2005

平成１７年度

金沢医科大学

共同研究成果報告書
奨励研究成果報告書

平成19年12月

金沢医科大学

はじめに

平成17年度金沢医科大学共同研究・奨励研究の成果報告書を発刊しましたのでお手元にお届けいたします。

本学では、平成15年度から若手研究者の育成を目的とした奨励研究や、学部、大学院、総合医学研究所、他大学等との有機的連携を目指す共同研究を展開することで本学研究の活性化を進めており、平成16年度までに共同研究に4研究課題、奨励研究に18研究課題を選定しております。また、平成17年度からは、奨励研究に萌芽的研究の枠を設けるなど研究の多様化にも対応しています。

本書は、平成17年度に学内公募で申請があった共同研究13件、奨励研究44件のうち、それぞれ5件、16件が採択された研究の成果をまとめたものであります。

今後、これらの共同研究と奨励研究を中心に学術研究がさらに発展し、本学の研究基盤が充実することを期待します。

最後に、本報告書の取りまとめの労をとられた研究推進評価委員会、研究助成センター事務課並びに関係各位に感謝します。

平成19年12月

金沢医科大学
学長　山田　裕一

目　　次

平成17年度
共同研究成果報告書

１．研究課題名：循環ショックの病態生理の解明と治療法の共同開発（研究番号　C2005-1）

２．キーワード：１）循環ショック（circulatory shock）
２）虚血再灌流（ischemia reperfusion）
３）肺水腫（pulmonary edema）
４）肝循環（hepatic circulation）
５）冠循環（coronary circulation）

３．研究代表者：芝本　利重・医学部・教　授・生理機能制御学　（生理学Ⅱ）
研究分担者：土田　英昭・医学部・教　授・侵襲制御学　（麻酔学）
佐久間　勉・医学部・教　授・呼吸機能治療学　（呼吸器外科）
久保　恵嗣・信州大学・医学部・教　授・内科学第一講座
倉田　康孝・医学部・助教授・生理機能制御学　（生理学Ⅱ）

４．研 究 目 的

循環ショックの病態は単に血圧低下にとどまらず、組織の微小循環障害から機能障害に発展する複雑な全身反応である。血行力学的に心原性ショックと非心原性ショックに大別され、前者は心臓ポンプ機能の失調による。一方、非心原性ショックの血圧低下とその臓器循環・機能障害の機序については十分には解明されてない。しかしながら、これらのショックに共通した病態として微小循環障害と虚血再灌流障害、それに基づく炎症反応としてのサイトカインをはじめとした mediator が病態形成に関わり多臓器不全を惹起し、肝臓では肝不全、肺では透過性亢進型肺水種である ARDS、心臓では冠不全、心不全にいたるものと考えられる。本研究の目的は心原性、出血性、アナフィラキシィー、敗血症による循環ショックの血圧低下機序とそれによる臓器循環障害の病態生理を肝循環、肺循環、冠循環に注目して whole animal、臓器、細胞、遺伝子レベルからの多面的アプローチにより明らかにすることである。

５．研 究 計 画

① ウサギとマウスで肺循環・門脈循環を in vivo でのモニター可能なモデルを作成し、血圧低下におけるそれらの役割を検討する（芝本,土田担当)。
② ラットとモルモットの摘出灌流肝において肝微小血管圧測定の micropuncture 法を確立し、血管閉塞法による微小血管圧と比較検討する。さらに micropuncture 法を in vivo 状態でも実施可能の系を確立し、エンドトキシンおよびアナフィラキシィー低血圧時に応用し､in vivo での肝微小循環の挙動を解明する(芝本担当)。
③ 麻酔下緬羊でアナフィラキシーショックを惹起し、ショック時の肝循環・肺循環動態を観察し、その役割を明らかにする（久保担当)。
④ 敗血症ラットの腸間膜細動脈を取りだして摘出灌流標本を作成し、各種血管収縮薬に対する反応の変化、内皮細胞の役割について検討する（土田担当)。
⑤ 急性膵炎ラットモデルで肺胞上皮細胞の Na^+と Cl^- channel, Na pump, β 受容体間のシグナル伝達を研究する（佐久間担当)。

⑥ ラット虚血再潅流肺傷害で肺胞上皮細胞の Na^+と Cl^- channel, Na pump, β 受容体間のシグナル伝達を研究する（佐久間担当）。

⑦ ヒト心室筋モデルの分岐構造解析によるバイオペースメーカーシステム設計原理の解明とその不整脈遺伝子治療への適用方法の検討（倉田担当）。

⑧ 致死的不整脈・心原性ショックの新しい予防・治療法としてのマウスおよびヒトＥＳ細胞由来ペースメーカー細胞システム設計（倉田担当）。

６．研 究 成 果　　（各項目末尾の番号は研究発表論文の番号である）

1. マウス肝血管アナフィラキシー解明の前段階としてその肝血管の特性とアナフィラキシーショックと心原性ショック時放出されるヒスタミンとノルエピネフリンの作用を明らかにした *(No. 1)*。
2. マウス肝臓の虚血再灌流障害における肝類洞圧の変化をマウス摘出灌流肝臓を確立して明らかにした *(No. 10)*。
3. マウス肝血管が血小板活性化因子に対する反応は弱く、さらに一酸化窒素に修飾されないことをラットとモルモットの肝血管反応と比較して示した *(No. 13)*。
4. マウスのアナフィラキシィーショックモデルを新規に確立し、血圧低下の機序を検討した。一酸化窒素は soluble guanylate cyclase 系を介さずに血圧低下に関与することを解明した *(No. 14)* 。
5. ウサギのアナフィラキシィーショックにおける肝血管収縮の有無と肝血管収縮部位について in vivo および ex vivo のウサギアナフィラキシーモデルを新規に確立して解明した *(No. 12)* 。
6. ラットのアナフィラキシィーショックにおける肝血管収縮の役割を肝摘除かつ腹腔血流遮断処置を施したラットと正常ラットと比較検討して解明した *(No. 2)* 。
7. アナフィラキシーショック時に肝臓の酸素消費量が減少する機序についてラット摘出灌流肝のアナフィラキシーモデルを作成して検討した。その結果、アナフィラキシー反応自体で酸素消費量が減少することを肝酸素消費量測定システムを新規に確立して明らかにした *(No. 6)*。
8. アナフィラキシー化学伝達物質である血小板活性化因子、トロンボキサン、ロイコトリエンのラット肝血管への作用を収縮部位、酸素消費量、胆汁産生量、肝内血液量について解明した *(No. 7)*。
9. ラット肝アナフィラキシーの一酸化窒素の役割を灌流血液との関係で明らかにした *(No. 8, 9)*。
10. モルモットのアナフィラキシィー肝血管収縮における化学伝達物質についてヒスタミン、プロスタグランジン、血小板活性化因子(PAF)とロイコトリエン(LT)の関与をそれぞれの受容体阻害剤を用いて検討し、PAF と LT がそれぞれ前類洞と後類洞収縮に関与していることを解明にした *(No. 4)*。
11. 選択的β_1-, β_2-交感神経刺激薬は肺胞水分クリアランスを亢進し，肺水腫の治療薬として有用な薬剤であることを明らかにした *(No. 5)*。
12. β_1-交感神経刺激薬は肺胞水分クリアランスを亢進するが，その機序に cystic fibrosis transmembrane conductance regulator が関与していることを明らかに

した *(No. 15)*。

13. ラットの肺動脈を慢性的に閉塞することにより肺胞水分クリアランスが亢進するを明らかにした *(No. 16)*。
14. ヒト心室筋細胞の分岐構造を解析して、内向き整流 K^+チャネル電流の抑制によりヒト心室筋に自動能が生じ得ること、また、その発現機構は本質的に洞結節の生理的自動能と同じであることを明らかにした。さらに、自動能発現における各イオンチャネル電流の役割を解明することにより、分岐構造解析が不整脈発生機序の統一的理解と記述、合理的な不整脈制御方法の開発（バイオペースメーカーシステム設計など）において有用（必要不可欠）であることを証明した。*(No. 3)*。
15. ヒト心室筋細胞由来バイオペースメーカー細胞の作成及び構造安定性強化のための最適システム修飾方法（各種ペースメーカー電流導入の効果）を検証し、過分極活性化陽イオンチャネル電流の導入がペースメーカー活性の発現を促進すること、構造安定性の強化には持続性内向き電流の導入が最も有効であることを明らかにした *(No. 11)*。

７．研究の考察・反省

各研究課題において当初に計画された多くのものは達成されたと考える。しかし、実験は終了しているにもかかわらず論文にまとめる作業が遅れているものもある。全体としては活発な研究活動が行われたものと考える。

８．研 究 発 表

1) Shibamoto T, Cui S, Ruan Z, Kurata Y. Effects of norepinephrine and histamine on vascular resistance in isolated perfused mouse liver. Jpn J Physiol 2005; 55: 143-148. (MLDB)

2) Shibamoto T, Cui S, Ruan Z, Liu W, Takano H, Kurata Y. Hepatic venoconstriction is involved in anaphylactic hypotension in rats. Am J Physiol Heart Circ Physiol 2005; 89: H1436-H1444. (MLDB)

3) Kurata Y, Hisatome I, Matsuda H, Shibamoto T. Dynamical mechanisms of pacemaker generation in IK1-downregulated human ventricular myocytes: Insights from bifurcation analyses of a mathematical model. Biophys J 2005; 89: 2865-2887. (MLDB)

4) Shibamoto T, Ruan Z, Cui S, Liu W, Kurata Y. Involvement of platelet-activating factor and leukotrienes in anaphylactic segmental venoconstriction in ovalbumin sensitized guinea pig livers. Prostaglandins Other Lipid Mediator 2005; 78: 218-230. (MLDB)

5) Sakuma T, Wang Z, Xu J, Maeda S, Sugita M, Sagawa M. Beta-adrenergic agonist

therapy for alveolar edema in postoperative pulmonary complications. J Kanazawa Med Univ 2005; 30: 6-11.

6) Cui S, Shibamoto T, Ruan Z, Takano H, Liu W, Kurata Y. Oxygen consumption, assessed with the oxygen absorption spectrophotometer, decreases during hepatic anaphylaxis in perfused rat liver. Shock 2006; 26: 62-68. (MLDB)

7) Cui S, Shibamoto T, Liu W, Takano H, Kurata Y. Effects of platelet-activating factor, thromboxane A_2 and leukotriene D_4 on isolated perfused rat liver. Prostaglandins Other Lipid Mediators 2006; 80: 35-45. (MLDB)

8) Shibamoto T, Ishibashi T, Shimo T, Cui S, Takano H, Tsuchida H, Nishio M, Kurata Y. N^G-nitro-L-arginine methyl ester potentiates anaphylactic venoconstriction in rat perfused livers. Clin Exp Pharmacol Physiol 2006; 33: 1073-1077. (MLDB)

9) Cui S, Shibamoto T, Liu W, Takano H, Z-S Zhao, Kurata Y. Effects of Hct on L-NAME-induced potentiation of anaphylactic presinusoidal constriction in perfused rat livers. J Cardiovasc Pharmacol 2006; 48: 827-833. (MLDB)

10) Shibamoto T, Ruan Z, Cui S, Liu W, Zhao Z-S, Koizumi T, Kubo K, Takano H, Kurata Y. The sinusoidal pressure during ischemia-reperfusion injury in perfused mouse liver pretreated with or without L-NAME. J Surg Res 2007; 139: 30-35. (MLDB)

11) Kurata Y, Matsuda H, Hisatome I, Shibamoto T. Effects of pacemaker currents on creation and modulation of human ventricular pacemaker: theoretical study with application to biological pacemaker engineering. Am J Physiol Heart Circ Physiol 2007; 292: H701-H718. (MLDB)

12) Karasawa N, Shibamoto T, Cui S, Takano H, Kurata Y, Tsuchida H. Hepatic pre-sinusoidal vessels contract in anaphylactic hypotension in rabbits. Acta Physiol (Oxf) 2007; 189: 15-22. (MLDB)

13) Cui S, Shibamoto T, Zhao ZS, Takano H, Kurata Y. L-NAME augments PAF-induced venoconstriction in isolated perfused livers of rat and guinea pig, but not mouse. Prostaglandins Leukotrienes Essential Fatty Acids 2007; 76: 277-283. (MLDB)

14) Takano H, Liu W, Zhao ZS, Cui S, Zhang W, Shibamoto T. N^G-Nitro-L-arginine

methyl ester, but not methylene blue, attenuates hypotension in anesthetized mice. J Pharmacol Sci 2007; 104: 212-217. (MLDB)

15) Gu X, Wang Z, Xu J, Maeda S, Sugita M, Sagawa M, Toga H, Sakuma T. Denopamine stimulates alveolar fluid clearance via cystic fibrosis transmembrane conductance regulator in rat lungs. Respirology 2006; 11: 566-571. (MLDB)

16) Wang Z, Xu J, Ma G, Sagawa M, Shimazaki M, Ueda Y, Sakuma T. Chronic pulmonary artery occlusion increases alveolar fluid clearance in rats. J Thorac Cardiovasc Surg 2007; 134: 1213-1219. (MLDB)

Short Communication

Japanese Journal of Physiology Vol. **55**, 143–148, 2005

Effects of Norepinephrine and Histamine on Vascular Resistance in Isolated Perfused Mouse Liver

Toshishige SHIBAMOTO, Sen CUI, Zonghai RUAN, and Yasutaka KURATA

Department of Physiology, Kanazawa Medical University, Uchinada Ishikawa, 920-0293 Japan

Abstract: Mice have frequently been used for a variety of physiological studies because of the development of genetic engineering. However, the characteristics of hepatic vessels such as the vascular resistance distribution and the reactivity to various vasoconstrictors are not known in mice. We therefore determined the basal levels of segmental vascular resistances and the effects of histamine and norepinephrine on the vascular resistance distribution of mice. The liver of male non-inbred ddY mice was excised and perfused via the portal vein with 5% bovine albumin-Krebs solution at a constant flow rate. The sinusoidal pressure was measured by the double occlusion pressure and used to determine the presinusoidal (R_{pre}) and postsinusoidal (R_{post}) resistances. The basal R_{post} comprised 53 ± 1% of the total hepatic vascular resistance. The norepinephrine and histamine increased R_{pre} in a greater magnitude than R_{post} with liver weight loss. However, the response to histamine was weaker than that to norepinephrine. Moreover, histamine-induced vasoconstriction showed tachyphylaxis. In conclusion, the presinusoidal and postsinusoidal resistances of mouse livers were similar in magnitude. The presinusoidal vessels predominantly contract in response to norepinephrine and histamine in mouse livers. [The Japanese Journal of Physiology 55: 143–148, 2005]

Key words: double occlusion pressure, isolated perfused mouse liver, sinusoidal pressure.

The passive blood mobilization to and from the liver, which influences the venous return to the heart, is critically dependent on the location and magnitude of intrahepatic vascular resistances in relation to the compliances [1]. There are species differences in the distribution of the hepatic vascular resistance. In canine livers, the presinusoidal resistance comprises approximately 50% of the total liver vascular resistance [2], but it comprises 56% and 59% in guinea pig [3] and rabbit livers [4–6], respectively, and more than 60% in rat livers [7, 8]. However, the basal hepatic vascular resistance distribution of mouse livers is not known, although mouse has been frequently used in physiological studies because of the development of genetic engineering.

Species differences are also found in the primary site of hepatic vasoconstriction. By using the vascular occlusion methods for measurement of the hepatic sinusoidal pressure [2, 9], we have recently shown that the hepatic longitudinal vascular responsiveness to vasoactive substances differs among different species, such as dogs, rabbits, rats, and guinea pigs [4–6, 9–11]. Histamine predominantly contracts the postsinusoidal veins with resultant hepatic congestion in dogs [9, 10] and guinea pigs [11], but this substance constricts presinusoidal vessels in rabbits [4]. In rat livers, histamine did not contract or dilate hepatic vessels [11]. On the other hand, norepinephrine predominantly contracts the presinusoidal veins over the postsinusoidal veins in dogs, rabbits, rats, and guinea pigs [4, 7, 9, 11]. However, the effects of these vasoconstrictors have not been determined on hepatic vascular resistance distribution in mice. Furthermore, norepinephrine is released during the critical circumstances of sympathoexcitation, such as hemorrhagic shock, but histamine could be released during liver transplantation and systemic anaphylaxis and thereby cause a disturbance of hepatic circulation [12].

Therefore we have herein established the isolated perfused mouse liver preparation, which permits the measurement of hepatic vascular pressures, including sinusoidal pressure and liver weight. We determined the basal hepatic vascular resistance distribution and the effects of histamine and norepinephrine on segmental vascular resistances in mouse livers.

Received on Feb 14, 2005; accepted on Apr 28, 2005; released online on Apr 29, 2005; DOI: 10.2170/jjphysiol.S642
Correspondence should be addressed to: Toshishige Shibamoto, Department of Physiology, Kanazawa Medical University, Uchinada Ishikawa 920-0293, Japan. Phone: +81-76-218-8104, Fax: +81-76-286-8010, E-mail: shibamo@kanazawa-med.ac.jp

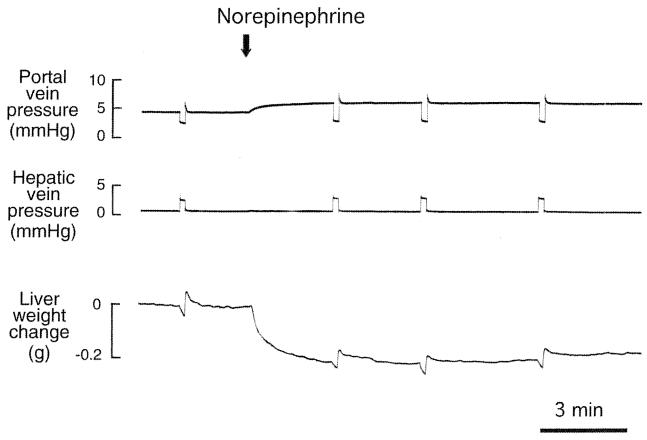

Fig. 1. A representative recording of the response to norepinephrine at 10 μM.

Methods

The study protocol was approved by the Animal Research Committee of Kanazawa Medical University in Uchinada, Japan. Thirty-two male specific-pathogen-free outbred ddY mice (43 ± 0.5 [SE] g; SLC Co., Hamamatsu, Japan), one of the most popular mouse strains in Japan, were anesthetized with pentobarbital sodium (50 mg/kg, ip) and mechanically ventilated with room air. After laparotomy, the bile duct was cut and the hepatic artery was ligated. At 5 min after an injection of heparin (500 mU/g) into the intraabdominal inferior vena cava (IVC), the IVC above the renal veins was ligated, and the portal vein was cannulated with a stainless cannula (OD 1.2 mm, ID 1.0 mm) for portal perfusion. After thoracotomy, the supradiaphragmatic IVC was cannulated through a right atrial incision with the same size stainless cannula, and portal perfusion was then begun with 5% albumin-Krebs buffer. The liver was rapidly excised, then suspended from an electric balance and weighed.

The basic method for liver perfusion was described previously [4], but each apparatus was the minimum size. The liver was perfused at a constant flow rate in a recirculating manner via the portal vein with the albumin-Krebs buffer that was pumped by a Masterflex pump from the venous reservoir through a heat exchanger (37°C). The recirculating blood volume was 30 ml. The height of the reservoir and the perfusate flow rate could be adjusted independently to maintain the portal and hepatic venous pressures at any desired level. The perfusate was oxygenated in the reservoir by continuous bubbling with 95% O_2 and 5% CO_2. We measured the portal venous (P_{pv}) and the hepatic venous (P_{hv}) pressures with pressure transducers connected to the corresponding side arm with the reference points at the hepatic hilus. To measure the double occlusion pressure (P_{do}), we placed two solenoid valves around the perfusion tubes upstream from the P_{pv} sidearm cannula and downstream from the P_{hv} sidearm cannula [4]. The perfusate flow rate (Q) was measured manually by collecting outflow perfusate for 1 min just before the baseline measurement. The same measurement was done at the end of the experiment to confirm the constancy of perfusate flow during the experimental period. The hepatic vascular pressures and liver weight (Wt) were monitored continuously and displayed through a thermal physiograph.

Hepatic hemodynamic parameters were observed for at least 20 min after the start of perfusion, during which an isogravimetric (no liver weight gain or loss) state was reached. After the baseline measurements, the perfused livers were challenged with either histamine (Sigma) or norepinephrine (Bitartrate salt, Sigma). They were injected as a bolus into the reservoir to attain the final perfusate concentration of 0.001–30 μM and 1–1,000 μM, respectively. The volume of each injected agent was adjusted to less than 0.5 ml.

The hepatic sinusoidal pressure was measured by the double occlusion method [2]. The inflow and outflow lines were simultaneously and instantaneously occluded with the solenoid valves, after which P_{pv} and P_{hv} rapidly equilibrated to a similar or identical pressure, which was P_{do}. In each experimental group, P_{do} was measured at baseline and maximal vasoconstriction.

The total portal-hepatic venous (R_t), presinusoidal (R_{pre}), and postsinusoidal (R_{post}) resistances were calculated as follows:

$$R_t = (P_{pv} - P_{hv})/Q \quad (1)$$

$$R_{pre} = (P_{pv} - P_{do})/Q \quad (2)$$

$$R_{post} = (P_{do} - P_{hv})/Q \quad (3)$$

All results are expressed as the mean ± SEM. The comparisons were made with Student's t-tests. A p value of less than 0.05 was considered significant.

Results

The final wet liver weight measured immediately after experiments was 1.91 ± 0.02 g. The P_{do} at the baseline states of 32 perfused mouse livers was 2.3 ± 0.1 mmHg, with P_{pv} 4.0 ± 0.1 mmHg and P_{hv} 0.5± 0.05 mmHg at Q 2.3 ± 0.05 ml/min/g liver wt. The calculated R_t was 1.55 ± 0.04 mmHg/ml/min/g liver wt. The segmental vascular resistances of R_{pre} and R_{post} were 0.74 ± 0.03 and 0.81 ± 0.02 mmHg/ml/min/g liver wt, respectively, and the R_{post}/R_t ratio was 0.53 ± 0.01. This indicates that 53% of the total portal-hepatic venous resistance of the isolated mouse livers exists in the postsinusoids.

Norepinephrine and histamine produced qualitatively the same responses: P_{pv} increased substantially, but

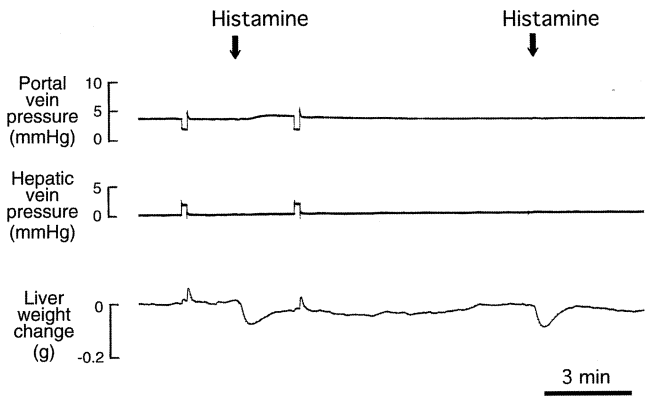

Fig. 2. Representative recordings of the responses to histamine at 1 mM. The second arrow indicates the injection of the same dose as the initial injection.

P_{do} either did not change or increased only minimally, with liver weight loss, as shown in Figs. 1 and 2. In livers treated with either norepinephrine or histamine, the P_{pv}-to-P_{do} gradient increased in a greater magnitude than the P_{do}-to-P_{hv} gradient, a finding indicating that R_{pre} was predominantly increased over R_{post}. However, the response to histamine was weaker than that to norepinephrine. Moreover, histamine-induced vasoconstriction showed tachyphylaxis (Fig. 2). Figure 3 shows the peak levels in R_{pre}, R_{post}, R_t, and Wt changes after injections of norepinephrine and histamine. R_t increased in a dose-dependent manner at 0.001–30 μM norepinephrine, reaching the maximum level of 151 ± 3% of baseline at 30 μM. This increase in R_t at 30 μM was mainly due to an increase in R_{pre} because the maximum levels of R_{pre} was 193 ± 3% of the baseline, and the corresponding levels of R_{post} was only 117 ± 3% of the baseline, as shown in Fig. 3. Histamine did not cause venoconstriction until the concentration increased to 100 μM, as shown in Fig. 3. Even at 1,000 μM histamine, R_{pre} inceased to only 145 ± 9% of the baseline, whereas R_{post} did not change significantly. Immediately after norepinephrine or histamine, the liver weight decreased and then gradually returned to the baseline. The maximal liver weight losses after injections of norepinephrine at 30 μM and histamine at 1,000 μM were approximately 0.15 and 0.03 g/g liver wt, respectively.

Discussion

There is a species difference in the distribution of segmental vascular resistances in the livers of animals, including dogs, rabbits, guinea pigs, and rats. We have recently shown by measuring the sinusoidal pressure, using the triple vascular occlusion method [9] and the double occlusion method [2], in isolated canine livers that R_{post} comprises approximately half of R_t. In contrast, R_{pre} in the other animals is greater in magnitude than R_{post}. Actually, we subsequently demonstrated that 59% of R_t exists in presinusoidal vessels in isolated rabbit livers [4, 5]. This agrees with the study of Maass-Moreno and Rothe [13], who reported that in intact rabbit livers the pressure gradient from the hepatic sinusoids averaged 59% of the total P_{pv} to the abdominal vena caval pressure gradient. Similar segmental vascular resistance distribution was found in guinea pig livers, in which R_{pre} comprises 61% of R_t [3, 11]. The rat livers show more marked predominance of R_{pre} over R_{post}; R_{pre} is 69% of R_t [11]. In the present study, for the first time we reported that the basal vascular resistance distribution of mouse livers was similar to that of canine livers because R_{pre} comprises 47% of R_t.

Species differences are also found in the hepatic vascular responsiveness to vasoactive substances. With respect to responses to histamine, this substance predominantly contracts the postsinusoidal vessels in dogs [9, 10, 14, 15] and guinea pigs [11]. On the other hand, in rabbit livers, histamine selectively increases R_{pre} in isolated-perfused liver [4], and this vasoactive amine also significantly increases R_{post} in in vivo preparations [19]. In contrast, histamine did not contract the hepatic vessels in rat livers [11, 16–18]. In the present study we showed that histamine selectively contracts the presinusoidal vessels of mouse livers, a finding similar to the results of studies on rabbit livers. The difference in the vasoconstrictive site for histamine might be ascribed, at least in part, to the different distribution of functionally active receptors between the presinusoidal vessels and the hepatic veins. The absence of vasoconstrictive responses to histamine in rat livers may be due to a lack of functional histamine receptors in rat hepatic vascular smooth muscles.

In the present study, the concentration of histamine required to produce significant hepatic vasoconstriction was 100 μM. The responsiveness of mouse hepatic vessels to histamine seems to be much weaker than to norepinephrine because the lower concentration of 0.1 μM norepinephrine can induce significant hepatic vasoconstriction, as shown in Fig. 3. Furthermore, 1,000 μM histamine increased R_t only to 1.2-fold baseline, whereas the 100 times lower concentration of 10 μM norepinephrine increased R_t to 1.4-fold baseline. A similar result was observed in isolated rabbit liver [4].

In contrast to histamine, norepinephrine predominantly contracts presinusoidal vessels over postsinusoidal vessels in dogs [7, 9], rabbits [4, 19], guinea pigs [11], and rats [11]. Actually, Rothe and colleagues, using the micropipette servonull pressure measurement technique, have recently demonstrated that the increase in the presinusoidal resistance is greater than in the postsinusoidal resistance in dogs [7], rats [7], and rabbits [19] during norepinephrine infusion. We added

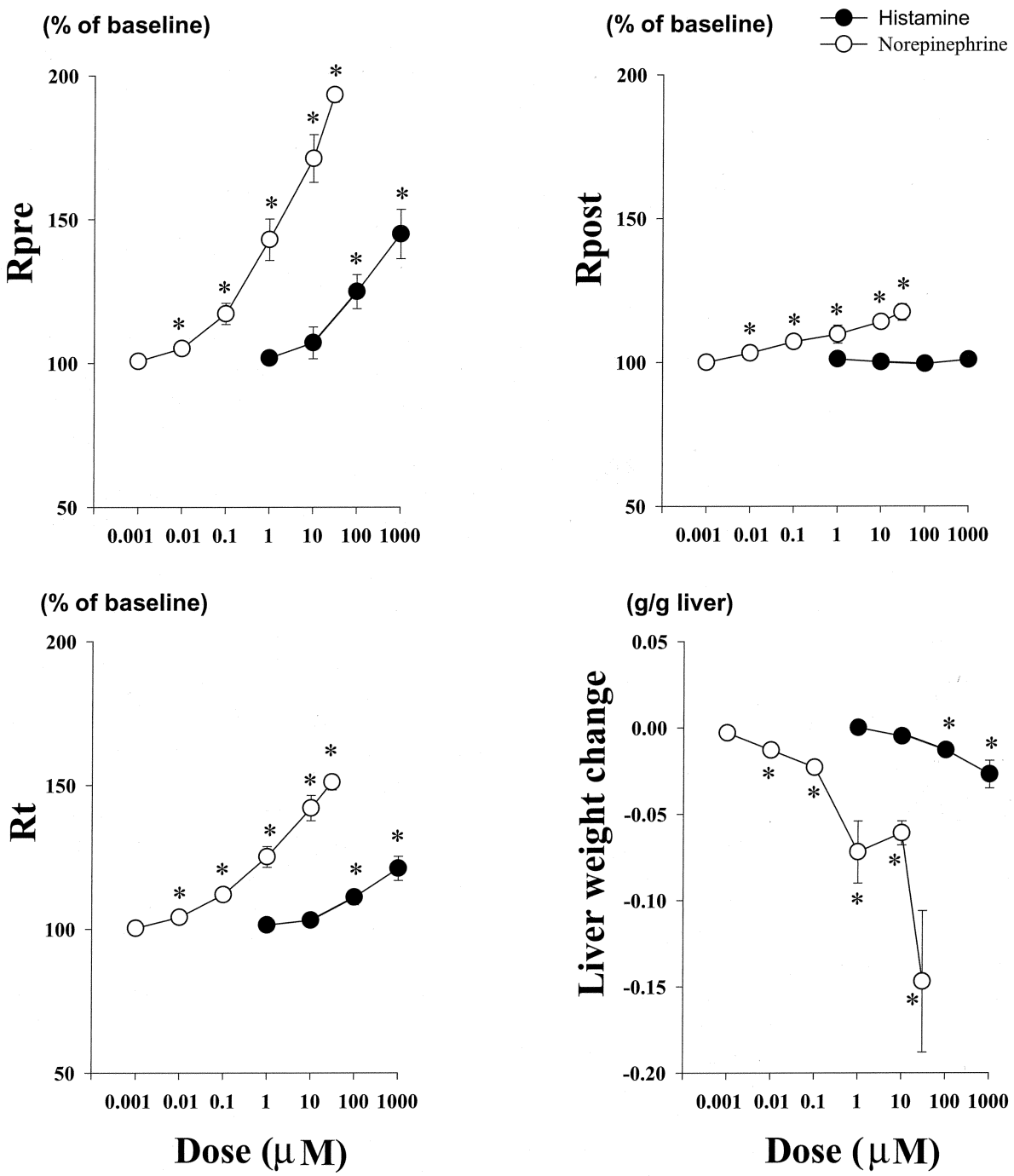

Fig. 3. The peak changes in the presinusoidal (R_{pre}) and postsinusoidal (R_{post}) resistances and total resistance (R_t) and the liver weight changes at 0.001–30 μM of norepinephrine (open circles) and at 1–1,000 μM of histamine (closed circles), as expressed by the percentage of the baseline in mouse livers. The values are given as mean ± SEM. n = 5–7. *$P < 0.05$ vs. the baseline.

new evidence that a similar response to norepinephrine was observed in isolated mouse livers. It is well known that norepinephrine causes a reduction in liver blood volume in cats [20], dogs [9, 21], rabbits [4, 19], guinea pigs [11], and rats [11]. In this respect, the present study showed that mouse livers also respond to norepinephrine with a reduction of liver weight, suggesting a decrease in liver blood volume. These findings suggest that norepinephrine, a mediator of the sympathetic nervous system, causes predominant presinusoidal constriction with a resultant decrease in liver blood volume beyond the species differences. The physiological significance of this finding is that the primitive response to life-threatening insults, which cause sympathoexcitation, may be similar among animals. In this respect, histamine, a mediator released from mast cells

in response to allergy or anaphylaxis, does not seem to be essential to life; therefore the hepatic responses may differ among animals.

In the present study, a decrease in *Wt* accompanied predominant presinusoidal vessel constriction, when norepinephrine or histamine was injected into mouse livers. The mechanism for this decrease cannot be currently clarified. However, it may be related to possible heterogeneous portal venule constriction. If heterogeneity existed in portal venule constriction among the hepatic lobules, that is, some vessels were closed and others open, the blood volume of sinusoids that was distal to the closed portal venules could be passively reduced because of a decrease in the distending pressure of the sinusoids. In contrast to this passive change in liver volume, another possibility exists that contractile elements exist in the walls of the hepatic sinusoids that may be stimulated by norepinephrine as well as endothelin [22–24]. Rothe and Maass-Moreno [24] infused norepinephrine into in vivo rabbit and found a decrease in liver volume, even though P_{pv} and hepatic venule pressure increased. This is clear proof of an active response and not a passive response to distending pressure.

As shown in Fig. 2, in response to the second bolus injection of histamine at 1 mM, hepatic venoconstriction was not observed, but the liver weight transiently decreased. The mechanism for this venoconstriction-independent decrease is unknown. We assumed that high osmolarity resulting from a bolus injection of 1 mM histamine might account for the decrease in liver weight: The hyperosmotic solution with 1 mM histamine might have caused osmosis and liver cell volume shrinkage, resulting in transient liver weight loss. Since the presence of structural pores of the sinusoidal endothelium enables free and rapid movement of drug and water molecules between the intravascular spaces and Disse's spaces, it is expected that an intravascular hyperosmolarity could easily cause osmosis at hepatocytes and at sinusoidal endothelial cells. Water derived from these cells might rapidly diffuse into the intravascular space through the endothelial pores and might be carried away extrahepatically via the blood stream. Indeed, we observed that a bolus injection of the solution with nonvasoactive sucrose at 1 mM, the volume and osmolarity of which are the same as those of the histamine solution, caused venoconstriction-independent liver weight loss in isolated perfused liver (data not shown).

There are limitations of the methods used in the present study. First, the livers were perfused via only the portal vein because of the technical difficulty to perfuse the hepatic artery. With the hepatic artery occluded, no clues were provided for the sensitivity of the hepatic arterioles to histamine and norepinephrine. Second, the livers were perfused with 5% bovine albumin-Krebs solution, but not with blood. There is a possibility that the oxygen sensitivity of the most metabolically active tissue may be limited. However, we confirmed previously that the bubbling with 95% oxygen of the albumin-Krebs perfusate produced the inflow perfusate PO_2, 300 mmHg [5]. We believe that the delivery of oxygen to the liver was adequate.

In conclusion, by measuring the hepatic sinusoidal pressure with the double occlusion method, we determined the basal vascular resistance distribution and the effects of histamine and norepinephrine on the segmental vascular resistances in isolated mouse livers perfused with blood-free albumin Krebs buffer. The presinusoidal and postsinusoidal resistances of mouse livers were similar in magnitude. In response to norepinephrine and histamine, presinusoidal vessels predominantly contract with a resultant decrease in hepatic vascular volume in mouse livers.

This work was supported by a Grant for Collaborative Research from Kanazawa Medical University (C2003-1, C2004-1, C2005-1) and a Grant-in-Aid for Scientific Research from the Ministry of Education, Culture, Sports, Sciences and Technology of Japan (No. 15591665).

REFERENCES

1. Maass-Moreno R and Rothe CF: Nonlinear resistances in hepatic microcirculation. Am J Physiol 269: H1922–H1930, 1995
2. Yamaguchi Y, Shibamoto T, Hayashi T, Saeki Y, and Tanaka S: Hepatic vascular response to anaphylaxis in isolated canine liver. Am J Physiol 267: R268–R274, 1994
3. Ruan Z, Shibamoto T, Shimo T, Tsuchida H, Koizumi T, and Nishio M: NO but not CO, attenuates anaphylaxis-induced postsinusoidal contraction and congestion in guinea pig liver. Am J Physiol Regul Integr Comp Physiol 286: R94–R100, 2004
4. Shibamoto T, Wang HG, Miyahara T, Tanaka S, Haniu H, and Koyama S: Presinusoidal vessels predominantly contract in response to norepinephrine, histamine, and KCl in rabbit liver. J Appl Physiol 87: 1404–1412, 1999
5. Wang HG, Shibamoto T, and Miyahara T: Endothelin-1 selectively contracts portal vein through ETA- and ETB-receptors in isolated rabbit liver. Am J Physiol 273: G1036–G1043, 1997
6. Wang HG, Shibamoto T, and Koyama S: The effect of platelet-activating factor on hepatic capillary pressure in isolated dog liver. Prostaglandins Leukot Essent Fatty Acids 57: 293–298, 1997
7. Bohlen HG, Maass-Moreno R, and Rothe CF: Hepatic venular pressures of rats, dogs, and rabbits. Am J Physiol 261: G539–G547, 1991
8. Ling YQ, Shibamoto T, Honda T, Kamikado C, Hironaka E, Hongo M, and Koyama S: Increased sinusoidal

pressure is associated with early liver weight gain in ischemia-reperfusion injury in isolated perfused rat liver. J Surg Res 88: 70–77, 2000
9. Shibamoto T, Wang HG, Tanaka S, and Koyama S: Hepatic capillary pressure is estimated using triple vascular occlusion method in isolated canine liver. Am J Physiol 271: R1130–R1141, 1996
10. Urayama H, Shibamoto T, Wang HG, and Koyama S: Thromboxane A_2 analogue contracts predominantly the hepatic veins in isolated canine liver. Prostaglandins 52: 483–495, 1996
11. Shibamoto T, Narushima M, Ling YQ, Shimo T, Tsuchida H, Kurata Y, and Ogura T: Different hepatic vascular response to noradrenaline and histamine between guinea pig and rat. Acta Physiol Scand 18: 255–263, 2004
12. Hansen CP, Man WK, Kirkegaad P, Jensen SL and Boesby S: Changes in plasma histamine during orthotopic liver transplantation in the pig. Agents Actions 23: 348–350, 1988
13. Maass-Moreno R and Rothe CF: Distribution of pressure gradients along hepatic vasculature. Am J Physiol 272: H2826–H2832, 1997
14. Lautt WW and Legare DJ: Effect of histamine, norepinephrine, and nerves on vascular pressures in dog liver. Am J Physiol 252: G472–G478, 1987
15. Mafhouz M and Geumei A: Pharmacodynamic of intrahepatic circulation in shock. Surgery 61, 755–762, 1967
16. Noguchi Y and Plaa GL: Effect of acetylcholine, serotonin and histamine on the hemodynamics on the isolated perfused rat liver. Arch int Pharmacodyn 188: 312–319, 1977
17. Cohen ML and Wiley KS: Comparison of arteries with longitudinal and circular venous muscle from the rat. Am J Physiol 232: H131–H139, 1977
18. Hogestatt ED, Hammarstrom LE, Andersson KE, and Holmin T: Contractile effects of various vasoactive agents in small rat portal veins and hepatic arteries and the influence of sympathetic denervation on the noradrenaline response. Acta Physiol Scand 128: 309–315, 1986
19. Rothe CF and Maass-Moreno R: Hepatic venular resistance responses to norepinephrine, isoproterenol, adenosine, histamine, and ACh in rabbits. Am J Physiol 274: H777–H785, 1998
20. Greenway CV and Lautt WW: Effects of infusions of catecholamines, angiotensin, vasopressin and histamine on hepatic blood volume in the anesthetized cat. Br J Pharmacol 44: 177–184, 1972
21. Bennett TD, Macanespie CL, and Rothe CF: Active hepatic capacitance responses to neural and humoral stimuli in dogs. Am J Physiol 242: H1000–H1009, 1982
22. Ito Y, Katori M, Majima M, and Kakita A: Constriction of mouse hepatic venules and sinusoids by endothelins through ETb receptor subtype. Int J Microcirc Clin Exp 16: 250–258, 1996
23. Kawada N, Tran-Thi T, Klein H, and Decker K: The contraction of hepatic stellate (Ito) cells stimulated with vasoactive substances. Possible involvement of endothelin 1 and nitric oxide in the regulation of the sinusoidal tonus. Eur J Biochem 213: 815–823, 1993
24. Rothe CF and Maass-Moreno R: Active and passive liver microvascular responses from angiotensin, endothelin, norepinephrine, and vasopressin. Am J Physiol 279: H1147–H1156, 2000

Am J Physiol Heart Circ Physiol 289: H1436–H1444, 2005.
First published May 27, 2005; doi:10.1152/ajpheart.00368.2005.

Hepatic venoconstriction is involved in anaphylactic hypotension in rats

Toshishige Shibamoto, Sen Cui, Zonghai Ruan, Wei Liu, Hiromichi Takano, and Yasutaka Kurata
Department of Physiology, Kanazawa Medical University, Uchinada Ishikawa 920-0293, Japan

Submitted 14 April 2005; accepted in final form 20 May 2005

Shibamoto, Toshishige, Sen Cui, Zonghai Ruan, Wei Liu, Hiromichi Takano, and Yasutaka Kurata. Hepatic venoconstriction is involved in anaphylactic hypotension in rats. *Am J Physiol Heart Circ Physiol* 289: H1436–H1444, 2005. First published May 27, 2005; doi:10.1152/ajpheart.00368.2005.—We determined the roles of liver and splanchnic vascular bed in anaphylactic hypotension in anesthetized rats and the effects of anaphylaxis on hepatic vascular resistances and liver weight in isolated perfused rat livers. In anesthetized rats sensitized with ovalbumin (1 mg), an intravenous injection of 0.6 mg ovalbumin caused not only a decrease in systemic arterial pressure from 120 ± 9 to 43 ± 10 mmHg but also an increase in portal venous pressure that persisted for 20 min after the antigen injection (the portal hypertension phase). The elimination of the splanchnic vascular beds, by the occlusions of the celiac and mesenteric arteries, combined with total hepatectomy attenuated anaphylactic hypotension during the portal hypertension phase. For the isolated perfused rat liver experiment, the livers derived from sensitized rats were hemoperfused via the portal vein at a constant flow. Using the double-occlusion technique to estimate the hepatic sinusoidal pressure, presinusoidal (R_{pre}) and postsinusoidal (R_{post}) resistances were calculated. An injection of antigen (0.015 mg) caused venoconstriction characterized by an almost selective increase in R_{pre} rather than R_{post} and liver weight loss. Taken together, these results suggest that liver and splanchnic vascular beds are involved in anaphylactic hypotension presumably because of anaphylactic presinusoidal contraction-induced portal hypertension, which induced splanchnic congestion resulting in a decrease in circulating blood volume and thus systemic arterial hypotension.

isolated perfused rat liver; anaphylaxis; hepatic circulation; portal hypertension; splanchnic congestion

ANAPHYLACTIC HYPOTENSION is primarily caused by alterations in the systemic circulation that decrease blood flow to the heart because left ventricular function is relatively well preserved during anaphylactic shock (4). Peripheral circulatory collapse is ascribed to hypovolemia, which results from a decrease in effective circulating blood volume. The latter could be because of vasodilation with the peripheral pooling and increased vascular permeability with a shift of intravascular fluid to the extravascular space (2).

In canine experimental models of anaphylactic shock, an increase in resistance to venous return is important in the pathogenesis of circulatory collapse (23); increased venous resistance decreases venous return with resultant decrease in stroke volume and systemic arterial pressure (P_{sa}). Indeed, eviscerated dogs did not develop anaphylactic shock (13). In addition, Enjeti et al. (5) reported that the severity of the anaphylactic shock could be decreased by occluding the descending aorta. In dogs, anaphylaxis-induced increase in venous resistance is partly caused by hepatic vasoconstriction, especially selective constriction of postsinusoidal hepatic veins in dogs (26). Indeed, anaphylaxis-induced hepatic venous constriction induces pooling of blood in liver itself, as well as in upstream splanchnic organs. However, in the rat, the roles of the splanchnic bed, and particularly the liver, are not known in the pathogenesis of anaphylactic hypotension, although, in the rat, portal venous pressure (P_{pv}) was increased during anaphylactic hypotension induced by ovalbumin (8). Thus the first purpose of the present study was to determine whether lesions of liver and splanchnic vascular bed contribute to anaphylactic hypotension in anesthetized rats. To resolve this question, P_{sa} changes were observed in sensitized rats with and without hepatic and splanchnic circulation after the antigen was intravenously administered.

In addition to canine livers (26), the guinea pig liver shows the anaphylactic response characterized by significant contraction of postsinusoidal vessel with resultant hepatic congestion (16). On the other hand, it is not known whether anaphylactic reaction in rats causes constriction of postsinusoidal hepatic veins, resulting in hepatic congestion, although anaphylactic venoconstriction is observed in isolated perfused livers of the sensitized rats (8). To clarify the anaphylactic disturbance of hepatic circulation, we herein established anaphylactic models of isolated portally perfused rat livers in which the sinusoidal pressure was measured by the double-occlusion method (20, 26). Thus the second purpose of the present study was to determine effects of anaphylaxis on hepatic vascular resistance distribution and liver weight in isolated perfused rat livers.

MATERIALS AND METHODS

Animals. Forty eight male Sprague-Dawley rats (Japan SLC, Shizuoka, Japan) weighing 372 ± 28 g were used in this study. Rats were maintained at 23°C under pathogen-free conditions on a 12:12-h dark-light cycle and allowed food and water ad libitum. The experiments conducted in the present study were approved by the Animal Research Committee of Kanazawa Medical University.

Sensitization. Rats were actively sensitized by the subcutaneous injection of an emulsion made by mixing equal volumes of complete Freund's adjuvant (0.5 ml) with 1 mg ovalbumin (grade V; Sigma) dissolved in physiological saline (0.5 ml). Nonsensitized rats were injected with complete Freund's adjuvant and ovalbumin-free saline. After injection (2 wk), the rats were used for the following in vivo or isolated perfused liver experiments.

In vivo experiment. After sensitization (2 wk), 35 rats were anesthetized with pentobarbital sodium (70 mg/kg ip) and placed on a thermostatically controlled heating pad (ATC-101B; Unique Medical) that maintained body temperature at 36–37°C throughout the experiment. The adequacy of anesthesia was monitored by the stability of blood pressure and respiration under control conditions and during a pinch of the hindpaw. Supplemental doses of anesthetic (10% of initial dose) were given as necessary. The left carotid artery was catheterized to measure P_{sa}. The right external jugular vein was

Address for reprint requests and other correspondence: T. Shibamoto, Dept. of Physiology, Kanazawa Medical Univ., Uchinada Ishikawa 920-0293, Japan (e-mail: shibamo@kanazawa-med.ac.jp).

The costs of publication of this article were defrayed in part by the payment of page charges. The article must therefore be hereby marked "*advertisement*" in accordance with 18 U.S.C. Section 1734 solely to indicate this fact.

catheterized, and the catheter tip was positioned at the confluence of the superior vena cava and the right atrium. This catheter was used for an intravenous injection of antigen and measurement of the central venous pressure (P_{cv}). Heart rate (HR) was measured by triggering the R wave of the electrocardiogram. The sensitized and nonsensitized animals were randomly divided into rats with gastrointestinal isolation and hepatectomy (GI-HptX) and intact rats. Thus the in vivo rats were randomly assigned to one of the following four groups: GI-HptX sensitized ($n = 11$), GI-HptX control ($n = 7$), intact sensitized ($n = 10$), and intact control ($n = 7$) groups. In the GI-HptX rats, through a 4-cm midline incision, ligation of the celiac artery and the mesenteric artery was followed by total hepatectomy, which consisted of resection of the median and left lateral lobe, the right lateral lobes, and the caudate lobes, as described by Gaub and Iversen (7). In the intact rats, after a midline incision, a catheter (0.47 mm ID, 0.67 mm OD) was inserted in the main portal vein without occlusion of the portal vein for continuous measurement of the P_{pv}. After closure of the abdomen, the baseline measurements were started.

The P_{sa}, P_{cv}, P_{pv}, and HR were continuously measured with pressure transducers (TP-400T; Nihon-Kohden) in the intact rats; P_{sa}, P_{cv}, and HR, but not P_{pv}, were measured in the GI-HptX rats. These pressures were continuously displayed on a thermal physiograph (RMP-6008; Nihon-Kohden). Outputs were also digitally recorded at 20 samples/s (PowerLab; ADInstruments). Hemodynamic parameters were observed for at least 20 min after surgery until a stable state was obtained. After the baseline measurements, 0.6 mg ovalbumin antigen was administered via the jugular vein catheter.

Isolated liver experiment. After sensitization (2 wk), these animals were anesthetized with pentobarbital sodium (70 mg/kg ip) and mechanically ventilated with room air. The basic methods for isolated perfused rat livers were described previously (18). In brief, a catheter was placed in the right carotid artery for later hemorrhage to obtain autologous blood for liver perfusion. After laparotomy, the hepatic artery was ligated, and the bile duct was cannulated with the polyethylene tube (0.5 mm ID, 0.8 mm OD). After intra-arterial heparinization (500 U/kg), 7–8 ml blood were withdrawn through the carotid arterial catheter. The intra-abdominal inferior vena cava (IVC) above the renal veins was ligated, and the portal vein was cannulated with a stainless cannula (1.3 mm ID, 2.1 mm OD) for portal perfusion. After thoracotomy, the supradiaphragmatic IVC was cannulated through a right atrium incision with a large-size stainless cannula (2.1 mm ID, 3.0 mm OD), and then portal perfusion was begun with the autologous blood diluted with 5% bovine albumin (Sigma-Aldrich, St. Louis, MO) in Krebs-Henseleit solution (in mM: 118 NaCl, 5.9 KCl, 1.2 $MgSO_4$, 2.5 $CaCl_2$, 1.2 NaH_2PO_4, 25.5 $NaHCO_3$, and 5.6 glucose) at Hct 8%. The liver was rapidly excised, suspended from an isometric transducer (TB-652T; Nihon-Kohden), and weighed continuously throughout the experimental period.

The livers were perfused at a constant flow rate in a recirculating manner via the portal vein with blood that was pumped using a Masterflex pump from the venous reservoir through a heat exchanger (37°C). The recirculating blood volume was 40 ml. The perfused blood was oxygenated in the venous reservoir by continuous bubbling with 95% O_2 and 5% CO_2. P_{pv} and hepatic venous pressure (P_{hv}) were measured with pressure transducers (TP-400T; Nihon-Kohden) attached by sidearm to the appropriate cannulas with the reference points at the hepatic hilus. To occlude inflow and outflow perfusion lines simultaneously for measurement of the double-occlusion pressure (P_{do}), two solenoid valves were placed in such a position that each sidearm cannula was between the corresponding solenoid valve and the liver. Portal blood flow rate (Q_{pv}) was measured with an electromagnetic flowmeter (MFV 1200; Nihon-Kohden), and the flow probe was positioned in the inflow line. Bile was collected drop by drop in a small tube suspended from the force transducer (SB-1T; Nihon-Kohden). One bile drop yielded 0.018 g, and the time between drops was measured for determination of the bile flow rate (11). The P_{pv}, P_{hv}, Q_{pv}, liver weight, and bile weight were monitored continuously and displayed through a thermal physiograph (RMP-6008; Nihon-Kohden). Outputs were also digitized by the analog-digital converter at a sampling rate of 100 Hz. These digitized values were displayed and recorded using a personal computer for later determination of P_{do}.

Hepatic hemodynamic parameters were observed for at least 20 min after the start of perfusion until an isogravimetric state (no weight gain or loss) was obtained by adjusting Q_{pv} and the height of the reservoir at a P_{hv} of 0–1 cmH_2O and at a Q_{pv} of 37 ± 6 $ml \cdot min^{-1} \cdot 10$ g liver wt^{-1}. After the baseline measurements, the perfused livers excised from the sensitized rats (anaphylaxis group, $n = 7$) and nonsensitized rats (control group, $n = 6$) were challenged with 0.015 mg ovalbumin injected in the reservoir.

The hepatic sinusoidal pressure was measured by the double-occlusion method (20, 26). Both the inflow and outflow lines were simultaneously and instantaneously occluded for 13 s using the solenoid valves, after which P_{pv} and P_{hv} rapidly equilibrated to a similar or identical pressure, which was P_{do}, using Liver software by Biomedical Science. In each experimental group, P_{do} was measured at baseline and at 3 and 6 min and then at 10-min intervals up to 30 min after antigen.

The total portal-hepatic venous (R_t) and presinusoidal (R_{pre}) and postsinusoidal (R_{post}) resistances were calculated as follows:

$$R_t = (P_{pv} - P_{hv})/Q_{pv} \quad (1)$$

$$R_{pre} = (P_{pv} - P_{do})/Q_{pv} \quad (2)$$

$$R_{post} = (P_{do} - P_{hv})/Q_{pv} \quad (3)$$

Statistics. All results are expressed as means ± SD. One-way ANOVA followed by Bonferroni's test was used to test for significant differences. Differences were considered as statistically significant at P values <0.05.

RESULTS

The response of the anesthetized rats to antigen. Figure 1*A* shows a representative example of the response to an intravenous injection of the ovalbumin antigen in an anesthetized intact rat sensitized with ovalbumin (the intact sensitized group). Figure 2 shows the summary data of time course changes in P_{pv} and P_{sa} of all four groups of anesthetized rats. After an antigen injection in the intact sensitized group, P_{sa} and P_{pv} simultaneously began to increase and decrease, respectively. P_{sa} rapidly decreased from the baseline of 120 ± 9 to 65 ± 11 mmHg at 1 min after the antigen and then continued to decrease progressively to the nadir of 43 ± 10 mmHg at 16 min, followed by a gradual recovery to 79 ± 18 mmHg at 60 min. P_{pv} increased from the baseline of 9.8 ± 0.9 cmH_2O to the peak of 24.3 ± 4.6 cmH_2O at 2.5 min after antigen and then gradually decreased to 10.9 ± 1.9 cmH_2O at 20 min. After that, P_{pv} remained at this level, which was not significantly different from the baseline. The postantigen period of up to 20 min during which P_{pv} remained elevated above the baseline (Fig. 2) was designated as the portal hypertension phase in the present study.

The surgical procedures of ligation of the celiac and the mesenteric arteries combined with total hepatectomy (GI-HptX) did not significantly affect the hemodynamic variables. Although P_{sa} transiently increased immediately after occlusion of the arteries, it returned to the pre-GI-HptX level during the baseline measurement after hepatectomy. Figure 1*B* shows a representative example in the GI-HptX sensitized group. The mean P_{sa} rapidly decreased from the baseline of 117 ± 12 to 80 ± 15 mmHg at 1 min. These levels were significantly

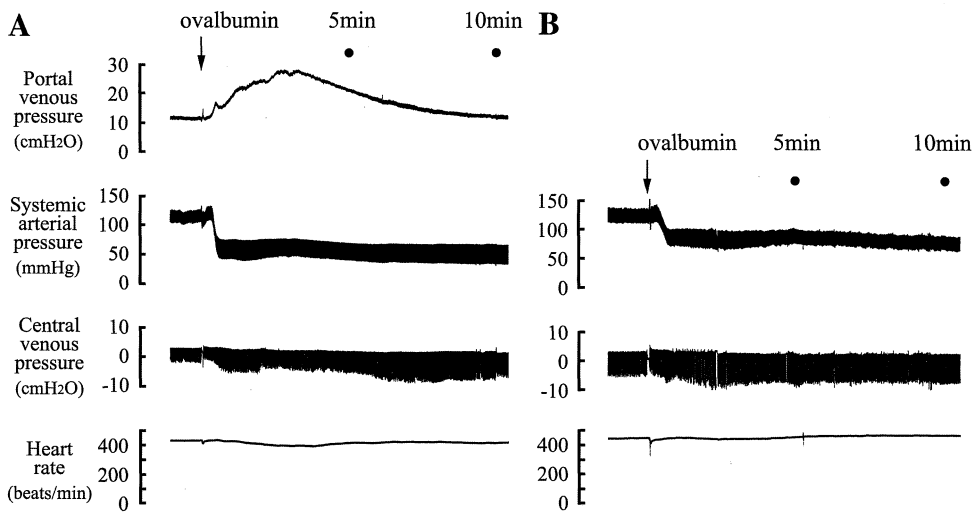

Fig. 1. Representative recording of the response to ovalbumin antigen (0.6 mg) in the intact sensitized group (*A*) and the gastrointestinal isolation and hepatectomy (GI-HptX) sensitized group (*B*). Portal venous pressure was not measured in the GI-HptX sensitized group because of no blood flow in the portal veins resulting from liver resection.

higher than the corresponding values of the intact sensitized group of 65 ± 11 mmHg. Thereafter, it did not further decrease but remained at this level throughout the experimental period, as shown in Fig. 2. Thus P_{sa} from 1 to 20 min after antigen in the GI-HptX sensitized group was significantly greater than that in the intact sensitized group. It should be noted that this period corresponded to the portal hypertension phase.

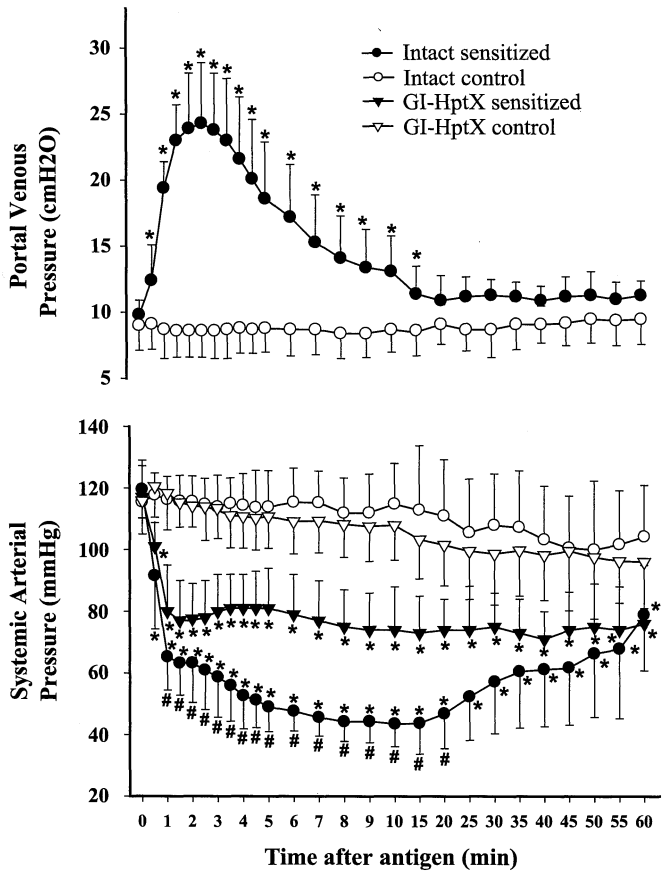

Fig. 2. Summary of changes in the systemic arterial pressure (P_{sa}) and portal venous pressure (P_{pv}) after antigen injection. Means ± SD; *$P < 0.05$ vs. baseline; #$P < 0.05$ vs. the intact sensitized group. P_{pv} was not measured in either the GI-HptX control or the GI-HptX sensitized group because the liver was excised.

At 10 min after antigen, P_{cv} in the intact sensitized group was significantly decreased from the baseline of 1.2 ± 0.3 to 0.1 ± 0.3 cmH_2O, whereas in the GI-HptX sensitized group, P_{cv} tended to decrease, but not significantly, from 0.8 ± 0.4 to 0.4 ± 0.8 cmH_2O. The changes in P_{cv} between the intact sensitized and GI-HptX sensitized groups at 10 min after antigen were significantly different (1.0 ± 0.3 vs. 0.4 ± 0.6 cmH_2O; $P < 0.05$). HR was not significantly changed after antigen in any groups studied, as shown in Fig. 1. Neither the P_{sa} nor the P_{pv} was significantly changed by the antigen in the control animals during the experimental periods of both the intact and GI-HptX groups (Fig. 2).

The response of the blood-perfused livers to antigen. The liver weight measured at the end of the perfusion experiment in the control and anaphylaxis groups was 9.3 ± 1.4 g ($n = 6$) and 9.0 ± 0.6 g ($n = 7$), respectively. The body weight in the control group was 0.288 ± 0.012 kg ($n = 6$), and that in the anaphylaxis group was 0.287 ± 0.021 kg ($n = 7$). There were no significant differences in the liver weight and body weight between the two groups. The liver weight-to-body weight ratio of all animals for the isolated perfusion study was 31.8 ± 3.1 g liver/kg body wt ($n = 13$).

An antigen injection caused hepatic venoconstriction, which was characterized by predominant presinusoidal constriction and liver weight loss, as shown in Fig. 3. Within 1 min after antigen, venoconstriction was evident by an increased P_{pv} that reached the peak value of 21.4 ± 4.9 cmH_2O from the baseline of 6.9 ± 0.1 cmH_2O (Fig. 4). The double-occlusion maneuver performed at 3 min after antigen revealed a P_{do} of 3.3 ± 0.3 cmH_2O that was significantly higher than that of the baseline of 2.3 ± 0.1 cmH_2O. Therefore, the P_{pv}-to-P_{do} gradient (in conjunction with the flow) defined the portal presinusoidal resistance (R_{pre}, *Eq. 2*). This resistance increased markedly from a baseline of 4.7 ± 0.2 to 18.1 ± 4.9 cmH_2O, whereas the P_{do}-to-P_{hv} gradient, the indicator of R_{post}, increased minimally, but significantly, from the baseline of 1.8 ± 0.1 to 2.8 ± 0.3 cmH_2O (Fig. 4). Thus R_{pre} increased by 250% the baseline from 0.13 ± 0.02 to 0.52 ± 0.19 $cmH_2O \cdot ml^{-1} \cdot min^{-1} \cdot 10$ g liver wt^{-1}, whereas R_{post} increased by only 67% from the baseline level of 0.05 ± 0.01 to 0.08 ± 0.01 $cmH_2O \cdot ml^{-1} \cdot min^{-1} \cdot 10$ g liver wt^{-1} (Fig. 4). This indicates that an injection of the antigen almost selectively increased R_{pre} rather than

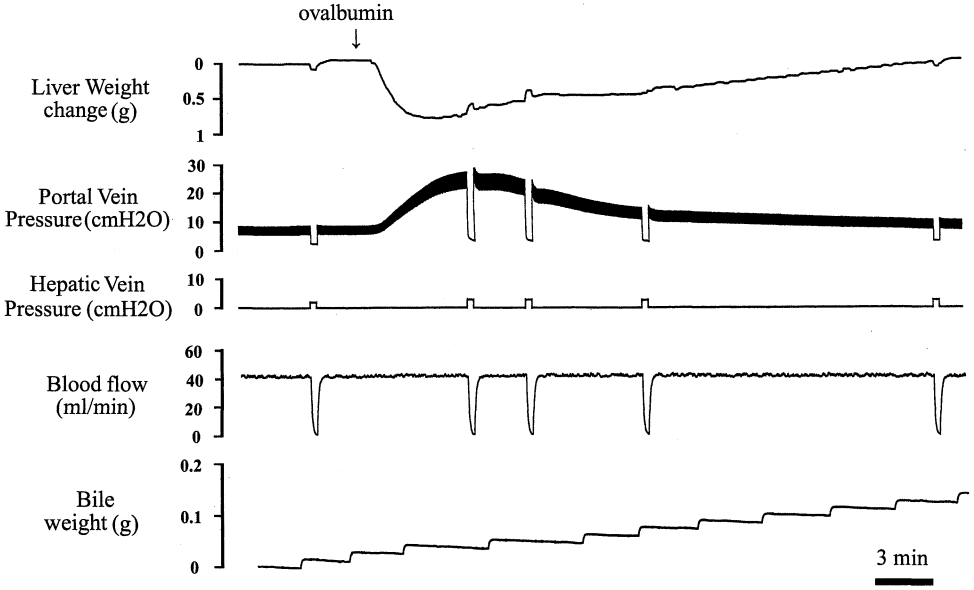

Fig. 3. Representative recording of the response to ovalbumin antigen (0.015 mg) in the blood-perfused liver isolated from a sensitized rat.

R_{post}, as reflected by a significant increase in the R_{pre}-to-R_t ratio from the baseline of 0.72 ± 0.01 to 0.86 ± 0.05. P_{pv}, and thus R_t, returned to the baseline at 30 min after antigen. Concomitant with venoconstriction, the liver weight showed a gradual decrease, reaching the nadir, −0.5 ± 0.4 g/10 g liver wt, at 3 min. Along with P_{pv}, the liver weight returned to the baseline at 30 min after antigen. The bile flow decreased to 67% of the baseline level of 0.01 ± 0.001 g·min^{-1}·10 g liver wt^{-1} during the maximal venoconstriction. In the control rat liver, no hemodynamic variables changed significantly after antigen (Fig. 4).

DISCUSSION

There are two major findings of the present study. The first finding (derived from the anesthetized rat experiments) is that elimination of the blood flow to the liver and splanchnic organs attenuated the antigen-induced decrease in P_{sa} during the portal hypertension phase. Another finding (derived from the isolated perfused rat liver experiments) is that hepatic anaphylactic venoconstriction is characterized by almost selective presinusoidal constriction and liver weight loss.

Hepatic anaphylactic postsinusoidal venoconstriction plays a crucial role in anaphylactic hypotension in dogs (6). In the present study, we have shown that immunological damage to the liver and splanchnic vascular beds also participated in the anaphylactic hypotension in rats. This is based on the finding that the elimination of hepatic and splanchnic circulation by ligation of the celiac and the mesenteric arteries combined with total hepatectomy attenuated the antigen-induced reduction of P_{sa} (Fig. 2). The mechanism for the beneficial effect of GI-

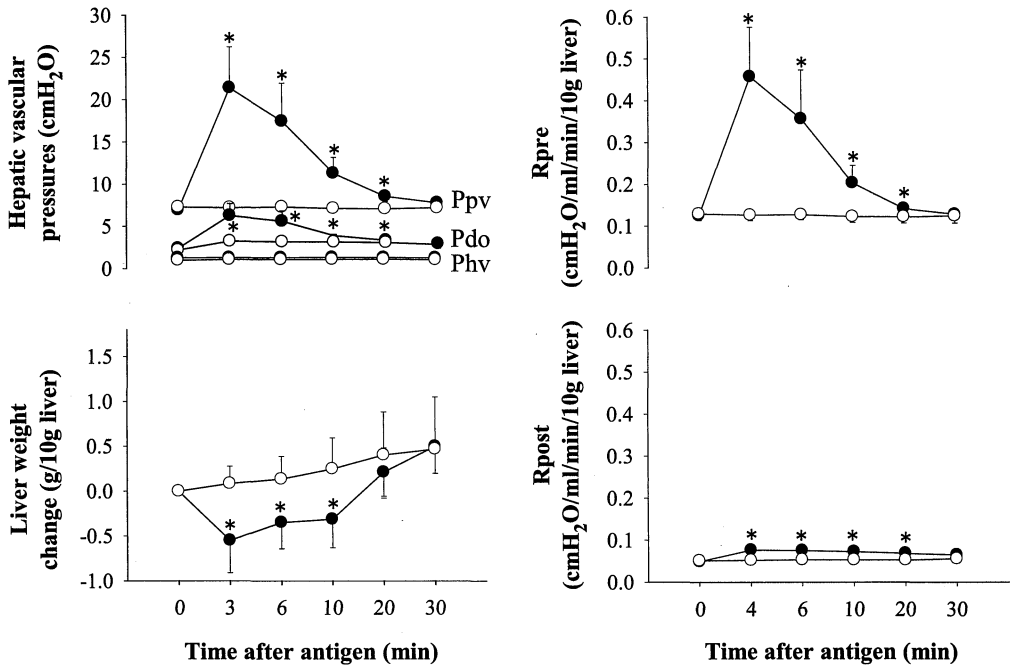

Fig. 4. Summary of changes in hepatic vascular pressures, liver weight changes, and pre (R_{pre})- and post (R_{post})-sinusoidal resistances after antigen injection in isolated perfused rat livers. Means ± SD; *P < 0.05 vs. baseline and the control group. P_{do}, double-occlusion pressure; P_{hv}, hepatic venous pressure; ●, anaphylaxis group; ○, control group.

HptX on the anaphylactic hypotension is not known. However, we assume that anaphylaxis-induced portal hypertension may account for the profound decrease in P_{sa} because the period during which attenuation of anaphylactic hypotension was observed corresponded to the portal hypertension phase during which the elevation of P_{pv} was sustained (Fig. 2). We speculate the following pathophysiological process: anaphylaxis causes hepatic venoconstriction, as observed in the isolated perfused sensitized liver, resulting in portal hypertension that then causes congestion of the upstream splanchnic organs, with resultant decrease in venous return and effective circulating blood volume, and finally augmentation of anaphylactic hypotension.

Another possible explanation may be related to the sources of mast cells that release vasoactive chemical mediators in response to antigens. Although mast cells occur throughout most tissues, they are more prevalent in gastrointestinal tract as well as the skin and lungs, the areas that come in contact with the external environment (14). A large number of mast cells in the gastrointestinal tract, including liver and intestines, may release substantial amounts of anaphylactic vasoactive substances in the systemic circulation. The elimination of these sources by the procedure of GI-HptX might have decreased the release of the anaphylaxis-related chemical mediators, resulting in a weak anaphylactic response.

Finally, there is a third possibility that anaphylaxis might be associated with significant splanchnic arterial vasodilation, as observed when platelet-activating factor (PAF), one of the mediators of anaphylaxis, was injected in the conscious rats (21). Splanchnic arterial dilation could contribute to both the reduced systemic pressure and increased P_{pv}. Moreover, splanchnic arterial ligation would attenuate these responses. However, there is currently no data that demonstrated splanchnic arterial vasodilation during anaphylactic hypotension in rats.

With respect to the mechanism for the early stage of anaphylactic hypotension in anesthetized rats, Bellou et al. (1) reported that histamine, serotonin, and nitric oxide are involved in the initial decrease in P_{sa} after ovalbumin antigen in the sensitized Brown Norway rats. Actually, either histamine or serotonin administered intravenously in the anesthetized rats causes a short-lasting decrease in P_{sa}, presumably because of dilatation of systemic arterioles (1). The initial arterial hypotension after antigen in the GI-HptX sensitized rats might be induced by the same mechanism proposed by Bellou et al. (1).

Anaphylactic hepatic venoconstriction, based on an increase in P_{pv}, was observed in rats (8), guinea pigs (16), and dogs (25, 26). However, a species difference between dog and guinea pig has been found in the hepatic vascular segments that preferentially contract during anaphylaxis: selective postsinusoidal constriction occurs in sensitized canine livers (26), whereas predominant presinusoidal but significant and substantial postsinusoidal constriction occurs in guinea pig livers (16). Using isolated, perfused, and sensitized rat livers, we have shown that anaphylactic hepatic venoconstriction in rats was different from that in dogs or guinea pigs and was characterized by a large presinusoidal contraction and only a minimal postsinusoidal contraction based on the double-occlusion method (20, 26) to estimate the sinusoidal pressure (P_{do}; see Figs. 3 and 4).

The mechanism for such a species-dependent response is not known. However, canine postsinusoidal hepatic veins anatomically contain smooth muscle sphincters in hepatic initial sublobular veins (4). Maass-Moreno and Rothe (12) also reported that major pressure gradients must lie upstream from the large (>2 mm) hepatic veins in dogs. Indeed, these postsinusoidal veins vigorously contract in response to various mediators of anaphylactic reaction, such as histamine (22), thromboxane A_2 (22), and PAF (24). In guinea pig livers, the anaphylactic presinusoidal constriction may be caused mainly by PAF, whereas the postsinusoidal constriction is caused by cysteinyl leukotrienes (19). Actually, PAF predominantly contracts presinusoidal vessels in guinea pig livers (17). However, effects of anaphylaxis-related vasoactive substances are not currently known on the segmental vascular resistances of rat livers. Further study is required to identify the chemical mediators responsible for the anaphylactic hepatic venoconstriction in rats.

In contrast to the liver weight gain response to the antigen of dogs (26) and guinea pigs (16), a liver weight loss was induced by marked anaphylactic presinusoidal constriction in isolated perfused rat livers. With the constant perfusion of the liver, the mechanism of the weight loss is unknown. This liver weight loss may be the result of hepatic vascular blood loss. Theoretically, the interstitial fluid volume loss also could contribute to a liver weight loss (10). Further study is required in this respect.

There are limitations of the present study. The first is related to the finding that the HR was high at baseline, as shown in Fig. 1, and that HR did not change in response to the marked drop in blood pressure during the anaphylactic shock. One of the reasons for high HR could be ascribed to the vagolytic property of pentobarbital sodium used in the present study (15). It is reported that pentobarbital decreases cardioinhibitory parasympathetic activity that dominates the control of HR (15). Indeed, in the pentobarbital-anesthetized rat study of others (3), the basal HR showed ~400 beats/min, as observed in the present study. With respect to the absence of the increase in HR in response to the antigen-induced marked drop in P_{sa}, that is, impairment of normal arterial baroreceptor reflex, Koyama et al. (9) demonstrated that systemic baroreceptor reflex control of HR and renal sympathetic nerve activity is reduced during anaphylactic hypotension in pentobarbital-anesthetized dogs. A similar impairment of arterial baroreceptor reflex might occur in the rat anaphylactic shock. Another shortcoming is the absence of hepatic arterial perfusion in the present isolated perfused livers. Hepatic arterial perfusion with normally oxygenated blood would improve the metabolic milieu of the liver. However, the perfusate was well oxygenated by bubbling with 95% O_2 and 5% CO_2, which provided perfusate oxygen tension of 290 ± 38 mmHg. Thus the isolated livers were perfused with hyperoxic blood, rather than hypoxic blood, and oxygenation was well done.

In summary, we determined the roles of splanchnic circulation in the anaphylactic hypotension in anesthetized rats sensitized with ovalbumin (1 mg). An intravenous injection of antigen (0.6 mg) caused not only a profound decrease in P_{sa} but also an increase in P_{pv}. The elimination of the splanchnic vascular beds, by the occlusions of the celiac and mesenteric arteries, combined with total hepatectomy attenuated anaphylactic hypotension during the portal hypertension phase. In addition, in isolated perfused sensitized rat livers, hepatic anaphylaxis caused almost selective presinusoidal constriction

and liver weight loss. Based on these findings, we conclude that liver and splanchnic vascular beds are partly involved in anaphylactic hypotension: anaphylactic presinusoidal contraction-induced portal hypertension and subsequent splanchnic congestion may cause a decrease in venous return and then hypotension.

ACKNOWLEDGMENTS

This study was supported by a Grant for Collaborative Research from Kanazawa Medical University (C2003–1, C2004–1, and C2005-1) and a Grant-in-Aid for Scientific Research from the Ministry of Education, Culture, Sports, Sciences, and Technology of Japan (No. 15591665).

REFERENCES

1. **Bellou A, Lambert H, Gillois P, Montemont C, Gerard P, Vauthier E, Sainte-Laudy J, Longrois D, Gueant JL, and Mallie JP.** Constitutive nitric oxide synthase inhibition combined with histamine and serotonin receptor blockade improves the initial ovalbumin-induced arterial hypotension but decreases the survival time in Brown Norway rats anaphylactic shock. *Shock* 19: 71–78, 2003.
2. **Brown AFT.** Anaphylactic shock: mechanism and treatment. *J Accid Emerg Med* 12: 89–100, 1995.
3. **Canyon SJ and Dobson GP.** Protection against ventricular arrhythmias and cardiac death using adenosine and lidocaine during regional ischemia in the in vivo rat. *Am J Physiol Heart Circ Physiol* 287: H1286–H1295, 2004.
4. **Ekataksin W and Kaneda K.** Liver microvascular architecture: an insight into the pathophysiology of portal hypertension. *Semin Liver Dis* 19: 359–382, 1999.
5. **Enjeti S, Bleecker ER, Smith PL, Rabson J, Permutt S, and Traystman RJ.** Hemodynamic mechanism in anaphylactic shock. *Circ Shock* 11: 297–309, 1983.
6. **Essex HE.** Anaphylactic and anaphylactoid reactions with special emphasis on the circulation. In: *Handbook of Physiology. Circulation.* Bethesda, MD: Am. Physiol. Soc., 1965, vol. III, chapt. 66, p. 2391–2408.
7. **Gaub J and Iversen J.** Rat liver regeneration after 90% partial hepatectomy. *Hepatology* 4: 902–904, 1984.
8. **Hines KL and Fisher RA.** Regulation of hepatic glycogenolysis and vasoconstriction during antigen-induced anaphylaxis. *Am J Physiol Gastrointest Liver Physiol* 262: G868–G877, 1992.
9. **Koyama S, Fujita T, Uematsu H, Shibamoto T, Aibiki M, and Kojima S.** Inhibitory effect of renal nerve activity during canine anaphylactic hypotension. *Am J Physiol Regul Integr Comp Physiol* 258: R383–R387, 1990.
10. **Lee JS, Lee LP, and Rothe CF.** Assessing microvascular volume change and filtration from venous hematocrit variation of canine liver and lung. *Ann Biomed Eng* 24: 25–36, 1996.
11. **Ling YQ, Shibamoto T, Honda T, Kamikado C, Hironaka E, Hongo M, and Koyama S.** Increased sinusoidal pressure is associated with early liver weight gain in ischemia-reperfusion injury in isolated perfused rat liver. *J Surg Res* 88: 70–77, 2000.
12. **Maass-Moreno R and Rothe CF.** Contribution of the large hepatic veins to postsinusoidal vascular resistance. *Am J Physiol Gastrointest Liver Physiol* 262: G14–G22, 1992.
13. **Manwaring WH.** The physiological mechanism of anaphylactic shock. *Bull Johns Hopkins Hosp* 21: 275–277, 1910.
14. **Metcalfe DD.** Mast cell mediators with emphasis on intestinal mast cells. *Ann Allergy* 53: 563–575, 1984.
15. **Murthy VS, Zagar ME, Vollmer RR, and Schmidt DH.** Pentobarbital-induced changes in vagal tone and reflex vagal activity in rabbits. *Eur J Pharmacol* 84: 41–50, 1982.
16. **Ruan Z, Shibamoto T, Shimo T, Tsuchida H, Koizumi T, and Nishio M.** NO, but not CO, attenuates anaphylaxis-induced postsinusoidal contraction and congestion in guinea pig liver. *Am J Physiol Regul Integr Comp Physiol* 286: R94–R100, 2004.
17. **Ruan Z, Shibamoto T, Shimo T, Koizumi T, Tsuchida H, Kurata Y, Ogura T, and Kubo K.** Effects of platelet-activating factor and thromboxane A_2 on isolated perfused-guinea pig liver. *Prostaglandins Other Lipid Mediat* 73: 73–85, 2004.
18. **Shibamoto T, Narushima M, Ling YQ, Shimo T, Tsuchida H, Kurata Y, and Ogura T.** Different hepatic vascular response to noradrenaline and histamine between guinea pig and rat. *Acta Physiol Scand* 180: 255–263, 2004.
19. **Shibamoto T and Ruan Z.** Chemical mediators responsible for hepatic vascular anaphylaxis in guinea pigs (Abstract). *Jpn J Physiol* 53: S167, 2003.
20. **Shibamoto T, Wang HG, Miyahara T, Tanaka S, Haniu H, and Koyama S.** Pre-sinusoidal vessels predominantly contract in response to norepinephrine, histamine, and KCl in rabbit liver. *J Appl Physiol* 87: 1404–1412, 1999.
21. **Siren AL and Feuerstein G.** Effects of PAF and BN 52021 on cardiac function and regional blood flow in conscious rats. *Am J Physiol Heart Circ Physiol* 257: H25–H32, 1989.
22. **Urayama H, Shibamoto T, Wang HG, and Koyama S.** Thromboxane A_2 analogue contracts predominantly the hepatic veins in isolated canine liver. *Prostaglandins* 52: 484–495, 1996.
23. **Wagner EM, Mitzner WA, and Bleecker ER.** Peripheral circulatory alterations in canine anaphylactic shock. *Am J Physiol Heart Circ Physiol* 251: H934–H940, 1986.
24. **Wang HG, Shibamoto T, and Koyama S.** Effect of platelet-activating factor on hepatic capillary pressure in isolated dog liver. *Prostaglandins Leukot Essent Fatty Acids* 57: 293–298, 1997.
25. **Weil R.** Studies in anaphylaxis. XXI. Anaphylaxis in dogs: a study of the liver in shock and peptone poisoning. *J Immunol* 2: 525–556, 1917.
26. **Yamaguchi Y, Shibamoto T, Hayashi T, Saeki Y, and Tanaka S.** Hepatic vascular response to anaphylaxis in isolated canine liver. *Am J Physiol Regul Integr Comp Physiol* 267: R268–R274, 1994.

Biophysical Journal Volume 89 October 2005 2865–2887

Dynamical Mechanisms of Pacemaker Generation in I_{K1}-Downregulated Human Ventricular Myocytes: Insights from Bifurcation Analyses of a Mathematical Model

Yasutaka Kurata,* Ichiro Hisatome,† Hiroyuki Matsuda,* and Toshishige Shibamoto*

*Department of Physiology, Kanazawa Medical University, Ishikawa 920-0293, Japan; and †Division of Regenerative Medicine and Therapeutics, Tottori University Graduate School of Medical Science, Yonago 683-0826, Japan

ABSTRACT Dynamical mechanisms of the biological pacemaker (BP) generation in human ventricular myocytes were investigated by bifurcation analyses of a mathematical model. Equilibrium points (EPs), periodic orbits, stability of EPs, and bifurcation points were determined as functions of bifurcation parameters, such as the maximum conductance of inward-rectifier K^+ current (I_{K1}), for constructing bifurcation diagrams. Stable limit cycles (BP activity) abruptly appeared around an unstable EP via a saddle-node bifurcation when I_{K1} was suppressed by 84.6%. After the bifurcation at which a stable EP disappears, the I_{K1}-reduced system has an unstable EP only, which is essentially important for stable pacemaking. To elucidate how individual sarcolemmal currents contribute to EP instability and BP generation, we further explored the bifurcation structures of the system during changes in L-type Ca^{2+} channel current ($I_{Ca,L}$), delayed-rectifier K^+ currents (I_K), or Na^+/Ca^{2+} exchanger current (I_{NaCa}). Our results suggest that 1), $I_{Ca,L}$ is, but I_K or I_{NaCa} is not, responsible for EP instability as a requisite to stable BP generation; 2), I_K is indispensable for robust pacemaking with large amplitude, high upstroke velocity, and stable frequency; and 3), I_{NaCa} is the dominant pacemaker current but is not necessarily required for the generation of spontaneous oscillations.

INTRODUCTION

The cardiac biological pacemaker (BP) was recently created by genetic suppression of the inward-rectifier K^+ current (I_{K1}) in guinea pig ventricular myocytes (1), suggesting possible development of the functional BP as a therapeutic alternative to the electronic pacemaker. A first step for creation of the functional BP would be engineering of single BP cells, which requires deep understanding of the BP mechanisms. Using the Luo-Rudy guinea pig ventricle model (2), Silva and Rudy (3) simulated BP activity by reducing I_{K1} conductance (g_{K1}) and investigated the ionic mechanisms of BP generation in the I_{K1}-downregulated ventricular myocyte. They reported that BP activity was yielded by 81% suppression of I_{K1}, concluding that Na^+/Ca^{2+} exchanger current (I_{NaCa}) was the dominant pacemaker current. However, the mechanistic difference between ventricular pacemaking and natural sinoatrial (SA) node pacemaking, as well as whether I_{K1} downregulation also induces BP activity in human ventricular myocytes (HVMs), remains to be clarified.

The aim of this study was to elucidate the mechanisms of BP generation in I_{K1}-downregulated HVMs and the roles of individual sarcolemmal currents in HVM pacemaking in terms of the nonlinear dynamics and bifurcation theory. In previous studies (4–11), bifurcation structures of ventricular or SA node models, i.e., ways of changes in the number or stability of equilibrium and periodic states of the model systems, were investigated for elucidating the mechanisms of normal and abnormal pacemaker activities. These theoretical works indicate that the mathematical approach provides a convenient way of understanding how individual currents contribute to pacemaker activities. In this study, therefore, local stability and bifurcation analyses, as well as numerical simulations, were performed for a mathematical model of the HVM. We constructed bifurcation diagrams by calculating equilibrium points (EPs), periodic orbits, stability of the EP, and saddle-node or Hopf bifurcation points as functions of bifurcation parameters (for details, see Theory and Methods). During I_{K1} suppression, BP activity abruptly emerged around an unstable EP via a saddle-node bifurcation at which a stable EP corresponding to the resting state disappeared. Our results suggested that BP activity could be developed by reducing I_{K1} alone in HVMs as well and that the instability of an EP at depolarized potentials is essentially important for BP generation.

To elucidate the ionic mechanisms of EP destabilization and BP generation in the I_{K1}-downregulated HVM, we further explored bifurcation structures of the I_{K1}-reduced BP system during decreases or increases in an L-type Ca^{2+} channel current ($I_{Ca,L}$), delayed-rectifier K^+ currents (I_K), and I_{NaCa}, which appear to be essentially important for pacemaker generation (3,11). Moreover, we determined stability of the BP system at the steady-state potential (V_0) during applications of the constant bias current (I_{bias}) and how the unstable V_0 and I_{bias} regions, where BP oscillations occur, change with decreasing or increasing the sarcolemmal currents. This would reveal the contributions of each current to EP instability and robustness of BP activity to hyperpolarizing or depolarizing loads (11). Our study suggests that the dynamical mechanism of the ventricular pacemaking is

Submitted February 7, 2005, and accepted for publication July 15, 2005.

Address reprint requests to Yasutaka Kurata, Dept. of Physiology, Kanazawa Medical University, 1-1 Daigaku, Uchinada-machi, Kahoku-gun, Ishikawa 920-0293, Japan, E-mail: yasu@kanazawa-med.ac.jp.

0006-3495/05/10/2865/23 $2.00

doi: 10.1529/biophysj.105.060830

essentially the same as that of the natural SA node pacemaking as reported by Kurata et al. (11).

This article clearly shows that bifurcation analyses of a mathematical model allow us to notice the essential importance of EP instability for pacemaker generation and to elucidate the roles of individual ionic currents in pacemaking. Thus, the nonlinear dynamical approach is useful for general understanding of the mechanisms of normal and abnormal pacemaker activities and may also be applicable to engineering of a functional BP as a therapeutic alternative to the electronic pacemaker. Definitions of the terms specific to the nonlinear dynamics and bifurcation theory are provided at the end of the Theory and Methods section to help understand the theory and methods for bifurcation analysis as well as our results and conclusions. Abbreviations and acronyms repeatedly used in this article are listed in Table 1.

THEORY AND METHODS

Development of a modified HVM model

A mathematical model of cardiac myocytes is described as an n-dimensional nonlinear dynamical system, i.e., a set of ordinary differential equations of the form

TABLE 1 Abbreviations and acronyms

AP	Action potential
APA	Action potential amplitude
$APD_{(90)}$	Action potential duration (at 90% repolarization)
βAS	β-adrenergic stimulation
BP	Biological pacemaker
CL	Cycle length
C-LTCC	High voltage-activated L-type Ca^{2+} channel
D-LTCC	Low voltage-activated L-type Ca^{2+} channel
EP	Equilibrium point
hESC	Human embryonic stem cell
HVM	Human ventricular myocyte
I_{bias}	Constant bias current
$I_{Ca,L}$	L-type Ca^{2+} channel current
I_K	Delayed-rectifier K^+ current
I_{Kr}	Rapidly activating component of I_K
I_{Ks}	Slowly activating component of I_K
I_{K1}	Inward-rectifier K^+ current
I_{Na}	Na^+ channel current
I_{NaCa}	Na^+/Ca^{2+} exchanger current
I_{to}	4-Aminopyridine-sensitive transient outward current
$I_{X,b}$	Background current carried by ion X
I_h	Hyperpolarization-activated current
MDP	Maximum diastolic potential
ODE	Ordinary differential equation
PB	Priebe-Beuckelmann
POP	Peak overshoot potential
SA	Sinoatrial
SR	Sarcoplasmic reticulum
V	Membrane potential
V_0	Steady-state potential at an EP
$[Ca^{2+}]_{rel}$	Free Ca^{2+} concentration in the junctional SR
$[Ca^{2+}]_{up}$	Free Ca^{2+} concentration in the network SR
$[X]_i$	Intracellular concentration of ion X
$[X]_o$	Extracellular concentration of ion X

$$dx_i/dt = f_i(x_1, x_2, \ldots, x_n), i = 1, 2, \ldots, n. \quad (1)$$

This is usually written in the vector form

$$d\boldsymbol{x}/dt = \boldsymbol{f}(\boldsymbol{x}), \quad (2)$$

where the state variable $\boldsymbol{x}$ is a vector-valued function of time t, and the vector field $\boldsymbol{f}$ is a function of the state variable $\boldsymbol{x}$ (12–14). For a model system to be suitable for bifurcation analysis, the vector field $\boldsymbol{f}$ should be continuous and smooth (i.e., sufficiently differentiable) and should not depend on time or initial conditions but depend only on the state variable $\boldsymbol{x}$. Such a system is called an "autonomous" system (see also Definitions of Terms at the end of this section).

On the basis of single-cell patch-clamp data from undiseased and failing HVMs, Priebe and Beuckelmann (15) have first developed a single HVM model (referred to as the Priebe-Beuckelmann (PB) model) as a modified version of the Luo-Rudy phase II model for the guinea pig ventricle (2). Recently, ten Tusscher et al. (16) and Iyer et al. (17) developed more elaborate HVM models based on detailed experimental data. Their models appear to be superior to the PB model in reproducing experimental data but less suitable for bifurcation analyses for the following reasons: 1), the ten Tusscher et al. model has the vector field containing many complex functions that are not continuous or smooth, thus they are not always differentiable or yield noncontinuous derivatives; and 2), the Iyer et al. model ($n = 67$) is much larger than the PB model ($n = 15$) or the ten Tusscher et al. model ($n = 17$), making bifurcation analyses practically much harder. We have therefore chosen to modify the PB model on the basis of recent experimental findings as well as other human or animal heart models. The original PB model explicitly contains time t in the formula for the sarcoplasmic reticulum (SR) Ca^{2+} release, making it nonautonomous. Thus, modifications of the PB model were required for converting it into an autonomous system, as well as for improving the capability of reproducing experimental data.

The standard model for the normal activity is described as a nonlinear dynamical system of 15 first-order ordinary differential equations. The membrane current system includes $I_{Ca,L}$, the rapid and slow components of I_K (denoted I_{Kr} and I_{Ks}, respectively), 4-aminopyridine-sensitive transient outward current (I_{to}), Na^+ channel current (I_{Na}), I_{K1}, background Na^+ ($I_{Na,b}$) and Ca^{2+} ($I_{Ca,b}$) currents, Na^+-K^+ pump current (I_{NaK}), I_{NaCa}, and Ca^{2+} pump current (I_{pCa}). The expressions for $I_{Ca,L}$ and I_{Ks} as well as SR Ca^{2+} release were reformulated, whereas the formulas for other ionic currents and intracellular Ca^{2+} handling are essentially the same as those in the original PB model or adopted from other existing models (16,18–20). Modifications of the model are summarized in Table 2; details on major modifications are described below. All expressions (Eqs. 3–64) and the standard parameter values used are provided in Appendix 1 and Table 5, respectively.

Formulation of $I_{Ca,L}$

The kinetics of $I_{Ca,L}$ was described by Eqs. 3–8 with the activation (d_L), voltage-dependent inactivation (f_L), and Ca^{2+}-dependent inactivation (f_{Ca}) gating variables. Voltage dependences of $I_{Ca,L}$ gating kinetics in the current (modified) and original human heart models are shown in Fig. 1 (*top*), together with temperature-corrected experimental values for comparison. As ten Tusscher et al. (16) pointed out, the steady-state activation and inactivation curves ($d_{L\infty}$, $f_{L\infty}$) yielded by the original PB formulas were somewhat unusual for unknown reasons (see Fig. 1, *left top*), resulting in a very large window current. We therefore renewed the expressions for $I_{Ca,L}$. For the steady-state activation and inactivation ($d_{L\infty}$, $f_{L\infty}$), we used the data of Bénitah et al. (21). The expression of the activation time constant (τ_{dL}) was adopted from the ten Tusscher et al. model (16). The formulas for the time constants of the voltage-dependent inactivation and recovery (τ_{fL}) employed by the original models appeared not to fit the experimental data for single HVMs from Bénitah et al. (21) or other articles (see Fig. 1, *right top*, and also Fig. 2 *E* of ten Tusscher et al. (16)). Therefore, we originally formulated τ_{fL} from the data of Bénitah et al. (21), which were corrected for

TABLE 2 Equations and parameter values adopted for individual components of the HVM model

Component	Expressions	Parameter values		PB*	TNNP*
$I_{Ca,L}$	$d_{L,\infty}$, $f_{L,\infty}$: Bénitah et al. (21) τ_{dL}: Same as the TNNP model (16) τ_{fL}: Original formula based on Bénitah et al. (21) $p_{a,\infty}$: Li et al. (24)	$g_{Ca,L}$ (nS/pF)	0.2496	*0.064*	
I_{Kr}	$p_{i,\infty}$: Same as the CRN model (19)† τ_{pa}: Same as the CRN model (19)† n_{∞}: Li et al. (24)	g_{Kr} (nS/pF)	0.012	*0.015*	*0.096*
I_{Ks}	τ_n: Original formula based on Virág et al. (34)	g_{Ks} (nS/pF)	0.036	*0.02*	*0.245*
I_{to}	Same as the PB model (15)	g_{to} (nS/pF)‡	0.3/0.4	0.3	*0.294*
I_{Na}	Same as Bernus et al. (18)§	g_{Na} (nS/pF)	7.8	*16*	*14.838*
I_{K1}	Same as the PB model (15)	g_{K1} (nS/pF)	3.9	2.5	5.405
$I_{Na,b}$	Same as the PB model (15)	$g_{Na,b}$ (nS/pF)	0.001	0.001	0.00029
$I_{Ca,b}$	Same as the PB model (15)	$g_{Ca,b}$ (nS/pF)	0.00051	0.00085	0.000592
I_{NaK}	Same as the PB model (15)	$I_{NaK,max}$ (pA/pF)	0.884	1.3	*1.362*
I_{NaCa}	Same as the PB model (15)	k_{NaCa}	1000	1000	1000
I_{pCa}	Same as the CRN model (19)¶	$I_{pCa,max}$ (pA/pF)	0.11	0	0.025
J_{rel}	Modified formulas base on Faber and Rudy (20)	P_{rel}	50	*22*	*24.696*
J_{up}	Same as the TNNP model (16)¶	P_{up}	0.00221	*0.0045*	*0.000425*
J_{tr}	Same as the PB model (15)	τ_{tr}	180	180	
Ca^{2+} buffers	Same as the PB model (15)				

*Parameter values used for the PB model (15) and ten Tusscher et al. (TNNP) model (16) are given for comparison. Values are shown in italics or not shown, when the formula is different from that of the current model and thus direct comparison is impossible.
†Formulas of the Courtemanche et al. (CRN) model for human atrial myocytes (19) were used. For details, see text.
‡The g_{to} (nS/pF) was set equal to 0.4, the value for epicardial cells (18), for the simulation of paced APs, and to 0.3, the value of the original PB model, for the BP simulations and bifurcation analyses.
§Formulas for I_{Na} were adopted from Bernus et al. (18) to reduce the number of state variables as well as to avoid the use of noncontinuous functions.
¶To reduce the diastolic $[Ca^{2+}]_i$ during pacing at 0.25–2 Hz to <0.3 μM, 1), a small amount of I_{pCa} was added, and 2), the formula for SR Ca^{2+} uptake was adopted from the TNNP model (16).

a temperature of 37°C with a Q_{10} of 2.2 and $[Ca^{2+}]_o$-dependent factor (16). The τ_{fL} data were fitted to a function similar to that used by Courtemanche et al. (19) for their human atrial model, using a least square minimization procedure. The formula for the Ca^{2+}-dependent inactivation ($f_{Ca,\infty}$) is also the same as used by Courtemanche et al. (19). Maximum $I_{Ca,L}$ was formulated as a fully selective Ca^{2+} current, with its reversal potential ($E_{Ca,L}$) fixed at a constant value of +52.8 mV as reported by Bénitah et al. (21) and the maximum conductance ($g_{Ca,L}$) set equal to 249.6 pS/pF at 2 mM $[Ca^{2+}]_o$.

The model-generated $I_{Ca,L}$ during voltage-clamp pulses and peak $I_{Ca,L}$-V relationship are depicted in Fig. 1 (*bottom*). The simulated peak $I_{Ca,L}$-V relation is comparable to the experimental data from Bénitah et al. (21), Pelzmann et al. (22), and Li et al. (23).

Formulation of I_{Kr}

The kinetics of I_{Kr} was described by Eqs. 9–14 with the activation (p_a) and inactivation (p_i) gating variables. Voltage dependences of I_{Kr} activation and inactivation in the current and original human heart models are shown in Fig. 2 (*top*), together with experimental data for comparison; the model-generated I_{Kr} during voltage-clamp pulses are also depicted. There are limited experimental data available for the gating kinetics of native I_{Kr} channels in HVMs. Nevertheless, experimentally observed activation of native I_{Kr} in human cardiac myocytes (24,25) appeared to be faster than the I_{Kr} activation simulated by the original PB formulas. To formulate I_{Kr} kinetics, the recently developed HVM models (16,17) employed the experimental data from human ether-a-go-go-related gene (HERG) channels expressed in human embryonic kidney (HEK) cells (26,27), Chinese hamster ovary cells (28), or *Xenopus* oocytes (29). However, voltage- and time-dependent kinetics of expressed HERG channels appear to depend on cell lines or conditions for expression, as well as conditions for current recordings such as temperatures, and thus may be different from those of native I_{Kr} channels in human hearts (26–28,30–32). We therefore adopted the data from HVMs of Li et al. (24) for the steady-state activation curve ($p_{a,\infty}$) and the formula of Courtemanche et al. (19) based on the data from human atrial myocytes of Wang et al. (25) for the activation time constant (τ_{pa}). We also employed the expression of Courtemanche et al. (19) for the steady-state inactivation curve ($p_{i,\infty}$). No detailed experimental data are available on the time constant of I_{Kr} inactivation (τ_{pi}) in intact HVMs. Inactivation and recovery of native I_{Kr} in animal hearts or expressed HERG channels are very rapid (28,33); thus, we assumed that I_{Kr} inactivation is instantaneous. The maximum I_{Kr} conductance (g_{Kr}) was set equal to 12 pS/pF, according to the data of Li et al. (24). With this g_{Kr} value, the complete block of I_{Kr} prolonged the action potential duration (APD) of the model HVM paced at 1 Hz by 34.6–48.9%; the simulated APD prolongation by I_{Kr} block is comparable to the experimentally observed effects of the selective I_{Kr} blocker E-4031 as reported by Li et al. (24).

Formulation of I_{Ks}

On the basis of the recent data from Li et al. (24) and Virág et al. (34), the kinetics of I_{Ks} was reformulated as Eqs. 15–18. Voltage dependences of I_{Ks} kinetics in the current and original models are shown in Fig. 2 (*bottom*), together with experimental data for comparison; the model-generated I_{Ks} during voltage-clamp pulses are also depicted. Steady-state I_{Ks} activation curve (n_{∞}) is from Li et al. (24). Virág et al. (34) recently reported that I_{Ks} in HVMs slowly activates and rapidly deactivates. According to their report, therefore, we reformulated the time constant of I_{Ks} activation (τ_n) as Eq. 18. The expression of E_{Ks} is the same as for the PB model. The maximum conductance (g_{Ks}) was set equal to 36 pS/pF so as to yield the APD at 90% repolarization (APD_{90}) during 1 Hz pacing of 336 ± 16 ms, as reported by Li et al. (24).

Formulation of SR Ca^{2+} release

In the original PB model, SR Ca^{2+} release kinetics was represented by the formula that explicitly contains time t and also $\Delta[Ca^{2+}]_{i,2}$, which is not

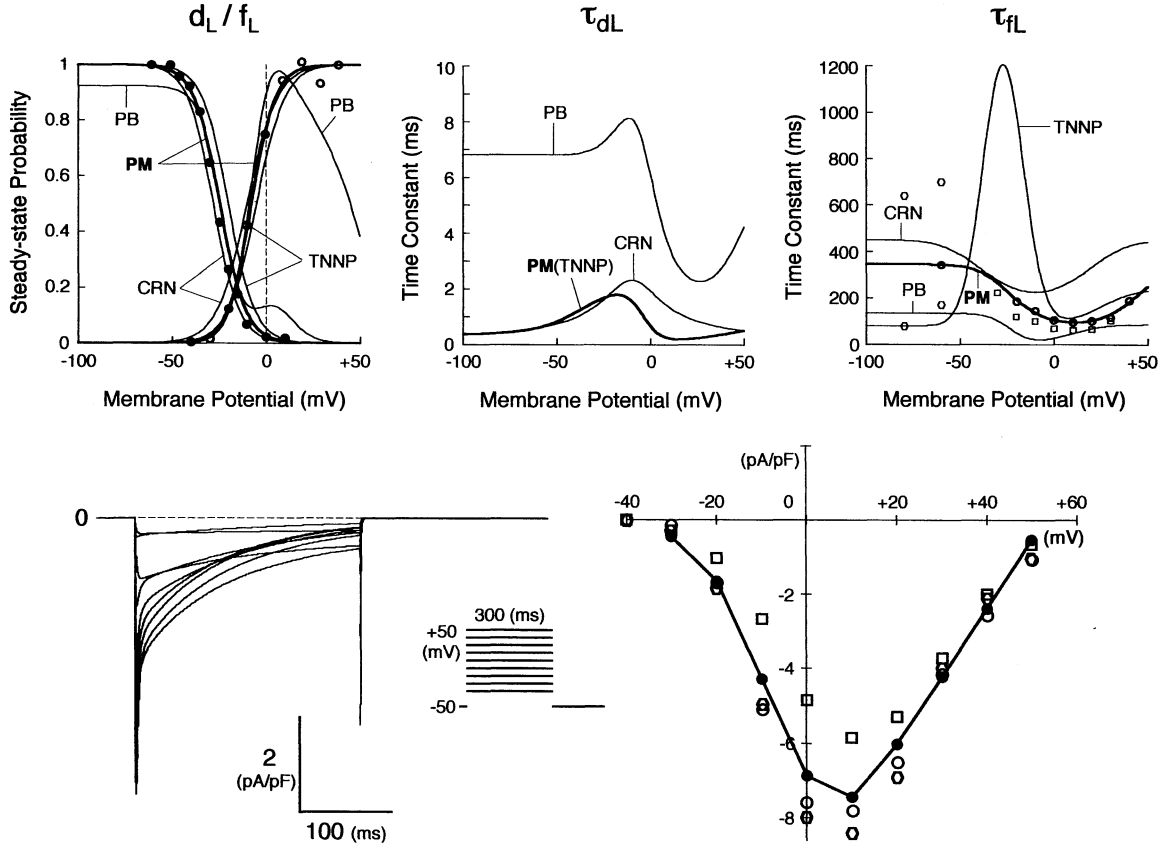

FIGURE 1 Kinetics of $I_{Ca,L}$. (*Top*) Voltage dependence of steady-state probabilities ($d_{L\infty}$, $f_{L\infty}$) and time constants for $I_{Ca,L}$ activation (τ_{dL}) and inactivation (τ_{fL}). Equations used for the current (modified) model are shown with the thick lines (labeled "PM"). For comparison, those for existing (original) models are also shown with the thin lines: PB, Priebe and Beuckelmann (15); TNNP, ten Tusscher et al. (16); CRN, Courtemanche et al. (19). The experimental data for $d_{L\infty}$, $f_{L\infty}$, and τ_{fL} are from Bénitah et al. (21) (*circles*), Pelzmann et al. (22) (*squares*), and Li et al. (23) (*hexagons*). (*Bottom*) Computed voltage-clamp records for $I_{Ca,L}$ (*left*) and peak $I_{Ca,L}$-V relationship (*right*). Currents were evoked by 300-ms step pulses from a holding potential of −50 mV to test potentials ranging from −30 to +50 mV in 10 mV increments. Simulating the whole-cell perforated-patch recording, $[Ca^{2+}]_i$ was not clamped, whereas $[Na^+]_i$ and $[K^+]_i$ were fixed at 5 and 140 mM, respectively. The experimental data for the peak $I_{Ca,L}$-V relation are from Bénitah et al. (21) (*open circles*), Pelzmann et al. (22) (*squares*), and Li et al. (23) (*hexagons*).

a state variable but the sum of net Ca^{2+} influx during the first 2 ms after initiation of the action potential (AP). Thus, the original PB model is a non-autonomous system, the vector field of which depends on time and initial conditions, not suitable for bifurcation analysis. We had therefore to renew the SR Ca^{2+} release formula to convert the model into an autonomous system. Owing to the lack of available data for updating the kinetic formulation of SR Ca^{2+} release in HVMs, we utilized simple expressions, Eqs. 47–51. The formula for conductance of the Ca^{2+} release channel (g_{rel}) was adopted from Faber and Rudy (20), with the P_{rel} value reduced to one-third of the original value to obtain the peak $[Ca^{2+}]_i$ transient of ~1 μM during APs elicited at 1 Hz. For gating behaviors of the Ca^{2+} release channel (d_R, f_R), we used the expressions similar to those for the $I_{Ca,L}$ gating variables to make the model an autonomous system suitable for bifurcation analyses.

Ion concentration homeostasis

The model also includes material balance expressions to define the temporal variation in $[Ca^{2+}]_i$, $[Na^+]_i$, and $[K^+]_i$, whereas $[Ca^{2+}]_o$, $[Na^+]_o$, and $[K^+]_o$ were fixed at 2, 140, and 5.4 mM, respectively. As pointed out by Hund et al. (35) and Krogh-Madsen et al. (36), the second-generation models incorporating ion concentration changes have two major problems: 1), drift, with very slow long-term trends in state variables; and 2), degeneracy, with nonuniqueness of steady-state solutions. The current model did not show a long-term drift in the intracellular ion concentrations but reached a steady state during pacing, as well as during BP oscillation, when the principle of charge conservation was taken into account (35).

An n-dimensional fully differential system formulated as a cardiac second-generation model can usually be converted into a differential-algebraic system composed of $n - 1$ differential equations and one algebraic equation, resulting in $n - 1$ equations for n unknowns (35,36). In such a system, the Jacobian matrix of which is singular, the EP or limit cycle is not unique but depends on initial conditions; e.g., our full system has a continuum of EPs, because Eq. 65 can be derived from Eqs. 66, 69, and 70 (see Appendix 2). Thus, second-generation models including our full system exhibit degeneracy not suitable for bifurcation analysis to be applicable to isolated equilibria. As suggested by Krogh-Madsen et al. (36), one of the ways to remove degeneracy and thus allow bifurcation analyses of isolated equilibria is to make some ionic concentrations fixed. Variations in $[K^+]_i$ during changes in parameters or stimulation rates (0.25–2 Hz) were relatively small (<5 mM), being too small to significantly alter the model cell behaviors. For stability and bifurcation analyses, therefore, $[K^+]_i$ was fixed at 140 mM. The degenerate system with the fixed $[K^+]_i$ has the finite number of EPs and limit cycles, being suitable for bifurcation analyses.

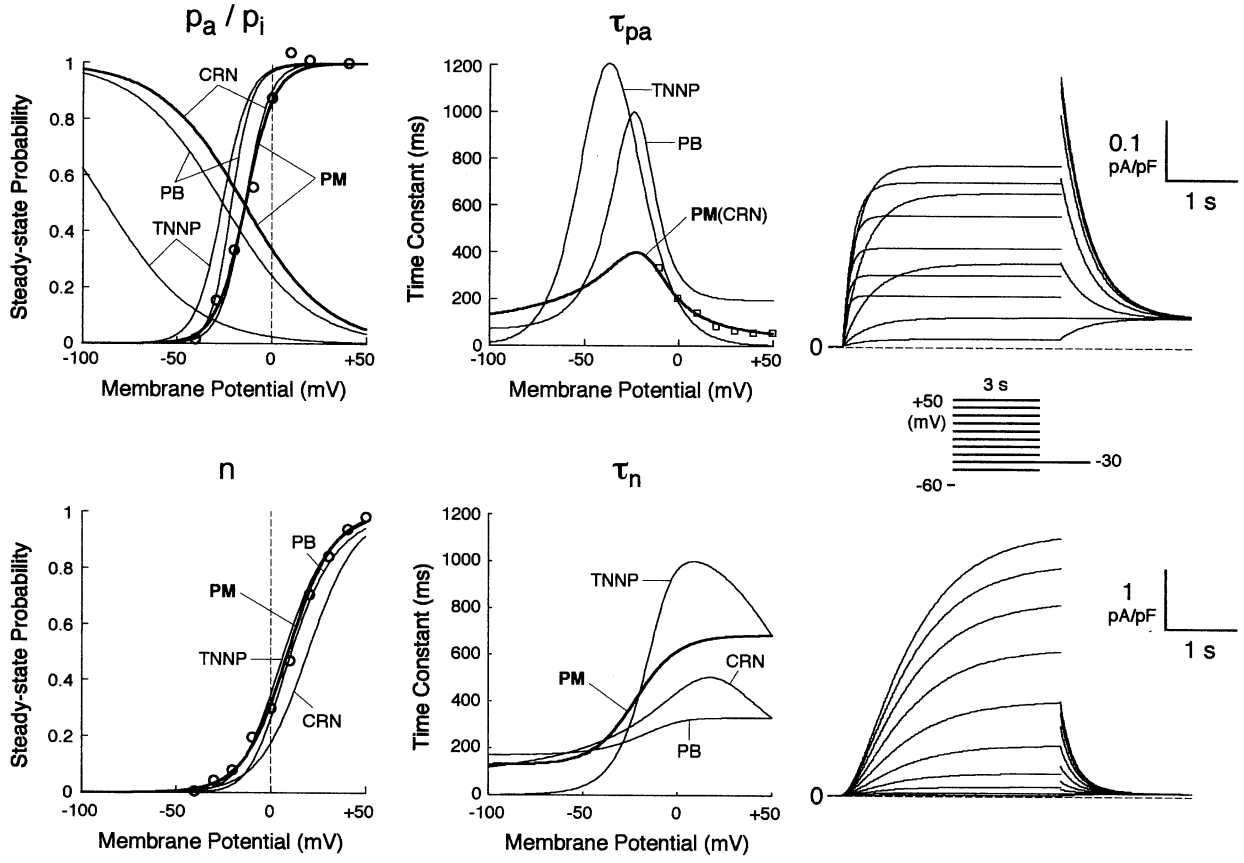

FIGURE 2 Kinetics of I_{Kr} (*top*) and I_{Ks} (*bottom*). (*Left, middle*) Voltage dependence of steady-state probabilities and time constants of I_{Kr} activation ($p_{a,\infty}$, τ_{pa}) and inactivation ($p_{i,\infty}$) as well as I_{Ks} activation (n_∞, τ_n). The thick lines are for this study (PM); the thin lines are from the existing models (PB, TNNP, CRN). The experimental data for $p_{a,\infty}$, τ_{pa}, and n_∞ are from Li et al. (24) (*circles*) and Wang et al. (25) (*squares*). (*Right*) Computed voltage-clamp records for I_{Kr} and I_{Ks}. Currents were elicited by 3-s step pulses from a holding potential of −60 mV to test potentials ranging from −50 to +50 mV in 10 mV increments.

Determination and validation of model HVM dynamics

Numerical methods for dynamic simulations of HVM behaviors

Dynamic behaviors of the model HVM were determined by solving a system of nonlinear ordinary differential equations numerically. Numerical integration, as well as bifurcation analyses, were performed on Power Macintosh G4 computers (Apple Computer, Cupertino, CA) with MATLAB 5.2 (The MathWorks, Natick, MA). We used the numerical algorithms available as MATLAB ODE solvers: 1), a fourth-order adaptive-step Runge-Kutta algorithm which includes an automatic step-size adjustment based on an error estimate (37), and 2), a variable time-step numerical differentiation approach selected for its suitability to stiff systems (38). The former (named *ode45*) is the best function for most problems. However, the latter (named *ode15s*) was much more efficient than *ode45* and both solvers usually yielded nearly identical results. Therefore, *ode15s* was usually used, and *ode45* was only sometimes used to confirm the accuracy of calculations. The maximum relative error tolerance for the integration methods was set to 1×10^{-6}.

Dynamic properties of the model HVM: simulated APs, ionic currents, and $[Ca^{2+}]_i$ dynamics

The steady-state AP, sarcolemmal currents, and $[Ca^{2+}]_i$ transient of the current model paced at 1 Hz with the standard parameter values are shown in Fig. 3 *A*. According to the report of Hund et al. (35), the stimulus current was assumed to carry K^+ ions into the cell for charge conservation. During pacing, the model cell dynamics reached a steady state, with no long-term drift in the state variables. Steady-state values of the resting potential, maximum upstroke velocity, and APD_{90} during 1 Hz pacing were −84.9 mV, 411 V/s, and 338 ms, respectively. The diastolic $[Ca^{2+}]_i$ and peak $[Ca^{2+}]_i$ transient in the model HVM paced at 1 Hz were 0.169 and 0.961 μM, respectively. The simulated AP parameters and $[Ca^{2+}]_i$ dynamics of the current and original HVM models are listed in Table 3, together with corresponding experimental data for comparison. The AP parameters and $[Ca^{2+}]_i$ dynamics of the current model appear to be in reasonable agreement with the mean experimental values recently determined for single HVMs, as well as those of the original PB and other HVM models. The values of $[Ca^{2+}]_{rel}$ and $[Ca^{2+}]_{up}$ were 0.41 mM (identical) for the resting state and 0.59–2.68 and 2.84–2.92 mM, respectively, in a steady state during 1 Hz pacing. These values are comparable to the experimental data from rat and rabbit ventricular myocytes (40,41), as well as those in the original PB model, although experimental values for HVMs are unknown.

Rate dependence of APD, $I_{Ca,L}$, $[Ca^{2+}]_i$ transients, and $[Na^+]_i$

We also tested the rate dependence of APD (dynamic restitution), as well as that of the $I_{Ca,L}$ waveform, $[Ca^{2+}]_i$ transients and $[Na^+]_i$ (Fig. 3 *B*). The steady-state values of APD_{90} at 0.5, 1, and 2 Hz were 369, 338, and 298 ms, respectively, compatible with the averaged experimental values (23,42).

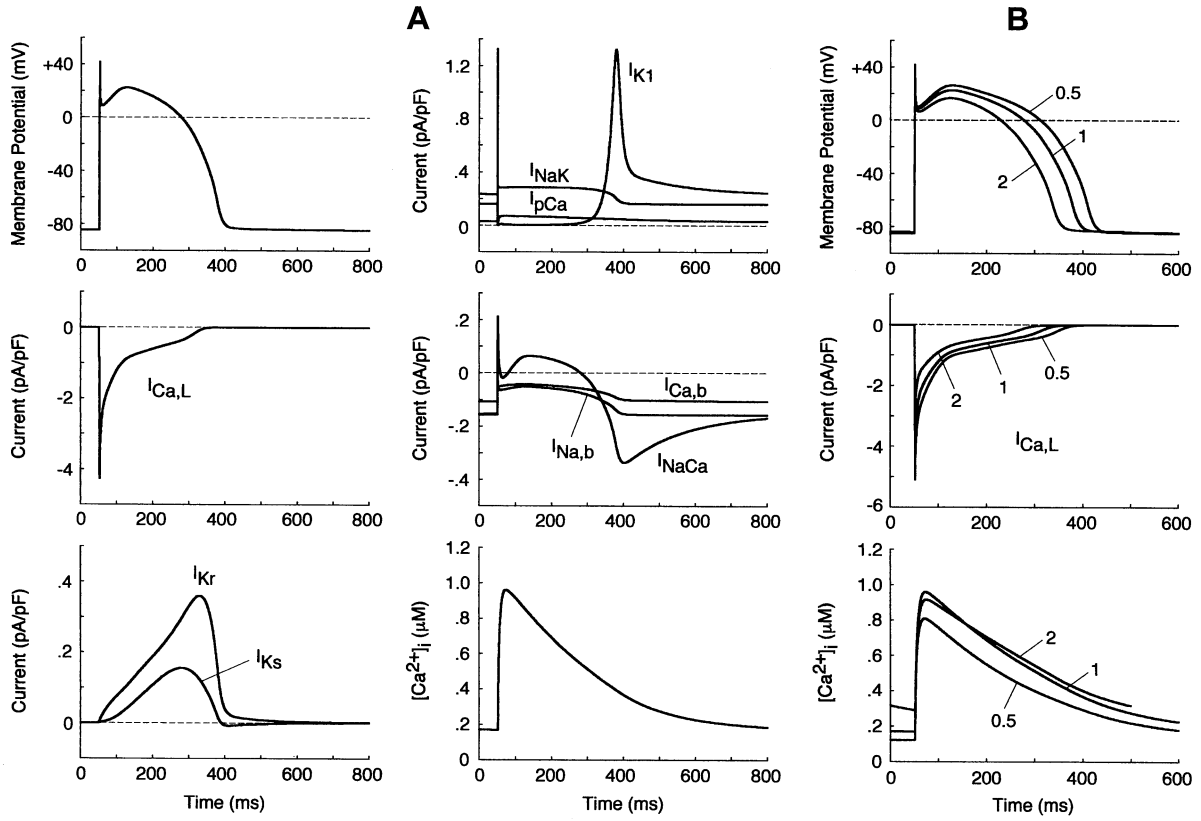

FIGURE 3 Simulated dynamics of the model HVM. (*A*) Steady-state behaviors of the AP, underlying sarcolemmal currents, and $[Ca^{2+}]_i$ transient. The model HVM was paced at 1 Hz with 1-ms stimuli of 80 pA/pF. Differential equations (Eqs. 55–64) were numerically solved for 20 min with the initial conditions appropriate to a resting state, which were determined by Eqs. 65–69 with $[K^+]_i$ fixed at 140 mM. Model cell behavior after the last stimulus (during the last AP) is depicted. (*B*) Rate dependence of APD, $I_{Ca,L}$, and $[Ca^{2+}]_i$ transients. The model HVM was paced at 0.5, 1, and 2 Hz with 1-ms stimuli of 80 pA/pF. The differential equations were numerically solved for 20 min at each pacing rate; model cell behaviors after the last stimulus are depicted.

$I_{Ca,L}$ attenuated with increasing the pacing rate as observed in the AP clamp experiment of Li et al. (23). The values of $[Na^+]_i$ during stimuli at 0 (resting state), 0.25, 0.5, 1, and 2 Hz averaged 6.14, 7.47, 8.26, 9.22, and 9.57 mM, respectively, comparable to experimental data (43,44).

The peak $[Ca^{2+}]_i$ transient predicted by the current model was a little smaller at 2 Hz than at 1 Hz. In most experiments, however, the peak $[Ca^{2+}]_i$ transient and/or developed tension increased as the pacing rate increased up to 2.5 Hz (45–47). This inconsistency may result from the lack of intracellular modulating factors such as those involved in the rate-dependent potentiation of $I_{Ca,L}$ (48,49). Alternatively, the kinetic formulation of $I_{Ca,L}$ and/or SR Ca^{2+} handling may be inappropriate. We found that the use of the τ_{fL} formula from the ten Tusscher et al. model (16) led to the successful reproduction of the rate-dependent increase in the peak $[Ca^{2+}]_i$ transient. Nevertheless, their τ_{fL} formula was not used, because it appeared not to fit the experimental data as shown in Fig. 1 and because a very large I_{Ks} (>8 times larger than the experimental values) was required to counteract the large $I_{Ca,L}$ during phase 2 (16). In the preliminary study, BP dynamics or bifurcation structures of the HVM model were not essentially altered by the use of different formulas for $I_{Ca,L}$ (τ_{fL}) or the change in the rate dependence of $[Ca^{2+}]_i$ transients.

Stability and bifurcation analyses

Constructing bifurcation diagrams

We examined how the stability and dynamics of the model cell alter with changes in bifurcation parameters and constructed bifurcation diagrams for one or two parameters. Bifurcation parameters chosen in this study were the maximum conductance of the ionic channels (g_{K1}, $g_{Ca,L}$, g_{Kr}, g_{Ks}) and amplitude of I_{NaCa} or I_{bias}; the maximum conductance and I_{NaCa} amplitude are expressed as normalized values, i.e., ratios to the control values.

In the HVM model with the fixed $[K^+]_i$, 14 state variables define a 14-dimensional state point in the 14-dimensional state space of the system. We calculated EPs and periodic orbits in the state space. An EP was determined as a point at which the vector field vanishes (i.e., $f(x) = 0$); steady-state values of the state variables were calculated by Eqs. 65–69 (see Appendix 2). Asymptotic stability of the EP was also determined by computing 14 eigenvalues of a 14 × 14 Jacobian matrix derived from the linearization of the nonlinear system around the EP (for more details, see Vinet and Roberge (7)). Periodic orbits were located with the MATLAB ODE solvers. When spontaneous oscillation (BP activity) appeared, the AP amplitude (APA) as a voltage difference between the maximum diastolic potential (MDP) and peak overshoot potential (POP), as well as the cycle length (CL), was determined for each calculation of a cycle. Numerical integration was continued until the differences in both APA and CL between the newly calculated cycle and the preceding one became $<1 \times 10^{-3}$ of the preceding APA and CL values. Potential extrema (MDP, POP) and CL of the steady-state oscillation were plotted against bifurcation parameters. When periodic behavior was irregular or unstable, model dynamics were computed for 60 s; all potential extrema and CL values were then plotted in bifurcation diagrams.

Codimension one and two bifurcations to occur in the model system were explored by constructing bifurcation diagrams with one and two parameters, respectively (10,11). For construction of one-parameter bifurcation diagrams in which values of a state variable at EPs or extrema of periodic orbits are shown as a function of one bifurcation parameter, a bifurcation parameter was systematically changed while keeping all other parameters at their

TABLE 3 AP parameters and $[Ca^{2+}]_i$ dynamics for single HVMs paced at 1 Hz: model-generated values and experimentally observed values

	$[Ca^{2+}]_o$ (mM)	$[K^+]_o$ (mM)	$[Na^+]_i$* (mM)	RP (mV)	V_{max} (V/s)	APD_{90} (ms)	$[Ca^{2+}]_{i,r}$† (nM)	$\Delta[Ca^{2+}]_i$ (nM)
Model values	2.0	4.0	10	−91.2	385	357	200	900
Priebe-Beuckelmann (15)‡	2.0	4.0	10	−90.2	386	357	400	0
Bernus et al. (18)	2.0	4.0	10	−90.4	369	333	119	784
Sachse et al. (39)	2.0	5.4	>11.5	−87.3	288	276	70	930
Ten Tusscher et al. (16)	2.0	4.0	9.80	−90.7	350	322	68	797
Iyer et al. (17)	2.0	5.4	9.18	−84.9	411	338	169	792
Current (modified) model								
Experimental values								
Peeters et al. (90)	1.2	4.0		−84 ± 6		381 ± 94		
Li et al. (24)	1.0	5.4	10	−83 ± 3		336 ± 16		
Li et al. (42)	2.0	5.4	10	−82 ± 2		298 ± 17		
Péréon et al. (91), epicardium	2.7	4.0		−86 ± 1	196 ± 20	324 ± 19		
Péréon et al. (91), midmyocardium	2.7	4.0		−86 ± 1	446 ± 46	432 ± 19		
Piacentino et al. (92)	1.0	5.4	12.5				153 ± 20	804 ± 197

*The steady-state mean $[Na^+]_i$ values during 1 Hz pacing are shown for the TNNP (16), Iyer et al. (17), and the current model; the resting state or fixed value is shown for others. The experimental values were for the perforated- or ruptured-patch recording. A $[Na^+]_i$ value was unknown (not shown) when the conventional microelectrode method was used.

†Minimum $[Ca^{2+}]_i$ values during the diastolic phase, i.e., $[Ca^{2+}]_i$ values at the end of phase 4.

‡Data for AP parameters are from Table 3 of Bernus et al. (18). The values of $[Ca^{2+}]_{i,r}$ (200) and $\Delta[Ca^{2+}]_i$ (900) are only approximations from the original figures.

Abbreviations: RP, resting potential; V_{max}, maximum upstroke velocity.

standard values. The membrane potential (V) at EPs (steady-state branches) and local potential extrema of periodic orbits (periodic branches) were determined and plotted for each value of the bifurcation parameter. The saddle-node bifurcation point at which two EPs coalesce and disappear was determined as a point at which the steady-state current-voltage (I/V) curve and zero-current axis come in touch with each other. The Hopf bifurcation point at which the stability of an EP reverses was also detected by the stability analysis as described above. For construction of two-parameter bifurcation diagrams in which codimension one bifurcation points are plotted in a parameter plane, the secondary parameter was systematically changed with the primary parameter fixed at various different values. The path of saddle-node and Hopf bifurcation points was traced in the parameter plane; i.e., bifurcation values for the secondary parameter were plotted as a function of the primary parameter.

Definition and evaluation of structural stability for the BP system

We also evaluated the structural stability of the BP system, which is defined as the robustness of pacemaker activity to various interventions or modifications that may cause a bifurcation to quiescence or irregular dynamics (11). Interventions or modifications leading to quiescence or irregular dynamics include injections of I_{bias}, electrotonic loads of normal HVMs, current leakage via myocardial injury, and intrinsic changes in channel conductance or gating kinetics. In this study, the structural stability of the BP system was tested for hyperpolarizing and depolarizing loads by exploring bifurcation structures during applications of I_{bias}.

The way of evaluating the structural stability to I_{bias} is essentially the same as in our previous study for the SA node pacemaker (11). Changes in V_0 and its stability with I_{bias} applications were depicted as the I_{bias}-V_0 curve (for more details, see Fig. 1 of Kurata et al. (11)). There are one or two Hopf bifurcation points and two saddle-node bifurcation points corresponding to the current exrema in the I_{bias}-V_0 curve. In the unstable I_{bias} region between two Hopf (or a Hopf and saddle-node) bifurcation points, the system has an unstable EP only, usually exhibiting stable limit cycles without annihilation (6,8). When the system removes to the stable I_{bias} region, it would come to rest at the stable EP via gradual decline of limit cycles, annihilation, or irregular dynamics, as reported by Guevara and Jongsma (8). Note that *system A* is considered structurally more stable than *system B* when the amplitude of I_{bias} required for stabilizing an EP or causing a bifurcation to quiescence is greater in *system A* than in *system B* (11). Thus, the larger the unstable I_{bias} range over which limit cycles continue is, the more structurally stable the system is.

The Hopf and saddle-node bifurcation points, as well as the control V_0 at $I_{bias} = 0$, in the I_{bias}-V_0 curve were determined as functions of bifurcation parameters and plotted on both the potential and current coordinates, as in previous studies (7,11). Exploring how the unstable V_0 and I_{bias} regions change with decreasing or increasing the sarcolemmal currents would enable us to determine the contribution of each current to the structural stability of the BP system to hyperpolarizing or depolarizing loads, as well as to EP instability itself, which is evaluated by positive real parts of eigenvalues of Jacobian matrices (see Fig. 4 of Kurata et al. (11)).

Definitions of terms specific to nonlinear dynamics and bifurcation theory

Autonomous system

An nth-order "autonomous" continuous-time dynamical system is defined by the state equation $d\boldsymbol{x}/dt = \boldsymbol{f}(\boldsymbol{x})$, where the vector field $\boldsymbol{f}$, a smooth function of the state variable $\boldsymbol{x} = \boldsymbol{x}(t)$, does not depend on time, but depends only on the state variable $\boldsymbol{x}$ (13).

Nonautonomous system

An nth-order "nonautonomous" continuous-time dynamical system is defined by the state equation $d\boldsymbol{x}/dt = \boldsymbol{f}(\boldsymbol{x}, t)$, where the vector field $\boldsymbol{f}$ depends on time, i.e., explicitly contains time t (13).

EP

A time-independent steady-state point at which the vector field vanishes (i.e., $d\boldsymbol{x}/dt = 0$) in the state space of an autonomous system, constructing the steady-state branch in one-parameter bifurcation diagrams. This state point corresponds to the zero-current crossing in the steady-state I/V curve, i.e., a quiescent state of a cell if it is stable.

Periodic orbit

A closed trajectory in the state space of a system, constructing the periodic branch in one-parameter bifurcation diagrams.

Limit cycle

A periodic limit set onto which a trajectory is asymptotically attracted in an autonomous system. A stable limit cycle corresponds to an oscillatory state, i.e., pacemaker activity, of a cell.

Bifurcation

A qualitative change in a solution of differential equations caused by altering parameters, e.g., a change in the number of EPs or periodic orbits, a change in the stability of an EP or periodic orbit, and a transition from a periodic to quiescent state. Bifurcation phenomena we can see in cardiac myocytes include a generation or cessation of pacemaker activity and occurrence of irregular dynamics such as skipped-beat runs and early afterdepolarizations.

Hopf bifurcation

This is a bifurcation at which the stability of an EP reverses with emergence or disappearance of a limit cycle, occurring when eigenvalues of a Jacobian matrix for the EP have a single complex conjugate pair and its real part reverses the sign through zero.

Saddle-node bifurcation

This is a bifurcation at which two EPs (steady-state branches) or two periodic solutions (periodic branches) emerge or disappear. The saddle-node bifurcation of EPs occurs when one of eigenvalues of a Jacobian matrix is zero.

Codimension

The codimension of a bifurcation is the minimum dimension of the parameter space in which the bifurcation may occur in a persistent way (12,50). In other words, the codimension is the number of independent conditions determining the bifurcation (14). A bifurcation with codimension one is a point in one-parameter bifurcation diagrams such as Fig. 6 or a line in two-parameter bifurcation diagrams such as Fig. 7, whereas a bifurcation with codimension two is a point in the two-parameter space.

RESULTS

BP generation in I_{K1}-downregulated HVM

BP activity appears in model HVM during I_{K1} suppression

We first examined whether I_{K1} downregulation leads to BP generation in the model HVM by decreasing g_{K1} at an interval of 0.01 (1%). Spontaneous oscillations (BP activity) abruptly appeared when g_{K1} was reduced to 0.15 (15%). Fig. 4 shows the simulated BP activity of the I_{K1}-downregulated HVM with g_{K1} of 0.15 or 0, depicting the membrane potential oscillations, underlying sarcolemmal currents, and $[Ca^{2+}]_i$ transients in steady state. The values of MDP, POP, APA, CL, and maximum upstroke velocity were determined for the BP oscillations at each g_{K1} value. The simulated AP parameters are listed in Table 4, together with the data from the guinea pig ventricle (3) and rabbit SA node (51) models, as well as from real BP systems (1,52), for comparison. The average $[Na^+]_i$ during the BP oscillations at g_{K1} of 0.15 and 0 were 6.55 and 6.42 mM, respectively. Decreasing g_{K1} caused the decrease of

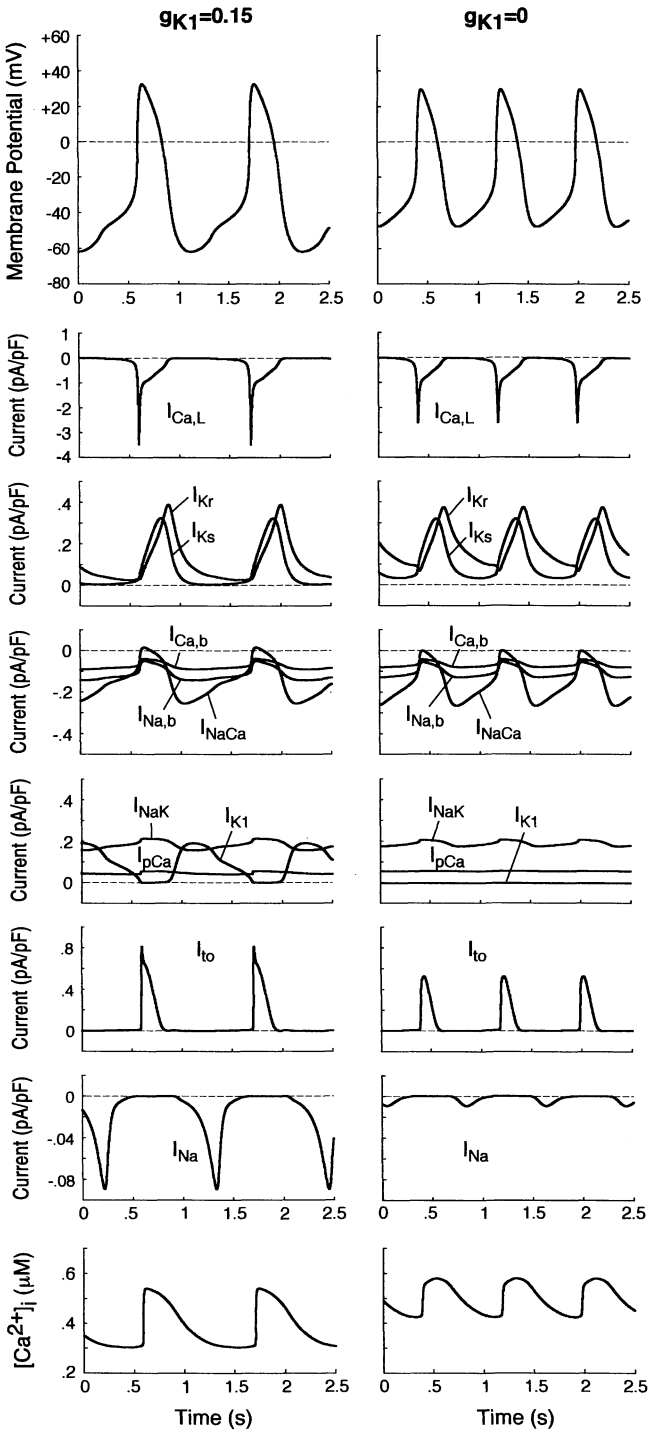

FIGURE 4 Simulated steady-state BP activities (spontaneous APs, ionic currents, and $[Ca^{2+}]_i$ dynamics) in the model HVM at $g_{K1} = 0.15$ (*left*) and 0 (*right*). Differential equations (Eqs. 55–63) were numerically solved for 20 min at each g_{K1} with initial conditions appropriate to an EP and a 1-ms stimulus of 1 pA/pF for triggering an AP; model cell behaviors during the last 2.5 s starting from MDP are depicted. Note the differences in the ordinate scales for individual currents.

TABLE 4 AP parameters for pacemaker systems: Model-generated values and experimental values

	Normalized g_{K1}	MDP (mV)	POP (mV)	APA (mV)	CL (ms)	V_{max} (V × s^{-1})
Model values						
Silva and Rudy (3)*	0.19	−67.3			594	15
	0				366	
This study	0.15	−61.9	+32.7	94.7	1117	3.2
	0.10	−54.3	+31.6	86.0	938	2.8
	0	−47.9	+29.8	77.7	795	2.3
Kurata et al. (51)†	0	−58.6	+16.6	75.2	308	6.4
Experimental values						
Miake et al. (1)*	0.20	−60.7			600	
Plotnikov et al. (52)‡					1091	

*Data from the model and real guinea pig ventricular myocytes.
†Primary pacemaker model for the rabbit SA node.
‡Data for Purkinje myocytes expressing I_h (HCN2) in the canine left ventricle.

APA with depolarization of MDP, decrease of CL, increase of $[Ca^{2+}]_i$, and decrease of $[Na^+]_i$. Consistent with the result from the guinea pig ventricular model (3), I_{NaCa} was the dominant inward current during phase 4 depolarization in the HVM pacemaking. In contrast, $I_{Ca,L}$ was very small during the early phase of the depolarization, although predominantly contributing to phase 0 upstroke. I_{Na} was also very small due to the voltage-dependent inactivation.

Ionic basis of phase 4 depolarization in simulated BP activity

Before investigating the dynamical mechanisms of BP generation via bifurcation analyses of the HVM model, we examined the ionic basis of phase 4 depolarization of the BP activity. The contributions of I_{Kr} and I_{Ks} deactivation, as well as individual inward currents ($I_{Ca,L}$, I_{Na}, I_{NaCa}, $I_{Na,b}$, $I_{Ca,b}$), to the pacemaker depolarization were assessed by the conventional freezing and blocking methods (53–55). Phase 4 depolarization of the I_{K1}-reduced BP system disappeared on clamping I_{Kr} deactivation (gating variable p_a) at the time of MDP, but not on clamping I_{Ks} deactivation (gating variable n). Thus, the g_{Kr}-decay theory for the natural SA node pacemaker (53–55) appears to be applicable to the HVM pacemaker as well. Removal of $I_{Ca,L}$ at the time of MDP little altered the initial phase of pacemaker depolarization, although reducing the rate of the later phase depolarization with cessation of BP activity. Eliminating I_{Na} did not significantly affect BP oscillations. Furthermore, in the I_{K1}-removed system, eliminating I_{NaCa} (the most dominant pacemaker current) at the MDP abolished phase 4 depolarization, leading to cessation of BP activity, whereas the removal of $I_{Na,b}$ (the second dominant pacemaker current) or $I_{Ca,b}$ only reduced the depolarization rate.

Bifurcation structure of HVM system during I_{K1} suppression

BP activity abruptly appears around unstable EP via saddle-node bifurcation

To elucidate the dynamical mechanisms of BP generation, we explored EP stability, dynamics, and bifurcation structures of the HVM system during I_{K1} suppression by constructing bifurcation diagrams for g_{K1}. As shown in Fig. 5, the zero-current potential in the steady-state I/V curve, as well as steady-state $[Ca^{2+}]_i$ and $[Na^+]_i$, was plotted as a function of g_{K1}; when BP activity appeared, AP parameters (MDP, POP, CL), extrema of $[Ca^{2+}]_i$, and average $[Na^+]_i$ were also plotted. There are three EPs corresponding to the zero-current crossings of the I/V curve in the state space of the system at $g_{K1} = 1$ (denoted as EP1, EP2, and EP3). The stability analysis revealed that EP1 with the most depolarized potential as well as EP2 is unstable, whereas EP3 with the most negative potential corresponding to the resting state is stable. The zero-current potential at EP3 positively shifted with decreasing g_{K1}; the stable EP3 (and EP2) disappeared via a saddle-node bifurcation when g_{K1} reduced to 0.154. After the bifurcation, the system has only one EP at depolarized potentials (EP1), which is always unstable, not stabilized during g_{K1} decreases. Limit cycles (BP oscillations) abruptly emerged around the unstable EP1 on occurrence of the saddle-node bifurcation, with APA and CL gradually decreasing during further reductions in g_{K1}.

Decrease in $[Na^+]_i$ accelerates BP generation

The steady-state $[Na^+]_i$, 6.14 mM in the control resting state (at $g_{K1} = 1$), reduced as g_{K1} decreased, reaching 4.64 mM just before the saddle-node bifurcation at $g_{K1} = 0.154$ (see Fig. 5, *right bottom*). This reduction in $[Na^+]_i$ during I_{K1} suppression was due to the enhancement of Na^+ efflux via the Na^+-K^+ pump, as well as decrease of Na^+ influx via the Na^+/Ca^{2+} exchanger and $I_{Na,b}$, with resting potential depolarization. To determine how the $[Na^+]_i$ decrease affects BP generation, we constructed bifurcation diagrams for g_{K1} using the reduced system with $[Na^+]_i$ fixed at the control value of 6.14 mM or critical value of 4.64 mM (data not shown). The critical g_{K1} at which BP activity emerges via a saddle-node bifurcation was larger in the system with the reduced $[Na^+]_i$ of 4.64 mM (0.153) than with the control $[Na^+]_i$ of 6.14 mM (0.117), suggesting that the $[Na^+]_i$ reduction facilitates BP generation during I_{K1} suppression.

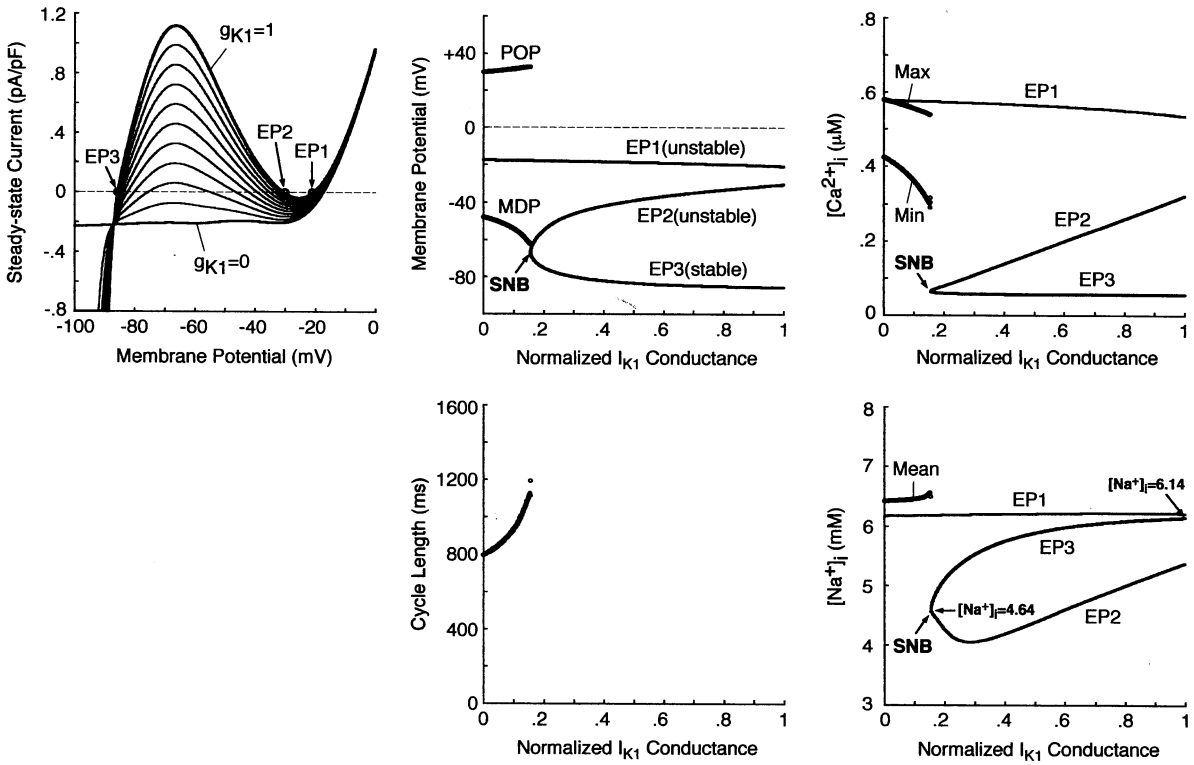

FIGURE 5 Bifurcation structure of the model HVM during g_{K1} decreases. (*Left*) Steady-state I/V relations for $g_{K1} = 0 - 1$, depicted at an interval of 0.1 with $[K^+]_i$ fixed at 140 mM. The zero-current crossings, corresponding to EPs, are designated by EP1, EP2, and EP3. (*Middle*) A bifurcation diagram for g_{K1} with the steady-state (*EP1–3*) and stable periodic (*MDP*, *POP*) branches (*top*), and CL plotted as a function of g_{K1} (*bottom*). EPs were determined by the algebraic equations (Eqs. 65–69). The model cell dynamics were computed by numerically solving the differential equations (Eqs. 55–63) for 10 min at each g_{K1}, which was reduced at an interval of 0.001, with the initial $[Na^+]_i$ at $g_{K1} = 1$ set equal to 6.14 mM. The saddle-node bifurcation point at which EP2 and EP3 merge together and disappear is located (labeled *SNB* at $g_{K1} = 0.154$). (*Right*) Steady-state $[Ca^{2+}]_i$ (*top*) and $[Na^+]_i$ (*bottom*) at EPs as functions of g_{K1}. The minimum (*Min*) and maximum (*Max*) of $[Ca^{2+}]_i$, as well as average $[Na^+]_i$, during the BP oscillations are also plotted. Note that the steady-state $[Na^+]_i$ at EP3 reduces with decreasing g_{K1}.

Ionic bases of EP instability and BP generation in I_{K1}-downregulated HVM

Instability of the EP at depolarized potentials (EP1) appears to be essentially important for BP generation. To elucidate the ionic mechanisms of EP instability and BP generation, therefore, we further explored how modulating individual sarcolemmal currents or $[Ca^{2+}]_i$ transients affects EP stability, oscillation dynamics, and bifurcation structures of the BP system. We focused on $I_{Ca,L}$, I_K, and I_{NaCa}, which appear to be essentially important for BP generation.

Influences of blocking $I_{Ca,L}$ or I_K on stability and dynamics of the BP system

Fig. 6 shows the effects of reducing the maximum conductance of $I_{Ca,L}$ ($g_{Ca,L}$), I_{Kr} (g_{Kr}), or I_{Ks} (g_{Ks}) on EP stability and BP dynamics of the I_{K1}-removed system. The zero-current potential (EP1) negatively shifted with decreasing $g_{Ca,L}$; the EP became stable via a Hopf bifurcation when $g_{Ca,L}$ was reduced by 86.6%. During the $g_{Ca,L}$ decreases, a limit cycle (BP oscillation) gradually contracted in size and finally disappeared at the Hopf bifurcation point. In contrast, a Hopf bifurcation to abolish BP activity did not occur during decreases in g_{Kr} or g_{Ks}, although APA significantly reduced with decreasing g_{Kr}. Spontaneous oscillation continued even when I_{Kr} or I_{Ks} was completely blocked, whereas it was abolished by eliminating both I_{Kr} and I_{Ks}.

As shown in Fig. 7, we also examined the effects of blocking $I_{Ca,L}$, I_{Kr}, or I_{Ks} on the unstable V_0 and I_{bias} regions in the I_{bias}-V_0 curve for further clarifying the contributions of the individual currents to EP instability and structural stability to depolarizing or hyperpolarizing loads of the BP system. Hopf and saddle-node bifurcation points in the I_{bias}-V_0 curve determined with decreasing conductance values were plotted on the potential and current coordinates to display how blocking each current shrinks the unstable ranges where BP oscillations occur (for more details, see Theory and Methods). The more prominent shrinkage in the unstable V_0 region is, the greater the contribution of the current to EP instability is; the more prominent shrinkage in the unstable I_{bias} region is, the greater the contribution to the robustness to depolarizing or hyperpolarizing loads is. The unstable regions, shrinking with decreases in $g_{Ca,L}$, disappeared via a codimension two saddle-node bifurcation at

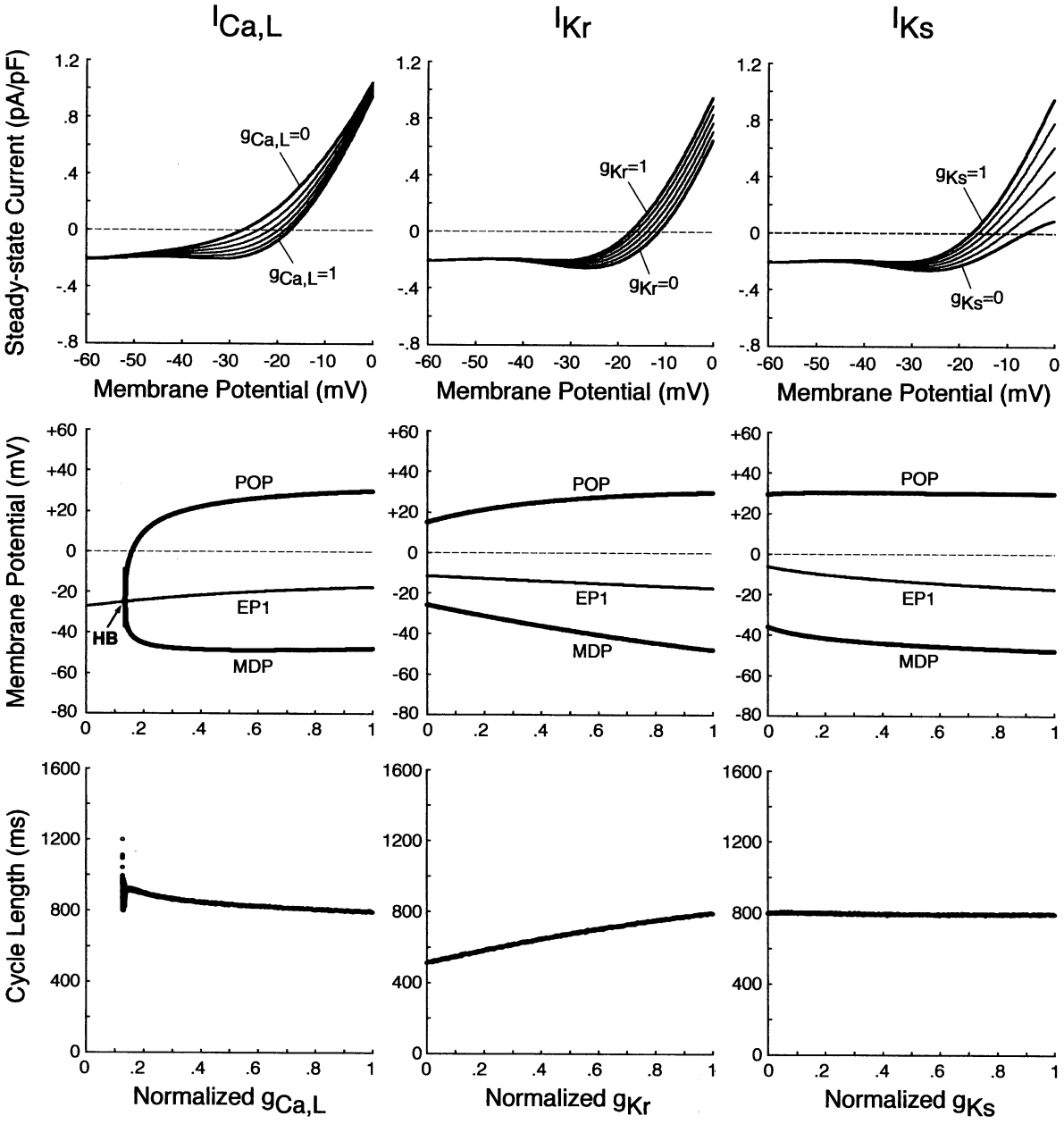

FIGURE 6 EP stability and BP dynamics of the I_{K1}-removed system during inhibition of $I_{Ca,L}$, I_{Kr}, or I_{Ks}. (*Top*) Steady-state I/V relations for $g_{Ca,L} = 0 - 1$ (*left*), $g_{Kr} = 0 - 1$ (*middle*), and $g_{Ks} = 0 - 1$ (*right*), depicted at an interval of 0.2. (*Middle, bottom*) Bifurcation diagrams with the steady-state (*EP1*) and stable periodic (*MDP, POP*) branches (*middle*), as well as CL (*bottom*), are shown as functions of $g_{Ca,L}$, g_{Kr}, or g_{Ks}, which was reduced at an interval of 0.001. The differential equations were numerically solved for 2–3 min at each conductance value. A Hopf bifurcation occurred at $g_{Ca,L} = 0.134$ (labeled *HB*), with the loci of MDP and POP converging at the bifurcation point.

a 87.4% reduction of $g_{Ca,L}$. Pacemaker activity never appeared in the system with $g_{Ca,L}$ reduced to less than the saddle-node bifurcation value. In contrast, reducing g_{Kr} or g_{Ks} little affected the unstable V_0 range, eigenvalues of Jacobian matrices at V_0 being not significantly altered. The unstable I_{bias} region shrunk with decreasing g_{Kr} or g_{Ks}, though it did not disappear even when I_{Kr} or I_{Ks} was completely blocked; the robustness to depolarizing I_{bias} was attenuated by decreasing g_{Kr} or g_{Ks}.

Effects of incorporating various K^+ currents on stability and automaticity of an I_K-removed system

The results shown in Figs. 6 and 7 suggest that I_{Kr} or I_{Ks} contributes little to the instability of the EP leading to the generation of spontaneous oscillations. To elucidate the roles of I_{Kr} and I_{Ks} in the HVM pacemaking, we tested how the stability and dynamics of the reduced BP system not including either I_{Kr} or I_{Ks} are affected by incorporating different K^+ currents. Both I_{Kr} and I_{Ks} were first removed from the

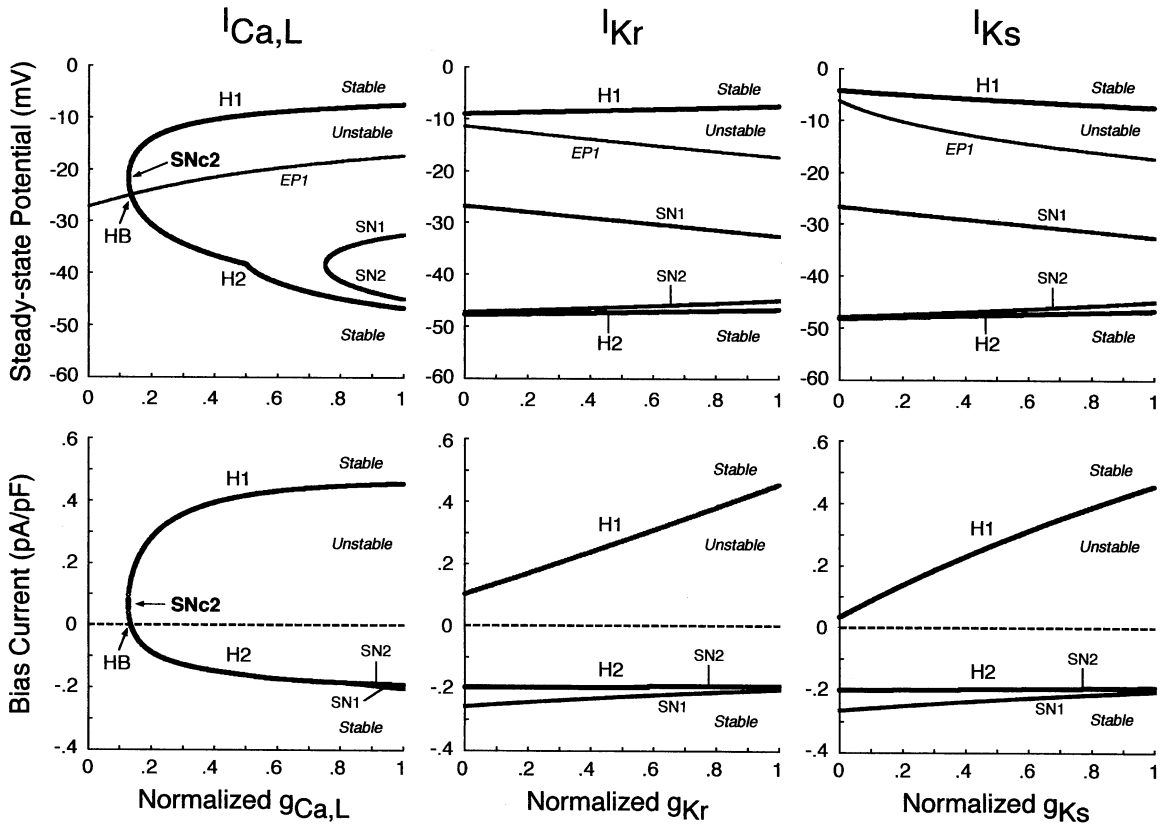

FIGURE 7 Changes in the unstable regions of the I_{bias}-V_0 curve during inhibition of $I_{Ca,L}$, I_{Kr}, or I_{Ks}. Displacements of Hopf (*H1*, *H2*) and saddle-node (*SN1*, *SN2*) bifurcation points in the I_{bias}-V_0 curve with decreasing $g_{Ca,L}$, g_{Kr}, or g_{Ks} at an interval of 0.001 are shown for the I_{K1}-removed BP system. Values of V_0 and I_{bias} at the bifurcation points were plotted on the potential (*top*) and current (*bottom*) coordinates, respectively, as functions of the conductance. The path of the control V_0 at $I_{bias} = 0$ (i.e., *EP1* in Fig. 6) is also shown on the potential coordinates, intersecting the locus of H2 at $g_{Ca,L} = 0.134$ (labeled *HB*). Note that the unstable region exists between H1 and H2 (or *H1* and *SN2*), where spontaneous oscillations occur. A codimension two saddle-node bifurcation at which the loci of H1 and H2 merge together, i.e., the unstable region disappears occurred at $g_{Ca,L} = 0.126$ (labeled *SNc2*).

standard I_{K1}-eliminated BP system, and the background K^+ current of linear I/V relation ($I_{K,b}$) or the original I_{Kr} or I_{Ks} (one of the three) was then incorporated. Eliminating both I_{Kr} and I_{Ks} abolished BP activity, with the model cell coming to a rest at a stable zero-current potential of +16.15 mV. Fig. 8 shows how EP stability and automaticity of the reduced system change with increasing the K^+ current conductance up to 10–50 pS/pF. As the K^+ conductance increased, the zero-current potential was negatively shifted and eventually destabilized via a Hopf bifurcation, with limit cycles emerging at the bifurcation. It should be noted that all the K^+ currents, including $I_{K,b}$, could individually create an unstable EP and induce spontaneous oscillations. However, $I_{K,b}$, the effect of which was very similar to the electrotonic influence of the adjacent normal HVM in a coupled-cell system (data not shown), produced the oscillation of relatively small amplitude and low upstroke velocity, as well as unstable CL and irregular dynamics. The $I_{K,b}$ conductance ($g_{K,b}$) range where an EP is unstable and spontaneous oscillations occur was very limited, with further increases in $g_{K,b}$ leading to quiescence via emergence of a stable EP. In contrast, I_{Kr} could yield the large amplitude oscillation with relatively high upstroke velocity and stable CL; however, I_{Kr} caused irregular dynamics at higher g_{Kr} values (>31.5 pS/pF), whereas I_{Ks} did not.

We further examined how incorporating the K^+ currents affects the structural stability of the reduced model to depolarizing or hyperpolarizing loads. The unstable regions in the I_{bias}-V_0 curve were determined for individual K^+ currents with the conductance increased up to 50 pS/pF (data not shown). Note that the structural stability to hyperpolarizing or depolarizing loads is considered as improved when the unstable I_{bias} region is enlarged, i.e., when larger I_{bias} is required to cause a bifurcation to quiescence. The results are summarized as follows: 1), Increasing I_{Kr} (g_{Kr}) continuously enlarged the unstable I_{bias} region, sufficiently improving the structural stability to depolarizing I_{bias}; 2), I_{Ks} could also enlarge the unstable I_{bias} region, but did not improve the structural stability as efficiently as I_{Kr}; and 3), $I_{K,b}$ could not enlarge the I_{bias} region of instability; with increasing $g_{K,b}$, the unstable regions shrunk and finally disappeared via a codimension two saddle-node bifurcation. These findings are essentially the same as those reported for the SA node pacemaker (see Fig. 9 of Kurata et al. (11)).

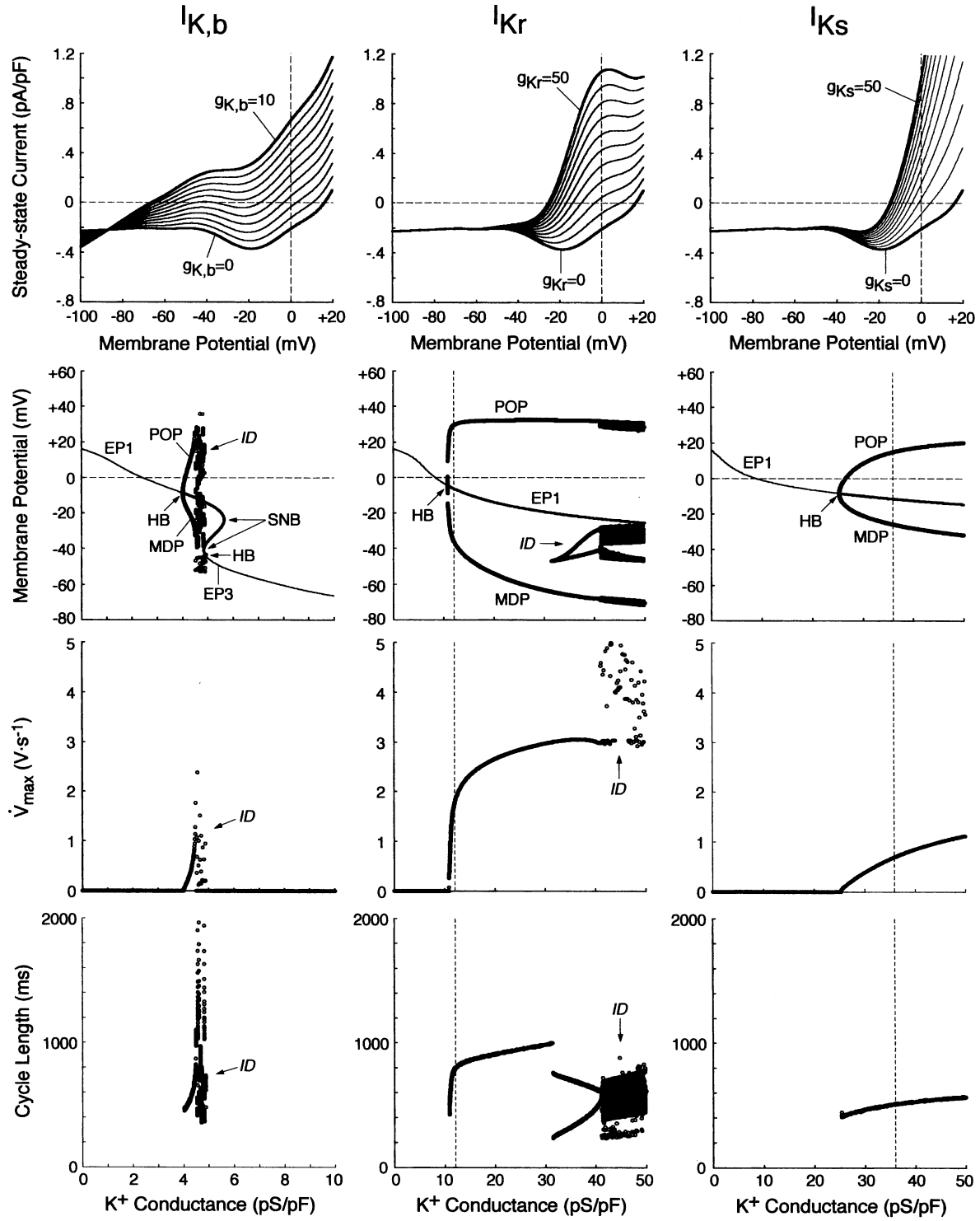

FIGURE 8 Effects of incorporating various K^+ currents with different kinetics ($I_{K,b}$, I_{Kr}, or I_{Ks}) on EP stability and dynamics of the I_K-removed model cell ($g_{K1} = 0$). (*Top*) Steady-state I/V relations for $g_{K,b} = 0$–10 pS/pF (*left*), $g_{Kr} = 0$–50 pS/pF (*middle*), and $g_{Ks} = 0$–50 pS/pF (*right*), depicted at an interval of 1 or 5 pS/pF. (*Middle, bottom*) Oscillatory behaviors, as well as zero-current potentials and their stability, of the model system, calculated during increases in $g_{K,b}$, g_{Kr}, or g_{Ks} at an interval of 0.01–0.1 pS/pF. Bifurcation diagrams with the steady-state (*EP1–3*) and periodic (*MDP*, *POP*) branches, as well as Hopf bifurcation (*HB*) and saddle-node bifurcation (*SNB*) points, were constructed for $g_{K,b}$, g_{Kr}, or g_{Ks} (*middle*). Maximum upstroke velocity (V_{max}) and CL of the potential oscillations were also plotted against $g_{K,b}$, g_{Kr}, or g_{Ks} (*bottom*). The vertical lines for I_{Kr} and I_{Ks} represent the standard values of g_{Kr} (12 pS/pF) and g_{Ks} (36 pS/pF). The symbol "*ID*" designates the irregular dynamics.

Influences of blocking I_{NaCa} or $[Ca^{2+}]_i$ transients on the stability and dynamics of the BP system

SR Ca^{2+} release, $[Ca^{2+}]_i$ transients, and activation of I_{NaCa} possibly play an important role in the generation and regulation of BP activity; as in the guinea pig ventricular pacemaking (3), I_{NaCa} was the dominant pacemaker current in the HVM pacemaking (Fig. 4). We therefore assessed the contributions of I_{NaCa} and $[Ca^{2+}]_i$ transients (SR Ca^{2+} release) to the EP instability and oscillation dynamics of the BP system by decreasing I_{NaCa} and/or clamping $[Ca^{2+}]_i$. As shown in Fig. 9 (*left*), BP oscillation ceased via a Hopf bifurcation when I_{NaCa} was reduced by 99.44% in the

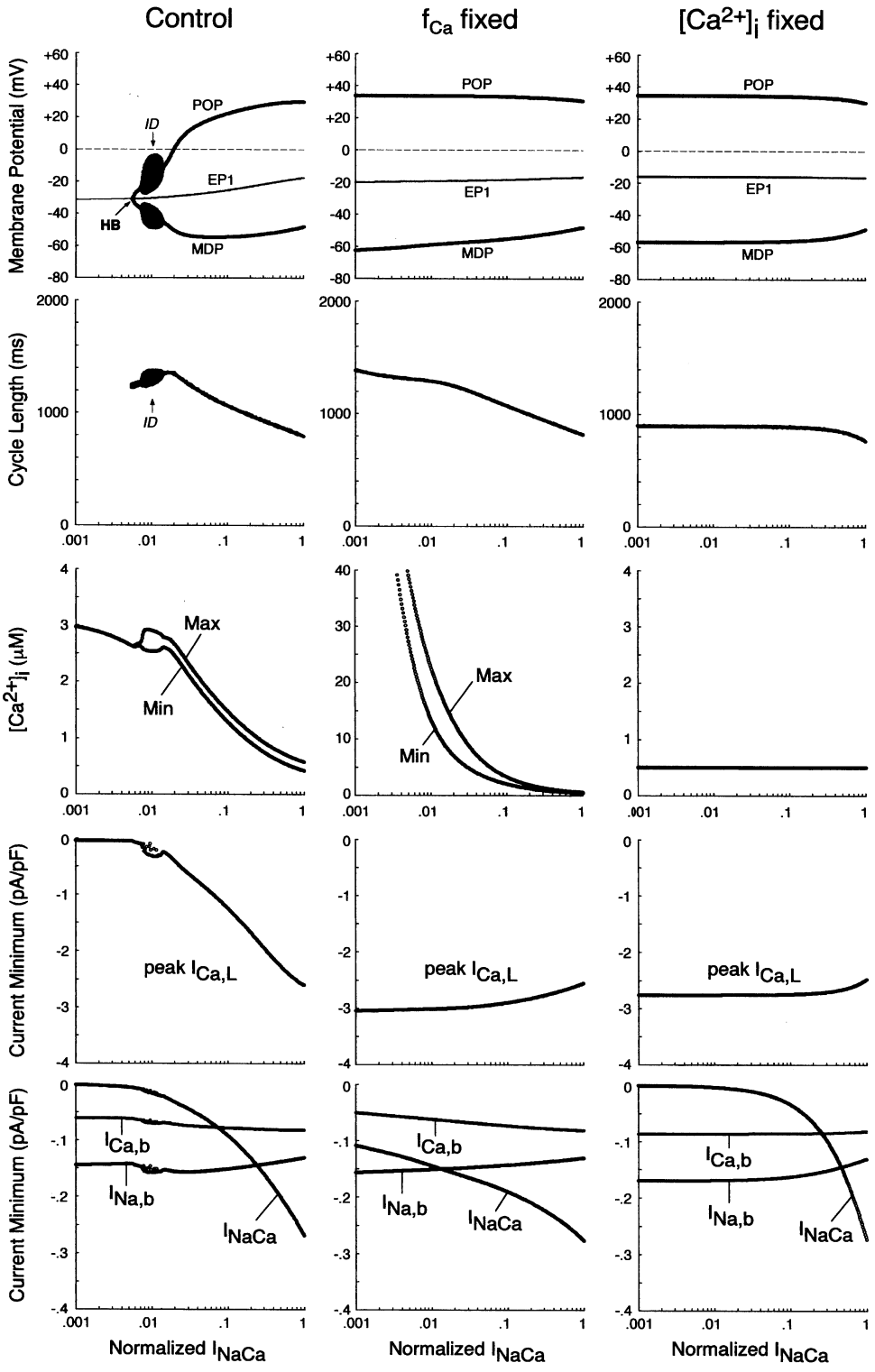

FIGURE 9 EP stability and BP dynamics of the I_{K1}-removed system during I_{NaCa} inhibition, determined for the unmodified system (*left*) and the modified system in which f_{Ca} was fixed at 0.412, the value for $[Ca^{2+}]_i = 0.5$ μM (*middle*), or $[Ca^{2+}]_i$ itself was fixed at 0.5 μM (*right*). The amplitude of I_{NaCa} as a ratio to the control value was decreased from 1 (control) to 0.001 (0.1%); practically, the $\log(I_{NaCa})$ value was reduced from 0 ($I_{NaCa} = 1$) to -3 ($I_{NaCa} = 1 \times 10^{-3}$) at an interval of 0.01. The zero-current potential (*EP1*) and BP dynamics (*MDP*, *POP*, *CL*), as well as the minimum (*Min*) and maximum (*Max*) of $[Ca^{2+}]_i$ and minimum values of the inward currents ($I_{Ca,L}$, I_{NaCa}, $I_{Na,b}$, $I_{Ca,b}$), are plotted as functions of $\log(I_{NaCa})$. Note that a Hopf bifurcation to abolish BP activity occurred only in the unmodified system (HB at $I_{NaCa} = 0.0056$).

I_{K1}-removed system. However, this may be due to the Ca^{2+}-dependent inactivation of $I_{Ca,L}$ after the induction of Ca^{2+}-overload conditions, rather than the decrease of I_{NaCa} itself. Therefore, we further tested the stability and dynamics during I_{NaCa} inhibition of the modified BP system for which $[Ca^{2+}]_i$ or Ca^{2+}-dependent $I_{Ca,L}$ inactivation (f_{Ca}) was fixed at a control value. In the modified systems, inhibition of I_{NaCa} caused neither EP stabilization nor BP cessation, with $I_{Ca,L}$ being not attenuated, although I_{NaCa} was still the dominant pacemaker current in control (Fig. 9, *middle, right*). Eliminating $[Ca^{2+}]_i$ transients or blocking SR Ca^{2+} release little altered BP dynamics.

We also examined the contributions of I_{NaCa} or $[Ca^{2+}]_i$ dynamics to the EP instability and structural stability to depolarizing or hyperpolarizing loads of the BP system by determining the unstable regions in the I_{bias}-V_0 curve during decreases in I_{NaCa} or $[Ca^{2+}]_i$ transients. As shown in Fig. 10 (*left*), inhibition of I_{NaCa} significantly shrunk the unstable regions, though a codimension two saddle-node bifurcation did not occur. When $[Ca^{2+}]_i$ or f_{Ca} was fixed at the control value, however, the unstable regions did not shrink during I_{NaCa} reduction (Fig. 10, *middle, right*). The influences of eliminating $[Ca^{2+}]_i$ transients or blocking SR Ca^{2+} release on the unstable regions were very small.

DISCUSSION

Mechanisms of BP generation in I_{K1}-downregulated HVM

Nonlinear dynamical aspects of BP generation

This study shows that pacemaker activity appears in the I_{K1}-downregulated HVM system via a saddle-node bifurcation (disappearance of a stable EP) or Hopf bifurcation (destabilization of an EP) and that the instability of an EP at depolarized potentials underlies the stable HVM pacemaking. The term "mechanisms of pacemaker generation" is usually interpreted as meaning how individual sarcolemmal currents drive or contribute to phase 4 depolarization. From the viewpoint of the nonlinear dynamics and bifurcation theory, however, "EP instability" seems to be most important for the generation of robust pacemaking: if the system has a stable EP, it will be quiescent at the stable EP or in a bistable zone where stable steady states and periodic states

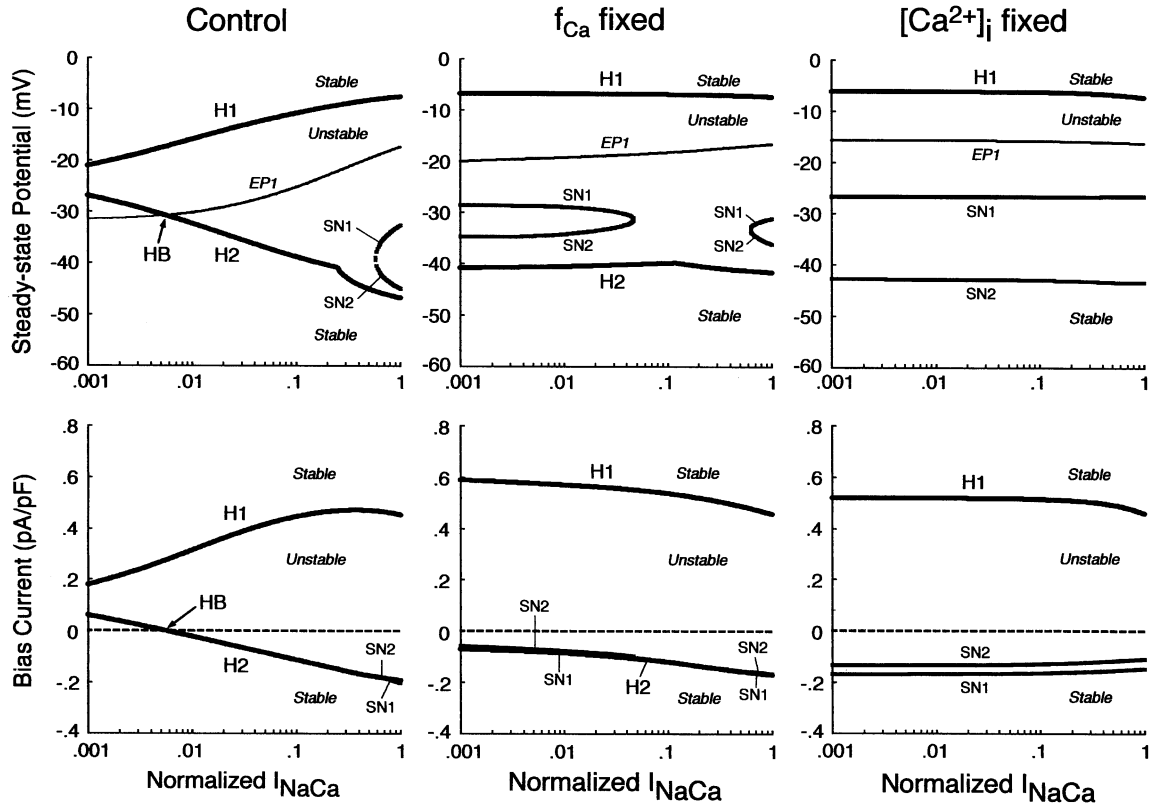

FIGURE 10 Changes in the unstable regions of the I_{bias}-V_0 curve during I_{NaCa} suppression in the I_{K1}-removed systems. Displacements of the bifurcation points (*H1–2, SN1–2*), as well as the control V_0 at $I_{bias} = 0$ (*EP1*), in the I_{bias}-V_0 curve with decreasing I_{NaCa} are shown for the unmodified system (*left*) and the modified system with f_{Ca} fixed at the value for $[Ca^{2+}]_i = 0.5$ μM (*middle*) or $[Ca^{2+}]_i$ itself fixed at 0.5 μM (*right*). The $\log(I_{NaCa})$ value was reduced from 0 to -3 at an interval of 0.01. As in Fig. 7, values of V_0 and I_{bias} at the bifurcation points are plotted on both the potential (*top*) and current (*bottom*) coordinates as functions of $\log(I_{NaCa})$. In the unmodified system, the path of EP1 intersected the locus of H2 at $I_{NaCa} = 0.0056$ (labeled *HB*).

coexist and thus annihilation occurs (for details on bistability and annihilation, see Landau et al. (6) and Guevara and Jongsma (8)). When considering the pacemaker mechanisms, therefore, one must elucidate the ionic mechanism of EP destabilization, which may be different from that of phase 4 depolarization. In the HVM pacemaker, $I_{Ca,L}$ is responsible for EP instability, whereas I_{NaCa} as well as I_{Kr} deactivation most contributes to phase 4 depolarization. Our study also suggests that the question "which current is dominant during phase 4" is relevant to the ionic mechanism not for EP instability as a requisite to stable pacemaking, but for the regulation of the destabilization rate (Figs. 4, 9, and 10). These viewpoints would be important particularly for engineering of functional BP cells to exhibit robust pacemaking.

It should be noted that the EP with the most depolarized potential (EP1) is always unstable, not stabilized during I_{K1} suppression (Fig. 5). The saddle-node bifurcation may also be yielded by increasing inward currents such as $I_{Na,b}$ or $I_{Ca,b}$. Nevertheless, increasing the inward currents would not lead to BP generation, because the positively shifted EP1 becomes stable via a Hopf bifurcation, resulting in an arrest at depolarized potentials. Another approach to create a BP cell may be overexpression of the hyperpolarization-activated current (I_h), which has been reported to induce BP activity in canine atrial or Purkinje myocytes (52,56). However, incorporating I_h did not cause a saddle-node bifurcation nor BP generation in the HVM model with normal I_{K1}, although accelerating BP generation during I_{K1} suppression via shifting the saddle-node bifurcation point toward higher g_{K1} values (data not shown). This discrepancy is at least in part due to the difference in I_{K1} density, which is much higher in ventricular cells than in atrial or Purkinje cells (56,57). These findings suggest that I_{K1} downregulation, ensuring both the occurrence of a saddle-node bifurcation and instability of EP1, is necessary and sufficient for constructing BP cells from HVMs.

Roles of individual sarcolemmal currents in HVM pacemaking

$I_{Ca,L}$

$I_{Ca,L}$ contributes little to the initial phase of pacemaker depolarization, although it contributes significantly to the terminal phase of the depolarization as well as to phase 0 upstroke (Fig. 4). Nevertheless, $I_{Ca,L}$ appears to be indispensable for the HVM pacemaking in that it is responsible for EP instability as a requisite to stable pacemaking (Figs. 7 and 8). The Ca^{2+} channel responsible for $I_{Ca,L}$ in the current model and original ventricular or SA node models corresponds to the high voltage-activated subtype (C-LTCC) formed by an α_{1C} subunit ($Ca_v1.2$), which is a major component in the heart of mouse or other species (58–60). However, the low voltage-activated subtype (D-LTCC), the α-subunit of which is α_{1D} ($Ca_v1.3$), activating at the pacemaker potential range, has recently been reported to contribute to phase 4 depolarization in the mouse SA node (61–63) and possibly in the rabbit SA node as well (64). Nevertheless, it is unlikely that D-LTCC plays an important role in the ventricular pacemaking, because $Ca_v1.3$ m-RNA is not present in the mouse or human ventricle (58,63).

I_K

In contrast to $I_{Ca,L}$, I_{Kr} or I_{Ks} was suggested to be inessential for EP destabilization leading to spontaneous activity, because 1), eliminating I_{Kr} and/or I_{Ks} did not significantly attenuate the EP instability as evaluated by positive real parts of eigenvalues of Jacobian matrices, little shrinking the unstable V_0 region in the I_{bias}-V_0 curve (Fig. 7); and 2), the I_K-removed BP system, quiescent in control (at $g_K = 0$), resumed automaticity when an EP was destabilized by incorporation of $I_{K,b}$ (Fig. 8) or electrotonic influences of adjacent normal HVMs (data not shown). Although I_{Kr} or I_{Ks} is not necessarily required for the generation of spontaneous oscillations, the K^+ currents appear to play pivotal roles in the modulation of BP dynamics. As suggested by Fig. 8, I_K would be necessary for the BP generation with large amplitude, high upstroke velocity, and stable frequency. Decreasing I_{Kr} or I_{Ks} shrunk the unstable I_{bias} region in the I_{bias}-V_0 curve, i.e., it attenuated the structural stability to depolarizing loads of the BP system (Fig. 7). The K^+ conductance region, as well as the I_{bias} region, where EPs are unstable and thus spontaneous oscillations occur, was much larger for the I_K-incorporated system than for the $I_{K,b}$-incorporated system (Fig. 8). Therefore, I_K may also contribute to the robust maintenance of BP activity, i.e., prevention of a bifurcation to quiescence.

I_{NaCa}

As in the guinea pig ventricular pacemaking (3), I_{NaCa} was suggested to be the dominant pacemaker current in the HVM pacemaking, with its removal leading to cessation of BP activity via a Hopf bifurcation (Figs. 4 and 9). However, the stabilization of an EP and cessation of BP activity during I_{NaCa} decreases appear to be a consequence of the Ca^{2+}-dependent inactivation of $I_{Ca,L}$, rather than the I_{NaCa} decrease itself: when f_{Ca} was fixed or when $[Ca^{2+}]_i$ was kept low by rapid Ca^{2+} buffering or tentative electroneutral Ca^{2+} transport, BP activity did not cease, being quite stable, during I_{NaCa} suppression (Fig. 9). It is also suggested that I_{NaCa} is not required for the destabilization of an EP or generation of spontaneous oscillations (Fig. 10). Thus, the major role of I_{NaCa} would be the maintenance of relatively low $[Ca^{2+}]_i$ to prevent Ca^{2+}-dependent inactivation of $I_{Ca,L}$ as well as cellular remodeling under Ca^{2+}-overload conditions, rather than the contribution to phase 4 depolarization as a pacemaker current. In all existing heart models, the Na^+/Ca^{2+} exchanger is assumed to mediate only the current I_{NaCa} via

the $3Na^+$:$1Ca^{2+}$ transport mode. However, it is also reported to carry a significant part of $I_{Na,b}$ via the Na^+-conducting mode (65,66). The background inward current $I_{Na,b}$ is the second dominant pacemaker current in the HVM model and the most dominant pacemaker current in most SA node models (51). Thus, the Na^+/Ca^{2+} exchanger may also contribute to pacemaker depolarization by generating $I_{Na,b}$.

Comparisons of HVM pacemaker with other pacemaker systems

Conditions for BP generation and BP dynamics

Real and model guinea pig ventricular myocytes exhibited spontaneous activities on 80–81% suppression of I_{K1} channels (1,3). In the HVM model, BP activity appeared when I_{K1} was suppressed by 84.6%, which is close to the critical values for BP generation in the guinea pig ventricle. The BP rates of the I_{K1}-reduced HVM (54–75 bpm), lower than those of the real or model guinea pig ventricular myocytes (100–164 bpm), appear to be in reasonable agreement with the mean human heart rate under normal conditions (refer to Table 4).

Pacemaker mechanisms

It has been reported for the rabbit SA node primary pacemaker that 1), $I_{Ca,L}$ is, but I_K is not, responsible for EP instability leading to spontaneous oscillations (11); 2), I_{Kr} contributes to the robust pacemaking with large amplitude and stable frequency (11); 3), I_{Kr} deactivation is crucial for phase 4 depolarization (53–55); and 4), $I_{Na,b}$ and I_{NaCa} are the predominant inward currents during phase 4 depolarization, with $I_{Ca,L}$ contributing only to the terminal phase of the depolarization as well as to phase 0 upstroke (51,55). These findings for the SA node pacemaker are in good agreement with our conclusions for the HVM pacemaker. As mentioned in the preceding section, the low voltage-activated $I_{Ca,L}$ mediated by D-LTCC may serve as a pacemaker current in the SA node pacemaking, but not in the ventricular pacemaking (61–63). However, the knockout of D-LTCC did not lead to sinus arrest, but led only to sinus bradycardia and arrhythmias (61–63), whereas the deletion of C-LTCC caused fetal death (60). These findings and our study suggest that the roles of C-LTCC and D-LTCC in pacemaking are different: C-LTCC would contribute mainly to EP destabilization as a requisite for basal pacemaking, whereas D-LTCC is not necessary for basal pacemaking, rather playing a pivotal role in pacemaker regulation by contributing mainly to phase 4 depolarization. Thus, the dynamical mechanism of the HVM pacemaking appears to be essentially the same as that of the basal SA node pacemaking. This consistency may reflect that cardiac myocytes, both pacemaker and nonpacemaker cells, in different regions or species share the common mechanism for the generation of basal pacemaking. Nevertheless, previous reports suggest the regional difference in pacemaker mechanisms. Blocking $I_{Ca,L}$ abolished spontaneous activity in central SA node tissues, but not in peripheral tissues (67,68); in the peripheral SA node, I_{Na} might contribute to EP destabilization and pacemaker generation. I_h is also suggested to play a predominant role in the subsidiary pacemaker mechanism (69,70). Bifurcation analyses of mathematical models for various regions or species are required for further investigations of the regional difference in pacemaker mechanisms.

Because there is transmural heterogeneity of electrophysiological properties of ventricular myocytes (16,18,71), one may also expect the transmural difference in BP mechanisms. Electrophysiological differences between epicardial, midmyocardial, and endocardial cells are attributable mainly to the differences in density and kinetics of I_{to} or I_{Ks}, and possibly I_{NaCa}, as summarized by ten Tusscher et al. (16). Reducing g_{to} only increased POP without affecting other AP parameters or EP stability (data not shown). Changing g_{Ks} or I_{NaCa} exerted only minor effects on stability and dynamics of the BP system (Figs. 6, 7, 9, and 10). These results suggest that bifurcation structures of epicardial, midmyocardial, and endocardial cells are essentially the same; thus we do not expect the transmural difference in BP mechanisms.

Responsiveness to β-adrenergic stimulation

As suggested by Silva and Rudy (3), a potential advantage of the BP over the electronic pacemaker is responsiveness to β-adrenergic stimulation (βAS). In the guinea pig ventricular model, BP responsiveness to βAS was very limited (3). We did not show the data on this issue, which is very important but out of the aim of this study. Nevertheless, we also found in the simulations according to the method of Silva and Rudy (3) that the HVM pacemaker did not exhibit a significant rate increase in response to βAS, suggesting that the ventricular pacemaker is less sensitive to βAS than the SA node pacemaker. The low sensitivity to βAS of the ventricular pacemaker may be at least in part due to the lack or low density of the regulatory inward currents, such as the low voltage-activated $I_{Ca,L}$, sustained-inward current (I_{st}) and I_h, which are known to be enhanced by βAS and abundant in SA node primary pacemaker cells (11,51,61–63,72–74).

Significance of applying bifurcation theory to BP system analysis and engineering

In this study, we used stability and bifurcation analyses to investigate the mechanisms of BP generation. As mentioned in the Introduction, the nonlinear dynamical approach is known to be useful for general understanding and systematic descriptions of the mechanisms of normal and abnormal pacemaker activities (4–11), as well as reentrant arrhythmias or conduction block (75–78). This study demonstrates that bifurcation theory also provides a reliable way of elucidating the roles of individual currents in pacemaker generation of I_{K1}-downregulated ventricular myocytes.

Our work suggests that exploring bifurcation structures of model cells can reveal the conditions and ways for oscillatory behavior to emerge or disappear in cardiac myocytes and possibly allow us to accurately predict and properly control the dynamics of real cells. Thus, the mathematical approach would also be applicable to engineering BP cells from native myocytes in vivo (1,52,56) or from human embryonic stem cells (hESCs) ex vivo (79–81) for the gene or cell therapy of bradyarrhythmias usually requiring implantation of an electronic pacemaker (for review, see Gepstein et al. (80)). Bifurcation analyses of model systems may lead to appropriate design of a functional BP, like the SA node, as a therapeutic alternative to the electronic pacemaker. Further investigations based on the bifurcation theory will possibly find out the most efficient ways to 1), create BP cells, 2), control BP dynamics, 3), improve the robustness of BP activity as well as BP sensitivity to βAS, and 4), improve BP ability to drive surrounding nonpacemaker tissues via modulating the existing currents or newly expressing the regulatory inward currents.

Limitations and perspectives of the study

Incompleteness of the HVM model

One limitation of this study is the incompleteness of the HVM model due to the lack of experimental data from HVMs. The formulas for $I_{Ca,L}$, I_{Kr}, SR Ca^{2+} release, and others were partly adopted from human atrial or animal heart models (see also Priebe and Beuckelmann (15)). In addition, for simplicity, the current model does not incorporate detailed descriptions of intracellular Ca^{2+} dynamics, SR Ca^{2+} handling, or the intracellular modulating factors such as cAMP and protein kinases, as in recently developed models (73, 82–84). More elaborate HVM models have recently been developed (16,17); however, these models with the larger number of equations and/or very complex formulas are less suitable for bifurcation analyses than the current model (for more details, see Theory and Methods). We believe that the current model is valuable and highly appropriate for exploring the essential mechanisms of BP generation. Nevertheless, further sophisticated but simplified HVM models with refinements of the formulas based on the data from HVMs, as well as incorporating more detailed descriptions of the intracellular Ca^{2+} handling and modulating factors, would have to be developed for future investigations.

The recently developed HVM models (16,17) are based mainly on the data from expressed channels whose electrophysiological properties may be different from those of native channels in HVMs. As suggested recently (79,81, 85), hESCs would provide an unlimited and renewable source of human cardiomyocytes for basic research as well as implantation therapies. Thus, cell system engineering to establish hESC-derived experimental models of HVMs may facilitate the development of more sophisticated HVM models.

Lack of experimental evidence

The conclusions in this study are of course the predictions from the model system; thus, they must be verified and supported by experimental works using real HVMs. However, there is no experimental study on BP activity in genetically modified HVMs. The hESC-derived experimental models of ventricular or nodal cells may also be useful for future investigations of BP mechanisms and thus verification of the model predictions. We hope that this study provides a stimulus to further experimentation on this issue.

Requirement of multicellular models involving electrotonic interactions

As suggested by Silva and Rudy (3), it should be recognized that the engineering of single BP cells is only a first step toward creation of the functional BP. Pacemaker mechanisms of the intact SA node are reported to involve electrotonic interactions with the atrium (86–88). BP cells in vivo would also suffer hyperpolarizing loads of adjacent nonpacemaker cells, which may abolish BP activity. Thus, BP ability to drive the heart would depend on its architecture to facilitate optimization of the electrical loading by the surrounding atrial or ventricular tissue (86,87). Recently, hESC-derived pacemaking cardiomyocytes implanted into the guinea pig ventricle in vivo have been found to integrate with the host tissue via forming gap junctions and drive the quiescent ventricle with nearly the same rate as in the isolated state (81). This suggested that the engrafted BP could efficiently interact with the surrounding nonpacemaker tissue to minimize the electrotonic load. However, the hESC-derived pacemaker may not be as robust to excessive hyperpolarizing loads as the native SA node pacemaker. Multicellular models such as for the SA node tissue (68,86,89) are required for further investigating the roles of electrotonic interactions in BP mechanisms in vivo and how to create a real functional BP with robust pacemaking.

APPENDIX 1: MODEL EQUATIONS

The mathematical expressions used in this study are given below. Units are mV, pA, nS, ms, nF, mM, and L. The temperature assumed for the model is 37°C. The symbols used and their definitions are the same as those in our rabbit SA node model (51) or the original PB model (15). The stimulus current I_{stim} in Eqs. 55 and 64 was assumed to carry K^+ ions into the cell for charge conservation during paced AP simulations, being set equal to zero for BP simulations. Standard parameter values and initial conditions for computations are given in Tables 5 and 6, respectively.

Sarcolemmal ionic currents

L-type Ca^{2+} channel current ($I_{Ca,L}$)

$$I_{Ca,L} = g_{Ca,L}(V - E_{Ca,L}) \times d_L \times f_L \times f_{Ca,\infty} \quad (3)$$

$$d_{L,\infty} = 1/\{1 + \exp[-(V + 7.64)/6.32]\} \quad (4)$$

$$f_{L,\infty} = 1/\{1 + \exp[(V + 24.6)/6.9]\} \quad (5)$$

TABLE 5 Standard parameter values

Parameters	Values	Parameters	Values
F	96485 (C/mol)	I_{pCamax}	0.11 (pA/pF)
R	8.3144 (J/mol/K)	K_{mCap}	0.0005 (mM)
T	310.15 (K)	P_{rel}	50 (ms^{-1})
C_m	153.4 (pF)	P_{up}	0.00221 (mM/ms)
V_{cell}	38 (pL)	P_{leak}	0.00026 (ms^{-1})
V_i	25.84 (pL)	K_{up}	0.00025 (mM)
V_{rel}	0.182 (pL)	τ_{tr}	180 (ms)
V_{up}	2.098 (pL)	$[CM]_{tot}$	0.05 (mM)
$[Na^+]_o$	140 (mM)	$[CQ]_{tot}$	10 (mM)
$[K^+]_o$	5.4 (mM)	$[TC]_{tot}$	0.07 (mM)
$[Ca^{2+}]_o$	2.0 (mM)	K_{dCM}	0.00238 (mM)
$g_{Ca,L}$	0.2496 (nS/pF)	K_{dCQ}	0.8 (mM)
g_{Kr}	0.012 (nS/pF)	K_{dTC}	0.0005 (mM)
g_{Ks}	0.036 (nS/pF)	k_{fTC}	400 ($mM^{-1} \times ms^{-1}$)
g_{to}	0.3 or 0.4 (nS/pF)	k_{bTC}	0.2 (ms^{-1})
g_{Na}	7.8 (nS/pF)		
g_{K1}	3.9 (nS/pF)		
$g_{Na,b}$	0.001 (nS/pF)		
$g_{Ca,b}$	0.00051 (nS/pF)		
$E_{Ca,L}$	+52.8 (mV)		
K_{mfCa}	0.00035 (mM)		
I_{NaKmax}	0.884 (pA/pF)		
K_{mNap}	10 (mM)		
K_{mKp}	1.5 (mM)		
k_{NaCa}	1000 (pA/pF)		
k_{sat}	0.1		
r_{NaCa}	0.35		
K_{mNaex}	87.5 (mM)		
K_{mCaex}	1.38 (mM)		

$$\tau_{dL} = (1.4/\{1 + \exp[-(V + 35)/13]\} + 0.25) \times 1.4/\{1 + \exp[(V + 5)/5]\} + 1/\{1 + \exp[-(V - 50)/20]\} \quad (6)$$

TABLE 6 State variable initial conditions for simulations of paced APs and BP oscillations

State variables	APs during 1 Hz pacing*	BP activity at $g_{K1} = 0.15^{\dagger}$	BP activity at $g_{K1} = 0^{\dagger}$
V	−84.86	−61.91	−47.88
d_L	4.941×10^{-6}	1.862×10^{-4}	1.714×10^{-3}
f_L	0.8873	0.5298	0.3868
p_a	9.095×10^{-3}	0.3382	0.5371
n	1.974×10^{-2}	0.1350	0.2321
q	0.9997	0.9890	0.8999
h	0.9925	0.2811	1.640×10^{-2}
$[Ca^{2+}]_i$	1.691×10^{-4}	3.502×10^{-4}	4.889×10^{-4}
$[Ca^{2+}]_{rel}$	2.683	5.207	6.378
$[Ca^{2+}]_{up}$	2.843	5.349	6.473
$[Na^+]_i$	9.224	6.548	6.418
$[K^+]_i$	136.4	140	140
d_R	4.941×10^{-6}	1.866×10^{-4}	1.718×10^{-3}
f_R	0.9998	0.9954	0.9645
f_{TC}	0.2529	0.4125	0.4949

*Initial conditions for simulations of paced APs in the standard system ($g_{K1} = 1$), obtained at 30 min during 1 Hz pacing, i.e., just before the 1801st stimulus, starting from a resting state.

†Initial conditions for simulations of BP activity in the I_{K1}-reduced systems, obtained at MDP after 15 min calculations starting from an EP.

$$\tau_{fL} = 17.925/\{0.1389 \times \exp[-(0.0358 \times (V - 10.9))^2] + 0.0519\} \quad (7)$$

$$f_{Ca,\infty} = 1/[1 + (K_{mfCa}/[Ca^{2+}]_i)] \quad (8)$$

Rapidly activating delayed-rectifier K^+ current (I_{Kr})

$$I_{Kr} = g_{Kr} \times (V - E_K) \times p_a \times p_{i,\infty} \quad (9)$$

$$p_{a,\infty} = 1/\{1 + \exp[-(V + 14)/7.7]\} \quad (10)$$

$$p_{i,\infty} = 1/\{1 + \exp[(V + 15)/22.4]\} \quad (11)$$

$$\tau_{pa} = 1/(\alpha_{pa} + \beta_{pa}) \quad (12)$$

$$\alpha_{pa} = 0.0003 \times (V + 14)/\{1 - \exp[-(V + 14)/5]\} \quad (13)$$

$$\beta_{pa} = 0.000073898 \times (V - 3.4328)/\{\exp[(V - 3.4328)/5.1237] - 1\} \quad (14)$$

Slowly activating delayed-rectifier K^+ current (I_{Ks})

$$I_{Ks} = g_{Ks} \times (V - E_{Ks}) \times n^2 \quad (15)$$

$$E_{Ks} = (RT/F) \times \ln[(0.01833 \times [Na^+]_o + [K^+]_o)/(0.01833 \times [Na^+]_i + [K^+]_i)] \quad (16)$$

$$n_\infty = 1/\{1 + \exp[-(V - 9.4)/11.8]\}^{0.5} \quad (17)$$

$$\tau_n = 555/\{1 + \exp[-(V + 22)/11.3]\} + 129 \quad (18)$$

Transient outward current (It_o)

$$I_{to} = g_{to} \times (V - E_{to}) \times q \times r_\infty \quad (19)$$

$$E_{to} = (RT/F) \times \ln[(0.043 \times [Na^+]_o + [K^+]_o)/(0.043 \times [Na^+]_i + [K^+]_i)] \quad (20)$$

$$r_\infty = \alpha_r/(\alpha_r + \beta_r) \quad (21)$$

$$\alpha_r = 0.5266 \times \exp[-0.0166 \times (V - 42.2912)]/\{1 + \exp[-0.0943 \times (V - 42.2912)]\} \quad (22)$$

$$\beta_r = \{0.5149 \times \exp[-0.1344 \times (V - 5.0027)] + 0.00005186 \times V\}/\{1 + \exp[-0.1348 \times (V - 0.00005186)]\} \quad (23)$$

$$q_\infty = \alpha_q/(\alpha_q + \beta_q) \quad (24)$$

$$\tau_q = 1/(\alpha_q + \beta_q) \quad (25)$$

$$\alpha_q = \{0.0721 \times \exp[-0.173 \times (V + 34.2531)] + 0.00005612 \times V\}/\{1 + \exp[-0.1732 \times (V + 34.2531)]\} \quad (26)$$

$$\beta_q = \{0.0767 \times \exp[-0.00000000166 \times (V + 34.0235)] + 0.0001215 \times V\}/\{1 + \exp[-0.1604 \times (V + 34.0235)]\} \quad (27)$$

Na^+ channel current (I_{Na})

$$I_{Na} = g_{Na} \times (V - E_{mh}) \times m_\infty^3 \times h^2 \quad (28)$$

$$E_{mh} = (RT/F) \times \ln[([Na^+]_o + 0.12 \times [K^+]_o)/([Na^+]_i + 0.12 \times [K^+]_i)] \quad (29)$$

$$m_\infty = \alpha_m/(\alpha_m + \beta_m) \quad (30)$$

$$\alpha_m = 0.32 \times (V + 47.13)/\{1 - \exp[-0.1 \times (V + 47.13)]\} \quad (31)$$

$$\beta_m = 0.08 \times \exp(-V/11) \quad (32)$$

$$h_\infty = 0.5 \times [1 - \tanh(7.74 + 0.12 \times V)] \quad (33)$$

$$\tau_h = 0.25 + 2.24 \times [1 - \tanh(7.74 + 0.12 \times V)]/\{1 - \tanh[0.07 \times (V + 92.4)]\} \quad (34)$$

Inward-rectifier K^+ channel current (I_{K1})

$$I_{K1} = g_{K1} \times (V - E_K) \times k_{1a}/(k_{1a} + k_{1b}) \quad (35)$$

$$k_{1a} = 0.1/\{1 + \exp[0.06 \times (V - E_K - 200)]\} \quad (36)$$

$$k_{1b} = \{3 \times \exp[0.0002 \times (V - E_K + 100)] + \exp[0.1 \times (V - E_K - 10)]\}/\{1 + \exp[-0.5 \times (V - E_K)]\} \quad (37)$$

Background Na^+/Ca^{2+} currents ($I_{Na,b}$, $I_{Ca,b}$)

$$I_{Na,b} = g_{Na,b} \times (V - E_{Na}) \quad (38)$$

$$I_{Ca,b} = g_{Ca,b} \times (V - E_{Ca}) \quad (39)$$

Na^+-K^+ pump current (I_{NaK})

$$I_{NaK} = I_{NaKmax} \times \{[K^+]_o/([K^+]_o + K_{mKp})\}/\{1 + (K_{mNap}/[Na^+]_i)^{1.5}\}/\{1 + 0.1245 \times \exp(-0.1 \times V \times F/RT) + 0.0365 \times [\exp([Na^+]_o/67.3) - 1]/7 \times \exp(-V \times F/RT)\} \quad (40)$$

Na^+/Ca^{2+} exchanger current (I_{NaCa})

$$I_{NaCa} = k_{NaCa}/(K_{mNaex}^3 + [Na^+]_o^3)/(K_{mCaex} + [Ca^{2+}]_o) \times \{[Ca^{2+}]_o \times [Na^+]_i^3 \times \exp(r_{NaCa} \times V \times F/RT) - [Na^+]_o^3 \times [Ca^{2+}]_i \times \exp[(r_{NaCa} - 1) \times V \times F/RT]\}/\{1 + k_{sat} \times \exp[(r_{NaCa} - 1) \times V \times F/RT]\} \quad (41)$$

Sarcolemmal Ca^{2+} pump current (I_{pCa})

$$I_{pCa} = I_{pCamax}/[1 + (K_{mCap}/[Ca^{2+}]_i)] \quad (42)$$

Total membrane current (I_{total})

$$I_{total} = I_{Ca,L} + I_{Kr} + I_{Ks} + I_{to} + I_{Na} + I_{K1} + I_{Na,b} + I_{Ca,b} + I_{NaK} + I_{NaCa} + I_{pCa} \quad (43)$$

Net ion fluxes

$$J_{Na,net} = (I_{Na} + I_{Na,b} + 3 \times I_{NaK} + 3 \times I_{NaCa}) \times C_m/F \quad (44)$$

$$J_{K,net} = (I_{Kr} + I_{Ks} + I_{to} + I_{K1} - 2 \times I_{NaK}) \times C_m/F \quad (45)$$

$$J_{Ca,net} = (I_{Ca,L} + I_{Ca,b} - 2 \times I_{NaCa} + I_{pCa}) \times C_m/(2 \times F) \quad (46)$$

Intracellular Ca^{2+} dynamics (SR Ca^{2+} handling)

SR Ca^{2+} release

$$J_{rel} = g_{rel} \times (d_R \times f_R)^3 \times ([Ca^{2+}]_{rel} - [Ca^{2+}]_i) \quad (47)$$

$$g_{rel} = P_{rel}/\{1 + \exp[(I_{Ca,L} + I_{Ca,b} - 2 \times I_{NaCa} + I_{pCa} + 5)/0.9]\} \quad (48)$$

$$d_{R\infty} = d_{L\infty} = 1/\{1 + \exp[-(V + 7.64)/6.32]\} \quad (49)$$

$$f_{R\infty} = f_{L\infty} = 1/\{1 + \exp[(V + 24.6)/6.9]\} \quad (50)$$

$$\tau_{dR} = \tau_{fR} = 4 \quad (51)$$

SR Ca^{2+} uptake via Ca^{2+} pump

$$J_{up} = P_{up} \times [Ca^{2+}]_i^2/([Ca^{2+}]_i^2 + K_{up}^2) \quad (52)$$

SR Ca^{2+} transfer and leak

$$J_{tr} = ([Ca^{2+}]_{up} - [Ca^{2+}]_{rel})/\tau_{tr} \quad (53)$$

$$J_{leak} = P_{leak} \times ([Ca^{2+}]_{up} - [Ca^{2+}]_i) \quad (54)$$

Differential equations for state variables

Membrane potential (V)

$$dV/dt = I_{stim} - I_{total} \quad (55)$$

Gating variables

$$dx/dt = (x_\infty - x)/\tau_x \; [x = d_L, f_L, p_a, n, q, h, d_R, f_R] \quad (56)$$

Ca^{2+} buffering flux

$$df_{TC}/dt = k_{fTC} \times [Ca^{2+}]_i \times (1 - f_{TC}) - k_{bTC} \times f_{TC} \quad (57)$$

$$B_{CM} = 1/\{1 + [CM]_{tot} \times K_{dCM}/(K_{dCM} + [Ca^{2+}]_i)^2\} \quad (58)$$

$$B_{CQ} = 1/\{1 + [CQ]_{tot} \times K_{dCQ}/(K_{dCQ} + [Ca^{2+}]_{rel})^2\} \quad (59)$$

Intracellular ion concentrations

$$d[Ca^{2+}]_i/dt = B_{CM} \times \{(-J_{Ca,net} + J_{rel} \times V_{rel} - J_{up} \times V_{up} + J_{leak} \times V_{up})/V_i - [TC]_{tot} \times df_{TC}/dt\} \quad (60)$$

$$d[Ca^{2+}]_{rel}/dt = B_{CQ} \times (J_{tr} - J_{rel}) \quad (61)$$

$$d[Ca^{2+}]_{up}/dt = J_{up} - J_{tr} \times V_{rel}/V_{up} - J_{leak} \quad (62)$$

$$d[Na^{+}]_i/dt = -J_{Na,net}/V_i \quad (63)$$

$$d[K^{+}]_i/dt = (I_{stim} \times C_m/F - J_{K,net})/V_i \quad (64)$$

APPENDIX 2: DETERMINATION OF EPS AS INITIAL CONDITIONS

To determine an EP (resting state) of the HVM system as initial conditions for AP simulations, steady-state values of the state variables V, $[Ca^{2+}]_i$, $[Na^{+}]_i$, $[K^{+}]_i$, $[Ca^{2+}]_{rel}$, and $[Ca^{2+}]_{up}$ were calculated numerically by the differential or algebraic method of Hund et al. (35). Differential equations given in Appendix 1 (Eqs. 55, 60–64) were used for the differential method with the MATLAB ODE solvers, whereas the following algebraic equations derived from the differential equations were used for the algebraic method with a nonlinear equation solver available in MATLAB.

$$I_{total} = 0\,(dV/dt = 0) \quad (65)$$

$$J_{Ca,net} = 0\,(d[Ca^{2+}]_i/dt = 0) \quad (66)$$

$$J_{rel} - J_{tr} = 0\,(d[Ca^{2+}]_{rel}/dt = 0) \quad (67)$$

$$J_{up} - J_{tr} \times V_{rel}/V_{up} - J_{leak} = 0\,(d[Ca^{2+}]_{up}/dt = 0) \quad (68)$$

$$J_{Na,net} = 0\,(d[Na^{+}]_i/dt = 0) \quad (69)$$

$$J_{K,net} = 0\,(d[K^{+}]_i/dt = 0) \quad (70)$$

$$V = (V_i \times F/C_m) \times ([K^{+}]_i + [Na^{+}]_i + 2[Ca^{2+}]_{i,tot} + 2 \times (V_{rel}/V_i) \times [Ca^{2+}]_{rel,tot} + 2 \times (V_{up}/V_i) \times [Ca^{2+}]_{up} - C_0) \quad (71)$$

$$[Ca^{2+}]_{i,tot} = [Ca^{2+}]_i + [CM]_{tot} \times [Ca^{2+}]_i/([Ca^{2+}]_i + K_{dCM}) + [TC]_{tot} \times [Ca^{2+}]_i/([Ca^{2+}]_i + K_{dTC}) \quad (72)$$

$$[Ca^{2+}]_{rel,tot} = [Ca^{2+}]_{rel} + [CQ]_{tot} \times [Ca^{2+}]_{rel}/([Ca^{2+}]_{rel} + K_{dCQ}) \quad (73)$$

The symbol C_0 in Eq. 71 is a constant of integration determined by initial conditions (35). Note that Eq. 65 can be derived from Eqs. 66, 69, and 70 (see Eqs. 43–46). The algebraic method for the full system with variable $[K^{+}]_i$ practically used Eqs. 66–70 and Eqs. 71–73 instead of Eq. 65, assuming that $[K^{+}]_i$ is equal to 140 mM under control conditions (e.g., at $g_{K1} = 1$). The differential and algebraic methods yielded nearly identical results. For BP simulations and bifurcation analyses using the $[K^{+}]_i$-fixed system, steady-state values of the state variables were calculated by Eqs. 65–69.

This work was supported in part by a Ministry for Education, Science, and Culture of Japan Grant-in-Aid for Scientific Research 15590195 and 17590192 (to Y. Kurata and T. Shibamoto) and a Kanazawa Medical University Grant for Collaborative Research C2003-1, C2004-1, and C2005-1 (to Y. Kurata and T. Shibamoto).

REFERENCES

1. Miake, J., E. Marbán, and H. B. Nuss. 2002. Gene therapy: biological pacemaker created by gene transfer. *Nature*. 419:132–133.
2. Luo, C. H., and Y. Rudy. 1994. A dynamic model of the cardiac ventricular action potential: I. Simulations of ionic currents and concentration changes. *Circ. Res.* 74:1071–1096.
3. Silva, J., and Y. Rudy. 2003. Mechanism of pacemaking in I_{K1}-downregulated myocytes. *Circ. Res.* 92:261–263.
4. Chay, T. R., and Y. S. Lee. 1985. Phase resetting and bifurcation in the ventricular myocardium. *Biophys. J.* 47:641–651.
5. Chay, T. R., and Y. S. Lee. 1990. Bursting, beating, and chaos by two functionally distinct inward current inactivations in excitable cells. *Ann. N. Y. Acad. Sci.* 591:328–350.
6. Landau, M., P. Lorente, D. Michaels, and J. Jalife. 1990. Bistabilities and annihilation phenomena in electrophysiological cardiac models. *Circ. Res.* 66:1658–1672.
7. Vinet, A., and F. A. Roberge. 1990. A model study of stability and oscillations in the myocardial cell membrane. *J. Theor. Biol.* 147:377–412.
8. Guevara, M. R., and H. J. Jongsma. 1992. Three ways of abolishing automaticity in sinoatrial node: ionic modeling and nonlinear dynamics. *Am. J. Physiol.* 262:H1268–H1286.
9. Gibb, W. J., M. B. Wagner, and M. D. Lesh. 1994. Effects of simulated potassium blockade on the dynamics of triggered cardiac activity. *J. Theor. Biol.* 168:245–257.
10. Varghese, A., and R. L. Winslow. 1994. Dynamics of abnormal pacemaking activity in cardiac Purkinje fibers. *J. Theor. Biol.* 168:407–420.
11. Kurata, Y., I. Hisatome, S. Imanishi, and T. Shibamoto. 2003. Roles of L-type Ca^{2+} and delayed-rectifier K^{+} currents in sinoatrial node pacemaking: insights from stability and bifurcation analyses of a mathematical model. *Am. J. Physiol. Heart Circ. Physiol.* 285:H2804–H2819.
12. Guckenheimer, J., and P. Holmes. 1983. Nonlinear Oscillations, Dynamical Systems, and Bifurcations of Vector Fields. Springer-Verlag, New York.
13. Parker, T. S., and L. O. Chua. 1989. Practical Numerical Algorithms for Chaotic Systems. Springer-Verlag, New York.
14. Kuznetsov, Y. A. 2003. Elements of Applied Bifurcation Theory, 3rd ed. Springer-Verlag, New York.
15. Priebe, L., and D. J. Beuckelmann. 1998. Simulation study of cellular electric properties in heart failure. *Circ. Res.* 82:1206–1223.
16. Ten Tusscher, K. H. W. J., D. Noble, P. J. Noble, and A. V. Panfilov. 2004. A model for human ventricular tissue. *Am. J. Physiol. Heart Circ. Physiol.* 286:H1573–H1589.
17. Iyer, V., R. Mazhari, and R. L. Winslow. 2004. A computational model of the human left-ventricular epicardial myocyte. *Biophys. J.* 87:1507–1525.
18. Bernus, O., R. Wilders, C. W. Zemlin, H. Verschelde, and A. V. Panfilov. 2002. A computationally efficient electrophysiological model of human ventricular cells. *Am. J. Physiol. Heart Circ. Physiol.* 282: H2296–H2308.
19. Courtemanche, M., R. J. Ramirez, and S. Nattel. 1998. Ionic mechanisms underlying human atrial action potential properties: insights from a mathematical model. *Am. J. Physiol.* 275:H301–H321.
20. Faber, G. M., and Y. Rudy. 2000. Action potential and contractility changes in $[Na^{+}]_i$ overloaded cardiac myocytes: a simulation study. *Biophys. J.* 78:2392–2404.
21. Bénitah, J. P., P. Bailly, M. C. D'Agrosa, J. P. Da Ponte, C. Delgado, and P. Lorente. 1992. Slow inward current in single cells isolated from adult human ventricles. *Pflugers Arch.* 421:176–187.
22. Pelzmann, B., P. Schaffer, E. Bernhart, P. Lang, H. Mächler, B. Rigler, and B. Koidl. 1998. L-type calcium current in human ventricular myocytes at a physiological temperature from children with tetralogy of Fallot. *Cardiovasc. Res.* 38:424–432.
23. Li, G. R., B. Yang, J. Feng, R. F. Bosch, M. Carrier, and S. Nattel. 1999. Transmembrane I_{Ca} contributes to rate-dependent changes of action potentials in human ventricular myocytes. *Am. J. Physiol.* 276: H98–H106.

24. Li, G. R., J. Feng, L. Yue, M. Carrier, and S. Nattel. 1996. Evidence for two components of delayed rectifier K^+ current in human ventricular myocytes. *Circ. Res.* 78:689–696.
25. Wang, Z., B. Fermini, and S. Nattel. 1994. Rapid and slow components of delayed rectifier current in human atrial myocytes. *Cardiovasc. Res.* 28:1540–1546.
26. Zhou, Z., Q. Gong, B. Ye, Z. Fan, J. C. Makielski, G. A. Robertson, and C. T. January. 1998. Properties of HERG channels stably expressed in HEK 293 cells studied at physiological temperature. *Biophys. J.* 74:230–241.
27. Mazhari, R., J. L. Greenstein, R. L. Winslow, E. Marbán, and H. B. Nuss. 2001. Molecular interactions between two long-QT syndrome gene products, HERG and KCNE2, rationalized by in vitro and in silico analysis. *Circ. Res.* 89:33–38.
28. Johnson, J. P., F. M. Mullins, and P. B. Bennett. 1999. Human *ether-à-go-go*-related gene K^+ channel gating probed with extracellular Ca^{2+}: evidence for two distinct voltage sensors. *J. Gen. Physiol.* 113:565–580.
29. Smith, P. L., and G. Yellen. 2002. Fast and slow voltage sensor movements in HERG potassium channels. *J. Gen. Physiol.* 119:275–293.
30. Sanguinetti, M. C., C. Jiang, M. E. Curran, and M. T. Keating. 1995. A mechanistic link between an inherited and an acquired cardiac arrhythmia: *HERG* encodes the I_{Kr} potassium channel. *Cell.* 81:299–307.
31. Weerapura, M., S. Nattel, D. Chartier, R. Caballero, and T. E. Hébert. 2002. A comparison of currents carried by HERG, with and without coexpression of MiRP1, and the native rapid delayed rectifier current. Is MiRP1 the missing link? *J. Physiol.* 540:15–27.
32. Berecki, G., J. G. Zegers, A. O. Verkerk, Z. A. Bhuiyan, B. de Jonge, M. W. Veldkamp, R. Wilders, and A. C. G. van Ginneken. 2005. HERG channel (dys)function revealed by dynamic action potential clamp technique. *Biophys. J.* 88:566–578.
33. Shibasaki, T. 1987. Conductance and kinetics of delayed rectifier potassium channels in nodal cells of the rabbit heart. *J. Physiol.* 387: 227–250.
34. Virág, L., N. Iost, M. Opincariu, J. Szolnoky, J. Szécsi, G. Bogáts, P. Szenohradsky, A. Varró, and J. G. Papp. 2001. The slow component of the delayed rectifier potassium current in undiseased human ventricular myocytes. *Cardiovasc. Res.* 49:790–797.
35. Hund, T. J., J. P. Kucera, N. F. Otani, and Y. Rudy. 2001. Ionic charge conservation and long-term steady state in the Luo-Rudy dynamic cell model. *Biophys. J.* 81:3324–3331.
36. Krogh-Madsen, T., P. Schaffer, A. D. Skriver, L. K. Taylor, B. Pelzmann, B. Koidl, and M. R. Guevara. 2005. An ionic model for rhythmic activity in small clusters of embryonic chick ventricular cells. *Am. J. Physiol. Heart Circ. Physiol.* 289:H398–H413.
37. Dormand, J. R., and P. J. Prince. 1980. A family of embedded Runge-Kutta formulae. *J. Comput. Appl. Math.* 6:19–26.
38. Shampine, L. F., and M. W. Reichelt. 1997. The MATLAB ODE Suite. *SIAM J. Sci. Comput.* 18:1–22.
39. Sachse, F. B., G. Seemann, K. Chaisaowong, and D. Weiß. 2003. Quantitative reconstruction of cardiac electromechanics in human myocardium: assembly of electrophysiologic and tension generation models. *J. Cardiovasc. Electrophysiol.* 14:S210–S218.
40. Shannon, T. R., and D. M. Bers. 1997. Assessment of intra-SR free [Ca] and buffering in rat heart. *Biophys. J.* 73:1524–1531.
41. Shannon, T. R., T. Guo, and D. M. Bers. 2003. Ca^{2+} scraps: local depletions of free $[Ca^{2+}]$ in cardiac sarcoplasmic reticulum during contractions leave substantial Ca^{2+} reserve. *Circ. Res.* 93:40–45.
42. Li, G. R., J. Feng, L. Yue, and M. Carrier. 1998. Transmural heterogeneity of action potentials and I_{to1} in myocytes isolated from the human right ventricle. *Am. J. Physiol.* 275:H369–H377.
43. Despa, S., M. A. Islam, C. R. Weber, S. M. Pogwizd, and D. M. Bers. 2002. Intracellular Na^+ concentration is elevated in heart failure but Na/K pump function is unchanged. *Circulation.* 105:2543–2548.
44. Pieske, B., L. S. Maier, V. Piacentino III, J. Weisser, G. Hasenfuss, and S. Houser. 2002. Rate dependence of $[Na^+]_i$ and contractility in non-failing and failing human myocardium. *Circulation.* 106:447–453.
45. Schmidt, U., R. J. Hajjar, P. A. Helm, C. S. Kim, A. A. Doye, and J. K. Gwathmey. 1998. Contribution of abnormal sarcoplasmic reticulum ATPase activity to systolic and diastolic dysfunction in human heart failure. *J. Mol. Cell. Cardiol.* 30:1929–1937.
46. Pieske, B., L. S. Maier, D. M. Bers, and G. Hasenfuss. 1999. Ca^{2+} handling and sarcoplasmic reticulum Ca^{2+} content in isolated failing and nonfailing human myocardium. *Circ. Res.* 85:38–46.
47. Maier, L. S., P. Barckhausen, J. Weisser, I. Aleksic, M. Baryalei, and B. Pieske. 2000. Ca^{2+} handling in isolated human atrial myocardium. *Am. J. Physiol. Heart Circ. Physiol.* 279:H952–H958.
48. Tiaho, F., C. Piot, J. Nargeot, and S. Richard. 1994. Regulation of the frequency-dependent facilitation of L-type Ca^{2+} currents in rat ventricular myocytes. *J. Physiol.* 477:237–252.
49. Yuan, W., and D. M. Bers. 1994. Ca-dependent facilitation of cardiac Ca current is due to Ca-calmodulin-dependent protein kinase. *Am. J. Physiol.* 267:H982–H993.
50. Fukai, H., S. Doi, T. Nomura, and S. Sato. 2000. Hopf bifurcations in multiple-parameter space of the Hodgkin-Huxley equations I. Global organization of bistable periodic solutions. *Biol. Cybern.* 82:215–222.
51. Kurata, Y., I. Hisatome, S. Imanishi, and T. Shibamoto. 2002. Dynamical description of sinoatrial node pacemaking: improved mathematical model for primary pacemaker cell. *Am. J. Physiol. Heart Circ. Physiol.* 283:H2074–H2101.
52. Plotnikov, A. N., E. A. Sosunov, J. Qu, I. N. Shlapakova, E. P. Anyukhovsky, L. Liu, M. J. Janse, P. R. Brink, I. S. Cohen, R. B. Robinson, P. Danilo Jr., and M. R. Rosen. 2004. Biological pacemaker implanted in canine left bundle branch provides ventricular escape rhythms that have physiologically acceptable rates. *Circulation.* 109: 506–512.
53. Brown, H. F., J. Kimura, D. Noble, S. J. Noble, and A. Taupignon. 1984. The ionic currents underlying pacemaker activity in rabbit sino-atrial node: experimental results and computer simulations. *Proc. R. Soc. Lond. B Biol. Sci.* 222:329–347.
54. Noble, D. 1984. The surprising heart: a review of recent progress in cardiac electrophysiology. *J. Physiol.* 353:1–50.
55. Dokos, S., B. Celler, and N. Lovell. 1996. Ion currents underlying sinoatrial node pacemaker activity: a new single cell mathematical model. *J. Theor. Biol.* 181:245–272.
56. Qu, J., A. N. Plotnikov, P. Danilo Jr., I. Shlapakova, I. S. Cohen, R. B. Robinson, and M. R. Rosen. 2003. Expression and function of a biological pacemaker in canine heart. *Circulation.* 107:1106–1109.
57. Joyner, R. W., Y.-G. Wang, R. Wilders, D. A. Golod, M. B. Wagner, R. Kumar, and W. N. Goolsby. 2000. A spontaneously active focus drives a model atrial sheet more easily than a model ventricular sheet. *Am. J. Physiol. Heart Circ. Physiol.* 279:H752–H763.
58. Takimoto, K., D. Li, J. M. Nerbonne, and E. S. Levitan. 1997. Distribution, splicing and glucocorticoid-induced expression of cardiac alpha 1C and alpha 1D voltage-gated Ca^{2+} channel mRNAs. *J. Mol. Cell. Cardiol.* 29:3035–3042.
59. Bohn, G., S. Moosmang, H. Conrad, A. Ludwig, F. Hofmann, and N. Klugbauer. 2000. Expression of T- and L-type calcium channel mRNA in murine sinoatrial node. *FEBS Lett.* 481:73–76.
60. Seisenberger, C., V. Specht, A. Welling, J. Platzer, A. Pfeifer, S. Kühbandner, J. Striessnig, N. Klugbauer, R. Feil, and F. Hofmann. 2000. Functional embryonic cardiomyocytes after disruption of the L-type α_{1C} ($Ca_v1.2$) calcium channel gene in the mouse. *J. Biol. Chem.* 275:39193–39199.
61. Platzer, J., J. Engel, A. Schrott-Fischer, K. Stephan, S. Bova, H. Chen, H. Zheng, and J. Striessnig. 2000. Congenital deafness and sinoatrial node dysfunction in mice lacking class D L-type Ca^{2+} channels. *Cell.* 102:89–97.
62. Zhang, Z., Y. Xu, H. Song, J. Rodriguez, D. Tuteja, Y. Namkung, H.-S. Shin, and N. Chiamvimonvat. 2002. Functional roles of $Ca_v1.3$ (α_{1D}) calcium channel in sinoatrial nodes: insight gained using gene-targeted null mutant mice. *Circ. Res.* 90:981–987.
63. Mangoni, M. E., B. Couette, E. Bourinet, J. Platzer, D. Reimer, J. Striessnig, and J. Nargeot. 2003. Functional role of L-type $Ca_v1.3$ Ca^{2+}

channels in cardiac pacemaker activity. *Proc. Natl. Acad. Sci. USA.* 100:5543–5548.

64. Verheijck, E. E., A. C. G. van Ginneken, R. Wilders, and L. N. Bouman. 1999. Contribution of L-type Ca^{2+} current to electrical activity in sinoatrial nodal myocytes of rabbits. *Am. J. Physiol. Heart Circ. Physiol.* 276:H1064–H1077.
65. Hilgemann, D. W. 2004. New insights into the molecular and cellular workings of the cardiac Na^+/Ca^{2+} exchanger. *Am. J. Physiol. Cell Physiol.* 287:C1167–C1172.
66. Kang, M., and D. W. Hilgemann. 2004. Multiple transport modes of the cardiac Na^+/Ca^{2+} exchanger. *Nature.* 427:544–547.
67. Kodama, I., M. R. Nikmaram, M. R. Boyett, R. Suzuki, H. Honjo, and J. M. Owen. 1997. Regional differences in the role of the Ca^{2+} and Na^+ currents in pacemaker activity in the sinoatrial node. *Am. J. Physiol. Heart Circ. Physiol.* 272:H2793–H2806.
68. Zhang, H., A. V. Holden, I. Kodama, H. Honjo, M. Lei, T. Varghese, and M. R. Boyett. 2000. Mathematical models of action potentials in the periphery and center of the rabbit sinoatrial node. *Am. J. Physiol. Heart Circ. Physiol.* 279:H397–H421.
69. Zhang, H., and M. Vassalle. 2000. Role of dual pacemaker mechanisms in sinoatrial node discharge. *J. Biomed. Sci.* 7:100–113.
70. Zhang, H., and M. Vassalle. 2001. Role of I_K and I_f in the pacemaker mechanisms of sino-atrial node myocytes. *Can. J. Physiol. Pharmacol.* 79:963–976.
71. Seemann, G., F. B. Sachse, D. L. Weiβ, and O. Dössel. 2003. Quantitative reconstruction of cardiac electromechanics in human myocardium: regional heterogeneity. *J. Cardiovasc. Electrophysiol.* 14:S219–S228.
72. Noma, A. 1996. Ionic mechanisms of the cardiac pacemaker potential. *Jpn. Heart J.* 37:673–682.
73. Demir, S. S., J. W. Clark, and W. R. Giles. 1999. Parasympathetic modulation of sinoatrial node pacemaker activity in rabbit heart: a unifying model. *Am. J. Physiol.* 276:H2221–H2244.
74. Mitsuiye, T., Y. Shinagawa, and A. Noma. 2000. Sustained inward current during pacemaker depolarization in mammalian sinoatrial node cells. *Circ. Res.* 87:88–91.
75. Chay, T. R., and Y. S. Lee. 1992. Studies on re-entrant arrhythmias and ectopic beats in excitable tissues by bifurcation analyses. *J. Theor. Biol.* 155:137–171.
76. Vinet, A., and F. A. Roberge. 1994. Analysis of an iterative difference equation model of the cardiac cell membrane. *J. Theor. Biol.* 170:201–214.
77. Chay, T. R. 1996. Proarrhythmic and antiarrhythmic actions of ion channel blockers on arrhythmias in the heart: model study. *Am. J. Physiol. Heart Circ. Physiol.* 271:H329–H356.
78. Landau, M., and P. Lorente. 1997. Conduction block and chaotic dynamics in an asymmetrical model of coupled cardiac cells. *J. Theor. Biol.* 186:93–105.
79. He, J.-Q., Y. Ma, Y. Lee, J. A. Thomson, and T. J. Kamp. 2003. Human embryonic stem cells develop into multiple types of cardiac myocytes: action potential characterization. *Circ. Res.* 93:32–39.
80. Gepstein, L., Y. Feld, and L. Yankelson. 2004. Somatic gene and cell therapy strategies for the treatment of cardiac arrhythmias. *Am. J. Physiol. Heart Circ. Physiol.* 286:815–822.
81. Xue, T., H. C. Cho, F. G. Akar, S.-Y. Tsang, S. P. Jones, E. Marbán, G. F. Tomaselli, and R. A. Li. 2005. Functional integration of electrically active cardiac derivatives from genetically engineered human embryonic stem cells with quiescent recipient ventricular cardiomyocytes: insights into the development of cell-based pacemakers. *Circulation.* 111:11–20.
82. Greenstein, J. L., and R. L. Winslow. 2002. An integrative model of the cardiac ventricular myocytes incorporating local control of Ca^{2+} release. *Biophys. J.* 83:2918–2945.
83. Shannon, T. R., F. Wang, J. Puglisi, C. Weber, and D. M. Bers. 2004. A mathematical treatment of integrated Ca dynamics within the ventricular myocyte. *Biophys. J.* 87:3351–3371.
84. Saucerman, J. J., L. L. Brunton, A. P. Michailova, and A. D. McCulloch. 2003. Modeling β-adrenergic control of cardiac myocyte contractility *in silico*. *J. Biol. Chem.* 278:47997–48003.
85. Mummery, C., D. Ward-van Oostwaard, P. Doevendans, R. Spijker, S. van den Brink, R. Hassink, M. van der Heyden, T. Opthof, M. Pera, A. B. de la Riviere, R. Passier, and L. Tertoolen. 2002. Differentiation of human embryonic stem cells to cardiomyocytes: role of coculture with visceral endoderm-like cells. *Circulation.* 107:2733–2740.
86. Boyett, M. R., H. Honjo, and I. Kodama. 2000. The sinoatrial node, a heterogeneous pacemaker structure. *Cardiovasc. Res.* 47:658–687.
87. Boyett, M. R., H. Dobrzynski, M. K. Lancaster, S. A. Jones, H. Honjo, and I. Kodama. 2003. Sophisticated architecture is required for the sinoatrial node to perform its normal pacemaker function. *J. Cardiovasc. Electrophysiol.* 14:104–106.
88. Verheijck, E. E., R. Wilders, and L. N. Bouman. 2002. Atrio-sinus interaction demonstrated by blockade of the rapid delayed rectifier current. *Circulation.* 105:880–885.
89. Garny, A., P. Kohl, P. J. Hunter, M. R. Boyett, and D. Noble. 2003. One-dimensional rabbit sinoatrial node models: benefits and limitations. *J. Cardiovasc. Electrophysiol.* 14:S121–S132.
90. Peeters, G. A., M. C. Sanguinetti, Y. Eki, H. Konarzewska, D. G. Renlund, S. V. Karwande, and W. H. Barry. 1995. Method for isolation of human ventricular myocytes from single endocardial and epicardial biopsies. *Am. J. Physiol.* 268:H1757–H1764.
91. Péréon, Y., S. Demolombe, I. Baró, E. Drouin, F. Charpentier, and D. Escande. 2000. Differential expression of KvLQT1 isoforms across the human ventricular wall. *Am. J. Physiol. Heart Circ. Physiol.* 278: H1908–H1915.
92. Piacentino III, V., C. R. Weber, X. Chen, J. Weisser-Thomas, K. B. Margulies, D. M. Bers, and S. R. Houser. 2003. Cellular basis of abnormal calcium transients of failing human ventricular myocytes. *Circ. Res.* 92:651–658.

ELSEVIER

Prostaglandins & other Lipid Mediators 78 (2005) 218–230

PROSTAGLANDINS
& other
LIPID MEDIATORS

Involvement of platelet-activating factor and leukotrienes in anaphylactic segmental venoconstriction in ovalbumin sensitized guinea pig livers

Toshishige Shibamoto *, Zonghai Ruan, Sen Cui, Wei Liu, Yasutaka Kurata

Department of Physiology, Kanazawa Medical University, Uchinada, Ishikawa 920-0293, Japan

Received 5 July 2005; received in revised form 18 August 2005; accepted 19 August 2005
Available online 19 September 2005

Abstract

The hepatic anaphylactic venoconstriction is partly involved in anaphylactic hypotension, and is characterized by significant post-sinusoidal constriction and liver congestion in guinea pigs. We determined what chemical mediators are involved in anaphylaxis-induced segmental venoconstriction and liver congestion in perfused livers isolated from ovalbumin sensitized guinea pigs. Livers were perfused portally and recirculatingly at constant flow with diluted blood. The sinusoidal pressure was measured by the double occlusion pressure (Pdo), and was used to determine the pre-sinusoidal (Rpre) and post-sinusoidal (Rpost) resistances. An antigen injection increased both the portal vein pressure and Pdo, resulting in 4.1- and 2.3-fold increases in Rpre and Rpost, respectively. Hepatic congestion was observed as reflected by liver weight gain. Pretreatment with TCV-309 (10 μM, platelet-activating factor (PAF) receptor antagonist) or ONO-1078 (100 μM, human cysteinyl-leukotriene (Cys-LT) receptor 1 antagonist), but not indomethacin (10 μM, cyclooxygenase inhibitor), ketanserin (10 μM, serotonin receptor antagonist), or diphenhydramine (100 μM, histamine H_1 antagonist), significantly attenuated this anaphylactic hepatic venoconstriction. Anaphylaxis-induced increases in Rpre and

Abbreviations: PAF, platelet-activating factor; Cys-LTs, cysteinyl-leukotrienes; $CysLT_1$, cysteinyl-leukotriene receptor 1; $CysLT_2$, cysteinyl-leukotriene receptor 2; Tx, thromboxane; IVC; inferior vena cava; Ppv, portal venous pressure; Phv, hepatic venous pressure; Pdo, double occlusion pressure; Q, portal blood flow rate; Rt, total portal-hepatic venous resistance; Rpre, pre-sinusoidal resistance; Rpost, post-sinusoidal resistance

* Corresponding author. Tel.: +81 76 218 8104; fax: +81 76 286 8010.
E-mail address: shibamo@kanazawa-med.ac.jp (T. Shibamoto).

1098-8823/$ – see front matter
doi:10.1016/j.prostaglandins.2005.08.003

Rpost were significantly inhibited by TCV-309 (by 48%) and ONO-1078 (by 36%), respectively. Combined TCV-309 and ONO-1078 pretreatment exerted additive inhibitory effects on anaphylactic hepatic venoconstriction. Anaphylactic hepatic weight gain was converted to weight loss when post-sinusoidal constriction was attenuated. It is concluded that anaphylaxis-induced pre-sinusoidal constriction is mainly caused by PAF and the post-sinusoidal constriction by Cys-LTs in guinea pig livers.

Keywords: Leukotriene; Platelet-activating factor; Histamine; Hepatic circulation; Antigen; Double occlusion pressure; Hepatic vascular resistance

1. Introduction

Anaphylactic hypotension is sometimes life-threatening, and is caused by a decrease in effective circulating blood volume [1]. It is reported that livers are partly involved in anaphylactic hypotension [2,3]. Anaphylaxis causes hepatic venoconstriction, as observed in rats [3,4], guinea pigs [5] and dogs [6,7], resulting in portal hypertension which then causes congestion of the upstream splanchnic organs, with resultant decrease in venous return and effective circulating blood volume, and finally augmentation of anaphylactic hypotension. Furthermore, if anaphylactic venoconstriction occurs substantially in the hepatic post-sinusoidal veins, hepatic congestion, pooling of blood in liver itself develops, which could contribute to anaphylactic hypotension, as observed in canine anaphylaxis [7,8]. We have recently reported that hepatic anaphylactic venoconstriction in guinea pigs is also accompanied by liver congestion [5]. Measurement of the sinusoidal pressure with the vascular occlusion method revealed that this hepatic congestion was caused by significant post-sinusoidal constriction, although the pre-sinusoidal constriction was predominant [5].

Anaphylaxis is the classic well-established immunoglobulin E dependent reaction [9]. Various inflammatory mediators, including histamine, serotonin, platelet-activating factor (PAF), and eicosanoids such as cysteinyl-leukotrienes (CysLTs), thromboxane (Tx) A_2, and prostaglandin D_2, are involved in the initiation and propagation of the anaphylactic responses [10–14]. However, the primary mediators responsible for the local anaphylactic response may differ among organs and tissues involved. The mediators responsible for hepatic anaphylaxis in any species including guinea pigs have not been determined. Indeed, histamine, which is stored in mast cells and released during degranulation, causes hepatic venoconstriction in guinea pigs [15]. PAF [16], TxA_2 [16] and LTD_4 [17,18], all of which are the products of the arachidonic acid cascade and are synthesized upon mast cell activation, induce hepatic venoconstriction. However, it is not known which mediator is mainly involved in the anaphylactic pre- or post-sinusoidal constriction, and hepatic congestion. Thus, the purpose of the present study was to determine the role of histamine, serotonin, eicosanoids, and PAF in the pre- and post-sinusoidal constriction and hepatic congestion during guinea pig hepatic anaphylaxis by using the corresponding receptor antagonists or enzyme-synthesis inhibitors.

2. Materials and methods

2.1. Animals

The experiments conducted in the present study were approved by the Animal Research Committee of Kanazawa Medical University.

Forty-two male Hartley guinea pigs weighing 356 ± 5 (S.E.) g were used in this study. The animals were housed in a temperature-controlled animal facility with alternating 12-h light/12-h dark cycles and fed standard lab chow ad libitum with free access to water.

2.2. Antigen sensitization

Guinea pigs were actively sensitized by the subcutaneous injection of an emulsion made by mixing complete Freund's adjuvant (0.5 ml) with 1 mg ovalbumin (grade V, Sigma) dissolved in physiological saline (0.5 ml).

2.3. Isolated liver preparation

Two weeks after sensitization, the animals were anesthetized with pentobarbital sodium (35 mg/kg, i.p.) and mechanically ventilated with room air. The methods of isolation and perfusion of guinea pig livers were previously described [5]. A polyethylene tube was placed in the right carotid artery. After laparotomy, the cystic duct and the hepatic artery were ligated and the bile duct was cannulated with the polyethylene tube (1.0 mm i.d., 1.3 mm o.d.). At 5 min after intraarterial heparinization (500 U/kg), 8–9 ml of blood was withdrawn with a plastic syringe through the carotid arterial catheter. The intra-abdominal inferior vena cava (IVC) above the renal veins was ligated, and the portal vein was cannulated with a stainless cannula (2.1 mm i.d., 3.0 mm o.d.) for portal perfusion. After thoracotomy, the supradiaphragmatic IVC was cannulated through a right atrium incision with the same size stainless cannula, then portal perfusion was begun with the heparinized autologous blood that was diluted with 5% bovine albumin (Sigma) in Krebs solution (118 mM NaCl, 5.9 mM KCl, 1.2 mM $MgSO_4$, 2.5 mM $CaCl_2$, 1.2 mM NaH_2PO_4, 25.5 mM $NaHCO_3$, and 5.6 mM glucose) at Hct of 8%. The liver was rapidly excised, suspended from an isometric transducer (TB-652T, Nihon-Kohden, Japan) and weighed continuously throughout the experimental period.

The sensitized livers were perfused at a constant flow rate in a recirculating manner via the portal vein with blood that was pumped using a Masterflex roller pump from the venous reservoir through a heat exchanger (37 °C). The recirculating blood volume was 40 ml. The height of the reservoir and the portal blood flow rate could be adjusted independently to maintain the portal and hepatic venous pressures at any desired level. The perfused blood was oxygenated in the venous reservoir by continuous bubbling with 95% O_2 and 5% CO_2. The portal venous (Ppv) and the hepatic venous (Phv) pressures were measured with pressure transducers (TP-400T, Nihon-Kohden, Japan) attached by sidearm to the appropriate cannulas with the reference points at the hepatic hilus. To occlude inflow and outflow perfusion lines simultaneously for measurement of the double occlusion pressure

(Pdo), two solenoid valves were placed in such a position that each sidearm cannula was between the corresponding solenoid valve and the liver. Portal blood flow rate (Q) was measured with an electromagnetic flow meter (MFV 1200, Nihon-Kohden, Japan), and the flow probe was positioned in the inflow line. Bile was collected drop by drop in a small tube suspended from the force transducer (SB-1T, Nihon-Kohden, Japan). One bile drop yielded 0.027 g and the time between drops was measured for determination of the bile flow rate [4]. The hepatic vascular pressures, blood flow rate, liver weight and bile weight were monitored continuously and displayed through a thermal physiograph (RMP-6008, Nihon-Kohden, Japan). Outputs were also digitized by the analog-digital converter at a sampling rate of 100 Hz. These digitized values were displayed and recorded using a personal computer for later determination of Pdo.

2.4. Experimental protocols

Hepatic hemodynamic parameters were observed for at least 20 min after the start of perfusion until an isogravimetric state (no weight gain or loss) was obtained by adjusting the flow rate and the height of the reservoir at a Phv of 0–1 cmH_2O, and at a Q of 44 ± 1 ml/min/10 g liver wt. After the baseline measurements, the perfused livers excised from the sensitized animals were randomly assigned to one of the following six groups.

In the Control group ($n=6$), ovalbumin 0.1 mg was injected into the reservoir. In all other groups, 10 min before an injection of antigen (0.1 mg), the following receptor antagonists or inhibitors were injected into the perfusate: (1) diphenhydramine HC1 (100 μM), a histamine H_1-receptor antagonist, for the Diphenhydramine group ($n=6$); (2) ketanserin (10 μM), a serotonin-receptor antagonist, for the Ketanserin group ($n=6$); (3) indomethacin (10 μM), a cyclooxygenase inhibitor, for the Indomethacin group ($n=6$); (4) TCV-309 (l0 μM; {3-bromo-5-[*N*-phenyl-*N*-(2-{[2-(1,2,3,4-tetrahydro-2-isoquinolyl-carbonyloxy)-ethyl]carbamoyl}ethyl)carbamyl]-l-propylpyridi nium nitrate}), a PAF-receptor antagonist [19], for the TCV-309 group ($n=6$); (5) ONO-1078 (100 μM; 4-oxo-8-[p-(4-phenylbutyloxy) benzoylamino]-2-(tetrazol-5-yl)-4H-1-benzopyran hemihydrate), a specific antagonist for human cysteinyl leukotriene receptor 1 ($CysLT_1$) [20], for the ONO-1078 group ($n=6$); and (6) both TCV-309 (10 μM) and ONO-1078 (100 μM) for the combined TCV-309 and ONO-1078 group ($n=6$).

The effects of each inhibitor or antagonist were evaluated by comparing the response of the agent-treated group with that of the Control group. The concentrations of TCV-309 (10 μM), diphenhydramine (100 μM), and ketanserin (10 μM) employed in this study were high enough to completely inhibit submaximal hepatic venoconstriction induced by 10 μM PAF, 100 μM histamine, and 10 μM serotonin, respectively, in the isolated guinea pig livers in our preliminary studies. The concentrations of indomethacin and ketanserin were chosen as previously described [21,22].

The hepatic sinusoidal pressure was measured by the double occlusion method [7]. Both the inflow and outflow lines were simultaneously and instantaneously occluded for 13 s using the solenoid valves, after which Ppv and Phv rapidly equilibrated to a similar or identical pressure, which was Pdo. Actually, Pdo values were obtained from the digitized data of Ppv and Phv using an original program (LIVER software, Biomedical

Science, Kanazawa, Japan). In each experimental group, Pdo was measured at baseline and 4, 6, and 10 min, and then at a 10-min intervals up to 120 min after an injection of ovalbumin.

The total portal-hepatic venous (Rt), pre-sinusoidal (Rpre) and post-sinusoidal (Rpost) resistances were calculated by the following equations.

$$\mathrm{Rt} = \frac{(\mathrm{Ppv} - \mathrm{Phv})}{Q} \tag{1}$$

$$\mathrm{Rpre} = \frac{(\mathrm{Ppv} - \mathrm{Pdo})}{Q} \tag{2}$$

$$\mathrm{Rpost} = \frac{(\mathrm{Pdo} - \mathrm{Phv})}{Q} \tag{3}$$

2.5. Drugs

TCV-309 and ONO-1078 were kindly provided by Takeda Chemical, (Osaka, Japan) and Ono Pharmaceutical (Osaka, Japan), respectively. Diphenhydramine-HCl, indomethacin and ketanserin were purchased from Sigma (St. Louis, MO, USA). TCV-309, ketanserin, and diphenhydramine-HC 1 were dissolved in saline. ONO-1078 was dissolved in 1N NaOH and ethanol. Indomethacin was dissolved in DMSO. Concentrations of drugs were expressed as a final concentration in the perfusate.

2.6. Statistics

All results are expressed as the means ± S.E. Data were analyzed by one- and two-way analysis of variance, using repeated-measures for two-way comparison within groups. Comparisons of individual points between groups and within groups were made by Bonferroni's test. Differences were considered as statistically significant at P-values less than 0.05.

3. Results

3.1. Antigen-induced hepatic segmental venoconstriction and hepatic weight gain

Fig. 1(left) shows a representative example of the response to 0.1 mg ovalbumin in the Control group. Within 1 min after an ovalbumin injection, venoconstriction occurred as evidenced by an increase in Ppv, which reached peak levels of 23.5 ± 1.2 cmH_2O from the baseline of 7.2 ± 0.2 cmH_2O. The Ppv-to-Phv gradient, the determinant of Rt, increased to 3.3 times the baseline, indicating that Rt increased by the same degree, as shown in Fig. 2. The double occlusion maneuver performed at 4 min after antigen revealed the sinusoidal pressure of Pdo (7.2 ± 0.4 cmH_2O) higher than that of the baseline (3.3 ± 0.1 cmH_2O). The Pdo-to-Phv gradient increased from the baseline of 2.9 ± 0.1 to 6.7 ± 0.4 cmH_2O, indicating an increase in Rpost (2.3-fold baseline). However, the increase in the Ppv-to-Pdo gradient (3.9 ± 0.2 cmH_2O versus 16.3 ± 1.1 cmH_2O, baseline versus peak) was greater than that

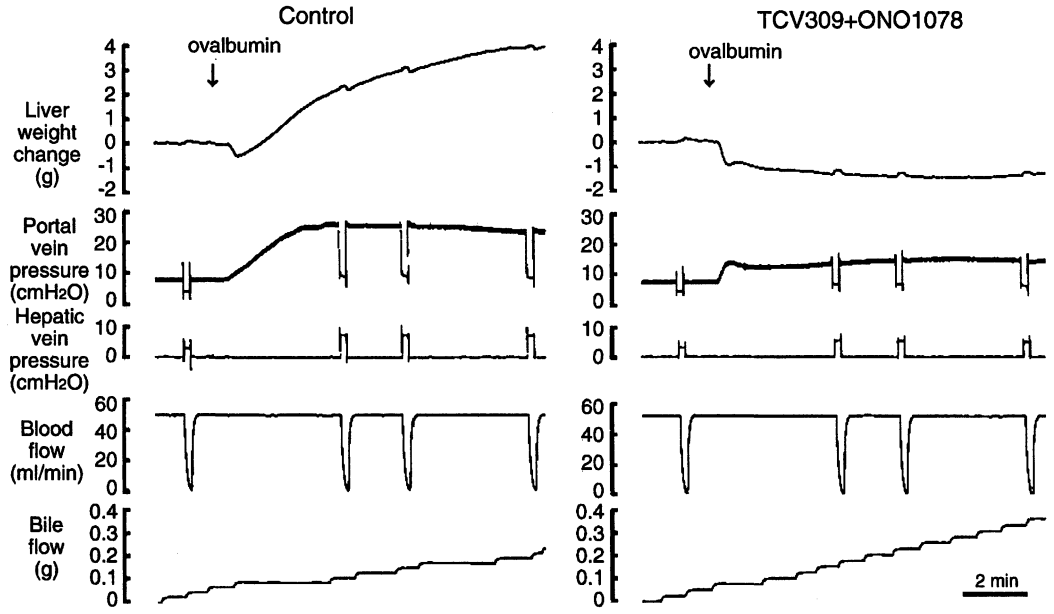

Fig. 1. Representative recordings of the response to the antigen, ovalbumin 0.1 mg in the Control (left) and the combined TCV-309 and ONO-1078 (right) groups.

in the Pdo-to-Phv gradient, indicating a greater increase in Rpre (4.2-fold baseline) than Rpost. At the same time the liver weight showed a gradual increase, reaching the peak of 2.1 ± 0.5 g/10 g liver weight at 10 min. Concomitant with venoconstriction, the bile flow rate decreased to 57% of the baseline of 0.03 ± 0.01 g/min/10 g liver wt.

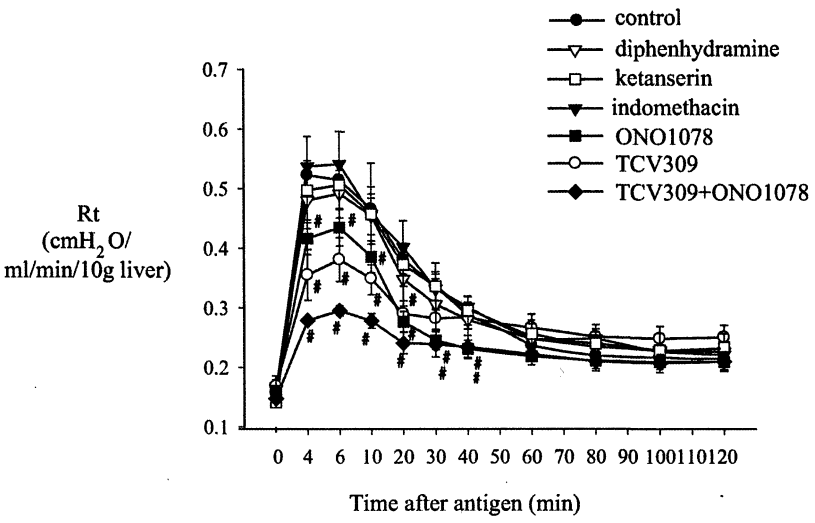

Fig. 2. Time course of total vascular resistance (Rt) in all seven groups. Values are means ± S.E.; $^{\#}P < 0.05$ vs. the Control group. All values of Rt after antigen in each group were significantly different from the corresponding baseline values.

3.2. *Effects of diphenhydramine, ketanserin, indomethacin, TCV-309, ONO-1078, and combined TCV-309 and ONO-1078 on antigen-induced hepatic segmental venoconstriction and hepatic weight gain*

Fig. 2 shows the time course of changes in Rt after antigen in all groups studied. In the control sensitized group, Rt increased from the baseline levels of 0.16 ± 0.01 to the peak levels of 0.52 ± 0.02 $cmH_2O/ml/min/10\,g$ liver wt. at 4 min after antigen, followed by a gradual return towards the baseline. Pretreatment with TCV-309, ONO-1078, or the combination of TCV-309 and ONO-1078 (TCV-309 + ONO-1078), but not indomethacin, ketanserin, or diphenhydramine, significantly attenuated this increase in Rt. The order of the degrees of the inhibition was the combined TCV-309 and ONO-1078 > TCV-309 > ONO-1078, as shown in Fig. 2. Actually the peak levels of Rt after antigen decreased to 54, 71, and 79% of that of the Control group in the TCV-309 + ONO-1078, TCV-309, and ONO-1078 group, respectively. Thus the inhibitory effect of the combination of TCV-309 and ONO-1078 seemed to be exerted in an additive, rather than synergistical, manner of an inhibitory effect of each drug. Fig. 3 shows the results for Rpre and Rpost. Anaphylaxis-

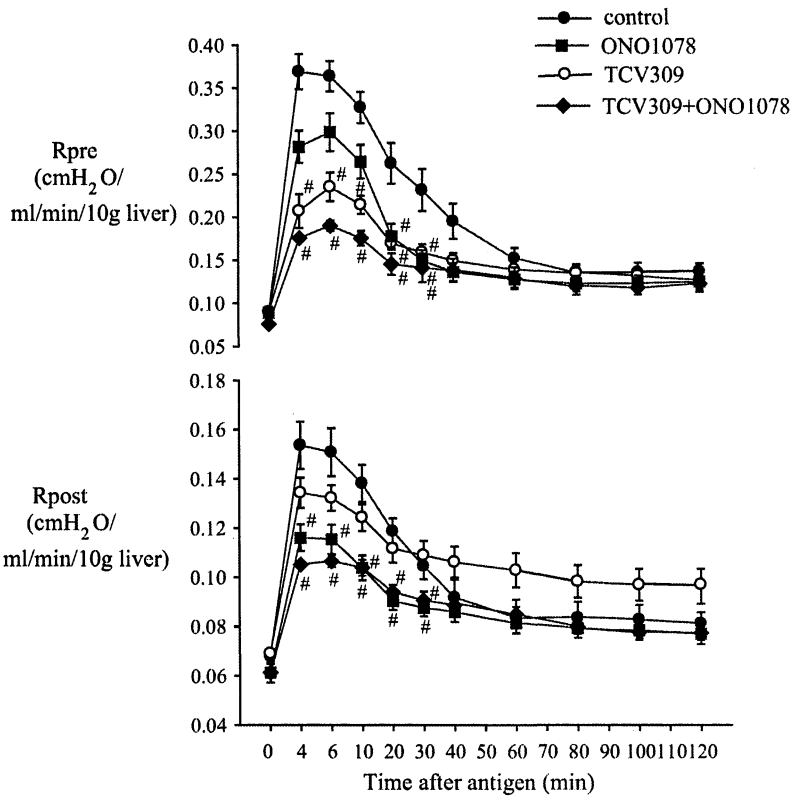

Fig. 3. Time course of the pre-sinusoidal resistance (Rpre) and post-sinusoidal resistance (Rpost) in the Control, the TCV-309, the ONO-1078, and the combined TCV-309 and ONO-1078 groups. Values are means ± S.E.; $^{\#}P < 0.05$ vs. the Control group. All values of Rpre and Rpost after antigen in each group were significantly different from the corresponding baseline values.

induced increases in Rpre and Rpost were significantly attenuated by TCV-309 (by 44%) and ONO-1078 (by 25%), respectively. Combined TCV-309 and ONO-1078 pretreatment exerted additive inhibitory effects on anaphylactic segmental venoconstriction, with pre- and post-sinusoidal vessel constriction decreased by 49 and 27%, respectively. Fig. 1 (right) shows a representative example of the response in the combined TCV-309 and ONO-1078 group.

Fig. 4 shows Pdo and liver weight changes in all groups studied. In the Control group the sinusoidal pressure of Pdo increased significantly from the baseline of 3.3 ± 0.1 cmH_2O to the peak of 7.2 ± 0.4 cmH_2O at 4 min after the antigen. Pretreatment with ONO-1078 and combined TCV-309 and ONO-1078 significantly attenuated the increase in Pdo after antigen, with the peak value of Pdo at 4 min in the ONO-1078 and the combined groups being 5.6 ± 0.2 and 5.2 ± 0.1 cmH_2O, respectively. Anaphylactic hepatic weight gain was observed in all groups but not in the ONO-1078, TCV-309, or the combined TCV-309 and ONO-1078 groups. In the ONO-1078 and the combined groups, the liver weight after antigen significantly decreased to the nadir of -1.0 ± 0.1 and -1.3 ± 0.1 g/10 g liver wt., respectively. In the TCV-309 group, the liver weight tended to decrease but not significantly after antigen.

4. Discussion

In the present study, we determined the chemical mediators responsible for anaphylactic hepatic segmental venoconstriction in isolated sensitized guinea pig livers perfused at a constant flow. The hepatic vascular resistances were assigned to the Rpre and Rpost by measuring the sinusoidal pressure with the vascular occlusion methods [7]. We found that hepatic anaphylactic venoconstriction was characterized by predominant pre-sinusoidal constriction and liver weight gain. This finding was consistent with our previous findings [5] although the method of sensitization of the guinea pigs with ovalbumin was different: the antigen was injected intraperitoneally in the previous study [5], while subcutaneously in the present study. The main finding of the present study was that anaphylaxis-induced pre-sinusoidal constriction was significantly inhibited by a PAF-receptor antagonist, TCV-309, and post-sinusoidal constriction by a $CysLT_1$ receptor antagonist, ONO-1078. The combined TCV-309 and ONO-1078 pretreatment exerted additive inhibitory effects on this segmental venoconstriction. On the other hand, inhibition of the receptor of histamine or serotonin, or inhibition of cyclooxygenase, alone did not affect the hepatic anaphylactic response. Another major finding was that anaphylactic hepatic weight gain was converted to weight loss when post-sinusoidal constriction was attenuated by ONO-1078 and combined TCV-309 and ONO-1078.

In the present study, pretreatment with TCV-309, a PAF antagonist, most intensely inhibited the increase in Rt after antigen (by 29%). This finding suggests that PAF is the primary mediator of the hepatic anaphylactic venoconstriction in guinea pigs. This hepatic venoconstriction was characterized by predominant pre-sinusoidal constriction rather than post-sinusoidal constriction. Actually, TCV-309 significantly attenuated this anaphylactic pre-sinusoidal constriction, but not the post-sinusoidal constriction, as shown in Fig. 3. With respect to the effects of PAF on the segmental hepatic vascular resistances of guinea pigs,

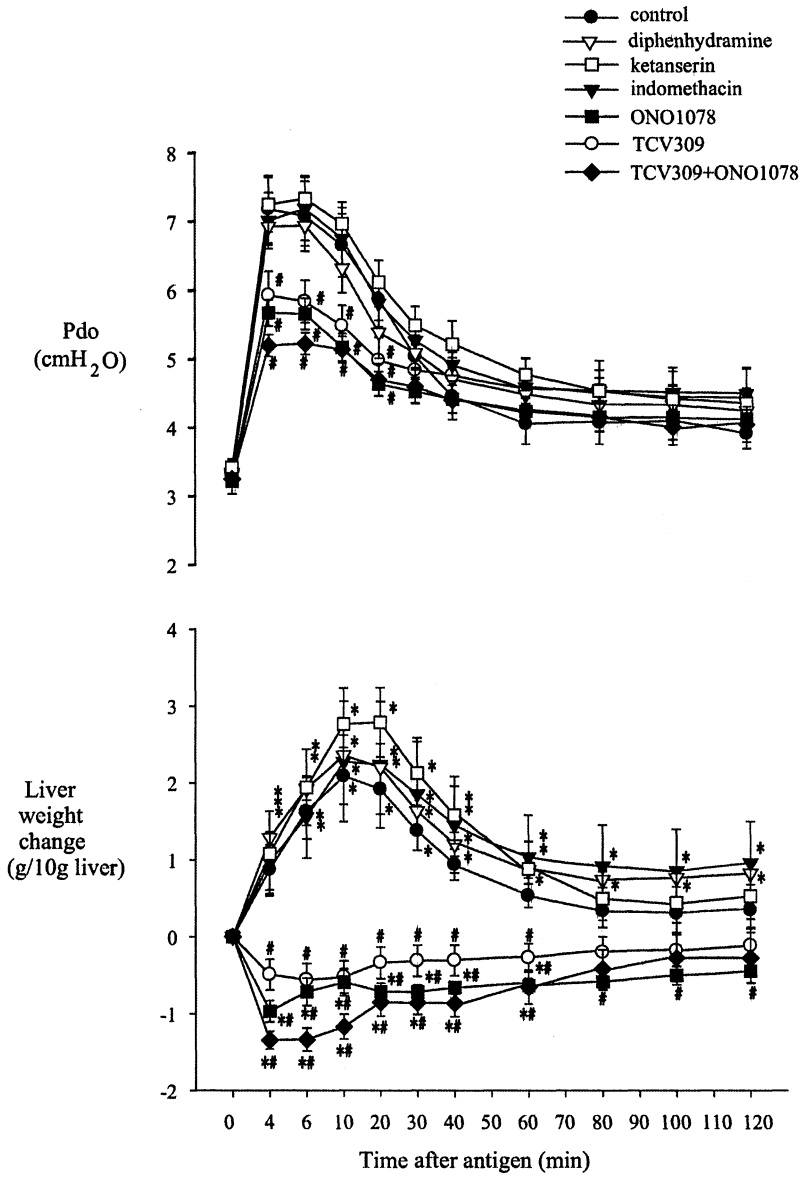

Fig. 4. Time course of the double occlusion pressure (Pdo) and the liver weight change in all seven groups. Values are means ± S.E.; $^{*}P < 0.05$ vs. baseline. The asterisks were not given in Pdo after antigen, because all these values were significantly different from the corresponding baseline values. $^{\#}P < 0.05$ vs. the Control group.

we have recently reported that PAF injected into the isolated guinea pig livers perfused in the same way as in the present study caused predominant pre-sinusoidal constriction with liver weight gain, the response similar to the anaphylactic response [16]. The crucial role of PAF was also reported in guinea pig anaphylaxis in vivo and in isolated lung parenchymal strips in vitro [23]. Darius et al. [23] demonstrated that the histamine- and leukotriene-independent component of anaphylactic hypotension and bronchoconstriction

in guinea pigs is mediated by PAF. These findings are consistent with the present results on the hepatic anaphylaxis in guinea pigs.

Cys-LTs are demonstrated to be as another main mediator in the guinea pig hepatic vascular anaphylaxis since pretreatment with ONO-1078 significantly attenuated the increase in Rt after antigen (by 21%). In contrast to TCV-309, which selectively inhibited the pre-sinusoidal constriction, ONO-1078, selective $CysLT_1$ antagonist, significantly inhibited anaphylactic post-sinusoidal constriction, but not the pre-sinusoidal constriction. Although Cys-LTs constrict hepatic vessels [17,18], it is not known which vascular segment of hepatic vessels is preferentially constricted by Cys-LTs. The present study suggests that Cys-LTs contract significantly the post-sinusoidal vessels of guinea pig livers via the $CysLT_1$ receptor, and substantially contribute to anaphylactic hepatic venoconstriction of this animal. It has been known that the vasoactive effects of Cys-LTs are mediated by at least 2 specific receptors, $CysLT_1$ and Cys-LT receptor 2 ($CysLT_2$) [24,25]. However there are only a limited number of studies that revealed the roles of these specific receptors in hepatic circulation [26]. Graupera et al. [26] reported using intact perfused rat livers that $CysLT_1$ receptor blockade mimics the effect on portal perfusion pressure caused by 5-lipoxygenase inhibition, suggesting that regulation of normal vascular tone by Cys-LTs is mediated by the activation of $CysLT_1$ receptors. We here show that anaphylactic post-sinusoidal constriction in guinea pigs is mediated by the activation of $CysLT_1$ receptors. However, the roles of $CysLT_2$ receptor and a third class of Cys-LT receptor could not be examined due to the lack of specific antagonists [24,25]. In future, further studies are required in this respect.

Combined TCV-309 and ONO-1078 pretreatment inhibited the anaphylaxis-induced increases in Rt, Rpre, and Rpost by 46, 49, and 27%, respectively. This suggests that PAF and Cys-LTs exert the hepatic venoconstrictive actions in not synegistical but additive manner.

In the present study, diphenhydramine, a histamine H_1-receptor antagonist, did not attenuate the venoconstriction induced by ovalbumin antigen. Histamine is known to be released during systemic anaphylaxis in humans [27] and in animals [12,28,29]. Actually, Selig et al. [13] showed, by using isolated perfused lungs of guinea pigs that were sensitized with ovalbumin, that the histamine H_1-receptor antagonist prevented the antigen-induced changes in pulmonary hemodynamics, intratracheal pressure, and edematogenic responses. Organ dependent difference in responsiveness to antigen may account for the difference in the effect of histamine antagonist between lungs and livers. Indeed, we have recently shown that in guinea pigs, the hepatic vascular response to histamine was relatively weak and short-lasting as observed in isolated perfused livers: even at high concentration of 100 μM, Rt increased only to 1.7-fold baseline, and this response lasted only 3 min [15]. Another explanation why a histamine antagonist did not prevent anaphylactic response is that histamine is released only early stage of anaphylaxis in guinea pigs [23,30]. Mest et al. [30] reported by examining the time course changes in chemical mediators during guinea pig anaphylaxis that histamine and serotonin were released immediately after antigen, reaching peak levels at 20–30 s, and then the release decreased rapidly within 60 s. Thus, when the maximum venoconstriction occurred in the present perfused guinea pig livers, histamine might have disappeared in perfusing blood. Failure of the histamine antagonist to prevent the physiological changes after the antigen administration in the present study suggests a minor role

of histamine in anaphylactic vasoconstriction in guinea pig livers. Finally, a more plausible explanation for the absence of the effect of diphenhydramine (histamine inhibitor), and also ketanserin (serotonin inhibitor) or indomethacin (cyclooxygenase inhibitor) on vasoconstriction is that more than one mediators are released at supramaximal concentrations, and thus inhibition of a single mediator has no effect on the magnitude of the constriction. For instance, even if the response to histamine, serotonin or TxA_2 is completely blocked, the response to PAF and Cys-LTs still remain intact, and no change in the constriction is observed.

In this study, liver weight gain was observed after antigen in the Control group but not in either TCV-309, ONO-1078, or the combined ONO-1078 and TCV-309 group. Moreover, the latter two groups showed the liver weight loss response. The weight gain in the Control group might be caused by post-sinusoidal venoconstriction as evidenced by a substantial increase in Rpost. This post-sinusoidal contraction could induce the upstream sinusoidal engorgement and increased extravascular fluid filtration caused by an increase in Pdo, the sinusoidal hydrostatic pressure. The absence of liver weight gain after antigen in the TCV-309, ONO-1078, or the combined groups may be due to the attenuation of post-sinusoidal constriction. Actually in these three groups, the sinusoidal pressure of Pdo, which is the indicator of post-sinusoidal resistance as well as the determinant of transvascular fluid movement and hepatic congestion, was not so much increased. We previously reported that the magnitude of an increase in Pdo in response to PAF and the TxA_2 analogue was strongly associated with the liver weight change in the same guinea pig liver preparation [16]. The perfused liver with pre-sinusoidal venoconstriction does not show liver weight gain until post-sinusoidal vessels contract enough to elevate Pdo to more than 6.5 cmH_2O. In the present study, the peak Pdo in the TCV-309, ONO-1078 and the combined ONO-1078 and TCV-309 groups was less than 6.5 cmH_2O (Fig. 4). On the other hand, the conversion from liver weight gain to liver weight loss after antigen in the ONO-1078 and the combined groups may be explained as follows: In these two groups, the anaphylaxis-induced post-sinusoidal constriction was substantially attenuated, but the pre-sinusoidal constriction was preserved. In the presence of pre-sinusoidal constriction, the blood volume of sinusoids, that was distal to the constricted pre-sinusoidal portal venules, could be passively reduced due to a decrease in distending pressure of the sinusoids. This reduction of blood volume may result in liver weight loss.

In summary, the chemical mediators responsible for the hepatic anaphylactic segmental venoconstriction induced by ovalbumin antigen were determined in isolated guinea pig livers. Anaphylaxis-induced pre- and post-sinusoidal constriction was inhibited markedly by the PAF inhibitor TCV-309 and the Cys-LT receptor 1 antagonist ONO-1078, respectively, whereas histamine, serotonin or cyclooxygenase inhibitors did not affect this response. We conclude that anaphylaxis-induced pre-sinusoidal constriction is mainly caused by PAF and the post-sinusoidal constriction by Cys-LTs in guinea pig livers.

Acknowledgements

The authors thank Takeda Chemical Industries (Osaka, Japan) and Ono Pharmaceutical Company (Osaka, Japan) for the gift of TCV-309 and ONO-1078, respectively.

This study was supported by a Grant for Collaborative Research from Kanazawa Medical University (C2004-1, C2005-1) and a Grant-in-Aid for Scientific Research from the Ministry of Education, Culture, Sports, Sciences and Technology of Japan (No. 15591665).

References

[1] Brown AFT. Anaphylactic shock: mechanism and treatment. J Accid Emerg Med 1995;12:89–100.
[2] Pavek K, Piper PJ, Smedegard G. Anaphylatoxin-induced shock and two patterns of anaphylactic shock: hemodynamics and mediators. Acta Physiol Scand 1979;105:393–403.
[3] Shibamoto T, Cui S, Ruan Z, Liu W, Takano H, Kurata Y. Hepatic venoconstriction is involved in anaphylactic hypotension in rats. Am J Physiol Heart Circ Physiol, May 27 [Epub], in press.
[4] Hines KL, Fisher RA. Regulation of hepatic glycogenolysis and vasoconstriction during antigen-induced anaphylaxis. Am J Physiol 1992;262:G868–77.
[5] Ruan Z, Shibamoto T, Shimo T, Tsuchida H, Koizumi T, Nishio M. NO, but not CO, attenuates anaphylaxis-induced postsinusoidal contraction and congestion in guinea pig liver. Am J Physiol Regul Integr Comp Physiol 2004;286:R94–100.
[6] Weil R. Studies in anaphylaxis. XXI Anaphylaxis in dogs: a study of the liver in shock and peptone poisoning. J Immunol 1917;2:525–56.
[7] Yamaguchi Y, Shibamoto T, Hayashi T, Saeki Y, Tanaka S. Hepatic vascular response to anaphylaxis in isolated canine liver. Am J Physiol Regul Integr Comp Physiol 1994;267:R268–74.
[8] Essex HE. Anaphylactic and anaphylactoid reactions with special emphasis on the circulation. In: Hamilton, W.F., editor. Handbook of physiology circulation, Section 2, vol. III, Chapter 66, Bethesda, MD: Am. Physiol. Soc.;1965, p. 2391–408.
[9] Patterson R, Roberts M, Pruzansky JJ. Comparisons of reaginic antibodies from three species. J Immunol 1969;102:466–75.
[10] Hagmann W, Hacker HJ, Buchholz U. Resident mast cells are the main initiators of anaphylactic leukotriene production in the liver. Hepatology 1992;16:1477–84.
[11] Lieberman PL. Specific and idiopathic anaphylaxis: pathophysiology and treatment. In: Bierman CW, Pearlman DL, Shapiro CG, et al., editors. Allergy, asthma, and immunology from infancy to adulthood. 3rd ed. Philadelphia: WB. Saunders; 1996. p. 297–319.
[12] Morel DR, Skoskiewicz M, Robinson DR, Bloch KJ, Hoaglin DC, Zapol WM. Leukotrienes, thromboxane A_2, and prostaglandins during systemic anaphylaxis in sheep. Am J Physiol Heart Circ Physiol 1991;261:H782–92.
[13] Selig WN, Tocker JE, Tannu SA, Cerasoli F, Durham SK. Pharmacologic modulation of antigen-induced pulmonary responses in the perfused guinea pig lung. Am Rev Respir Dis 1993;147:262–9.
[14] Terashita Z, Imura Y, Nishikawa K. Possible pathophysiological roles of platelet-activating factor in shock and the PAF antagonists, CV-3988 and CV-6209. In: Handley DA, Sauders RN, Houlihan WJ, Tomesch JC, editors. Platelet-activating factor in endotoxin and immune diseases. New York: Marcel Dekker; 1990. p. 547–75.
[15] Shibamoto T, Narushima M, Ling YQ, et al. Different hepatic vascular response to noradrenaline and histamine between guinea pig and rat. Acta Physiol Scand 2004;180:255–63.
[16] Ruan Z, Shibamoto T, Shimo T, et al. Effects of platelet-activating factor and thromboxane A_2 on isolated perfused-guinea pig liver. Prostaglandins Other Lipid Mediat 2004;73:73–85.
[17] Bilzer M, Lauterburg BH. Peptidoleukotrienes increase the efflux of glutathione from perfused rat liver. Prostaglandins Leukot Essent Fatty Acids 1993;49:715–21.
[18] Haussinger D, Stehle T, Gerok W. Effects of leukotrienes and the thromboxane A2 analogue U-46619 in isolated perfused rat liver. Metabolic, hemodynamic and ion-flux responses. Biol Chem Hoppe Seyler 1988;369:97–107.
[19] Terashita Z, Kawamura M, Takatani M, Tsuchima S, Imura Y, Nishikawa K. Beneficial effects of TCV-309, a novel potent and selective platelet activating factor antagonist in endotoxin and anaphylactic shock in rodents. J Pharmacol Exp Ther 1992;260:748–55.

[20] Lynch KR, O'Neill GP, Liu Q, et al. Characterization of the human cysteinyl leukotriene CysLT1 receptor. Nature 1999;399:789–93.
[21] Martin GR. Vascular receptors for 5-hydroxytryptamine: distribution, function and classification. Pharmacol Ther 1994;62:283–324.
[22] vom Dahl S, Wettstein M, Gerok W, Haussinger D. Stimulation of release of prostaglandin D2 and thromboxane B2 from perfused rat liver by extracellular adenosine. Biochem J 1990;270:39–44.
[23] Darius HD, Lefer DJ, Smith JB, Lefer AM. Role of platelet-activating factor-acether in mediating guinea pig anaphylaxis. Science 1986;232:58–60.
[24] Hui Y, Funk CD. Cysteinyl leukotrienes receptors. Biochem Pharmacol 2002;64:1549–57.
[25] Capra V. Molecular and functional aspects of human cysteinyl leukotriene receptors. Pharmacol Res 2004;50:1–11.
[26] Graupera M, Garcia-Pagan J-C, Titos E, et al. 5-Lipoxygenase inhibition reduces intrahepatic vascular resistance of cirrhotic rat livers: A possible role of cysteinyl-leukotrienes. Gastroenterology 2002;122:387–93.
[27] Smith PL, Sobotka AK, Bleecker ER, et al. Physiologic manifestations of human anaphylaxis. J Clin Invest 1980;66:1072–80.
[28] Krell RD. Investigation of the role of histamine in antigen-induced bronchoconstriction in the ascaris-hypersensitive dog. Br J Pharmacol 1978;62:519–28.
[29] Silverman HJ, Taylor WR, Smith PL, et al. Effects of antihistamines on the cardiopulmonary changes due to canine anaphylaxis. J Appl Physiol 1988;64:210–7.
[30] Mest HJ, Ponicke K, Heinroth-Hoffmann I, Meissner N, Giessler C. Relevance of mediators to cardiac parameters of isolated anaphylactic guinea-pig heart. Prostaglandins Leukot Essent Fatty Acids 1995;53:21–9.

金医大誌（J. Kanazawa Med. Univ.）30：6－11，2005

Beta-Adrenergic Agonist Therapy for Alveolar Edema in Postoperative Pulmonary Complications

Tsutomu Sakuma, Zheng Wang, Jin Xu, Sumiko Maeda, Makoto Sugita, Motoyasu Sagawa

Abstract: Over the past one and a half decade, we have established and developed an *ex vivo* human lung model for the investigation of alveolar fluid reabsorption (alveolar fluid clearance) in the human lung. Alveolar fluid clearance primarily depends on active sodium transport via apical sodium channel and basolateral Na^+-K^+ ATPase on alveolar epithelial cells. Beta-adrenergic agonists stimulate β_1- and β_2-, but not β_3-adrenergic receptors followed by the increase of cAMP and alveolar fluid clearance. Cystic fibrosis transmembrane conductance regulator plays a role in β-adrenergic agonist stimulated alveolar fluid clearance. Hypothermia followed by rewarming preserves alveolar fluid clearance capacity and the function of β-receptors, the results are favorable in the preservation of donor lung for lung transplantation. Since there was a species difference between alveolar fluid clearance among animals, our date from human lungs have contributed to the research area of ion and fluid transport on the alveolar epithelial cells and to the clinical area of pulmonary edema and lung injury.

Key words: pulmonary edema, alveolar epithelium, ion transport, beta-adrenergic agonist

Introduction

There are a number of postoperative pulmonary complications in which fluid accumulates in the alveolar spaces (Table 1). In such diseases, excess alveolar fluid deteriorates alveolar gas exchange and exposes the patients to hypoxemia. If the therapy for the diseases was not successful, the patient will be exposed to high mortality because of respiratory failure followed by multiple organ failure.

Alveolar fluid clearance plays an important role in resolution of alveolar edema in a number of diseases that occur during intra- and post-operative period in patients who undergo pulmonary resection. Over the past two decades, the mechanism responsible for alveolar fluid clearance has been studied in normal and pathological lungs of sheep (1-3), goats (4) , dogs (5, 6) , rats (7-18), rabbits (19), and mice (20-24). Those studies indicated that apical sodium channel and basolateral Na^+-K^+ ATPase on alveolar type II epithelial cells drive excess alveolar fluid out of the alveolar spaces. In human, active ion and fluid transport was suggested by the

Department of Thoracic Surgery, Kanazawa Medical University, Ishikawa 920-0293, Japan
Corresponding to: Tsutomu Sakuma
Accepted: August 22, 2005

Table 1. Postoperative pulmonary complications in which fluid accumulates in the alveolar spaces

Hydrostatic pulmonary edema
Cardiogenic pulmonary edema
Hyperperfusion pulmonary edema
Post-pneumonectomy pulmonary edema
Increased permeability pulmonary edema
Acute respiratory distress syndrome
Re-expansion pulmonary edema
Ischemia-reperfusion lung injury
Ventilator-induced lung injury
Pulmonary reimplantation response
Interstitial inflammation
Idiopathic interstitial pneumonias
Drug-induced interstitial pneumonia
Alveolar inflammation
Aspiration pneumonia: gastric juice, pleural effusion
Bronchopneumonia
Atelectasis

observation that protein concentration increased greater in pulmonary edema fluid than in simultaneously obtained plasma (25-29), but it was not possible to examine the effect of known inhibitors or agonists of alveolar fluid clearance in the clinical setting. We have established and developed the method to measure alveolar fluid clearance in *ex vivo* human lung, and studied the mechanism responsible for alveolar fluid clearance in human lungs. In this article, human studies for alveolar ion and fluid clearance are summarized.

Methods for alveolar fluid clearance in ex vivo human lung

Since we had studied that alveolar fluid clearance occurred in the presence of pulmonary blood flow in sheep (2), we have advanced the method and tested if alveolar fluid clearance occurred in the isolated human lungs. The instillate consisted of a physiologic albumin solution that was adjusted to be isosmolar (290 mOsm/l) with human serum. The solution consisted of total protein 5.0 g/dl; albumin>99 %; Na^+ 155 mEq/l; K^+ 0.3 mEq/l; Cl^- 115 mEq/l; Ca^{2+} 1.8 mEq/l; HCO_3^- 11 mEq/l; glucose 10 mg/dl; and pH 6.8. Human lungs were obtained from patients who underwent pulmonary resection for bronchogenic carcinoma. The age of the patients was 65 ± 8 years. Preoperative pulmonary function test revealed to be normal. Within 10 minutes of surgical removal, a segmental bronchus was occluded by a balloon catheter. Through the catheter, 40 – 50 ml of isosmolar 5% human albumin solution warmed to 37°C was instilled into the occluded segmental lobe followed by 40 ml of air to advance the instilled solution into the alveolar spaces. The lungs were inflated with 100% oxygen at an airway pressure of 7 cmH_2O. The lung was placed in a plastic bag and a humidified incubator at 37°C in order to minimize dehydration (Figure 1). At the conclusion of the experiment over 1 – 4 h, the lung was removed and alveolar fluid was aspirated with a small catheter (0.75 mmID). Aspirated alveolar fluid (1 – 2 ml) was centrifuged at 3,000 rpm for 10 min. The supernatant of the fluid was obtained for measurement of the protein concentration. The total protein concentrations of the instilled albumin solution and the final alveolar fluid were measured by a biuret method. The albumin content was measured by electrophoresis using a cellulose acetate membrane.

Alveolar fluid clearance was estimated by measuring the increase in the protein concentration of the instilled albumin solution. Since protein leaves the air space very slowly (30), the change of the albumin concentration in the alveolar spaces over 1 – 4 h was used as an index of alveolar fluid clearance. Alveolar liquid clearance (AFC) (% of instilled) was calculated according to the following equation:

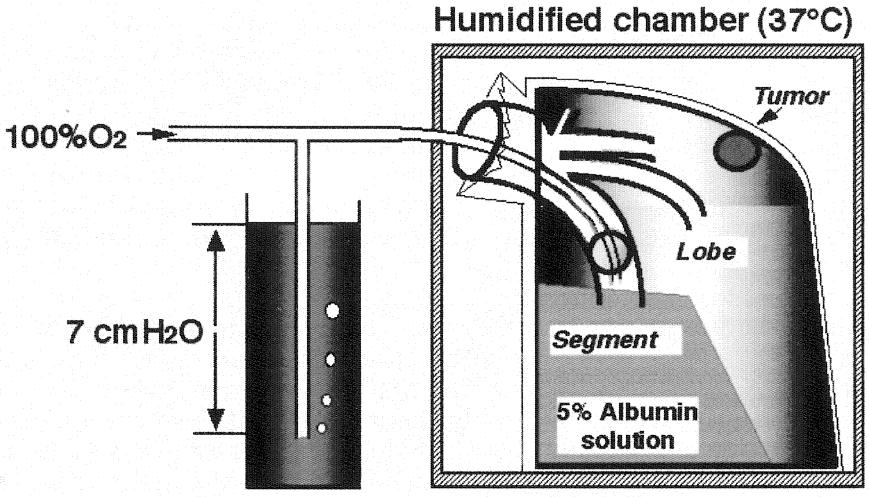

Fig 1. Schematic diagram of the experiment. An isosmolar albumin solution was instilled through the segmental bronchus that was located distant from the tumor.

AFC = (Vi X Fwi-Vf X Fwf) / (Vi X Fwi) X 100
in which V is the volume of the instilled albumin solution (i) and the final alveolar fluid (f), Fw is the water content of the instilled albumin solution (i) and the final alveolar fluid (f). Water content was measured by the albumin concentration. Vf (ml) is measured by the following equation:
Vf (ml) = (Vi X Pi) / Pf
in which P is the albumin concentration of the instilled albumin solution (i) and the final alveolar fluid (f).

Alveolar fluid clearance in ex vivo human lung

Basal alveolar fluid clearance in *ex vivo* human lung in the absence of pulmonary perfusion was 12 ± 2 % over 4 h (31). Amiloride (10^{-5} M), an inhibitor of apical sodium uptake, and ouabain (10^{-3} M), an inhibitor of Na^+-K^+ ATPase activity, reduced alveolar fluid clearance by 40% and 49%, respectively. Hypothermia (8° C) completely inhibited alveolar fluid clearance. These data provided the first direct evidence for active metabolic processes and sodium transport as the major mechanism driving alveolar fluid clearance in *ex vivo* human lung.

β-adrenergic agonists stimulate alveolar fluid clearance

There was a species difference in the effect of β-adrenergic agonists on alveolar fluid clearance. Although β-adrenergic agonists increased alveolar fluid clearance in sheep (1), dogs (5), rats (7), and mice (20), β-adrenergic agonists did not in rabbits (19) and hamsters (32). Therefore, it was an urgent and important issue to determine if β-adrenergic agonists increased alveolar fluid clearance in human lungs.

We determined if a β-adrenergic agonist, terbutaline, stimulated alveolar fluid clearance in *ex vivo* human lungs (31). Terbutaline (10^{-3} or 10^{-4} M) doubled alveolar liquid clearance to 28 ± 9 % over 4 h. Propranolol (10^{-4} M) and amiloride (10^{-5} M) inhibited the terbutaline-increased alveolar fluid clearance. In a subsequent study, salmeterol, a lipophilic β_2-adrenergic agonist, was more potent stimulator of alveolar fluid clearance than terbutaline in ex vivo human lungs (8).

In terms of the distribution of b-receptors in the human alveolar epithelium, 70% are β_2-adrenoceptors and 30% are β_1-adrenoceptors in the human alveolar walls (33). Similar to β_2-agonists, a β_1-adrenergic agonist can increase alveolar fluid clearance in rat lungs (12). Norepinephrine increased alveolar fluid reabsorption via the activation of both α_1- and β-adrenergic receptors in rats (10, 34). However, it is yet uncertain if a β_1-adrenergic agonist and norepinephrine increase alveolar alveolar fluid clearance in human lungs.

Recently we found that endogenous catecholamine concentrations in pulmonary edema fluid increased to the level of 10^{-9} – 10^{-8} M and that administration of exogenous epinephrine (10^{-7} M), but neither epinephrine (10^{-9} M) nor norepinephrine (10^{-7} M), into the distal airspaces could stimulate alveolar fluid clearance in the human lung (22). These results indicate that endogenous catecholamine concentrations in pulmonary edema fluid are probably not sufficient to stimulate alveolar fluid clearance and that administration of exogenous β-agonists into the distal airspaces can be a potent therapy for patients with pulmonary edema.

Glibenclamide(10^{-5}M) and $CFTR_{inh}$-172(10^{-5}M), cystic fibrosis transmembrane conductance regulator (CFTR) inhibitors, inhibited the epinephrine-induced stimulation of alveolar fluid clearance in ex vivo human lungs (18). Our results are consistent with the results that glibenclamide inhibited isoproterenol-stimulated alveolar fluid clearance in human lungs that were obtained from human lung donors whose lungs were rejected for transplantation (22).

Human lung versus rat lung

We determined if there was a difference in the rate of basal alveolar fluid clearance between *ex vivo* human and *ex vivo* rat lungs, and if there was a difference in the effect of β-adrenergic agonist therapy on alveolar epithelial fluid clearance between *ex vivo* human and *ex vivo* rat lungs (8). The results indicated that basal alveolar fluid clearance in rat lungs was significantly faster than in human lungs (24 ± 4% over 4 h in rat lungs compared to 11 ± 2% over 4 h in human lungs). Comparison of equivalent doses of salmeterol indicated that stimulated clearance rates were also faster in rat lungs than in human lungs. Very low doses of salmeterol were effective in *ex vivo* rat lungs (10^{-8} M). Relatively low doses were effective in the *ex vivo* human lungs (10^{-6} M) as a treatment for increasing alveolar fluid clearance. In summary, there are significant differences in the basal and stimulated rates of alveolar epithelial fluid clearance between rat and human lungs. The human lung responds well to relatively low doses of β-adrenergic agonist, a finding with potentially important clinical implications for hastening the resolution of alveolar edema.

Temperature dependent alveolar fluid clearance

Since hypothermia abolished alveolar fluid clearance in the excised human lungs (35), we advanced the study to determine whether alveolar fluid clearance resumed in the human lungs that were rewarmed after severe hypothermia (36). An isosmolar albumin solution was instilled into *ex vivo* human lungs that were rewarmed to 37°C after hypothermia (7 ± 3°C) over 5 h, and then alveolar fluid clearance was measured by the concentration of albumin in the alveolar fluid sample after 4 h. Although hypothermia completely abolished alveolar fluid clearance, alveolar fluid clearance resumed to a normal level of 12 ± 1% over 4 h in the lungs that were rewarmed after hypothermia. Amiloride decreased alveolar fluid clearance by 47% in the rewarmed lungs. Terbutaline increased alveolar fluid clearance by nearly 300% in the rewarmed lungs.

Alveolar fluid clearance was also measured in human lungs that were obtained from human lung donors whose lungs were rejected for transplantation (14, 17). The donor lungs were transported under hypothermic conditions and then warmed to 37°C over 3 – 4 h. Next, 60 – 120 ml of isosmolar 5% human albumin solution containing 5 mCi ^{131}I-albumin that was used for calculation of alveolar fluid clearance. Alveolar fluid clearance capacity in donor lungs was similar to that in *ex vivo* human lungs from patients with bronchogenic carcinoma (36).

These studies indicated that basal and stimulated alveolar fluid clearance is normal in the excised human lung that has been exposed to severe hypothermia followed by rewarming to human body temperature. Amiloride-sensitive sodium transport and β-adrenoceptors that mediate alveolar fluid clearance are preserved in the rewarmed human lungs after hypothermia. The results provide further evidence of the resistance of alveolar epithelial transport mechanisms to injury, a finding that has been documented under a variety of clinically relevant pathological conditions.

In addition, a study was conducted to determine whether hypothermia inhibited alveolar epithelial injury in the resected human lung during preservation (37). A hyposmolar albumin solution, 248 mOsm/kg, was instilled into the alveolar spaces of the resected human lungs which were inflated with an airway pressure of 7 cmH_2O and stored at either 37°C or 8°C for 4 h. Alveolar fluid was aspirated and the influx of lactate dehydrogenase (LDH) and globulin into the alveolar spaces, as markers of alveolar epithelial injury, was measured. Ion transport and fluid clearance across the alveolar epithelium were calculated by the changes in electrolyte and albumin concentrations in the alveolar fluid, respectively. While the LDH levels and globulin concentrations increased significantly in the hyposmolar experiments at 37°C, hypothermia inhibited these increases. Alveolar fluid clearance at 37°C increased to 20% in the hyposmolar experiments compared with 12% in the control isosmotic experiments, however, sodium and chloride transport in the hyposmolar experiments was not significantly different from that in the isosmolar experiments. This study indicates that hypothermia at 8°C inhibits alveolar epithelial injury caused by the hyposmolar solution in excised human lungs. Moreover, alveolar ion and fluid clearance mechanisms were preserved across the injured alveolar epithelial cells.

K_{ATP} channel opener stimulates alveolar fluid clearance

Since the effect of ATP-sensitive potassium channel (K_{ATP} channel) opener on the function of alveolar epithelial cells is unknown, the effect of YM-934, a newly synthesized K_{ATP} channel opener, on potassium influx into the alveolar spaces and alveolar fluid clearance was determined in the resected human lung (38). An isosmolar albumin solution with a low potassium concentration was instilled into the distal airway of the resected human lungs. Net potassium transport and alveolar fluid clearance were measured for 4 h using both the changes in the potassium concentration of the alveolar fluid as well as changing the alveolar fluid volume. YM934 (10^{-4} M) increased net influx of potassium by 76% into the alveolar spaces and also increased alveolar fluid clearance by 48 % in the experiments with a potassium concentration of 0.3 mEq/l. Glibenclamide (10^{-4} M), a K_{ATP} channel blocker, inhibited the YM934-increased influx of potassium transport and the increase in alveolar fluid clearance. Also amiloride (10^{-5} M) blocked the YM934-increase in alveolar fluid clearance. These results indicate that a K_{ATP} channel opener can affect potassium transport and net vectorial fluid movement across the human alveolar epithelium.

Recently, Kir channel (Kir6.1) and sulfonylurea receptor (SUR 2B) forming K_{ATP} channel were detected in freshly isolated and cultured rat alveolar type II cells (39). Glibenclamide reduced amiloride-sensitive sodium current and abolished chloride current stimulation by forskolin in

cultured monolayer of alveolar type II epithelial cells. In addition, K_{ATP} channel activation by pinacidil increased sodium and chloride transepithelial transport. Although further studies are necessary to elucidate the relationships among K_{ATP} channel, β-adrenoceptor and chloride channel in the alveolar epithelial cells, it is noted that K_{ATP} channels may be necessary for β-agonist mediated stimulation of chloride transport.

Alveolar fluid clearance in the remaining lung after thoractomy

We studied the effect of thoracotomy on alveolar fluid clearance in the remaining lungs in a patient who underwent exploratory thoracotomy (40). The first exploratory thoracotomy was carried out 9 days before the second thoracotomy. Since the tumor was malignant, the second thoracotomy was carried out and alveolar fluid clearance was measured in the excised lungs. We found that alveolar sodium and fluid clearance increased by nearly 200 %. Histological examination showed that the number of alveolar type II epithelial cells was markedly increased particularly in the alveoli near the visceral pleura (41). These results suggest that an increase in the number of alveolar type II cells may accelerate alveolar fluid clearance under certain clinical conditions.

Summary

We have established a method to study ion and fluid transport across the alveolar epithelium in *ex vivo* human lung and determined the mechanisms responsible for alveolar fluid clearance. The principle results were as follows. Alveolar fluid clearance occurred in the excised human lung. Active ion transports mediated by amiloride-sensitive sodium channels and Na^+-K^+ ATPase accounted for the mechanisms responsible for alveolar fluid clearance. β_2-adrenergic agonists (terbutaline, salmeterol, and epinephrine) were potent stimulators of alveolar liquid clearance via β-adrenergic receptors and sodium channels. A potassium channel opener (YM934) also increased alveolar fluid clearance. Hypothermia abolished alveolar fluid clearance and rewarm following hypothermia resumed normal alveolar fluid clearance. Proliferation of type II alveolar epithelial cells played a role in the increase in alveolar fluid clearance in a patient who had undergone partial pneumonectomy of the lung. CFTR may play a potential role in epinephrine stimulated alveolar fluid clearance. These observations have important clinical implications because stimulation of alveolar fluid clearance may accelerate the resolution of alveolar edema in many diseases (Table 2). However, further studies are needed because little data are available regarding alveolar fluid clearance in *in vivo* human lungs.

Table 2. Strategies to accelerate the resolution of pulmonary edema in the human lung

Increase alveolar fluid clearance capacity
Aerosolized b-adrenergic agonists
β_1-adrenergic agonist (Denopamine)
β_2-adrenergic agonist (Salmeterol, Terbutaline, Epinephrine)
Intravenous administration
Dobutamine
Dopamine
Potassium channel opener
Prevent collapse of the alveolar spaces
Proliferation of type II alveolar epithelial cells
Nutrition

These studies were supported by Grant for Project Research from High-Technology Center of Kanazawa Medical University (H2003-7, H2004-7, H2005-7), Grant for Collaborative Research from Kanazawa Medical University (C2003-1, C2004-1, C2005-1), Grant-In-Aid for Scientific Research from the MEXT, Japan (14571289, 17591492).

References

1. Berthiaume Y, Staub NC, Matthay MA: Beta-adrenergic agonists increase lung liquid clearance in anesthetized sheep. J Clin Invest 1987; **79:** 335-43.
2. Sakuma T, Pittet JF, Jayr C et al: Alveolar liquid and protein clearance in the absence of blood flow or ventilation in sheep. J Appl Physiol 1993; **74:** 176-85.
3. Campbell AR, Folkesson HG, Berthiaume Y et al: Alveolar epithelial fluid clearance persists in the presence of moderate left atrial hypertension in sheep. J Appl Physiol 1999; **86:** 139-51.
4. Serikov VB, Grady M, Matthay MA: Effect of temperature on alveolar liquid and protein clearance in an in situ perfused goat lung. J Appl Physiol 1993; **75:** 940-7.
5. Berthiaume Y, Broaddus VC, Gropper MA et al: Alveolar liquid and protein clearance from normal dog lungs. J Appl Physiol 1988; **65:** 585-93.
6. Sugita M, Ferraro P, Dagenais A et al: Alveolar liquid clearance and sodium channel expression are decreased in transplanted canine lungs. Am J Respir Crit Care Med 2003; **167:** 1440-50.
7. Crandall ED, Heming TA, Palombo RL et al: Effects of terbutaline on sodium transport in isolated perfused rat lung. J Appl Physiol 1986; **60:** 289-94.
8. Sakuma T, Folkesson HG, Suzuki S et al: Beta-adrenergic agonist stimulated alveolar fluid clearance in ex vivo human and rat lungs. Am J Respir Crit Care Med 1997; **155:** 506-12.
9. Sakuma T, Tsukano C, Ishigaki M et al: Lung deflation impairs alveolar epithelial fluid transport in ischemic rabbit and rat lungs. Transplantation 2000; **69:** 1785-93.

10. Sakuma T, Hida M, Nambu Y et al: Effects of hypoxia on alveolar fluid transport capacity in rat lungs. J Appl Physiol 2001; **91:** 1766-74.
11. Sakuma T, Hida M, Nambu Y et al: Beta1-adrenergic agonist is a potent stimulator of alveolar fluid clearance in hyperoxic rat lungs. Jpn J Pharmacol 2001; **85:** 161-6.
12. Sakuma T, Tuchihara C, Ishigaki M et al: Denopamine, a beta(1)-adrenergic agonist, increases alveolar fluid clearance in ex vivo rat and guinea pig lungs. J Appl Physiol 2001; **90:** 10-6.
13. Sakuma T, Sagawa M, Hida M et al: Time-dependent effect of pneumonectomy on alveolar epithelial fluid clearance in rat lungs. J Thorac Cardiovasc Surg 2002; **124:** 668-74.
14. Sakuma T, Zhao Y, Sugita M et al: Malnutrition impairs alveolar fluid clearance in rat lungs. Am J Physiol Lung Cell Mol Physiol 2004; **286:** L1268-74.
15. Sakuma T, Zhao Y, Sugita M et al: A prostacyclin analogue, OP-41483alpha-CD, restores the ability of a beta2-adrenergic agonist to stimulate alveolar fluid clearance in rats. Surg Today 2004; **34:** 429-36.
16. Sakuma T, Gu X, Sugita M et al: Uridine 5'-triphosphate stimulates alveolar fluid clearance in the isolated rat lungs. J Pharmacol Sci 2004; **95:** 420-5.
17. Sakuma T, Gu X, Sugita M et al: Catecholamine clearance from alveolar spaces of rat and human lungs. Respiration 2005; **72:** 189-96.
18. Sakuma T, Gu X, Maeda S et al: Epinephrine dependent stimulation of alveolar fluid clearance in the human lung is CFTR dependent. Am J Respir Crit Care Med 2005; **2:** A299.
19. Smedira N, Gates L, Hastings R et al: Alveolar and lung liquid clearance in anesthetized rabbits. J Appl Physiol 1991; **70:** 1827-35.
20. Garat C, Carter EP, Matthay MA: New in situ mouse model to quantify alveolar epithelial fluid clearance. J Appl Physiol 1998; **84:** 1763-7.
21. Fukuda N, Folkesson HG, Matthay MA: Relationship of interstitial fluid volume to alveolar fluid clearance in mice: ventilated vs. in situ studies. J Appl Physiol 2000; **89:** 672-9.
22. Fang X, Fukuda N, Barbry P et al: Novel role for CFTR in fluid absorption from the distal airspaces of the lung. J Gen Physiol 2002; **119:** 199-207.
23. Mutlu GM, Dumasius V, Burhop J et al: Upregulation of alveolar epithelial active Na+ transport is dependent on beta2-adrenergic receptor signaling. Circ Res 2004; **94:** 1091-100.
24. Mutlu GM, Koch WJ, Factor P: Alveolar epithelial beta 2-adrenergic receptors: their role in regulation of alveolar active sodium transport. Am J Respir Crit Care Med 2004; **170:** 1270-5.
25. Matthay MA, Wiener-Kronish JP: Intact epithelial barrier function is critical for the resolution of alveolar edema in humans. Am Rev Respir Dis 1990; **142:** 1250-7.
26. Matthay MA, Folkesson HG, Verkman AS: Salt and water transport across alveolar and distal airway epithelia in the adult lung. Am J Physiol 1996; **270:** L487-503.
27. Ware LB, Matthay MA: The acute respiratory distress syndrome. N Engl J Med 2000; **342:** 1334-49.
28. Ware LB, Matthay MA: Alveolar fluid clearance is impaired in the majority of patients with acute lung injury and the acute respiratory distress syndrome. Am J Respir Crit Care Med 2001; **163:** 1376-83.
29. Ware L, Wang Y, Fang X et al: Assessment of lungs rejected for transplantation and implications for donor selection. Lancet 2002; **360:** 619.
30. Hastings RH, Grady M, Sakuma T et al: Clearance of different-sized proteins from the alveolar space in humans and rabbits. J Appl Physiol 1992; **73:** 1310-6.
31. Sakuma T, Okaniwa G, Nakada T et al: Alveolar fluid clearance in the resected human lung. Am J Respir Crit Care Med 1994; **150:** 305-10.
32. Goodman BE: Lung fluid clearance. In R. C. Effros, HK, editor (Eds). Fluid and solute transport in the air spaces of the lungs. New York. Marcel Dekker, 1993; 139-83.
33. Carstairs JR, Nimmo AJ, Barnes PJ: Autoradiographic visualization of beta-adrenoceptor subtypes in human lung. Am Rev Respir Dis 1985; **132:** 541-7.
34. Azzam ZS, Adir Y, Crespo A et al: Norepinephrine increases alveolar fluid reabsorption and Na, K-ATPase activity. Am J Respir Crit Care Med 2004; **170:** 730-6.
35. Sakuma T, Okaniwa G, Nakada T et al: Effects of hypothermia and hyperpotassium on alveolar fluid clearance in the resected human lung. Surg Today 1995; **25:** 694-700.
36. Sakuma T, Suzuki S, Usuda K et al: Preservation of alveolar epithelial fluid transport mechanisms in rewarmed human lung after severe hypothermia. J Appl Physiol 1996; **80:** 1681-6.
37. Sakuma T, Nishimura T, Usude K et al: Hypothermia inhibits the alveolar epithelial injury caused by hyposmotic albumin solution during preservation of the resected human lung. Surg Today 1997; **27:** 527-33.
38. Sakuma T, Takahashi K, Ohya N et al: Effects of ATP-sensitive potassium channel opener on potassium transport and alveolar fluid clearance in the resected human lung. Pharmacol Toxicol 1998; **83:** 16-22.
39. Leroy C, Dagenais A, Berthiaume Y et al: Molecular identity and function in transepithelial transport of K(ATP) channels in alveolar epithelial cells. Am J Physiol Lung Cell Mol Physiol 2004; **286:** L1027-37.
40. Sakuma T, Usuda K, Handa M et al: Increased alveolar fluid clearance following thoracotomy: report of a case and results of an analysis. Surg Today 1997; **27:** 762-5.
41. Sakuma T: Proliferation of alveolar type II epithelial cells in residual lungs following thoracotomy. Jpn J Thorac Cardiovasc Surg 1999; **47:** 43-6.

SHOCK, Vol. 26, No. 1, pp. 62–68, 2006

OXYGEN CONSUMPTION, ASSESSED WITH THE OXYGEN ABSORPTION SPECTROPHOTOMETER, DECREASES INDEPENDENTLY OF VENOCONSTRICTION DURING HEPATIC ANAPHYLAXIS IN PERFUSED RAT LIVER

Sen Cui, Toshishige Shibamoto, Zonghai Ruan, Hiromichi Takano, Wei Liu, and Yasutaka Kurata

Department of Physiology, Kanazawa Medical University, Uchinada, Ishikawa, Japan

Received 15 Jul 2005; first review completed 22 Sep 2005; accepted in final form 23 Jan 2006

ABSTRACT—Anaphylactic shock is accompanied by a decrease in oxygen consumption. However, it is not well known whether oxygen consumption decreases during local anaphylactic reaction in liver. We determined the effects of anaphylaxis and norepinephrine on oxygen consumption in isolated rat livers perfused portally and recirculatingly at constant flow with blood (hematocrit, 12%). Oxygen consumption was continuously measured by monitoring the portal–hepatic venous oxygen saturation differences using the absorption spectrophotometer, the probes of which were built in perfusion lines. Hepatic anaphylaxis was induced by an injection of ovalbumin (0.01 or 0.1 mg) into the perfusate of the isolated liver of the rat sensitized with subcutaneous ovalbumin (1 mg). Hepatic venoconstriction and liver weight loss were similarly observed in response to norepinephrine (0.01–10 μmol L^{-1}) and anaphylaxis. However, hepatic anaphylaxis reduced oxygen consumption, whereas norepinephrine increased it. There was a possibility that anaphylactic venoconstriction could reduce the perfused surface area, resulting in decreased oxygen consumption. However, pretreatment with a vasodilator of sodium nitroprusside substantially attenuated venoconstriction but not the decrease in oxygen consumption during anaphylaxis. Thus, we conclude that local hepatic anaphylaxis decreases oxygen consumption independently of venoconstriction in isolated blood-perfused rat livers.

KEYWORDS—Anaphylactic shock, hepatic circulation, norepinephrine, hepatic venoconstriction, portal venous pressure

INTRODUCTION

Circulatory shock is characterized by generalized cellular hypoxia and a decrease in oxygen consumption of organs and tissues (1–3). The severity and the mortality after shock is strongly associated with decreased oxygen consumption (2, 4). Indeed, anaphylactic shock is accompanied by decreased oxygen consumption (5, 6). There is a possibility that anaphylactic reaction itself reduces oxygen consumption. However, there are only a limited number of studies (7) to determine the effect of local anaphylaxis on oxygen consumption of organs such as the liver.

Therefore, for determination of the effect of local anaphylaxis on oxygen consumption of the liver, we used the isolated perfused liver, which was free from the influences of the other organs or many humoral mediators released from other organs during the time course of anaphylactic shock. We continuously measured the oxygen consumption of isolated blood-perfused livers during hepatic anaphylaxis by monitoring the oxygen (O_2) saturation differences between the inflow and outflow blood using a custom-made absorption spectrophotometer. To check the validity of this absorption spectrophotometer, we also measured the oxygen consumption during administration of norepinephrine because norepinephrine is known to increase oxygen consumption in the perfused rat liver (8–10). Another reason for investigating the effect of norepinephrine is that it induces hepatic venoconstriction. Oxygen consumption depends not only on metabolic factors but also on hemodynamic factors. From the hemodynamic point of view, isolated perfused rat livers showed similar predominant presinusoidal constrictive responses to anaphylaxis (11) and norepinephrine (12). In addition, to determine the effect of hepatic anaphylaxis on oxygen consumption without its hemodynamic influence, anaphylaxis-induced venoconstriction was suppressed by pretreatment with sodium nitroprusside (SNP) and then changes in oxygen consumption were determined during hepatic anaphylaxis.

MATERIALS AND METHODS

Animals

Seventy-four male Sprague-Dawley rats (Japan SLC, Shizuoka, Japan) weighing 270 to 370 g (mean ± SD, 325 ± 4 g) were used in this study. Rats were maintained at 23°C and under pathogen-free conditions on a 12-h dark/light cycle and received food and water *ad libitum*. The study protocol was approved by the Animal Research Committee of Kanazawa Medical University.

Sensitization

Twenty-one rats were sensitized by subcutaneous injection of an emulsion made by mixing complete Freund's adjuvant (0.5 mL) with 1 mg ovalbumin (grade V, Sigma, Saint Louis, MO) dissolved in physiological saline (0.5 mL) as previously described (11). Two weeks after injection, rats were used for the isolated perfused liver experiments.

Isolated liver preparation

The animals were anesthetized with pentobarbital sodium (50 mg kg^{-1} i.p.) and were mechanically ventilated with room air. The method for perfusion of isolated rat livers was previously described (11). In brief, after the right carotid artery

Address reprint requests to Toshishige Shibamoto, Department of Physiology, Kanazawa Medical University, Uchinada Ishikawa 920-0293, Japan. E-mail: shibamo@kanazawa-med.ac.jp.

This work was supported by a grant for collaborative research from Kanazawa Medical University (C2004-1, C2005-1).
DOI: 10.1097/01.shk.0000215315.76370.8a

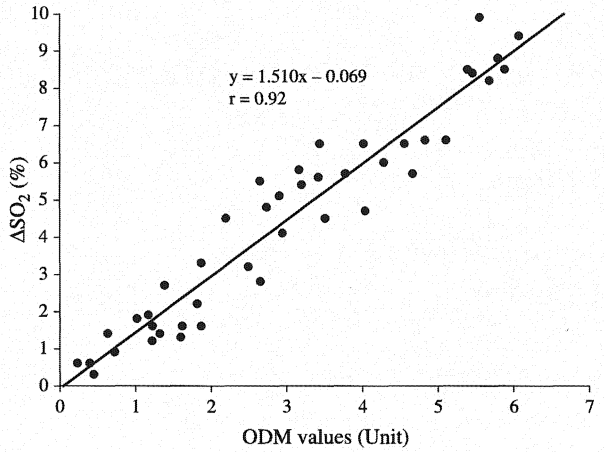

FIG. 1. **The relationship between the ODM values and the measured ΔSo_2 that were obtained in 10 intact livers.** The regression line equation is $\Delta So_2 = 1.5103 \times ODM - 0.0685$ ($r = 0.92$, $P < 0.05$).

cannulation and laparotomy, the hepatic artery was ligated, and the bile duct was cannulated with polyethylene tube (inner diameter [ID], 0.5 mm; outer diameter [OD], 0.8 mm). After intra-arterial heparinization (500 U kg^{-1}), 8 to 9 mL of blood was withdrawn through the carotid arterial catheter. The intra-abdominal inferior vena cava above the renal veins was ligated, and the portal vein was cannulated with a stainless cannula (ID, 1.3 mm; OD, 2.1 mm) for portal perfusion. After thoracotomy, the supradiaphragmatic inferior vena cava was cannulated through a right atrium incision with a larger stainless cannula (ID, 2.1 mm; OD, 3.0 mm), then portal perfusion was begun with the heparinized autologous blood diluted with 5% bovine albumin (Sigma-Aldrich, St. Louis, Mo) in Krebs solution (118 mmol L^{-1} NaCl, 5.9 mmol L^{-1} KCl, 1.2 mmol L^{-1} $MgSO_4$, 2.5 mmol L^{-1} $CaCl_2$, 1.2 mmol L^{-1} NaH_2PO_4, 25.5 mmol L^{-1} $NaHCO_3$, and 5.6 mmol L^{-1} glucose) at hematocrit of 12%. The liver was rapidly excised, suspended from an isometric transducer (TB-652T, Nihon-Kohden, Tokyo, Japan), and weighed continuously throughout the experimental period.

The livers were perfused at a constant flow rate in a recirculating manner *via* the portal vein with blood that was pumped using a Masterflex roller pump from the venous reservoir through a heat exchanger (37°C). The recirculating blood volume was 40 mL. The perfused blood was oxygenated in the venous reservoir by continuous bubbling with 95% O_2 and 5% carbon dioxide (perfusate Po_2 = 300 mmHg). The portal and hepatic venous pressures (Ppv and Phv, respectively) were measured using pressure transducers (TP-400T, Nihon-Kohden) attached by sidearm to the appropriate cannulas with the reference points at the hepatic hilus. Portal blood flow rate was measured with an electromagnetic flow meter (MFV 1200, Nihon-Kohden), and the flow probe was positioned in the inflow line. Bile was collected drop by drop in a small tube suspended from the force transducer (SB-1T, Nihon-Kohden). One bile drop yielded 0.018 g, and the time between drops was measured for determination of the bile flow rate. To determine the oxygen consumption, the blood oxygen saturation difference between the portal and hepatic venous blood was monitored continuously with a custom-made absorption spectrophotometer (ODM-1, Biomedical Science, Kanazawa, Japan), the probe of which consisted of a 660-nm wavelength light-emitting diode, a cuvette, and a photodiode detector. These 2 probes were built in the inflow and outflow perfusion lines. The blood oxygen saturation differences measured with this absorption spectrophotometer were expressed as the oxygen difference meter (ODM) values. The hepatic vascular pressures, ODM values, blood flow rate, liver weight, and bile weight were monitored continuously and displayed through a thermal physiograph (RMP-6008, Nihon-Kohden). All output were also digitized by the analog–digital converter at a sampling rate of 100 Hz. These digitized values were also displayed and recorded using a personal computer.

Measurement of oxygen consumption

Oxygen consumption was calculated according to the Fick principle by the following equation

$$\text{Portalbloodflow/liverweight(g)} \times 1.39\text{(mL/g)} \times \text{hemoglobin(g/mL)} \times \Delta So_2 \quad (1)$$

where ΔSo_2 is the oxygen saturation difference between the inflow (portal) and outflow (hepatic vein) blood. To estimate ΔSo_2 by the ODM value of the absorption spectrophotometer, the validity of the ODM values was examined by comparing the ODM values with the ΔSo_2, which was determined by measuring the oxygen saturation of the inflow and outflow blood with the use of automatic blood gas analyzer. To determine the correlation of ODM value and ΔSo_2, the intact isolated rat livers (n = 10) were perfused at various blood flow rates (12 – 60 mL/min) to obtain various inflow-to-outflow oxygen saturation differences. Blood samples were collected simultaneously from the inflow (portal) and outflow (hepatic venous) lines at a given flow rate and the oxygen saturation of the inflow (So_2in) and outflow (So_2out) blood were measured by the blood gas analyzer (AVL OMNI Modular System, AVL Scientific Corp., Roswell, GA). The calculated oxygen saturation differences ($\Delta So_2 = So_2\text{in} - So_2\text{out}$) were compared with the corresponding ODM values. We obtained the regression line equation for So_2 measured and ODM values.

Experimental protocol

Hepatic hemodynamic parameters were observed for at least 20 min after the start of perfusion until an isogravimetric state (no weight gain or loss) was obtained by adjusting the portal blood flow rate and the height of the reservoir at a Phv of 0 to 1 cmH_2O and at a portal blood flow of 37 ± 1 mL min^{-1} per 10 g of liver. After the baseline measurements, the perfused livers excised from nonsensitized animals were randomly assigned to the control group or norepinephrine group and those from sensitized animals to the anaphylaxis group. In the norepinephrine group (n = 35), norepinephrine was administered into the perfusate to get the final concentration of 0.001, 0.01, 0.1, 1, and 10 μmol L^{-1}. The concentrations of norepinephrine were randomly assigned for individual preparations. In the anaphylaxis group, ovalbumin 0.01 (n = 7) or 0.1 mg (n = 7) was administered into the perfusate. In addition, to eliminate a possible effect of anaphylaxis-induced venoconstriction on oxygen consumption, a vasodilator of SNP at 100 μmol L^{-1} was administered 10 min before injection of 0.01 mg of ovalbumin (SNP group, n = 7). In the control group (n = 8), ovalbumin 0.1 mg was administered into the perfusate of the livers from nonsensitized rats.

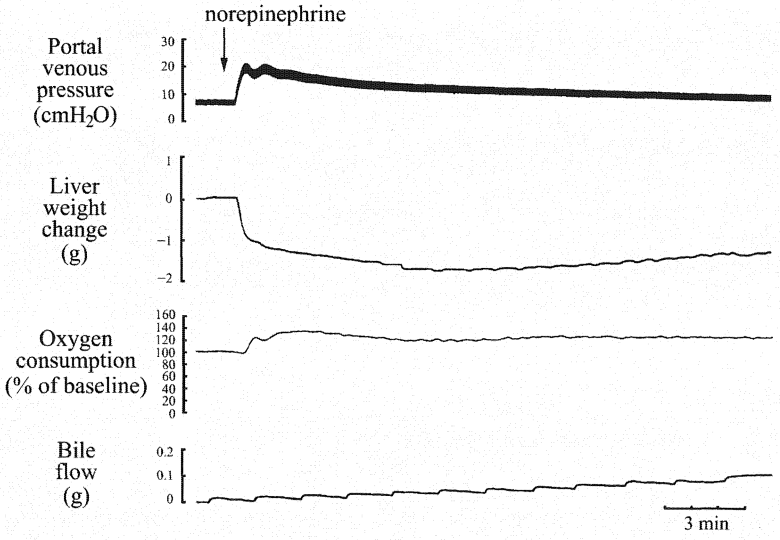

FIG. 2. **A representative recording of the response to norepinephrine at 1 μmol L^{-1}.**

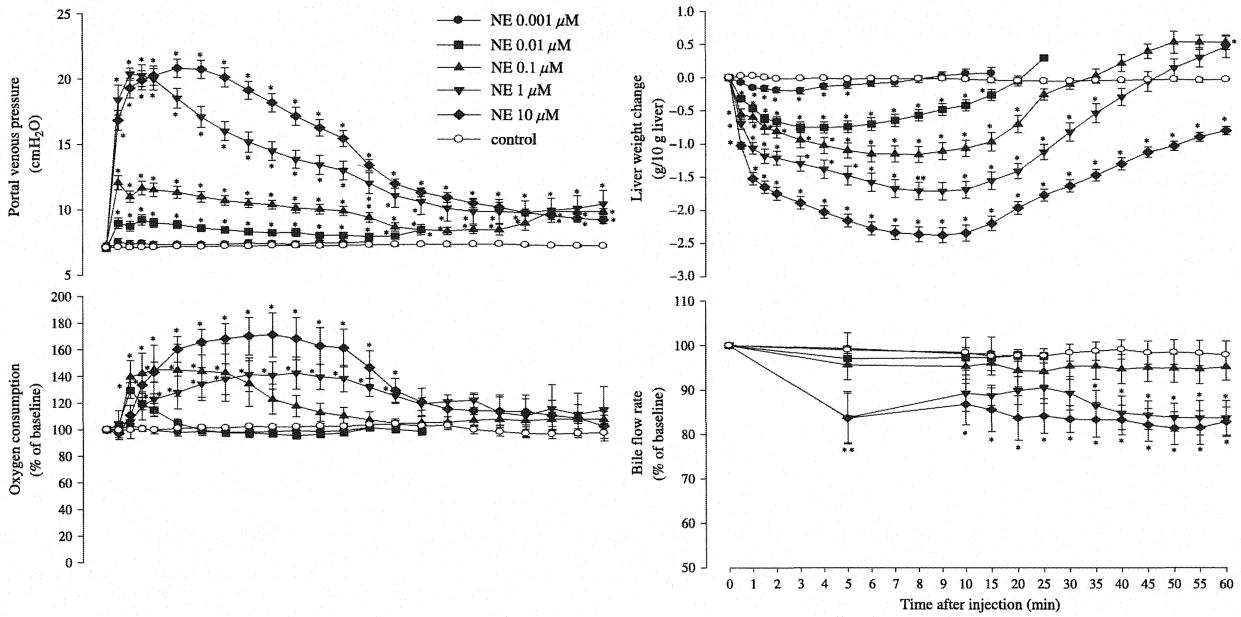

FIG. 3. **The time course changes in the Ppv, liver weight changes, oxygen consumption, and bile flow rate in the norepinephrine (n = 35) and control (n = 8) groups.** Values are given as means ± SE. *$P < 0.05$ versus the baseline. NE indicates norepinephrine.

Statistics

All results are expressed as means ± SE. Data were analyzed by one- and two-way analysis of variance, using repeated measures for 2-way comparison within groups. Comparisons of individual points between groups and within groups were made by Bonferroni test. The correlation between the ODM values and the measured oxygen saturation differences was analyzed by linear regression. Differences were considered as statistically significant at P values of <0.05.

RESULTS

Relationship between the ODM values and the measured oxygen saturations

Figure 1 shows the relationship between the ODM values and the measured ΔSo_2 that were obtained in 10 intact livers. The regression line equation is

$$\Delta S_{O_2} = 1.510 \times \mathrm{ODM} - 0.069 \; (r = 0.92, \; P < 0.05). \qquad (2)$$

This indicates that the ΔSo_2 can be estimated by ODM values in isolated perfused rat liver. The basal oxygen consumption calculated using the ODM values in the control, 0.1-mg ovalbumin, 0.01-mg ovalbumin, SNP, and 0.001-, 0.01-, 0.1-, 1-, and 10-μmol L^{-1} norepinephrine groups were 0.0072 ± 0.0005, 0.0078 ± 0.0002, 0.0054 ± 0.0005, 0.0055 ± 0.0003, 0.0065 ± 0.0008, 0.0069 ± 0.0009, 0.0066 ± 0.0008, 0.0070 ± 0.0008, and 0.0064 ± 0.0005 mL min^{-1} per gram of liver, respectively. In the present study, the changes in oxygen consumption in a given perfused liver were directly proportional to the ODM values because the other determinants of oxygen consumption such as perfusate hemoglobin and portal blood flow rate were not changed during the experimental period. Thus, oxygen consumption was expressed as the percentage of the baseline ODM value.

Effects of norepinephrine on hepatic oxygen consumption, Ppv, liver weight, and bile flow

Figure 2 shows a representative example of the hepatic response to administration of norepinephrine at 1 μmol L^{-1}. Figure 3 shows the summary data of the time-dependent changes in Ppv, liver weight, hepatic oxygen consumption, and bile flow rate of the norepinephrine groups. Significant changes in the variables were observed in response to norepinephrine at concentrations higher than 0.01 μmol L^{-1}. Hepatic oxygen consumption increased dose-dependently after norepinephrine, with the peak values being 129% ± 13% of the baseline at 0.01 μmol L^{-1}, 145% ± 42% at 0.1 μmol L^{-1}, 142% ± 27% at 1 μmol L^{-1}, and 171% ± 43% at 10 μmol L^{-1}. Norepinephrine at 0.01, 0.1, and 1 μmol L^{-1} dose-dependently increased Ppv to the peak, 9.2 ± 0.3, 12.1 ± 0.5, and 20.4 ± 0.8 cmH_2O, respectively, within 3 min. Maximal venoconstriction was observed at 1 μmol L^{-1}; the peak of Ppv after norepinephrine at 10 μmol L^{-1} (20.8 ± 0.7 cmH_2O) was comparable to that at 1 μmol L^{-1}. After administration of norepinephrine at 0.01, 0.1, 1, and 10 μmol L^{-1}, the liver weight decreased by 0.8 ± 0.1, 1.2 ± 0.2, 1.7 ± 0.2, and 2.4 ± 0.2 g per 10 g of liver, respectively. The bile flow rates decreased after norepinephrine administration at 1 and 10 μmol L^{-1} to 84% ± 6% and 84% ± 8% of the baseline of 8.6 ± 0.4 and 9.8 ± 0.5 mg min^{-1} per 10 g of liver, respectively.

Effects of anaphylaxis on hepatic oxygen consumption, Ppv, liver weight, and bile flow

Figure 4 shows a representative example of the response of the sensitized liver to the antigen (0.01 mg of ovalbumin). Figure 5 shows the summary data of the time course changes in Ppv, liver weight, hepatic oxygen consumption, and bile flow rate of the 0.01-mg ovalbumin group along with the data

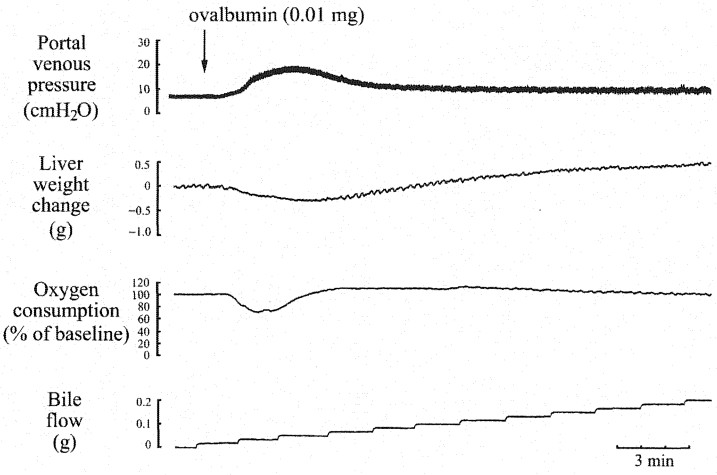

FIG. 4. **A representative recording of the responses to the antigen of ovalbumin (0.01 mg).**

of the 0.1-mg ovalbumin, 1- and 10-μmol L^{-1} norepinephrine, and control groups. After injection of 0.01 mg of ovalbumin, Ppv increased from the baseline of 6.9 ± 0.13 cmH_2O to the peak of 20.0 ± 1.4 cmH_2O at 4 min. Hepatic oxygen consumption decreased to the nadir of 75% ± 6% of the baseline at 2 min and then recovered to the baseline level at 4 min after administration of 0.01 mg of ovalbumin. The decrease in oxygen consumption after antigen administration contrasts with its increase after norepinephrine administration in that hepatic venoconstriction was similar in magnitude between the 0.01-mg ovalbumin group and the high dose of norepinephrine (1 or 10 μmol L^{-1}) group. The liver weight showed a rapid decrease, reaching the bottom of −0.4 ± 0.1 g per 10 g of liver at 4 min after 0.01 mg ovalbumin administration. The bile flow rate significantly decreased to 86% ± 1% of the baseline of 8.7 ± 0.5 mg min^{-1} per 10 g of liver at 5 min after antigen (0.01 mg of ovalbumin) administration and then gradually recovered. The responses of the variables to the high-dose ovalbumin (0.1 mg) were qualitatively similar to that of the low-dose ovalbumin (0.01 mg), but greater in magnitude, as shown in Figure 5.

Effects of SNP on Hepatic Anaphylactic Response

Figure 6 shows a representative example of the response of the sensitized liver to the antigen (0.01 mg of ovalbumin) after pretreatment with SNP at 100 μmol L^{-1}. Figure 7 shows the summary data of the time course changes of the 0.01-mg ovalbumin and SNP groups. The increase in Ppv in response to the 0.01-mg ovalbumin antigen was much smaller with SNP than without SNP. However, the decrease in hepatic oxygen consumption was similarly observed with or without pretreatment with SNP. At 2 min after antigen administration, hepatic oxygen consumption decreased to the nadir of 79% ± 3% of the baseline, which was not significantly different from that of the 0.01-mg ovalbumin group without administration of SNP. In contrast, Ppv increased only slightly to the peak of 9.9 ± 1.2 cmH_2O at 4 min from the baseline of 6.6 ± 0.15 cmH_2O. The liver weight showed a mild, but significant, decrease, reaching the nadir of −0.2 ± 0.1 g per 10 g of liver at 3 min after ovalbumin administration. The bile flow rate significantly decreased to 89% ± 1% of the baseline of 8.6 ± 0.5 mg min^{-1} per 10 g of liver at 5 min after antigen administration and did not return to the baseline.

DISCUSSION

In the present study, oxygen consumption was for the first time measured continuously by a custom-made absorption spectrophotometer, the probes of which were built in the perfusing circuit to monitor the portal–hepatic venous oxygen saturation difference of isolated perfused rat livers. We have shown that anaphylaxis decreased hepatic oxygen consumption, whereas norepinephrine increased it, although both caused similar hepatic venoconstriction and liver weight loss. Pretreatment with a vasodilator of SNP did not prevent the anaphylaxis-induced decrease in hepatic oxygen consumption, whereas it substantially attenuated the anaphylaxis-induced hepatic venoconstriction. These findings suggest that the decrease in hepatic oxygen consumption during anaphylactic shock could be caused by local hepatic anaphylaxis itself, and that it is independent of hepatic venoconstriction.

We demonstrated that there was a significant and good correlation between the ODM values of the absorption spectrophotometer and ΔS_{O_2} measured with the blood gas analyzer. This indicates that the ΔS_{O_2} and oxygen consumption can be indirectly measured by the absorption spectrophotometer in isolated perfused liver. Oxygen consumption of the perfused liver is usually measured with a Clark-type oxygen electrode (7, 13–15). However, this oxygen electrode monitors only the effluent, but not the influent, oxygen concentration and, thus, it alone cannot directly assess the portal– hepatic venous oxygen difference, which is the determinant of oxygen consumption. The application of the custom-made oxygen absorption spectrophotometer permits the continuous measurement of the portal–hepatic venous oxygen difference of the perfused livers.

An increase in oxygen consumption has been observed after norepinephrine administration in perfused rat livers (8, 16). In these studies, oxygen consumption was determined by measuring the effluent oxygen concentration with a Clark-type oxygen electrode. In the present study, we confirmed by using the oxygen absorption spectrophotometer that norepinephrine at concentrations higher than 0.01 μmol L^{-1}

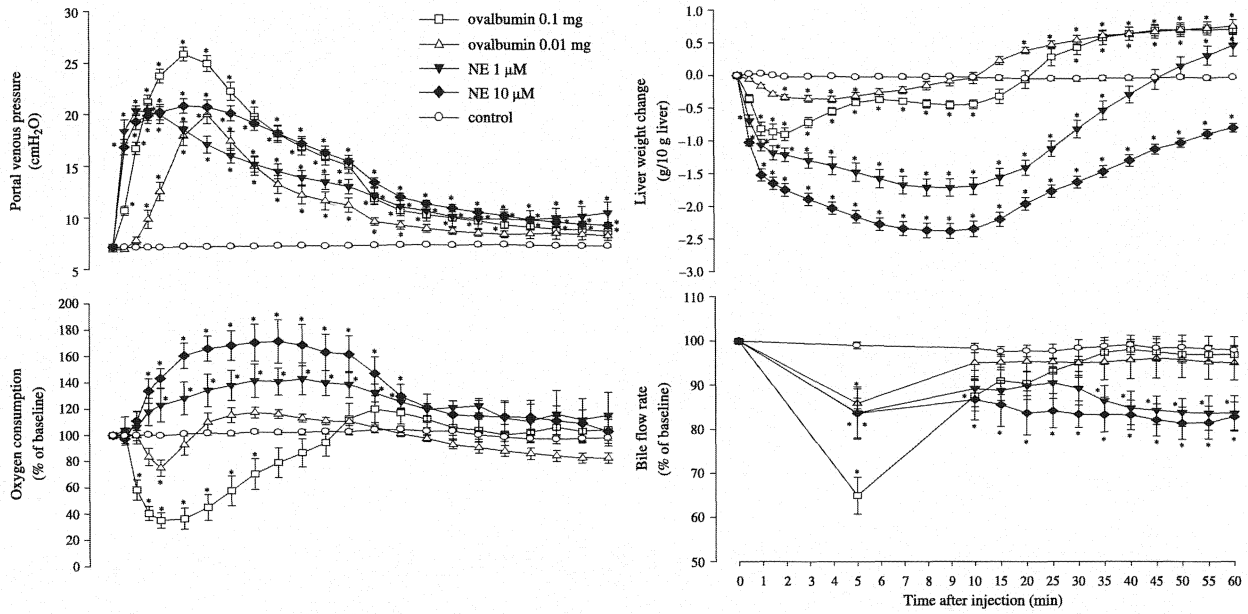

FIG. 5. **The time course changes in the Ppv, liver weight changes, oxygen consumption, and bile flow rate in the 0.1-mg ovalbumin (n = 7), 0.01-mg ovalbumin (n = 7), 1-μmol L^{-1} norepinephrine (n = 7), 10-μmol L^{-1} norepinephrine (n = 8), and control (n = 8) groups.** Values are given as means ± SE. *$P < 0.05$ versus the baseline. NE indicates norepinephrine.

increased hepatic oxygen consumption in isolated blood-perfused livers. This effect is ascribed to the metabolic effect of norepinephrine; norepinephrine is known to increase glycogenolysis using energy, which is reflected by an increase in oxygen consumption. Indeed, norepinephrine increases oxygen consumption of isolated cultured hepatocytes (17).

In the present study, in contrast to norepinephrine administration increasing hepatic oxygen consumption, anaphylaxis obviously reduced hepatic oxygen consumption (35% and 75% of baseline with ovalbumin at 0.1 and 0.01 mg, respectively). This finding is consistent with the investigation of Hines and Fisher (7), in which hepatic oxygen consumption initially increased and then largely decreased to about 24% during the antigen infusion. However, their experimental method was different from that of this study: In their study, the isolated rat livers were perfused with blood-free solutions in a nonrecirculating manner, whereas the livers in the present study were perfused more physiologically with blood. Another difference is that oxygen consumption was determined by measuring only the effluent oxygen concentration with an oxygen electrode in the previous study, whereas it was measured by directly determining the portal–hepatic venous oxygen saturation difference with the oxygen absorption spectrophotometer in the present study.

Hepatic oxygen consumption is regulated by the factors that affect metabolic and hemodynamic components of the liver. Thus, metabolic and hemodynamic factors may be involved in the anaphylaxis-induced decrease in oxygen consumption observed in the present study. With respect to the metabolic factors, pharmacologically active mediators, such as leukotrienes, thromboxane A_2 (TXA_2), platelet-activating factor, histamine, and serotonin are released during anaphylactic reaction. These mediators could directly inhibit oxygen consumption. Indeed, leukotriene C_4 and D_4 reduced oxygen consumption by 29% ± 3% and 30% ± 3% of baseline, respectively, and these inhibitory effects were independent of

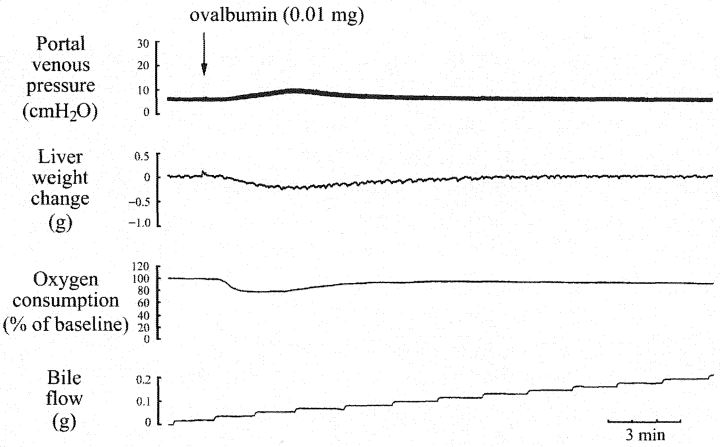

FIG. 6. **A representative recording of the responses to the antigen of ovalbumin (0.01 mg) after pretreatment with SNP at 100 μmol L^{-1}.**

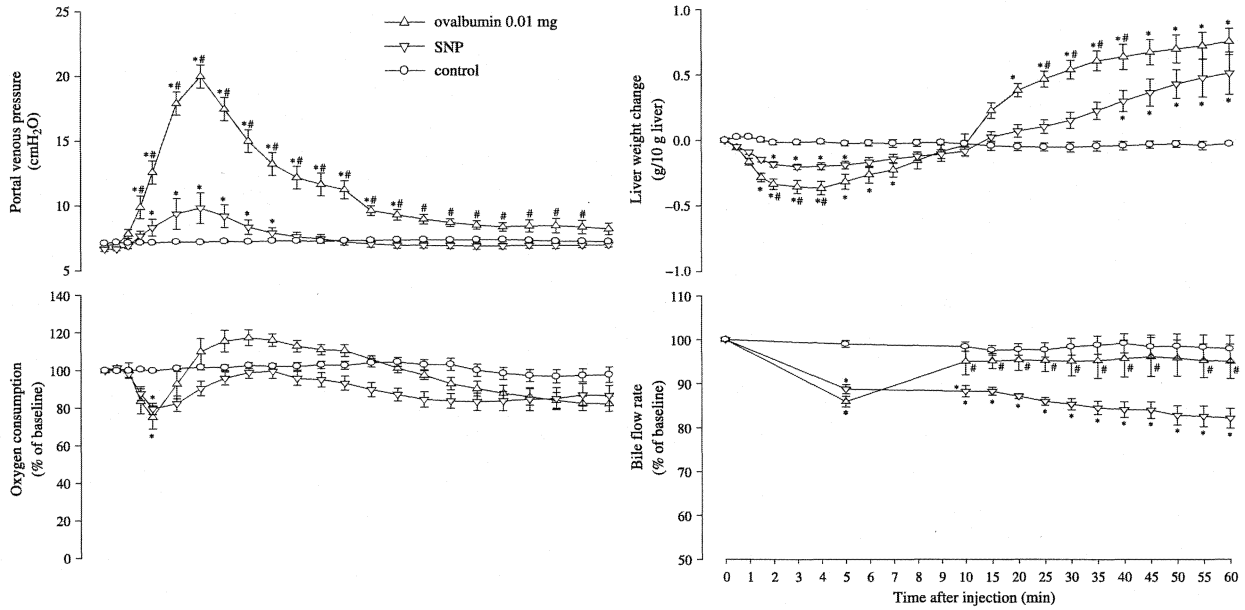

FIG. 7. **The time course changes in the Ppv, liver weight changes, oxygen consumption, and bile flow rate in the 0.01-mg ovalbumin (n = 7), SNP (n = 7), and control (n = 8) groups.** Values are given as means ± SE. $^{*}P < 0.05$ versus the baseline, $^{\ddagger}P < 0.05$ versus SNP group.

changes in hemodynamic factors (13). U-46619, a TXA_2 analogue, also decreased oxygen consumption by 27% in perfused rat livers (13). Altin and Bygrave (14) also found that ONO-11113, another TXA_2 analogue, induced an initial small transient stimulation followed by a marked and sustained inhibition of oxygen uptake in perfused rat livers. Finally, platelet-activating factor increased glucose production concomitant with suppression of oxygen consumption in perfused rat livers (15). On the other hand, from the hemodynamic point of view, presinusoidal constriction observed during anaphylactic venoconstriction of the perfused sensitized rat livers (11) may account for decreased oxygen consumption—presinusoidal constriction caused a decrease in hepatic vascular surface area, which might result in a decrease in the number of active hepatocytes. However, even when anaphylactic hepatic venoconstriction to be induced by 0.01 mg of ovalbumin was substantially suppressed by pretreatment with SNP, a potent vasodilator, the anaphylaxis-induced decrease in oxygen consumption was still preserved (Fig. 7). Thus, although hemodynamic changes might partially contribute to the anaphylaxis-induced decrease in oxygen consumption, the contribution of the hemodynamic effect seems to be small.

To the best of our knowledge, this is the first study to measure oxygen consumption of perfused rat liver using absorption spectrophotometer, although this method has been well adopted for isolated perfused heart experiments (18, 19). Kameyama et al. (18) reported that the basal oxygen consumption of isolated perfused rat hearts measured with an absorption spectrophotometer (AVOX system) was 0.65 to 0.70 $\mu L\ g^{-1}\ beat^{-1}$ (about 0.16 mL min^{-1} per gram of heart weight). Oxygen consumption of isolated perfused rat hearts measured with an oxygen content difference analyzer (model PWA-200S, Shoe Technica, Chiba, Japan) was about 0.5 $\mu L\ g^{-1}\ beat^{-1}$ (0.15 mL min^{-1} per gram of heart weight) (19). The basal oxygen consumption of the present perfused rat livers calculated from the ODM values was 0.0054 to 0.0078 mL min^{-1} per gram of liver. Thus, these values are approximately one twentieth of those of perfused hearts (18, 19). This difference in oxygen consumption between heart and liver was also observed when a Clark-type oxygen electrode was used for the perfused rat heart (20–23) and perfused rat liver (8, 24–27): 28 to 49 $\mu mol\ L^{-1}\ min^{-1}$ per gram of heart (20–23) and 1.78 to 3.0 $\mu mol\ L^{-1}\ min^{-1}$ per gram of liver (8, 23–26), respectively. This indicates that the absorption spectrophotometer used in the present study can be used to measure oxygen consumption continuously in isolated perfused liver experiments.

In the present study, the bile flow rate decreased after norepinephrine at concentrations of 1 and 10 $\mu mol\ L^{-1}$. The reason for this decrease is not known, but it seems to be secondary to the hemodynamic effects (28). In hepatic anaphylaxis, the bile flow rate also reduced significantly at 5 min after antigen administration, even when the hemodynamic effect was eliminated by SNP. We therefore speculate that it is related to the reduction of hepatocyte activity, as reflected by a decrease in oxygen consumption during anaphylaxis.

In summary, we measured the changes in oxygen consumption during hepatic anaphylaxis and norepinephrine administration using a custom-made absorption spectrophotometer in isolated perfused rat livers. Hepatic venoconstriction and liver weight loss were similarly observed in response to norepinephrine and anaphylaxis. However, hepatic anaphylaxis caused a decrease in oxygen consumption, whereas norepinephrine increased oxygen consumption, as reported previously. Pretreatment with a vasodilator of SNP substantially attenuated anaphylaxis-induced venoconstriction, but not anaphylaxis-induced decrease in oxygen consumption. We conclude that local hepatic anaphylaxis decreases oxygen consumption independently of venoconstriction in isolated perfused rat livers.

REFERENCES

1. Ba ZF, Wang P, Koo DJ, Cioffi WG, Bland KI, Chaudry IH: Alterations in tissue oxygen consumption and extraction after trauma and hemorrhagic shock. *Crit Care Med* 28:2837–2842, 2000.
2. Roy JW, Graham MC, Griffin AM, Gainer JL: A novel fluid resuscitation therapy for hemorrhage shock. *Shock* 10:213–217, 1998.
3. Ottosson J, Persson T, Dawidson I: Oxygen consumption and central hemodynamics in septic shock treated with antibiotics, fluid infusions, and corticosteroids. *Crit Care Med* 17:772–779, 1989.
4. Dawidson I, Eriksson B, Gelin LE, Soderberg R: Oxygen consumption and recovery from surgical shock in rats: a comparison of the efficacy of different plasma substitutes. *Crit Care Med* 7:460–465, 1979.
5. Brown SG: Clinical features and severity grading of anaphylaxis. *J Allergy Clin Immunol* 114:371–376, 2004.
6. Catala JC, Llagunes J, Marin JP, Aguar F, Grau F: Oxygen consumption during anaphylactic shock. *Rev Esp Anestesiol Reanim* 44:154–156, 1997.
7. Hines KL, Fisher RA: Regulation of hepatic glycogenolysis and vasoconstriction during antigen-induced anaphylaxis. *Am J Physiol* 262: G868–G877, 1992.
8. Beckh K, Otto R, Ji S, Jungermann K: Control of oxygen uptake, microcirculation and glucose release by circulating noradrenaline in perfused rat liver. *Biol Chem Hoppe Seyler* 366:671–678, 1985.
9. Becker G, Beuers U, Jungermann K: Modulation by oxygen of the actions of noradrenaline, sympathetic nerve stimulation and prostaglandin F_2 α on carbohydrate metabolism and hemodynamics in perfused rat liver. *Biol Chem Hoppe Seyler* 371:983–990, 1990.
10. Binet A, Claret M: α-Adrenergic stimulation of respiration in isolated rat hepatocytes. *Biochem J* 210:867–873, 1983.
11. Shibamoto T, Cui S, Ruan Z, Liu W, Takano H, Kurata Y: Hepatic venoconstriction is involved in anaphylactic hypotension in rats. *Am J Physiol Heart Circ Physiol* 289:H1436–H1441, 2005.
12. Shibamoto T, Narushima M, Ling YQ, Shimo T, Tsuchida H, Kurata Y, Ogura T: Different hepatic vascular response to noradrenaline and histamine between guinea pig and rat. *Acta Physiol Scand* 18:255–263, 2004.
13. Haussinger D, Stehle T, Gerok W: Effects of leukotrienes and the thromboxane A_2 analogue U-46619 in isolated perfused rat liver. *Biol Chem Hoppe Seyler* 369:97–107, 1988.
14. Altin JG, Bygrave FL: Prostaglandin F_2 α and the thromboxane A_2 analogue ONO-11113 stimulate Ca^{2+} fluxes and other physiological responses in rat liver. Further evidence that prostanoids may be involved in the action of arachidonic acid and platelet-activating factor. *Biochem J* 249:677–685, 1988.
15. Kimura K, Moriyama M, Nishisako M, Kannan Y, Shiota M, Sakurada K, Musashi M, Sugano T: Modulation of platelet activating factor–induced glycogenolysis in the perfused rat liver after administration of endotoxin *in vivo*. *J Biochem (Tokyo)* 123:142–149, 1998.
16. Taylor WM, Reinhardt PH, Bygrave FL: Stimulation by α-adrenergic agonists of Ca^{2+} fluxes, mitochondrial oxidation and gluconeogenesis in perfused rat liver. *Biochem J* 212:555–565, 1983.
17. Dehaye JP, Hughes BP, Blanckmore PF, Exton JH: Insulin inhibition of α-adrenergic actions in liver. *Biochem J* 194:949–956, 1981.
18. Kameyama T, Chen Z, Bell SP, VanBuren P, Maughan D, LeWinter MM: Mechanoenergetic alterations during the transition from cardiac hypertrophy to failure in Dahl salt–sensitive rats. *Circulation* 98:2919–2929, 1998.
19. Hata Y, Sakamoto T, Hosogi S, Ohe T, Suga H, Takaki M: Linear O_2 use-pressure-volume area relation from curved end-systolic pressure-volume relation of the blood-perfused rat left ventricle. *Jpn J Physiol* 48:197–204, 1998.
20. Kurzelewski M, Duda M, Stanley WC, Boemke W, Beresewicz A: Nitric oxide synthase inhibition and elevated endothelin increase oxygen consumption but do not affect glucose and palmitate oxidation in the isolated rat heart. *J Physiol Pharmacol* 55:27–38, 2004.
21. Kreutzer U, Jue T: Role of myoglobin as a scavenger of cellular NO in myocardium. *Am J Physiol* 286:H985–H991, 2004.
22. Lopaschuk GD, Barr R, Thomas PD, Dyck JR: Beneficial effects of trimetazidine in *ex vivo* working ischemic hearts are due to a stimulation of glucose oxidation secondary to inhibition of long-chain 3–ketoacyl coenzyme a thiolase. *Circ Res* 93:e33–e37, 2003.
23. Schlenker EH, Tamura T, Gerdes AM: Gender-specific effects of thyroid hormones on cardiopulmonary function in SHHF rats. *J Appl Physiol* 95: 2292–2298, 2003.
24. Nakagawa Y, Matsumura T, Goto M, Qu W, Kauffman FC, Thurman RG: Increase in oxygen uptake due to arachidonic acid is oxygen dependent in the perfused liver. *Am J Physiol* 266:G953–G959, 1994.
25. Qu W, Zhong Z, Arteel GE, Thurman RG: Stimulation of oxygen uptake by prostaglandin E_2 is oxygen dependent in perfused rat liver. *Am J Physiol* 275:G542–G549, 1998.
26. Ji S, Beckh K, Jungermann K: Regulation of oxygen consumption and microcirculation by α-sympathetic nerves in isolated perfused rat liver. *FEBS Lett* 167:117–122, 1984.
27. Matsumura T, Yoshihara H, Jeffs R, Takei Y, Nukina S, Hijioka T, Evans RK, Kauffman FC, Thurman RG: Hormones increase oxygen uptake in periportal and pericentral regions of the liver lobule. *Am J Physiol* 262:G645–G650, 1992.
28. Lenzen R, Funk A, Kolb-Bachofen V, Strohmeyer G: Norepinephrine-induced cholestasis in the isolated perfused rat liver is secondary to its hemodynamic effects. *Hepatology* 12:314–321, 1990.

ELSEVIER

Prostaglandins & other Lipid Mediators 80 (2006) 35–45

PROSTAGLANDINS & other LIPID MEDIATORS

Effects of platelet-activating factor, thromboxane A_2 and leukotriene D_4 on isolated perfused rat liver

Sen Cui, Toshishige Shibamoto *, Wei Liu, Hiromichi Takano, Yasutaka Kurata

Department of Physiology, Kanazawa Medical University, Uchinada 920-0293, Japan

Received 21 January 2006; received in revised form 17 March 2006; accepted 30 March 2006
Available online 11 May 2006

Abstract

Vasoconstrictive lipid mediators, thromboxane A_2 (TxA_2), platelet-activating factor (PAF) and leukotriene D_4 (LTD_4) have been implicated as mediators of liver diseases. There are species differences in the primary site of hepatic vasoconstriction in response to these mediators. We determined the effects of a TxA_2 analogue (U-46619), PAF and LTD_4 on the vascular resistance distribution, weight and oxygen consumption of isolated rat livers portally perfused with blood. The sinusoidal pressure was measured by the double occlusion pressure (P_{do}), and was used to determine the pre- (R_{pre}) and post-sinusoidal (R_{post}) resistances. All these three mediators increased the hepatic total vascular resistance (R_t). The responsiveness to PAF was 100 times greater than that to U-46619 or LTD_4. Both of PAF and U-46619 predominantly increased R_{pre} over R_{post}. At the comparable increased R_t levels, U-46619 more preferentially increased R_{pre} than PAF. In contrast, LTD_4 increased both the R_{pre} and R_{post} to similar extent. U-46619 caused liver weight loss, while high concentrations of either LTD_4 or PAF produced liver weight gain, which was caused by substantial post-sinusoidal constriction and increased P_{do}. PAF and U-46619 decreased hepatic oxygen consumption while LTD_4 induced biphasic change of an initial transient decrease followed by an increase. In conclusion, PAF is the most potent vasoconstrictor of rat hepatic vessels among these three mediators. Both TxA_2 and PAF constrict the pre-sinusoidal veins predominantly. TxA_2 more preferentially constricts the pre-sinusoids than PAF, resulting in liver weight loss. However LTD_4 constricts both the pre- and post-sinusoidal veins similarly. High concentrations of LTD_4 and PAF cause liver weight gain by substantial post-sinusoidal constriction. PAF and TxA_2 decrease hepatic oxygen consumption, whereas LTD_4 causes a biphasic change of it.

Keywords: PAF; The double occlusion pressure; Hepatic circulation; U-46619; Sinusoidal pressure; Microcirculation; LTD_4; Oxygen consumption

1. Introduction

Lipid mediators such as platelet-activating factor (PAF), thromboxane A_2 (TxA_2) and leukotriene D_4 (LTD_4) are potent vasoconstrictors, and are released from a variety of cells including platelets, neutrophils, macrophages (e.g., Kupffer cells), monocytes, lymphocytes, endothelial and smooth muscle cells in response to various stimuli [1–3]. Each substance is implicated as a mediator of various types of liver diseases such as hepatic anaphylaxis [3,4], endotoxin

Abbreviations: IVC, inferior vena cava; PAF, platelet-activating factor; R_{pre}, pre-sinusoidal resistance; R_{post}, post-sinusoidal resistance; R_t, total portal-hepatic venous resistance; P_{pv}, portal venous pressure; P_{hv}, hepatic venous pressure; P_{do}, double occlusion pressure; Q, portal blood flow rate; Wt, liver weight; LT, leukotriene; TxA_2, thromboxane A_2

* Corresponding author. Tel.: +81 76 218 8104; fax: +81 76 286 8010.
E-mail address: shibamo@kanazawa-med.ac.jp (T. Shibamoto).

1098-8823/$ – see front matter © 2006 Elsevier Inc. All rights reserved.
doi:10.1016/j.prostaglandins.2006.03.004

liver injury [5–7], ischemia-reperfusion liver injury [8–10] and hepatic resection [9–11]. The microcirculation of the hepatic sinusoid plays a crucial role in the integrity of liver function [12]. PAF, TxA_2 and LTD_4 may influence the sinusoidal circulation, as a result of their vasoconstrictive action. Indeed, an infusion of a TxA_2 analogue or LTD_4 into the isolated perfused rat liver increases portal vein pressure, indicative of constriction of the hepatic vasculature [13,14]. PAF also causes an increase in the portal vein pressure in in vivo animals [15] and isolated perfused livers [16]. We have reported by measuring the sinusoidal pressure with the hepatic vascular occlusion methods in isolated blood-perfused canine livers that a TxA_2 analogue predominantly constricts the post-sinusoidal veins [17], while PAF constricts both the pre- and post-sinusoidal veins similarly [18]. On the other hand, both agents predominantly constrict the pre-sinusoidal veins over the post-sinusoidal veins in the isolated blood-perfused guinea pig livers [19]. These investigations indicated that there are species differences in the primary site of hepatic vasoconstriction for these mediators. However, the dominant vascular segments that these lipid mediators constrict in rat livers are not well known. Using the hepatic vascular occlusion method for measurement of the sinusoidal pressure [20], therefore, we determined the effects of PAF, a TxA_2 mimetic of U-46619 and LTD_4 on hepatic vascular resistance distribution and liver weight in isolated blood-perfused rat livers. Simultaneously, their effects on hepatic oxygen consumption were also determined with a custom-made oxygen absorption spectrophotometer [21].

2. Materials and methods

Sixty-seven male Sprague-Dawley rats (Japan SLC, Shizuoka, Japan) weighing 327 ± 3 g were used in this study. Rats were maintained at 23 °C and under pathogen-free conditions on a 12/12-h dark/light cycle, and received food and water ad libitum. The experiments conducted in the present study were approved by the Animal Research Committee of Kanazawa Medical University.

2.1. Isolated liver preparation

The animals were anesthetized with pentobarbital sodium (50 mg kg^{-1}, i.p.) and were mechanically ventilated with room air. The methods for the isolated perfused rat liver preparation were previously described [22]. In brief, a polyethylene tube was placed in the right carotid artery. After laparotomy, the hepatic artery was ligated and the bile duct was cannulated with the polyethylene tube (0.5 mm i.d., 0.8 mm o.d.). At 5 min after intraarterial heparinization (500 U kg^{-1}), 8–9 ml of blood was withdrawn through the carotid arterial catheter. The intra-abdominal inferior vena cava (IVC) above the renal veins was ligated, and the portal vein was cannulated with a stainless cannula (1.3 mm i.d., 2.1 mm o.d.). After thoracotomy, the supradiaphragmatic IVC was cannulated through a right atrium incision with a larger stainless cannula (2.1 mm i.d., 3.0 mm o.d.), then portal perfusion was begun with the heparinized autologous blood diluted with 5% bovine albumin (Sigma–Aldrich Co., St. Louis, MO) in Krebs solution (118 mM NaCl, 5.9 mM KCl, 1.2 mM $MgSO_4$, 2.5 mM $CaCl_2$, 1.2 mM NaH_2PO_4, 25.5 mM $NaHCO_3$, and 5.6 mM glucose) at Hct of 12%. The liver was rapidly excised, suspended from an isometric transducer (TB-652T, Nihon-Kohden, Japan) and weighed continuously throughout the experimental period.

The liver was perfused at a constant flow rate in a recirculating manner via the portal vein with blood that was pumped using a Masterflex roller pump from the venous reservoir through a heat exchanger (37 °C). The recirculating blood volume was 40 ml. The perfused blood was oxygenated in the venous reservoir by continuous bubbling with 95% O_2 and 5% CO_2 (perfused $PO_2 = 300$ mmHg).

2.2. Measurement of hepatic vascular pressures and vascular resistances

The portal venous (P_{pv}) and the hepatic venous (P_{hv}) pressures were measured using pressure transducers (TP-400T, Nihon-Kohden, Japan) attached by sidearm to the appropriate cannulas with the reference points at the hepatic hilus. Portal blood flow rate (Q) was measured with an electromagnetic flow meter (MFV 1200, Nihon-Kohden, Japan), and the flow probe was positioned in the inflow line. The hepatic sinusoidal pressure was measured by the double occlusion pressure (P_{do}) [20,23]. Both the inflow and outflow lines were simultaneously and instantaneously occluded for 13 s using the solenoid valves, after which P_{pv} and P_{hv} rapidly equilibrated to a similar or identical pressure, which was P_{do}. The principle of the double occlusion method to estimate the sinusoidal pressure [20] is derived from the concept of the mean circulating filling pressure (P_{mcf}) of the systemic circulation [24]. The P_{mcf} in the systemic circulation

represents the pressure of the most compliant vascular segments, and therefore the P_{do}, the P_{mcf} in the isolated perfused livers, represents the pressure of the most compliant vessels in the liver, that is the sinusoids. Actually, P_{do} values were obtained from the digitized data of P_{pv} and P_{hv} using an original program (LIVER software, Biomedical Science, Kanazawa, Japan). The total portal-hepatic venous (R_t), pre-sinusoidal (R_{pre}) and post-sinusoidal (R_{post}) resistances were calculated by the following equations:

$$R_t = (P_{pv} - P_{hv})/Q \quad (1)$$

$$R_{pre} = (P_{pv} - P_{do})/Q \quad (2)$$

$$R_{post} = (P_{do} - P_{hv})/Q \quad (3)$$

2.3. Bile flow rate measurement

Bile was collected drop-by-drop in a small tube suspended from the force transducer (SB-1T, Nihon-Kohden, Japan). One bile drop yielded 0.018 g and the time between drops was measured for determination of the bile flow rate [22].

2.4. Hepatic oxygen consumption measurement

To determine the oxygen consumption, the blood oxygen saturation difference between the inflow and outflow blood (ΔSO_2) was monitored continuously with a custom-made oxygen absorption spectrophotometer (ODM-1, Biomedical Science, Kanazawa, Japan), the cuvettes and sensors of which were built in the inflow and outflow perfusion lines [21]. The measured ΔSO_2 was expressed as the ODM values [21]. ΔSO_2 was calculated using the following regression line equation as determined in our previous study [21]:

$$\Delta SO_2 = 1.5103 \times \text{ODM} - 0.0685 \quad (4)$$

Using ΔSO_2, oxygen consumption (ml min^{-1} 10 g liver $weight^{-1}$) was calculated according to the Fick principle by the following equation:

$$\text{Portal blood flow/liver weight (g)} \times 10 \times 1.39\ (\text{ml/g}) \times \text{Hb (g/ml)} \times \Delta SO_2 \quad (5)$$

where Hb is the perfusing blood hemoglobin measured using spectrophotometer (UV-1200, SHIMADZU, Japan).

2.5. Data recording

The hepatic vascular pressures, blood flow rate, liver weight, bile weight and ODM values were monitored continuously and displayed through a thermal physiograph (RMP-6008, Nihon-Kohden, Japan). All outputs were also digitized by the analog-digital converter at a sampling rate of 100 Hz. These digitized values were also displayed and recorded using a personal computer for later determination of P_{do}.

2.6. Experimental protocol

Hepatic hemodynamic parameters were observed for at least 20 min after the start of perfusion until an isogravimetric state (no weight gain or loss) was obtained by adjusting the portal blood flow rate and the height of the reservoir at a P_{hv} of 0–1 cmH_2O, and at a Q of 36 ± 0.5 ml min^{-1} 10 g liver wt^{-1}. After the baseline measurements, the perfused livers were randomly divided into the three groups of the PAF, U-46619 and LTD_4 groups. To determine the concentration dependence, the drug was administered as a bolus into the reservoir to gain the final concentration of 0.0001–1 μM for PAF, 0.001–3 μM for U-46619 and 0.001–1 μM for LTD_4. The concentrations were randomly assigned for individual preparations.

In each experimental group, P_{do} was measured at baseline and maximal venoconstriction (when P_{pv} reached the peak), 6, 10, 20 and 30 min after injection of PAF, U-46619 or LTD_4.

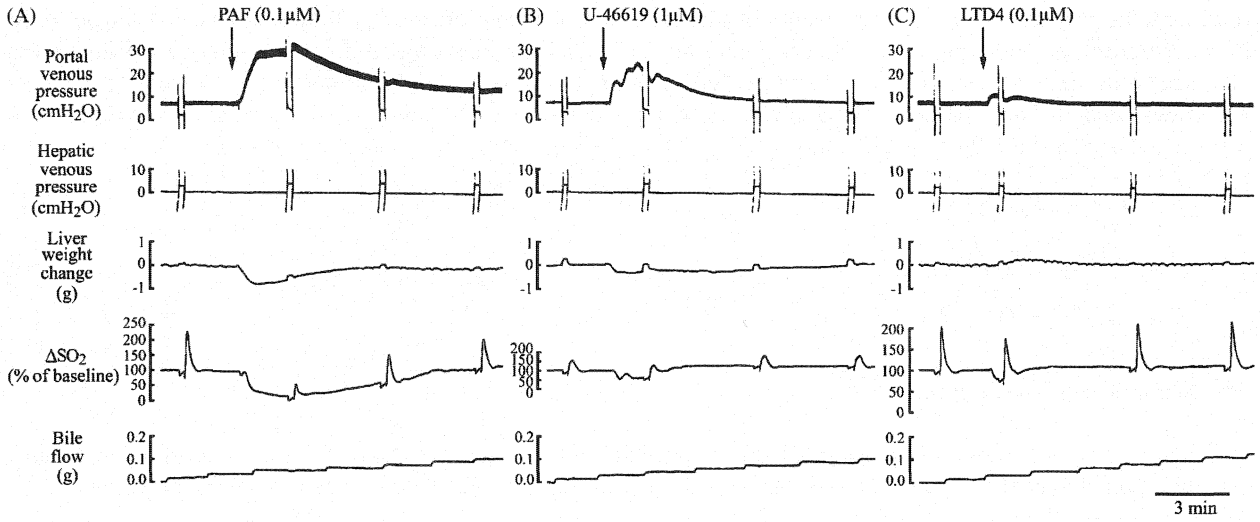

Fig. 1. Representative recordings of the responses of rat livers to PAF at 0.1 μM (A), to U-46619 at 1 μM (B) and to LTD_4 at 0.1 μM (C). ΔSO_2, the blood oxygen saturation difference between the inflow and outflow blood.

2.7. Statistics

All results are expressed as the means ± S.E. Data were analyzed by one- and two-way analysis of variance, using repeated-measures for two-way comparison within groups. Comparisons of individual points between groups and within groups were made by Bonferroni's test. Differences were considered as statistically significant at P-values less than 0.05.

3. Results

3.1. Effects of PAF, U-46619 and LTD_4 on hepatic hemodynamic variables

Fig. 1 shows the representative examples of variables after injections of PAF at 0.1 μM (A), U-46619 at 1 μM (B) and LTD_4 at 0.1 μM (C). Fig. 2 shows the summary data of the time-dependent changes in P_{pv}, P_{do}, liver weight, hepatic oxygen consumption and bile flow rate of all groups.

Soon after administrations of PAF (0.0001–1 μM), vasoconstriction occurred, as evidenced by the increase in P_{pv} (Figs. 1A and 2A). At 0.1 μM, P_{pv} increased to the peak of 25.5 ± 1.9 cmH_2O from the baseline of 7.1 ± 0.1 cmH_2O within 1.5–2.5 min after injection. The double occlusion maneuver revealed that P_{do} increased from the baseline of 2.5 ± 0.1 to 4.4 ± 0.3 cmH_2O. The pressure gradient of P_{do}-to-P_{hv} was significantly increased from the baseline of 2.2 ± 0.1 to 4.1 ± 0.1 cmH_2O, indicating the increase in R_{post}. However, the increase in the P_{pv}-to-P_{do} gradient, from 4.7 ± 0.1 to 21.2 ± 0.9 cmH_2O, was much greater than that in the P_{do}-to-P_{hv} gradient, indicating that the increase in R_{pre} was greater than that in R_{post}. Fig. 3 shows the peak levels of segmental vascular resistance, liver weight change and bile flow after PAF (closed column). R_t and R_{pre} showed concentration-dependent increases with peak levels of 3.7-fold and 4.6-fold the baseline at 0.1 μM PAF. In contrast, R_{post} at 0.1 μM PAF reached only 1.9-fold the baseline. Thus, the R_{post}/R_t ratio decreased with increasing concentrations of PAF, as shown in Fig. 3. The peaks of R_t, R_{pre} and R_{post} at 1 μM PAF were not significantly different from those at 0.1 μM PAF.

U-46619 caused venoconstriction at concentrations higher than 0.01 μM (Figs. 1B and 2B). Similar to PAF, the U-46619-induced venoconstriction was also characterized by dominant pre-sinusoidal constriction: the increase in Pdo was relatively smaller than that in P_{pv}, as shown in Fig. 2B. Actually, at the maximal vasoconstriction with 3 μM U-46619, the increase in P_{pv}-to-P_{do} gradient (from 4.8 ± 0.1 to 23.1 ± 0.5 cmH_2O) was much greater than that in the P_{do}-to-P_{hv} gradient (from 2.3 ± 0.1 to 3.3 ± 0.1 cmH_2O). Indeed, in response to 3 μM U-46619, R_{pre} increased to 4.8 times the baseline, while R_{post} increased to only 1.3 times the baseline (Fig. 3). This predominant pre-sinusoidal constriction over post-sinusoidal constriction was reflected by a progressive decrease in R_{post}/R_t ratio (Fig. 3). The U-

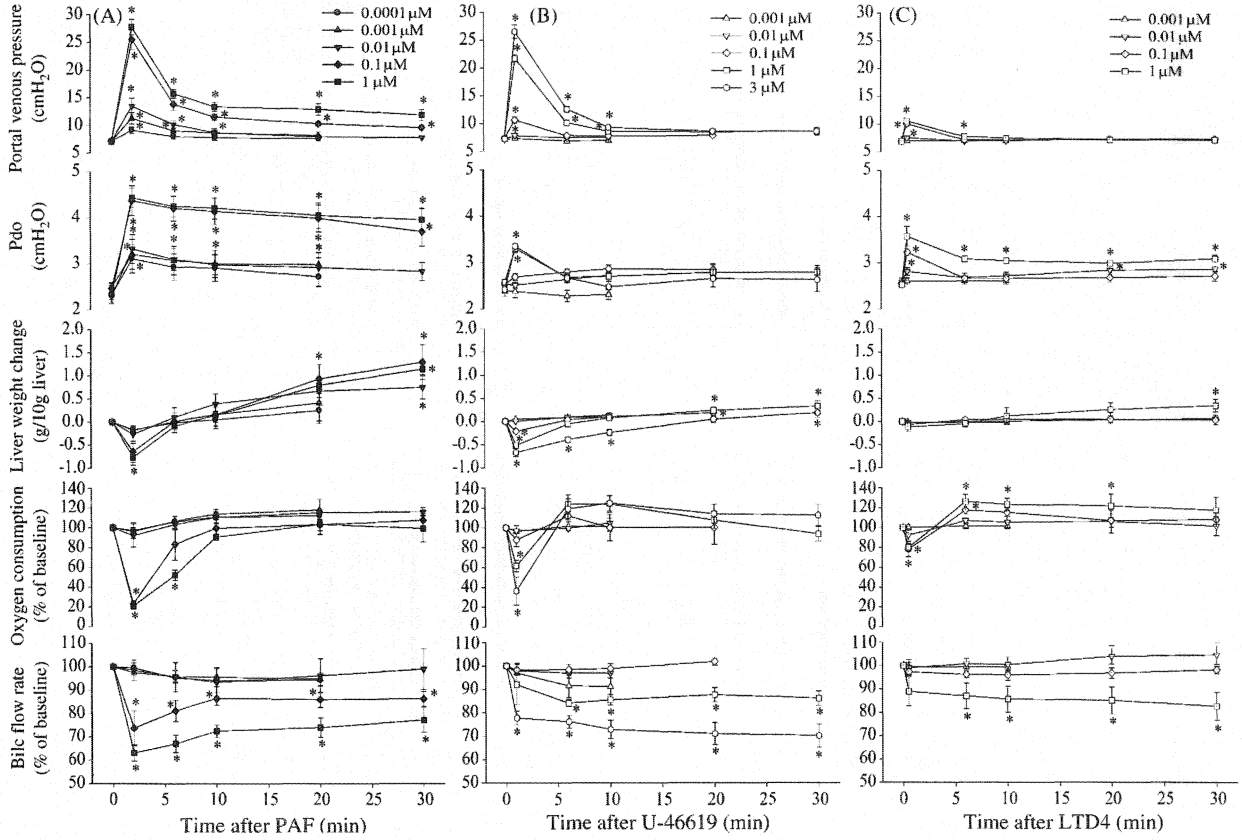

Fig. 2. The summary data of time course changes in portal venous pressure, double occlusion pressure (P_{do}), liver weight change, hepatic oxygen consumption and bile flow rate in the PAF (A), U-46619 (B) and LTD_4 (C) groups. Values are given as mean ± S.E. $n = 4$–6. $^*P < 0.05$ vs. the baseline.

46619-induced increase in R_t was smaller in magnitude than that at the corresponding concentration of PAF. However, at the comparable increased R_t levels, the R_{post}/R_t ratio in U-46619 groups was smaller than that in PAF groups, indicating that U-46619 more preferentially constricts the pre-sinusoids than PAF. R_t, R_{pre} and R_{post} recovered almost to the baseline levels within 20 min after U-46619.

LTD_4 caused a dose-dependent increase in P_{pv} at concentrations higher than 0.01 μM, as shown in Figs. 1C and 2C. The vasoconstrictive effect of LTD_4 is much weaker than that of PAF or U-46619. However, the venoconstrictive responsiveness of either pre- or post-sinusoids to LTD_4 was almost the same: the increase in R_{pre} (1.6 times the baseline) was nearly the same as that of R_{post} (1.3 times the baseline) with 0.1 μM LTD_4. This was also reflected by no significant change in R_{post}/R_t ratio (Fig. 3). R_t, R_{pre} and R_{post} recovered almost to the baseline levels within 10 min after LTD_4.

Table 1 shows the basal hemodynamic variables in all groups.

3.2. *Effects of PAF, U-46619 and LTD_4 on liver weight*

Concomitant with hepatic vasoconstriction at high concentrations of PAF (0.01–1 μM), the liver weight showed a biphasic change characterized by an initial decrease followed by an increase, as shown in Fig. 2A. There are no significant differences in peak liver weight levels between the 0.1 and 1 μM PAF groups.

U-46619 caused a progressive and dose-dependent decrease in the liver weight, resulting in the nadirs of -0.22 ± 0.02, -0.51 ± 0.05, and -0.67 ± 0.09 g 10 g liver wt^{-1}, at 0.1, 1 and 3 μM, respectively, at 1 min (Fig. 2B).

In contrast to PAF and U-46619, LTD_4, did not significantly change liver weight for 20 min, but slightly increased it at 30 min after 1 μM LTD_4 (Fig. 2C).

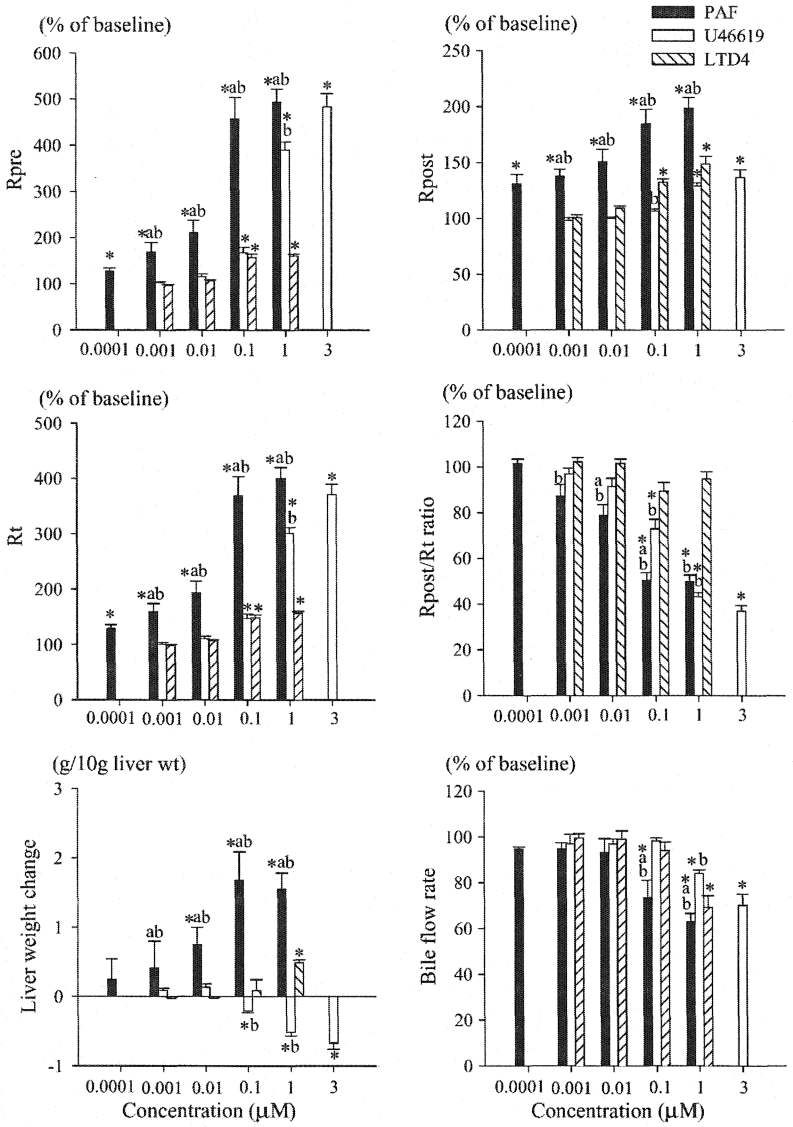

Fig. 3. The peak changes in the total (R_t), pre- (R_{pre}) and post-sinusoidal (R_{post}) resistances, the R_{post}/R_t ratio, bile flow rate and liver weight change at 0.0001–3 μM of PAF, U-46619 and LTD_4. Percent changes are expressed by those of the baseline. Values are given as mean ± S.E. $n = 4$–6. $^{*}P < 0.05$ vs. the baseline, $^{a}P < 0.05$ vs. U-46619, $^{b}P < 0.05$ vs. LTD_4.

Table 1
Basal hemodynamic variables of isolated perfused rat livers in the PAF, U-46619 and LTD_4 groups

	PAF	U-46619	LTD_4
Number of preparations	22	27	18
Portal venous pressure (cmH_2O)	7.1 ± 0.1	7.2 ± 0.1	7.0 ± 0.1
Hepatic venous pressure (cmH_2O)	0.20 ± 0.02	0.18 ± 0.02	0.21 ± 0.03
Double occlusion pressure (cmH_2O)	2.4 ± 0.1	2.5 ± 0.1	2.6 ± 0.1
Blood flow rate ($ml^{-1}\ min^{-1}\ 10\,g^{-1}$)	35 ± 1	38 ± 1	34 ± 1
Total vascular resistance ($cmH_2O\ ml^{-1}\ min^{-1}\ 10\,g^{-1}$)	0.20 ± 0.01	0.19 ± 0.01	0.20 ± 0.01
Pre-sinusoidal resistance ($cmH_2O\ ml^{-1}\ min^{-1}\ 10\,g^{-1}$)	0.14 ± 0.01	0.13 ± 0.01	0.13 ± 0.01
Post-sinusoidal resistance ($cmH_2O\ ml^{-1}\ min^{-1}\ 10\,g^{-1}$)	0.06 ± 0.01	0.06 ± 0.01	0.07 ± 0.01
R_{post}/R_t ratio	0.32 ± 0.01	0.33 ± 0.01	0.34 ± 0.01

Values are given as mean ± S.E.

3.3. Effects of PAF, U-46619 and LTD_4 on bile flow rate

Basal bile flow rate in livers studied was 8.7 ± 0.1 mg min^{-1} 10 g liver wt^{-1}. After PAF at 0.1 and 1 μM, bile flow rate significantly decreased to nadirs of 74 ± 8 and $63 \pm 4\%$ of the baseline, respectively, at 2 min and then gradually recovered. In response to U-46619 at 1 and 3 μM, it also significantly decreased to 84 ± 5 and $70 \pm 5\%$ of the baseline. In contrast, a significant decrease in the bile flow rate was observed after LTD_4 only at 1 μM, and it decreased to $69 \pm 5\%$ of the baseline at 30 min.

3.4. Effects of PAF, U-46619 and LTD_4 on hepatic oxygen consumption

The hepatic oxygen consumption was not significantly changed by PAF at 0.0001–0.01 μM, but significantly decreased at 0.1 and 1 μM (Figs. 1A and 2A). It recovered to the baseline at 10 min. There was no significant difference between the nadirs of hepatic oxygen consumption, $23 \pm 3\%$ of the baseline of 0.049 ± 0.006 ml min^{-1} 10 g liver wt^{-1} at 0.1 μM and $21 \pm 2\%$ of the baseline of 0.053 ± 0.010 ml min^{-1} 10 g liver wt^{-1} at 1 μM.

In response to U-46619, the hepatic oxygen consumption was also not significantly changed at lower concentrations (0.001–0.1 μM), but was significantly decreased at higher concentrations (1 and 3 μM). It reached the nadirs, 62 ± 6 and $36 \pm 14\%$ of the baseline of 0.041 ± 0.005 and 0.044 ± 0.008 ml min^{-1} 10 g liver wt^{-1}, respectively, at 1 min, and then recovered quickly, as shown in Fig. 2B. The magnitude of decrease in the hepatic oxygen consumption was smaller with U-46619 than with PAF at corresponding concentrations.

In contrast, LTD_4 induced biphasic changes at high concentrations of 0.1 and 1 μM. It initially decreased to $78 \pm 8\%$ and $80 \pm 4\%$ of the baseline at 0.5 min, and then quickly and significantly increased to the peak of $118 \pm 4\%$ and $126 \pm 7\%$, at 0.1 and 1 μM, respectively (Fig. 2C).

4. Discussion

In the present study, we determined the effects of a TxA_2 analogue (U-46619), PAF and LTD_4 on the vascular resistance distribution, liver weight and oxygen consumption in isolated rat livers portally perfused with blood. The main findings are that both PAF and U-46619 predominantly constricted the pre-sinusoidal veins over the post-sinusoidal veins, with U-46619 more preferentially constricting the pre-sinusoids than PAF. In contrast, LTD_4 constricted both the pre- and post-sinusoidal veins similarly in isolated blood-perfused rat livers. U-46619 caused liver weight loss, while PAF and LTD_4 at the high concentrations increased liver weight via substantial post-sinusoidal constriction. PAF and U-46619 decreased hepatic oxygen consumption, but LTD_4 induced a biphasic change of an initial transient decrease followed by an increase.

Hepatic vascular responsiveness to various vasoactive substances differs depending on the vascular segments and the animal species. Histamine causes marked constriction of the hepatic vein in dogs [25] and guinea pigs [26], while it does not constrict hepatic vessels of cats [27] and rats [26]. In contrast, norepinephrine preferentially constricts the pre-sinusoidal vessels similarly in dog [28,29], rat [28,29], rabbit [23,28], guinea pig [26] and mouse [30]. With respect to the venoconstrictive site of PAF and TxA_2, we previously reported using canine isolated blood-perfused livers that TxA_2 predominantly constricts the hepatic vein [17], while PAF constricts both portal veins and hepatic veins similarly [18]. We have recently shown that both PAF and TxA_2 predominantly constrict pre-sinusoidal veins over post-sinusoidal veins in guinea pigs, although the post-sinusoidal action of TxA_2 was weaker than that of PAF [19]. In rat livers, we herein demonstrated that both PAF and TxA_2 predominantly constricted pre-sinusoidal veins over post-sinusoidal veins, and TxA_2 more preferentially constricted the pre-sinusoids than PAF in rat livers. In contrast, LTD_4 constricted both the pre- and post-sinusoidal veins similarly in rat livers. Thus the hepatic vascular responsiveness to PAF and TxA_2 of rats appears to be similar to that of guinea pigs rather than dogs. Furthermore, we have shown that the order of vasoconstrictive effects was PAF > TxA_2 > LTD_4.

We have recently reported using the same isolated rat liver preparation that hepatic anaphylaxis induced by antigen of ovalbumin causes marked pre-sinusoidal venoconstriction and liver weight change of initial loss followed by a gradually increase, which could account for the portal hypertension and hepatic congestion associated with anaphylactic shock [21,22]. Anaphylactic reaction is accompanied by an increased release of vasoactive substances such as PAF [31], TxA_2 [31] and LTD_4 [32]. In the present study, PAF induced substantial pre-sinusoidal constriction, and an initial slight liver weight loss followed by liver weight gain. The response to PAF may be compatible with the hepatic anaphylactic

response in rats [21,22]. In contrast, TxA_2or LTD_4 seems not to be a main mediator responsible for the rat hepatic anaphylaxis, because the vasoconstriction induced by these mediators was very weak, as shown in the present study. However, in this respect, further pharmacological studies are required using the antagonists of these lipid mediators.

The mechanism whereby PAF or U-46619 predominantly constricts the pre-sinusoids over the post-sinusoids in rat is not known. One possibility is related to platelet and neutrophil aggregation, because both PAF and TxA_2 can activate these cells, resulting in intravascular aggregation [1,2]. The aggregation of neutrophils and platelets may obstruct the sinusoids, which could represent an increase in the pre-sinusoidal resistance. However, this assumption seems unlikely because heparin that was used in the present study has been shown not only to inhibit adhesion of leukocyte in the endothelium [33] but also to cause platelet dysfunction [34]. Thus, even if platelet or leukocyte aggregation occurs, they might play a minor role in the vascular resistance change. The second, contraction of the hepatic pericytes, hepatic stellate cells, may account for either PAF or U-46619-induced pre-sinusoidal venoconstriction. Hepatic stellate cells are located around the endothelial cells and their multiple cellular appendages reach out to wrap around the sinusoid [35]. Hepatic stellate cells are highly contractile in response to PAF and TxA_2 [36]. PAF and TxA_2 could constrict sinusoidal hepatic stellate cells directly, resulting in increased sinusoidal resistance, which might represent increased pre-sinusoidal resistance. However, other investigators could not confirm the physiological contractility of the stellate cells [37,38]. Finally, a more plausible explanation is that functional PAF and TxA_2 receptors are distributed more abundantly in the smooth muscle cells of the rat pre-sinusoidal vein than in those of the post-sinusoidal vein. However, there is no direct evidence of the presence of nonhomogenous distribution of PAF or TxA_2 receptors in rat hepatic vessels.

We believe that the hepatic vasoconstrictive response to PAF, U-46619 or LTD_4 in the present study was due to the direct effects of these substances, because the vasoconstriction occurred immediately after injection without a latent period that might have been required for activation, release or synthesis of other vasoconstrictors. However, we cannot rule out a possibility of modulation of an endogenous hepatic vasoconstrictor that could be released in response to U-46619, PAF or LTD_4. In organs other than livers, some of the vasoconstrictive effects of TxA_2 seem to be mediated by the induction of LTC_4 and LTD_4 [39], and endothelins [40]. PAF is also able to activate the hepatic intravascular macrophages of Kupffer cells, with resultant release of the cyclooxygenase metabolites [41]. LTD_4 could stimulate the synthesis of TxA_2 [42,43]. Further studies are required to examine the interactions among these mediators.

We measured liver weight changes to know the intrahepatic blood volume alterations. U-46619 induced obvious liver weight loss. In contrast, PAF mainly induced liver weight gain although it initially and transiently caused liver weight loss. Liver weight also increased in response to LTD_4 at the highest concentration of 1 μM. The decrease in liver weight may be produced by pre-sinusoidal constriction, which may prevent the entrance of blood into the liver capillaries, resulting in weight loss. The liver weight gain after PAF and LTD_4 may be caused by substantial post-sinusoidal constriction and an increase in P_{do}, both of which would lead to hepatic congestion, enhanced extravascular fluid filtration and interstitial water accumulation. The magnitude of increased P_{do} may represent the liver weight change. Fig. 4 shows the relationship between the peak P_{do} and liver weight change in all groups studied. There was a significant correlation between the peak P_{do} and liver weight change ($r=0.746$, $p<0.0001$) after administrations of PAF, U-46619 and LTD_4. This finding indicated that the liver weight change was strongly associated with the P_{do} increase, as described previously in our study [19].

In the present study, we have demonstrated that PAF and U-46616 decreased hepatic oxygen consumption, while LTD_4 caused a biphasic change of it. These results are in agreement with the previous studies [44–46]. Haussinger et al. reported that U-46619 decreased oxygen consumption by 27% in perfused rat livers [44]. ONO-11113, another TXA_2 analogue, induced an initial small stimulation followed by a marked inhibition of oxygen uptake in perfused rat livers [45]. PAF also suppressed oxygen consumption in perfused rat livers [46]. However, Haussinger et al. reported that LTC_4 and LTD_4 of 20 nM reduced oxygen consumption by $29 \pm 3\%$ and $30 \pm 3\%$ of baseline, respectively, in isolated rat livers [44]. The difference may be related to the different perfusion methods. In the study of Haussinger et al., the livers were perfused without recirculation with blood-free Krebs solution [44]. In addition, in the present study, a biphasic change in oxygen consumption was observed only at high concentrations (0.1 and 1 μM) of LTD_4. In contrast, Haussinger et al. examined only one small dose (20 nM) of LTD_4, but not the high dose of LTD_4.

There is a criticism that the relevance of the present findings to the in vivo situation seems to be limited by the fact that the experiments were done in an isolated organ, and perfusion was done using diluted blood. However, one of the main purposes of the present study is to determine the venoconstrictive site of the lipid mediators in rat hepatic circulation. Currently, this could not be accomplished in in vivo intact animals, if the measurement of the hepatic

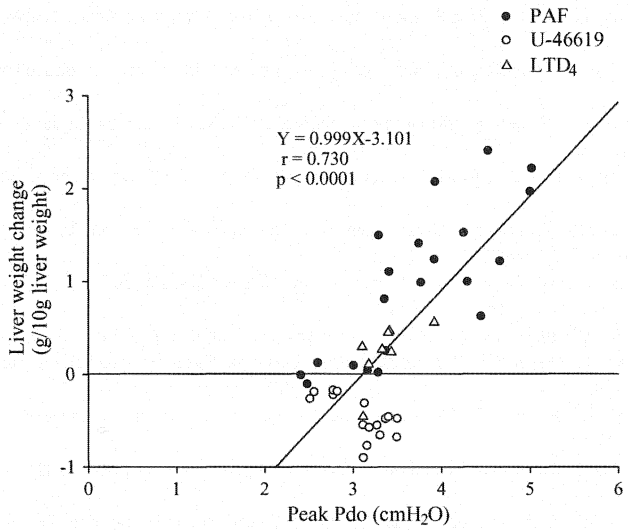

Fig. 4. Relationship between peak P_{do} values and liver weight changes after injections of PAF (closed circle), U-46619 (open circle) and LTD_4 (triangle). Equations of linear lines are given in the text.

microvascular pressures using the micropipette method were not performed [47]. However, no measurement of the hepatic microvessels with micropipettes in in vivo animals has been performed so far to determine the effects of lipid mediators such as PAF, TxA_2, and LTD_4 on the hepatic vascular resistance distribution. Although limitations inherent to isolated perfused livers exist, we think that P_{do} [20] in the present perfused livers has provided estimation of the sinusoidal pressure and therefore the pre- and post-sinusoidal resistances in the livers exposed to the lipid mediators studied.

In conclusion, both TxA_2 and PAF predominantly constrict pre-sinusoidal veins, and TxA_2 more preferentially constricts the pre-sinusoids than PAF. However LTD_4 constricts both pre- and post-sinusoidal veins similarly. The order of the extent of hepatic venoconstrictive effects was PAF > TxA_2 > LTD_4. TxA_2 causes liver weight loss at high concentrations, while LTD_4 and PAF increase liver weight via substantial post-sinusoidal constriction in isolated rat livers. PAF and TxA_2 decrease hepatic oxygen consumption, whereas LTD_4 induces a biphasic change of it in isolated blood-perfused rat livers.

Acknowledgement

This work was supported by a Grant for Collaborative Research from Kanazawa Medical University (C2004-1, C2005-1).

References

[1] Braquet P, Touqui L, Shen TY, Vargaftig BB. Perspective in platelet-activating factor research. Pharmacol Rev 1987;39:97–145.
[2] Samuelsson B, Goldyne M, Granstrom E, Hamberg M, Hammarstrom S, Malmsten C. Prostaglandins and thromboxanes. Ann Rev Biochem 1978;47:997–1029.
[3] Hagmann W, Hacher HJ, Buchholz U. Resident mast cells are the main initiators of anaphylactic leukotriene production in the liver. Hepatology 1992;16:1477–84.
[4] Shibamoto T, Ruan Z, Cui S, Liu W, Kurata Y. Involvement of platelet-activating factor and leukotrienes in anaphylactic segmental venoconstriction in ovalbumin sensitized guinea pig livers. Prostaglandins Other Lipid Mediat 2005;78:218–30.
[5] Guarner F, Wallace JL, MacNaughton WK, Ibbotson GC, Arroyo V, Rodes J. Endotoxin-induced ascites formation in the rat: partial mediation by platelet-activating factor. Hepatology 1989;10:788–94.
[6] Ishiguro S, Arii S, Monden K, et al. Identification of the thromboxane A_2 receptor in hepatic sinusoidal endothelial cells and its role in endotoxin-induced liver injury in rats. Hepatology 1994;20:1281–6.
[7] Tiegs G, Wendel A. Leukotriene-mediated liver injury. Biochem Pharmacol 1988;37:2569–73.
[8] Ishiguro S, Arii S, Monden K, et al. Involvement of thromboxane A2–thromboxane A2 receptor system of the hepatic sinusoid in pathogenesis of cold preservation/reperfusion injury in the rat liver graft. Transplantation 1995;59:957–61.

[9] Iwazaki S, Takeyoshi I, Ohawada S, et al. FR128998 ameliorates liver injury in extended liver resection with ischemia in dogs. Hepatogastroenterology 2001;48:197–202.
[10] Takeyoshi I, Sunose Y, Iwazaki S, et al. The effect of a selective cycloxygenase-2 inhibitor in extended liver resection with ischemia in dogs. J Surg Res 2001;100:25–31.
[11] Shimada M, Matsumata T, Taketomi A, Shirabe K, Yamamoto K, Sugimachi K. The role of prostaglandins in hepatic resection. Prostaglandins Leukot Essent Fatty Acids 1994;50:65–8.
[12] Chun K, Zhang J, Biewer J, Ferguson D, Clemens MG. Microcirculatory failure determines lethal hepatocyte injury in ischemic/reperfusion rat livers. Shock 1994;1:3–9.
[13] Fisher RA, Robertson SM, Olson MS. Stimulation of glycogenolysis and vasoconstriction in the perfused rat liver by the thromboxane A2 analogue U-46619. J Biol Chem 1987;262:4631–8.
[14] Haussinger D, Stehle T, Gerok W. Effects of leukotrienes and the thromboxane A2 analogue U-46619 in isolated perfused rat liver. Metabolic, hemodynamic and ion-flux responses. Biol Chem 1988;369:97–107.
[15] Hines KL, Braillon A, Fisher RA. PAF increases hepatic vascular resistance and glycogenolysis in vivo. Am J Physiol 1991;260:G471–80.
[16] Buxton DB, Fisher RA, Hanahan DJ, Olson MS. Platelet-activating factor mediated vasoconstriction and glycogenolysis in the perfused rat liver. J Biol Chem 1986;261:644–9.
[17] Urayama H, Shibamoto T, Wang HG, Koyama S. Thromoboxane A_2 analogue contracts predominantly the hepatic veins in isolated canine livers. Prostaglandins 1996;52:483–95.
[18] Wang HG, Shibamoto T, Koyama S. Effect of platelet-activating factor on hepatic capillary pressure in isolated dog liver. Prostaglandins Leukot Essent Fatty Acids 1997;57:293–8.
[19] Ruan Z, Shibamoto T, Shimo T, et al. Effects of platelet-activating factor and thromboxane A_2 on isolated perfused guinea pig liver. Prostaglandins Other Lipid Mediat 2004;73:73–85.
[20] Yamaguchi Y, Shibamoto T, Hayashi T, Saeki Y, Tanaka S. Hepatic vascular response to anaphylaxis in isolated canine liver. Am J Physiol 1994;267:R268–74.
[21] Cui S, Shibamoto T, Ruan Z, Takano H, Liu W, Kurata Y. Oxygen consumption, assessed with the oxygen absorption spectrophotometer, decreases independently of venoconstriction during hepatic anaphylaxis in perfused rat liver. Shock; in press.
[22] Shibamoto T, Cui S, Ruan Z, Liu W, Takano H, Kurata Y. Hepatic venoconstriction is involved in anaphylactic hypotension in rats. Am J Physiol Heart Circ Physiol 2005;289:H1436–41.
[23] Shibamoto T, Wang HG, Miyahara T, Tanaka S, Haniu H, Koyama S. Presinusoidal vessels predominantly contract in response to norepinephrine, histamine, and KCl in rabbit liver. J Appl Physiol 1999;87:1404–12.
[24] Rothe CF. Mean circulatory filling pressure: its meaning and measurement. J Appl Physiol 1993;74:499–509.
[25] Lautt WW, Legare DJ. Effect of histamine, norepinephrine, and nerves on vascular pressures in dog liver. Am J Physiol 1987;252:G472–8.
[26] Shibamoto T, Narushima M, Ling YQ, et al. Different hepatic vascular response to norepinephrine and histamine between guinea pig and rat. Acta Physiol Scand 2004;180:255–63.
[27] Greenway CV, Lautt WW. Effects of infusions of catecholamines, angiotensin, vasopressin and histamine on hepatic blood volume in the anaesthetized cat. Br J Pharmacol 1972;44:177–84.
[28] Bohlen HG, Maass-Moreno R, Rothe CF. Hepatic venular pressures of rats, dogs, and rabbits. Am J Physiol 1991;261:G539–47.
[29] Shibamoto T, Wang HG, Tanaka S, Koyama S. Hepatic capillary pressure is estimated using triple vascular occlusion method in isolated canine liver. Am J Physiol 1996;271:R1130–41.
[30] Shibamoto T, Cui S, Ruan Z, Kurata Y. Effects of norepinephrine and histamine on vascular resistance in isolated perfused mouse liver. Jpn J Physiol 2005;55:143–8.
[31] Kemp SF, Lockey RF. Anaphylaxis: a review of causes and mechanisms. J Allergy Clin Immunol 2002;110:341–8.
[32] Foster A, Letts G, Charleson S, Fitzsimmons B, Blacklock B, Rokach J. The in vivo production of peptide leukotrienes after pulmonary anaphylaxis in the rat. J Immunol 1988;141:3544–50.
[33] Bazzoni G, Beltran NA, Mascellani G, Bianchini P, Dejana E, Del Maschio A. Effect of heparin, dermatan sulfate, and related oligo-derivatives on human polymorphonuclear leukocyte functions. J Lab Clin Med 1993;121:268–75.
[34] Khuri SF, Valeri CR, Loscalzo J, et al. Heparin causes platelet dysfunction and induces fibrinolysis before cardiopulmonary bypass. Ann Thorac Surg 1995;60:1008–14.
[35] Wake K. Perisinusoidal stellate cells (fat-storing cells, interstitial cells, lipocytes), their related structure in and around the liver sinusoids, and vitamin A-storing cells in extrahepatic organs. Int Rev Cytol 1980;66:303–53.
[36] Rockey DC. Hepatic blood flow regulation by stellate cells in normal and injured liver. Semin Liver Dis 2001;21:337–49.
[37] McCuskey R, Ito Y, McCuskey M, et al. Morphological mechanism for regulating blood flow through hepatic sinusoids: 1998 update and overview. In: Wisse E, Knock D, De Zanger R, editors. Cell of the hepatic sinusoid. Rijswijk: Kupffer Cell Foundation; 1999. p. 129–34.
[38] Ekataksin W, Kaneda K. Liver microvascular architecture: an insight into the pathophysiology of portal hypertension. Semin Liver Dis 1999;19:359–82.
[39] Soifer SJ, Schreiber MD, Heymann MA. Leukotriene antagonists attenuate thromboxane-inducible pulmonary hypertension. Pediatr Res 1989;26:83–7.
[40] Yamamoto T, Hosoki K, Karasawa T. Possible involvement of endothelin in thromboxane A_2 receptor agonist (U-46619)-induced angina in the rat. Eur J Pharmacol 1993;250:189–91.
[41] Altin JG, Dieter P, Bygrave FL. Evidence that Ca^{2+} fluxes and respiratory, glycogenolytic and vasoconstrictive effects induced by the action of platelet-activating factor and L-α-lysophosphatidylcholine in the perfused rat liver are mediated by products of the cyclo-oxygenase pathway. Biochem J 1987;245:145–50.

[42] Smith LJ, Shamsuddin M, Houston M. Effect of leukotriene D_4 and platelet-activating factor on human alveolar macrophage eicosanoid and PAF synthesis. Am Rev Respir Dis 1993;148:682–8.
[43] Bochnwicz S, Underwood DC. Dose-dependent mediation of leukotriene D4-induced airway microvascular leakage and bronchoconstriction in the guinea pig. Prostaglandins Leukot Essent Fatty Acids 1995;52:403–11.
[44] Haussinger D, Stehle T, Gerok W. Effects of leukotrienes and the thromboxane A_2 analogue U-46619 in isolated perfused rat liver. Biol Chem 1988;369:97–107.
[45] Altin JG, Bygrave FL. Prostaglandin F_2 alpha and the thromboxane A_2 analogue ONO-11113 stimulate Ca^{2+} fluxes and other physiological responses in rat liver. Further evidence that prostanoids may be involved in the action of arachidonic acid and platelet-activating factor. Biochem J 1988;249:677–85.
[46] Kimura K, Moriyama M, Nishisako M, et al. Modulation of platelet activating factor-induced glycogenolysis in the perfused rat liver after administration of endotoxin in vivo. J Biochem (Tokyo) 1998;123:142–9.
[47] Rothe CF, Maass-Moreno R. Active and passive liver microvascular responses from angiotensin, endothelin, norepinephrine, and vasopressin. Am J Physiol Heart Circ Physiol 2000;279:H1147–56.

N^G-NITRO-L-ARGININE METHYL ESTER POTENTIATES ANAPHYLACTIC VENOCONSTRICTION IN RAT PERFUSED LIVE

Toshishige Shibamoto,* Takaharu Ishibashi,† Tomohiro Shimo,‡ Sen Cui,* Hiromichi Takano,* Hideaki Tsuchida,‡ Matomo Nishio† and Yasutaka Kurata*

*Departments of *Physiology, †Pharmacology and ‡Anaesthesiology, Kanazawa Medical University, Uchinada, Ja*

SUMMARY

1. The effects of the nitric oxide (NO) synthase inhibitor N^G-nitro-L-arginine methyl ester (L-NAME) on anaphylaxis-induced venoconstriction were examined in rat isolated livers perfused with blood-free solutions in order to clarify the role of NO in anaphylactic venoconstriction.

2. Rats were sensitized with ovalbumin (1 mg) and, 2 weeks later, livers were excised and perfused portally in a recirculating manner at a constant flow with Krebs'–Henseleit solution. The antigen (ovalbumin; 0.1 mg) was injected into the reservoir 10 min after pretreatment with L-NAME (100 μmol/L) or D-NAME (100 μmol/L) and changes in portal vein pressure (Ppv), hepatic vein pressure (Phv) and perfusate flow were monitored. In addition, concentrations of the stable metabolites of NO (NO_2^- and NO_3^-) were determined in the perfusate using an HPLC–Griess system.

3. The antigen caused hepatic venoconstriction, as evidenced by an increase in Ppv from a mean (±SEM) baseline value of 7.7 ± 0.1 cmH_2O to a peak of 21.4 ± 1.1 cmH_2O at 3 min in D-NAME-pretreated livers. Pretreatment with L-NAME augmented anaphylactic venoconstriction, as reflected by a higher Ppv (27.4 ± 0.8 cmH_2O) after antigen than observed following D-NAME pretreatment. The addition of L-arginine, a precursor for the synthesis of NO, reversed the augmentation of anaphylactic venoconstricion by L-NAME. This suggests that hepatic anaphylaxis increased the production of NO, which consequently attenuated anaphylactic venoconstriction. However, perfusate NO_x levels did not increase significantly after antigen in livers pretreated with either L-NAME or D-NAME.

4. In conclusion, L-NAME potentiates rat anaphylactic hepatic venoconstriction, suggesting that NO contributes to the attenuation of the venoconstriction. However, this functional evidence was not accompanied by corresponding changes in perfusate NO_x concentrations.

Key words: anaphylactic shock, HPLC–Griess system, isolated perfused rat liver, nitric oxide, NO_x.

Correspondence: Dr Toshishige Shibamoto, Department of Physiology, Kanazawa Medical University, Daigaku 1-1, Uchinada, Ishikawa 920-0293, Japan. Email: shibamo@kanazawa-med.ac.jp

Received 8 October 2005; revision 2 April 2006; accepted 18 April 2006.

INTRODUCTION

Anaphylactic hypotension is sometimes life threatening caused by a decrease in effective circulating blood v Nitric oxide (NO), which is produced in endothelial response to either hormonal or physical stimuli, such as she regulates the vascular system.[2,3] Nitric oxide seems to important pathophysiological role in modulating the s changes associated with anaphylaxis. An NO synthase inhibitor was shown to attenuate hypotension and haemo tration and decrease venous return in this condition, alt did not improve cardiac depression.[4] Conversely, NO fun antagonizes the effects of vasoconstrictors released duri phylaxis and there is experimental evidence that NO may some pathophysiological changes associated with anap except for vasodilatation.[4]

It is well known that vasoconstriction of the liver cor to the control of systemic circulation: passive blood mob to and from the liver, which is caused by hepatic vasocons influences venous return to the heart and, hence, systemic tion.[5] Indeed, it has been reported that hepatic venocon is involved, in part, in anaphylactic hypotension.[6,7] Anap causes hepatic venoconstriction, as observed in rats,[7,8] pigs[9] and dogs,[10,11] resulting in portal hypertension th causes congestion of the upstream splanchnic organs, resultant decrease in venous return and effective cir blood volume and finally augmentation of anaphylacti tension. We have shown recently that hepatic venocons is observed in response to antigen in sensitized guinea-p and that NO attenuates constriction of these vessels phylactic hepatic venoconstriction, based on an increase i venous pressure, was also observed in rats.[7,8] However, known whether NO can be released in rat liver vasc exposed to anaphylaxis and can modulate anaphylactic venoconstriction.

Thus, to investigate these issues, anaphylactic venocon was examined with rat isolated livers that were perfuse blood-free solution under constant flow in the presenc NOS inhibitor N^G-nitro-L-arginine methyl ester (L-NA D-NAME, an inactive enantiomer of L-NAME. The e L-NAME was further examined with simultaneous pret with L-arginine. In addition to this functional study, we at to provide physical evidence by measuring perfusate NO_2^- a (stable metabolites of NO) with the sophisticated HPLC system (ENO-10) to elucidate the contribution of NO to fu effects observed.

METHODS

Animals

Twenty-three male Sprague-Dawley rats (Japan SLC, Shizuoka, Japan) weighing 333 ± 4 g were used in the present study. Rats were maintained under pathogen-free conditions on a 12 h dark–light cycle and allowed food and water *ad libitum*. The experiments conducted in the present study were approved by the Animal Research Committee of Kanazawa Medical University. Rats were actively sensitized by the subcutaneous injection of an emulsion made by mixing equal volumes of complete Freund's adjuvant (0.5 mL) with 1 mg ovalbumin (grade V; Sigma, St Louis, MO, USA) dissolved in physiological saline (0.5 mL).

Isolated perfused liver

Two weeks after sensitization, animals were anaesthetized with pentobarbital sodium (70 mg/kg, i.p.) and ventilated mechanically with room air. The basic methods for rat isolated perfused livers have been described elsewhere.[7] Briefly, a catheter was placed in the right carotid artery for the injection of heparin. After laparotomy, the hepatic artery was ligated. After intra-arterial heparinization (500 U/kg), the intra-abdominal inferior vena cava (IVC) above the renal veins was ligated and the portal vein was cannulated with a stainless-steel cannula (1.3 mm ID, 2.1 mm OD) for portal perfusion. After thoracotomy, the supradiaphragmatic IVC was cannulated through an incision in the right atrium with a large stainless-steel cannula (2.1 mm ID, 3.0 mm OD). Then, portal perfusion was started at a constant flow rate (43 mL/min) with Krebs'–Henseleit solution (composition (in mmol/L): NaCl 118; KCl 5.9; $MgSO_4$ 1.2; $CaCl_2$ 2.5; NaH_2PO_4 1.2; $NaHCO_3$ 25.5; glucose 5.6). Initially, livers were perfused in a non-recirculating manner with perfusate that was pumped using a Masterflex pump (Cole-Parmer, Chicago, IL, USA) from the venous reservoir through a heat exchanger (37°C). When the colour of the effluent became translucent, the perfusion mode was changed to recirculating. The recirculating perfusate volume was 40 mL. The perfusate was oxygenated in the venous reservoir by continuous bubbling with 95% O_2 and 5% CO_2. The portal venous (Ppv) and hepatic venous (Phv) pressures were measured with pressure transducers (TP-400T; Nihon-Kohden, Tokyo, Japan) attached by a sidearm to the appropriate cannulas with the reference points at the hepatic hilus. Portal perfusate flow rate (Qpv) was measured with an electromagnetic flow meter (MFV 1200; Nihon-Kohden) and the flow probe was positioned in the inflow line. The Ppv, Phv and Qpv were monitored continuously and displayed through a thermal physiograph (RMP-6008; Nihon-Kohden). Outputs were also digitized by the analogue–digital converter at a sampling rate of 100 Hz using a personal computer.[7]

Hepatic haemodynamic parameters were observed for at least 20 min after the start of perfusion. Then, the livers were divided into three groups: (i) D-NAME ($n = 9$), in which 100 μmol/L D-NAME (Sigma) was administered into the reservior; (ii) L-NAME ($n = 9$), in which 100 μmol/L L-NAME (Sigma) was administered into the reservior; and (iii) L-arginine + L-NAME ($n = 5$), in which L-arginine (1 mmol/L; Sigma) plus L-NAME (100 μmol/L) were administered into the reservoir. Thus, any livers studied were pretreated with either L-NAME or D-NAME. Ovalbumin (0.1 mg) was injected into the reservoir 10 min after the injection of L-NAME or D-NAME. In each experimental group, measurements were performed up to 30 min after the administration of antigen. The total portal–hepatic venous (Rt) resistance was calculated using the formula:

$$Rt = (Ppv - Phv)/Qpv$$

Measurement of NO_x

Portal (inflow) and hepatic venous (outflow) perfusate samples (0.5 mL) were simultaneously and instantaneously obtained from the inflow and outflow lines, respectively, before injection of L- or D-NAME just before antigen injection (baseline) and 0.5, 1, 3 and 6 min after antigen injection. NO_2^- and NO_3^- were separated and measured using the HPLC–Griess system (ENO-10; Eicom, Kyoto, Japan). The detection limit and the sensitivity for NO_3^- were 10 nmol/L under routine setup, whereas under the highly sensitive mode for NO_2^- (the reduction column was omitted and 100 μL sample was loaded without deproteinization), the detection limit was 2 nmol/L and the sensitivity was 1–2 nmol/L. The inter- and intra-assay coefficients of variation were below 0.5% for NO_3^- and approximately 5% for NO_2^- for highly sensitive quantification.[12,13] Special attention was paid to avoid any contamination with NO_x throughout the entire procedure.[14]

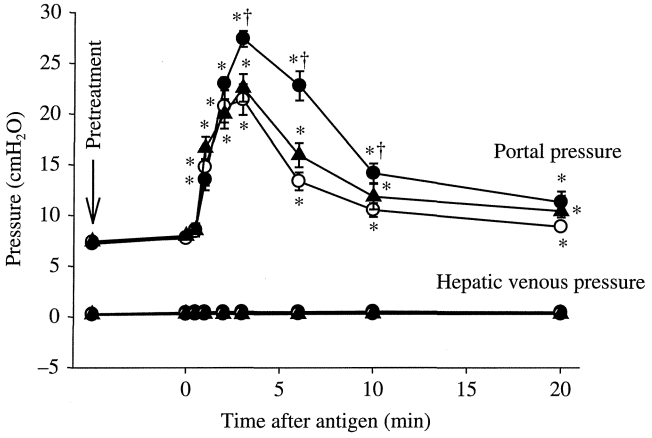

Fig. 1 Summary of changes in portal venous pressure and hepatic venous pressure after antigen injection in N^G-nitro-D-arginine methyl ester (D-NAME; $n = 9$; ○), N^G-nitro-L-arginine methyl ester (L-NAME; $n = 9$; ●) and L-arginine + L-NAME ($n = 5$; ▲) groups. Data are the mean±SEM. *$P < 0.05$ compared with baseline; †$P < 0.05$ compared with the D-NAME and L-arginine + L-NAME groups.

Statistics

All results are expressed as the mean±SEM. Analysis of variance followed by Bonferroni's test was used to test the significance of differences. Differences were considered statistically significant at $P < 0.05$.

RESULTS

Response of Ppv to antigen

After injection of L-NAME or D-NAME into the blood-free constant-flow perfused liver, Ppv did not change significantly. As shown in Fig. 1, after injection of 0.1 mg ovalbumin into a D-NAME-pretreated liver, venoconstriction occurred, as evidenced by an increase in Ppv. The Ppv reached peak levels of 21.4 ± 1.1 cmH_2O 3 min after the injection of antigen from a baseline value of 7.7 ± 0.1 cmH_2O. The Ppv-to-Phv gradient, the determinant of Rt, increased 2.9-fold baseline, indicating that Rt increased by the same degree, as indicated in Table 1. In fact, Rt increased from a baseline value of 0.17 ± 0.01 to 0.47 ± 0.04 cmH_2O/mL per min per 10 g. Thereafter, Ppv and Rt decreased gradually towards baseline values.

In the L-NAME group, Ppv also increased after the injection of antigen, but the peak Ppv levels of 27.4 ± 0.8 cmH_2O 3 min after antigen injection were significantly greater than those seen in the D-NAME group (21.4 ± 1.1 cmH_2O). Thus, the peak Rt level in the L-NAME group was 1.7-fold greater than that in the D-NAME group. This significant difference was observed until 10 min after antigen injection (Fig. 1). However, as shown in Fig. 1, the augmentation of antigen-induced venoconstriction induced by L-NAME was

Table 1 Effects of N^G-nitro-L-arginine methyl ester (L-NAME) and N^G-nitro-D-arginine methyl ester (D-NAME) on haemodynamic variables and antigen injection in rat isolated perfused livers

Groups	L-NAME			D-NAME			L-Arginine + L-NAME		
	Pretreatment	Baseline	3 min	Pretreatment	Baseline	3 min	Pretreatment	Baseline	
Ppv (cmH_2O)	7.2 ± 0.2	7.8 ± 0.4	27.4 ± 0.8*	7.4 ± 0.1	7.7 ± 0.1	21.4 ± 1.1*	7.4 ± 0.2	8.0 ± 0.4	22.(
Phv (cmH_2O)	0.3 ± 0.1	0.4 ± 0.2	0.5 ± 0.2	0.2 ± 0.1	0.3 ± 0.1	0.3 ± 0.1	0.3 ± 0.1	0.3 ± 0.1	0.:
Qpv (mL/min per 10 g)	41 ± 3	41 ± 3	41 ± 3	42 ± 2	42 ± 2	42 ± 2	38 ± 1	38 ± 1	3{
Rt	0.19 ± 0.03	0.20 ± 0.04	0.74 ± 0.10*	0.17 ± 0.01	0.17 ± 0.01	0.47 ± 0.04*	0.19 ± 0.01	0.20 ± 0.01	0.5
NO_x concentration (μmol/L)									
Inflow	0.45 ± 0.05	0.51 ± 0.05	0.54 ± 0.05	0.45 ± 0.02	0.52 ± 0.02	0.55 ± 0.02	0.40 ± 0.05	0.50 ± 0.05	0.5
Outflow	0.45 ± 0.06	0.50 ± 0.06	0.54 ± 0.06	0.53 ± 0.03	0.45 ± 0.06	0.54 ± 0.02	0.41 ± 0.05	0.48 ± 0.05	0.5

Values are the mean±SEM. *$P < 0.05$ compared with baseline.
Ppv, portal vein pressure; Phv, hepatic venous pressure; Qpv, perfusate flow; Rt, vascular resistance (in cmH_2O/mL per min per 10 g).

reversed by additional perfusion with L-arginine (1 mmol/L). The pressure response in the L-arginine + L-NAME group was similar in magnitude to that in the D-NAME group. These results suggest that the anaphylactic reaction in rat livers produced NO, which then attenuated the anaphylactic hepatic venoconstriction.

Perfusate concentrations of NO_x

Perfusate levels of either NO_2^- or NO_3^- did not change significantly after antigen injection in any group studied (Table 1). Moreover, differences in NO_2^- and NO_3^- between the outflow and inflow did not change significantly in any group and the differences between the two groups were not significant throughout the experimental period, as shown in Fig. 2.

DISCUSSION

The present study showed that the NOS inhibitor L-NAME augmented anaphylactic venoconstriction in rat isolated livers perfused with blood-free solution under constant flow. L-Arginine completely reversed enhancement of the anaphylactic venoconstriction by L-NAME. This finding suggests that, similar to guinea-pig livers,[5] rat livers produce NO during the anaphylactic reaction and that the NO released then attenuates anaphylactic hepatic venoconstriction. We also measured perfusate concentrations of NO metabolites before and after antigen in order to confirm the production of NO. However, unexpectedly, we could not detect significant differences in perfusate NO_x concentrations between the outflow and inflow perfusate, even though we used the highly sensitive HPLC–Griess system (ENO-10) for measurement of NO_x.

We have reported previously that anaphylactic venocostriction occurs in rat isolated blood-perfused livers.[7] In the present study, a similar response was observed in rat livers perfused with blood-free solution. This indicates that the intrahepatic mast cells rather than circulating blood cells, such as basophils and platelets, were involved in the hepatic regional anaphylaxis in the present study.

N^G-Nitro-L-arginine methyl ester is widely used to inhibit endothelial synthesis of NO. However, multiple non-specific actions of L-NAME other than simple inhibition of NO synthesis have also been reported.[15–18] These include generation of superoxide anions and prostaglandin endoperoxides, both of which cause vasoconstriction. Thus, NO-independent mechanism may ha involved in the effect of L-NAME in the present study. I we found that the addition of L-arginine completely reve augmentation by L-NAME. This finding suggests that the L-NAME is due to inhibition of NO synthesis rather tha the production of vasoconstrictors, such as superoxide an prostaglandin endoperoxide.

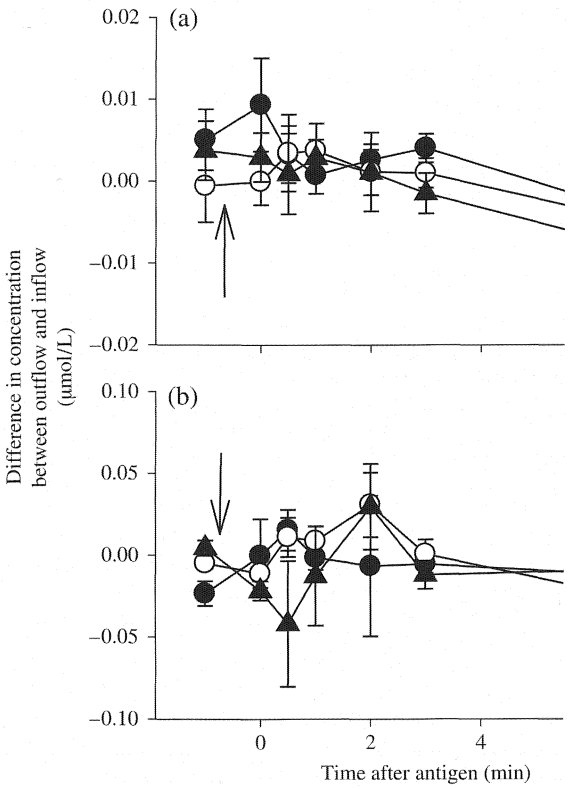

Fig. 2 Summary of changes in differences in (a) NO_2^- and concentrations between inflow and outflow perfusate after antigen in the N^G-nitro-D-arginine methyl ester (D-NAME; ○), N^G-nitro-I methyl ester (L-NAME; ●) and L-arginine + L-NAME (▲) gr arrows indicate the time of pretreatment. Data are the mean±SE *$P < 0.05$ compared with baseline.

The mechanism responsible for NO release during hepatic anaphylaxis may be ascribed to shear stress-dependent and -independent mechanisms.[19] In rat livers perfused at constant flow, anaphylaxis contracted hepatic vessels, where shear stress could be increased, resulting in NO release from the constricted endothelium. Conversely, the shear stress-independent mechanism may be related to humoral substances released by the anaphylactic reaction *per se*. We assume that chemical mediators, such as platelet-activating factor (PAF), thromboxane (TX) A_2, histamine, cysteinyl leukotrienes and serotonin, may act on their corresponding receptors on the endothelium, resulting in the subsequent activation of endothelial (e) NOS and production of NO. In fact, it has been reported that most mediators of anaphylaxis, such as histamine,[20,21] leukotrienes,[22] TXA_2[21] and PAF,[23] all stimulate NO release from the vascular endothelium.

The percentage proportion of NO counter-regulation in anaphylactic venoconstriction of the portal vein in rats was approximately 28% (6.0 cmH_2O). This seems to be smaller than that of similarly examined guinea-pig livers, in which NO inhibition augmented the anaphylaxis-induced increase in Ppv by 80% (18.1 cmH_2O).[9] The relatively lesser augmentation induced by L-NAME in the present study may be ascribed to differences in the perfusate, as well as species differences. The Krebs' solution used in the present study had a very low viscosity and, thus, produced a low vascular resistance, resulting in low shear stress and small NO production compared with the diluted blood used in the previous guinea-pig liver study.[6] The reason why we used blood-free Krebs' solution as the perfusate in the present study was that a solution including free haemoglobin could prevent accurate measurement of perfusate NO_2^- and NO_3^- concentrations.[24] Haemolysis and, thus, the presence of free haemoglobin in the perfusate could not be avoided in the present experimental set up including a roller pump. Because NO_2^- has been suggested to be a more sensitive and specific marker of NO than NO_3^-[25] and it has been suggested that NO_2^- is the main metabolite of NO in haemoglobin-free medium,[26] we endeavoured to quantify the substance at nmol/L levels. The possible reasons why the highly sensitive HPLC–Griess system could not detect the expected increase in NO_2^- as a reflection of enhanced NO release during anaphylaxis in rat isolated perfused livers reamin obscure. However, some possible causes may be derived from the following. The device we used may still be insufficient to detect smaller changes in NO_2^- from the vascular bed in an excised organ with a large volume of perfusate compared with changes in a whole body and the substance may be easily influenced by the surrounding atmosphere. In addition, we have experienced disappearance of NO_2^- or NO_3^- after perfusion of certain organs.[12,13]

In conclusion, we are able to present functional evidence that NO production may be increased during rat hepatic anaphylaxis. This hepatic anaphylactic response was independent of circulating blood cells. However, perfusate NO_x measurements using the highly sensitive HPLC–Griess system could not detect physical evidence of increased intrahepatic NO production in rat isolated perfused anaphylactic livers; thus, this issue requires further examination.

ACKNOWLEDGEMENTS

This work was supported by a Grant for Collaborative Research (C2004-1, C2005-1) and a Grant for Promoted Research (S2005-10) from Kanazawa Medical University.

REFERENCES

1. Brown AFT. Anaphylactic shock: Mechanism and treatment. *J. Accid. Emerg. Med.* 1995; **12**: 89–100.
2. Moncada S, Higgs A. The L-arginine–nitric oxide pathway. *N. Engl. J. Med.* 1993; **329**: 2002–12.
3. Rees DD, Palmer RMJ, Moncada S. Role of endothelium-derived nitric oxide in regulation of blood pressure. *Proc. Natl Acad. Sci. USA* 1989; **86**: 3375–8.
4. Mitsuhata H, Shimizu R, Yokoyama MM. Role of nitric oxide in anaphylactic shock. *J. Clin. Immunol.* 1995; **15**: 277–83.
5. Maass-Moreno R, Rothe CF. Nonlinear resistances in hepatic microcirculation. *Am. J. Physiol.* 1995; **269**: H1922–30.
6. Pavek K, Piper PJ, Smedegard G. Anaphylatoxin-induced shock and two patterns of anaphylactic shock: Hemodynamics and mediators. *Acta Physiol. Scand.* 1979; **105**: 393–403.
7. Shibamoto T, Cui S, Ruan Z, Liu W, Takano H, Kurata Y. Hepatic venoconstriction is involved in anaphylactic hypotension in rats. *Am. J. Physiol. Heart Circ. Physiol.* 2005; **289**: H1436–41.
8. Hines KL, Fisher RA. Regulation of hepatic glycogenolysis and vasoconstriction during antigen-induced anaphylaxis. *Am. J. Physiol.* 1992; **262**: G868–77.
9. Ruan Z, Shibamoto T, Shimo T, Tsuchida H, Koizumi T, Nishio M. NO, but not CO, attenuates anaphylaxis-induced postsinusoidal contraction and congestion in guinea pig liver. *Am. J. Physiol. Regul. Integr. Comp. Physiol.* 2004; **286**: R94–100.
10. Weil R. Studies in anaphylaxis. XXI. Anaphylaxis in dogs: A study of the liver in shock and peptone poisoning. *J. Immunol.* 1917; **2**: 525–56.
11. Yamaguchi Y, Shibamoto T, Hayashi T, Saeki Y, Tanaka S. Hepatic vascular response to anaphylaxis in isolated canine liver. *Am. J. Physiol.* 1994; **267**: R268–74.
12. Ishibashi T, Matsubara T, Ida T *et al.* Negative NO_3^- balance in human coronary circulation with severe atherosclerotic stenosis. *Life Sci.* 2000; **66**: 173–84.
13. Ishibashi T, Himeno M, Kubota K *et al.* Decrease in plasma NO_x concentration by isosorbide dinitrate, an organic nitrate ester. *J. Cardiovasc. Pharmacol.* 2003; **41**: 40–8.
14. Ishibashi T, Himeno M, Imaizumi N *et al.* NO_x contamination in laboratory ware and effect of countermeasures. *Nitric Oxide Biol. Chem.* 2000; **4**: 516–25.
15. Buxton IL, Cheek DJ, Eckman D, Westfall DP, Sanders KM, Keef KD. N^G-Nitro-L-arginine methyl ester and other alkyl esters of arginine are muscarinic receptor antagonists. *Circ. Res.* 1993; **72**: 387–95.
16. Peterson DA, Peterson DC, Archer S, Weir EK. The non specificity of specific nitric oxide synthase inhibitors. *Biochem. Biophys. Res. Commun.* 1992; **187**: 797–801.
17. Nakaike R, Shimokawa H, Yasutake H *et al.* Effects of L-arginine analogues on vasomotion of isolated porcine coronary arteries. *Am. J. Physiol.* 1995; **268**: H1966–72.
18. Heim KF, Thomas G, Ramwell PW. Effect of substituted arginine compounds on superoxide production in the rabbit aorta. *J. Pharmacol. Exp. Ther.* 1991; **257**: 1130–5.
19. Shibamoto T, Ruan Z, Cui S, Kurata Y, Koizumi T, Kubo K. Anaphylactic hepatic venoconstriction is attenuated by nitric oxide released via shear stress-dependent and -independent mechanisms in guinea-pig. *Clin. Exp. Pharmacol. Physiol.* 2005; **32**: 288–93.
20. Lantoine F, Iouzalen L, Devynck MA *et al.* Nitric oxide production in human endothelial cells stimulated by histamine requires Ca^{2+} influx. *Biochem. J.* 1998; **330**: 695–9.
21. Levi R, Gross SS, Lamparter B *et al.* Evidence that L-arginine is the biosynthetic precursor of vascular and cardiac nitric oxide. In: Moncada S, Higgs EA (eds). *Nitric Oxide From l-Arginine: A Bioregulatory System.* Elsevier, Amsterdam. 1990; 35–45.
22. Sakuma I, Gross S, Levi R. Peptidoleukotrienes induce an endothelium-dependent relaxation of guinea pig main pulmonary artery and thoracic aorta. *Prostaglandins* 1987; **34**: 685–96.

23. Kamata K, Mori T, Shigenobu K, Kasuya Y. Endothelium-dependent vasodilator effects of platelet activating factor on rat resistance vessels. *Br. J. Pharmacol.* 1989; **98**: 1360–4.
24. Ishibashi T, Kubota K, Himeno M *et al.* Respiratory alkalosis does not alter NO_x concentrations in human plasma and erythrocytes. *Am. J. Physiol. Heart Circ. Physiol.* 2001; **281**: H2757–61.
25. Kleinbongard P, Dejam A, Lauer T *et al.* Plasma nitrit constitutive nitric oxide synthase activity in mammals. *Fr Biol. Med.* 2003; **35**: 790–6.
26. Williams DLH. A chemist's view of the nitric oxide story. *Or Chem.* 2003; **1**: 441–9.

Effects of Hct on L-NAME–induced Potentiation of Anaphylactic Presinusoidal Constriction in Perfused Rat Livers

Sen Cui, MD, Toshishige Shibamoto, MD, PhD, Wei Liu, MD, Hiromichi Takano, PhD, Zhan-Sheng Zhao, MD, PhD, and Yasutaka Kurata, MD, PhD

Abstract: Effects of hematocrit (Hct) on N^G-nitro-L-arginine methyl ester (L-NAME)–induced modulation of anaphylactic venoconstriction were determined in isolated perfused rat livers. The rats were sensitized with ovalbumin (1 mg), and the livers were excised 2 weeks later and perfused portally and recirculat-ingly under constant flow at Hct of 0%, 5%, 16%, and 22%. The hepatic sinusoidal pressure was estimated via the double occlusion pressure (Pdo), and the presinusoidal resistance (Rpre) and the postsinusoidal resistance (Rhv) were calculated. The antigen of ovalbumin 0.1 mg was injected into the reservoir at 10 minutes after pretreatment with L-NAME (100 μM) or D-NAME (100 μM). Perfusate viscosity, a determinant of vascular resistance and shear stress, was increased in parallel with Hct. In the D-NAME groups, antigen caused predominant presinusoidal constriction. The magnitude of venoconstriction was significantly smaller at Hct 0% than at Hct 5% to 22%, whereas no significant differences were found among Hct 5% to 22%. L-NAME potentiated the antigen-induced increase in Rpre, but not in Rpost at Hct 5% to 22% as compared with D-NAME. But the augmentative effects of L-NAME were similar in magnitude among Hct 5% to 22%. These findings suggest that hepatic anaphylaxis increases production of nitric oxide, which consequently attenuates anaphylactic presinusoidal constriction in rat livers, and that these effects are independent of perfusate Hct or viscosity in blood-perfused rat livers.

Key Words: anaphylactic shock, nitric oxide, viscosity, shear stress, hepatic circulation

(*J Cardiovasc Pharmacol*™ 2006;48:827–833)

Anaphylactic hypotension is sometimes life-threatening, and is caused by a decrease in effective circulating blood volume.[1] It is reported that the liver is partly involved in animal models of anaphylactic hypo-tension.[2,3] Anaphylactic hepatic venoconstriction, as observed in rats,[3,4] guinea pigs,[5] and dogs,[6,7] causes portal hypertension which then induces congestion of the upstream splanchnic organs, with resultant decrease in venous return and effective circulating blood volume, and finally augmentation of anaphylactic hypotension.

Nitric oxide (NO), a potent vasodilator, regulates the vascular system,[8,9] and seems to play an important pathophysiologic role in modulating the systemic changes associated with anaphylaxis.[10] We have recently reported that N^G-nitro-L-arginine methyl ester (L-NAME), a NO synthase inhibitor, augmented anaphylactic hepatic venoconstriction in guinea pig.[5] And further, we demonstrated, using the vascular occlusion method for measurement of the hepatic sinusoidal pressure, that the anaphylactic venoconstriction of the presinusoids, but not the postsinusoids, was enhanced by L-NAME.[5] However, it is not known whether L-NAME also induces augmentation of anaphylactic hepatic venoconstriction in other animals such as rats.

NO is produced by the activation of the NO synthase 3 present in endothelial cells either by hormonal or physical stimuli such as shear stress.[8,9] The viscosity, an important determinant of shear stress and vascular resistance, highly depends on hematocrit (Hct). Indeed, the vascular resistance increased as Hct elevates at a given blood flow in rat liver, as we previously reported.[11] However, it is not well known how the changes in blood viscosity modulate anaphylactic hepatic segmental venoconstriction.

Thus, we herein determined the effect of Hct on the L-NAME–induced modulation of anaphylactic hepatic segmental venoconstriction in rats. To accomplish this purpose, we measured the sinusoidal pressure with the vascular occlusion method, and determined the pre and postsinusoidal resistances during hepatic anaphylaxis in isolated rat livers perfused portally and recirculatingly under constant flow at different Hct of 0%, 5%, 16%, or 22% in the presence of L-NAME or D-NAME (an inactive enantiomer of L-NAME). In addition, we determined the anaphylaxis-induced changes in hepatic oxygen consumption and bile production.

METHODS

Animals and Sensitization

Forty male Sprague-Dawley rats (Japan SLC, Shizuoka, Japan) weighing 341 ± 3 g were maintained at 23°C and under

Received for publication January 24, 2006; accepted May 23, 2006.
From the Department of Physiology, Kanazawa Medical University, Uchinada 920-0293, Japan.
Supported by a Grant for Collaborative Research from Kanazawa Medical University (C2004-1, C2005-1) and a Grant-in-Aid for Scientific Research (18591730) from the Ministry for Education, Culture, Science and Technology of Japan.
Reprints: Toshishige Shibamoto, MD, PhD, Department of Physiology, Kanazawa Medical University, Daigaku 1-1, Uchinada, Ishikawa 920-0293, Japan (e-mail: shibamo@kanazawa-med.ac.jp).

pathogen-free conditions on a 12/12-hours dark/light cycle, and received food and water ad libitum. The experiments conducted in the present study were approved by the Animal Research Committee of Kanazawa Medical University. Rats were actively sensitized by the subcutaneous injection of an emulsion made by mixing equal volumes of complete Freund's adjuvant (0.5 mL) with 1 mg ovalbumin (grade V, Sigma) dissolved in physiologic saline (0.5 mL).[3]

Isolated Liver Preparation

Two weeks after sensitization, the animals were anesthetized with pentobarbital sodium (50 mg kg^{-1}, IP) and were mechanically ventilated with room air. The methods for the isolated perfused rat liver preparation were previously described.[3] In brief, a polyethylene tube was placed in the right carotid artery. After laparotomy, the hepatic artery was ligated and the bile duct was cannulated with the polyethylene tube (0.5 mm ID, 0.8 mm OD). At 5 minutes after intra-arterial heparinization (500 U kg^{-1}), 8 to 9 mL of blood was withdrawn through the carotid arterial catheter. The intra-abdominal inferior vena cava above the renal veins was ligated, and the portal vein was cannulated with a stainless cannula (1.3 mm ID, 2.1 mm OD). After thoracotomy, the supra-diaphragmatic inferior vena cava was cannulated through a right atrium incision with a larger stainless cannula (2.1 mm ID, 3.0 mm OD), then portal perfusion was begun with the heparinized blood diluted with 5% bovine albumin (Sigma-Aldrich Co, St Louis, MO) in Krebs solution (118 mM NaCl, 5.9 mM KCl, 1.2 mM $MgSO_4$, 2.5 mM CaCl2, 1.2 mM NaH_2PO_4, 25.5 mM $NaHCO_3$, and 5.6 mM glucose) at the following Hct levels: 0% (n = 10), 5% (n = 10), 16% (n = 10), and 22% (n = 10). At Hct 5%, only the autologous blood was used, while at Hct 16% and 22%, additional blood was obtained by exsanguination of an anesthetized and heparinized intact donor rat. At Hct 0%, the liver was perfused with only 5% albumin-Krebs solution without blood. The liver was rapidly excised, suspended from an isometric transducer (TB-652T, Nihon-Kohden, Japan), and weighed continuously throughout the experimental period.

The liver was perfused at a constant flow rate in a recirculating manner via the portal vein using perfusate with or without blood that was pumped using a Masterflex roller pump from the venous reservoir through a heat exchanger (37°C). The recirculating perfusate volume was 40 mL. The perfusate was oxygenated in the venous reservoir by continuous bubbling with 95% O_2 and 5% CO_2 (perfusate PO_2 = 300 mm Hg).

The viscosity of the perfusate was measured using cone plate type of viscometer (Biorheolizer, Tokyo Keiki, Japan).

Measurement of Hepatic Vascular Pressures and Vascular Resistances

The portal venous (Ppv) and the hepatic venous (Phv) pressures were measured using pressure transducers (TP-400T, Nihon-Kohden, Japan) attached by sidearm to the appropriate cannulas with the reference points at the hepatic hilus. Portal blood flow rate (Q) was measured with an electromagnetic flow meter (MFV 1200, Nihon-Kohden, Japan), and the flow probe was positioned in the inflow line. The hepatic sinusoidal pressure was measured by the double occlusion pressure (Pdo).[7] Both the inflow and outflow lines were simultaneously and instantaneously occluded for 17 seconds using the solenoid valves, after which Ppv and Phv rapidly equilibrated to a similar or identical pressure, which was Pdo. Actually, Pdo values were obtained from the digitized data of Ppv and Phv using an original program (LIVER software, Biomedical Science, Kanazawa, Japan). The total portal-hepatic venous (Rt), presinusoidal (Rpre), and postsinu-soidal (Rpost) resistances were calculated as follows:

$$Rt = (Ppv - Phv)/Q \quad (1)$$

$$Rpre = (Ppv - Pdo)/Q \quad (2)$$

$$Rpost = (Pdo - Phv)/Q \quad (3)$$

Bile Flow Rate Measurement

Bile was collected drop by drop in a small tube suspended from the force transducer (SB-1T, Nihon-Kohden, Japan). One bile drop yielded 0.018 g and the time between drops was measured for determination of the bile flow rate.[3]

Hepatic Oxygen Consumption Measurement

To determine the oxygen consumption, the blood oxygen saturation difference between the inflow and outflow blood (ΔSO_2) was monitored continuously with a custom-made oxygen absorption spectrophotometer (ODM-1, Biomedical Science, Kanazawa, Japan), the cuvettes and sensors of which were built in the inflow and outflow perfusion lines.[12] The measured ΔSO_2 was expressed as the oxygen consumption difference meter (ODM) values.[12] ΔSO_2 was calculated using the following regression line equation as determined in our previous study[12]:

$$\Delta SO_2 = 1.5103 \times ODM - 0.0685 \quad (4)$$

Using ΔSO_2, oxygen consumption (mL min^{-1} 10 g liver wt^{-1}) was calculated according to the Fick principle by the following equation:

$$\text{Portal blood flow/liver weight } (g) \times 10 \times 1.39 \text{ (ml/g)} \times \text{Hb (g/ml)} \times \Delta SO_2 \quad (5)$$

where Hb is the perfusing blood hemoglobin measured by cyanmethohemoglobin method (Hb-B test Wako, Wako, Japan) with a spectrophotometer (UV-1200, Shimadzu, Japan).

Data Recording

The hepatic vascular pressures, blood flow rate, liver weight, bile weight, and ODM values, were monitored continuously and displayed through a thermal physiograph (RMP-6008, Nihon-Kohden, Japan). All outputs were also digitized through the analog-digital converter at a sampling rate of 100 Hz. These digitized values were also displayed and recorded using a personal computer for later determination of Pdo.

Experimental Protocol

Hepatic hemodynamic parameters were observed for at least 20 minutes after the start of perfusion until an isogravimetric state (no weight gain or loss) was obtained by adjusting the portal blood flow rate and the height of the reservoir at a Phv of 0 to 1 cm H_2O, and at a Q of 36 ± 0.5 mL min^{-1} 10 g liver wt^{-1}. Then, the livers perfused at various Hct were further divided into the following 2 groups of the D-NAME and L-NAME groups, in which D-NAME (100 μM: Sigma) and L-NAME (100 μM: Sigma), respectively, were administered into the reservoir. Thus, any liver studied was pretreated with either D-NAME or L-NAME. Ovalbumin 0.1 mg was injected into the reservoir at 10 minutes after injection of D-NAME or L-NAME. In each experimental, measurement was performed up to 30 minutes after antigen.

In each experimental group, the double occlusion was performed at baseline, just before antigen injection, and at the maximal venoconstriction (when Ppv reached the peak), 6, 10, 20, and 30 minutes after injection of antigen.

Statistics

All results are expressed as the means ± SE. Data were analyzed by 1 and 2-way analysis of variance, using repeated-measures for 2-way comparison within groups. Comparisons of individual points between groups and within groups were made by Bonferroni test. Differences were considered as statistically significant at P values less than 0.05.

RESULTS

Perfusate Hct and Viscosity

The perfusate viscosity increased in parallel with Hct from 0% to 22% in both D-NAME and L-NAME groups. The viscosity was 0.879 ± 0.007 mPa s^{-1} at Hct 0%, 1.232 ± 0.014 mPa s^{-1} at Hct 5%, 1.706 ± 0.019 mPa s^{-1} at Hct 16%, and 2.222 ± 0.039 mPa s^{-1} at Hct 22%.

The Basal Hepatic Vascular Resistances

Figure 1 shows basal Ppv, Rpre, and Rpost. Basal Rpre was higher than basal Rpost in livers of any Hct (0% to 22%), resulting in basal Rpost/Rt ratio of 0.3 to 0.35. The basal Ppv and vascular resistances of Hct 22% groups were significantly greater than those of other Hct groups. D-NAME pretreatment did not change basal Ppv or resistances at any Hct level. However, basal Ppv and Rpre were significantly increased by L-NAME pretreatment at Hct 16% and 22%.

Effects of Hct on the Responses of D-NAME Pretreated Livers to Antigen

Figure 2 shows the summary data of the time-dependent changes in Ppv, Pdo, liver weight, oxygen consumption, and bile flow rate of D-NAME groups. Antigen induced venoconstriction, as reflected by an increase in Ppv. Ppv peaked at 3 minutes after antigen and gradually decreased towards baseline at 30 minutes. The magnitude of venoconstriction at Hct 0% was significantly smaller than that at Hct 5% to 22%: The Ppv peak at Hct 0% was 20.9 ± 1.4 cm H_2O, and that at Hct 5% was 27.8 ± 0.8 cm H_2O. However, no significant differences were found in the peak values of Ppv

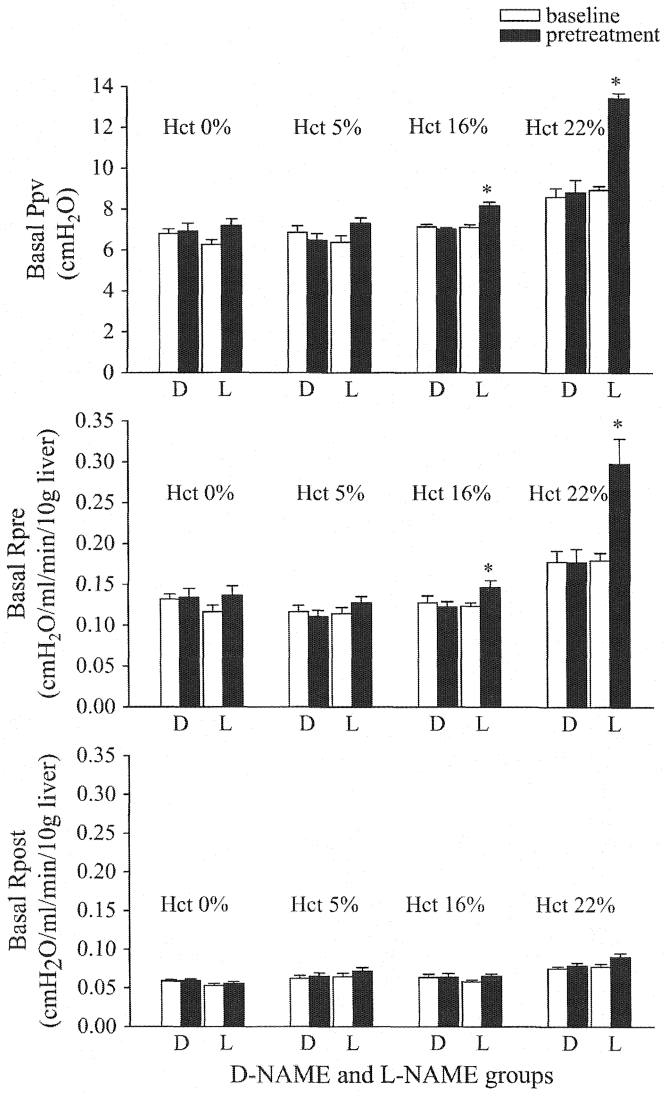

FIGURE 1. The basal portal venous pressure (Ppv), presinusoidal resistance (Rpre), and postsinusoidal resistance (Rpost) of the baseline and after pretreatment with D-NAME (D) and L-NAME (L) at Hct of 0%, 5%, 16%, and 22%. *$P < 0.05$ versus the baseline.

after antigen among Hct 5%, 16%, and 22%. Pdo increased slightly but significantly after antigen, and the increase at Hct 0% was smaller than that at Hct 5% to 22%.

Figure 3 shows changes in Rpre and Rpost after antigen. In the D-NAME groups, both Rpre and Rpost significantly increased after antigen. However, the magnitudes of the increases in Rpre were much larger than that in Rpost: At Hct 16%, Rpre increased 0.612 ± 0.067 cmH_2O mL^{-1} min^{-1} 10 g^{-1} liver, whereas Rpost increased only 0.050 ± 0.003 cm H_2O mL^{-1} min^{-1} 10 g^{-1} liver $weight^{-1}$. The antigen-induced increases in Rpre and Rpost in blood-perfused livers (Hct 5% to 22%) were significantly greater than those in livers perfused without blood (Hct 0%). However, there were no significant differences in increases of Rpre or Rpost among Hct 5%, 16%, and 22%. These results indicate that the antigen induces

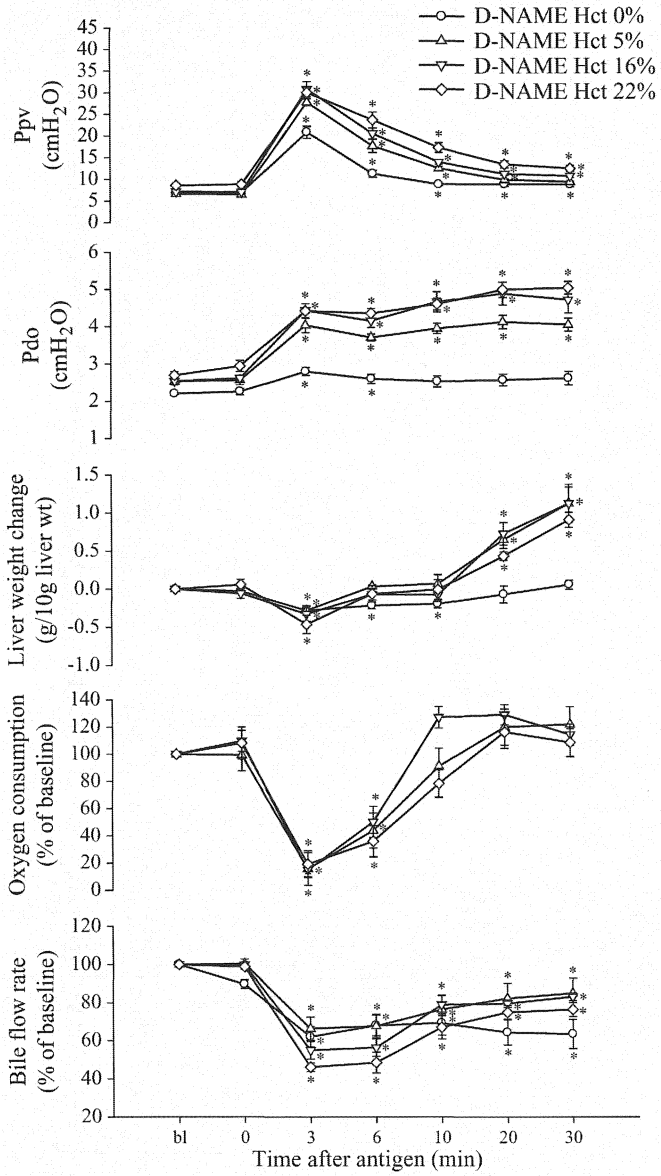

FIGURE 2. The summary data of time course changes in the portal venous pressure (Ppv), double occlusion pressure (Pdo), liver weight change, hepatic oxygen consumption, and bile flow rate after antigen injection at Hct of 0%, 5%, 16%, and 22% in the D-NAME groups. Values are given as mean ± SE, n = 5. *$P < 0.05$ versus the baseline.

predominant presinusoidal constriction independently of blood Hct (5% to 22%) in blood-perfused rat livers.

The liver weight showed a biphasic change of an initial decrease followed by an increase in response to antigen, as shown in Figure 2. The lowest nadir was -0.521 ± 0.054 g 10 g^{-1} liver at Hct 22%. There were no significant differences in the nadirs among all D-NAME groups.

Bile flow rate decreased Hct dependently, reaching 47 ± 3% of the baseline of 8.7 ± 0.6 mg min^{-1} 10 g^{-1} liver at Hct 22% group, as shown in Figure 2. It did not recover to the baseline at the end of experiment.

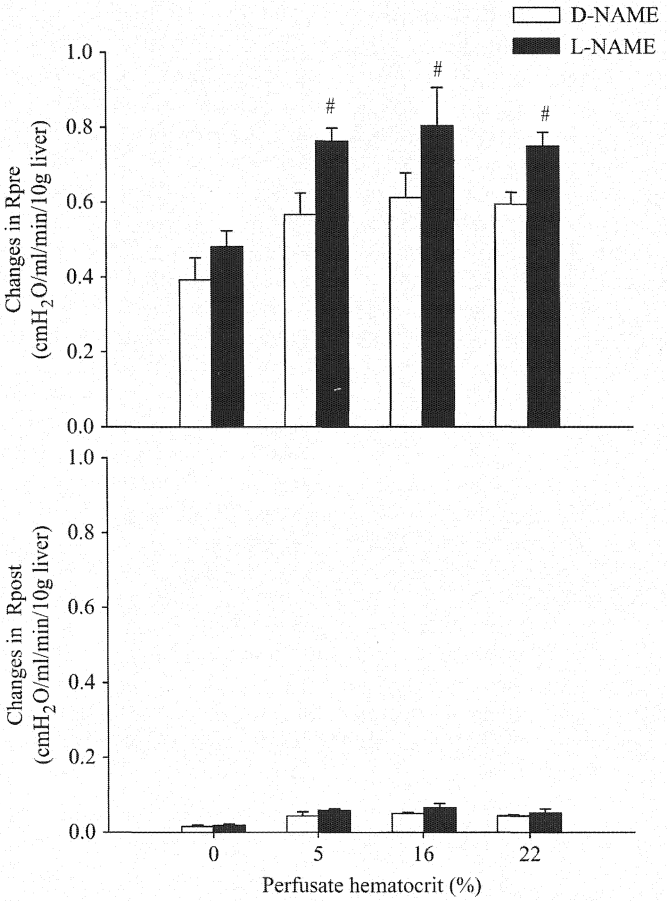

FIGURE 3. The changes in Rpre and Rpost after antigen injection at Hct of 0%, 5%, 16%, and 22% in D-NAME and L-NAME groups. Values are given as mean ± SE. All values in both D-NAME and L-NAME groups were significantly different from the corresponding baseline, and therefore asterisks were omitted. #$P < 0.05$ versus the D-NAME group.

The basal hepatic oxygen consumption increased as Hct increased: The basal levels were 0.015 ± 0.002 for Hct 5%, 0.070 ± 0.005 for Hct 16%, and 0.096 ± 0.034 mL min^{-1} 10 g^{-1} liver for Hct 22%. The oxygen consumption in livers of Hct 0% could not be determined in the present system because of absence of red blood cells in the perfusate. The hepatic oxygen consumption was significantly decreased after antigen injection. It reached the lowest value, 13.5 ± 4.1% of the baseline of 0.072 ± 0.006 mL min^{-1} 10 g^{-1} liver at Hct 16%. Actually, the decreases of hepatic oxygen consumption were similar in magnitudes among Hct 5% to 22%. Oxygen consumption almost recovered to the baseline at 20 minutes after antigen.

Effects of L-NAME on Hepatic Responses to Antigen Under Different Hct

Figure 4 shows the summary data of the time course changes in Ppv, Pdo, liver weight, oxygen consumption, and bile flow rate of the L-NAME groups. As compared with D-NAME groups, the antigen-induced increases in Ppv in the L-NAME groups were qualitatively similar but greater in

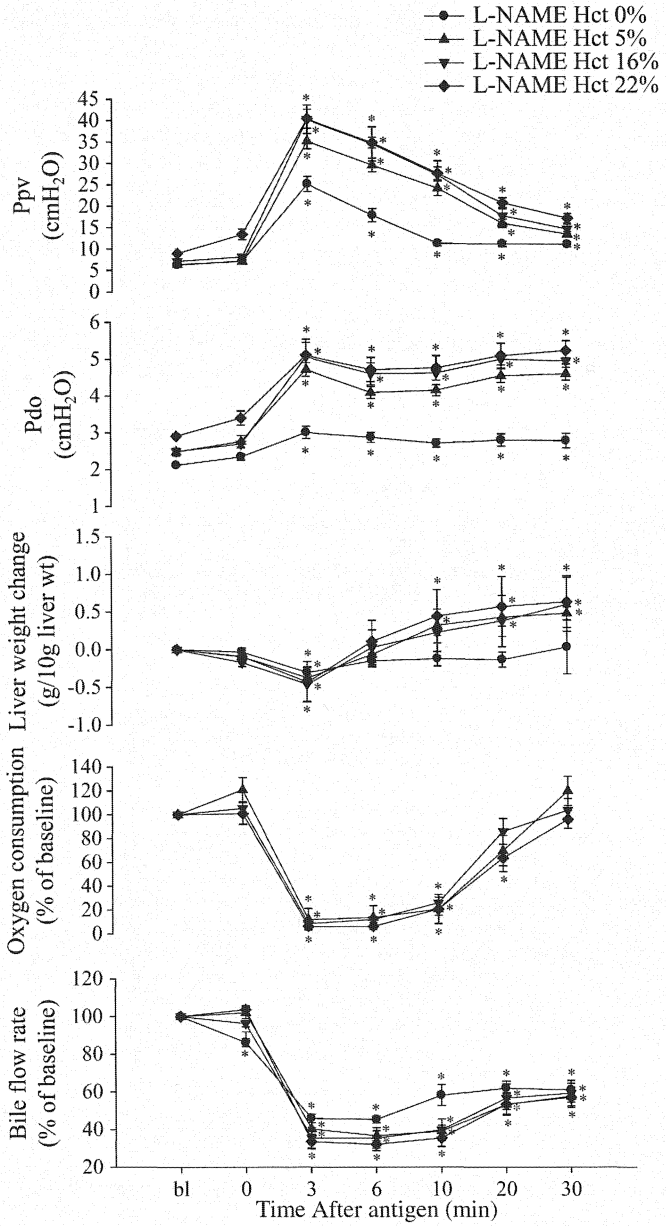

FIGURE 4. The summary data of time course changes in the portal venous pressure (Ppv), double occlusion pressure (Pdo), liver weight change, hepatic oxygen consumption, and bile flow rate after antigen injection at Hct of 0%, 5%, 16%, and 22% in the L-NAME groups. Values are given as mean ± SE. n = 5. *$P < 0.05$ versus the baseline.

magnitude, although the increases in Pdo were comparable. Thus, as shown in Figure 3, the amplitudes of the increase in Rpre, but not in Rpost, were significantly larger in the L-NAME groups than in the D-NAME groups at any Hct level. However, the increases in Rpre were not significantly different among Hct levels of 5% to 22%, although they were significantly higher than those at Hct 0%.

The antigen-induced changes in liver weight, bile flow rate, and oxygen consumption in L-NAME groups were similar to those in D-NAME groups. However, bile flow rates more profoundly decreased than in D-NAME groups at corresponding Hct level: the nadir, 31.2 ± 3.6% of the baseline of 8.9 ± 1.1 mg min^{-1} 10 g^{-1} liver at Hct 22% was much lower than in D-NAME groups. Although there were no significant differences in the nadir of hepatic oxygen consumption in all groups studied, it was much lower at 6, 10, and 20 minutes after antigen in the L-NAME groups than in the D-NAME group, as shown in Figure 4.

DISCUSSION

In the present study, we examined anaphylactic venoconstriction in isolated perfused rat livers pretreated with either L-NAME or D-NAME under various Hct. The first of the main findings is that L-NAME augmented the antigen-induced increase in Rpre, but not Rpost. This suggested that hepatic anaphylaxis increases production of NO, which consequently attenuates presinusoidal constriction in rats. The second is that the magnitudes of the L-NAME–induced augmentation of the anaphylactic presinusoidal constriction were similar at various Hct (5% to 22%), although the perfusate viscosity increased depending on Hct.

In the present study, we first confirmed the previous finding that anaphylaxis induced predominant presinusoidal constriction in rat livers perfused with blood at Hct 12%,[3] and further extended it by showing the same result at various Hct ranging 0% to 22%.

The basal levels of Ppv and Rpre of Hct 22% groups were significantly greater than those of other Hct groups (Fig. 1). According to Poiseuille's law, this increase in basal hepatic vascular resistance could be attributed to the perfusate Hct-dependent increase in perfusate viscosity. We have here shown that L-NAME pretreatment increased the basal hepatic resistances, especially Rpre, only at Hct 16% and 22% (Fig. 1). This indicated that NO is not involved in the regulation of basal hepatic vascular tone of isolated rat livers perfused with blood at Hct of 5% or less. This finding is consistent with that on rat livers perfused with a blood-free solution, in which inhibition of NO did not increase basal vascular tone.[13] It is suggested that the low perfusate viscosity results only in small shear stress and thus low amount of NO production in livers perfused with low Hct. This might account for a negligible role of NO in maintenance of basal vascular tone in livers perfused at Hct of 5% or less.

The present study showed that L-NAME significantly potentiated the antigen-induced increase in Rpre, but not in Rpost, in rat livers, a finding similar to that observed in guinea pig livers.[5] This suggests that NO might be released selectively from presinusoidal vessels during anaphylaxis, and then attenuated the anaphylactic presinusoidal constriction. The mechanism for this selective vulnerability of presinusoids to NO may be considered as follows: anaphylaxis predominantly constricted presinusoidal vessels as shown in D-NAME groups, where elevated shear stress increased NO release from the same presinusoidal endothelium, leading to relaxation of the adjacent presinusoidal vascular smooth muscle cells in a paracrine manner. Indeed, the wall shear stress in isolated perfused vessels is inversely proportional to the third

power of internal radius theoretically.[14] The decrease in vascular internal radius caused by anaphylactic venoconstriction should result in an increase in shear stress. It would further be increased if turbulence did increase at the constricted site.[14] Thus, the NO release from vascular endothelium of the contracted presinusoids would be increased via the shear stress mechanism during anaphylactic venoconstriction.

In the present study, the magnitudes of the L-NAME–induced potentiation of anaphylactic venoconstriction were similar among livers perfused with blood at Hct 5% to 22% (Fig. 3), although perfusate viscosity increased depending on Hct. However, these results were unexpected, because the Hct-dependent increase in perfusate viscosity could produce more shear-stress,[14] and then increase production of NO, resulting in more dilation of the constricted vessels. Thus, we initially expected that L-NAME–induced potentiation of anaphylactic venoconstriction might increase when the perfusate Hct increased. With respect to the mechanisms for the absence of exaggerated venoconstriction by L-NAME at high Hct, it might be attributed to the concomitant increase in perfusate Hb concentration. It is reported that oxygenated Hb, even in extremely small amounts, inactivates NO, resulting in inhibition of its vasodilatory action.[15,16] Thus, augmented vasodilatory effect due to the over-produced NO at high perfusate Hct might be attenuated by elevated perfusate Hb, which could inactivate NO. Another possible explanation could be related to the isolated rat liver preparation perfused at a constant flow. It is possible that the hepatic vessels perfused at a low Hct of 5% in the presence of L-NAME contracted mechanically to the maximal levels and could not constrict further even when the perfusate Hct increased. In the present isolated perfused rat liver preparation, Ppv might not be able to increase to the levels higher than 45 cm H_2O. Actually, Ppv did not increase higher than 45 cm H_2O even when supraphysiologically high concentrations (>3 μM) of PAF, a potent vasoconstrictor, were administered into the similar perfused rat liver preparations.[17]

Hepatic oxygen consumption was significantly and markedly decreased to the level less than 20% of baseline, regardless of different perfusate Hct or pretreatment with L-NAME or D-NAME. This finding of anaphylaxis-induced reduction of hepatic oxygen consumption was consistent with previous studies.[4,12] The mechanisms for this decrease in oxygen consumption may be due to hemodynamic or non-hemodynamic factors. Nonhemodynamic factors may be anaphylaxis-related chemical mediators, such as PAF,[18,19] TXA_2,[20,21] and LTD_4,[19,21] all of which can decrease hepatic oxygen consumption. On the other hand, from the hemodynamic point of view, presinusoidal constriction observed during anaphylactic venoconstriction may account for the decreased oxygen consumption: presinusoidal constriction reduced hepatic vascular surface area, resulting in a decrease in the number of active hepatocytes. Actually, the difference in the recovery of decreased oxygen consumption between the L-NAME (slow recovery) and D-NAME (quick recovery) groups seems to be correlated to the difference in the time course changes in Ppv, hence hepatic venoconstriction, as shown in Figures 2 and 4. Thus, the hemodynamic factors might substantially contribute to the late phase of the anaphylaxis-induced decrease in oxygen consumption in the L-NAME group.

In summary, ovalbumin-induced anaphylactic hepatic venoconstriction is characterized by predominant presinusoidal constriction in all rat livers with Hct 0% to 22%, and L-NAME pretreatment augmented the antigen-induced venoconstriction, by increasing Rpre, but not Rpost. This suggests that hepatic anaphylaxis increases production of NO, which consequently attenuates anaphylactic presinusoidal constriction in isolated perfused rat livers. However, the magnitude of L-NAME–induced augmentation of anaphylactic venoconstriction was not variable and independent of perfusate Hct and viscosity in blood perfused rat livers. Anaphylaxis reduced hepatic oxygen consumption independently of perfusate Hct 5% to 22%.

REFERENCES

1. Brown AFT. Anaphylactic shock: mechanism and treatment. *J Accid Emerg Med.* 1995;12:89–100.
2. Pavek K, Piper PJ, Smedegard G. Anaphylatoxin-induced shock and two patterns of anaphylactic shock: hemodynamics and mediators. *Acta Physiol Scand.* 1979;105:393–403.
3. Shibamoto T, Cui S, Ruan Z, et al. Hepatic venoconstriction is involved in anaphylactic hypotension in rats. *Am J Physiol Heart Circ Physiol.* 2005; 289:H1436–H1441.
4. Hines KL, Fisher RA. Regulation of hepatic glycogenolysis and vasoconstriction during antigen-induced anaphylaxis. *Am J Physiol Gastrointest Liver Physiol.* 1992;262:G868–G877.
5. Ruan Z, Shibamoto T, Shimo T, et al. NO, but not CO, attenuates anaphylaxis-induced postsinusoidal contraction and congestion in guinea pig liver. *Am J Physiol Regul Integr Comp Physiol.* 2004;286:R94–R100.
6. Weil R. Studies in anaphylaxis. XXI Anaphylaxis in dogs: a study of the liver in shock and peptone poisoning. *J Immunol.* 1917;2:525–556.
7. Yamaguchi Y, Shibamoto T, Hayashi T, et al. Hepatic vascular response to anaphylaxis in isolated canine liver. *Am J Physiol Regul Integr Comp Physiol.* 1994;267:R268–R274.
8. Moncada S, Higgs A. The L-arginine-nitric oxide pathway. *N Engl J Med.* 1993;329:2002–2012.
9. Rees DD, Palmer RMJ, Moncada S. Role of endothelium-derived nitric oxide in regulation of blood pressure. *Proc Natl Acad Sci USA.* 1989;86: 3375–3378.
10. Osada S, Ichiki H, Oku H, et al. Participation of nitric oxide in mouse anaphylactic hypotension. *Eur J Pharmacol.* 1994;252:347–350.
11. Kamikado C, Shibamoto T, Hongo M, et al. Effects of Hct and norepinephrine on segmental vascular resistance distribution in isolated perfused rat livers. *Am J Physiol Heart Circ Physiol.* 2004;286:H121–H130.
12. Cui S, Shibamoto T, Ruan Z, et al. Oxygen consumption, assessed with the oxygen absorption spectrophotometer, decreases independently of venoconstriction during hepatic anaphylaxis in perfused rat liver. *Shock.* 2006. In press.
13. Suematsu M, Goda N, Sano T, et al. Carbon monoxide: an endogenous modulator of sinusoidal tone in the perfused rat liver. *J Clin Invest.* 1995; 96:2431–2437.
14. Kamiya A, Togawa T. Adaptive regulation of wall shear stress to flow change in the canine carotid artery. *Am J Physiol.* 1980;239:H14–H21.
15. Casadevall M, Pique JM, Cirera I, et al. Increased blood hemoglobin attenuates splanchnic vasodilation in portal-hypertensive rats by nitric oxide inactivation. *Gastroenterology.* 1996;110:1156–1165.
16. Rimar S, Gillis CN. Selective pulmonary vasodilation by inhaled nitric oxide is due to hemoglobin inactivation. *Circulation.* 1993;88:2884–2887.
17. Cui S, Shibamoto T, Liu W, et al. Effects of platelet-activating factor, thromboxane A_2 and leukotriene D_4 on isolated perfused rat liver. *Prostaglandins Other Lipid Mediat.* In press.
18. Kimura K, Moriyama M, Nishisako M, et al. Modulation of platelet activating factor-induced glycogenolysis in the perfused rat liver after administration of endotoxin in vivo. *J Biochem (Tokyo).* 1998;123:142–149.

19. Shibamoto T, Ruan Z, Cui S, et al. Involvement of platelet-activating factor and leukotrienes in anaphylactic segmental venoconstriction in ovalbumin sensitized guinea pig livers. *Prostaglandins Other Lipid Mediat.* 2005;78:218–230.
20. Altin JG, Bygrave FL. Prostaglandin F_2 alpha and the thromboxane A_2 analogue ONO-11113 stimulate Ca^{2+} fluxes and other physiological responses in rat liver. Further evidence that prostanoids may be involved in the action of arachidonic acid and platelet-activating factor. *Biochem J.* 1988;249:677–685.
21. Haussinger D, Stehle T, Gerok W. Effects of leukotrienes and the thromboxane A_2 analogue U-46619 in isolated perfused rat liver. *Biol Chem Hoppe Seyler.* 1988;369:97–107.

Journal of Surgical Research **139,** 30–35 (2007)
doi:10.1016/j.jss.2006.07.052

The Sinusoidal Pressure During Ischemia-Reperfusion Injury in Perfused Mouse Liver Pretreated With or Without L-NAME

Toshishige Shibamoto, M.D.,*,[1] Zonghai Ruan, M.D.,* Sen Cui, M.D.,* Wei Liu, M.D.,* Zhan-Sheng Zhao, M.D.,* Hiromichi Takano, Ph.D.,* Yasutaka Kurata, M.D.,* Tomonobu Koizumi, M.D.,† and Keishi Kubo, M.D.†

**Department of Physiology, Kanazawa Medical University, Uchinada Ishikawa, Japan; †First Department of Internal Medicine, Shinshu University School of Medicine, Matsumoto, Japan*

Submitted for publication April 5, 2006

Background. **Hepatic ischemia-reperfusion (I/R) is accompanied by liver weight gain and ascites formation possibly caused by an increase in the sinusoidal pressure, a determinant of hepatic transvascular fluid movement. However, changes in the sinusoidal pressure during hepatic I/R in mice are not known. It is also controversial whether nitric oxide (NO) exerts a beneficial or detrimental effect on hepatic I/R injury. We determined the changes in hepatic sinusoidal pressure and liver weight, and the effect of a NO synthase inhibitor, N^G-nitro-L-arginine methyl ester (L-NAME) on I/R injury of isolated mouse liver.**

Materials and methods. **Isolated liver from 20 male outbred ddY mice was perfused portally with diluted blood (Hct 3%). After pretreatment with L-NAME (100 μM) or D-NAME (100 μM), ischemia was induced at room temperature by occlusion of the inflow line of the portal vein for 1 h followed by 1-h reperfusion in a recirculating manner. The sinusoidal pressure was assessed by the double vascular occlusion pressure (Pdo), and pre- and postsinusoidal resistance was determined. Liver injury was assessed by blood levels of alanine aminotransferase (ALT).**

Results. **In the D-NAME group (n = 7), immediately after reperfusion, the portal pressure increased by 2.8 ± 0.1 (SE) mmHg, which was accompanied by an increase in Pdo of 1.5 ± 0.1 mmHg, indicating increases in pre- and postsinusoidal resistance to a similar degree. Then, presinusoidal, but not postsinusoidal, resistance sustained increased until 60 min after reperfusion. Liver weight increased to 0.14 ± 0.04 g/g liver after reperfusion, followed by a gradual return to baseline. Blood ALT levels increased at 60 min after reperfusion. There were no significant differences in changes in the variables between the D- and L-NAME (n = 7) groups. In the time-matched non- I/R control group (n = 6), no changes in variables were observed for 2 h.**

Conclusions. **Mouse hepatic I/R causes marginal liver weight gain associated with a small and transient increase in the sinusoidal pressure, and nitric oxide does not play any significant roles in this injury.**

Key Words: **hepatic circulation; double occlusion pressure; nitric oxide; hepatic vascular resistance.**

INTRODUCTION

Ischemia followed by reperfusion causes a series of complex pathophysiological events that could finally lead to irreversible cell injury. Ischemia-reperfusion (I/R) injury may be involved in hepatic dysfunction in liver transplantation [1] and in hepatic surgery requiring temporal occlusion of hepatic vessels [2]. Liver weight gain and ascites formations are among the manifestations of the liver injuries caused by I/R [3]. Increased capillary (sinusoidal) pressure of the liver causes the transvascular fluid movement resulting in liver weight gain and ascites formation. We previously reported that an increase in hepatic sinusoidal pressure, assessed by the vascular occlusion method, is involved in edematogenic changes in rat liver after reperfusion after ischemia [4]. However, the change in the sinusoidal pressure after I/R is not known in other mammals such as the mouse, the most frequently used experimental animal. Recently, we have established

[1] To whom correspondence and reprint requests should be addressed at Department of Physiology, Kanazawa Medical University, Uchinada, Ishikawa 920-0293. E-mail: shibamo@kanazawa-med.ac.jp.

0022-4804/07 $32.00

the isolated perfused mouse liver preparation in which the sinusoidal pressure can be measured with the double occlusion method [5].

Nitric oxide (NO) is a potent vasodilator and can induce vasodilation at the level of the sinusoids as well as at presinusoidal sites in liver exposed to vasoconstrictors [6–8]. Microcirculatory disturbances and nonperfused sinusoids are well-recognized phenomena that cause reperfusion injury after hepatic ischemia [9–11]. In this respect, the vasodilator action of NO serves a beneficial purpose in hepatic I/R. On the other hand, NO can react with superoxide to form the potent cytotoxic oxidant peroxynitrite [12]. Thus, it is still controversial whether inhibition of NO is beneficial [13, 14] or detrimental [15, 16] in hepatic I/R injury.

Therefore, the first purpose of the present study was to determine the effect of reperfusion following ischemia on the hepatic sinusoidal pressure, vascular resistance distribution, and liver weight in isolated mouse liver. Ischemia was induced at room temperature by occlusion of the inflow line while keeping the outflow line open. The second purpose was to determine the effect of a NO synthase inhibitor, N^G-nitro-L-arginine methyl ester (L-NAME), on the I/R injury in isolated portally perfused mouse liver.

MATERIALS AND METHODS

The study protocol was approved by the Animal Research Committee of Kanazawa Medical University, Uchinada, Japan.

Isolated Perfused Mouse Liver Preparation

Twenty male specific-pathogen-free, outbred ddY mice [41.5 ± 0.4 (SE) g; SLC Co., Hamamatsu, Japan], one of the most popular mouse strains in Japan, were anesthetized with pentobarbital sodium (50 mg/kg, i.p.) and mechanically ventilated with room air. After laparotomy, the bile duct was cut and the hepatic artery was ligated. Before cannulation of the portal vein, the perfusion circuit was initially filled with diluted blood; 1.3 mL blood was initially obtained by exanguination of an intact anesthetized and heparinzed donor mouse, and this blood was diluted with 5% bovine albumin (Fraction V powder-A2153; Sigma, St. Louis, MO) in a Krebs solution (118 mM NaCl, 5.9 mM KCl, 1.2 mM $MgSO_4$, 2.5 mM $CaCl_2$, 1.2 mM NaH_2PO_4, 25.5 mM NaHCO3, and 5.6 mM glucose). At 5 min after an injection of heparin (500 mU/g) into the intra-abdominal inferior vena cava (IVC), autologous blood was obtained through the abdominal IVC and added to the reservoir. Then, IVC above the renal veins was ligated, and the portal vein was cannulated with a stainless cannula (OD 1.2 mm, ID 1.0 mm) for portal perfusion. After thoracotomy, the supradiaphragmatic IVC was cannulated through a right atrial incision with the same size stainless cannula, and then portal perfusion was begun with diluted blood. The liver was rapidly excised, suspended from an electric balance, and weighed.

The basic method for liver perfusion was described previously [5]. The liver was perfused at a constant flow rate in a recirculating manner via the portal vein with the diluted blood. Blood was pumped using a Masterflex pump from the venous reservoir through a heat exchanger (37°C). The recirculating blood volume was 30 mL and the final hematocrit was 3%. The height of the reservoir and the blood flow rate could be adjusted independently to maintain the portal and hepatic venous pressures at any desired level. The blood was oxygenated in the reservoir by continuous bubbling with 95% O_2 and 5% CO_2. The portal venous (Ppv) and the hepatic venous (Phv) pressures were measured with pressure transducers connected to the corresponding side arm with the reference point at the hepatic hilus. To measure the double occlusion pressure (Pdo), two solenoid valves were placed around the perfusion tubes upstream from the Ppv sidearm cannula and downstream from the Phv sidearm cannula [5]. Blood flow rate (Q) was measured manually by collecting outflow blood for 1 min just before the baseline measurement. The same measurement was done at the end of the experiment to confirm the constancy of blood flow during experimental period. The hepatic vascular pressures and liver weight (Wt) were monitored continuously and displayed through a thermal physiograph.

Experimental Protocol

Initially, the hepatic hemodynamic variables were observed for at least 30 min after the start of perfusion until an isogravimetric state (no weight gain or loss) was obtained at the highest levels of Q by adjusting Ppv and Phv to a level within the normal perfusion range, i.e., a Ppv of 4.5 to 5.5 mmHg and a Phv of 0 to 1 mmHg. After the baseline measurement, the perfused liver was pretreated with either of L-NAME (100 μM, n = 7) or the biological inactive enantiomer of N^G-nitro-D-arginine methyl ester (D-NAME, 100 μM, n = 7).

The mouse liver was then exposed to ischemia, which was induced by occlusion of the portal inflow line for 1 h followed by 1-h reperfusion. In the time-matched non-I/R control group (n = 6), the liver was perfused without ischemia for 2 h. In all liver studied, the pump speed for portal perfusion, once determined at baseline, was not changed throughout the experimental period. The hepatic sinusoidal pressure was measured by the double occlusion method [17]. Both the inflow and outflow lines were simultaneously and instantaneously occluded using the solenoid valves, after which Ppv and Phv rapidly equilibrated to an identical pressure, which was Pdo. In each experimental group, Pdo was measured at baseline before ischemia, and 1.5, 3, 10, 20, 30, 40, 50, and 60 min after reperfusion. In the control group, Pdo was measured at the corresponding time after 60-min observation. For measurement of blood concentration of alanine aminotransferase (ALT) with the automated analyzer (HITACHI 7250, Hitachi, Japan), the perfusing blood (1 mL) was sampled before ischemia and at 1.5 and 60 min after reperfusion. The total portal-hepatic venous (Rt), pre- (Rpre) and postsinusoidal (Rpost) resistance values were calculated by the following equations:

$$Rt = \frac{Ppv - Phv}{Q} \quad (1)$$

$$Rpre = \frac{Ppv - Pdo}{Q} \quad (2)$$

$$Rpost = \frac{Pdo - Phv}{Q} \quad (3)$$

Statistics

All results are expressed as the means ± SE. Data were analyzed by one- and two-way analysis of variance (ANOVA), using repeated-measures for two-way comparison within groups. Comparisons of individual points between groups and within groups were made by Bonferroni-Dunn post hoc test. A P values less than 0.05 was considered significant.

RESULTS

Administration of either L-NAME or D-NAME into the blood of isolated mouse liver did not change basal Ppv. Figure 1 shows a recording example of variables

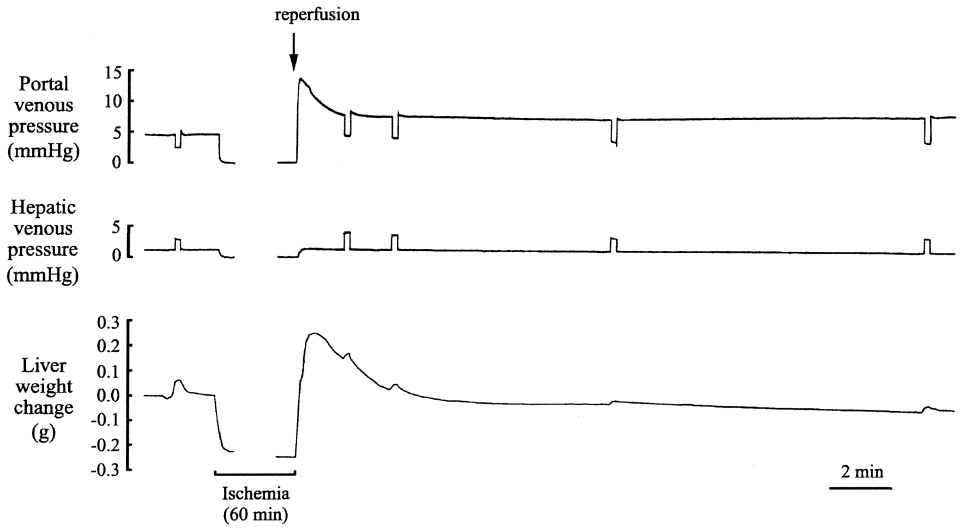

FIG. 1. Representative recordings of portal venous pressure, hepatic venous pressure, and liver weight change after reperfusion following 1-h ischemia in the D-NAME group.

during 60 min after reperfusion following 1-h ischemia in the D-NAME group. Ppv increased steeply from the preischemia baseline of 5.1 ± 0.1 to 7.9 ± 0.3 mmHg at 1.5 min after start of reperfusion, and then it remained elevated even at the end of the experimental period, as shown in Table 1. Phv (0.2 ± 0.1 mmHg) did not change because of constant flow perfusion. Double occlusion maneuver revealed that Pdo increased from the baseline of 2.5 ± 0.1 to 4.0 ± 0.1 mmHg at 1.5 min, and then it returned to the almost baseline levels of 2.8 ± 0.1 mmHg at 60 min after reperfusion (Fig. 2, Table 1). During reperfusion, Wt changed in a manner similar to the change in Pdo: Wt increased steeply and reached the peak value of 0.14 ± 0.04 g/g liver above the baseline at 1.5 min, and then quickly returned to the lower levels, which were not significantly different from the baseline at 10 min, as shown in Fig. 2. The hepatic hemodynamic responses were also similarly observed in the L-NAME group. There were no significant differences in the hemodynamic variables between the L-NAME and D-NAME groups, as shown in Figs. 2 and 3, and Table 1. In the control group, Ppv showed a minimal but significant increase at 120 min after the baseline measurement.

At 1.5 min after reperfusion in the D-NAME group, the Ppv-to-Pdo gradient increased from the baseline of 2.6 ± 0.1 to 3.9 ± 0.2 mmHg, and the Pdo-to-Phv gradient also increased from 2.4 ± 0.1 to 3.8 ± 0.1 mmHg. The increase in the Ppv-to-Pdo gradient (1.5 mmHg) was similar to that in the Pdo-to-Phv gradient (1.4 mmHg), indicating that the increases in Rpre and Rpost were similar in degree after reperfusion. The similar changes in pressure gradients were observed in the L-NAME group. Figure 3 shows changes in Rpre, Rpost, and Rt after reperfusion. The time course changes in Rt were parallel to those of Ppv because of constant perfusion. At 1.5 min after reperfusion, Rpre increased by 60% after reperfusion in both I/R groups (from 1.06 ± 0.05 to 1.78 ± 0.13 mmHg · mL^{-1} · min · g liver in the D-NAME group; from 1.08 ± 0.05 to 1.62 ± 0.06 mmHg · mL^{-1} · min · g liver in the L-NAME group). Rpost also significantly increased about 60% in

TABLE 1

The Changes in the Portal Venous, Hepatic Venous, Double Vascular Occlusion Pressures, Portal Venous Blood Flow, and Blood Alanine Aminotransferase after Reperfusion following 1-hour Ischemia

Groups	Baseline	1.5 min	60 min
Ppv (mmHg)			
L-NAME (n = 7)	4.9 ± 0.1	7.8 ± 0.2*#	6.9 ± 0.4*#
D-NAME (n = 7)	5.1 ± 0.1	7.9 ± 0.3*#	6.8 ± 0.3*#
non I/R control (n = 6)	4.9 ± 0.1	5.2 ± 0.2	5.9 ± 0.2*
Phv (mmHg)			
L-NAME (n = 7)	0.4 ± 0.1	0.4 ± 0.1	0.4 ± 0.1
D-NAME (n = 7)	0.2 ± 0.1	0.2 ± 0.1	0.2 ± 0.1
non I/R control (n = 6)	0.3 ± 0.1	0.3 ± 0.1	0.3 ± 0.1
Pdo (mmHg)			
L-NAME (n = 7)	2.5 ± 0.1	4.1 ± 0.2*#	2.9 ± 0.2
I/R D-NAME (n = 7)	2.5 ± 0.1	4.0 ± 0.1*#	2.8 ± 0.1
non I/R control (n = 6)	2.5 ± 0.1	2.6 ± 0.1	2.7 ± 0.1
Q (mL · min^{-1} · g $liver^{-1}$)			
L-NAME (n = 7)	2.4 ± 0.1	2.4 ± 0.1	2.4 ± 0.1
D-NAME (n = 7)	2.5 ± 0.1	2.5 ± 0.1	2.5 ± 0.1
non I/R control (n = 6)	2.5 ± 0.1	2.5 ± 0.1	2.5 ± 0.1
ALT (U/L)			
L-NAME (n = 7)	3 ± 1	11 ± 3	60 ± 20*#
D-NAME (n = 7)	2 ± 1	9 ± 4	51 ± 19*#
non I/R control (n = 6)	3 ± 1	6 ± 2	9 ± 3

Ppv, portal venous; phv, hepatic venous; pdo, double vascular occlusion; Q, portal venous blood flow; ALT, blood alanine aminotransferase.
Values are means ± SE.
* $P < 0.05$ vs. baseline.
# $P < 0.05$ vs. the non I/R control group.

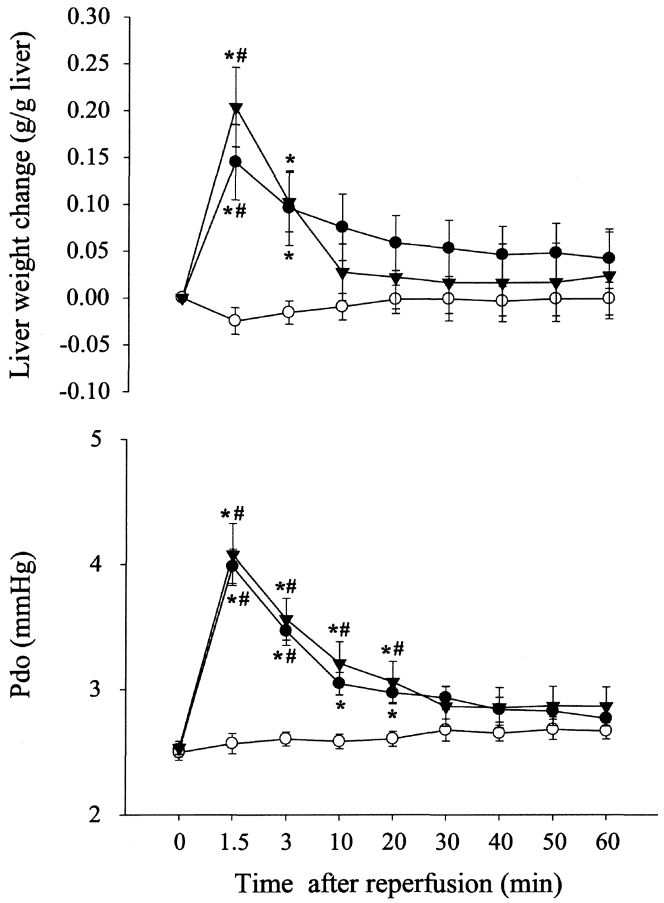

FIG. 2. Time course changes in liver weight change and double occlusion pressure (Pdo) in the L-NAME (closed circle, $n = 7$), D-NAME (closed triangle, $n = 7$), and non-I/R control (open circle, $n = 6$) groups. Values are means ± SE. $*P < 0.05$ *vs.* baseline. $\#P < 0.05$ *vs.* non-I/R control group.

both D-NAME and L-NAME groups. Thus, the Rpost to Rt ratio (Rpost/Rt ratio) did not significantly change: It changed from the baseline value of 0.52 ± 0.07 to 0.49 ± 0.01 at 1.5 min in D-NAME group, and from 0.46 ± 0.01 to 0.49 ± 0.01 at 1.5 min in the L-NAME group. This indicates that increased hepatic vascular resistance could be ascribed to a similar increase in both Rpre and Rpost. Rpost returned to the baseline levels within 30 min after reperfusion, while Rpre remained elevated at the end of the experimental period. In the non-I/R control group, there were no significant changes in the Rpost throughout the experimental period, while Rpre did not significantly increased until 120 min after reperfusion. The liver dysfunction was also confirmed by increased liver enzyme release into blood after reperfusion. Table 1 shows the results of blood levels of ALT. The enzyme levels at 60 min after reperfusion in both I/R groups were significantly higher than the corresponding levels of the control group. In the D-NAME group, ALT levels increased to 28 times the baseline levels. The increased levels in the D-NAME group were not significantly different from those in the L-NAME group.

DISCUSSION

In the present study we determined the changes in liver weight and the sinusoidal pressure, which was assessed by Pdo [17], in the I/R injury of isolated mouse liver perfused with diluted blood via the portal vein.

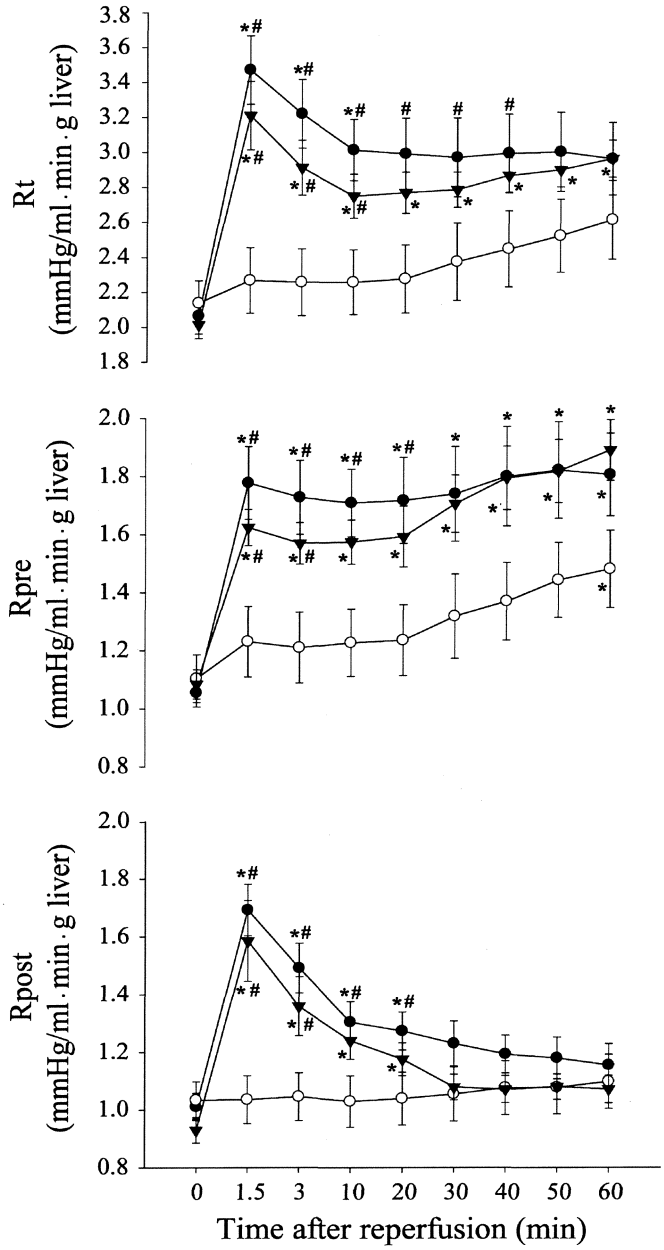

FIG. 3. Time course changes in total vascular resistance (Rt), presinusoidal resistance (Rpre), and postsinusoidal resistance (Rpost) in the L-NAME (closed circle, $n = 7$), D-NAME (closed triangle, $n = 7$), and non-I/R control (open circle, $n = 6$) groups. Values are means ± SE. $*P < 0.05$ *vs.* baseline. $\#P < 0.05$ *vs.* non-I/R control group.

Immediately after reperfusion, Pdo, the determinant of transvascular fluid movement and hepatic congestion, increased slightly but significantly because of an increase in Rpost. Concomitant with an increase in Pdo, liver weight increased (14%), and then quickly declined to baseline without secondary liver weight gain at the end of the experimental period. This finding suggests that the sinusoidal pressure does not so much increase after I/R that the associated edematous changes might be small in mouse liver during I/R. Another major finding is that both Rpre and Rpost increased in a similar magnitude immediately after reperfusion. Then Rpre remained elevated throughout the postreperfusion period, whereas Rpost returned to the baseline levels within 30 min after reperfusion.

Although the reperfusion-induced increase in vascular resistance was previously reported in isolated portally perfused rat liver [18, 19], we have recently demonstrated that the increased vascular resistance after reperfusion was mainly because of the increase in Rpre, that is, the inflow resistance [4]. In the present study, however, Rpost in mouse liver increased in nearly the same magnitude as Rpre during reperfusion after ischemia. The differences in reperfusion-induced changes in segmental vascular resistance between rats [4] and mice may be attributed to the greater increase in Rpre in rats (230%) than in mice (60%), because the increase in Rpost was similar between these species (100% in rats and 60% in mice). The reason for this difference is not know; however, the hepatic venoconstriction in mice generally seems to be smaller than rats. One possibility is that contractile smooth muscle cells may not be so much distributed in portal venules of mice, as compared with rats. However, no morphological studies that support this assumption are currently available.

The increase in Rpre might be explained on a mechanical basis by the phenomenon of vascular occlusion. Ischemia-induced mechanical collapse and cell swelling of portal venules and sinusoids can lead to a physical obliteration of lumen of portal venules and the sinusoids. Actually, Ischemia stress does cause hepatocyte swelling [20]. Such a swelling of parenchymal cells would cause narrowing of the vascular spaces and thus impede microvascular blood flow. After I/R, Kupffer cells can also physically enlarge and impinge on luminal diameter [21]. These possible changes in the portal venules and sinusoids might have appeared as an increase in the inflow resistance after reperfusion in the present study. The mechanism for the increase in the Rpost is also not known from the present study. We speculate that activation of Kupffer cells and perhaps endothelial cells might have released potent vasoconstrictor substances, resulting in hepatic venous constriction. Kupffer cell activation has been shown to occur mainly on reperfusion [22], and these activated Kupffer cells could release a variety of vasoactive substances, such as eicosanoids, platelet-activating factor, reactive oxygen intermediate [23]. Further studies are required in this respect.

In the present study, hepatocellular injury was evident by an increase in blood ALT at 60 min after reperfusion, but the associated liver weight gain was not observed. This contrasted with the previous finding on rat hepatic I/R injury [4], in which liver weight gain was accompanied by hepatocellular damages, because no differences were found in the perfusate Hct and the ischemia time between the present mouse and the previous rat studies. The absence of hepatocellular injury associated liver weight gain in mouse liver could be ascribed to presence of the persistent elevated Rpre, as shown in Fig. 3. Although the mechanism for persistent increase in Rpre is not known, presinusoidal venoconstriction or obstruction could cause a decrease in downstream sinusoidal blood volume, resulting in liver weight loss. This possible liver weight loss associated with increased Rpre might have been counteracted by liver damage-associated liver weight gain, resulting in apparent absence of liver weight changes at the end of experimental periods. Another possibility may be related to the difference in the ischemia tolerance between rats and mice: mice might be more resistant to hepatic I/R injury than rats. However, this assumption may be unlikely. In the additional *in vivo* experiments, we could not find any significant differences in plasma ALT, an indicator of hepatocellular damage, after reperfusion following a 60-min ischemia of 70% liver (occlusion of the portal vein and hepatic artery to the left and middle lobes) between ddY mice and SD rats (baseline; 33 ± 9 *versus* 21 ± 1 U/L, 60 min after reperfusion; 557 ± 84 *versus* 401 ± 64 U/L, mice *versus* rats, respectively).

NO has been reported to play a beneficial role in hepatic I/R injury [24]. NO can induce vasodilation at the level of the sinusoid as well as at presinusoidal sites, resulting in improvement of microcirculatory disturbances and non-perfused sinusoids. Indeed, any NOS inhibitors that affect eNOS reduce microvascular perfusion and aggravate liver injury during I/R [14, 25]. NO also has anti-inflammatory effects, such as inhibition of platelet aggregation and neutrophil adherence to endothelium [26, 27]. In addition, other beneficial effects of NO, such as protection of mitochondria and induction of heat shock proteins, may also be involved [28]. However, in the present study, pretreatment with L-NAME did not augment the I/R injury. This suggests that NO does not play a substantial role in the present perfused mouse hepatic I/R injury model. One of the reasons for the absence of beneficial effects of NO may be related to diluted perfusing blood. In the present study to measure the sinusoidal pressure, the liver was isolated and perfused, resulting in a

large perfusate volume as compared with the mouse liver mass. In the present perfused liver preparation, neutrophils could not have exerted injurious actions because of too much dilution. The diluted blood has a low viscosity, resulting in a decrease in shear stress, a key factor of NO generation. Finally, NO may only be relevant in conditions of microhemodynamic deterioration. If there are no serious disorders, as observed in the present study, NO may not be produced in relevant amounts, and thus, inhibition may not affect the hepatic circulation.

In conclusion, we determined the changes in the sinusoidal pressure, hepatic vascular resistance distribution, and liver weight in the I/R injury of isolated mouse liver perfused portally with diluted blood. Pre- and postsinusoidal resistance was similarly increased immediately after I/R, followed by a sustained increase in presinusoidal resistance. Reperfusion caused marginal liver weight gain associated with a small and transient increase in the sinusoidal pressure. NO synthase inhibition does not affect hepatic I/R injury in this isolated perfused mouse liver model.

ACKNOWLEDGMENTS

This work was supported by a Grant for Collaborative Research from Kanazawa Medical University (C2005-1, 2 C2006) and a Grant-in-Aid for Scientific Research (18591730) from the Ministry for Education, Culture, Science and Technology of Japan.

REFERENCES

1. Clavien PA, Harvey PR, Strasberg SM. Preservation and reperfusion injuries in liver allografts. Transplantation 1992;53:957.
2. Delva E, Barberousse JP, Nordlinger B, et al. Hemodynamic and biochemical monitoring during major liver resection with use of hepatic vascular exclusion. Surgery 1984;95:309.
3. Wang KS, Monden M, Kanai T, et al. Protective effects of a PAF antagonist against liver injury induced by warm ischemia or cold preservation. Transplant Proc 1992;24:1596.
4. Ling YQ, Shibamoto T, Honda T, et al. Increased sinusoidal pressure is associated with early liver weight gain in ischemiareperfusion injury in isolated perfused rat liver. J Surg Res 2000;88:70.
5. Shibamoto T, Cui S, Ruan Z, et al. Effects of norepinephrine and histamine on vascular resistance in isolated perfused mouse liver. Jpn J Physiol 2005;55:143.
6. McCuskey RS. Morphological mechanisms for regulating blood flow through hepatic sinusoids. Liver 2000;20:3.
7. Ming Z, Han C, Lautt WW. Nitric oxide mediates hepatic arterial vascular escape from norepinephrine-induced constriction. Am J Physiol Gastrointest Liver Physiol 1999;277:G1200.
8. Wiest R, Groszmann RJ. The paradox of nitric oxide in cirrhosis and portal hypertension: too much, not enough. Hepatology 2002;35:478.
9. Chun K, Zhang J, Biewer J, et al. Microcirculatory failure determines lethal hepatocyte injury in ischemic/reperfused rat livers. Shock 1994;1:3.
10. Koo A, Komatsu H, Tao G, et al. Contribution of noreflow phenomenon to hepatic injury after ischemia-reperfusion: Evidence for a role for superoxide anion. Hepatology 1991;15:507.
11. Vollmar B, Glasz J, Leiderer R, et al. Hepatic microcirculatory perfusion failure is a determinant of liver dysfunction in warm ischemia-reperfusion. Am J Pathol 1994;145:1421.
12. Squadrito GL, Pryor WA. Oxidative chemistry of nitric oxide: The role of superoxide, peroxynitrite and carbon dioxide. Free Radic Biol Med 1998;25:392.
13. Menezes J, Hierholzer C, Watkins SC, et al. A novel nitric oxide scavenger decreases liver injury and improves survival after hemorrhagic shock. Am J Physiol 1999;277:G144.
14. Meguro M, Katsuramaki T, Nagayama M, et al. A novel inhibitor of inducible nitric oxide synthase (ONO-1714) prevents critical warm ischemia-reperfusion injury in the pig liver. Transplantation 2002;73:1439.
15. Wang Y, Mathews WR, Guido DM, et al. Inhibition of nitric oxide synthesis aggravates reperfusion injury after hepatic ischemia and endotoxemia. Shock 1995;4:282.
16. Liu P, Yin K, Nagele R, Wong PY. Inhibition of nitric oxide synthase attenuates peroxynitrite generation, but augments neutrophil accumulation in hepatic ischemiareperfusion in rats. J Pharmacol Exp Ther 1998;284:1139.
17. Yamaguchi Y, Shibamoto T, Hayashi T, et al. Hepatic vascular response to anaphylaxis in isolated canine liver. Am J Physiol 1994;267:R268.
18. Kukan M, Bezek S, Tmovec T. Role of hepatovasculature in warm ischemiareperfusion injury of rat liver. Physiol Res 1996; 45:427.
19. Minor T, Isselhard W. Role of the hepatovasculature in free radical mediated reperfusion damage of the liver. Eur Surg Res 1993;25:287.
20. Gores GJ, Flarsheim CE, Dawson TL, et al. Swelling, reductive stress and cell death during chemical hypoxia in hepatocytes. Am J Physiol 1989;257:C347.
21. McCuskey RS, McCuskey PA, Urbaschek R, et al. Kupffer cell function in host defense. Rev Infect Dis 1987;9:S616.
22. Caldwell-Kenkel JC, Currin RT, Tanaka Y, et al. Kupffer cell activation and endothelial damage after storage of rat livers: Effects of reperfusion. Hepatology 1991;13:83.
23. Decker K. Biologically active products of stimulated liver macrophages (Kupffer cells). Eur J Biochem 1990;192:245.
24. Jaeschke H. Molecular mechanisms of hepatic ischemia-reperfusion injury and preconditioning. Am J Physiol Gastrointest Liver Physiol 2003;284:G15.
25. Harbrecht BG, Wu B, Watkins SC, et al. Inhibition of nitric oxide synthase during hemorrhagic shock increases hepatic injury. Shock 1995;332.
26. Gauthier TW, Davenpeck KL, Lefer AM. Nitric oxide attenuates leukocyte-endothelial interaction via P-selectin in splanchnic ischemia-reperfusion. Am J Physiol 1994;G562.

Am J Physiol Heart Circ Physiol 292: H701–H718, 2007.
First published September 22, 2006; doi:10.1152/ajpheart.00426.2006.

Effects of pacemaker currents on creation and modulation of human ventricular pacemaker: theoretical study with application to biological pacemaker engineering

Yasutaka Kurata,[1] Hiroyuki Matsuda,[1] Ichiro Hisatome,[2] and Toshishige Shibamoto[1]

[1]*Department of Physiology, Kanazawa Medical University, Ishikawa, and* [2]*Division of Regenerative Medicine and Therapeutics, Tottori University Graduate School of Medical Science, Yonago, Japan*

Submitted 28 April 2006; accepted in final form 16 September 2006

Kurata Y, Matsuda H, Hisatome I, Shibamoto T. Effects of pacemaker currents on creation and modulation of human ventricular pacemaker: theoretical study with application to biological pacemaker engineering. *Am J Physiol Heart Circ Physiol* 292: H701–H718, 2007. First published September 22, 2006; doi:10.1152/ajpheart.00426.2006.—A cardiac biological pacemaker (BP) has been created by suppression of the inward rectifier K^+ current (I_{K1}) or overexpression of the hyperpolarization-activated current (I_h). We theoretically investigated the effects of incorporating I_h, T-type Ca^{2+} current ($I_{Ca,T}$), sustained inward current (I_{st}), and/or low-voltage-activated L-type Ca^{2+} channel current ($I_{Ca,LD}$) on *1*) creation of BP cells, *2*) robustness of BP activity to electrotonic loads of nonpacemaking (NP) cells, and *3*) BP cell ability to drive NP cells. We used a single-cell model for human ventricular myocytes (HVMs) and also coupled-cell models composed of BP and NP cells. Bifurcation structures of the model cells were explored during changes in conductance of the currents and gap junction. Incorporating the pacemaker currents did not yield BP activity in HVM with normal I_{K1} but increased the critical I_{K1} conductance for BP activity to emerge. Expressing I_h appeared to be most helpful in facilitating creation of BP cells via I_{K1} suppression. In the coupled-cell model, I_{st} significantly enlarged the gap conductance (G_C) region where stable BP cell pacemaking and NP cell driving occur, reducing the number of BP cells required for robust pacemaking and driving. In contrast, I_h enlarged the G_C region of pacemaking and driving only when I_{K1} of the NP cell was relatively low. $I_{Ca,T}$ or $I_{Ca,LD}$ exerted effects similar to those of I_{st} but caused shrinkage or irregularity of BP oscillations. These findings suggest that expressing I_{st} most effectively improves the structural stability of BPs to electrotonic loads and the BP ability to drive the ventricle.

mathematical model; bifurcation analysis; computer simulation

A CARDIAC BIOLOGICAL PACEMAKER (BP) has recently been created by genetic suppression of the inward rectifier K^+ current (I_{K1}) in guinea pig ventricular myocytes (28) or overexpression of the hyperpolarization-activated current (I_h) in canine atrial or Purkinje myocytes (32, 36), suggesting possible development of the functional BP as a therapeutic alternative to the electronic pacemaker (8, 37).

A first step for creation of the functional BP would be engineering of single BP cells, which requires deep understanding of the BP mechanisms. By bifurcation analyses of a mathematical model for human ventricular myocytes (HVMs), we have elucidated (22) the dynamical mechanisms of BP generation in I_{K1}-downregulated HVMs and the roles of individual sarcolemmal currents in HVM pacemaking. We have suggested that *1*) BP activity can be developed by reducing I_{K1} alone in HVMs as in guinea pig ventricular myocytes (41), *2*) the instability of an equilibrium point (EP) with depolarized potentials is essentially important for BP generation, and *3*) the dynamical mechanism of ventricular pacemaking is essentially the same as that of natural sinoatrial (SA) node pacemaking as reported by Kurata et al. (21). In the previous study, however, whether BP cells can be developed from HVMs by incorporating "pacemaker currents," which contribute to phase 4 depolarization in SA node pacemaking, was not clearly shown, with the most efficient way to create BP cells remaining unknown; the pacemaker currents include I_h, T-type Ca^{2+} channel current ($I_{Ca,T}$), sustained inward current (I_{st}), and low-voltage-activated L-type Ca^{2+} channel current ($I_{Ca,LD}$). Therefore, we first investigated whether incorporating these pacemaker currents can yield BP activity and how this affects BP generation during I_{K1} suppression in the model HVM. Our findings suggested that I_h facilitates BP generation during I_{K1} suppression in combination with the other pacemaker currents, although I_{K1} downregulation is necessary for constructing BP cells from HVMs.

Our preliminary study also revealed some drawbacks of the I_{K1}-downregulated HVM pacemaker, compared with the SA node pacemaker, to prevent the creation of functional BPs. They include *1*) relatively low robustness to hyperpolarizing (electrotonic) loads and *2*) low ability to drive adjacent nonpacemaker cells, which may be due to the lack of pacemaker currents. Using a coupled-cell model composed of I_{K1}-deleted BP cells and a nonpacemaking HVM [referred to as "nonpacemaking (NP) cell"], therefore, we further explored the effects of incorporating pacemaker currents on the structural stability of BP cells (robustness of BP activity) to electrotonic modulations and BP cell ability to drive the adjacent NP cell. Our results suggested that $I_{Ca,T}$, I_{st}, and $I_{Ca,LD}$ can, but I_h cannot, significantly improve the structural stability of BPs to electrotonic loads of HVMs and the BP ability to drive the ventricle.

This study indicates that the theoretical approach based on nonlinear dynamics and bifurcation theory may allow us to predict the effects of current modulations on pacemaker cell dynamics accurately and find out how to control the dynamical properties of real myocytes properly. Exploring bifurcation structures of the mathematical model would provide a theoret-

Address for reprint requests and other correspondence: Y. Kurata, Dept. of Physiology, Kanazawa Medical Univ., 1-1 Daigaku, Uchinada-machi, Kahoku-gun, Ishikawa 920-0293, Japan (e-mail: yasu@kanazawa-med.ac.jp).

The costs of publication of this article were defrayed in part by the payment of page charges. The article must therefore be hereby marked "*advertisement*" in accordance with 18 U.S.C. Section 1734 solely to indicate this fact.

ical background for engineering of BP cells and functional BPs from native cardiomyocytes or embryonic stem (ES) cells, i.e., for gene or cell therapy of bradyarrhythmias (8, 37). This study also provides novel insights into the roles of the pacemaker currents in natural SA node pacemaking. Definitions of terms specific to nonlinear dynamics and bifurcation theory are given at the end of THEORY AND METHODS (see also Refs. 21–23, 30).

THEORY AND METHODS

Base Mathematical Model for Human Ventricular Myocytes

We used our HVM model (22) as a modified version of the Priebe-Beuckelmann model (33). More elaborate HVM models were recently developed by Iyer et al. (12) and ten Tusscher et al. (42), which are probably superior to the original or modified Priebe-Beuckelmann model in reproducing experimental data. Nevertheless, these models are much more complex or include vector field functions that are not continuous or smooth, being less suitable for bifurcation analyses (for more details, see Ref. 22). We have therefore chosen to use our model, which is more suitable for bifurcation analyses.

The standard model for the normal activity of single HVMs is described as a nonlinear dynamical system of 15 first-order ordinary differential equations. The membrane current system includes the L-type Ca^{2+} channel current ($I_{Ca,L}$), rapid and slow components of delayed rectifier K^+ currents (denoted I_{Kr} and I_{Ks}, respectively), 4-aminopyridine-sensitive transient outward current (I_{to}), Na^+ channel current (I_{Na}), I_{K1}, background Na^+ ($I_{Na,b}$) and Ca^{2+} ($I_{Ca,b}$) currents, Na^+-K^+ pump current (I_{NaK}), Na^+/Ca^{2+} exchanger current (I_{NaCa}), and Ca^{2+} pump current (I_{pCa}). Time-dependent changes in the membrane potential (V) are described by the equation

$$dV/dt = I_{stim} - (I_{Ca,L} + I_{Kr} + I_{Ks} + I_{to} + I_{Na} + I_{K1} + I_{Na,b} + I_{Ca,b} + I_{NaK} + I_{NaCa} + I_{pCa}) \quad (1)$$

where I_{stim} represents the stimulus current (in pA/pF), being set equal to zero for simulations of BP activity. Details on modifications and expressions of the HVM model are described in our previous article (22).

Our full system includes material balance expressions to define the temporal variation in intracellular Ca^{2+}, Na^+, and K^+ concentrations ($[Ca^{2+}]_i$, $[Na^+]_i$, and $[K^+]_i$), whereas extracellular Ca^{2+}, Na^+, and K^+ concentrations ($[Ca^{2+}]_o$, $[Na^+]_o$, and $[K^+]_o$) were fixed at 2, 140 and 5.4 mM, respectively. As pointed out by Hund et al. (11) and Krogh-Madsen et al. (18), the second-generation model incorporating ion concentration changes exhibits degeneracy (i.e., nonuniqueness of steady-state solutions), not suitable for bifurcation analysis to be applicable to isolated equilibria. One of the ways to remove degeneracy and thus allow bifurcation analyses of isolated equilibria is to make some ionic concentrations fixed (18). Variations in $[K^+]_i$ during changes in bifurcation parameters were relatively small, not significantly altering the model cell behaviors. For stability and bifurcation analyses, therefore, $[K^+]_i$ was fixed at 140 mM.

Incorporation of Pacemaker Currents

To investigate how pacemaker currents contributing to phase 4 depolarization in SA node pacemaking affect bifurcation structures of HVM model cells, we incorporated the formulas of I_h, $I_{Ca,T}$, and I_{st}, which were used for our SA node model (20) or experimentally determined for human cardiomyocytes. The low voltage-activated L-type Ca^{2+} channel (D-LTCC) was recently reported to activate at pacemaker potential regions, i.e., at potentials 10–20 mV more negative than the high-voltage-activated Ca^{2+} channel, contributing to mouse SA node pacemaking (16, 27, 31, 51). Therefore, we also tested the effect of the current mediated by D-LTCC (denoted as $I_{Ca,LD}$). The formulas for individual pacemaker currents are given in APPENDIX B. The origins of the expressions and conductance values tested for each current, as well as those chosen for the original SA node models as mean experimental values, are summarized in Table 1 (for details, see below).

For comparison of the voltage-dependent gating behaviors of the currents tested, steady-state probabilities and time constants of gating variables, as well as the steady-state (window) currents calculated by the steady-state equations for the gating variables, are shown in Fig. 1. To determine the conductance range to be tested for individual currents, we first examined their effects on stability and dynamics of a single BP cell (Fig. 2). Higher conductance of I_h caused a saddle-node bifurcation and cessation of BP activity with drastic increases in $[Na^+]_i$ and $[Ca^{2+}]_i$; higher conductance of $I_{Ca,T}$, I_{st}, or $I_{Ca,LD}$ caused shrinkage of BP oscillations with decrease in upstroke velocity and then cessation of BP activity via Hopf bifurcations. The maximum conductance value to be tested was limited for each current so as not to significantly shrink BP oscillations or not to cause Na^+- or Ca^{2+}-overload conditions (for more details, see below).

I_h. The expressions for I_h were adopted from the rabbit SA node model (20, 49), as well as from experimental studies for human I_h (3, 29). Although all the I_h formulas exerted qualitatively the same effects, the effect of the rabbit SA node I_h was most dramatic, which is probably due to the most positive activation threshold. Thus we show data only for the rabbit SA node I_h. The maximum conductance (g) value for I_h (g_h), 0.375 nS/pF in the original SA node model (20, 49), was limited to 0.12 nS/pF (for the effects on BP generation) or 0.5 nS/pF (for the effects on pacemaking and driving ability of BP cells); higher g_h caused inaccurate calculations of steady states with drastic increases of $[Na^+]_i$ and $[Ca^{2+}]_i$ to unreasonable values.

$I_{Ca,T}$. The expressions for $I_{Ca,T}$ were adopted from the rabbit SA node (5, 20) and ventricular (34) models. The effects of these $I_{Ca,T}$ currents were qualitatively the same, with the effect of the SA node $I_{Ca,T}$ being more remarkable; thus the data for the rabbit SA node $I_{Ca,T}$ are shown. Relatively high $g_{Ca,T}$ was required to affect dynamical properties of the model cell, probably because the window region (i.e., overlap of activation and inactivation curves) of the model $I_{Ca,T}$ is relatively small (see Fig. 1). Therefore, the $g_{Ca,T}$ value was increased up to 3 nS/pF, although it was 0.458 nS/pF in the original SA node model (5, 20). Further

Table 1. *Equations and conductance values tested for individual pacemaker currents*

Species and Expression Systems	References	Conductance, nS/pF	
		BP	SAN
I_h			
Rabbit SA node	Kurata et al. (20), Wilders et al. (49)	0–0.5	0.375
Human ventricle	Cerbai et al. (3)	0–1	
HCN2 (expressed in HEK cells)	Moroni et al. (29)	0–1	
$I_{Ca,T}$			
Rabbit SA node	Kurata et al. (20), Demir et al. (5)	0–3	0.458
Rabbit ventricle	Puglisi and Bers (34)	0–3	
I_{st}			
Rabbit SA node	Kurata et al. (20)	0–0.02	0.015
Rat SA node	Shinagawa et al. (40)	0–0.1	0.0669
$I_{Ca,LD}$			
Mouse SA node	Mangoni et al. (27), Platzer et al. (31)	0–1	0.58

I_h, hyperpolarization-activated current; $I_{Ca,T}$, T-type Ca^{2+} current; I_{st}, sustained inward current; $I_{Ca,LD}$, low-voltage-activated L-type Ca^{2+} channel current; SA, sinoatrial; SAN, SA node; BP, biological pacemaker. BP values are ranges of the maximum conductance tested for each current in this study. SAN values are the maximum conductance of each current used for the original SA node models (5, 20, 40, 49); the value used for the SA node high-voltage-activated Ca^{2+} channel current ($I_{Ca,LC}$) (20) is shown for $I_{Ca,LD}$.

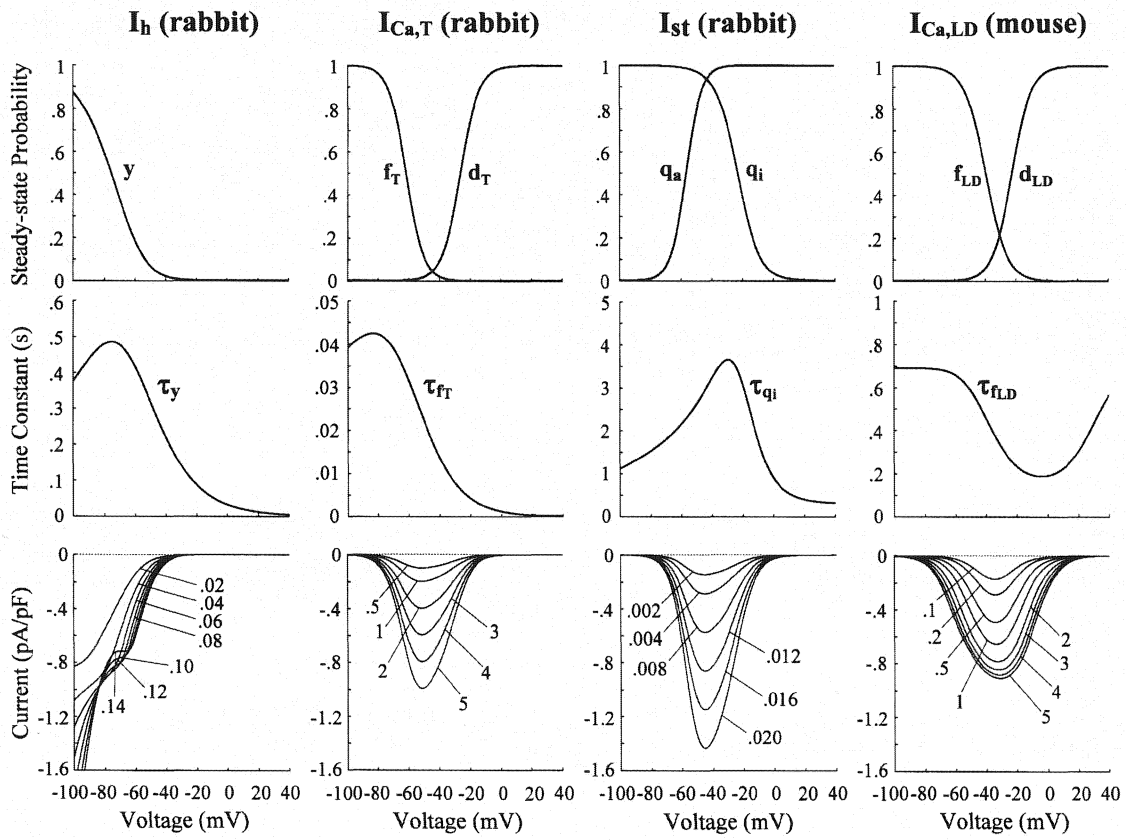

Fig. 1. Voltage-dependent kinetics of the rabbit sinoatrial (SA) node hyperpolarization-activated current (I_h), T-type Ca^{2+} current ($I_{Ca,T}$), and sustained inward current (I_{st}) as well as mouse SA node low-voltage-activated L-type Ca^{2+} channel current ($I_{Ca,LD}$). *Top* and *middle*: voltage dependence of the steady-state probabilities (*top*) and time constants (τ, *middle*) for activation and inactivation gating variables of individual pacemaker currents. *Bottom*: steady-state (window) currents calculated by the steady-state equations for the gating variables. Numbers in each panel represent the maximum current conductance in nS/pF. See APPENDIX A for symbol definitions.

increases in $g_{Ca,T}$ caused shrinkage of BP oscillations and stabilization of an EP via a Hopf bifurcation (see Fig. 2).

I_{st}. The formulas for I_{st} were adopted from the rabbit SA node model (20) and the experimental report for the rat SA node (40). The effects of the two I_{st} currents were essentially the same; thus only data for the rabbit SA node I_{st} are shown. The g_{st} value, 0.015 nS/pF in the original SA node model (20), was limited to 0.02 nS/pF; further increases in g_{st} yielded extremely large window currents leading to Na^+-overload conditions, because the window region of the model I_{st} is relatively large (see Fig. 1).

$I_{Ca,LD}$. The kinetics of $I_{Ca,LD}$ was formulated on the basis of experimental data from mouse SA node cells (27, 31, 51) and human embryonic kidney cells expressing D-LTCC (16). These previous studies suggested that *1*) the voltage dependence of the activation and inactivation of $I_{Ca,LD}$ is 10–20 mV more negative than that of the high-voltage-activated Ca^{2+} channel current ($I_{Ca,LC}$), *2*) the activation of $I_{Ca,LD}$ is faster than that of $I_{Ca,LC}$, and 3) the inactivation of $I_{Ca,LD}$ is 1.5–2 times slower than that of $I_{Ca,LC}$. According to these data, therefore, we formulated the kinetics of $I_{Ca,LD}$ as provided in APPENDIX B (*Eqs. A38–A42*). Because the effects on model cell dynamics of the model $I_{Ca,LD}$ were relatively small, the $g_{Ca,LD}$ value was increased up to 1 nS/pF. Further increases in $g_{Ca,LD}$ caused Ca^{2+}-overload conditions as well as shrinkage of BP oscillations (see Fig. 2).

Formulation of Coupled-Cell Model

To investigate the electrotonic influences of adjacent HVMs on stability and dynamics of BP cells as well as BP cell ability to drive adjacent HVMs, we used a coupled-cell model (Fig. 3), in which I_{K1}-deleted BP cells were connected to a NP cell with normal or reduced I_{K1} via the gap junction conductance (G_C) of 0–20 nS. One NP cell was connected with one to seven BP cells; more than one BP cells were assumed to be well-coupled enough to synchronize completely and act as a cluster of isopotential cells (or assumed to connect with the NP cell via an identical G_C). Pacemaker currents were incorporated into the BP cells only (not into the NP cell).

Time-dependent changes in the membrane potentials of the BP (V_{BP}) and NP (V_{NP}) cells were calculated by the equations

$$dV_{BP}/dt = I_{stim} - I_{total(BP)} - I_{GJ}/C_{BP} \quad (2)$$

$$dV_{NP}/dt = -I_{total(NP)} + I_{GJ}/C_{NP} \quad (3)$$

where C_{BP} and C_{NP} represent the membrane capacitance of the BP and NP cells, respectively. $I_{total(BP)}$ and $I_{total(NP)}$ are the sum of sarcolemmal ionic currents in the BP and NP cells, with I_{GJ} denoting the gap junction current. I_{stim} is the stimulus current applied to the BP cells, usually set equal to zero. The units for V, C, I_{total} (I_{stim}), and I_{GJ} are millivolts, picofarads, picoamperes per picofarad, and picoamperes, respectively. Time-dependent changes in all the other state variables of the BP and NP cells were computed independently, as described for the single HVM in our previous article (22).

Numerical Methods for Dynamic Simulations and Bifurcation Analyses

Dynamic behaviors of the model cells were determined by solving a system of nonlinear ordinary differential equations numerically. Numerical integration as well as bifurcation analyses were performed

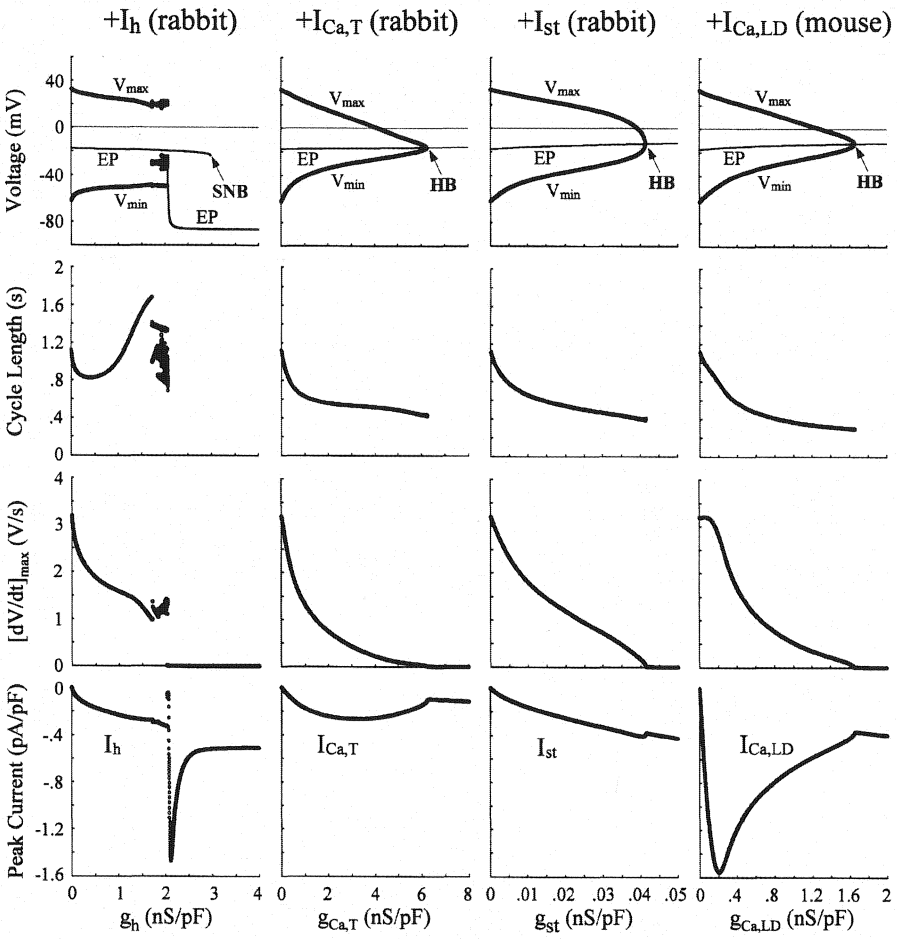

Fig. 2. Changes in stability and dynamics of a single biological pacemaker (BP) cell with increase of each pacemaker current. To induce BP activity, the inward rectifier K^+ current (I_{K1}) conductance (g_{K1}) was reduced to 15% of the control. The steady-state (equilibrium point, EP) and stable periodic [maximum diastolic potential (V_{min}) and peak overshoot potential (V_{max})] branches (*top*), as well as the cycle length (CL) (*second*) and maximum upstroke velocity ($[dV/dt]_{max}$) (*third*) of potential oscillations, are shown as functions of the maximum conductance (g). Peak amplitudes of the pacemaker currents during BP oscillations are also plotted (*bottom*). Steady-state BP dynamics were computed by numerically solving differential equations for 1 min at each conductance value (for details, see Ref. 22), with the initial Na^+ concentration ($[Na^+]_i$) set equal to 6.55 mM in the absence of pacemaker currents; the conductance value was increased at an interval of 1 pS/pF (for g_h, $g_{Ca,T}$, and $g_{Ca,LD}$) or 0.01 pS/pF (for g_{st}) until a bifurcation occurred. Hopf bifurcation points at which stability of an EP reverses (labeled HB at $g_{Ca,T}$ = 6.253, g_{st} = 0.04141, and $g_{Ca,LD}$ = 1.654 nS/pF) and a saddle-node bifurcation point at which an EP disappears (labeled SNB at g_h = 2.982 nS/pF) are shown.

on Workstation CELSIUS X630 (Fujitsu, Tokyo, Japan) with MATLAB 7 (MathWorks, Natick, MA). We used the numerical algorithms available as MATLAB ODE solvers: *1*) a fourth-order adaptive-step Runge-Kutta algorithm that includes an automatic step-size adjustment based on an error estimate (*ode45*) (6) and *2*) a variable time-step numerical differentiation approach selected for its suitability to stiff systems (*ode15s*) (39). Both solvers usually yielded nearly identical results. The latter, much more efficient than the former, was usually used; the former as the best function for most problems was only sometimes used to confirm the accuracy of calculations. The maximum relative error tolerance for the integration methods was set to 1×10^{-6}.

Stability and Bifurcation Analyses

We examined how the stability and dynamics of the model cells alter with changes in bifurcation parameters and constructed bifurcation diagrams for one or two parameters. Bifurcation parameters chosen in this study were the maximum conductance of I_{K1} (g_{K1}) and pacemaker currents (g_h, $g_{Ca,T}$, g_{st}, $g_{Ca,LD}$) as well as G_C; g_{K1} is expressed as a normalized value, i.e., in ratio to the control value of 3.9 nS/pF, unless otherwise stated. The methods for bifurcation analyses of the single BP or NP cell are described in our previous article (22).

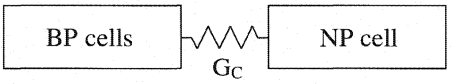

Fig. 3. Coupled-cell model. NP, nonpacemaking; G_C, gap conductance.

Although the methods of bifurcation analyses for the coupled-cell system are essentially the same as for the single cell, the number of state variables increases twice: in the coupled-cell system with fixed $[K^+]_i$, 28 state variables define a 28-dimensional state point in the 28-dimensional state space of the system. We calculated EPs, i.e., steady-state values of the variables, and periodic orbits in the state space of the coupled-cell system. Steady-state values of the variables were calculated by *Eqs. A53–A58* in APPENDIX C. Asymptotic stability of the EP was also determined by computing 28 eigenvalues of a 28 × 28 Jacobian matrix derived from the linearization of the nonlinear system around the EP (for details, see Ref. 45). Periodic orbits were located with the MATLAB ODE solvers. When spontaneous oscillation (BP activity) appeared, the action potential amplitude (APA) as a voltage difference between the maximum diastolic potential (V_{min}) and peak overshoot potential (V_{max}) as well as the cycle length (CL) were determined for each calculation of a cycle. Numerical integration was continued until the differences in both APA and CL between the newly calculated cycle and the preceding one became $<1 \times 10^{-3}$ of the preceding APA and CL values. Potential extrema (V_{min}, V_{max}) and CL of the steady-state oscillation were plotted against bifurcation parameters. When periodic behavior was irregular or unstable, model dynamics were computed for 60 s; all potential extrema and CL values were then plotted.

We constructed one-parameter bifurcation diagrams for G_C and two-parameter bifurcation diagrams for G_C and pacemaker current conductance. For construction of one-parameter bifurcation diagrams, the membrane potential at EPs (steady-state branches) and local potential extrema (V_{min}, V_{max}) of periodic orbits (periodic branches) were determined and plotted as a function of G_C, which was system-

atically changed while keeping all other parameters at their standard values. The saddle-node bifurcation point at which two EPs coalesce and disappear with emergence of robust BP activity was determined; the Hopf bifurcation point at which an unstable EP is stabilized with cessation of BP activity was also located. For construction of two-parameter bifurcation diagrams, the critical G_C values at bifurcation points were determined as functions of the secondary parameters such as the pacemaker current conductance, the number of BP cells, and NP cell g_{K1}; the primary parameter (G_C) was systematically changed, with the secondary parameter fixed at various different values. The path of Hopf and saddle-node bifurcation points was traced in the parameter plane, i.e., bifurcation values for the primary parameter were plotted as a function of the secondary parameter.

We also evaluated the "structural stability" of BP cells, which is defined as the robustness of BP activity to various interventions or modifications that may cause a bifurcation to quiescence or irregular dynamics (21, 22). In this study, we tested the structural stability of BP cells to electrotonic (hyperpolarizing) loads of an adjacent NP cell, using the coupled-cell system, which is also useful in exploring BP cell ability to drive the adjacent NP cell. The method of evaluating the structural stability to electrotonic loads is essentially the same as that for constant bias currents as described in our previous articles (21, 22). In the unstable G_C region where the system has no stable EP, the system usually exhibited robust pacemaking and driving without annihilation (9, 24). When the system removes to the stable G_C region with a stable EP, it will come to a rest at the stable EP via gradual decline of limit cycles, annihilation, or irregular dynamics, as reported by Guevara and Jongsma (9). In the coupled-cell system, the larger the G_C region over which all EPs are unstable (there is no stable EP) and thus BP activity appears is, the more structurally stable the BP system is (for more detail, see Ref. 22).

Definitions of Terms Specific to Nonlinear Dynamics and Bifurcation Theory

Equilibrium point. The equilibrium point (EP) is a time-independent steady-state point at which the vector field vanishes in the state space of a dynamical system, constructing the steady-state branch in one-parameter bifurcation diagrams. This state point corresponds to the zero-current crossing in the steady-state current-voltage (*I-V*) curve, i.e., a quiescent (resting) state of a cell if it is stable.

Periodic orbit. A periodic orbit is a closed trajectory in the state space of a system, constructing the periodic branch in one-parameter bifurcation diagrams.

Limit cycle. The limit cycle is a periodic limit set onto which a trajectory is asymptotically attracted. A stable limit cycle corresponds to an oscillatory state, i.e., pacemaker activity, of a cell.

Bifurcation. Bifurcation is a qualitative change in a solution of differential equations caused by altering parameters, e.g., a change in the number of EPs or periodic orbits, a change in the stability of an EP or periodic orbit, and a transition from a periodic to a quiescent state. Bifurcation phenomena we can see in cardiac myocytes include generation or cessation of pacemaker activity and occurrence of irregular dynamics such as skipped-beat runs and early afterdepolarizations.

Saddle-node bifurcation. Saddle-node bifurcation is a bifurcation at which two EPs (steady-state branches) or two periodic solutions (periodic branches) emerge or disappear. The saddle-node bifurcation of EPs occurs when one of the eigenvalues of a Jacobian matrix for the EP is zero.

Hopf bifurcation. The Hopf bifurcation is a bifurcation at which the stability of an EP reverses with emergence or disappearance of a limit cycle, occurring when eigenvalues of a Jacobian matrix have a single complex conjugate pair and its real part reverses the sign through zero.

RESULTS

Effects of Pacemaker Currents on BP Generation in Single HVM Model

Our preceding study (22) suggests that I_{K1} downregulation, ensuring both the occurrence of a saddle-node bifurcation and instability of the EP with depolarized potentials, yields spontaneous oscillations (BP activity) in HVMs without incorporating any pacemaker current. However, a saddle-node bifurcation to induce BP activity may also be yielded by incorporating pacemaker currents such as I_h, $I_{Ca,T}$, I_{st}, and $I_{Ca,LD}$, which are abundant in SA node primary pacemaker cells but absent or very small in native HVMs. In the preliminary study, we found that these pacemaker currents could not yield BP generation in the model HVM with normal I_{K1} (g_{K1} = 1): BP activity did not appear when g_h, $g_{Ca,T}$, g_{st}, and $g_{Ca,LD}$ were increased up to the limited values of 0.12, 3, 0.02 and 1 nS/pF, respectively (see THEORY AND METHODS) or even when $g_{Ca,T}$, g_{st}, or $g_{Ca,LD}$ was further increased to the critical value above which an EP at depolarized potentials would be stable and thus BP oscillations could not occur (see Fig. 2). Nevertheless, incorporating the pacemaker currents is expected to accelerate BP generation during I_{K1} suppression by increasing the critical g_{K1} value at which a saddle-node bifurcation occurs and thus BP oscillations emerge. We therefore investigated how these currents affect the saddle-node bifurcation and BP generation during I_{K1} suppression.

Effects of incorporating each pacemaker current on BP generation during I_{K1} suppression. As clearly shown in Fig. 4, the saddle-node bifurcation point below which BP oscillations occur shifted toward higher g_{K1} values with increasing g_h, suggesting that expression of I_h accelerates BP generation during I_{K1} suppression by increasing the critical g_{K1} value to induce BP activity. To further examine the effects of incorporating the pacemaker currents on BP generation in the I_{K1}-reduced HVM, we determined the critical g_{K1} value for BP generation (i.e., g_{K1} value at a saddle-node bifurcation) as functions of g_h, $g_{Ca,T}$, g_{st}, or $g_{Ca,LD}$, as well as exploring the influences of the pacemaker currents on the steady-state *I-V* relation at g_{K1} = 1 (Fig. 5). The inward pacemaker currents counteracted the outward component of I_{K1}, inwardly shifting the steady-state *I-V* curve. The critical g_{K1} value increased with increasing g_h; however, it did not reach the control g_{K1} value but reached the maximum of 0.287 (28.7%) at g_h = 0.1039 nS/pF. $I_{Ca,T}$ at higher densities ($g_{Ca,T} \leq 3$ nS/pF) also increased the critical g_{K1}, with its increase limited to <0.266 (26.6%). The effects of I_{st} and $I_{Ca,LD}$ were relatively small within the limited conductance ranges of ≤0.02 and ≤1 nS/pF, respectively.

Effects of coexpression of I_h and other pacemaker currents on BP generation. The critical g_{K1} value did not reach the control g_{K1} value when the conductance of individual currents was increased up to the limited values, or even when $g_{Ca,T}$, g_{st}, or $g_{Ca,LD}$ was increased to more than the Hopf bifurcation point at which BP oscillation would disappear (see Fig. 2). However, the critical g_{K1} may further be increased by coexpression of I_h and the other pacemaker currents that have a different voltage range of activation. As shown in Fig. 6, therefore, we also examined the effects of coexpressing I_h and $I_{Ca,T}$, I_{st}, or $I_{Ca,LD}$ on BP generation

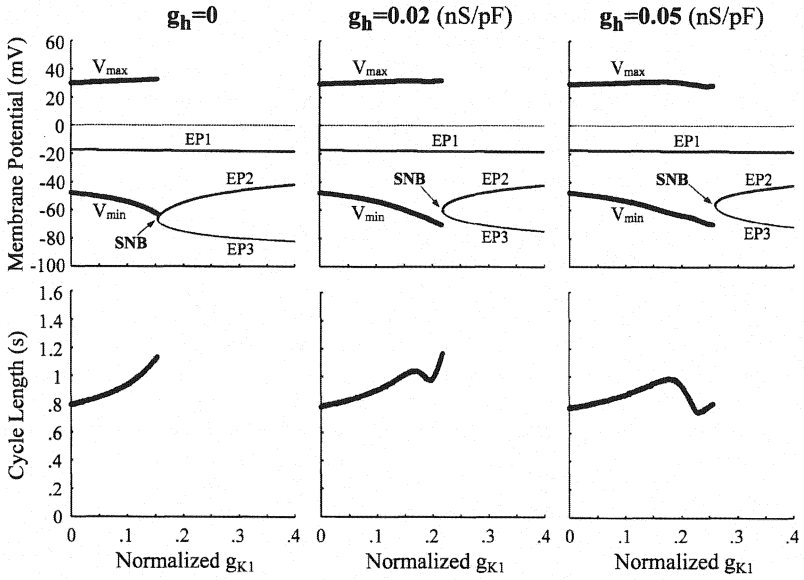

Fig. 4. Bifurcation structures during g_{K1} decreases of the model human ventricular myocyte (HVM) in the absence or presence of the rabbit SA node type I_h. One-parameter bifurcation diagrams for g_{K1} with the steady-state (EP1–3) and stable periodic (V_{min}, V_{max}) branches (*top*), as well as CL of potential oscillations as a function of g_{K1} (*bottom*), are shown for g_h of 0 (*left*), 0.02 (*center*), and 0.05 (*right*) nS/pF. Steady-state BP dynamics were computed by numerically solving differential equations for 60 min at each g_{K1} value (for details see APPENDIX B). The g_{K1} value was reduced at an interval of 0.001, with the initial $[Na^+]_i$ set equal to 5.75 mM at g_{K1} = 0.4. The saddle-node bifurcation point at which EP2 and EP3 merge together and disappear is shown (labeled SNB at g_{K1} = 0.154, 0.219, and 0.260).

during I_{K1} suppression. $I_{Ca,T}$, I_{st}, or $I_{Ca,LD}$ coexpressed with I_h further increased the critical g_{K1} value, i.e., enhanced the accelerating effect of I_h. Nevertheless, the increase in the critical g_{K1} was limited even when I_h and the other pacemaker currents were coexpressed. Drastic increases of $[Na^+]_i$ and $[Ca^{2+}]_i$ at the bifurcation points were caused by coexpression of I_h and the other currents at higher conductance.

Structural Stability and Driving Ability of HVM Pacemaker

One of the drawbacks of the I_{K1}-downregulated HVM pacemaker may be the relatively low structural stability to hyperpolarizing loads such as electrotonic modulations of surrounding nonpacemaker cells, because it lacks the pacemaker currents that are abundant in SA node primary pacemaker cells and contribute to pacemaker depolarization. We therefore ex-

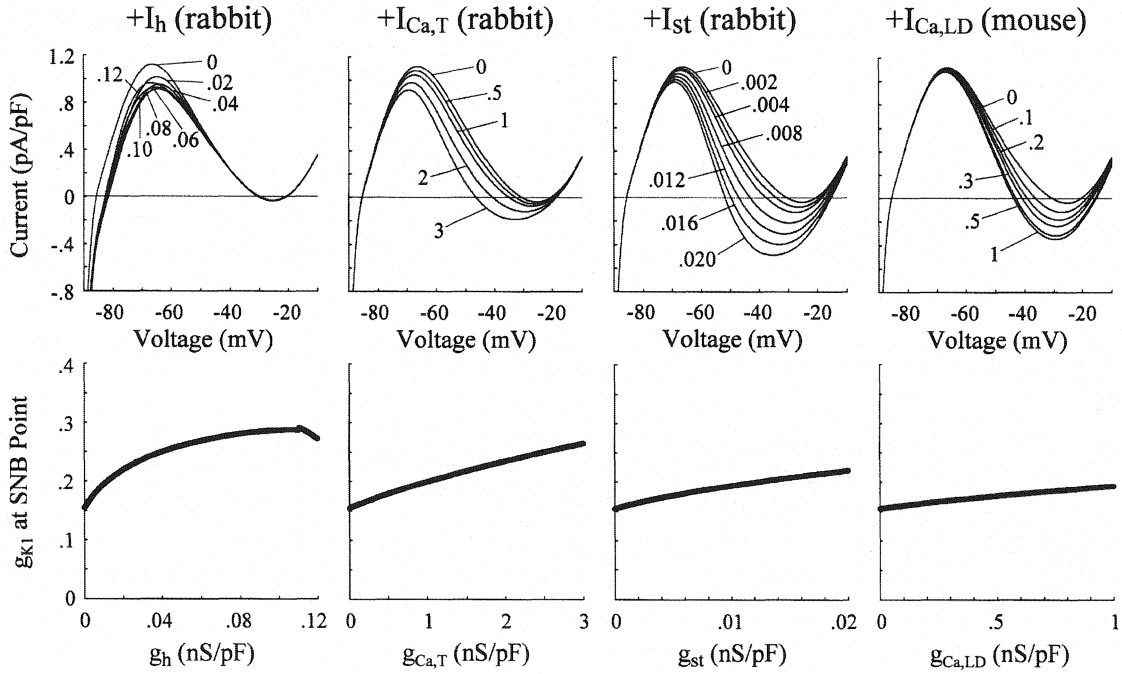

Fig. 5. Effects of incorporating the rabbit SA node I_h, $I_{Ca,T}$, or I_{st} or the mouse SA node $I_{Ca,LD}$ on the steady-state current-voltage (*I-V*) relation and BP generation during I_{K1} inhibition. *Top*: effects on the steady-state *I-V* curve for a HVM with normal I_{K1}. $[K^+]_i$ was fixed at 140 mM. The values of g_h, $g_{Ca,T}$, g_{st}, and $g_{Ca,LD}$ were increased up to 0.12, 3, 0.02, and 1 nS/pF, respectively. *Bottom*: 2-parameter bifurcation diagrams for g_{K1} (*y*-axis) and g_h, $g_{Ca,T}$, g_{st}, or $g_{Ca,LD}$ (*x*-axis), depicting changes in the critical g_{K1} value, i.e., displacements of saddle-node bifurcation points at which BP activity emerges, with increasing g_h, $g_{Ca,T}$, g_{st}, or $g_{Ca,LD}$ at an interval of 0.1 (for g_h and g_{st}) or 1 (for $g_{Ca,T}$ and $g_{Ca,LD}$) pS/pF. The g_{K1} value was reduced at an interval of 0.001–0.0001 for searching for bifurcation points.

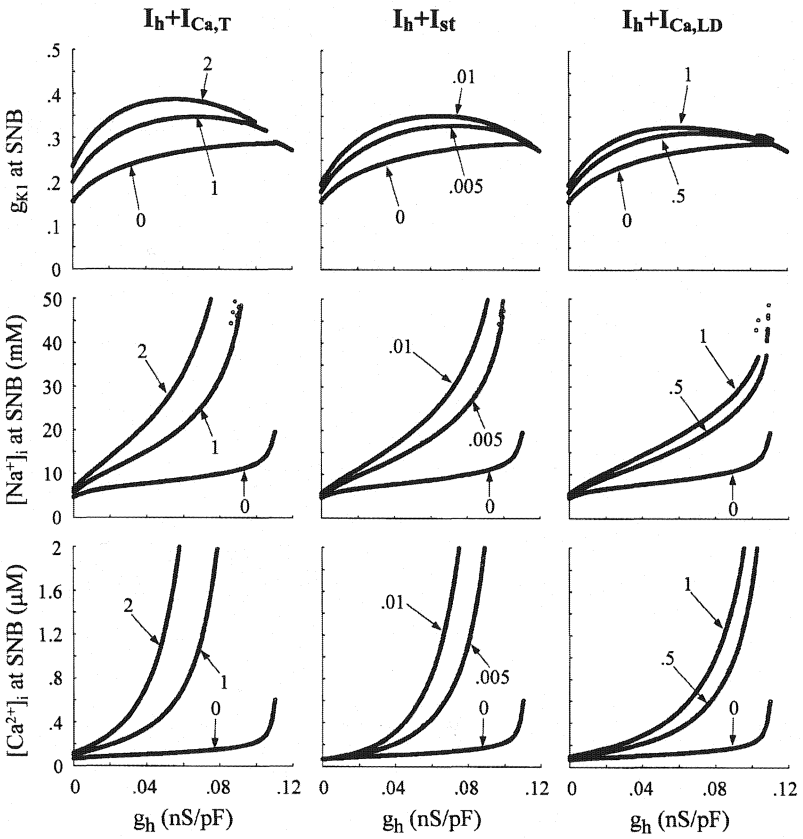

Fig. 6. Effects of coexpression of I_h and $I_{Ca,T}$ (*left*), I_{st} (*center*), or $I_{Ca,LD}$ (*right*) on BP generation during I_{K1} inhibition. *Top*: 2-parameter bifurcation diagrams for g_{K1} (*y*-axis) and g_h (*x*-axis) depicting displacements of saddle-node bifurcation points with increasing g_h at an interval of 0.1 pS/pF. $I_{Ca,T}$, I_{st}, or $I_{Ca,LD}$ was incorporated with maximum conductance set equal to 1–2, 0.005–0.01, and 0.5–1 nS/pF, respectively. The g_{K1} value was reduced at an interval of 0.0001 for searching for bifurcation points. Calculations were stopped when $[Na^+]_i$ exceeded extracellular Na^+ concentration ($[Na^+]_o$) or when $[Ca^{2+}]_i$ exceeded $[Ca^{2+}]_o$. *Middle* and *bottom*: steady-state $[Na^+]_i$ (*middle*) and $[Ca^{2+}]_i$ (*bottom*) at the bifurcation points are shown as functions of g_h.

amined the structural stability of BP cells to electrotonic loads of the adjacent NP cell, using a coupled-cell model in which BP cells (g_{K1} = 0) were connected to a NP cell (g_{K1} = 0.2–1) via the G_C ranging from 0 to 20 nS. The coupled-cell system is also useful in exploring BP cell ability to drive adjacent NP cells.

G_C-dependent behaviors of the coupled-cell system. In the system with one BP cell and one normal HVM (g_{K1} = 1), an EP was stabilized via a Hopf bifurcation at G_C = 0.689 nS, with the BP cell not exhibiting pacemaker activity at G_C values higher than the bifurcation value. Thus the coupling of one BP cell to one normal HVM produced either *1*) BP cell pacemaking at slower rates without driving the NP cell for lower G_C values or *2*) inhibition of BP cell pacemaking for higher G_C values. We could not find a G_C value for which one BP cell could exhibit pacemaking itself and drive the normal HVM but found that three or more BP cells, assumed to be well coupled to form a cluster, were required for driving the normal HVM.

Figure 7 shows the simulated membrane potentials and I_{GJ} at various G_C values for the coupled-cell system composed of five BP cells and one normal HVM. With increasing G_C, the BP rate decreased, with the oscillation amplitude getting larger. The BP cells could induce only subthreshold responses of the HVM at G_C = 2.0 nS, whereas they induced driven action potentials at G_C = 2.5–3.5 nS. Further increase in G_C to 5.0 nS abolished BP activity, which was probably due to hyperpolarizing loads of the NP cell as indicated by positive I_{GJ}.

Influences of size factor and NP cell g_{K1} on G_C-dependent bifurcation structures. The structural stability and driving ability of pacemaker systems are known to depend on the size factor (i.e., the number of BP cells relative to that of NP cells) and g_{K1} of adjacent NP cells (13, 14, 19, 47), which are practically important for engineering of functional BPs in vivo. Therefore, we more minutely explored the effects of the size factor and NP cell g_{K1} on G_C-dependent bifurcation structures of coupled-cell systems.

Stability and dynamics during G_C increases of the coupled-cell system composed of one to seven BP cells and one normal HVM are shown in Fig. 8*A*. EPs and potential extrema were determined for both the BP and NP cells, plotted as functions of G_C values. Hopf and saddle-node bifurcation points were also determined and located in the bifurcation diagrams. In the systems with one to five BP cells, hyperpolarizing loads of the NP cell caused *1*) prolongation of CL with an increase in oscillation amplitude, *2*) irregular dynamics, and then *3*) a bifurcation to quiescence (Hopf bifurcation), with increasing G_C. These behaviors are essentially the same as those reported for interactions of the SA node cell and the atrial or ventricular myocyte (13, 44, 47, 48). The critical G_C value at the Hopf bifurcation to cause stabilization of EPs and cessation of BP activity increased with increasing number of BP cells. One or two BP cells could not drive the normal HVM. With three to five BP cells, the increase in G_C yielded a BP cell ability to drive the normal HVM; however, further increases in G_C led to the cessation of pacemaking and driving via the Hopf bifurcation. The G_C region of driving the normal HVM was very limited with three to five BP cells, whereas it dramatically enlarged when the number of BP cells increased to more than five. With six or more BP cells, a saddle-node bifurcation at which two EPs (EP2, EP3) disappear occurred to ensure the

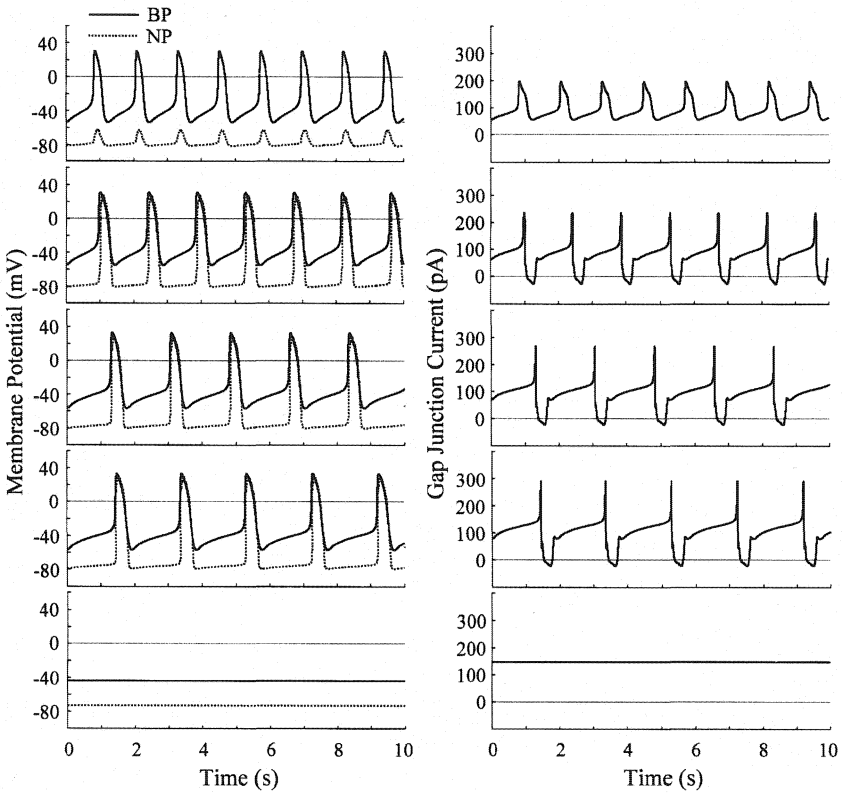

Fig. 7. Simulated dynamic behaviors of a coupled-cell system at various G_C values of 2.0, 2.5, 3.0, 3.5, and 5 nS (from *top* to *bottom*). One normal HVM (g_{K1} = 1) was connected to 5 BP cells (g_{K1} = 0), which were assumed to be well coupled enough to act as a cluster. Membrane potentials of the BP cells and normal HVM (NP), as well as gap junction currents, were computed by numerically solving differential equations for 60 min at each G_C value (for details, see APPENDIX B); the potential and current behaviors during the last 10 s are shown.

robust pacemaking and driving without annihilation (see Fig. 8*A*, *far right*, for 7 BP cells).

The relatively low ability to drive the normal HVM and low structural stability to electrotonic loads of the BP cell appeared to be due to the relatively high I_{K1} density in the normal HVM (14). Therefore, we also explored stability and dynamics during G_C increases of a coupled-cell system consisting of one BP cell and one NP cell with reduced I_{K1}, as shown in Fig. 8*B* for the normalized NP cell g_{K1} of 0.35, 0.30, and 0.25. With the reduced g_{K1} of 0.30 (1.17 nS/pF) or less, increasing G_C did not cause a Hopf bifurcation to quiescence but yielded a saddle-node bifurcation to ensure robust pacemaking and driving.

Effects of Pacemaker Currents on Structural Stability and Driving Ability of HVM Pacemaker

Using the coupled-cell model, we examined how incorporating the pacemaker currents affects the structural stability of BP cells to electrotonic loads of the adjacent NP cell, as well as BP cell ability to drive the NP cell. Figure 8 suggests that a Hopf bifurcation point is just at or close to the point at which BP activity is abolished by hyperpolarizing loads of the NP cell, whereas a saddle-node bifurcation point is the point above which robust pacemaking and driving occur. To assess the effects of the pacemaker currents on the structural stability and driving ability of BP cells, therefore, we focused on the shift in the Hopf bifurcation point, as well as emergence of a saddle-node bifurcation.

Effects of incorporating pacemaker currents on G_C-dependent bifurcation structures. Bifurcation structures during G_C increases were first determined at various conductances of each pacemaker current. We constructed two-parameter bifurcation diagrams in which the critical G_C value at Hopf or saddle-node bifurcation points was plotted as functions of the maximum current conductance. Figure 9 shows the effects of incorporating I_h, $I_{Ca,T}$, I_{st}, or $I_{Ca,LD}$ on the bifurcation structure during G_C increases of the coupled-cell system in which three BP cells were connected to one normal HVM or one BP cell was connected to one NP cell with reduced I_{K1} (g_{K1} = 0.35). Stability and dynamics during G_C increases of the coupled-cell systems incorporating each pacemaker current are illustrated in Fig. 10. The results suggest that individual pacemaker currents affect the G_C-dependent bifurcation structure of the system in different ways.

I_H EFFECT. In the coupled-cell system with three BP cells and one normal HVM, incorporation of I_h (~0.5 nS/pF) did not significantly change the critical G_C value at Hopf bifurcations where an EP is stabilized and BP activity is abolished, not enlarging the region of pacemaking labeled "$P^+D^{\pm}$" (Fig. 9, *top*). As shown in Fig. 10*A*, I_h (0.2 nS/pF) did not enlarge the G_C region where all EPs are unstable and BP activity appears. When I_{K1} of the NP cell was relatively small (g_{K1} = 0.35), however, I_h enlarged the pacemaking and driving region labeled P^+D^+ by producing a saddle-node bifurcation (Fig. 9, *bottom*; Fig. 10*B*). Overexpression of I_h ($g_h > 0.2043$ nS/pF) caused cessation of BP activity at higher G_C values, with a stable resting potential dramatically hyperpolarized probably via drastic increases in $[Na^+]_i$ and $[Ca^{2+}]_i$.

$I_{CA,T}$ EFFECT. Similar to I_h, $I_{Ca,T}$ (~3 nS/pF) did not significantly change the critical G_C value at Hopf bifurcations, not enlarging the $P^+D^{\pm}$ region, in the coupled-cell system with three BP cells and one normal HVM (Fig. 9, *top*). However, higher densities of $I_{Ca,T}$ yielded a saddle-node bifurcation and

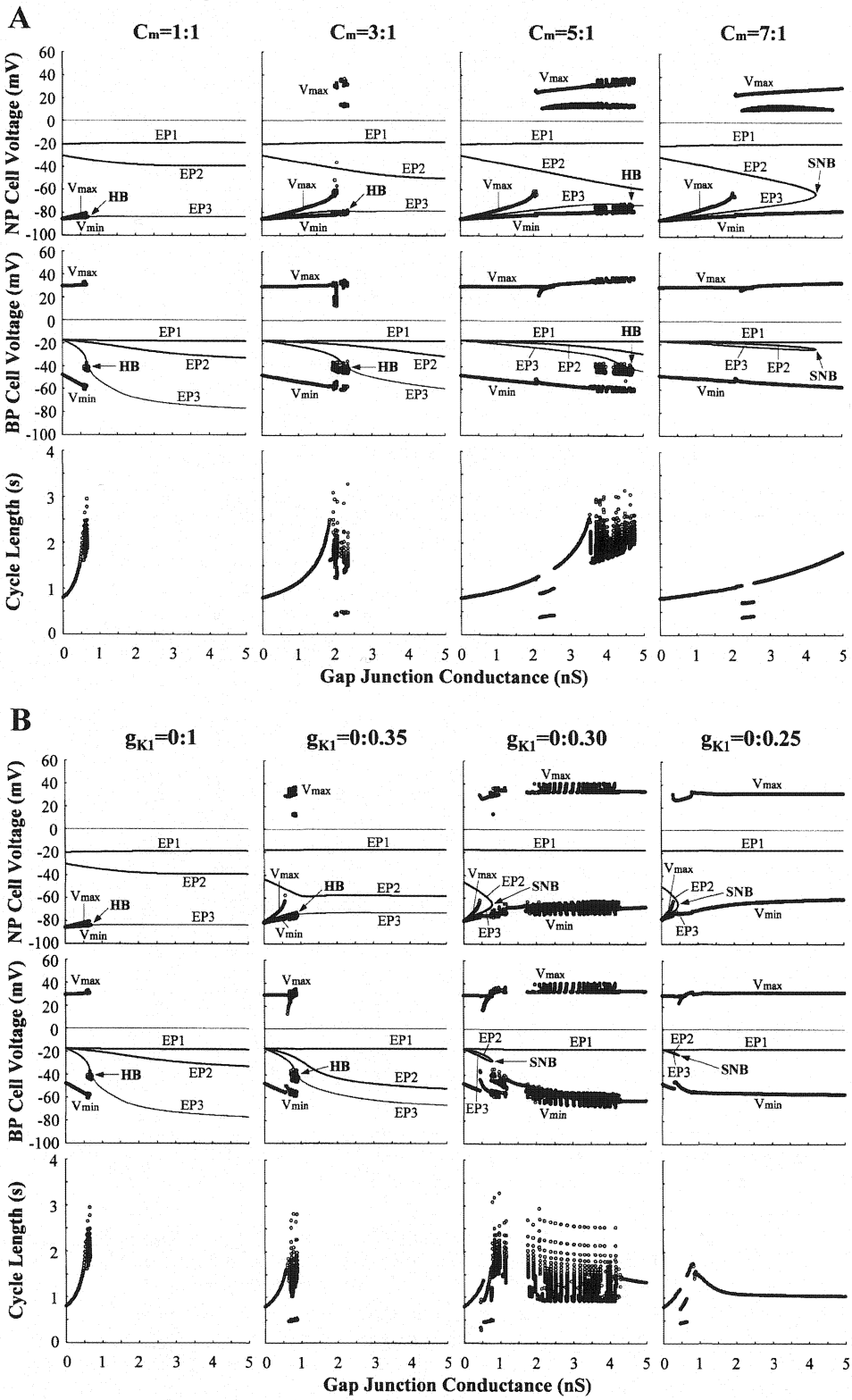

Fig. 8. Stability and dynamics during G_C increases of the coupled-cell systems with various size factors (*A*) or NP cell g_{K1} (*B*). One normal HVM was connected to 1, 3, 5, or 7 I_{K1}-deleted BP cells with all the BP cells assumed to be well coupled (*A*), or 1 I_{K1}-reduced NP cell (g_{K1} = 0.35, 0.30, 0.25) was connected to 1 BP cell (*B*). One-parameter bifurcation diagrams for G_C depicting EPs, Hopf bifurcation, and saddle-node bifurcation points, as well as extrema of potential oscillations (V_{min}, V_{max}), of NP (*top*) and BP (*middle*) cells are shown; CL of BP oscillations is also shown as functions of G_C (*bottom*). Steady-state model cell dynamics were computed by numerically solving the differential equations for 60–120 min at each G_C value. The G_C value was increased up to 5 nS at an interval of 0.01 nS. C_m, cell membrane capacitance.

thus enlarged the P^+D^+ region; $I_{Ca,T}$ at 2 nS/pF enlarged the G_C region where all EPs are unstable and BP activity appears (Fig. 10*A*). When the NP cell I_{K1} was relatively small, $I_{Ca,T}$ dramatically enlarged the P^+D^+ region by producing a saddle-node bifurcation (Fig. 9, *bottom*; Fig. 10*B*). With relatively high conductance of $I_{Ca,T}$, the amplitudes of BP oscillations and driven action potentials of the NP cell were relatively small.

I_{ST} EFFECT. In contrast to I_h or $I_{Ca,T}$, incorporation of I_{st} (~0.02 nS/pF) dramatically shifted Hopf bifurcation points

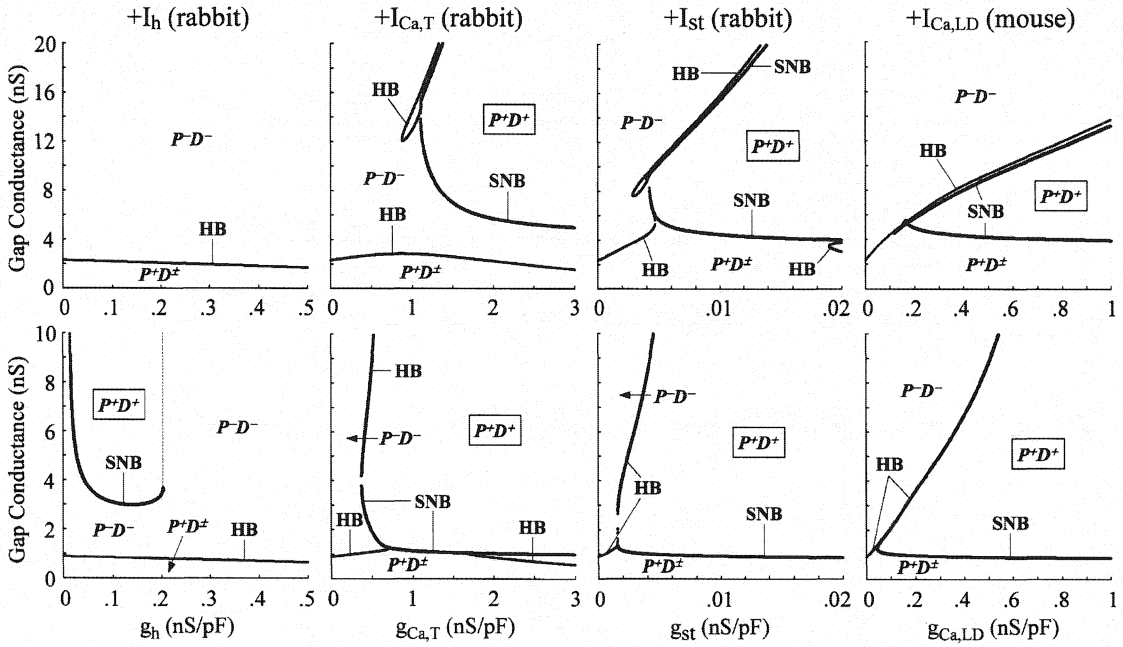

Fig. 9. Effects of incorporating pacemaker currents on bifurcation structures during G_C increases of the coupled-cell model. Three BP cells were connected to 1 normal HVM (*top*), or 1 BP cell was connected to 1 NP cell with a reduced g_{K1} of 0.35 (*bottom*). The rabbit SA node I_h (g_h = 0–0.5 nS/pF), $I_{Ca,T}$ ($g_{Ca,T}$ = 0–3 nS/pF), or I_{st} (g_{st} = 0–0.02 nS/pF) or mouse SA node $I_{Ca,LD}$ ($g_{Ca,LD}$ = 0–1 nS/pF) was incorporated into the BP cells. Two-parameter bifurcation diagrams for G_C and the pacemaker current conductance are shown; the critical G_C values at Hopf bifurcation and saddle-node bifurcation points were plotted as functions of the maximum current conductance. The G_C value was increased up to 10–20 nS at an interval of 0.01 nS for searching for bifurcations. The parameter plane should be divided into 3 areas with different steady states: *1*) nonpacemaking and nondriving (P^-D^-), where BP activity is abolished; 2) pacemaking and driving (P^+D^+), where BP cells exhibit pacemaker activity and drive the NP cell; and *3*) pacemaking and nondriving (P^+D^-), where BP cells exhibit pacemaker activity but do not drive the NP cell. The loci of Hopf and saddle-node bifurcation points actually divided the parameter plane into 3 areas, P^-D^-, P^+D^+, and $P^+D^\pm$ (not P^+D^-). The symbol $P^+D^\pm$ was used for the G_C region lower than the 1st bifurcation point, because NP cell driving might appear in the vicinity of the 1st bifurcation point (see Fig. 8), but it was not possible to determine the critical G_C value at which NP cell driving occurs by this analysis.

toward higher G_C values and further produced a saddle-node bifurcation to ensure robust pacemaking and driving, i.e., enlarged the P^+D^+ region (Fig. 9). I_{st} at 0.01 nS/pF dramatically enlarged the G_C region where BP oscillations occur, with CL of BP oscillations being relatively stable during increases in G_C (Fig. 10).

$I_{CA,LD}$ EFFECT. The effects of $I_{Ca,LD}$ were similar to those of I_{st}, although much larger conductance was required for $I_{Ca,LD}$ to exert the effects as dramatically as I_{st}. Incorporation of $I_{Ca,LD}$ (~1 nS/pF) increased the Hopf bifurcation value and produced a saddle-node bifurcation to enlarge the P^+D^+ region (Fig. 9). As shown in Fig. 10, $I_{Ca,LD}$ (0.5 nS/pF) enlarged the G_C region where BP oscillations occur. However, $I_{Ca,LD}$ at high densities of 0.5–1 nS/pF caused unstable CL and irregular dynamics during increases in G_C.

Influences of altering pacemaker current kinetics on their modulation of bifurcation structures. Individual pacemaker currents affected the G_C-dependent bifurcation structure in different ways, as well as with different potencies. The effects of I_h were completely different from those of the other pacemaker currents, which probably resulted from the difference in the voltage range of activation. Furthermore, the effects of $I_{Ca,T}$, I_{st}, and $I_{Ca,LD}$ were apparently different in the system with three BP cells and one normal HVM: the locus of Hopf bifurcation points at lower G_C was separated from that of saddle-node bifurcation points with $I_{Ca,T}$, but not with I_{st} or $I_{Ca,LD}$. The differences in their effects may result from the large differences in their inactivation kinetics, whereas the different potencies are probably due to the different degrees of the overlap of activation and inactivation curves (see Fig. 1). Thus we examined the effects of incorporating the modified $I_{Ca,T}$ or I_{st} with slowed or accelerated inactivation on G_C-dependent bifurcation structures of the system with three BP cells and one normal HVM (Fig. 11). Changing the inactivation kinetics altered the loci of Hopf bifurcations: the modified $I_{Ca,T}$ with the inactivation time constant (τ_{fT}) 10 times higher than the control yielded a bifurcation diagram similar to that for the original I_{st}; in contrast, the modified I_{st} with the inactivation time constant (τ_{qi}) decreased to 0.01 of the control yielded a locus of Hopf bifurcations separated from that of saddle-node bifurcations, like the original $I_{Ca,T}$. Thus the different effects of the pacemaker currents are at least in part ascribable to the difference in their inactivation kinetics, which appeared to affect the Hopf bifurcation, i.e., stability of EPs, but not the saddle-node bifurcation.

Effects of pacemaker currents on size factor or NP cell g_{K1}-dependent bifurcation structures. To further examine how the pacemaker currents affect the pacemaking and driving of BP cells, bifurcation structures during G_C increase were determined with change in the size factor (the number of BP cells) or NP cell g_{K1} for the modified systems with BP cells incorporating I_h, $I_{Ca,T}$, I_{st}, or $I_{Ca,LD}$, as well as for the standard system not including a pacemaker current (control). We constructed two-parameter bifurcation diagrams in which the critical G_C value at saddle-node or Hopf bifurcation points was plotted as functions of the size factor or normalized NP cell

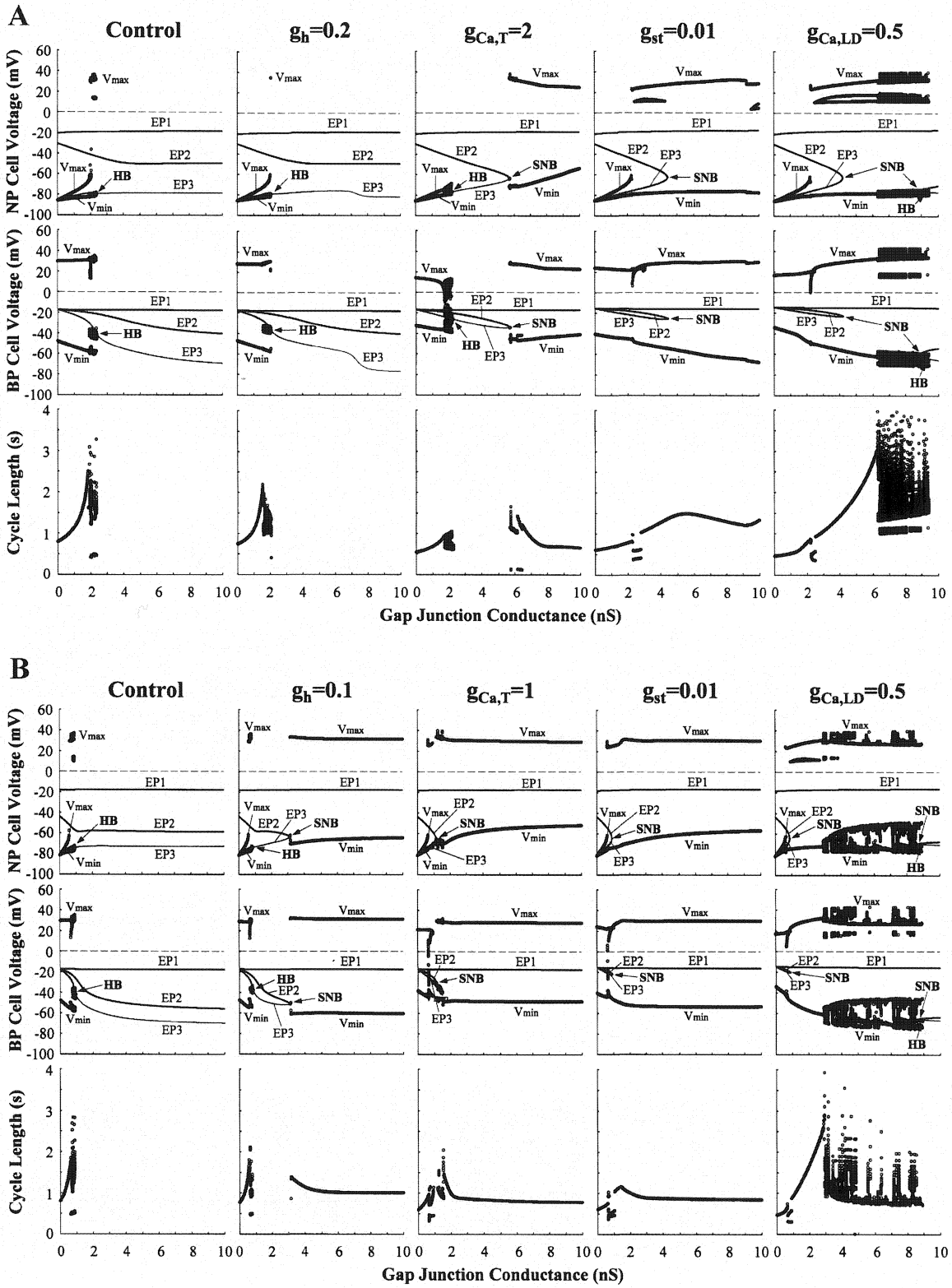

Fig. 10. Stability and dynamics during G_C increases of the coupled-cell systems composed of 3 BP cells and 1 normal HVM (*A*) or 1 BP cell and 1 NP cell with reduced g_{K1} of 0.35 (*B*). I_h (g_h = 0.1–0.2 nS/pF), $I_{Ca,T}$ ($g_{Ca,T}$ = 1–2 nS/pF), I_{st} (g_{st} = 0.01 nS/pF), or $I_{Ca,LD}$ ($g_{Ca,LD}$ = 0.5 nS/pF) was incorporated into the BP cells. Bifurcation diagrams depicting EPs, Hopf bifurcation, and/or saddle-node bifurcation points, as well as dynamics (V_{min}, V_{max}, CL) of the NP and BP cells, are shown as functions of G_C. Steady-state dynamics were computed by numerically solving the differential equations for 30–60 min at each G_C value, which was increased up to 10 nS at an interval of 0.01 nS.

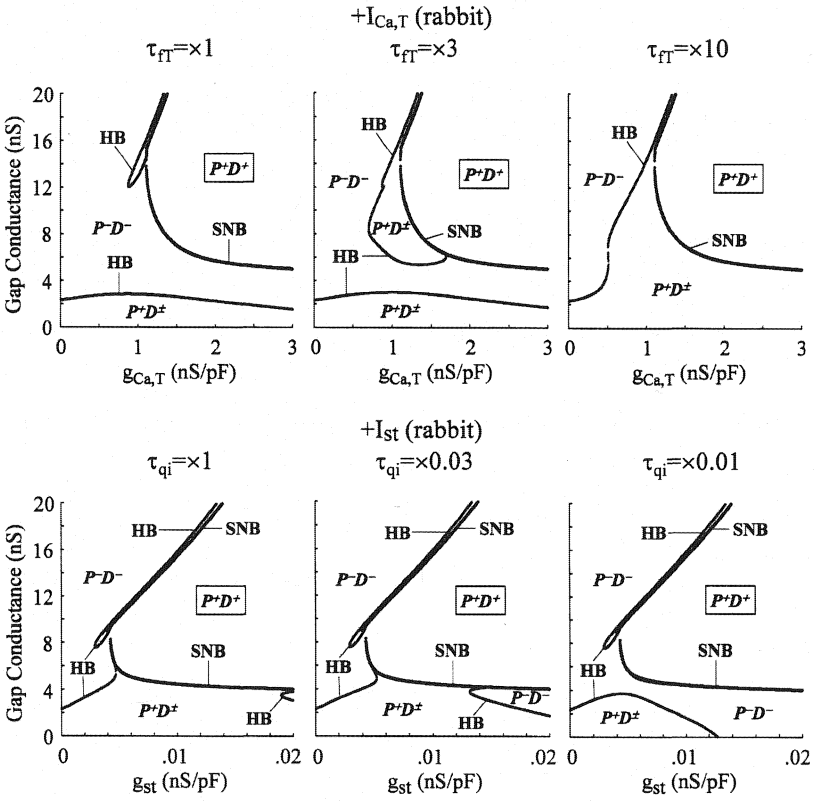

Fig. 11. Effects of the pacemaker currents with different inactivation kinetics on G_C-dependent bifurcation structures of the coupled-cell system composed of 3 BP cells and 1 normal HVM. $I_{Ca,T}$ ($g_{Ca,T}$ = 0–3 nS/pF) or I_{st} (g_{st} = 0–0.02 nS/pF) was incorporated into the BP cells, with their inactivation time constants (τ_{fT}, τ_{qi}) increased or decreased to the values shown as ratios to the control values. Two-parameter bifurcation diagrams for G_C and the pacemaker current conductance were constructed as for Fig. 9.

g_{K1}; one to six BP cells were connected to one normal HVM (Fig. 12) or one BP cell was connected to one NP cell with reduced g_{K1} of 0.2–0.7 (Fig. 13).

Incorporating I_h (0.1–0.2 nS/pF) exerted relatively small effects on the size factor-dependent bifurcation structure of the coupled-cell system with a normal HVM, enlarging the P^+D^+ area only in the region of relatively large size factors and high G_C values (Fig. 12). Decreasing g_{K1} of the NP cell, I_h enlarged the P^+D^+ area by producing a saddle-node bifurcation at relatively low g_{K1} values (Fig. 13). In contrast to I_h, I_{st} (0.01–0.02 nS/pF) dramatically enlarged the P^+D^+ area by facilitating the emergence of saddle-node bifurcations at

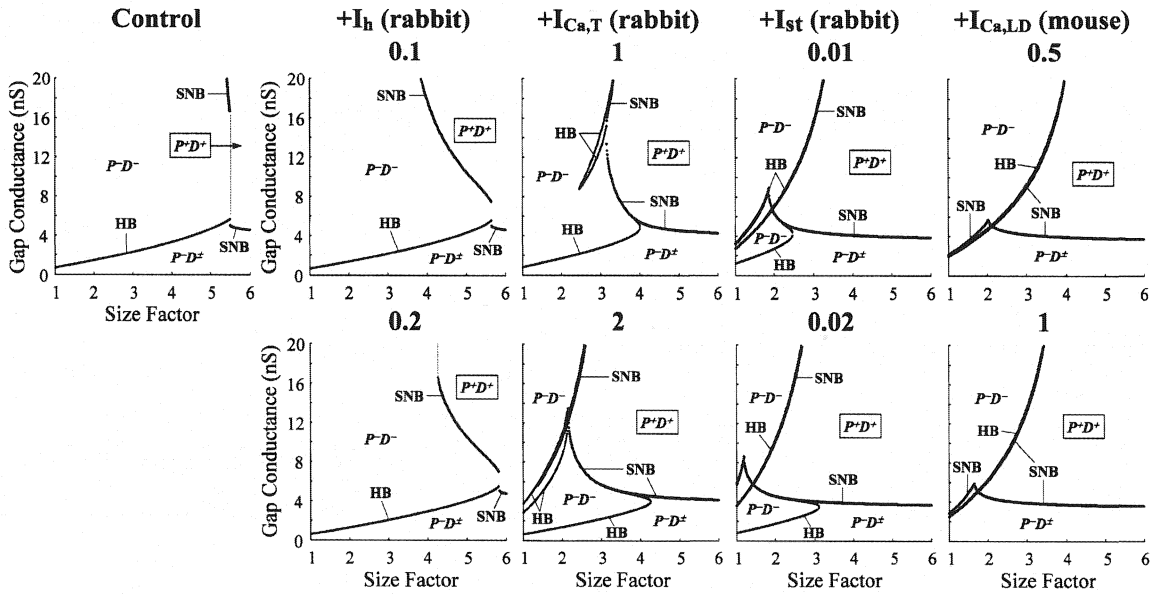

Fig. 12. Effects of incorporating the pacemaker currents on size factor-dependent bifurcation structures of the coupled-cell systems. One to six BP cells were connected to 1 normal HVM. Rabbit SA node I_h (g_h = 0.1–0.2 nS/pF), $I_{Ca,T}$ ($g_{Ca,T}$ = 1–2 nS/pF), or I_{st} (g_{st}=0.01–0.02 nS/pF) or mouse SA node $I_{Ca,LD}$ ($g_{Ca,LD}$ = 0.5–1 nS/pF) was incorporated into the BP cells. Two-parameter bifurcation diagrams depicting the displacement of saddle-node bifurcation and Hopf bifurcation points are shown; the critical G_C value at the bifurcation points was plotted as functions of the size factor (i.e., the number of BP cells) increased at an interval of 0.01. The G_C value was increased up to 20 nS at an interval of 0.01 nS for searching for bifurcations.

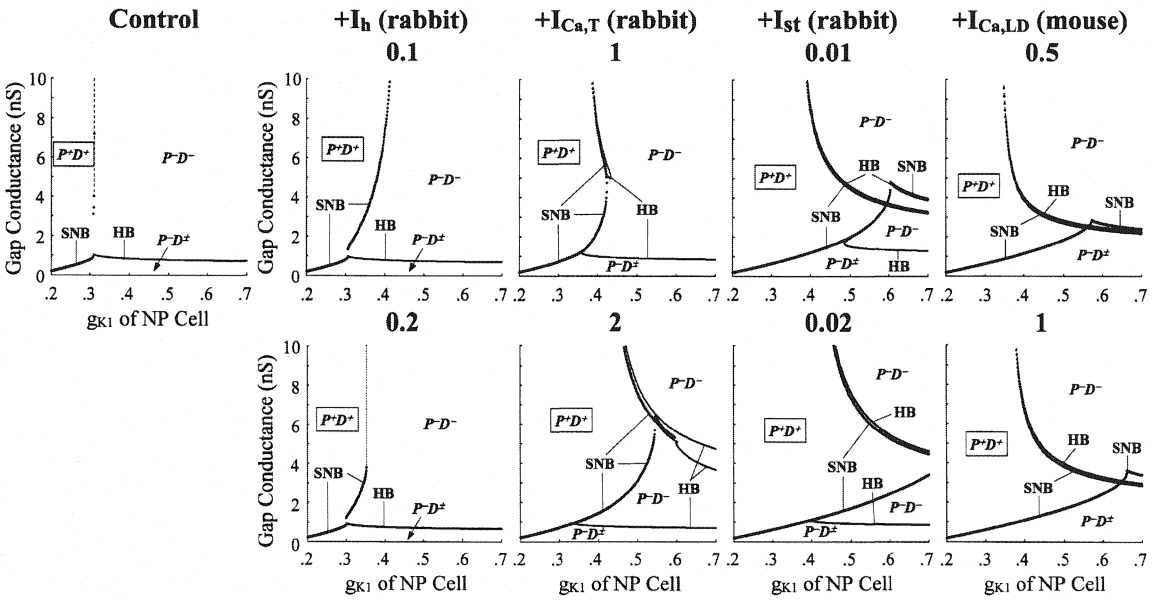

Fig. 13. Effects of incorporating the pacemaker currents on NP cell g_{K1}-dependent bifurcation structures of the coupled-cell systems. One BP cell was connected to 1 NP cell with g_{K1} = 0.2–0.7. I_h (g_h = 0.1–0.2 nS/pF), $I_{Ca,T}$ ($g_{Ca,T}$ = 1–2 nS/pF), I_{st} (g_{st} = 0.01–0.02 nS/pF), or $I_{Ca,LD}$ ($g_{Ca,LD}$ = 0.5–1 nS/pF) was incorporated into the BP cell. The critical G_C value at the bifurcation points was plotted as functions of the normalized g_{K1} of the NP cell decreased at an interval of 0.001. The G_C value was increased up to 10 nS at an interval of 0.01 nS for searching for bifurcations.

smaller size factors and higher g_{K1} values. The effects of $I_{Ca,T}$ (1–2 nS/pF) or $I_{Ca,LD}$ (0.5–1 nS/pF) were similar to those of I_{st}, although much larger conductance was required for $I_{Ca,T}$ or $I_{Ca,LD}$ to exert effects as dramatically as I_{st}.

DISCUSSION

Possible Roles of Pacemaker Currents in Creation of BP Cells

We first investigated whether incorporating pacemaker currents exerts beneficial effects on creation of BP cells by constructing two-parameter bifurcation diagrams in which the critical g_{K1} value (saddle-node bifurcation point) to produce BP activity was plotted as functions of the maximum current conductance.

Pacemaker currents facilitate BP generation during I_{K1} suppression. Our results suggest that the pacemaker currents, especially I_h, can facilitate BP generation during I_{K1} suppression, although their effects were limited (Fig. 5). The mechanism underlying the facilitation of BP generation appears to be relatively simple: the inward pacemaker currents counteract the outward component of I_{K1}, inwardly shift the steady-state *I-V* curve, and thus lead to a saddle-node bifurcation at a higher g_{K1} value (see Fig. 5, *top*). Nevertheless, the critical g_{K1} value never reached the control value of 1, suggesting that any pacemaker currents cannot yield BP activity in the HVM with normal I_{K1}.

I_{K1} downregulation is a requisite for BP generation in HVM. The limited effects of the pacemaker currents appear to be due to the induction of intracellular Na^+ and Ca^{2+} overloads: as shown in Fig. 6, overexpressions of the pacemaker currents cause increases in $[Na^+]_i$ and $[Ca^{2+}]_i$, which enhance the outward Na^+-K^+ pump current, attenuate the inward background Na^+ and Ca^{2+} currents (by decreasing the driving force for Na^+ and Ca^{2+}), and thus counteract the inward shift of *I-V* curves that leads to a saddle-node bifurcation. When $[Na^+]_i$, which is a state variable in the standard system, was fixed at the control value of 6.14 mM (for g_{K1} = 1) to prevent the pacemaker currents causing Na^+ and Ca^{2+} overloads, increasing the pacemaker currents led to BP generation via a saddle-node bifurcation without inhibition of I_{K1}, albeit with the requirement of very high conductance (e.g., $g_h > 0.996$ nS/pF) (data not shown). Thus Na^+ and Ca^{2+} overloads would prevent a bifurcation to BP generation during enhancements of the pacemaker currents. In conclusion, incorporating I_h and/or the other pacemaker currents would not yield BP generation in HVMs with normal I_{K1}, and thus I_{K1} downregulation would be necessary for constructing a BP cell system from HVMs. Inconsistent with our result, Viswanathan et al. (46) reported that the rabbit SA node I_h could induce BP activity in the Luo-Rudy guinea pig ventricular model without reducing I_{K1}. We are not sure about the reason for this inconsistency. Further studies are required to clarify whether the effects of I_h and other pacemaker currents depend on species (human vs. guinea pig) or on the property of a model itself as well as whether expressing I_h can actually induce BP activity in real NP myocytes of the ventricle.

Overexpression of I_h has been reported to induce BP activity (or increase BP rates) in canine atrial or Purkinje myocytes (32, 36). Figure 5 indicates that increasing I_h alone can induce BP activity via a saddle-node bifurcation if g_{K1} is smaller than the control value of 3.9 nS/pF, e.g., when a g_{K1} value is 25% of the control value (0.975 nS/pF), increasing g_h to 0.0403 nS/pF or more yields BP generation. Koumi et al. (17) reported that a slope conductance at a reversal (K^+ equilibrium) potential of the human atrial I_{K1} (0.134 nS/pF) is only 18.3% of that of the human ventricular I_{K1} (0.732 nS/pF). As suggested by previous reports (14, 32, 36), expression of I_h alone would induce pacemaker activity in myocytes with relatively low density of I_{K1}, such as atrial and Purkinje myocytes.

Possible Roles of Pacemaker Currents in Robust Pacemaking and Driving of Functional BP

Using the coupled-cell model, we examined whether incorporation of pacemaker currents exerts beneficial effects on BP functions, i.e., whether it improves the structural stability of BPs to electrotonic loads of adjacent NP cells and the BP ability to drive the ventricle. The results suggest that individual pacemaker currents affect the BP functions in different ways.

I_h effect is relatively small and NP cell g_{K1} dependent. The effects of I_h on G_C-dependent bifurcation structures were quite different from those of the other pacemaker currents, which is probably due to the difference in the voltage range of activation. I_h did not significantly improve the structural stability of BP cells to electrotonic loads of the normal HVM or the BP cell ability to drive the normal HVM (Figs. 9 and 10*A*). When NP cell I_{K1} was relatively small, however, I_h improved the structural stability and driving ability of BP cells by producing a saddle-node bifurcation (Figs. 9 and 10*B*). Moreover, the effects of I_h were shown to depend on I_{K1} density of the NP cell, as well as the size factor (Figs. 12 and 13). These results suggest that I_h can support the robust pacemaking and driving of BPs only when I_{K1} density in adjacent NP cells is relatively small. I_{K1} density is much larger in the human ventricle than in the human atrium (17); thus I_h may support the robust pacemaking and driving of BPs (as well as the SA node) in the atrium with relatively small I_{K1}, but not in the ventricle with relatively large I_{K1}. Possible roles of I_h in the working of ventricular BPs could be to modulate pacemaker frequency in response to autonomic regulations, as well as to prevent excess hyperpolarization, rather than to improve the structural stability and driving ability by destabilizing EPs or yielding saddle-node bifurcations.

$I_{Ca,T}$ effect is NP cell g_{K1} dependent and characterized by shrinkage of voltage oscillations. Similar to I_h, $I_{Ca,T}$ did not improve the structural stability of BP cells to electrotonic loads of the normal HVM by shifting the Hopf bifurcation point at lower G_C values (Fig. 9, *top*); the low efficacy of $I_{Ca,T}$ appeared to be due to the rapid inactivation kinetics, because the modified $I_{Ca,T}$ with slowed inactivation significantly increased the Hopf bifurcation value (Fig. 11). Nevertheless, higher densities of $I_{Ca,T}$ improved the structural stability and driving ability of BP cells by producing a saddle-node bifurcation. The effects of $I_{Ca,T}$ also depend on the NP cell I_{K1}, as well as the size factor (Figs. 9, 12, and 13); $I_{Ca,T}$ may effectively improve the functions of BPs in the atrium, whereas much larger $I_{Ca,T}$ is required for the ventricle. However, higher densities of $I_{Ca,T}$ caused shrinkage in BP oscillations and driven action potentials of the NP cell (Fig. 10), which is probably due to the rapid kinetics of $I_{Ca,T}$ inactivation and is not desirable for functional BPs.

I_{st} most dramatically improves structural stability and driving ability of BP cells. In contrast to I_h or $I_{Ca,T}$, I_{st} at relatively low conductance dramatically improved the structural stability and driving ability of BP cells by shifting Hopf bifurcation points toward higher G_C values and yielding a saddle-node bifurcation (Fig. 9), producing BP oscillations with stable frequency over the broad G_C range (Fig. 10). Furthermore, I_{st}, as well as $I_{Ca,T}$ and $I_{Ca,LD}$, may contribute to reducing the critical size of a BP system (i.e., the number of BP cells) to be required for driving the ventricle: with I_{st} at 0.01 nS/pF, four BP cells are enough to yield robust pacemaking and driving of a normal HVM via creation of a saddle-node bifurcation, whereas more than five BP cells are required without a pacemaker current (see Fig. 12). Our results suggest that I_{st}, exhibiting relatively slow inactivation kinetics, most dramatically improves the structural stability and driving ability of the HVM pacemaker. I_{st} may be indispensable for robust pacemaking and driving of ventricular BPs.

$I_{Ca,LD}$ effect is similar to I_{st} effect but characterized by generation of irregular dynamics. The effects of $I_{Ca,LD}$ were qualitatively similar to those of I_{st}, although its potency was much smaller (Figs. 9, 12, and 13). However, $I_{Ca,LD}$ at high densities caused unstable CL and irregular dynamics during increases in G_C, which is possibly a consequence of producing Ca^{2+} overload conditions, not desirable for functional BPs. We suppose that the role of $I_{Ca,LD}$ in the working of pacemaker systems is essentially the same as that of $I_{Ca,LC}$: $I_{Ca,LD}$ may play a major role in producing the action potential upstroke as well as excitation-contraction coupling, rather than in supporting robust pacemaking and driving.

Implications and Significance of Study

In the present study, we used stability and bifurcation analyses to investigate the effects of pacemaker currents on creation and modulations of the HVM pacemaker. Previous reports indicate that exploring bifurcation structures of SA node or ventricular models is useful for general understanding and systematic descriptions of the dynamical mechanisms of normal and abnormal pacemaker activities, e.g., the roles of individual currents in pacemaking (4, 9, 21, 22, 24, 45). Pacemaker currents are not indispensable for basal pacemaking of SA node cells (20, 21) or BP cells (22, 46). As shown in this study for BP cells, however, the pacemaker currents may be necessary for constructing a pacemaker system with high structural stability and high driving ability, as well as for finer regulations of pacemaking rates.

Bifurcation analyses of model cell systems may also allow us to accurately predict and properly control the dynamics and bifurcation structures of real cells, possibly applicable to cell system engineering to develop functional BPs from native cardiomyocytes or ES cells for gene or cell therapy of bradyarrhythmias (8, 10, 15, 25, 28, 32, 36, 50). Pacemaker currents are not necessarily required for creating BP cells (22, 46). Nevertheless, stable transfection of pacemaker channel genes or transplantation of BP cells expressing pacemaker channels (e.g., ES cell-derived SA node cells) to host tissues may be helpful or even necessary for creating functional BPs with robust pacemaking and driving, as well as responsiveness to autonomic regulations. This study suggests that *1*) expression of I_h (or the other pacemaker currents) is not indispensable but is helpful for creating BP cells from HVMs, *2*) expression of I_h improves structural stability and driving ability of BPs when I_{K1} density in adjacent NP cells is relatively small, as in the atrium, and *3*) expression of I_{st}, i.e., a pacemaker current with relatively slow inactivation kinetics, may especially be effective in yielding robust BP activity with stable frequency.

Limitations and Perspectives of Study

As mentioned in our previous article (22), the limitations of our study include incompleteness of the HVM model due to the

lack of experimental data from HVMs as well as the lack of experimental evidence for bifurcation structures of real myocytes. More elaborate HVM models, such as recently published ones (12, 42), with refinements of formulas to be suitable for bifurcation analyses would have to be developed for more detailed investigations using the theoretical approach. In addition, the pacemaker current formulas based on experiments for human cardiomyocytes should be used in future studies.

As suggested by Silva and Rudy (41), a potential advantage of the BP over the electronic pacemaker is responsiveness to β-adrenergic stimulation (β-AS). BP responsiveness to β-AS was very limited in the guinea pig ventricular model (41). We also found in the simulations according to their method that the HVM pacemaker did not exhibit a significant rate increase in response to β-AS, suggesting that the ventricular pacemaker is less sensitive to β-AS than the SA node pacemaker. Such low sensitivity to β-AS of the ventricular pacemaker would be due at least in part to the lack of the pacemaker currents that are abundant in SA node primary pacemaker cells (20, 21, 27, 31, 51) and are known to be enhanced by β-AS (26, 35, 43). Nevertheless, we did not show the data on this issue, because it is very important but beyond the aim of this study and because our model lacks the intracellular modulating factors such as cAMP and protein kinases. Further sophisticated models incorporating the modulating factors, as developed by Saucerman et al. (38), would be required.

We used the simple coupled-cell system to investigate the structural stability and driving ability of BP cells, believing that this study is valuable as a first step toward development of a theoretical background for engineering of functional BPs. Nevertheless, a real pacemaker system such as the intact SA node has much more complex architectures to facilitate optimization of the electrical loading by surrounding atrial or ventricular tissues (1, 2, 14, 44). Thus more elaborate multicellular models are required for investigation of the structural stability to electrotonic loads and ability to drive the heart of a BP system in vivo and of how to create BP systems with robust pacemaking and driving. In the coupled-cell model, the critical size factor (the critical number of BP cells) for stable driving of a normal HVM was quite large, e.g., at least six BP cells were required in the absence of a pacemaker current (see Figs. 8*A* and 12). A similar size effect, a size factor of 5, was previously reported for other coupled-cell systems composed of SA node cells and ventricular myocytes (19, 47). However, the coupled-cell model cannot predict the critical size of a BP to be required for stable driving of the ventricle. Using a two-dimensional system in which real atrioventricular node or model SA node cells were coupled to ventricular or atrial model cells, Joyner et al. (14) determined the critical size of the pacemaker cells for driving the surrounding quiescent cells and suggested that the critical size depends on the scale of the systems, I_{K1} density in surrounding NP cells, G_C values, and many other factors. Moreover, the roles of pacemaker currents in pacemaking and driving of BPs may also change depending on the dimension of the systems, as well as the number of BP cells, I_{K1} of adjacent NP cells, and G_C values (see Figs. 12 and 13). Further studies using multicellular (2 or 3 dimensional) models are required to determine the critical BP size for driving the ventricle and to determine how incorporating pacemaker currents affects critical BP size and BP functions.

APPENDIX A: GLOSSARY

General

F	Faraday constant
V	Membrane potential (mV)

Cell Geometry

C_m	Cell membrane capacitance
C_{BP}	C_m of BP cells
C_{NP}	C_m of NP cells
V_i	Myoplasmic volume available for Ca^{2+} diffusion
V_{rel}	Volume of junctional SR (Ca^{2+} release store)
V_{up}	Volume of network SR (Ca^{2+} uptake store)

Ionic Concentrations

$[Na^+]_o$	Extracellular Na^+ concentration
$[K^+]_o$	Extracellular K^+ concentration
$[Ca^{2+}]_o$	Extracellular Ca^{2+} concentration
$[Na^+]_i$	Intracellular Na^+ concentration
$[K^+]_i$	Intracellular K^+ concentration
$[Ca^{2+}]_i$	Myoplasmic Ca^{2+} concentration
$[Ca^{2+}]_{rel}$	Ca^{2+} concentration in junctional SR
$[Ca^{2+}]_{up}$	Ca^{2+} concentration in network SR

Equilibrium Potentials

E_{Na}	Equilibrium (Nernst) potential for Na^+
E_K	Equilibrium (Nernst) potential for K^+

Sarcolemmal Ionic Currents

g_h	Maximum I_h conductance
$g_{Ca,T}$	Maximum $I_{Ca,T}$ conductance
g_{st}	Maximum I_{st} conductance
$g_{Ca,LD}$	Maximum $I_{Ca,LD}$ conductance
d_L	Activation gating variable for $I_{Ca,L}$
f_L	Voltage-dependent inactivation gating variable for $I_{Ca,L}$
d_T	Activation gating variable for $I_{Ca,T}$
f_T	Inactivation gating variable for $I_{Ca,T}$
p_a	Activation gating variable for I_{Kr}
n	Activation gating variable for I_{Ks}
q	Inactivation gating variable for I_{to}
y	Activation gating variable for I_h
q_a	Activation gating variable for I_{st}
q_i	Inactivation gating variable for I_{st}
α_{qa}	Opening rate constant for q_a
β_{qa}	Closing rate constant for q_a
α_{qi}	Opening rate constant for q_i
β_{qi}	Closing rate constant for q_i
d_{LD}	Activation gating variable for $I_{Ca,LD}$
f_{LD}	Voltage-dependent inactivation gating variable for $I_{Ca,LD}$
$f_{Ca,\infty}$	Ca^{2+}-dependent inactivation gating variable for $I_{Ca,LD}$
h	Inactivation gating variable for I_{Na}
x_∞	Steady-state value of a gating variable x
τ_x	Time constant for a gating variable x
$J_{Ca,net}$	Net Ca^{2+} flux through the sarcolemmal membrane
$J_{Na,net}$	Net Na^+ flux through the sarcolemmal membrane

Intracellular Ca^{2+} Dynamics (SR Function and Ca^{2+} Buffering)

J_{rel}	Ca^{2+} release flux from junctional SR to subspace
J_{up}	Ca^{2+} uptake flux from myoplasm to network SR

J_{tr}	Ca^{2+} transfer flux from network SR to junctional SR
J_{leak}	Ca^{2+} leak flux from network SR to myoplasm
$[CM]_{tot}$	Total calmodulin concentration
$[CQ]_{tot}$	Total calsequestrin concentration
$[TC]_{tot}$	Total concentration of troponin-Ca complex
f_{TC}	Fractional occupancy of troponin-Ca complex by Ca^{2+}
f_{CM}	Fractional occupancy of calmodulin by Ca^{2+} in myoplasm
f_{CQ}	Fractional occupancy of calsequestrin by Ca^{2+}
K_{dCM}	Ca^{2+}-binding constant for calmodulin
K_{dCQ}	Ca^{2+}-binding constant for calsequestrin
B_{CM}	Scaling factor for fast Ca^{2+} buffering by calmodulin
B_{CQ}	Scaling factor for fast Ca^{2+} buffering by calsequestrin

APPENDIX B: MODEL EQUATIONS

The mathematical expressions used for the pacemaker currents (I_h, $I_{Ca,T}$, I_{st}, $I_{Ca,LD}$), as well as differential equations for state variables of the coupled-cell system, are given below. Units are millivolts, picoamperes, nanosiemens, picofarads, milliseconds, millimolar, and liters. The temperature assumed for the model is 37°C. The symbols used and their definitions are the same as those in our rabbit SA node model (20). Expressions for other currents and dynamics of SR Ca^{2+} handling, as well as standard parameter values and initial conditions for computations, are given in our previous article (22). See APPENDIX A for symbol definitions.

Hyperpolarization-Activated Current (I_h)

Rabbit SA node I_h from Kurata et al. (20) model [adopted from Wilders et al. (49) model].

$$I_{hK} = 0.6167 \cdot g_h \cdot (V - E_K) \cdot y^2 \quad (A1)$$

$$I_{hNa} = 0.3833 \cdot g_h \cdot (V - E_{Na}) \cdot y^2 \quad (A2)$$

$$I_h = I_{hK} + I_{hNa} \quad (A3)$$

$$y_\infty = 1/\{1 + \exp[(V + 64)/13.5]\} \quad (A4)$$

$$\tau_y = 0.71665/\{\exp[-(V + 386.9)/45.302] + \exp[(V - 73.08)/19.231]\} \quad (A5)$$

Human ventricle I_h from Cerbai et al. (3).

$$I_{hK} = 0.6167 \cdot g_h \cdot (V - E_K) \cdot y \quad (A6)$$

$$I_{hNa} = 0.3833 \cdot g_h \cdot (V - E_{Na}) \cdot y \quad (A7)$$

$$I_h = I_{hK} + I_{hNa} \quad (A8)$$

$$y_\infty = 1/\{1 + \exp[(V + 80.6)/6.8]\} \quad (A9)$$

$$\tau_y = 1{,}000/[\exp(-2.9\text{–}0.04 \cdot V) + \exp(3.6 + 0.11 \cdot V)] \quad (A10)$$

Human HCN2 current from Moroni et al. (29).

$$I_{hK} = 0.6167 \cdot g_h \cdot (V - E_K) \cdot y^2 \quad (A11)$$

$$I_{hNa} = 0.3833 \cdot g_h \cdot (V - E_{Na}) \cdot y^2 \quad (A12)$$

$$I_h = I_{hK} + I_{hNa} \quad (A13)$$

$$y_\infty = 1/\{1 + \exp[(V + 83.1)/7.89]\} \quad (A14)$$

$$\tau_y = 438.6/[0.00053 \cdot \exp(-V/13.16) + 141.17 \cdot \exp(V/13.16))] \quad (A15)$$

T-type Ca^{2+} Channel Current ($I_{Ca,T}$)

Rabbit SA node $I_{Ca,T}$ from Kurata et al. (20) model [adopted from Demir et al. (5) model].

$$I_{Ca,T} = g_{Ca,T} \cdot (V - 45) \cdot d_{T,\infty} \cdot f_T \quad (A16)$$

$$d_{T,\infty} = 1/\{1 + \exp[-(V + 26.3)/6]\} \quad (A17)$$

$$f_{T,\infty} = 1/\{1 + \exp[(V + 61.7)/5.6]\} \quad (A18)$$

$$\tau_{fT} = 1/(0.0153 \cdot \exp[-(V + 61.7)/83.3] + 0.015 \cdot \exp[(V + 61.7)/15.38)] \quad (A19)$$

Rabbit ventricle $I_{Ca,T}$ from Pugligi-Bers (34) model.

$$I_{Ca,T} = g_{Ca,T} \cdot (V - E_{Ca}) \cdot d_{T,\infty} \cdot f_T \quad (A20)$$

$$d_{T,\infty} = 1/\{1 + \exp[-(V + 48)/6.1]\} \quad (A21)$$

$$f_{T,\infty} = 1/\{1 + \exp[(V + 66)/6.6]\} \quad (A22)$$

$$\tau_{fT} = 32/\{1 + \exp[(V + 65)/5]\} + 8 \quad (A23)$$

Sustained Inward Current (I_{st})

Rabbit SA node I_{st} from Kurata et al. (20) model.

$$I_{st} = g_{st} \cdot (V - 37.4) \cdot q_{a,\infty} \cdot q_i \quad (A24)$$

$$q_{a,\infty} = 1/\{1 + \exp[-(V + 57)/5]\} \quad (A25)$$

$$\alpha_{qi} = 1[3{,}100 \cdot \exp(V/13) + 700 \cdot \exp(V/70)] \quad (A26)$$

$$\beta_{qi} = 1/[95 \cdot \exp(-V/10) + 50 \cdot \exp(-V/700)] + 0.000229/[1 + \exp(-V/5)] \quad (A27)$$

$$q_{i,\infty} = \alpha_{qi}/(\alpha_{qi} + \beta_{qi}) \quad (A28)$$

$$\tau_{qi} = 6.65/(\alpha_{qi} + \beta_{qi}) \quad (A29)$$

Rat SA node I_{st} from Shinagawa et al. (40).

$$I_{st} = g_{st} \cdot (V - 18) \cdot q_{a,\infty} \cdot q_i \quad (A30)$$

$$\alpha_{qa} = 1/[0.15 \cdot \exp(-V/11) + 0.2 \cdot \exp(-V/700)] \quad (A31)$$

$$\beta_{qa} = 1/[16 \cdot \exp(V/8) + 15 \cdot \exp(V/50)] \quad (A32)$$

$$q_{a,\infty} = \alpha_{qa}/(\alpha_{qa} + \beta_{qa}) \quad (A33)$$

$$\alpha_{qi} = 1/[3{,}100 \cdot \exp(V/13) + 700 \cdot \exp(V/70)] \quad (A34)$$

$$\beta_{qi} = 1/[95 \cdot \exp(-V/10) + 50 \cdot \exp(-V/700)] + 0.000229/[1 + \exp(-V/5)] \quad (A35)$$

$$q_{i,\infty} = \alpha_{qi}/(\alpha_{qi} + \beta_{qi}) \quad (A36)$$

$$\tau_{qi} = 1/(\alpha_{qi} + \beta_{qi}) \quad (A37)$$

Low-Voltage-Activated L-Type Ca^{2+} Channel Current ($I_{Ca,LD}$)

$$I_{Ca,LD} = g_{Ca,LD} \cdot (V - 52.8) \cdot d_{LD,\infty} \cdot f_{LD} \cdot f_{Ca,\infty} \quad (A38)$$

$$d_{LD,\infty} = 1/\{1 + \exp[-(V + 7.64)/6.32]\} \quad (A39)$$

$$f_{LD,\infty} = 1/\{1 + \exp[(V + 24.6)/6.9]\} \quad (A40)$$

$$\tau_{fLD} = 17.925/(0.1389 \cdot \exp\{-[0.0358 \cdot (V - 10.9)]^2\} + 0.0519) \quad (A41)$$

$$f_{Ca,\infty} = 1/[1 + ([Ca^{2+}]_i/0.00035)] \quad (A42)$$

Differential Equations for State Variables

Membrane potential (V).

$$dV_{BP}/dt = I_{stim} - I_{total(BP)} - I_{GC}/C_{BP} \quad (A43)$$

$$dV_{NP}/dt = -I_{total(NP)} + I_{GC}/C_{NP} \quad (A44)$$

$$I_{total} = I_{Ca,L} + I_{Kr} + I_{Ks} + I_{to} + I_{Na} + I_{K1} + I_{Na,b} + I_{Ca,b} + I_{NaK} + I_{NaCa} + I_{pCa} + I_h + I_{Ca,T} + I_{st} + I_{Ca,LD} \quad (A45)$$

Gating variables.

$$dx/dt = (x_\infty - x)/\tau_x \quad [x = d_L, f_L, p_a, n, q, h, d_R, f_R, y, d_T, f_T, q_a, q_i, d_{LD}, f_{LD}] \tag{A46}$$

Intracellular ion concentrations.

$$d[Ca^{2+}]_i/dt = B_{CM} \cdot [(-J_{Ca,net} + J_{rel} \cdot V_{rel} - J_{up} \cdot V_{up} + J_{leak} \cdot V_{up})/V_i - [TC]_{tot} \cdot df_{TC}/dt] \tag{A47}$$

$$B_{CM} = 1/\{1 + [CM]_{tot} \cdot K_{dCM}/(K_{dCM} + [Ca^{2+}]_i)^2\} \tag{A48}$$

$$d[Ca^{2+}]_{rel}/dt = B_{CQ} \cdot (J_{tr} - J_{rel}) \tag{A49}$$

$$B_{CQ} = 1/\{1 + [CQ]_{tot} \cdot K_{dCQ}/(K_{dCQ} + [Ca^{2+}]_{rel})^2\} \tag{A50}$$

$$d[Ca^{2+}]_{up}/dt = J_{up} - J_{tr} \cdot V_{rel}/V_{up} - J_{leak} \tag{A51}$$

$$d[Na^{2+}]_i/dt = -J_{Na,net}/V_i \tag{A52}$$

$$J_{Ca,net} = (I_{Ca,L} + I_{Ca,b} - 2 \cdot I_{NaCa} + I_{pCa} + I_{Ca,T} + I_{Ca,LD}) \cdot C_m/(2 \cdot F) \tag{A53}$$

$$J_{Na,net} = (I_{Na} + I_{Na,b} + 3 \cdot I_{NaK} + 3 \cdot I_{NaCa} + I_{hNa} + I_{st}) \cdot C_m/F \tag{A54}$$

APPENDIX C: DETERMINATION OF EPS AS INITIAL CONDITIONS

The methods for determination of EPs as initial conditions for the single cell were described previously (22). To determine an EP of the coupled-cell system, steady-state values of the state variables V, $[Ca^{2+}]_i$, $[Na^+]_i$, $[Ca^{2+}]_{rel}$, and $[Ca^{2+}]_{up}$ for BP and NP cells were calculated numerically by the algebraic method with a nonlinear equation solver available in MATLAB 7. For bifurcation analyses and simulations using the $[K^+]_i$-fixed system, steady-state values of the state variables for BP and NP cells were computed by the following algebraic equations derived from the differential equations.

$$I_{total(BP)} + I_{GJ}/C_{BP} = 0 \ (dV_{BP}/dt = 0) \tag{A55}$$

$$I_{total(NP)} - I_{GJ}/C_{NP} = 0 \ (dV_{NP}/dt = 0) \tag{A56}$$

$$J_{Ca,net} = 0 \ (d[Ca^{2+}]_i/dt = 0) \tag{A57}$$

$$J_{rel} - J_{tr} = 0 \ (d[Ca^{2+}]_{rel}/dt = 0) \tag{A58}$$

$$J_{up} - J_{tr} \cdot V_{rel}/V_{up} - J_{leak} = 0 \ (d[Ca^{2+}]_{up}/dt = 0) \tag{A59}$$

$$J_{Na,net} = 0 \ (d[Na^+]_i/dt = 0) \tag{A60}$$

Equations A57–A60 are for either the BP or the NP cell; in total, 10 equations are required for calculating the steady state of the coupled-cell system.

ACKNOWLEDGMENTS

Present address of H. Matsuda: Group in Leading Project for Biostimulation, Kyoto Univ., Kyoto, Japan.

GRANTS

This work was supported in part by Ministry for Education, Science, Sports and Culture of Japan Grant-in-Aid for Scientific Research (C) 17590192 (to Y. Kurata and T. Shibamoto), Kanazawa Medical University Grant for Collaborative Research C2005-1 (to Y. Kurata and T. Shibamoto), and Kanazawa Medical University Grant for Promoted Research S2006-6 (to Y. Kurata).

REFERENCES

1. **Boyett MR, Dobrzynski H, Lancaster MK, Jones SA, Honjo H, Kodama I.** Sophisticated architecture is required for the sinoatrial node to perform its normal pacemaker function. *J Cardiovasc Electrophysiol* 14: 104–106, 2003.
2. **Boyett MR, Honjo H, Kodama I.** The sinoatrial node, a heterogeneous pacemaker structure. *Cardiovasc Res* 47: 658–687, 2000.
3. **Cerbai E, Pino R, Portiatti F, Sani G, Toscano M, Maccherini M, Giunti G, Mugelli A.** Characterization of the hyperpolarization-activated current, I_f, in ventricular myocytes from human failing heart. *Circulation* 95: 568–571, 1997.
4. **Chay TR, Lee YS.** Phase resetting and bifurcation in the ventricular myocardium. *Biophys J* 47: 641–651, 1985.
5. **Demir SS, Clark JW, Murphey CR, Giles WR.** A mathematical model of a rabbit sinoatrial node cell. *Am J Physiol Cell Physiol* 266: C832–C852, 1994.
6. **Dormand JR, Prince PJ.** A family of embedded Runge-Kutta formulae. *J Comput Appl Math* 6: 19–26, 1980.
7. **Garny A, Kohl P, Hunter PJ, Boyett MR, Noble D.** One-dimensional rabbit sinoatrial node models: benefits and limitations. *J Cardiovasc Electrophysiol* 14: S121–S132, 2003.
8. **Gepstein L, Feld Y, Yankelson L.** Somatic gene and cell therapy strategies for the treatment of cardiac arrhythmias. *Am J Physiol Heart Circ Physiol* 286: H815–H822, 2004.
9. **Guevara MR, Jongsma HJ.** Three ways of abolishing automaticity in sinoatrial node: ionic modeling and nonlinear dynamics. *Am J Physiol Heart Circ Physiol* 262: H1268–H1286, 1992.
10. **He JQ, Ma Y, Lee Y, Thomson JA, Kamp TJ.** Human embryonic stem cells develop into multiple types of cardiac myocytes: action potential characterization. *Circ Res* 93: 32–39, 2003.
11. **Hund TJ, Kucera JP, Otani NF, Rudy Y.** Ionic charge conservation and long-term steady state in the Luo-Rudy dynamic cell model. *Biophys J* 81: 3324–3331, 2001.
12. **Iyer V, Mazhari R, Winslow RL.** A computational model of the human left-ventricular epicardial myocyte. *Biophys J* 87: 1507–1525, 2004.
13. **Joyner RW, Kumar R, Golod DA, Wilders R, Jongsma HJ, Verheijck EE, Bouman L, Goolsby WN, van Ginneken AC.** Electrical interactions between a rabbit atrial cell and a nodal cell model. *Am J Physiol Heart Circ Physiol* 274: H2152–H2162, 1998.
14. **Joyner RW, Wang YG, Wilders R, Golod DA, Wagner MB, Kumar R, Goolsby WN.** A spontaneously active focus drives a model atrial sheet more easily than a model ventricular sheet. *Am J Physiol Heart Circ Physiol* 279: H752–H763, 2000.
15. **Kehat I, Khimovich L, Caspi O, Gepstein A, Shofti R, Arbel G, Huber I, Satin J, Itskovitz-Eldor J, Gepstein L.** Electromechanical integration of cardiomyocytes derived from human embryonic stem cells. *Nat Biotechnol* 22: 1282–1289, 2004.
16. **Koschak A, Reimer D, Huber I, Grabner M, Glossmann H, Engel J, Striessnig J.** α_{1C} ($Ca_v1.3$) subunits can form L-type Ca^{2+} channels activating at negative voltages. *J Biol Chem* 276: 22100–22106, 2001.
17. **Koumi S, Backer CL, Arentzen CE.** Characterization of inwardly rectifying K^+ channel in human cardiac myocytes: alterations in channel behavior in myocytes isolated from patients with idiopathic dilated cardiomyopathy. *Circulation* 92: 164–174, 1995.
18. **Krogh-Madsen T, Schaffer P, Skriver AD, Taylor LK, Pelzmann B, Koidl B, Guevara MR.** An ionic model for rhythmic activity in small clusters of embryonic chick ventricular cells. *Am J Physiol Heart Circ Physiol* 289: H398–H413, 2005.
19. **Kumar R, Wilders R, Joyner RW, Jongsma HJ, Verheijck EE, Golod DA, van Ginneken ACG, Goolsby WN.** Experimental model for an ectopic focus coupled to ventricular cells. *Circulation* 94: 833–841, 1996.
20. **Kurata Y, Hisatome I, Imanishi S, Shibamoto T.** Dynamical description of sinoatrial node pacemaking: improved mathematical model for primary pacemaker cell. *Am J Physiol Heart Circ Physiol* 283: H2074–H2101, 2002.
21. **Kurata Y, Hisatome I, Imanishi S, Shibamoto T.** Roles of L-type Ca^{2+} and delayed-rectifier K^+ currents in sinoatrial node pacemaking: insights from stability and bifurcation analyses of a mathematical model. *Am J Physiol Heart Circ Physiol* 285: H2804–H2819, 2003.
22. **Kurata Y, Hisatome I, Matsuda H, Shibamoto T.** Dynamical mechanisms of pacemaker generation in I_{K1}-downregulated human ventricular myocytes: insights from bifurcation analyses of a mathematical model. *Biophys J* 89: 1–23, 2005.
23. **Kuznetsov YA.** *Elements of Applied Bifurcation Theory* (3rd ed.). New York: Springer, 2003.
24. **Landau M, Lorente P, Michaels D, Jalife J.** Bistabilities and annihilation phenomena in electrophysiological cardiac models. *Circ Res* 66: 1658–1672, 1990.
25. **Lin G, Cai J, Jiang H, Shen H, Jiang X, Yu Q, Song J.** Biological pacemaker created by fetal cardiomyocyte transplantation. *J Biomed Sci* 12: 513–519, 2005.

26. **Lonardo G, Cerbai E, Casini S, Giunti G, Bonacchi M, Battaglia F, Fiorani B, Stefano PL, Sani G, Mugelli A.** Pharmacological modulation of the hyperpolarization-activated current (I_f) in human atrial myocytes: focus on G protein-coupled receptors. *J Mol Cell Cardiol* 38: 453–460, 2005.
27. **Mangoni ME, Couette B, Bourinet E, Platzer J, Reimer D, Striessnig J, Nargeot J.** Functional role of L-type $Ca_v1.3$ Ca^{2+} channels in cardiac pacemaker activity. *Proc Natl Acad Sci USA* 100: 5543–5548, 2003.
28. **Miake J, Marbán E, Nuss HB.** Gene therapy: biological pacemaker created by gene transfer. *Nature* 419: 132–133, 2002.
29. **Moroni A, Barbuti A, Altomare C, Viscomi C, Morgan J, Baruscotti M, DiFrancesco D.** Kinetic and ionic properties of the human HCN2 pacemaker channel. *Pflügers Arch* 439: 618–626, 2000.
30. **Parker TS, Chua LO.** *Practical Numerical Algorithms for Chaotic Systems*. New York: Springer, 1989.
31. **Platzer J, Engel J, Schrott-Fischer A, Stephan K, Bova S, Chen H, Zheng H, Striessnig J.** Congenital deafness and sinoatrial node dysfunction in mice lacking class D L-type Ca^{2+} channels. *Cell* 102: 89–97, 2000.
32. **Plotnikov AN, Sosunov EA, Qu J, Shlapakova IN, Anyukhovsky EP, Liu L, Janse MJ, Brink PR, Cohen IS, Robinson RB, Danilo P Jr, Rosen MR.** Biological pacemaker implanted in canine left bundle branch provides ventricular escape rhythms that have physiologically acceptable rates. *Circulation* 109: 506–512, 2004.
33. **Priebe L, Beuckelmann DJ.** Simulation study of cellular electric properties in heart failure. *Circ Res* 82: 1206–1223, 1998.
34. **Puglisi JL, Bers DM.** LabHEART: an interactive computer model of rabbit ventricular myocyte ion channels and Ca transport. *Am J Physiol Cell Physiol* 281: C2049–C2060, 2001.
35. **Qu Y, Baroudi G, Yue Y, El-Sherif N, Boutjdir M.** Localization and modulation of α_{1D} (Cav1.3) L-type Ca channel by protein kinase A. *Am J Physiol Heart Circ Physiol* 288: H2123–H2130, 2005.
36. **Qu J, Plotnikov AN, Danilo P Jr, Shlapakova I, Cohen IS, Robinson RB, Rosen MR.** Expression and function of a biological pacemaker in canine heart. *Circulation* 107: 1106–1109, 2003.
37. **Robinson RB, Brink PR, Cohen IS, Rosen MR.** I_f and the biological pacemaker. *Pharmacol Res* 53: 407–415, 2006.
38. **Saucerman JJ, Brunton LL, Michailova AP, McCulloch AD.** Modeling β-adrenergic control of cardiac myocytes contractility in silico. *J Biol Chem* 278: 47997–48003, 2003.
39. **Shampine LF, Reichelt MW.** The MATLAB ODE Suite. *SIAM J Sci Comput* 18: 1–22, 1997.
40. **Shinagawa Y, Satoh H, Noma A.** The sustained inward current and inward rectifier K^+ current in pacemaker cells dissociated from rat sinoatrial node. *J Physiol* 523: 593–605, 2000.
41. **Silva J, Rudy Y.** Mechanism of pacemaking in I_{K1}-downregulated myocytes. *Circ Res* 92: 261–263, 2003.
42. **ten Tusscher KHWJ, Noble D, Noble PJ, Panfilov AV.** A model for human ventricular tissue. *Am J Physiol Heart Circ Physiol* 286: H1573–H1589, 2004.
43. **Toyoda F, Ding WG, Matsuura H.** Responses of the sustained inward current to autonomic agonists in guinea-pig sino-atrial node pacemaker cells. *Br J Pharmacol* 144: 660–668, 2005.
44. **Verheijck EE, Wilders R, Bouman LN.** Atrio-sinus interaction demonstrated by blockade of the rapid delayed rectifier current. *Circulation* 105: 880–885, 2002.
45. **Vinet A, Roberge FA.** A model study of stability and oscillations in the myocardial cell membrane. *J Theor Biol* 147: 377–412, 1990.
46. **Viswanathan PC, Coles JA Jr, Sharma V, Sigg DC.** Recreating an artificial biological pacemaker: insights from a theoretical model. *Heart Rhythm* 3: 824–831, 2006.
47. **Wagner MB, Golod D, Wilders R, Verheijck EE, Joyner RW, Kumar R, Jongsma HJ, van Ginneken ACG, Goolsby WN.** Modulation of propagation from an ectopic focus by electrical load and by extracellular potassium. *Am J Physiol Heart Circ Physiol* 272: H1759–H1796, 1997.
48. **Watanabe EI, Honjo H, Anno T, Boyett MR, Kodama I, Toyama J.** Modulation of pacemaker activity of sinoatrial node cells by electrical load imposed by an atrial cell model. *Am J Physiol Heart Circ Physiol* 269: H1735–H1742, 1995.
49. **Wilders R, Jongsma HJ, van Ginneken ACG.** Pacemaker activity of the rabbit sinoatrial node: a comparison of mathematical models. *Biophys J* 60: 1202–1216, 1991.
50. **Xue T, Cho HC, Akar FG, Tsang SY, Jones SP, Marbán E, Tomaselli GF, Li RA.** Functional integration of electrically active cardiac derivatives from genetically engineered human embryonic stem cells with quiescent recipient ventricular cardiomyocytes: insights into the development of cell-based pacemakers. *Circulation* 111: 11–20, 2005.
51. **Zhang Z, Xu Y, Song H, Rodriguez J, Tuteja D, Namkung Y, Shin HS, Chiamvimonvat N.** Functional roles of $Ca_v1.3$ (α_{1D}) calcium channel in sinoatrial nodes: insight gained using gene-targeted null mutant mice. *Circ Res* 90: 981–987, 2002.

Acta Physiol 2007, 189, 15–22

Hepatic pre-sinusoidal vessels contract in anaphylactic hypotension in rabbits

N. Karasawa,[1,2] T. Shibamoto,[1] S. Cui,[1] H. Takano,[1] Y. Kurata[1] and H. Tsuchida[2]

1 *Department of Physiology and*

2 *Department of Anaesthesiology, Kanazawa, Medical University, Uchinada, Japan*

Received 24 July 2006, revision requested 26 August 2006, final revision received 9 September 2006, accepted 16 September 2006

Correspondence: T. Shibamoto, Department of Physiology, Kanazawa Medical University, Uchinada Ishikawa 920-0293 Japan. E-mail: shibamo@kanazawa-med.ac.jp

Abstract

Aim: The purpose of this study was to determine whether anaphylactic hypotension in rabbits is accompanied by hepatic venoconstriction, and the effects of anaphylaxis on hepatic segmental vascular resistances and liver weight in isolated perfused rabbit livers.

Methods: The rabbits were sensitized by subcutaneous injection of antigen of 2.5 mg ovalbumin with complete Freund's adjuvant three times at 1 week interval. One week after sensitization, anaphylaxis was induced by an injection of 2.5 mg ovalbumin into the jugular vein of pentobarbital anaesthetized rabbits or the perfusate of rabbit livers perfused via the portal vein at a constant flow. Using the double occlusion technique to estimate the hepatic sinusoidal pressure, pre- (R_{pre}) and post-sinusoidal (R_{post}) resistances were calculated for the isolated perfused livers.

Results: An antigen injection into the sensitized rabbits caused not only a decrease in systemic arterial pressure from 79 ± 2 to 40 ± 4 mmHg, but also an increase in portal venous pressure (P_{pv}) from 9.5 ± 2.2 to 24.1 ± 3.9 cmH_2O. Portal hypertension persisted for 8 min after the antigen injection. An injection of antigen into the perfusate caused a marked increase in P_{pv} from 5.4 ± 0.1 to 28.6 ± 2.4 cmH_2O at 6 min, but only a slight increase in double occlusion pressure from 2.2 ± 0.2 to 3.8 ± 0.2 cmH_2O, resulting in a selective increase in R_{pret} rather than R_{post}. Concomitant with the hepatic pre-sinusoidal constriction, liver weight loss occurred.

Conclusion: Anaphylactic hypotension in rabbits is accompanied by hepatic venoconstriction which is characterized by pre-sinusoidal contraction.

Keywords anaphylaxis, hepatic circulation, isolated perfused rabbit liver, portal hypertension.

The incidence of anaphylaxis is estimated between 1 in 10 000 and 1 in 20 000 anaesthesia, and any drug administered in the perioperative period can potentially produce life-threatening anaphylactic shock (Mertes & Laxenaire 2004). Anaphylactic hypotension is primarily caused by alterations in the systemic circulation that decrease blood flow to the heart (Brown 1995). Peripheral circulatory collapse is ascribed to hypovolemia, which results from a decrease in effective circulating blood volume. The latter could be due to vasodilation with the peripheral pooling and increased vascular permeability with a shift of intravascular fluid to the extravascular space (Brown 1995). However, the exact hemodynamic mechanism for the peripheral pooling during anaphylactic shock is not well known. We have been putting an emphasis on the existence of antigen-induced hepatic venoconstriction and portal hypertension during anaphylactic shock.

Indeed, in canine experimental models of anaphylactic shock, antigen-induced selective constriction of

 doi: 10.1111/j.1748-1716.2006.01629.x

post-sinusoidal hepatic veins (Yamaguchi *et al.* 1994) play an important role in the pathogenesis of circulatory collapse (Wagner *et al.* 1986); anaphylaxis-induced hepatic venous constriction induces pooling of blood in liver itself, as well as in upstream splanchnic organs, both of which reduce venous return with resultant decrease in stroke volume and systemic arterial pressure. In addition, in rats, antigen-induced hepatic venoconstriction is also involved in anaphylactic hypotension (Shibamoto *et al.* 1999, 2005b). On the basis of these previous findings, we have proposed that antigen-induced hepatic venoconstriction plays an important role in pathogenesis of anaphylactic shock, and possibly serves as a common shock-inducing cause among mammals. However, in rabbits, the role of the liver is not known in anaphylactic hypotension, although right heart overload due to anaphylactic pulmonary hypertension is recognized as a factor causative of hypotension in this species (Cohen *et al.* 1951, Halonen *et al.* 1980). Thus, the first purpose of the present study was to determine whether anaphylactic hypotension is accompanied by hepatic venoconstriction in anaesthetized rabbits. To resolve this question, systemic arterial pressure and portal venous pressure were observed in sensitized rabbits after the antigen was intravenously administered.

Species difference has been found in the hepatic vascular segments that preferentially contract during anaphylaxis: selective post-sinusoidal constriction occurs in sensitized canine livers (Yamaguchi *et al.* 1994), while predominant pre-sinusoidal but significant and substantial post-sinusoidal constriction occurs in guinea pig livers (Ruan *et al.* 2004a). Finally in rats, almost selective pre-sinusoidal constriction was observed (Shibamoto *et al.* 2005b). On the other hand, it is not known whether anaphylactic reaction in rabbits causes constriction of post-sinusoidal hepatic veins, resulting in hepatic congestion. To clarify the anaphylaxis-induced changes in hepatic vascular resistance distribution in rabbits, we herein established anaphylactic models of isolated portally perfused rabbit livers, in which the sinusoidal pressure was measured by the double occlusion method (Yamaguchi *et al.* 1994). Thus, the second purpose of the present study was to determine the effects of anaphylaxis on hepatic vascular resistance distribution and liver weight in isolated perfused rabbit livers.

Methods

Animals

Twenty-six male New Zealand white rabbits (Japan SLC, Shizuoka, Japan) weighing 2.8 ± 0.1 kg were used in this study. Rabbits were maintained at 22 °C and under pathogen-free conditions on a 12 : 12-h dark/light cycle, and allowed food and water *ad libitum*. The experiments conducted in the present study were approved by the Animal Research Committee of Kanazawa Medical University.

Sensitization

Rabbits were actively sensitized by the subcutaneous injection of an emulsion made by mixing equal volumes of complete Freund's adjuvant (0.5 mL) with 2.5 mg ovalbumin (grade V; Sigma, St Louis, MO, USA) dissolved in physiological saline (0.5 mL) three times at 1 week interval. Non-sensitized rabbits were injected with complete Freund's adjuvant and ovalbumin-free saline. One week after the third injection, the rabbits were used for the following *in vivo* or isolated perfused liver experiments.

In vivo *experiment*

One week after sensitization, sensitized ($n = 6$) and non-sensitized ($n = 5$) rabbits were anaesthetized with pentobarbital sodium (50 mg kg^{-1}, i.v.) and placed on a thermostatically controlled heating pad (ATC-101B; Unique Medical, Tokyo, Japan). The adequacy of anaesthesia was monitored by the stability of blood pressure and respiration under control conditions and during a pinch of the hindpaw. Supplemental doses of anaesthetic (10% of initial dose) were given if necessary. The right femoral artery and vein were catheterized to measure systemic arterial pressure (P_{sa}), and to inject antigen respectively. The right external jugular vein was catheterized, and the catheter tip was positioned at the confluence of the superior vena cava and the right atrium for measurement of the central venous pressure (P_{cv}). Heart rate (HR) was measured by triggering the R wave of electrocardiogram. Following an abdominal midline incision, the gastroduodenal vein was catheterized, and the catheter tip was positioned in the main portal vein for continuous measurement of the portal venous pressure (P_{pv}). After closure of the abdomen, the baseline measurements were started.

The P_{sa}, P_{cv} and P_{pv} were continuously measured with pressure transducers (TP-400T; Nihon-Kohden, Tokyo, Japan), and these pressures and HR were continuously displayed on a thermal physiograph (RMP-6008; Nihon-Kohden). Outputs were also digitally recorded at 20 Hz (PowerLab, ADInstruments). Haemodynamic parameters were observed for at least 20 min after surgery until a stable state was obtained. After the baseline measurements, 2.5 mg of the ovalbumin antigen was administered via the femoral vein catheter and the changes in variables were observed for 60 min.

 doi: 10.1111/j.1748-1716.2006.01629.x

Isolated liver experiment

One week after sensitization, the rabbits were anaesthetized with pentobarbital sodium (50 mg kg^{-1}, i.v.) and mechanically ventilated with room air. The basic method for isolated perfused rabbit liver was previously described (Shibamoto *et al.* 1999). Catheters were placed in the right carotid artery. After laparotomy, loose ligatures were placed around the hepatic artery, portal vein, inferior vena cava and common bile duct. At 5 min after heparinization (500 U kg^{-1} i.v.), the rabbit was rapidly bled through the carotid arterial catheter. The aforementioned vessels and bile duct were ligated, and thoracotomy was performed. Then, the liver was rapidly excised and weighed. The portal vein and vena cava were cannulated with stainless cannulas (5 mm ID), whereas the hepatic artery was ligated to simplify analysis of the intrahepatic vascular circuit. The common bile duct was also cannulated with polyethylene tubing. Perfusion was begun within 5 min after excision of the liver.

The cannulated liver was suspended from an isometric transducer (TB-652T; Nihon-Kohden) and perfused via the portal vein at a constant flow rate with 200 mL of the heparinized autologous blood diluted with 5% bovine albumin (Sigma-Aldrich, St Louis, MO, USA) in Krebs solution (118 mM NaCl, 5.9 mM KCl, 1.2 mM $MgSO_4$, 2.5 mM $CaCl_2$, 1.2 mM NaH_2PO_4, 25.5 mM $NaHCO_3$, and 5.6 mM glucose) at Hct of 8% in a recirculating fashion. The blood was maintained at 37 °C by using a water bath, and the blood in the reservoir was continuously bubbled with 95% O_2–5% CO_2, which could provide perfusate oxygen tension of approx. 290 mmHg (Shibamoto *et al.* 1999, 2005a). A bubble trap was placed in the inflow line. P_{pv} and hepatic venous (P_{hv}) pressures were measured through the corresponding sidearm cannula by using pressure transducers (TP-400T; Nihon-Kohden) referenced to the level of the portal vein at the hepatic hilus. The portal blood flow rate (Q_{pv}) was measured with an electromagnetic flowmeter (MFV 1200; Nihon-Kohden), and the flow probe was positioned in the inflow line. To occlude the portal and hepatic venous lines simultaneously for measurement of the double occlusion pressure (P_{do}), solenoid valves were placed around the perfusion tubes upstream from the P_{pv} sidearm cannula and downstream from the P_{hv} sidearm cannula. Bile was continuously collected in a small tube suspended from the force transducer (45196A; NEC-Sanei, Tokyo, Japan). The weight of the tube was continuously measured, and the bile flow rate was expressed as grams per minute per 10 g liver weight. The P_{pv}, P_{hv}, Q_{pv}, liver weight and bile weight were monitored continuously and displayed through a thermal physiograph (RMP-6008; Nihon-Kohden). Outputs were also digitized by the analogue–digital converter at a sampling rate of 100 Hz. These digitized values were displayed and recorded using a personal computer for later determination of P_{do}.

Hepatic haemodynamic parameters were observed for at least 20 min after the start of perfusion until an isogravimetric state (no weight gain or loss) was obtained by adjusting Q_{pv} and the height of the reservoir at a P_{hv} of 0–1 cmH_2O, and at a Q_{pv} of 27 ± 1 mL min^{-1} (10 g liver weight)$^{-1}$. After the baseline measurements, the perfused livers excised from the sensitized rabbits (anaphylaxis group, $n = 9$) and non-sensitized rabbits (control group, $n = 6$) were challenged with ovalbumin 2.5 mg injected into the reservoir.

The hepatic sinusoidal pressure was measured by the double occlusion method (Yamaguchi *et al.* 1994), using the custom-made software (LIVER SOFTWARE, Biomedical Science, Kanazawa, Japan). Both the inflow and outflow lines were simultaneously and instantaneously occluded for 15 s with the solenoid valves, after which P_{pv} and P_{hv} rapidly equilibrated to a similar or identical pressure, which was P_{do}. The principle of the double occlusion method to estimate the sinusoidal pressure is derived from the concept of the mean circulating filling pressure of the systemic circulation (Rothe 1993). In each experimental group, P_{do} was measured at baseline and at 2, 4 and 6 min, and then at 10 min intervals up to 60 min after antigen.

The total portal-hepatic venous (R_t), pre-sinusoidal (R_{pre}) and post-sinusoidal (R_{post}) resistances were calculated as follows:

$$R_t = (P_{pv} - P_{hv})/Q_{pv} \quad (1)$$

$$R_{pre} = (P_{pv} - P_{do})/Q_{pv} \quad (2)$$

$$R_{post} = (P_{do} - P_{hv})/Q_{pv} \quad (3)$$

Statistics

All results are expressed as the means ± SE. Statistical analyses were performed with repeated measures analysis of variance, and a P-value <0.05 was considered significant. When a significant difference was obtained, *post hoc* analysis was performed with the Bonferroni post-test correction method.

Results

The response of the anaesthetized rabbits to antigen

Figure 1 shows a representative example of the response to an intravenous injection of the ovalbumin antigen in an anaesthetized rabbit sensitized with ovalbumin. Figure 2 shows the summary data of time course changes in P_{pv}, P_{sa} and P_{cv}. After an injection of antigen, P_{pv} initially increased and then P_{sa} and P_{cv}

 doi: 10.1111/j.1748-1716.2006.01629.x

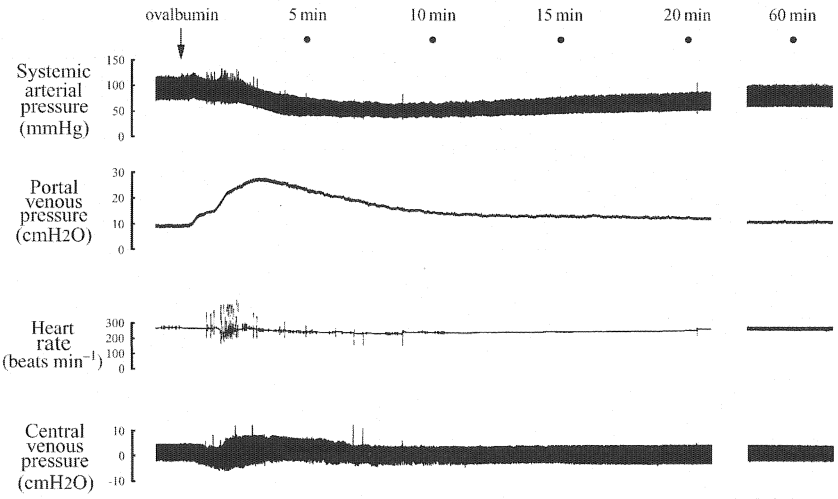

Figure 1 A representative recording of the response to ovalbumin antigen (2.5 mg) in an anaesthetized sensitized rabbit.

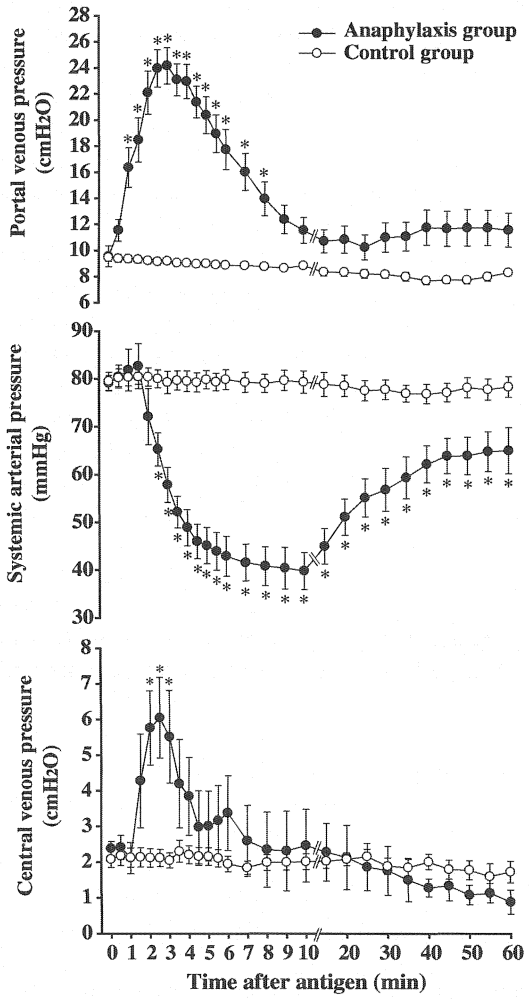

Figure 2 The summary of changes in the systemic arterial pressure, portal venous pressure and central venous pressure after antigen injection. Means ± SE; *$P < 0.05$ vs. baseline; closed circles, the anaphylaxis group ($n = 6$); open circles, the control group ($n = 5$).

decreased and increased, respectively. Actually, approx. 1 min after an antigen injection, P_{sa} decreased from the baseline of 79 ± 2 mmHg to the nadir of 40 ± 4 mmHg at 10 min, followed by a gradual recovery to 65 ± 5 mmHg at 60 min. In contrast, after the shorter latent period following the antigen, P_{pv} began to increase gradually from the baseline of 9.5 ± 2.2 cmH_2O to the peak of 24.1 ± 3.9 cmH_2O at 3 min after antigen, and then decreased to 12 ± 1 cmH_2O at 10 min. After that, P_{pv} remained at this level, which was not significantly different from the baseline. The post-antigen period of up to 10 min during which P_{pv} remained elevated above the baseline (Fig. 2) was designated as the portal hypertension phase in the present study. It should be noted that P_{sa} persistently decreased during the portal hypertension phase (Fig. 2). After antigen, P_{cv} initially increased from the baseline of 2.4 ± 0.2 to 6.1 ± 1.1 cmH_2O at 2.5 min, and thereafter gradually decreased along with a decrease in P_{sa}. Heart rate did not increase but decreased in the presence of a fall in P_{sa}: heart rate significantly decreased from 278 ± 12 to 243 ± 15 beats min^{-1} at 8 min after antigen in the anaphylaxis group. Neither of P_{sa}, P_{pv} nor P_{cv} was significantly changed by the antigen in the control animals during the experimental periods (Fig. 2).

The response of the blood-perfused livers to antigen

The excised liver weight measured just before perfusion experiment in the control and anaphylaxis group was 88 ± 4 and 90 ± 3 g respectively. An antigen injection caused hepatic venoconstriction, which was characterized by predominant pre-sinusoidal constriction and liver weight loss, as shown in Figs 3 and 4. Within 1 min after antigen, venoconstriction was evident by an

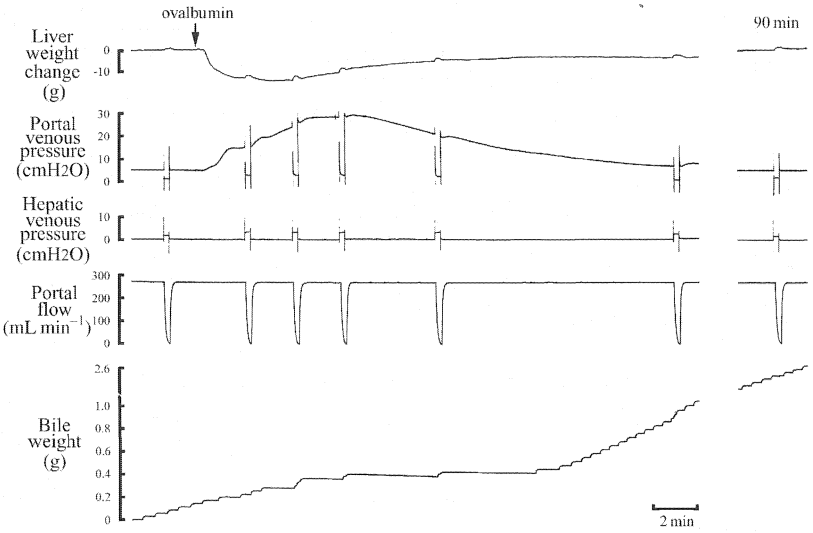

Figure 3 A representative recording of the response to ovalbumin antigen (2.5 mg) in the blood-perfused liver isolated from a sensitized rabbit.

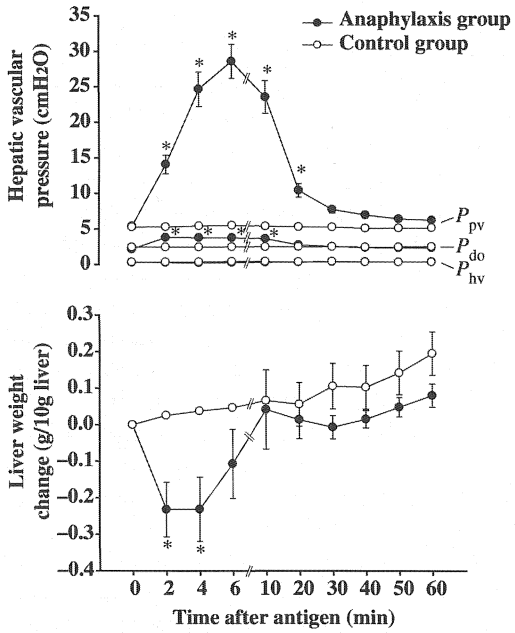

Figure 4 The summary of changes in hepatic vascular pressures and liver weight changes after antigen injection in isolated perfused rabbit livers. Means ± SE; $^*P < 0.05$ vs. baseline and the control group; P_{pv}, portal venous pressure; P_{do}, double occlusion pressure; P_{hv}, hepatic venous pressure; closed circles, the anaphylaxis group ($n = 9$); open circles, the control group ($n = 6$).

increased P_{pv}. P_{pv} gradually increased to the peak value of 28.6 ± 2.4 cmH_2O from the baseline of 5.4 ± 0.1 cmH_2O at 6 min after antigen (Fig. 4). The double occlusion maneuver performed at 6 min after antigen revealed a P_{do} of 3.8 ± 0.2 cmH_2O that was significantly higher than that of the baseline of 2.2 ± 0.2 cmH_2O. Therefore, the P_{pv}-to-P_{do} gradient (in conjunction with the flow), the indicator of R_{pre} (eqn 2), increased markedly from the baseline of 3.3 ± 0.1 to 24.8 ± 2.1 cmH_2O, while the P_{do}-to-P_{hv} gradient, the indicator of R_{post} (eqn 3), increased only slightly, but significantly, from the baseline of 1.9 ± 0.1 to 3.5 ± 0.2 cmH_2O (Fig. 4). Thus, R_{pre} increased by 680% the baseline from 0.12 ± 0.01 to 0.94 ± 0.10 cmH_2O mL min^{-1} (10 g liver weight), while R_{post} increased by only 85% from 0.07 ± 0.01 to 0.13 ± 0.01 cmH_2O mL min^{-1} (10 g liver weight) (Fig. 5). This indicates that the antigen almost selectively increased R_{pre} rather than R_{post}, as reflected by a significant increase in R_{pre}/R_t ratio from the baseline of 0.64 ± 0.03 to 0.87 ± 0.01. P_{pv}, and thus R_t, returned close to the baseline at 20 min after antigen. Concomitant with venoconstriction, the liver weight showed a decrease, reaching the nadir, −0.2 ± 0.1 g (10 g liver - weight)$^{-1}$, at 2 min. Then, the liver weight returned to nearly the baseline at 10 min after antigen. The bile flow decreased to 20% of the baseline level of 3.7 ± 0.5 g min^{-1} (10 g liver weight)$^{-1}$ during the maximal venoconstriction, as shown in Fig. 3. In the control rabbit liver, any haemodynamic variables did not change significantly after antigen (Figs 4 and 5).

Discussion

In this study, we examined whether hepatic venoconstriction occurs during rabbit anaphylactic hypotension. There are two major findings of the present study. The first finding (derived from the anaesthetized rabbit experiments) is that P_{pv} markedly increased during anaphylactic hypotension induced by an intravenous injection of the ovalbumin antigen in anaesthetized rabbits. Another finding (derived from the isolated perfused rabbit liver experiments) is that hepatic anaphylactic venoconstriction is characterized by almost selective pre-sinusoidal constriction and liver weight loss.

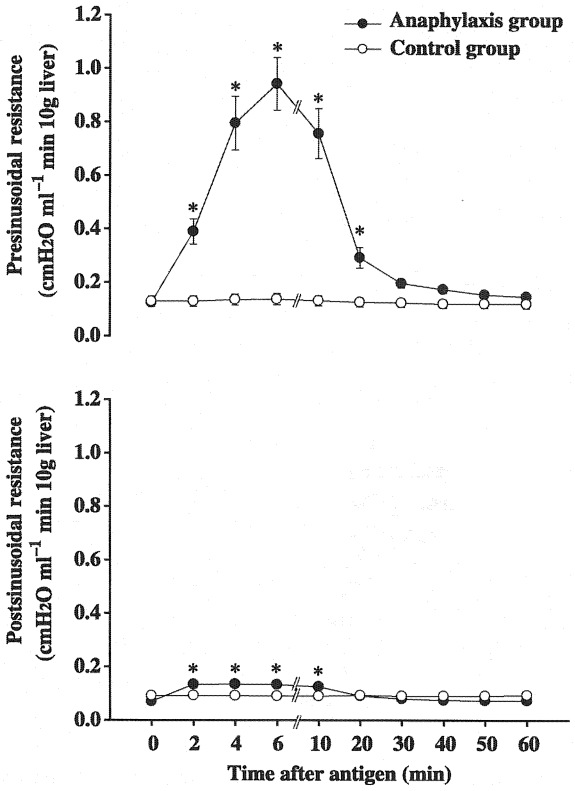

Figure 5 The summary of changes in pre- and post-sinusoidal resistances after antigen injection in isolated perfused rabbit livers. Means ± SE; $*P < 0.05$ vs. baseline and the control group; closed circles, the anaphylaxis group ($n = 9$); open circles, the control group ($n = 6$).

To the best of our knowledge, this is the first study to demonstrate that anaphylactic hypotension in rabbits is accompanied by substantial hepatic venoconstriction. Indeed, anaphylactic hepatic venoconstriction has been reported in rats (Hines & Fisher 1992, Shibamoto *et al.* 2005b), guinea pigs (Ruan *et al.* 2004a) and dogs (Weil 1917, Yamaguchi *et al.* 1994). With respect to the physiological significance of hepatic venoconstriction in anaphylactic hypotension, we speculate the following pathophysiological process: anaphylactic hepatic venoconstriction results in portal hypertension which then causes congestion of the upstream splanchnic organs, blood pooling, with resultant decrease in venous return and effective circulating blood volume, and finally augmentation of anaphylactic hypotension.

In the present study, P_{cv} increased significantly but slightly by 3.7 cmH_2O, which may be primarily caused by increased right ventricular load probably due to anaphylaxis-induced pulmonary vascular resistance (Cohen *et al.* 1951, Halonen *et al.* 1980). Unlikely, this increase in P_{cv} substantially contributed to the increase in P_{pv}, because this increase in P_{cv} was very small and short-lasting, when compared with that in P_{pv}. We think that the increase in P_{pv} was primarily caused by hepatic venoconstriction, as demonstrated in the isolated perfused rabbit livers.

Concerning species difference in the hepatic vascular segments that preferentially contract during anaphylaxis: post-sinusoids selectively contract in canine livers (Yamaguchi *et al.* 1994), while predominant pre-sinusoidal but substantial post-sinusoidal constriction occurs in guinea pig livers (Ruan *et al.* 2004a), and finally almost selective pre-sinusoidal constriction occurs in rat livers (Shibamoto *et al.* 2005b). In the present study, by measuring the sinusoidal pressure with the double occlusion method (Yamaguchi *et al.* 1994) in perfused sensitized rabbit livers, we here clearly showed that anaphylactic hepatic venoconstriction in rabbits was characterized by a marked pre-sinusoidal contraction and only a slight post-sinusoidal contraction (Figs 3 and 4), which was different from that in dogs or guinea pigs, but similar to that in rats.

The mechanism for such a species-dependent response is not clear. Canine post-sinusoidal hepatic veins anatomically contain smooth muscle sphincters in hepatic initial sublobular veins (Ekataksin & Kaneda 1999), which may cause selective post-sinusoidal contraction. Maass-Moreno & Rothe (1992) also reported that major pressure gradients must lie upstream from the large (>2 mm) hepatic veins in dogs. Indeed, these post-sinusoidal veins vigorously contract in response to various mediators of anaphylactic reaction, such as histamine (Urayama *et al.* 1996), thromboxane A_2 (Urayama *et al.* 1996), and platelet-activating factor (PAF) (Wang *et al.* 1997). In guinea pig livers, the anaphylactic pre-sinusoidal constriction may be caused mainly by PAF, while the post-sinusoidal constriction is caused by cysteinyl-leukotrienes (Shibamoto *et al.* 2005a). Actually, PAF predominantly contracts pre-sinusoidal vessels in guinea pig livers (Ruan *et al.* 2004b). However, the studies on effects of anaphylaxis-related vasoactive substances are limited on the segmental vascular resistances of rabbit livers. We have previously reported that histamine selectively contracts pre-sinusoids of isolated rabbit livers perfused with blood-free perfusate (Shibamoto *et al.* 1999). This finding is consistent with the present finding of predominant pre-sinusoidal constriction of the antigen challenged liver. However, the vasoconstrictive sites of the anaphylaxis-related chemical mediators other than histamine, were currently unknown. Further study is required to identify the chemical mediators responsible for the anaphylactic hepatic venoconstriction in rabbits and their vasoconstrictive sites.

In contrast to the liver weight gain response to the antigen of dogs (Yamaguchi *et al.* 1994) and guinea pigs (Ruan *et al.* 2004a), a liver weight loss was induced by marked anaphylactic pre-sinusoidal constriction in isolated perfused rabbit livers. With the constant perfusion

of the liver, the mechanism of the weight loss is unknown. This liver weight loss may be due to hepatic vascular blood loss. Likely the blood volume of the sinusoids, which were situated downstream to the selectively constricted pre-sinusoids, might be reduced. On the other hand, we believe that this possible reduction of intrahepatic blood volume as reflected by liver weight loss in isolated anaphylactic livers occurs similarly in anaesthetized animals. The hepatic vascular blood loss could serve as autotransfusion which might counteract the decrease in circulating blood volume and systemic hypotension in rats. Although the anaphylactic liver itself might have expelled the intrahepatic reserve blood to the systemic circulation and then contributed to supplementation of circulating blood volume, anaphylactic hypotension had occurred. This suggests that the blood mobilized from the liver is not enough to compensate fully the blood pressure fall induced by systemic anaphylaxis. Actually, in the present study, the maximum liver weight loss, which may serve as autotransfusion, was -0.2 g (10 g liver)$^{-1}$. With an active increase in the tension developed by the smooth muscle in the hepatic vessel walls, up to 50% of the hepatic blood volume can be mobilized (Greenway & Lautt 1989). Since the liver blood volume is 350 mL kg liver^{-1}, a 50% of liver blood volume is thus equivalent to a 1.75 mL (10 g liver)$^{-1}$ (Rothe & Maass-Moreno 1998). The liver volume loss of 0.2 mL (10 g liver)$^{-1}$ estimated from the liver weight loss in the present study is only 11% of the maximal mobilized blood volume. We suppose that this small volume of autotransfusion might not effectively contribute to compensation of anaphylaxis-induced circulating blood volume loss.

Conclusion

We determined the response of rabbit hepatic circulation to the antigen in anaesthetized rabbits and in isolated perfused rabbit livers. An intravenous injection of antigen (2.5 mg ovalbumin) caused not only a profound decrease in P_{sa} but also an increase in P_{pv}. In addition, in isolated perfused sensitized rabbit livers, hepatic anaphylaxis caused almost selective pre-sinusoidal constriction, and liver weight loss. On the basis of these findings, we conclude that anaphylactic hypotension in rabbit is accompanied by almost selective pre-sinusoidal contraction of the liver, which could induce splanchnic congestion and subsequent decrease in venous return and then contribute to hypotension.

Conflict of interest

The authors declare that there is no conflict of interest.

This study was supported by a Grant for Collaborative Research from Kanazawa Medical University (C2005-1, 2006) and a Grant-in-Aid for Scientific Research (18591730) from the Ministry of Education, Culture, Sports, Sciences and Technology of Japan.

References

Brown, A.F.T. 1995. Anaphylactic shock: mechanism and treatment. *J Accid Emerg Med* **12**, 89–100.

Cohen, S.G., Franke, F.R. & Karlson, E.L. 1951. Studies on the mechanism of fatal anaphylaxis in the rabbit. *J Allergy* **22**, 160–164.

Ekataksin, W. & Kaneda, K. 1999. Liver microvascular architecture: an insight into the pathophysiology of portal hypertension. *Semin Liver Dis* **19**, 359–382.

Greenway, C.V. & Lautt, W.W. 1989. Hepatic circulation. In: S.D. Schultz, J.D. Wood, B.B. Raunner (eds.) *Handbook of Physiology. The Gastrointestinal System. Motility and Circulation*, section 6, vol. 1, pt 2, chapter 41, pp. 1519–1564. American Physiological Society: Bethesda, MD.

Halonen M., Palmer, J.D., Lohman, I.C., McManus, L.M. & Pinckard, R.N. 1980. Respiratory and circulatory alterations induced by acetyl glyceryl ether phosphorylcholine, a mediator of IgE anaphylaxis in the rabbit. *Am Rev Respir Dis* **122**, 915–924.

Hines, K.L. & Fisher, R.A. 1992. Regulation of hepatic glycogenolysis and vasoconstriction during antigen-induced anaphylaxis. *Am J Physiol* **262**, G868–G877.

Maass-Moreno, R. & Rothe, C.F. 1992. Contribution of the large hepatic veins to postsinusoidal vascular resistance. *Am J Physiol* **262**, G14–G22.

Mertes, P.M. & Laxenaire, M.C. 2004. Allergy and anaphylaxis in anaesthesia. *Minerva Anestesio* **70**, 285–291.

Rothe, C.F. 1993. Mean circulatory filling pressure: its meaning and measurement. *J Appl Physiol* **74**, 499–509.

Rothe, C.F. & Maass-Moreno, R. 1998. Hepatic venular resistance responses to norepinephrine, isoproterenol, adenosine, histamine, and ACh in rabbits. *Am J Physiol* **274**, H777–H785.

Ruan, Z., Shibamoto, T., Shimo, T., Tsuchida, H., Koizumi, T. & Nishio, M. 2004a. NO, but not CO, attenuates anaphylaxis-induced postsinusoidal contraction and congestion in guinea pig liver. *Am J Physiol* **286**, R94–R100.

Ruan, Z., Shibamoto, T., Shimo, T., Koizumi, T., Tsuchida, H., Kurata, Y., Ogura, T. & Kubo, K. 2004b. Effects of platelet-activating factor and thromboxane A_2 on isolated perfused-guinea pig liver. *Prostaglandins Other Lipid Mediators* **73**, 73–85.

Shibamoto, T., Wang, H.G., Miyahara, T., Tanaka, S., Haniu, H., & Koyama, S. 1999. Pre-sinusoidal vessels predominantly contract in response to norepinephrine, histamine, and KCl in rabbit liver. *J Appl Physiol* **87**, 1404–1412.

Shibamoto, T., Ruan, Z., Cui, S., Liu, W. & Kurata, Y. 2005a. Involvement of platelet-activating factor and leukotrienes in anaphylactic segmental venoconstriction in ovalbumin sensitized guinea pig livers. *Prostaglandins Other Lipid Mediator* **78**, 218–230.

 doi: 10.1111/j.1748-1716.2006.01629.x

Shibamoto, T., Cui, S., Ruan, Z., Liu, W., Takano, H. & Kurata, Y. 2005b. Hepatic venoconstriction is involved in anaphylactic hypotension in rats. *Am J Physiol* **289**, H1436–H1441.

Urayama, H., Shibamoto, T., Wang, H.G. & Koyama, S. 1996. Thromboxane A_2 analogue contracts predominantly the hepatic veins in isolated canine liver. *Prostaglandins* **52**, 484–495.

Wagner, E.M., Mitzner, W.A. & Bleecker, E.R. 1986. Peripheral circulatory alterations in canine anaphylactic shock. *Am J Physiol* **251**, H934–H940.

Wang, H.G., Shibamoto, T. & Koyama, S. 1997. Effect of platelet-activating factor on hepatic capillary pressure in isolated dog liver. *Prostagland Leukot Essent Fatty Acid* **57**, 293–298.

Weil, R. 1917. Studies in anaphylaxis. XXI Anaphylaxis in dogs: a study of the liver in shock and peptone poisoning. *J Immunol* **2**, 525–556.

Yamaguchi, Y., Shibamoto, T., Hayashi, T., Saeki, Y. & Tanaka, S. 1994. Hepatic vascular response to anaphylaxis in isolated canine liver. *Am J Physiol* **267**, R268–R274.

Available online at www.sciencedirect.com
ScienceDirect
ELSEVIER
Prostaglandins, Leukotrienes and Essential Fatty Acids 76 (2007) 277–283
Prostaglandins Leukotrienes and Essential Fatty Acids
www.elsevier.com/locate/plefa

L-NAME augments PAF-induced venoconstriction in isolated perfused livers of rat and guinea pig, but not mouse

Sen Cui, Toshishige Shibamoto*, Zhansheng Zhao, Hiromichi Takano, Yasutaka Kurata

Department of Physiology, Kanazawa Medical University, Uchinada 920-0293, Japan

Received 11 September 2006; received in revised form 21 November 2006; accepted 29 December 2006

Abstract

Platelet-activating factor (PAF), one of vasoconstrictive lipid mediators, is involved in systemic anaphylaxis. On the other hand, nitric oxide (NO) is known to attenuate anaphylactic venoconstriction of the pre-sinusoids in isolated guinea pig and rat livers. However, it is not known whether NO attenuates PAF-induced hepatic venoconstriction. We therefore determined the effects of L-NAME, a NO synthase inhibitor, on PAF-induced venoconstriction in blood- and constant flow-perfused isolated livers of mice, rats and guinea pigs. The sinusoidal pressure was measured by the double occlusion pressure (Pdo), and was used to determine the pre- (Rpre) and post-sinusoidal (Rpost) resistances. PAF (0.01–1 μM) concentration-dependently caused predominant pre-sinusoidal constriction in all livers of three species studied. The guinea pig livers were the most sensitive to PAF, while the mouse livers were the weakest in responsiveness. L-NAME pretreatment selectively increased the basal Rpre in all of three species. L-NAME also significantly augmented the PAF-induced increases in Rpre, but not in Rpost, in rat and guinea pig livers. This augmentation was stronger in rat livers than in guinea pig livers at the high concentration of 0.1 μM PAF. However, L-NAME did not augment PAF-induced venoconstriction in mouse livers. In conclusion, in rat and guinea pig livers, NO may be released selectively from the pre-sinusoids in response to PAF, and then attenuate the PAF-induced pre-sinusoidal constriction. In mouse liver, PAF-induced venoconstriction is weak and not modulated by NO.

1. Introduction

Platelet-activating factor (PAF), one of lipid mediators which have a potent vasoconstrictive action, is released from a variety of cells including platelets, neutrophils, macrophages (e.g., Kupffer cells), monocytes, lymphocytes, endothelial cells and smooth muscle cells in response to various stimuli [1,2]. It is implicated as a mediator in various types of liver diseases such as hepatic anaphylaxis [3], endotoxin liver injury [4], ischemia-reperfusion liver injury, and hepatic resection [5]. The microcirculation of the hepatic sinusoid plays a crucial role in the integrity of liver function [6]. PAF may influence the sinusoidal circulation via its vasoconstrictive action [7,8]. We have reported by measuring the sinusoidal pressure with the hepatic vascular occlusion methods in isolated blood-perfused canine livers that PAF similarly constricts both the pre- and post-sinusoidal veins [9]. On the other hand, it predominantly constricts the pre-sinusoidal veins over the post-sinusoidal veins in the isolated blood perfused guinea pig [10] and rat livers [11]. These investigations indicated that there are species differences in the primary site of hepatic venoconstriction for PAF. However, the vascular segments that PAF predominantly constricts in mouse livers are not well known.

Abbreviations: IVC, inferior vena cava; PAF, platelet-activating factor; Rpre, pre-sinusoidal resistance; Rpost, post-sinusoidal resistance; Rt, total portal–hepatic venous resistance; Phv, portal venous pressure; Phv, hepatic venous pressure; Pdo, double occlusion pressure; Qpv, portal blood flow rate; Wt, liver weight; TxA_2, thromboxane A_2; L-NAME, N^G-nitro-L-arginine methyl ester; D-NAME, N^G-nitro-D-arginine methyl ester; NO, nitric oxide; Pmcf, the mean circulating filling pressure

*Corresponding author. Tel.: +81 76 218 8104; fax: +81 76 286 8010.
E-mail address: shibamo@kanazawa-med.ac.jp (T. Shibamoto).

0952-3278/$ - see front matter © 2007 Elsevier Ltd. All rights reserved.
doi:10.1016/j.plefa.2006.12.007

Nitric oxide (NO), a potent vasodilator produced by the activation of the NO synthase 3 present in endothelial cells in response to hormonal or physical stimuli such as shear stress [12,13], regulates the vascular system [12,13], and seems to play an important pathophysiological role in modulating the systemic changes associated with anaphylaxis [14]. We have recently reported that N^G-nitro-L-arginine methyl ester (L-NAME), a NO synthase inhibitor, augmented anaphylactic venoconstriction of the pre-sinusoids in isolated guinea pig [15] and rat [16] livers. However, it is not known whether L-NAME also augments hepatic venoconstriction induced by PAF, one of the main mediators for anaphylaxis.

The first purpose of the present study was to compare the effects of PAF on hepatic vascular resistance distribution in isolated perfused mouse, rat and guinea pig livers. Another purpose was to determine the effects of L-NAME on PAF-induced hepatic segmental venoconstriction, and to explore whether there are species differences in the effects among these three animals. To accomplish these purposes, we measured the sinusoidal pressure by the vascular occlusion method [17], and determined the pre- (Rpre) and post-sinusoidal resistances (Rpost) during hepatic venoconstriction induced by PAF in isolated mouse, rat and guinea pig livers perfused portally and recirculatingly with blood under constant flow in the presence of either L-NAME or N^G-nitro-D-arginine methyl ester (D-NAME) (an inactive enantiomer of L-NAME).

2. Materials and methods

Fourteen male ddY mice (40 ± 1 g), 12 male Sprague–Dawley rats (311 ± 3 g) and 12 male Hartley guinea pigs (320 ± 3 g) were used in this study. Animals were maintained at 23 °C and under pathogen-free conditions on a 12/12-h dark/light cycle, and received food and water ad libitum. The experiments conducted in the present study were approved by the Animal Research Committee of Kanazawa Medical University. All animals were purchased from Japan SLC (Hamamatsu, Japan).

2.1. Isolated liver preparation

The animals were anesthetized with intraperitoneal pentobarbital sodium and were mechanically ventilated with room air. The methods for the isolated perfused liver preparation were previously described [5,18,19]. After laparotomy, the hepatic artery was ligated; the bile duct was cannulated with the polyethylene tube in rats and guinea pigs. At 5 min after heparinization ($500\ U\ kg^{-1}$) via right carotid artery for rats and guinea pigs or via intra-abdominal inferior vena cava (IVC) for mice, blood (8–9 ml in rat or guinea pig, or 1.1 ml in mouse) was withdrawn through the carotid arterial or IVC catheter. The IVC above the renal veins was ligated, and the portal vein was cannulated with a stainless cannula. After thoracotomy, the supradiaphragmatic IVC was cannulated through a right atrium incision with a stainless cannula, then portal perfusion was begun with the heparinized autologous blood diluted with 5% bovine albumin (Sigma-Aldrich Co., St. Louis, MO) in Krebs solution (118 mM NaCl, 5.9 mM KCl, 1.2 mM $MgSO_4$, 2.5 mM $CaCl_2$, 1.2 mM NaH_2PO_4, 25.5 mM $NaHCO_3$, and 5.6 mM glucose) at Hct of 12% for rat and guinea pig livers and 3.6% for mouse livers. The liver was rapidly excised, suspended from an isometric transducer (TB-652 T, Nihon-Kohden, Japan) and weighed continuously throughout the experimental period.

The liver was perfused at a constant flow rate in a recirculating manner via the portal vein with blood that was pumped using a Masterflex roller pump from the venous reservoir through a heat exchanger (37 °C). The recirculating blood volume was 15 ml for mouse nd 40 ml for rat or guinea pig liver. The perfused blood was oxygenated in the venous reservoir by continuous bubbling with 95% O_2 and 5% CO_2 (perfused $PO_2 = 300$ mmHg).

2.2. Measurement of hepatic vascular pressures and vascular resistances

The portal venous (Ppv) and the hepatic venous (Phv) pressures were measured with pressure transducers (TP-400 T, Nihon-Kohden, Japan) attached by sidearm to the appropriate cannulas with the reference points at the hepatic hilus. Portal blood flow rate (Qpv) was measured with an electromagnetic flow meter (MFV 1200, Nihon-Kohden, Japan), the flow probe of which was positioned in the inflow line in rat and guinea pig livers. In mouse livers, Qpv was measured manually by collecting outflow perfusate for 1 min just before the baseline measurement. The hepatic sinusoidal pressure was measured using the double occlusion pressure (Pdo) [17,20]. Both the inflow and outflow lines were simultaneously and instantaneously occluded for 17 s in rat and guinea pig livers and 10 s in mouse livers using the solenoid valves, after which Ppv and Phv rapidly equilibrated to a similar or identical pressure, which was Pdo. The principle of the double occlusion method to estimate the sinusoidal pressure [17] is derived from the concept of the mean circulating filling pressure (Pmcf) of the systemic circulation [21]. Actually, Pdo values were obtained from the digitized data of Ppv and Phv using an original program (LIVER software, Biomedical Science, Kanazawa, Japan). The total portal–hepatic venous (Rt), Rpre and Rpost resistances were calculated

as follows:

$$Rt = (Ppv - Phv)/Qpv, \quad (1)$$

$$Rpre = (Ppv - Pdo)/Qpv, \quad (2)$$

$$Rpost = (Pdo - Phv)/Qpv. \quad (3)$$

2.3. Data recording

The hepatic vascular pressures, Qpv and liver weight (Wt) were monitored continuously and displayed through a thermal physiograph (RMP-6008, Nihon-Kohden, Japan). All outputs were also digitized via the analog–digital converter at a sampling rate of 100 Hz. These digitized values were also displayed and recorded using a personal computer for later determination of Pdo.

2.4. Experimental protocol

Hepatic hemodynamic parameters were observed for at least 20 min after the start of perfusion until an isogravimetric state (no weight gain or loss) was obtained by adjusting Qpv and the height of the reservoir at a Phv of 0–1 cmH_2O. After the baseline measurements, the perfused livers were randomly divided into the D-NAME and L-NAME groups, in which D-NAME and L-NAME (100 μM: Sigma-Aldrich Co., St. Louis, MO) were administered into the reservoir, respectively. Thus, any liver studied was pretreated with either D-NAME or L-NAME. At 10 min after injection of D-NAME or L-NAME, PAF was administered as a bolus into the reservoir in a cumulative manner to gain the concentrations of 0.00001-1 μM. In each experimental group, a double occlusion maneuver was performed at baseline and maximal venoconstriction (when Ppv reached the peak) after an injection of PAF.

2.5. Statistics

All results are expressed as the means ± SE. Data were analyzed by one- and two-way analysis of variance, using repeated-measures for two-way comparison within groups. Comparisons of individual points between groups and within groups were made by Bonferroni's test. Differences were considered as statistically significant at P-values less than 0.05.

3. Results

3.1. The basal hepatic hemodynamic variables

Table 1 shows basal hemodynamic variables of isolated perfused mouse, rat and guinea pig livers. Basal Ppv values were similar among three species, but Qpv values were different: Qpv were 22 ± 1, 38 ± 1 and 48 ± 2 ml min^{-1} 10 g liver Wt for mouse, rat, and guinea pig livers, respectively. Therefore, the order of Rt was mouse > rat > guinea pig. The Rpost-to-Rt ratios were also different, higher in the mouse (0.43 ± 0.01) and guinea pig (0.42 ± 0.01) and lower in the rat (0.24 ± 0.01).

3.2. Effects of L-NAME on basal hepatic hemodynamic variables

Basal Rt and Rpre, but not Rpost, were significantly increased by L-NAME pretreatment in all of three species. Rt and Rpre after L-NAME increased substantially in guinea pig livers, reaching 119 ± 3 and 130 ± 4% of the baselines, respectively. In contrast, the increases in both Rt and Rpre after L-NAME in mouse and rat

Table 1
Basal hemodynamic variables of isolated perfused livers of mouse, rat and guinea pig

	Mouse	Rat	Guinea pig
Number of animals	14	12	12
Wet liver weight (g)	1.7 ± 0.1	10.5 ± 0.2	13.3 ± 0.5
Ppv (cmH_2O)	6.6 ± 0.1[a,b]	7.2 ± 0.1	7.0 ± 0.1
Phv (cmH_2O)	0.21 ± 0.03	0.22 ± 0.03	0.27 ± 0.05
Pdo (cmH_2O)	3.0 ± 0.1[a]	1.9 ± 0.1[b]	3.1 ± 0.1
Qpv (ml min^{-1} per 10 g liver)	22 ± 1[a,b]	38 ± 1[b]	48 ± 2
Rt (cmH_2O ml^{-1} min per 10 g liver)	0.299 ± 0.010[a,b]	0.185 ± 0.004[b]	0.142 ± 0.007
Rpre (cmH_2O ml^{-1} min per 10 g liver)	0.170 ± 0.007[a,b]	0.140 ± 0.003[b]	0.083 ± 0.004
Rpost(cmH_2O ml^{-1} min per 10 g liver)	0.129 ± 0.004[a,b]	0.045 ± 0.001[b]	0.060 ± 0.004
Rpost-to-Rt ratio	0.43 ± 0.01[a]	0.24 ± 0.01[b]	0.42 ± 0.01

Values are given as means ± SE; Ppv, portal venous pressure; Phv, hepatic venous pressure; Pdo, double occlusion pressure; Qpv, portal blood flow rate; Rt, total vascular resistance; Rpre, pre-sinusoidal resistance; Rpost, post-sinusoidal resistance.
[a] $P < 0.05$ vs. rat;
[b] $P < 0.05$ vs. guinea pig.

livers were similarly smaller than those in the guinea pig livers. D-NAME pretreatment did not affect any basal hemodynamic variables.

3.3. The hepatic vasoconstrictive responses of D-NAME pretreated livers to PAF

Fig. 1 shows the concentration-dependent responses of hepatic vascular pressures to PAF (0.00001–1 μM) in mouse, rat and guinea pig livers after pretreatment with D-NAME and L-NAME. In D-NAME groups, PAF concentration-dependently induced hepatic venoconstriction, as reflected by a significant increase in Ppv. Almost maximal constriction was observed at a high concentration of 0.1 μM in all species studied, as shown in Fig. 1. Guinea pig liver was the most sensitive to PAF since the significant increase of Ppv was found at 0.0001 μM, while at 0.01 μM for mouse and rat livers. The responsiveness to PAF of mouse livers was the weakest: PAF at 0.1 μM increased Ppv only by $2.9 \pm 0.2\,cmH_2O$. In contrast, in rat and guinea pig livers, the increases of Ppv were 22.5 ± 2.1 and $19.1 \pm 0.9\,cmH_2O$, respectively, at the corresponding concentration of 0.1 μM PAF. PAF caused a slight but significant increase in Pdo in all of three species, as shown in Fig. 1. These findings indicate that PAF-induced increase in the Ppv-to-Pdo gradient, an indicator of Rpre (Eq. (2)) was greater than that in the Pdo-to-Phv gradient, an indicator of Rpost (Eq. (3)).

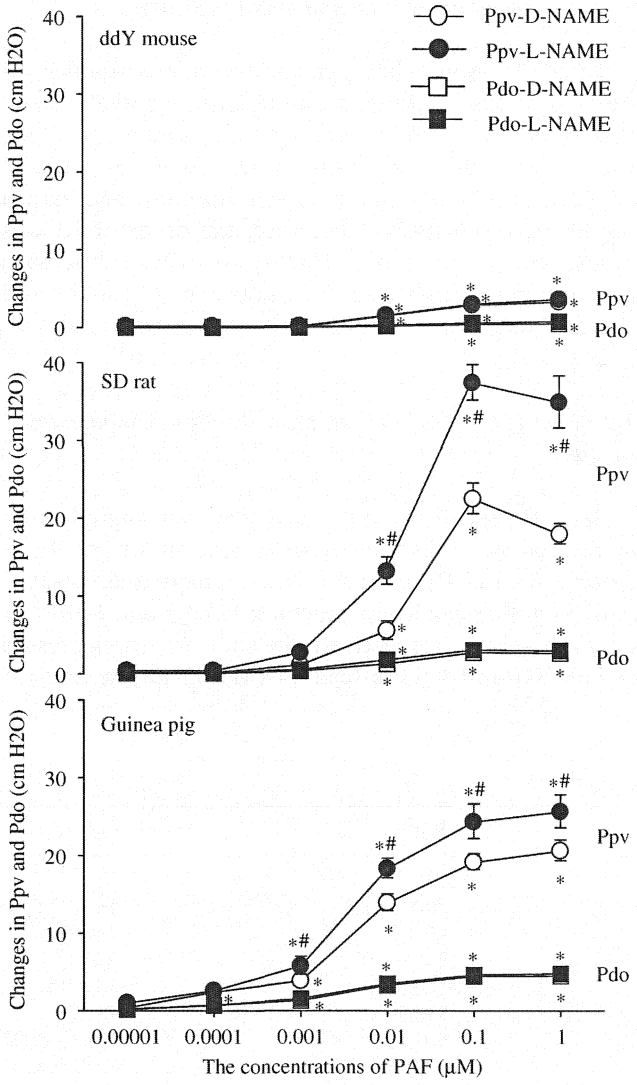

Fig. 1. The concentration-dependent changes in the portal venous pressure (Ppv, circle) and double occlusion pressure (Pdo, square) after PAF injection in mouse, rat and guinea pig livers in the D-NAME (opened symbols) and L-NAME (closed symbols) groups. Values are given as mean ± SE. $n = 6$–7. $^{*}P < 0.05$ vs. the baseline, $^{\#}P < 0.05$ vs. D-NAME group.

Fig. 2 shows summary data of hepatic vascular resistances in D-NAME and L-NAME groups. PAF concentration-dependently increased Rpre and Rpost, and the increases of Rpre were higher than those of Rpost in all D-NAME groups of mouse, rat and guinea pig livers. These results indicate that PAF predominantly constricts the pre-sinusoids in mouse, rat and guinea pig livers. At the concentration of PAF to induce the maximum responses (0.1–1 μM), the Rpre and Rpost were similar between rats and guinea pigs, but they were much lower in mice (Fig. 2).

3.4. Effects of L-NAME on hepatic vascular responses to PAF

In L-NAME groups, PAF-induced hepatic vascular responses were qualitatively similar to those of the D-NAME groups in all three species of animals, as shown in Figs. 1 and 2. In mouse livers, the increases in hepatic vascular pressures and resistances induced by PAF were comparable to those of D-NAME groups, and any significant difference in hepatic hemodynamic variables was not observed between the D- and L-NAME groups. In contrast, in rat and guinea pig livers, the PAF-induced increases in Ppv and Rpre, but not Pdo or Rpost, were significantly greater than those of D-NAME groups. This indicated that L-NAME augmented PAF-induced pre-sinusoidal constriction in rats and guinea pigs. The lowest concentration of PAF at which L-NAME can induce significant augmentative effect was lower in guinea pigs than in rats. However, the augmented venoconstriction at the high concentration of 0.1 μM PAF was significantly larger in magnitude in rat livers than in guinea pig livers: Ppv increased by $37.4 \pm 2.4\,cmH_2O$ in rats, but only by $24.3 \pm 2.4\,cmH_2O$ in guinea pigs; Rpre increased to $744 \pm 55\%$ of the baseline in rats, but to $649 \pm 54\%$ of the baseline in guinea pigs. These results indicated that the augmentation by L-NAME of PAF-induced hepatic vasoconstriction was more sensitive in the guinea pig, but was stronger in the rat.

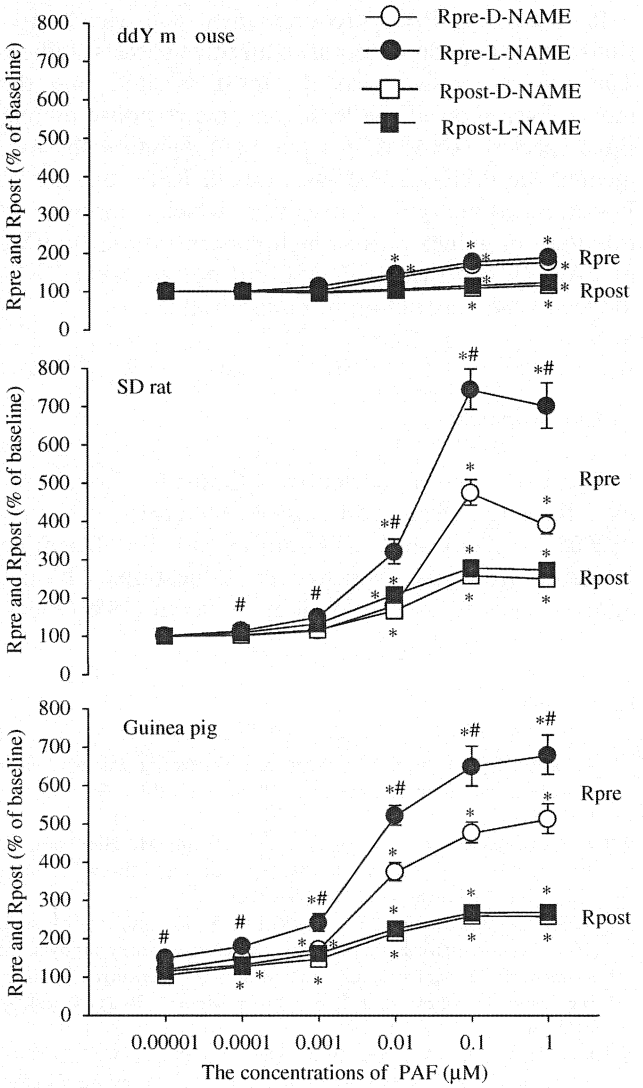

Fig. 2. The summary data of pre-sinusoidal resistance (Rpre, circle) and post-sinusoidal resistance (Rpost, square) in percent of the baselines in mouse, rat and guinea pig livers in the D-NAME (opened symbols) and L-NAME (closed symbols) groups. Values are given as mean ± SE. $n = 6$–7. $^{*}P<0.05$ vs. the baseline, $^{\#}P<0.05$ vs. the D-NAME group.

4. Discussion

We here examined the effects of PAF on the vascular resistance distribution in isolated perfused mouse, rat and guinea pig livers pretreated with either L-NAME or D-NAME. There are two main findings in the present study. The first is that PAF concentration-dependently constricted the pre-sinusoids predominantly over the post-sinusoids in all species of mouse, rat and guinea pig, and that the sensitivity to PAF was the greatest in guinea pig livers and the responsiveness was the weakest in mouse livers. Another main finding was that L-NAME significantly augmented the PAF-induced increases in Rpre, but not in Rpost, in rat and guinea pig livers. This augmentation by L-NAME is stronger in rat livers than in guinea pig livers at the high concentration (0.1 μM) of PAF. In contrast, L-NAME did not significantly augment PAF-induced increases of vascular resistances in mouse livers.

Hepatic segmental vascular responsiveness to PAF differs depending on the animal species: both pre- and post-sinusoidal veins contract in a similar magnitude in dogs [9], while pre-sinusoidal veins predominantly contract over post-sinusoidal veins in guinea pigs [10] and rats [11]. In the present study, we confirmed the previous findings on the effects of PAF on Rpre and Rpost resistances in rat and guinea pig livers, and further demonstrated that PAF also predominantly constricted the pre-sinusoids over the post-sinusoids in mouse livers. However, the venoconstrictive effect of PAF was much weaker on mouse livers than on rat and guinea pig livers (Fig. 2). The reasons of weak venoconstrictive response of mouse livers to PAF were unclear. We speculated that it may be related to the density of PAF receptors on the hepatic vessels, which might be lower in mouse liver than in rat and guinea pig livers, and/or there may be a different subtype of PAF receptor in mice. Another possible explanation is that there might be little amount of contractile elements, i.e., smooth muscle cells, distributed on the portal vein wall of the mouse. This assumption is derived from our previous investigation that the hepatic vascular response was weaker in mice than in rats or guinea pigs under various insults such as norepinephrine [19,22], anaphylaxis [18] and ischemia-reperfusion injury [23,24]. In response to norepinephrine (10 μM), a physiological sympathetic vasoconstrictor, Ppv increased by only 2.0 cmH_2O in mouse livers [19], while 13.1 cmH_2O in rat livers [22] and 9.9 cmH_2O in guinea pig livers [22]. During anaphylactic hypotension, the antigen-induced increase in Ppv was only 3.8 cmH_2O in anesthetized ovalbumin-sensitized mice (unpublished observation), but 14.5 cm H_2O in anesthetized similarly sensitized rats [18]. Finally, during reperfusion following one-hour ischemia, Ppv increased by 19.2 cm H_2O in rat livers [24], while only 3.8 cmH_2O in mouse livers [23]. Further studies are required on structural and functional mechanisms for weak reactivity of the mouse hepatic vessels to determine the amount and distribution of vascular smooth muscle cells and receptors for PAF, and vasoreactivity to PAF in the mouse portal and hepatic veins.

The present study showed in rat and guinea pig livers that L-NAME significantly augmented the PAF-induced increases in Rpre, but not in Rpost. This suggested that NO might be selectively released from pre-sinusoidal vessels during PAF-induced venoconstriction, and then attenuated the PAF-induced pre-sinusoidal constriction. These findings are similar to our previous observations on the effect of L-NAME on the anaphylactic hepatic

venoconstriction in rats [16] and guinea pigs [15], and consistent with the concept that PAF is one of the main mediators for hepatic anaphylaxis [3,7]. The mechanism for this selective vulnerability of pre-sinusoids to NO under PAF-induced venoconstriction may be considered as follows: PAF predominantly constricted pre-sinusoidal vessels as shown in D-NAME groups, where elevated shear stress increased NO release from the same pre-sinusoidal endothelium, leading to relaxation of the adjacent pre-sinusoidal vascular smooth muscle cells in a paracrine manner. Indeed, the wall shear stress in isolated perfused vessels is inversely proportional to the third power of internal radius theoretically [25]. The decrease in vascular internal radius caused by PAF-induced venoconstriction should result in an increase in shear stress. It would further be increased if turbulence did increase at the constricted site [26]. Thus, the NO release from vascular endothelium of the contracted pre-sinusoids would be increased via the shear stress mechanism during PAF-induced venoconstriction.

There is another possibility that is not related to shear stress. PAF could directly stimulate NO release from the vascular endothelium [27–29], by acting on the PAF receptors of the endothelium, resulting in the subsequent activation of endothelial nitric oxide synthase (eNOS) and production of NO. Indeed, PAF, following the binding to its receptor, induces translocation and activation of protein kinase C-alpha [30], which then phosphorylates and activates eNOS [28]. The preponderance of PAF receptors to distribute in the pre-sinusoids rather than the post-sinusoids could account for this vulnerability of the pre-sinusoids to L-NAME.

In the present study, L-NAME augmented the hepatic venoconstrictive responses of rats and guinea pigs, but not mice. These results indicate that there is a species difference in effects of L-NAME on PAF-induced hepatic venoconstriction. We think that this difference depends on the degree of PAF-induced vascular constriction: The stronger venoconstriction, as observed in rats and guinea pigs, could produce bigger shear stress, resulting in more production of NO, which was reflected by exaggerated augmentation of hepatic venoconstriction by L-NAME. In contrast, the mouse liver did not show substantial venoconstriction, which resulted in small shear stress and thus small amount of NO produced, which was reflected by absence of L-NAME-induced augmentation. On the other hand, NO synthesis could be stimulated by PAF via the shear stress-independent mechanism, as mentioned above [28]. This shear stress-independent mechanism also might have not operated in mouse livers challenged with PAF. These findings suggest that mouse hepatic vasculatures seem to be either less sensitive to stimuli for NO synthesis or resistant to the vasodilator action of NO released.

In summary, PAF predominantly constricted pre-sinusoids over post-sinusoids in all three species studied. The guinea pig liver was the most sensitive and the mouse liver showed the least sensitive response among three species. L-NAME pretreatment significantly augmented the PAF-induced increases in Rpre, but not in Rpost, in rat and guinea pig livers, which is stronger in rats than in guinea pigs at high concentration (0.1 μM) of PAF. In contrast, L-NAME did not augment PAF-induced venoconstriction in mouse livers.

Acknowledgments

This work was supported by a Grant for Collaborative Research from Kanazawa Medical University (C2005-1, 2006) and a Grant-in-Aid for Scientific Research from the Ministry of Education, Culture, Sports, Sciences and Technology of Japan (18591730).

References

[1] P. Braquet, L. Touqui, T.Y. Shen, B.B. Vargaftig, Perspective in platelet-activating factor research, Pharmacol. Rev. 39 (2) (1987) 97–145.
[2] B. Samuelsson, M. Goldyne, E. Granstrom, M. Hamberg, S. Hammarstrom, C. Malmsten, Prostaglandins and thromboxanes, Ann. Rev. Biochem. 47 (1978) 997–1029.
[3] T. Shibamoto, Z. Ruan, S. Cui, W. Liu, Y. Kurata, Involvement of platelet-activating factor and leukotrienes in anaphylactic segmental venoconstriction in ovalbumin sensitized guinea pig livers, Prostaglandins Other Lipid Mediat. 78 (1–4) (2005) 218–230.
[4] F. Guarner, J.L. Wallace, W.K. MacNaughton, G.C. Ibbotson, V. Arroyo, J. Rodes, Endotoxin-induced ascites formation in the rat: partial mediation by platelet-activating factor, Hepatology 10 (5) (1989) 788–794.
[5] S. Iwazaki, I. Takeyoshi, S. Ohwada, et al., FR128998 ameliorates liver injury in extended liver resection with ischemia in dogs, Hepatogastroenterology 48 (37) (2001) 197–202.
[6] K. Chun, J. Zhang, J. Biewer, D. Ferguson, M.G. Clemens, Microcirculatory failure determines lethal hepatocyte injury in ischemic/reperfusion rat livers, Shock 1 (1) (1994) 3–9.
[7] K.L. Hines, A. Braillon, R.A. Fisher, PAF increases hepatic vascular resistance and glycogenolysis in vivo, Am. J. Physiol. 260 (3 pt 1) (1991) G471–G480.
[8] D.B. Buxton, R.A. Fisher, D.J. Hanahan, M.S. Olson, Platelet-activating factor mediated vasoconstriction and glycogenolysis in the perfused rat liver, J. Biol. Chem. 261 (2) (1986) 644–649.
[9] H.G. Wang, T. Shibamoto, S. Koyama, Effect of platelet-activating factor on hepatic capillary pressure in isolated dog liver, Prostaglandins Leukot. Essent. Fatty Acids 57 (3) (1997) 293–298.
[10] Z. Ruan, T. Shibamoto, T. Shimo, et al., Effects of platelet-activating factor and thromboxane A_2 on isolated perfused guinea pig liver, Prostaglandins Other Lipid Mediat. 73 (1–2) (2004) 73–85.
[11] S. Cui, T. Shibamoto, W. Liu, H. Takano, Y. Kurata, Effects of platelet-activating factor, thromboxane A_2 and leukotriene D_4 on isolated perfused rat liver, Prostaglandins Other Lipid Mediat. 80 (1–2) (2006) 35–45.

[12] S. Moncada, A. Higgs, The L-arginine–nitric oxide pathway, N. Engl. J. Med. 329 (27) (1993) 2002–2012.
[13] D.D. Rees, R.M. Palmer, S. Moncada, Role of endothelium-derived nitric oxide in regulation of blood pressure, Proc. Natl. Acad. Sci. USA 86 (9) (1989) 3375–3378.
[14] S. Osada, H. Ichiki, H. Oku, K. Ishiguro, M. Kunitomo, M. Semma, Participation of nitric oxide in mouse anaphylactic hypotension, Eur. J. Pharmacol. 252 (3) (1994) 347–350.
[15] Z. Ruan, T. Shibamoto, T. Shimo, H. Tsuchida, T. Koizumi, M. Nishio, NO, but not CO, attenuates anaphylaxis-induced post-sinusoidal contraction and congestion in guinea pig liver, Am. J. Physiol. Regul. Integr. Comp. Physiol. 286 (1) (2004) R94–R100.
[16] S. Cui, T. Shibamoto, W. Liu, H. Takano, Z.S. Zhao, Y. Kurata, Effects of Hct on L-NAME-induced potentiation of anaphylactic presinusoidal constriction in perfused rat livers, J. Cardiovasc. Pharmacol. 48 (1) (2006) 827–833.
[17] Y. Yamaguchi, T. Shibamoto, T. Hayashi, Y. Saeki, S. Tanaka, Hepatic vascular response to anaphylaxis in isolated canine liver, Am. J. Physiol. 267 (1, Part 2) (1994) R268–R274.
[18] T. Shibamoto, S. Cui, Z. Ruan, W. Liu, H. Takano, Y. Kurata, Hepatic venoconstriction is involved in anaphylactic hypotension in rats, Am. J. Physiol. Heart Circ. Physiol. 289 (4) (2005) H1436–H1441.
[19] T. Shibamoto, S. Cui, Z. Ruan, Y. Kurata, Effects of norepinephrine and histamine on vascular resistance in isolated perfused mouse liver, Jpn. J. Physiol. 55 (2) (2005) 143–148.
[20] T. Shibamoto, H.G. Wang, T. Miyahara, S. Tanaka, H. Haniu, S. Koyama, Presinusoidal vessels predominantly contract in response to norepinephrine, histamine, and KCl in rabbit liver, J. Appl. Physiol. 87 (4) (1999) 1404–1412.
[21] C.F. Rothe, Mean circulatory filling pressure: its meaning and measurement, J. Appl. Physiol. 74 (2) (1993) 499–509.
[22] T. Shibamoto, M. Narushima, Y.Q. Ling, et al., Different hepatic vascular response to noradrenaline and histamine between guinea pig and rat, Acta Physiol. Scand. 180 (3) (2004) 255–263.
[23] T. Shibamoto, Z. Ruan, S. Cui, et al., The sinusoidal pressure during ischemia-reperfusion injury in perfused mouse liver pretreated with or without L-NAME, J. Surg. Res., in press.
[24] Y.Q. Ling, T. Shibamoto, T. Honda, et al., Increased sinusoidal pressure is associated with early liver weight gain in ischemia-reperfusion injury in isolated perfused rat liver, J. Surg. Res. 88 (2) (2000) 70–77.
[25] A. Kamiya, T. Togawa, Adaptive regulation of wall shear stress to flow change in the canine carotid artery, Am. J. Physiol. 239 (1) (1980) H14–H21.
[26] D. Lamontagne, U. Pohl, R. Busse, Mechanical deformation of vessel wall and shear stress determine the basal release of endothelium-derived relaxing factor in the intact rabbit coronary vascular bed, Circ. Res. 70 (1) (1992) 123–130.
[27] K. Kamata, T. Mori, K. Shigenobu, Y. Kasuya, Endothelium-dependent vasodilator effects of platelet activating factor on rat resistance vessels, Br. J. Pharmacol. 98 (4) (1989) 1360–1364.
[28] W.N. Duran, A. Seyama, K. Yoshimura, et al., Stimulation of NO production and of eNOS phosphorylation in the microcirculation in vivo, Microvasc. Res. 60 (2) (2000) 104–111.
[29] L. Zhu, P. He, Platelet-activating factor increases endothelial [Ca2+]i and NO production in individually perfused intact microvessels, Am. J. Physiol. Heart Circ. Physiol. 288 (6) (2005) H2869–H2877.
[30] S. Dearn, M. Rahman, A. Lewis, Z. Ahmed, M.C. Eggo, A. Ahmed, Activation of platelet-activating factor (PAF) receptor stimulates nitric oxide (NO) release via protein kinase C-alpha in HEC-1B human endometrial epithelial cell line, Mol. Med. 6 (1) (2000) 37–49.

J Pharmacol Sci **104**, 212 – 217 (2007)

Journal of Pharmacological Sciences

Full Paper

N^G-Nitro-L-arginine Methyl Ester, but Not Methylene Blue, Attenuates Anaphylactic Hypotension in Anesthetized Mice

Hiromichi Takano[1], Wei Liu[1], Zhansheng Zhao[1], Sen Cui[1], Wei Zhang[1], and Toshishige Shibamoto[1,*]

[1]*Department of Physiology II, Kanazawa Medical University, Uchinada, Ishikawa 920-0293, Japan*

Received January 19, 2007; Accepted May 1, 2007

Abstract. To clarify the role of NO in mouse anaphylactic hypotension, effects of a nitric oxide (NO) synthase inhibitor, N^G-nitro-L-arginine methyl ester (L-NAME), on antigen-induced hypotension and portal hypertension were determined in anesthetized BALB/c mice. Systemic arterial pressure (Psa), central venous pressure (Pcv), and portal venous pressure (Ppv) were directly and simultaneously measured. Mice were first sensitized with ovalbumin, and then the injection of antigen was used to decrease Psa and increase Ppv. Pretreatment with L-NAME (1 mg/kg) attenuated this antigen-induced systemic hypotension, but not the increase in Ppv. The effect of inhibitors of soluble guanylate cyclase on anaphylactic hypotension were studied with either methylene blue (3.0 mg/kg) or 1*H*-[1,2,4]oxadiazole[4,3-*a*]quinoxalin-1-one (10 mg/kg). Neither modulated any antigen-induced changes. Furthermore, methylene blue did not improve systemic hypotension induced by Compound 48/80 (4.5 mg/kg), a mast cell degranulator, which can produce non-immunological anaphylactoid reactions. These data show in anesthetized BALB/c mice that L-NAME attenuated anaphylactic hypotension without affecting portal hypertension. This beneficial effect of L-NAME appears not to depend on the soluble guanylate cyclase pathway.

Keywords: anaphylactic shock, portal venous pressure, N^G-nitro-L-arginine methyl ester (L-NAME), methylene blue

Introduction

Anaphylactic hypotension is sometimes fatal (1) and is primarily caused by a decreased blood flow to the heart because left ventricular function is relatively well preserved during anaphylactic shock (2). However, hemodynamic mechanisms responsible for anaphylactic hypotension are not fully understood. We have proposed that the liver and splanchnic vascular beds are involved in anaphylactic hypotension (3 – 6). Indeed, the liver plays a crucial role in the pathogenesis of circulatory collapse in canine anaphylactic shock (3, 7). Anaphylaxis-induced hepatic venous constriction induces pooling of blood in the liver, as well as in upstream splanchnic organs. Both effects reduce venous return with a resultant decrease in stroke volume and systemic arterial pressure. In addition, in sensitized rabbits, anaphylactic hypotension is accompanied by substantial portal hypertension (4), although right heart overload due to pulmonary hypertension is recognized as a causative factor (8). In rats, antigen-induced hepatic venoconstriction also contributes to anaphylactic hypotension (5), and we have recently reported that the liver and splanchnic vascular beds are also involved in mouse anaphylactic hypotension (6).

Nitric oxide (NO) has been shown to play a primary and harmful role in circulatory shock, causing progressive refractory hypotension which ultimately leads to multiple organ dysfunction and death (9 – 11). Although mice have been frequently used for a variety of physiological studies because of development of genetic engineering, few studies have examined a possible role for NO in mouse anaphylactic hypotension (10, 12). Furthermore, it is not known how NO affects anaphylactic hepatic venoconstriction in mice.

The objective of this study was to investigate the role of NO on both systemic and hepatic circulation during anaphylactic hypotension in anesthetized mice.

*Corresponding author. shibamo@kanazawa-med.ac.jp
Published online in J-STAGE: June 29, 2007
doi: 10.1254/jphs.FP0070169

To achieve this, systemic arterial pressure and portal venous pressure were directly measured in sensitized mice intravenously administered ovalbumin antigen. In addition, we determined the effects of methylene blue or 1*H*-[1,2,4]oxadiazole[4,3-*a*]quinoxalin-1-one (ODQ), both inhibitors of soluble guanylate cyclase, on anaphylactic hypotension to define any role for activation of guanylate cyclase and subsequent generation of cGMP in the vasorelaxant action of NO (13). A key reason for studying the effect of methylene blue in mouse anaphylactic hypotension in the present study is the suggestion that methylene blue might be a potential therapeutic drug in anaphylactic shock (14).

Materials and Methods

Animals

The experiments conducted in the present study were approved by the Animal Research Committee of Kanazawa Medical University. We used 57 male BALB/c mice (SLC, Shizuoka) weighing 27 ± 3 g in this study. Mice were maintained at 23°C and under pathogen-free conditions on a 12:12-h dark/light cycle, with food and water ad libitum.

Sensitization

Mice were actively sensitized by the subcutaneous injection of an emulsion made by mixing aluminum potassium sulfate adjuvant (2 mg) with 0.01 mg ovalbumin (grade V; Sigma Chemical Co., St. Louis, MO, USA) dissolved in physiological saline (0.2 ml). The antigen emulsion was injected again one week after the first antigen injection. Non-sensitized (control) mice were injected with aluminum potassium sulfate adjuvant and ovalbumin-free saline. One week after the second injection, the mice were used for the following experiments except the experiment for compound 48/80 (C48/80), a mast cell degranulating agent.

Protocol

Mice were anesthetized with pentobarbital sodium (90 mg/kg, i.p.) and placed on a thermostatically controlled heating pad (ATC-101B; Unique Medical, Tokyo) to maintain body temperature at 37 ± 0.2°C throughout the experiment. The adequacy of anesthesia was monitored by the stability of blood pressure and respiration under control conditions and during tail pinch. Supplemental doses of anesthetic (10% of initial dose) were given intraperitoneally if necessary. To ensure airway patency, tracheotomy followed by insertion of a tracheal tube (18G stainless steel needle) was performed. The right femoral artery was catheterized to measure systemic arterial pressure (Psa) with a transducer (TP-400T; Nihon Kohden, Tokyo). The right external jugular vein was catheterized, and the catheter tip was positioned at the confluence of the superior vena cava and the right atrium to measure the central venous pressure (Pcv). Following a laparotomy, a catheter (ID 0.47 mm, OD 0.67 mm) was inserted into the main portal vein for continuous measurement of portal venous pressure (Ppv). The Psa, Pcv, and Ppv were continuously measured and continuously displayed on a thermal physiograph (RMP-6008, Nihon-Kohden). Outputs were also digitally recorded at 20 Hz (PowerLab; AD Instruments, Sydney, Australia).

The following three experimental protocols were employed:

1) The effect of an NO synthesis inhibitor, N^G-nitro-L-arginine methyl ester (L-NAME), on anaphylactic hypotension: either L-NAME (1.0 mg/kg, 25 μl; n = 8) or N^G-nitro-D-arginine methyl ester (D-NAME) (1.0 mg/kg, 25 μl; n = 8) was intravenously administered. After 10 min, 0.01 mg of ovalbumin antigen (in 100 μl saline) was intravenously administered.

2) The effect of inhibitors of soluble guanylate cyclase, methylene blue or ODQ, on anaphylactic hypotension: either methylene blue (3.0 mg/kg, 25 μl; n = 7) or saline (25 μl, n = 5) was intravenously administered into sensitized mice. After 2 min, the ovalbumin antigen was administered as above. In 6 mice, ODQ (10 mg/kg in 50 μl DMSO) was intraperitoneally administered 1.5 h prior to the injection of ovalbumin antigen.

3) The effect of methylene blue on anaphylactoid reactions induced by C48/80: either methylene blue (3.0 mg/kg; 25 μl, n = 5) or saline (25 μl, n = 5) was intravenously administered into non-sensitized mice. After 2 min, C48/80 (4.0 mg/kg, 100 μl) was intravenously administered.

The following drugs were used: methylene blue (Waldech GmbH & Co., Muenster, Germany); L-NAME, D-NAME, ODQ, and C48/80 (Sigma).

Statistics

All results are expressed as the means ± S.D. Statistical analysis was performed by repeated measures analysis of variance. Comparison of individual points within groups was made by analysis of variance followed by the Bonferroni post-test correction method. Comparison of individual points between two groups and among four groups was made by Student's *t*-test and analysis of variance followed by the Bonferroni post-test correction method, respectively. Differences were considered statistically significant at $P<0.05$.

Results

Intravenous injection of L-NAME, an inhibitor of NO synthase, significantly increased Psa from a baseline of 99 ± 6 to 116 ± 6 mmHg at 10 min, while injection of D-NAME, an inactive isomer of L-NAME, did not change Psa. At 10 min after injection of either L-NAME or D-NAME, ovalbumin antigen was injected to induce anaphylactic hypotension. Figure 1 shows representative examples of the response to intravenous injection of ovalbumin antigen in sensitized mice pretreated with L-NAME or D-NAME. Figure 2 shows the summary data for the time course of changes in Psa, Ppv, and Pcv. After an antigen injection, Psa and Ppv increased in the D-NAME group. Psa increased to the peak of 107 ± 5 mmHg initially and then progressively and significantly decreased to 50 ± 8 mmHg. Ppv increased from the baseline of 5.6 ± 0.7 cmH_2O to the peak of 9.8 ± 0.8 cmH_2O in the D-NAME groups. In the L-NAME group, after antigen, Psa increased to a peak of 135 ± 7 mmHg and then declined but not significantly from baseline until 9, 10, and 20 min. Significant differences in Psa between the L-NAME and D-NAME group were observed up to 50 min after antigen. In contrast to the Psa response, Ppv in the L-NAME group increased in a similar way to the D-NAME group: Ppv increased from the baseline of 5.6 ± 0.7 cmH_2O to a peak of 9.9 ± 0.8 cmH_2O after antigen. Pcv did not significantly change after antigen in either the L-NAME or D-NAME group.

To examine how NO may attenuate anaphylactic hypotension, we used pretreatment with methylene blue in anesthetized mice sensitized with ovalbumin. Intravenous injection of methylene blue did not change the baseline values of Psa, Ppv, and Pcv. After 2 min, antigen was injected to evoke anaphylactic hypotension. Figure 3 shows anaphylactic hypotension in the presence of methylene blue. Pretreatment with methylene blue

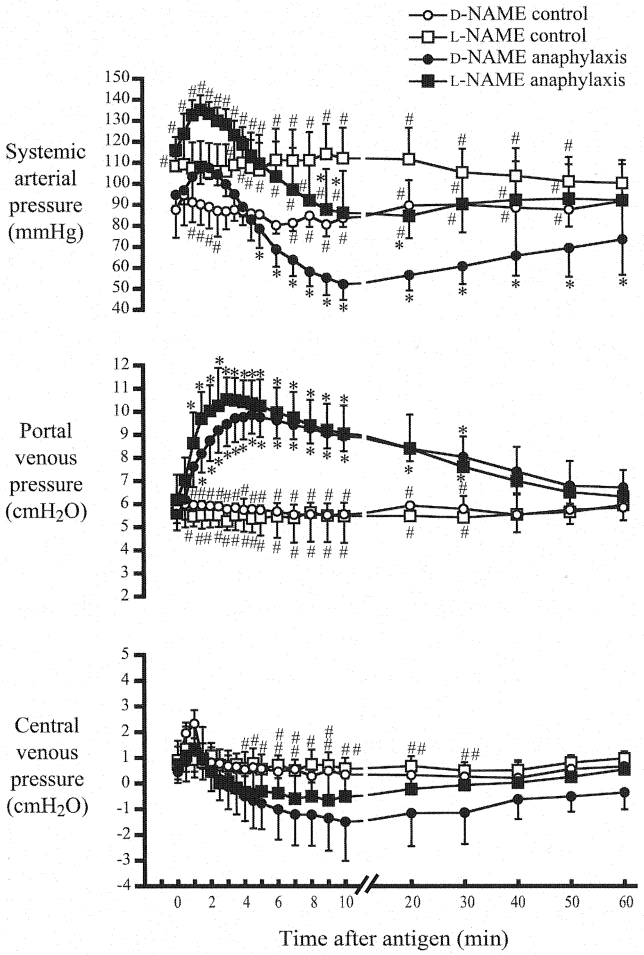

Fig. 2. The summary of changes in the systemic arterial pressure, portal venous pressure, and central venous pressure after an ovalbumin antigen injection in the presence of D-NAME or L-NAME. Open circle, D-NAME control (non-sensitized) (n = 4); closed circle, D-NAME anaphylaxis (n = 8); open square, L-NAME control (non-sensitized) (n = 4); closed square, L-NAME anaphylaxis (n = 8). Values are means ± S.D.; **P*<0.05 *vs* the baseline values, #*P*<0.05 *vs* the D-NAME anaphylaxis group.

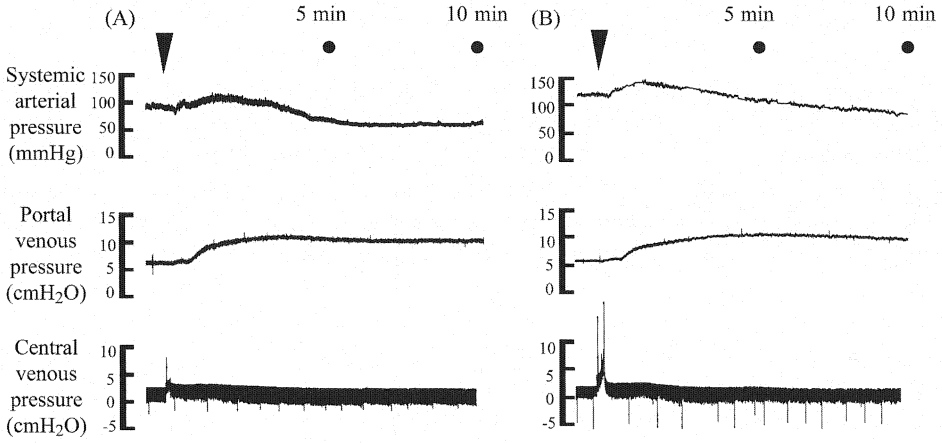

Fig. 1. Representative recordings of the response to ovalbumin antigen of an anesthetized mouse pretreated with D-NAME (A) and L-NAME (B). The arrow on each trace indicates the antigen injection.

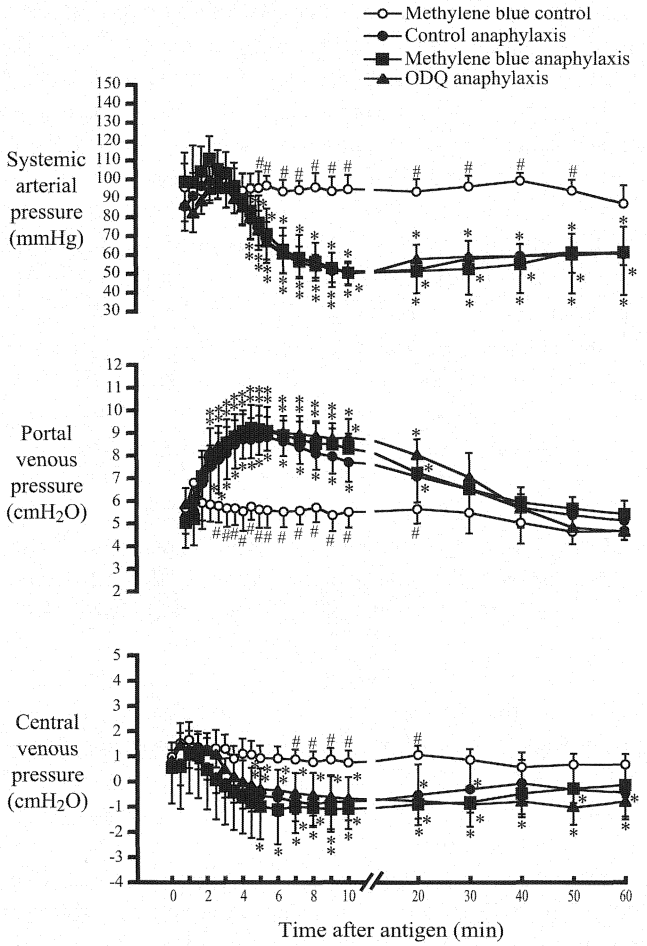

Fig. 3. The summary of changes in the systemic arterial pressure, portal venous pressure, and central venous pressure after an antigen injection in the presence of methylene blue or ODQ. Open circle, methylene blue control (non-sensitized) (n = 4); closed circle, control anaphylaxis (n = 6); closed square, methylene blue anaphylaxis (n = 7); closed triangle, ODQ anaphylaxis (n = 6). Values are means ± S.D. **P*<0.05 *vs* the baseline values, #*P*<0.05 *vs* the control anaphylaxis group.

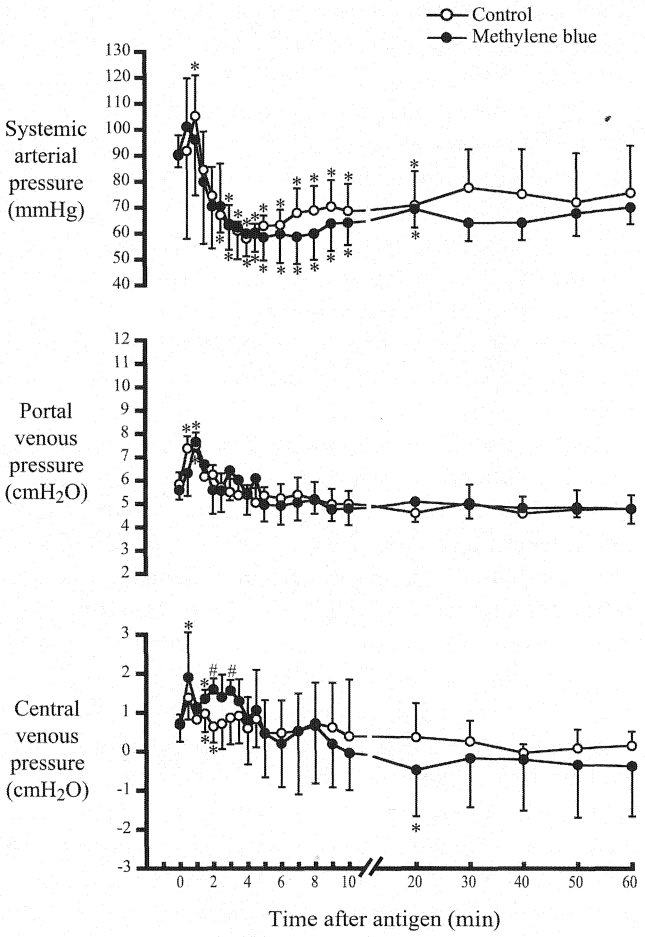

Fig. 4. The summary of changes in the systemic arterial pressure, portal venous pressure, and central venous pressure after Compound 48/80 injection in the control group (open circles, n = 5) and the methylene blue group (closed circles, n = 5). Values are means ± S.D. **P*<0.05 *vs* the baseline values, #*P*<0.05 *vs* the control group.

did not significantly affect the antigen-induced changes in Psa, Ppv, or Pcv. In addition, use of ODQ (10 mg/kg), more specific soluble guanylate cyclase inhibitor, also failed to influence the anaphylactic response.

The fact that methylene blue had no effect on mouse anaphylactic hypotension was unexpected, because Buzato et al. (15) reported that methylene blue improved systemic hypotension induced by C48/80, a mast cell degranulator in the rabbit. So the effect of methylene blue on systemic hypotension induced by C48/80 was also examined in non-sensitized BALB/c mice. Figure 4 shows the summary data for time course changes in Psa, Ppv, and Pcv after an intravenous injection of C48/80 in non-sensitized mice pretreated with or without methylene blue. In control mice, Psa initially increased to 114 ± 15 mmHg from a baseline of 90 ± 8 mmHg after C48/80. Thereafter, Psa dropped to 58 ± 2 mmHg at 8 min and then gradually recovered. Ppv was modestly increased, from a baseline of 5.9 ± 0.5 to 8.3 ± 0.6 cmH_2O at 2 min after an injection of C48/80. Ppv then returned to the baseline levels by 8 min. Pcv was only slightly decreased after C48/80. Pretreatment with methylene blue did not significantly attenuate the C48/80-induced decrease in Psa (Fig. 4), and likewise, there were no substantial differences in Ppv or Pcv to C48/80 with methylene blue (Fig. 4).

Discussion

The present study showed the NO synthesis inhibitor, L-NAME, attenuated anaphylactic systemic hypotension, but not anaphylactic portal hypertension, in anesthetized BALB/c mice. Although attenuation of

anaphylactic hypotension with L-NAME has been reported previously (10, 12), the present study reports the new observation that L-NAME does not affect anaphylactic portal hypertension. Furthermore, use of the soluble guanylate cyclase inhibitor methylene blue unexpectedly failed to have any effect against anaphylactic hypotension in the mouse. Methylene blue also failed to improve systemic hypotension induced by C48/80, a mast cell degranulator, that caused a systemic hypotension similar to anaphylaxis.

Anaphylactic hypotension is primarily caused by a decrease in blood flow to the heart (2). An increased resistance to venous return is important in the pathogenesis of circulatory collapse in anaphylactic shock (3). We have previously reported that anaphylaxis-induced increase in venous resistance is in part caused by hepatic vasoconstriction in dogs (7), guinea pigs (16), rats (5), and rabbits (4). We speculate that anaphylaxis causes hepatic venoconstriction and portal hypertension, resulting in congestion of the upstream splanchnic organs, with a resultant decrease in venous return and effective circulating blood volume, and finally augmentation of anaphylactic hypotension. Indeed, elimination of the liver and splanchnic circulation by total hepatectomy combined with ligation of the celiac and mesenteric arteries attenuates anaphylactic hypotension in anesthetized rats (5). More recently, the same surgical procedures (hepatectomy and elimination of the splanchnic vascular bed) have been shown to attenuate mouse anaphylactic hypotension (6). However, in the present study, antigen-induced increases in Ppv were observed in both L-NAME and D-NAME groups, although a significantly smaller decrease in Psa after antigen occurred in the L-NAME group compared to the D-NAME group. This suggests that L-NAME does not affect anaphylactic hepatic venoconstriction and that the beneficial anti-hypotensive effect of L-NAME may be exerted not on the hepatic vessels but at extrahepatic sites, possibly systemic arterioles. In this regard, we recently showed that mouse hepatic vessels display weak responses to L-NAME: L-NAME did not increase the basal Ppv of hepatic vascular tone in isolated perfused mouse liver nor did it augment hepatic venoconstriction to either the anaphylaxis-related mediator of platelet-activating factor (PAF) (17) or thromboxane A_2 (unpublished observation).

NO relaxes vascular smooth muscle cells mainly through activation of soluble guanylate cyclase (sGC) and subsequent cyclic GMP-dependent modification of several intracellular processes, including the phosphorylation of proteins of the contractile apparatus and of pumps or channels involved in modulating intracellular calcium levels (13). Recent studies by Evora's group reported that one inhibitor of sGC, methylene blue, can reverse clinical anaphylactic shock induced by injected contrast media (12) and prolong the survival of rabbits during experimental anaphylaxis (15). However, in the present study, methylene blue did not prevent anaphylactic hypotension to the same extent. Furthermore, we could not find any beneficial effects of methylene blue against C48/80-induced hypotension, as reported by Buzato et al. (15), in anesthetized mice. In addition, we also failed to alter the anaphylactic responses with another sGC inhibitor, ODQ. The reason for this disparity is not clear, but it might possibly reflect a species difference. In agreement with our data, Cauwels et al. showed that ODQ did not protect against shock induced by PAF in the mouse and that deficiency of 1 of the 2 isoforms of the α subunit of the heterodimeric sGC enzyme ($sGC_{\alpha 1}^{-/-}$ mice) did not protect against PAF-induced shock (10). They proposed that downstream effects of NO, independent of sGC, are important during PAF-induced shock.

On the other hand, NO is involved in the sympathoinhibition during anaphylactic hypotension in anesthetized dogs (18, 19). So, L-NAME stimulation of sympathetic nerve activity may underlie the increase in systemic arterial pressure recorded during anaphylaxis in the present study.

In summary, we investigated the role of NO during anaphylactic hypotension in anesthetized mice. Pretreatment with L-NAME attenuated a fall in Psa, but not an increase in Ppv, after antigen injection. The results suggest that NO partially contributes to anaphylactic hypotension but does not affect the hepatic circulation. Furthermore, pretreatment with either methylene blue or ODQ did not improve systemic hypotension induced by antigen. Thus, it is suggested that sGC independent events downstream from the NO produced during anaphylaxis in the mouse underlie the beneficial action of NO synthase inhibition on anaphylactic hypotension.

Acknowledgments

We thank Professor Chris J Garland and Dr. Kim A Dora for carefully reading a draft version of the manuscript and suggesting many improvements. This study was supported by a Grant for Promoted Research from Kanazawa Medical University (S2006-8), Collaborative Research from Kanazawa Medical University (C2005-1), and a Grant-in-Aid for Scientific Research (18591730) from the Ministry of Education, Culture, Sports, Sciences, and Technology of Japan.

References

1 Kemp SF, Lockey RF. Anaphylaxis: a review of causes and mechanisms. J Allergy Clin Immunol. 2002;110:341–348.
2 Brown ATF. Anaphylactic shock: mechanisms and treatment. J Accid Emerg Med. 1995;12:89–100.
3 Wagner EM, Mitzner WA, Bleecker ER. Peripheral circulatory alterations in canine anaphylactic shock. Am J Physiol. 1986;251:H934–H940.
4 Karasawa N, Shibamoto T, Cui S, Takano H, Kurata Y, Tsuchida H. Hepatic pre-sinusoidal vessels contract in anaphylactic hypotension in rabbits. Acta Physiol (Oxf). 2007;189:15–22.
5 Shibamoto T, Cui S, Ruan Z, Liu W, Takano H, Kurata Y. Hepatic venoconstriction is involved in anaphylactic hypotension in rats. Am J Physiol Heart Circ Physiol. 2005;289: H1436–H1441.
6 Liu W, Shibamoto T, Cui S, Takano H, Kurata Y. Role of liver in anaphylactic hypotension of anesthetized mice. J Physiol Sci. 2006;56:S134.
7 Yamaguchi Y, Shibamoto T, Hayashi T, Saeki Y, Tanaka S. Hepatic vascular response to anaphylaxis in isolated canine liver. Am J Physiol. 1994;267:R268–R274.
8 Halonen M, Palmer JD, Lohman IC, McManus LM, Pinckard RN. Respiratory and circulatory alterations induced by acetyl glyceryl ether phosphorylcholine, a mediator of IgE anaphylaxis in the rabbit. Am Rev Respir Dis. 1980;122:915–924.
9 Amir S, English AM. An inhibitor of nitric oxide production, N^G-nitro-L-arginine-methyl ester, improves survival in anaphylactic shock. Eur J Pharmacol. 1991;203:125–127.
10 Cauwels A, Janssen B, Buys E, Sips P, Brouckaert P. Anaphylactic shock depends on PI_3K and eNOS-derived NO. J Clin Invest. 2006;116:2244–2251.
11 Thiemermann C. Nitric oxide and septic shock. Gen Pharmacol. 1997;29:159–166.
12 Osada S, Ichiki H, Oku H, Ishiguro K, Kunitomo M, Semma M. Participation of nitric oxide in mouse anaphylactic hypotension. Eur J Pharmacol. 1994;252:347–350.
13 Lucas KA, Pitari GM, Kazerounian S, Ruiz-Stewart I, Park J, Schulz S, et al. Guanylyl cyclases and signaling by cyclic GMP. Pharmacol Rev. 2000;52:375–414.
14 Oliveira Neto AM, Duarte NM, Vicente WV, Viaro F, Evora PR. Methylene blue: an effective treatment for contrast medium-induced anaphylaxis. Med Sci Monit. 2003;9:CS102–CS106.
15 Buzato MA, Viaro F, Piccinato CE, Evora PR. The use of methylene blue in the treatment of anaphylactic shock induced by compound 48/80: experimental studies in rabbits. Shock. 2005;23:582–587.
16 Ruan Z, Shibamoto T, Shimo T, Tsuchida H, Koizumi T, Nishio M. NO, but not CO, attenuates anaphylaxis-induced postsinusoidal contraction and congestion in guinea pig liver. Am J Physiol Regul Integr Comp Physiol. 2004;286:R94–R100.
17 Cui S, Shibamoto T, Zhao Z, Takano H, Kurata Y. L-NAME augments PAF-induced venoconstriction in isolated perfused livers of rat and guinea pig, but not mouse. Prostaglandins Leukot Essent Fatty Acids. 2007;76:277–283.
18 Sakuma I, Togashi H, Yoshioka M, Saito H, Yanagida M, Tamura M, et al. N^G-methyl-L-arginine, an inhibitor of L-arginine-derived nitric oxide synthesis, stimulates renal sympathetic nerve activity in vivo. A role for nitric oxide in the central regulation of sympathetic tone? Circ Res. 1992;70:607–611.
19 Shibamoto T, Wang HG, Tanaka S, Miyahara T, Koyama S. Participation of nitric oxide in the sympathetic response to anaphylactic hypotension in anesthetized dogs. Neurosci Lett. 1996;212:99–102.

Respirology (2006) **11**, 566–571 doi: 10.1111/j.1400-1843.2006.00898.x

ORIGINAL ARTICLE

Denopamine stimulates alveolar fluid clearance via cystic fibrosis transmembrane conductance regulator in rat lungs

XIU GU,[1,2] ZHENG WANG,[1] JIN XU,[1] SUMIKO MAEDA,[1] MAKOTO SUGITA,[1] MOTOYASU SAGAWA,[1] HIROHISA TOGA[3] AND TSUTOMU SAKUMA[1]

[1]*Thoracic Surgery,* [3]*Respiratory Medicine, Kanazawa Medical University, Ishikawa, Japan, and* [2]*Respiratory Department, The Second Affiliated Hospital of China Medical University, Shenyang, Liaoning, China*

Denopamine stimulates alveolar fluid clearance via cystic fibrosis transmembrane conductance regulator in rat lungs
GU X, WANG Z, XU J, MAEDA S, SUGITA M, SAGAWA M, TOGA H, SAKUMA T. *Respirology* 2006; **11**: 566–571

Objective: The objective of this study was to test the hypothesis that cystic fibrosis transmembrane conductance regulator (CFTR) plays a role in β_1-adrenergic agonist-stimulated alveolar fluid clearance.

Methods: Isotonic 5% albumin solutions containing different pharmacological agents were instilled into the alveolar spaces of the isolated rat lungs. The lungs were inflated with 100% oxygen at an airway pressure of 7 cm H_2O and placed in a humidified incubator at 37°C. Alveolar fluid clearance was estimated by the progressive increase in the albumin concentration over 1 h. To test the hypothesis, we determined whether CFTR Cl^- channel inhibitors (glibenclamide and $CFTR_{inh}$-172) inhibited the effect of denopamine, a β_1-adrenergic agonist, on stimulation of alveolar fluid clearance in the isolated rat lungs.

Results: Denopamine increased alveolar fluid clearance in a dose-dependent manner. Atenolol, a β_1-adrenergic antagonist, abolished the effects of denopamine on stimulation of alveolar fluid clearance. Although glibenclamide alone or $CFTR_{inh}$-172 alone did not change basal alveolar fluid clearance, these CFTR inhibitors inhibited the effect of denopamine on alveolar fluid clearance.

Conclusion: CFTR plays a role in β_1-adrenergic agonist-stimulated alveolar fluid clearance in rat lungs.

Key words: alveolar fluid clearance, beta-adrenergic agonist, cystic fibrosis transmembrane conductance regulator, glibenclamide, pulmonary oedema.

INTRODUCTION

The mechanisms responsible for reabsorption of excess oedema fluid in the alveolar spaces have been studied over the past two decades.[1] Alveolar epithelium consisting of type I and type II alveolar epithelial cells drives excess alveolar fluid out of the alveolar spaces into the pulmonary interstitial spaces.[2–4] The primary mechanism responsible for alveolar fluid clearance (AFC) is active sodium transport via apical sodium channels and basolateral Na^+-K^+ ATPase.[5–7] Osmotic gradients generated by ion transport withdraw excess alveolar fluid through unknown pathways,[2,8] probably through both paracellular and transcellular pathways. Transported interstitial fluid is then removed through pulmonary circulation, lymph flow and pleural pathways.[9,10] Although β-adrenoceptors on alveolar epithelial cells do not play a role in basal AFC, activation of β-adrenoceptors by β-adrenergic agonists increases AFC[11–13] and accelerates the resolution of pulmonary oedema.[14]

In terms of the distribution of β-receptors in human alveolar cells, 70% are β_2-adrenoceptors and 30% are β_1-adrenoceptors.[15] Terbutaline,[16,17] epinephrine,[18,19] isoproterenol[20] and dobutamine[21] are potent hydrophilic β_2-adrenergic agonists and stimulators of AFC. Salmeterol is a lipophilic β_2-adrenergic agonist and is more potent than the hydrophilic β_2-adrenergic

Correspondence: Tsutomu Sakuma, Thoracic Surgery, Kanazawa Medical University, Uchinada, Ishikawa 920-0293, Japan. Email: sakuma-t@kanazawa-med.ac.jp

Received 3 November 2005; invited to revise 23 December 2005; revised 21 February 2006; accepted 15 March 2006 (Associate Editor: YC Gary Lee).

agonists in stimulating AFC.[17] Similar to β_2-adrenergic agonists, denopamine, a selective β_1-adrenergic agonist, can increase AFC in rat lungs.[22,23] In guinea pig lungs, isoproterenol increased AFC, an effect that was inhibited by atenolol, a selective β_1-adrenergic antagonist.[24] Recent reports have indicated that Cl^- transport is necessary for β_2-agonist-stimulated AFC,[25,26] and that the cystic fibrosis transmembrane conductance regulator (CFTR) Cl^- channel is responsible for Cl^- transport in β_2-agonist-stimulated AFC.[27,28] However, it is not known whether β_1-agonist-stimulated AFC is mediated via CFTR. Therefore, the objective of this study was to determine if β_1-agonist-stimulated AFC is mediated via the CFTR Cl^- channel.

METHODS

Materials

Denopamine (a β_1-adrenergic agonist) was obtained from Tanabe Pharmaceutical Co., Ltd. (Tokyo, Japan). Atenolol (a β_1-adrenergic antagonist) and glibenclamide (a sulphonylurea) were obtained from Sigma (St Louis, MO, USA). $CFTR_{inh}$-172 (a selective CFTR inhibitor) was donated by Dr A.S. Verkman (University of California, San Francisco, CA, USA).

Experimental protocol

All rats received humane care. The study was approved by the Committee for Animal Experiments at Kanazawa Medical University. AFC was measured in the isolated rat lungs in the absence of pulmonary perfusion or ventilation.[17,22,29] Briefly, 8- to 10-week-old male Sprague–Dawley rats (290 ± 35 g, Japan SLC, Inc., Hamamatsu, Japan) were anesthetized with intraperitoneal pentobarbital sodium (50 mg/kg). An endotracheal tube was inserted through a tracheostomy. The rats were exsanguinated via the abdominal aorta and the trachea, and lungs and heart were isolated *en bloc*. Isotonic saline solution (6 mL/kg body weight, 37°C) containing 5% bovine albumin was instilled into both lungs, followed by 4 mL of oxygen to deliver all the instilled solution into the alveolar spaces. The lungs were placed in a humidified incubator at 37°C and inflated with 100% oxygen at an airway pressure of 7 cm H_2O. Alveolar fluid was aspirated 1 h after incubation. The oxygen concentration does not affect AFC for 1 h in isolated rat lungs.[30]

Albumin concentrations in the instilled and aspirated solutions were measured by the pyrogallol red protein dye-binding method (SRL Inc., Tokyo, Japan). AFC was estimated as the progressive increase in the albumin concentration:

$$AFC = [(Vi - Vf)/Vi] \times 100$$

$$Vf = Vi \times Pi/Pf$$

where Vi indicates the volume of instilled albumin fluid and Vf the volume of final alveolar fluid. Pi indicates the protein concentration in the instilled albumin fluid and Pf the protein concentration in the final alveolar fluid.

The term alveolar does not imply that all fluid reabsorption occurs across the alveolar epithelium, because the distal bronchial epithelium can also transport sodium and fluid.

Effects of denopamine on AFC

The dose-dependent effects of denopamine on AFC were determined. Isotonic 5% albumin solutions containing denopamine (10^{-9} M, $n = 4$; 10^{-8} M, $n = 4$; 10^{-7} M, $n = 5$; 10^{-6} M, $n = 9$, 10^{-5} M, $n = 6$) were instilled into the alveolar spaces of rat lungs. As a control, isotonic 5% albumin solutions without denopamine were instilled into the alveolar spaces of rat lungs ($n = 10$).

Effects of atenolol, glibenclamide and $CFTR_{inh}$-172 on denopamine-stimulated AFC

As denopamine increased AFC in a dose-dependent manner, we determined the mechanisms responsible for denopamine-stimulated AFC. First, to determine if denopamine-stimulated AFC was mediated via β_1-adrenoceptors, atenolol (a selective β_1-adrenergic antagonist, 10^{-4} M) was added to the albumin solutions containing denopamine (10^{-6} M) and instilled into the alveolar spaces of rat lungs ($n = 5$). Second, to determine if denopamine-stimulated AFC was mediated via the CFTR Cl^- channel, glibenclamide (10^{-4} M, $n = 6$) or $CFTR_{inh}$-172 (10^{-5} M, $n = 7$) was added to the albumin solutions containing denopamine (10^{-6} M) and instilled into the alveolar spaces of rat lungs. The concentration of $CFTR_{inh}$-172 (10^{-5} M) completely abolished ion transport in intestinal fluid secretion in mice[31] and in cultured human alveolar epithelial type II cells.[32] Third, to determine if combined treatment with atenolol and a CFTR inhibitor had an additive effect on denopamine-stimulated AFC, isotonic 5% albumin solutions containing atenolol (10^{-4} M), glibenclamide (10^{-4} M) and denopamine (10^{-6} M) were instilled into the alveolar spaces of rat lungs ($n = 5$). Isotonic 5% albumin solutions containing atenolol (10^{-4} M), $CFTR_{inh}$-172 (10^{-5} M) and denopamine (10^{-6} M) were also instilled into the alveolar spaces of rat lungs ($n = 5$).

Effects of atenolol, glibenclamide and $CFTR_{inh}$-172 on basal AFC

Finally, we determined whether atenolol, glibenclamide, or $CFTR_{inh}$-172 had effects on basal AFC in the absence of denopamine. Isotonic 5% albumin solutions containing atenolol (10^{-4} M), glibenclamide (10^{-4} M, $n = 4$), or $CFTR_{inh}$-172 (10^{-5} M, $n = 6$) were instilled into the alveolar spaces of rat lungs.

Statistics

Data are summarized as the mean and SD. The data were analysed by one-way analysis of variance

(ANOVA) with the Student–Newman–Keuls *post hoc* test. Differences with a P-value <0.05 were regarded as significant.

RESULTS

Basal AFC was 8.2 ± 1.5% of instilled volume and there was a dose-dependent effect of denopamine on AFC in the rat lungs (Fig. 1). Although 10^{-9} and 10^{-8} M denopamine did not increase AFC, 10^{-7}–10^{-5} M denopamine increased AFC by up to 115% ($P < 0.05$). Atenolol abolished the effect of denopamine on stimulation of AFC ($P < 0.01$, Fig. 2). Glibenclamide and $CFTR_{inh}$-172 partly inhibited the effect of denopamine on stimulation of AFC ($P < 0.05$). Neither glibenclamide nor $CFTR_{inh}$-172 had an additive effect to that of atenolol on denopamine-stimulated AFC (Fig. 3). Atenolol, glibenclamide and $CFTR_{inh}$-172 did not change basal AFC (Fig. 4).

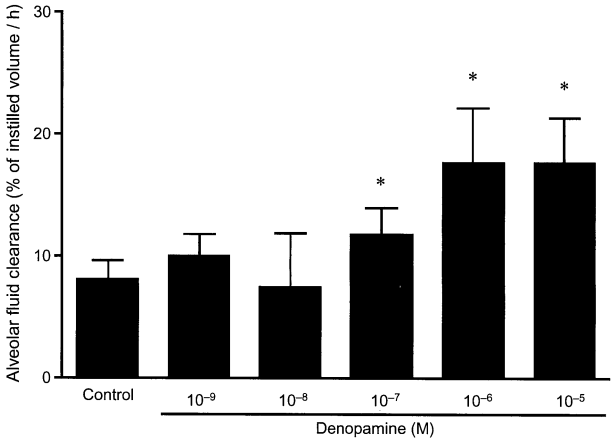

Figure 1 Dose-dependent effects of denopamine on alveolar fluid clearance in rat lungs. *$P < 0.05$ versus control. ED50 = 6.7×10^{-7} M.[23]

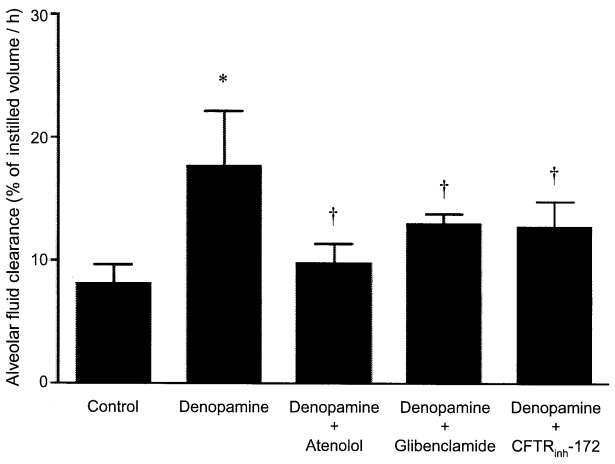

Figure 2 Effects of atenolol, glibenclamide and $CFTR_{inh}$-172 on denopamine-stimulated alveolar fluid clearance. *$P < 0.01$ versus control; †$P < 0.05$ versus denopamine. CFTR, cystic fibrosis transmembrane conductance regulator.

DISCUSSION

There are two major findings from the current study. First, denopamine increased AFC in a dose-dependent manner. Second, the effect of denopamine on AFC was mediated by β_1-adrenoceptors and in part, by CFTR Cl^- channels.

Recently, aerosolized β-agonist therapy has been considered for hydrostatic pulmonary oedema and acute lung injury.[1,33] Interestingly, inhaled salmeterol, a lipophilic β_2-adrenergic agonist, reduced the incidence of pulmonary oedema in subjects susceptible to high-altitude pulmonary oedema.[34] We previously reported that a β_1-adrenergic agonist, denopamine, stimulated AFC in isolated rat lungs.[23] The effect of denopamine persisted in rat lungs with mild injury caused by hyperoxia.[35] As the distribution of β_2-adrenoceptors is greater than that of

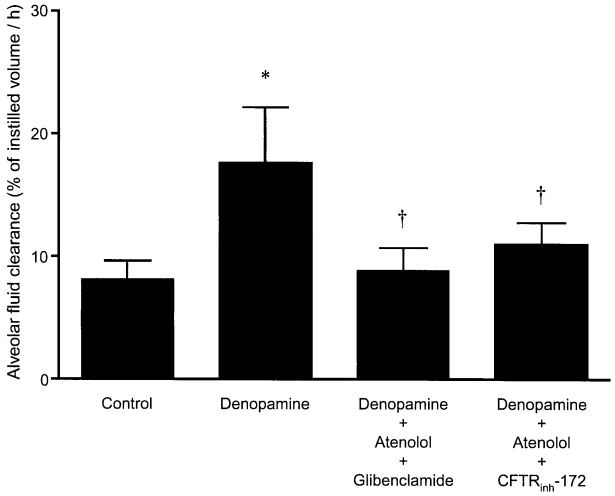

Figure 3 Effects of combined treatment with atenolol and cystic fibrosis transmembrane conductance regulator (CFTR) blockers on denopamine-stimulated alveolar fluid clearance. *$P < 0.01$ versus control; †$P < 0.05$ versus denopamine.

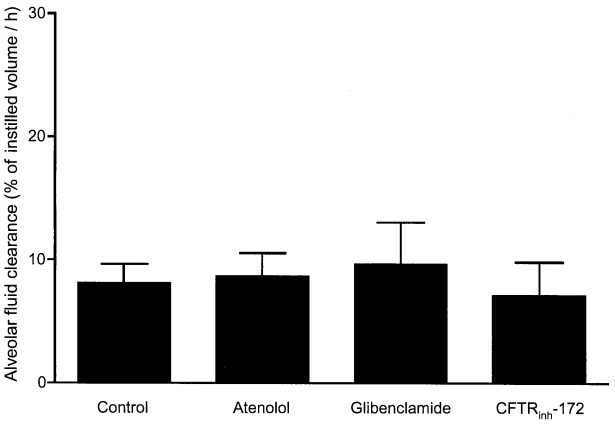

Figure 4 Effects of atenolol, glibenclamide and $CFTR_{inh}$-172 on basal alveolar fluid clearance. CFTR, cystic fibrosis transmembrane conductance regulator.

β_1-adrenoceptors,[15] a β_2-adrenergic agonist should be considered as the first candidate for β-agonist therapy for pulmonary oedema. However, the use of β_2-agonists induces downregulation of β_2-adrenoceptors thereby impairing the efficacy of β_2-agonist therapy.[36] In such circumstances, β_1-agonist therapy would be considered as a second option for treatment of pulmonary oedema.

What is the minimal concentration of β_1-agonist that is required to stimulate AFC? To answer this question, we initially determined the dose–response effect of denopamine on AFC, and found that concentrations of 10^{-7}–10^{-5} M in the pulmonary oedema fluid are necessary to stimulate AFC (Fig. 1). One possible method may be aerosol therapy, because a study reported that standard aerosolized delivery of a generic β_2-agonist (albuterol) in patients with acute pulmonary oedema achieved concentrations in the distal air spaces of the lung in the range of 10^{-6} M,[37] a concentration that should be on the plateau of the dose–response curve for cAMP-mediated stimulation of AFC in human lungs.[17] Therefore, dose–response studies indicate that an adequate concentration of denopamine may be achieved by aerosol therapy.

In our previous study, atenolol, a selective β_1-adrenergic antagonist, inhibited the effect of denopamine, but ICI-118551, a selective β_2-adrenergic antagonist, did not.[23] In the current study, although we did not test the effect of ICI-118551, the β-adrenoceptor subtype that was activated by denopamine may be the β_1-adrenoceptor, because atenolol completely inhibited the effect of denopamine on AFC. Previously, isoproterenol increased AFC and the effect of isoproterenol in guinea pig lungs was inhibited by atenolol.[24] Recently, isoproterenol stimulated AFC in mice with targeted deletions of the β_2-adrenoceptor ($\beta_1AR^{+/+}/\beta_2AR^{-/-}$), although the magnitude of stimulated AFC was less than in wild-type ($\beta_1AR^{+/+}/\beta_2AR^{+/+}$) mice.[13] These reports and the current study confirm that the stimulation of β_1-adrenoceptors actually increases AFC in rats.

To determine if CFTR Cl^- channels play a role in denopamine-stimulated AFC, we tested two inhibitors of CFTR Cl^- channels. One is glibenclamide, a sulphonylurea, that has been used for patients with diabetes mellitus.[38,39] The other inhibitor is $CFTR_{inh}$-172, a newly synthesized specific CFTR inhibitor that is more potent than glibenclamide.[40,41] As $CFTR_{inh}$-172 inhibited AFC, it is likely that denopamine-stimulated AFC was mediated by CFTR.

There are high-conductance, voltage-dependent chloride channels in rat alveolar type II cells, but CFTR is the only cAMP-activated chloride channel known to be present.[42] A role for CFTR was indicated by studies demonstrating AFC in the presence, but not in the absence, of beta-adrenergic agonists.[27,32] However, similar to chloride transport in the presence of β-adrenergic agonists, chloride transport occurs in parallel with sodium transport during basal AFC,[43] suggesting that there must be an intracellular relationship between sodium and chloride channels. However, previous reports indicated that unselective Cl^- channel inhibitors had little effect on basal AFC in normal lungs.[44,45] Both $CFTR_{inh}$-172 and glibenclamide had no effect on basal AFC in the current study. These results suggest that there must be non-CFTR chloride pathways that play a role in basal AFC. However, as there is no specific non-CFTR chloride channel antagonist available, the role of a non-CFTR chloride pathway is uncertain. Further studies are needed to determine the molecular basis for chloride transport across the alveolar epithelium under basal conditions.

Although atenolol abolished the effect of denopamine in stimulating AFC, CFTR inhibitors only partly inhibited the effect of denopamine and did not add to the inhibitory effect of atenolol on denopamine-stimulated AFC. The relationship between β-adrenoceptors and CFTR in AFC has not been sufficiently elucidated. However, Fang *et al.* reported that a β-adrenergic agonist did not accelerate AFC in $CFTR^{-/-}$ mice.[27] Mutlu *et al.* reported that neither β_2-adrenoceptor overexpression in $CFTR^{-/-}$ mice nor CFTR overexpression in $\beta_1AR^{-/-}/\beta_2AR^{-/-}$ mice increased AFC.[28] These studies have indicated that there exists an interdependence between β-adrenoceptors and CFTR Cl^- channels.

Denopamine increased AFC in a dose-dependent manner. This increase was mediated via β_1-adrenoceptors and, in part, via CFTR Cl^- channels. Although the interdependence between β_1-adrenoceptor and CFTR Cl^- channel mechanisms is unknown, it is likely that CFTR plays an important role in β_1-adrenergic agonist-stimulated AFC.

ACKNOWLEDGEMENTS

This study was supported by a Grant for Project Research from High-Technology Center of Kanazawa Medical University (H2005-7), a Grant for Collaborative Research from Kanazawa Medical University (C2005-1) and a Grant-In-Aid for Scientific Research from the MEXT of Japan (17591492).

REFERENCES

1 Matthay MA, Folkesson HG, Clerici C. Lung epithelial fluid transport and the resolution of pulmonary edema. *Physiol. Rev.* 2002; **82**: 569–600.
2 Matthay MA, Landolt CC, Staub NC. Differential liquid and protein clearance from the alveoli of anesthetized sheep. *J. Appl. Physiol.* 1982; **53**: 96–104.
3 Goodman BE, Crandall ED. Dome formation in primary cultured monolayers of alveolar epithelial cells. *Am. J. Physiol.* 1982; **243**: C96–100.
4 Dobbs LG, Gonzalez R, Matthay MA *et al.* Highly water-permeable type I alveolar epithelial cells confer high water permeability between the airspace and vasculature in rat lung. *Proc. Natl. Acad. Sci. USA* 1998; **95**: 2991–6.
5 Basset G, Crone C, Saumon G. Significance of active ion transport in transalveolar water absorption: a study on isolated rat lung. *J. Physiol.* 1987; **384**: 311–24.
6 Goodman BE, Kim KJ, Crandall ED. Evidence for active sodium transport across alveolar epithelium of isolated rat lung. *J. Appl. Physiol.* 1987; **62**: 2460–6.

7 Effros RM, Mason GR, Hukkanen J *et al.* New evidence for active sodium transport from fluid-filled rat lungs. *J. Appl. Physiol.* 1989; **66**: 906–19.
8 Fukuda N, Folkesson HG, Matthay MA. Relationship of interstitial fluid volume to alveolar fluid clearance in mice: ventilated vs. *in situ* studies. *J. Appl. Physiol.* 2000; **89**: 672–9.
9 Wiener-Kronish JP, Broaddus VC, Albertine KH *et al.* Relationship of pleural effusions to increased permeability pulmonary edema in anesthetized sheep. *J. Clin. Invest.* 1988; **82**: 1422–9.
10 Sakuma T, Pittet JF, Jayr C *et al.* Alveolar liquid and protein clearance in the absence of blood flow or ventilation in sheep. *J. Appl. Physiol.* 1993; **74**: 176–85.
11 Crandall ED, Heming TA, Palombo RL *et al.* Effects of terbutaline on sodium transport in isolated perfused rat lung. *J. Appl. Physiol.* 1986; **60**: 289–94.
12 Berthiaume Y, Staub NC, Matthay MA. Beta-adrenergic agonists increase lung liquid clearance in anesthetized sheep. *J. Clin. Invest.* 1987; **79**: 335–43.
13 Mutlu GM, Dumasius V, Burhop J *et al.* Upregulation of alveolar epithelial active Na^+ transport is dependent on beta2-adrenergic receptor signaling. *Circ. Res.* 2004; **94**: 1091–100.
14 Frank JA, Wang Y, Osorio O *et al.* Beta-adrenergic agonist therapy accelerates the resolution of hydrostatic pulmonary edema in sheep and rats. *J. Appl. Physiol.* 2000; **89**: 1255–65.
15 Carstairs JR, Nimmo AJ, Barnes PJ. Autoradiographic visualization of beta-adrenoceptor subtypes in human lung. *Am. Rev. Respir. Dis.* 1985; **132**: 541–7.
16 Sakuma T, Okaniwa G, Nakada T *et al.* Alveolar fluid clearance in the resected human lung. *Am. J. Respir. Crit. Care Med.* 1994; **150**: 305–10.
17 Sakuma T, Folkesson HG, Suzuki S *et al.* Beta-adrenergic agonist stimulated alveolar fluid clearance in *ex vivo* human and rat lungs. *Am. J. Respir. Crit. Care Med.* 1997; **155**: 506–12.
18 Pittet JF, Wiener-Kronish JP, McElroy MC *et al.* Stimulation of lung epithelial liquid clearance by endogenous release of catecholamines in septic shock in anesthetized rats. *J. Clin. Invest.* 1994; **94**: 663–71.
19 Maron MB. Dose-response relationship between plasma epinephrine concentration and alveolar liquid clearance in dogs. *J. Appl. Physiol.* 1998; **85**: 1702–7.
20 Saldias FJ, Comellas A, Ridge KM *et al.* Isoproterenol improves ability of lung to clear edema in rats exposed to hyperoxia. *J. Appl. Physiol.* 1999; **87**: 30–5.
21 Tibayan FA, Chesnutt AN, Folkesson HG *et al.* Dobutamine increases alveolar liquid clearance in ventilated rats by beta-2 receptor stimulation. *Am. J. Respir. Crit. Care Med.* 1997; **156**: 438–44.
22 Sakuma T, Tuchihara C, Ishigaki M *et al.* Beta1-adrenoceptor stimulation by high-dose terbutaline downregulates terbutaline-stimulated alveolar fluid clearance in *ex vivo* rat lung. *Exp. Lung Res.* 2001; **27**: 453–68.
23 Sakuma T, Tuchihara C, Ishigaki M *et al.* Denopamine, a β_1-adrenergic agonist, increases alveolar fluid clearance in *ex vivo* rat and guinea pig lungs. *J. Appl. Physiol.* 2001; **90**: 10–16.
24 Norlin A, Finley N, Abedinpour P *et al.* Alveolar liquid clearance in the anesthetized ventilated guinea pig. *Am. J. Physiol.* 1998; **274**: L235–43.
25 Jiang X, Ingbar DH, O'Grady SM. Adrenergic stimulation of Na^+ transport across alveolar epithelial cells involves activation of apical Cl^- channels. *Am. J. Physiol.* 1998; **275**: C1610–20.
26 Jiang X, Ingbar DH, O'Grady SM. Adrenergic regulation of ion transport across adult alveolar epithelial cells: effects on Cl^- channel activation and transport function in cultures with an apical air interface. *J. Membr. Biol.* 2001; **181**: 195–204.
27 Fang X, Fukuda N, Barbry P *et al.* Novel role for CFTR in fluid absorption from the distal airspaces of the lung. *J. Gen. Physiol.* 2002; **119**: 199–207.
28 Mutlu GM, Adir Y, Jameel M *et al.* Interdependency of beta-adrenergic receptors and CFTR in regulation of alveolar active Na^+ transport. *Circ. Res.* 2005; **96**: 999–1005.
29 Sakuma T, Zhao Y, Sugita M *et al.* Malnutrition impairs alveolar fluid clearance in rat lungs. *Am. J. Physiol. Lung Cell Mol. Physiol.* 2004; **286**: L1268–74.
30 Sakuma T, Hida M, Nambu Y *et al.* Effects of hypoxia on alveolar fluid transport capacity in rat lungs. *J. Appl. Physiol.* 2001; **91**: 1766–74.
31 Ma T, Thiagarajah JR, Yang H *et al.* Thiazolidinone CFTR inhibitor identified by high-throughput screening blocks cholera toxin-induced intestinal fluid secretion. *J. Clin. Invest.* 2002; **110**: 1651–8.
32 Fang X, Song Y, Hirsch J *et al.* Contribution of CFTR to apical-basolateral fluid transport in cultured human alveolar epithelial type II cells. *Am. J. Physiol. Lung Cell Mol. Physiol.* 2006; **290**: L242–9.
33 Crandall ED, Matthay MA. Alveolar epithelial transport. Basic science to clinical medicine. *Am. J. Respir. Crit. Care Med.* 2001; **163**: 1021–9.
34 Sartori C, Allemann Y, Duplain H *et al.* Salmeterol for the prevention of high-altitude pulmonary edema. *N. Engl. J. Med.* 2002; **346**: 1631–6.
35 Sakuma T, Hida M, Nambu Y *et al.* Beta1-adrenergic agonist is a potent stimulator of alveolar fluid clearance in hyperoxic rat lungs. *Jpn J. Pharmacol.* 2001; **85**: 161–6.
36 Matthay MA, Abraham E. Beta-adrenergic agonist therapy as a potential treatment for acute lung injury. *Am. J. Respir. Crit. Care Med.* 2006; **173**: 254–5.
37 Atabai K, Ware LB, Snider ME *et al.* Aerosolized β_2-adrenergic agonists achieve therapeutic levels in the pulmonary edema fluid of ventilated patients with acute respiratory failure. *Intensive Care Med.* 2002; **28**: 705–11.
38 Sakuma T, Takahashi K, Ohya N *et al.* Effects of ATP-sensitive potassium channel opener on potassium transport and alveolar fluid clearance in the resected human lung. *Pharmacol. Toxicol.* 1998; **83**: 16–22.
39 Leroy C, Dagenais A, Berthiaume Y *et al.* Molecular identity and function in transepithelial transport of K(ATP) channels in alveolar epithelial cells. *Am. J. Physiol. Lung Cell Mol. Physiol.* 2004; **286**: L1027–37.
40 Salinas DB, Pedemonte N, Muanprasat C *et al.* CFTR involvement in nasal potential differences in mice and pigs studied using a thiazolidinone CFTR inhibitor. *Am. J. Physiol. Lung Cell Mol. Physiol.* 2004; **287**: L936–43.
41 Thiagarajah JR, Song Y, Haggie PM *et al.* A small molecule CFTR inhibitor produces cystic fibrosis-like submucosal gland fluid secretions in normal airways. *FASEB J* 2004; **18**: 875–7.

42 O'Grady SM, Lee SY. Chloride and potassium channel function in alveolar epithelial cells. *Am. J. Physiol. Lung Cell Mol. Physiol.* 2003; **284**: L689–700.
43 Sakuma T, Suzuki S, Usuda K *et al.* Preservation of alveolar epithelial fluid transport mechanisms in rewarmed human lung after severe hypothermia. *J. Appl. Physiol.* 1996; **80**: 1681–6.
44 Matthay MA, Folkesson HG, Verkman AS. Salt and water transport across alveolar and distal airway epithelia in the adult lung. *Am. J. Physiol.* 1996; **270**: L487–503.
45 Saumon G, Basset G. Electrolyte and fluid transport across the mature alveolar epithelium. *J. Appl. Physiol.* 1993; **74**: 1–15.

Chronic pulmonary artery occlusion increases alveolar fluid clearance in rats

Zheng Wang, MD,[a] Jin Xu, MD,[a] Gang Ma, MD,[a] Motoyasu Sagawa, MD, PhD,[a] Miyako Shimazaki, BS,[b] Yoshimichi Ueda, MD, PhD,[b] and Tsutomu Sakuma, MD, PhD[a]

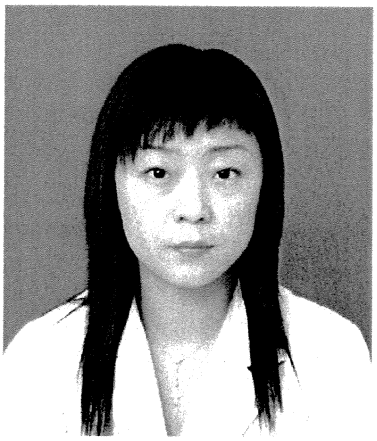

Dr Wang

From the Departments of Thoracic Surgery[a] and Pathology II,[b] Kanazawa Medical University, Uchinada, Ishikawa, Japan.

This study was supported by Grant for Project Research from High-Technology Center of Kanazawa Medical University (H2006-7), Grant for Collaborative Research from Kanazawa Medical University (C2005-1), and Grant-In-Aid for Scientific Research from the MEXT of Japan (17591492).

Received for publication Dec 14, 2006; revisions received May 12, 2007; accepted for publication May 23, 2007.

Address for reprints: Tsutomu Sakuma, MD, PhD, Department of Thoracic Surgery, Kanazawa Medical University, Daigaku, Uchinada, Ishikawa 920-0293, Japan (E-mail: sakuma-t@kanazawa-med.ac.jp).

J Thorac Cardiovasc Surg 2007;134:1213-9

0022-5223/$32.00

doi:10.1016/j.jtcvs.2007.05.027

Objective: We had observed that pulmonary artery ligation for 14 days did not induce lung infiltration in a patient who had undergone a lobectomy for lung cancer. Our hypothesis was that long-term pulmonary artery ligation decreased lung water volume and/or increased alveolar fluid clearance. We determined the mechanism responsible for lung water balance in rats with chronic pulmonary artery occlusion for 14 days.

Methods: Sprague–Dawley rats (n = 45) were used. Through a left thoracotomy, the left pulmonary artery was ligated for 14 days. Then, we measured lung water volume, alveolar fluid clearance, the effects of β-adrenergic agonist and antagonist, mRNA expression, and protein expression in the lungs.

Results: Chronic left pulmonary artery occlusion increased both lung water volume and alveolar fluid clearance in the left lungs, but not in the right lungs with pulmonary perfusion. Neither a β-agonist nor a β-antagonist changed the increase in alveolar fluid clearance. Real-time polymerase chain reaction revealed an increase in α_1-Na,K-ATPase mRNA and a decrease of β_2-adrenoreceptor mRNA, but no change in β_1-Na,K-ATPase mRNA and α-, β-, γ-epithelial sodium channel mRNA, in the left lung without pulmonary perfusion. Western blot analysis revealed an increase in α_1-Na,K-ATPase subunit, but no change in β_1-Na,K-ATPase subunit.

Conclusion: Chronic pulmonary artery occlusion increases alveolar fluid clearance via α_1-Na,K-ATPase overexpression in rats.

Surgery is the most common form of treatment for non–small cell lung cancer. However, there are some complications during surgery. While silicotic hilar lymph nodes (11R inferior) were dissected from the pulmonary artery, we had observed an unexpected hemorrhage from a distal pulmonary artery that was thereafter ligated at the base of the branches to stop the hemorrhage. Fortunately, no abnormal infiltration such as pulmonary edema was found in the lung lobe with pulmonary artery ligation by a chest x-ray film and a computed tomograpic scan 14 days after the operation. However, questions remained regarding lung water balance, especially whether lung water volume decreased or whether alveolar fluid clearance increased.

The amount of alveolar fluid volume is determined by the balance between formation and clearance of alveolar fluid.[1] If the formation exceeds the clearance of

Abbreviations and Acronyms

ATPase	= adenosine triphosphatase
cDNA	= complementary deoxyribonucleic acid
DNA	= deoxyribonucleic acid
ENaC	= epithelial sodium channel
GAPDH	= glyceraldehyde-3-phosphate dehydrogenase
Na,K-ATPase	= sodium–potassium–adenotriphosphatase
PCR	= polymerase chain reaction
RNA	= ribonucleic acid

alveolar fluid, as in cases of hydrostatic pulmonary edema and acute lung injury, the amount of alveolar edema fluid increases and oxygen exchange deteriorates across the alveolar epithelial barrier.[2] The mechanisms responsible for alveolar fluid clearance have been studied in the past 2 decades.[3] Alveolar epithelial type I and II cells drive Na^+ from the alveolar spaces through the apical epithelial sodium channel (ENaC) and basolateral sodium–potassium–adenotriphosphatase (Na,K-ATPase).[4] Ion gradients generated with transported ions drive fluid out of the alveolar spaces.[1] Inasmuch as stimulation of β-adrenergic receptors augmented the rate of alveolar fluid clearance and accelerated the resolution of pulmonary edema,[5,6] some β_2-adrenergic agonists have been considered to be an effective medicine for patients with pulmonary edema.[7]

The impairment of pulmonary blood flow sometimes occurs in patients with pulmonary edema and acute respiratory distress syndrome; therefore, the effect of pulmonary perfusion on alveolar fluid clearance has been studied in in vivo and ex vivo models. Acute pulmonary ischemia did not affect alveolar fluid clearance in sheep.[8,9] Although the rate of alveolar fluid clearance is impaired in the isolated lungs than as in vivo lungs,[10] alveolar fluid clearance continued in the isolated lungs without any pulmonary perfusion in several species including human lungs.[6,10,11] Interestingly, β-adrenergic agonists increase alveolar fluid clearance in these ex vivo and in vivo lungs.[10] However, the duration of pulmonary ischemia was no longer than 8 hours in those studies. Chronic pulmonary artery occlusion occurs in several circumstances in clinical practice. For example, pulmonary artery obstruction can occur as a result of anastomotic stenosis, kinking, or extrinsic compression in a recipient of lung transplantation. Branches of the pulmonary artery are often obstructed by the invasion of lung cancer. Postoperative pulmonary thromboembolism obstructs the stem and branches of pulmonary arteries. It is uncertain whether chronic pulmonary artery occlusion affects the rate of alveolar fluid clearance.

The first objective in the current study was to determine whether chronic pulmonary artery occlusion affected lung water volume and alveolar fluid clearance. Inasmuch as alveolar fluid clearance increased in the rat lungs with chronic pulmonary artery occlusion, the second objective was to determine the mechanism responsible for the increase in alveolar fluid clearance. The third objective was to determine whether a β_2-adrenergic agonist increased alveolar fluid clearance in the rat lungs with chronic pulmonary artery occlusion.

Materials and Methods

Propranolol (a nonselective β-adrenergic antagonist) and terbutaline (a β_2-adrenergic agonist) were obtained from Sigma Chemical Company (St Louis, Mo). RNA probes (α_1-, β_1-Na,K-ATPase, α-, β-, γ-ENaC, β_2-adrenoreceptor) and antibodies (α_1-, β_1- Na,K-ATPase) were obtained from Applied Biosystems (Foster, Calif).

General Protocol

This study was approved by the Committee on Animal Experiments at Kanazawa Medical University. Specific pathogen-free male Sprague–Dawley rats (250–300 g, Japan SLC Inc, Hamamatsu, Japan) received humane care in compliance with guidelines from the University Committee on Animal Resources. Rats were anesthetized with intraperitoneal injection of pentobarbital sodium (50 mg/kg). The rats were orally intubated with Surflo Teflon IV catheters (18G; Terumo, Tokyo, Japan), placed in the right lateral decubitus position, and ventilated with an animal respirator (Harvard Apparatus, Dover, Mass) with 100% oxygen at a peak airway pressure of 7 cm H_2O combined with a positive end-expiratory pressure of 2 cm H_2O. The tidal volume and respiratory rate were 2.0 mL and 70 cycles/min, respectively. Body temperature was maintained at 37°C ± 1°C. Through the fourth intercostal space, a left thoracotomy was performed. The apex of the left lung was pressed with a cotton pad gently toward the diaphragm, and the left pulmonary artery was separated from the left main bronchus gently and then ligated with a 3–0 silk suture. The lung was inflated and the thoracotomy incision was closed.

After the operation, the rats were awakened from the anesthesia and allowed free access to rat chow and water ad libitum for 14 days. After left pulmonary artery occlusion for 14 days, alveolar fluid clearance was measured in the isolated rat lungs.[12-14] In brief, rats were anesthetized with intraperitoneal injection of pentobarbital sodium (50 mg/kg) and exsanguinated via the abdominal aorta. Blood samples were obtained for the measurement of plasma catecholamine levels. The trachea, bilateral lungs, and heart were excised en bloc through a median sternotomy. Isotonic saline solution (37°C) containing 5% bovine albumin was instilled separately into the left lung (6 mL/kg) and right lung (8 mL/kg). Because the right lung is larger than the left lung, a larger volume of albumin solution was instilled into the right lungs. Neither instilled volume (ranging from 6–8 mL/kg) nor oxygen concentration used to inflate lungs had an effect on alveolar fluid clearance.[11-14] The lungs were placed in a humid incubator at 37°C and inflated with 100% oxygen at an airway pressure of 7 cm H_2O over 1 hour. Alveolar fluid was aspirated from the right lung and then from the left lung separately 1 hour after instillation. Protein concentrations in the instilled and aspired alveolar fluid samples

were measured with the pyrogallol red protein dye–binding method.[13]

Specific Protocol

Group 1. The effect of left pulmonary artery occlusion on lung water volume. Lung water volume was estimated by the ratio of lung water to dry lung weight. The lung water/dry lung weight ratio was measured in rats with left pulmonary artery occlusion for 14 days (n = 6). As a control, the lung water/dry lung weight ratio was measured in rats that underwent left thoracotomy without left pulmonary artery occlusion 14 days before the measurement (n = 4).

Group 2. The effect of left pulmonary artery occlusion on alveolar fluid clearance. Alveolar fluid clearance was measured in rats with left pulmonary artery occlusion for 14 days (n = 7). As a sham control, alveolar fluid clearance was measured in rats that underwent left thoracotomy without left pulmonary artery occlusion 14 days before the measurement (n = 4).

Group 3. The effects of propranolol and terbutaline on alveolar fluid clearance in rats with left pulmonary artery occlusion. Inasmuch as alveolar fluid clearance increased in the left lungs in rats with pulmonary artery occlusion, we determined whether endogenous catecholamine played a role in the increase in alveolar fluid clearance. To inhibit the effect of endogenous catecholamine, we instilled an isotonic 5% albumin solution containing propranolol (10^{-4} mol/L) separately into the right and left lungs from rats that underwent left pulmonary artery occlusion for 14 days (n = 4). Because propranolol did not inhibit the increase in alveolar fluid clearance in rats with pulmonary artery occlusion for 14 days, we determined whether chronic pulmonary artery occlusion preserved the effect of terbutaline, a β_2-adrenergic agonist, on alveolar fluid clearance. An isotonic 5% albumin solution containing terbutaline (10^{-6} mol/L) was instilled separately into the right and left lungs from rats that underwent left pulmonary artery occlusion for 14 days (n = 5). As a control, an isotonic 5% albumin solution was instilled into the individual lungs from rats that underwent sham left thoracotomy without left pulmonary artery occlusion 14 days before the measurement (n = 4).

Group 4. Real-time polymerase chain reaction and Western blot analysis. Because chronic pulmonary artery occlusion increased alveolar fluid clearance, we determined the mechanisms responsible for the increase in alveolar fluid clearance. First, we measured the expression levels of ENaC mRNA, Na,K-ATPase mRNA, and β_2-adrenoreceptor mRNA by real-time polymerase chain reaction (RT-PCR) (5 rats with left pulmonary artery occlusion, 4 sham rats without pulmonary artery occlusion). Second, since the expression of α_1- Na,K-ATPase mRNA increased, we measured the Na,K-ATPase protein levels by Western blot analysis (2 rats with pulmonary artery occlusion, 2 sham rats without pulmonary artery occlusion, and 2 control rats without thoracotomy).

Measurements

Lung water volume. Left and right lungs were excised separately and weighed immediately for the measurement of wet lung weight. Thereafter, the lungs were dried in an oven (65°C) for 4 days for the measurement of dry lung weight. The lung water (LW)/dry lung (DL) weight ratio was calculated as follows[13]:

$$LW/DL = (\text{Wet lung weight} - \text{Dry lung weight})/\text{Dry lung weight} \quad (1)$$

Alveolar fluid clearance. Alveolar fluid clearance was estimated by the progressive increase of the albumin concentration in the alveolar spaces.[6,10,11] Alveolar fluid clearance (AFC) was calculated as follows:

$$AFC = ([V_i - V_f]/V_i) \times 100 \quad (2)$$

where V represents the instilled volume of the albumin solution (i) and final volume of alveolar fluid (f).

$$V_f = (V_i \times P_i)/P_f \quad (3)$$

where P represents the concentration of albumin in the instilled solution (i) and in the final alveolar fluid (f).

Plasma catecholamine. Catecholamine (epinephrine, norepinephrine, and dopamine) levels in plasma were measured as reported in prior studies.[12]

Real-time quantitative PCR. After left pulmonary artery occlusion for 14 days, rats were exsanguinated under anesthesia with pentobarbital sodium. The distal lung tissue samples were freshly frozen in liquid nitrogen and stored at −80°C. Total RNA was extracted from the lung tissue with RNA isolative reagent (Isogen; Wako, Osaka, Japan) according to the manufacturer's manual. cDNA was synthesized from 5 μg of total RNA in the DNA engine (PTC-200; MJ Research, Watertown, Mass). Then 3.5 μLcDNA was performed with a 1-step RT-PCR reagent (TaqMan; Applied Biosystems) in a final volume of 20 μL containing 1 μL TaqMan probes, diethylpyrocarbonate water 5.5 μL, and TaqMan universal PCR master mixture 10 μL, at 50°C 2 minutes, 95°C for 10 minutes, 95°C for 15 seconds, and 60°C for 1 minute, totally 40 cycles in sequence detection system (ABI PRISM 7700; Applied Biosystems). Oligonucleotide primers and TaqMan probes of α-, β-, γ-ENaC, α_1-, β_1-Na,K-ATPase, β_2-adreneoreceptor, and glyceraldehyde-3-phosphate dehydrogenase (GAPDH) genes were purchased from Assays-On Demand Gene Expression Products (Applied Biosystems). We picked the sample with lowest Ct value* in all of samples as the standard sample. The standard curve was made of the degressive concentration of standard samples at 5-fold. Gene expression levels, quantified by the standard curve method according to the manufacturer's instructions and standardized with the expression levels of GAPDH gene, were used to analyze the relative amount of target mRNA expressions.

Western blot analysis. Proteins were extracted from the lung tissues with a lysis buffer containing 50 mmol/L Tris-HCl (pH 7.6), 10% glycerol, 5 mmol/L magnesium acetate, 0.2 mmol/L ethylenediamine tetraacetic acid, 1 mmol/L phenylmethylsulfonyl fluoride, and 1% sodium dodecylsulfate. Protein extract was quantified by the Bradford method (Bio-Rad, Hercules, Calif) and 20 μg of the extracted protein was applied to electrophoresis with a 15% polyacrylamide gel and then transferred to a nitrocellulose membrane (Atoh, Tokyo, Japan). After blocking with 5% nonfat milk, 0.05% Tween-20 in Tris-buffered saline, the nitrocellulose membrane was reacted with anti-α_1- and β_1-Na,K-ATPase monoclonal antibodies (1:2000) overnight at 4°C. Blots were washed

*The number of cycles at which fluorescence goes over the cutoff value.

and incubated with peroxidase-labeled rabbit anti-mouse antibodies (1:2000) for 1 hour at room temperature. After incubation, blots were washed 3 times with blocking solution with 0.05% Tween-20 in Tris-buffered saline. The membranes were incubated with chemiluminescence luminol reagent (Supersignal; Pierce, Rockford, Ill) and immunoreactive bands were visualized and photographed digitally by ATTO Light-Capture (AE-6971; ATTO Corporation, Tokyo, Japan).

Morphologic examination. The lung were fixed by injection of 10% formalin solution through the trachea at a pressure of 20 cm H_2O and immersed in 10% formalin solution. A 3-mm thick section was obtained from the center of the each piece of both lungs. These sections were embedded in paraffin and then sectioned serially at 5 μm and stained with hematoxylin and eosin. All sections were coded randomly. Microscopic fields using magnifications of ×100 and ×200 were examined in each section.

Statistics

Data are summarized as the mean and standard error (mean ± SE). The data were analyzed by a 1-way analysis of variance with the Student–Newman–Keuls post hoc test (GraphPad Prism 4; GraphPad Software Inc, San Diego, Calif).

Results

Left Pulmonary Artery Occlusion Increased Lung Water Volume and Alveolar Fluid Clearance

The lung water/dry lung weight ratio was 10% greater in the left lungs with left pulmonary artery occlusion (4.32 ± 0.10 g/g; $P < .05$) than in the right lungs in the same rats (4.00 ± 0.03 g/g) and in left lungs in sham rats without pulmonary artery occlusion (3.90 ± 0.03 g/g) (Figure 1, *A*). In sham rats, there was no difference between the lung water/dry lung weight ratios in the left lungs and in the right lungs. Alveolar fluid clearance significantly increased in the left lungs in rats with left pulmonary artery occlusion (13.6% ± 1.0%; $P < .05$) than in the right lungs in the same rats (9.6% ± 0.5%) and in the left lungs in sham rats without pulmonary artery occlusion (8.6% ± 0.5%) (Figure 1, *B*). In sham rats, there was no difference between alveolar fluid clearance in the left lungs and that in the right lungs. RT-PCR revealed that the expression level of α_1-Na,K-ATPase mRNA (Figure 1, *C*), but not β_1-Na,K-ATPase mRNA (Figure 1, *D*), increased in the left lungs in rats with pulmonary arterial occlusion. Thoracotomies in sham rats did not change the expression levels of α_1- and β_1-Na,K-ATPase mRNA. Western blotting revealed that the α_1-Na,K-ATPase subunit protein level increased in the left lungs in rats with pulmonary artery occlusion (Figure 1, *E*), whereas a statistical analysis was impossible because of small number of samples. However, the β_1-Na,K-ATPase subunit protein level did not change in the left lungs in rats with pulmonary artery occlusion. Neither a thoracotomy nor pulmonary artery occlusion changed the expression levels of α-, β-, and γ-ENaC mRNA.

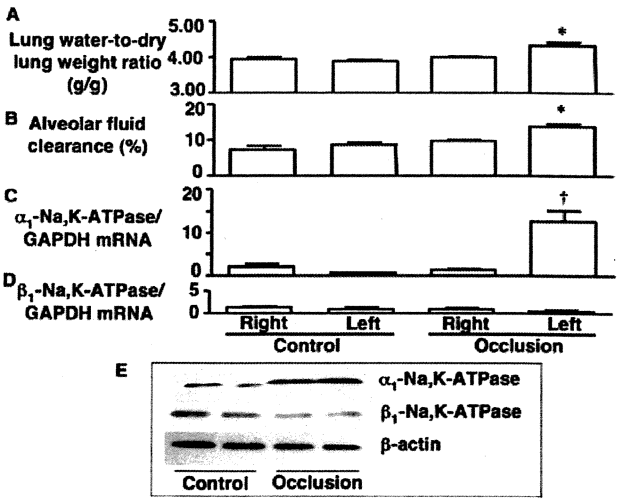

Figure 1. The effect of pulmonary artery occlusion on lung water volume (A), alveolar fluid clearance (B), on Na,K-ATPase mRNA (C and D),and protein levels (E). Left pulmonary artery occlusion increased both the lung water/dry lung weight ratio (A) and alveolar fluid clearance (percent of instilled volume over 1 hour, B) in the left lungs, but not in the right lungs, in rats with left pulmonary artery occlusion. RT-PCR demonstrated that left pulmonary artery occlusion increased the α_1-Na,K-ATPase mRNA levels (C), but not β_1-Na,K-ATPase mRNA levels (D), in the left lungs in rats with left pulmonary artery occlusion. The protein levels of α_1-Na,K-ATPase, but not β_1-Na,K-ATPase, increased in the left lung in rats with pulmonary artery occlusion (occlusion, n = 2) compared with the left lungs in sham control (control, n = 2) (E). *P <.05 vs sham control and right lungs in rats with pulmonary artery occlusion. †P <.01 vs values of Na,K-ATPase mRNA over GAPDH mRNA in the right lungs in rats with left pulmonary artery occlusion and in sham rats without pulmonary artery occlusion. Means ± standard errors. *GAPDH,* Glyceraldehyde-3-phosphate dehydrogenase.

The Effects of Propranolol and Terbutaline on Alveolar Fluid Clearance in Rats With Left Pulmonary Artery Occlusion

Propranolol (10^{-4} mol/L) did not change alveolar fluid clearance in bilateral lungs in rats with left pulmonary artery occlusion (Figure 2, *A*). Terbutaline (10^{-6} mol/L) increased alveolar fluid clearance in the right lungs in rats with pulmonary artery occlusion. However, terbutaline did not increase alveolar fluid clearance in the left lungs in rats with left pulmonary artery occlusion. Plasma catecholamine levels 14 days after surgery were not different from the normal values.[13] The expression levels of a β_2-adrenergic receptor mRNA decreased in the left lung in rats with pulmonary artery occlusion (Figure 2, *B*).

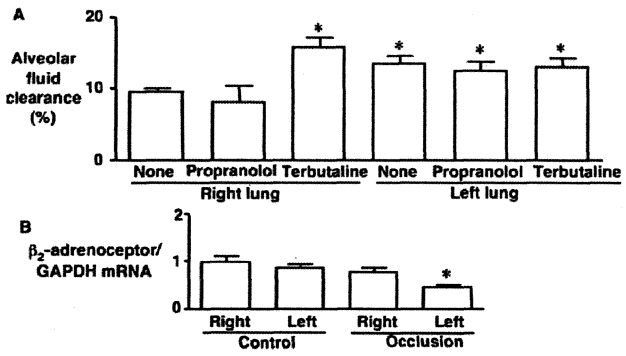

Figure 2. The effects of terbutaline and propranolol on alveolar fluid clearance in rats with left pulmonary artery occlusion (A). Terbutaline (10^{-6} mol/L) increased alveolar fluid clearance in the right lungs, but not in the left lungs, in rats with left pulmonary artery occlusion. Propranolol (10^{-4} mol/L) had no effect on alveolar fluid clearance in both lungs in rats with left pulmonary artery occlusion. *$P < .05$ vs the rates of alveolar fluid clearance in the right lungs in rats with pulmonary artery occlusion. *None,* No treatment of propranolol or terbutaline. The effect of pulmonary artery occlusion on β_2-adrenoceptor mRNA level (B). RT-PCR demonstrated that the level of β_2-adrenoceptor mRNA over GAPDH mRNA decreased in the left lungs in rats with left pulmonary artery occlusion. *$P < .05$ vs the mRNA levels in the right lungs in rats with left pulmonary artery occlusion and in bilateral lungs in control rats. Means ± standard errors. *GAPDH,* Glyceraldehyde-3-phosphate dehydrogenase; *RT-PCR,* real-time polymerase chain reaction; *mRNA,* messenger ribonucleic acid.

Morphologic Examination

The formation of edema fluid was absent in the right lungs in rats with left pulmonary artery occlusion and in the bilateral lungs in sham rats (Figure 3, *A*). Although the formation of edema fluid was absent in the alveolar spaces, perivascular cuffing was present in the left lungs in rats with pulmonary artery occlusion for 14 days (Figure 3, *B* and *C*). Pulmonary infarction and thrombus formation were absent in the lungs with pulmonary artery occlusion.

Discussion

In this study, we found that pulmonary artery occlusion for 14 days increased lung water volume by 10% and also alveolar fluid clearance by 40%. Although α-, β-, γ-ENaC mRNA and β_1-Na,K-ATPase mRNA levels did not increase in the lungs in rats with pulmonary artery occlusion, mRNA and protein levels of α_1-Na,K-ATPase increased. We also found that pulmonary artery occlusion for 14 days abolished the effect of a β_2-adrenergic agonist on alveolar fluid clearance.

Inasmuch as pulmonary artery occlusion decreases the hydrostatic force in the Starling equation,[1] we hypothesized that lung water volume would decrease in the rat lungs without pulmonary perfusion. However, lung water volume measured by a gravimetric method increased. There may be two explanations for the increase in lung water volume because perivascular cuffing was present around the ligated pulmonary artery. First, because lung interstitial fluid drains primarily through the pathway via pulmonary circulation,[8] the decease in pulmonary blood flow impaired the clearance capacity of interstitial fluid and resulted in the increase in lung water volume. Second, whereas lung lymph flow also plays a role in the drainage of interstitial lung fluid and the rate of lung lymph flow is impaired in lungs without pulmonary perfusion,[9,15] it is also likely that decreased lung lymph flow impaired the drainage capacity and resulted in the increase in lung water volume. Because there was no fluid accumulation around bronchi, it is unlikely that bronchial circulation played an important role in the increase in lung water volume.

An amiloride-sensitive sodium channel and basolateral Na,K-ATPase play a primary role in alveolar fluid clearance.[16] We determined whether pulmonary arterial occlusion changed the expression of the sodium channel and Na,K-ATPase. First, since the sodium channel consists of three homologous subunits: α-, β-, and γ-ENaC,[17] we measured the mRNA levels of three subunits and found that RT-PCR did not reveal a significant change in the mRNA levels. Second, although the overexpression of β_1-Na,K-ATPase increased alveolar fluid clearance,[18] we found that pulmonary arterial occlusion did not change the expression of β_1-Na,K-ATPase. In this study, because pulmonary artery occlusion increased both mRNA and protein expressions of α_1-Na,K-ATPase, it is likely that α_1-Na,K-ATPase played a role in the increase in alveolar fluid clearance. Although we did not measure the activity of Na,K-ATPase, our data are supported by a report that the overexpression of α_1-Na,K-ATPase by catecholamine correlated with the increase in the of Na,K-ATPase activity.[19]

Endogenous catecholamines,[20,21] exogenous β_2-adrenergic agonists,[5,6] and the overexpression of β_2-adrenoceptors[22] increased alveolar fluid clearance. Therefore, we determined whether the mechanism mediated by a β-adrenoceptor played a role in the increase in alveolar fluid clearance in the lungs with pulmonary artery occlusion. First, because the endogenous catecholamine levels in plasma did not increase in rats with pulmonary artery occlusion, it is unlikely that the increase in plasma catecholamine was responsible for the increase in alveolar fluid clearance. Second, although it was reported that propranolol inhibited the effect of endogenous catecholamine on alveolar fluid clearance in rats with shock,[20] propranolol did not inhibit the increase in alveolar fluid clearance in this study. Third, although there was a possibility that terbutaline, a potent β_2-adrenergic agonist, did not stimulate alveolar fluid clearance because of a plateau of alveolar fluid clearance, it is unlikely because the increased alveolar fluid clearance in this

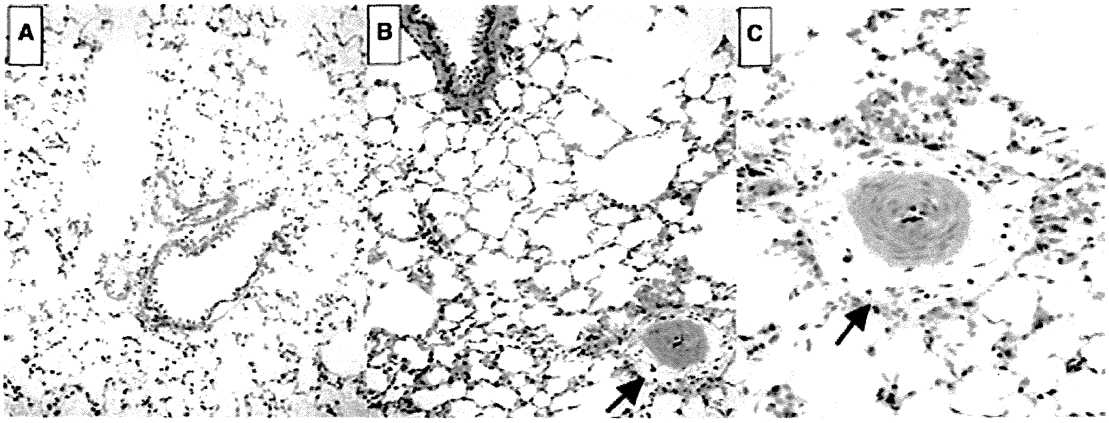

Figure 3. Morphologic examination of the lungs in rats with pulmonary artery occlusion for 14 days. Periarterial cuffing was absent in the right lungs (A) but present in the left lungs (B, ×100, C, ×200) in rats without pulmonary perfusion. *Arrows*, Perivascular cuffing.

study was smaller than the plateau of alveolar fluid clearance.[14] Finally, because the expression of β_2-adrenoceptor mRNA decreased, the decreased expression may be associated with the impaired effect of terbutaline. The impaired function of β-adrenoceptors has been indicated in hemorrhagic shock,[21] hyperoxic lung injury,[23] and ventilator-induced lung injury.[24] However, it is uncertain whether the impaired function of β-adrenoceptors is due to downregulation of β-adrenoceptor, the defect of receptor signaling, or some combination of impaired alveolar epithelial function.[25]

There are several limitations in this study. First, the role of bronchial circulation and lymph flow that may play an important role in lung fluid balance was not determined. Second, the activity of Na,K-ATPase was not determined and the number of lungs used for protein analysis is small. Third, the protein level, trafficking, and signaling of β-adrenoceptors were not determined.

In clinical relevance in thoracic surgery, the results of this study indicate that a treatment increasing alveolar fluid clearance should be considered to eliminate alveolar edema fluid in the lung with pulmonary artery occlusion. In addition, it is unlikely that a β_2-adrenergic agonist is a useful agent for resolution of pulmonary edema in the lung without pulmonary blood flow.

In conclusion, chronic pulmonary artery occlusion increases alveolar fluid clearance via the overexpression of α_1-Na,K-ATPase in rats.

References

1. Matthay MA, Folkesson HG, Clerici C. Lung epithelial fluid transport and the resolution of pulmonary edema. *Physiol Rev.* 2002;82:569-600.
2. Frank JA, Wang Y, Osorio O, Matthay MA. Beta-adrenergic agonist therapy accelerates the resolution of hydrostatic pulmonary edema in sheep and rats. *J Appl Physiol.* 2000;89:1255-65.
3. Matthay MA, Landolt CC, Staub NC. Differential liquid and protein clearance from the alveoli of anesthetized sheep. *J Appl Physiol.* 1982;53:96-104.
4. Borok Z, Liebler JM, Lubman RL, Foster MJ, Zhou B, Li X, et al. Na transport proteins are expressed by rat alveolar epithelial type I cells. *Am J Physiol Lung Cell Mol Physiol.* 2002;282:L599-608.
5. Berthiaume Y, Staub NC, Matthay MA. Beta-adrenergic agonists increase lung liquid clearance in anesthetized sheep. *J Clin Invest.* 1987;79:335-43.
6. Sakuma T, Okaniwa G, Nakada T, Nishimura T, Fujimura S, Matthay MA. Alveolar fluid clearance in the resected human lung. *Am J Respir Crit Care Med.* 1994;150:305-10.
7. Ware LB, Matthay MA. Alveolar fluid clearance is impaired in the majority of patients with acute lung injury and the acute respiratory distress syndrome. *Am J Respir Crit Care Med.* 2001;163:1376-83.
8. Jayr C, Matthay MA. Alveolar and lung liquid clearance in the absence of pulmonary blood flow in sheep. *J Appl Physiol.* 1991; 71:1679-87.
9. Sakuma T, Pittet JF, Jayr C, Matthay MA. Alveolar liquid and protein clearance in the absence of blood flow or ventilation in sheep. *J Appl Physiol.* 1993;74:176-85.
10. Sakuma T, Folkesson HG, Suzuki S, Okaniwa G, Fujimura S, Matthay MA. Beta-adrenergic agonist stimulated alveolar fluid clearance in ex vivo human and rat lungs. *Am J Respir Crit Care Med.* 1997;155:506-12.
11. Sakuma T, Suzuki S, Usuda K, Handa M, Okaniwa G, Nakada T, et al. Preservation of alveolar epithelial fluid transport mechanisms in rewarmed human lung after severe hypothermia. *J Appl Physiol.* 1996; 80:1681-6.
12. Sakuma T, Hida M, Nambu Y, Osanai K, Toga H, Takahashi K, et al. Effects of hypoxia on alveolar fluid transport capacity in rat lungs. *J Appl Physiol.* 2001;91:1766-74.
13. Sakuma T, Sagawa M, Hida M, Nambu Y, Osanai K, Toga H, et al. Time-dependent effect of pneumonectomy on alveolar epithelial fluid clearance in rat lungs. *J Thorac Cardiovasc Surg.* 2002;124:668-74.
14. Sakuma T, Tuchihara C, Ishigaki M, Osanai K, Nambu Y, Toga H, et al. Denopamine, a b_1-adrenergic agonist, increases alveolar fluid clearance in ex vivo rat and guinea pig lungs. *J Appl Physiol.* 2001;90:10-6.
15. Fukuda N, Folkesson HG, Matthay MA. Relationship of interstitial fluid volume to alveolar fluid clearance in mice: ventilated vs. in situ studies. *J Appl Physiol.* 2000;89:672-9.
16. Matalon S, O'Brodovich H. Sodium channels in alveolar epithelial cells: molecular characterization, biophysical properties, and physiological significance. *Annu Rev Physiol.* 1999;61:627-61.

17. Eaton DC, Chen J, Ramosevac S, Matalon S, Jain L. Regulation of Na+ channels in lung alveolar type II epithelial cells. *Proc Am Thorac Soc.* 2004;1:10-6.
18. Azzam ZS, Dumasius V, Saldias FJ, Adir Y, Sznajder JI, Factor P. Na,K-ATPase overexpression improves alveolar fluid clearance in a rat model of elevated left atrial pressure. *Circulation.* 2002;105:497-501.
19. Azzam ZS, Adir Y, Crespo A, Comellas A, Lecuona E, Dada LA, et al. Norepinephrine increases alveolar fluid reabsorption and Na,K-ATPase activity. *Am J Respir Crit Care Med.* 2004;170:730-6.
20. Pittet JF, Wiener-Kronish JP, McElroy MC, Folkesson HG, Matthay MA. Stimulation of lung epithelial liquid clearance by endogenous release of catecholamines in septic shock in anesthetized rats. *J Clin Invest.* 1994;94:663-71.
21. Modelska K, Matthay MA, Brown LA, Deutch E, Lu LN, Pittet JF. Inhibition of beta-adrenergic–dependent alveolar epithelial clearance by oxidant mechanisms after hemorrhagic shock. *Am J Physiol.* 1999;276:L844-57.
22. Mutlu GM, Adir Y, Jameel M, Akhmedov AT, Welch L, Dumasius V, et al. Interdependency of beta-adrenergic receptors and CFTR in regulation of alveolar active Na+ transport. *Circ Res.* 2005;96:999-1005.
23. Saldias FJ, Comellas A, Ridge KM, Lecuona E, Sznajder JI. Isoproterenol improves ability of lung to clear edema in rats exposed to hyperoxia. *J Appl Physiol.* 1999;87:30-5.
24. Frank JA, Pittet JF, Lee H, Godzich M, Matthay MA. High tidal volume ventilation induces NOS2 and impairs cAMP-dependent air space fluid clearance. *Am J Physiol Lung Cell Mol Physiol.* 2003;284:L791-8.
25. Mutlu GM, Koch WJ, Factor P. Alveolar epithelial beta 2-adrenergic receptors: their role in regulation of alveolar active sodium transport. *Am J Respir Crit Care Med.* 2004;170:1270-5.

CSP

１．研究課題名：肺癌の新しい機能的および形態的診断法の確立と分子標的治療法を指向した標的遺伝子の特定に関する研究（研究番号　C2005-2）

２．キーワード：１）肺癌（lung　cancer）
２）DNA microarray（DNA microarray）
３）微小乳頭状成分（micropapillary component）
４）仮想気管支鏡（Virtual Bronchoscopy）
５）Furanonaphthoquinone（Furanonaphthoquinone）

３．研究代表者：東　光太郎・医学部・教　授・放射線診断治療学（放射線医学）
研究分担者：竹上　　勉・総合医学研究所・教　授・分子腫瘍学研究部門
上田　善道・医学部・教　授・病理病態学（病理学Ⅱ）
栂　　博久・医学部・教　授・呼吸機能治療学（呼吸器内科学）
佐川　元保・医学部・教　授・呼吸機能治療学（呼吸器外科）
小林　　健・金沢大学・医学部・講師・放射線科
松成　一朗・先端医学薬学研究センター・臨床研究開発部長
郭　　建飛・中国医科大学・医学部・講師・放射線科

４．研 究 目 的

平成１５年度の肺癌による死亡者は５６０００人と癌死の一位を占め、さらに増加傾向にある。肺癌の治療成績は不良で、再発をきたしやすい。肺癌の予後を改善するためには、新たな診断法および治療法の開発が不可欠である。以下の１）、２）、３）、４）、５）により、肺癌の予後改善に寄与することが本研究の最終的な目標である。

１）細胞組織の腫瘍化・進展における遺伝子発現の差異を明らかにする。(担当：竹上)

２）近年肺腺癌の新たな予後不良亜型として提唱された微小乳頭状成分に関して、その高悪性度に関わる遺伝子を癌細胞・宿主間質細胞間応答に着目して明らかにする。(担当：上田)

３）極細経の気管支鏡と CT を用いた Virtual Bronchoscopy を組み合わせることにより，末梢型微小肺癌の確実な形態的診断法を確立する。(担当：佐川)

４）新しい肺癌治療薬として furanonaphthoquinone 誘導体(J103)に注目し、furanonaphthoquinone 誘導体(J103)の肺癌細胞に対する抗腫瘍効果を明らかにし、その機構を解明する。さらに、gefitinib の抗腫瘍効果の機序を解明する。(担当：栂)

５）cDNA マイクロアレイ及びプロテオミクス解析により遺伝子及び蛋白発現プロファイリングとして腫瘍の生物学的活性を捉え、肺癌の新たな機能的診断法を開発、確立する（担当：東、小林、松成、郭)。

５．研 究 計 画

１）細胞組織の腫瘍化・進展における遺伝子発現の差異について DNA microarray 法による網羅的解析および Real time RT-PCR 法による標的遺伝子の活性状態を探索し、

がん細胞・宿主細胞相互応答に関わる遺伝子について調べ、さらに関与が推定されるタンパク分子群の実態を共焦点顕微鏡等を駆使して解析を行う。(担当:竹上)

2）肺腺癌の微小乳頭状成分に関して、その高悪性度に関わる遺伝子について cDNA マイクロアレイ法による遺伝子発現プロファイリング解析を行う。(担当：上田)

3）Virtual Bronchoscopy の末梢微小陰影に関する画像再構成の至適条件を確立し，実際の症例で観察および組織採取を行う。また，より採取効率の良い組織・細胞採取の device の開発を行う。(担当：佐川)

4）マウスを用いた in vivo の実験では、Lewis lung carcinoma 2 (LL/2)を移植し furanonaphthoquinone 誘導体の抗腫瘍効果を測定し、副作用の有無を調べる。(担当：栂)

5）非小細胞性肺癌の血管新生因子の一種である angiopoietin-2 の mRNA 発現を測定する。さらに、hypoxia-inducible factor-2α の発現を測定し、これらと FDG PET により測定した糖代謝活性との関連を明らかにする。これにより、血管新生因子を標的とした分子標的治療法の適応を明らかにする。(担当：東、小林、松成、郭)

6．研 究 成 果

1）細胞内シグナル伝達に重要なタンパクである RhoGDIβ の分子端が欠如する場合は正常なタンパク機能を果たせず、細胞の異常増殖、転移能の上昇がみられた (Ota T, et al., 2006 及び 2007)。また肝細胞癌発症におけるＣ型肝炎ウイルスの役割、発癌に関わるウイルス遺伝子・タンパク、中でも NS3 タンパクと宿主細胞タンパクとの相互作用についても引き続き解析を行い、p53 経路に関わる SRCAP タンパクの関与を明らかにした (論文準備中)。(担当：竹上)

2）Unsupervise な状態でのクラスター解析でも微小乳頭状成分を有する肺腺癌と有さない肺腺癌は有意に異なるクラスターに分類された。更に微小乳頭状腺癌では、低進行度と高進行度の間でも異なるクラスターに分類された。Ranking 解析から両者間で有意に発現差のある遺伝子が選別され、real time RT-PCR 法および免疫染色でも検証された。中でも chemokine ligand 14 (CXCL 14) の発現低下と S100P 遺伝子の発現亢進は微小乳頭状腺癌成分の生物学的侵襲性に関わることが明らかになり、現在その詳しい機序に関し検索を進めている。この研究結果に関しては現在論文作成中である。(担当：上田)

3）平成１７年度までに，Virtual Bronchoscopy に関して，種々の画像再構成条件を試行し，末梢微小陰影に関する至適条件を検討した。実際の微小肺癌症例に Virtual Bronchoscopy を行い，その結果を条件検討に反映させた。おおむね５次から７次気管支までの Virtual Bronchoscopy 画像再構成に関しては，安定して可能となるような条件を設定しえた。８次ないし９次気管支に関しては，症例の条件の違いもあり不安定なため，今後若干の検討が必要である。(担当：佐川)

4）①Furanonaphthoquinone 誘導体(J103)は 1.0-2.5 ・g/body の範囲で量依存性にマウスに移植された LL/2 腫瘍の増殖を抑制した。同時に J103 は同腫瘍細胞表面の Fas 発現を増強し、Fas mRNA の発現を増強した。LL/2 腫瘍細胞のアポトーシスを増加させた。J103 は脾臓由来の T リンパ球数を減少させず、同細胞表面に FasL

を発現させた。以上から、J103 の抗腫瘍作用機序は Fas/FasL システムを介したアポトーシスの増強と T リンパ球の活性化であることが示された。(担当：栂) ②A549 細胞に抗腫瘍薬 VP-16 1-4g/ml を投与する時、クラリスロマイシン(CAM) 10-50g/ml を上乗せ投与すると、VP-16 の抗腫瘍効果が量依存性に増強した。CAM は VP-16 の腫瘍細胞内への取り込みを促進することにより、その抗腫瘍効果を増強する可能性が示された。(担当:栂)③A549 細胞に抗腫瘍薬 gefitinib 0.25-20・M を投与すると、A549 の IL-8 産生が量依存性に増加した。gefitinib の抗腫瘍効果の一部は IL-8 産生に関連していることが示唆された。また、これは gefitinib の重篤な副作用である急性肺傷害の発症機序に IL-8 産生が関わる可能性も示すものである。(担当：栂)

５)肺癌の血管新生因子である angiopoietin-2 の mRNA 発現および hypoxia-inducible factor-2α の発現の程度は肺癌の悪性度により異なり、angiopoietin-2 の mRNA 発現あるいは hypoxia-inducible factor-2α の発現が強い肺癌は悪性度が高く予後が悪いこと明らかにした。また、FDG PET で測定した肺癌の糖代謝活性は angiopoietin-2 の mRNA 発現および hypoxia-inducible factor-2α の発現と相関していた。このことから、FDG PET により angiopoietin-2 および hypoxia-inducible factor-2α を標的とした分子標的治療法の適応を決定できることが判明した。(担当：東、小林、松成、郭)

７．研究の考察・反省

１）今後さらに発癌過程におけるタンパクータンパクの相互作用とその役割・影響について詳細を DNA microarray 法、Real time RT-PCR 法、タンパク発現ベクター導入、レポーターアッセイ法等を用いて解析していくことが必要である。(担当：竹上)

２）気管支鏡の条件設定および組織採取・検体処理に関する多くの知見が得られ，今後の研究の基盤整備に役立てることができた．今後は，自動描画システムの開発による更なる診断技術の開発に取り組んでいく予定である。(担当：佐川)

３）肺癌の治療効果の予測に、Fas/FasL システムを介したアポトーシスの増強、CAM の抗腫瘍薬の作用増強効果、IL-8 産生の関与が有用であることが示唆された。腫瘍細胞を直接調べればこのような予測が可能になると思われる。今回の研究では、このような関連蛋白および遺伝子の発現をアイソトープなどを用いて画像化するところまでは出来なかった。今後の課題である。(担当：栂)

８．研 究 発 表

Takegami T. Japanese encephalitis virus RNA synthesis *in vivo* and *in vitro*. J Kanazawa Med Univ 2005; 30: 560-566.

Ota T, Maeda M, Suto S, Zhou X, Murakami M, Takegami T, Tatsuka M. RhoGDIβ lacking the N-terminal regulatory domain suppresses metastasis by promoting anoikis in v-src transformed cells. Clinical and Experimental Metastasis 2006;

23: 323-334. (MLDB)

Ota T, Maeda M, Murakami M, Takegami T, Suto S, Tatsuka M. Activation of Rac1 by Rho-guanine nucleotide dissociation inhibitor-β with defective isoprenyl-binding pocket. Cell Biology International 2007; 31: 92-96. (MLDB)

Guo J, Higashi K, Ueda Y, Oguchi M, Takegami T, Toga H, Sakuma T, Yokota H, Katsuda S, Tonami H, Yamamoto I. Microvessel density: correlation with F-18 FDG uptake and prognostic impact in lung adenocarcinomas. J Nucl Med 2006; 47: 419-425 (MLDB)

Sagawa M, Higashi K, Sugita M, Ueda Y, Maeda S, Toga H, Sakuma T. Fluorodeoxyglucose uptake correlates with the growth pattern of small peripheral pulmonary adenocarcinoma. Surg Today 2006; 36: 230-234. (MLDB)

Guo J. Tumor angiogenesis in lung adenocarcinomas: correlation with FDG uptake and prognosis. J Kanazawa Med Univ 2006; 31: 10-16.

高橋知子. FDG 集積度, HRCT 所見, および血清 CEA 値による肺腺癌（３ｃｍ以下）の術後再発予測. 金医大誌 2006; 31: 185-193.

東　光太郎, 上田善道. PET の現状　肺癌の診断, 評価. Pharma Medica 2006; 24: 27-29.

J Kanazawa Med Univ 30 : 560−566, 2005

Japanese encephalitis virus RNA synthesis *in vivo* and *in vitro*

Tsutomu Takegami

Abstract: In order to investigate the mechanism of Japanese encephalitis virus (JEV) RNA replication, viral RNA syntheses *in vivo* and *in vitro* were analyzed. First, an appearance of viral specific RNA in JEV-infected cells was examined by northern blot analysis. Minus RNA-probe recognized a negative strand of JEV-specific RNA synthesized in JEV-infected cells as early as 6 hrs post infection (p.i.). Full length genomic 42S positive RNAs were detected in the cells at 12 hrs p.i. Relative amounts of the 42 S positive RNA was much larger in the membrane fraction than the supernatant fraction of JEV-infected cells. To investigate the mechanism of RNA synthesis, it is important to establish the *in vitro* system of RNA synthesis. It was found that JEV specific positive RNAs were efficiently synthesized *in vitro* in the crude membrane and nuclear fractions prepared from the JEV-infected cells. The analyses by SDS-PAGE and immunofluorescence assay indicated that nonstructural proteins NS3 and NS5, considered to be RNA helicase, protease and RNA polymerase, respectively, were membrane associated proteins, even though they were hydrophilic proteins. Maybe other NS proteins, including NS4a and 4b, are responsible to the membrane association, because of the hydrophobicity. The data that monospecific antisera against NS3 and NS5 inhibited *in vitro* RNA synthesis indicate that those proteins strongly contributed for viral RNA synthesis in the JEV-infected cells.

Key Words : Japanese encephalitis virus, RNA replication, *in vitro* system

Introduction

Japanese encephalitis (JE) is an acute viral infection of the central nervous system in humans, with an estimation of 50,000 cases of encephalitis and 10,000 death annually in the world (1-3). Japanese encephalitis virus (JEV) is the leading cause of viral encephalitis in Asia. Even though recently JE cases in Japan are less than 10 in each year, still JE viruses circulate in wide area including Ishikawa (4). The genome of JEV, a member of the Flaviviridae, is a single-stranded, positive sense RNA ca 11kb in length which has no poly A at the 3'untranslated region (UTR) (5). Several process of JEV-RNA synthesis in the infected cells is unknown, although some studies related to this problem have been reported (6-8). Generally, it is thought that a negative stranded RNA must be synthesized in the early stage of JEV reproduction in cells, similarly to the early events of other positive RNA virus infections. The negative strand copied from positive genomic RNA leads to the formation of double-stranded replicative form (RF), which may have recycling role as a template (6). In order to examine the early events during JEV-RNA replication, it is essential to detect and distinguish the negative and positive strand.

The entire nucleotide sequence of JEV genomic RNA has been determined (9-11). It is suggested that JEV genomic RNA has a specific secondary structure at the 3' end, and this structure plays a significant role in the RNA replication of JEV and other flaviviruses (5-6,11-12). Sequencing data indicate that the genome organization of several flaviviruses is very similar to each other, though not identical (6), and suggest that these viruses have common features in their mechanism of RNA replication. The functions of nonstructural proteins including NS3 and NS5 in the replication complex (RC) is gradually clarified but not enough. Here we report the feature of JEV-RNA synthesis in JEV-infected cells and *in vitro* system using membrane fraction derived from JEV-infected cells.

Division of Molecular Oncology and Virology,
Medical Research Institute, Kanazawa Medical University
Uchinada, Ishikawa, 920-0293, Japan
Accepted: March 11, 2006

Materials and Methods

Cells, Viruses and RNA:

Mosquito cells C6/36 and Vero cells were cultured in the medium MEM containing 5-10% fetal bovine serum. Those cells were infected with JEV, JaGAr01 or Nakayama strains. Culture fluids were taken at proper time post-infection (p.i.) and subjected to the virus titration. Virus titer was estimated by plaque forming using confluent monolayer of BHK cells, as previously described (13). JEV virion were prepared from culture fluids by ultra-centrifugation method using discontinuous density gradient containing 10-40% sucrose. Viral RNA was extracted from virions with SDS-phenol/chroloform and precipitated with ethanol. To prepare RNA from JEV-infected cells, cells were washed with phosphate buffered saline (PBS) and harvested by the addition of 50 mM Tris buffer (pH7.5) containing 0.5% SDS and 1 mM EDTA.

Preparation of cell extracts

To obtain subcellular fractions, infected cells were dissolved in Tris buffer (pH7.5) containing 1.5 mM $MgCl_2$ and 10 mM KCl, and disrupted by 20 strokes in a Dounce homogenizer. Cellular homogenates were subjected to successive centrifugations, i.e. 500 x g for 10 min and then 10,000 x g for 30 min (7). The resulting pellets, nuclear and membrane fractions, were resuspended in 50 mM Tris buffer (pH8.0) containing 1.5 mM $MgCl_2$ and 50 mM KCl, and used for *in vitro* assay reactions.

Procedure of hybridization including Northern blot

Plasmid pJB11 has JEV cDNA sequences corresponding to the 3' end of JEV genomic RNA (9). DNA fragment at nucleotides 9183 to 10883 was prepared from pJB11, and inserted into pSPT18 and pSPT19, and then constructed new plasmids pJT18V and pJT19V (8). Each plasmid was then digested with restriction enzymes to prepare fragments. RNA probes were prepared through the RNA synthesis reaction carried out in the presence of T7 RNA polymerase (Toyobo, Tokyo) and α-^{32}P-UTP. The JT18V and JT19V probes could detect intracellular viral specific negative-sense RNA and positive-sense JEV-RNA including virion RNA, respectively.

For northern blot analysis, sample RNAs were denatured at 50℃ for 60 min in the presence of 1 M glyoxal and 50% DMSO and then were electrophoresed on 1% agarose gel in 10 mM phosphate buffer (pH7.0) which was recirculated continuously. Molecular weight standards were 23S (3.3 kb) and 16S (1.7 kb) *E. coli* rRNAs. RNAs were transferred to a nylon membrane (Pall, USA) with 20 x SSC (1xSSC:0.15M NaCl and 0.015M sodium citrate) and baked. The baked nylon membrane was treated with prehybridization buffer and then hybridized with ^{32}P labeled RNA probe at 42℃ for 16 hr. After hybridization, the nylon membrane was washed repeatedly with 2 x SSC containing 0.1% SDS. Slot hybridization was performed as similar protocol as described above. The dried filters were exposed to Fuji RX films.

In vitro assay of RNA synthesis.

In vitro RNA synthesis was carried out in 30 μl reaction mixture containing 50 mM HEPES (pH8.0), 3.5 mM MgCl2, 50 mM KCl, 5 mM DTT, 10 μg/ml actinomycin-D (Act-D), 0.7% NP40, 0.5 mM each of ATP, CTP and GTP, 10 μCi α-^{32}P-UTP and subcellular fractions (ca 5 μg protein). After an incubation at 30℃ for 60 min, 120 μl of 0.5% SDS solution was added, followed quickly by 150 μl of phenol. The RNAs in aqueous phase were precipitated with ethanol. To detect *in vitro* RNA product, 1% native agarose gels were used. Electrophoresis was carried out in TBE buffer (90 mM Tris-borate (pH 8.0) and 2 mM EDTA). To identify ds- and ss-RNA, RNAs were treated with 2M LiCl and fractionated by a centrifugation after the overnight-incubation. In ultra-centrifugation using 15-30% sucrose density gradient, ultra-centrifuge (Beckman) was used. The dried gels were exposed to Fuji RX films.

Labeling of protein with ^{35}S methionine

In a long labeling experiment, cells were pretreated with 1 μg/ml Act-D. After 4-hr pretreatment, cells were infected with JEV and added with 5 μCi/ml of ^{35}S-methionine (Met), and then cultured for further 24 hr and harvested. Subcellular fractions were prepared by centrifugation and subjected to SDS-10% polyacrylamide gel electrophoresis (SDS-PAGE) (7). The gels were exposed to X ray films.

Indirect immunofluorescence antibody assay (IFA)

For the IFA, JEV-infected Vero cells were fixed with acetone and incubated with specific antisera, as previously described (14). The specific antisera including anti-E, anti-NS3 and anti-NS5 were prepared from rabbits which were immunized with JEV proteins purified by the method using SDS-PAGE (14-15). After incubation with FITC conjugated goat anti-rabbit IgG, the cells were observed by a fluorescence microscope.

Results

Viral RNA in JEV-infected cells

JEV specific RNA in the infected cells was detected by hybridization using RNA probes. In order to examine the size of JEV-specific in the infected cells, RNA samples were subjected to glyoxal gel electrophoresis. The JT19V probe could detect positive-sense JEV-RNA including virion RNA, while the proves JT18V recognized only intracellular viral

specific negative-sense RNA. Since 2 kinds of genome sized RNA (42S) were detected in the hybridization with ^{32}P-plus (JT19V) and ^{32}P-minus probes (JT18V), we used both probes to examine viral RNAs in the infected cells (Fig.1). By using the minus probes, it was elucidated that the negative stranded viral RNA (42S) was synthesized in the early stage of infection. As shown in Fig. 1B, the amounts of

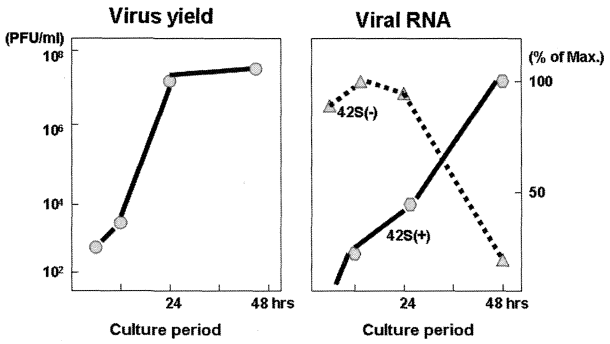

Fig. 1. Virus reproduction and appearance of JEV-specific RNAs in the infected cells.
(Left) JEV growth in C6/36 cells. Cells were infected with 10 m.o.i. of JEV and virus titers were assayed by plaque forming method.
(Right) RNAs were prepared from JEV-infected C6/36 cells at different times after virus infection. After glyoxal gel electrophoresis, RNA samples were transferred to nylon membrane and hybridized first with plus, ^{32}P-JT19V and second with minus probes, ^{32}P-JT18V. The amount of 42S vRNA were estimated and relative amounts are shown.

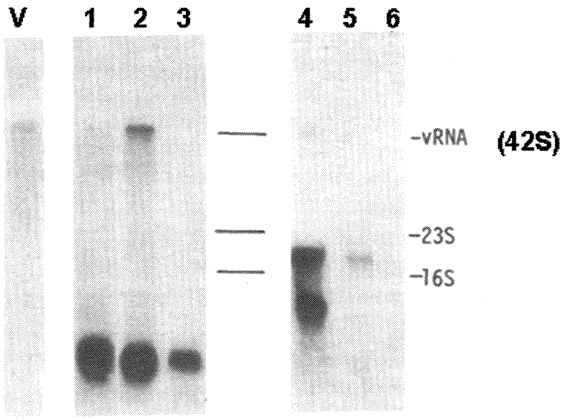

Fig. 2. Northern blot analysis of JEV-specific RNAs from the infected cells.
RNAs were extracted from virions or from the subcellular fractions of JEV-infected cells (48 hr p.i.) and electrophoresed using glyoxal gel, as described in the text. Lane V, JEV-vRNA. Lanes show RNAs from supernatant (lanes 1,4), crude membrane (lanes 2,5) and nuclear fractions (lanes 3, 6), respectively. After the transfer, hybridization was carried out by using RNA probes as described in the legend to Fig.1. Lanes V, 1-3 hybridized with JT19V. Lanes 4-6, JT18V.

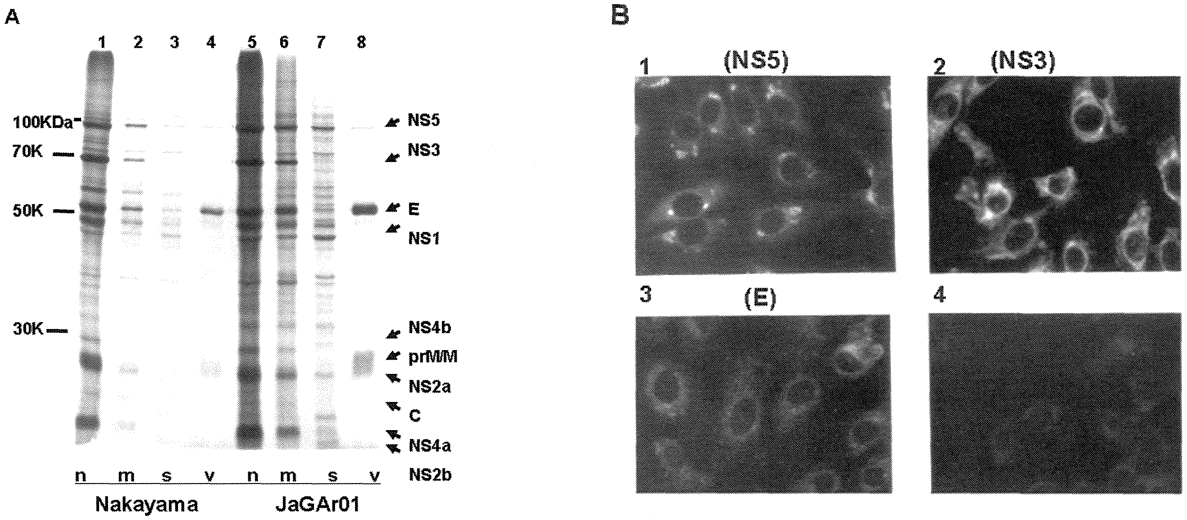

Fig. 3. Localization of viral proteins in JEV-infected cells.
A: JEV-infected cells labeled with ^{35}S-Met for 2hr were disrupted and fractionated into subcellular fractions including nuclear (lanes 1, 5), crude membrane (lanes 2, 6) and supernatant fractions (lanes 3, 7) by the centrifugation. Here we used 2 kinds of JEV strains for analysis. Lanes 4 and 8 indicate the partially purified JEV virion.
B: Indirect immunofluorescence assay (IFA) of JEV-infected cells.
Feature of JEV-proteins NS5, NS3 and E were shown in panels 1, 2 and 3. Panel 4 indicates IFA using preimmune rabbit sera.

negative stranded viral RNA reached a maximum level around 12 hr p.i. and then decreased. Appearance of the positive RNA (42S), however, was delayed, and it was obviously detected as 12 hr p.i. and then increased in amounts gradually. The accumulation of 42 S (+) RNA was similar to that of the virus growth curve assayed by plaque forming methods, as shown in Fig1.

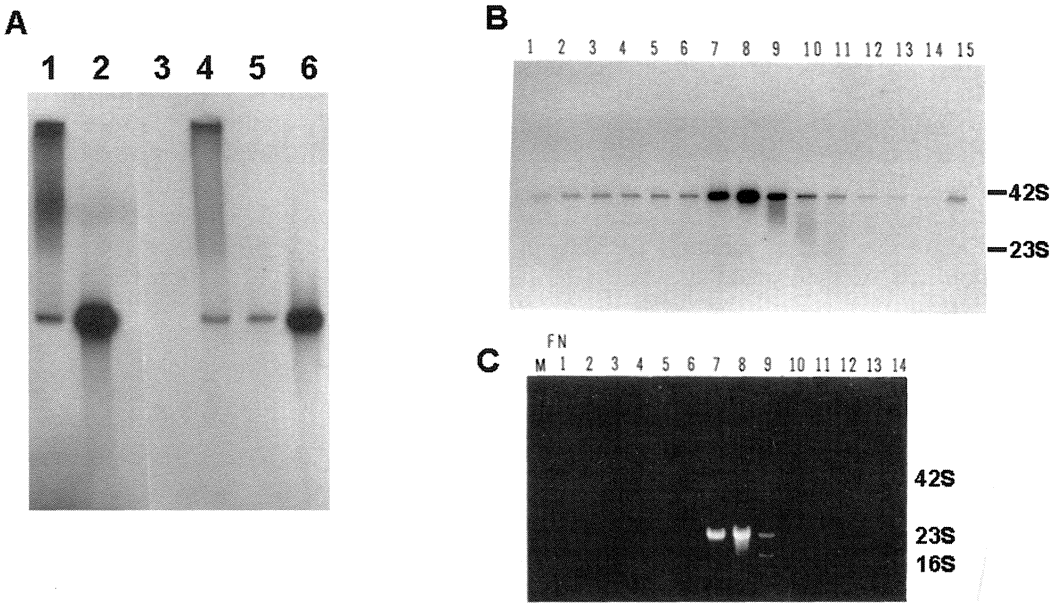

Fig. 4. Electrophoretic analysis of RNA products synthesized *in vitro*.
A: RNA synthesis *in vitro* using the crude membrane fraction were carried out in the absence (lane 1) or presence (lane 2) of NP40, and then ^{32}P RNA products were analyzed on the solubility in 2M LiCl. Lanes 3 and 5 were insoluble, and lanes 4 and 6 were soluble fractions.
B: ^{32}P RNA products were fractionated by the centrifugation using 15-30% sucrose density gradient.
C: *E.coli* ribosomal RNA was used as size marker in the fractionation by the ultra-centrifugation. 42S genomic RNAs were fractionated in the same fraction as *E. coli* rRNA by the ultra-centrifugation, since they formed duplex.

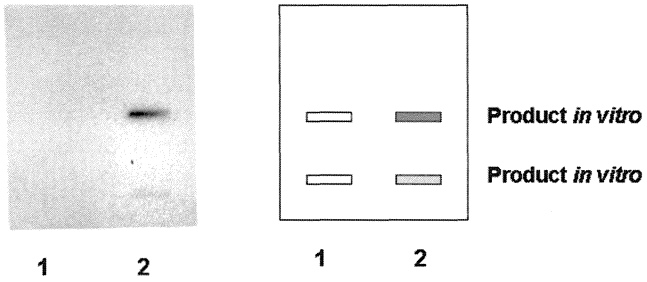

Fig. 5. Northern blot analysis of ^{32}P RNA *in vitro* products.
To determine polarity of ^{32}P RNA *in vitro* products, slot hybridization method was carried out. In the hybridization, both RNA fragments, JT18V (lane 1) and JT19V (lane 2) unlabeled were reacted with ^{32}P-RNA *in vitro* products used as probe. RNA fragment in upper side of figure contains 2 times higher than that of bottom.

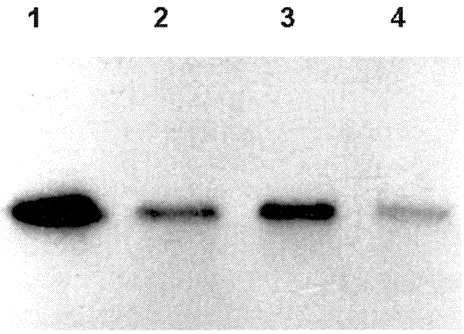

Fig. 6. Effect of antisera, anti- NS3 and -NS5 on *in vitro* RNA synthesis.
Preincubation of the crude membrane fraction and antisera was carried out prior to the addition of α-^{32}P-UTP. The procedure for *in vitro* reaction was the same as described in the text. Lane 1 (control); Products *in vitro* by treatment with preimmune sera at dilution 1:5. Lanes 2-3; treatment with anti-NS5 at dilution of 1:5 and 1:10, respectively. Lane 4; treatment with anti-NS3 at dilution of 1:5.

Localization of JEV-specific RNA in the infected cells.

To examine the localization of JEV-specific RNA in the cells, RNAs prepared from each of the subcellular fractions were subjected to Northern blot analysis. Fig. 2 shows the data of the hybridization using JT18V (right) and 19V (left) probes, respectively. In this experiment, the same sample filter was used and hybridized with both plus and minus probes. The 42S (+) RNA was abundantly in the crude membrane fraction (Fig. 2, lane 2). On the other hand, the amounts of the 42 S (-) RNA in the membrane fraction was almost same as those in the supernatant fraction (Fig.2, lanes 4 and 5). A large amount of small RNAs was observed in plus and minus hybridization shown in Fig. 2. Positive small 10S RNA was now clarified to contain the fragment at 3' end of genomic RNA (16) (data not shown).

Distribution of JEV-specific proteins in infected cells

To clarify the function of viral proteins, it is important to know the distribution of proteins in the cells. Fig.3A indicates the localization of viral proteins of 2 kinds of JEV strains (Nakayama and JaGAr01) labeled with ^{35}S-Met. Most of viral proteins were detected in nuclear and membrane fractions (Fig.3A, lanes 1, 2, 5 and 6). This nuclear fraction means not only nucleus but also nuclear membrane associated fraction. RNA dependent RNA polymerase (replicase) (NS5, 100KDa) and RNA helicase (NS3, 70KDa) were detected in the nuclear and membrane fractions. IFA indicated that both NS5 and NS3 were localized perinuclear fraction (Fig.3). NS5 appears to form some kinds of aggregates at the perinuclear site of the infected cells, as shown in Fig.3B, panel 1. NS3 also indicated the similar aggregates (Fig.3B, panel 2), which was different from the case of the distribution of E protein (Fig.3B, panel 3). E proteins were dispersed in the cytoplasm.

Viral RNA synthesis in vitro

In order to investigate viral RNA synthesis, it is useful to develop *in vitro* reaction system. By using crude membrane fractions from JEV-infected cells, we developed viral RNA synthesis system *in vitro*. As shown in Fig. 4, RNA products were clearly detected in cell-free fraction from JEV-infected cells at 48 hr p.i. In the presence of 0.7% NP-40 (Fig.4A, lane 2), larger quantities of RNA were synthesized. Next, RNA products were analyzed on solubility in LiCl, to identify ds- or ss-RNA. In the presence of 2M LiCl, most of RNA products were in the LiCl-soluble fraction (lanes 4 and 6), meaning dsRNA. By the ultra-centrifugation using sucrose density gradient 15-30%, products were fractionated at the position about 20S (Fig.4B and 4C). These indicate that *in vitro* RNA products are mainly of ds-RNA, may be replication form (RF). Next, in order to identify whether RNA product is positive RNA or negative, hybridization method using same probes JT18V (Fig.5, lane 1) and 19V (lane 2) was performed. Only JT19V probe could hybridized with ^{32}P-products *in vitro*, meaning that the products are positive strand (Fig.5).

Viral proteins influencing in vitro reaction of RNA synthesis

Viral proteins NS3 and NS5 are thought as helicase and RNA-dependent RNA polymerase, respectively and the important members of replication complex. In order to know the functions of NS3 and NS5 in viral RNA synthesis, we examined the effect of antisera, anti-NS3 and anti-NS5 on RNA synthesis *in vitro*. In the presence of antisera, anti-NS3 and anti-NS5, RNA synthesis level *in vitro* was decreased (Fig.6). The inhibitory effect of anti-NS3 on RNA syntheis was much more remarkable (Fig.6, lane 4). This was confirmed by repeated experiments.

Discussion

As described in the result, JEV-RNAs in the infected cells were clearly detected by the hybridization using the specific probes. The data indicated that the negative stranded JEV-RNA was synthesized before 6hr p.i. It is reasonable that the negative stranded RNA appears earlier than the positive stranded RNA during JEV infection. The facts that the positive JEV-RNAs (42S) were accumulated in the membrane fraction in the infected cells and it differed from the distribution of the negative RNAs suggest that the positive RNAs are continuously synthesized at the membrane, maybe endoplasmic reticulum (ER) and outer nuclear membrane during viral replication, as reported else about flavivirus replication (6). This fact seems to be related with the data of JEV-RNA synthesis *in vitro* that the membrane fractions have a high activity of RNA (mainly positive-stranded) synthesis (Fig.4).

Although several reports have been published describing flavivirus RNA synthesis, the mechanism of RNA synthesis is not yet fully understood (6-7,8,14). Here we described the *in vitro* RNA synthesis using the crude membrane fraction. The data indicated that RNAs produced *in vitro* were JEV specific, ds-RNA including positive strand labeled with ^{32}P. This *in vitro* RNA synthesis system, however, includes endogenous RNA template, so that most of the RNA polymerase reaction is probably a chain elongation. It is not obvious that the initiation occurs during the *in vitro* reaction (17).

The amounts of *in vitro* RNA products in the presence of non-ionic detergents such as NP40 and

Triton X 100 increased, and clear bands were detected in the agarose gel. It is thought that RNA synthesized *in vitro* formed duplex structure like replication intermediate (RI) or replication form (RF) under the native condition (6-7,18-19). Actually *in vitro* synthesized poliovirus RF (19) migrated slower than did genomic ssRNA in the native agarose gel. Most of products synthesized here, in the presence of NP40 seem to be RF, which migrates to the similar site with ssRNA (42S) in 1% native gel. The data that *in vitro* synthesized RNAs were in the LiCl-soluble fraction and fractionated at the similar site to rRNA of *E. coli* in the centrifugation also indicate that most of products are of dsRNA. The result that the clear band was observed in the agarose gel (Fig.4) is explainable as follows; It is likely that during the incubation in the presence of NP40, RI was degraded by some endogenous RNase and only RF was accumulated, since in the absence of NP40 some larger bands including RI were detected (Fig.4A).

It should be noted that the *in vitro* JEV-RNA synthetic activity was high in the crude membrane fraction including outer nuclear membrane. The study on West Nile virus RNA synthesis also showed that outer nuclear membrane contained RNA dependent RNA polymerase (20). Here, ^{35}S-labeling and immunofluorescence experiments indicated so much NS3 and NS5 proteins were accumulated in the crude nuclear and membrane fraction (Fig.3). It is obvious that NS3 is strongly associated with the nuclear and membrane fractions, although sequence data suggest that NS3 is hydrophilic and not a transmembrane protein (21). This phenomenon seems to be due to the function of hydrophobic and transmembrane protein NS4a/b (22). NS4 may work as an anchor for NS3. Actually we could see the NS4 band in the crude nuclear and membrane fractions as shown in the result (Fig.3A). Now it is well known that NS3 has protease activity at amino terminal region, and ATPase and RNA helicase in other region (21,23). Recently it has been reported that flavivirus (HCV) NS3 influences IFN pathway (24). Putative viral replication proteins NS3 and also NS5 actually work together in RNA replication (25), because anti-NS3 and anti-NS5 could inhibit RNA synthesis *in vitro* (Fig.6).

As previously described, even though recently JE cases in Japan are less than 10 in each year, still JE viruses circulate in wide area of Japan (4). In addition, it was found that recently isolated viruses including Ishikawa strains belonged to genotype I which differs from previous JEV strains (genotype III) (4,26). Now we need to be careful about the change in the pathogenesity of new genotype JEV. It is also necessary to develop new drug against JEV infection (27). To develop new drugs, it is important to elucidate the mechanism of virus reproduction including RNA replication.

Taken together the results here indicate that the membrane fractions have high activity for viral RNA synthesis, and contain a large amount of NS3, NS5 and other NS proteins which make the replication complex in the infected cells. In addition, we reported the sensitive probes for the detection of JEV specific RNAs. To know the mechanism of JEV-RNA synthesis, further study will be essential.

Acknowledgements

This study was supported in part by a Project Research from High-Technology Center (2005-8) and Grant for Collaborative Research (C2004-2 and C2005-2) of Kanazawa Medical University. The author is grateful to K. Hori and staffs in the Division of Molecular Oncology and Virology, Medical Research Institute for their assistance.

References

1. Williams DT, Wang L, Daniels PW et al: Molecular characterization of the first Australian isolate of Japanese encephalitis virus, the FU strain. J Gen Virol 2000; **81:** 2471-80.
2. Weissenbock H, Kolodziejek J, Url A et al: Emergence of Usutu virus, an African mosquito-borne flavivirus of the Japanese encephalitis virus group, central Europe. Emerg Infect Dis 2002; **8:** 652-6.
3. Solomon T, Dung NM, Wills B et al: Interferon alpha-2a in Japanese encephalitis: a randominised double-blind placebo-controlled trial. Lancet 2003; **361:** 821-6.
4. Takegami T, Ishak H, Miyamoto C et al: Isolation and molecular comparison of Japanese encephalitis virus in Ishikawa, Japan. Jpn J Infect Dis 2000; **53:** 178-9.
5. Takegami T, Washizu M, Yasui K: Nucleotide sequence at the 3' end of Japanese encephalitis virus genomic RNA. Virology 1986; **152:** 483-6.
6. Lindenbach BD, Rice CM: Flaviviridae: The viruses and their replication. Knipe DM (Eds), Virology (Fields) (4th ed), Philadelphia, Lippincott Williams & Wikins 2001; 991-1041.
7. Takegami T, Hotta S: In vitro synthesis of Japanese encephalitis virus (JEV) RNA: membrane and nuclear fractions of JEV-infected cells possess high levels of virus-specific RNA polymerase activity. Virus Res 1989; **13:** 337-50.
8. Takegami T, Hotta S: Synthesis and localization of Japanese encephalitis virus RNAs in the infected cells. Microbiol Immunol 1990; **34:** 849-57.
9. Hashimoto H, Nomoto A, Watanabe K et al: Molecular cloning and complete nucleotide sequence of the genome of Japanese encephalitis virus Beijin strain. Virus Genes 1988; **1:** 305-17.
10. Sumiyoshi H, Mori C, Fuke I et al: Complete nucleotide sequence of the Japanese encephalitis virus genome RNA. Virology 1987; **161:** 497-510.
11. Mangada MNM, Takegami T: Molecular characterization of the Japanese encephalitis virus representative immunotype strain JaGAr01. Virus Res 1999; **59:** 101-12.
12. Rice CM, Lenches EM, Eddy SR et al: Nucleotide sequence of yellow fever virus: Implication for flavivirus gene expression and evolution. Science 1985; **229:** 726-35.
13. Takegami T, Sahara M, Hotta S: A sensitive method for detection of flavivirus envelope protein and virus titration using a monospecific antiserum against Japanese encephalitis virus envelope protein. J Kanazawa Med Univ 1990; **15:** 73-9.
14. Takegami T, Miyamoto H, Nakamura H et al: Difference in the biological activity of the V3 envelope protein of two Japanese encephalitis virus. Acta Virol 1982; **26:** 321-27.
15. Zulkarnain E, Takegami T: Localization and functions of Japanese encephalitis virus nonstructural proteins NS3 and NS5 for viral RNA

synthesis in the infected cells. Microbiol Immunol 1993; **37:** 239-43.
16. Lin K, Chang H, Chang R: Accumulation of a 3'-terminal genome fragment in Japanese encephalitis virus-infected mammalian and mosquito cells. J Gen Virol 2004; **78:** 5133-38.
17. Chu PEG, Westaway EG: Characterization of Kunjin virus RNA-dependent RNA polymerase: Reinitiation of synthesis *in vitro* Virology 1987; **157:** 330-7.
18. Takegami T, Semler BL, Anderson CW et al: Membrane fractions active in poliovirus RNA replication contain VPg precursor polypeptides. Virology 1983; **128:** 33-47.
19. Takegami T, Kuhn RJ, Anderson CW et al: Membrane dependent uridylylation of the genome linked protein VPg of poliovirus. Proc Natl Acad Sci USA 1983; **80:** 7447-451.
20. Grun JB, Brinton NA: Dissociation of NS5 from cell fraction containing West Nile virus-specific polymerase activity. J Virol 1987; **61:** 3641-44.
21. Takegami T, Sakamuro R, Furukawa T: Japanese encephalitis virus nonstructural protein NS3 has RNA binding and ATPase activities. Virus Genes 1994; **9:** 105-12.
22. Tautz N, Kaiser A, Thiel H: NS3 serine protease of bovine viral diarrhea virus: Characterization of active site residues NS4A cofactor domain, and protease-cofactor interactions. Virology 2000; **273:** 351-63.
23. Utama A, Shimizu H, Hasebe F et al: Role of the DExH motif of the Japanese encephalitis virus and hepatitis C virus NS3 protein in the ATPase and RNA helicase activities. Virology 2000; **273:** 316-24.
24. Foy E, Li K, Wang C et al: Regulation of interferon regulatory factor-3 by the hepatitis C virus serine protease. Science 2003; **300:** 1145-8.
25. Uchil PD, Satchidanandam V: Characterization of RNA synthesis, replication mechanism, and in vitro RNA-dependent RNA polymerase activity of Japanese encephalitis virus. Virology 2003; **15:** 358-71.
26. Solomon T, Haolin N, Beasley DWC et al: Origin and evolution of Japanese encephalitis virus in southeast Asia. J Virol 2003; **77:** 3091-98.
27. Murakami M, Ota T, Nukuzuma S et al: Inhibitory effect of RNAi on Japanese encephalitis virus replication *in vitro* and *in vivo*. Microbiol Immunol 2005; **49:** 1047-56.

Clin Exp Metastasis (2006) 23:323–334
DOI 10.1007/s10585-006-9041-y

ORIGINAL PAPER

RhoGDIβ lacking the N-terminal regulatory domain suppresses metastasis by promoting anoikis in v-src-transformed cells

Takahide Ota · Masayo Maeda · Shiho Sakita-Suto · Xinwen Zhou · Manabu Murakami · Tsutomu Takegami · Masaaki Tatsuka

Received: 21 April 2006 / Accepted: 29 September 2006 / Published online: 17 November 2006

Abstract Rho guanine nucleotide dissociation inhibitors (RhoGDIs) regulate the activity of Rho family GTPases. RhoGDIβ (LyGDI/GDID4/RhoGDI2) has two caspase cleavage sites after Asp19 and Asp55. The resulting cleavage products, ΔN(1–19)RhoGDIβ and ΔN(1–55)RhoGDIβ, are expressed in cells under conditions that activate caspases. ΔN(1–19)RhoGDIβ, which can inhibit GDP dissociation, is implicated in the process of apoptosis, whereas the physiological roles for ΔN(1–55)RhoGDIβ, which lacks the ability to inhibit GDP dissociation, are largely unknown. To explore the roles of ΔN(1–55)RhoGDIβ, we examined the phenotypes of v-src-transformed metastatic fibroblasts transfected with plasmids for expressing ΔN(1–55)RhoGDIβ. Although the expression of ΔN(1–55)RhoGDIβ had no effect on the rate of growth in vitro, it suppressed experimental metastasis and decreased the rate of growth in vivo. In addition, ΔN(1–55)RhoGDIβ-expressing cells had enhanced adhesion to fibronectin, laminin, and collagens but reduced retention in the lung after intravenous injection. Also, the expression of ΔN(1–55)RhoGDIβ promoted anoikis without affecting the levels of activated Rac1 or Cdc42. Furthermore, ΔN(1–55)RhoGDIβ did not affect the expression or phosphorylation of focal adhesion kinase, p44/p42 mitogen-activated protein kinases, or Akt1 before or after induction of anoikis. Thus, ΔN(1–55)RhoGDIβ appears to promote anoikis by undefined mechanisms, thereby suppressing metastasis in v-src-transformed fibroblasts.

Keywords Anoikis · Apoptosis · Caspase · Metastasis · RhoGDI · Src

Abbreviations

BSA	Bovine serum albumin
EMEM	Eagle's minimum essential medium
ECM	Extracellular matrix
FAK	Focal adhesion kinase
FBS	Fetal bovine serum
HBSS	Hanks' balanced salt solution
MAPK	Mitogen-activated protein kinase
PAK1	p21/Cdc42/Rac1-activated kinase 1
PBS	Phosphate-buffered saline
RhoGDI	Rho guanine nucleotide dissociation inhibitor
RhoGEF	Rho guanine nucleotide exchange factor
SDS	Sodium dodecyl sulfate

Introduction

Rho family GTPases function as molecular switches and play crucial roles in signaling pathways controlling

T. Ota (✉) · M. Murakami · T. Takegami
Division of Molecular Oncology and Virology, Medical Research Institute, Kanazawa Medical University, Uchinada, Ishikawa 920-0293, Japan
e-mail: takahide@kanazawa-med.ac.jp

M. Maeda
Department of Chemistry, Kanazawa Medical University, Uchinada, Ishikawa 920-0293, Japan

S. Sakita-Suto · M. Tatsuka
Department of Regulatory Radiobiology, Research Institute for Radiation Biology and Medicine, Hiroshima 734-8553, Japan

X. Zhou
School of Radiation Medicine and Public Health, Suzhou University, Jiang Su 215007, China

cytoskeletal organization, cell polarity, gene transcription, cell cycle progression, microtubule dynamics, and vesicular transport [1]. Rho guanine nucleotide dissociation inhibitors (RhoGDIs) maintain Rho family GTPases in an inactive state in the cytosol and shuttle them between the cytosol and effector sites [2–4]. RhoGDIβ (LyGDI/GDID4/RhoGDI2) is abundantly expressed in hematopoietic cells [5], however non-hematopoietic cells, such as keratinocytes, fibroblasts, amnion cells, lung cancer cells, and colon cancer cells also express RhoGDIβ [6, 7].

RhoGDI β is cleaved by caspases at least at two sites, specifically, C-terminal to Asp19 and Asp55 [8]. A cleavage product produced by caspase-3, ΔN(1–19)RhoGDIβ, is generated during apoptosis induced by ionizing radiation [9], anti-Fas antibody [10], anti-IgM antibody [11], tumor necrosis factor-α [12], staurosporine [13], or taxol [14]. In addition, during apoptosis induced by ionizing radiation in thymic cells [9], drug treatment in myelocytic leukemia cells [13], and anti-Fas antibody in Jurkat T cells [15], ΔN(1–19)RhoGDIβ translocates to the nucleus, suggesting that it participates in apoptotic signaling. Another cleavage product, ΔN(1–55) RhoGDIβ, is found in inflammatory leukocytes and may contribute to the activation of Rho family GTPases because it lacks the ability to inhibit GDP dissociation [8]. Interestingly, ΔN(1–55)RhoGDIβ has been reported to be constitutively expressed in normal polymorphonuclear neutrophils [12]. These observations suggest that ΔN(1–55)RhoGDIβ has a specific although currently unknown physiological role.

We previously isolated a gene capable of a conferring a metastatic phenotype to non-metastatic cancer cells from human tumors [16]. This gene encodes ΔC(166–201)RhoGDIβ, a form of RhoGDIβ lacking the C-terminal 36 amino acids [7]. In addition, full-length wild-type RhoGDIβ is thought to play a role in cancer progression [17–20] and has been reported to suppress metastasis in human cancer [21]. These observations collectively indicate that RhoGDIβ is important in signaling pathways leading to a metastatic phenotype.

In this report, we investigated the physiological function of ΔN(1–55)RhoGDIβ to help clarify the roles of RhoGDIβ in cancer metastasis. We found that expression of ΔN(1–55)RhoGDIβ suppresses metastasis by promoting detachment-induced apoptosis (anoikis) in v-src-transformed fibroblasts. The N-terminal flexible domain of RhoGDIs has also been shown to be important in the regulation of Rho GTPases [22–28]. RhoGDIs lacking this N-terminal regulatory region bind with much lower affinity to and do not inhibit the function of Rho GTPases in vitro [8, 23, 28]. Thus, our finding that ΔN(1–55)RhoGDIβ represses metastasis suggests that RhoGDIβ has a function other than the inhibition of Rho GTPase signaling. Finally, we discuss the possible use of RhoGDIs lacking the N-terminal regulatory region to elucidate the cellular functions of RhoGDIs.

Materials and methods

Cells and culture

BALB/c 3T3 A31-1-1 cells were established by Kakunaga and Crow [29] and show different cancer phenotypes when transformed by src and ras oncogenes [30]. The 1-1src cell line, derived by transforming A31-1-1 with v-src, is tumorigenic and highly metastatic [30]. These cells were cultured in Eagle's minimum essential medium (EMEM) supplemented with 10% fetal bovine serum (FBS) and were maintained at 37 °C in a humidified atmosphere of 5% CO_2 in air.

Antibodies

Anti-RhoGDIβ, anti-focal adhesion kinase (FAK), and anti-pY925-FAK antibodies were purchased from Santa Cruz Biotechnology Inc. (Santa Cruz, CA, USA). Anti-α-tubulin (clone B-5-1-2) was purchased from Sigma-Aldrich (St Louis, MO, USA). Anti-pY397-FAK (clone 18), anti-Rac1 (clone 102), anti-Cdc42 (clone 44), and anti-Bcl-2 (clone 7) antibodies were purchased from BD Biosciences (San Jose, CA, USA). Anti-p44/p42 mitogen-activated protein kinase (MAPK), anti-phospho-p44/p42 MAPK (Thr202/Tyr204) (clone E10), anti-Akt1, and anti-phospho-Akt1 (Ser473) (clone 193H12) antibodies were purchased from Cell Signaling Technology Inc. (Danvers, MA, USA). Anti-Xpress antibody was purchased from Invitrogen (Carlsbad, CA, USA). Peroxidase-conjugated anti-mouse IgG and anti-rabbit IgG antibodies were purchased from DakoCytomation (Glostrup, Denmark). Peroxidase-conjugated anti-goat IgG (414161) was purchased from Nichirei Corporation (Tokyo, Japan). A rhodamine-conjugated secondary antibody was purchased from Chemicon (Temecula, CA, USA).

Immunoblotting

Samples were lysed with Laemmli buffer, resolved by sodium dodecyl sulfate–polyacrylamide gel electrophoresis, and transferred to immobilon-P membranes

(Millipore, Billerica, MA, USA). The membranes were then probed with a primary antibody, followed by a peroxidase-conjugated secondary antibody. Immunoreactive proteins were visualized using ECL or ECL Plus reagents (Amersham Biosciences, Little Chalfont, UK).

Plasmids and transfection

To construct expression vectors for full-length RhoGDIβ and ΔN(1–55)RhoGDIβ, the entire and truncated sequences were amplified by PCR using the SW480 cDNA library, which was constructed by "lone-linker"-generated PCR-based cDNA construction methods [7]. The products were then subcloned into hygromycin-resistant pEF/hyg1 [31] and designated pEF/hyg1-RhoGDIβ and pEF/hyg1-ΔN(1–55)RhoGDIβ, respectively. Xpress-tagged pcDNA3.1 expression vector for the ΔN(1–55)RhoGDIβ was generated and designated pcDNA3.1-ΔN(1–55)RhoGDIβ. Cells were transfected with plasmids using LipofectAMINE^{TM} plus or Lipofectamine 2000 (Invitrogen). To obtain stable cell lines, hygromycin-resistant cells were isolated in medium containing 800 U/ml hygromycin (Wako Pure Chemical, Osaka, Japan).

Animals

Five-week-old male BALB/c nude mice and 6-week-old male BALB/c normal mice were obtained from Japan SLC Inc. (Shizuoka, Japan) and were maintained under specific pathogen-free conditions. Experiments were performed in accordance with guidelines of The Committee on Experimental Animals in Kanazawa Medical University. Mice were used for experiments at 7 weeks of age.

Assay of metastasis and tumor growth in vivo

The cells were harvested by brief trypsinization, after which they were washed once with medium containing 10% FBS and twice with Hanks' balanced salt solution (HBSS). Cells were suspended in 0.2 ml of HBSS and injected into the lateral tail veins of BALB/c nude mice. Three weeks later, the mice were sacrificed and the number of lung tumor nodules was counted after insufflation with 15% India ink [32]. To assay tumorigenicity, cells were suspended in 0.1 ml of HBSS and subcutaneously injected to BALB/c nude mice. Palpable tumors were measured with a caliper, and the tumor weight was estimated as described previously [33].

In vitro transformation assay

In vitro transformation was assayed using a method similar to a previous report [34]. Briefly, exponentially growing cells (5,000 cells) were seeded onto six-well plates in 2.0 ml of culture medium containing 10% FBS. After 24 h, the cells were cotransfected with a ΔN(1–55)RhoGDIβ expression vector and pcDsrc (v-Src expression plasmid) [35] using Lipofectamine 2000. Cells were cultured for 12 days with a medium change every 3 days, fixed with ethanol, and stained with Giemsa solution. Morphological transformation was determined under a dissecting microscope according to previously described criteria [36].

Assay of retention of tumor cells in the lung

The retention of tumor cells in the lung was measured as previously described [37]. Briefly, the cells were labeled with 4 μM PKH26 (Zynaxis Cell Science Inc., Malvern, PA, USA), and 5×10^5 of labeled cells were injected intravenously into BALB/c normal mice. After 24 h, the mice were killed, and PKH26 was extracted from their lungs. The fluorescence intensity of PKH26 was measured with a fluorescence spectrophotometer (MPF4, Hitachi Ltd, Tokyo, Japan; excitation, 551 nm; emission, 567 nm). There was a linear correlation between the fluorescence intensity and the number of labeled cells between 2,000 and 400,000 cells. The retention of tumor cells in the lung was determined by calculating the percentage of the total injected fluorescence intensity that was found in the lung extract. PKH26 labeling had a negligible effect on metastatic capacity.

Assay of adhesion to extracellular matrix proteins

Ninety-six-well plates were filled with 100 μl/well of fibronectin (20 μg/ml), laminin (20 μg/ml), collagen type I (50 μg/ml), or collagen type IV (50 μg/ml) (Nitta Gelatin, Osaka, Japan) and air-dried. The wells were then incubated with 0.5% bovine serum albumin (BSA) in phosphate-buffered saline (PBS) for 60 min, after which 2×10^4 cells suspended in 0.1 ml of 0.5% BSA in serum free-culture medium were added to each well and allowed to attach for 90 min at 37°C. The attached cells were counted by colorimetric assay using a highly water-soluble formazan dye (WST-1) [38].

Induction of anoikis

Exponentially growing cells were harvested by brief trypsinization and washed once with medium

containing FBS and once with HBSS. Cells (1×10^5) in 5 ml of serum-free EMEM were plated in 60-mm bacteriological dishes (BD Biosciences, San Jose, CA, USA) precoated overnight at 37 °C with 1% BSA to avoid cell anchorage. Cells were cultured in suspension for 6 or 8 h.

Annexin V staining

Cells were washed twice with PBS at 4 °C and stained with an Annexin V-FITC Apoptosis Detection Kit I (BD Biosciences, San Jose, CA, USA) according to the manufacturer's protocol and analyzed by flow cytometry within 1 h. For double-staining with anti-Xpress antibody, the cells stained with Annexin V-FITC were fixed with 4% paraformaldehyde in PBS for 10 min at room temperature, permeabilized with 0.1% Triton X-100, and then stained with rhodamine-conjugated secondary antibody.

Rac1 and Cdc42 activation assay

Pull-down assays were performed using a Rac and Cdc42 activation assay kit (Cytoskeleton Inc., Denver, CO, USA) according to the manufacturer's instructions. The cells were washed with PBS and lysed on the dish in cell lysis buffer (2 mM phenylmethylsulphonylfluoride, 10 μg/ml aprotinin, 10 μg/ml leupeptin, 10 mM $MgCl_2$, 150 mM NaCl, 5% sucrose, 1.0% NP-40, 25 mM Tris–HCl, pH 7.5). Rac1-GTP and Cdc42-GTP were pulled down using the p21 binding domain (PBD) of p21/Cdc42/Rac1-activated kinase 1 (PAK1).

Statistical analysis

Differences between values were analyzed using a two-tailed Welch's *t*-test.

Results

ΔN(1–55)RhoGDIβ suppresses the metastatic capacity of 1-1src cells

To examine the role of ΔN(1–55)RhoGDIβ, we transfected 1-1src cells with pEF/hyg1-full-RhoGDIβ or pEF/hyg1ΔN(1–55)RhoGDIβ and then selected cell lines stably expressing the exogenously introduced genes (Fig. 1a). These cells were intravenously injected into nude mice, and the numbers of metastatic nodules in the lungs were counted after 3 weeks. Fewer nodules were formed in mice injected with clones expressing ΔN(1–55)RhoGDIβ than in mice injected with cells expressing an empty vector (Fig. 1b, c). The levels of ΔN(1–55)RhoGDIβ expressed by the clones correlated with the degree to which metastasis was repressed (Fig. 1a). Expression of full-length RhoGDIβ repressed metastasis, but it was not as potent as ΔN(1–55)RhoGDIβ (Fig. 1b, c).

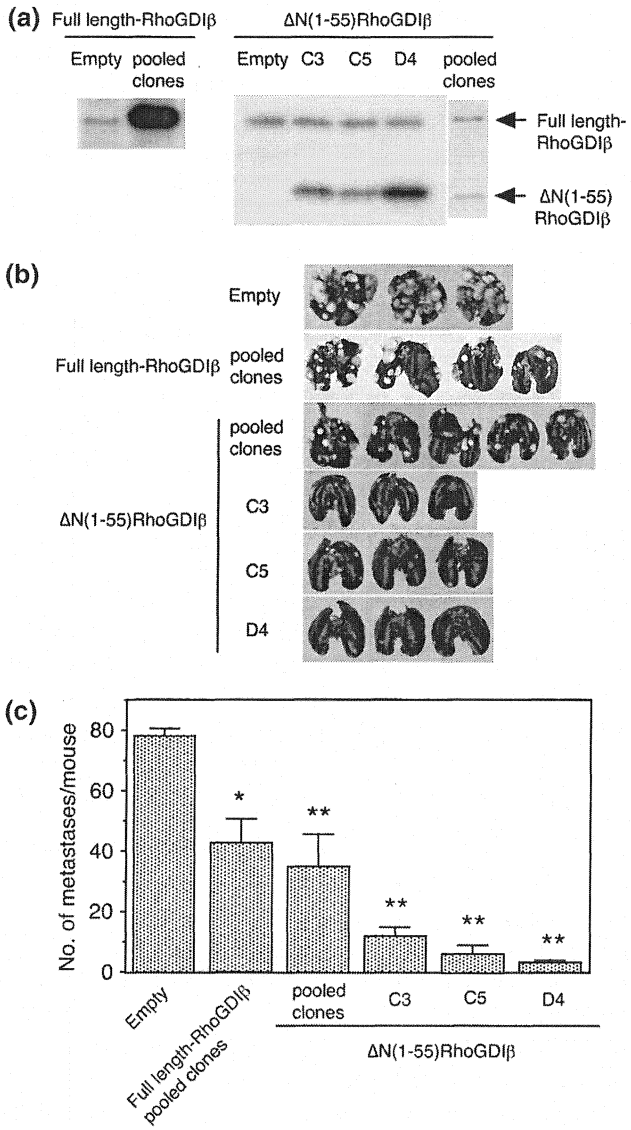

Fig. 1 Decrease of metastatic capacity in 1-1src cells stably expressing ΔN(1–55)RhoGDIβ. **a** The expression of introduced genes in stable transfectants. Whole cell lysates from cells expressing full-length RhoGDIβ or ΔN(1–55)RhoGDIβ were examined by immunoblotting with an anti-RhoGDIβ antibody. **b** Macroscopic appearance of metastatic lungs. Nude mice were injected intravenously with 4×10^5 cells. After 3 weeks, the mice were sacrificed and the lungs were examined for metastases. Metastatic nodules were not observed in organs other than the lung. **c** The number of lung tumor nodules in (**b**) was counted. Values indicate means ± S.E. of three to five mice. $^*P < 0.01$ and $^{**}P < 0.0001$ compared with the empty vector-transfected control

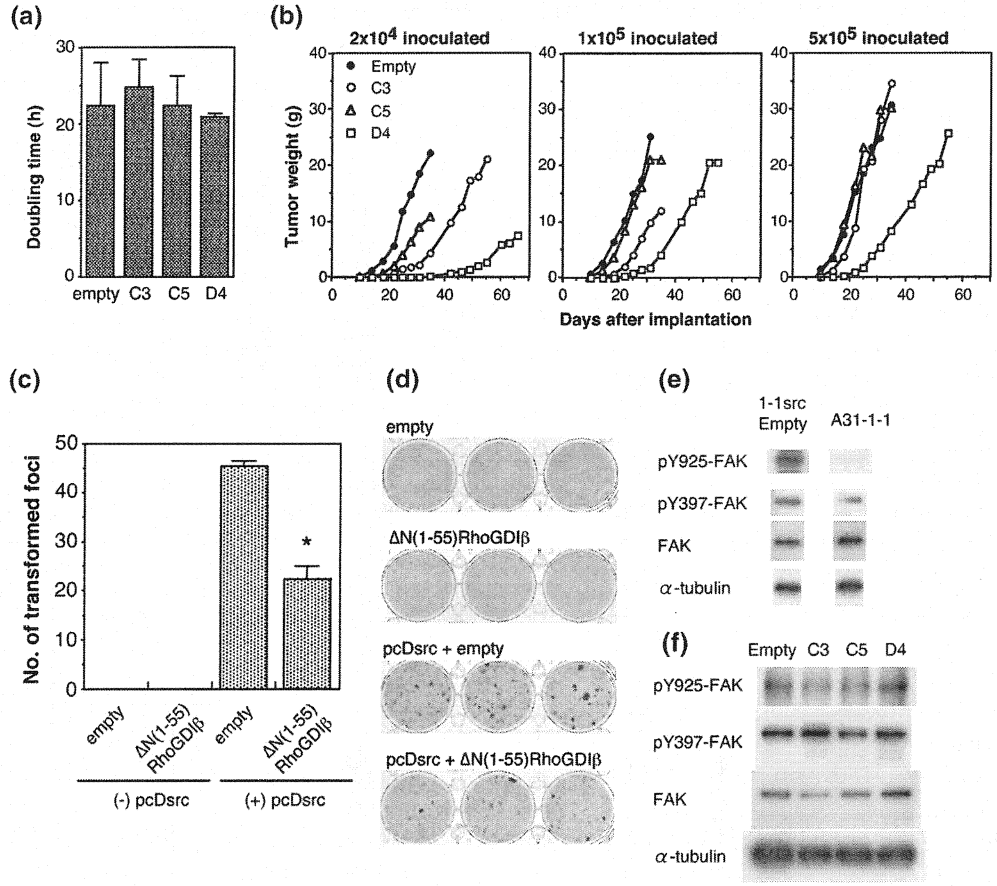

Fig. 2 Growth properties of cells expressing ΔN(1–55)RhoGDIβ. **a** In vitro doubling times of clones stably expressing ΔN(1–55)RhoGDIβ. Values indicate means ± S.D. of three independent experiments. **b** The indicated numbers of cells were subcutaneously injected into three nude mice per group. The sizes of palpable tumors were measured with a caliper and used to estimate the tumor weight. Values indicate means from three mice. **c** A31-1-1 cells were cotransfected with pcDsrc and either empty vector or the ΔN(1–55)RhoGDIβ expression vector. The number of foci was counted 12 days after transfection. Values indicate means ± S.D. of three plates. $^*P < 0.005$ compared with the control cells cotransfected with pcDsrc and empty vector. **d** Photographs of plates in (**c**). **e** Whole cell lysates of empty vector-transfected 1-1src cells and A31-1-1 cells were examined by immunoblotting with antibodies to FAK phosphorylated at Tyr925 (pY925-FAK), FAK phosphorylated at Tyr397 (pY397-FAK), total FAK, and α-tubulin. A representative blot from two independent experiments is shown. **f** Whole cell lysates of empty vector-transfected 1-1src cells and ΔN(1–55)RhoGDIβ-expressing cells were examined by immunoblotting with anti-pY925-FAK, -pY397-FAK, -FAK, and -α-tubulin antibodies. A representative blot from four independent experiments is shown

Suppression of transformed phenotypes by ΔN (1–55)RhoGDIβ

To determine the mechanisms by which metastasis is suppressed by ΔN(1–55)RhoGDIβ, we first examined the growth rate of the clones in vitro. We found that the doubling time of clones expressing ΔN(1–55)RhoGDIβ were not significantly different than cells transfected with an empty vector (Fig. 2a). In contrast, after subcutaneous inoculation of the cells into nude mice, the in vivo growth rate of ΔN(1–55)RhoGDIβ-expressing clones was lower than that of cells transfected with an empty vector (Fig. 2b). When mice were inoculated with 2×10^4 or 1×10^5 cells, the tumor growth rate of ΔN(1–55)RhoGDIβ-expressing clones was lower and the latency period longer than cells transfected with an empty vector. Even when mice were inoculated with 5×10^5 cells, clone D4, which had the highest level of ΔN(1–55)RhoGDIβ expression, showed repressed in vivo growth and prolonged latency. Furthermore, the level of ΔN(1–55)RhoGDIβ expression correlated with the extent to which the in vivo growth rate was repressed (Figs. 1a, 2b).

We also examined the effects of ΔN(1–55)RhoGDIβ on transformed phenotypes in the in vitro transformation assay. The expression of ΔN(1–55)RhoGDIβ reduced the frequency of transformation of A31-1-1 cells by v-src (Fig. 2c, d) but not by H-ras (data not

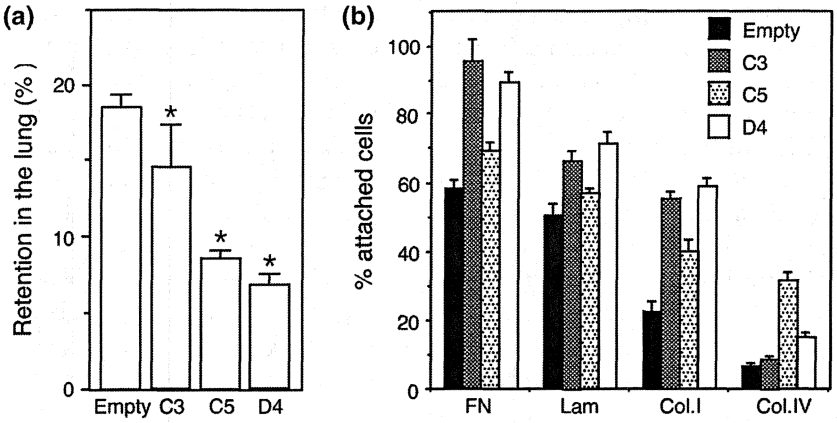

Fig. 3 Decrease of the retention in the lung after intravenous injection of ΔN(1–55)RhoGDIβ-expressing cells. **a** Normal mice were injected intravenously with 5×10^5 PKH26-labeled cells. After 24 h, the mice were killed, PKH26 was extracted from their lungs, and the fluorescence intensity of PKH26 was measured. The retention of tumor cells in the lung was determined by calculating the percentage of the injected fluorescence intensity that was found in the lung extract. Values indicate means ± S.D. of four mice. $^*P < 0.01$ compared with the empty vector-transfected control. **b** Cells (2×10^4) were added to each well of a 96-well plate coated with the indicated ECM proteins and allowed to attach for 90 min at 37°C. The number of attached cells was determined using a colorimetric assay. Values indicate means ± S.D. of eight samples

shown). The expression of ΔN(1–55)RhoGDIβ alone did not transform A31-1-1 cells. Thus, ΔN(1–55)RhoGDIβ did not influence the in vitro growth rate and did not act as an oncogene.

To determine whether ΔN(1–55)RhoGDIβ influences the activity of v-Src, we examined the extent of FAK phosphorylation at Tyr925, which is specifically phosphorylated by Src [39], and at Tyr397, which is autophosphorylated by FAK [40]. Although the degree of autophosphorylation (Tyr397) in 1-1src and untransformed parental A31-1-1 cells was similar, the level of phosphorylation at Tyr925 was much higher in 1-1src cells than in the parental cells (Fig. 2e). Expression of ΔN(1–55)RhoGDIβ in 1-1src cells did not influence the level of phosphorylation at either Tyr925 or Tyr397 (Fig. 2f). These results indicate that ΔN(1–55)RhoGDIβ affects both in vivo tumorigenicity in v-src-transformed cells and v-src-induced transformation in vitro without altering Src activity.

ΔN(1–55)RhoGDIβ decreases the retention of tumor cells in the lung

To examine which metastatic processes were affected by ΔN(1–55)RhoGDIβ, we next measured the retention of tumor cells in the lung. Cells were labeled with a fluorescent marker, PKH26, and intravenously injected into mice. The number of cells retained in the lung was determined after 24 h by measuring the fluorescence in lung extracts. We found that fewer ΔN(1–55)RhoGDIβ-expressing cells were retained in the lung than cells transfected with the empty vector (Fig. 3a). These observations indicate that ΔN(1–55)RhoGDIβ influenced during an early step of metastasis, either the attachment or survival of the cells in the lung.

We therefore explored the ability of the cells to attach to extracellular matrix (ECM) proteins, namely, fibronectin, laminin, collagen type I, and collagen type IV. We found that the ΔN(1–55)RhoGDIβ-expressing cells adhered more rapidly to these proteins than cells transfected with an empty vector (Fig. 3b). Thus, the repression of metastasis by ΔN(1–55)RhoGDIβ is likely due to a decrease in survival in the lung rather than a decrease in ability to attach to the ECM.

Increase of sensitivity to anoikis in ΔN (1–55)RhoGDIβ-expressing cells

On the basis of these results, we speculated that the decreased survival of ΔN(1–55)RhoGDIβ-expressing cells in the lung during metastasis is due to an increased sensitivity to cell death. We therefore measured the sensitivity of the clones to detachment-induced apoptosis (anoikis). Anoikis is thought to serve as a physiological barrier to metastasis, and resistance to anoikis contributes to the malignancy of cancer cells [41, 42]. To induce anoikis, we cultured the cells as a single-cell suspension for 6–8 h, and measured the extent of apoptosis with an Annexin V assay. Highly metastatic 1-1src cells showed a higher resistance to anoikis than the parental normal A31-1-1 cells (Fig. 4a). The resistance to anoikis observed in 1-1src cells was repressed by the expression of

ΔN(1–55)RhoGDIβ (Fig. 4a). This repression does not appear to be due to inactivation of Src kinase because ΔN(1–55)RhoGDIβ had no effect on Src in ΔN (1–55)RhoGDIβ-expressing 1-1src cells (Fig. 2e, f). Therefore, ΔN(1–55)RhoGDIβ likely promotes anoikis in 1-1src cells via pathways other than Src kinase signaling. To further confirm this causal relationship between anoikis sensitivity and expression of ΔN (1–55)RhoGDIβ, we transiently introduced Xpress-tagged ΔN(1–55)RhoGDIβ into 1-1src cells and measured the sensitivity to anoikis. The results clearly showed that transient expression of ΔN(1–55)RhoGDIβ enhanced cell death after the induction of anoikis (Fig. 4b).

Evaluation of signaling pathways involved in the promotion of anoikis by ΔN(1–55)RhoGDIβ

To evaluate the signaling pathways participating in the change in the sensitivity of 1-1src cells to anoikis, we examined the expression levels of FAK, p44/p42-MAPK, Akt1, and Bcl-2, proteins known to regulate cell survival during anoikis [42, 43]. When attached the substrate, the levels of these proteins were similar in cells expressing empty control vector or ΔN(1–55) RhoGDIβ (Figs. 2f, 5a). Furthermore, the phosphorylation levels of FAK, p44/p42-MAPK, and Akt1 were similar in these cells (Figs. 2f, 5a). After the induction of anoikis, in all cell lines, the level of FAK, p44/p42-MAPK, Akt1, and Bcl-2 was unchanged, but the phosphorylation of FAK on Tyr925, p44/p42-MAPK on Thr202/Tyr204, and Akt1 on Ser473 were clearly reduced within 1 h (Fig. 5b). These changes in phosphorylation may participate in anoikis signaling, but there was no difference between cells expressing the empty vector and those expressing ΔN(1–55)RhoGDIβ.

Finally, we examined the possibility that Rac or Cdc42 participates in the enhancement of sensitivity to anoikis by ΔN(1–55)RhoGDIβ. Dominant-negative mutants of Rac1 and Cdc42 induce anoikis in fibroblast cells [44], and it is possible that the amount of GTP-bound Rac1 and Cdc42 are reduced in ΔN (1–55)RhoGDIβ-expressing cells. Unexpectedly, the amounts of GTP-bound Rac1 and Cdc42 were not reduced by ΔN(1–55)RhoGDIβ expression (Fig. 5c).

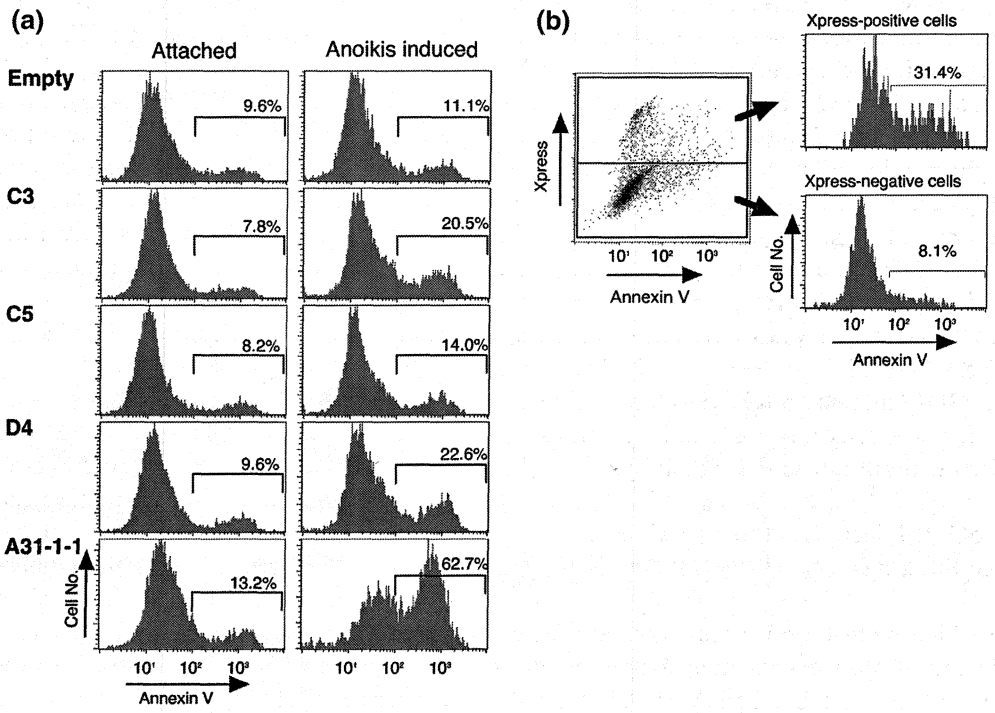

Fig. 4 Increase of anoikis in ΔN(1–55)RhoGDIβ-expressing cells. **a** Cells (1×10^5) in 5 ml of serum-free EMEM were plated in 60-mm bacteriological dishes precoated with 1% BSA to induce anoikis. After 8 h, the cells were harvested, stained with Annexin V-FITC, and analyzed by flow cytometry within 1 h. The percentage of apoptotic cells is shown in the figures. A representative from four independent experiments is shown. **b** 1-1src cells were transfected with pcDNA3.1-ΔN(1–55)RhoGDIβ. After 24 h, anoikis was induced for 6 h. The cells were then stained with Annexin V-FITC, fixed with 4% paraformaldehyde, stained with anti-Xpress antibody followed by rhodamine-conjugated secondary antibody, and analyzed by flow cytometry. The percentage of apoptotic cells is shown in the figures

Therefore, ΔN(1–55)RhoGDIβ functions in 1-1src cells via pathways other than Src kinase, Rac1, and Cdc42 signaling.

On the basis of these findings, we concluded that ΔN(1–55)RhoGDIβ represses metastasis by increasing the sensitivity to anoikis through undefined mechanisms in v-src-transformed fibroblast cells.

Discussion

Activation of Rho GTPase pathways stimulates cell growth, cell motility, and invasion [45], and the active form of Rho GTPases and Rho guanine nucleotide exchange factors (RhoGEFs) are oncogenic [46–48]. Furthermore, the forced expression of RhoGDIβ suppresses the malignancy of cancer cells [21]. Therefore, it is plausible that full-length RhoGDIβ inhibits metastasis by down-regulating Rho GTPase signaling. In addition, the N-terminal flexible domain of RhoGDIs have significant functions in the regulation of Rho GTPases [22–28], and RhoGDIs lacking this domain cannot inhibit GDP dissociation from Rho GTPases in vitro [8, 23, 28]. In the current studies, we showed that expression of ΔN(1–55)RhoGDIβ does not decrease Rac1 or Cdc42 activation in 1-1src cells. Therefore, unlike full-length RhoGDIβ, the repression of metastasis by ΔN(1–55)RhoGDIβ is not due to the inhibition of Rho GTPases, and molecules other than Rho family proteins may be the intracellular targets of ΔN(1–55)RhoGDIβ.

ΔN(1–55)RhoGDIβ decreased the growth rate of 1-1src cells in nude mice, suppressed transformation of A31-1-1 cells by v-src in vitro, and increased the

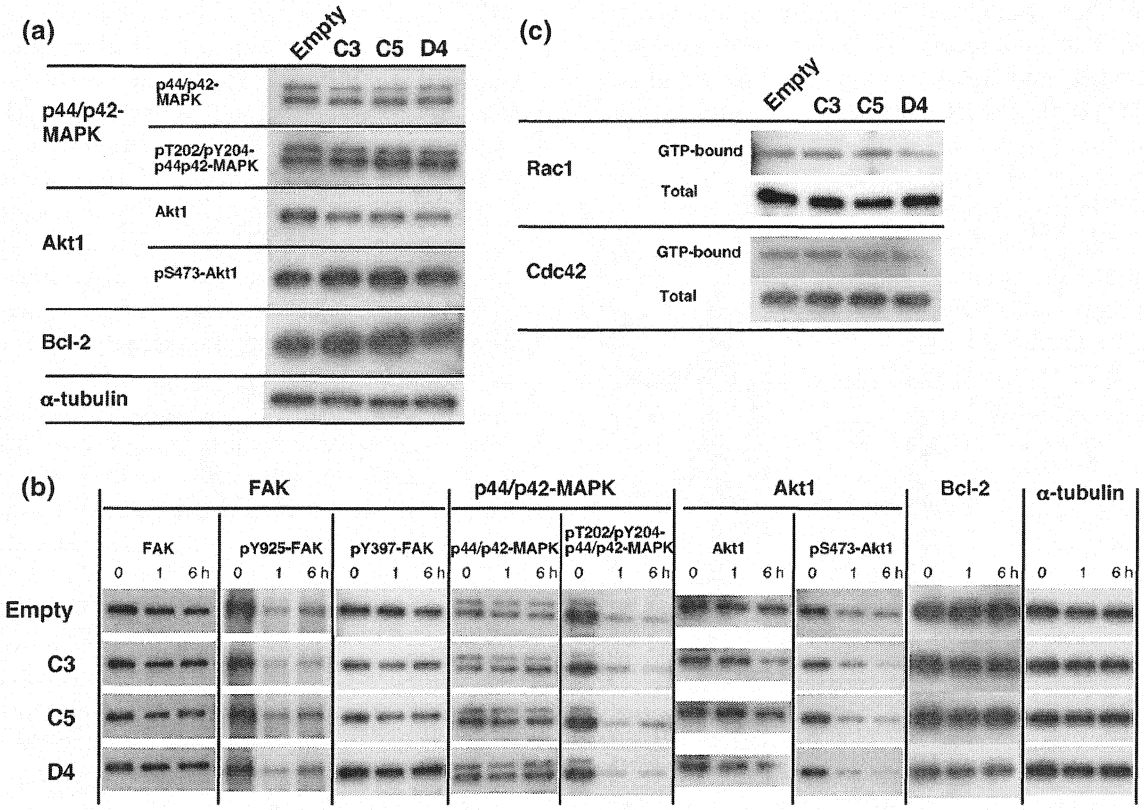

Fig. 5 Effect of ΔN(1–55)RhoGDIβ on the expression and phosphorylation of signaling molecules regulating cell survival. **a** Whole cell lysates of empty vector-transfected 1-1src cells and ΔN(1–55)RhoGDIβ-expressing cells in monolayer cultures were examined by immunoblotting with anti-p44/p42 MAPK, anti-p44/p42 MAPK phosphorylated at Thr202/Tyr204 (pT202/pY204), anti-Akt1, anti-Akt1 phosphorylated at Ser473 (pS473), anti-Bcl-2, and anti-α-tubulin. A representative blot from two independent experiments is shown. **b** After 1 and 6 h of the induction of anoikis, cells were lysed and examined by immunoblotting with anti-FAK, anti-FAK phosphorylated at Tyr925 (pY925-FAK), anti-FAK phosphorylated at Tyr397 (pY397-FAK), anti-p44/p42 MAPK, anti-p44/p42 MAPK phosphorylated at Thr202/Tyr204 (pT202/pY204), anti-Akt1, anti-Akt1 phosphorylated at Ser473 (pS473), anti-Bcl-2, and anti-α-tubulin. A representative blot from two independent experiments is shown. **c** Activation levels of Rac1 and Cdc42 in ΔN(1–55)RhoGDIβ-expressing cells. Rac1-GTP and Cdc42-GTP were pulled down from cell lysate with GST-PBD. Bound proteins and whole cell lysates were characterized by immunoblotting with anti-Rac1 and anti-Cdc42 antibodies. A representative blot from two independent experiments is shown

sensitivity of 1-1src cells to anoikis. These results suggest that sensitivity to anoikis is an important biological factor influencing tumorigenic growth during not only growth of tumor xenografts in vivo but also transformation-focus formation in vitro. Consistent with this finding, anoikis has been previously suggested to serve as a physiological barrier to metastasis [41, 42], and resistance to anoikis is known to contribute to the malignancy of both epithelial [49–51] and non-epithelial cancers [52–54].

It seems contradictory that the increased adhesiveness to the ECM in vitro is associated with a higher sensitivity to anoikis in ΔN(1–55)RhoGDIβ-expressing cells. This apparent contradiction could be due to the difference in the time points between the two assays: adhesiveness was measured after 90 min, whereas the sensitivity to anoikis was measured after 6 or 8 h. Specifically, ΔN(1–55)RhoGDIβ-expressing cells attached more rapidly to the ECM than control cells but also died more quickly when maintained in suspension for more than 90 min. Thus, signals occurring later than 90 min after detachment appear to be important for cell survival. Further studies are needed to determine the point at which the cells commit to anoikis.

Many intracellular signaling factors have been implicated in anoikis of tumor cells [42, 55, 56], and ΔN(1–55)RhoGDIβ may be a new candidate for an endogenous factor regulating anoikis sensitivity during cancer progression. Truncated proteins produced by protein processing such as ΔN(1–55)RhoGDIβ are generally difficult to detect in situ. Such a factor could regulate tumor growth under specific conditions, for example during the process of micrometastasis. We detected a band at the size expected for mouse RhoGDIβ cleaved at Asp54 (corresponding to Asp55 in human RhoGDIβ) within 1 h after the induction of anoikis in A31-1-1 cells; however, Ac-YVAD-FMK (an inhibitor of caspase-1) did not inhibit the production of this band (unpublished data). These findings are consistent with a previous report showing that RhoGDIβ is cleaved at Asp55 by caspase-1 in vitro but that caspase-1 inhibitors do not block the cleavage at this site in vivo [8]. Therefore, a caspase other than caspase-1 seems to be responsible for the in vivo cleavage at this site. Even if there is a cleavage product other than ΔN(1–55)RhoGDIβ, the deletion of this domain is expected to cause a similar phenotype because the N-terminal flexible domain is important for the regulatory function of RhoGDIβ [22–28].

Rac1, Cdc42 [44, 57], Src [58–60], FAK, p44/p42-MAPK, Akt1, and Bcl-2 [42, 43] are known to regulate cell survival during anoikis. The proteolytic removal of the N-terminal 55 amino acids of RhoGDIβ eliminates its ability to inhibit Rho GTPases [8]. Consequently, as proposed by Danley et al. [8], production of ΔN(1–55) RhoGDIβ should lead to increased activity of Rho family GTPases. In the current studies, we found that the expression of ΔN(1–55)RhoGDIβ in 1-1src cells does not induce the activation of Rac1 or Cdc42. We also found that the levels of FAK, MAPK, Akt1, and Bcl-2 and the phosphorylation of FAK, MAPK, and Akt1 are similar in the empty vector control and ΔN (1–55)RhoGDIβ-expressing cells before and after the induction of anoikis. Therefore, the increased sensitivity to anoikis in ΔN(1–55)RhoGDIβ-expressing cells could not be attributed to the difference in the expression or phosphorylation of these molecules. Nevertheless, ΔN(1–55)RhoGDIβ appears to play a key role in determining the sensitivity to anoikis when expressed in highly metastatic anoikis-resistant 1-1src cells. Our findings suggest that undefined signaling pathways mediate the ability of ΔN(1–55)RhoGDIβ to enhance the sensitivity to anoikis.

We have not yet tested the effect of ΔN(1–55)RhoGDIβ on anoikis and metastasis in a range of metastatic cancer cells, but we found that ΔN(1–55) RhoGDIβ suppresses transformation induced by v-src but not by H-ras in BALB/c 3T3 A31-1-1 cells. Thus, the effect of ΔN(1–55)RhoGDIβ is likely to be v-src specific. The deregulation of Src tyrosine kinase has been implicated as a central factor in various human cancers [61]. It is possible that human cancers with abnormal Src tyrosine kinase activity are potential targets of the effect of ΔN(1–55)RhoGDIβ.

Rho guanine nucleotide dissociation inhibitors have three known functions: inhibition of dissociation of GDP from Rho proteins, inhibition of GTPase activity of Rho proteins, and regulation of the localization of Rho proteins [62–66]. ΔN(1–59)RhoGDIα can associate with Cdc42, but the affinity of this interaction is approximately 500-fold lower than that for full-length RhoGDIα [23]. Therefore, the direct interaction of ΔN(1–55)RhoGDIβ with Rho family proteins is unlikely. RhoGDIs also interact with other molecules, including Ezrin Radixin Moesin proteins [3, 7, 67], RhoGEFs [68], p75 neurotrophin receptor [69], and PAK1 [70]. In addition, the C-terminus of RhoGDIβ and RhoGDIα can interact with Vav [68] and Radixin [71], respectively. Recently, it has been proposed that RhoGDI-associated multimolecular complexes are key regulators of RhoGDI activity and function [66], and it is possible that ΔN(1–55)RhoGDIβ interacts with these complexes. Further studies using RhoGDIs lacking the N-terminal flexible region should help determine the physiological significance of RhoGDIs and whether they could be used to prevent metastasis.

Acknowledgments This research was supported in part by Grants-in-Aid for Scientific Research from the Japan Society for the Promotion of Science, by the Nature Science Foundation of China (30570548), Project Research from High Technology Center (H2006-8), Grant for Collaborative Research (C2005-2) of Kanazawa Medical University, the Science Research Promotion Fund of The Promotion and Mutual Aid Corporation for Private Schools of Japan, and by the Two Cell Co. Ltd.

References

1. Etienne-Manneville S, Hall A (2002) Rho GTPases in cell biology. Nature 420(6916):629–635
2. Ueda T, Kikuchi A, Ohga N, Yamamoto J, Takai Y (1990) Purification and characterization from bovine brain cytosol of a novel regulatory protein inhibiting the dissociation of GDP from and the subsequent binding of GTP to rhoB p20, a ras p21-like GTP-binding protein. J Biol Chem 265(16):9373–9380
3. Takahashi K, Sasaki T, Mammoto A, Takaishi K, Kameyama T, Tsukita S, Takai Y (1997) Direct interaction of the Rho GDP dissociation inhibitor with ezrin/radixin/moesin initiates the activation of the Rho small G protein. J Biol Chem 272(37):23371–23375
4. Del Pozo MA, Kiosses WB, Alderson NB, Meller N, Hahn KM, Schwartz MA, Takebe H (2002) Integrins regulate GTP-Rac localized effector interactions through dissociation of Rho-GDI. Nat Cell Biol 4(3):232–239
5. Lelias JM, Adra CN, Wulf GM, Guillemot JC, Khagad M, Caput D, Lim B (1993) cDNA cloning of a human mRNA preferentially expressed in hematopoietic cells and with homology to a GDP-dissociation inhibitor for the rho GTP-binding proteins. Proc Natl Acad Sci USA 90(4):1479–1483
6. Leffers H, Nielsen MS, Andersen AH, Honore B, Madsen P, Vandekerckhove J, Celis JE (1993) Identification of two human Rho GDP dissociation inhibitor proteins whose overexpression leads to disruption of the actin cytoskeleton. Exp Cell Res 209(2):165–174
7. Ota T, Maeda M, Suto S, Tatsuka M (2004) LyGDI functions in cancer metastasis by anchoring Rho proteins to the cell membrane. Mol Carcinog 39(4):206–220
8. Danley DE, Chuang TH, Bokoch GM (1996) Defective Rho GTPase regulation by IL-1 beta-converting enzyme-mediated cleavage of D4 GDP dissociation inhibitor. J Immunol 157(2):500–503
9. Zhou X, Suto S, Ota T, Tatsuka M (2004) Nuclear translocation of cleaved LyGDI dissociated from Rho and Rac during Trp53-dependent ionizing radiation-induced apoptosis of thymus cells in vitro. Radiat Res 162(3):287–295
10. Na S, Chuang TH, Cunningham A, Turi TG, Hanke JH, Bokoch GM, Danley DE (1996) D4-GDI, a substrate of CPP32, is proteolyzed during Fas-induced apoptosis. J Biol Chem 271(19):11209–11213
11. Rickers A, Brockstedt E, Mapara MY, Otto A, Dorken B, Bommert K (1998) Inhibition of CPP32 blocks surface IgM-mediated apoptosis and D4-GDI cleavage in human BL60 Burkitt lymphoma cells [published erratum appears in Eur J Immunol 1998 Mar; 28(3):1122]. Eur J Immunol 28(1):296–304
12. Kettritz R, Xu YX, Faass B, Klein JB, Muller EC, Otto A, Busjahn A, Luft FC, Haller H (2000) TNF-alpha-mediated neutrophil apoptosis involves Ly-GDI, a Rho GTPase regulator. J Leukoc Biol 68(2):277–283
13. Krieser RJ, Eastman A (1999) Cleavage and nuclear translocation of the caspase 3 substrate Rho GDP-dissociation inhibitor, D4-GDI, during apoptosis. Cell Death Differ 6(5):412–419
14. Essmann F, Wieder T, Otto A, Muller EC, Dorken B, Daniel PT (2000) GDP dissociation inhibitor D4-GDI (Rho-GDI 2), but not the homologous rho-GDI 1, is cleaved by caspase-3 during drug-induced apoptosis. Biochem J 346(Pt 3):777–783
15. Thiede B, Siejak F, Dimmler C, Rudel T (2002) Prediction of translocation and cleavage of heterogeneous ribonuclear proteins and Rho guanine nucleotide dissociation inhibitor 2 during apoptosis by subcellular proteome analysis. Proteomics 2(8):996–1006
16. Tatsuka M, Ota T, Maeda M, Wada M, Yamagishi N, Taniguchi S, Seiki M, Odashima S (1997) A BALB/c 3T3-transformed cell line suitable for transfection assay of metastasis-inducing genes. Int J Cancer 71(1):88–93
17. Jiang WG, Watkins G, Lane J, Cunnick GH, Douglas-Jones A, Mokbel K, Mansel RE (2003) Prognostic value of rho GTPases and rho guanine nucleotide dissociation inhibitors in human breast cancers. Clin Cancer Res 9(17):6432–6440
18. Seraj MJ, Harding MA, Gildea JJ, Welch DR, Theodorescu D (2000) The relationship of BRMS1 and RhoGDI2 gene expression to metastatic potential in lineage related human bladder cancer cell lines. Clin Exp Metastasis 18(6):519–525
19. Tapper J, Kettunen E, El-Rifai W, Seppala M, Andersson LC, Knuutila S (2001) Changes in gene expression during progression of ovarian carcinoma. Cancer Genet Cytogenet 128(1):1–6
20. Yanagawa T, Watanabe H, Takeuchi T, Fujimoto S, Kurihara H, Takagishi K (2004) Overexpression of autocrine motility factor in metastatic tumor cells: possible association with augmented expression of KIF3A and GDI-beta. Lab Invest 84(4):513–522
21. Gildea JJ, Seraj MJ, Oxford G, Harding MA, Hampton GM, Moskaluk CA, Frierson HF, Conaway MR, Theodorescu D (2002) RhoGDI2 is an invasion and metastasis suppressor gene in human cancer. Cancer Res 62(22):6418–6423
22. Keep NH, Barnes M, Barsukov I, Badii R, Lian LY, Segal AW, Moody PC, Roberts GC (1997) A modulator of rho family G proteins, rhoGDI, binds these G proteins via an immunoglobulin-like domain and a flexible N-terminal arm. Structure 5(5):623–633
23. Gosser YQ, Nomanbhoy TK, Aghazadeh B, Manor D, Combs C, Cerione RA, Rosen MK (1997) C-terminal binding domain of Rho GDP-dissociation inhibitor directs N-terminal inhibitory peptide to GTPases. Nature 387(6635):814–819
24. Longenecker K, Read P, Derewenda U, Dauter Z, Liu X, Garrard S, Walker L, Somlyo AV, Nakamoto RK, Somlyo AP, Derewenda ZS (1999) How RhoGDI binds Rho. Acta Crystallogr D Biol Crystallogr 55(Pt 9):1503–1515
25. Hoffman GR, Nassar N, Cerione RA (2000) Structure of the Rho family GTP-binding protein Cdc42 in complex with the multifunctional regulator RhoGDI. Cell 100(3):345–356
26. Scheffzek K, Stephan I, Jensen ON, Illenberger D, Gierschik P (2000) The Rac–RhoGDI complex and the structural basis for the regulation of Rho proteins by RhoGDI. Nat Struct Biol 7(2):122–126
27. Lian LY, Barsukov I, Golovanov AP, Hawkins DI, Badii R, Sze KH, Keep NH, Bokoch GM, Roberts GC (2000) Mapping the binding site for the GTP-binding protein Rac-1 on its inhibitor RhoGDI-1. Struct Fold Des 8(1):47–55
28. Golovanov AP, Chuang TH, DerMardirossian C, Barsukov I, Hawkins D, Badii R, Bokoch GM, Lian LY, Roberts GC (2001) Structure–activity relationships in flexible protein

domains: regulation of rho GTPases by RhoGDI and D4 GDI. J Mol Biol 305(1):121–135
29. Kakunaga T, Crow JD (1980) Cell variants showing differential susceptibility to ultraviolet light-induced transformation. Science 209(4455):505–507
30. Tatsuka M, Ota T, Yamagishi N, Kashihara Y, Wada M, Matsuda N, Mitsui H, Seiki M, Odashima S (1996) Different metastatic potentials of ras- and src-transformed BALB/c 3T3 A31 variant cells. Mol Carcinog 15(4):300–308
31. Terada Y, Tatsuka M, Suzuki F, Yasuda Y, Fujita S, Otsu M (1998) AIM-1: a mammalian midbody-associated protein required for cytokinesis. EMBO J 17(3):667–676
32. Ota T, Maeda M, Tatsuka M, Matsui T, Tanino M, Tanaka T (1999) Decrease of metastatic ability after selection for intravasating ability in Lewis lung carcinoma (3LL) cell line. Cancer Lett 139(1):105–108
33. Ota T, Suto S, Katayama H, Han ZB, Suzuki F, Maeda M, Tanino M, Terada Y, Tatsuka M (2002) Increased mitotic phosphorylation of histone H3 attributable to AIM-1/Aurora-B overexpression contributes to chromosome number instability. Cancer Res 62(18):5168–5177
34. Tatsuka M, Maeda M, Ota T (2001) Anticarcinogenic effect and enhancement of metastatic potential of BALB/c 3T3 cells by ginsenoside Rh(2). Jpn J Cancer Res 92(11):1184–1189
35. Yagi T, Sasayama S, Sasai H, Kakunaga T (1989) Cotransfection of plasmids with ras and myc oncogenes to diploid cells derived from rodent fetuses: alteration of neoplastic transformation frequency depending on the gestation period. Mol Carcinog 1(4):222–228
36. Kakunaga T (1985) Critical review of the use of established cell lines for in-vitro cell transformation. IARC Sci Publ 67:55–73
37. Ota T, Matsui T, Kohno H, Maeda M, Tanino M, Odashima S (1995) CD44 participates in tumor cell adhesion to endothelial cells in the experimental metastatic process in B16BL6 melanoma cells. Anticancer Res 15(4):1215–1219
38. Ota T, Maeda M, Tanino M, Tatsuka M (2001) Functional suppression of integrin beta 4-mediated adhesion caused by in vivo sequential selection for cancer cell intravasation. Anticancer Res 21(1A):205–211
39. Brunton VG, Avizienyte E, Fincham VJ, Serrels B, Metcalf CA 3rd, Sawyer TK, Frame MC (2005) Identification of Src-specific phosphorylation site on focal adhesion kinase: dissection of the role of Src SH2 and catalytic functions and their consequences for tumor cell behavior. Cancer Res 65(4):1335–1342
40. Schaller MD, Hildebrand JD, Shannon JD, Fox JW, Vines RR, Parsons JT (1994) Autophosphorylation of the focal adhesion kinase, pp125FAK, directs SH2-dependent binding of pp60src. Mol Cell Biol 14(3):1680–1688
41. Frisch SM, Ruoslahti E (1997) Integrins and anoikis. Curr Opin Cell Biol 9(5):701–706
42. Frisch SM, Screaton RA (2001) Anoikis mechanisms. Curr Opin Cell Biol 13(5):555–562
43. Gilmore AP (2005) Anoikis. Cell Death Differ 12(Suppl. 2):1473–1477
44. Zugasti O, Rul W, Roux P, Peyssonnaux C, Eychene A, Franke TF, Fort P, Hibner U (2001) Raf-MEK-Erk cascade in anoikis is controlled by Rac1 and Cdc42 via Akt. Mol Cell Biol 21(19):6706–6717
45. Jaffe AB, Hall A (2002) Rho GTPases in transformation and metastasis. Adv Cancer Res 84:57–80
46. Sahai E, Marshall CJ (2002) RHO-GTPases and cancer. Nat Rev Cancer 2(2):133–142
47. Rossman KL, Der CJ, Sondek J (2005) GEF means go: turning on RHO GTPases with guanine nucleotide-exchange factors. Nat Rev Mol Cell Biol 6(2):167–180
48. Schmidt A, Hall A (2002) Guanine nucleotide exchange factors for Rho GTPases: turning on the switch. Genes Dev 16(13):1587–1609
49. Yawata A, Adachi M, Okuda H, Naishiro Y, Takamura T, Hareyama M, Takayama S, Reed JC, Imai K (1998) Prolonged cell survival enhances peritoneal dissemination of gastric cancer cells. Oncogene 16(20):2681–2686
50. Streuli CH, Gilmore AP (1999) Adhesion-mediated signaling in the regulation of mammary epithelial cell survival. J Mammary Gland Biol Neoplasia 4(2):183–191
51. Shanmugathasan M, Jothy S (2000) Apoptosis, anoikis and their relevance to the pathobiology of colon cancer. Pathol Int 50(4):273–279
52. McGill G, Shimamura A, Bates RC, Savage RE, Fisher DE (1997) Loss of matrix adhesion triggers rapid transformation-selective apoptosis in fibroblasts. J Cell Biol 138(4):901–911
53. Petitclerc E, Stromblad S, von Schalscha TL, Mitjans F, Piulats J, Montgomery AM, Cheresh DA, Brooks PC (1999) Integrin alpha(v)beta3 promotes M21 melanoma growth in human skin by regulating tumor cell survival. Cancer Res 59(11):2724–2730
54. Diaz-Montero CM, McIntyre BW (2003) Acquisition of anoikis resistance in human osteosarcoma cells. Eur J Cancer 39(16):2395–2402
55. Rennebeck G, Martelli M, Kyprianou N (2005) Anoikis and survival connections in the tumor microenvironment: is there a role in prostate cancer metastasis? Cancer Res 65(24):11230–11235
56. Valentijn AJ, Zouq N, Gilmore AP (2004) Anoikis. Biochem Soc Trans 32(Pt 3):421–425
57. Cheng TL, Symons M, Jou TS (2004) Regulation of anoikis by Cdc42 and Rac1. Exp Cell Res 295(2):497–511
58. Loza-Coll MA, Perera S, Shi W, Filmus J (2005) A transient increase in the activity of Src-family kinases induced by cell detachment delays anoikis of intestinal epithelial cells. Oncogene 24(10):1727–1737
59. Wei L, Yang Y, Zhang X, Yu Q (2004) Altered regulation of Src upon cell detachment protects human lung adenocarcinoma cells from anoikis. Oncogene 23(56):9052–9061
60. Windham TC, Parikh NU, Siwak DR, Summy JM, McConkey DJ, Kraker AJ, Gallick GE (2002) Src activation regulates anoikis in human colon tumor cell lines. Oncogene 21(51):7797–7807
61. Frame MC (2002) Src in cancer: deregulation and consequences for cell behaviour. Biochim Biophys Acta 1602(2):114–130
62. Sasaki T, Takai Y (1998) The Rho small G protein family-Rho GDI system as a temporal and spatial determinant for cytoskeletal control. Biochem Biophys Res Commun 245(3):641–645
63. Zalcman G, Dorseuil O, Garcia-Ranea JA, Gacon G, Camonis J (1999) RhoGAPs and RhoGDIs, (His)stories of two families. Prog Mol Subcell Biol 22:85–113
64. Olofsson B (1999) Rho guanine dissociation inhibitors: pivotal molecules in cellular signalling. Cell Signal 11(8):545–554
65. DerMardirossian C, Bokoch GM (2005) GDIs: central regulatory molecules in Rho GTPase activation. Trends Cell Biol 15(7):356–363
66. Dovas A, Couchman JR (2005) RhoGDI: multiple functions in the regulation of Rho family GTPase activities. Biochem J 390(Pt 1):1–9

67. Maeda M, Matsui T, Imamura M, Tsukita S (1999) Expression level, subcellular distribution and rho-GDI binding affinity of merlin in comparison with ezrin/radixin/moesin proteins. Oncogene 18(34):4788–4797
68. Groysman M, Russek CS, Katzav S (2000) Vav, a GDP/GTP nucleotide exchange factor, interacts with GDIs, proteins that inhibit GDP/GTP dissociation. FEBS Lett 467(1):75–80
69. Yamashita T, Tohyama M (2003) The p75 receptor acts as a displacement factor that releases Rho from Rho-GDI. Nat Neurosci 6(5):461–467
70. DerMardirossian C, Schnelzer A, Bokoch GM (2004) Phosphorylation of RhoGDI by Pak1 mediates dissociation of Rac GTPase. Mol Cell 15(1):117–127
71. Dransart E, Olofsson B, Cherfils J (2005) RhoGDIs revisited: novel roles in Rho regulation. Traffic 6(11):957–966

ELSEVIER

Cell Biology International 31 (2007) 92–96

Cell Biology International

www.elsevier.com/locate/cellbi

Short communication

Activation of Rac1 by Rho-guanine nucleotide dissociation inhibitor-β with defective isoprenyl-binding pocket

Takahide Ota [a,*], Masayo Maeda [b], Manabu Murakami [a], Tsutomu Takegami [a], Shiho Suto [c], Masaaki Tatsuka [c]

[a] *Division of Molecular Oncology and Virology, Medical Research Institute, Kanazawa Medical University, Daigaku, Uchinada, Ishikawa 920-0293, Japan*
[b] *Department of Chemistry, Kanazawa Medical University, Daigaku, Uchinada, Ishikawa 920-0293, Japan*
[c] *Department of Molecular Radiobiology, Research Institute for Radiation Biology and Medicine, Hiroshima University, Hiroshima 734-8553, Japan*

Received 25 August 2006; accepted 1 September 2006

Abstract

Rho-guanine nucleotide dissociation inhibitor-β (RhoGDIβ), a regulator for Rho GTPases, is implicated in cancer cell progression. We reported that C-terminal truncated RhoGDIβ (ΔC(166–201)-RhoGDIβ) promoted metastasis through activating Rac1 signaling pathway in ras-transformed fibroblast cells. To better understand the mechanism of Rac1 activation by ΔC(166–201)-RhoGDIβ during metastasis, the amount of GTP-bound Rac1 was measured as the activation level of Rac1 in cells expressing various mutant RhoGDIβ with sequential C-terminal deletions. Three C-terminal hydrophobic amino acid residues (Trp191, Leu193, and Ile195) supposed to interact with isoprenyl groups of Rac1, was indispensable for a proper regulation of Rac1 activation/inhibition. Deletion of this region led RhoGDIβ to continuously associate with GTP-bound Rac1, provoking constitutive activation of Rac1. Thus, impaired interaction of RhoGDIβ with Rac1 isoprenyl groups possibly makes RhoGDIβ function as a positive regulator for Rac1 during metastasis.

Keywords: RhoGDI; Rac1; Prenylation; Metastasis

1. Introduction

Rho GTPases play crucial roles in various cellular events, such as cytoskeletal organization, cell polarity, gene transcription, cell cycle progression, microtubule dynamics, and vesicular transport (Etienne-Manneville and Hall, 2002). We had identified Rho-guanine nucleotide dissociation inhibitor-β (RhoGDIβ) lacking the C-terminal 36 amino acids (ΔC(166–201)-RhoGDIβ) as a metastasis-inducing gene (Tatsuka et al., 1997; Ota et al., 2004). In several reports, RhoGDIs are also implicated in the progression of cancer cells, however their roles are still controversial. RhoGDIα was upregulated in ovarian cancer (Jones et al., 2002), and breast cancer (Fritz et al., 2002). RhoGDIβ was also upregulated in ovarian cancer (Tapper et al., 2001) and in metastatic fibrosarcoma cells generated by overexpression of autocrine motility factor (Yanagawa et al., 2004). In contrast, downregulation of RhoGDIα was reported in breast cancer (Jiang et al., 2003) and expression of RhoGDIβ was inversely correlated with the invasive capacity in human bladder cancer cell lines (Seraj et al., 2000). Furthermore, RhoGDIβ was reported as an invasion and metastasis suppressor gene (Gildea et al., 2002). Although these observations collectively indicate that RhoGDIs regulate the metastatic processes, their roles are elusive. We reported earlier that the promotion of metastasis by ΔC(166–201)-RhoGDIβ was mediated by the activation of Rac1 signaling pathway (Ota et al., 2004). In this study, to better understand how RhoGDIβ functions in the regulation of metastasis, we examined which region of the 36 amino acid sequence was important for affecting the Rac1 signaling

* Corresponding author. Tel.: +81 76 286 2211; fax: +81 76 286 0521.
E-mail address: takahide@kanazawa-med.ac.jp (T. Ota).

1065-6995/$ - see front matter © 2006 International Federation for Cell Biology. Published by Elsevier Ltd. All rights reserved.
doi:10.1016/j.cellbi.2006.09.002

pathway. We found that the deletion of the C-terminal region containing Trp191, Leu193, and Ile195, hydrophobic residues supposed to participate in the interaction with isoprenyl group of Rac1 (Gosser et al., 1997; Hoffman et al., 2000; Grizot et al., 2001), was critical for the promotion of Rac1 activation and the association of ΔC-RhoGDIβ with GTP-bound Rac1. Our results indicate that the destruction of the interaction of RhoGDIβ with isoprenyl group on Rac1 makes RhoGDIβ function as a positive regulator for Rac1 during metastasis.

2. Materials and methods

2.1. Cells and culture

The 1-1ras1000 cell line, derived from BALB/c 3T3 A31-1-1 cells transfected with an activated c-Ha-ras oncogene (Tatsuka et al., 1996), was used for assay. In this cell line, the expression of ΔC(166–201)-RhoGDIβ induces metastatic phenotype by activating Rac1 signaling pathways (Ota et al., 2004). Cells were cultured in Eagle's minimum essential medium supplemented with 10% fetal bovine serum and were maintained at 37 °C in a humidified atmosphere of 5% CO_2 in air.

2.2. Plasmids and transfection

To construct expression vectors for wild type and C-terminal truncated RhoGDIβ, the entire and truncated sequences were amplified by PCR using pcDNA3.1-LyGDI, which is an expression vector for wild type RhoGDIβ (Ota et al., 2004). The products were then subcloned into Xpress-tagged pcDNA3.1 expression vector. Cells were transfected with plasmids using LipofectAMINE™ plus (Invitrogen, Carlsbad, CA).

2.3. Rac activation assay

Pull-down assays for measuring the Rac activation were performed using Rac activation assay kits (Cytoskeleton Inc., Denver, CO) according to the manufacturer's instructions. The cells were washed with PBS and lysed on the dish in cell lysis buffer. Rac1-GTP was pulled down using the GST tagged PBD (p21 binding domain) of Pak1 (p21/Cdc42/Rac1-activated kinase 1) protein beads.

2.4. Immunoblotting

Samples were lysed with Laemmli buffer, resolved by sodium dodecyl sulfate-polyacrylamide gel electrophoresis, and transferred to Immobilon-P membranes (Millipore, Billerica, MA). The membranes were then probed with a primary antibody, followed by a peroxidase-conjugated secondary antibody. Immunoreactive proteins were visualized using ECL Plus reagents (Amersham Biosciences, Little Chalfont, UK). For densitometric analysis of immunoblots the films were scanned and the intensity of the bands was measured using the ImageJ program (NIH, Bethesda, MD, USA), and the Rac1 and Xpress-RhoGDIβ values in PBD-bound fraction were normalized with respect to those in total cell lysate.

2.5. Antibodies

Anti-Xpress, anti-α-tubulin (clone B-5-1-2), and anti-Rac1 (clone 102) antibodies were purchased from Invitrogen (Carlsbad, CA), Sigma-Aldrich (St. Louis, MO), and BD Biosciences (San Jose, CA), respectively. Peroxidase-conjugated anti-mouse IgG was purchased from DakoCytomation (Glostrup, Denmark).

3. Results and discussion

We had reported that C-terminal truncated RhoGDIβ (ΔC(166–201)-RhoGDIβ) promoted the metastasis by activating Rac1 signaling pathways in *ras*-transformed fibroblast cells (1-1ras1000 cells) (Ota et al., 2004). In this report we attempted to define which region within the 36 residues deleted in ΔC(166–201)-RhoGDIβ was important for Rac signaling. Fig. 1A shows the amino acid sequences of

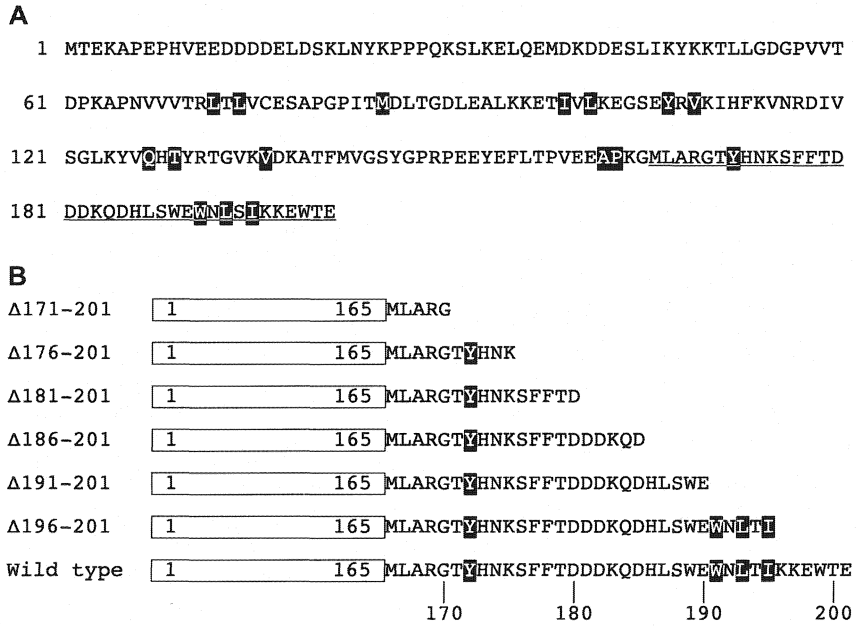

Fig. 1. Amino acid sequences of human RhoGDIβ. (A) Hydrophobic residues of RhoGDIβ corresponding to the residues of RhoGDIα that participate in the interaction with isoprenyl groups of Rho GTPases (Gosser et al., 1997; Hoffman et al., 2000; Grizot et al., 2001) are indicated as black boxes. Residues 166–201, which are deleted in metastasis-inducing ΔC-RhoGDIβ (Ota et al., 2004), are underlined. (B) A schematic representation of sequential C-terminal deleted RhoGDIβ. Four hydrophobic residues in 166–201 of RhoGDIβ proposed to participate in the formation of isoprenyl-binding pocket are indicated as black boxes.

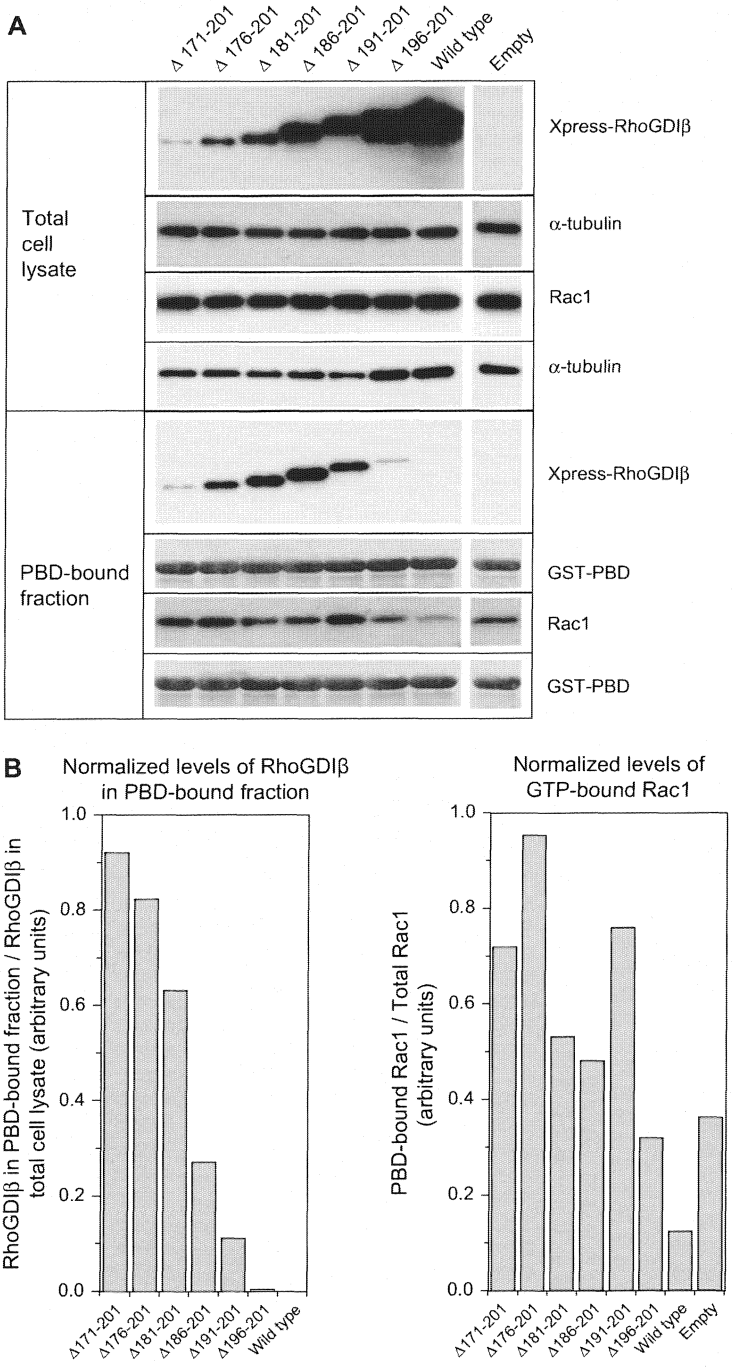

Fig. 2. Increase of GTP-bound Rac1 and association of ΔC-RhoGDIβ with GTP-bound Rac1 in cells expressing ΔC-RhoGDIβ. (A) Cells were transfected with Xpress-tagged pcDNA3.1 expression vectors of various ΔC-RhoGDIβ. After 48 h cells were lysed and Rac1-GTP was pulled down using the GST tagged PBD protein beads. Total cell lysate and PBD-bound fraction were immunoblotted with anti-Xpress antibody or anti-Rac1 antibody. As a loading control, α-tubulin was stained in total cell lysate and GST-PBD was stained with Coomassie brilliant blue in PBD-bound fraction. When Xpress-RhoGDIβ was overexpressed, an unidentified band smaller than expected size was observed in total cell lysate. The amount of this smaller band was less than 5% of major band. (B) The blots in Fig. 2A were analyzed by NIH ImageJ analysis software, and the values of Xpress-RhoGDIβ and Rac1 in PBD-bound fractions were normalized to those values in total cell lysate.

RhoGDIβ. In the deleted region of ΔC(166–201)-RhoGDIβ, four hydrophobic residues (Tyr172, Trp191, Leu193, and Ile195) are supposed to participate in the formation of an isoprenyl-binding pocket involved in interaction with isoprenyl groups of Rac1 (Gosser et al., 1997; Hoffman et al., 2000; Grizot et al., 2001). We constructed Xpress-tagged pcDNA3.1 expression vectors of various length for ΔC-RhoGDIβ with residues sequentially deleted from C-terminus (Fig. 1B). These expression vectors were transfected into the 1-1ras1000 cells and the amount of GTP-bound Rac1 were determined by pull-down assay using GST tagged PBD protein beads. Although the expression levels of introduced

genes varied among transfectants (Fig. 2A), cells expressing ΔC-RhoGDIβ lacking the three C-terminal hydrophobic amino acids Trp191, Leu193, and Ile195 (Δ171–201, Δ176–201, Δ181–201, Δ186–201, and Δ191–201) showed higher levels of GTP-bound Rac1 than empty control cells (Fig. 2A). Furthermore, ΔC-RhoGDIβ was detected in PBD-bound fraction, whereas wild type RhoGDIβ was not detected in PBD bound fraction despite its highest expression level (Fig. 2A). When the amounts of ΔC-RhoGDIβ in PBD-bound fraction were normalized to those in total cell lysate, ΔC(196–201)-RhoGDIβ, which retains C-terminal three hydrophobic amino acid residues, was detectible only at trace level (Fig. 2B). These results further support our previous observation that C-terminal truncated RhoGDIβ (ΔC(166–201)-RhoGDIβ) induces metastasis by constitutive activation of Rac1 and associates with GTP-bound Rac1 (Ota et al., 2004).

Wild type RhoGDIβ and ΔC(196–201)-RhoGDIβ, which retain the three hydrophobic amino acid residues at the C-terminal, could not increase the amount of GTP-bound Rac1 and yielded hardly detectible levels in the PBD-bound fraction (Fig. 2). These results clearly indicate that the absence of the C-terminal hydrophobic amino acids Trp191, Leu193, and Ile195, which are supposed to interact with isoprenyl groups of Rho GTPases, is crucial for ΔC-RhoGDIβ to express its phenotype. The isoprenyl group of Rho GTPase is not essential for the binding of Rho GTPases to RhoGDI (Lian et al., 2000; Faure and Dagher, 2001; Thapar et al., 2002). Indeed, we found that ΔC-RhoGDIβ lacking an intact isoprenyl binding-pocket could associate with GTP-bound Rac1 (Fig. 2). However, the interaction of the isoprenyl groups of Rho GTPases with RhoGDIs are important for the proper intracellular localization and functions of Rho GTPase (Hori et al., 1991; Regazzi et al., 1992; Michaelson et al., 2001; Sun and Barbieri, 2004; Wennerberg and Der, 2004). Therefore, RhoGDIβ defective in the isoprenyl binding pocket probably binds Rac1, but is expected to differ from wild type RhoGDIβ in the intracellular localization and function. Previously, we had shown that ΔC(166–201)-RhoGDIβ anchored Rac1 at the membrane to activate its effector molecules (Ota et al., 2004). In another report, a mutant RhoGDIα, defective in extracting the isoprenyl moiety of Cdc42 off the membrane through an isoprenyl-binding pocket, forms a complex with Cdc42 and retains it on the membrane (Sun and Barbieri, 2004). To explain the ability of RhoGDIα to release Cdc42 from membrane a two-step model has been proposed (Nomanbhoy et al., 1999; Hoffman et al., 2000). In this model, the N-terminal regulatory domain of RhoGDIα binds to Cdc42 on the membrane and subsequently the C-terminal isoprenyl-binding pocket of RhoGDIα extracts the membrane-buried isoprenyl moiety of Cdc42 from the membrane. Furthermore, it has been reported that RhoGDIα more efficiently interacted with GDP-bound Rac1 than with GTP-bound Rac1 (Sasaki et al., 1993) and the conversion of GTP-bound Rac1 to GDP-bound Rac1 was the rate-limiting step in the dissociation from membrane (Moissoglu et al., 2006). On the other hand, RhoGDIα can bind GTP-bound Rac1 and can inhibit GTP hydrolysis by Rac1. This interaction is suggested to be a mechanism that maintains Rac1 in an active form (Chuang et al., 1993). According to these findings, the function of ΔC-RhoGDIβ with the defective isoprenyl-binding pocket in our experiment should act as depicted in Fig. 3. GTP-bound Rac1 is converted to the GDP-bound form and then wild type RhoGDIβ binds GDP-bound Rac1 by an N-terminal regulatory domain and, through extraction of the hydrophobic,

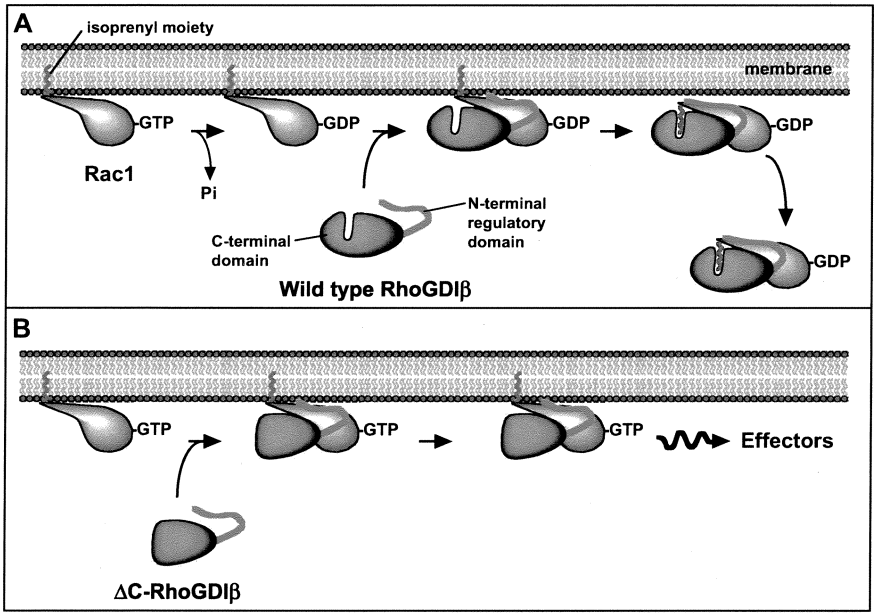

Fig. 3. Schematic drawing of proposed function of ΔC-RhoGDIβ. (A) GTP-bound Rac1 is converted to GDP-bound form and then the N-terminal regulatory domain of wild type RhoGDIβ binds GDP-bound Rac1 and the C-terminal isoprenyl-binding pocket of RhoGDIβ extracts the membrane-buried isoprenyl moiety of Rac1 from membrane, thereby releasing Rac1 from membrane. (B) ΔC-RhoGDIβ binds GTP-bound Rac1 by the N-terminal regulatory domain, but can not remove Rac1 from membrane due to the defect of the isoprenyl-binding pocket. Therefore, ΔC-RhoGDIβ remains attached to GTP-bound Rac1 on membrane and supports Rac1 activation of effectors.

membrane-buried isoprenyl moiety of Rac1, removes GDP-bound Rac1 from the membrane (Fig. 3A). On the other hand, ΔC-RhoGDIβ binds GTP-bound Rac1 by the N-terminal regulatory domain but can not remove Rac1 from the membrane due to the defective isoprenyl-binding pocket, therefore ΔC-RhoGDIβ keeps GTP-bound Rac1 on the membrane and supports Rac1 activation of the effectors (Fig. 3B).

The expression level of RhoGDIs is correlated to cancer progression, both positively (Tapper et al., 2001; Fritz et al., 2002; Jones et al., 2002; Yanagawa et al., 2004) and negatively (Seraj et al., 2000; Gildea et al., 2002; Jiang et al., 2003). RhoGDIs are often thought to function as inhibitors, however, we had shown that RhoGDIβ could positively regulate Rac1 (Ota et al., 2004). Several other studies also suggest a positive regulatory role for RhoGDIs (O'Sullivan et al., 1996; Tolias et al., 1998). Our observations in this report suggest that the interaction of RhoGDIβ with the isoprenyl moiety of Rac1 is a crucial determinant of the nature of regulatory functions of RhoGDIβ. The apparently opposite roles of RhoGDIs in cancer progression may reflect different regulation mechanisms of Rho GTPases by RhoGDIs mediated by interaction of RhoGDIs with the isoprenyl moiety of Rho GTPases.

Acknowledgements

This research was supported in part by Grants-in-Aid for Scientific Research from the Japan Society for the Promotion of Science, Project Research from High Technology Center (H2006-8), Grant for Collaborative Research (C2005-2) of Kanazawa Medical University, the Science Research Promotion Fund of The Promotion and Mutual Aid Corporation for Private Schools of Japan and by the Two Cell Co. Ltd.

References

Chuang TH, Xu X, Knaus UG, Hart MJ, Bokoch GM. GDP dissociation inhibitor prevents intrinsic and GTPase activating protein-stimulated GTP hydrolysis by the Rac GTP-binding protein. J Biol Chem 1993;268:775–8.

Etienne-Manneville S, Hall A. Rho GTPases in cell biology. Nature 2002; 420:629–35.

Faure J, Dagher M. Interactions between Rho GTPases and Rho GDP dissociation inhibitor (Rho-GDI). Biochimie 2001;83:409–14.

Fritz G, Brachetti C, Bahlmann F, Schmidt M, Kaina B. Rho GTPases in human breast tumours: expression and mutation analyses and correlation with clinical parameters. Br J Cancer 2002;87:635–44.

Gildea JJ, Seraj MJ, Oxford G, Harding MA, Hampton GM, Moskaluk CA, et al. RhoGDI2 is an invasion and metastasis suppressor gene in human cancer. Cancer Res 2002;62:6418–23.

Gosser YQ, Nomanbhoy TK, Aghazadeh B, Manor D, Combs C, Cerione RA, et al. C-terminal binding domain of Rho GDP-dissociation inhibitor directs N-terminal inhibitory peptide to GTPases. Nature 1997;387:814–9.

Grizot S, Faure J, Fieschi F, Vignais PV, Dagher MC, Pebay-Peyroula E. Crystal structure of the Rac1-RhoGDI complex involved in nadph oxidase activation. Biochemistry 2001;40:10007–13.

Hoffman GR, Nassar N, Cerione RA. Structure of the Rho family GTP-binding protein Cdc42 in complex with the multifunctional regulator RhoGDI. Cell 2000;100:345–56.

Hori Y, Kikuchi A, Isomura M, Katayama M, Miura Y, Fujioka H, et al. Post-translational modifications of the C-terminal region of the rho protein are important for its interaction with membranes and the stimulatory and inhibitory GDP/GTP exchange proteins. Oncogene 1991;6: 515–22.

Jiang WG, Watkins G, Lane J, Cunnick GH, Douglas-Jones A, Mokbel K, et al. Prognostic value of rho GTPases and rho guanine nucleotide dissociation inhibitors in human breast cancers. Clin Cancer Res 2003;9: 6432–40.

Jones MB, Krutzsch H, Shu H, Zhao Y, Liotta LA, Kohn EC, et al. Proteomic analysis and identification of new biomarkers and therapeutic targets for invasive ovarian cancer. Proteomics 2002;2:76–84.

Lian LY, Barsukov I, Golovanov AP, Hawkins DI, Badii R, Sze KH, et al. Mapping the binding site for the GTP-binding protein Rac-1 on its inhibitor RhoGDI-1. Structure Fold Des 2000;8:47–55.

Michaelson D, Silletti J, Murphy G, D'Eustachio P, Rush M, Philips MR. Differential localization of Rho GTPases in live cells: regulation by hypervariable regions and RhoGDI binding. J Cell Biol 2001;152:111–26.

Moissoglu K, Slepchenko BM, Meller N, Horwitz AF, Schwartz MA. In vivo dynamics of Rac-membrane interactions. Mol Biol Cell 2006;17: 2770–9.

Nomanbhoy TK, Erickson JW, Cerione RA. Kinetics of Cdc42 membrane extraction by Rho-GDI monitored by real-time fluorescence resonance energy transfer. Biochemistry 1999;38:1744–50.

O'Sullivan AJ, Brown AM, Freeman HN, Gomperts BD. Purification and identification of FOAD-II, a cytosolic protein that regulates secretion in streptolysin-O permeabilized mast cells, as a rac/rhoGDI complex. Mol Biol Cell 1996;7:397–408.

Ota T, Maeda M, Suto S, Tatsuka M. LyGDI functions in cancer metastasis by anchoring Rho proteins to the cell membrane. Mol Carcinog 2004; 39:206–20.

Regazzi R, Kikuchi A, Takai Y, Wollheim CB. The small GTP-binding proteins in the cytosol of insulin-secreting cells are complexed to GDP dissociation inhibitor proteins. J Biol Chem 1992;267:17512–9.

Sasaki T, Kato M, Takai Y. Consequences of weak interaction of rho GDI with the GTP-bound forms of rho p21 and rac p21. J Biol Chem 1993;268: 23959–63.

Seraj MJ, Harding MA, Gildea JJ, Welch DR, Theodorescu D. The relationship of BRMS1 and RhoGDI2 gene expression to metastatic potential in lineage related human bladder cancer cell lines. Clin Exp Metastasis 2000;18:519–25.

Sun J, Barbieri JT. ExoS Rho GTPase-activating protein activity stimulates reorganization of the actin cytoskeleton through Rho GTPase guanine nucleotide disassociation inhibitor. J Biol Chem 2004;279:42936–44.

Tapper J, Kettunen E, El-Rifai W, Seppala M, Andersson LC, Knuutila S. Changes in gene expression during progression of ovarian carcinoma. Cancer Genet Cytogenet 2001;128:1–6.

Tatsuka M, Ota T, Yamagishi N, Kashihara Y, Wada M, Matsuda N, et al. Different metastatic potentials of ras- and src-transformed BALB/c 3T3 A31 variant cells. Mol Carcinog 1996;15:300–8.

Tatsuka M, Ota T, Maeda M, Wada M, Yamagishi N, Taniguchi S, et al. A BALB/c 3T3-transformed cell line suitable for transfection assay of metastasis-inducing genes. Int J Cancer 1997;71:88–93.

Thapar R, Karnoub AE, Campbell SL. Structural and biophysical insights into the role of the insert region in Rac1 function. Biochemistry 2002;41: 3875–83.

Tolias KF, Couvillon AD, Cantley LC, Carpenter CL. Characterization of a Rac1- and RhoGDI-associated lipid kinase signaling complex. Mol Cell Biol 1998;18:762–70.

Wennerberg K, Der CJ. Rho-family GTPases: it's not only Rac and Rho (and I like it). J Cell Sci 2004;117:1301–12.

Yanagawa T, Watanabe H, Takeuchi T, Fujimoto S, Kurihara H, Takagishi K. Overexpression of autocrine motility factor in metastatic tumor cells: possible association with augmented expression of KIF3A and GDI-beta. Lab Invest 2004;84:513–22.

Microvessel Density: Correlation with ^{18}F-FDG Uptake and Prognostic Impact in Lung Adenocarcinomas

JianFei Guo, MD[1,2]; Kotaro Higashi, MD[1]; Yoshimichi Ueda, MD[3]; Manabu Oguchi, MD[1]; Tsutomu Takegami, MD[4]; Hirohisa Toga, MD[5]; Tsutomu Sakuma, MD[6]; Hajime Yokota, MD[1]; Shogo Katsuda, MD[3]; Hisao Tonami, MD[1]; and Itaru Yamamoto, MD[1]

[1]Department of Radiology, Kanazawa Medical University, Ishikawa, Japan; [2]Department of Radiology, First Affiliated Hospital, China Medical University, Shenyang, People's Republic of China; [3]Department of Pathology, Kanazawa Medical University, Ishikawa, Japan; [4]Department of Medical Research Institute, Kanazawa Medical University, Ishikawa, Japan; [5]Division of Respiratory Disease, Department of Internal Medicine, Kanazawa Medical University, Ishikawa, Japan; and [6]Department of Thoracic Surgery, Kanazawa Medical University, Ishikawa, Japan

Although researched for many years, the prognostic value of tumor angiogenesis reflected by microvessel density (MVD) is still controversial, and there have been no previous reports regarding the correlation with ^{18}F-FDG uptake in lung adenocarcinomas. Therefore, in the present study, we investigated the correlation between MVD determined with different endothelial cell antibodies and ^{18}F-FDG uptake and compared the prognostic impact of those factors in lung adenocarcinomas. **Methods:** Forty-four patients with 45 lung adenocarcinomas underwent ^{18}F-FDG PET before surgery. Consecutive paraffin-embedded sections obtained from each resected tumor were immunostained for CD31 (a panendothelial cell marker), CD105 (a proliferation-related endothelial cell marker), and CD34/α-SMA (for double labeling of endothelial cells and mural cells). Four high-power fields in the area with the highest MVD were selected for analysis. Computer-assisted image analysis was used to assess MVD. **Results:** MVD staining results for panendothelial cell markers can be classified into 3 microvessel patterns: diffuse, alveolar, and mixed. The highly ordered alveolar pattern is believed to represent preexisting alveolar vessels trapped in lung adenocarcinomas and may have no significant meaning for the aggressiveness of tumors. Preexisting alveolar cells also do not contribute to ^{18}F-FDG uptake. CD105 staining of MVD (CD105-MVD) showed a significantly positive correlation with ^{18}F-FDG uptake ($P < 0.0001$), whereas CD31 staining of MVD (CD31-MVD) showed a marginally negative correlation with it ($P = 0.057$). Although CD105-MVD correlated negatively with prognosis, patients with low CD105-MVD, compared with those with high or moderate CD105-MVD, had a much better prognosis in both disease-free and overall survival analyses ($P = 0.017$ and $P = 0.013$, respectively). Patients with low CD31-MVD had the worst prognosis ($P = 0.032$ for disease-free survival analysis and $P = 0.179$ for overall survival analysis). **Conclusion:** There is no positive correlation between ^{18}F-FDG uptake and MVD determined with panendothelial cell markers (CD31 and CD34); in contrast, there is a marginally negative correlation between them. MVD determined with CD105, which is a proliferation-related endothelial cell marker, reflects active angiogenesis, correlates positively with ^{18}F-FDG uptake, and is a better indicator of prognosis in lung adenocarcinomas.

Key Words: PET; ^{18}F-FDG; lung cancer; microvessel density; prognosis

J Nucl Med 2006; 47:419–425

Lung cancer is the leading reason for cancer-related deaths in Japan and most Western countries. Surgery is the main method of therapy and also can be combined with radiotherapy and chemotherapy. However, the mortality of lung cancer is still very high; the 5-y survival expectation is only 70%–80%, even in the very early stages (*1,2*). Adenocarcinoma is the most common histologic type of lung cancer and accounts, to a great extent, for the increasing incidence of lung cancer in recent years (*3*). The established prognostic criteria for patients with non–small cell lung carcinoma (NSCLC), such as pathologic stage, can serve as a good indicator of a patient's outcome; however, this staging system does not determine accurately an individual patient's prognosis. Therefore, there is an urgent need to identify and validate new molecular markers and imaging techniques to better identify patients at risk for recurrent disease and metastatic disease, so that patients who might benefit from adjuvant therapy after surgery can be selected.

Tumor angiogenesis is an essential requirement for the development, progression, and metastasis of malignant tumors (*4*). Immunohistochemical staining measurements of angiogenesis with antibodies to factor VIII, CD31, CD34, or CD105 can be used to determine microvessel density (MVD), an important prognostic factor that is independent of other known prognostic variables in several

Received Aug. 16, 2005; revision accepted Nov. 30, 2005.

For correspondence or reprints contact: Kotaro Higashi, MD, Department of Radiology, Kanazawa Medical University, 1-1, Daigaku, Uchinada, Kahoku-gun, Ishikawa 920-0293, Japan.

E-mail: h550208@kanazawa-med.ac.jp

cancer types (*5*), including lung cancer (*6–12*). However, whereas some reports have found that MVD is an important prognostic factor in lung cancer (*6,7,10,12*), some reports have failed to do so (*8,9,11*). Therefore, although MVD estimation has promising prognostic prospects, a consensus as to whether MVD is a prognostic marker in lung cancer has yet to be reached.

^{18}F-FDG PET has been applied in many kinds of tumors and is regarded as a good imaging technique for predicting prognosis in some tumors (*13,14*), especially lung cancer (*15–19*). In previous studies, it was demonstrated that ^{18}F-FDG uptake is a significant prognostic factor in patients with NSCLC or adenocarcinoma (*16,19*)—and is even better than pathologic stage (*16*). Furthermore, some studies showed that there is a significant correlation between ^{18}F-FDG uptake and blood flow in breast cancer (*20*). However, although tumor angiogenesis showed a correlation with blood flow, the 2 factors are still quite different from each other. To date, there has been no report regarding the correlation between MVD and ^{18}F-FDG uptake in lung adenocarcinoma. Therefore, in the present study, we investigated not only whether tumor angiogenesis reflected by MVD determined with CD31 or CD105 is a good prognostic factor but also whether there is any correlation between MVD and ^{18}F-FDG uptake in patients with lung adenocarcinoma.

MATERIALS AND METHODS

Patients

Forty-four patients (20 men and 24 women; age range, 47–82 y; mean age, 65 y) with 45 lung adenocarcinomas were included in this study. Twelve patients had bronchioloalveolar carcinoma (BAC), 12 had well-differentiated adenocarcinoma, 14 had moderately differentiated adenocarcinoma, 5 had poorly differentiated adenocarcinoma, and 1 had 2 types of cancer (moderately differentiated adenocarcinoma and poorly differentiated adenocarcinoma). All patients underwent a thoracotomy within 4 wk after their ^{18}F-FDG PET study. No patient had received neoadjuvant chemotherapy or radiotherapy before surgery. Final diagnoses were established histologically (via the thoracotomy) in all patients, and the pathologic stage of each tumor was recorded with the TNM staging system. The sizes of the tumors were determined from the resected specimens and ranged in diameter from 1.2 to 5.5 cm. None of the patients had insulin-dependent diabetes, and the serum glucose levels in all patients just before ^{18}F-FDG injection were less than 120 mg/dL. Informed consent was obtained from all patients participating in this study.

^{18}F-FDG PET Imaging

^{18}F-FDG PET was performed by use of a PET camera (Headtome IV; Shimadzu) with a 10-cm axial field of view. The Headtome IV has 4 detector rings with 768 bismuth germanate crystals per ring. It uses direct and cross-plane coincidence detection to generate 14 slices per bed position. For the thorax, 2 bed positions (28 slices at 6.5-mm intervals) were obtained. Reconstruction in a 128 × 128 matrix with a Hann filter (0.5 cutoff) yielded 5-mm intrinsic resolution at the center. Transmission scans were obtained in all subjects before ^{18}F-FDG administration for attenuation correction with a ^{68}Ge ring source. x-Ray fluoroscopy was used to ascertain the location of the pulmonary nodule, and marks were made on the skin to aid in positioning the patient for the transmission scan. A transmission scan was acquired for 10–20 min in each bed position, depending on the specific radioactivity of the ring sources at the time of the study, for at least 2 million counts per slice. During the transmission scan, marks were made on the patient's skin to aid in repositioning for the emission scan. However, because of the limitation of the available equipment, we could not perform respiratory gating to avoid respiratory motion, which may affect the standardized uptake value (SUV) to some degree. Blood (1 mL) was drawn for baseline blood glucose estimation, and the data were recorded. Immediately after the transmission scan, ^{18}F-FDG was administered intravenously. The average injected dose of ^{18}F-FDG was 185 MBq. After a 40-min uptake period, the patient was repositioned in the scanner. An emission scan was acquired for 10 min in each bed position; the process took a total of 20 min.

For semiquantitative analysis of ^{18}F-FDG uptake, regions of interest (ROIs) were manually defined on the transaxial tomograms that showed the highest uptake to be in the middle of the tumor. The ROIs placed on the lesions encompassed all pixels within lesions that had uptake values of greater than 90% the maximum uptake in that slice, and the average count rate in each ROI was calculated. In patients in whom no nodules were detectable by PET, the ROIs were extrapolated from chest CT scans. After correction for radioactive decay, we analyzed the ROIs by computing the SUVs as follows: PET counts per pixel per second times calibration factor per injected dose (MBq) per kilogram of body weight, where the calibration factor was (MBq/mL)/(counts/pixel/s).

Immunohistochemical Analysis

Immunohistochemical Analysis with a Panendothelial Cell Marker. Monoclonal antibody (mAb) JC70 (Dako), recognizing panendothelial cell antigen CD31 (platelet/endothelial cell adhesion molecule), was used for microvessel staining of 5-μm paraffin-embedded sections. Sections were dewaxed, rehydrated, and microwaved (3 times for 4 min each time) for antigen retrieval. Endogenous peroxidase activity was blocked by incubation in 0.3% hydrogen peroxide in methanol. Nonspecific protein binding was inhibited by treatment with 10% normal serum for 10 min at 37°C. The specimens then were incubated with mAb JC70 overnight at 4°C. The slides were preincubated and rinsed in phosphate-buffered saline and then treated with the biotinylated secondary antibody and peroxidase-conjugated streptavidin. The final reaction product was revealed by exposure to 0.03% diaminobenzidine, and the nuclei were counterstained with Mayer hematoxylin. As a negative control, appropriately diluted nonimmune sera were applied instead of the primary antibody.

Immunohistochemical Analysis with a Proliferation-Related Endothelial Cell Marker. CD105 was stained with mAb SN6 h (1:100; Dako) (*21*) by use of a sensitive immunohistochemical staining system (CSA System; Dako). All of the procedures were performed in accordance with the manufacturer's protocol. Sections were incubated with the anti-CD105 mAb diluted 1:100 for 1 h at room temperature. Normal mouse IgG was used instead of the primary antibody as a negative control.

Double-Labeling Immunohistochemical Technique for CD34 and α-SMA. A double-labeling immunohistochemical technique with a specific double-labeling kit (Envision+ System; Dako) was

used to simultaneously stain endothelial cells (CD34) and mural cells (α-SMA) (*22*) to quantitatively assess the pericyte coverage of microvessels. Peroxidase activity was blocked in deparaffinized and rehydrated tissue sections, and the sections were trypsinized, incubated with blocking serum, and then doubly stained for CD34 to label endothelial cells and for α-SMA to detect pericytes and smooth muscle cell expression. For CD34 staining, sections were incubated with a mouse mAb (clone BI-3C5, 1:50 dilution; Zymed) overnight at 4°C. A biotinylated secondary antibody, streptavidin–alkaline phosphatase complex, and diaminobenzidine as a substrate were used to visualize binding of the CD34 antibody. For subsequent staining of α-SMA, sections were incubated with a mouse anti–human α-SMA mAb (clone 1A4, 1:50 dilution; Sigma) for 2 h at room temperature. The color was developed by 20 min of incubation with new fuchsin solution.

Assessment of MVD

Assessment of MVD was performed by computer-assisted image analysis as suggested previously but with some modifications (*23,24*). Vessels with a clearly defined lumen or well-defined linear vessel shape but not single endothelial cells were considered for microvessel assessment. The areas with the highest vascularization were scanned and chosen at low power (×100), and 4 chosen ×200 fields with the highest vascularization were recorded with a digital camera. The captured images were 24 bit and had a resolution of 2,272 × 1,704 pixels. Adobe Photoshop (version 6.0; Adobe Systems Inc.) was used to outline microvessels and convert the images into binary, black-and-white images; the converted images were imported into the image analysis package NIH image 1.62 (http://rsb.info.nih.gov/nih-image/) to calculate the percentage of stained microvessel area corresponding to the total section area. The average MVDs of the 4 selected areas were grouped into 3 grade categories. For CD31 staining of MVD (CD31-MVD), the categories were as follows: low, 0%–4%; moderate, 4%–8%; and high, >8%. For CD105 staining of MVD (CD105-MVD), the categories were as follows: low, 0%–0.8%; moderate, 0.8%–1.6%; and high, >1.6%.

Statistical Methods

All data are reported as the mean ± 1 SD. All statistical analyses were performed with SPSS for Windows (version 12.0; SPSS Inc.). The χ-square test was used to compare the distributions of values across categoric variables. Differences between continuous variables and dichotomous variables were tested by 1-way ANOVA. Overall and disease-free survival probabilities were calculated with the Kaplan–Meier life table method. Differences between survival probabilities were analyzed by the log-rank test. Probability values of less than 0.05 were considered statistically significant.

RESULTS

Vascular Architecture in Lung Adenocarcinomas

On the basis of the immunohistochemical staining results obtained with antibody against CD31, the vascular architecture in lung adenocarcinomas usually can be classified into 3 kinds of patterns: diffuse, alveolar, and mixed. The diffuse pattern is an angiogenic pattern. Normal lung architecture is replaced diffusely. Vessels and stroma are scattered randomly throughout the tumor (Fig. 1A). The alveolar pattern is a nonangiogenic pattern. Tumor cells fill up the alveoli, exploiting the existing alveolar vessels instead of destroying them (Fig. 1B). The mixed pattern consists of both diffuse and alveolar patterns.

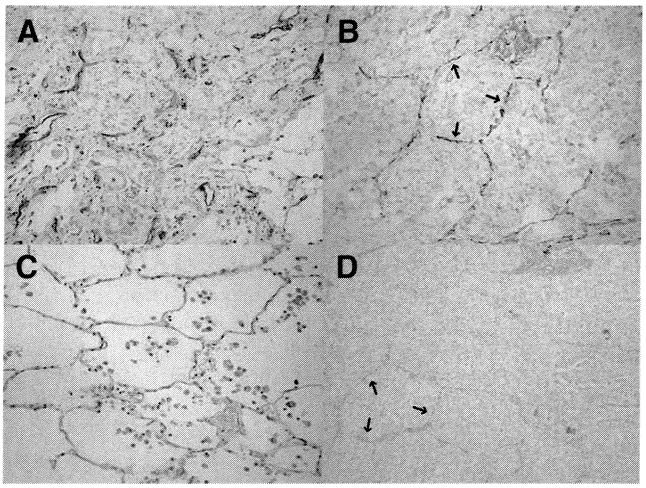

FIGURE 1. (A) Adenocarcinoma with diffuse pattern stained by mAb to CD31. Normal structure was destroyed, and vessels were randomly and diffusely distributed throughout tumor. (B) Adenocarcinoma with alveolar pattern stained by mAb to CD31. Vessels (arrows) in alveolar pattern area were in original distribution; tumor cells filled up alveoli instead of destroying them. (C) Normal alveoli. (D) Consecutive section of same tumor as in B stained by mAb to CD105. Trapped vessels showed negative staining (arrows).

Comparison Between CD34/α-SMA and CD105

For serial sections of lung adenocarcinomas, we compared immunohistochemical staining by mAbs against CD34 (Fig. 2A) and CD105 (Fig. 2B). For CD34 staining, we used a double-labeling technique, staining CD34-positive vessels and vascular pericytes simultaneously. Because the mAb against α-SMA is targeted specifically to pericytes and smooth muscle cells (*22*), vessels with α-SMA expression are mature vessels, and vessels without α-SMA expression are newly formed immature vessels. The total vessel number is usually much higher with CD34 staining and lower with CD105 staining in the same sample; however, as shown in Figure 2, CD34 staining was seen for both mature and immature vessels, whereas CD105 staining was seen mainly for immature vessels. Staining by a mAb against CD31 showed results similar to those for CD34; both mature and immature vessels were stained in the tumors.

Correlation Between MVD and Clinicopathologic Parameters

Table 1 shows the results of a comparison of CD31-MVD and CD105-MVD with clinicopathologic parameters. CD31-MVD showed a correlation with patient age (P = 0.042), sex (P = 0.049), and histologic findings (P = 0.017), whereas CD105-MVD showed a correlation with stage (P = 0.004), tumor size (P = 0.031), and histologic findings (P = 0.007). Our data showed that solitary BAC, a

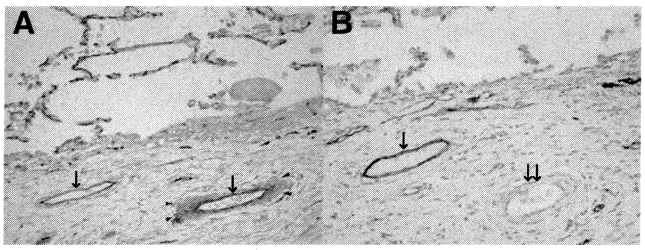

FIGURE 2. Comparison between CD34/α-SMA double labeling and CD105 in serial sections. (A) Double labeling of CD34 (arrow) and α-SMA (arrowheads). Left vessel was immature vessel showing staining only with CD34. Right vessel was mature vessel showing staining with both CD34 and α-SMA. (B) CD105 staining. Only left, immature vessel was positive for CD105 (arrow). Right, mature vessel was negative for CD105 (double arrows).

subcategory of lung adenocarcinoma with a good prognosis and an MVD that is different from those of other types of adenocarcinoma, had moderate or high CD31-MVD and CD34-MVD but low CD105-MVD.

Correlation Between MVD and ^{18}F-FDG Uptake

Figure 3 shows the correlation of CD31-MVD and CD105-MVD with ^{18}F-FDG uptake. ^{18}F-FDG uptake showed a marginally negative correlation with CD31-MVD ($P = 0.057$), whereas it showed a significantly positive correlation with CD105-MVD ($P < 0.0001$).

Correlation Between MVD and Postoperative Prognosis

Using the Kaplan–Meier method, we analyzed the prognostic impact of CD31-MVD and CD105-MVD in lung adenocarcinomas (Fig. 4). Patients with moderate CD31-MVD had the best disease-free and overall survival probabilities, and patients with low CD31-MVD had the worst prognosis ($P = 0.032$ for disease-free survival analysis and $P = 0.179$ for overall analysis). CD105-MVD correlated negatively with prognosis; patients with low CD105-MVD had the best disease-free and overall survival probabilities ($P = 0.017$ and $P = 0.013$, respectively).

Figures 5 and 6 show 2 representative cases in this study.

DISCUSSION

The present study demonstrated that there is no positive correlation between ^{18}F-FDG uptake and MVD determined with panendothelial cell markers (CD31 and CD34); in contrast, there is a marginally negative correlation between them. Furthermore, MVD determined with CD105, which is a proliferation-related endothelial cell marker, reflects active angiogenesis, correlates positively with ^{18}F-FDG uptake, and is a better indicator of prognosis in lung adenocarcinomas.

Angiogenesis is essential for neoplastic proliferation, progression, invasion, and metastasis because solid tumors cannot grow beyond 1–2 mm in diameter without angiogenesis (*25*). MVD is assumed to reflect the intensity of tumor angiogenesis; indeed, it has been established as a good indicator of prognosis in several cancer types (*5*). However, conflicting results on the prognostic impact of MVD in lung cancer make it difficult to determine the prognostic importance of tumor angiogenesis in lung cancer (*6–12*). Variations in survival results among studies could be explained by the heterogeneity in methodologies used to stain and count microvessels in tumors in addition to variations in patient populations. Differences in reactivity between anti–endothelial cell antibodies used to highlight intratumoral microvessels represent a major bias that should be considered. Although antibodies to CD31 and

TABLE 1
Relationship of Clinicopathologic Parameters to MVD

Parameter	CD31-MVD*			*P*	CD105-MVD*			*P*
	Low	Moderate	High		Low	Moderate	High	
Age				0.042				0.254
≤65	10	9	3		11	5	6	
>65	4	9	10		6	8	9	
Sex				0.049				0.376
Male	10	5	6		6	6	9	
Female	4	13	7		11	7	6	
Stage				0.223				0.004
I	11	13	7		16	9	6	
II, III	3	2	5		0	3	7	
Size				0.234				0.031
≤3 cm	8	14	11		16	9	8	
>3 cm	6	4	2		1	4	7	
Histologic findings				0.017				0.007
BAC	0	8	4		9	2	1	
Non-BAC	14	10	9		8	11	14	

*Data are reported as number of tumors.
Non-BAC = well-differentiated adenocarcinoma, moderately differentiated adenocarcinoma, and poorly differentiated adenocarcinoma.

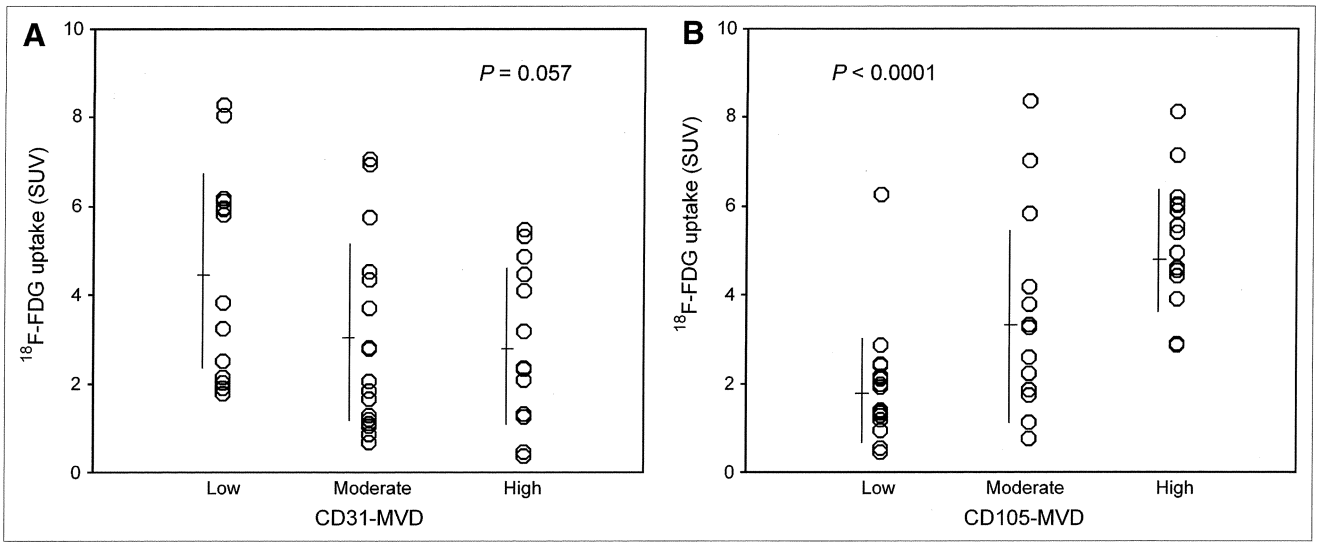

FIGURE 3. (A) CD31-MVD showed negative correlation with ^{18}F-FDG uptake ($P = 0.057$). (B) CD105-MVD showed significantly positive correlation with ^{18}F-FDG uptake ($P < 0.0001$).

CD34 are recommended as standard antibodies for assessing MVD in solid tumors (*26,27*), the variations among studies with these antibodies imply their limitations in lung cancer.

Endothelium in healthy adults is considered quiescent because the turnover of endothelial cells is very low (*28*). However, endothelial cells of tumor-associated neovasculature proliferate 20–2,000 times more rapidly than do endothelial cells of normal tissues (*29*). CD105 (endoglin) is a homodimeric cell membrane glycoprotein expressed on endothelial cells and is thought to be a proliferation-associated marker of endothelial cells (*30,31*). In fact, a correlation has been found between levels of CD105 expression and markers of cell proliferation (i.e., cyclin A and Ki-67) in tumor endothelia (*32*), and some studies have indicated that a greater intensity of staining for CD105 is detectable in blood vessel endothelia within neoplastic tissues than in those within normal tissues (*31,33*). Consistent with these findings, CD105 has been shown to represent an ideal marker for quantifying tumor angiogenesis and to be an independent indicator of prognosis in some tumors (*34,35*), including lung cancer (*21*).

In the present study, by comparing staining results for CD105 and CD34/α-SMA in serial sections of lung adenocarcinomas, we found that CD105 was expressed specifically in immature vessels but not in mature vessels. In areas with an alveolar pattern, we could see clearly the difference between CD31 expression and CD105 expression. The trapped vessels were in the same distribution as in normal alveoli; however, these kinds of vessels were CD31 positive but CD105 negative. Taken together, these findings indicated the following. First, there may be a different mechanism of tumor angiogenesis in lung adenocarcinomas—involving tumor cells filling the alveolar spaces and entrapping, but not destroying, the alveolar septa and co-opting the preexisting blood vessels. Second, because of the presence of the alveolar pattern, comparing the proliferation-related endothelial cell marker CD105 with panendothelial cell markers, such as factor VIII, CD31, and CD34, may not reflect exactly the tumor-associated neovasculature; this may be one of the explanations for the conflicting results regarding MVD studies in lung cancer. Third, although there is a marginally significant correlation between CD31-MVD and prognosis, CD105-MVD has a much more significant prognostic impact than does CD31-MVD; therefore, CD105-MVD is a much better indicator of prognosis in lung adenocarcinomas.

Furthermore, we also found that BAC usually has moderate or high CD31-MVD and CD34-MVD but low CD105-MVD. BAC, as a subcategory of lung adenocarcinoma, has a fairly good prognosis for surgically treated patients. The key pathologic feature of BAC is preservation of the underlying architecture of the lung, with cylindric tumor cells growing on the walls of preexisting alveoli. Therefore, because CD31 and CD34 staining was seen for both mature and immature vessels, it is reasonable to assume that the moderate or high CD31-MVD and CD34-MVD involved mainly preexisting vessels; serial sections stained with CD105 further proved that those vessels were negative for CD105. Although the pathophysiologic impact of preexisting vessels for tumor progression is still unclear, it seems that these kinds of vessels make no contribution to ^{18}F-FDG uptake in lung adenocarcinomas, because most solitary BACs are almost negative in ^{18}F-FDG PET (*36*), even though these BACs have moderate or high CD31-MVD and CD34-MVD.

Regarding the correlation between ^{18}F-FDG uptake and MVD in NSCLC, only 1 previous study mentioned a positive correlation between ^{18}F-FDG uptake and CD34-MVD (*37*). The present study is the first research concentrating

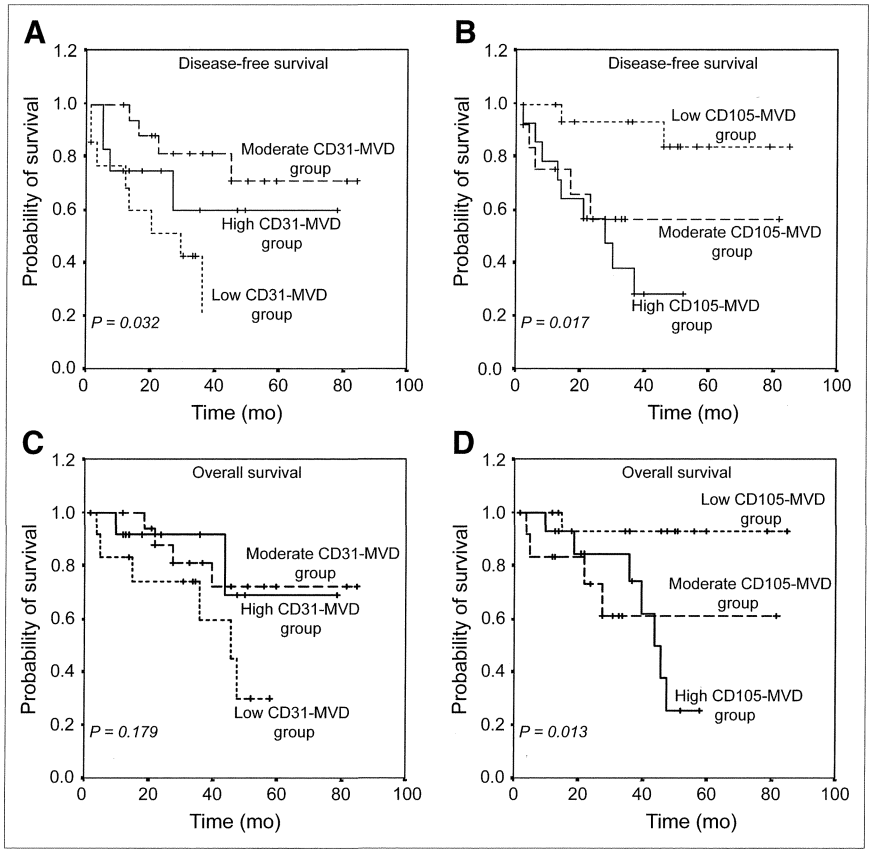

FIGURE 4. Kaplan–Meier survival curves based on MVDs in lung adenocarcinomas. Patients with low CD31-MVD had worst disease-free and overall survival probabilities (A and C), whereas patients with low CD105-MVD had best disease-free and overall survival probabilities (B and D).

on the correlation in lung adenocarcinomas. In contrast to that previous study, our findings suggested that ^{18}F-FDG uptake shows a marginally negative correlation with CD31-MVD but a significantly positive correlation with CD105-MVD. However, the underlying mechanism of this difference is still unclear, and further study is warranted. Although the prognostic impact of MVD in NSCLC is complicated and further study is needed, a new treatment for malignant tumors (antiangiogenic therapy) recently provided new hope for cancer therapy (*38*). Therefore, there is

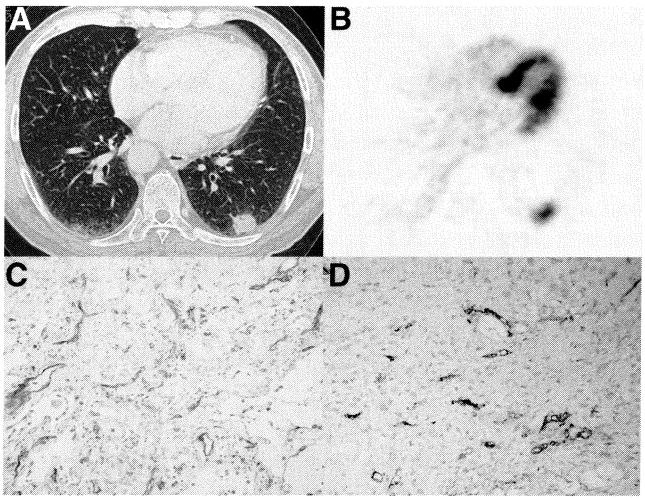

FIGURE 5. Moderately differentiated adenocarcinoma (2.9 cm) with recurrence in 23 mo. (A) CT scan shows nodule in left lung. (B) ^{18}F-FDG PET shows intense uptake of ^{18}F-FDG in tumor (SUV = 5.76). (C) CD31 immunohistochemical analysis shows high MVD. (D) CD105 immunohistochemical analysis also shows high MVD.

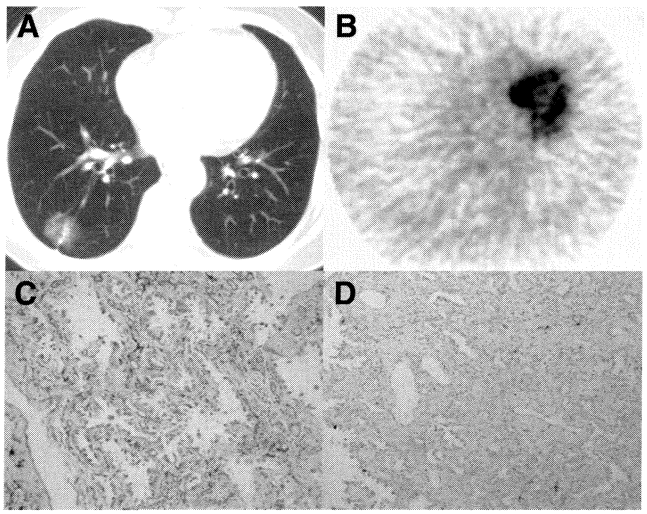

FIGURE 6. BAC (2.0 cm) without recurrence in 50 mo. (A) CT scan shows nodule in right lung. (B) ^{18}F-FDG PET shows modest uptake of ^{18}F-FDG in tumor (SUV = 1.32). (C) CD31 immunohistochemical analysis shows moderate MVD. (D) CD105 immunohistochemical analysis shows low MVD.

an urgent need for assessing pretreatment angiogenic status and evaluating the response to this therapy in clinical studies. In the present study, we found that ^{18}F-FDG uptake not only can reflect the angiogenic status in lung adenocarcinomas but also, and more importantly, can reflect active angiogenesis in lung adenocarcinomas. These properties may have further applications in assessing and monitoring antiangiogenic therapy in the near future.

CONCLUSION

In contrast to CD31-MVD, CD105-MVD reflects active tumor angiogenesis and is a better indicator of prognosis in patients with lung adenocarcinomas. ^{18}F-FDG uptake correlated significantly with the active angiogenesis determined by CD105-MVD. This property may have applications in assessing and monitoring antiangiogenic therapy.

ACKNOWLEDGMENTS

This work was supported by a Grant of Collaborative Research from Kanazawa Medical University (C2005-2), by a Grant-in-Aid for Cancer Research (16-5) from the Ministry of Health and Welfare, Japan, and by Grants-in-Aid (16591232 and 17590320) for Scientific Research from the Ministry of Education, Japan.

REFERENCES

1. Kurokawa T, Matsuno Y, Noguchi M, Mizuno S, Shimosato Y. Surgically curable "early" adenocarcinoma in the periphery of the lung. *Am J Surg Pathol.* 1994;18:431–438.
2. Takise A, Kodama T, Shimosato Y, Watanabe S, Suemasu K. Histopathologic prognostic factors in adenocarcinomas of the peripheral lung less than 2 cm in diameter. *Cancer.* 1988;61:2083–2088.
3. Charloux A, Quoix E, Wolkove N, Small D, Pauli G, Kreisman H. The increasing incidence of lung adenocarcinoma: reality or artefact? A review of the epidemiology of lung adenocarcinoma. *Int J Epidemiol.* 1997;26:14–23.
4. Hanahan D, Folkman J. Patterns and emerging mechanisms of the angiogenic switch during tumorigenesis. *Cell.* 1996;86:353–364.
5. Weidner N. Tumoural vascularity as a prognostic factor in cancer patients: the evidence continues to grow. *J Pathol.* 1998;184:119–122.
6. Giatromanolaki A, Koukourakis MI, Theodossiou D, et al. Comparative evaluation of angiogenesis assessment with anti-factor-VIII and anti-CD31 immunostaining in non-small cell lung cancer. *Clin Cancer Res.* 1997;3:2485–2492.
7. Fontanini G, Lucchi M, Vignati S, et al. Angiogenesis as a prognostic indicator of survival in non-small-cell lung carcinoma: a prospective study. *J Natl Cancer Inst.* 1997;89:881–886.
8. Pastorino U, Andreola S, Tagliabue E, et al. Immunocytochemical markers in stage I lung cancer: relevance to prognosis. *J Clin Oncol.* 1997;15:2858–2865.
9. Chandrachud LM, Pendleton N, Chisholm DM, Horan MA, Schor AM. Relationship between vascularity, age and survival in non-small-cell lung cancer. *Br J Cancer.* 1997;76:1367–1375.
10. O'Byrne KJ, Koukourakis MI, Giatromanolaki A, et al. Vascular endothelial growth factor, platelet-derived endothelial cell growth factor and angiogenesis in non-small-cell lung cancer. *Br J Cancer.* 2000;82:1427–1432.
11. Liao M, Wang H, Lin Z, Feng J, Zhu D. Vascular endothelial growth factor and other biological predictors related to the postoperative survival rate on non-small cell lung cancer. *Lung Cancer.* 2001;33:125–132.
12. Cox G, Jones JL, Andi A, Waller DA, O'Byrne KJ. A biological staging model for operable non-small cell lung cancer. *Thorax.* 2001;56:561–566.
13. Miller TR, Pinkus E, Dehdashti F, Grigsby PW. Improved prognostic value of ^{18}F-FDG PET using a simple visual analysis of tumor characteristics in patients with cervical cancer. *J Nucl Med.* 2003;44:192–197.
14. Franzius C, Bielack S, Flege S, Sciuk J, Jurgens H, Schober O. Prognostic significance of ^{18}F-FDG and ^{99m}Tc-methylene diphosphonate uptake in primary osteosarcoma. *J Nucl Med.* 2002;43:1012–1017.
15. Pandit N, Gonen M, Krug L, Larson SM. Prognostic value of [^{18}F]FDG-PET imaging in small cell lung cancer. *Eur J Nucl Med Mol Imaging.* 2003;30:78–84.
16. Higashi K, Ueda Y, Arisaka Y, et al. ^{18}F-FDG uptake as a biologic prognostic factor for recurrence in patients with surgically resected non–small cell lung cancer. *J Nucl Med.* 2002;43:39–45.
17. Hicks RJ, Kalff V, MacManus MP, et al. ^{18}F-FDG PET provides high-impact and powerful prognostic stratification in staging newly diagnosed non–small cell lung cancer. *J Nucl Med.* 2001;42:1596–1604.
18. Dhital K, Saunders CA, Seed PT, O'Doherty MJ, Dussek J. [(18)F]Fluorodeoxyglucose positron emission tomography and its prognostic value in lung cancer. *Eur J Cardiothorac Surg.* 2000;18:425–428.
19. Guo J, Higashi K, Yokota H, et al. In vitro proton magnetic resonance spectroscopic lactate and choline measurements, ^{18}F-FDG uptake, and prognosis in patients with lung adenocarcinoma. *J Nucl Med.* 2004;45:1334–1339.
20. Zasadny KR, Tatsumi M, Wahl RL. FDG metabolism and uptake versus blood flow in women with untreated primary breast cancers. *Eur J Nucl Med Mol Imaging.* 2003;30:274–280.
21. Tanaka F, Otake Y, Yanagihara K, et al. Evaluation of angiogenesis in non-small cell lung cancer: comparison between anti-CD34 antibody and anti-CD105 antibody. *Clin Cancer Res.* 2001;7:3410–3415.
22. Eberhard A, Kahlert S, Goede V, Hemmerlein B, Plate KH, Augustin HG. Heterogeneity of angiogenesis and blood vessel maturation in human tumors: implications for antiangiogenic tumor therapies. *Cancer Res.* 2000;60:1388–1393.
23. King TW, Brey EM, Youssef AA, Johnston C, Patrick CW Jr. Quantification of vascular density using a semiautomated technique for immunostained specimens. *Anal Quant Cytol Histol.* 2002;24:39–48.
24. Lee JS, Jung JJ, Kim J. Quantification of angiogenesis by a computerized image analysis system in renal cell carcinoma. *Anal Quant Cytol Histol.* 2000;22:469–474.
25. Weidner N, Semple JP, Welch WR, Folkman J. Tumor angiogenesis and metastasis: correlation in invasive breast carcinoma. *N Engl J Med.* 1991;324:1–8.
26. Vermeulen PB, Gasparini G, Fox SB, et al. Quantification of angiogenesis in solid human tumours: an international consensus on the methodology and criteria of evaluation. *Eur J Cancer.* 1996;32A:2474–2484.
27. Vermeulen PB, Gasparini G, Fox SB, et al. Second international consensus on the methodology and criteria of evaluation of angiogenesis quantification in solid human tumours. *Eur J Cancer.* 2002;38:1564–1579.
28. Risau W. Differentiation of endothelium. *FASEB J.* 1995;9:926–933.
29. Hobson B, Denekamp J. Endothelial proliferation in tumours and normal tissues: continuous labelling studies. *Br J Cancer.* 1984;49:405–413.
30. Kumar P, Wang JM, Bernabeu C. CD 105 and angiogenesis. *J Pathol.* 1996;178:363–366.
31. Burrows FJ, Derbyshire EJ, Tazzari PL, et al. Up-regulation of endoglin on vascular endothelial cells in human solid tumors: implications for diagnosis and therapy. *Clin Cancer Res.* 1995;1:1623–1634.
32. Miller DW, Graulich W, Karges B, et al. Elevated expression of endoglin, a component of the TGF-beta-receptor complex, correlates with proliferation of tumor endothelial cells. *Int J Cancer.* 1999;81:568–572.
33. Wang JM, Kumar S, Pye D, Haboubi N, al Nakib L. Breast carcinoma: comparative study of tumor vasculature using two endothelial cell markers. *J Natl Cancer Inst.* 1994;86:386–388.
34. Kumar S, Ghellal A, Li C, et al. Breast carcinoma: vascular density determined using CD105 antibody correlates with tumor prognosis. *Cancer Res.* 1999;59:856–861.
35. Wikstrom P, Lissbrant IF, Stattin P, Egevad L, Bergh A. Endoglin (CD105) is expressed on immature blood vessels and is a marker for survival in prostate cancer. *Prostate.* 2002;51:268–275.
36. Higashi K, Ueda Y, Seki H, et al. Fluorine-18-FDG PET imaging is negative in bronchioloalveolar lung carcinoma. *J Nucl Med.* 1998;39:1016–1020.
37. Tateishi U, Nishihara H, Tsukamoto E, Morikawa T, Tamaki N, Miyasaka K. Lung tumors evaluated with FDG-PET and dynamic CT: the relationship between vascular density and glucose metabolism. *J Comput Assist Tomogr.* 2002;26:185–190.
38. Yang JC, Haworth L, Sherry RM, et al. A randomized trial of bevacizumab, an anti-vascular endothelial growth factor antibody, for metastatic renal cancer. *N Engl J Med.* 2003;349:427–434.

Surg Today (2006) 36:230–234
DOI 10.1007/s00595-005-3123-3

SURGERY TODAY

Fluorodeoxyglucose Uptake Correlates with the Growth Pattern of Small Peripheral Pulmonary Adenocarcinoma

MOTOYASU SAGAWA[1], KOTARO HIGASHI[2], MAKOTO SUGITA[1], YOSHIMICHI UEDA[3], SUMIKO MAEDA[1], HIROHISA TOGA[4], and TSUTOMU SAKUMA[1]

Departments of [1]Thoracic Surgery, [2]Radiology, [3]Pathology II, and [4]Respiratory Medicine, Kanazawa Medical University, 1-1 Daigaku, Uchinada, Ishikawa 920-0293, Japan

Abstract

Purpose. Noguchi and colleagues reported that the growth pattern of small-sized adenocarcinoma was related to the vascular involvement and the prognosis of the patient. Noguchi's type A/B tumors had no lymph node metastasis, rare vascular involvement, and an excellent prognosis, which meant that Noguchi's type A/B tumors were preinvasive tumors of the peripheral type. Although Noguchi's classification was usually determined based on resected specimens, it would be useful to make a decision about the therapeutic strategy if the classification could be determined preoperatively based on the fluorodeoxyglucose (FDG) uptake.

Methods. The FDG uptake in 61 pulmonary adenocarcinomas measuring 3 cm or smaller in diameter was compared with the mediastinal uptake and was classified into five grades. The relationship between the FDG uptake and Noguchi's classification (A to F) was analyzed.

Results. The FDG uptake was significantly lower in Noguchi's type A/B tumors than in type C or in type D/E/F. Eleven of 12 tumors (92%) with no increased or a weak FDG uptake were classified as type A/B, whereas 32 of 33 tumors (97%) with a strong or very strong FDG uptake were classified as type C–F.

Conclusions. The FDG uptake is helpful for making an accurate diagnosis of Noguchi's classification preoperatively in patients with pulmonary adenocarcinoma.

Key words ^{18}F-Fluorodeoxyglucose positron emission tomography · Noguchi's classification · Adenocarcinoma · Lung cancer · Limited resection

Reprint requests to: M. Sagawa
Received: April 1, 2005 / Accepted: July 12, 2005

Introduction

Lung cancer is the leading cause of cancer death in Japan as well as in the United States. Recently, thoracic computed tomography (CT) screening for the detection of early lung cancer has been suggested as a possible tool to decrease lung cancer mortality.[1–3] Using CT screening, a number of small-sized pulmonary adenocarcinomas have thus been detected and treated, and several characteristics of small-sized adenocarcinomas have also been elucidated. Noguchi and colleagues introduced a novel classification where small-sized pulmonary adenocarcinomas were classified according to their growth pattern. Noguchi's classification was strongly related with vascular involvement and the prognosis of the patient.[4] In particular, Noguchi's type A/B tumors had characteristics with no lymph node metastasis, rare vascular involvement, and an excellent prognosis (5-year survival rate: 100%).[4] Although Noguchi's classification was usually determined with resected specimens, it would be useful to decide the therapeutic strategy if the classification could be determined preoperatively.

Positron emission tomography imaging with ^{18}F-fluorodeoxyglucose (FDG PET) provides physiologic and metabolic information of pulmonary nodules, which cannot be provided by morphological examinations such as CT.[5–7] To date, little is known concerning the relationship between the FDG uptake and Noguchi's classification in small-sized primary pulmonary adenocarcinomas, which we retrospectively analyzed in this study.

Patients and Methods

Positron emission tomography scanning was performed with a PET camera, Headtome IV (Shimazu, Kyoto, Japan) or Advance (GE Medical System, Milwaukee,

WI, USA). Until March 2003, FDG PET was performed in 110 patients with 118 primary lung cancers, which were surgically resected at our university. Of them, 61 lesions of adenocarcinoma which pathologically measured 3 cm or smaller in diameter were analyzed.

All of the patients studied fasted for 6 h before undergoing scanning. Blood (1 ml) was drawn for baseline blood glucose estimation, and the data were recorded. Fluorodeoxyglucose was administered intravenously. The average injection dose of FDG was 370 MBq. After a 40–50-min uptake period, an emission scan was acquired. Transmission scans were obtained in all subjects for attenuation correction. Fluorodeoxyglucose accumulation within the primary lung cancer on the attenuation- and decay-corrected images was graded independently. A 5-point visual grading system (a modified method of Vansteenkiste et al.[8]) was used to interpret the FDG uptake within the primary lesions without any pathological information: no increased uptake (similar to background), weak uptake (lower than mediastinum), medium uptake (similar to mediastinum), strong uptake (higher than mediastinum), very strong uptake (remarkably higher than mediastinum).

Histological typing was classified according to the World Health Organization classification[9] without any radiological information. The growth pattern of the tumors was classified according to Noguchi's classification[4]: A, localized bronchiolo-alveolar carcinoma (LBAC); B, LBAC with foci of collapse of alveolar structure; C, LBAC with foci of active fibroblastic proliferation; D, poorly differentiated adenocarcinoma; E, tubular adenocarcinoma; and F, papillary adenocarcinoma with compressive and destructive growth. Type A/B/C tumors show a growth pattern involving replacement of alveolar lining cells, whereas type D/E/F tumors are nonreplacement-type adenocarcinomas. A statistical analysis was performed using the Mann–Whitney *U*-test.

Table 1. Characteristics of the patients in this study

Factor	*n*
Sex	
Male	21
Female	35
Age	
59 and below	19
60–69	16
70–79	18
80 and above	3
Histology	
Bronchiolo-alveolar carcinoma	9
Well-differentiated adenocarcinoma	28
Moderately differentiated adenocarcinoma	21
Poorly differentiated adenocarcinoma	3
Noguchi's classification	
A	2
B	14
C	16
D	4
E	7
F	18
Maximum diameter	
10 mm or less	4
11–15 mm	10
16–20 mm	17
21–25 mm	14
26–30 mm	16
FDG uptake	
0	6
1	6
2	16
3	17
4	16

FDG, fluorodeoxyglucose

Results

Table 1 shows the characteristics of the 61 lesions of the 56 patients. Figure 1 shows FDG PET findings of representative cases. The FDG uptake of each tumor according to Noguchi's classification and the tumor size are shown in Fig. 2.

Fifty-five of all the 61 adenocarcinomas (90%) had a positive FDG uptake. According to the tumor size, all 16 adenocarcinomas measuring from 26 to 30 mm in diameter (100%), 12 of 14 tumors measuring from 21 to 25 mm in diameter (86%), all 17 tumors measuring from 16 to 20 mm in diameter (100%), and 10 of 14 tumors measuring from 1 to 15 min in diameter (71%) had a positive FDG uptake. In the adenocarcinomas measuring from 1 to 15 mm in diameter, 9 of 10 Noguchi's type C–F tumors had a positive FDG uptake (90%), whereas only 1 of 4 Noguchi's type A/B tumors had (25%).

Although 11 of 16 type A/B tumors (69%) had a positive FDG uptake, 10 of the 11 FDG-positive type A/B tumors had a medium FDG uptake or weaker. On the other hand, 15 of 16 type C tumors (94%) and 29 of 29 type D/E/F tumors (100%) had a positive FDG uptake, and all of the FDG-positive type C–F tumors had a medium FDG uptake or stronger. The FDG uptake was lower in Noguchi's type A/B tumors than in type C tumors ($P = 0.0002$) or in type D/E/F tumors ($P < 0.0001$). The FDG uptake in type C tumors was not statistically different from that in type D/E/F tumors ($P = 0.104$).

Table 2 shows the number of tumors according to Noguchi's classification and the FDG uptake. Eleven of 12 tumors with no FDG uptake or a weak one (92%) were classified as Noguchi's type A/B. On the other hand, 32 of 33 tumors with strong or very strong FDG uptake (97%) were classified as Noguchi's type C, D, E, or F.

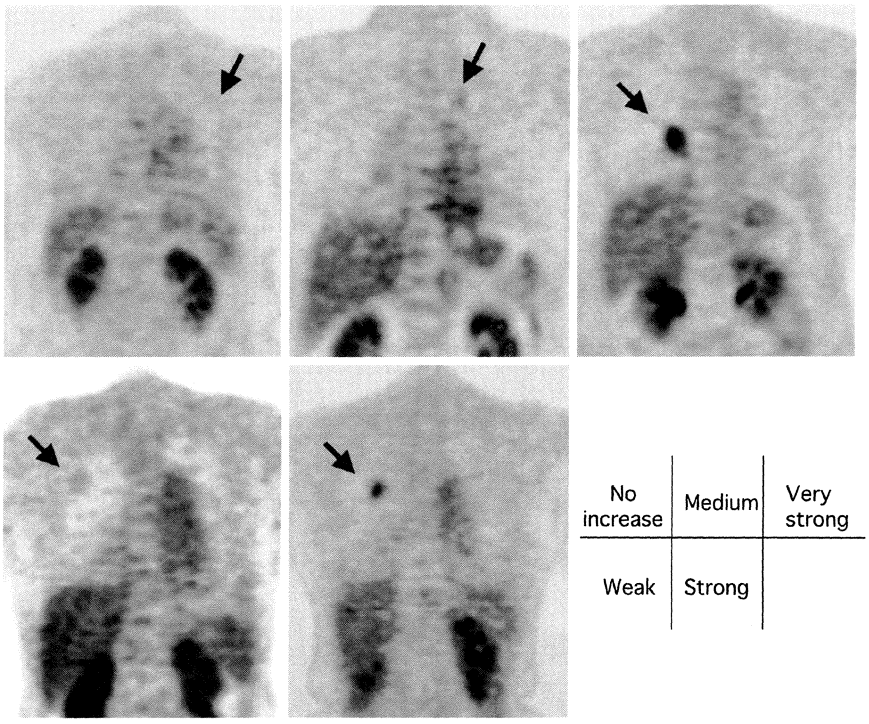

Fig. 1. ^{18}F-Fluorodeoxyglucose positron emission tomography findings in representative cases

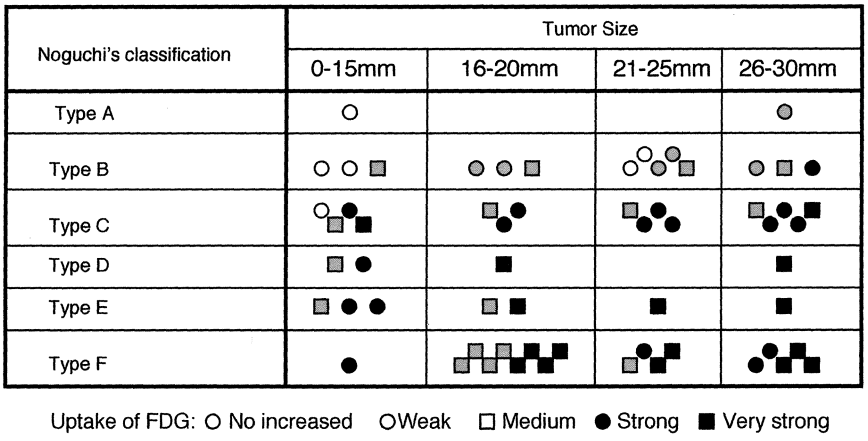

Fig. 2. Relationships among the fluorodeoxyglucose (*FDG*) uptake, Noguchi's classification, and the tumor size. Most of Noguchi's type A/B tumors had a medium FDG uptake or weaker, whereas most of Noguchi's type C–F had a medium FDG uptake or stronger, regardless of the size of the tumor

Table 2. Number of tumors according to Noguchi's classification and FDG uptake

FDG uptake	Noguchi's classification					
	A	B	C	D	E	F
No increased uptake	1	4	1	0	0	0
Weak uptake	1	5	0	0	0	0
Medium uptake	0	4	4	1	2	5
Strong uptake	0	1	9	1	2	4
Very strong uptake	0	0	2	2	3	9

Discussion

Recently a number of small pulmonary adenocarcinomas have been found due to advances in diagnostic radiology.[1–3] Noguchi et al. published a classification with which the aggressiveness of small adenocarcinomas was evaluated.[4] In this study, we examined the relationship between FDG uptake and Noguchi's classification with resected small-sized adenocarcinomas.

Our results showed that 90% of adenocarcinomas were FDG-positive even though the tumors measured

3 cm in size or smaller. According to the tumor size, 96% of the tumors measuring from 16 to 30 mm in diameter had a positive FDG uptake, whereas the sensitivity decreased to 71% in the tumors measuring 15 mm or smaller. However, 90% of type C–F tumors measuring 15 mm or smaller in diameter still had a positive FDG uptake. These results indicate that FDG PET is useful for detecting type C–F small adenocarcinomas. On the other hand, only 25% of type A/B tumors 15 mm or smaller in diameter were FDG-positive, thus indicating that FDG PET could not detect type A/B small adenocarcinoma.

A number of early adenocarcinomas detected by thoracic CT screening have raised a question as to whether a lobectomy would be indispensable for such kinds of tumor. A randomized trial concerning a limited resection for clinical T1N0M0 lung cancers revealed that a limited resection is not recommended for patients with clinical T1N0M0 diseases.[10] However, Noguchi's type A/B tumor is not the same as usual T1N0M0 lung cancer because it has rare nodal and vascular involvement,[4] and a limited resection might thus be sufficient for such a tumor.[11] Actually a clinical trial, where a wedge resection of the lung without nodal dissection would be performed instead of a lobectomy with systematic nodal dissection when the lung cancer was Noguchi's type A/B, is now being planned in Japan. Nevertheless, it is sometimes difficult to accurately differentiate type A/B from type C–F by transbronchial lung biopsy specimens or intraoperative frozen sections, which thus remains a great obstacle for conducting such a clinical trial.

Our results revealed that 92% of the pulmonary adenocarcinomas 3 cm or smaller in diameter with no increased or weak FDG uptake were Noguchi's type A/B tumors, and 97% of the pulmonary adenocarcinomas 3 cm or smaller in diagmeter with a strong or very strong FDG uptake were Noguchi's type C–F. Although the negative predictive values were not so high, the positive predictive values were considerably high. This means that FDG PET may therefore help us to make an accurate diagnosis of Noguchi's classification pre- and intraoperatively, and would also be useful for conducting a clinical trial where a wedge resection of the lung would be performed instead of a lobectomy for Noguchi's type A/B lung cancer.

In the present study there are some issues that remain to be discussed. First, a five-point visual grading system was used to interpret FDG uptake within the primary lesions, and the standard uptake value (SUV)threshold was not used. Vansteenkiste et al. reported that a visual scale was as accurate as the use of an SUV threshold for lymph nodes in the distinction between benign and malignant nodes.[8] The SUV is affected by many factors, including the partial volume effect, the method of drawing regions of interest, the period between FDG administration and the start of an emission scan, and whether the image is attenuation-corrected or nonattenuation-corrected.[12] Iterative reconstruction with segmented attenuation correction resulted in a significantly lower mean SUV and maximum SUV values compared to a filtered back-projection with measured attenuation correction.[13] Therefore, a visual scale was found to be more adequate than the SUV threshold in this study.

Second, the results of this study did not describe the sensitivity or positive predictive value of FDG PET to differentiate malignant tumors from benign tumors, which has already been reported by many investigators.[14–17] This study focused on the positive predictive value (probability) to differentiate Noguchi's type A/B from type C–F, which would be important for selecting appropriate candidates for a limited resection. Therefore, all of the patients in this study were lung cancer patients.

Third, this study did not focus on the negative predictive value or false-negative cases, such as type A/B tumors with a medium FDG uptake. The standard surgical procedure for lung cancer is a pulmonary lobectomy with a systematic nodal dissection, because a randomized trial revealed that the patients with clinical T1N0M0 lung cancer who underwent a limited resection had a significantly worse prognosis than those who underwent a pulmonary lobectomy.[10] At present, the important strategy in selecting candidates for a limited resection should be not to reduce the number of false-negative cases, but to reduce the number of false-positive cases. Therefore, this study focused on the positive predictive value to differentiate type A/B from type C–E.

Although the number of cases in this study was limited, the results were informative. FDG PET is useful for detecting Noguchi's type C–F small adenocarcinomas, but not type A/B small adenocarcinomas. FDG PET may be helpful for achieving an accurate diagnosis of Noguchi's classification, thus enabling us to conduct a clinical trail where a wedge resection would be performed instead of a lobectomy for selected lung cancer patients. Further studies will be required to clarify whether a limited resection is actually beneficial for such patients.

Acknowledgments. This study was supported in part by Grants for Collaborative Research from Kanazawa Medical University (C2003-2, C2004-2, C2005-2), Grant-in-Aid from Kurokawa Research Foundation (2005), and Grant-in-Aid for Scientific Research No. 16591419.

References

1. Henschke CI. Early lung cancer action project: overall design and findings from baseline screening. Cancer 2000;89:2474–82.

2. Sone S, Li F, Yang ZG, Honda T, Maruyama Y, Takashima S, et al. Results of three-year mass screening programme for lung cancer using mobile low-dose spiral computed tomography scanner. Br J Cancer 2001;84:25–32.
3. Kaneko M, Kusumoto M, Kobayashi T, Moriyama N, Naruke T, Ohmatsu H, et al. Computed tomography screening for lung carcinoma in Japan. Cancer 2000;89:2485–8.
4. Noguchi M, Morikawa A, Kawasaki M, Matsuno Y, Yamada T, Hirohashi S, et al. Small adenocarcinoma of the lung: histologic characteristics and prognosis. Cancer 1995;75:2844–52.
5. Coleman RE. PET in lung cancer. J Nucl Med 1999;40:814–20.
6. Vesselle H, Schmidt RA, Pugsley JM, Li M, Kohlmyer SG, Vallieres E, et al. Lung cancer proliferation correlates with [F-18]fluorodeoxyglucose uptake by positron emission tomography. Clin Cancer Res 2000;6:3837–44.
7. Higashi K, Ueda Y, Yagishita M, Arisaka Y, Sakurai A, Oguchi M, et al. FDG PET measurement of the proliferative potential on non-small cell lung cancer. J Nucl Med 2000;41:85–92.
8. Vansteenkiste JF, Stroobants SG, De Leyn PR, Dupont PJ, Bogaert J, Maes A, et al. Lymph node staging in non-small-cell lung cancer with FDG-PET scan: a prospective study on 690 lymph node stations from 68 patients. J Clin Oncol 1998;16:2142–9.
9. WHO. Histological typing of lung and pleural tumours. 3rd ed. Berlin: Springer; 1999. p. 31–47.
10. Lung cancer study group. Randomized trial of lobectomy versus limited resection for T1N0 non-small cell lung cancer. Ann Thorac Surg 1995;60:615–23.
11. Nakata M, Sawada S, Saeki H, Takashima S, Mogami H, Teramoto N, et al. Prospective study of thoracoscoic limited resection for ground-glass opacity selected by computed tomography. Ann Thorac Surg 2003;75:1601–6.
12. Keyes J. SUV: standard uptake or silly useless value? J Nucl Med 1995;36:1836–9.
13. Chin BB, Lyengar S, Sabundayo BP, Schwartz D. Standardized uptake values in 2-deoxy-2-[18F]Fluoro-d-glucose with positron emission tomography. Clinical significance of iterative reconstruction and segmented attenuation compared with conventional filtered back projection and measured attenuation correction. Mol Imaging Biol 2002;4:294–300.
14. Kubota K, Matsuzawa T, Fujiwara T, Ito M, Hatazawa J, Ishiwata K, et al. Differential diagnosis of lung tumor with positron emission tomography: a prospective study. J Nucl Med 1990;31:1927–32.
15. Gupta NC, Maloof J, Gunel E. Probability of malignancy in solitary pulmonary nodules using fluorine-18-FDG and PET. J Nucl Med 1996;37:943–8.
16. Lowe VJ, Fletcher JW, Gobar L, Lawson M, Kirchner P, Valk P, et al. Prospective investigation of positron emission tomography in lung nodules. J Clin Oncol 1998;16:1075–84.
17. Gould MK, Maclean CC, Kuschner WG, Rydzak CE, Owens DK. Accuracy of positron emission tomography for diagnosis of pulmonary nodules and mass lesions: a meta-analysis. JAMA 2001;285:914–25.

J Kanazawa Med Univ 31 : 10−16, 2006

Tumor Angiogenesis in Lung Adenocarcinomas: Correlation with FDG Uptake and Prognosis

JianFei Guo

Abstract: PURPOSE
To investigate correlation of angiogenic factors (VEGF, Angiopoietin-2) expression and hypoxia inducible factors (HIF-1α, HIF-2α) expression with FDG uptake and prognosis in lung adenocarcinomas.
MATERIALS AND METHODS
Forty-four patients with forty-five lung adenocarcinomas were performed FDG PET before surgery. FDG-PET measurements were performed 40 minutes after intravenous injection of approximately 185 MBq FDG on a dedicated PET scanner. Consecutive paraffin-embedded sections obtained from each resected tumor were immunostained for VEGF, Angipoietin-2, HIF-1α, HIF-2α and Glut-1, respectively. The Kaplan-Meier survival method was used to calculate survival rates, and the log-rank test was used to compare groups with respect to survival.
RESULTS
FDG uptake significantly correlated with VEGF (P=0.05) and Angiopoietin-2 (P=0.003) expression; higher FDG uptake usually means higher VEGF and Angiopoietin-2 expression. While HIF-1α expression had no significant correlation with FDG uptake, HIF-2α expression had a significant correlation with FDG uptake (P=0.009) and Glut-1 expression (P=0.004). The patients with SUV≤5 (P=0.00001), low VEGF (P=0.006), low Angiopoietin-2 (P=0.0002), low HIF-1α (P=0.04) or low HIF-2 α (P=0.0001) expression had a significantly better disease-free survival probabilities than the others.
CONCLUSION
Angiogenic factors (VEGF, Angiopoietin-2) expression and HIF-2α expression significantly correlated with FDG uptake and prognosis in lung adenocarcinomas. This may have applications in assessing and monitoring antiangiogenic therapy.

Key Words: PET, fluorine-18-fluorodeoxyglucose, lung adenocarcinoma, angiogenesis, prognosis

Introduction

Tumor growth and metastasis are critically dependent on the tumor's supply of blood vessels. Many studies have demonstrated that angiogenesis is stimulated by a variety of tumor-secreted angiogenic factors and inhibited by angiogenic inhibitors(1). Vascular endothelial growth factor (VEGF) is one of the most potent endothelial cell-specific growth factors and can promote differentiation and proliferation of endothelial cells and the formation of immature vessels(2). VEGF overexpression has been noted in human cancers of the brain, colon, breast, and lung and is reported to correlate with an adverse prognosis in these cancers, including non-small-cell lung cancer (NSCLC)(3,4). Angiopoietin-2 (Ang-2) has also recently been reported to have angiogenic activity and is related to vascular remodelling and sprouting, which occur in a complementary and coordinated fashion during vascular development, along with VEGF(5). The upregulated expression of Ang-2 has been noted in some human malignant tumors, including NSCLC(6).

Several factors have been identified as involved in the regulation of VEGF, including signal-transduction molecules, specific growth factors and cytokines, the

Department of Diagnostic Radiology and Radiation Oncology, Kanazawa Medical University, Uchinada, Ishikawa 920-0293, Japan
Correspondent to: JianFei Guo, Department of Diagnostic Radiology, First Affiliated Hospital, China Medical University, Shenyang, People's Republic of China
Accepted: February 13, 2006

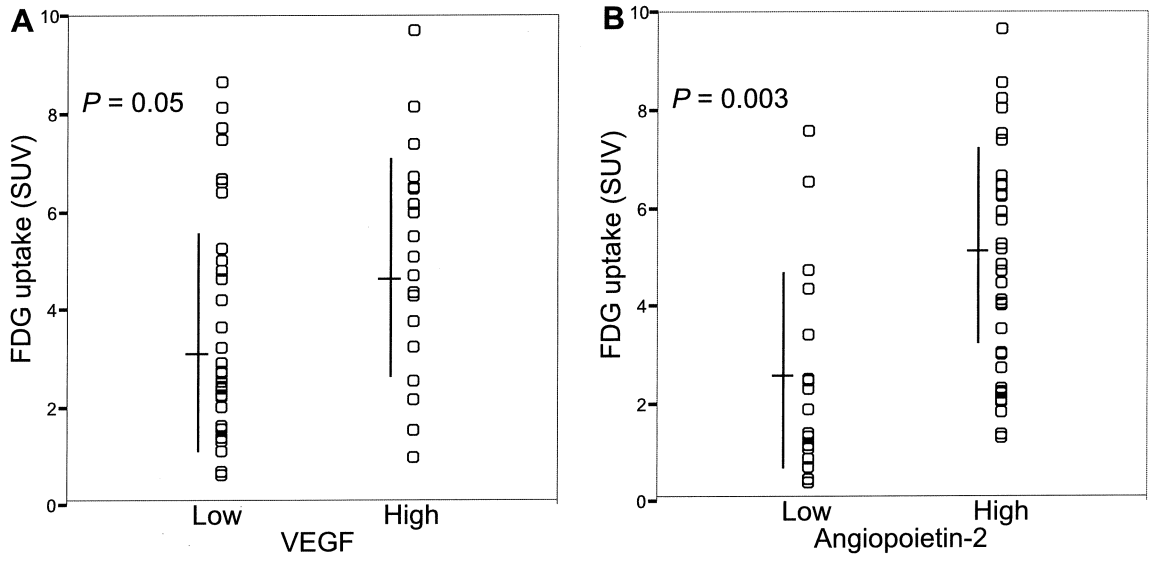

Fig. 1 . Correlation of VEGF and Ang-2 expression with FDG uptake in lung adenocarcinomas. (A) VEGF expression shows a significant correlation with FDG uptake (P = 0.05). (B) Ang-2 expression also has a much more significant correlation with FDG uptake (P = 0.003). (SUV: standardized uptake value)

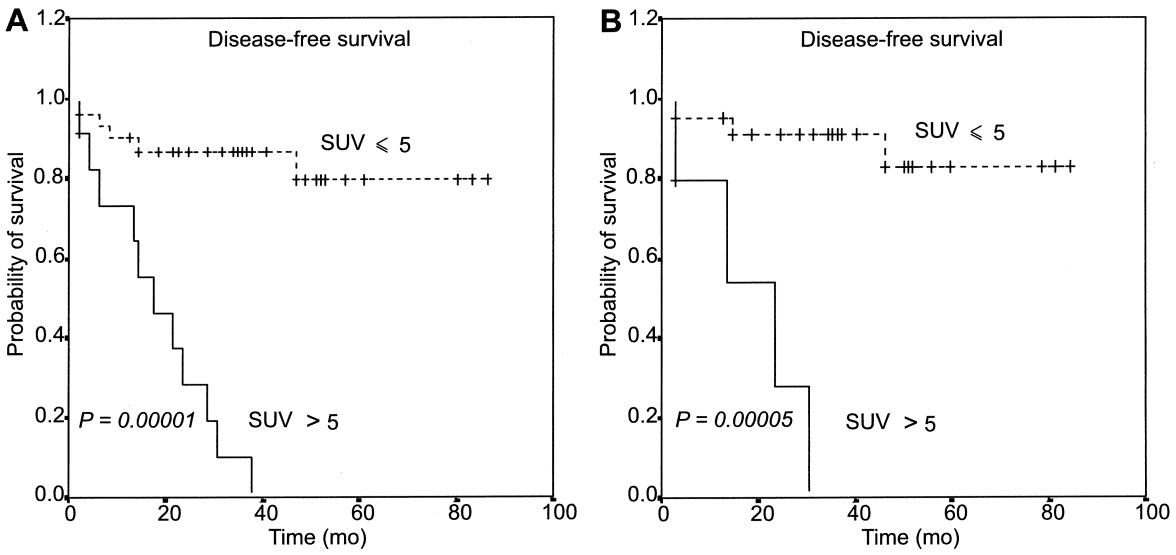

Fig. 2 . Kaplan-Meier analysis of disease-free survival according to FDG uptake (SUV>5 and SUV< or =5). (A) Analysis in the total patients shows that SUV is a significant prognostic factor (P = 0.00001) in the patiens with lung adenocarcinoma. (B) Analysis in the patients with stage I disease (35 patients) shows that SUV is still a significant prognostic factor (P = 0.00005).

most important of which may be hypoxia(7). Two of the most important transcription factors mediating the cellular response to hypoxia are hypoxia inducible factor-1α (HIF-1α) and hypoxia inducible factor-2α (HIF-2α). These transactivate many target genes, including glucose transporters (Gluts), glycolytic enzymes, and VEGF(8). Overexpression of HIF-1α and HIF-2α has been linked to upregulated angiogenic factors expression and poor outcome in some tumors, including NSCLC(9).

FDG PET imaging has been applied in many kinds of tumors and regarded as a good imaging modality for predicting prognosis in lung cancer(10-12). In previous study(13), we have found that active tumor angiogenesis reflected by CD105 microvessel density (MVD) significantly correlated with FDG uptake and prognosis in lung adenocarcinomas. However, until now, there is no previous report regarding the correlation between FDG uptake and angiogenic factors expression in lung adenocarcinomas and there is no reports regarding the correlation between FDG uptake and HIF expression in lung adenocarcinomas either. Therefore, the aims of this study were to investigate (a) correlation of VEGF and Ang-2 expression with FDG uptake in lung adenocarcinomas; (b) correlation of HIF-1α and HIF-2α expression with FDG uptake and Glut-1 expression; and (c) the prognostic value of those angiogenic factors involved in this study.

Materials and Methods

Patients

Forty-four patients (20 men, 24 women; age range, 47-82 y; mean age, 65 y) with forty-five lung adenocarcinomas, who underwent complete resection at Kanazawa Medical University from January, 1995, through December, 1999, were included in this study. All patients underwent thoracotomy within 4 weeks after their FDG PET study. Final diagnoses were established histologically in all patients. Follow-up of the postoperative clinical course was conducted by outpatient medical records and by inquiries by telephone or letter. The sizes of the tumors were determined from the resected specimens and ranged in diameter from 1.2 to 5.5 cm. None of the patients had insulin-dependent diabetes, and the serum glucose levels in all patients just before FDG injection were less than 120 mg / dl. Our institutional review board approved our research study and did not require patient informed consent for the retrospective study. We did obtain written informed consent from all patients for the PET examinations.

Table 1. Correlation of HIF-1α and HIF-2α expression with FDG uptake and Glut-1 expression in lung adenocarcinomas.

	FDG uptake			Glut-1		
	SUV ≤ 5	SUV > 5	pValue	Low	High	pValue
HIF-1α			0.42			0.30
Low	14	4		17	8	
High	19	8		10	8	
HIF-2α			0.01			0.02
Low	20	2		17	6	
High	13	10		8	18	

SUV: standardized uptake value

FDG PET Imaging

FDG PET was performed using a PET camera (Headtome IV, Shimazu, Kyoto, Japan) with a 10-cm axial field of view. The Headtome IV has 4 detector rings with 768 bismuth germanate (BGO) crystals per ring. It uses direct and crossplane coincidence detection to generate 14 slices per bed position. For the thorax, two-bed positions (28 slices at 6.5 mm intervals) were obtained. Reconstruction in a 128 x 128 matrix using a Hann filter (0.5 cutoff) yielded 5-mm intrinsic resolution at the center. Transmission scans were obtained in all subjects before FDG administration for attenuation correction by using a germanium-68 ring source. X-ray fluoroscopy was used to ascertain the location of the pulmonary nodule, and marks were made on the skin to aid in positioning the patient for the transmission scan. A transmission scan was acquired for 10 to 20 minutes in each bed position, depending on the specific radioactivity of the ring sources at the time of the study, for at least 2 million counts per slice. During the transmission scan, marks were made on the patient's skin to aid in repositioning for the emission scan. Blood (1 ml) was drawn for baseline blood glucose estimation and the data was recorded. Immediately after the transmission scan, FDG was administered intravenously. The average injection dose of FDG was 185 MBq. After a 40-minute uptake period, the patient was repositioned in the scanner. An emission scan was acquired at 10 minutes for each bed position, and the process took a total of 20 minutes.

For semiquantitative analysis of the FDG uptake, regions of interest (ROIs) were manually defined on the transaxial tomograms that showed the lesion's highest uptake to be in the middle of the tumour. The ROIs placed on the lesions encompassed all pixels within that lesion which had uptake values of greater than 90% of the maximum uptake in that slice, and the average counted rate in each ROI was calculated. In patients in whom no nodules were detectable by PET, the ROI was extrapolated from chest CT scans. After correction for radioactive decay, we analyzed

the ROIs by computing the standardized uptake values (SUVs), PET counts / pixel / sec × calibration factor / injected dose (MBq) / body weight, where the calibration factor = (MBq / ml) / (counts / pixel / sec).

Immunohistochemical Staining

Consecutive 5-μm sections were cut from each paraffin-embedded study block and were stained for VEGF, Angipoietin-2, HIF-1α, HIF-2α and Glut-1 using the immunoperoxidase technique. Appropriate positive and negative controls were included with each set of stains. The primary antibodies used were a mouse monoclonal antibody (clone VG1, Zymed) at a 1:100 dilution for VEGF, a goat monoclonal antibody (clone C-19, Santa Cruz Biotechnology) at a 1:50 dilution for Angipoietin-2, a mouse monoclonal antibody (clone ESEE122, Novus biologicals) at a 1:200 dilution for HIF-1α, a mouse monoclonal antibody (clone EP190b, Novus biologicals) at a 1:500 dilution for HIF-2α and a mouse monoclonal antibody (clone MYM, Chemicon International) at a 1:500 dilution for Glut-1. Sections were deparaffinized, rehydrated and microwaving (4 min × 3) for antigen retrieval was applied. They were further processed by the addition of primary antibodies and rinses, horseradish peroxidaseconjugated secondary antibody and rinses, and color development with diaminobenzidine tetrahydrochloride and the nuclei were counterstained with Mayer's hematoxylin.

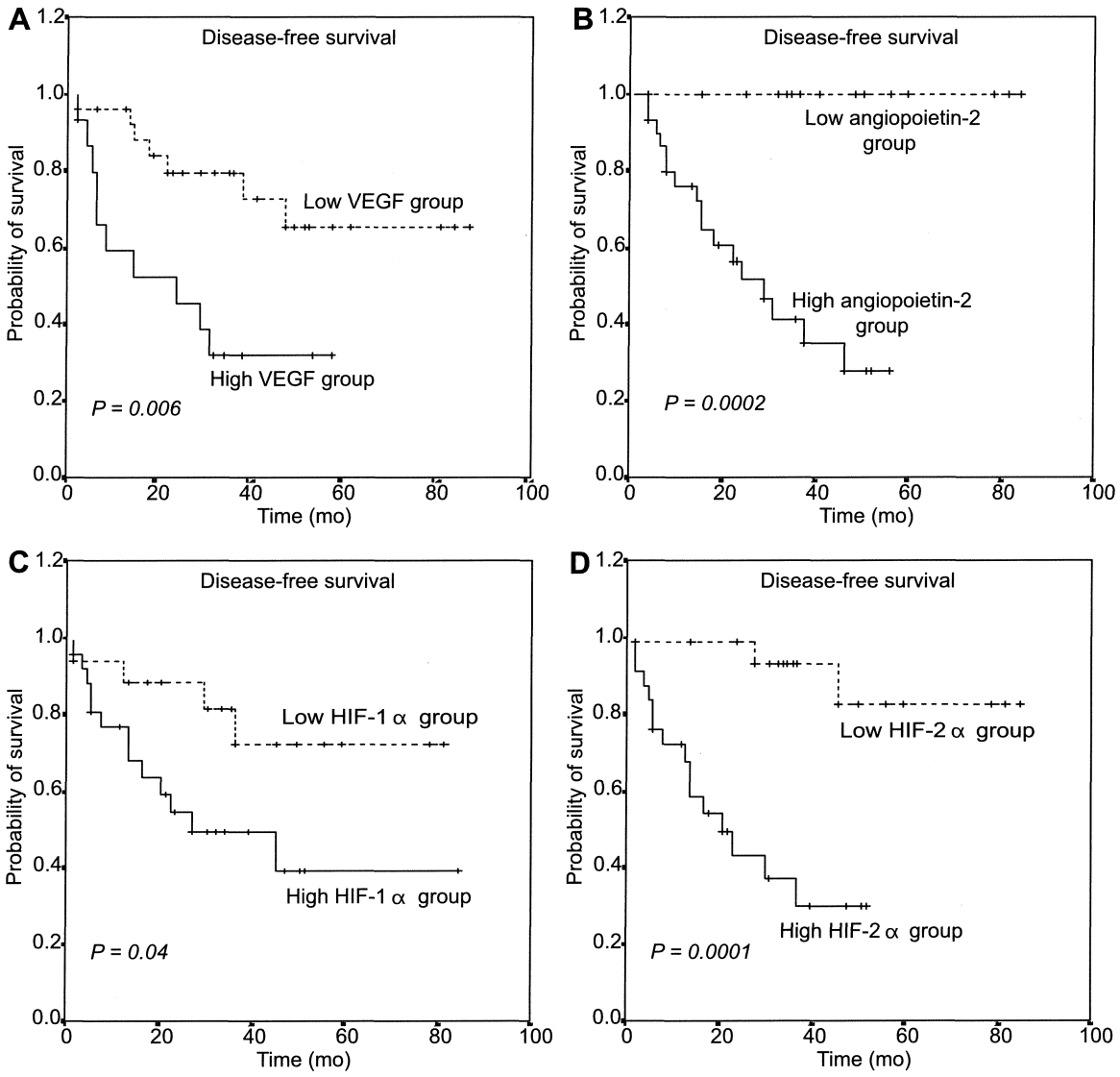

Fig. 3. Kaplan-Meier analysis of disease-free survival for VEGF (A), Ang-2 (B), HIF-1α (C) and HIF-2α (D) in the total patients.

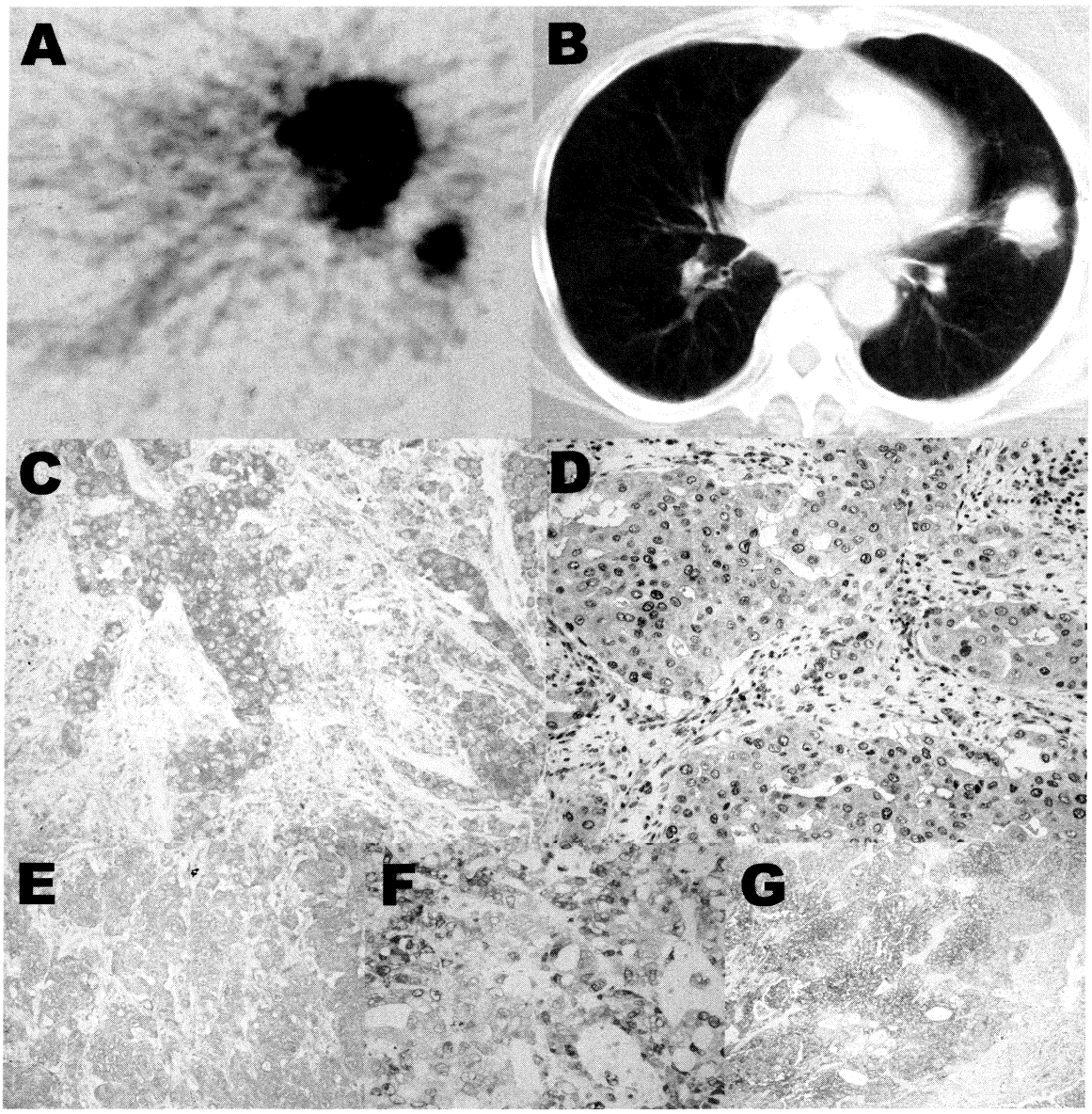

Fig. 4 . A moderately differentiated adenocarcinoma with recurrence in 17 months. (A) FDG PET shows intense uptake of FDG in the tumor (SUV 6.94). (B) CT scan shows a nodule in the left lung. VEGF (C), Ang-2 (D), HIF-1α (E), HIF-2α (F) and Glut-1 (G) immunohistochemistry demonstrate strong expression.

Immunohistochemical interpretation

All immunohistochemical evaluation was performed by two investigators without knowledge of patient outcome. The VEGF and Ang-2 expression was assessed according to the percentage of immunoreactive cells, and the median level was chosen as cut-off point to define low and high expression(6,14).

HIF-1α and HIF-2α expression was both cytoplasmic and nuclear. Cytoplasmic staining was scored as absent, weak, moderate and strong. Nuclear expression usually was accompanied with moderate/strong cytoplasmic reactivity, pure nuclear expression was more often noted in HIF-2α staining than HIF-1α staining. Tumors were grouped as low and high expression according to the intensity and

extent of staining: low HIF expression, tumors without nuclear reactivity and with absent or weak cytoplasmic reactivity; high HIF expression, tumors with a clear nuclear reactivity and/or with moderate/strong cytoplasmic reactivity. This scoring method is performed according to previous study with some modifications(9).

Glut-1 staining was scored by combining both the percentage of positive tumor cells and the staining intensity, according to the previous study with some modifications(15).

Statistical Methods

All data are shown as the mean ± 1 standard deviation. All statistical analyses were carried out with the use of SPSS for Windows (version 12.0; SPSS Inc, Chicago, IL, USA). Chi-square test was used to compare the distribution of values across categorical variables. Differences in continuous variables between dichotomous variables were tested using one-way analysis of variance (ANOVA). Disease-free survival probability was calculated with the Kaplan-Meier life table method. Differences between survival probabilities were analyzed using the log-rank test. Probability values of less than or equal to 0.05 were considered statistically significant.

Results

Figure 1 shows the correlation of VEGF and Ang-2 expression with FDG uptake. Campared with VEGF expression, Ang-2 expression has a much more significant correlation with FDG uptake (P = 0.003).

As summarized in Table 1, Chi-squire analysis shows that HIF-1α expression has no significant correlation with FDG uptake and Glut-1 expression, while HIF-2α expression has a significant correlation with FDG uptake and Glut-1 expression (P = 0.009, P = 0.004) (Table 1).

Using Kaplan-Meier method, we analyzed the prognostic impact of FDG uptake and angiogenic factors invoved in this study. According to the previous report(11), the patients were classified into two groups of SUV>5 and SUV< or =5. Among all of the factors investigated in this study, SUV is the most significant prognostic factor in disease-free survival analysis (P = 0.00001)(Fig. 2A). Even in patients only with stage I disease (35 patients), SUV still is a significantly prognostic factor (P = 0.00005)(Fig. 2B). Both of VEGF and Ang-2 expression are significantly prognostic factors in this study (P = 0.006, P = 0.0002) (Fig. 3A, Fig. 3B). HIF expression is also significant prognostic factor, however, compared to HIF-1α expression (P = 0.04) (Fig. 3C), HIF-2α expression is a much more significantly prognostic factor (P = 0.0001) (Fig. 3D). Figure 4 shows a representative case in this study. A patient with a moderately differentiated adenocarcinoma had a recurrence in 17 months. FDG PET shows intense uptake of FDG in the tumor (SUV 6.94). VEGF, Ang-2, HIF-1α , HIF-2α and Glut-1 immunohistochemistry demonstrate strong expression.

Discussion

The present study demonstrated that angiogenic factors (VEGF, Ang-2) expression and HIF-2α expression significantly correlated with FDG uptake and prognosis in lung adenocarcinomas.

Angiogenesis is required for tumor growth and metastasis. The process of angiogenesis is stimulated or inhibited by a variety of factors(1). VEGF is one of the most potent endothelium-specific angiogenic factors, and its overexpression is reported to be associated with high microvessel density, rapid tumor progression, and poor prognosis in several human cancers, including NSCLC(3,4). The recent discovery of Ang-1 and Ang-2 has also provided novel and important insights into the molecular mechanism of blood vessel formation. Ang-1 and Ang-2 bind with similar affinity to the endothelial cell tyrosine kinase receptor Tie 2(16). Ang-1 leads to endothelial cell stability, but Ang-2 antagonizes the stabilizing action of Ang-1. Ang-2 results in destabilization of vessels and causes regression of newly formed vessels by endothelial cell apoptosis, unless VEGF is present, in which case the two collaborate to promote angiogenesis(5). In Tanaka et al's study(6), they found that Ang-2 expression significantly correlated with prognosis, as well as with aggressive angiogenesis in NSCLC that was enhanced in the presence of high VEGF expression. Our findings are consistent with that report, and indicate that tumor angiogenesis mediated by VEGF and Ang-2 can be assessed by FDG uptake. Moreover, our findings also confirm our previous study(13), in which we found that tumor angiogenesis reflected by CD105-MVD is a significant prognostic factor and significantly correlate with FDG uptake in lung adenocarcinomas. Taken together, these results indicate that FDG PET imaging may be a good imaging modality to noninvasively assess tumor angiogenesis in lung adenocarcinomas.

To our knowledge, there was no previous report regarding the correlation between FDG uptake and tumor angiogenesis in lung adenocarcinomas. The underlying mechanism of this correlation also remains unclear. In one hand, in-vitro cell line study shows that FDG uptake is significantly unregulated under hypoxic condition(17), it is assumed that glucose transporter protein (Glut-1) expression mediated by hypoxia may be one of important time-limiting steps for FDG uptake. The important role of Glut-1

expression increasing FDG uptake in NSCLC are already investigated in the previous study(18), however, the relationship of hypoxia with FDG uptake and Glut-1 expression in lung adenocarcinomas is not determined yet. On the other hand, angiogenic factors expression, for example, VEGF expression can be significantly enhanced by hypoxia through both transcriptional and post-transcriptional mechanisms(7). Based on this complicated connection, we can assume that hypoxia may be the important linkage between tumor angiogenesis and FDG uptake. In the present study, we investigated two important transcription factors mediating the cellular response to hypoxia, that is, HIF-1α and HIF-2α. We found that although both of them are regulated by hypoxia and have similar function, they have different prognostic value and relationship with FDG uptake. This result implies that they may play different role in lung adenocarcinomas, in fact, some previous reports indicated that HIF-1α and HIF-2α did have different function in different tumors and HIF-2α may be more abundant in lung cancer(19,20). Furthermore, we found that HIF expression is also a significant prognostic factor in lung adenocarcinomas, in addition to its important role in tumorigenesis, targeting HIF pathway may also be important in the treatment of lung cancer.

As a functional imaging modality, FDG PET has been proved very useful tool for staging many kinds of tumors, including NSCLC. FDG uptake is also recognized as an important and independent prognostic factor in some tumors including NSCLC. Using FDG PET imaging to assess tumor angiogenesis will be a good choice in face of the forthcoming antiangiogenic therapy.

In summary, our results indicate that angiogenic factors (VEGF, Ang-2) expression and HIF-2α expression significantly correlated with FDG uptake and prognosis in lung adenocarcinomas. This may have applications in assessing antiangiogenic therapy in the near future.

The author is grateful to Professor Hisao Tonami, Professor Shogo Katsuda, Professor Hirohisa Toga, Professor Tsutomu Sakuma, Professor Yoshimichi Ueda, Professor Tsutomu Takegami and Professor Kotaro Higashi for their critical reviews and comments on the manuscript.

This work was supported by a Grant of Collaborative Research from Kanazawa Medical University (C2005-2), by a Grand-in Aid for Cancer Research (16-5) from the Ministry of Health and Welfare, Japan and by a Grand-in Aid (16591232) for Scientific Research from the Ministry of Education, Japan.

References

1. Folkman J: Angiogenesis in cancer, vascular, rheumatoid and other disease. Nat Med 1995; **1**: 27-31.
2. Leung DW, Cachianes G, Kuang WJ et al: Vascular endothelial growth factor is a secreted angiogenic mitogen. Science 1989; **246**: 1306-9.
3. Fontanini G, Vignati S, Boldrini L et al: Vascular endothelial growth factor is associated with neovascularization and influences progression of non-small cell lung carcinoma. Clin Cancer Res 1997; **3**: 861-5.
4. Imoto H, Osaki T, Taga S et al: Vascular endothelial growth factor expression in non-small-cell lung cancer: prognostic significance in squamous cell carcinoma. J Thorac Cardiovasc Surg 1998; **115**: 1007-14.
5. Yancopoulos GD, Davis S, Gale NW et al: Vascular-specific growth factors and blood vessel formation. Nature 2000; **407**: 242-8.
6. Tanaka F, Ishikawa S, Yanagihara K et al: Expression of angiopoietins and its clinical significance in non-small cell lung cancer. Cancer Res 2002; **62**: 7124-9.
7. Shweiki D, Itin A, Soffer D, Keshet E: Vascular endothelial growth factor induced by hypoxia may mediate hypoxia-initiated angiogenesis. Nature 1992; **359**: 843-5.
8. Blancher C, Moore JW, Talks KL et al: Relationship of hypoxia-inducible factor (HIF)-1alpha and HIF-2alpha expression to vascular endothelial growth factor induction and hypoxia survival in human breast cancer cell lines. Cancer Res 2000; **60**: 7106-13.
9. Giatromanolaki A, Koukourakis MI, Sivridis E et al: Relation of hypoxia inducible factor 1 alpha and 2 alpha in operable non-small cell lung cancer to angiogenic/molecular profile of tumours and survival. Br J Cancer 2001; **85**: 881-90.
10. Hicks RJ, Kalff V, MacManus MP et al: (18)F-FDG PET provides high-impact and powerful prognostic stratification in staging newly diagnosed non-small cell lung cancer. J Nucl Med 2001; **42**: 1596-604.
11. Higashi K, Ueda Y, Arisaka Y et al: 18F-FDG uptake as a biologic prognostic factor for recurrence in patients with surgically resected non-small cell lung cancer. J Nucl Med 2002; **43**: 39-45.
12. Guo J, Higashi K, Yokota H et al: In vitro proton magnetic resonance spectroscopic lactate and choline measurements, 18F-FDG uptake, and prognosis in patients with lung adenocarcinoma. J Nucl Med 2004; **45**: 1334-9.
13. Guo J, Higashi K, Ueda Y et al: Microvessel Density: Correlation with FDG Uptake and Prognostic Impact in Lung Adenocarcinomas. J Nucl Med (In Press).
14. Giatromanolaki A, Koukourakis MI, Kakolyris S et al: Vascular endothelial growth factor, wild-type p53, and angiogenesis in early operable non-small cell lung cancer. Clin Cancer Res 1998; **4**: 3017-24.
15. Higashi T, Tamaki N, Torizuka T et al: FDG uptake, GLUT-1 glucose transporter and cellularity in human pancreatic tumors. J Nucl Med 1998; **39**: 1727-35.
16. Maisonpierre PC, Suri C, Jones PF et al: Angiopoietin-2, a natural antagonist for Tie2 that disrupts in vivo angiogenesis. Science 1997; **277**: 55-60.
17. Burgman P, Odonoghue JA, Humm JL et al: Hypoxia-Induced increase in FDG uptake in MCF7 cells. J Nucl Med 2001; **42**: 170-5.
18. Higashi K, Ueda Y, Sakurai A et al:Correlation of Glut-1 glucose transporter expression with. Eur J Nucl Med 2000; **27**: 1778-85.
19. Hu CJ, Wang LY, Chodosh LA et al: Differential roles of hypoxia-inducible factor 1alpha (HIF-1alpha) and HIF-2alpha in hypoxic gene regulation. Mol Cell Biol 2003; **23**: 9361-74.
20. Wiesener MS, Jurgensen JS, Rosenberger C et al: Widespread hypoxia-inducible expression of HIF-2alpha in distinct cell populations of different organs. FASEB J 2003; **17**: 271-3.

金医大誌（J Kanazawa Med Univ）31：185－193, 2006

FDG集積度，HRCT所見，および血清CEA値による肺腺癌 (3cm以下) の術後再発予測

髙　橋　知　子

要　約：【目的】本研究の目的は，術前画像診断 (原発巣のFDG集積度，HRCT所見) および術前血清CEA値により肺腺癌 (3cm以下) の術後再発を予測しうるか否かを明らかにすることである。【対象と方法】対象は，術前にFDG PETおよびHRCT検査，血清CEA値測定が行われた肺腺癌 (3cm以下) 標準手術症例75例である。原発巣のFDG集積度は視覚的に縦隔の血中濃度を基準として2群に分類した。HRCT所見はGGOの割合を半定量的に計測し，solid patternとGGO patternの2群に分類した。術前の血清CEA値は20ng/mlを基準として2群に分類した。術後，病理組織学的浸潤性 (血管侵襲・リンパ管侵襲・胸膜浸潤) および術後再発と術前画像所見および血清CEA値の関連を統計学的に解析した。【結果】原発巣のFDG集積度・HRCT所見，血清CEA値と浸潤性および術後再発との間には有意な関連が認められた。GGO pattern群では浸潤性と術後再発は認められなかった。また，solid pattern群ではFDG集積度と病理病期分類が独立した予後予測因子であった。さらに，solid patternかつFDG高集積度の症例では血清CEA値20ng/ml以上の群は有意に術後再発率が高かった。【結論】肺腺癌 (3cm以下) において原発巣のFDG集積度，HRCT所見，および血清CEA値を組み合わせることにより，術後再発をより高い精度で予測できることが判明した。

キーワード：肺腺癌，^{18}F-FDG PET，GGO component，血清CEA値，術後再発

緒　　言

近年，画像診断の向上やCT検査の日常化，胸部CT検診の普及によって小型肺癌の発見が飛躍的に増加している(1,2)。肺癌の手術的治療では肺葉以上の切除および肺門・縦隔リンパ節郭清が標準術式とされているが，小型肺癌発見の増加に伴い，縮小手術である区域切除または部分切除の適応に対する議論がされている(1-3)。さらに，病期分類Ⅰ期にもかかわらず術後早期に再発を認める症例も散見され，補助的化学療法の有効性が検討されている(4,5)。また，病理組織学的に浸潤性 (血管侵襲・リンパ管侵襲・胸膜浸潤) が認められた症例は術後再発率が高いことが報告されている(6-8)。したがって，非浸潤性肺癌を術前に予測することができれば，縮小手術の標準化を進めることが可能になり，さらには術前あるいは術後化学療法の併用を考慮するうえでの一助となるとも考えられる。

このような考えから，術前画像所見による原発巣の浸潤性評価の試みが行われている。その一つとして，high resolution computed tomography (以下HRCT) における原発巣のground-glass opacity (以下GGO) の割合が挙げられている。GGOは非浸潤癌である細気管支肺胞上皮癌 (broncioloalveolar carcinoma: 以下BAC) 型の進展をよく反映しており(9,10)，GGOの割合は浸潤性やリンパ節転移，さらには術後予後との間に相関が認められたと報告されている(11-16)。

一方，^{18}F-fluorodeoxyglucose (以下FDG) を用いた positron emission tomography (以下PET) は，glucoseのOH基一つを^{18}Fに置換したブドウ糖類似物質を用いて生体の糖代謝を画像化する方法である。多くの腫瘍細胞は糖代謝が活発であるためFDGは強く集積し，糖代謝の低い全身組織とのコントラストで高感度の診断が可能である。腫瘍へのFDG集積は腫瘍の増殖速度・細胞密度・分化度とも相関し(17)，中でも肺腺癌では原発巣のFDG集積度は生物学的悪性度を反映することが報告されている(18)。

また，術前血清carcinoembryonic antigen (以下CEA) 値も肺腺癌の予後予測因子としての有用性が検討されており，術前CEA高値の症例では術後予後が悪いことが報告されている(19-21)。

本研究の目的は，術前画像診断 (原発巣のFDG集積度，HRCT所見) および術前血清CEA値により肺腺癌 (3cm以下) の術後再発を予測しうるか否かを明らかにすることである。

金沢医科大学放射線診断治療学
石川県河北郡内灘町大学1-1
平成19年２月５日受理

実 験 方 法

1. 対象

1997年4月から2005年1月の間に金沢医科大学病院にて標準手術 (縦隔リンパ節郭清を伴う肺葉切除術) が行われた原発性肺腺癌 (3cm以下) 症例で，術前にFDG PETおよびHRCT検査，血清CEA値測定が行われ，なおかつ術後再発の追跡調査が可能であった75症例を対象とした。追跡調査困難であった群の患者背景因子は対象との間に大きな違いは認められなかった。FDG投与直前の採血において高血糖でありFDG集積に影響が認められた症例や体動などにより画像評価に影響が及んだ症例は除外した。なお，本研究は術前評価に用いることを考慮してTNM分類で用いられている腫瘍径 (3cm) を基準として腫瘍径3cm以下の症例を対象とした。

2. 方法

1) FDG PET

PET装置は，HEADTOME-Ⅳ (Shimazu, Kyoto, Japan)，Advance (General Electric Medical Systems, Milwaukee, WI, USA)，ECAT ACCEL (Siemens Medical Solutions, Knoxville, TN, USA) の3機種を使用した。検査前6時間以上の絶食とし，全例に血糖値測定のため1mlの採血を行った。平均370MBqのFDGを単回静脈内投与し，40～60分後より撮像開始した。HEADTOME-ⅣおよびAdvanceは2次元収集，ECAT ACCELは3次元収集にてemission scanを施行した。また，全例に吸収補正のためにtransmission scanを施行した。再構成法はHEADTOME-ⅣおよびECAT ACCELはfiltered back projection法，Advanceは逐次近似画像構成法である。

2) HRCT

CT装置は，SOMATOM Plus (Siemens Medical Solutions, Erlangen, Germany)，SOMATOM Sensation 16 (Siemens Medical Solutions, Erlangen, Germany) の2機種を使用した。始めに肺野全体をhelical mode (table speed 10 mm/sec，10 mm section thickness) にて撮像し，病変部分をthin section (2.0 mm section thickness) にて追加撮像した。再構成したCT画像は一定の条件でフィルム化した (window center -700 HU, width 1500 HU)。

3) 画像評価

FDG PETおよびHRCT画像はそれぞれ2人の核医学医，放射線科医が独立して評価し，相違が認められた場合は合議により評価の一致を得た。原発巣のFDG集積度は，多機種での比較検討のため視覚的に縦隔の血中濃度を基準として評価した。すなわち，縦隔と同程度以下のFDG低集積度群と縦隔より高いFDG高集積度群の2群に分類した。HRCT上の原発巣におけるGGOは内部の肺血管が透見認識可能な比較的均一な淡い広がり (すりガラス状陰影) と定義され，GGOの割合はAokiらの提唱した方法を参照して腫瘍断面の最大径 (D_{GGO}) とGGO以外の腫瘍部分の最大径 (D) を用いて半定量的に計測した：$([D_{GGO}-D]/D_{GGO})\times 100$ (%) (11)。これをもとに，GGO50%未満のsolid patternとGGO50%以上のGGO patternの2群に分類した。

4) 血清CEA値

血清CEA値は喫煙や糖尿病・腎不全・肝疾患などの良性疾患でも高値となることがあり，その値は基準値上限の2倍程度 (10ng/ml) までがほとんどであると報告されている(22,23)。したがって肺腺癌術後再発予測因子として血清CEA値を用いる場合，正常値上限をカットオフとすると肺腺癌以外の影響が否定できないと考えられた。本研究では明らかな異常値として血清CEA値20ng/mlをカットオフ値に設定し，20ng/ml未満と20ng/ml以上の2群に分類した。

5) 病理組織学的評価

浸潤性は手術標本を病理組織学的にhematoxylin and eosin (HE) 染色とelastica van Gieson染色にて，血管侵襲・リンパ管侵襲・胸膜浸潤の有無を病理医2名の同一の見解のもとで評価した。

6) 追跡調査

金沢医科大学病院で術後経過が観察された症例は診療記録を参照し，他病院で術後経過が観察された症例は当該病院の担当医に再発の有無を問い合わせた。いずれも患者の同意を得たうえで各施設の倫理規定に則り情報収集を行った。さらに各症例のデータを扱う場合，個人情報の流出を防いだ。

術後再発は，局所・リンパ節転移・遠隔転移にて評価し，術後から再発診断までの期間を無再発生存期間と設定した。

7) 統計学的解析

統計学的処理はSPSS (Dr. SPSS Ⅱ for Windows; SPSS Inc., Chicago, IL, USA) を用いて行った。術前画像所見 (原発巣のFDG集積度，HRCT所見) および術前血清CEA値と病理組織学的浸潤性の関連は，2×2分割表を作成し期待値のうち最も小さいものが5以下のためFisher's exact testで検討した(24)。また術前画像所見 (原発巣のFDG集積度，HRCT所見) および術前血清CEA値と術後再発の関連は，事象発生までの期間を考慮する必要があるためKaplan-Meier法 (log rank test) で検討した。さらにHRCT上のsolid pattern群に限定して，前述の解析方法と同様に，病理組織学的浸潤性とFDG集積度の関連をFisher's exact test，術後再発とFDG集積度の関連をKaplan-Meier法 (log rank test) で検討した。さらに，solid pattern群で術後再発に関与する因子として，年齢 (65歳未満，65歳以上)・性別・術前血清CEA値・病理病期分類 (I期，II・III期)・FDG集積度の5因子を選択し，Cox比例ハザードモデルによる多変量解析を行った。加えてHRCT上のsolid pattern群でFDG集積度と血清CEA値を組み合わせた場合の術後再発についてKaplan-Meier法 (log rank test) で検討した。なお，$p<0.05$を統計学的有意とした。

結　　果

対象の性別は男性35人女性40人，年齢は42-84歳 (平均年齢63.85歳) である。術後に評価された病理病期分類 (pStage) は，ⅠA期57症例，ⅠB期4症例，ⅡA期3症例，ⅡB期0症例，ⅢA期

表1. 対象患者背景

因子	症例数	%
年齢		
65歳未満	36	48.0
65歳以上	39	52.0
性別		
男性	35	46.7
女性	40	53.3
血清CEA値		
20.0ng/ml未満	70	93.3
20.0ng/ml以上	5	6.7
病理病期分類		
ⅠA	57	76.0
ⅠB	4	5.3
ⅡA	3	4.0
ⅡB	0	0.0
ⅢA	9	12.0
ⅢB	2	2.7
HRCT所見		
GGO pattern	13	17.3
solid pattern	62	82.7
FDG集積度		
低集積度群	38	50.7
高集積度群	37	49.3

9症例，ⅢB期2症例で，ⅠB期およびⅢB期は全て胸膜浸潤が認められた症例である。観察期間は2-102ヶ月 (平均観察期間28.37ヶ月) である(表1)。

病理組織学的浸潤性の有無は72症例で確認でき，浸潤性あり30症例 (41.7%)，浸潤性なし42症例 (58.3%) であった。

術後再発は16症例 (22.0%) で認められ，再発までの期間は2-47ヶ月 (平均17.88ヶ月) であった。

1. 原発巣のFDG集積度

原発巣のFDG集積度は，低集積度群38症例 (50.6%)，高集積度群37症例 (49.4%) であった。

1) 病理組織学的浸潤性との関連(表2)

浸潤性は，FDG低集積度群では16.2% (6/37)，FDG高集積度群では68.6% (24/35) で認められ，Fisher's exact testにてFDG高集積度群ではFDG低集積度群よりも有意に浸潤性を認める症例が多かった (p<0.0001)。

2) 術後再発との関連(図1)

術後再発は，FDG低集積度群では5.3% (2/38)，FDG高集積度群では37.8% (14/37) で認められた。Kaplan-Meier法で，FDG高集積度群は低集積度群よりも有意に術後再発率が高かった (p=0.0006)。

表2. 原発巣のFDG集積度と病理組織学的浸潤性との関連

	浸潤性		
	−	+	%
FDG集積度			
FDG低集積度群	31	6	16.2
FDG高集積度群	11	24	68.6

Fisher's exact testにてp<0.0001と統計学的有意差が認められた。

表3. 原発巣のHRCT所見と病理組織学的浸潤性との関連

	浸潤性		
	−	+	%
HRCT所見			
GGO pattern	13	0	0.0
solid pattern	29	30	50.8

Fisher's exact testにてp<0.0001と統計学的有意差が認められた。

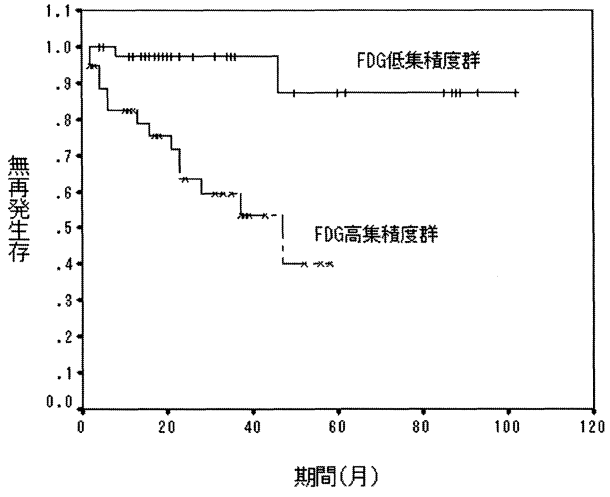

図1. 原発巣のFDG集積度と術後再発との関連(Kaplan-Meier法)
log rank testにてp=0.0006と統計学的有意差が認められた。

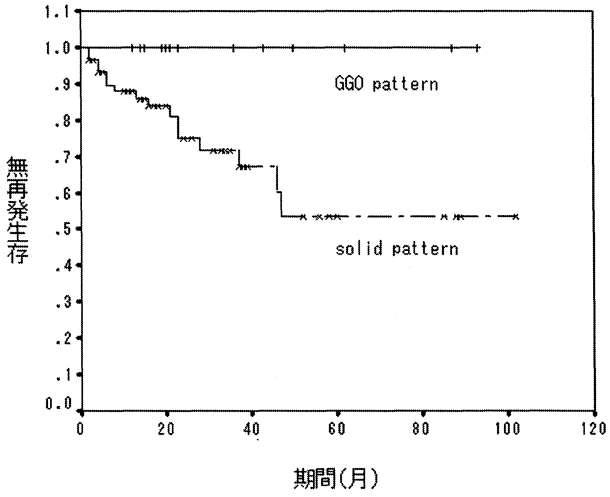

図2. 原発巣のHRCT所見と術後再発との関連(Kaplan-Meier法)
log rank testにてp=0.0359と統計学的有意差が認められた。

2. 原発巣のHRCT所見

原発巣のHRCT所見は，GGO pattern群13症例 (17.3%)，solid pattern群62症例 (82.7%) であった。

1) 病理組織学的浸潤性との関連(表3)

浸潤性は，GGO pattern群では0% (0/13)，solid pattern群では50.8% (30/59) で認められ，Fisher's exact testにてsolid pattern群ではGGO pattern群よりも有意に浸潤性を認める症例が多かった (p<0.0001)。

2) 術後再発との関連(図2)

術後再発は，GGO pattern群では0% (0/13)，solid pattern群では25.8% (16/62) で認められた。Kaplan-Meier法で，solid pattern群はGGO pattern群よりも有意に術後再発率が高かった (p=0.0359)。

3. 術前血清CEA値

術前血清CEA値20ng/ml未満は70症例 (93.3%)，20ng/ml以上は5症例 (6.7%) であった。

1) 病理組織学的浸潤性との関連(表4)

浸潤性は，術前血清CEA値20ng/ml未満の群では37.3% (25/67)，20ng/ml以上の群では100.0% (5/5) で認められ，Fisher's exact testにて術前血清CEA値20ng/ml以上の群では20ng/ml未満の群よりも有意に浸潤性を認める症例が多かった (p=0.010)。

2) 術後再発との関連(図3)

術後再発は，術前血清CEA値20ng/ml未満の群では17.1% (12/70)，20ng/ml以上の群では80.0% (4/5) で認められた。Kaplan-Meier法で，血清CEA値20ng/ml以上の群は20ng/ml未満の群より有意に術後再発率が高かった (p=0.0002)。

4. Solid pattern群に限定した場合の解析結果

GGO pattern群では病理組織学的浸潤性および術後再発が共に認められなかったため，対象をsolid pattern群 (62症例) に限定した場合の検討を行った。

1) 原発巣のFDG集積度と病理組織学的浸潤性(表5)

浸潤性はFDG低集積度群では24.0% (6/25)，FDG高集積度群では70.6% (24/34) で認められ，Fisher's exact testにてFDG高集積度群ではFDG低集積度群よりも有意に浸潤性を認める症例が多かった (p=0.001)。

2) 原発巣のFDG集積度と術後再発(図4)

術後再発はFDG低集積度群では7.7% (2/26)，FDG高集積度群

表4. 術後血清CEA値と病理組織学的浸潤性との関連

	浸潤性		
	−	+	%
血清CEA値			
20ng/ml未満	42	25	37.3
20ng/ml以上	0	5	100.0

Fisher's exact testにてp=0.010と統計学的有意差が認められた。

表5. Solid patternにおける原発巣のFDG集積度と浸潤性

	浸潤性		
	−	+	%
FDG集積度			
低集積度群	19	6	24.0
高集積度群	10	24	70.6

Fisher's exact testにてp=0.001と統計学的有意差が認められた。

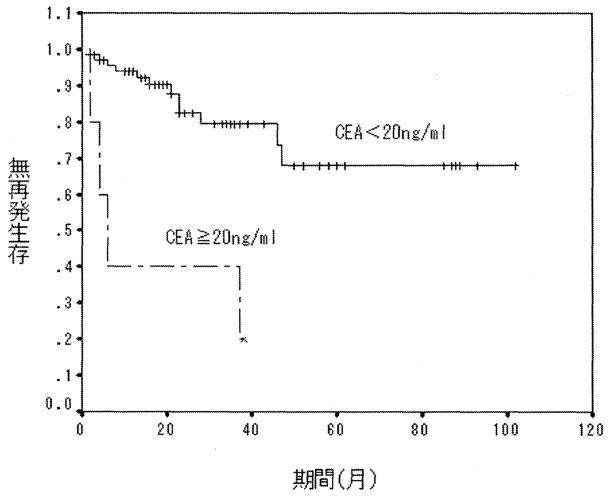

図3. 術前血清CEA値と術後再発との関連(Kaplan-Meier法)
log rank testにてp=0.0002と統計学的有意差が認められた。

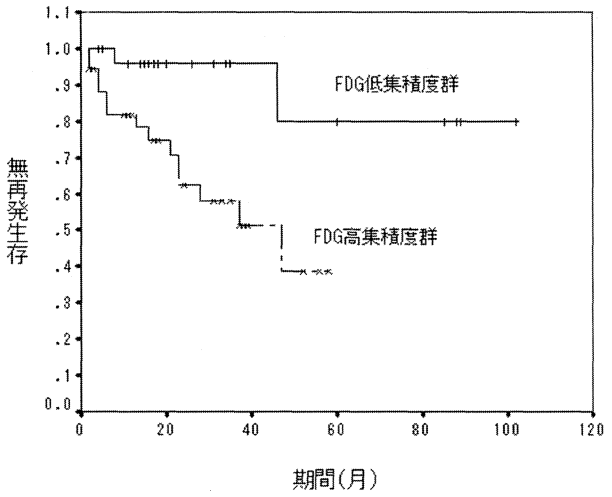

図4. Solid patternにおける原発巣のFDG集積度と術後再発(Kaplan-Meier法)
log rank testにてp=0.0079と統計学的有意差が認められた。

では38.9% (14/36) で認められた。対象をsolid pattern群に限定した場合も，Kaplan-Meier法でFDG高集積度群は低集積度群よりも有意に術後再発率が高かった (p=0.0079)。例として共にsolid pattern・術前血清CEA正常値・pStage ⅠAであるが，FDG高集積度群であり術後再発が認められた症例(図5)とFDG低集積度群であり観察期間中に術後再発が認められなかった症例(図6)を提示した。

3) 術後再発に関与する主要因子の多変量解析(表6)

年齢・性別・術前血清CEA値・病理病期分類・FDG集積度の5因子のなかでは，病理病期分類 (p=0.040) とFDG集積度 (p=0.040) のみが独立した術後再発予測因子であった。

4) 原発巣のFDG集積度と血清CEA値を組み合わせた場合の術後再発(図7)

Solid patternでなおかつFDG高集積度の症例では，術前血清

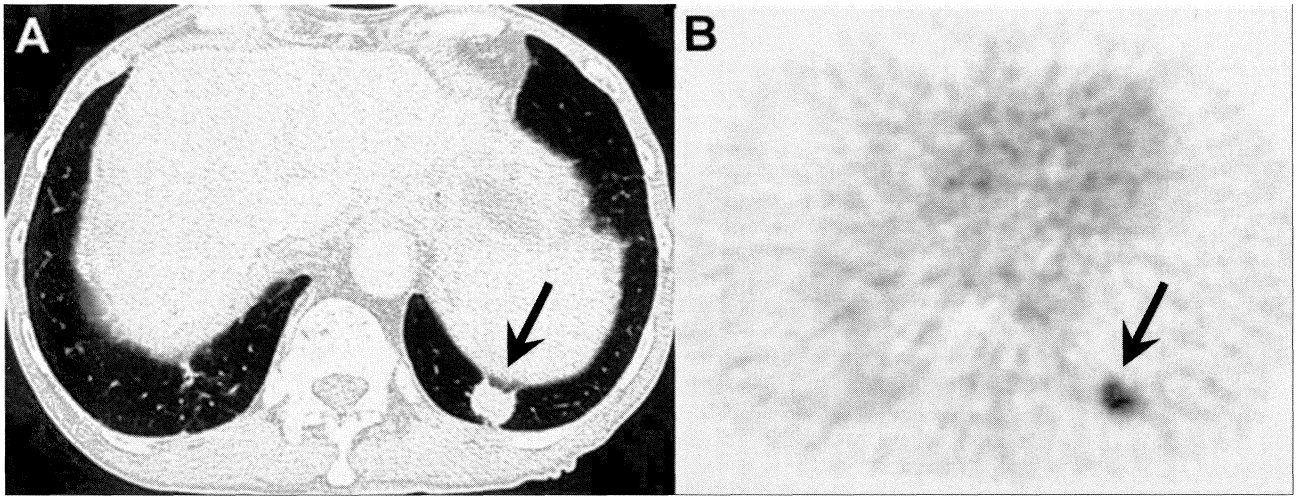

図5. HRCT上solid patternでFDG高集積度を呈した肺腺癌症例
A. CT上、左下葉にsolid patternの腫瘤影を認める(矢印)。
B. FDG PET上、CTの腫瘤影に一致して縦隔より高い集積を認める(FDG高集積度群)(矢印)。
この症例では術後2ヶ月で肝転移による再発が認められた。

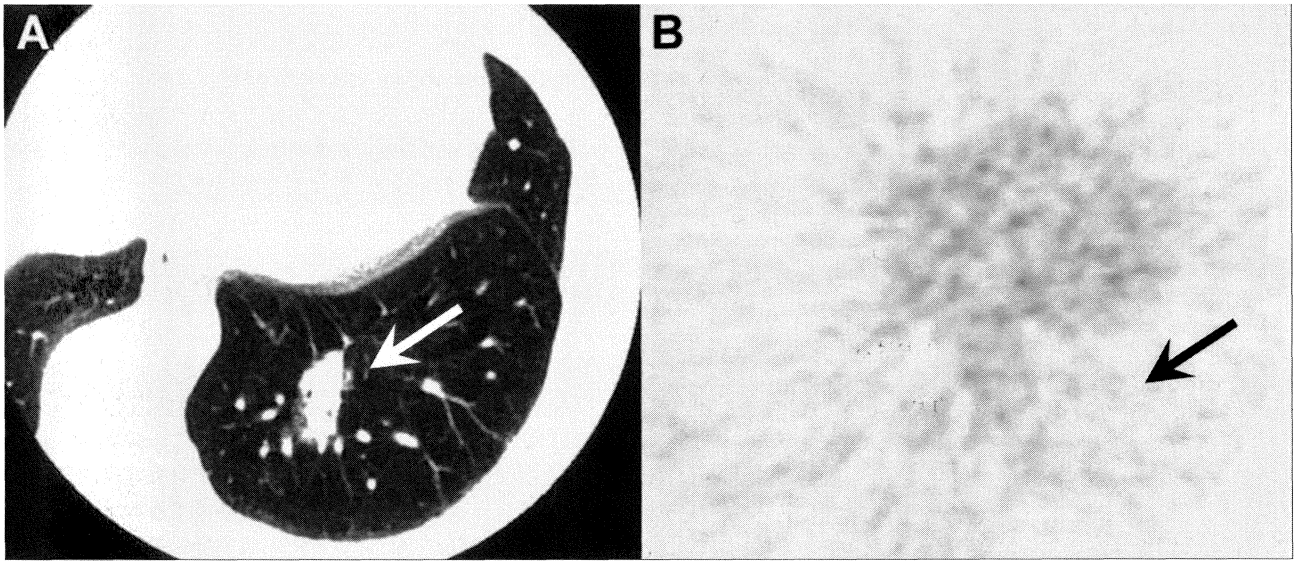

図6. HRCT上solid patternでFDG低集積度を呈した肺腺癌症例
A. CT上、左下葉にsolid patternの腫瘤影を認める(矢印)。
B. FDG PET上、CTの腫瘤影に一致した集積は指摘困難である(FDG低集積度群)(矢印)。
この症例では術後85ヶ月の時点で再発は認められていない。

表6. Solid patternにおける再発に関する主要因子の多変量解析 (Cox比例ハザードモデル)

因子	再発			多変量解析	
	−	+	%	相対危険度(95%信頼区間)	p値
年齢					
65歳未満	22	9	29.0	1.00	0.483
65歳以上	24	7	22.6	0.63(0.17-2.32)	
性別					
男性	21	11	34.4	1.00	0.128
女性	25	5	16.7	0.37(0.10-1.34)	
血清CEA値					
20ng/ml未満	45	12	21.1	1.00	0.996
20ng/ml以上	1	4	80.0	0.99(0.19-5.26)	
病理病期分類					
Ⅰ期	41	7	14.6	1.00	0.040*
Ⅱ・Ⅲ期	5	9	64.3	4.40(1.07-18.11)	
FDG集積度					
低集積度群	24	2	7.7	1.00	0.040*
高集積度群	22	14	38.9	5.47(1.08-27.71)	

*: 統計学有意
相対危険度は全ての因子を含めた結果である。

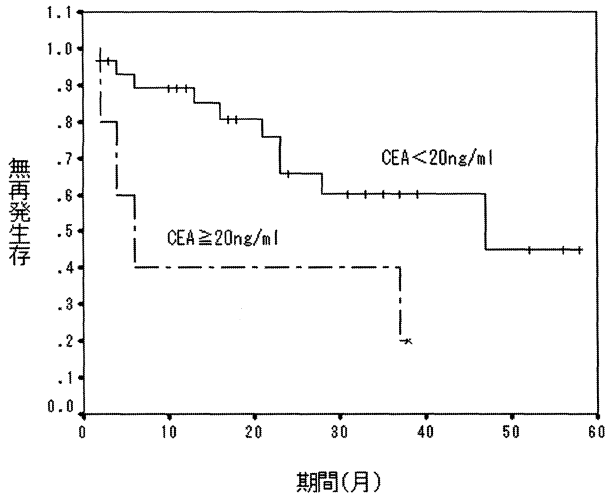

図7. Solid patternかつFDG高集積度群における術前血清CEA値と術後再発(Kaplan-Meier法)
log rank testにてp=0.0461と統計学的有意差が認められた。

CEA値20ng/ml未満の群では32.3% (10/31), 20ng/ml以上の群では80.0% (4/5) で術後再発が認められた。Kaplan-Meier法で, 血清CEA値20ng/ml以上の群は20ng/ml未満の群より有意に術後再発率が高かった (p=0.0461)。

考　　察

1. 肺腺癌原発巣のFDG集積度と浸潤性および術後再発

肺癌における原発巣のFDG集積度は浸潤性予測や予後予測因子としての有用性が報告されている(18,25-28)。FDG集積度の評価方法としては視覚的評価法や半定量的評価法があり, 半定量的評価法では単位体重あたりのFDG投与量に対する集積比であるstandardized uptake value (以下SUV) が多く用いられている。しかし, SUV値は撮像装置や関心領域の選択法, FDG投与から撮像までの時間などに影響される。したがって, 本研究では多機種での比較評価のために視覚的評価を行った。これまでの報告では視覚的評価と半定量的評価法の間には大きな差異は認められなかったとも報告されているが(29), 縦隔と同程度の集積では評価に迷う可能性があることも示唆されている(30)。本研究では2人の核医学医による独立した評価にて差異が認められた場合は合議にて評価の一致が得られた。

本研究では, 原発巣のFDG集積度と病理組織学的浸潤性および術後再発との間に有意な相関が認められた。つまり, 原発巣FDG高集積度群では低集積度群に比較して有意に浸潤性を認める症例が多く, 術後再発率も高いとの結果である。これまでも非小細胞肺癌や肺腺癌においてFDG集積度と病変の生物学的悪性度や予後との関連性が検討され, FDG集積度は分化度や浸潤性と関連し, 予後との相関も認められたことが報告されている(18,25-28)。これらは本研究と一致する結果であった。

2. 肺腺癌原発巣のHRCT所見と浸潤性および術後再発

HRCT所見におけるGGOとは，内部の肺血管が透見認識可能な比較的均一な淡い広がり (すりガラス状陰影) をいう。病理組織学的には肺胞腔内に含気が保たれており，病変が肺胞上皮を置換するように進展し壁の著しい破壊を生じていない状態であり，肺腺癌ではいわゆるBACパターンの腫瘍進展を呈するものである。一方，solid patternは，内部の肺血管が透見困難な充実性陰影と定義し，病理組織学的には肺胞腔内の含気が乏しく，肺腺癌では肺胞上皮非置換性の破壊性・圧排性・充実性増殖や線維化巣の存在が認められるものである(11,31)。BACは間質浸潤のない肺胞上皮置換性進展を示す癌として定義され，理論的には非浸潤癌であるために縮小手術の良い適応と考えられる。したがって，HRCT上のGGO割合がBAC成分の占める割合をよく反映し，生物学的悪性度や予後と相関すると報告されている(9-16)。

GGO割合の計測法には視覚的に面積や径を計測する方法，ソフトウエアを用いる方法などが報告されている。Matsugumaらは過去の報告での計測法を比較検討し，視覚的評価の不確実性を問題としている(14)。本研究ではAokiらの提唱した方法を参照し，腫瘍断面の最大径およびGGO以外の腫瘍部分の最大径から半定量的にGGO割合を算出した(11)。さらに，Matsugumaらは原発巣の病理組織学的浸潤性と術後再発との関連についてGGO割合を10%毎に細分化して比較検討した結果，GGO50%が最適カットオフ値であったと報告している。本研究ではGGO50%を基準として2群に分類したが，GGO50%以上のGGO patternでは病理組織学的浸潤性および術後再発が認められず，統計学的解析でもGGO patternではsolid patternより有意に浸潤性を認める症例が少なく，術後再発率も低いとの結果が得られた。したがって，GGO割合50%が予測因子として一つの基準となる可能性が考えられた。

しかしsolid patternでの更なる評価はHRCTのみでは限界があり，BACの中にはHRCTにてsolid patternを呈するものも存在すること(32)を考慮すると，他検査との総合評価が重要であると考えられた。

3. 術前血清CEA値と病理組織学的浸潤性および術後再発

血清CEAは肺腺癌の腫瘍マーカーの一つであり，予後予測因子としての有用性が検討されている。これまでの文献では血清CEA正常値を基準として検討しているものが多く，病期分類Ⅰ期で再発やリンパ節転移との相関が認められたとの報告や(19-21)，病期分類Ⅰ期以上の症例も含む検討では血清CEA値10ng/mlを基準とした場合に予後との相関が認められたとする報告がある(33,34)。しかし正常値 (5ng/ml以下) をカットオフとした場合では喫煙や糖尿病・腎不全・肝疾患などの良性疾患の影響が否定できないため，本研究では明らかな異常値として血清CEA値20ng/mlを基準値として用いた。結果，血清CEA値と浸潤性および術後再発との間には有意な関連が認められ，術前血清CEA値20ng/ml以上の群では20ng/ml未満の群よりも有意に浸潤性を認める症例が多く，術後再発率も高いことが示された。

4. 原発巣のFDG集積度・HRCT所見，血清CEA値を組み合わせた場合の病理組織学的浸潤性および術後再発との関連

これまでも術後予後予測因子として，血清CEA値とHRCT所見を含む多変量解析結果や原発巣のFDG集積度とHRCT所見を合わせた検討結果が報告されている(35-37)。Sakaoらは臨床病期分類ⅠA期の症例では血清CEA異常値およびHRCT所見にてGGO割合10%未満の群で術後予後不良であったと報告している(35)。しかし，原発巣のFDG集積度・HRCT所見，血清CEA値を含む検討は，検索した限りでは認められなかった。

前述のように，HRCT所見におけるGGO pattern群では病理組織学的浸潤性および術後再発を認めた症例はなく，HRCT上GGO割合50%以上はそれだけで強い予後良好の所見と考えられたが，solid pattern群では他検査との総合評価が必要であることが示唆された。そこで，solid pattern群に限定したうえで術後再発予測因子として，年齢・性別・術前血清CEA値・病理病期分類・FDG集積度を挙げ，多変量解析にて比較検討を行った。結果はFDG集積度が病理病期分類と並んで独立した予後予測因子となった。したがって，solid patternでは原発巣FDG集積度が特に重要な術後再発予測因子であることが証明された。血清CEA値は単変量解析のみで有意な関連が示されたが，これは血清CEA値20ng/ml以上では症例数が少なく全例solid patternかつFDG高集積度群の症例であったことが結果に影響した可能性が考えられた。そこで，solid patternかつFDG高集積度群に限定して更なる検討を行ったところ，血清CEA値と術後再発の間には有意な関連が認められた。したがって，血清CEA値20ng/ml以上も強い予後不良の所見であることが示された。

5. まとめ

肺腺癌 (3cm以下) において原発巣のFDG集積度・HRCT所見，血清CEA値と浸潤性および術後再発との間には，有意な関連が認められた。HRCT上GGO patternを呈した症例では術後再発が認められずGGO patternは強い予後良好の所見と考えられた。HRCT上solid patternを呈した症例ではFDG集積度が独立して重要な術後再発予測因子であることが判明した。さらに，血清CEA値20ng/ml以上は強い予後不良の所見であった。

以上より，肺腺癌 (3cm以下) において原発巣のFDG集積度，HRCT所見，および血清CEA値を組み合わせることにより，術後再発をより高い精度で予測できることが判明した。

稿を終えるにあたり，終始御指導と御高閲を賜りました金沢医科大学放射線診断治療学　利波久雄教授および東光太郎教授，ならびに本論文を御高閲，御教示賜りました病理病態学　勝田省吾教授，呼吸機能治療学 (呼吸器内科学)　栂博久教授，呼吸機能治療学 (呼吸器外科学)　佐川元保教授に深甚なる謝意を表します。また，統計解析の御指導を賜りました健康増進予防医学　三浦克之助教授に深謝いたします。さらに本研究の遂行に際し多大な御支援，御協力をいただきました放射線診断治療学教室員一同に心

より感謝いたします。

なお，本論文の内容は第65回日本医学放射線学会学術集会 (2006年4月　横浜) において発表した。

本研究の一部は，文部科学省科学研究費 (16591232)，厚生労働省がん研究助成(16-5)，日本私立学校振興・共済事業団の学術研究振興資金，および金沢医科大学共同研究 (C2005-2) の補助を受けた。

文　　献

1. 渡辺俊一，小田 誠，野崎善成ほか：組織型と縮小手術. 日胸臨 1999; **58:** 473-9.
2. 小池輝明，寺島雅範，滝沢恒世ほか：縮小手術の適応. 日胸臨 1999; **58:** 463-7.
3. 児玉 憲，東山聖彦，横内秀起ほか：QOLを目的とした縮小手術. 肺癌の臨床 1998; **1:** 537-45.
4. Nakagawa M, Tanaka F, Tsubota N et al: A randomized phase Ⅲ trial of adjuvant chemotherapy with UFT for completely resected pathological stage Ⅰ non-small-cell lung cancer: the West Japan Study Group for Lung Cancer Surgery (WJSG) -the 4th study. Ann Onc 2005; **16:** 75-80.
5. Kato H, Ichinose Y, Ohta M et al: A randomized trial of adjuvant chemotherapy with uracil-tegafur for adenocarcinoma of the lung. N Engl J Med 2004; **350:** 1713-21.
6. Suzuki H, Kawaguchi T, Sio Y et al: Clinicopathologic features of local and metastatic recurrences in primary lung adenocarcinoma. Fukushima J Med Sci 1998; **44:** 13-21.
7. Fu XL, Zhu XZ, Shi DR et al: Study of prognostic predictors for non-small cell lung cancer. Lung Cancer 1999; **23:** 143-52.
8. Osaki T, Nagashima A, Yoshimatsu T et al: Visceral pleural involvement in nonsmall cell lung cancer: prognostic significance. Ann Thorac Surg 2004; **77:** 1769-73.
9. Okada M, Nishio W, Sakamoto T et al: Correlation between computed tomographic findings, bronchioloalveolar carcinoma component, and biologic behavior of small-sized lung adenocarcinomas. J Thorac Cardiovasc Surg 2004; **127:** 857-61.
10. Kuriyama K, Sato M, Kasugai T et al: Ground-grass opacity on thin-section CT: value in differentiating subtypes of adenocarcinoma. AJR Am J Roentgenol 1999; **173:** 465-9.
11. Aoki T, Tomoda Y, Watanabe H et al: Peripheral lung adenocarcinoma: correlation of thin-section CT findings with histologic prognostic factors and survival. Radiology 2001; **220:** 803-9.
12. Kim EA, Johkoh T, Lee KS et al: Quantification of ground-grass opacity on high-resolution CT of small peripheral adenocarcinoma of the lung. AJR Am J Roentgenol 2001; **177:** 1417-22.
13. Matsuguma H, Yokoi K, Anraku M et al: Proportion of ground-glass opacity on high-resolution computed tomography in clinical T1 N0 M0 adenocarcinoma of the lung: A predictor of lymph node metastasis. J Thorac Cardiovasc Surg 2002; **124:** 278-84.
14. Matsuguma H, Nakahara R, Anraku M et al: Objective definition and measurement method of ground-glass opacity for planning limited resection in patients with clinical stage ⅠA adenocarcinoma of the lung. Eur J Cardiothorac Surg 2004; **25:** 1102-6.
15. Ohde Y, Nagai K, Yoshida J et al: The proportion of consolidation to ground-grass opacity on high resolution CT is a good predictor for distinguishing the population of non-invasive peripheral adenocarcinoma. Lung Cancer 2003; **42:** 303-10.
16. Kodama K, Higashiyama M, Yokouchi H et al: Prognostic value of ground-glass opacity found in small lung adenocarcinoma on high-resolution CT scanning. Lung Cancer 2001; **33:** 17-25.
17. 佐々木雅之. 腫瘍FDG-PETの臨床: 日本医放会誌 2001; **61:** 414-20.
18. Higashi K, Ueda Y, Ayabe K et al: FDG PET in the evaluation of the aggressiveness of pulmonary adenocarcinoma: correlation with histopathological features. Nucl Med Commun 2000; **21:** 707-14.
19. Okada M, Sakamoto T, Nishio W et al: Characteristics and prognosis of patients after resection of nonsmall cell lung carcinoma measuring 2 cm or less in greatest dimension. Cancer 2003; **98:** 535-41.
20. Sakao Y, Tomimitsu S, Takeda Y et al: Carcinoembryonic antigen as a predictive factor for postoperative tumor relapse in early-stage lung adenocarcinoma. Eur J Cardiothorac Surg 2004; **25:** 520-2.
21. Tomita M, Matsuzaki Y, Edogawa M et al: Prognostic significance of preoperative serum carcinoembryonic antigen level in lung adenocarcinoma but not squamous cell carcinoma. Ann Thorac Cardiovasc Surg 2004; **10:** 76-9.
22. Frost MA, Coates AS: Plasma carcinoembryonic antigen in an Australian hospital population. Med J Aust 1976; **19:** 950-3.
23. Loewenstein MS, Zamcheck N: Carcinoembryonic antigen (CEA) levels in benign gastrointestinal disease states. Cancer 1978; **42:** 1412-8.
24. Cochran WG: Some methods for strengthening the common χ 2 tests. Biometrics 1954; 417-51.
25. Higashi K, Ueda Y, Yagishita M et al: FDG PET measurement of the proliferative potential of non-small cell lung cancer. J Nucl Med 2000; **41:** 85-92.
26. Higashi K, Ueda Y, Arisaka Y et al: 18F-FDG uptake as a biologic prognostic factor for recurrence in patients with surgically resected non-small cell lung cancer. J Nucl Med 2002; **43:** 39-45.
27. Cheran SK, Nielsen ND, Patz EF Jr.: False-negative findings for primary lung tumors on FDG positron emission tomography: staging and prognostic implications. AJR Am J Roentgenol 2004; **182:** 1129-32.
28. Marom EM, Sarvis S, Herndon JE Ⅱ et al: T1 Lung cancers: sensitivity of diagnosis with fluorodeoxyglucose PET. Radiology 2002; **223:** 453-9.
29. Lowe VJ, Hoffman JM, DeLong DM et al: Semiquantitative and visual analyses of FDG-PET images in pulmonaly abnormalities. J Nucl Med 1994; **35:** 1771-6.
30. Nomori H, Watanabe K, Ohtsuka T et al: Visual and semiquantitative analyses for F-18 fluorodeoxyglucose PET scanning in pulmonary nodules 1 cm to 3 cm in size. Ann Thorac Surg 2005; **79:** 984-8.
31. Aoki T, Nakata H, Watanabe H et al: Evolution of peripheral lung adenocarcinomas: CT findings correlated with histology and tumor dubling time. AJR Am J Roentgenol 2000; **174:** 763-8.
32. Mihara N, Ichikado K, Johkoh T et al: The subtypes of localized bronchioloalveolar carcinoma: CT-pathologic correlation in 18 cases. AJR Am J Roentgenol 1999; **173:** 75-9.
33. Tomita M, Matsuzaki Y, Shimizu T et al: Prognostic determinants for lung cancer patients with preoperative high serum carcinoembryonic antigen levels. Thorac Cardiovasc Surg 2005; **53:** 300-4.
34. Tomita M, Matsuzaki Y, Shimizu T et al: Serum carcinoembryonic antigen levels in pT1 non-small cell lung cancer patients. Anticancer Res 2005; **25:** 3601-5.
35. Sakao Y, Nakazono T, Sakuragi T et al: Predictive factors for survival in surgically resected clinical ⅠA peripheral adenocarcinoma of the lung. Ann Thorac Surg 2004; **77:** 1157-61.
36. Lee KS, Jeong YJ, Han J et al: T1 non-small cell lung cancer: imaging and histopathologic findings and their prognostic implications. RadioGraphics 2004; **24:** 1617-36.
37. Nomori H, Watanabe K, Ohtsuka T et al: Evaluation of F-18 fluorodeoxyglucose (FDG) PET scanning for pulmonary nodules less than 3 cm in diameter, with special reference to the CT images. Lung Cancer 2004; **45:** 19-27.

FDG集積度、HRCT所見、血清CEA値による肺腺癌の術後再発予測

FDG Uptake within the Primary Tumor, HRCT Findings and Serum Level of CEA as Predictors of Recurrence in Patients with Surgically Resected Lung Adenocarcinoma Smaller than 3 cm.

Tomoko Takahashi

Department of Radiology, Kanazawa Medical University, Uchinada, Ishikawa 920-0293, Japan

Recently, small lung cancers have been frequently detected by screening with low-dose computed tomography (CT) examination. The candidates for limited resection are thought to be a group of patients that have less invasive tumors and a better prognosis. In addition, to improve prognosis, pre- and post-operative therapy regimens have been studied in clinical trials. The extent of ground-glass opacity (GGO) within the tumor on high resolution CT (HRCT) findings correlates with aggressiveness and prognosis in patients with lung adenocarcinoma. Positron emission tomography (PET) with ^{18}F-fluorodeoxyglucose (FDG), an *in-vivo* imaging method that measures glucose metabolism, has been used to detect tumors with increased glucose metabolism. FDG uptake within the primary lesion is related to aggressiveness in patients with lung adenocarcinoma. The aim of this study was to clarify the prognostic importance for recurrence of FDG uptake, HRCT findings and serum level of carcinoembryonic antigen (CEA) in patients with lung adenocarcinoma.

Methods: The subjects were 75 patients with lung adenocarcinoma smaller than 3 cm in largest diameter, who underwent standard surgical procedures. Before surgery, FDG PET, HRCT and serum level of CEA were examined. On visual assessment, FDG uptakes within the primary lesions were classified into two grades in comparison with the mediastinal blood pool. The tumor contents were classified into two groups according to the extent of the GGO assessed by HRCT. In addition, CEA level was classified into two groups (<20 ng/ml, >or=20 ng/ml).

Results: FDG uptake, GGO components and serum level of CEA were significantly correlated with aggressiveness (vascular invasion, lymphatic permeation and pleural involvement) in univariate analyses. These were also significant prognostic factors for poor outcome in the Kaplan-Meier method (log rank test). Recurrence was not found in the patients with GGO pattern (GGO>or=50%). Of the patients with solid pattern (GGO<50%), FDG uptake and serum level of CEA were significantly correlated with recurrence. The degree of FDG uptake was found to be an independent prognostic factor in multivariate analyses.

Conclusions: The combination of FDG uptake, HRCT findings and serum level of CEA could be useful for predicting the postoperative prognosis for recurrence.

Key Words: lung adenocarcinoma, ^{18}F-FDG PET, GGO component, serum level of CEA, recurrence

１．研究課題名：モデル動物を利用した肥満・高脂血症の発がんへの関与とその阻止に関する研究（研究番号 C2005-3）

２．キーワード：１）非アルコール性脂肪性肝炎（nonalcoholic steatohepatitis,NASH）
２）肥満（obesity）
３）高脂血症（hyperlipidemia）
４）オーラプテン（auraptene）
５）TOP-GFP マウス（TOP-GFP mouse）

３．研究代表者：杉江　茂幸・医学部・教　授・腫瘍病理学　（病理学Ⅰ）
研究分担者：吉谷新一郎・医学部・助手・消化器外科治療学　（消化器外科学）
甲野　裕之・医学部・助教授・腫瘍病理学　（病理学Ⅰ）
堤　　幹宏・奈良医科大学・先端医学研究機構・教授・医療情報学
山田　泰広・岐阜大学・大学院医学系研究科・講師・腫瘍病理学

４．研 究 目 的

高脂肪食に代表される食事の欧米化や運動不足等が大腸等の発がんを促進することが疫学や動物実験から示唆されている。肥満は生活習慣病の根底をなす病態とされ、これらライフスタイルの変化は肥満者の急増をももたらしている。肥満の発症に関与する遺伝子群(肥満関連遺伝子)にはレプチンや PPARγ等あるが、大腸発がんの危険因子として肥満の重要性あるいは肥満関連遺伝子との関係についての解析は乏しい。一方、肝臓においては、肥満に伴う脂肪肝はよく知られるが、肥満、高脂血症からの非アルコール性脂肪性肝炎(NASH)の増加が近年報告され、高率に肝硬変、肝癌へ進行するとの報告も見られ、肥満者・高脂血症患者における肝がんの発生を阻止することは重要と考えられる。本研究では、柑橘類化合物（auraptene、nobiletin）についてレプチン受容体欠損のため高レプチン血症を伴う db マウスや高脂血症を伴う Min マウスを用いて、大腸発がん及び肝発がんに対する修飾効果を検討する。これにより、肥満阻止、大腸・肝発がん阻止のための基礎的資料を得、柑橘類化合物等の天然物の肥満に係る発がん阻止物質としての可能性を探る。

５．研 究 計 画

１） Azoxymethane (AOM)誘発 db/db マウス大腸前駆病変モデル系を用いたがん化学予防物質の検索:レプチン受容体欠損の db/db マウスを用いて、柑橘由来成分である auraptene による AOM 誘発大腸がん前駆病変の修飾作用について検討した。

２） Min マウス炎症性大腸発がんモデルにおける血中脂質との関連性の検討：Apc 遺伝子に異常をもつ Min マウスに大腸炎誘発物質である dextran sodium sulfate (DSS)を投与し、大腸がんの発生頻度と血中脂質成分との関連について検討した。

３） 肥満および高脂血症と脂肪肝の関連性を明らかにするために、OLETF ラットを長期間飼育し、内臓肥満の程度、血糖値、血清コレステロール値と中性脂肪値、血清 AST、ALT 値および脂肪肝の程度を経時的に検討する。次いで、高脂血症あるいは脂肪肝の発生した時点から FEN を投与し、FEN の脂肪肝に対する有用性について検討を行う。

４） Beta-catenin/tcf 転写活性を可視化するために、Tcf binding elements (TBE)の下流に EGFP を結合したトランスジーンを持つマウス(TOP-GFP マウス)を作製し、高脂肪食投与によるその活性化を検討する。

６．研 究 成 果

１） AOM 誘発 db/db マウス大腸前駆病変モデル系を用いたがん化学予防物質の検索：Auraptene は大腸がん前駆病変である aberrant crypt foci (ACF) およびβ-catenin accumulated crypt (BCAC)の発生を有意に抑制した。また、Auraptene の投与により血中中性脂肪濃度の低下を認めた。

２） Min マウス炎症性大腸発がんモデルにおける血中脂質との関連性の検討：大腸腫瘍発生頻度および個数と血中中性脂肪濃度が正の相関を示し、大腸がん発生に対し中性脂肪が深く関わっている可能性が示唆された。

３） 脂肪肝の発生は、１２週齢から生じ、２４週齢には肝の約５０％に脂肪変性が認められた。血清 AST および ALT 値は、両群間で明らかな差は認められなかった。血清 Cholesterol および Triglyceride 値は、OLETF では LETO に比べて高値であったが、５６週間の飼育中には、大きな変化が認められなかった。OLEFT 群の血中インシュリン値は、 １２週齢より増加し始め LEOT の約２倍の値を示した。この成績を基に、１２週齢から FEN の投与を開始した。FEN 投与後２４週まで、２週間隔でラットを屠殺し、脂肪肝の程度と内臓肥満の程度および血糖値、血清コレステロール値、中性脂肪値、血清 AST と ALT 値の測定を行った。FEN 投与群では、血清コレステロールおよび中性脂肪値は、非投与群に比べ、有意に低下したが、血糖値、血清 AST 値および血清 ALT 値には明らかな差は認められなかった。脂肪肝および内臓脂肪の程度についての詳細な検討を現在行っている。

４） TOP-GFP マウスは 3 つの異なるラインを確立した。このマウスでは、脾臓細胞の初代培養にて、GSK-3beta の阻害剤であるリチウムクロライド処理により、GFP 発現の増加が確認され、生体において beta-catenin/tcf 転写活性の検出が可能であることが分かった。さらに、このレポーターマウスを家族性大腸腺腫症のモデルマウスである Apc Min マウスに交配し、大腸腫瘍での beta-catenin/tcf 転写活性を検討した。その結果、大腸腫瘍では著しい転写活性の亢進が確認され、この pathway の活性化が大腸発がんに重要な役割を果たすことが示唆された。

７．研究の考察・反省

１，２）柑橘由来成分である auraptene が db/db マウス大腸前駆病変モデル系において、肥満による大腸前駆病変の有意な抑制を示し、同時に血中中性脂肪濃度を低下させた。また、Min マウスを用いた炎症性大腸発がんモデル系においても、大腸腫瘍発生頻度および個数と血中中性脂肪濃度が正の相関を示しており、肥満マウス系と同様、大腸がん発生において血清脂質深く関わっていると考えられ、血清脂質濃度をコントロールすることにより大腸がんの発生を予防できる可能性が示唆された。

３）内臓肥満、2 型糖尿病、高脂血症、脂肪肝を自然に発症する OLETF ラットを用いて、NASH に対する FEN の有用性について検討を行ったが、脂肪肝は認められるものの明らかな脂肪肝炎を誘発させるまでには至らなかった。しかし、FEN の投与が、自然発症する脂肪

肝および高脂血症に対しては、有効であることが示唆された。

4）TOP-GFP マウスは生体において beta-catenin/tcf 転写活性を検出可能であり、個体レベルでの複雑な生体現象における Wnt pathway 活性化の意義を明らかにするために、非常に有用であると考えられる。期間内には実施できなかったが、今後はこのマウスモデルにおいて高脂肪食投与による、beta-catenin/tcf 転写活性への影響を検討し、大腸発がんへの関与を明らかにしたい。一方で GFP は生体臓器において高いバックグラウンドを示し、本来の転写活性との区別が場合によっては困難であることが明らかとなった。現在、GFP の代わりに luciferase をレポーターに持つマウス（TOP-Luc マウス）を作製している所である。

８．研 究 発 表

Hata K, Tanaka T, Kohno H, Suzuki R, Qiang SH, Yamada Y, Oyama T, Kuno T, Hirose Y, Hara A, Mori H. β-Catenin-accumulated crypts in the colonic mucosa of juvenile *Apc*$^{Min/+}$ mice. Cancer Lett 2006; 239: 123-128.

Miyamoto S, Kohno H, Suzuki R, Sugie S, Murakami A, Ohigashi H, Tanaka T. Preventive effects of chrysin on the development of azoxymethane-induced colonic aberrant crypt foci in rats. Oncol Rep 2006; 15: 1169-1173.

Available online at www.sciencedirect.com
SCIENCE DIRECT
ELSEVIER
Cancer Letters 239 (2006) 123–128
CANCER Letters
www.elsevier.com/locate/canlet

β-Catenin-accumulated crypts in the colonic mucosa of juvenile $Apc^{Min/+}$ mice

Kazuya Hata[a,b], Takuji Tanaka[c,*], Hiroyuki Kohno[c], Rikako Suzuki[c], Sheng Hong Qiang[b], Yasuhiro Yamada[b], Takeshi Oyama[b], Toshiya Kuno[b], Yoshinobu Hirose[b], Akira Hara[b], Hideki Mori[b]

[a]*BMR Laboratories, Sunplanet Co., Ltd, 4388 Hagiwara, Kamiishidu, Yourou, Gifu 503-1602, Japan*
[b]*Department of Tumor Pathology, Gifu University School of Medicine, 1-1 Yanagido, Gifu 501-1194, Japan*
[c]*Department of Oncologic Pathology, Kanazawa Medical University, 1-1 Daigaku, Uchinada, Ishikawa 920-0293, Japan*

Received 2 May 2005; received in revised form 25 July 2005; accepted 28 July 2005

Abstract

Although $Apc^{Min/+}$ mice are widely used for an animal model of human familial adenomatous polyposis (FAP), a majority of intestinal polyps locate in the small intestine. We recently reported that numerous β-catenin-accumulated crypts (BCAC), which are reliable precursor lesions for colonic adenocarcinoma, develop in the large bowel of aged $Apc^{Min/+}$ mice. In this study, we determined the presence and location of BCAC in the large intestine of juvenile $Apc^{Min/+}$ mice (3 and 5 weeks of age). Surprisingly, BCAC were noted in the colon of even $Apc^{Min/+}$ mice of both ages, and mainly located in the distal and middle segments of the colon. Also, a few microadenomas were detected in $Apc^{Min/+}$ mice of 5-week old. Our results may indicate need of further investigation of the colorectal mucosa of $Apc^{Min/+}$ mice for examining colorectal carcinogenesis using $Apc^{Min/+}$ mice.

Keywords: β-Catenin-accumulated crypts; C57BL/6J-$Apc^{Min/+}$; Juvenile mice

1. Introduction

Aberrant crypt foci (ACF) and BCAC are widely used as markers for evaluating colorectal carcinogenic risk in rodents [1,2] and humans [3]. ACF proposed by Bird [1,2], are morphologically distinguished from their surrounding crypts on colonic mucosa stained with methylene blue [1]. While they are considered as putative precursor lesions for colonic adenocarcinoma and frequently used for preclinical cancer chemoprevention studies [4,5], we have recently proposed that β-catenin-accumulated crypts (BCAC) rather than ACF are reliable precancerous lesions for colonic adenocarcinoma [6–8].

Mutant mouse lineage being predisposed to $Apc^{Min/+}$ is regarded as one of the models for colorectal tumorigenesis [9]. Originally, this lineage was established from an ethylnitrosourea-treated

* Corresponding author. Tel.: +81 76 286 2211x3611; fax: +81 76 286 6926.
E-mail address: takutt@kanazawa-med.ac.jp (T. Tanaka).

0304-3835/$ - see front matter © 2005 Elsevier Ireland Ltd. All rights reserved.
doi:10.1016/j.canlet.2005.07.033

C57BL/6J male mouse, and its phenotype is a fully penetrate autosomal dominant trait. The dominant mutation is known to be located in Apc, the mouse homologue of the human *APC* gene, resulting in truncation of the gene product at amino acid 850 [10]. Although homozygous $Apc^{Min/Min}$ mice die as embryos [11], $Apc^{Min/+}$ mice develop multiple intestinal tumors in the small intestine. However, unlike in human familial adenomatous polyposis (FAP), colonic neoplasms are rarely detected in the large intestine. We previously documented that numerous BCAC, which could be useful for detecting the modifying effects of xenobiotics in colon carcinogenesis in mice and rats [6,12], develop in the colorectal mucosa of adult $Apc^{Min/+}$ mice aged over 20 weeks [13]. The presence of spontaneous ACF [14] or dysplastic ACF (ACF_{Min}) [15] are also known in $Apc^{Min/+}$ mice, but their frequency is low.

Since certain hit(s) on the BCAC may lead to tumor development in $Apc^{Min/+}$ mice [16], we, in the present study, turned attention to the presence of BCAC in the large bowel of juvenile $Apc^{Min/+}$ mice and determined where BCAC develop.

2. Materials and methods

2.1. Animals

The mice were bred at our laboratory, from inbred mice originally purchased from The Jackson Laboratory (Bar Harbor, ME). The $Apc^{Min/+}$ pedigree was maintained by mating $Apc^{+/+}$ females with $Apc^{Min/+}$ males, and procedures to secure inbreeding were followed. The $Apc^{Min/+}$ mice were identified by allele-specific PCR on DNA isolated from tail. All mice used for the experiment were maintained in the well-controlled room with a high-efficiency particulate air (HEPA) filter, a 12 h lighting (7:00–19:00), 25 ± 2 °C room temperature, and 55 ± 15% humidity. Mice (5 mice/cage) were housed in polycarbonate cages measuring W225 × D338 × H140 mm (Japan CLEA, Inc., Tokyo, Japan) with the floor covered with a sheet of roll paper (Japan SLC). Water and diet were given ad libitum. The mice were given a basal diet, MF (Oriental Yeast Co., Ltd, Tokyo, Japan), during gestation and until 5 weeks of age. We fully complied with the 'Guidelines Concerning Experimental Animals' issued by the Japanese Association for Laboratory Animal Science and exercised due consideration so as not to cause any ethical problem.

2.2. Experimental procedure

A total of 54 mice were used in this study: $Apc^{Min/+}$ mice of 3 weeks of age (7 females and 8 males) or 5 weeks of age (7 females and 6 males)) and $Apc^{+/+}$ mice of 3 weeks of age (8 females and 6 males) or 5 weeks of age (5 females and 7 males). The $Apc^{Min/+}$ mice were autopsied at 3-week and 5-week of age respectively for measurement of the large intestines as well as detection of ACF and BCAC in the large intestinal mucosa. At sacrifice the large bowels were removed, flushed with saline, fixed flat in 10% buffered formalin for 24 h at room temperature, and then processed for histopathological evaluation by routine procedures [17]. To identify aberrant classical ACF [1], mucosal surface of the colons were stained with methylene blue. In brief, fixed colons were placed in 0.5% solution of methylene blue in distilled water for 30 s. They were then placed mucosal side up on a microscope slide and ACF were counted under a light microscope at a magnification of ×40.

2.3. Tissue preparation

To identify intramucosal lesions ACF and BCAC, colon was divided into three (distal, middle, and proximal) segments and embedded in paraffin. A total of 162 segments were examined by using an en face preparation and 3–5-μm thick serial sections were made [6,7]. For each case, two serial sections were used to analyze the intramucosal lesions.

2.4. Histopathology and immunohistochemistry

Two serial sections were subjected to hematoxylin and eosin (H and E) staining for histopathology and β-catenin immunohistochemistry for enumeration of BCAC [12]. Immunohistochemistry for β-catenin was performed on 4-μm-thick paraffin-embedded sections from all segments of the colons, using the labeled streptavidin-biotin method (LSAB KIT; DAKO, Glostrup, Denmark) with microwave

accentuation. The paraffin-embedded sections were heated for 30 min at 65 °C, deparaffinized in xylene, and rehydrated through graded alcohols at room temperature. A 0.05 M Tris–HCl buffer (pH 7.6) was used to prepare solutions and for washes between various steps. Sections were treated for 40 min at room temperature with 2% bovine serum albumin and incubated overnight at 4 °C with a primary antibody against β-catenin protein (diluted 1:1000, Transduction Laboratories, Lexington, KY, USA). Horseradish peroxidase activity was visualized by treatment with H_2O_2 and diaminobenzidine for 5 min. Negative control sections were immunostained without the primary antibody. Immunoreactivities were regarded as positive if the apparent stainings were detected in cytoplasm and/or nuclei for determining BCAC.

2.5. Statistical analysis

Data on the frequency of BCAC were analyzed by two-way ANOVA, Bonferroni post hoc tests, and a $P<0.05$ was considered significant.

3. Results

The classical ACF proposed by Bird [1] were not observed in any mice examined, but BCAC (Fig. 1), mostly less than 50 μm in diameter, were identified in the colon of $Apc^{Min/+}$ mice of both sexes. There were no BCAC in $Apc^{+/+}$ mice of both sexes. As shown in Table 1, the mean numbers of BCAC in 5 weeks old $Apc^{Min/+}$ of both sexes were significantly greater than those in 3 weeks old $Apc^{Min/+}$ mice of both sexes ($P<0.001$). As for the distribution of BCAC, the lesions mainly located in the distal and middle segments with a few in the proximal part: 3 weeks of age: distal vs. proximal parts, $P<0.01$ for females and males, middle vs. proximal parts. $P<0.01$ for females and $P<0.001$ for males; and 5 weeks of age: distal vs. proximal parts, $P<0.001$ for females and $P<0.001$ for males, middle vs. proximal parts. $P<0.01$ for females and $P<0.001$ for males). The mean numbers of BCAC at the distal and middle parts in 5 weeks old $Apc^{Min/+}$ of both sexes were also significantly greater than those in 3 weeks old $Apc^{Min/+}$ mice of both sexes (the distal part:

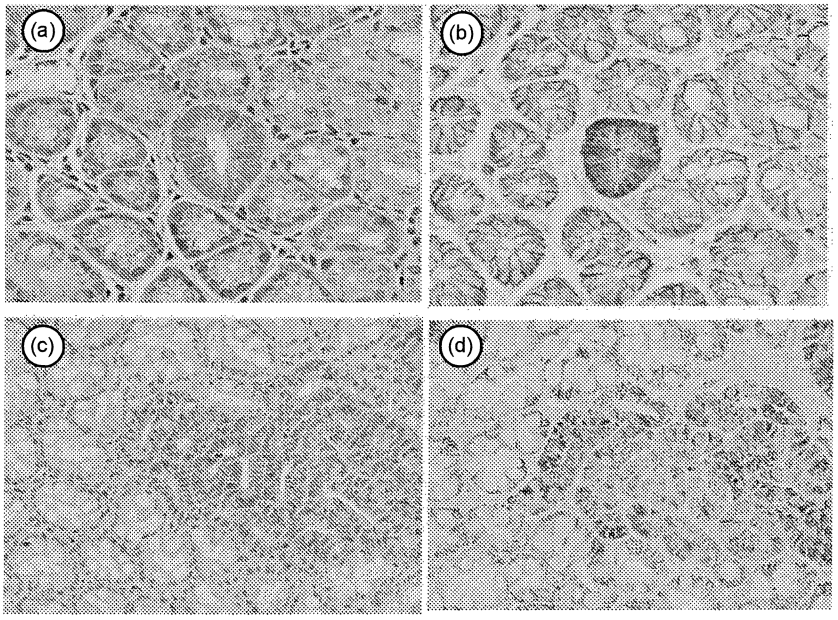

Fig. 1. A BCAC (a, b) found in the middle segment of the colon of a $Apc^{Min/+}$ female mouse aged 5 weeks and a microadenoma (c, d) observed in the middle segment of the colon of a $Apc^{Min/+}$ male mouse aged 5 weeks. A BCAC is consisted of one crypt (a) and positive for β-catenin immunohistochemistry (b). A microadenoma compresses surrounding crypts (c) and shows positive reactivity for β-catenin the cytoplasm (d). (a, c) H and E stain and (b, d) β-catenin immunohistochemistry. Original magnification, (a–d) ×100.

Table 1
Numbers of BCAC in C57BL/6J-$APC^{Min/+}$ and $APC^{+/+}$ mice at 3 and 5 weeks of age

Weeks of age	Genotype	Sex	No. of mice examined	No. of BCAC per segment			
				Total	Distal	Middle	Proximal
3	$Apc^{Min/+}$	Female	7	3.43±1.13[a]	1.71±0.76	1.57±0.79	0.14±0.38
	$Apc^{+/+}$	Female	8	0	0	0	0
	$Apc^{Min/+}$	Male	8	4.50±1.85	1.88±0.99	2.50±1.31	0.13±0.35
	$Apc^{+/+}$	Male	6	0	0	0	0
5	$Apc^{Min/+}$	Female	7	9.86±2.34	4.71±0.76	4.71±1.98	0.43±0.53
	$Apc^{+/+}$	Female	5	0	0	0	0
	$Apc^{Min/+}$	Male	6	9.67±2.66	4.83±1.17	4.50±2.17	0.33±0.52
	$Apc^{+/+}$	Male	7	0	0	0	0

($P<0.01$) ($P<0.001$) ($P<0.001$) ($P<0.01$) ($P<0.01$) ($P<0.001$) ($P<0.001$) ($P<0.001$) ($P<0.05$) ($P<0.001$) ($P<0.001$)

[a]Mean SD.
Statistical analysis was done by two-way ANOVA, Bonferroni post hoe tests.

$P<0.001$ for males and females; and the middle part: $P<0.01$ for females and $P<0.05$ for males). As illustrated in Fig. 1, most BCAC consisted of one or two crypts at both ages. A single microadenoma developed in a male and a female $Apc^{+/+}$ mice of 5 weeks old.

4. Discussion

$Apc^{Min/+}$ mice are heterozygous for a nonsense mutation in the *Apc* gene [13,15]. They develop spontaneously $Apc^{Min/+}$ mice similarly to the FAP syndrome in humans [13,15]. However, the distributing pattern of intestinal tumors in $Apc^{Min/+}$ mice is different from that in human FAP. Most adenomatous polyps in the FAP patients arise in the colon and, if left untreated, lead to colonic cancers [18]. In contrast, the highest frequency of tumors (adenomas) in $Apc^{Min/+}$ mice is seen in the small intestine, whereas small number of tumors develop in the colon [19]. Our results described here showed that there are BCAC that are hardly identified in the whole mount preparations in the colonic mucosa of the $Apc^{Min/+}$ mice.

Dysplastic ACF (ACF_{Min}) were reported to be present in he colon of $Apc^{Min/+}$ mice at 7 weeks of age and were positive for β-catenin [15]. Their number was small, but increased when $Apc^{Min/+}$ mice were treated with a colonic carcinogen azoxymethane (AOM) [15]. We considered that BCAC described here are similar lesions as dysplastic ACF (ACF_{Min}), because of similar size (less than 50 μm), their increase in number with aging and carcinogen treatment [15] like in the case of BCAC [13]. However, the frequency of spontaneous dysplastic ACF (ACF_{Min}) in the $Apc^{Min/+}$ mice at 7 weeks of age [15] was much lower than that found our mice at 3 and 5 weeks of ages. In contrast to classical ACF, ACF_{Min} are not elevated lesions above the surrounding mucosa, their detection depends on methylene blue staining and transillumination [20]. Also, the tissue preparation (cross section vs. whole mount) may contribute to the difference in the numbers of spontaneous dysplastic ACF (ACF_{Min}) [20] and BCAC in the current study. However, our findings that there were no classic ACF in the colon of juvenile $Apc^{Min/+}$ mice are in agreement with the reported absence or vaery rare development of ACF in the colon of $Apc^{\Delta 716}$ knockout mice and Min mice [20–23].

Surprisingly we observed a microadenomas in the $Apc^{Min/+}$ mice of either sex even at 5 weeks of age. In our previous work with aged $Apc^{Min/+}$ mice (20–23 weeks of age), the frequency of microadenomas were $17.85 \pm 9.86/cm^2$ with a diameter of 176.04 ± 410.84 μm in the colon [13]. Thus, our previous [13] and present findings may suggest that BCAC with a few microadenomas are already present in the colon of juvenile $Apc^{Min/+}$ mice and increase in their number and growth with aging. This may be likely in the case of human FAP. However, we [13] and others [15] did not observe colonic adenocarcinomas in untreated $Apc^{Min/+}$ mice, although multiple exposure of AOM produced a number of this malignancy [24]. As reported microadenomatous crypts have lost of the remaining allele of *Apc* in old $Apc^{Min/+}$ mice, suggesting that loss of *Apc* function in such crypts. However, our recent work [16] has demonstrated that exposure of a colitis-inducing agent dextran sodium sulfate results in numerous colonic adenocarcinomas in $Apc^{Min/+}$ mice of either sex. Additional promotion (inflammation [25]) stimuli are enough to produce colonic epithelial malignancy in the colon of $Apc^{Min/+}$ mice. The findings may indicate the importance of inflammatory stimuli in the progression of BCAC through microadenomas to colonic malignancy in $Apc^{Min/+}$ mice, although detailed mechanisms that what kinds of factors involve in a powerful promotion effect of this agent should be clarified.

In conclusion, our findings may offer a valuable clue to detection of precancerous colonic lesions and provide a new insight that experimentation using $Apc^{Min/+}$ mice can be applied for investigation of colon carcinogenesis as well as small intestinal tumorigenesis.

Acknowledgements

We wish to thank Kyoko Takahashi, Tomoko Kajita and Misato Yasuda for their technical assistance, and Yoshihisa Wakita and Shinya Tanahashi for care of the animals. This study was supported in part by the Grant-in-Aid for Cancer Research from the Ministry of Health, Labour and Welfare of Japan; the Grant-in-Aid for the 3rd Term for a Comprehensive 10-year Strategy for Cancer Control from the Ministry of Health, Labour and Welfare of Japan; the Grants-in-Aid for Scientific Research (Nos. 15-2052 and 15592007) from the Ministry of Education, Culture, Sports, Science and Technology of Japan; and the grants (H2005-6 and C2005-3) from Kanazawa Medical University.

References

[1] R.P. Bird, Observation and quantification of aberrant crypts in the murine colon treated with a colon carcinogen: preliminary findings, Cancer Lett. 37 (1987) 147–151.
[2] R.P. Bird, Role of aberrant crypt foci in understanding the pathogenesis of colon cancer, Cancer Lett. 93 (1995) 55–71.
[3] I.M. Siu, T.G. Pretlow, S.B. Amini, T.P. Pretlow, Identification of dysplasia in human colonic aberrant crypt foci, Am. J. Pathol. 150 (1997) 1805–1813.
[4] D.E. Corpet, S. Tache, Most effective colon cancer chemopreventive agents in rats: a systematic review of aberrant crypt foci and tumor data, ranked by potency, Nutr, Cancer 43 (2002) 1–21.
[5] D.E. Corpet, F. Pierre, Point: From animal models to prevention of colon cancer. Systematic review of chemoprevention in min mice and choice of the model system, Cancer Epidemiol. Biomarkers Prev. 12 (2003) 391–400.
[6] Y. Yamada, N. Yoshimi, Y. Hirose, K. Kawabata, K. Matsunaga, M. Shimizu, A. Hara, H. Mori, Frequent β-catenin gene mutations and accumulations of the protein in the putative preneoplastic lesions lacking macroscopic aberrant crypt foci appearance, in rat colon carcinogenesis, Cancer Res. 60 (2000) 3323–3327.
[7] Y. Yamada, N. Yoshimi, Y. Hirose, K. Matsunaga, M. Katayama, K. Sakata, M. Shimizu, T. Kuno, H. Mori, Sequential analysis of morphological and biological properties of β-catenin-accumulated crypts, provable premalignant lesions independent of aberrant crypt foci in rat colon carcinogenesis, Cancer Res. 61 (2001) 1874–1878.
[8] Y. Yamada, N. Yoshimi, Y. Hirose, A. Hara, M. Shimizu, T. Kuno, M. Katayama, Z. Qiao, H. Mori, Suppression of occurrence and advancement of β-catenin-accumulated crypts, possible premalignant lesions of colon cancer, by selective cyclooxygenase-2 inhibitor, celecoxib, Jpn. J. Cancer Res. 92 (2001) 617–623.
[9] A.R. Moser, H.C. Pitot, W.F. Dove, A dominant mutation that predisposes to multiple intestinal neoplasia in the mouse, Science 247 (1990) 322–324.
[10] L.K. Su, K.W. Kinzler, B. Vogelstein, A.C. Preisinger, A.R. Moser, C. Luongo, K.A. Gould, W.F. Dove, Multiple intestinal neoplasia caused by a mutation in the murine homolog of the APC gene, Science 256 (1992) 668–670.
[11] M. Oshima, H. Oshima, K. Kitagawa, M. Kobayashi, C. Itakura, M. Taketo, Loss of *Apc* heterozygosity and abnormal tissue building in nascent intestinal polyps in mice carrying a truncated *Apc* gene, Proc. Natl. Acad. Sci. USA 92 (1995) 4482–4486.

[12] K. Hata, Y. Yamada, T. Kuno, Y. Hirose, A. Hara, S.H. Qiang, H. Mori, Tumor formation is correlated with expression of β-catenin-accumulated crypts in azoxymethane-induced colon carcinogenesis in mice, Cancer Sci. 95 (2004) 316–320.
[13] Y. Yamada, K. Hata, Y. Hirose, A. Hara, S. Sugie, T. Kuno, N. Yoshimi, T. Tanaka, H. Mori, Microadenomatous lesions involving loss of *Apc* heterozygosity in the colon of adult *ApcMin/+* mice, Cancer Res. 62 (2002) 6367–6370.
[14] T.P. Pretlow, W. Edelmann, R. Kucherlapati, T.G. Pretlow, L.H. Augenlicht, Spontaneous aberrant crypt foci in *Apc1638N* mice with a mutant *Apc* allele, Am. J. Pathol. 163 (2003) 1757–1763.
[15] J.E. Paulsen, I.L. Steffensen, E.M. Loberg, T. Husoy, E. Namork, J. Alexander, Qualitative and quantitative relationship between dysplastic aberrant crypt foci and tumorigenesis in the *Min/+* mouse colon, Cancer Res. 61 (2001) 5010–5015.
[16] T. Tanaka, H. Kohno, R. Suzuki, K. Hata, S. Sugie, N. Niho, K. Sakano, M. Takahashi, K. Wakabayashi, Dextran sodium sulfate strongly promotes colorectal carcinogenesis in *ApcMin/+* mice: Inflammatory stimuli by dextran sodium sulfate results in development of multiple colonic neoplasms, Int. J. Cancer, in press.
[17] K. Kawabata, T. Tanaka, T. Murakami, T. Okada, H. Murai, T. Yamamoto, A. Hara, M. Shimizu, Y. Yamada, K. Matsunaga, T. Kuno, N. Yoshimi, S. Sugie, H. Mori, Dietary prevention of azoxymethane-induced colon carcinogenesis with rice-germ in F344 rats, Carcinogenesis 20 (1999) 2109–2115.
[18] K.W. Kinzler, B. Vogelstein, Lessons from hereditary colorectal cancer, Cell 87 (1996) 15–170.
[19] C.V. Rao, I. Cooma, J.G. Rodriguez, B. Simi, K. El-Bayoumy, B.S. Reddy, Chemoprevention of familial adenomatous polyposis development in the APC^{min} mouse model by 1,4-phenylene bis(methylene)selenocyanate, Carcinogenesis 21 (2000) 617–621.
[20] J.E. Paulsen, E. Namork, I.L. Steffensen, T.J. Eide, J. Alexander, Identification and quantification of aberrant crypt foci in the colon of Min mice—a murine model of familial adenomatous polyposis, Scand. J. Gastroenterol. 35 (2000) 534–539.
[21] H. Oshima, M. Oshima, M. Kobayashi, M. Tsutsumi, M.M. Taketo, Morphological and molecular processes of polyp formation in $Apc^{\Delta 716}$ knockout mice, Cancer Res. 57 (1997) 1644–1649.
[22] R.F. Jacoby, D.J. Marshall, M.A. Newton, K. Novakovic, K. Tutsch, C.E. Cole, R.A. Lubet, G.J. Kelloff, A. Verma, A.R. Moser, W. Dove, Chemoprevention of spontaneous intestinal adenomas in the *ApcMin* mouse model by the nonsteroidal anti-inflammatory drug piroxicam, Cancer Res. 56 (1996) 710–714.
[23] A.H. Reitmair, J.C. Cai, M. Bjerknes, M. Redston, H. Cheng, M. Pind, K. Hay, A. Mitri, B. Bapat, T.W. Mak, S. Gallinger, MSH2 deficiency contributes to accelerated APC-mediated intestinal tumorigenesis, Cancer Res. 56 (1996) 2922–2926.
[24] M. Suzui, M. Okuno, T. Tanaka, H. Nakagama, H. Moriwaki, Enhanced colon carcinogenesis induced by azoxymethane in min mice occurs via a mechanism independent of β-catenin mutation, Cancer Lett. 183 (2002) 31–41.
[25] M. Philip, D.A. Rowley, H. Schreiber, Inflammation as a tumor promoter in cancer induction, Semin. Cancer Biol. 14 (2004) 433–439.

Preventive effects of chrysin on the development of azoxymethane-induced colonic aberrant crypt foci in rats

SHINGO MIYAMOTO[1], HIROYUKI KOHNO[2], RIKAKO SUZUKI[2], SHIGEYUKI SUGIE[2], AKIRA MURAKAMI[1], HAJIME OHIGASHI[1] and TAKUJI TANAKA[2]

[1]Division of Food Science and Biotechnology, Graduate School of Agriculture, Kyoto University, Kyoto 606-8502; [2]Department of Oncologic Pathology, Kanazawa Medical University, 1-1 Daigaku, Uchinada, Ishikawa 920-0293, Japan

Received October 4, 2005; Accepted December 2, 2005

Abstract. The modifying effects of dietary feeding with chrysin (5,7-dihydroxyflavone) on the development of azoxymethane (AOM)-induced colonic aberrant crypt foci (ACF) were investigated in male F344 rats. We also assessed the effect of chrysin on mitosis and apoptosis in 'normal appearing' crypts. To induce ACF, rats were given two weekly subcutaneous injections of AOM (20 mg/kg body weight). They also received an experimental diet containing chrysin (0.001 or 0.01%) for 4 weeks, starting 1 week before the first dose of AOM. AOM exposure produced a substantial number of ACF (73±13/rat) at the end of the study (week 4). Dietary administration of chrysin caused significant reduction in the frequency of ACF: 0.001% chrysin, 37±17/rat (49% reduction, $P<0.001$); and 0.01% chrysin, 40±10/rat (45% reduction, $P<0.001$). In addition, chrysin administration significantly reduced the mitotic index and significantly increased the apoptotic index in 'normal appearing' crypts. These findings might suggest a possible chemopreventive activity of chrysin in the early step of colon tumorigenesis through modulation of cryptal cell proliferation activity and apoptosis.

Introduction

Colorectal cancer is one of the leading causes of cancer death in Western countries. Globally, colorectal cancer accounted for approximately 1 million new cases in 2002 (9.4% of the world) and mortality is approximately one half that of incidence (~529,000 deaths in 2002) (1). In Japan, its incidence has been increasing and colonic malignancy is now the third leading cause of cancer death. In this context, primary prevention, including chemoprevention, is important for fighting this malignancy.

Flavonoids are plant secondary metabolites ubiquitously distributed throughout the plant kingdom, and numerous reports have shown their biological effects, such as anti-oxidative and anti-inflammatory activity. They also act as inhibitors of several enzymes that are activated in certain inflammatory conditions (2), while a variety of cell types associated with the immune system are down-regulated by certain flavonoids *in vitro* (3). Further, most flavonoids show potent anti-oxidative/radical scavenging effects (4). A natural flavonoid, chrysin (5,7-dihydroxyflavone, Fig. 1), which is a potent inhibitor of the enzyme, CYP1A (5), and aromatase (6), is present in many plants, honey, and propolis (7,8). Studies have shown that chrysin suppresses lipopolysaccharide (LPS)-induced cyclooxygenase (COX)-2 and inducible nitric oxide synthase (iNOS) expression through the activation of peroxisome proliferator-activated receptor (PPAR)-γ (9). In our previous studies, a polymethoxy flavonoid, nobiletin (5,6,7,8,3',4'-hexamethoxyflavone), suppressed the expression of proinflammatory genes, such as iNOS and COX-2, *in vitro* (10) and inhibited azoxymethane (AOM)-induced rat colon carcinogenesis (11). In addition, pomegranate (*Punica granatum L.*) seed oil, which contains more than 70% conjugated linolenic acids, in the diet suppressed AOM-induced colon carcinogenesis in rats through an up-regulation of PPARγ protein in the non-tumorous colonic mucosa (12). Thus, proinflammatory genes and PPARγ are good targets for chemoprevention of colon carcinogenesis.

Recently, several *in vitro* studies have shown that chrysin is able to inhibit the growth of Hela cells by downregulating the expression of proliferating cell nuclear antigen (PCNA) (13), induce apoptosis via caspase activation and Akt inactivation in U937 leukemia cells (14), and cause cell-cycle arrest in human colon cancer cells (15), and C6 glioma cells (16). However, there are few reports investigating whether chrysin has cancer chemopreventive effects on the colon in experimental animal studies.

In the current study, we investigated the possible suppressing effect of chrysin on the occurrence of AOM-induced aberrant crypt foci (ACF), which are putative preneoplastic lesions for colonic adenocarcinoma (17-19), with a short-term rat ACF bioassay. In addition, we assess

Correspondence to: Dr Shingo Miyamoto, Division of Food Science and Biotechnology, Graduate School of Agriculture, Kyoto University, Kyoto 606-8502, Japan
E-mail: shingo7@kanazawa-med.ac.jp

Key words: chrysin, aberrant crypt foci, mitosis, apoptosis

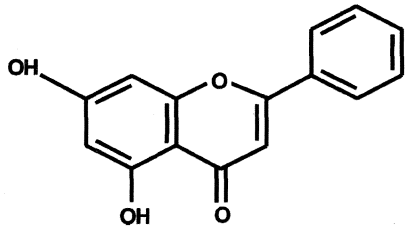

Figure 1. Chemical structure of chrysin.

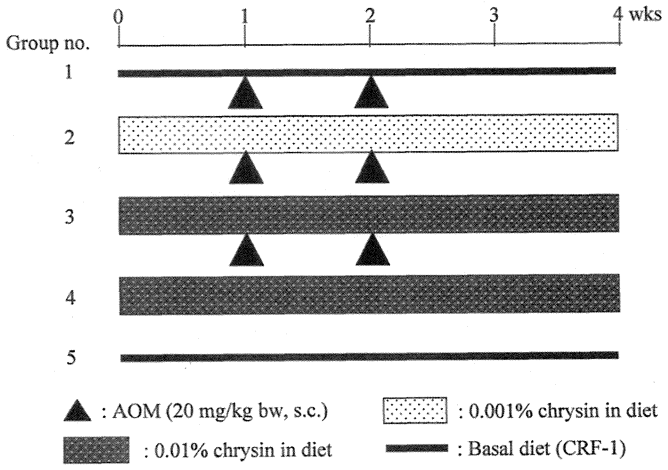

Figure 2. Experimental protocol.

whether dietary chrysin affects cell proliferation activity and induces apoptosis in the colonic epithelium, since certain chemopreventive agents exert cancer inhibitory action through reduction of cell proliferating activity (20) and induction of apoptosis (21) in the target tissue.

Materials and methods

Animals, chemicals and diet. Male F344 rats (Charles River Japan, Inc, Kanazawa, Japan), aged 4 weeks, were used for an ACF assay. The animals were maintained in Kanazawa Medical University Animal Facility according to the Institutional Animal Care Guidelines. All animals were housed in plastic cages (4 rats/cage) with free access to tap water and a basal MF diet (Oriental Yeast, Co., Ltd., Nagoya, Japan) under controlled conditions of humidity (50±10%), lighting (12-h light/dark cycle), and temperature (23±2˚C). They were quarantined for 7 days after arrival, and randomized by body weight into experimental and control groups. AOM for ACF induction was purchased from Sigma-Aldrich Chemical Co. (St. Louis, MO, USA). Chrysin was obtained from Funakoshi Co. (Tokyo, Japan).

Experimental procedure for ACF. A total of 32 male F344 rats were divided into five experimental and control groups (Fig. 2). Animals in groups 1 through 3 were initiated with AOM by two weekly subcutaneous injections (20 mg/kg body weight) to induce colonic ACF. Rats in groups 2 and 3 were fed diets containing 0.001% and 0.01% chrysin for 4 weeks, respectively, starting one week before the first dose of AOM. Group 4 did not receive AOM and were given the diet containing 0.01% chrysin. Group 5 served as an untreated control. At week 4, rats were sacrificed under ether anesthesia to assess the occurrence of colonic ACF and we performed a careful necropsy, with emphasis on the colon, liver, kidney, lung, and heart. All grossly abnormal lesions in any tissue and the organs, e.g. liver (caudate lobe), kidney, lung, and heart, were fixed in 10% buffered formalin solution for histopathology.

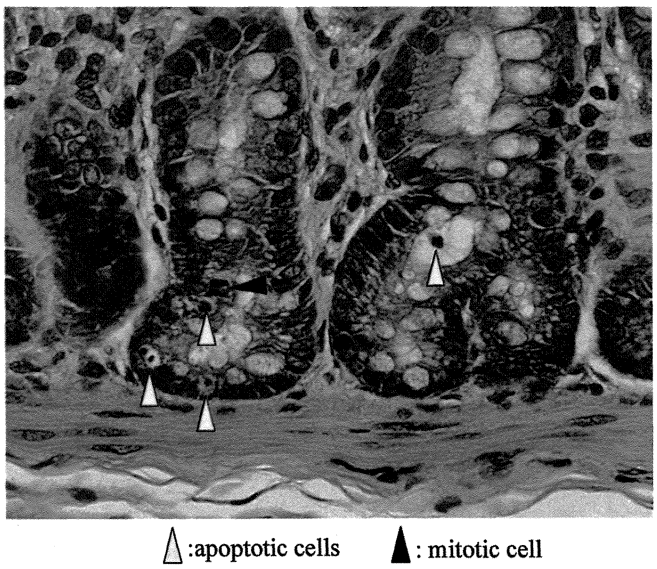

Figure 3. Apoptotic and mitotic cells in the crypt from the distal colon, which was stained with hematoxylin and eosin, from a rat in group 3 (AOM+0.01% chrysin). Apoptotic cells are identified by cell shrinkage, homogeneous basophilic and condensed nuclei, nuclear fragments (apoptotic bodies), marked eosinophilic condensation of cytoplasm and sharply delineated cell borders surrounded by a clear halo. Yellow arrowheads indicate apoptotic cells and the black arrowhead indicates a mitotic cell.

Determination of ACF. The frequency of ACF was determined according to the method described in our previous report (22). At necropsy, the colons were flushed with saline, excised, cut open longitudinally along the main axis, and then washed with saline. They were cut and fixed in 10% buffered formalin for at least 24 h. The fixed colons were dipped in a 0.5% solution of methylene blue in distilled water for 30 sec, and placed on a microscope slide to count the ACF.

Counting mitotic and apoptotic cells. To identify intramucosal apoptotic and mitotic cells in the crypts, the distal colon (2 cm from the anus) was cut out, embedded in paraffin, and 4 μm-thick serial sections were made. The paraffin-embedded sections were stained with hematoxylin and eosin (H&E) and evaluated under a light microscope for apoptotic and mitotic cells at a magnification of 400 (Fig. 3). Apoptotic cells were identified by cell shrinkage, homogeneous basophilic and condensed nuclei, nuclear fragments (apoptotic bodies), marked eosinophilic condensation of the cytoplasm, and sharply delineated cell borders surrounded by a clear halo (23). The apoptotic and mitotic indices in the colonic crypts were determined on longitudinal sections that allowed evaluation of the whole crypt from the top to the base.

Table I. Body, liver, and relative liver weights.

Group no.	Treatment (no. of rats examined)	Body weight (g)	Liver weight (g)	Relative liver weight (g/100 g body weight)
1	AOM alone (8)	194±8[a]	9.7±0.7	5.00±0.68
2	AOM+0.001% chrysin (8)	192±7	10.5±1.1	5.47±0.45
3	AOM+0.01% chrysin (8)	195±5	9.9±0.5	5.10±0.18
4	0.01% chrysin (4)	203±7	10.5±0.9	5.14±0.28
5	No treatment (4)	196±9	9.4±0.5	4.80±0.17

[a]Mean ± SD.

Table II. Effect of chrysin on AOM-induced ACF formation in male F344 rats.

Group no.	Treatment (no. of rats examined)	Incidence (%)	Total no. of ACF/colon	Total no. of aberrant crypts/colon	No. of aberrant crypts/focus
1	AOM alone (8)	8/8 (100%)	73±13[a]	145±28	1.98±0.10
2	AOM+0.001% chrysin (8)	8/8 (100%)	37±17[b]	67±29[b]	1.81±0.14[c]
3	AOM+0.01% chrysin (8)	8/8 (100%)	40±10[b]	69±21[b]	1.73±0.09[b]
4	0.01% chrysin (4)	0/4 (0%)	0	0	0
5	No treatment (4)	0/4 (0%)	0	0	0

[a]Mean ± SD, [b]significantly different from group 1 by one-way ANOVA with Bonferroni correction (P<0.001), [c]significantly different from group 1 by one-way ANOVA with Bonferroni correction (P<0.05).

Table III. Effect of chrysin on size of ACF induced by AOM.

Group no.	Treatment	% of ACF containing:			
	(no. of rats examined)	1 crypt	2 crypts	3 crypts	≥ 4 crypts
1	AOM alone (8)	43.1±4.7[a]	27.9±5.9	19.1±5.2	9.9±2.7
2	AOM+0.001% chrysin (8)	44.2±3.8	38.4±4.7[b]	0.3±4.1[b]	7.1±6.1
3	AOM+0.01% chrysin (8)	47.3±5.5	34.4±6.4	16.3±3.9[c]	2.0±3.1[b]

[a]Mean ± SD, [b]significantly different from group 1 by one-way ANOVA with Bonferroni correction (P<0.01), [c]significantly different from group 2 by one-way ANOVA with Bonferroni correction (P<0.05).

Randomly chosen crypts (28-57 crypts/colon) with well-oriented crypt structure from the mouth to the base were evaluated for counting apoptosis and mitosis. The apoptotic and mitotic indices were determined by dividing the total number of apoptotic or mitotic cells by the number of epithelial cells evaluated.

Statistical evaluation. Where applicable, data were analyzed using one-way ANOVA with Bonferroni correction (GraphPad Instat version 3.05, GraphPad Softwear, San Diego, CA, USA) with P<0.05 as the criterion of significance.

Results

General observation. All animals remained healthy throughout the experimental period. Food consumption (g/day/rat) did not differ significantly among the groups (data not shown). As shown in Table I, the mean body, liver and relative liver weights (g/100 g body weight) in all groups did not differ significantly at the end of the study. Further, no significant pathological alternations were found in organs other than the colon.

Frequency of ACF. Table II summarizes the data on colonic ACF formation. All rats belonging to groups 1 through 3, which were treated with AOM, developed ACF. In groups 4 and 5, there was no microscopically observable change, including ACF, in colonic morphology. The mean number of ACF/colon in group 1 was 73±13. Dietary administration of chrysin (groups 2 and 3) significantly reduced the ACF incidence when compared to group 1: 49% reduction by 0.001% chrysin (group 2), P<0.001; and 45% reduction by

Table IV. Epithelial proliferative kinetics in the distal colon.

Group no.	Treatment (no. of crypts examined)	Mitotic index (%)	Apoptotic index (%)	Crypt column height
1	AOM alone (44)	4.3±2.5[a,b]	1.2±1.6	44.2±10.1[b]
2	AOM+0.001% chrysin (38)	3.2±2.5	3.2±2.3[c]	43.3±6.9
3	AOM+0.01% chrysin (57)	1.4±1.4[c]	3.7±2.1[c]	55.4±10.2[c]
4	0.01% chrysin (56)	1.8±1.4	1.2±1.2	54.0±11.1[d]
5	No treatment (28)	1.3±1.4	0.8±1.0	62.0±11.7

[a]Mean ± SD, [b]significantly different from group 5 by one-way ANOVA with Bonferroni correction (P<0.001), [c]significantly different from group 1 by one-way ANOVA with Bonferroni correction (P<0.001), [d]significantly different from group 5 by one-way ANOVA with Bonferroni correction (P<0.01)

0.01% chrysin (group 3), P<0.001. In addition, there were significant decreases in the total number of aberrant crypts (ACs) per colon (P<0.001), and in the number of ACs per focus in group 2 (9% reduction, P<0.05) and group 3 (13% reduction, P<0.001) when compared to group 1. The size distribution of ACF induced by AOM in groups 1-3 showed in Table III. The percentages of ACF consisting of one crypt did not significantly differ among these three groups. Although the percentage of ACF with 2 crypts in group 2 was significantly greater than that in group 1 (P<0.01), the values of ACF with 3 crypts in groups 2 and 3 were significantly smaller than in group 1 (P<0.01 and P<0.05, respectively). As for the percentage of ACF with ≥ 4 crypts, the value in group 3 was significantly lower than that in group 1 (P<0.01).

Indices of mitosis and apoptosis in colonic crypts. The data on the epithelial proliferative kinetics in 'normal appearing' distal colon are summarized in Table IV. The mitotic index was significantly higher in group 1 (4.3±2.5, 331% increase, P<0.001) than in group 5. The dietary administration of chrysin (groups 2 and 3) reduced the mitotic index in a dose-dependent manner when compared to group 1: 26% reduction by 0.001% chrysin (group 2); and 67% reduction by 0.01% chrysin, P<0.001 (group 3). Feeding with 0.01% chrysin alone (group 4) did not affect the mitotic index in the crypts. The apoptotic indices of groups 1, 4 and 5 were comparable, but the values in groups 2 and 3 were significantly increased when compared to group 1 (P<0.001). As for the crypt column height (no. of cells/crypt), the value in group 1 was significantly smaller than in group 5 (P<0.001). The crypt column height of group 3 was significantly larger than that of group 1 (P<0.001). The value in group 4 was significantly lower than in group 5 (P<0.01).

Discussion

The results described here clearly indicate that dietary administration of chrysin at dose levels of 0.001% and 0.01% significantly inhibited AOM-induced ACF formation in male F344 rats. Moreover, the percentage of ACF that consisted of 4 or more aberrant crypts was significantly reduced by feeding with the diet supplemented with 0.01% chrysin. These findings indicate that dietary chrysin effectively suppresses the early phase of chemically-induced rat colon tumorigenesis. Also, the inhibitory effect of chrysin (0.001%) in the diet on the formation of large ACF may suggest suppression of the late stage of AOM-induced colon carcinogenesis, since the number of large ACF is well correlated with the incidence of colonic adenocarcinoma induced by a colonic carcinogen, AOM (18,19,24). Our results are the first to show the chemopreventive ability of chrysin in ACF formation in an *in vivo* study with a colon carcinogenesis model.

The oral disposition of the dietary flavonoid, chrysin, in humans has been reported (25). Seven healthy subjects were administered 400 mg chrysin orally and the areas under the plasma concentration-time curves (AUCs) and urinary recoveries of chrysin and metabolites were measured. As a result, peak plasma chrysin concentrations were only 3-16 ng ml^{-1} with AUCs of 5-193 ng ml^{-1} h, whereas chrysin sulphate concentrations were 30-fold higher (AUC 450-4220 ng ml^{-1} h). In urine, chrysin and chrysin glucuronide accounted for 0.2-3.1 mg and 2-26 mg, respectively. Most of the dose appeared in faeces as unchanged chrysin. These findings, together with our data, might suggest that unchanged chrysin exists, not in plasma but in intestine, and directly affects the proliferation activity of cryptal cells.

Chrysin is a natural flavonoid that is contained in many plants, honey and propolis. Flavonoids are dietary polyphenols derived from fruits and vegetables (26). Epidemiological observations strongly suggest flavonoids to be preventive in coronary heart disease (27,28), stroke (29) and certain cancers (30). In this study, dietary administration of chrysin reduced the number of mitotic cells and increased the number of apoptotic cells. Recent studies have shown that chrysin induces apoptosis through caspase activation and Akt inactivation in U937 leukemia cells (14), and G2/M cell-cycle arrest in human colon carcinoma SW480 cells (15). Our results are in accordance with those in these *in vitro* studies. Certain components, such as caffeic acid esters and artepillin C, of propolis, which is used as a traditional medicine with a long history in Eastern Europe and Brazil, have been reported to exert antimutagenic and anticarcinogenic effects (31-33). The findings in this study suggest that other components, like chrysin in propolis (0.8 mmol chrysin/100 g of Brazilian propolis) (34), may serve as cancer chemopreventive agents.

In conclusion, this study demonstrates for the first time that dietary administration of chrysin significantly inhibits the development of AOM-induced colonic ACF in rats.

Although the exact mechanisms by which chrysin inhibits ACF development remain to be elucidated, it would appear that the modulation of colon tumorigenesis by chrysin in diet is associated with the alteration of cell proliferation activity and apoptosis.

Acknowledgements

This work was supported in part by a Grant-in-Aid for Cancer Research, for the Third-Term Comprehensive 10-Year Strategy for Cancer Control from the Ministry of Health, Labour and Welfare of Japan; a Grant-in-Aid (no. 15•2052) for Scientific Research from the Ministry of Education, Culture, Sports, Science and Technology of Japan; a grant (H2005-6) for the Project Research from the High-Technology Center of Kanazawa Medical University; and a grant (C2005-3) for Collaborative Research from Kanazawa Medical University.

References

1. Parkin DM, Bray F, Ferlay J and Pisani P: Global cancer statistics, 2002. CA Cancer J Clin 55: 74-108, 2005.
2. Havsteen B: Flavonoids, a class of natural products of high pharmacological potency. Biochem Pharmacol 32: 1141-1148, 1983.
3. Middleton EJ and Kandaswami C: Effects of flavonoids on immune and inflammatory cell functions. Biochem Pharmacol 43: 1167-1179, 1992.
4. Mora A, Paya M, Rios JL and Alcaraz MJ: Structure-activity relationships of polymethoxyflavones and other flavonoids as inhibitors of non-enzymic lipid peroxidation. Biochem Pharmacol 40: 793-797, 1990.
5. Tsyrlov IB, Mikhailenko VM and Gelboin HV: Isozyme- and species-specific susceptibility of cDNA-expressed CYP1A P-450s to different flavonoids. Biochim Biophys Acta 1205: 325-335, 1994.
6. Sanderson JT, Hordijk J, Denison MS, Springsteel MF, Nantz MH and van den Berg M: Induction and inhibition of aromatase (CYP19) activity by natural and synthetic flavonoid compounds in H295R human adrenocortical carcinoma cells. Toxicol Sci 82: 70-79, 2004.
7. Williams CA, Harborne JB, Newman M, Greenham J and Eagles J: Chrysin and other leaf exudate flavonoids in the genus Pelargonium. Phytochemistry 46: 1349-1353, 1997.
8. Rapta P, Misik V, Stasko A and Vrabel I: Redox intermediates of flavonoids and caffeic acid esters from propolis: an EPR spectroscopy and cyclic voltammetry study. Free Radic Biol Med 18: 901-908, 1995.
9. Liang YC, Tsai SH, Tsai DC, Lin-Shiau SY and Lin JK: Suppression of inducible cyclooxygenase and nitric oxide synthase through activation of peroxisome proliferator-activated receptor-gamma by flavonoids in mouse macrophages. FEBS Lett 496: 12-18, 2001.
10. Murakami A, Matsumoto K, Koshimizu K and Ohigashi H: Effects of selected food factors with chemopreventive properties on combined lipopolysaccharide- and interferon-gamma-induced IkappaB degradation in RAW264.7 macrophages. Cancer Lett 195: 17-25, 2003.
11. Suzuki R, Kohno H, Murakami A, *et al*: Citrus nobiletin inhibits azoxymethane-induced large bowel carcinogenesis in rats. Biofactors 22: 111-114, 2004.
12. Kohno H, Suzuki R, Yasui Y, Hosokawa M, Miyashita K and Tanaka T: Pomegranate seed oil rich in conjugated linolenic acid suppresses chemically induced colon carcinogenesis in rats. Cancer Sci 95: 481-486, 2004.
13. Zhang T, Chen X, Qu L, Wu J, Cui R and Zhao Y: Chrysin and its phosphate ester inhibit cell proliferation and induce apoptosis in Hela cells. Bioorg Med Chem 12: 6097-6105, 2004.
14. Woo KJ, Jeong YJ, Park JW and Kwon TK: Chrysin-induced apoptosis is mediated through caspase activation and Akt inactivation in U937 leukemia cells. Biochem Biophys Res Commun 325: 1215-1222, 2004.
15. Wang W, VanAlstyne PC, Irons KA, Chen S, Stewart JW and Birt DF: Individual and interactive effects of apigenin analogs on G2/M cell-cycle arrest in human colon carcinoma cell lines. Nutr Cancer 48: 106-114, 2004.
16. Weng MS, Ho YS and Lin JK: Chrysin induces G1 phase cell cycle arrest in C6 glioma cells through inducing p21Waf1/Cip1 expression: involvement of p38 mitogen-activated protein kinase. Biochem Pharmacol 69: 1815-1827, 2005.
17. Pretlow TP, Barrow BJ, Ashton WS, *et al*: Aberrant crypts: putative preneoplastic foci in human colonic mucosa. Cancer Res 51: 1564-1547, 1991.
18. Pretlow TP, O'Riordan MA, Somich GA, Amini SB and Pretlow TG: Aberrant crypts correlate with tumor incidence in F344 rats treated with azoxymethane and phytate. Carcinogenesis 13: 1509-1512, 1992.
19. Bird RP: Role of aberrant crypt foci in understanding the pathogenesis of colon cancer. Cancer Lett 93: 55-71, 1995.
20. Kohno H, Maeda M, Honjo S, *et al*: Prevention of colonic preneoplastic lesions by the ß-cryptoxanthin and hesperidin rich powder prepared from *Citrus Unshiu* Marc. juice in male F344 rats. J Toxicol Pathol 12: 209-215, 1999.
21. Pereira MA: Prevention of colon cancer and modulation of aberrant crypt foci, cell proliferation, and apoptosis by retinoids and NSAIDs. Adv Exp Med Biol 470: 55-63, 1999.
22. Tanaka T, Kawabata K, Kakumoto M, *et al*: Citrus auraptene inhibits chemically induced colonic aberrant crypt foci in male F344 rats. Carcinogenesis 18: 2155-2161, 1997.
23. Wyllie AH, Kerr JF and Currie AR: Cell death: the significance of apoptosis. Int Rev Cytol 68: 251-306, 1980.
24. McLellan EA, Medline A and Bird RP: Sequential analyses of the growth and morphological characteristics of aberrant crypt foci: putative preneoplastic lesions. Cancer Res. 51: 5270-5274, 1991.
25. Walle T, Otake Y, Brubaker JA, Walle UK and Halushka PV: Disposition and metabolism of the flavonoid chrysin in normal volunteers. Br J Clin Pharmacol 51: 143-146, 2001.
26. Hertog MGL, Hollman PCH and van de Putte B: Content of potentially anticarcinogenic flavonoids of tea infusions, wines, and fruit juices. J Agric Food Chem 41: 1242-1246, 1993.
27. Hertog MG, Feskens EJ, Hollman PC, Katan MB and Kromhout D: Dietary antioxidant flavonoids and risk of coronary heart disease: The Zutphen Elderly Study. Lancet 342: 1007-1011, 1993.
28. Knekt P, Jarvinen R, Reunanen A and Maatela J: Flavonoid intake and coronary mortality in Finland: A cohort study. BMJ 312: 478-481, 1996.
29. Keli SO, Hertog MG, Feskens EJ and Kromhout D: Dietary flavonoids, antioxidant vitamins, and incidence of stroke: The Zutphen study. Arch Intern Med 156: 637-642, 1996.
30. Le Marchand L, Murphy SP, Hankin JH, Wilkens LR and Kolonel LN: Intake of flavonoids and lung cancer. J Natl Cancer Inst 92: 154-160, 2000.
31. Rao CV, Desai D, Kaul B, Amin S and Reddy BS: Effect of caffeic acid esters on carcinogen-induced mutagenicity and human colon adenocarcinoma cell growth. Chem Biol Interact 84: 277-290, 1992.
32. Frenkel K, Wei H, Bhimani R, *et al*: Inhibition of tumor promoter-mediated processes in mouse skin and bovine lens by caffeic acid phenethyl ester. Cancer Res 53: 1255-1261, 1993.
33. Kimoto T, Arai S, Kohguchi M, *et al*: Apoptosis and suppression of tumor growth by artepillin C extracted from Brazilian propolis. Cancer Detect Prev 22: 506-515, 1998.
34. Shimizu K, Ashida H, Matsuura Y and Kanazawa K: Anti-oxidative bioavailability of artepillin C in Brazilian propolis. Arch Biochem Biophys 424: 181-188, 2004.

１．研究課題名：細胞膜リピッドラフト制御による新規抗癌剤および免疫抑制剤の開発
（研究番号　C2005-4）

２．キーワード：１）リピッドラフト（lipid rafts）
２）アポトーシス（apoptosis）
３）活性化シグナル（activation signal）
４）T 細胞（T cells）
５）スフィンゴミエリン（sphingomyelin）

３．研究代表者：梅原　久範・医学部・教　授・血液免疫制御学（血液免疫内科学）
研究分担者：岡崎　俊朗・鳥取大学・医学部・教　授・血液内科
南　　康博・神戸大学・医学部・教　授・ゲノム科学
小川　法良・医学部・助教授・血液免疫制御学（血液免疫内科学）
（現：浜松医科大学第３内科）

４．研 究 目 的

細胞膜からの活性化シグナル伝達の足場としてマイクロドメイン（ラフト）の存在が近年注目を浴びている。Fas 依存性アポトーシスにおいてもラフトの関与が証明され、ラフト凝集におけるセラミドの必要性が示唆されている。ある種の抗癌剤は Fas 依存性アポトーシスを誘導するが､薬剤耐性を獲得した場合この過程に障害が生じる。しかし、アポトーシスおよびラフト機能の解析において、細胞膜スフィンゴ脂質の解析はほとんどなされていなかった。我々は、下記に示す如く、スフィンゴミエリン合成酵素の遺伝子同定と、細胞膜スフィンゴミエリン欠失細胞および機能回復株を樹立しえた。ここに至り、アポトーシスにおける Fas およびラフトの凝集過程、DISC 形成過程、セラミド合成過程におけるスフィンゴミエリンの解析が可能となり、アポトーシスの詳細な解析と薬剤耐性機序の解明が可能となりえた。今回の研究課題では、世界に先駆けてアポトーシスおよび細胞活性化機構におけるラフト・フィンゴミエリンの機能解析を行いたい。

５．研 究 計 画

A) スフィンゴミエリン欠失細胞株における Fas 誘導 apoptosis の解析

１） 薬剤耐性を示す HL60 細胞株(WR/Mock)から調整した cDNA library を PIRES 2-EGFP ヒトベクターに組み込み、G418 およびグルコシルセラミド合成酵素阻害剤の存在下に、スフィンゴミエリン合成回復株(WR22)を樹立した。スフィンゴミエリン合成細胞および欠失細胞からスフィンゴミエリン合成酵素(SMS-1)をクローニングした（岡崎、梅原)。

２） WR22 および WR/Mock 細胞における細胞膜リピッドラフトを confocal microscopy による解析を行う（梅原、金)。

３） 両細胞における Fas 誘導シグナルおよび T 細胞活性化シグナルの差異を検討する（梅原、南)。

４） 細胞膜リピッドラフトを sucrose gradient による分離し組成の相違を解析する（梅原、金)。

５） ラフト分画における ganglioside GM1 量とスフィンゴミエリン量を比較検討する（梅原、岡崎)。

６） アポトーシスおよび活性化刺激によるラフト分画でのセラミド合成能を検討する（梅原、岡崎)。

B) スフィンゴミエリン欠失 T 細胞株の樹立と T 細胞活性化シグナルの解析

１） ヒトＴ細胞株 Jurkat 細胞に SMS-1 遺伝子 Si-RNA を遺伝子導入し、スフィンゴミエリン合成低下株を樹立する(Jurkat/kd)（梅原、金)。

２） さらに限界希釈法および薬剤耐性機序を用いてスフィンゴミエリン合成低下株を樹立する(Jurkat/kd)（梅原、金)。

３） 両細胞を抗 CD3 抗体で架橋刺激し、細胞増殖活性を MTT アッセイで評価する（梅原、岡崎、金)。

４） CD３架橋刺激によるラフト凝集能および TCR 凝集能を共焦点顕微鏡で検討する（梅原、岡崎、南)。

５） CD3 刺激細胞増殖において､Lck、Fyn などのチロシンキナーゼ活性化を in vitro kinase assay で、アダプター蛋白 LAT のリン酸化を抗 LAT 抗体の免疫沈降物を抗チロシンリン酸化抗体による免疫ブロット法で検討する（梅原、南)。

６） 両細胞において CD3 分子のリピッドラフトへの移行量をショ糖比重密度勾配により分画したラフト内で検討する（梅原、金)。

６．研 究 成 果

A) スフィンゴミエリン欠失細胞株細胞株における Fas 誘導 apoptosis の解析

１）スフィンゴミエリン欠質細胞およびコントロール細胞を抗 Fas 抗体（CH11）で刺激し、apoptosis を sub G1 法で FACS で解析し、両細胞における apoptosis の差異を明らかにした。Fas 架橋刺激による、DISC 形成の検出、Caspase 活性の測定、ミトコンドリア膜電位の測定を行なった。

２）細胞膜 lipid raft の confocal microscopy による解析

スフィンゴミエリン欠失細胞株における lipid raft の形態および機能を明らかにした。細胞膜でのスフィンゴミエリンの局在を明らかにするために、スフィンゴミエリンに特異的に結合する MBP 結合 lysenin と PE 標識抗 MBP 抗体を用いて染色した。Fas 架橋刺激による Cluster 形成を FITC-、 PE-標識 Fas 抗体で検出し、ラフト構成における ganglioside GM1 とスフィンゴミエリンおよび Fas の動態を明らかにした。 スフィンゴミエリン欠失細胞株では、Fas の凝集が抑制されていた。

３）Fas 誘導シグナルの差異の検討:Fas 架橋刺激に伴う、FADD、 Caspase-8 と Fas との結合を western blotting および免疫沈降法を用いて検討した。リピッドラフトを sucrose gradient 法により分画し、ganglioside GM1 量とスフィンゴミエリン量を比較検討した。Fas 刺激に伴う FADD や Caspase などのシグナル伝達物質の lipid raft への移行を検討した。スフィンゴミエリン欠失細胞では、Fas 刺激による caspase-8、caspase-3 活性が抑制されていた。また､Fas に会合する FADD、Caspase-8

量も低下していた。その結果 Fas によるアポトーシスがスフィンゴミエリン欠失細胞では障害されていることが明らかになった。

B) スフィンゴミエリン欠失 T 細胞株の樹立と T 細胞活性化シグナルの解析

１） ヒト T 細胞株 Jurkat 細胞に SMS-1 遺伝子 Si-RNA を遺伝子導入し、スフィンゴミエリン合成低下株（Jurkat/kd）の樹立に成功した。

２） 両細胞を抗 CD3 抗体で架橋刺激し、細胞増殖活性を MTT アッセイで評価したところ、Jurkat/kd 細胞では有意に低下していた。

３） CD３架橋刺激によるラフト凝集能および TCR 凝集能を共焦点顕微鏡で検討したところ、Jurkat/kd 細胞では TCR 凝集能が有意に低下していた。

４） CD3 刺激細胞増殖において、Lck、Fyn などのチロシンキナーゼ活性化を in vitro kinase assay で、アダプター蛋白 LAT のリン酸化を抗 LAT 抗体の免疫沈降物を抗チロシンリン酸化抗体による免疫ブロット法で検討したところ、Jurkat/kd 細胞では細胞内チロシン化蛋白、LAT のチロシンリン酸化が有意に低下していた。

５） 両細胞において CD3 分子のリピッドラフトへの移行量をショ糖比重密度勾配により検討したところ、Jurkat/kd 細胞では CD3 分子のリピッドラフトへの移行量が有意に低下していた。

７．研究の考察・反省

上記の結果より、細胞膜スフィンゴミエリンはリピッドラフトの機能の本質を担う細胞膜脂質である事が明らかとなった。その欠質は、Fas を介した細胞のアポトーシスの障害、T 細胞レセプターを介した細胞活性化の障害に直結する結果を得た。今後は、細胞膜リピッドラフトを制御しうる薬物の検討に入り、抗がん剤抵抗性を獲得した腫瘍細胞をアポトーシスに引き込む手法を開発する。また、その逆に、リピッドラフト機能を抑制する手法で、自己免疫疾患の活性化 T 細胞を抑制する手法を検討する。

８．研 究 発 表

Dong L, Masaki Y, Takegami T et al. Cloning and expression of two human recombinant monoclonal Fab fragments specific for EBV viral capsid antigen. Int Immunol 2007; 19: 331-336.

梅原久範、 リピッドラフト（Lipid Raft）－細胞活性化のための“脂肪の筏”－. 金医大誌 2005; 30: 374-382.

Dong L et al. Clonality analysis of lymphoproliferative disorders in lymphocytes infiltration from patients with Sjögren’s syndrome (SS). 2007. (in press)

金医大誌（J Kanazawa Med Univ）30：374－382, 2005

免疫最前線：リピッドラフト (Lipid Raft) 細胞活性化のための“脂肪の筏”

梅　原　久　範

要　約：近年，スフィンゴミエリンとコレステロールからなる細胞膜マイクロドメイン (リピッドラフト) が，細胞活性化シグナルの足場として注目をあびている。リピッドラフトには，細胞活性化に重要なシグナル伝達物質が局在している。免疫シナプス形成に重要なT細胞レセプターの凝集やアポトーシスに重要なFasの凝集過程にもリピッドラフトは深く関わっている。リピッドラフトは，T細胞に限らずあらゆる血球系細胞の細胞膜に存在するため，その異常は自己免疫疾患，抗癌剤耐性機序，病原体感染症などさまざまな病態に関連する。我々は，リピッドラフトの主要構成脂質であるスフィンゴミエリン合成酵素遺伝子の同定に成功した。さらに，スフィンゴミエリン欠失細胞にこの合成遺伝子を導入し，Fas誘導アポトーシスにおけるリピッドラフトと細胞膜スフィンゴミエリンの重要性を証明した。リピッドラフトの制御は，新たな免疫抑制剤や抗癌剤の開発につながるものと期待される。

キーワード：　リピッドラフト，スフィンゴミエリン，T細胞レセプター，Fas，アポトーシス

はじめに

免疫学における近年の最も注目すべきトピックは，SimonsとIkonenらによる細胞膜が外界からの刺激を効率良く細胞内へ伝達する仕組みについてのlipid rafts (ラフト) の概念であろう。すなわち，彼らは「スフィンゴミエリンとコレステロールからなる細胞膜のマイクロドメインが，特定の膜構造を輸送するための“筏”として且つ細胞内シグナル伝達のための足場として働く」というラフトモデルを提唱した(1)。その後，細胞膜レセプターや細胞内シグナル伝達物質がラフトに局在することが続々と一流紙に発表され，このモデルの正当性が一躍脚光を浴びるようになった。また，近年の蛍光イメージング技術の進歩に伴い，細胞接触面を詳細に観察出来るようになり，T細胞抗原受容体 (TCR) と抗原提示細胞 (antigen presenting cell: APC) 上のMHC／抗原ペプチド複合体 (pMHC) との接触面 (免疫シナプス) について詳しく調べられるようになった。TCRをはじめ細胞膜レセプターの凝集過程にこのリピッドラフトが深く関わっていることが証明された。本稿では，リピッドラフトがいかなるものかを紹介しつつ，ラフトに関する我々の研究の軌跡を紹介したい。

金沢医科大学血液免疫制御学（血液免疫内科学）
石川県河北郡内灘町大学1-1
平成18年２月28日受理

1．細胞膜とLipid rafts (ラフト)

細胞膜は，リン脂質，スフィンゴ脂質，コレステロールよりなる脂質二重構造である。細胞膜を界面活性剤で溶解しショ糖密度勾配遠心法で分画すると，界面活性剤に不溶性のコンパートメントが上層に浮いて来る。この分画は，DIG (detergent-insoluble glycolipid-enriched domain), DRM (detergent resistant membrane), TIFF (Triton-insoluble floating fraction), GEM (glycolipid-enriched membrane) など，さまざまな名称で呼ばれていた(2)。Simonsらは，この構成脂質の違いによるコンパートメントをlipid raftsと名付け，その合成経路やシグナル伝達における重要性について報告した(1)。一般にリン脂質は，水素受容体を持つが水素供与体が無いためにリン脂質同士では結合しにくく，多価不飽和脂肪酸を含んでいる部分がねじれているためにネットワークの形成も起こりにくい。一方，脂肪酸側鎖が飽和型であるスフィンゴ脂質は，水素結合に必要な水素受容体と水素供与体の両方を持っており，脂質二重層の中でネットワークを形成する。これに加え，コレステロールは飽和アシル鎖を介してスフィンゴ脂質に結合しやすいために，スフィンゴ脂質ネットワークの間隙を埋めるように配置する。これがラフトの本体で，スフィンゴ脂質とコレステロールが強固にパックされた領域が形成されている (図1A) (1,3-5)。

従来より，ラフトとカベオラ (caveolae) との異同が取り沙汰れていた(6)。カベオラはカベオリン (caveolin) により形成される細胞膜の小さなくぼみでバソラテラル膜に存在する。カベオ

ラとラフトは多くの点で非常に類似している。大きさもカベオラが50～80nmでラフトが70nmである。細胞膜からコレステロールを除去すると両者とも破壊される。両者には多くのシグナル伝達物質が局在しており，低分子の取り込み，細胞内カルシウムの調節，活性化刺激の伝達に関わっている。結局，ラフトもカベオラも脂質組成や機能の面からは同一のもので，蛋白をゴルジ複合体から細胞膜へと輸送するtransport vesicle (lipid shells)を形成されるが，運搬する蛋白がカベオリンかアピカル膜蛋白かの相違によりvesicleの形態や輸送先が異なってくるのではないであろうか (図1B) (3,6,7)。

BrownとRoseは GPI-anchored 蛋白がスフィンゴ脂質と共にdetergent不溶性分画に存在し，細胞先端のマイクロドメインに輸送されることを見いだし(8)，StefanovaらはCD14, CD24, CD48, CD55, CD59などのGPI-anchored蛋白が細胞内ドメインを持たないにも関わらず細胞内でチロシンキナーゼLckと会合していることを見いだした(9)。現在までに判明しているだけでもRas, チロシンキナーゼ，アダプター蛋白など様々なシグナル伝達物質がラフトに局在している。蛋白がラフトに局在するためには，蛋白質N末端のグリシン (Gly) 残基にアミド結合を介したミリスチン酸化かシスチン残基 (Cys) にチオエステル結合を介したパルミチン酸化およびC末端のシスチン残基のファルネシル化が必要である。例えば，Ras はパルミチン酸化とファルネシル化の両方を受けており，ほとんどのSrc型チロシンキナーゼはミリスチン酸化とパルミチン酸化を受けラフトに局在している(10)。

2．ラフトと免疫シナプス

細胞接着面における細胞膜変化は，形態学的に神経シナプスに似ていることより免疫シナプス (Immunological synapse) と呼ばれている(5,11,12)。T細胞抗原受容体 (TCR) と抗原提示細胞 (antigen presenting cell: APC) 上のMHC／抗原ペプチド複合体 (pMHC) との接触について詳しく調べられている。TCRとpMHCとの距離は約15 nmと極めて短いために，初期のT細胞とAPC との接着は細胞外領域の長いLFA-1とICAM-1 (およそ42 nm) 或いはCD2とCD58 (およそ40nm)によって担われている。接着後数分以内に，細胞表面レセプター群が接着面に環状に集

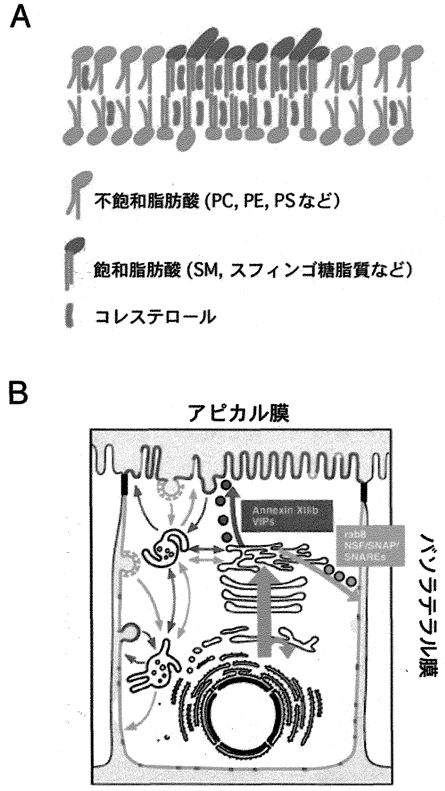

図1．ラフトの構造
(A) 飽和型脂肪酸を有するスフィンゴミエリン (SM)，スフィンゴ糖脂質などのスフィンゴ脂質は細胞膜側外層に局在している。一方，フォスファチジルコリン (PC)，フォスファチジルエタノールアミン (PE)，フォスファチジルセリン (PS) などのリン脂質は細胞膜側外層および細胞質側内層の両方に存在する。スフィンゴ脂質のアシル鎖は直線的でネットワークを形成するのに対し，リン脂質のアシル鎖は不飽和脂肪酸のためにねじれていてネットワークを形成しにくい。コレステロールは飽和脂肪酸と親和性が高いために，スフィンゴ脂質ネットワークの間隙を埋めるように存在する。このように，ラフトはスフィンゴ脂質とコレステロールが密にパックされた領域 (マイクロドメイン)である。(文献3より改変)
(B) 細胞内蛋白輸送システム
極性化した上皮細胞 (MDCK細胞) には，アピカル膜とバソラテラル膜とがある。赤色細胞膜はスフィンゴ脂質-コレステロールからなるラフト領域で，青色細胞膜はリン脂質豊富な領域である。新たに合成された蛋白はゴルジ複合体を通過する間に，各々ことなる脂質小胞のなかに包埋されてアピカル側 (赤矢印) かバソラテラル側 (青矢印) かに輸送されるべく運命付けされる。(文献3より改変)

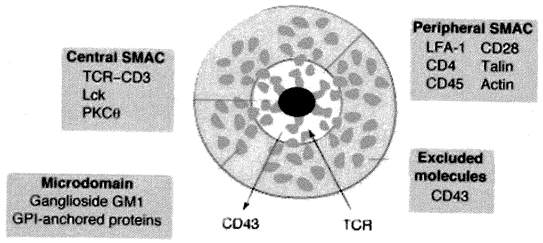

図2．免疫シナプスの構造
T細胞と抗原提示細胞との接着面には，supramolecular activation cluster (SMAC) が形成される。成熟免疫シナプスでは，TCR/CD3はcentral SMAC (cSMAC) に凝集する。cSMACには，*Lck*，*Fyn*，PKC θ などのシグナル物質が集積する。一方，peripheral SMAC には，LFA-1，CD4，CD28，CD45などがcSMACを囲むように配列する。(文献3より改変)

合しsupramolecular activation clusters (SMACs) という配列を形成する。初期の免疫シナプスでは，SMACの中心部 (central SMAC : cSMAC) にLFA-1/ICAM-1とCD2/CD58が集積し，その周辺部 (peripheral SMAC: pSMAC) にTCR/pMHC が局在している。しかし，この構成が5～15分の間に逆転し，TCR/pMHCがcSMACに集積しその周りをLFA-1/ICAM-1とCD2/CD58が取り囲むようになる (図2)。この状態の細胞接着形態を成熟免疫シナプスと呼び，T細胞活性化には一定時間この成熟免疫シナプスが維持されることが必要である。成熟免疫シナプスの形成と維持の詳細なメカニズムは不明であるが，アクチン重合阻害剤やアクチンの凝集に重要なVav の欠損マウスでは免疫シナプス形成が阻害されることより，細胞骨格機能を制御するVav, SLP-76, Nck, WASPなどのシグナル伝達物質が関与していると考えられている(5)。

3．T細胞活性化とラフト

免疫学の中でラフトの解析が最も進んでいるのはCD4陽性T細胞で，T細胞の活性化に重要なキナーゼやアダプター蛋白がラフトに局在していることや，TCR刺激後に新たにシグナル伝達物質がラフトに凝集してくることが明らかにされている(3,12)。TCRは抗原感受性が非常に高いにもかかわらず，個々のTCRとpMHCとの親和性は弱く，平均数秒～数分で解離すると言われている。また，T細胞の活性化は1分子のTCRの活性化によって起こるものではなく，次々に起こるTCRの活性化シグナルの蓄積によって起こると考えられている。一説には，TCRの活性化が8000分子を越えた時にT細胞の活性化が起こるとも報告されている。このようにT細胞の活性化には細胞膜での効率の良いTCRの凝集と活性化シグナルの蓄積が必要であり，その機序を説明するのに魅力的なモデルがラフトの概念である。

TCRシグナルとラフトとの関連を明らかにした重要な発見は，米国癌研究所のSamelsonらによるラフトに局在するアダプター蛋白LAT (linker for activation of T cell) の発見である(13)。TCRからのシグナル経路は，TCRとpMHCとの結合により*Lck*や*Fyn*などのチロシンキナーゼが活性化しCD3ζ鎖のITAM (immunoreceptor tyrosine-based activation motif) がチロシンリン酸化を受ける。このリン酸化ITAMにSyk tyrosine kinase familyのZAP-70が結合し，*Lck*との協調作用によりLAT, SLP-76などのアダプター蛋白をチロシンリン酸化する。さらに，リン酸化LATを介してSLP-76, PLC-γ, Grb2, PI 3-kinase, Cbl, Vav, SKP-76などのシグナル物質がラフトに新たに集積してくることが報告されている(14)。LAT以降のシグナル経路として，Grb2やSOSを介してRasの活性化へ，Gads, SLP-76, Vavを介してRac/cdc42の活性化へ，Nck, Waspを介してアクチンの重合化へと刺激が伝達されていく。このように，ラフトに局在するLATが，あたかもT細胞活性化の“足場”として機能していることが判明した (図3)。

LATは恒常的にラフト内に局在するが，TCRは非刺激時には存在しない。すると，どのような仕組みでTCRがラフトへ移行するのであろうか？ T細胞活性化はTCRの凝集により起こるが，この過程でTCRとラフト局在分子との親和性が増強することが考えられる。*Lck*はラフトに局在しており，近傍のTCRが抗原と結合した際に活性しTCRζ鎖ITAMのチロシンリン酸化を誘導する。その後，ZAP-70は自己のSH2ドメインを介してITAMのリン酸化チロシンと結合し，活性化および自己のチロシンリン酸化を起こす。その結果，*Lck*のSH2ドメインがリン酸化ZAP-70と結合することによりTCR/ZAP-70複合体をラフト内に引き寄せるというモデルが想定される。これに加えて，TCRの凝集を誘導するシグナルは細胞骨格の凝集を介してラフト自体をも凝集させているのかもしれない(15)。

4．NK細胞活性化とラフト

NK細胞活性化レセプター群には，CD16,やCD2に加え，レクチンタイプのMHC非特異的Natural cytotoxicity receptor (NKp46, NKp30, NKp44) とMHCクラスIを認識するレセプター群 (KIR2SD, NKG2C/CD94) 等がある(16,17)。そして，これらのレセプター群はITAMを有するCD3/ζ鎖，FcεRIγ鎖およびDAP12と機能的に会合している(18)。NK細胞活性化シグナルはTCRシグナル経路と類似しており，*Lck*や*Fyn*の活性化によりITAMのチロシンリン酸化が誘導され，さらに*ZAP-70*, *Syk*の会合およびPI 3-キナーゼの活性化が起こる。

我々は，CD2を介したNK細胞の活性化では，①CD2架橋刺激により有意な細胞内顆粒の放出が起こること。②この現象が

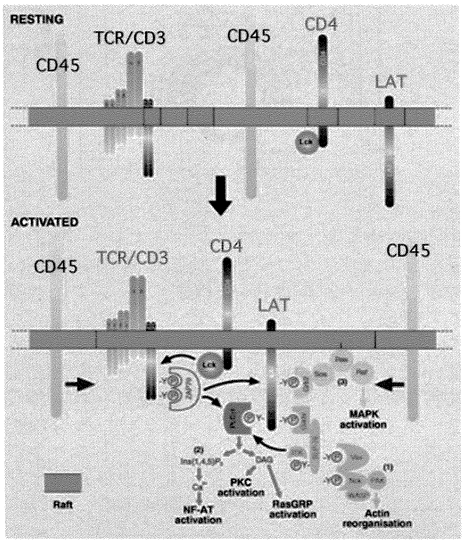

図３．TCRとLATを介したシグナル経路
LAT以降のシグナル経路として，Grb2やSOSを介してRasの活性化へ，Gads, SLP-76, Vavを介してRac/cdc42の活性化へ，Nck, Waspを介してアクチンの重合化へ，PLC-γ, Gads, SLP-76を介して細胞内カルシウム流入へと刺激が伝達されていく。ラフトに局在するLATが，あたかもT細胞活性化の“足場”として機能している。(文献3より改変)

チロシンキナーゼ阻害剤であるHerbimycinとPI 3-キナーゼ阻害剤であるWortmanninによって完全に抑制されること。③CD2架橋刺激によって*Syk*チロシンキナーゼの活性化が増強し，細胞内蛋白のチロシンリン酸化が増強すること。④チロシンリン酸化蛋白に会合したPI 3-キナーゼの活性が有意に増強していることを報告した(19)。さらに，TCR刺激と同様にNK細胞のCD2架橋刺激でも，Cbl, Grb2, Shcなどの細胞内アダプター蛋白のリン酸化と各々の結合増強が起こることを明らかにした(20)。CD2は細胞内ドメインにチロシンキナーゼ部位を持たないにも関わらず，*Lck*依存性にCD3/ζ鎖およびFcεRIγ鎖のチロシンリン酸化を誘導することが報告されていた(21)。CD2シグナルとラフトとの関連をさらに検討した結果，①ショ糖密度勾配遠心法で分画されるNK細胞膜のラフト分画に非刺激状態でもCD2が存在することを認めた。②共焦点顕微鏡の解析では，CD2架橋刺激によるCD2凝集と一致してラフトが凝集することを確認した。③CD2架橋刺激により，ラフト局在アダプター蛋白であるLATのチロシンリン酸化が強く誘導され，このチロシンリン酸化LATにPI 3-キナーゼとPLC-γが会合することを認めた。すなわち，チロシンキナーゼ領域を有しないCD2のNK細胞活性化メカニズムは，CD2架橋刺激によりラフト凝集が起こり，ラフトに局在するチロシンキナーゼ*Lck*の活性化とラフト局在アダプター蛋白であるLATのチロシンリン酸化により，PI 3-キナーゼやPLC-γの会合が起こることを証明した(22)。実際に，共焦点顕微鏡でNK細胞と感受性標的細胞との接触面にラフトとCD2およびそのリガンドであるCD58の凝集が確認される (図4)。さらに，コレステロール除去剤であるmethyl-β-cyclodextrinによりラフトを破壊すると，NK細胞からの顆粒放出と細胞傷害活性は著明に減弱することを認めている(22,23)。

従来，NK細胞はMHC拘束性に標的細胞を殺傷するCTLと異なり，MHC非拘束性に腫瘍細胞を殺傷すると考えられていた。1990年にLjunggren とKarreはNK細胞は正常なMHCを欠失した細胞を認識し殺傷するという“自己喪失 (missing self) 仮説”を提唱した(24)。” missing self-MHC” という概念は，“NK細胞はMHCクラスI分子の正常な発現を監視しており，MHCクラスI分子の発現が異常か欠失した時に，その標的細胞を傷害する”というものである。実際のNK細胞による標的細胞認識は，NK活性化レセプター群；killer-cell activatory receptors (KARs) とNK抑制性レセプター群；killer-cell inhibitory receptors (KIRs) とのバランスによって決定されている(25,26)。標的細胞上のMHCクラスI分子は，NK細胞による細胞傷害から回避させる働きを持つと考えられている。

NK細胞におけるシグナルのユニークな点は，活性化レセプターと抑制性レセプターが免疫シナプス内で共存することである。抑制性レセプターとMHCクラスIとの結合距離は，およそ15 nmとTCR/MHC間距離と同程度であり，理論的にはT細胞で見られるcSMACを形成できるはずである。しかし，標的細胞上にMHC class I分子が存在すると，抑制性レセプターとの結合によりITIM にSHP-1が会合しチロシンキナーゼの活性化を抑制する。このために，チロシンキナーゼ依存的であるラフトの凝集と成熟免疫シナプスの形成が起こらないと考えられる。すなわち，NK細胞による標的細胞の認識・殺傷は免疫シナプスにおける活性化レセプター (チロシンキナーゼの活性化) と抑制性レセプター (チロシンキナーゼの鎮静化) との強弱により調節されていると考えられる (図5) (16,17,23,25,27,28)。

5．ラフトと臨床病態

近年になりラフトの機能が明らかになるにつれ種々の病態と

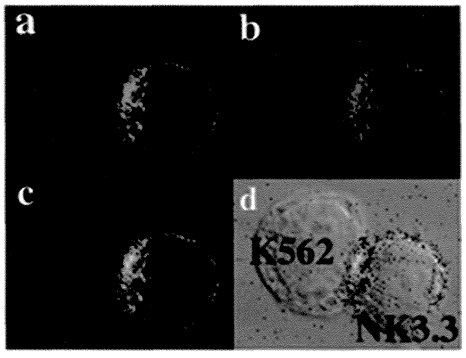

図4．NK細胞におけるCD2とラフトの凝集
NK細胞と標的細胞 (K562) との接着面に，CD2 (赤色) とラフト (緑色) が凝集し共存する (黄色)。(文献22より引用)

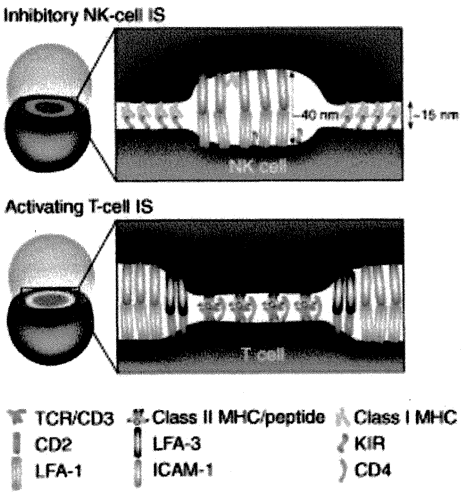

図5．抑制性NK細胞免疫シナプス
活性化T細胞の免疫シナプスでは，LFA-1/ICAM-1やCD2/LFA-3によって囲まれた中心にTCR/CD3とMHC class II分子が凝集するのに対し (下図)，抑制性NK細胞免疫シナプスでは，killer cell Ig-like receptor (KIR) とMHC class Iとの結合が分断したままである (上図)。(文献3より改変)

の関与が注目されている。ラフトの主要な構成脂質であるスフィンゴミエリンは神経系細胞に多量に存在しており，アルツハイマー病やパーキンソン病発症におけるラフトの関与が報告されている。アミロイドーβ-蛋白の沈着はアルツハイマー病の重要な指標であるが，これはβ-secretase, γ-secretaseによりアミロイド前駆蛋白から生成される。動物モデルでは高コレステロール食によりアミロイド蛋白合成が増加し，スタチン系の高脂血症薬がアルツハイマー発症予防に有効であると報告されている。In vitroの系でコレステロール除去剤によりアミロイド蛋白の合成が減少することから，アミロイド前駆蛋白がラフト内に貯蔵されている可能性が示唆されている(29)。

多くのウイルスや細菌が細胞内への進入窓口としてラフトを利用していることが判明してきた。ラフトにはコレステロールやスフィンゴ糖脂質が多量に存在するが，細菌毒素やウイルスの産生する赤血球凝集素やノイラミニダーゼは脂質-脂質結合や脂質-蛋白結合力を介してラフトに結合する。また，HIVウイルス感染の補助レセプターとして働くCD4やケモカインレセプターであるCCR5, CXCR4はラフトに存在する。このように種々の病原体がラフトに局在する分子に結合した後にエンドサイトーシスにより細胞内へ取り込まれ，そのまま自己増殖の場としてラフトを利用 (ラフトをハイジャックする) することが報告されている(29,30)。

自己免疫疾患である全身性エリテマトーデス (SLE) において，IsenbergのグループとTsokosのグループはラフトに局在するTCRζ鎖と*Lck*について解析し，SLE患者T細胞ではラフトに結合したTCRζ鎖や*Lck*が減少していることを報告している(31,32)。SLE 患者T細胞は，非刺激状態で既にラフトに結合した*Lck*がチロシンリン酸化を受けており，慢性的な活性化状態にある可能性がある。さらにJuryらは，SLE患者ではガングリオシドGM1で検出されるラフト発現の増強とCD45やユビキチン化を促進するCblのラフトでの増加を報告している(33)。両グループともラフトに結合したTCRζ鎖や*Lck*も過剰なユビキチン修飾を受けていることを認め，SLEにおけるTCRζ鎖や*Lck*の減少がこのユビキチン依存性の蛋白分解による可能性を報告している(31,32,34)。33例のSLE 患者において我々が行った検討でも，各リンパ球サブセットにおけるラフトの発現はSLEDAIに基づいた疾患活動性に応じて増強しており，その増強はCD45陽性メモリーT細胞で著しかった (論文執筆中)。

6．ラフト研究の新展開

1）スフィンゴミエリン合成酵素遺伝子の発見

従来，ラフトの同定はラフト内に局在するガングリオシドGM1に結合するコレラトキシンBサブユニット (CTx) を用いて行われ，ラフト機能の解析はコレステロール除去剤であるメチル-β-サイクロデキストリン (MβCD) を用いて判定されてきた。しかし，ラフトの重要構成脂質であるスフィンゴミエリンについての検討は，スフィンゴミエリン合成酵素が発見されていなかったこともあり詳しく報告されていなかった。近年，岡崎と我々のグループは，ヨーロッパのグループとほぼ同時にスフィンゴミエリン合成酵素 (SMS1) の遺伝子クローニングに成功し(35,36)，スフィンゴミエリンに特異的に結合するライセニンを用いて，細胞膜上のスフィンゴミエリンの発現様式とライセニン感受性について明らかにした。さらに我々は，スフィンゴミエリン欠失細胞WR/Fas-SM(-)細胞にSMS1遺伝子を導入し，スフィンゴミエリン合成を回復させた細胞株 (WR/Fas-SMS1) を樹立した。WR/Fas-SM(-)細胞およびWR/Fas-SMS1細胞におけるヒトFasの発現および細胞膜コレステロール量とガングリオシドGM1量は同等であったが，ライセニンで確認される細胞膜スフィンゴミエリンはWR/Fas-SMS1細胞にのみ発現していた。この両者を用いることにより初めて，ラフトの凝集やアポトーシスにおける細胞膜スフィンゴミエリンの機能を解析することが可能になった。

2）Fas依存性アポトーシスのシグナル経路

Fasを介するアポトーシス経路には大きく分けて2通りある。WR/19L細胞に代表されるType I細胞では，Fas架橋によりDISCが形成され活性化Caspase-8が直接その下流のCaspase-3を活性化しアポトーシスが進行する。一方，Type II細胞ではFasの架橋は不十分であるが，活性化された少量のCaspase-8がBcl-2ファミリーのBidを切断し，切断型Bid (tBid) がミトコンドリア内膜に存在するチトクロームCの放出を引き起こす。その結果，チトクロームCはApaf-1 (apoptotic protease-activating factor 1)およびcaspase-9と複合体を形成し，下流のcaspase-3, -7を活性化する (図6) (37,38)。

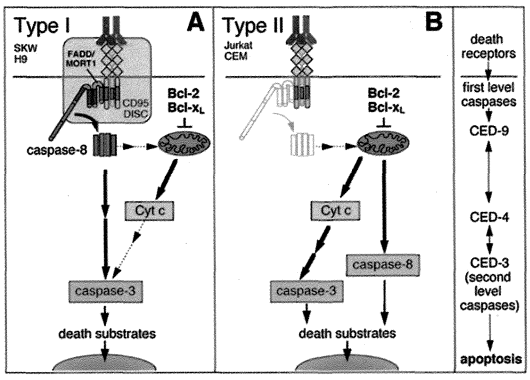

図6．Type IとType IIアポトーシス
Type I細胞では，Fas架橋によりFas-FADD-Caspase8からなるDISCが形成され，Caspase-8が活性化される。その後，下流のCaspase-3を活性化しアポトーシスが進行する。一方，Type II細胞ではFasの架橋およびcaspase-8の活性化は不十分であるが，活性化された少量のCaspase-8がBcl-2ファミリーのBidを切断し，切断型Bid (tBid) がミトコンドリア内膜に存在するチトクロームCの放出を引き起こす。その結果，チトクロームCは下流のcaspase-3およびcaspase-8を活性化しアポトーシスを起こす。(文献18より引用)。

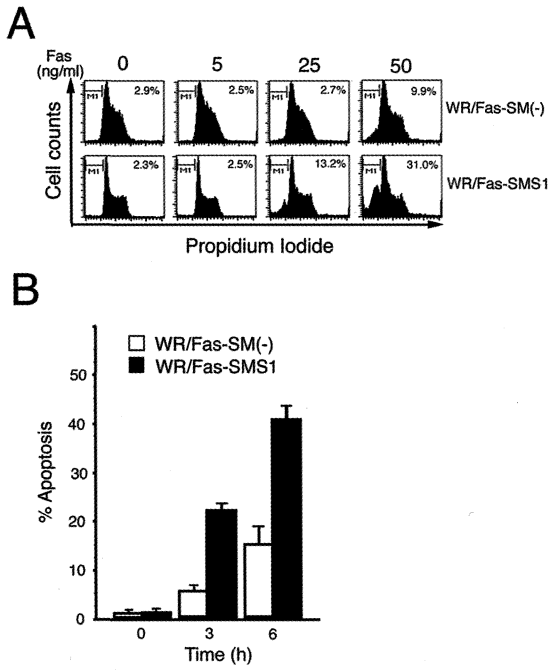

図7．細胞膜スフィンゴミエリン欠失細胞と回復株におけるFas誘導アポトーシス (文献42より改変)
WR/Fas-SM(-)細胞 (スフィンゴミエリン欠失細胞) およびWR/Fas-SM1 (スフィンゴミエリン合成回復株) をFas抗体で架橋刺激し，アポトーシスにより断片化DNAを有する細胞をFACS解析した。(A) 抗Fas抗体濃度依存性アポトーシス，(B) アポトーシスの時間経過

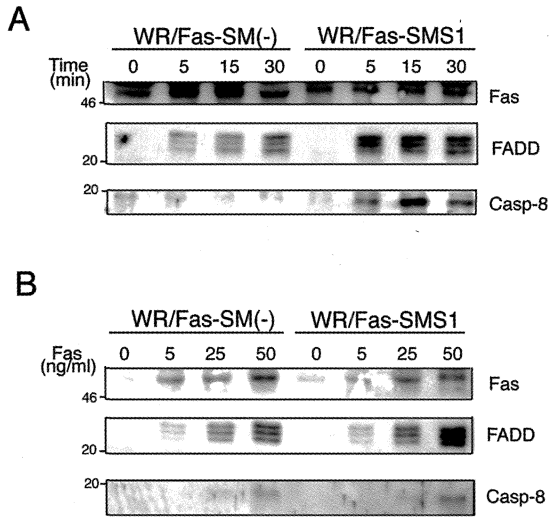

図8．細胞膜スフィンゴミエリン欠失細胞と回復株におけるDISC形成 (文献42より改変)
WR/Fas-SM(-)細胞 (スフィンゴミエリン欠失細胞) およびWR/Fas-SM1 (スフィンゴミエリン合成回復株) をFas抗体で架橋刺激し，Fasを免疫沈降した。会合するFADDおよびCaspase-8量をウエスタンブロットにて検出した。(A) 時間依存性DISC形成，(B) 抗Fas抗体濃度依存性DISC形成

IgM抗Fas抗体(CH11)を用いてWR/Fas-SM(-)細胞とWR/Fas-SMS1細胞におけるアポトーシスについて検討した結果，①スフィンゴミエリンが欠失しているWR/Fas-SM(-)細胞ではアポトーシスが障害されているが，スフィンゴミエリンを回復することにより著明にアポトーシスが誘導された (図7)。②抗Fas抗体で両細胞を刺激後，Fasを免疫沈降しFADDおよびカスパーゼ8の会合を検討した結果，WR/Fas-SM(-)細胞に比べスフィンゴミエリンを回復させたWR/Fas-SM1細胞では，著明にFADDおよびカスパーゼ8の会合量が時間依存的かつ刺激強度依存的に増加していた (図8)。Fasは細胞外のPLADを介して三量体を形成し細胞膜上に存在している(39)。しかし，Fasリガンド (Fas-L) を固層化してFasを刺激した場合，可溶型のFas-Lに比べ1000倍のアポトーシスを誘導出来ることが示されている(40)。Fas単量体の分子量は約45Kdであるが，架橋刺激によりFasが凝集した場合，2%SDSおよび5%2MEに対して抵抗性の多量体が形成される(41)。すなわち，効率の良いアポトーシスを実行するためには，3量体Fasの凝集が必須である。③WR/Fas-SM(-)細胞と WR/Fas-SMS1細胞におけるFas凝集能の違いについて検討した結果，WR/Fas-SMS1細胞ではWR/Fas-SM(-)細胞に比べ，Fasの多量体形成が著明に亢進していた (図9)。さらに，

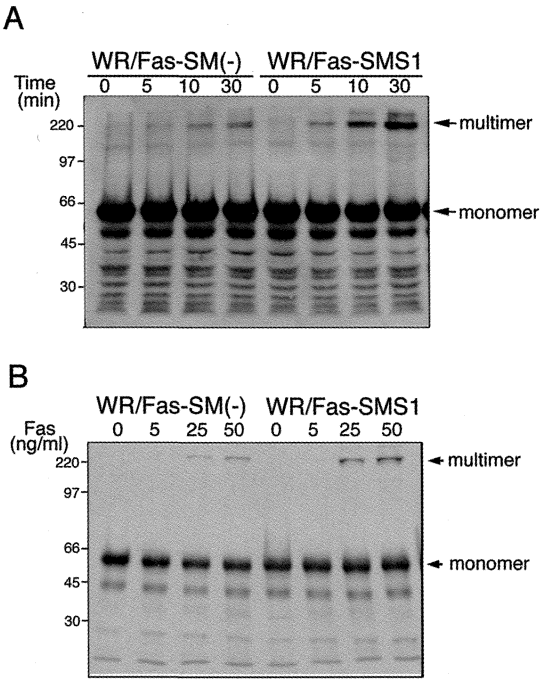

図9．細胞膜スフィンゴミエリン欠失細胞と回復株におけるFas多量体形成能およびFas凝集能 (文献42より改変)
WR/Fas-SM(-)細胞 (スフィンゴミエリン欠失細胞) およびWR/Fas-SM1 (スフィンゴミエリン合成回復株) をFas抗体で架橋刺激し，多量体Fasをウェスタンブロット法で検出した。(A) 時間依存性変化，(B) 抗Fas抗体濃度依存性変化

共焦点顕微鏡を用いて細胞膜上Fasの凝集能を検討したところ，WR/Fas-SMS1細胞におけるFas凝集が著明に増強していた(42)。

3）**Fasとリピッドラフト**

近年のラフトの研究よりT細胞レセプター (TCR) をはじめB細胞レセプター，CD2, CD44, CD11a/CD18など多くの細胞膜レセプターがラフトに凝集することが判明した(2,3,22,23,43)。Fasも例外では無く，ラフトへの集積が効率の良いアポトーシスの実行に重要であることが分かっている(44,45)。

我々は，WR/Fas-SM(-)細胞と WR/Fas-SMS1細胞を用いて，Fas架橋刺激前後におけるFasのラフト内局在について検討した。細胞を1% Triton-Xで可溶化後，ショ糖密度超遠心法で細胞膜からリピッドラフト分画を分離し，ラフト分画におけるFasを免疫ブロット法で検出した。両細胞におけるFasは，すでに非刺激状態でラフト分画内に存在していた。しかし，Fas架橋刺激を加えても，WR/Fas-SM(-)細胞ではラフト分画のFasが増加しないのに対し，WR/Fas-SMS1細胞ではFas架橋刺激により2.5倍の増加を認めた。Type Iアポトーシスの実行には，Fasの凝集とDISCを介したカスパーゼの活性化が必須である。すなわち，FasLにより細胞膜上のFasが微小な凝集を起こし，これにFADDが結合してDISCが形成される。その後に，より大きなFasの凝集が形成されてcaspase-8とその下流のcaspase-3の十分な活性化によりアポトーシスが誘導される。このように，我々はスフィンゴミエリン欠損WR/Fas-SM(-)細胞とその合成回復細胞WR/Fas-SMS-1細胞を用いて，細胞膜スフィンゴミエリンがFas誘導アポトーシスにおけるリピッドラフト内へのFasの移行，Fasの凝集，DISCの形成，カスパーゼの活性化の全ての過程において重要な役割を果たしていることを明らかにした (図10) (42)。

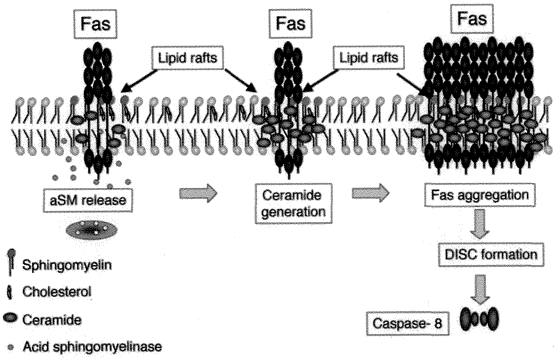

図10．Fas誘導アポトーシスにおけるリピッドラフト
Fas刺激によりFasが細胞膜へ移行する。ラフト内のスフィンゴミエリンはセラミドに変換され，コレステロールを膜から遊離しセラミド同士が結合する。その結果，より大きなFasのclusterが形成され，DISCの形成，カスパーゼの活性が起こる。

7．ラフトとセレンディピティー

1990年頃，NIH留学中の筆者は接着分子の凝集とNK細胞活性化シグナルの研究に没頭していた。当時は，細胞接着面への膜蛋白や細胞骨格蛋白の凝集とその直下へのGolgi/microtube organic centerの移動が報告されていたが，接着分子が活性化シグナルを伝達するレセプターであるとは考えられていなかった。私は，接着分子の凝集がNK細胞活性化シグナルを伝達すると仮定し実験を進め，接着分子LFA-1の凝集がセカンドメッセンジャーIP3の産生増強や細胞内顆粒放出を誘導することを明らかにした(46)。しかし，細胞膜レセプターの凝集自体は既成事実として捉え，凝集メカニズムを深く考える事無く，細胞内でのシグナル伝達のみを追い求めていた。1997年にSimonsらがラフトの概念をNature誌に報告して以来(1)，1998年，1999年代はラフト関連の論文が，Nature, Science, Cellなどの超一流学術誌を席巻していた。私もこの流れに遅れまいと，NK細胞活性化過程におけるラフトの重要性に関する論文をNature, Scienceに投稿したが，レフリーからのコメントは「ラフトの重要性はT細胞で既に報告されており，B細胞でも好塩基球でも報告された。NK細胞で同じことが起こってもおかしくない」と評価されなかった。あるreviewerからは，私も私もという"me too paper" だとまで言われ悔しい思いをした。しかし，結局，ラフトの大ブレークまで目の前の現象の重要性に気づかず，違った方向に興味を持ち研究を進めて行った自分の未熟さのためである。

ノーベル賞級の大発見には「セレンディピティー」が必要だと言われる。セレンディピティーとは，セイロンのおとぎ話「セレンディップの3人の王子」から，イギリスの小説家であるホーレス・ウォルポールが作った造語で，「偶然に幸運な予想外の発見をする能力」と訳される。アルキメデスの原理，ニュートンの万有引力，ジェンナーの種痘，ペニシリン，X線，ダイナマイト，マジックテープなどこれまでの多くの大発見は偶然の産物であるが，鋭い洞察力を持った研究者がセレンディピティーによって真理を見つけ出したものである(47)。しかし，セレンディピティーはノーベル賞になるような大発見にのみ必要な訳ではなく，各人が遭遇する日常の些細な場面においても重要である。今回のリピッドラフトの研究を通じて，自分にセレンディピティーが欠けていたことを残念に思う。一方で，宝の山を気付かずに通り過ぎていた自分を後になって知り，研究のおもしろさを再確認している。

終　わ　り　に

医学研究とは，生体の構造や機能に関する自然科学の発見を病気の原因解明や治療法に結びつけることである。我々は，これまでのラフトに関する成果を臨床に役立てる手懸かりを模索しなければならない。おそらくラフトは免疫担当細胞全般の活性化やアポトーシスに深く関わっており，臨床的には自己免疫疾患やアレルギー性疾患での免疫系の異常活性化，移植臓器に

対する拒絶反応，感染細胞や癌細胞の殺傷などにも関与しているであろう。リピッドラフトは免疫担当細胞全般の活性化やアポトーシスにも深く関わっている。もし，細胞活性化あるいはアポトーシスをラフト機能の面より制御できれば，自己免疫疾患やアレルギー性疾患に対する新たな治療法に結びつく可能性がある(34)。また，ある種の抗癌剤はFasの凝集を介して効果を発揮している。抗癌剤耐性細胞ではこのFasの凝集が抑制されているものがある。ラフトの主要構成脂質であるスフィンゴミエリンを制御することによって，新たな機序の抗癌剤や免疫調節剤が開発される可能性がある。それを実現するためには，細胞生物学や免疫学，血液学，アレルギー学にとどまらず，脂質生化学，薬理学など広い分野の知識の結集が必要と思われる。昨年，全国から第一線の研究者に集まって頂き「第1回血液免疫ネットワークin 金沢」を開催し今後も継続していく予定である。今年度は，スフィンゴ・テラピー研究会 (鳥取大学血液内科教授　岡崎俊朗代表) を準備し共同研究や研究協力体制を模索中である。一人でも多くの研究者にこの領域に興味を持っていただき，この分野の研究に加わって頂けることを心から望んでいる (連絡先：金沢医科大学血液免疫制御学　梅原久範，umehara@kanazawa-med.ac.jp)。

本研究の遂行にあたり，多くの研究者の先生方にご協力を頂きました。鳥取大学医学部血液内科　岡崎俊朗教授，山岡昇平博士，関西医科大学第一内科　福原資郎教授，尼川龍一先生，宮地理彦先生，京都大学大学院医学研究科臨床免疫学　三森経世教授，山口拓郎博士，大阪歯科大学内科学講座　堂前尚親教授，合田征司先生，井上博先生に深謝致します。

本研究は，文部省科学研究費補助金 萌芽的研究 (13877075)，基盤研究Ｂ (展開，13557160)，基盤研究Ｂ (15024236，15390313)，特定領域研究 (がん生物15024236)，特定領域研究 (感染症，13226124)，厚生労働科学研究費補助金　免疫アレルギー疾患予防治療研究事業，日本学術振興会 (特別研究員奨励費，外国人研究者Ｐ04244)，上原生命科学財団　外国人留学生，上原生命科学財団　研究助成金，金沢医科大学共同研究助成金の援助を受けて遂行された。

文　　献

1. Simons K, Ikonen E: Functional rafts in cell membranes. Nature 1997; **387**: 569-72.
2. Ilangumaran S, He H-T, Hoessli DC: Microdomains in lymphocyte signaling: beyond GPI-anchored proteins. Immunol. Today 2000; **21**: 2-7.
3. 梅原久範, 宮地理彦, 岡崎俊朗: “Lipid rafts” 細胞活性化のための “脂肪の筏”. 臨床免疫学会会誌 2003; **26**: 9-20.
4. Brown RE: Sphingolipid organization in biomembranes: what physical studies of model membranes reveal. J Cell Sci 1998; **111**: 1-9.
5. Bromley SK, Burack WR, Johnson KG et al: The immunological synapse. Annu Rev Immunol 2001; **19**: 375-96.
6. Galbiati F, Razani B, Lisanti MP: Emerging themes in lipid rafts and caveolae. Cell 2001; **106**: 403-11.
7. Anderson RG, Jacobson K: A role for lipid shells in targeting proteins to caveolae, rafts and other lipid domains. Science 2002; **296**: 1821-5.
8. Brown DA, Rose JK: Sorting of GPI-anchored proteins to glycolipid-enriched membrane subdomains during transport to the apical cell surface. Cell 1992; **68**: 533-44.
9. Stefanova I, Horejsi V, Ansotegui IJ et al: GPI-anchored cell-surface molecules complexed to protein tyrosine kinases. Science 1991; **254**: 1016-9.
10. Reth MD: Myristylation and palmitoylation of Src family members: the fats of the matter. Cell 1994; **76**: 411-3.
11. Davis DM: Assembly of the immunological synapse for T cell and NK cells. Trends Immunol 2002; **23**: 356-63.
12. 梅原久範, 宮地理彦, 岡崎俊朗: T細胞シグナル伝達におけるraftの役割. 炎症と免疫 2003; **11**: 100-9.
13. Zhang W, Sloan-Lancaster J, Kitchen J et al: LAT: The ZAP-70 tyrosine kinase substrate that links T cell receptor to cellular activation. Cell 1998; **92**: 83-92.
14. Samelson LE: Signal transduction mediated by the T cell antigen receptor: The role of adapter proteins. Annu Rev Immunol 2002; **20**: 371-94.
15. Viola A: The amplification of TCR signaling by dynamic membrane microdomains. Trends Immunol 2001; **22**: 322-7.
16. Cerwenka A, Lanier LL: Natural killer cells, viruses and cancer. Nat. Review (Immunoogy) 2001; **1**: 41-9.
17. Smyth MJ, Hayakawa Y, Takeda K et al: New aspects of natural-killer-cell surveillance and therapy of cancer. Nat Reveiw Cancer 2002; **2**: 850-61.
18. Lanier LL: On guard-activating NK cell receptors. Nature Immunol 2001; **2**: 23-7.
19. Umehara H, Huang J-Y, Kono T et al: Involvement of protein tyrosine kinase $p72^{syk}$ and phosphatidylinositol 3-kinase in CD2-mediated granular exocytosis in natural killer cell line. J Immunol 1997; **159**: 1200-7.
20. Umehara H, Inoue H, Huang J-Y et al: Role for adapter proteins in costimulatory signals of CD2 and IL-2 on NK cell activation. Mol Immunol 2002; **38**: 587-96.
21. 梅原久範, 井上 博, 堂前尚親: CD2 (LFA-2) とCD58. T細胞の分化と機能発現に関わる分子. 臨床免疫別冊 2000; **33**:
22. Inoue H, Yoneda O, Minami Y et al: Lipid rafts as the signaling scaffold for NK cell activation: Tyrosine phosphorylation and association of LAT with PI 3-kinase and PLC-γ following CD2 stimulation. Eur J Immunol 2002; **32**: 2188-98.
23. 梅原久範, 井上 博, 宮地理彦: NK細胞活性化におけるlipid raftの関与. 臨床免疫 2003; **26**: 9-20.
24. Ljunggren H-G, Karre K: In search of the missing self: MHC molecules and NK cell recognition. Immunol. Today 1990; **11**: 237-44.
25. Raulet DH, Held W: Natural killer cell receptors: The offs and ons of NK cell recognition. Cell 1995; **82**: 697-700.
26. 梅原久範, 長野 豊, 堂前尚親: NK細胞の活性化と細胞内シグナル伝達. 臨床免疫 1997; **29**: 1161-70.
27. 梅原久範, 米田 修, 堂前尚親: NK活性とCD2. 臨床免疫 1999; **31:** 32-9.
28. Moretta A, Bottino C, Mingari CM et al: What is a natural killer cell? Nat Immunol 2002; **3**: 6-8.
29. Simons K, Ehehalt R: Cholesterol, lipid rafts, and disease. J Clin Invest 2002; **110**: 597-603.
30. Manes S, del Real G, Martinez-A C: Pathogens: raft hijackers. Nat Rev Immunol 2003; **3**: 557-68.
31. Nambiar MP, Enyedy E, Fisher CU et al: Abnormal expression of various molecular forms and distribution of T cell receptor zeta chain in patients with systemic lupus erythematosus. Arthritis Rheum 2002; **46**: 163-74.
32. Jury EC, Kabouridis PS, Abba A et al: Increased ubiquitination and reduced expression of LCK in T lymphocytes from patients with systemic lupud erythematosus. Arthritis Rheum 2003; **48**: 1343-54.
33. Jury EC, Kabouridis PS, Flores-Borja F et al: Altered lipid raft-associated signaling and ganglioside expression in T lymphocytes from patients with systemic lupus erythematosus. J Clin Invest 2004; **113**: 1176-87.
34. 梅原久範, 山口拓郎, 三森経世: 細胞活性化シグナルにおけるlipid raftの役割と自己免疫病. 分子リウマチ 2004; **1**: 54-60。
35. Yamaoka S, Miyaji M, Kitano T et al: Expression cloning of a human cDNA restoring sphingomyelin synthesis and cell growth in sphingomyelin synthase-defficient cells. J Biol Chem 2004; **279**: 18688-93.
36. Huitema K, Dikkenberg Jvd, Brouwers JF et al: Identification of a family of animal sphingomyelin synthases. The EMBO J 2004; **23**: 33-44.
37. Scaffidi C, Fulda S, Srinivasan A et al: Two CD95 (APO-1/Fas) signaling pathways. The EMBO J 1998; **17**: 1675-87.
38. 梅原久範, 金 哲雄, 宮地理彦ほか: Fas依存性アポトーシスにおけるスフィンゴミエリンの役割. 臨床免疫 2004; **42**: 292-299.

39. Siegel RM, Frederiksen JK, Zacharias DA et al: Fas preassociation required for apoptosis signaling and dominant inhibition by pathogenic mutations. Science 2000; **288**: 2354-7.
40. Schneider P, Holler N, Bodmer J-L et al: Conversion of membrane-bound Fas (CD95) ligand to its soluble form is associated with downregulation of its proapoptotic activity and loss of liver toxicity. J Exp Med 1998; **187**: 1205-13.
41. Kamitani T, Nguyen HP, Yeh ETH: Activation-induced aggregation and processing of the human Fas antigen. J Biol Chem 1997; **272**: 22307-14.
42. Miyaji M, Jin ZX, Yamaoka S et al: Role of membrane sphingomyelin and ceramide in platform formation for Fas-mediated apoptosis. J Exp Med 2005; **202**: 249-59.
43. Brown DA, London E: Functions of lipid rafts in biological membranes. Annu Rev Cell Dev Biol 1998; **14**: 111-36.
44. Hueber A-O, Bernard A-M, Herincs Z et al: An essential role for membrane rafts in the initiation of Fas/CD95-triggered cell death in mouse thymocytes. EMBO reports 2002; **31**: 190-6.
45. Muppidi J, Siegel RM: Ligand-independent redistribution of Fas (CD95) into lipid rafts mediates clonotypic death. Nat Immunol 2004; **5**: 182-9.
46. Umehara H, Takashima A, Minami Y et al: Signal transduction via phosphorylated adhesion molecule, LFA-1 β (CD18), is increased by culture of natural killer cells with IL-2 in the generation of lymphokine-activated killer cells. Int Immunol 1993; **5**: 19-27.
47. RMロバーツ著, 安藤喬志訳: セレンディピティー —思いがけない発見・発明のドラマ—科学同人社, 2002年

Frontier in Immunology: Lipid Raft

Hisanori Umehara

Department of Hematology and Immunology, Kanazawa Medical University, Uchinada, Ishikawa 920-0293, Japan

Aggregation and clustering of cell surface receptors upon binding to their specific ligands has been reported for a variety of receptors, including T cell receptor (TCR)/CD3 complex, B-cell receptor (BCR), TNF-R, epithelial-derived growth factor receptor (EGF-R), CD2, CD44, CD11a/CD18 and Fas, and is facilitated by localization of receptor and proximal signaling components within cholesterol, glycosphingolipids and sphingomyelin (SM) rich membrane microdomains, known as lipid rafts. It has been suggested that membrane rafts provide a milieu for spatial segregation of specific sets of receptor/ligand at the plasma membrane and enhance the efficacy and specificity of interactions between enzymes involved in signal transduction. Recently, there is accumulating evidence that rafts are involved in Fas-induced apoptosis through translocation and clustering of Fas into rafts upon stimulation. Engagement of the Fas receptor (CD95) on type I cells initiates multiple signaling pathways leading to apoptosis, such as formation of death-inducing signaling complex (DISC), activation of caspase cascades and generation of the lipid messenger, ceramide. Sphingomyelin (SM) is a major component of lipid rafts, which are specialized structures that enhance the efficiency of membrane receptor signaling and are a main source of ceramide. However, the functions of SM in Fas-mediated apoptosis have yet to be clearly defined due to lack of molecular cloning of its responsible genes. After cloning cDNA responsible for SM synthesis (SMS-1), we established SM-synthase-defective WR19L cells transfected with human Fas gene (WR/Fas-SM(-)) and cells that have been functionally restored by transfection with SMS-1 (WR/Fas-SMS1). Here we show that expression of membrane SM enhances Fas-mediated apoptosis through increasing DISC formation, activation of caspases, efficient translocation of Fas into lipid rafts and subsequent clustering. Furthermore, WR/Fas-SMS1 cells, but not WR/Fas-SM(-), showed a significant increase in ceramide generation within lipid rafts upon Fas stimulation. These data suggest that membrane SM plays a crucial role in Fas clustering through aggregation of lipid rafts, leading to Fas-mediated type I apoptosis.

Key Words: lipid raft, sphingomyelin, TCR, Fas, apoptosis

１．研究課題名：分子生物学的手法による顎関節症の発症メカニズム解明と新規治療法開発
（研究番号　C2005-5）

２．キーワード：１）顎関節症（Temporomandibular joint disorders）
２）発症メカニズム（Pathogenesis）
３）生化学的解析（Biochemical analysis）
４）遺伝子学的解析（Genetic analysis）

３．研究代表者：瀬上　夏樹・医学部・教　授・顎口腔機能病態学（口腔科学）
研究分担者：金山　景錫・医学部・講　師・顎口腔機能病態学（口腔科学）
高橋　　克・京都大学・医学部・講　師・感覚運動系外科学講座口腔外科学分野
佐藤　　淳・北海道大学・歯学部・助　手・口腔病態学
出村　　昇・医学部・講　師・顎口腔機能病態学（口腔科学）

４．研究目的

近年、世界的規模で高齢化社会への移行が進んでおり、我国でも高齢化社会への移行につれてリウマチや変形性関節症などの老人性疾患の急増が社会的問題になりつつある。歯科領域でもう蝕・歯周病と並んで三大疾患にあげられる変形性関節症に属する顎関節症は臨床的に関節疼痛と開口障害など日常生活に多大な影響を及ぼすことから、この疾患の発症機構の解明と治療薬の開発が社会的に強く要望されている。われわれもこれまで顎関節症における臨床的・基礎的研究によりその主病態が滑膜炎であることを明らかにするとともに、サイトカインや発痛物質がその病態に関与して関節疼痛と機能障害に関連していることを世界に先駆けて報告してきた。他方、昨今では遺伝子レベルでの病態解明と治療が非常に注目されているが、顎関節症においてはいまだ未開拓の分野となっている。今研究では遺伝子に着眼し、これまでの成果をさらに推し進め、世界に先駆けて遺伝子レベルで顎関節症の発症メカニズムを明らかにし、あわせて遺伝子組み換えなどによる抗サイトカイン療法など新規治療法の開発を行うことを目的とした。

５．研究計画

（基礎的検討）①現在我々が開発中の顎関節症の動物モデル（ウサギ）に対して、ターゲットとするサイトカインおよび受容体の抗体を注入し、経時的な病理組織学的効果を判定して、サイトカイン療法の臨床応用の発展への可能性を模索する。②ヒトおよびウサギの滑膜細胞の培養細胞株を樹立して、ターゲットとする抗体の遺伝子のベクターを導入する。③ウサギの顎関節症モデルの顎関節部に同培養細胞を注入して病理組織学効果を判定して、遺伝子治療の臨床応用の可能性を検索する。④正常ウサギにおける薬剤による関節構造への影響を経時的に評価して、合併症の可能性への配慮を行う。

（臨床的検討）①顎関節症患者の滑膜組織中における炎症性サイトカインおよびその受容体のタンパク、mRNA の局在を組織学的、組織化学的染色手法により同定する。②患者の滑液中ならびに滑膜組織中の発痛物質（Bradykinin など）の定量的評価を行い、サイトカインとの関連を検討する。③顎関節症患者のなかで、通常の治療法で関節疼痛のコントロールが困難な症例を選択し、抗サイトカイン製剤（ヒト型の抗 TNF-α抗体、抗 IL-6 受容体抗体など）の関節腔内への局所注入

を開始する。この際には、術前の患者管理、インフォームドコンセントの確立、術後の症状、画像所見の変化を記録すべくプロトコールを作製のうえ慎重に臨床応用する。

なお、臨床検体ならびに動物実験におけるゲノム解析、遺伝子検索に際しては、本学の倫理委員会における申請と承認を受けることが前提となる。

6．研究成果

顎関節症、とくに最も発症頻度の高い顎関節症 III 型（顎関節内障）のより詳細な病態を明らかにするために以下の臨床的基礎的研究を遂行した。

（1）55 例の顎関節症患者と５名の無症状対照者の上関節腔から滑液を希釈採取して TNF-α、IL-6、IL-1β、可溶性 TNF-α receptor-1 および-II（sTNFR-I、sTNFR-II）、IL-6 可溶性 receptor（IL-6sR）、IL-1 可溶性 receptor II、IL-1 拮抗 receptor を ELISA 法で測定した。この結果、患者群の TNF-α、IL-6、IL-1β、sTNFR-I、sTNFR-II、IL-6sR 濃度が対照群よりも有意に高値であった [1]。これらのサイトカインならびに receptor は滑膜炎の up-regulate に作用し顎関節内障の発症過程で重要な役割を担うことが示された。

（2）家兎６羽６顎関節に対してスプリングを用いた外力を４週間負荷して作成した顎関節炎において、滑液を採取し総蛋白量を測定後、蛋白２μｇを SDS-PAGE に用いた。電気泳動で分離した各蛋白バンドをデンシトメトリック解析し、その強度を総バンド量に対する割合として数量化した。この結果、負荷群では非負荷群に比べて蛋白濃度が有為に高値を示した（1824μg vs. 398μg）。さらに泳動解析で負荷群では 140kd 以上のバンドが多く検出された [2]。外力付加による顎関節症モデルにおいても同様に患者と類似して滑液蛋白量は増加することが解明され、今後、本モデルを応用した病態解明および薬剤など新規治療法の開発に有用と考えられる。

（3）54 関節 54 例の顎関節内障患者と 8 例 10 関節の習慣性顎関節脱臼患者（対照群）について上腔鏡視下に滑膜組織をパンチ生検し Substance-P（SP）の免疫組織化学的染色を施行して両群を比較検討した。この結果、陽性細胞は滑膜表層細胞付近の血管内皮細胞に主に認められたが、患者群（陽性率 87%）では対照群（陽性 5/10 関節）よりも有意に陽性細胞数が多く認められた（P=.002）。しかしながら陽性細胞率と関節疼痛度あるいは鏡視下滑膜炎 score との関連はみられなかった [3]。以上より、SP は顎関節内障の病態形成に深く関与し、とくに疼痛発現との関連が示唆されるが、今後症例を追加して詳細な検討が必要と考えられる。

（4）46 関節 44 例の顎関節内障患者と 8 例 10 関節の習慣性顎関節脱臼患者（対照群）について上腔鏡視下に滑膜組織をパンチ生検し Interleukin-8（IL-8）の免疫組織化学的染色を施行して両群を比較検討した。この結果、陽性細胞は滑膜表層細胞付近の血管組織に主に認められたが、患者群（陽性率 80%）では対照群（陽性 2/10 関節）よりも有意に陽性細胞数が多く認められた（P=.004）。しかしながら陽性率と臨床所見との関連は明らかでなかった [4]。以上より、IL-8 は円板後方滑膜における炎症性変化を二次的に up-regulate し、病態形成に深く関与する可能性が示された。

（5）MR 画像において関節円板転位がなく正常円板位を示した 14 例 14 関節の顎関節内障クローズドロック症例についてその病態を検討した。全体の平均ロック期間は３か月で、その他、平均開口量は 28mm（15-32mm）、自覚的疼痛度（0-10）は平均 5（2-10）であった。全例で関節洗浄療法を施行したが、その際得られた上腔よりの滑液解析（9 関節）では平均蛋白量は 343μ

g/ml(36-791)と以前に行った非復位性転位を伴う同症例に比して低値を呈した。関節洗浄療法が無効であった５例に対しては関節鏡視下剥離授動術を施行したが、その際の鏡視下所見の定量的評価(0-10 点)では、滑膜炎が平均６点(2-7)、線維性癒着が平均７点(6-8)と通常のクローズドロック例と同等であった[5]。以上の検討により、典型的所見とされる関節円板前方転位を伴わないクローズドロック例が存在し典型例と類似した症状と病態を示すこと、また通法による治療法でコントロール可能なことが明らかとされた。

（6）一次治療として関節腔洗浄療法を施行した 66 例 66 関節の顎関節内障クローズドロック症例について、その際に希釈回収した上腔滑液の発痛物質すなわち Bradykinin (BK)、Leukotrien B4 (LTB4)、Prostaglandin E2 (PGE2)、Substance P (SP)について奏効群(51 関節)と非奏効群(15 関節)の両群で比較した。この結果、LTB4 の検出率は奏効群(47%)は非奏効群(16%)よりも有意に高かった(P<.05)。また BK の平均濃度は奏効群(425pg/ml)が非奏効群(144pg/ml)よりも有意に高値を示した(P<.0005)。さらに LTB4 と PGB4 の相互検出率は有意であった(P<.01)[6]。以上の結果により、本症の罹患関節では発痛物質の活性が up-regulate され治療奏効度に関与することを明らかにした。

（7）26 例の顎関節症患者（顎関節内障 16 例、変形性顎関節症 10 例）および対照群：(無症候者 7 名）の上関節腔滑液を希釈回収して総蛋白量を測定後、蛋白２μｇを SDS-PAGE に用いた。電気泳動で分離した各蛋白バンドをデンシトメトリック解析し、その強度を総バンド量に対する割合として数量化した。この結果、滑液中の平均総蛋白量は患者群（変形性顎関節症：2485μg、顎関節内障：1353μg）が対照群（615μg）より有為に高値を示した。電気泳動解析では、22 種の分子量の異なる糖鎖バンド（14ー700kd）が検出されたが、患者群では 140kd より大きな分子量の糖鎖が多く検出された[7]。以上より、罹病顎関節では炎症性変化の波及に伴い滑液蛋白の変化が惹起されることが明らかとなった。(本研究期間の掲載論文であるが謝辞記載欠落のため参考文献)

７．研究の考察・反省

以上の当該研究期間に得られた結果ならびにこれまで当講座で報告した結果から、顎関節症 III 型（顎関節内障クローズドロック）では、関節円板の非復位性前方転位の発現に伴って開口障害と関節運動痛が出現するが、この際に関節内でみられる病的所見は滑膜炎、線維性癒着が主体である。しかしながら滑膜炎の程度は組織学的には比較的経度であり、むしろ活性化された炎症性サイトカイン、発痛物質の up-regulation が顕著に認められたことから疼痛症状の大きな要因と考えられる。これらの種々の関節マーカーの活性化に伴う滑液中蛋白の増加が併せて特徴であるが、その発生起源は滑膜表層付近の血管内皮細胞であり円板の位置異常と機械的負荷に伴って増生した血管が反応性に炎症発現に貢献するものと考えられる。

反省点として、

１）市販キットなどを応用した主な関節マーカーの濃度測定あるいは免疫組織化学的染色は比較的容易に遂行できたが、滑液の微小蛋白の解析が困難であり、より詳細な病因解明として今後の課題である。

２）臨床検体ならびに動物実験におけるゲノム解析、遺伝子検索について倫理委員会の承認は得られたが、とくに骨変形に関する遺伝子解析の遂行が遅れ結果が未だ得られていない。本検討について継続して行う必要がある。

３）関節内のマーカーの活性上昇の結果をもとに、とくに新たな薬剤治療法の開発が急務である。

８．研究発表

Sato J, Segami N, Yoshitake Y, Kaneyama K, Abe A, Yoshimura H. Expression of capsaicin receptor TRPV-1 in synovial tissues of patients with symptomatic internal derangement of the temporomandibular joint and joint pain. Oral Surg Oral Med Oral Pathol Oral Radiol Endod 2005; 100: 674-681. (MLDB)

Fujimura K, Kobayashi S, Yoshitake Y, Tsuruoka N, Kaneyama K, Segami N. Electrophoretically separation of the synovial fluid proteins in rabbit temporomandibular arthritis induced by mechanical loading. J Oral Pathol Med 2005; 34: 546-551. (MLDB)

Sato J, Segami N, Nishimura M, Yoshitake Y, Kaneyama K, Yoshimura H, Kitagawa Y. Specific expression of substance P in synovial tissues of patients with symptomatic, non-reducing internal derangement of the temporomandibular joint: Comparison with clinical findings. Br J Oral Maxillofac Surg 2007; 45: 372-377. (MLDB)

Sato J, Segami N, Nishimura M, Yoshitake Y, Kaneyama K, Kitagawa Y. Expression of interleukin 8 in synovial tissues in patients with internal derangement of the temporomandibular joint and its relationship with clinical variables. Oral Surg Oral Med Oral Pathol Oral Radiol Endod 2007; 103: 467-474. (MLDB)

Kaneyama K, Segami N, Tsurusako S, Fujimura K, Sato J, Nagao T. Anchored disc phenomenon with a normally positioned disc in the temporomandibular joint: Characteristics and behaviour. Br J Oral Maxillofac Surg 2007; 45: 279-283. (MLDB)

Kaneyama K, Segami N, Sato J, Fujimura K, Nagao T, Yoshimura H. Prognostic factors in arthrocentesis of the temporomandibular joint: Comparison of bradykinin, leukotriene B4, prostaglandin E2, and substance P level in synovial fluid between successful and unsuccessful cases. J Oral Maxillofac Surg 2007; 65: 242-247. (MLDB)

Expression of capsaicin receptor TRPV-1 in synovial tissues of patients with symptomatic internal derangement of the temporomandibular joint and joint pain

Jun Sato, DDS, PhD,[a] Natsuki Segami, DDS, PhD,[b] Yoshino Yoshitake, PhD,[c]
Keiseki Kaneyama, DDS, PhD,[a] Atsuko Abe, DDS,[d] Hiroshi Yoshimura, DDS, PhD,[e]
and Kazuma Fujimura, DDS, PhD,[e] Ishikawa, Japan
KANAZAWA MEDICAL UNIVERSITY

Objective. To elucidate expression of capsaicin receptor TRPV-1 in synovial tissues of the human temporomandibular joint (TMJ) with internal derangement and discuss its relationship with joint pain.
Study design. Fifty-four TMJs in 54 patients were examined using an immunohistochemical technique. As controls, 10 TMJs with habitual dislocation without pain were also examined.
Results. TRPV-1 was expressed mainly in the blood vessels beneath the lining cells in synovial tissues from 31 of the 54 joints with internal derangement and from 8 of the 10 control joints. The extent score of TRPV-1–stained cells with internal derangement was not significantly higher than that of controls. The extent score of TRPV-1 showed no correlation with joint pain.
Conclusions. TRPV-1 was detected in the region of the posterior disk attachment of synovial tissues from the TMJ in patients with internal derangement and controls. TRPV-1 may play a role in maintenance of the physiologic condition of the TMJ.
(Oral Surg Oral Med Oral Pathol Oral Radiol Endod 2005;100:674-81)

Although pain allows the recognition of injury and triggers appropriate protective responses,[1] severe or continuous pain has a negative effect on overall quality of life. Many patients with internal derangement of the temporomandibular joint (TMJ) suffer from pain in the TMJ region. Although synovitis has been suggested to be one of the causes of TMJ pain, the pathophysiologic mechanisms of local pain are not completely understood.

Quinn and Bazan[2] first detected high levels of prostaglandin E2 in the synovial fluid of inflamed joints and demonstrated a strong correlation with pain. Many subsequent studies have demonstrated significant correlations between proinflammatory cytokines, such as interleukin 1β (IL-1β),[3,4] IL-6,[5] and tumor necrosis factor α (TNF-α)[6] in synovial fluids and joint pain. Previously, we demonstrated the expression of proinflammatory cytokines and growth factors, including IL-1β, IL-6, TNF-α, fibroblast growth factor 2 (FGF-2), and vascular endothelial growth factor (VEGF), in synovial tissues or synovial fluids of the TMJ and shown that these proinflammatory cytokines and growth factors were upregulated in symptomatic internal derangement.[7-11] Moreover, other types of chemical mediators, including neuropeptides such as substance P, calcitonin gene–related peptide (CGRP), and serotonin, have been detected in the TMJ.[12-14] These neuropeptides are released from activated peripheral nerve terminals into the surrounding tissues and cause an inflammatory response, which is known as neurogenic inflammation.[14] Recently, these neurogenic factors were recognized as keys to understanding the pathophysiology of arthritis.[15] These neuropeptides, such as substance P and CGRP, are present mainly in nociceptive C-fibers.[16-18] Small afferent unmyelinated C-fibers are usually correlated with nociception and the sensation of pain. In general, pain is induced when noxious stimuli excite the peripheral terminals of specialized primary afferent neurons called nociceptors.[19] Many different types of inotropic receptors are known to be involved in this process.[20-22] In 1997, one of these receptors, capsaicin receptor TRPV-1, was cloned and shown to play a key role in nociception and inflammatory pain.[23-25] Modulation of TRPV-1 activity is a promising pharmacologic target for analgesics in many conditions.[25] We

This study was partially supported by a Grant for Collaborative Research from Kanazawa Medical University (C2005-5) and Grant-in-Aid for Young Scientists (B-16791265) from the Ministry of Education, Culture, Sports, Science and Technology of Japan.
[a]Lecturer, Department of Oral and Maxillofacial Surgery.
[b]Professor and Chairman, Department of Oral and Maxillofacial Surgery.
[c]Associate Professor, Department of Biochemistry.
[d]Resident, Department of Oral and Maxillofacial Surgery.
[e]Associate Professor, Department of Oral and Maxillofacial Surgery.
Received for publication Dec 2, 2004; returned for revision Feb 12, 2005; accepted for publication Mar 17, 2005.
1079-2104/$ - see front matter

doi:10.1016/j.tripleo.2005.03.008

Table I. Patient and TRPV-1–staining score

Patient number	*Age (years)/sex*	*VAS*	*Synovitis score*	*TRPV-1 score*
1	23/F	4	8	0
2	24/F	8	8	0
3	70/F	7	7	5
4	36/F	7	5	0
5	61/M	7	5	3
6	70/F	5	3	0
7	38/F	8	7	66
8	55/M	9	5	44
9	22/F	4	6	0
10	40/F	7	8	75
11	28/F	6	6	18
12	41/F	10	3	5
13	21/F	5	6	45
14	23/F	5	5	80
15	56/F	3	5	0
16	55/F	4	4	5
17	50/M	8	6	33
18	50/F	6	10	0
19	18/F	6	6	0
20	17/F	6	5	0
21	84/F	3	2	0
22	35/M	6	5	0
23	35/F	6	4	0
24	76/F	5	2	7
25	73/F	5	5	0
26	52/F	1	6	20
27	40/F	4	9	55
28	18/F	8	2	45
29	33/F	7	4	0
30	17/F	9	4	80
31	24/F	9	8	78
32	58/F	6	4	6
33	31/F	7	4	0
34	39/M	2	9	65
35	52/F	1	3	15
36	56/F	10	2	0
37	36/F	8	5	41
38	35/F	4	6	0
39	58/F	6	5	0
40	52/F	5	2	82
41	61/F	5	6	0
42	38/F	7	3	0
43	48/M	5	4	0
44	23/F	7	6	0
45	53/F	3	7	65
46	55/F	8	9	20
47	32/F	7	4	15
48	36/M	5	7	0
49	25/F	3	6	35
50	19/F	7	7	85
51	56/F	4	8	90
52	13/F	5	9	70
53	40/F	8	5	75
54	22/F	5	8	82
55*	23/M	0	0	0
56*	66/F	0	0	35
57*	27/M	0	0	3
58*	46/M	0	0	2
59*	72/M	0	0	0
60*	72/M	0	0	4
61*	25/F	0	2	4
62*	25/F	0	0	15
63*	29/F	0	1	33
64*	55/F	0	0	20

Synovitis score, the degree of synovitis evaluated by arthroscopy[29];
TRPV-1 score, extent score of TRPV-1–positive cells (%).
*Control subjects with habitual dislocation.

hypothesized that TRPV-1 may be involved in joint pain in patients with internal derangement of the TMJ. Because the expression and distribution of TRPV-1 in synovial tissues of the human TMJ have not been reported, we performed an immunohistochemical study of synovial tissues of the TMJ and assessed the correlation between the expression of TRPV-1 and joint pain.

PATIENTS AND METHODS

Patients (Table I)

Fifty-four TMJs in 54 patients with symptomatic internal derangement were included in the present study. The patient population consisted of 7 men and 47 women with an average age of 41 years (range 13-84). MRI showed that all of the patients had anterior disk displacement without reduction. Their mean maximum interincisal opening was 33 mm and the mean duration of symptoms was 5 months. All of the patients underwent arthroscopic surgery following failure of nonsurgical treatment, consisting of occlusal appliances, nonsteroidal antiinflammatory drugs (NSAIDs), and physiotherapy, to resolve their clinical symptoms. Just before the operation, the degree of subjective pain from jaw movement was indicated by the patients on a visual analog scale (VAS) of 0 to 10: The VAS score ranged from 1 to 10, with a mean of 5.8.

The control group was comprised of 10 joints in 8 subjects (4 men and 4 women) with a mean age of 43 years (range 23 to 72) who had habitual dislocation without pain. All control patients underwent arthroscopic eminoplasty.[26] The validity of adopting these patients as controls has been discussed in detail previously and is outlined briefly below.[27]

All of the participants gave their informed consent to arthroscopy, synovial biopsy, and histologic examination.

Synovial tissues and immunohistochemical staining

Two or 3 synovial tissue biopsy specimens approximately 2 mm in diameter were obtained arthroscopically from each patient from a portion of the posterior

Table II. Scoring with intensity of synovitis[29]

Score	Findings
0	Normal pale, almost translucent, synovial lining with a fine network of anastomosing small blood vessels
1	Increased vascularity and capillary hyperemia (mild)
2	Increased vascularity and capillary hyperemia (moderate)
3	Increased vascularity and capillary hyperemia (severe)
4	Capillary dilatation and increasing network (mild to moderate)
5	Capillary dilatation and increasing network (severe)
6	Contact bleeding occurs on probe palpation (mild to moderate)
7	Contact bleeding occurs on probe palpation (severe)
8	Microbleeding and effusion
9	Granulative change, effusion and debris (mild to moderate)
10	Granulative change, effusion and debris (severe)

disk attachment using the triangular technique under direct visualization. Immediately after resection, the specimens were fixed in 4% paraformaldehyde for 8 hours and embedded in paraffin. Sections were prepared and stained immunohistochemically by the avidin-biotin technique (Vector Laboratories, Burlingame, Calif) as described previously.[9-11,27] After blocking nonspecific binding with 1.5% normal horse serum for 10 minutes at room temperature, the sections were treated with primary antibody to TRPV-1 (sc-20813, 1:200 dilution; Santa Cruz Biotechnology, Santa Cruz, Calif) and left overnight at 4°C. This antibody (sc-20813) was a purified polyclonal rabbit IgG derived from amino acids 1-150 of human TRPV-1, and its specificity was confirmed by the manufacturer. The following day, the specimens were incubated in a 1:200 dilution of antirabbit biotinylated antibody (Dako, Carpinteria, Calif) for 30 minutes at room temperature, and avidin/biotinylated horseradish peroxidase complex was added for 20 minutes at room temperature. The color was developed with 3-amino-9-ethyl carbazole followed by counterstaining with hematoxylin. Negative controls in which the primary antibody was replaced with normal rabbit IgG were run with each specimen. The TRPV-1–stained cells were counted in 2 to 5 regions of maximal immunohistochemical density (under light microscopy, magnification ×200), and the percentage of TRPV-1–stained cells was calculated. The extent score of TRPV-1–stained cells was calculated as the percentage of immunopositive blood vessels. About 10 to 100 blood vessels were evaluated in each specimen. This work was performed by 2 of the authors (KK and JS), who were unaware of which specimens had come from which patients.

Arthroscopy

Diagnostic arthroscopy was performed by the standard technique in the whole of the upper joint compartment, and all findings were recorded.[28] The degree of synovitis was evaluated according to the criteria of Murakami et al. (Table II).[29] This evaluation was performed by 2 of the authors (NS and JS) without knowledge of other information about the patients. The mean synovitis scores of patients with internal derangement and controls were 5.5 and 0.2, respectively.

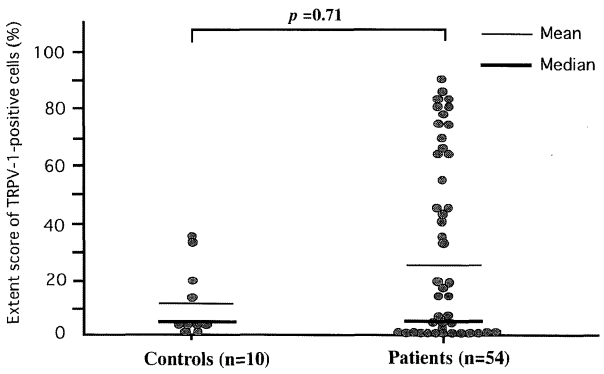

Fig 1. The extent score of TRPV-1–positive cells in synovial tissues of patients with internal derangement and controls. The extent score of TRPV-1–positive cells is not significantly different between the internal derangement group and control group. (P = .71; Mann-Whitney U-test)

Statistical analysis

The Mann-Whitney U-test was used to compare the extent score of TRPV-1–positive cells between the internal derangement and control groups. The Spearman correlation coefficient was used to assess correlations between the extent score of TRPV-1–positive cells and joint pain (VAS) and between the extent score of TRPV-1–positive cells and the degree of synovitis. Stat View J-5.0 (Abacus Concepts, Berkeley, Calif) was used for all statistical analyses. P values of less than .05 were considered significant.

RESULTS

Immunohistochemical staining

Cells that stained positively for TRPV-1 were seen in the synovial tissue specimens from 31 of the 54 joints (58%) in the internal derangement group, and from 8 of the 10 joints in the control group. The mean ± SD (median) extent score of TRPV-1–positive cells was 26.1 ± 32.1 (5.5) in the internal derangement specimens vs 11.6 ± 13.5 (4.0) in the control. The extent score of TRPV-1 was not significantly different between the internal derangement group and the control group (P = .71) (Fig 1).

In the internal derangement group, cells positive for TRPV-1 were seen mainly in the blood vessels beneath the lining cells. Cells positive for TRPV-1 were also

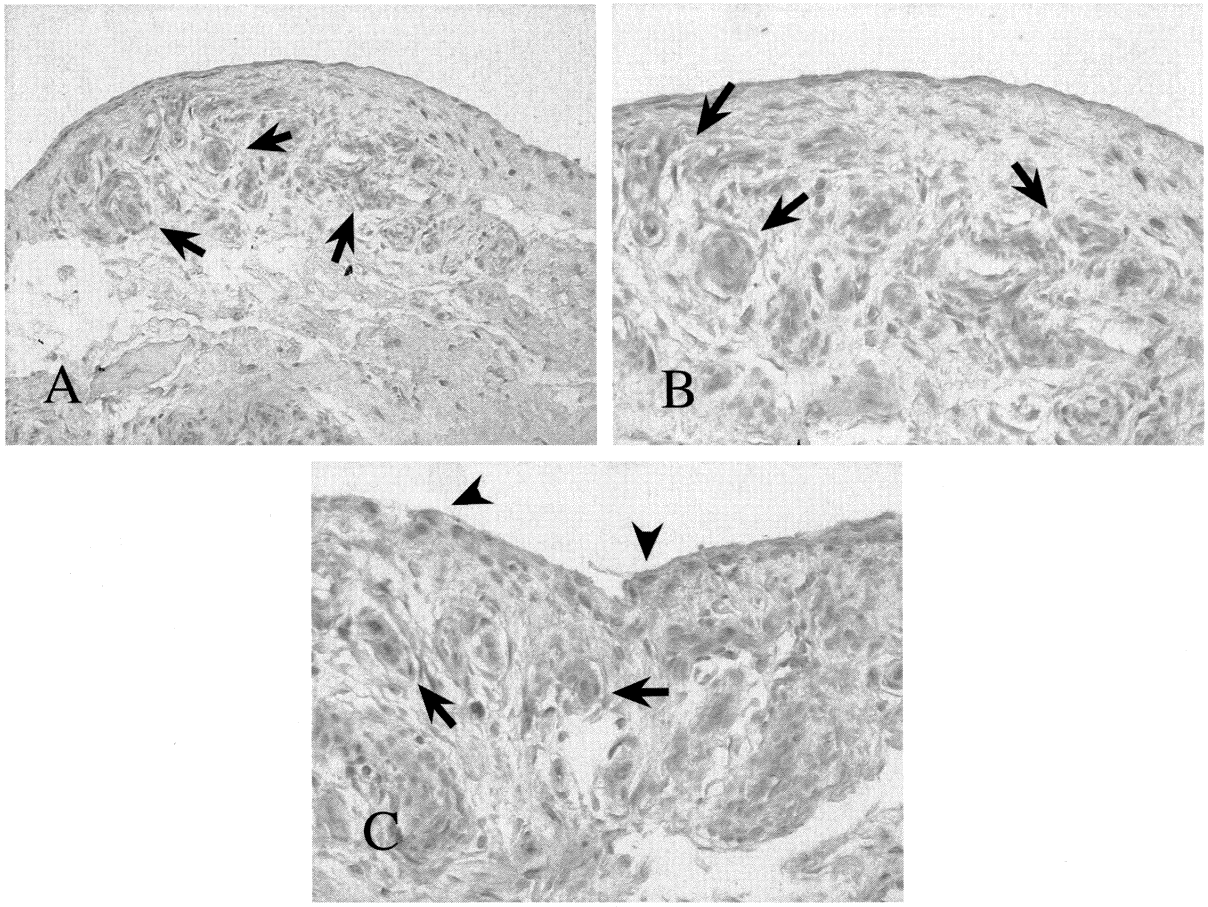

Fig 2. TRPV-1–stained sections obtained from patients with internal derangement (**A**, **B**, case number 45; **C**, case number 53). Immunoreactivities are observed in the blood vessels beneath the lining cells (*arrows*) and some cells lining the synovium (*arrowheads*) (original magnification: **A**: ×100; **B**, **C**: ×200).

seen in some lining cells (Fig 2). In the control specimens, TRPV-1–positive cells were seen in the blood vessels beneath the lining cells (Fig 3). The negative control sections showed only background staining (Fig 4).

Correlation of expression of TRPV-1 with joint pain (VAS), and the degree of synovitis

In the internal derangement group, there were no significant correlations between the extent score of TRPV-1–positive cells and joint pain (VAS) ($P = .606$, $r = 0.05$) (Fig 5). However, there was a significant positive correlation between the extent score of TRPV-1–positive cells and the degree of synovitis ($P = .048$, $r = 0.32$) (Fig 6).

DISCUSSION

The capsaicin receptor TRPV-1 is a sensory neuron–specific ion channel that serves as a polymodal detector of pain-producing physical and chemical stimuli.[1] Previous studies have shown that tissue inflammation heightens the sense of pain by producing an array of chemical mediators that activate or sensitize nociceptor terminals and increase the number of nociceptors such as TRPV-1.[1,19,22] Moreover, some inflammatory mediators, such as bradykinin and ATP, have been shown to induce excitation of nociceptors in many tissues.[30,31] The activation of TRPV-1–positive nerves is thought to induce the release of neuropeptides around the tissues,[32] and these neuropeptides increase the inflammatory response known as neurogenic inflammation.[1] This is a major factor leading to the vicious circle of chronic inflammation.

Internal derangement of the TMJ is often accompanied with synovitis. When synovitis occurs, the inflammatory changes in the synovial tissues include hyperplasia of the cells lining the synovial membrane and growth of small new blood vessels.[33,34] In a previous study, we demonstrated that the level of expression of CGRP, which is one of the major neuropeptides, was

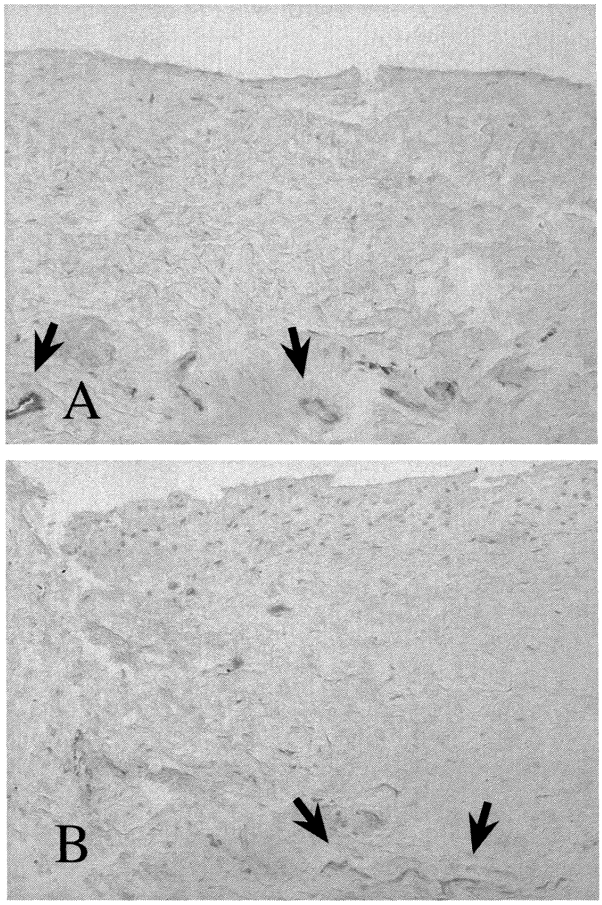

Fig 3. TRPV-1–stained sections obtained from control subjects (**A**, case number 63; **B**, case number 56). Immunoreactivities for TRPV-1 can be seen in the blood vessels beneath the lining cells (*arrows*) (original magnification ×200).

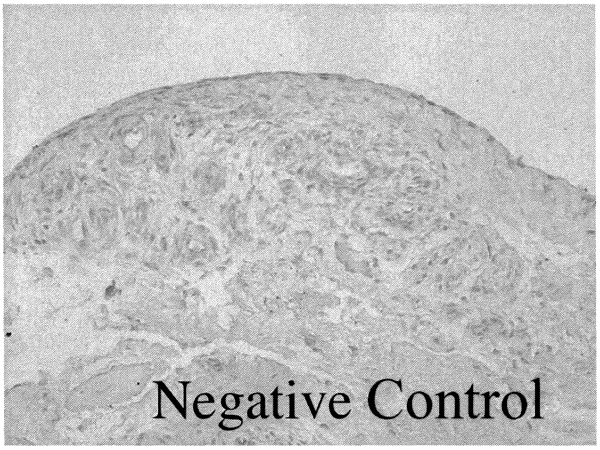

Fig 4. Immunohistochemical finding for negative control using normal rabbit IgG in the section obtained from a patient case number 45 with internal derangement. The section shows only background staining. (×100)

significantly higher in synovial tissues of the TMJ from the internal derangement group as compared with controls, and this neuropeptide seems to play an important role in the mechanism of pain production in patients with symptomatic internal derangement.[18]

The unexpected results obtained in the present study suggest that expression of TRPV-1 in synovial tissues of the TMJ may be involved in physiologic functions, such as reflex and protective responses. In fact, TRPV-1–sensitive nerves are thought to participate in a variety of reflex responses.[25] Moreover, TRPV-1 is thought to play a pivotal role in the mucosal defensive mechanism in gut lesions by controlling mucosal cell proliferation and submucosal blood flow.[24,32] We speculate that TRPV-1 may also play a defensive role in the synovial membrane. Nociceptors have been shown to play major roles in reflex responses and maintenance of homeostasis. The results of the present study indicated that TRPV-1–positive cells were present in the region of posterior disk attachment of the synovial tissues of patients with internal derangement and habitual dislocation (controls) of the TMJ. The extent score of TRPV-1–positive cells was not significantly higher in the internal derangement group than in the control group. Moreover, there was no significant correlation between the expression of TRPV-1and joint pain (VAS). These results were unexpected because we hypothesized that the expression of TRPV-1in synovial tissues would be increased in the internal derangement group as compared with controls.

In the internal derangement group, there was a weak positive correlation between TRPV-1 expression and the degree of synovitis evaluated by arthroscopy. This result may support our previous hypothesis that TRPV-1 is an important regulator of joint pain. However, because the correlation was weak and TRPV-1 expression was detected also in the noninflammatory (control) synovial tissues, we speculated that TRPV-1 may be a factor in the maintenance of physiologic conditions. Unfortunately, we were unable to determine the contribution of TRPV-1 to pathologic conditions in TMJ synovial tissues in the present study. Our observations suggested that TRPV-1 may not be a good candidate for pharmacologic targeting by analgesics for the treatment of TMJ pain. However, further studies using not only immunohistochemical techniques but also other biologic methods are required to elucidate the possible contributions of TRPV-1 to pathologic conditions.

In the present study, TRPV-1–immunopositive cells were detected around the blood vessels under the lining cells in specimens from both the internal derangement and the control groups. To our knowledge, this is the first report of the expression of TRPV-1 in synovial tissue of

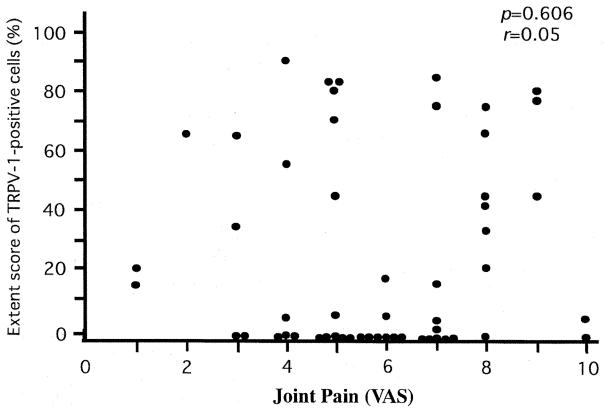

Fig 5. The extent score of TRPV-1–positive cells and VAS of pain. Significant correlation is not indicated by the Spearman correlation coefficient. ($P = .606$, $r = 0.05$)

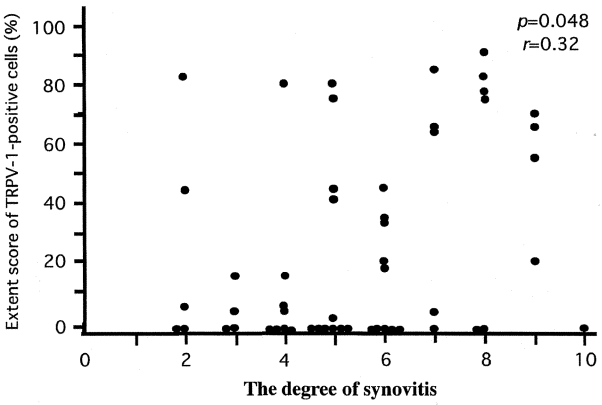

Fig 6. The extent score of TRPV-1–positive cells and the degree of synovitis. Significant positive correlation is indicated by the Spearman correlation coefficient. ($P = .048$, $r = 0.32$)

the human TMJ. Until recently, it was thought that TRPV-1 protein and mRNA expression were restricted to tissues of the central nervous system.[20,25] However, most internal organs have now been shown to possess peripheral nerve fibers containing TRPV-1, and the presence of TRPV-1 mRNA has been demonstrated in various nonneural tissues.[25,35] In a previous immunohistochemical study, Nozawa et al.[24] detected distinct TRPV-1–positive cells around blood vessels in the submucosa of the rat stomach. Generally, capsaicin-sensitive sensory neurons contain neuropeptides, such as substance P.[32] Although there have been no previous reports of the expression of TRPV-1 in human synovial tissues of the TMJ, Henry et al.[14] demonstrated cells immunopositive for substance P mainly within the walls of the vasculature in synovial tissues of the human TMJ. The results of both the present and these previous studies indicate that TRPV-1 is present at least in the blood vessels under synovial lining cells.

The major limitations of the present study were the small number and characteristics of the control patients. These problems are difficult to overcome, as it is impossible to obtain fresh samples of synovial tissues from healthy individuals.[11] However, we feel that these patients with dislocation were suitable controls because they were nonsymptomatic except for occasional difficulty in closing their mouths and MRI revealed a normal disk position in the closed-mouth position. None of the control subjects reported pain. In our previous immunohistochemical study,[10] the number of small blood vessel (microvessel density) in the synovial tissues were significantly lower in patients with habitual dislocation without pain than in those with symptomatic internal derangement. Moreover, in the present study, the mean synovitis score evaluated by arthroscopy in the control group was 0.2. These results suggest that the synovial tissues of patients with habitual dislocation without pain are very similar to normal synovial tissues in both morphologic and histologic respects. In the present study, TRPV-1–positive cells were also present in the control synovial tissues at a high rate, and the distribution pattern of TRPV-1 in the control synovial tissues was almost the same as that in the internal derangement group. Previous studies indicated that sensory joint nerve fibers are indispensable for control of joint movement and for protection of joint structures.[36,37]

Because we performed punch biopsy from the posterior disk attachment, it was not possible to determine the distribution of TRPV-1 of the whole intracapsular structure of the TMJ. Beacuse the pathologic mechanisms underlying joint pain are very complex, we therefore cannot exclude the possibility that TRPV-1 is involved in the pathologic conditions. Another problem in the present study was the relatively low expression rate of TRPV-1–positive cells in synovial tissues. TRPV-1–positive cells were detected in synovial tissue specimens from 31 of 54 (57%) joints with internal derangement as compared with 8 of the 10 control joints with habitual dislocation. If TRPV-1 is involved mainly in physiologic rather than pathologic functions, it should have been detected in all of the internal derangement and control specimens. The relatively low rate may have been due to limitations of sensitivity of the primary antibody on paraffin-embedded sections.

In conclusion, TRPV-1 was detected in the region of posterior disk attachment of the synovial tissues in patients with internal derangement and controls with habitual dislocation of the TMJ. TRPV-1 may play an important role in the maintenance of physiologic

conditions in the TMJ. Further studies are required to elucidate the possible contribution of TRPV-1 to pathologic conditions in patients with internal derangement of the TMJ.

REFERENCES

1. Numazaki M, Tominaga T, Toyooka H, Tominaga M. Direct phosphorylation of capsaicin receptor VR1 by protein kinase Cε and identification of two target serine residues. J Biol Chem 2002;277:13375-8.
2. Quinn JH, Bazan NG. Identification of prostaglandin E2 and leukotriene B4 in the synovial fluid of painful, dysfunctional temporomandibular joints. J Oral Maxillofac Surg 1990;48: 968-71.
3. Takahashi T, Kondoh T, Fukuda M, Yamazaki Y, Toyosaki T, Suzuki R. Proinflammatory cytokines detectable in synovial fluids from patients with temporomandibular disorders. Oral Surg Oral Med Oral Pathol Oral Radiol Endod 1998;85:135-41.
4. Takahashi T, Nagai H, Seki H, Fukuda M. Relationship between joint effusion, joint pain, and protein levels in joint lavage fluid of patients with internal derangement and osteoarthritis of the temporomandibular joint. J Oral Maxillofac Surg 1999;57: 1187-93.
5. Fu K, Ma X, Zhang Z, Pang X, Chen W. Interleukin-6 in synovial fluid and HLA-DR expression in synovium from patients with temporomandibular disorders. J Orofac Pain 1995;9:131-7.
6. Shafer DM, Assael L, White LB, Rossomando EF. Tumor necrosis factor-α as a biochemical marker of pain and outcome in temporomandibular joints with internal derangements. J Oral Maxillofac Surg 1994;52:786-91.
7. Suzuki T, Segami N, Kaneyama K, Nishimura M, Nojima T. Specific expression of interleukin 1β in temporomandibular joints with internal derangement: correlation with clinical findings. Oral Surg Oral Med Oral Pathol Oral Radiol Endod 1999;88:413-7.
8. Suzuki T, Segami N, Nishimura M, Nojima T. Co-expression of interleukin-1β and tumor necrosis factor-α in synovial tissues and synovial fluids of temporomandibular joint with internal derangement: comparison with histologic grading of synovial inflammation. J Oral Pathol Med 2002;31:549-57.
9. Sato J, Segami N, Nishimura M, Demura N, Yoshimura H, Yoshitake Y, et al. Expression of interleukin 6 in synovial tissues in patients with internal derangement of the temporomandibular joint. Br J Oral Maxillofacial Surg 2003;41:95-101.
10. Sato J, Segami N, Yoshitake Y, Nishikawa K. Correlation of the expression of fibroblast growth factor-2, vascular endothelial growth factor, and their receptors with angiogenesis in synovial tissues from patients with internal derangement of the temporomandibular joint. J Dent Res 2003;82:272-7.
11. Sato J, Segami N, Kaneyama K, Konishi H, Yoshitake Y, Nishikawa K. Levels of fibroblast growth factor-2 in synovial fluids in human patients with internal derangement of the temporomandibular joint. Oral Surg Oral Pathol Oral Radiol Endod 2003;96:673-9.
12. Holmlund A, Ekblom A, Hansson P, Lind J, Lundeberg T, Theodorsson E. Concentrations of neuropeptides substance P, neurokinin A, calcitonin gene—related peptide, neuropeptide Y and vasoactive intestinal polypeptide in synovial fluid of the human temporomandibular joint. Int J Oral Maxillofac Surg 1991;20:228-31.
13. Kopp S. The influence of neuropeptides, serotonin, and interleukin 1β on temporomandibular joint pain and inflammation. J Oral Maxillofac Surg 1998;56:189-91.
14. Henry CH, Wolford LM. Substance P and mast cells: preliminary histologic analysis of the human temporomandibular joint. Oral Surg Oral Med Oral Pathol Oral Radiol Endod 2001;92: 384-9.
15. Deal CL, Schnitzer TJ, Lipstein E, Seibold JR, Levy MD, Albert D, et al. Treatment of arthritis with topical capsaicin: a double-blind trial. Clin Ther 1991;13:383-95.
16. Wiesenfeld-Hallin Z, Hokfelt T, Lundberg JM, Forssmann WG, Reinecke M, Tscopp FA. Immunoreactive calcitonin gene—related peptide and substance P coexist in sensory neurons to the spinal cord and interact in spinal behavioral response of the rat. Neurosci Lett 1984;52:199-204.
17. Pedersen-Bjergaard U, Nielsen LB, Jensen K, Edvinsson L, Jansen I, Olesen J. Calcitonin gene—related peptide, neurokinin A and substance P: effects on nociception and neurogenic inflammation in human skin and temporal muscle. Peptides 1991;12:333-7.
18. Sato J, Segami N, Kaneyama K, Yoshimura H, Fujimura K, Yoshitake Y. Relationship of calcitonin gene—related peptide in synovial tissues and temporomandibular joint pain in humans. Oral Surg Oral Med Oral Pathol Oral Radiol Endod 2004;98: 533-40.
19. Tominaga M, Wada M, Masu M. Potentiation of capsaicin receptor activity by metabotropic ATP receptors as a possible mechanism for ATP-evoked pain and hyperalgesia. Proc Natl Acad Sci USA 2001;98:6951-6.
20. Cateria MJ, Julius D. Sense and specificity: a molecular identity for nociceptors. Curr Opin Neurobiol 1999;9:523-30.
21. Julius D, Basbaum AI. Molecular mechanisms of nociception. Nature 2001;413:203-10.
22. Numazaki M, Tominaga M. Molecular mechanisms of nociception and thermosensation: structures, expressions and functions of capsaicin receptor and its homologues. Seikagaku 2003;75: 359-71.
23. Cateria MJ, Schumacher MA, Tominaga M, Rosen TA, Levine JD, Julius D. The capsaicin receptor: a heat-activated ion channel in the pain pathway. Nature 1997;389:816-24.
24. Nozawa Y, Nishihara K, Yamamoto A, Nakano M, Ajioka H, Matsuura N. Distribution and characterization of vanilloid receptors in the rat stomach. Neurosci Lett 2001;309:33-6.
25. Szallasi A. Vanilloid receptor ligands: hope and realities for the future. Drug Aging 2001;18:561-73.
26. Segami N, Kaneyama K, Tsurusako S, Suzuki T. Arthroscopic eminoplasty for habitual dislocation of the temporomandibular joint: preliminary study. J Craniomaxillofac Surg 1999;27:390-7.
27. Sato J, Segami N, Suzuki T, Kaneyama K, Yoshitake Y, Nishikawa K. The expression of vascular endothelial growth factor in synovial tissues in patients with internal derangement of the temporomandibular joint. Oral Surg Oral Med Oral Pathol Oral Radiol Endod 2002;93:251-6.
28. McCain JP, de la Rua H, LeBlanc WG. Puncture technique and portals of entry for diagnostic and operative arthroscopy of the temporomandibular joint. Arthroscopy 1991;7:221-32.
29. Murakami k, Segami N, Fujimura K, Iizuka T. Correlation between pain and synovitis in patients with internal derangement of the temporomandibular joint. J Oral Maxillofac Surg 1991;49: 1159-61.
30. Chuang H, Prescott ED, Kong H, Scields S, Jordt SE, Basbaum AI, et al. Bradykinin and nerve growth factor release the capsaicin receptor from ptdlns (4,5) P2-mediated inhibition. Nature 2001;411:957-62.
31. Sugiura T, Tominaga M, Katsuya H, Mizumura K. Bradykinin lowers the threshold temperature for heat activation of vanilloid receptor 1. J Neurophysiol 2001;88:544-8.
32. Kido MA, Muroya H, Yamaza T, Terada Y, Tanaka T. Vanilloid receptor expression in the rat tongue and palate. J Dent Res 2003;82:393-7.
33. Mefill RG, Yih WY, Langan MJ. A histologic evaluation of the accuracy of TMJ diagnostic arthroscopy. Oral Surg 1990;70: 393-8.
34. Gynther GW, Holmlund AB, Reinholt FP. Synovitis in internal derangement of the temporomandibular joint: correlation between arthroscopic and histologic findings. J Oral Maxillofac Surg 1994;52:913-7.

35. McIntyre P, McLatchie LM, Chambers A, Phillips E, Clarke M, Savidge J, et al. Pharmacological differences between the human and rat vanolloid receptor 1 (VR1). Br J Pharmacol 2001;132: 1084-94.
36. Connolly DT. Vascular permeability factor, a unique regulator of blood vessel function. J Cell Biochem 1991;47:219-23.
37. Cohen T, Nahari D, Cerem LW, Neufeld G, Levi BZ. Interleukin 6 induces the expression of vascular endothelial growth factor. J Biol Chem 1996;271:736-41.

Reprint requests:
Jun Sato, DDS, PhD
Department of Oral and Maxillofacial Surgery
Kanazawa Medical University Daigaku
Uchinada-machi, Kahoku-gun, Ishikawa
920-0293, Japan
jun-s@kanazawa-med.ac.jp

J Oral Pathol Med (2005) 34: 546–51

www.blackwellmunksgaard.com/jopm

Electrophoretically separation of the synovial fluid proteins in rabbit temporomandibular arthritis induced by mechanical loading

K. Fujimura[1], S. Kobayashi[1], Y. Yoshitake[2], N. Tsuruoka[2], K. Kaneyama[1], N. Segami[1]

Departments of [1]Oral and Maxillofacial Surgery; and [2]Biochemistry, Kanazawa Medical University, Ishikawa, Japan

BACKGROUND: The concentration of protein in synovial fluid (SF) of temporomandibular joints (TMJs) with disorders tends to be increased. We investigated the protein composition of SF of rabbits in which arthritis of the TMJ was induced.

METHOD: Arthritis was induced in six TMJs in six rabbits by exertion of a load for 4 weeks. Six non-loaded TMJs in six rabbits served as controls. The protein concentration and content in TMJ SF of the two groups were compared.

RESULTS: The mean protein concentration was higher in the SF of the loaded group than in that of the non-loaded group (1824 μg/ml vs. 398 μg/ml, $P = 0.002$). Proteins with molecular weights of more than 95 kDa were abundant in the loaded group ($P < 0.05$).

CONCLUSION: Temporomandibular arthritis induced by mechanical loading in rabbit is accompanied by an increase in the abundance of relatively high molecular weight proteins in SF.

J Oral Pathol Med (2005) **34**: 546–51

Keywords: arthritis; mechanical loading; proteins of synovial fluid; rabbits; SDS-PAGE; temporomandibular joint disorders

Introduction

A diverse range of studies on the pathophysiological mechanism of temporomandibular joint disorders (TMD) has been performed to date. It has been revealed that synovitis observed by arthroscopy is consistent with synovitis seen in biopsy specimens (1–4), the total protein concentration of the synovial fluid (SF) is increased in cases of TMD with joint pain and/or joint effusion (5, 6), and proinflammatory cytokines, such as tumor necrosis factor-α (TNF-α), interleukin-1β (IL-1β) and IL-6, are also involved (7–12). The increase in TNF-α and IL-1 may contribute to degradation of the cartilage because, in synovial fibroblast cultures, IL-1 or TNF-α, either independently or together, induce matrix metalloproteinase-1 (MMP-1), MMP-3 and MMP-13 (13), which can cleave type II collagen in the articular cartilage (14). In addition, the hyaluronic acid, one of main components of SF, from patients with TMD was also degraded (15, 16), inferred from the mechanism of reactive oxidative radical species generated by hypoxic-reperfusion injury (17, 18). In short, the temporomandibular joints (TMJ) with inflammatory changes might fail to maintain proper homeostasis.

Synovial fluid in extremities in healthy subjects contains about one-third as much total protein as in plasma and a large amount of low-molecular weight albumin, and a smaller amount of gamma-globulin, with consequent increase in the albumin/globulin ratio (7.8 in contrast to 2.7 in normal sera) (19). In addition, SF has a lower percentage of high molecular weight proteins (20, 21).

These alterations in the composition of SF can therefore give us clues to the pathology of the TMJ. In order to further our understanding of TMD, in this study, we analyzed the composition of SF from rabbit TMJs in which arthritis had been induced by exerting a continuous force on the glenoid fossa. We choose this animal model, which we have previously described (22), because excessive force on the glenoid fossa is thought to be a key factor in the induction of TMD.

Material and methods

This study was conducted in accordance with the guidelines for animal experiments in Kanazawa Medical University. The rabbits were chosen because their size is suitable for good anatomic observation.

Preparation of arthritis model induced by mechanical loading

The animal model of arthritis has been described previously (22). In brief, six Japanese male white rabbits,

Correspondence: Dr Kazuma Fujimura, Department of Oral and Maxillofacial Surgery, Kanazawa Medical University, 1-1 Uchinada, Ishikawa 920-0293, Japan. Fax: +81 76 286 2010. E-mail: 1-kkk@kanazawa-med.ac.jp
Accepted for publication May 25, 2005

weighing 3.0–3.3 kg, were anesthetized by injecting 30 mg/kg of sodium pentobarbital into the marginal vein of the ear. The left submandibular skin was incised and the inferior margin of the mandibular ramus was exposed. Two holes were made in the antegonial notch, and stainless steel wire 0.5 mm in diameter was passed through them. The orbital edge and the proximal area of the zygomatic arch were exposed, and two holes were made approximately 7 mm from the TMJ capsule. Stainless steel wire 0.4 mm in diameter was introduced through the holes. The subcutaneous tissue and skin were sutured tightly, and a coil spring (Helical Extension Spring; SUS304WPB, JIS-G 4314, Accurate Sales Co. Ltd., Saitama, Japan) was placed in one side of the TMJ and attached to the wires. The coil exerted a force of 1-N (Fig. 3). Six joints in another three rabbits that served as control group were not subjected to any treatment.

Sampling of synovial fluids and plasma

Four weeks after the surgery, the rabbits in both groups were anesthetized by intravenous injection of pentobarbital. SF was then collected using a modification of the method described by Tominaga et al. (23) In this procedure, we shaved the TMJ area, and then made an incision in the skin covering the temple to expose the articular capsule. From the posterior aspect of the articular eminence, we inserted a disposable butterfly needle (27G, Neonatal Scalp Vein Needle, Atom Medical Co., Japan) through the articular capsule and into the superior compartment of the TMJ cavity. We inserted a second butterfly needle of the same type by the side of the first needle, to serve as an outflow. Saline solution was injected into the cavity and the rabbits were made to open and close their mouth ten times to mix the saline with the SF. About 500 μl of the SF diluted with saline was aspirated from the cavity at a flow rate of 0.05 ml/min by using an infusion pump. The diluted SF was centrifuged (800 *g* for 20 min at 4°C) to remove the blood cells and micro-tissue fragments, and aliquots were stored at −80°C. Only samples containing < 0.5 μl/ml of red blood cells in the centrifuged pellet were used in this study. In addition, the plasma from animals in the both groups was also collected, centrifuged and stored at −80°C.

SDS-PAGE analysis

The protein content of each SF sample and plasma was determined using the bicinchoninic acid (BCA) protein assay (Pierce Chemical Co., Rockford, IL, USA). Samples of each fluid and plasma containing 2 μg of total protein were subjected to SDS-PAGE (24) on 5–20% gradient acrylamide gels (90 × 83 × 1 mm). Each protein band was visualized by staining with silver (Silver Stain II Kit, Wako Pure Chemical Industries Ltd., Osaka, Japan) and quantified by densitometric analysis (Scion Image, version 4.02, Scion Co., Frederick, MD, USA). Each value of intensity obtained in the densitometric analysis was expressed as a percentage of the sum value of the intensities and, averaged for each specified range of MWs.

Confirmation of arthritis in loaded TMJs

To confirm the occurrence of synovial inflammation in the loaded TMJ and to evaluate the level of synovitis, TMJ tissue was histopathologically graded and the concentration of inflammatory cytokines in the SF was assayed. The rabbits were killed by intravenous injection of excess pentobarbital after the SF had been collected. Their heads were fixed in 4% paraformaldehyde, and 20 × 20 mm specimens of the TMJ and surrounding tissue were removed and decalcified with 10% ethylenediaminetetraacetic acid (EDTA) solution and then embedded in paraffin. Serial sagittal sections 3–5 μm in thickness were stained with hematoxylin and eosin, and histopathologically graded according to Gynther's system (25). In brief, the intensity of inflammation in the synovium was quantified using the following criteria; synovial lining cell layers: (i) normal, one to two cell layers (0 points), (ii) two to three cell layers (1 point), (iii) three to five cell layers (2 points), (iv) five or more cell layers (3 points). The inflammatory cytokines in rabbit, IL-1β and TNF-α, in the collected SF and plasma were assayed using an enzyme-linked immunosorbent assay kit (Quantikine ELISA; R & D System Inc, Minneapolis, MN, USA) with limits of detection of 0.0625 pg/ml for IL-1β and 0.008 for TNF-α, as previously described (23).

Statistical analysis

The mean total protein and cytokine concentrations, and histopathologic grades, as well as the intensity of protein bands quantified by densitometric analysis, were compared using the *F*-test and either Student's *t*-test or Welch's *t*-test. *P*-values < 0.05 were considered significant.

Results

Confirmation of arthritis

As shown in Fig. 1, there were histological signs of arthritis in the loaded TMJs: there was hyperplasia of the synovium in the upper joint cavity; there were vascularity and vascular dilatations under the synovial lining cells (Fig. 1a,b); and the cartilage layer in the surface of the articular eminence was thin and it was in the condylar surface had disappeared. In contrast, there were no histological signs of arthritis in the non-loaded TMJs: the synovial membrane in the upper joint compartment generally consisted of a layer of only one or two cells, under which there were no inflammatory cells (Fig. 2a,b); the surfaces of the articular eminence and condyle were covered with smooth, thin fibrous tissue; and the layers of cartilage in the articular eminence and the condyle was of constant thickness.

As expected, synovial inflammation was also more intense in the loaded group, with the mean score being 1.4 ± 0.5 as compared with 0.4 ± 0.5 in the control group ($P = 0.0174$). Furthermore, the mean concentrations of TNF-α and IL-1β, indices of arthritis, in SF-saline mixture were higher in the loaded group than in the non-loaded group ($P = 0.0247$ and $P = 0.037$, respectively; Table 1). On the contrary, the

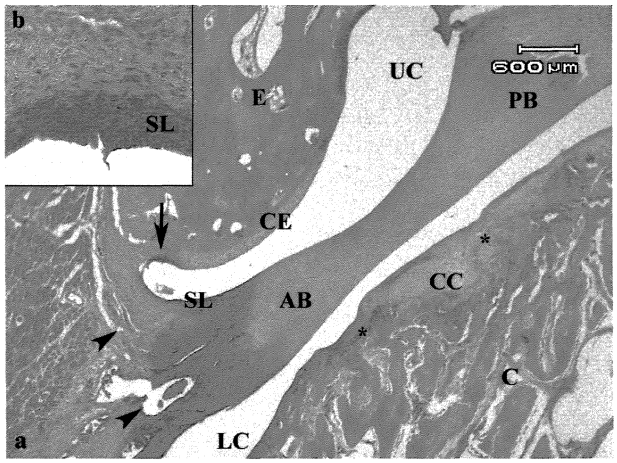

Figure 1 (a) Low-power microphotograph of a mid-sagittal section of TMJ in the loaded group with three point of histopathologic score (H&E stain, original magnification, ×12.5). (b) High-power microphotograph of arrowed area in (a) (H&E stain, original magnification, ×100). Abbreviations: AB, anterior band of disc; C, condylar head; CC, condylar cartilage; CE, cartilage of eminence; E, articular eminence; LC, lower compartment; PB, posterior band of disc; SL, synovial lining cells; UC, upper compartment. Hyperplasia of the synovial lining cells in the upper joint cavity (arrow, b) and increased vascular dilatations under the synovial lining cells (arrowheads). The cartilage layer in the surface of the articular eminence and condylar had decreased. The asterisks indicate degraded cartilage.

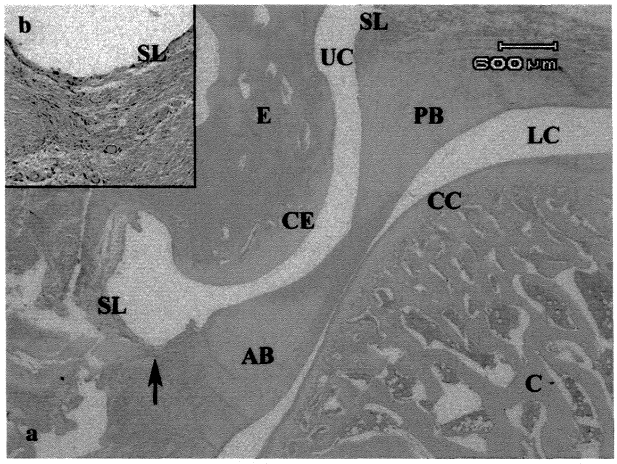

Figure 2 (a) Low-power microphotograph of a mid-sagittal section of TMJ in the non-loaded group with one point of histopathologic score (H&E stain, original magnification ×12.5). (b) High-power microphotograph of arrowed area in (a) (H&E stain, original magnification, ×100). Layers, generally, one or two cells thick, and no inflammatory cells under the synovial lining. The cartilage layer in the surface of the articular eminence and condylar was clear.

concentrations of these cytokines in the plasma from both groups were undetectable.

Protein in SF and plasma

The mean total protein concentration in the SF was 1824 μg/ml (range: 1114–3984 μg/ml) in the loaded group compared with 398 μg/ml (range: 164–724 μg/ml) in the non-loaded group ($P = 0.002$; Table 1). There was no significant difference between the total protein concentrations in the plasma of the two groups.

Typical SDS-PAGE band patterns of protein in SF from the loaded and non-loaded groups are shown in Fig. 4. The SF of both groups contained 21 different proteins, with molecular weights (MW) ranging from 14 to 500 kDa. In both groups, the intensities of the bands of the proteins with MW between 40 and 84 kDa were relatively high, and were similar to those of the proteins analyzed from plasma. The most abundant proteins, whose MWs were 66, 50 and 25 kDa, were probably albumin, IgG heavy-chain, and IgG light-chain, respectively, based on the abundance and MW of proteins in human SF (26, 27).

The size of the predominant proteins, along with the mean intensity of each protein band for SF and plasma are shown in Table 2. The concentrations of proteins with MWs of 280, 180, 175, 140, 126, 116 and 95 were higher in the loaded group ($P < 0.05$), while the concentrations of the protein with an MW of 66 kDa was lower in the loaded group ($P < 0.05$). For both groups, the concentration of proteins with relatively high MW, that is, more than 84 kDa, and the concentration of the 40 kDa proteins were lower in the SF than in the plasma. There were no significant quantitative differences between the plasma samples of the two groups.

Discussion

We have previously shown that the method used to induce arthritis in the rabbit TMJs is reliable (22). In our previous study, the intensity of synovitis gradually increased from 1 week after the start of loading and peaked at 4 weeks during an 8-week observation period, and type II collagen was degraded in the cartilage of the articular eminence and condyle with time. Four weeks after the start of loading, the intensity of synovitis, assessed by Gynther's reliable system, was similar in degree to that in specimens obtained arthroscopically from patients with TMD (3). In the present study, we confirmed that arthritis was induced in the loaded group at 4 weeks, but not in the non-loaded group: the histopathologic scores were significantly higher in the loaded group than in the non-loaded group; and the levels of TNF-α and IL-1β, which are indices of arthritis, were also significantly higher in the SF of the loaded group than in the SF of the non-loaded group.

In an antigen-induced arthritis model (28), IL-1β was observed predominately in inflammatory cells, synovial cells and subsynovial fibroblasts within 3 days in the acute stage and was observed in chodrocytes at 6 weeks in the chronic stage. IL-1β is synthesized by macrophages stimulated by TNF-α, and is known to cause bone resorption (29). We observed in our mechanical loading model that the cartilage of articular eminence and condylar head was degraded (Fig. 1). IL-1β and TNF-α might closely mediate the induction of synovitis and the subsequent degradation of type II collagen in TMJ cartilage, by a mechanism similar to that in antigen-induced arthritis.

Table 1 Concentrations of total protein and cytokines in the synovial fluid and plasma

	Total protein (μg/ml)	*TNF α (pg/ml)*	*IL 1β (pg/ml)*
Loaded group ($n = 6$)	1824 ± 806* (1114–3984)	0.99 ± 0.53* (0.33–1.57)	25.35 ± 18.93* (1.19–50.07)
Non-loaded group ($n = 6$)	398 ± 298 (164–724)	0.40 ± 0.39 (0.02–1.11)	4.52 ± 6.23 (0.00–12.99)
Plasma ($n = 12$)	13595 ± 681 (12410–14320)		
Loaded group ($n = 6$)	13420 ± 978 (12410–14320)	ND	ND
Non-loaded group ($n = 6$)	13703 ± 410 (13290–14110)	ND	ND

*Significant difference between loaded and non-loaded groups, $P < 0.05$.
Values are mean ± SD. Range of values are given in parentheses. ND, undetectable.

Table 2 Mean abundance of proteins from synovial fluid and plasma (%)

	Synovial fluid		*Plasma*	
Molecular weight (kDa)	*Load*	*Non-load*	*Load**	*Non-load***
500	0.1	0.1	1.0b	0.8c
280	1.1a	0.3	1.5	1.7c
180	2.4a	0.8	5.5b	5.2c
175	0.9a	0.6	1.1	1.2c
140	2.0a	1.2	3.2b	3.1c
126	2.2a	1.1	1.9	1.9
116	2.0a	1.1	4.9b	4.8c
95	1.9a	0.9	2.0	2.0c
84	3.6	3.1	3.9	3.8c
76	7.1	6.8	6.0b	5.9c
66	26.1a	32.0	24.4	28.2
50	17.5	19.6	13.5	10.3c
42	3.7	3.6	1.4b	1.2c
40	4.8	2.7	5.2b	4.8c
36	1.9	1.4	1.2b	1.5
34	1.4	1.0	1.1	0.9
28	1.6	1.9	2.3	2.4
27	4.2	5.1	5.7	5.9
24	7.9	8.6	5.9b	6.4c
16	2.2	1.5	0.9b	0.8
14	5.4	6.6	7.4	7.2
Total	100.0	100.0	100.0	100.0

Values are expressed as a percentage of protein band intensities. Load: loaded group ($n = 6$); Non-load: non-treatment subjects as a control group ($n = 6$); *PL from loading group ($n = 6$); **PL from control group ($n = 6$). a, b, c: significant differences ($P < 0.05$); a: synovial fluid (SF) of Load vs. SF of non-Load; b: SF of Load vs. plasma (PL) of Load; c: SF of Non-Load vs. PL of Non-Load.

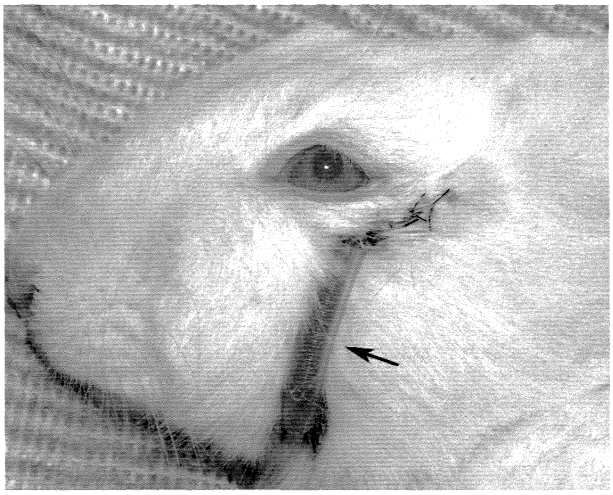

Figure 3 Left lateral view of the head after treatment in 1-N loaded group. The facial skin under the coil spring was protected with a silicon tube (internal diameter: 5 mm) indicated by the arrow.

In this study, we analyzed the protein content of the SF in TMJs of rabbits in which arthritis had been induced and compared it to that of non-loaded rabbits. The mean protein content in the SF of the loaded group was significantly higher than that of the non-loaded group, and this difference was primarily the result of an increased concentration of relatively high MW proteins (>95 kDa). In addition, the expression pattern of protein observed in the SF of TMJs from the non-loaded group significantly differed from that seen in plasma. Although there were 10 significant differences between the loaded group in the bands of proteins in the SF and plasma, the pattern of expressed proteins was similar well each other. Recently, we also observed a similar pattern of expressed proteins in the SF of patients with TMD (30). Namely, the mean protein concentration in SF from the patients with TMD was significantly higher than that observed in the asymptomatic healthy subjects, mainly because of an increased abundance of relatively high molecular polypeptides (>140 kDa).

The synovium controls the fluid flow from the synovial capillary to the joint cavity and subsynovium, (31, 32) and thus might function like a blood-synovial barrier (BSB), maintaining the unique protein composition of the SF. A continuous force on the glenoid fossa might induce synovitis in the synovial joint cavity, resulting in failure to function like a BSB and in increased total protein concentration in SF. The proliferation of synovial lining cells in arthritic joints might affect the drainage of fluid to the subsynovium, especially, drainage of high MW proteins in the fluid, which would result in an altered protein composition of the SF (33).

Although high MW glycoproteins could not be separated by SDS-PAGE in this study (34), it is likely that these molecules, along with glycosaminoglycans from cartilage or other components of the extra cellular matrix, must be eluted into the SF of TMJ. To elucidate the pathophysiological mechanism of TMD, it is necessary to further study these high MW polysaccharides which bind to diverse core proteins and exhibit a physiological function in synovial joints.

In conclusion, load-induced arthritis of the TMJ of rabbit is associated with increased total protein concen-

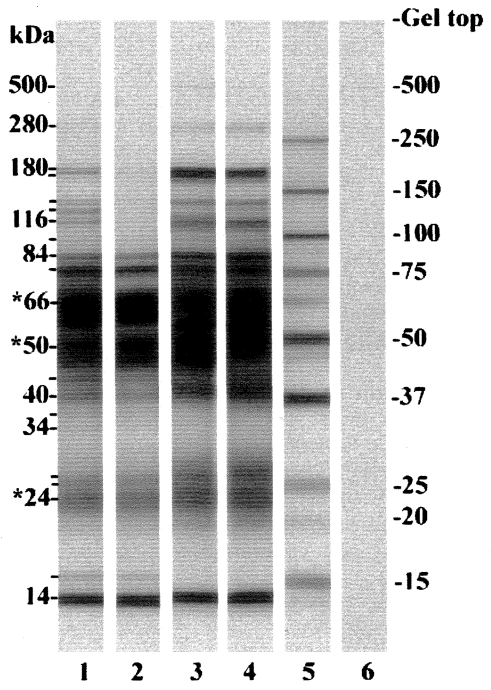

Figure 4 Proteins in synovial fluid (SF) and plasma for the both groups separated by SDS-PAGE. Two microgram of proteins from SF was analyzed using 5–20% gradient SDS-PAGE as described in the Material and methods. Lane 1 shows a typical band pattern of proteins for the loaded group. Lane 2 shows a typical band pattern of SF proteins for the non-loaded group, while lane 3 and 4 show typical band patterns of plasma proteins in rabbit from the loaded and non-loaded group respectively. Lane 5 shows SDS-PAGE molecular weight standards. Lane 6 shows the expected 500 kDa fibronectin standard from reactions performed under non-reducing conditions. The 66, 50 and 24 kDa bands are probably albumin, IgG heavy and light chain, respectively. Proteins with molecular weight 95–280 kDa in the loaded group were higher than that in the non-loaded group Table 1.

tration in SF, and particularly increase in proteins with a MW higher than 95 kDa. Unlike in healthy TMJs, the protein composition of SF in the loaded TMJ approaches that in the plasma, suggesting an inability of TMJ with load-induced synovitis to properly maintain a normal intra-articular environment.

References

1. Holmlund AB, Gynther GW, Reinholt FP. Disk derangement and inflammatory changes in the posterior disk attachment of the temporomandibular joint: a histologic study. *Oral Surg Oral Med Oral Pathol* 1992; **73**: 9–12.
2. Gynther GW, Holmlund AB, Reinholt FP. Synovitis in internal derangement of the temporomandibular joint: correlation between arthroscopic and histologic findings. *J Oral Maxillofac Surg* 1994; **52**: 913–7.
3. Segami N, Suzuki T, Sato J, Miyamaru M, Nishimura M, Yoshimura H. Does joint effusion on T2 magnetic resonance images reflect synovitis? Part 3. Comparison of histologic findings of arthroscopically obtained synovium in internal derangements of the temporomandibular joint. *Oral Surg Oral Med Oral Pathol Oral Radiol Endod* 2003; **95**: 761–6.
4. Sato J, Segami N, Nishimura M, et al. Correlation between the arthroscopic diagnosis of synovitis and microvessel density in synovial tissues in patients with internal derangement of the temporomandibular joint. *J Craniomaxillofac Surg* 2003; **31**: 101–6.
5. Takahashi T, Nagai H, Seki H, Fukuda M. Relationship between joint effusion, joint pain, and protein levels in joint lavage fluid of patients with internal derangement and osteoarthritis of the temporomandibular joint. *J Oral Maxillofac Surg* 1999; **57**: 1187–93.
6. Segami N, Miyamaru M, Nishimura M, Suzuki T, Kaneyama K, Murakami K. Does joint effusion on T2 magnetic resonance images reflect synovitis? Part 2. Comparison of concentration levels of proinflammatory cytokines and total protein in synovial fluid of the temporomandibular joint with internal derangements and osteoarthrosis. *Oral Surg Oral Med Oral Pathol Oral Radiol Endod* 2002; **94**: 515–21.
7. Kubota E, Kubota T, Matsumoto J, Shibata T, Murakami KI. Synovial fluid cytokines and proteinases as markers of temporomandibular joint disease. *J Oral Maxillofac Surg* 1998; **56**: 192–8.
8. Nordahl S, Alstergren P, Kopp S. Tumor necrosis factor-alpha in synovial fluid and plasma from patients with chronic connective tissue disease and its relation to temporomandibular joint pain. *J Oral Maxillofac Surg* 2000; **58**: 525–30.
9. Emshoff R, Puffer P, Rudisch A, Gassner R. Temporomandibular joint pain: relationship to internal derangement type, osteoarthrosis, and synovial fluid mediator level of tumor necrosis factor-alpha. *Oral Surg Oral Med Oral Pathol Oral Radiol Endod* 2000; **90**: 442–9.
10. Emshoff R, Puffer P, Strobl H, Gassner R. Effect of temporomandibular joint arthrocentesis on synovial fluid mediator level of tumor necrosis factor-alpha: implications for treatment outcome. *Int J Oral Maxillofac Surg* 2000; **29**: 176–82.
11. Kaneyama K, Segami N, Nishimura M, Suzuki T, Sato J. Importance of proinflammatory cytokines in synovial fluid from 121 joints with temporomandibular disorders. *Br J Oral Maxillofac Surg* 2002; **40**: 418–23.
12. Nishimura M, Segami N, Kaneyama K, Sato J, Fujimura K. Comparison of cytokine level in synovial fluid between successful and unsuccessful cases in arthrocentesis of the temporomandibular joint. *J Oral Maxillofac Surg* 2004; **62**: 284–7.
13. Fuchs S, Skwara A, Bloch M, Dankbar B. Differential induction and regulation of matrix metalloproteinases in osteoarthritic tissue and fluid synovial fibroblasts. *Osteoarthritis Cartilage* 2004; **12**: 409–18.
14. Mitchell PG, Magna HA, Reeves LM, et al. Cloning, expression, and type II collagenolytic activity of matrix metalloproteinase-13 from human osteoarthritic cartilage. *J Clin Invest* 1996; **97**: 761–8.
15. Takahashi T, Tominaga K, Takano H, et al. A decrease in the molecular weight of hyaluronic acid in synovial fluid from patients with temporomandibular disorders. *J Oral Pathol Med* 2004; **33**: 224–9.
16. Nitzan DW. The process of lubrication impairment and its involvement in temporomandibular joint disc displacement: a theoretical concept. *J Oral Maxillofac Surg* 2001; **59**: 36–45.
17. Grootveld M, Henderson EB, Farrell A, Blake DR, Parkes HG, Haycock P. Oxidative damage to hyaluronate and glucose in synovial fluid during exercise of the inflamed rheumatoid joint. Detection of abnormal low-molecular-mass metabolites by proton-NMR spectroscopy. *Biochem J* 1991; **273**: 459–67.

18. Nitzan DW. Intraarticular pressure in the functioning human temporomandibular joint and its alteration by uniform elevation of the occlusal plane. *J Oral Maxillofac Surg* 1994; **52**: 671–79.
19. Sandson J, Hamerman D. Paper electrophoresis of human synovial fluid. *Proc Soc Exp Biol Med* 1958; **98**: 564–6.
20. Sundblad L, Jonsson E, Nettelbladt E. Permeability of the synovial membrane to glycoproteins. *Nature* 1961; **192**: 1192.
21. Schur PH, Sandson J. Immunologic studies of the proteins of human synovial fluid. *Arthritis Rheum* 1963; **6**: 115–29.
22. Fujimura K, Kobayashi S, Suzuki T, Segami N. Histological evaluation of temporomandibular arthritis induced by mild mechanical loading in rabbits. *J Oral Pathol Med* 2005; **34**: 157–63.
23. Tominaga K, Alstergren P, Kurita H, Matsukawa A, Fukuda J, Kopp S. Interleukin-1beta in antigen-induced arthritis of the rabbit temporomandibular joint. *Arch Oral Biol* 2001; **46**: 539–44.
24. Laemmli UK. Cleavage of structural proteins during the assembly of the head of bacteriophage T4. *Nature* 1970; **227**: 680–5.
25. Gynther GW, Dijkgraaf LC, Reinholt FP, Holmlund AB, Liem RS, de Bont LG. Synovial inflammation in arthroscopically obtained biopsy specimens from the temporomandibular joint: a review of the literature and a proposed histologic grading system. *J Oral Maxillofac Surg* 1998; **56**: 1281–86.
26. Anderson L, Anderson NG. High resolution two-dimensional electrophoresis of human plasma proteins. *Proc Natl Acad Sci U S A* 1977; **74**: 5421–5.
27. Sanchez JC, Appel RD, Golaz O, et al. Inside SWISS-2DPAGE database. *Electrophoresis* 1995; **16**: 1131–51.
28. Habu M, Tominaga K, Sukedai M, et al. Immunohistochemical study of interleukin-1beta and interleukin-1 receptor antagonist in an antigen-induced arthritis of the rabbit temporomandibular joint. *J Oral Pathol Med* 2002; **31**: 45–54.
29. Kopp S. Neuroendocrine, immune, and local responses related to temporomandibular disorders. *J Orofac Pain* 2001; **15**: 9–28.
30. Fujimura K, Segami N, Yoshitake Y, Tsuruoka N, Kaneyama K, Sato J. Electrophoretically separation of the synovial fluid proteins in patients with temporomandibular joint disorders. *Oral Surg Oral Med Oral Pathol Oral Radiol Endod* 2005; **95**: in press.
31. Levick JR, Levick JR. Microvascular architecture and exchange in synovial joints. *Microcirculation* 1995; **2**: 217–33.
32. Scott D, Bertin K, Poli A, Levick JR, Miserocchi GA. Interstitial pressure gradients around joints; location of chief resistance to fluid drainage from the rabbit knee. *Exp Physiol* 2001; **86**: 739–47.
33. Kushner I, Somerville JA. Permeability of human synovial membrane to plasma proteins. Relationship to molecular size and inflammation. *Arthritis Rheum* 1971; **14**: 560–70.
34. Schulz BL, Packer NH, Karlsson NG. Small-scale analysis of O-linked oligosaccharides from glycoproteins and mucins separated by gel electrophoresis. *Anal Chem* 2002; **74**: 6088–97.

Acknowledgement

This work was supported by a Grant for Collaborative Research from Kanazawa Medical University (C2005-5) and by a Grant-in-Aid for Young Scientists (B-16791265) from the Ministry of Education, Culture, Sports, Science and Technology of Japan.

Available online at www.sciencedirect.com
ScienceDirect
ELSEVIER
British Journal of Oral and Maxillofacial Surgery 45 (2007) 372–377
BRITISH Journal of Oral and Maxillofacial Surgery
www.bjoms.com

Specific expression of substance P in synovial tissues of patients with symptomatic, non-reducing internal derangement of the temporomandibular joint: Comparison with clinical findings

Jun Sato [a,c,*], Natsuki Segami [a], Yoshino Yoshitake [b], Keiseki Kaneyama [a], Hiroshi Yoshimura [a], Kazuma Fujimura [a], Yoshimasa Kitagawa [c]

[a] *Department of Oral and Maxillofacial Surgery, Kanazawa Medical University, Daigaku, Uchinada-machi, Kahoku-gun, Ishikawa 920-0293, Japan*
[b] *Department of Biochemistry, Kanazawa Medical University, Japan*
[c] *Oral Diagnosis and Medicine, Department of Oral Pathobiological Science, Hokkaido University Graduate School of Dental Medicine, North 13, West 7, Kita-ward, Sapporo City 060-8586, Japan*

Accepted 21 September 2006
Available online 13 November 2006

Abstract

Our aim was to find out the extent of expression of substance P in synovial tissue from the human temporomandibular joints (TMJ) with symptomatic, non-reducing internal derangement, and to investigate the relationship between substance P and clinical findings. Fifty-four joints in 54 patients were examined immunohistochemically. Specimens of synovial tissue from 10 joints in 8 subjects with habitual dislocation of the TMJ with no pain were examined as controls. Cells that stained for substance P were found mainly among the endothelial cells in the blood vessels beneath the lining cells in synovial tissues from 47 of the 54 joints (87%) with internal derangement and from 5 of the 10 control joints. The extent score of cells that stained for substance P in joints with internal derangement was significantly higher than that in controls ($p = 0.02$). The extent score of these cells did not correlate with pain in the joint or the degree of synovitis. These results suggest that substance P may have some roles in both the physiological and pathological conditions in patients with symptomatic internal derangement of the TMJ.

Keywords: Substance P; Synovial tissue; Neurogenic inflammation; Temporomandibular joint

Introduction

Internal derangement of the temporomandibular joint (TMJ) is often accompanied by synovitis. Neuropeptides are now recognised as a key to understanding the pathophysiology of arthritis.[1] These neuropeptides, including substance P and calcitonin gene-related peptide (CGRP), are present mainly in nociceptive C-fibres, which usually correlate with nociception and the sensation of pain.[2,3] These neuropeptides are released by activated peripheral nerve terminals into the surrounding tissues and cause an inflammatory response, known as neurogenic inflammation.[4] Substance P is a member of the tachykinin family, and it has been suggested that it is one of the most important neuropeptides that modulate the inflammatory process of arthritis.[5] Substance P acts not only as a transmitter of pain signals, "but also stimulates macrophages, neutrophils, and endothelial cells to induce phagocytosis, chemotaxis, and plasma to extravasate".[5,6] Recently, we showed that CGRP and the capsaicin receptor TRPV-1 are expressed in synovial tissues of the TMJ. Transient receptor

* Corresponding author at: Oral Diagnosis and Medicine, Department of Oral Pathobiological Science, Hokkaido University Graduate School of Dental Medicine, North 13, West 7, Kita-ward. Sapporo City 060-8586, Japan. Tel.: +81 11 716 2111; fax: +81 11 706 4280.
E-mail address: jun-s@den.hokudai.ac.jp (J. Sato).

0266-4356/$ – see front matter
doi:10.1016/j.bjoms.2006.09.011

Table 1
Patient and substance P-staining score

Case number	Age /sex (years)	VAS for pain	Synovitis score (evaluated by arthroscopy)	Extent score for number of cells stained for substance P
1	23/F	4	8	6
2	24/F	8	8	40
3	70/F	7	7	40
4	36/F	7	5	3
5	61/M	7	5	25
6	70/F	5	3	0
7	38/F	8	7	4
8	55/M	9	5	7
9	22/F	4	6	4
10	40/F	7	8	66
11	28/F	6	6	18
12	41/F	10	3	10
13	21/F	5	6	25
14	23/F	5	5	40
15	56/F	3	5	18
16	55/F	4	4	0
17	50/M	8	6	20
18	50/F	6	10	0
19	18/F	6	6	16
20	17/F	6	5	8
21	84/F	3	2	38
22	35/M	6	5	14
23	35/F	6	4	20
24	76/F	5	2	30
25	73/F	5	5	0
26	52/F	1	6	40
27	40/F	4	9	35
28	18/F	8	2	45
29	33/F	7	4	10
30	17/F	9	4	12
31	24/F	9	8	85
32	58/F	6	4	10
33	31/F	7	4	8
34	39/M	2	9	25
35	52/F	1	3	33
36	56/F	10	2	0
37	36/F	8	5	70
38	35/F	4	6	2
39	58/F	6	5	40
40	52/F	5	2	36
41	61/F	5	6	25
42	38/F	7	3	10
43	48/M	5	4	20
44	23/F	7	6	26
45	53/F	3	7	40
46	55/F	8	9	8
47	32/F	7	4	0
48	36/M	5	7	18
49	25/F	3	6	12
50	19/F	7	7	0
51	56/F	4	8	40
52	13/F	5	9	22
53	40/F	8	5	36
54	22/F	5	8	33
Control subjects with habitual dislocation:†				
55†	23/M	0	0	36
56†	66/F	0	0	0
57†	27/M	0	0	0
58†	46/M	0	0	6
59†	72/M	0	0	10
60†	72/M	0	0	0
61†	25/M	0	2	0
62†	25/F	0	0	4
63†	29/F	0	1	0
64†	55/F	0	0	12

potential V1 (TRPV-1) is one of the major nociceptors and has a key role in inflammatory pain.[7,8] We showed that the expression of CGRP is correlated significantly with joint pain in patients with symptomatic internal derangement,[9,10] and that there is a possibility that some neuropeptides and neurogenic inflammation are involved in the pathophysiological mechanisms of pain in the TMJ. The expression and clinical relevance of substance P in synovial tissues in patients with symptomatic internal derangement of the TMJ have not been investigated fully. Before the present study, we hypothesised that substance P may be involved in pain in the joint in much the same way as CGRP in patients with non-reducing internal derangement of the TMJ. Here, we have made an immunohistochemical examination of synovial tissues of the TMJ and assessed the correlation between expression of substance P and clinical findings.

Patients and methods

Patients (Table 1)

We studied 54 joints in 54 patients with symptomatic non-reducing internal derangement of the TMJ. There were 7 men and 47 women, with a mean (S.D.) age of 41 (17) years (range 13–84) (Table 1). Magnetic resonance imaging showed that all of the patients had anterior disc displacement without reduction. The median duration of symptoms was 4 months (range 1–24). All of the patients had had arthroscopy after failure of non-surgical treatment—occlusal appliance, non-steroidal anti-inflammatory drugs (NSAIDS), and physiotherapy. Just before operation, the patients indicated the degree of subjective pain caused by moving the jaw on a visual analogue scale (VAS) of 0–10. This ranged from 1 to 10, with a mean (S.D.) of 5 (2).

The control group consisted of 10 joints in eight subjects, four men and four women, with a mean (S.D.) age of 43 (20) years (range 23–72), who had habitual dislocation without pain. All control patients had had arthroscopic eminoplasty.[11] The validity of adopting these patients as controls has been discussed in detail previously.[9,10] The patients with internal derangement and the control subjects also participated in our previous studies.[9,10,12] None of the subjects in either group had had arthroscopy of the TMJ before this study.

All the participants gave their informed consent to arthroscopy, synovial biopsy, and histological examination.

Synovial tissues and immunohistochemical staining

Two or three synovial tissue biopsy specimens roughly 2 mm in diameter were obtained arthroscopically from each patient from a portion of the posterior disc attachment using the triangular technique under direct visualisation.[9,10,12] Immediately after resection, the specimens were fixed in 4% paraformaldehyde for 4 h and embedded in paraffin. Sections were prepared and stained immunohistochemically by the avidin–biotin–peroxidase complex method with a Vectastain ABC kit (Vector Laboratories, Burlingame, CA) as described previously.[9,10,12] The sections were treated with primary antibody to substance P (1:100 dilution, Santa Cruz Biotechnology, Santa Cruz, CA; sc-21715) and left overnight at 4 °C. This antibody was purified monoclonal rat IgG to substance P in multiple species, and its specificity has been confirmed by the manufacturer. The following day the specimens were incubated in a solution of biotinylated anti-rat antibody (1:200 dilution; Dako, Carpinteria, CA) for 30 min at room temperature, and avidin /biotinylated horseradish peroxidase complex was added for 30 min at room temperature. The colour was developed using 3-amino-9-ethyl carbazole followed by counterstaining with heamatoxylin. The cells that reacted to substance P stained red. Negative controls in which the primary antibody was replaced with normal rat IgG were run with each specimen. The cells stained for substance P were evaluated in two to five regions of maximal immunohistochemical density under light microscopy at a magnification of ×200. The extent score of cells stained for substance P was calculated as the percentage of blood vessels containing those cells. About 10 to 100 blood vessels were evaluated in each specimen. This work was done by two of the authors (KK and JS) who were unaware of the identities of the patients from whom the specimens had been obtained.

Arthroscopy

Diagnostic arthroscopy was done by a standard technique throughout the whole area of the upper joint compartment.[13] The degrees of synovitis and intra-articular adhesion were evaluated according to the criteria of Murakami et al. (Tables 2 and 3)[14–16] by two of the authors (NS and JS) who were unaware of other information about the patients. The mean (S.D.) synovitis and adhesion scores were 5.1 (2.1) and 6.4 (1.6) in the internal derangement group, compared with 0.3 (0.7) and 0.8 (0.9) in the control group.

Statistical analysis

The Mann–Whitney test was used to compare the extent scores of cells stained for substance P between the internal derangement and control groups. The Spearman correlation coefficient was used to assess correlations between the extent score of cells stained for substance P and the clinical findings. StatView J-5.0 (Abacus Concepts, Berkeley, CA) was used for all statistical analyses. $p < 0.05$ were considered significant.

Table 2
Scoring of intensity of synovitis

Score	Findings
0	Normal pale, almost translucent, synovial lining with a fine network of anastomosing small blood vessels
1	Increased vascularity and capillary hyperaemia (mild)
2	Increased vascularity and capillary hyperaemia (moderate)
3	Increased vascularity and capillary hyperaemia (severe)
4	Capillary dilatation and increasing network (mild to moderate)
5	Capillary dilatation and increasing network (severe)
6	Contact bleeding on palpation with probe (mild to moderate)
7	Contact bleeding on palpation with probe (severe)
8	Microbleeding and effusion
9	Granulative change, effusion, and debris (mild to moderate)
10	Granulative change, effusion, and debris (severe)

Table 3
Scoring of intensity of adhesion

Score	Findings
0	No adhesion or fibrous change
1	Filmy adhesion (mild)
2	Filmy adhesion (moderate to severe)
3	Fibrosynovial band (mild to moderate)
4	Fibrosynovial band (severe)
5	Fibrous band (mild to moderate)
6	Fibrous band (severe)
7	Formation of pseudowall (mild to moderate)
8	Formation of pseudowall (severe)
9	Capsular fibrosis (mild to moderate)
10	Capsular fibrosis (severe)

Results

Immunohistochemical staining

Cells that stained for substance P were seen in synovial tissue specimens from 47 of the 54 joints (87%) in the internal derangement group (Fig. 1). All the negative control specimens showed only background staining (data not shown). The specimens from 5 of the 10 control subjects with habitual dislocation also stained for substance P (Fig. 2A and B). The mean (S.D.; median) extent score of cells that stained for substance P was 23 (19; 20) in the internal derangement specimens compared with 7 (11; 2) in the control specimens, the difference being significant ($p = 0.02$) (Fig. 3). Cells that stained for substance P were mostly located in the endothelial cells in the blood vessels beneath the lining cells, with some lining the synovium (Figs. 1 and 2B).

Expression of substance P and clinical findings

There were no significant correlations between the extent score of cells stained for substance P and the duration

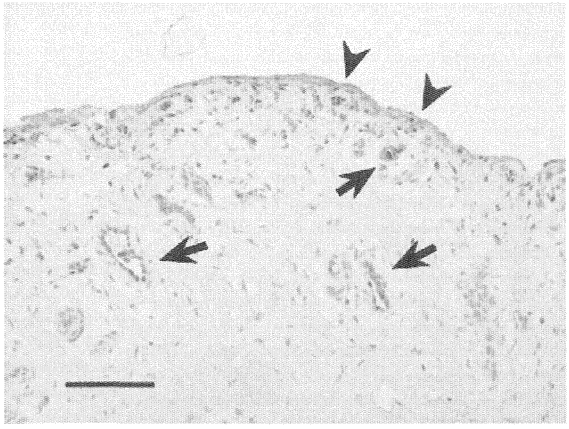

Fig. 1. Section stained for substance P from a patient with internal derangement (case 31). Immunoreactivities for substance P (arrows) can be seen in the endothelial cells in the blood vessels beneath the lining cells and lining the synovium (arrow heads) (original magnification: ×100, bar: 50 μm).

of symptoms in the internal derangement group ($p=0.14$, $r=-0.09$) (Fig. 4), the degree of synovitis ($p=0.31$, $r=0.14$) (Fig. 5), the degree of adhesion ($p=0.19$, $r=-0.22$) or the severity of pain in the joint (VAS) ($p=0.75$, $r=0.01$) (Fig. 6).

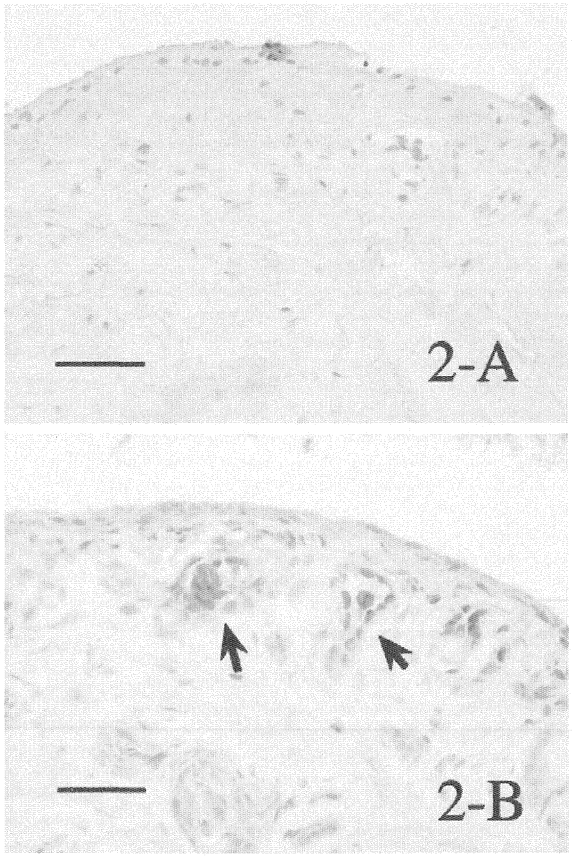

Fig. 2. (A and B). Specimens stained for substance P from control patients (A: case 61, B: case 55). There is no immunoreactivity for substance P in the synovial tissue (A), and only a few stained cells in the blood vessels (B: arrows) (original magnification A: ×100 and B: ×200, bar: 50 μm).

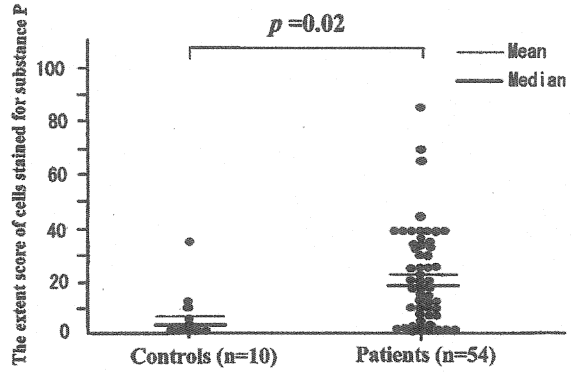

Fig. 3. The extent score of cells stained for substance P in the synovial tissues of patients with internal derangement and controls. The extent score of these cells is significantly higher in the internal derangement group than in the control group (Mann–Whitney test; $p=0.02$).

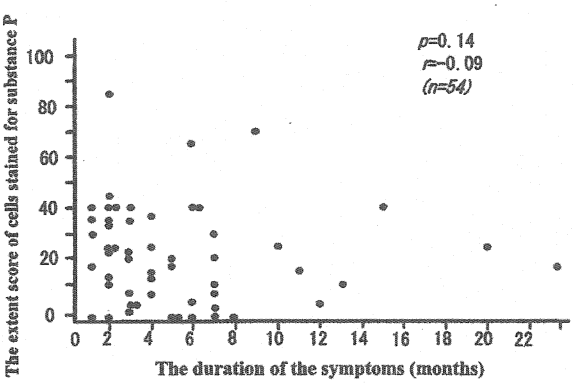

Fig. 4. The extent score of cells stained for substance P and the duration of the symptoms are not correlated significantly (Spearman correlation coefficient; $p=0.14$, $r=-0.09$).

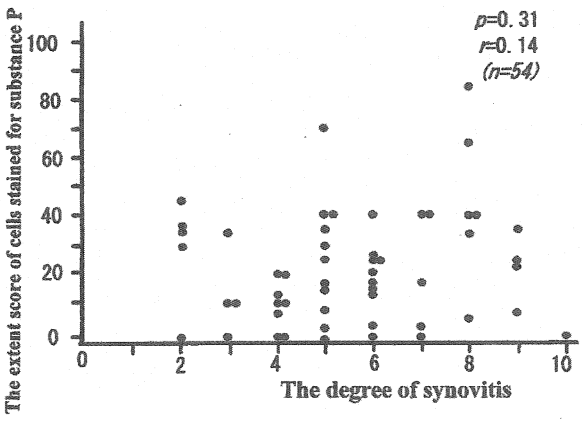

Fig. 5. The extent score of cells stained for substance P and the degree of synovitis are not correlated significantly (Spearman correlation coefficient; $p=0.31$, $r=0.14$).

Discussion

The contribution of neuropeptides to arthritis is currently a matter of debate.[16] In the present study, we have shown

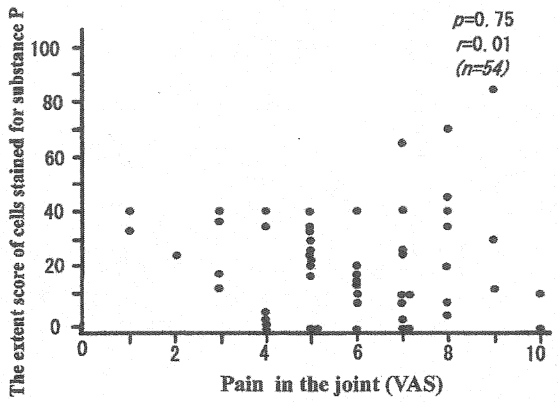

Fig. 6. The extent score of cells stained for substance P and the VAS of pain are not correlated significantly (Spearman correlation coefficient; $p=0.75$, $r=0.01$).

the presence of cells stained for substance P in the specimens of synovial tissue in the posterior disc attachment in patients with symptomatic internal derangement of the TMJ. The extent score of these cells was significantly higher in the internal derangement group than in the control group.

Substance P has been suggested as not only one of the most important neuropeptides that modulate the inflammatory process of arthritis,[17] but also one of the most important to act as a local regulator of blood flow and pain.[1,18] Although we expected a close relation between the expression of substance P and joint pain (the degree of synovitis), we were unable to confirm our hypothesis from the results of the present study.

We know of a few previous studies of substance P in the TMJ region. In a preliminary study, Henry and Wolford[3] showed that cells that stained for substance P were present mainly within the walls of the vasculature in synovial tissues of the human TMJ. As they obtained synovial tissues from only nine women, they did not investigate the relation between the expression of substance P and clinical findings. Our immunohistochemical study supports their observation that cells that stained for substance P were present in the blood vessels. Appelgren et al.[18] reported that substance P-like immunoreactivity in the synovial fluids from patients with arthritic TMJs was correlated with intra-articular temperature and pain. Holmlund et al.[19] detected substance P-like immunoreactivity in 17 of 19 synovial fluid samples from patients with internal derangement, osteoarthrosis (OA), and rheumatoid arthritis (RA). They concluded that there were no significant correlations between the concentrations of substance P in the synovial fluids and the arthroscopic findings, including the degrees of synovitis and OA. They also concluded that these unexpected results were the results of the relatively small number of patients with pronounced synovitis who were included in their study. Marshal et al.[20] reported that the concentrations of substance P in synovial fluids in patients with RA did not differ significantly from those found in patients with OA. Mapp et al.[17] found a large number of afferent fibres of substance P in normal synovial tissues, but few such fibres in patients with RA. They speculated that large amounts of neuropeptides, including substance P, may be released from the sensory terminals in the early phases of inflammation, resulting in permanent depletion. They concluded that substance P and other neuropeptides may be involved in the pathogenesis of inflammation of the joint in the early rather than the chronic phases. However, we found no significant correlation between the extent score of cells stained for substance P and the duration of symptoms. This discrepancy may have been caused by the difference in pathogenesis between internal derangement of the TMJ and RA. As the degree of inflammation of the synovial tissues in patients with internal derangement of the TMJ is usually much less than that in patients with RA, neuropeptides may never be permanently depleted.

We detected substance P at low concentrations in the synovial tissues from control subjects. This suggests that it may play some part in the maintenance of physiological conditions in the TMJ. Substance P has been suggested to regulate vascular functions (such as blood flow) under normal conditions,[17] and its expression may be a protective response to tissue injury.[18,21]

The main limitations of the present study were the small number of observations and characteristics of the control patients. These problems are difficult to overcome, as it is impossible to obtain fresh samples of synovial tissues from healthy people.[9,10] We have explained the validity of our control subjects in previous reports,[9,10,12] and think that these patients with dislocations were suitable control subjects for the present study.

As we performed punch biopsies on the posterior disc attachment, it was not possible to assess the distribution of substance P in the whole intracapsular structure of the TMJ. As the pathological mechanisms underlying joint pain are complex, we are aware that it is not possible to work out the mechanisms of all cases of TMJ based pain from our results.

In conclusion, we have shown that substance P may be involved in the pathogenesis of symptomatic internal derangement of the TMJ. However, it is unlikely that its important physiological and pathological roles of are mediated independently. Substance P has been suggested to play an important part in the pathogenesis of arthritis by up-regulation of production of other cytokines,[22] and it stimulates synovial cells and lymphocytes to produce prostaglandins[23] and to release cytokines, such as IL-1.[24] It is therefore important to examine the relations between substance P and other chemical mediators in more depth. Further studies are required to elucidate the possible contribution of substance P to physiological and pathological conditions in patients with internal derangement of the TMJ.

Acknowledgements

This study was partially supported by a Grant for Collaborative Research from Kanazawa Medical University (C20005-5), Grant-in-Aid for Young Scientists (B-16791265) and for

Scientific Researcher (17390527) from the Ministry of Education, Culture, Sports, Science and Technology of Japan.

References

1. Kido MA, Kiyoshima T, Kondo T, et al. Distribution of substance P and calcitonin gene-related peptide-like immunoreactive nerve fibers in the rat temporomandibular joint. *J Dent Res* 1993;**72**:592–8.
2. Pedersen-Bjergaard U, Nielsen LB, Jensen K, Edvinsson L, Jansen I, Olesen J. Calcitonin gene-related peptide, neurokinin A and substance P: effects on nociception and neurogenic inflammation in human skin and temporal muscle. *Peptides* 1991;**12**:333–7.
3. Henry CH, Wolford LM. Substance P and mast cells: preliminary histologic analysis of the human temporomandibular joint. *Oral Surg Oral Med Oral Pathol Oral Radiol Endod* 2001;**92**:384–9.
4. Rosenfeld MG, Mermod JJ, Amara SG, et al. Production of a novel neuropeptide encoded by the calcitonin gene via tissue-specific RNA processing. *Nature* 1983;**304**:129–35.
5. Saito T, Koshino T. Distribution of neuropeptides in synovium of the knee with osteoarthritis. *Clin Orthop Relat Res* 2000;**376**:172–82.
6. Lembeck F, Holzer P. Substance P as neurogenic mediator of antidromic vasodilation and neurogenic plasma extravasation. *Naunyn Schmiedebergs Arch Pharmacol* 1979;**310**:175–83.
7. Numazaki M, Tominaga M. Molecular mechanisms of nociception and thermosensation: structures, expressions and functions of capsaicin receptor and its homologues. *Seikagaku* 2003;**75**:359–71.
8. Caterina MJ, Schumacher MA, Tominaga M, Rosen TA, Levine JD, Julius D. The capsaicin receptor: a heat-activated ion channel in the pain pathway. *Nature* 1997;**389**:816–24.
9. Sato J, Segami N, Kaneyama K, Yoshimura H, Fujimura K, Yoshitake Y. Relationship of calcitonin gene-related peptide in synovial tissues and temporomandibular joint pain in humans. *Oral Surg Oral Med Oral Pathol Oral Radiol Endod* 2004;**98**:533–40.
10. Sato J, Segami N, Yoshitake Y, et al. Expression of capsaicin receptor TRPV-1 in synovial tissues of patients with symptomatic internal derangement of the temporomandibular joint and joint pain. *Oral Surg Oral Med Oral Pathol Oral Radiol Endod* 2005;**100**:674–81.
11. Segami N, Kaneyama K, Tsurusako S, Suzuki T. Arthroscopic eminoplasty for habitual dislocation of the temporomandibular joint: preliminary study. *J Craniomaxillofac Surg* 1999;**27**:390–7.
12. Sato J, Segami N, Yoshitake Y, Nishikawa K. Correlations of the expression of fibroblast growth factor-2, vascular endothelial growth factor, and their receptors with angiogenesis in synovial tissues from patients with internal derangement of the temporomandibular joint. *J Dent Res* 2003;**82**:272–7.
13. McCain JP, de la Rua H, LeBlanc WG. Puncture technique and portals of entry for diagnostic and operative arthroscopy of the temporomandibular joint. *Arthroscopy* 1991;**7**:221–32.
14. Murakami K, Segami N, Fujimura K, Iizuka T. Correlation between pain and synovitis in patients with internal derangement of the temporomandibular joint. *J Oral Maxillofac Surg* 1991;**49**:1159–62.
15. Murakami K, Segami N, Moriya Y, Iizuka T. Correlation between pain and dysfunction and intra-articular adhesions in patients with internal derangement of the temporomandibular joint. *J Oral Maxillofac Surg* 1992;**50**:705–8.
16. Sato J, Segami N, Nishimura M, et al. Expression of interleukin 6 in synovial tissues in patients with internal derangement of the temporomandibular joint. *Br J Oral Maxillofac Surg* 2003;**41**:95–101.
17. Mapp PI, Kidd BL, Gibson SJ, et al. Substance P-, calcitonin gene-related peptide- and C-flanking peptide of neuropeptide Y-immunoreactive fibres are present in normal synovium but depleted in patients with rheumatoid arthritis. *Neuroscience* 1990;**37**:143–53.
18. Appelgren A, Appelgren B, Kopp S, Lundeberg T, Theodorsson E. Substance P-associated increase of intra-articular temperature and pain threshold in the arthritic TMJ. *J Orofac Pain* 1998;**12**:101–7.
19. Holmlund A, Ekblom A, Hansson P, Lind J, Lundeberg T, Theodorsson E. Concentrations of neuropeptides substance P, neurokinin A, calcitonin gene-related peptide, neuropeptide Y and vasoactive intestinal polypeptide in synovial fluid of the human temporomandibular joint. A correlation with symptoms, signs, and arthroscopic findings. *Int J Oral Maxillofac Surg* 1991;**20**:228–31.
20. Marshall KW, Chiu B, Inman RD. Substance P and arthritis: analysis of plasma and synovial fluid levels. *Arthritis Rheum* 1990;**33**:87–90.
21. Walsh DA, Mapp PI, Wharton J, et al. Localisation and characterisation of substance P binding to human synovial tissue in rheumatoid arthritis. *Ann Rheum Dis* 1992;**51**:313–7.
22. Komuro H, Tanabe T, Ogushi S, et al. Participation of substance P distribution in the cytokine production of rheumatoid synovium. *Mod Rheumatol* 2000;**10**:83–7.
23. Lotz M, Carson DA, Vaughan JH. Substance P activation of rheumatoid synoviocytes: neural pathway in pathogenesis of arthritis. *Science* 1987;**235**:893–5.
24. Kimball ES, Persico FJ, Vaught JL. Substance P, neurokinin A, and Neurokinin B induce generation of IL-1-like activity in P388D1 cells. Possible relevant to arthritic disease. *J Immunol* 1988;**141**: 3564–9.

Expression of interleukin 8 in synovial tissues in patients with internal derangement of the temporomandibular joint and its relationship with clinical variables

Jun Sato, DDS, PhD, [a,d] Natsuki Segami, DDS, PhD,[b] Masaaki Nishimura, DDS, PhD,[a]
Yoshino Yoshitake, PhD,[c] Keiseki Kaneyama, DDS, PhD,[a] and
Yoshimasa Kitagawa, DDS, PhD,[e] Uchinada-machi and Kita-Ward Sapporo, Japan
KANAZAWA MEDICAL UNIVERSITY AND HOKKAIDO UNIVERSITY

Objectives. The objectives of this study were to assay interleukin 8 (IL-8) in synovial tissues of the temporomandibular joint (TMJ) with symptomatic internal derangement, and to assess its relationship with clinical variables.

Study design. Forty-six joints in 44 patients were examined using an immunohistochemical technique. As controls, 8 joints in 7 subjects with habitual dislocation without pain were also examined.

Results. IL-8 was expressed mainly in the blood vessels beneath the lining cells in 37 of the 46 joints (80%) with internal derangement and in 2 of the 8 control joints. The percentage of IL-8-positive cells was significantly higher in the internal derangement group than in the control group ($P = .004$). The percentage of IL-8-positive cells showed no correlation with joint pain or number of infiltrating cells.

Conclusions. IL-8 was up-regulated in inflamed synovial tissues in patients with internal derangement. Because IL-8 has no significant correlation with clinical variables, IL-8 may play a secondary role in the pathogenesis of the internal derangement of the TMJ. **(Oral Surg Oral Med Oral Pathol Oral Radiol Endod 2007;103:467-74)**

Internal derangement of the temporomandibular joint (TMJ) is often accompanied by synovitis. Chronic synovial inflammation results in hyperplasia of the cells lining the synovium, growth of new small blood vessels, and infiltration of inflammatory cells around the blood vessels.[1,2] Previous studies have shown appreciable amounts of proinflammatory cytokines, including interleukin 1β (IL-1β), IL-6, and tumor necrosis factor α (TNF-α) in synovial fluid or synovial tissue in patients with internal derangement of the TMJ.[3-7] Recently we reported the presence of other kinds of chemical mediators, including neuropeptides such as substance P and calcitonin gene-related peptide (CGRP), in the TMJ.[8,9] These chemical mediators are thought to contribute to the pathogenesis and clinical findings of internal derangement of the TMJ.

IL-8, previously referred to as neutrophil-activating protein-1 or monocyte-derived neutrophil chemotactic factor,[10,11] is a chemokine with the ability to induce chemotaxis and active neutrophils.[8,12] This chemokine has been implicated in several disease states, especially in angiogenic diseases such as rheumatoid arthritis (RA).[10,13] In RA, IL-8 is known to cause the infiltration of neutrophils into synovial fluid and promote joint inflammation.[10] As TMJs with internal derangement are inflamed, it is reasonable to suspect involvement of IL-8, and we have previously showed that appropriate levels of IL-8 exist in synovial fluid taken from patients with internal derangement of the TMJ.[7] There are few reports, however, concerning expression of IL-8 in synovial tissue of the TMJ. In the present study, we immunohistochemically investigated the expression of IL-8 in synovial tissue of the deranged TMJ and evaluated its correlations with clinical findings.

As the RA synovial macrophage is capable of producing IL-8,[10] we also performed an exploratory study to see if the macrophage-like cells are present in the inflamed synovial tissues in the TMJ.

This study was partially supported by a Grant for Collaborative Research from Kanazawa Medical University (C20005-5) and for Scientific Research (17390527) from the Ministry of Education, Culture, Sports, Science and Technology of Japan.

[a]Lecturer, Department of Oral and Maxillofacial Surgery, Kanazawa Medical University.
[b]Professor and Chairman, Department of Oral and Maxillofacial Surgery, Kanazawa Medical University.
[c]Associate Professor, Department of Biochemistry, Kanazawa Medical University.
[d]Associate Professor, Department of Oral and Oral Diagnosis and Medicine, Pathobiological Science, Hokkaido University Graduate School of Dental Medicine.
[e]Professor and Chairman, Oral Diagnosis and Medicine, Department of Oral Pathobiological Science, Hokkaido University Graduate School of Dental Medicine.

Received for publication Apr 16, 2006; accepted for publication Jun 15, 2006.
1079-2104/$ - see front matter

doi:10.1016/j.tripleo.2006.06.058

PATIENTS AND METHODS

Patients

We studied 46 TMJs with internal derangement in 44 patients: 6 men and 38 women with a mean age of 43 years (range 17 to 84 years) (Table I). Magnetic resonance imaging (MRI) showed that all of the patients had anterior disc displacement without reduction. Their mean maximum interincisal opening was 33 mm and the mean duration of symptoms was 6 months. Because of failure of nonsurgical treatment, including occlusal appliance, nonsteroidal anti-inflammatory drugs (NSAIDS), and physiotherapy, to resolve the clinical symptoms, all patients underwent arthroscopic surgery. Just before the operation, the degree of subjective arthralgia from jaw movement was indicated by the patients on a visual analogue scale (VAS) of 0 to10. The mean VAS score was 6.0.

A control group comprised 8 joints in 7 patients: 4 men and 3 women with a mean age of 42 years (range 23 to 72 years) who had habitual dislocation without pain and underwent arthroscopic eminoplasty.[14] MRI confirmed the normal position of the disc in all control patients with the mouth closed. The validity of adopting these patients as controls has been discussed in detail previously.[15]

Twenty-two joints from 20 internal derangement subjects and 4 joints from 3 control subjects were available for measurement of the level of IL-8 in the synovial fluid. To our regret, the other 24 joints with internal derangement were not available for measurement of the levels of IL-8 because their synovial fluids were used for measurement of other cytokines. Because of lack of the control samples, synovial fluid from 2 healthy volunteers (2 men aged 26 and 28) were added to the control group, making a total of 6 joints from 5 people.

All participants gave their informed consent to arthroscopy, extraction of synovial fluid, collection of a synovial biopsy specimen, and histological examination.

Synovial tissues and immunohistochemical staining

IL-8. Two or 3 biopsy specimens of synovial tissues about 2 mm in diameter were obtained from each patient arthroscopically from a portion of the posterior disk attachment using the triangular technique under direct visualization.[16] Immediately after resection, the specimens were fixed in 4% paraformaldehyde for 8 hours and embedded in paraffin. Sections were prepared and stained immunohistochemically by an avidin-biotin technique (Vector Laboratories, Burlingame, CA) as previously described.[15] After blocking nonspecific binding with 1.5% normal horse serum for 20 minutes at room temperature, the sections were treated with primary antibody to IL-8 (1:1000 dilution: ENDOGEN, Woburn, MA; P-801, polyclonal) and left overnight at 4°C. This antibody binds IL-8 on cells. The next day, the specimens were left in a 200 dilution of anti-rabbit biotinylated antibody (Dako, Carpinteria, CA) for 30 minutes at room temperature. Avidin/biotinylated horseradish peroxidase complex was then added for 30 minutes at room temperature. The color was developed by 3-amino-9-ethyl carbazole followed by counterstaining with hematoxylin. Negative controls in which the primary antibody was replaced with normal rabbit immunoglobulin G were run with each specimen. The IL-8-positive cells were counted in 2 regions chosen at random, under light microscope at ×200 magnification, and the percentage of IL-8-positive cells was calculated. This work was done by 2 of the authors (K.K. and J.S.) who were unaware of which patients the specimens came from.

The number of the infiltrating cells around the blood vessels was evaluated as the total number of the infiltrating cells per 5 blood vessels. The 5 largest blood vessels were selected for evaluation. The counts were made without knowledge of any other information regarding the patients (K.K. and J.S.).

Microvessel density (MVD). MVD of the biopsy specimens was determined by staining the endothelial cells with a monoclonal antibody to CD34 (1:50, Nichirei, Tokyo, Japan: NU-4A1), according to Weidner's method with minor modifications, as described previously.[17-19] MVD was evaluated as the total number of blood vessels in 2 areas of maximal vascularization under a light microscope (×20 objective and ×10 ocular, 0.74 mm^2 per field). This work was done by 2 of the authors (K.K. and J.S.).

Detection of macrophages in the synovium. Thirteen sections from the internal derangement group and 2 sections from the control group were selected at random to investigate the presence of synovial macrophages. Macrophages were detected by applying monoclonal antibody to CD68 overnight at 4°C (1:100 dilution: Zymed Laboratories, Inc, San Francisco, CA, mouse monoclonal: 00761325). This antibody reacts with CD68 antigen that is expressed primarily on macrophages in a wide variety of human tissues, and also on peripheral blood monocytes. These sections were treated with a 200 dilution of anti-mouse biotinylated antibody (Dako) for 30 minutes. After the color development, CD68-positive cells were assessed. For a positive control section, we selected specimens taken from patients with squamous cell carcinoma of the parotid gland.

Synovial fluid sample preparation. Synovial fluid samples were collected from the superior joint com-

Table I. Patient and clinical variables, IL-8 staining, IL-8 in synovial fluids, CD68 staining

Patient no.	*Age, y/Sex*	*MIO, mm*	*VAS*	*Synovitis score*	*MVD*	*IL-8 staining, %*	*IL-8 level in SF*	*Infiltrating cell*	*CD68*	*Patient no.*	*Age, Sex*	*MIO, mm*	*VAS*	*Synovitis score*	*MVD*	*IL-8 staining, %*	*IL-8 level in SF*	*Infiltrating cell*	*CD68*
1	23/F	27	4	8	32	30	1.1	48		29	76/F	30	5	2	3	45		38	
2	24/F	30	8	8	15	15	1.7	38		30	73/F	29	5	5	25	34		34	
3	70/F	35	7	7	30	40	0	38		31	52/F	36	1	6	3	44		44	
4*	36/F	35	7	5	33	0	14.7	40		32	40/F	30	4	9	19	38		62	
5*	36/F	35	7	5	18	58		16	No	33	18/F	30	8	2	10	12		36	
6	61/M	34	7	5	10	55	13.0	46	No	34	33/F	28	7	4	6	10		36	
7	70/F	42	5	3	10	0	18.0	54		35	17/F	40	9	4	31	41	0	50	
8*	38/F	31	8	5	17	9	13.0	40	Yes	36	24/F	36	9	8	20	15		54	
9*	38/F	31	8	7	38	0	16.3	62		37	58/F	30	6	4	15	0		32	
10	55/M	20	9	5	16	56		34		38	31/F	23	7	4	35	10		28	
11	55/M	33	10	3	4	0		26		39	39/M	33	2	9	59	9		54	
12	33/F	48	3	4	12	32		44		40	52/F	32	1	3	14	88		62	No
13	22/F	30	4	6	48	12	0.8	48		41	56/F	38	10	2	8	48		72	
14	40/F	40	7	8	45	35	1.7	46		42	36/F	42	8	5	56	62		40	No
15	28/F	37	6	6	19	48	8.0	52	Yes	43	35/F	28	4	6	29	98		30	No
16	41/F	32	10	3	5	50	32.6	20		44	58/F	30	6	5	75	40		34	
17	21/F	32	5	6	10	22	30.6	40		45	52/F	25	5	2	12	38		50	
18	45/F	34	7	4	17	12	0	36		46	61/F	31	5	6	65	18		38	
19	23/F	36	5	5	36	10	0.8	60	No	47†	23/M	44	0	0	6	15		22	
20	56/F	32	3	5	58	8		48	No	48†	66/F	42	0	0	20	18	3.4	30	No
21	55/F	27	4	4	7	0	5.3	24	No	49†	27/M	52	0	0	5	0		20	
22	50/M	35	8	6	3	0		28	No	50†	46/M	40	0	0	5	0		42	
23	50/F	37	6	10	25	0	14.5	42	No	51*†	25/F	50	0	0	14	0	0	24	
24	18/F	33	6	6	25	3	0	50		52*†	25/F	50	0	2	9	0	0	24	
25	17/F	33	6	5	29	0		34		53†	55/F	30	0	0	15	0		24	
26	84/F	45	5	2	6	35	0.5	38		54†	72/M	50	0	0	10		0	16	No
27	35/M	33	7	5	43	36		46	Yes	55‡	28/M	49	0				0		
28	35/F	39	6	4	33	50	4.2	52		56‡	26/M	55	0				0		

M, male; *F,* female; *MIO,* maximum interincisal opening; *VAS,* visual analogue scale of pain; *MVD,* microvessel density in synovial tissue; *IL-8 staining,* the percentage of IL-8 positive cells (%); *IL-8 level in SF,* IL-8 level in synovial fluid (pg/mL); *infiltrating cell,* the number of the infiltrating cells around the blood vessels; *CD68,* presence of CD8-positive cells.

*Bilateral joints.

†Control subjects with habitual dislocation.

‡Healthy volunteer.

Table II. Scoring with intensity of synovitis

Score	Findings
0	Normal pale, almost translucent, synovial lining with a fine network of anastomosing small blood vessels
1	Increased vascularity and capillary hyperemia (mild)
2	Increased vascularity and capillary hyperemia (moderate)
3	Increased vascularity and capillary hyperemia (severe)
4	Capillary dilatation and increasing network (mild to moderate)
5	Capillary dilatation and increasing network (severe)
6	Contact bleeding occurs on probe palpation (mild to moderate)
7	Contact bleeding occurs on probe palpation (severe)
8	Microbleeding and effusion
9	Granulative change, effusion and debris (mild to moderate)
10	Granulative change, effusion and debris (severe)

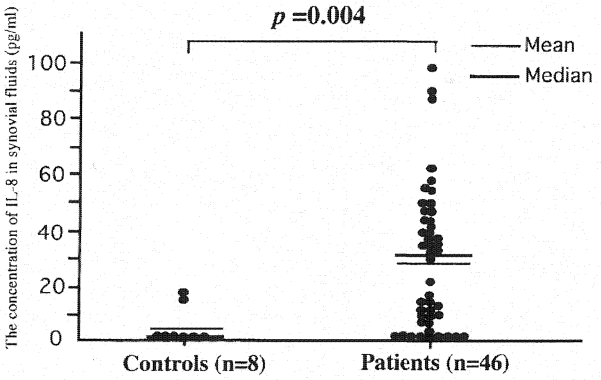

Fig. 1. The percentage of IL-8-positive cells in synovial tissues of patients with internal derangement and controls. The percentage of IL-8-positive cells is significantly higher in the internal derangement group than in the control group (P = .004; Mann-Whitney test).

partment during arthroscopic surgery for a therapeutic purpose except in the cases of the 2 healthy volunteers. In the 2 healthy volunteers, synovial fluid samples were collected under local anesthesia. The surgeons (N.S. and J.S.) injected 2.0 mL of saline solution into the superior joint space with a 21-gauge needle and aspirated the diluted the synovial fluid, and re-injected it a total of 10 times before drawing off the final sample.[7] The samples were centrifuged (800 g for 20 minutes) and stored at −80°C until assayed.

Measurement of IL-8 levels in the synovial fluid. The concentration of IL-8 in the synovial fluid was determined by using an enzyme-linked immunosorbent assay (ELISA) kit (Quantikine ELIZA, R & D Systems, Minneapolis, MN) according to the manufacturer's instructions.[7] This assay recognizes natural human IL-8. The minimum detectable level of IL-8 was 0.98 pg/mL. The measurement was done by 2 of the authors (M.N. and J.S.) blind as to which patients the samples came from.

Arthroscopy

Conventional diagnostic arthroscopy was done according to a standard technique in the whole area of the upper joint compartment and all findings were videotaped.[16] The degree of synovitis was evaluated according to the criteria of Murakami et al.[20] In short, the highest degree of synovitis in the upper compartment was scored on a scale of 0 to10 (Table II). This evaluation was performed by 2 of the authors (N.S. and J.S.) without knowledge of other information about the patients. The mean arthroscopic synovitis scores was 5.1 in patients with internal derangement and 0.3 in the control subjects.

Statistical analysis

The Mann-Whitney U test was used to compare the percentage of IL-8-positive cells in the synovial tissues and IL-8 concentrations in the synovial fluids between the internal derangement and control groups. The Spearman correlation coefficient was used to assess correlations between the percentage of IL-8-positive cells and clinical variables. StatView J-5.0 (Abacus Concepts, Berkeley, CA) was used for all statistical analyses. P values of less than .05 were considered significant.

RESULTS

Immunohistochemical staining for IL-8

In the internal derangement group, IL-8-positive cells were found in the biopsy specimens from 37 (80%) of the 46 joints, but in only 2 of the 8 control joints. The mean ± SD (median) percentage of IL-8-positive cells was 29.4% ± 25.4% (31%) in the internal derangement specimens versus 4.1% ± 7.6% (0%) in the control specimens, the difference being significant (P = .004) (Fig. 1).

In the internal derangement group, the IL-8-positive cells were mainly seen in the blood vessels beneath the lining cells and in some lining cells (Fig. 2, *A*) The negative control sections showed only background staining (Fig. 2, *B*).

IL-8 concentrations in synovial fluids

IL-8 was detected in the synovial fluid from18 joints (82%) of the 22 internal derangement joints but in only 1 (concentration: 3.4 pg/mL) of the 6 control joints. The mean ± SD (median) concentration of IL-8 was 8.7 ± 9.8 (6.6) pg/mL in the internal derangement group. The concentration of IL-8 was significantly higher in the internal derangement group than in the control group (P = .009) (Fig. 3). In the 22 deranged joints, there was no

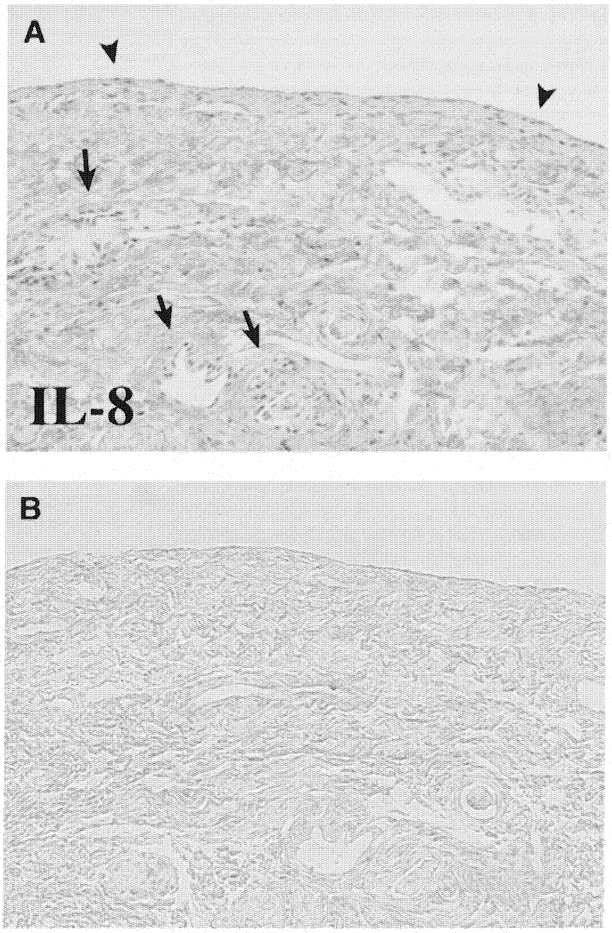

Fig. 2. IL-8-stained sections obtained from a patient with internal derangement (case number 15). **A**, Immunoreactivities are seen in the blood vessels beneath the lining cells (arrows) and in some lining cells (arrow heads). **B**, The negative control sections showed only background staining. (Original magnification ×100.)

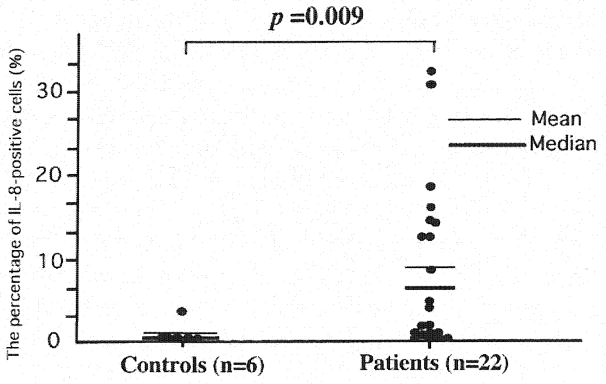

Fig. 3. IL-8 concentrations in synovial fluid of patients with internal derangement and controls. IL-8 concentration is significantly higher in the internal derangement group than in the control group (P = .009; Mann-Whitney test).

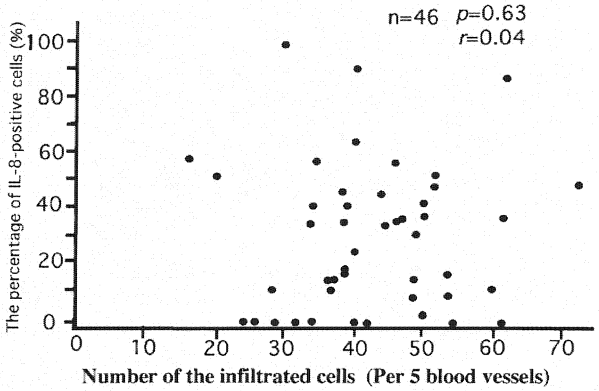

Fig. 4. The percentage of IL-8-positive cells in synovial tissues and the number of infiltrating cells around the blood vessels. Significant correlation is not indicated by the Spearman correlation coefficient (P = .63, r = 0.04).

significant correlation between the percentage of IL-8-positive cells in the synovial tissues and the concentration of IL-8 in the synovial fluids (P = .91, r = 0.09).

Relationship between IL-8 expression and clinical variables

In the internal derangement group, there was no significant correlation between the percentage of IL-8-positive cells in the synovial tissues and VAS of pain (P = .74, r = −0.06), degree of synovitis (P = .48, r = −015), and MVD (P = .73, r = −0.06). Moreover, there was no significant correlation between the percentage of IL-8-positive cells and the number of infiltrating cells around the blood vessels (P = .63, r = 0.04) (Fig. 4).

Immunohistochemical staining of macrophages with anti-CD68 antibody

In the positive control section from the patient with squamous cell carcinoma of the parotid gland, many macrophage-like cells that were positive for anti-CD68 antibody were seen around the cancer cells and in the connective tissues (Fig. 5, *A*). In the internal derangement group, 3 of the 13 sections showed weak staining in the synovial lining cells (Fig. 5, *B*), while 2 of the control sections showed no staining (data not shown). The negative control sections showed only background staining (Fig. 5, *C* and *D*).

DISCUSSION

To our knowledge, there are few reports about the expression of IL-8 in synovial tissue of TMJs. In the present study, IL-8 was immunohistochemically detected in 80% of the synovial tissue specimens taken from the TMJs with internal derangement. The expres-

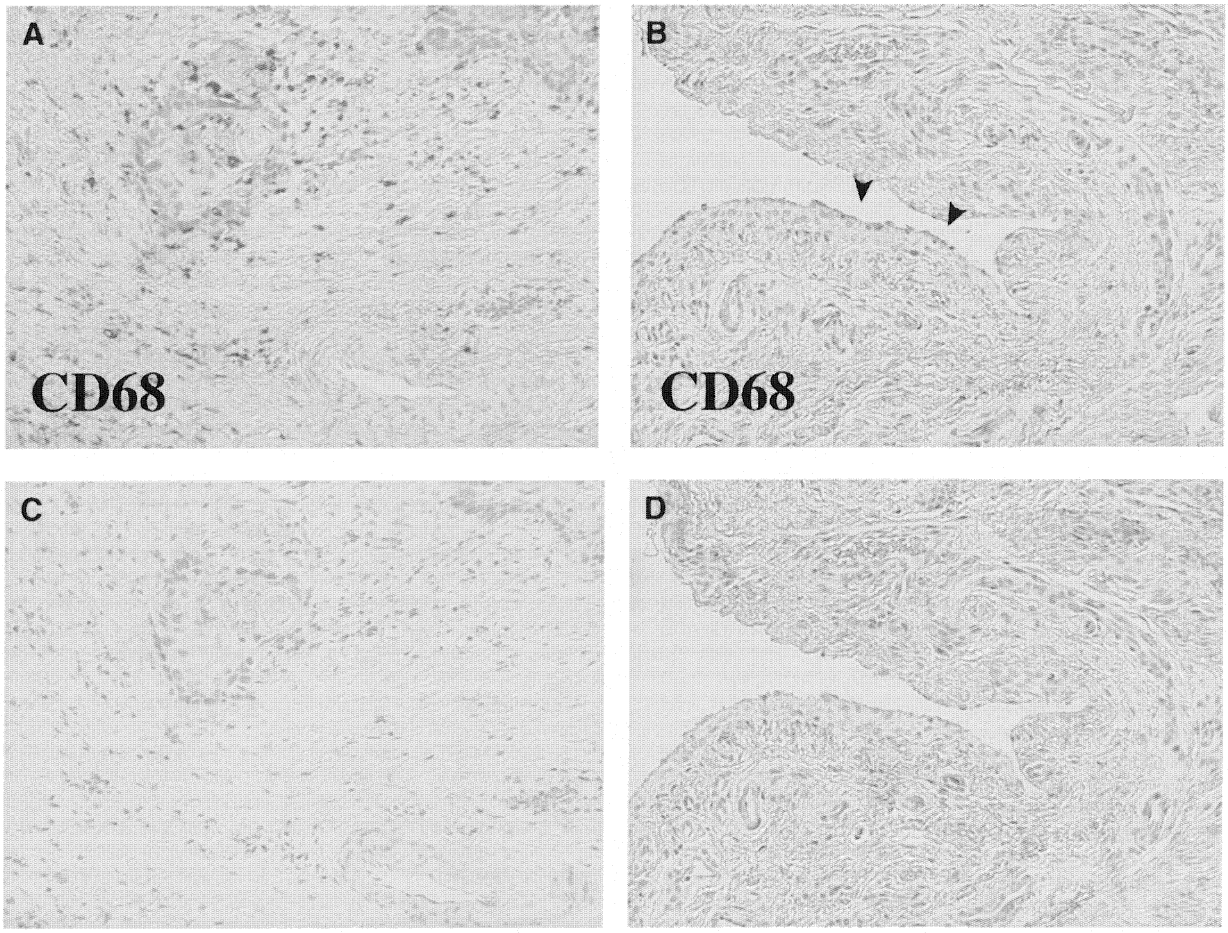

Fig. 5. Immunohistochemical finding of macrophages with anti-CD68 antibody. Many macrophage-like cells that are positive for anti-CD68 antibody are seen around the cancer cells and in the connective tissues (**A**, Positive control section). In the internal derangement section, weak staining is seen in the synovial lining cells (arrow heads) (**B**, patient number 27). Both negative control sections show no staining (**C**, **D**). (Original magnification ×200.)

sion of IL-8 in the synovial tissues was significantly up-regulated in the internal derangement group compared with the control group, suggesting that IL-8 may be a key cytokine in the production of the pathological conditions in the internal derangement of the TMJ.

Koch et al.[10] reported that, compared with patients with osteoarthritis, patients with RA had significantly higher levels of IL-8 in their synovial fluids. Takahashi et al.[21] reported that IL-8 mRNA was detected in synovial tissues from patients with RA but not, except rarely, in normal synovial tissues. However, in the present study, there were no significant correlations between the level of IL-8 expression in the synovial tissues and the clinical variables. Synovitis often occurs with internal derangement of the TMJ, and the inflammatory changes include infiltration of inflammatory cells around the blood vessels.[1,2] In patients with internal derangement of the TMJ, the degree of synovitis is remarkably milder than that in patients with RA.[22] Histologically, synovitis occurring with the internal derangement of the TMJ is chronic inflammation rather than acute inflammation.[1,2] Therefore, IL-8 may to some extent be involved in the synovitis in the TMJ.

Moreover, Koch[13] reported that IL-8 is an important potent macrophage-derived mediator of angiogenesis, and that IL-8 is involved in angiogenic diseases such as RA. In the present study, there was no significant correlation between the level of IL-8 expression in the synovial tissues and MVD. In our previous study,[15,19] there was a significant correlation among the level of expression of vascular endothelial growth factor (VEGF), its receptor (VEGF-receptor 1: Flt-1) in synovial tissues, and MVD of the TMJ. As VEGF is an endothelial cell–specific angiogenic inducer,[23,24] VEGF rather than IL-8 may be a key regulator in angiogenesis in synovial tissues of the TMJ.

Other proinflammatory cytokines such as IL-1β and TNF-α also have important functions in the pathogenesis of internal derangement of the TMJ.[5,25] IL-8, however, differs from IL-1β and TNF-α in its failure to stimulate production of prostaglandin E_2 and collagenase in joint tissue.[26,27] This may be one of the reasons why there was no correlation between the expression of IL-8 in synovial tissue and the clinical variables such as pain.

The percentage of infiltrating inflammatory cells in synovium of the TMJ was reported to range from only 3% to 12% by Dijkgraaf et al.[28] and Carls et al.[29] The biological activities of IL-8 are mediated by its binding to receptors, which are expressed mainly on leukocytes.[30] Even if expression of IL-8 is increased in the synovial tissues of the internal derangement TMJs, its effects may not be noticeable because of a lack of its receptors. These results suggest that IL-8 may play a secondary role in the pathogenesis of internal derangement of the TMJ.

Moreover, as we performed a punch biopsy in the posterior disk attachment, it was not possible to determine the distribution of IL-8 throughout the whole intracapsular structure. This may be another reason for the unexpected results in the present study.

In our previous study,[22] the number of total white blood cells (WBC) in synovial fluid was about 1000-fold higher in RA joints than in those with internal derangement of the TMJ (30000/mm^3 versus 30/mm^3). Kopp[31] demonstrated that some synovial fluids contained many lymphocytes and very few neutrophils. These results suggest that IL-8 does not play a major role in the activation of neutrophils in the TMJ.

As in other joints, synovial lining cells in the TMJ can be categorized according to their ultrastructural characteristics into at least 2 main cell types.[32,33] Type A cells are frequently described as macrophage-like and type B cells as fibroblast-like.[32] Synovial tissue macrophages have been suggested to be a source of IL-8 in joints with RA.[10] Therefore, we may expect the synovial lining cells in the TMJ to stain positive for anti-CD68 antibody. However, only 3 of 13 specimens were positive, and only weakly so. We do not think that this unexpected result stems from the technical problems, because the positive control specimen taken from the patients with carcinoma clearly stained positive. Synovial cells expressing macrophage-associated antigens were reported to be increased in inflamed synovial tissues.[33] Only low levels of expression of macrophage-associated cells in the TMJ may be involved in the limitation of the function of IL-8 in the internal derangement of the TMJ.

The major weakness of the present study is the limited number and characteristics of the control subjects. Unfortunately, finding appropriate control subjects is an immense challenge, as it is difficult to obtain fresh samples of synovial tissue and fluid from healthy individuals. As we have explained before,[8,15] the patients with dislocation were suitable for controls.

In conclusion, IL-8 was detected in the posterior disk attachment in patients with internal derangement. Although IL-8 was up-regulated in the inflamed synovial tissues from patients with internal derangement, IL-8 was not implicated in the clinical variables. IL-8 may play a secondary role in the pathogenesis of TMJ disorders. However, as the pathological mechanisms underlying joint disorders are very complex, we cannot exclude the possibility of IL-8 being involved in the pathological conditions. Further studies are required to elucidate the possible contribution of IL-8 to pathological conditions in patients with internal derangement of the TMJ.

REFERENCES

1. Gynther GW, Holmlund AB, Reinholt FP. Synovitis in internal derangement of the temporomandibular joint: correlation between arthroscopic and histologic findings. J Oral Maxillofac Surg 1994;52:913-7.
2. Merill RG, Yih WY, Langan MJ. A histologic evaluation of the accuracy of TMJ diagnostic arthroscopy. Oral Surg 1990;70:393-8.
3. Quinn JH, Bazan NG. Identification of prostaglandin E2 and leukotrien B4 in the synovial fluid of painful, dysfunctional temporomandibular joints. J Oral Maxillofac Surg 1990;48: 968-71.
4. Takahashi T, Kondoh T, Fukuda M, Yamazaki Y, Toyosaki T, Suzuki R. Proinflammatory cytokines detectable in synovial fluids from patients with temporomandibular disorders. Oral Surg Oral Med Oral Pathol Oral Radiol Endod 1998;85:135-41.
5. Suzuki T, Segami N, Nishimura M, Nojima T. Co-expression of interleukin-1β and tumor necrosis factor-α in synovial tissues and synovial fluids of temporomandibular joint with internal derangement: comparison with histologic grading of synovial inflammation. J Oral Pathol Med 2002;31:549-57.
6. Sato J, Segami N, Nishimura M, Demura N, Yoshimura H, Yoshitake Y, et al. Expression of interleukin 6 in synovial tissues in patients with internal derangement of the temporomandibular joint. Br J Oral Maxillofacial Surg 2003;41:95-101.
7. Nishimura M, Segami N, Kaneyama K, Suzuki T, Miyamaru M. Proinflammatory cytokines and arthroscopic findings of patients with internal derangement and osteoarthritis of the temporomandibular joint. Br J Oral Maxillofac Surg 2002;40:68-71.
8. Sato J, Segami N, Kaneyama K, Yoshimura H, Fujimura K, Yoshitake Y. Relationship of calcitonin gene-related peptide in synovial tissues and temporomandibular joint pain in humans. Oral Surg Oral Med Oral Pathol Oral Radiol Endod 2004;98:533-40.
9. Sato J, Segami N, Yoshitake Y, Kaneyama K, Yoshimura Y, Fujimura K, et al. Specific expression of substance p in human synovial tissues of patients with symptomatic internal derangement of the temporomandibular joint: comparison with clinical variants. Br J Oral Maxillofac Surg 2006. In press.
10. Koch AE, Kunkel SL, Burrows JC, Evanoff HL, Haines GK, Pope RM, et al. Synovial tissues macrophage as a source of the chemotactic cytokine IL-8. J Immunol 1991;147:2187-95.

11. Matsushima K, Morishita K, Yoshimura T, Lavu S, Obayashi Y, Lew W, et al. Molecular cloning of human monocyte-derived neutrophil chemotactic factor (MDNCF) and induction of MDNCF by interleukin-1 and tumor necrosis factor. J Exp Med 1988;167:1883-92.
12. Mukaida N, Sciroo M, Matsushima K. Genomic structure of human monocyte-derived neutrophil chemotactic factor IL-8. J Immunol 1989;143:1366-71.
13. Koch AE, Polverini PJ, Kunkel SL, Harlow LA, DiPietro LA, Elner VN, et al. Interleukin-8 as a macrophage-derived mediator of angiogenesis. Science 1992;258:1798-801.
14. Segami N, Kaneyama K, Tsurusako S, Suzuki T. Arthroscopic eminoplasty for habitual dislocation of the temporomandibular joint: preliminary study. J Craniomaxillofac Surg 1999;27:390-7.
15. Sato J, Segami N, Suzuki T, Kaneyama K, Yoshitake Y, Nishikawa K. The expression of vascular endothelial growth factor in synovial tissues in patients with internal derangement of the temporomandibular joint. Oral Surg Oral Med Oral Pathol Oral Radiol Endod 2002;93:251-6.
16. McCain JP, de la Rua H, LeBlanc WG. Puncture technique and portals of entry for diagnostic and operative arthroscopy of the temporomandibular joint. Arthroscopy 1991;7:221-32.
17. Weidner N, Carrol PR, Flax J, Blumenfeld W, Folkman J. Tumor angiogenesis correlates with metastasis in invasive prostate carcinoma. Am J Pathol 1993;143:401-9.
18. Decaussin M, Sartelet F, Robert C, Moro D, Claraz C, Brambilla C, et al. Expression of vascular endothelial growth factor (VEGF) and its two receptors (VEGF-R1-Flt1 and VEGF-R2-Flk1/KDR) in non-small cell lung carcinoma (NSCLCs): correlation with angiogenesis and survival. J Pathol 1999;188:369-77.
19. Sato J, Segami N, Yoshitake Y, Nishikawa K. Correlation of the expression of fibroblast growth factor-2, vascular endothelial growth factor, and their receptors with angiogenesis in synovial tissues from patients with internal derangement of the temporomandibular joint. J Dent Res 2003;82:272-7.
20. Murakami K, Segami N, Fujimura K, Iizuka T. Correlation between pain and synovitis in patients with internal derangement of the temporomandibular joint. J Oral Maxillofac Surg 1991;49:1159-61.
21. Takahashi Y, Kasahara T, Sawai T, Rikimaru A, Mukaida N, Matsushima K, et al. The participation of IL-8 in the synovial lesions at an early stage of rheumatoid arthritis. Tohoku J Exp Med 1999;188:75-87.
22. Nishimura M, Segami N, Shimada H. White blood cell analysis of the synovial fluids in patients with internal derangement of the tempotomandibular joints. J Kanazawa Med Univ 2000; 25:194-201.
23. Pepper MS, Ferrara N, Orci L, Montesano R. Potent synergism between vascular endothelial growth factor and basic fibroblast growth factor in the induction of angiogenesis in vitro. Biochem Biophys Res Commun 1992;189:824-34.
24. Decaussin M, Sartelet H, Robert C, Moro D, Claraz C, Brambilla C, et al. Expression of vascular endothelial growth factor (VEGF) and its two receptors (VEGF-R1-Flt1 and VEGF-R2-Flk1/KDR) in non-small cell lung carcinomas (NSCLCs): correlation with angiogenesis and survival. J Pathol 1999; 188:369-77.
25. Sandler NA, Buckely M, Cillo JE, Braun TW. Correlation of inflammatory cytokines with arthroscopic findings in patients with temporomandibular joint. J Oral Maxillofac Surg 1998;56:534-43.
26. Guerne PA, Zuraw BL, Vaughan JH, Carson DA, Lotz M. Synovium as a souce of interleukin 6 in vitro: contribution to local and systemic manifestations of arthritis. J Clin Invest 1989;83:585-92.
27. Jorgensen C, Apparailly F, Sany J. Immunological evaluation of cytokine and anticytokine immunotherapy in vivo: what have we learnt? Ann Rheum Dis 1999;58:136-41.
28. Dijkgraaf LC, Liem RSB, de Bont LGM. Synovial membrane involvement in osteoarthritic temporomandibular joints: a light microscopic study. Oral Surg Oral Med Oral Pathol Oral Radiol Endod 1997;83:373-86.
29. Carls FR, von Hochstetter A, Makek M, Engelke W. Diagnostic accuracy of TMJ arthroscopy in correlation to histological findings. J Craniomaxillofac Surg 1995;23:75-80.
30. Murphy PM, Tiffany HL. Cloning of complementary DNA encoding a functional human interleukin-8 receptor. Science 1991;253:1280-2.
31. Kopp S, Wenneberg B, Clemensson E. Clinical microscopical and biochemical investigation of synovial fluid from temporomandibular joint. Scand J Dent Res 1983;91:33-41.
32. Dijkgraaf LC, de Bont LGM, Boering G, Liem RSB. Structure of the normal synovial membrane of the temporomandibular joint: a review of the literature. J Oral Maxillofac Surg 1996;54:332-8.
33. Athanasou NA, Quinn J, Heryet A, Puddle B, Woods CG, McGee JO. The immunohistology of synovial lining cells in normal and inflamed synovium. J Pathol 1988;155:133-42.

Reprint requests:

Jun Sato, DDS, PhD
Oral Diagnosis and Medicine
Department of Oral Pathobiological Science
Hokkaido University Graduate School of Dental Medicine
North 13, West 7
Kita-Ward Sapporo 060-8586, Japan
jun-s@den.hokudai.ac.jp

Available online at www.sciencedirect.com
ScienceDirect
ELSEVIER
British Journal of Oral and Maxillofacial Surgery 45 (2007) 279–283
BRITISH Journal of Oral and Maxillofacial Surgery
www.bjoms.com

Anchored disc phenomenon with a normally positioned disc in the temporomandibular joint: Characteristics and behaviour

Keiseki Kaneyama [a,*], Natsuki Segami [a], Tsurusako Shin-Ichi [b], Kazuma Fujimura [a], Jun Sato [c], Toshikazu Nagao [a]

[a] *Department of Oral and Maxillofacial Surgery, Kanazawa Medical University, 1-1 Daigaku, Uchinada-cho, Kahoku-gun, Ishikawa-pref. 920-0293, Japan*
[b] *Department of Oral and Maxillofacial Surgery, Seirei Hospital, 56 Kawanayama-cho, Showaku, Nagoya-city, Aichi-pref. 466-8633, Japan*
[c] *Department of Oral Diagnosis and Oral Medicine, Graduate School of Dental Medicine, Hokkaido University, N-13, W-7, Kita-ku, Sapporo, Hokkaido 060-8586, Japan*

Accepted 21 August 2006
Available online 23 October 2006

Abstract

We aimed to elucidate the pathogenesis and evaluate the therapeutic behaviour of patients with an anchored disc phenomenon but a normally positioned disc of the temporomandibular joint (TMJ). Fourteen patients with internal derangement including closed lock of one TMJ were examined. All had normally positioned discs. Synovial fluid was collected from the TMJ by arthrocentesis. Their symptoms, and the protein concentration in the synovial fluid, were evaluated. Their median duration of illness was 3 months (range 0.5–12), and the median protein concentration was low (343 μg/ml; range 36–791). Arthrocentesis was successful in nine. Arthroscopic findings in the five unsuccessful cases showed severe intra-articular adhesions of the TMJ. The main intra-articular pathological feature was the presence of adhesions, which might be affected by low protein concentrations in the synovial fluid. These findings may provide a new treatment in patients with normally positioned discs, despite the small number studied.

Keywords: Temporomandibular joint (TMJ); Anchored disc phenomenon; Normally positioned disc; Synovial fluid; protein

Introduction

The clinical behaviour and treatment of internal derangement of the temporomandibular joint (TMJ) with closed lock have been well documented.[1–4] Although patients usually have anterior displacement of the disc without reduction, Nitzan and Marmary reported that the anchored disc in the TMJ is a condition in which the integrity of the joint is preserved but the disc adheres so tightly to the fossa that it prevents the condyle from sliding.[5] This is characterised by sudden onset and severe limitation of mouth opening, associated with clinical and radiological evidence of no condylar sliding, probably as a result of the disc being adherent to the fossa in either a normal or displaced position.[5,6] However, the characteristics and treatment are still not clear. In the present study, therefore, we investigated the pathogenesis of patients with an anchored, but normally positioned disc of the TMJ. We also evaluated the response to treatment of patients with normally positioned discs.

* Corresponding author at: 1-1 Daigaku, Uchinada-cho, Kahoku-gun, Ishikawa-ken., Japan. Tel.: +81 76 286 2211x7018; fax: +81 76 286 2010.
E-mail address: k-k@kanazawa-med.ac.jp (K. Kaneyama).

0266-4356/$ – see front matter
doi:10.1016/j.bjoms.2006.08.021

Table 1
Details of anchored disc phenomenon with normally positioned disc of the temporomandibular joint

Case no.	Age (years)	Sex (M/F)	History of present illness (months)	Opening degree (mm)	Visual analogue scale	Osseous changes of the condyle on magnetic resonance imaging
1	70	M	0.5	20	5	Biconcave
2	29	F	9	28	2	Biconcave
3	25	F	1	29	10	Biconcave
4	20	F	3	31	2	Biconcave
5	29	M	0.5	28	6	Biconcave
6	38	F	12	31	2	Biconcave
7	15	F	3	32	3	Biconcave
8	16	F	12	30	3	Biconcave
9	26	F	5	30	7	Biconcave
10	55	M	1	20	9	Biconcave
11	34	F	3	25	8	Biconcave
12	38	F	1	15	10	Biconcave
13	50	M	4	27	8	Osteophytic
14	35	M	1	23	5	Deformed
Median (range)	32 (15–70)		3 (0.5–12)	28 (15–32)	5 (2–10)	

In all cases the position of the disc was normal and it was biconcave.

Patients and methods

Subjects

We examined 14 patients who had all had an internal derangement with closed lock of a TMJ, and who had had therapeutic arthrocentesis. Diagnoses were based on primary clinical symptoms and findings on magnetic resonance imaging (MRI).[5,7] The scans were done just before arthrocentesis and sampling of the synovial fluid. MRIs were taken in sagittal mouth-closed and mouth-open positions with a single excitation with a 256 × 157 matrix, using a 1.5-T MRI scanner (Siemens, Erlangen, Germany) and with bilateral 3-in. surface coils. Continuous proton density (TR/TE 2000/20 ms) sagittal images of sections 3 mm thick were taken. Internal derangement of the TMJ was defined as derangement of the disc with locking of the TMJ, which was associated with considerably impaired mobility of the joint and pain. MRI findings showed that internally deranged TMJs had a normally positioned disc. When the disc is positioned normally, the posterior band of the TMJ is located at the apex of the condyle when the mouth is closed, and the disc assumes a "bow-tie" appearance. Lack of change in the position of the disc was defined as a stuck or fixed disc. The characteristics of the 14 patients and their symptoms are shown in Table 1.

Preparation of synovial fluid from the TMJ, and perfusion

Synovial fluid was collected from each TMJ by puncture with a 21 gauge needle that was inserted inferolaterally into the superior joint space under local anaesthesia.[8,9] A solution of 2 ml normal saline was injected into the space, and the synovial fluid aspirated. The patients were asked to open and close their mouths to mix the saline solution with the synovial fluid, and the mixture was aspirated and re-injected 10 times before it was collected. Samples that were contaminated with blood were excluded. Samples were centrifuged immediately (3000 rpm for 20 min) to remove cells, and the supernatants were stored at −85 °C until the protein was assayed.

An 18 gauge needle was inserted into the articular eminence by the anterolateral approach to let the perfusate drain. The perfusate, 400 ml of Ringer's lactate, was allowed to flow freely through the superior joint space. The perfusion bag containing the Ringer's was set 1.5 m above the level of the joint and the solution was perfused at a constant flow rate of 10–12 ml/min. After 400 ml had been perfused, 2.5 mg of betamethasone was injected into the joint space. Finally, each patient practised opening the mouth as wide as possible.

After arthrocentesis, antibiotics were prescribed (sawacillin 750 mg per day, three times daily for 3 days, respectively) and a non-steroidal anti-inflammatory drug were prescribed (loxonin 180 mg per day, three times daily for 7 days, respectively). The patients used an occlusal appliance for 1–2 months postoperatively. They also continued opening, protrusive, and lateral excursive exercises.

Protein assay

Total protein concentration in the synovial fluid of the TMJ was measured by dye-binding assay using a protein assay kit (Bio-Rad Co., Hercules, CA, USA) with a detection limit of more than 20 μg/ml.

Statistics

The significance of differences among the signs and symptoms (age, duration of illness, degree of opening, and the visual analogue scale for pain (VAS) of arthralgia) were assessed using the Mann–Whitney *U*-test, as were those

Table 2
Median (range) volume and concentration of protein in synovial fluid aspirated from the superior joint compartment of the TMJ in patients with a normally positioned disc ($n = 9$)

Number of joints	9
Volume (ml)	1.8 (1.6–2)
Protein (μg/ml)	343 (36–791)

between total concentrations of protein in the two groups. Probabilities of less than 0.05 were accepted as significant.

Results

Total concentration of protein in synovial fluid

Nine synovial samples were obtained that were not contaminated with blood. The median concentration of protein was 343 μg/ml (range 36–791) (Table 2).

Clinical course and success rate

The criteria of "success" for arthrocentesis were judged in the same way as previous reports[8,9]; that is, arthralgia disappeared or was mild, the median width of mouth opening was more than 38 mm, and the patients were taking a normal diet. Nine cases were judged as successful (Table 3). There were no significant differences in the symptoms between successful (cases 1–9) and unsuccessful cases (numbers 10–14). During the follow-up period, which ranged from 4 to 48 weeks (median 8 weeks), the median width of mouth opening in the unsuccessful group was lower than that in the successful group (27 mm compared with 44 mm) ($p < 0.001$, Table 3). In addition, there were no improvements in pain scores in the unsuccessful group (Table 3). The patients in the unsuccessful group found eating a normal diet difficult.

Table 4
Arthroscopic findings in the unsuccessful cases with normally positioned discs

Case no.	Score of arthroscopic findings (0–10)	
	Synovitis	Adhesion
10	7	8
11	6	6
12	2	9
13	7	7
14	5	7
Median (range)	6 (2–7)	7 (6–8)

Case 13 had a degenerating articular cartilage.

Evaluation of arthroscopic findings

Five patients in whom arthrocentesis had been unsuccessful then had arthroscopic lysis and lavage. We did a conventional diagnostic arthroscopy of the whole area of the superior joint compartment and recorded it on videotape for about 10 min. The degrees of synovitis and degeneration of articular cartilage and adhesions were estimated by inspection and palpation with a probe according to the criteria described previously[10]: the most pronounced degree of synovitis in the superior compartment was given a score on a scale of 0–10 by two oral and maxillofacial surgeons (KK and NS) who were unaware of the patient's name and condition. In Table 4

Table 3
Outcomes after arthrocentesis in patients with normally positioned discs

Case no.	Follow-up period (weeks)	Opening (mm)	Length of time before patient pain free
Successful cases			
1	4	50	1
2	8	45	4
3	12	44	6
4	48	48	1
5	4	52	1
6	8	45	1
7	12	43	1
8	16	40	1
9	16	33	1
Median (range)	12 (4–48)	45 (33–52)	1 (1–6)
Unsuccessful cases			
10	4	20	–
11	8	28	–
12	4	23	–
13	8	35	–
14	8	29	–
Median (range)	8 (4–8)	28 (20–35)	
Total: median (range)	8 (4–48)	41.5 (20–52)	

No unsuccessful case became painful.

we summarise the arthroscopic findings, the most common of which were severe intra-articular adhesions and moderate synovitis.

Discussion

The median duration of illness in patients with normally positioned discs was 4 months, which was significantly shorter than that in the patients with anterior displacement of the disc that had been reported previously (12–22 months).[1,3] In particular, in the case of diagnostic arthroscopy in our patients, severe adhesions were present despite the illness having been symptomatic for only a month, as in previous studies.[5,11] Previous studies have suggested that the anchored disc phenomenon may be caused by a vacuum cap effect, which is compression of the disc against the fossa and may be the first chain reaction which would result in anterior displacement with adhesion.[5,11] However, it is likely that the condition does not always progress to anterior displacement because this might depend on the development of adhesions. In the cases without adhesions, a vacuum cap effect may induce anterior displacement. In contrast, a patient may have adhesions that do not induce displacement because of the reduced mobility of the disc. Intra-articular adhesion may therefore be a key factor in the progression from normal positioning to anterior displacement. In particular, a vacuum cap effect of the TMJ might prevent the exchange of synovial fluid and induce the breakdown of the lubrication system in the TMJ and degradation of hyaluronic acid.[5,11] Adhesions that caused no symptoms might then form gradually.

In cases with the sudden onset of symptoms, the duration of illness may be relatively short. One previous study hypothesised that overloading of the joint may induce degradation of the molecular components of the cartilage, resulting in excessive release of the degradation products of proteoglycans into the synovial fluid.[12] Increased levels of protein in the synovial fluid may therefore indicate degradation of the molecular components of the cartilage matrix.

Increased concentrations of protein were associated with arthralgia of the TMD.[7,12,13] Interestingly, although it has been reported that the range of protein concentrations in the synovial fluid of patients with anterior displacement was 1105–1830 μg/ml,[7,12] our results indicate that the mean protein concentrations were 353 μg/ml and less. There might be no excessive release of the molecular components of the cartilage, because the morphology of the disc and condyle in most patients were normal. We therefore, speculate that arthralgia of the TMJ in these patients with normally positioned discs may not be induced by mediators in the synovial fluid, but by tractional pain accompanied by fibrous adhesions.

Arthrocentesis is a simple yet effective method of treatment for anterior displacement of the disc of the TMJ with confirmed long-term results.[9,14,15] We know of only one report that both arthrocentesis and arthroscopic surgery are efficient procedures for the management of patients with normally positioned discs, but it was not clear which of these methods was superior.[11] This raises the question of what is the best treatment for these patients. In the present study, arthrocentesis was successful in 9 of 14 patients, which was similar to the results of previous reports of patients with anterior displacement.[9,15] Arthrocentesis may therefore be a better first choice for the treatment of patients with both conditions. However, as diagnostic arthroscopy in the unsuccessful cases indicated severe fibrous adhesions, arthrocentesis may not always be suitable.[4] That is, it is likely that arthrocentesis will have more effects in the treatment of sudden-onset closed lock, which arose as a result of the vacuum cap effect. Some that are resistant to arthrocentesis may have adhesions in the TMJ, and arthroscopic surgery should be attempted as early as possible. However, it is not clear which cases will respond to arthrocentesis in the early stage. Because most of our successful cases had less pain within 1 week of arthrocentesis, improvement in arthralgia might be useful for predicting the prognosis of such patients. That is, in unsuccessful cases, arthralgia may have arisen in the TMJ because of tractional pain derived from severe fibrous adhesions. It will therefore be important to target fibrous adhesions when treating patients with normally positioned as well as anteriorly displaced discs.

Despite the small number of patients, the main condition of an immobile disc might be a vacuum cup effect together with adhesions, which might be affected by low concentrations of protein in the synovial fluid. Consequently, normally positioned discs may be included in the "closed lock" category, and be treated similarly. Further studies are required to gain a better understanding of this.

Acknowledgements

This study was partially supported by a Grant-in-Aid for Young Scientists (B-16791265) and Grant-Aid for Scientific Research (17592118) from the Ministry of Education, Culture, Sports, Science, and Technology of Japan, and by a Grant for Collaborative Research from Kanazawa Medical University (C2005-5).

References

1. Indresano AT. Arthroscopic surgery of the temporomandibular joint: report of 64 patients with long-term follow-up. *J Oral Maxillofac Surg* 1989;**47**:439–41.
2. McCain JP, Sanders B, Koslin MG, Quinn JH, Peters PB, Indresano AT. Temporomandibular joint arthroscopy: a 6-year multicenter retrospective study of 4831 joints. *J Oral Maxillofac Surg* 1992;**50**:926–30.
3. Kaneyama K, Segami N, Sato J, Murakami K, Iizuka T. Outcomes of 152 temporomandibular joints following arthroscopic antero-lateral capsular release by Holmium:YAG laser or electrocautery. *Oral Surg Oral Med Oral Pathol Oral Radiol Endod* 2004;**97**:546–52.
4. Murakami K, Hosaka H, Moriya Y, Segami N, Iizuka T. Short-term treatment outcome study for the management of temporomandibular joint closed lock. A comparison of arthrocentesis to nonsurgical therapy

and arthroscopic lysis and lavage. *Oral Surg Oral Med Oral Pathol Oral Radiol Endod* 1995;**80**:253–7.
5. Nitzan DW, Marmary Y. The "anchored disc phenomenon": a proposed etiology for sudden-onset, severe, and persistent closed lock of the temporomandibular joint. *J Oral Maxillofac Surg* 1997;**55**:797–803.
6. Rao VM, Liem MD, Farole A, Razek AA. Elusive "stuck" disk in the temporomandibular joint: diagnosis with MR imaging. *Radiology* 1993;**189**:823–7.
7. Kaneyama K, Segami N, Nishimura M, Suzuki T, Sato J. Importance of proinflammatory cytokines in synovial fluid from 121 joints with temporomandibular disorders. *Br J Oral Maxillofac Surg* 2002;**40**:418–23.
8. Nishimura M, Segami N, Kaneyama K. Prognostic factors in arthrocentesis of the temporomandibular joint: evaluation of 100 patients with internal derangement. *J Oral Maxillofac Surg* 2001;**59**:874–8.
9. Kaneyama K, Segami N, Nishimura M, Sato J, Fujimura K, Yoshimura H. The ideal lavage volume for removing bradykinin, interleukin-6 and protein from the temporomandibular joint by arthrocentesis. *J Oral Maxillofac Surg* 2004;**62**:657–61.
10. Segami N, Nishimura M, Kaneyama K, Miyamaru M, Sato J, Murakami KI. Does joint effusion on T2 magnetic resonance images reflect synovitis? Comparison of arthroscopic findings in internal derangements of the temporomandibular joint. *Oral Surg Oral Med Oral Pathol Oral Radiol Endod* 2001;**92**:341–5.
11. Sanroman JF. Closed lock (MRI fixed disc): a comparison of arthrocentesis and arthroscopy. *Int J Oral Maxillofac Surg* 2004;**33**:344–8.
12. Takahashi T, Nagai H, Seki H, Fukuda M. Relationship between joint effusion, joint pain, and protein levels in joint lavage fluid of patients with internal derangement and osteoarthritis of the temporomandibular joint. *J Oral Maxillofac Surg* 1999;**57**:1187–94.
13. Segami N, Miyamaru M, Nishimura M, Suzuki T, Kaneyama K, Murakami K. Does joint effusion on T2 magnetic resonance images reflect synovitis? Part 2. Comparison of concentration levels of proinflammatory cytokines and total protein in synovial fluid of the temporomandibular joint with internal derangements and osteoarthrosis. *Oral Surg Oral Med Oral Pathol Oral Radiol Endod* 2002;**94**:515–21.
14. Nitzan DW, Samson B, Better H. Long-term outcome of arthrocentesis for sudden-onset, persistent, severe closed lock of the temporomandibular joint. *J Oral Maxillofac Surg* 1997;**55**:151–8.
15. Hosaka H, Murakami K, Goto K, IIzuka T. Outcome of arthrocentesis for temporomandibular joint with closed lock at 3 years follow-up. *Oral Surg Oral Med Oral Pathol Oral Radiol Endod* 1996;**82**:501–4.

Prognostic Factors in Arthrocentesis of the Temporomandibular Joint: Comparison of Bradykinin, Leukotriene B4, Prostaglandin E2, and Substance P Level in Synovial Fluid Between Successful and Unsuccessful Cases

Keiseki Kaneyama, DDS, PhD, Natsuki Segami, DDS, PhD,†*
Jun Sato, DDS, PhD,‡ Kazuma Fujimura, DDS, PhD,§
Toshikazu Nagao, DDS, PhD,‖ and
Hiroshi Yoshimura, DDS, PhD¶

Purpose: To compare levels of bradykinin (BK), leukotriene B4 (LTB4), prostaglandin E2 (PGE2), and substance P (SP) between successful and unsuccessful cases of arthrocentesis of temporomandibular joint disorders (TMDs).

Patients and Methods: A total of 66 joints in 66 patients with TMDs who underwent arthrocentesis were evaluated in this study. Synovial fluid diluted with saline solution was aspirated from the superior joint compartment before arthrocentesis and their concentrations of BK, LTB4, PGE2, and SP were determined by enzyme-linked immunosorbent assay. The differences in the detection rate and concentration of each mediator between successful cases and unsuccessful cases of arthrocentesis were analyzed statistically.

Results: Arthrocentesis was successful for 77% (51/66) of the joints. The mean detection rate of LTB4 was significantly ($P < .05$) higher in the unsuccessful cases (47%) than in the successful cases (16%). The mean concentration of BK was significantly ($P < .0005$) higher in the unsuccessful cases (425 pg/mL) than in the successful cases (144 pg/mL). There was also a statistical correlation between the detection of LTB4 and PGE2 ($P < .01$).

Conclusions: Increased levels of BK and LTB4 in the synovial fluid of patients with TMDs may indicate that arthrocentesis is less likely to be a successful treatment.

J Oral Maxillofac Surg 65:242-247, 2007

Arthrocentesis has been recognized as a simple and effective treatment for temporomandibular joint disorders (TMDs).[1-5] Because there are few reports on the prognostic factors of this procedure,[3-5] little is known as to which cases will respond well to this procedure. Our previous studies showed that severe preoperative pain of the temporomandibular joint (TMJ) may be a clinical predictor of unsuccessful arthrocentesis for TMDs.[3] Murakami et al[4] also reported that a patient's age and duration of locking

Received from the Department of Oral and Maxillofacial Surgery, Kanazawa Medical University, Ishikawa, Japan.
*Lecturer.
†Professor and Chairman.
‡Lecturer.
§Associate Professor.
‖Assistant Professor.
¶Associate Professor.
This study was partially supported by Grant-in-Aid for Young Scientists (B-16791265) from the Ministry of Education, Culture, Sports, Science and Technology of Japan and by a Grant for Collaborative Research (C2005-5) from Kanazawa Medical University.
Address correspondence and reprint requests to Dr Kaneyama: 1-1 Daigaku, Uchinada-machi, Kahoku-gun, Ishikawa-Ken, 920-0293 Japan; e-mail: k-k@kanazawa-med.ac.jp

0278-2391/07/6502-0014$32.00/0
doi:10.1016/j.joms.2005.10.068

may be predictors of the outcome of arthrocentesis. To the best of our knowledge, there has been only 1 report concerning analysis of synovial fluid of the TMJ in an attempt to find prognostic indicators.[5] That study found that interleukin (IL)-1β and IL-6 in the synovial fluid may be indicators of nonsuccess after arthrocentesis. On the other hand, previous studies showed that pain-related chemical mediators such as bradykinin (BK), leukotriene B4 (LTB4), prostaglandin E2 (PGE2), and substance P (SP), which are pain-inducible mediators, may be related to synovitis and arthralgia of the TMJ.[6-12] We previously showed that arthrocentesis can reduce the concentration of BK in the synovial fluid of the TMJ, and we speculate that its reduction might lead to reduced arthralgia.[6] However, whether those pain mediators as well as BK may be predictors of the outcome of arthrocentesis is unclear. To determine this, we compared levels of BK, LTB4, PGE2, and SP between successful and unsuccessful cases of arthrocentesis for patients with TMDs.

Patients and Methods

PATIENTS

Sixty-six TMJs with internal derangement (ID) and osteoarthritis (OA) in 62 women and 4 men were examined. All of the patients complained of limited mouth opening and pain in the affected TMJ. The patients' average age was 36 years (range, 14 to 73 years). Preoperative symptoms of painful locking ranged from 1 month to 24 months (mean, 2 months). Preoperative magnetic resonance imaging (MRI) showed that the 51 joints with ID had anterior disc displacement without reduction, with no bony changes or flattening of the condyle. MRI also showed that all 15 joints with OA had anterior disc displacement without reduction and bony changes such as osteophytes and erosion, either alone or in combination. Before arthrocentesis, each patient rated, on a visual analog scale (VAS) from 0 to 10 points, his or her degree of joint pain on mouth opening. The average VAS score was 5 points (range, 0 to 9 points).

ARTHROCENTESIS AND PREPARATION OF TMJ SYNOVIAL FLUID

All patients underwent therapeutic arthrocentesis at Kanazawa Medical University Hospital. The patients were instructed to maintain a normal diet regimen. Arthrocentesis was performed as described previously.[3,5,6] In brief, a local anesthetic (2% lidocaine) was injected subcutaneously to infiltrate into the pericapsular tissue, with care taken to prevent the anesthetic from entering the TMJ. Then 2 mL of saline solution was injected through a 21-gauge needle inserted through an inferolateral approach into the superior joint compartment of the TMJ. The patient was instructed to open and close the mouth to mix the saline with the synovial fluid. The mixture of synovial fluid and saline was aspirated and reinjected a total of 10 times using a syringe, and then an average of 2 mL (range, 1.8 to 2.4 mL) was collected. After the samples were confirmed to be free of blood contamination, they were immediately centrifuged at 3,000 rpm for 20 minutes to remove the cells. The supernatants were stored at −85°C until they were assayed. An 18-gauge needle was inserted into the articular eminence through an anterolateral approach to serve as an outlet for perfusate. The perfusate, 400 mL of lactated Ringer's solution, was allowed to flow freely through the superior joint space. The perfusion bag containing the Ringer's solution was set 1.5 m above the level of the joint, and the solution was perfused at a constant flow rate of 10 to 12 mL/minute. After the perfusion, 2.5 mg of betamethasone was injected into the joint space.

MEASUREMENT OF CONCENTRATIONS OF PAIN-RELATED CHEMICAL MEDIATORS

The concentrations of BK, LTB4, PGE2, and SP were determined using enzyme-linked immunosorbent assay kits, obtained from Dai-Nippon Pharmaceutical Corp (Osaka, Japan) for BK (sensitivity, <4.9 pg/mL) and from Assay Designs (Ann Arbor, MI) for LTB4 (sensitivity, <48 pg/mL), PGE2 (sensitivity, <36 pg/mL), and SP (sensitivity, <8 pg/mL).

STATISTICS

Statistical analyses of BK, LTB4, PGE2, and SP concentrations were done using the Mann-Whitney U test. The prevalence of BK, LTB4, PGE2, and SP was analyzed using the χ^2 test for independence. P values less than .05 were considered significant.

Results

CLINICAL COURSE AND SUCCESS RATE

The criteria for "success" have been described previously.[3,5,6] The arthralgia disappeared or was very mild. The average width of mouth opening was greater than 38 mm, and the average lateral and protrusion movement was greater than 6 mm. The patients were given a normal diet regimen. In the follow-up period, which ranged from 2 to 13 months (mean, 3 months), arthrocentesis was successful for 77% (51 of 66) of the joints. The 15 unsuccessful joints still had severe arthralgia and locking.

Table 1. VOLUME AND YIELD IN SYNOVIAL FLUID OF THE TMJ

	Successful Cases (n = 51)	Unsuccessful Cases (n = 15)	Total (n = 66)
*Volume (mL)	2.0 ± 0.13	2.0 ± 0.16	2.0 ± 0.14
Yield (%)	101	104	102

*Volume of diluted synovial fluid aspirated from the superior joint compartment. Mean ± SD: mL.

Kaneyama et al. Prognostic Factors in Arthrocentesis of the TMJ. J Oral Maxillofac Surg 2007.

VOLUME AND YIELD IN TMJ SYNOVIAL FLUID

There was no significant difference between successful cases and unsuccessful cases in terms of the volume and yield of diluted synovial fluid (Table 1).

DETECTION OF PAIN-RELATED CHEMICAL MEDIATORS

BK was detected in 86% (57) of all 66 joints, LTB4 in 23% (15), PGE2 in 11% (7), and SP in 12% (8). BK was detected in 82% (42) of the 51 successful joints, LTB4 in 16% (8), PGE2 in 8% (4), and SP in 8% (4). BK was detected in 100% (15) of the 15 unsuccessful joints, LTB4 in 47% (7), PGE2 in 20% (3), and SP in 27% (4). A statistically significant difference between successful and unsuccessful cases was seen only in LTB4 ($P < .05$) (Table 2).

CONCENTRATIONS OF PAIN-RELATED CHEMICAL MEDIATORS

In the synovial fluid of successful cases, the mean concentration of BK was 144 pg/mL, that of LTB4 was 116 pg/mL, that of PGE2 was 10 pg/mL, and that of SP was 5 pg/mL. In the unsuccessful cases, mean concentrations were 425 pg/mL for BK, 342 pg/mL for LTB4, 48 pg/mL for PGE2, and 22 pg/mL for SP. A statistically significant difference in mediator concentration between successful and unsuccessful cases was seen only for BK ($P < .0005$) (Table 3; Fig 1).

Table 2. DETECTION RATE OF PAIN-RELATED CHEMICAL MEDIATORS IN SYNOVIAL FLUID OF THE TMJ

	Successful Cases (n = 51)	Unsuccessful Cases (n = 15)	Total (n = 66)
BK			
Detection rate: joint	42	15	57
%	82	100	86
LTB4			
Detection rate: joint	8	7	15
%	*16	*47	23
PGE2			
Detection rate: joint	4	3	7
%	8	20	11
SP			
Detection rate: joint	4	4	8
%	8	27	12

*$P < .05$.

Kaneyama et al. Prognostic Factors in Arthrocentesis of the TMJ. J Oral Maxillofac Surg 2007.

Table 3. CONCENTRATION OF PAIN-RELATED CHEMICAL MEDIATORS IN SYNOVIAL FLUID OF THE TMJ

	Successful Cases (n = 51)	Unsuccessful Cases (n = 15)	Total (n = 6)
BK	*144 ± 144	*425 ± 295	208 ± 221
LTB4	116 ± 357	342 ± 642	168 ± 443
PGE2	10 ± 41	48 ± 149	18 ± 80
SP	5 ± 20	22 ± 50	9 ± 30

Mean ± SD pg/mL.
*$P < .0005$.

Kaneyama et al. Prognostic Factors in Arthrocentesis of the TMJ. J Oral Maxillofac Surg 2007.

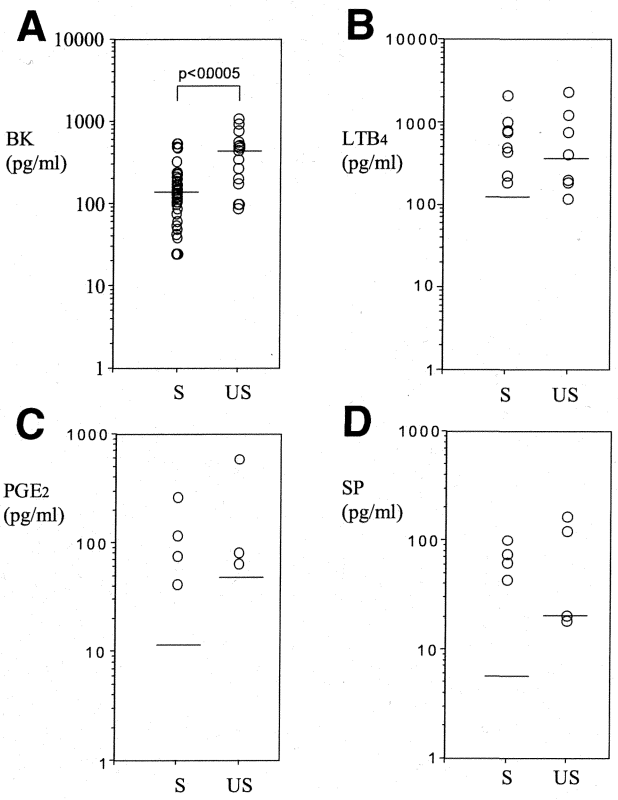

FIGURE 1. Concentration of the pain-related chemical mediators in successful cases and unsuccessful cases. The horizontal bars indicate the mean concentration. *S*, successful cases; *US*, unsuccessful cases.

Kaneyama et al. Prognostic Factors in Arthrocentesis of the TMJ. J Oral Maxillofac Surg 2007.

Table 4. CORRELATION OF PAIN-RELATED CHEMICAL MEDIATORS IN SYNOVIAL FLUID OF THE TMJ

	PGE2	
	ND	D
LTB4		
ND	*49	2
D	10	*5

Abbreviations: D, detected; ND, not detected.
*$P < .01$.

Kaneyama et al. Prognostic Factors in Arthrocentesis of the TMJ. J Oral Maxillofac Surg 2007.

CORRELATIONS OF PAIN-RELATED CHEMICAL MEDIATORS

With respect to each pain-related chemical mediator, all of the joints were classified into 2 groups according to whether or not each pain-related chemical mediator was detected. As shown in Table 4, there was a significant correlation between PGE2 and LTB4 ($P < .01$). In addition, the concentration of LTB4 (1049 pg/mL) was higher in the group with detected PGE2 than in the group without detected PGE2 (63 pg/mL; $P < .05$) (Fig 2). However, no significant differences in the detection and concentrations of other pain-related chemical mediators were seen.

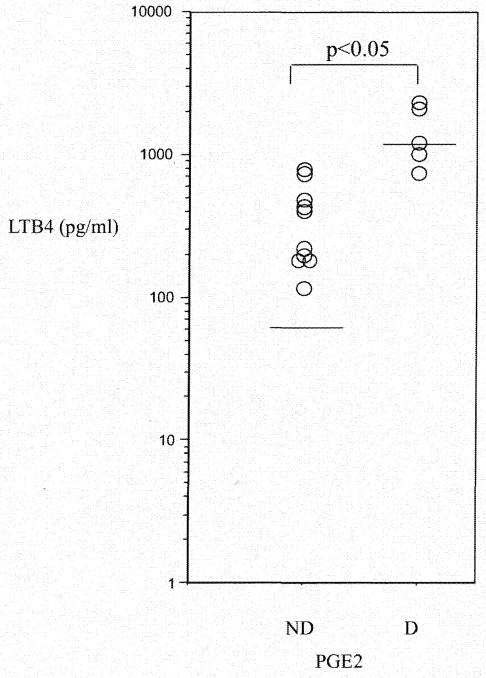

FIGURE 2. Correlation between LTB4 and PGE1. *D*, detected. *ND*, not detected.

Kaneyama et al. Prognostic Factors in Arthrocentesis of the TMJ. J Oral Maxillofac Surg 2007.

Table 5. CORRELATIONS BETWEEN CLINICAL SIGNS AND PAIN RELATED CHEMICAL MEDIATORS

	Age	Duration of Illness	Opening Degree	VAS
BK	0.001	0.20	0.01	0.03
LTB4	0.13	0.02	0.05	0.15
PGE2	0.20	0.05	0.02	0.06
SP	0.10	0.08	0.002	0.09

Abbreviation: VAS, visual analog scale.
Number is a correlation coefficient.

Kaneyama et al. Prognostic Factors in Arthrocentesis of the TMJ. J Oral Maxillofac Surg 2007.

ASSOCIATION OF CLINICAL SYMPTOMS WITH PAIN-RELATED CHEMICAL MEDIATORS

There were no correlations among the concentrations of BK, LTB4, SP, and PGE2 and age, duration of illness, width of mouth opening, and VAS score (Table 5).

Discussion

In the present study, the detection rate of BK was very high, especially in the unsuccessful cases of arthrocentesis, and the concentration of BK was higher in the unsuccessful cases than in the successful cases. BK is a potent inflammatory, pain-inducible mediator that can provoke release of other mediators, such as PGE2, leukotrienes, and cytokines.[13-15] BK has also been identified in various arthritic joints, including TMJ, and has been correlated with synovitis, which can cause joint arthralgia.[11,13-15] Because BK in the synovial fluid of diseased TMJs was significantly correlated with arthroscopic synovitis,[12] it is reasonable to speculate that elimination of BK may be important in terms of treatment. In our previous study, we confirmed that the BK level is reduced by the amount dose-dependent perfusate in arthrocentesis[6]; however, this method of reducing the BK level did not necessarily result in reduced arthralgia, and no correlation between BK concentration and VAS score was seen. This may be related to the greater production and faster recovery of BK and the character of the VAS, which is too subjective and somewhat unclear.[6] How quickly the levels of BK and other pain mediators can increase again in the TMJ has not yet been studied. To the best of our knowledge, there has been only 1 report investigating how quickly and how much protein was recovered in the synovial fluid of the TMJ.[16] In that report, which was based on only a single case of arthrocentesis, by day 14 the protein levels had returned to 70% of the prearthrocentesis level, due to gradual permeation from plasma and secretion by synovial cells. In the unsuccessful cases

in which the BK concentration is higher, rapid recovery of large amounts of BK may occur due to severe synovial inflammation. Therefore, high levels of BK before arthrocentesis may be a key regulator affecting the success of arthrocentesis of the TMJ. In addition, in such cases, even if a high level of BK in the synovial fluid was significantly eliminated by initial arthrocentesis, subsequent arthrocentesis may be required for successful treatment.

Some of the pain-related chemical mediators in the TMJ are involved in the arachidonic acid cascade. Arachidonic acid, released from a major lipid component of the cell membrane after the activation of phosholipase A2, is converted into leukotrienes by lipooxygenase or converted into prostaglandins by cyclooxygenase. LTB4 is a powerful chemoattractant that activates inflammatory cells and increases vascular permeability.[7,17] PGE2 plays a major role in inflammation, increases vascular permeability, and causes vasodilatation of capillaries.[7-9] Quinn et al[7] reported a strong correlation between LTB4 and PGE2 levels in the synovial fluid of the TMJ and also between their levels and the severity of acute synovitis. Alstergren et al[8] also demonstrated that PGE2 in the synovial fluid of the TMJ is related to TMJ allodynia. On the other hand, Murakami et al[9] reported that the amount of PGE2 in the synovial fluid of the TMJ is not correlated with pain or arthroscopic synovitis. In the present study, the detection rate of LTB4 in synovial fluid was statistically higher in unsuccessful cases of arthrocentesis than in successful cases. In addition, the mean concentrations of LTB4 and PGE2 were higher in the unsuccessful cases than in the successful cases, and there was a statistically positive correlation between them. These findings indicate that LTB4 and PGE2 may aggravate the intra-articular condition of the TMJ and may play a role in the pathology of TMDs. Due to inflammation of the TMJ, phospholipase A2 is secreted into the joint space and, on activation, triggers the arachidonic acid cascade; therefore, LTB4 and PGE2 may be released into the synovial fluid of the TMJ, and there is the possibility of a connection between them. In unsuccessful cases, these reactions may occur more readily or on an increased scale.

SP, which has been found in the synovial fluid of the TMJ, may be a pain mediator and may induce vasodilatation and increase capillary permeability.[10,11] Alstergren et al[10] showed that the SP concentration correlated with the concentration of other neuropeptides in the synovial fluid of the TMJ with various inflammatory diseases. Holmlund et al[11] found SP in the synovial fluid of 16 of 19 TMJs, but its concentration did not correlate with clinical symptoms. In the present study, SP concentration also did not correlate with clinical symptoms, and the detection rate of SP was much lower. However, this discrepancy may be explained by differences in patients, sampling procedures, and assay methods.[10-12] Therefore, whether SP is related to the pathogenesis of TMDs remains unclear; histological studies are needed.

In this study, we did not use asymptomatic healthy volunteers as controls, due to the difficulty in obtaining synovial samples from healthy volunteers. More importantly, we do not believe that such controls would have been useful because our aim was to compare successful and unsuccessful cases of arthrocentesis, and arthrocentesis cannot be expected to be successful in healthy controls. In addition, numerous studies involving identification of inflammation pain mediators in synovial fluid have been carried out without control samples.[7,9-12] On the other hand, it was reported that PGE2 was undetectable in synovial fluid of the TMJ from healthy subjects.[8] In the future, it will be necessary to investigate the pain-related chemical mediators in normal joints to clarify the pathogenesis of the TMDs.

In conclusion, BK and LTB4 levels in synovial fluid of the TMJ were higher in unsuccessful cases of arthrocentesis than in successful cases. In particular, the detection rate of BK was extremely high in unsuccessful cases, and thus this may be a useful prognostic factor of arthrocentesis of the TMJ. Further work is needed to explain the pathophysiologic role and clinical relevance of the pain-related mediators in the TMJ.

References

1. Nitzan DW, Dolwick MF, Martinez GA: Temporomandibular joint arthrocentesis: A simplified treatment for severe, limited mouth opening. J Oral Maxillofac Surg 49:1163, 1991
2. Nitzan DW, Samson B, Better H: Long-term outcome of arthrocentesis for sudden-onset, persistent, severe closed lock of the temporomandibular joint. J Oral Maxillofac Surg 55:151, 1997
3. Nishimura M, Segami N, Kaneyama K, et al: Prognostic factors in arthrocentesis of the temporomandibular joint: Evaluation of 100 patients with internal derangement. J Oral Maxillofac Surg 59:874, 2001
4. Murakami K, Hosaka H, Moriya Y, et al: Short-term treatment outcome study for the management of temporomandibular joint closed lock. A comparison of arthrocentesis to nonsurgical therapy and arthroscopic lysis and lavage. Oral Surg Oral Med Oral Pathol Oral Radiol Endod 80:253, 1995
5. Nishimura M, Segami N, Kaneyama K, et al: Comparison of cytokine level in synovial fluid between successful and unsuccessful cases in arthrocentesis of the temporomandibular joint. J Oral Maxillofac Surg 62:284, 2004
6. Kaneyama K, Segami N, Nishimura M, et al: The ideal lavage volume for removing bradykinin, interleukin-6 and protein from the temporomandibular joint by arthrocentesis. J Oral Maxillofac Surg 62:657, 2004
7. Quinn JH, Bazan NG: Identification of prostaglandin E2 and leukotriene B4 in the synovial fluid of painful, dysfunctional temporomandibular joints. J Oral Maxillofac Surg 48:968, 1990
8. Alstergren P, Kopp S: Prostaglandin E2 in temporomandibular joint synovial fluid and its relation to pain and inflammatory disorders. J Oral Maxillofac Surg 58:180, 2000
9. Murakami K, Shibata T, Kubota E, et al: Intra-articular levels of prostaglandin E2, hyaluronic acid, and chondroitin-4 and −6 sulfates in the temporomandibular joint synovial fluid of pa-

tients with internal derangement. J Oral Maxillofac Surg 56:199, 1998
10. Alstergren P, Appelgren A, Appelgren B, et al: Co-variation of neuropeptide Y, calcitonin gene-related peptide, substance P and neurokinin A in joint fluid from patients with temporomandibular joint arthritis. Arch Oral Biol 40:127, 1995
11. Holmlund A, Ekblom A, Hansson P, et al: Concentrations of neuropeptides, substance P, neurokinin A, calcitonin gene-related peptide, neuropeptide Y and vasoactive intestinal polypeptide in synovial fluid of the human temporomandibular joint. A correlation with symptoms, signs and arthroscopic findings. Int J Oral Maxillofac Surg 20:228, 1991
12. Nishimura M, Segami N, Kaneyama K, et al: Relationships between pain-related mediators and both synovitis and joint pain in patients with internal derangements and osteoarthritis of the temporomandibular joint. Oral Surg Oral Med Oral Pathol Oral Radiol Endod 94:328, 2002
13. Sharma JN, Buchanan WW: Pathogenic responses of bradykinin system in chronic inflammatory rheumatoid disease. Exp Toxicol Pathol 46:421, 1994
14. Bond AP, Lemon M, Dieppe PA, et al: Generation of kinins in synovial fluid from patients with arthropathy. Immunopharmacology 36:209, 1997
15. Rahman MM, Bhoola KD, Elson CJ, et al: Identification and functional importance of plasma kallikrein in the synovial fluid of patients with rheumatoid, psoriatic, and osteoarthritis. Ann Rheum Dis 54:345, 1995
16. Ishimaru JI, Ogi N, Mizui T, et al: Effects of a single arthrocentesis and a COX-2 inhibitor on disorders of temporomandibular joints. A preliminary clinical study. Br J Oral Maxillofac Surg 41:323, 2003
17. Davis P, Bailey PJ, Goldenberg MM, et al: The role of arachidonic acid oxygenation products in pain and inflammation. Annu Rev Immunol 2:335, 1984

平成17年度
奨励研究成果報告書

１．研究課題名：Gene33/mig-6 による心肥大シグナルの制御（研究番号　S2005-1）

２．キーワード：１）細胞内情報伝達（intracellular signal transduction）
２）心筋細胞（cardiac myocytes）
３）早期誘導遺伝子（immediate early gene）
４）酸化ストレス（oxidative stress）

３．研究代表者：竹田　健史・医学部・助手・循環制御学（循環器内科学）

４．研 究 目 的

スーパーオキシドや過酸化水素などの活性酸素(ROS)が、心血管系細胞から直接産生され、動脈硬化、虚血性心疾患、心不全、心肥大、高血圧などさまざまな循環器疾患の病態に関与していることが知られている。したがって、ROS によって特異的に活性化されるレドックス感受性シグナル伝達経路を明らかにすることは、これら心血管病態の解明と新しい治療法の開発に非常に重要であると思われる。

Gene33/mig-6 は、酸化ストレス刺激や様々な増殖因子の刺激で急速に誘導される早期誘導遺伝子の一つとして知られていたが、長い間その機能が不明なままであった。近年、活性化した ErbB family や Grb2、Cdc42 等が、Gene33 と結合することにより負の制御を受けることが報告されている。特に心筋細胞において、ErbB family に属する上皮成長因子受容体（EGFR）は、ROS によっても活性化され（トランスアクチベーション）、下流のレドックス感受性シグナル伝達経路を介して心肥大や心筋細胞障害に重要な役割を果たすことが知られている。

本研究では、ほとんど明らかにされていない心筋細胞における Gene33 の発現調節機構と機能解析、特にレドックス感受性シグナル伝達系への内因性の負の制御因子として機能するのか否かを明らかにすることを目的とする。

５．研 究 計 画

I.　血管壁や心筋ミトコンドリアにおいて産生される活性酸素（スーパーオキシド）は、スーパーオキシドジスムターゼ（SOD）によって安定な過酸化水素にすばやく代謝されることが知られている。したがって、過酸化水素は酸化ストレスシグナルの伝達因子として重要な役割を果たしていると考えられる。そこで、過酸化水素の外的投与により心筋細胞（ラット心臓由来 myoblasts H9c2）に酸化ストレスを与え、心筋における Gene33 の遺伝子発現に関わるシグナル伝達因子を同定する。また、他のレドックス感受性転写因子との遺伝子発現様式の違いを明らかにする。

II.　過酸化水素刺激により活性化されたレドックス感受性シグナル伝達系における、Gene33 の役割を明らかにするために、Gene33 発現ベクターを心筋細胞へ導入し、細胞内シグナル伝達系の変化を解析する。また、Gene33 過剰発現により影響を受ける遺伝子も同定する。

III.　*gene33* 遺伝子の発現調節機構を解明するために、*gene33* 遺伝子の転写開始点より上流約 1200bp の領域をルシフェラーゼベクターへクローニングし、プロモーターアッセイにより、この遺伝子の転写に係わる領域を同定する。

６．研 究 成 果

1) 心筋への酸化ストレス刺激による *gene33* 遺伝子の発現調節

過酸化水素の外的投与により、H9c2 細胞において濃度依存的に *gene33* の遺伝子発現が誘導された。この誘導は、200μM で効果がもっとも強く、投与後約１時間で発現レベルはピークに達した。また、この発現パターンは心肥大のシグナル伝達系において、レドックス感受性転写因子として重要な役割を果たす早期誘導遺伝子である、*early growth response gene-1*（*egr-1*）や *c-fos* 遺伝子の発現と類似していた。次に、これらの発現調節に関わるレドックス感受性シグナル伝達因子を解析するために、MAPK 経路や EGFR の阻害剤の前処理による遺伝子発現パターンの変化を調べた。その結果、*gene33* の発現誘導は MEK-1 阻害剤によりほぼ完全に抑制され、EGFR や ERK1/2、p38、JNK 阻害剤によって部分的に抑制された。一方で、*egr-1* と *c-fos* の遺伝子発現の誘導は、MEK-1 阻害剤で完全に、EGFR 阻害剤で部分的に抑制されたが、JNK や p38 阻害剤ではほとんど効果を示さなかった。またこれら遺伝子レベルで観察された結果は、Western blot 法によるタンパクレベルでの解析においても確認できた。

2) *gene33* 遺伝子導入によるレドックス感受性シグナル伝達系への影響

心筋細胞で発現誘導された Gene33 の機能を解析するために、ラット心筋よりクローニングした全長の *gene33* cDNA を発現ベクターpcDNA3.1 へサブクローニングし、H9c2 細胞へトランスフェクションした。遺伝子導入 48 時間後、顕微鏡下で細胞の状態を観察したところ、empty vector を導入した細胞と比べて、*gene33* 遺伝子発現 vector の導入細胞において明らかに浮遊した死細胞数が多かった。過酸化水素の投与によって活性化されるレドックス感受性シグナル伝達系を解析するために、細胞から抽出した全タンパクを用いた Western Blot 解析を行ったところ、ERK1/2 のリン酸化レベルおよび ERK1/2 の活性が Gene33 の過剰発現により減少していた（図１）。一方で、JNK1/2 や Akt、ERK5 は、過酸化水素刺激により速やかに活性化されたが、*gene33* 遺伝子導入による影響は認められなかった。さらに、Gene33 を過剰発現した H9c2 細胞では、過酸化水素刺激により誘導される Egr-1

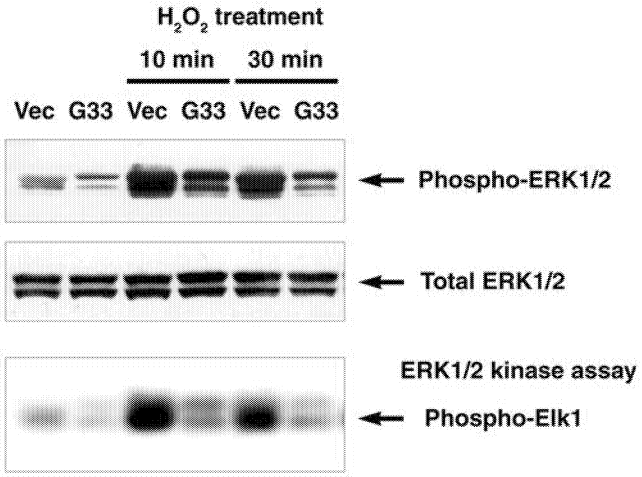

図１　*gene33*遺伝子導入による ERK1/2活性化の抑制効果

過酸化水素で刺激したH9c2細胞におけるERK1/2のリン酸化レベルと、おのおのの細胞からERK1/2を免疫沈降し、Elk1組替え蛋白を基質として用いて、 ERK1/2の活性を調べた。Gene33導入細胞においてERK1/2のリン酸化レベルと活性が抑制されている。

の発現が抑制されていた。これらの結果は、先の RT-PCR 解析の結果において、過酸化水素刺激による Egr-1 の発現誘導が ERK1/2 の上流に位置する MEK1 の阻害剤により、完全に抑制されたことと一致する。以上の結果から、Gene33 は ERK1/2 経路を抑制することによ

り、Egr－1 の発現を妨げることを示唆した。

3) *gene33* 遺伝子の転写調節機構の解析

心筋細胞における *gene33* 遺伝子の転写に関わる調節領域を同定するために、ラットゲノム DNA から *gene33* 遺伝子の上流約 1.2kbp の領域を単離し、レポーターベクターへクローニングした。さらにこのクローンを元にして、いくつかの上流領域を欠損した deletion mutant も作製し、これらを用いてルシフェラーゼアッセイを行った（図２）。

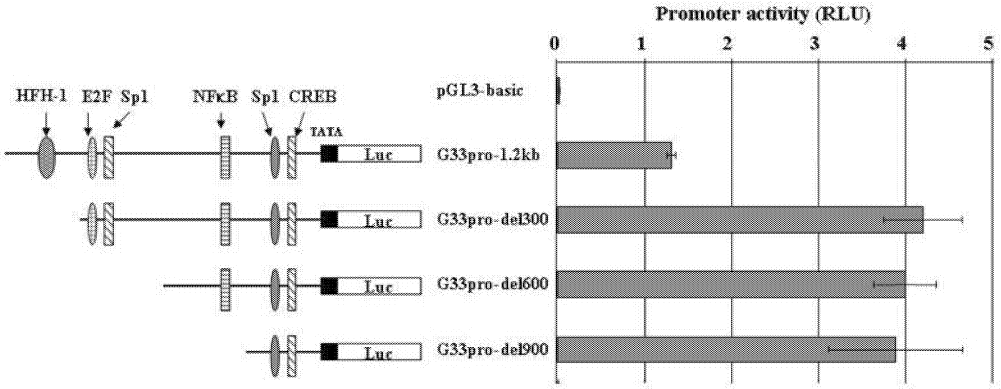

図２　*gene33*遺伝子プロモーターの解析

*gene33*遺伝子の転写開始点から上流約1.2kbpの領域をfirefly luciferase expression vectorへクローニングし、レポーターアッセイを行った。また、上流から約300bpずつ削ったdeletion mutantも作製し同様に解析した。得られた測定値(RLU)は、co-transfectionした*Renilla* luciferase expression vectorの測定値で補正した。

1.2kbp の領域を含んだレポーターベクターは、プロモーターを含まないコントロールベクター（pGL3-basic）と比較して約 65 倍ルシフェラーゼ活性が高かった。さらに、興味深いことに、上流から 300bp を欠損させると、約４倍プロモーター活性が上昇した。このことは、欠損させた領域内に転写を負に制御する領域（サイレンサー）が存在することを示唆した。

７．研究の考察・反省

本研究により、心筋細胞への *gene33* 遺伝子導入によって酸化ストレス刺激による ERK1/2 の活性化を抑制し、下流の早期誘導遺伝子である Egr-1 の発現誘導レベルを減少させることが明らかとなった。Egr-1 は、少なくとも 300 個の遺伝子の発現を制御する master regulator として働き、多くの心血管系疾患（アテローム性動脈硬化症、血管形成術後再狭窄、心肥大、血管新生など）に重要な役割を果たしていることが知られている。特に、病的な心肥大シグナルを負に制御する転写抑制因子として NAB1 が同定されているが、これは Egr-1 と結合し負に制御する調節因子である。Gene33 が Egr-1 との結合能を有しているという報告は無いが、Egr-1 を転写レベルで抑制することで心肥大シグナルを負に制御できる可能性が考えられる

また、今回のレポーターアッセイの解析結果により、*gene33* 遺伝子のプロモーター領域にはこの遺伝子の発現を負に制御する領域が存在することを示唆した。この領域には、転

写因子 HFH-1 の結合コンセンサス配列と 100%相同な領域が存在する。今後はこの領域を含めてさらなる詳細な解析を行い人為的に *gene33* 遺伝子の発現量を制御することで、心血管系疾患の新たな治療法の確立を目指したい。

８．研究発表

Egr-1 発現の抑制機構、*gene33* 遺伝子のプロモーター機構の解析結果を含めて投稿準備中。

１．研究課題名：骨粗鬆症への応用を目的としたコラーゲントリペプチドの生理活性作用の解析（研究番号　S2005-2）

２．キーワード：１）コラーゲントリペプチド（Collagen tripeptide）
２）オステリックス（Osterix）
３）DNAマイクロアレイ（DNA microarray）
４）骨芽細胞　（Osteoblast）

３．研究代表者：鶴岡　直樹・医学部・助手・ゲノム医科学（生化学）

４．研 究 目 的

本研究の目的は、新たな骨粗鬆症治療への応用を目指して、コラーゲンの酵素消化産物であるトリペプチド（コラーゲントリペプチド、Ctp）が骨形成に与える効果とその作用機構を明らかにすることである。

国内における骨粗鬆症患者は予備軍を含めると既に2,000万人に達している推定され、患者のQOLの維持、医療・介護費用の面で深刻な問題となっている。効果的な治療法の確立や対応策が早急に望まれるが、既存の骨粗鬆症治療は主に骨量低下を抑制するものであり、すでに骨量が低下している高齢者においては顕著な回復効果が得られない。

我々はこれまでに、豚皮I型コラーゲンから培養細胞や動物実験に利用可能な非抗原性・低アレルゲン性のコラーゲントリペプチド（Ctp）を高純度で生産する系を確立している。Ctpの骨形成における効果を解析してきた結果、Ctpを経口投与することによりラットの骨折治癒が亢進することが明らかとなった。また、平成16年度学内奨励研究の助成を受けて行った研究では、培養骨芽細胞のI型コラーゲン合成や石灰化をCtpが促進させることを明らかにした。平成17年度は、これらCtpが骨形成にもたらす効果の作用機構を明らかにすることを目的とし、Ctpが培養骨芽細胞の遺伝子発現に与える影響についてDNAマイクロアレイや定量的RT-PCRにより解析した。

５．研 究 計 画

1) DNAマイクロアレイを用いて、Ctpが培養ヒト骨芽細胞（hFOB1.19）の遺伝子発現に与える影響を解析する。
2) 発現量に変化があった遺伝子群から転写因子を抽出し、Ctpのシグナルを受けてI型コラーゲン遺伝子（*Col1a1*）の発現を促進させる因子を推定する。推定された因子については定量的RT-PCRを行ってその発現変化をより詳細に解析する。
3) DNAマイクロアレイの解析結果を用いて、発現量の変動した遺伝子群が多く含まれるシグナル伝達経路を統計的な解析により抽出し、Ctpのシグナル伝達経路を推定する。

６．研 究 成 果

1）DNAマイクロアレイ解析

10 ・g/ml のCtpで24 h処理した培養骨芽細胞（hFOB 1.19）から全RNAを抽出し、ヒト全ゲノム解析用GeneChip® Human Genome U133 Plus 2.0 Array （Affymetrix）によるDNAマイクロアレイ解析に使用した。各遺伝子の発現量をCtp処理群とコントロール群で比較し、発現倍率に基づいて遺伝子群を8つに分類した。Ctpの添加によって2.1倍以上の発現増加を示した遺伝子は169個存在し、同遺伝子群からGeneOntologyのアノテーション情報に従って転写因子を検索したところ19個が抽出された（表1）。最も高い発現増加を示したのは、Sp7 transcripiton factor/Osterix (Osx)で発現量はコントロールの3.9倍となった。

表．Ctp によって発現が増加した転写因子

Gene	Fold Change
Sp7 transcription factor (osterix)	3.92
Far upstream element (FUSE) binding protein 1	3.13
Runt-related transcription factor 1; translocated to, 1 (cyclin D-related)	2.84
Ets variant gene 6	2.69
Calreticulin	2.69
Cullin-associated and neddylation-dissociated 1	2.55
Checkpoint suppressor 1	2.48
Endothelial PAS domain protein 1	2.41
Peroxisome proliferative activated receptor, gamma	2.38
AT rich interactive domain 1B (SWI1-like)	2.32
PRKC, apoptosis, WT1, regulator	2.31
Enhancer of zeste homolog 2 (Drosophila)	2.28
Zinc finger protein 544	2.24
SWI/SNF related, matrix associated, actin dependent regulator of chromatin	2.20
Nuclear antigen Sp100	2.19
Runt-related transcription factor 1	2.18
Signal transducer and activator of transcription 3	2.18
Nuclear receptor subfamily 4, group A, member 2	2.15
Forkhead box P1	2.14

2）Osterixとその関連因子の発現変化

DNAアレイ試験で*Osx*遺伝子の発現増加がみられたことから、Ctp添加後の*Osx*の発現量を定量的RT-PCRによって経時的に解析し、*Col1a1*の発現変化と比較した。その結果、図に示した様にオステリックス遺伝子の発現はCtp添加後12h、24hで優位に増加し、これに追従する形で24h後以降*Col1a1*の発現量が増加した。

Osxを制御する因子として報告されているRunt related transcription factor 2/Cbfa1 (Runx2)や、Runx2の上流または下流の因子であるBMP-2、Dlx5、MSX2についても遺伝子発現の変化を定量的RT-PCRによって解析した。しかしRunx2やその他既知の関連因子についてはCtp処理による発現変化が認められなかった。

3）Ctpによって変動したシグナルの伝達経路の抽出

DNAマイクロアレイによる解析で発現増加を示した因子が、既知の各シグナル伝

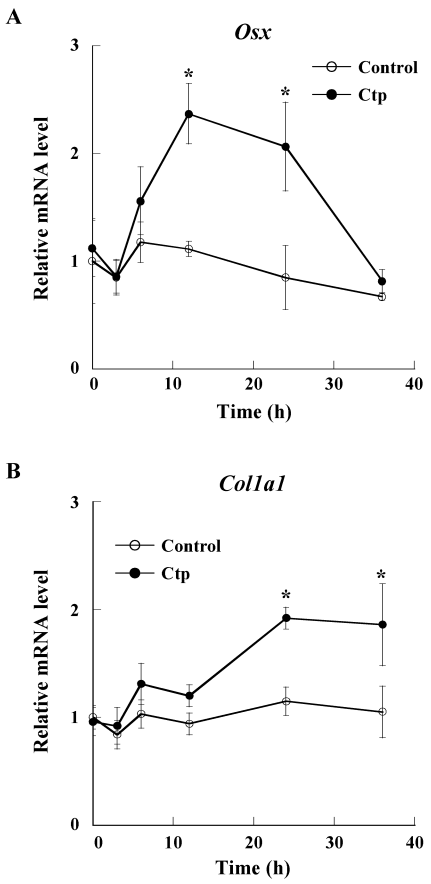

図. Ctp 処理による *Osx* と *Col1a1* の発現変化

達経路に出現する頻度とKEGGに登録された全シグナル伝達経路に出現する頻度を比較し、Fisher’s Exact Testによる統計処理を行って優位に変化した経路を抽出した。これにより、MAPK、接着結合、Chondroitin / Heparan sulfateの各シグナル伝達経路が上位に抽出された（それぞれp = 0.00137、0.00155、0.00157)。

７．研究の考察・反省

培養骨芽細胞、hFOB1.19株の全RNAを用いたDNAマイクロアレイ解析により、Ctp処理によって転写因子Osxの発現が増加することがわかった。Osxは骨芽細胞に特異的に発現する転写因子で，骨形成に必須であることが報告されている（Nakashima K., et al., *Cell*, 108, 17-29, 2002)。そのC末端に内包されたZinc fingerモチーフは*Col1a1*のプロモーター領域を認識し、コラーゲン遺伝子の発現を誘導することもわかっている。Ctpによる刺激でも*Osx*の発現増加が検出され，これに続いて*Col1a1*の増加が認められたことから、CtpはOsxを介して*Col1a1*の発現を促進しているものと推測された。一方、オステリックスを制御すると報告されているRunx2についてはCtpによる有意な発現変化が認められなかった。Runx2は間葉系細胞を骨芽細胞へ分化させるBMP-2シグナルを伝達する因子であり、骨基質の発現を直接、あるいはOsxやDlx5、MSX2などの転写因子を介して制御するとされている。しかし、Ctpは*Runx2*やその他*Osx*以外の関連因子の発現に影響を与えなかったことから、CtpとOsxの間には別の伝達経路が存在すると推測された。

BMP-2に比較すると効果は低いが、IGF-1によっても*Osx*が誘導されることが報告されている(Ayse B. Celil and Phil G. Campbell, *J. Biol. Chem.*, 280, 31353-9, 2005)。IGF-1のシグナルはProtein Kinase C、 Dが仲介し数種のMAPK（p38、 JNK、 ERK1/2）が活性化された後*Osx*の発現量が増加する。 BMP-2による*Osx*の発現増加は約30-100倍、IGF-1による増大は3-5倍程度であることが報告されており、CtpはIGF-1とほぼ同程度のレベルで*Osx*の発現を誘導していることになる。また、DNAマイクロアレイのデータをもとにCtp処理によって変動したシグナル伝達経路を検索した結果、MAPK経路が変動している可能性が高いことがわかった. したがって、CtpはIGF-1と同様にp38、 JNK、 ERK1/2を活性化し、これによって下流の*Osx*の発現が誘導されている可能性がある。今後はこれらMAPKの活性化をリン酸化抗体や阻害剤を用いて同シグナル伝達経路が実際に活性化されているか検証する必要がある。

８．研 究 発 表

Tsuruoka N, Yamato R, Sakai Y, Yoshitake Y, Yonekura H, Promotion B. Collagen tripeptide of type I collagen gene expression in human osteoblastic cells and fracture healing of rat femur. Biosci Biotech Biochem (in press) (MLDB)

Biosci. Biotechnol. Biochem., **71**, 70287-1–8, 2007

Promotion by Collagen Tripeptide of Type I Collagen Gene Expression in Human Osteoblastic Cells and Fracture Healing of Rat Femur

Naoki TSURUOKA,[1,†] Rumiko YAMATO,[2] Yasuo SAKAI,[2]
Yoshino YOSHITAKE,[1] and Hideto YONEKURA[1]

[1]*Department of Biochemistry, Kanazawa Medical University School of Medicine, 1-1 Daigaku, Uchinada, Kahoku-gun, Ishikawa 920-0293, Japan*
[2]*Central Research Institute, Jellice Co., Ltd., 4-1-4 Wakabayashi, Wakabayashi-ku, Sendai, Miyagi 984-0826, Japan*

Received May 11, 2007; Accepted August 2, 2007; Online Publication, November 7, 2007
[doi:10.1271/bbb.70287]

Peptides produced by the enzymatic degradation of collagens are reported to have various activities of biological and medical interest. The mechanisms underlying their actions are, however, poorly understood. We have produced, by collagenase digestion of type I collagen, a highly purified, non-antigenic, and low allergenic tripeptide fraction (collagen tripeptide, Ctp). We report here the effects of Ctp on the *in vivo* bone fracture healing and *in vitro* calcification of osteoblastic cells. An oral administration of Ctp to rats with a femur fracture accelerated the fracture healing. Ctp apparently stimulated the calcification of human osteoblastic cells in culture. This osteotrophic effect was accompanied by a significant increase in type I collagen protein production and its mRNA levels. DNA microarray and quantitative RT-PCR analyses demonstrated that Ctp upregulated the bone-specific transcription factor, Osterix, suggesting that the induction of type I collagen gene expression by Ctp was mediated by upregulation of this factor.

Key words: collagen peptide; Osterix; osteoblast; fracture healing; DNA microarray

Collagen is a major component of the extracellular matrix in almost all tissues of vertebrates and is produced in large quantities as a byproduct of the livestock industry. Collagen molecules form triple helical structures from three α chains which comprise a highly repetitive sequence of Gly-Xaa-Yaa (Xaa and Yaa are arbitrary but are often occupied by proline, hydroxyprolin, and alanine). This unique sequence and structure enables collagen molecules to show resistance to general proteinases. The degradation of collagen and preparation of collagen peptides thus require collagenolytic proteinases, collagenases.

Collagen peptides (the enzymatic degradation products of collagens) have recently been shown to have several biological activities, and have been used as preservatives[1)] and immunotherapeutic agents.[2,3)] Although these applications of collagen peptides have become very popular, the mechanisms underlying their actions are not fully understood.

Using a bacterial collagenase that degrades the peptide bonds of collagen at the amino-terminal end of Gly,[4)] we have prepared from porcine type I collagen a highly purified, non-antigenic, and low-allergenic tripeptide fraction (collagen tripeptide, Ctp) containing Gly-Xaa-Yaa sequences.[5)] We recently found that rats that were orally administered with Ctp showed accelerated recovery of fractured bones.[6)]

We show in this paper the osteotrophic effects of Ctp on bone fracture healing in a rat model, and examine the effects of Ctp on type I collagen synthesis and on overall gene expression in human osteoblastic cells in culture.

Materials and Methods

Materials. Ctp was prepared as previously described.[4)] The purity of Ctp is expressed as the content of tripeptides in the fractions, this being estimated from the peak integral of the absorbance at 215 nm by HPLC with a Superdex Peptide gel filtration column (Pharmacia Biotech, Sweden). Briefly, collagen peptide was prepared from porcine skin collagen by collagenase digestion. The digest was deionized with an ion exchanger (DAION type SK, Mitsubishi Chemical, Tokyo, Japan) and then passed through a 0.2-μm filter, the

† To whom correspondence should be addressed. Fax: +81-76-218-8111; E-mail: tsuruoka@kanazawa-med.ac.jp

Abbreviations: Ctp, collagen tripeptide; *Col1a1*, type I collagen α-chain gene; Osx, Sp7 transcription factor/Osterix; Runx2/Cbfa1, runt-related transcription factor 2; Msx2, Msh homeobox 2; Dlx5, distal-less homeobox 5; BMP2, bone morphogenetic protein 2; Pept1, peptide transporter 1; TOR, target of rapamycin

resulting fraction (20% purity) being used for *in vivo* experiments. Further purification was performed for *in vitro* experiments by eliminating the endotoxins, using an ACP-0013 module (Asahi Chemical, Tokyo, Japan) and fractionation of the tripeptide fraction by reverse-phase HPLC. The tripeptide content was more than 90% after this purification. A D-MEM/F-12 medium (1:1) was purchased from Sigma (St. Louis, MO, USA), and HEPES, G418 and L-ascorbic acid were from Nacalai Tesque (Kyoto, Japan). CELLYARD Beads™ comprising high-purity hydroxyapatite were from Pentax (Tokyo, Japan), rat normal feed, CRF-1, was from Oriental Yeast (Tokyo, Japan), and oligonucleotides were produced by Texas Genomics Japan (Tokyo, Japan).

Oral administration of Ctp to the fracture-model rats. The procedures for the animal experiments were approved by the institutional animal care and use committee guidelines of the Central Research Institute of Jellice Co., Ltd. We used 7-week-old IGS male rats as the bone-fracture model. The middle of the left femur of each rat was cut in an operation, and the fractured bone was fixed with wires. These rats were divided into three groups (N = 10 in each group). From day 1 after the operation, the rats of each group received 0, 80, or 500 mg/kg/day of Ctp (20% purity) for 12 weeks (84 days). The left (fractured) and right (control) femurs were then extirpated, and the progression of fracture healing was observed by soft X-ray exposure. The bone strength (stiffness and breaking load) was measured by the three-point bending test[7] with MZ-500D apparatus (Maruto, Tokyo, Japan). An isolated bone was horizontally fixed at both ends in the machine, and a probe was moved down (20 mm/min) at the mid-point of the bone. The stiffness and breaking load parameters were recorded when the bone was broken according to the manufacturer's instructions.

Cell culture. Human osteoblastic hFOB1.19 cells were purchased from American Tissue Culture Collection (Manassas, VA, USA). The hFOB1.19 cells were immortalized by transfection with the temperature-sensitive SV40 large T antigen gene.[8] Cell proliferation is permitted at 34 °C and restricted at 39 °C. At the restrictive temperature, the cells show osteoblastic phenotypes including the expression of osteoblast-specific genes and increased collagen production. The cells were maintained at 34 °C in a D-MEM/F-12 medium containing 10% (v/v) FBS, 15 mM HEPES, and 0.3 mg/ml of G418 (growth medium). For the mineralization assay, the cells were seeded at 50,000 cells/cm^2 in 6-well plates and were cultured at 34 °C in the growth medium. When the cells became confluent, the culture medium was replaced with a D-MEM/F-12 medium containing 1% (v/v) FBS, 15 mM HEPES, 0.3 mg/ml of G418, and 50 μg/ml of L-ascorbic acid (assay medium), and the cells were incubated with Ctp (highly purified, >90%) at 10 μg/ml at 37 °C for 7 days. The culture medium was replaced with a fresh assay medium containing 10 μg/ml of Ctp every 2 days. After 7 days of culture, the cells were fixed with ice-cold 70% (v/v) ethanol and stained for calcium deposition by the Alizarin Red S method as described previously.[9] For the collagen production, cells were seeded at 50,000 cells/cm^2 in 6-well plates and were cultured at 34 °C in the growth medium. When cells became confluent, the culture medium was replaced with the assay medium, and the cells were incubated at 39 °C for 24 h. Ctp was then added to the culture medium at 10 μg/ml, and the cells were further incubated for 48 h at 39 °C.

Production of type I collagen. To quantify collagen production by the hFOB1.19 cells, we detected the c-terminal extension peptides (CICP) released into the culture medium. Collagen is synthesized as procollagen containing extension peptides at the N- and C-termini. After the procollagen molecule is secreted from cells, these extension peptides are cleaved and released as soluble peptides. Thus, these peptides provide a stoichiometric representation of collagen synthesis.[10] The culture medium of the hFOB1.19 cells was centrifuged at 16,000 × *g* and assayed with a Metra™ CICP EIA kit (Quidel, San Diego, CA, USA). Total protein concentration was determined by the Bradford method[11] with bovine serum albumin as a standard.

Quantitative real-time RT-PCR analysis. Cells for the gene expression assay were seeded at 50,000 cells/cm^2 in 6-well plates and were cultured at 34 °C in the growth medium. When the cells became confluent, the culture medium was replaced with the assay medium and the cells were incubated at 39 °C for 24 h. The cells were then incubated with Ctp (highly purified, >90%) at the indicated concentrations for the indicated periods at 39 °C. Total RNA was isolated from the treated and untreated hFOB1.19 cells with an RNeasy mini-kit (Qiagen, Chatsworth, CA, USA). For the type I collagen expression in the presence of hydroxyapatite, the cells were incubated with hydroxyapatite beads (1 mg/ml) at 39 °C for 24 h, and then Ctp was added to the culture medium at various concentrations, before the cells were further incubated at 39 °C for 24 h. The gene expression of type I collagen and other genes was analyzed by quantitative real-time PCR, using an ABI Prism 7700 sequence detector (Applied Biosystems, Foster City, CA, USA). Primers were designed by Primer Express software (Applied Biosystems) as shown in Table 1. Total RNA of 10–100 ng and 0.1–1.0 μM sequence-specific primers were used for the reaction in 20 μl with a one-step SYBR® RT-PCR kit (Takara, Kyoto, Japan). The reaction mixtures were incubated at 42 °C for 15 min for reverse transcription and then at 95 °C for 2 min for denaturation; the thermal cycling parameters were 95 °C/5 s for denaturation, and 60 °C/30 s for annealing and elongation (40 cycles). After detection by an ABI

Table 1. Primer Sequences for Quantitative Real-Time RT-PCR

Gene	Sense primer	Antisense primer
Col1a1	AGGGCCAAGACGAAGACATCCC	TGTCGCAGACGCAGATCCG
Osx	GCAAGAGGTTCACTCGTTCGGATG	TGTTTGCTCAGGTGGTCGCTTC
Runx2/Cbfa1	TGGACGAGGCAAGAGTTTCACC	CTTCTGTCTGTGCCTTCTGGGTTC
Msx2	CCGCCTCGGTCAAGTCGGAAA	AGGGCTCATATGTCTTGGCGG
Dlx5	TGCCGACTATAGCTACGCTAGCTCC	CACTTCTTTCTCTGGCTGGTTGGTG
Bmp2	AACACTGTGCGCAGCTTCC	CCTAAAGCTTGCATCTGTTCTC
Gapdh	ATCACCATCTTCCAGGAGCGAGA	TGGTGAAGACGCCAGTGGACTC

Prism 7700 sequence detector, the data were analyzed by SDS 2.1 software (Applied Biosystems), and the average Ct value was calculated from triplicate reactions. The average Ct value was normalized by that of the internal standard gene, GAPDH, and the relative mRNA expression levels of samples with added Ctp and the control were calculated.

DNA microarray analysis. A DNA microarray analysis was performed by using GeneChip® Human Genome U133 Plus 2.0 and the analysis system (Affymetrix, Santa Clara, CA, USA). Total RNA was extracted from Ctp-treated or untreated (10 μg/ml, 24 h) hFOB1.19 cells with an RNeasy mini-kit, and the concentration and purity were checked by a UV spectrophotometric analysis. Using a One-cycle Target Labeling kit (Affymetrix), total RNA was reverse-transcribed with a T7-Oligo (dT) primer and SuperScript II reverse transcriptase, this being followed by second-strand cDNA synthesis with DNA polymerase, and the cDNAs were used for *in vitro* transcription with T7 RNA polymerase. The resulting complimentary RNAs were biotinylated, fragmented, and hybridized to GeneChip® arrays according to the manufacturer's instructions. After washing and staining the probe arrays with a Fluidics station 450 (Affymetrix), they were scanned by a GeneChip® 3000 scanner (Affymetrix). Gene expression data were normalized to a target intensity of 500, and were then used for a comparative analysis between the control and Ctp-treated samples.

Results and Discussion

Effects of Ctp on rat bone fracture healing

To assess the effects of Ctp on bone formation *in vivo*, we used an artificial rat bone fracture model.[7] During fracture healing, the broken areas generally are initially filled with calluses, this being followed by mineralization from the periosteum, reduction, and finally, disappearance of the calluses.[7,12]

The rats with a fracture of the left femur were divided into three groups of 10 each that respectively received a daily oral administration of 0, 80, or 500 mg/kg/day of Ctp for 12 weeks (84 days). Each femur was then extirpated and exposed to soft X-rays. Figure 1A presents typical pictures of the femurs showing no conjugation or a clear fracture line and large callus (a)

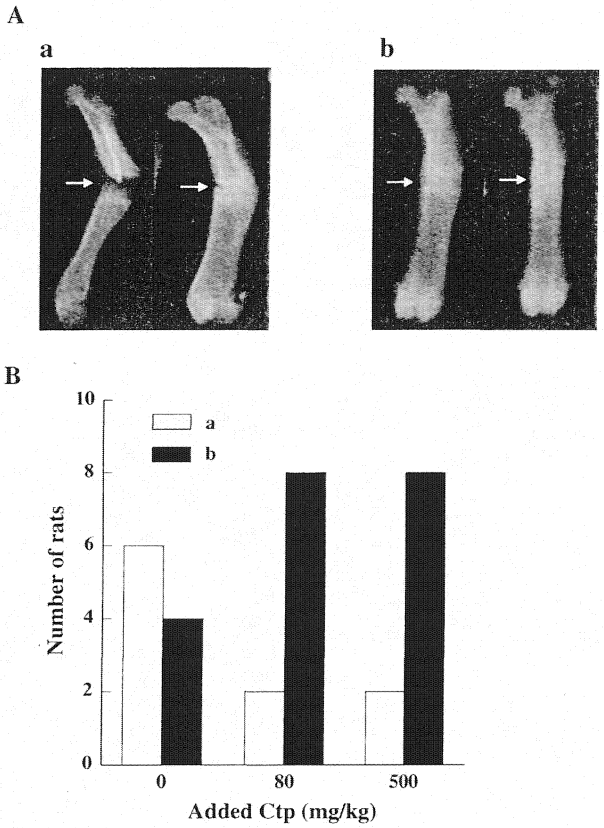

Fig. 1. Effects of Ctp on Fracture Healing of the Rat Femur.

Rats whose left femur had been cut in an operation received daily oral Ctp in the indicated amounts for 12 weeks (84 days) and the femurs were then extirpated and observed by soft X-rays.[6] A, (a), typical pictures of femurs showing no conjugation or a clear fracture line and a large callus; (b), typical pictures of femurs with an obscure or undetectable fracture line and cortex continuity. Arrows indicate the fracture position. B, Fracture healing of rats with and without Ctp. Open and closed bars indicate the numbers of rats with an unhealed femur (a) and those with a healed femur (b), respectively.

and of the femurs with an obscure or undetectable fracture line and cortex continuity (b). As shown in Fig. 1B, six of the ten rats that received no Ctp showed incomplete fracture healing; two of these showed no conjugation of the fractured bone and large calluses on both sides (Fig. 1Aa, left) and four showed conjugated bone but still with large calluses and clear fracture lines (Fig. 1Aa, right), indicating that they were still at an early stage of fracture healing. In contrast, the rats that

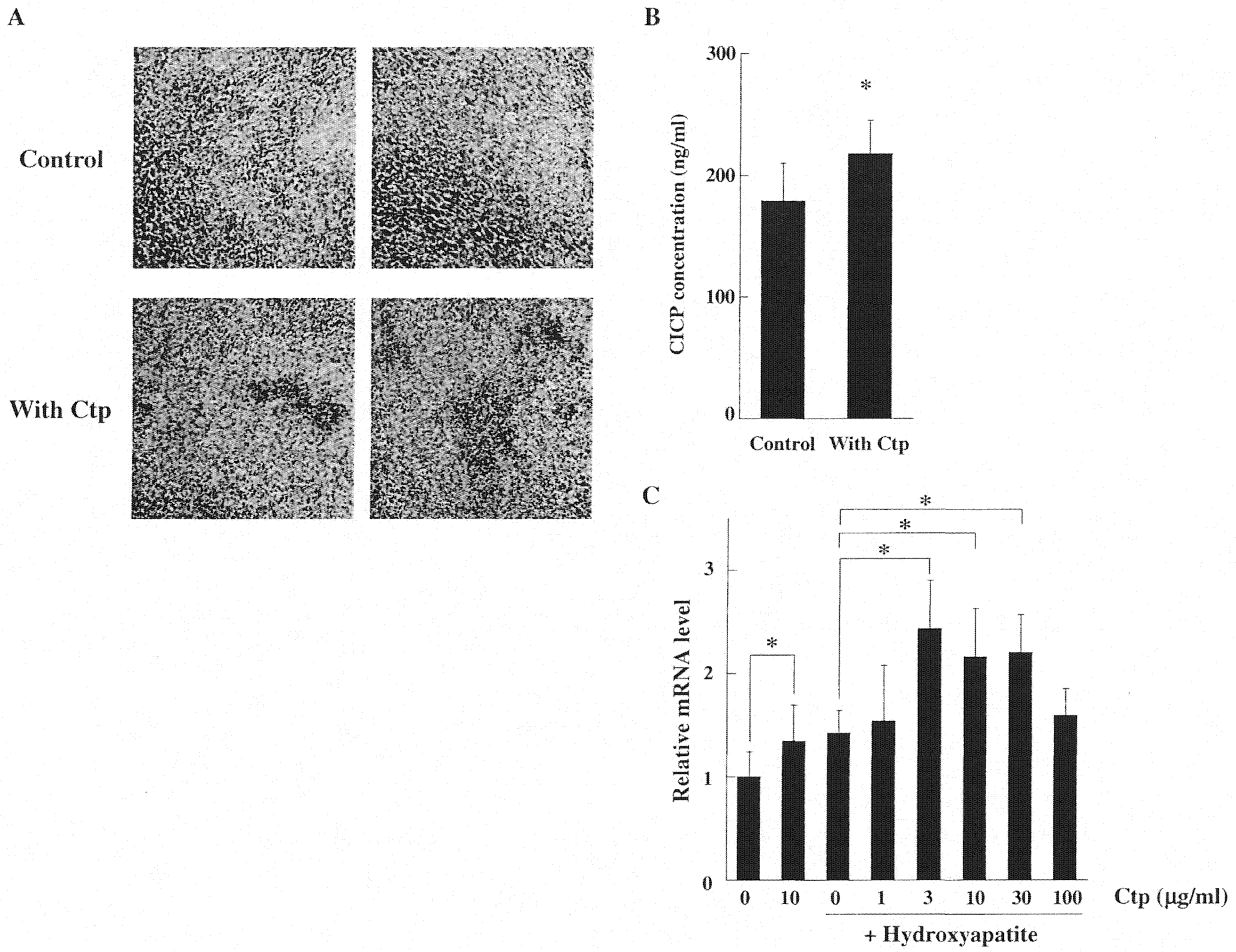

Fig. 2. Effects of Ctp on Human Osteoblastic Cells.

A, Mineralization of hFOB 1.19 cells. Cells were cultured at 37 °C for 7 days with and without 10 μg/ml of Ctp. Mineralization was analyzed by staining with Alizarin Red S. Typical pictures are shown; the red-stained areas correspond to the mineralized matrix. B, Type I collagen protein production. hFOB1.19 cells were cultured under a restrictive condition for 48 h with and without 10 μg/ml of Ctp. The C-terminal extension peptide (CICP) concentration in each culture supernatant was analyzed by ELISA. Columns and bars indicate the mean (N = 3) and standard deviation, respectively, $^*p < 0.05$. C, Type I collagen mRNA level. hFOB1.19 cells were treated with the indicated concentrations of Ctp under restrictive conditions for 24 h in the presence or absence of 1 mg/ml of hydroxyapatite beads. *Col1a1* mRNA expression was analyzed by quantitative real-time RT-PCR. The intensity of each *Col1a1* mRNA signal was normalized with that of GAPDH and related to that of the control. Columns and bars indicate the mean (N = 3) and standard deviation, respectively, $^*p < 0.05$.

received 80 or 500 mg/kg/day of Ctp showed significantly accelerated fracture healing (Fig. 1B). Only two of the ten rats showed large calluses and clear fracture lines; the others had an obscure or undetectable fracture line (Fig. 1Ab). Compared with the control, the healed bone of the Ctp-treated rats showed a significant improvement in stiffness (0.86 ± 0.07 [500 mg/kg/day of Ctp] *vs.* 0.47 ± 0.10 [untreated]) and a breaking load (0.86 ± 0.11 [500 mg/kg/day of Ctp] *vs.* 0.62 ± 0.11 [untreated]). Each value is expressed as the ratio of the left femur (fractured and healed) to the right femur (control), and the normal value is 1.0.[6]

Effects of Ctp on the mineralization of a human osteoblastic cell culture

To examine the effects of Ctp on osteoblastic cells, we first looked at the mineralization of hFOB cells in the presence of Ctp. After 7 days of culture, we detected an apparent increase of mineralized nodules in the cultures treated with 10 μg/ml of Ctp (Fig. 2A). The results suggest that Ctp accelerated bone fracture healing though the stimulation of osteoblast calcification. We looked at the proliferation and alkaline phosphatase activity of the Ctp-treated cells, but they were essentially unchanged when compared with the untreated cells (data not shown). These results indicate that Ctp affected factors other than these in the stimulation of mineralization.

Type I collagen expression in the Ctp-treated human osteoblastic cells

We next examined collagen production in the Ctp-treated hFOB1.19 cells. Type I collagen is a major component of osteoblastic cells and is involved in the

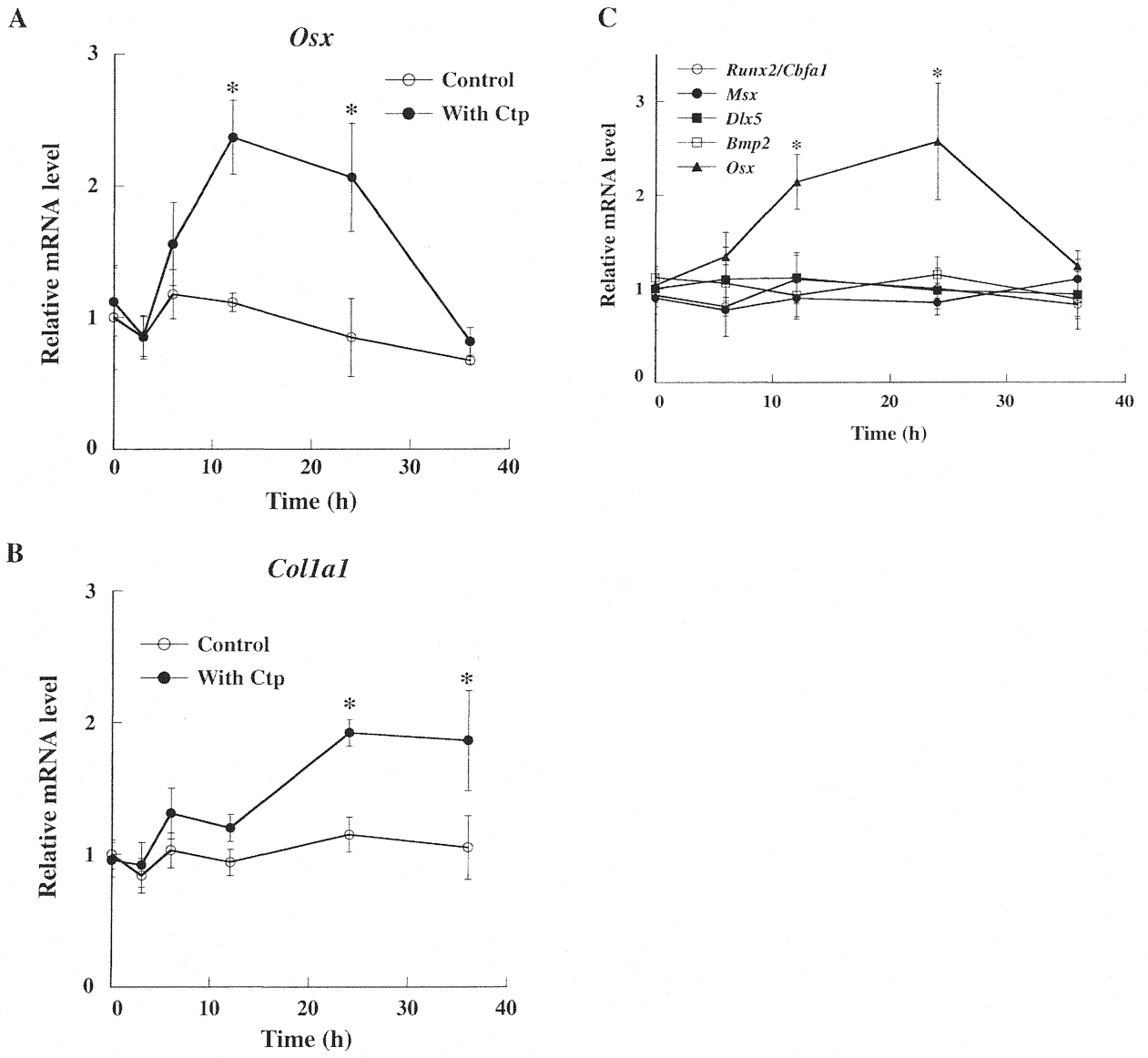

Fig. 3. Time-Course Characteristics of the mRNA Levels of *Osx* (A), *Col1a1* (B) and *Osx*-Related Genes (C).

A and B, hFOB1.19 cells were treated with (filled circles) and without (unfilled circles) 10 μg/ml of Ctp for the indicated periods, and total RNA was isolated and analyzed by quantitative real-time RT-PCR. Each value is the mean (N = 3) and bars indicate the standard deviation, $^*p < 0.05$ (*vs.* the value without Ctp). C, mRNA expression analysis of *Osx*-related genes. hFOB1.19 cells were treated with 10 μg/ml of Ctp for the indicated periods, and total RNA was isolated and analyzed by quantitative real-time RT-PCR. Runx2/Cbfa1, runt-related transcription factor 2; Msx2, Msh homeobox 2; Dlx5, distal-less homeobox 5: Bmp2, bone morphogenetic protein 2; Osx, Sp7 transcription factor/Osterix. Each value is the mean (N = 3) and bars indicate the standard deviation, $^*p < 0.05$ (*vs.* the value at 0 h).

mineralization process.[13] hFOB1.19 cells were cultured in the presence or absence of 10 μg/ml of Ctp for 2 days, and type I collagen production was analyzed by measuring CICP in the culture medium. As shown in Fig. 2B, Ctp significantly increased the release of CICP (1.3-fold), indicating that Ctp induced a 1.3-fold increase of type I collagen protein production. We then examined the type I collagen mRNA levels in Ctp-treated cells by quantitative real-time RT-PCR. The levels of mRNA for the α-chain of type I collagen were significantly higher (1.3–1.7-fold) in the presence of 10 μg/ml of Ctp (Figs. 2C and 3B), suggesting that Ctp stimulated type I collagen protein production through the upregulation of type I collagen α-chain gene (*Col1a1*) expression.

We further examined the effects of Ctp on *Col1a1* expression in the presence of high-purity hydroxyapatite beads in hFOB1.19. Hydroxyapatite [$Ca_{10}(PO_4)_6OH_2$] has been reported to increase *Col1a1* expression in mouse osteoblastic cells.[14] It is thought that the attachment of osteoblasts to hydroxyapatite may induce osteoblastic cell differentiation at an early stage and stimulate the synthesis of extracellular matrix proteins, including type I collagen.[14,15] As expected, Ctp gave 1.7-fold higher *Col1a1* mRNA levels at 3 μg/ml (1.7-

Table 2. Affymetrix Analysis of Genes Upregulated by Ctp in hFOB1.19 Cells

Gene name	Gene bank	No.-fold change
Sp7 transcription factor/Osterix	NM_152860	3.92
Far upstream element (FUSE) binding protein 1	NM_003902	3.13
Runt-related transcription factor 1, translocated to 1	NM_004349	2.84
Ets variant gene 6	NM_001987	2.69
Calreticulin	NM_004343	2.69
Cullin-associated and neddylation-dissociated 1	NM_018448	2.55
Checkpoint suppressor 1	NM_005197	2.48
Endothelial PAS domain protein 1	NM_001430	2.41
Peroxisome proliferative activated receptor γ	NM_005037	2.38
AT rich interactive domain 1B (SWI1-like)	NM_017519	2.32
PRKC, apoptosis, WT1, regulator	NM_002583	2.31
Enhancer of zeste homolog 2	NM_004456	2.28
Zinc finger protein 544	NM_014480	2.24
SWI/SNF related, matrix associated, actin dependent regulator of chromatin	NM_003070	2.20
Nuclear antigen Sp100	NM_003113	2.19
Runt-related transcription factor 1	NM_001754	2.18
Signal transducer and activator of transcription 3	NM_003150	2.18
Nuclear receptor subfamily 4, group A, member 2	NM_006186	2.15
Forkhead box P1	NM_032682	2.14

Each value is the mean of three independent experiments.

fold) in the presence of hydroxyapatite when compared with the control (Fig. 2C).

These results suggest that the stimulation of osteoblast mineralization by Ctp can be accounted for by the induction of type I collagen production by Ctp.

Affymetrix microarray analysis for the genes upregulated by Ctp

To examine the effects of Ctp on overall gene expression, we performed a DNA microarray analysis of the gene expression in Ctp-treated hFOB1.19 cells by using an Affymetrix GeneChip® array and detected 169 probe sets that were upregulated more than 2.12-fold. Among them, Gene Ontology annotations identified 19 genes that are thought to be involved in transcriptional regulation. These genes were reproducibly upregulated by the Ctp treatment in three independent experiments, with Sp7 transcription factor/Osterix (Osx) showing the greatest change in expression (3.92-fold on average) (Table 2).

Osx has been reported to be an essential factor for osteoblast differentiation.[16] It contains a C_2H_2-zinc finger motif, binds to the *Col1a1* promoter and regulates the expression of major bone matrix protein genes, including *Col1a1*, bone sialoprotein, and osteocalcin.[16] Osx knockout mice die soon after birth and show impaired bone formation and reduced expression of *Col1a1*.[16] Along with these findings, our microarray results suggest that Osx is involved in the Ctp upregulation of *Col1a1* gene expression. A quantitative real-time RT-PCR analysis clearly demonstrated that the induction of *Col1a* gene expression by Ctp was preceded by the upregulation of Osx expression (Fig. 3A and B).

Expression of Osx-related genes

Osx null mice show a phenotype similar to that of runt-related transcription factor 2 (Runx2/Cbfa1) knockout mice.[17] In Runx2/cbfa1 null embryos, Osx is not expressed, and osteoblast differentiation is arrested, whereas Runx2/Cbfa1 is expressed in Osx null cells. These observations suggest that Osx acts downstream of Runx2/Cbfa1.[16] To examine whether the Runx2/Cbfa1 signaling pathway would be affected by Ctp, we analyzed the mRNA levels of Runx2/Cbfa1, Msh homeobox 2 (Msx2), distal-less homeobox 5 (Dlx5),[18] and bone morphogenetic protein 2 (BMP2).[19] BMP2 initiates osteoblastic cell differentiation and acts upstream of Runx2/Cbfa1, while Msx2 and Dlx5 are known to act downstream of Runx2/Cbfa1.[16,19–21] As shown in Fig. 3C, the mRNA levels of these genes remained unchanged, and only Osx was upregulated in the Ctp-treated hFOB1.19 cells. These results suggest that Ctp did not directly affect the expression of the Runx2/Cbfa1 or BMP2-induced signaling pathways.

The mechanisms underlying the osteotrophic effects of Ctp are currently unknown. How Ctp activates *Osx* gene expression is the most important issue to be clarified. Two possible mechanisms can be considered. First, Ctp stimulates *Osx* gene expression through a peptide hormone-like mechanism, *i.e.*, through binding to a cell surface receptor. Second, Ctp enters the osteoblast cells and directly or indirectly activates *Osx* gene expression through intracellular peptide sensor proteins similar to the target of rapamycin (TOR). TOR has been reported to sense amino acids and short peptides, and to stimulate the transcription, translation, and degradation of the proteins involved in protein synthesis.[22] We do not have any data suggesting which possibility is more likely, but it should be noted here that we detected the expression of mRNA for peptide transporter 1 (Pept1) in hFOB1.19 cells with the DNA

microarray analysis of this study (data not shown). Pept1 has been reported to be specifically expressed in intestinal epithelial cells and to mediate the uptake of short peptides such as di- and tripeptides.[23] We have previously prepared ^{3}H-labeled Gly-Pro-Hyp (Gly-Pro-Hyp is a representative tripeptide in Ctp and Pro was labeled with ^{3}H), and observed that when rats orally received this radiolabeled tripeptide, radioactivity could be detected in the blood and in those tissues that actively produce collagens, such as bone, skin, tendon, and kidney, more rapidly than the rats which received [^{3}H]Pro.[6] We, however, have not yet confirmed whether the radiolabeled tripeptide remained intact in the blood and tissues, this being an urgent issue to be examined for understanding the *in vivo* effect of Ctp. Collagen-derived di- and tripeptides have recently been identified in the blood of human volunteers who had orally received a gelatin hydrolysate (average molecular weight of 5,000 to 14,500) and the tripeptides had Gly at their carboxyl termini (Xaa-Hyp-Gly).[24,25] Their sequences were distinct from those of our Ctp (Gly-Xaa-Yaa) and it is unclear whether the Xaa-Hyp-Gly tripeptides had osteotrophic effects or other biological activities.

In conclusion, this study has revealed the osteotrophic effects of Ctp. Ctp can accelerate bone fracture healing in a rat model and stimulate type I collagen production by osteoblastic cells in culture through upregulation of the transcription factor, Osx. Although more studies are needed to clarify the mechanisms of Ctp action, the present findings show new regulatory features in osteoblast differentiation and bone formation that may assist in developing preventive measures against bone loss and treatments for bone fractures.

Acknowledgment

We thank Dr. Yasuhito Ishigaki for his kind guidance with the Affymetrix microarray analysis. We also thank Kazumi Tanaka for her assistance. This work was supported by grants for promoted research from Kanazawa Medical University (nos. S2004-15 and S2005-2) and by from the Ministry of Education, Culture, Sports, Science and Technology of Japan grant-aid for young scientists (B) (no. 16790858).

References

1) Gaffney, P. J., Edgell, T. A., Dawson, P. A., Ford, A. W., and Stocker, E., A pig collagen peptide fraction. A unique material for maintaining biological activity during lyophilization and during storage in the liquid state. *J. Pharm. Pharmacol.*, **48**, 896–898 (1996).
2) Khare, S. D., Krco, C. J., Griffiths, M. M., Luthra, H. S., and David, C. S., Oral administration of an immunodominant human collagen peptide modulates collagen-induced arthritis. *J. Immunol.*, **155**, 3653–3659 (1995).
3) Ku, G., Kronenberg, M., Peacock, D. J., Tempst, P., Banquerigo, M. L., Braun, B. S., Reeve Jr., J. R., and Brahn, E., Prevention of experimental autoimmune arthritis with a peptide fragment of type II collagen. *Eur. J. Immunol.*, **23**, 591–599 (1993).
4) Sakai, Y., Yamato, R., Onuma, M., Kikuta, T., Watanabe, M., and Nakayama, T., Non-antigenic and low allergic gelatin produced by specific digestion with an enzyme-coupled matrix. *Biol. Pharm. Bull.*, **21**, 330–334 (1998).
5) Tsuruoka, N., Nakayama, T., Ashida, M., Hemmi, H., Nakao, M., Minakata, H., Oyama, H., Oda, K., and Nishino, T., Collagenolytic serine-carboxyl proteinase from *Alicyclobacillus sendaiensis* strain NTAP-1: purification, characterization, gene cloning, and heterologous expression. *Appl. Environ. Microbiol.*, **69**, 162–169 (2003).
6) Yamato, R., Effect of HACP on the process of fracture healing in rat. *Food Processing* (in Japanese, anecdotal report), **39**, 54–55 (2001).
7) Li, C., Mori, S., Li, J., Kaji, Y., Akiyama, T., Kawanishi, J., and Norimatsu, H., Long-term effect of incadronate disodium (YM-175) on fracture healing of femoral shaft in growing rats. *J. Bone Miner. Res.*, **16**, 429–436 (2001).
8) Harris, S. A., Enger, R. J., Riggs, B. L., and Spelsberg, T. C., Development and characterization of a conditionally immortalized human fetal osteoblastic cell line. *J. Bone Miner. Res.*, **10**, 178–186 (1995).
9) Reinholz, G. G., Getz, B., Pederson, L., Sanders, E. S., Subramaniam, M., Ingle, J. N., and Spelsberg, T. C., Bisphosphonates directly regulate cell proliferation, differentiation, and gene expression in human osteoblasts. *Cancer Res.*, **60**, 6001–6007 (2000).
10) Melkko, J., Niemi, S., Risteli, L., and Risteli, J., Radioimmunoassay of the carboxyterminal propeptide of human type I procollagen. *Clin. Chem.*, **36**, 1328–1332 (1990).
11) Bradford, M. M., A rapid and sensitive method for the quantitation of microgram quantities of protein utilizing the principle of protein-dye binding. *Anal. Biochem.*, **72**, 248–254 (1976).
12) Li, J., Mori, S., Kaji, Y., Mashiba, T., Kawanishi, J., and Norimatsu, H., Effect of bisphosphonate (incadronate) on fracture healing of long bones in rats. *J. Bone Miner. Res.*, **14**, 969–979 (1999).
13) Stein, G. S., and Lian, J. B., Molecular mechanisms mediating proliferation/differentiation interrelationships during progressive development of the osteoblast phenotype. *Endocr. Rev.*, **14**, 424–442 (1993).
14) Ogata, K., Imazato, S., Ehara, A., Ebisu, S., Kinomoto, Y., Nakano, T., and Umakoshi, Y., Comparison of osteoblast responses to hydroxyapatite and hydroxyapatite/soluble calcium phosphate composites. *J. Biomed. Mater. Res. A*, **72**, 127–135 (2005).
15) Kim, H. W., Kim, H. E., and Salih, V., Stimulation of osteoblast responses to biomimetic nanocomposites of gelatin-hydroxyapatite for tissue engineering scaffolds. *Biomaterials*, **26**, 5221–5230 (2005).
16) Nakashima, K., Zhou, X., Kunkel, G., Zhang, Z., Deng, J. M., Behringer, R. R., and de Crombrugghe, B., The novel zinc finger-containing transcription factor osterix is required for osteoblast differentiation and bone formation. *Cell*, **108**, 17–29 (2002).
17) Komori, T., Yagi, H., Nomura, S., Yamaguchi, A.,

Sasaki, K., Deguchi, K., Shimizu, Y., Bronson, R. T., Gao, Y. H., Inada, M., Sato, M., Okamoto, R., Kitamura, Y., Yoshiki, S., and Kishimoto, T., Targeted disruption of Cbfa1 results in a complete lack of bone formation owing to maturational arrest of osteoblasts. *Cell*, **89**, 755–764 (1997).

18) Takahashi, T., Kato, S., Suzuki, N., Kawabata, N., and Takagi, M., Autoregulatory mechanism of Runx2 through the expression of transcription factors and bone matrix proteins in multipotential mesenchymal cell line, ROB-C26. *J. Oral Sci.*, **47**, 199–207 (2005).

19) Lee, K. S., Kim, H. J., Li, Q. L., Chi, X. Z., Ueta, C., Komori, T., Wozney, J. M., Kim, E. G., Choi, J. Y., Ryoo, H. M., and Bae, S. C., Runx2 is a common target of transforming growth factor beta1 and bone morphogenetic protein 2, and cooperation between Runx2 and Smad5 induces osteoblast-specific gene expression in the pluripotent mesenchymal precursor cell line C2C12. *Mol. Cell. Biol.*, **20**, 8783–8792 (2000).

20) Phimphilai, M., Zhao, Z., Boules, H., Roca, H., and Franceschi, R. T., BMP signaling is required for RUNX2-dependent induction of the osteoblast phenotype. *J. Bone Miner. Res.*, **21**, 637–646 (2006).

21) Yagi, K., Tsuji, K., Nifuji, A., Shinomiya, K., Nakashima, K., DeCrombrugghe, B., and Noda, M., Bone morphogenetic protein-2 enhances osterix gene expression in chondrocytes. *J. Cell. Biochem.*, **88**, 1077–1083 (2003).

22) Chou, M. M., and Blenis, J., The 70 kDa S6 kinase: regulation of a kinase with multiple roles in mitogenic signalling. *Curr. Opin. Cell Biol.*, **7**, 806–814 (1995).

23) Adibi, S. A., Regulation of expression of the intestinal oligopeptide transporter (Pept-1) in health and disease. *Am. J. Physiol. Gastrointest. Liver Physiol.*, **285**, G779–788 (2003).

24) Iwai, K., Hasegawa, T., Taguchi, Y., Morimatsu, F., Sato, K., Nakamura, Y., Higashi, A., Kido, Y., Nakabo, Y., and Ohtsuki, K., Identification of food-derived collagen peptides in human blood after oral ingestion of gelatin hydrolysates. *J. Agric. Food Chem.*, **53**, 6531–6536 (2005).

25) Ohara, H., Matsumoto, H., Ito, K., Iwai, K., and Sato, K., Comparison of quantity and structures of hydroxyproline-containing peptides in human blood after oral ingestion of gelatin hydrolysates from different sources. *J. Agric. Food Chem.*, **55**, 1532–1535 (2007).

１．研究課題名：ヒト型モノクローナル抗体によるEBウイルス関連蛋白を標的とした特異的治療法の開発（研究番号　S2005-3）

２．キーワード：１）EBウイルス（EB virus）
２）ファージ・ディスプレイ（Phage display）
３）ヒト型モノクローナル抗体（Human monoclonal antibody）
４）発現クローニング（Expression cloning）
５）悪性リンパ腫（Malignant lymphoma）

３．研究代表者：正木　康史・医学部・助教授・血液免疫制御学（血液免疫内科学）

４．研究目的

バクテリオ・ファージ表面に抗体 Fab 分子を発現する Combinatorial antibody library system が開発され、ヒト型のモノクローナル抗体の作成が可能となり、モノクローナル抗体の応用範囲が従来の診断研究主体から治療応用主体へと大きく変遷しつつある。今回は、悪性リンパ腫に対する抗 Epstein Barr ウイルス（EBV）抗体による標的療法の開発に重点を起き研究を行う。まずEBウイルス関連蛋白に高い親和性を有するヒト型の抗EBV抗体をクローニングする事を第一目標とする。更に、ヒト型の抗EBV抗体がEBV関連悪性リンパ腫細胞にも結合することを確認した上で、まずはそれを用いた免疫染色などによる診断的利用法の確立、次いで、その抗体に抗癌剤を結合させ腫瘍特異的な標的療法を開発する事を最終目標とする。

５．研究計画

EBV に対する抗体を高力価で有する患者由来のファージ・ディスプレイ型のライブラリーを種々の抗原に対してファージ・パンニングを行い、EBV もしくはEBV関連蛋白に対するヒト型のモノクローナル抗体Fabをクローニングする。

強く反応する Fab が得られたら、塩基配列の決定、エピトープの解析等を行う。また、EBV陽性悪性リンパ腫組織に対しての親和性を免疫染色やFACSにて検討する。親和性が確認されたら、ラジオアイソトープ標識したFabを、EBウイルス関連リンパ腫組織を移植したSCIDマウスに投与し、組織に到達しうるかどうかを判定する。

６．研究成果

各種EBV関連蛋白のうち、EBV-VCA（viras capsid antigen）に反応するFabが５クローン得られた。そのうち、２クローンは EBV-VCA と強く特異的に反応し、免疫染色においてEBV感染細胞に陽性を示した。EBV関連腫瘍の診断目的として有用なFabが得られた。

７．研究の考察・反省

様々なEBV関連蛋白に対するヒト型モノクローナル抗体が得られる予定であったが、得られたものはVCAに対するもののみであった。VCAは細胞表面に表出する抗原ではな

いため、当初目的とした、Fab を用いた標的療法としては使えなかった。今後は、細胞表面抗原に対するモノクローナル Fab をクローニングするべく計画中である。

８．研 究 発 表

Dong L, Masaki Y, Takegami T, Kazanami T, Itoh K, Jin ZX, Huang CR, Tong XP, Fukushima T, Tanaka M, Sawaki T, Sakai T, Sugai S, Okazaki T, Hirose Y, Umehara H. Cloning and expression of two human recombinat monoclonal Fab fragments specific for EBV viral capsid antigen. Int Immunol 2007; 19: 331-336.

International Immunology, Vol. 19, No. 3, pp. 331–336
doi:10.1093/intimm/dxl150

Cloning and expression of two human recombinant monoclonal Fab fragments specific for EBV viral capsid antigen

Lingli Dong[1,3], Yasufumi Masaki[1], Tsutomu Takegami[2], Takafumi Kawanami[1], Kunihiko Itoh[4], Zhe-Xiong Jin[1], Cheng-Ri Huang[1], Xiao-Peng Tong[1], Toshihiro Fukushima[1], Masao Tanaka[1], Toshioki Sawaki[1], Tomoyuki Sakai[1], Susumu Sugai[1], Toshiro Okazaki[5], Yuko Hirose[1] and **Hisanori Umehara[1]**

[1]Department of Hematology and Immunology and [2]Department of Molecular Oncology and Virology, Kanazawa Medical University, Uchinada, Ishikawa 920-0293, Japan
[3]Department of Hematology and Immunology, Tongji Hospital, Huazhong University of Science and Technology, Wuhan, Hubei 430030, China
[4]Department of Clinical Pharmacology and Genetics, School of Pharmaceutical Science, University of Shizuoka, Shizuoka 422-8526, Japan
[5]Department of Clinical Laboratory, Medicine/Hematology, Faculty of Medicine, Tottori University, Yonago, Tottori 683-8504, Japan

Keywords: antibodies, human, molecular biology

Abstract

Serum titers of antibody to Epstein–Barr virus (EBV) viral capsid antigen (VCA) have been positively correlated with malignancies of lymphoid proliferation, such as Burkitt's lymphoma and Hodgkin's lymphoma. We have constructed a phage display combinatorial antibody Fab library from a patient with marginal zone B cell lymphoma associated with Sjögren's syndrome and carrying high serum anti-EBV-VCA IgG titer. Fab fragments were selected by panning against EBV-VCA protein coated onto ELISA plates, and selected Fab clones were characterized by ELISA, western blotting (WB), indirect immunofluorescence assay and immunohistochemistry. We have established two Fab clones, Fab-aVCA1 and Fab-aVCA21, which specifically recognize EBV-VCA by ELISA and WB. Inhibition ELISA competition showed that both clones could significantly reduce the binding of specific anti-EBV-VCA mAb to its relevant proteins. Furthermore, these two Fab clones could localize VCA protein in the EBV-positive P3HR1 and Daudi cell lines, as well as in tissue samples from patients with EBV-infected lymphoid malignancies. These results indicate that our two Fab clones are novel human mAbs specific for EBV-VCA protein and may have potential benefits for development of novel diagnostic and therapeutic approaches in EBV-related lymphoid malignancies.

Introduction

Epstein–Barr virus (EBV) is the first virus to be directly implicated in carcinogenesis in humans. EBV infects >90% of the world's adult population, and primary infection in a young adult can lead to infectious mononucleosis. Although most humans co-exist with the virus without serious sequels, this virus is strongly associated with several malignancies, including Burkitt's lymphoma (BL), nasopharyngeal carcinoma (NPC) and Hodgkin's lymphoma (HL) (1, 2). In cancer cells, EBV is present in a latent state, in which a subset of EBV genes is expressed, or in lytic cycles, which are characterized by the production of viral particles. Because viral capsid antigen (VCA) and early antigen, like the recently described EBV transactivator protein (ZEBRA), are expressed during EBV replication, cells expressing those EBV genes are more readily recognized by the immune system (3, 4). Therefore, high anti-VCA IgG titers are considered to be a marker of EBV reactivity (5). Remarkably, anti-VCA antibody titer is considerably higher in the sera of patients with BL, HL and NPC patients than in age-matched controls (1, 2). Although the presence of serum anti-VCA IgG has been widely used for the diagnosis of EBV infection, the molecular profiles of this human antibody remain unknown. In addition, EBV was

Correspondence to: Y. Masaki; E-mail: yasum@kanazawa-med.ac.jp

Transmitting editor: K. Okumura

Received 4 September 2006, *accepted* 22 December 2006

Advance Access publication 31 January 2007

recently found to be associated with autoimmune diseases, such as systemic lupus erythematosus (6, 7). Thus, the generation of EBV-VCA-specific human mAbs from human combinatorial Fab libraries could be of assistance in studies of molecular profiles of these antibodies and in the diagnosis of EBV infection at various stages.

The preparation of combinatorial libraries on the filamentous phage surface has been demonstrated to be an efficient route for the production of high affinity human mAbs (8, 9). Their advantages over mouse mAb include the ability to alter antibody fragments by protein engineering methods. Thus, there have been many studies of recombinant Fab selected by target antigens, including viruses such as HIV types 1 and 2, human rotavirus and SARS by phage display (10–12).

We have constructed a human antibody library from a patient carrying a high titer of serum anti-EBV-VCA IgG and successfully established two Fab clones by panning the Fab library against EBV-VCA. These two Fab fragments were found to bind to EBV-VCA with high affinity and were suitable for detecting EBV-VCA in EBV-infected malignant cells.

Methods

Library construction and phage display

After obtaining informed consent, we isolated 10 million bone marrow lymphocytes from a patient with Sjögren's syndrome and marginal zone B cell lymphoma carrying a high titer of EBV-VCA IgG. Total RNA was isolated and used to generate cDNA, which was used as a template for PCR amplification of sequences in the region of Vh-Ch1 of the heavy chain and light chain κ/λ (13). An antibody Fab library was constructed by the pComb3 M13 surface display system (13, 14).

Panning selection of EBV-VCA antigen binding phage

Human Fab antibodies were selected by panning against commercially obtained EBV-VCA (Biogenesis Company, UK) as described (13). A total of four cycles of panning were performed on 96-well ELISA plates pre-coated with 5 μg per well of EBV-VCA. Unbound phages were removed by washing 10 times with PBS/0.05% Tween 20. Bound human Fabs were detected with alkaline phosphatase (AP)-labeled goat anti-human IgG $F(ab)_2$ (Pierce, Rockford, IL, USA), and visualized with *p*-Nitrophenyl phosphate disodium salt (pNPP) substrate (Pierce) by reading the absorbance at 405 nm.

DNA sequencing

DNA was amplified using a BigDye Terminator v3.1 Cycle Sequencing Kit (Applied Biosystems, CA, USA). The primers for the variable region of the heavy (V_H) chain were T3 (5′-GAAGTAGTCCTTGACCAG-3′ forward) and Gz (5′-GAAGTAGTCCTTGACCAG-3′, reverse), and the primers for the variable region of the light (V_L) chain were KEF (5′-GAATTCTAAACTAGCTAGTCG-3′, forward) and Kb (5′-ATAGAAGTTGTTCAGCAGGCA-3′, reverse). The products were sequenced on the ABI PRISM 310 Genetic Analyzer (Applied Biosystems).

Purification of Fab fragments

Monoclonal Fabs were purified by immunoaffinity chromatography, using polyclonal Goat anti-human IgG $F(ab')_2$ (Pierce) conjugated to Gammabind G Sepharose (Amersham Bioscience, Piscataway, NJ, USA). After cross-linking with dimethyl pimelimidate (Pierce), Fab was purified (15) and its concentration was determined using the Bio-Rad protein microassay (CA, USA), and antibody purity was assessed by 12% SDS–PAGE followed by Quick-CBB staining (Wako, Osaka, Japan).

ELISA and inhibition analysis

To determine the reactivity of Fabs to EBV-VCA, 96-well microtiter plates were coated with 5 μg ml^{-1} EBV-VCA protein. After blocking with 3% BSA in PBS, the plates were washed with PBS/0.05% Tween 20 and incubated with two-fold serial dilutions of purified Fab (0.625–10 μg per well in PBS), followed by 1:2500 diluted AP-conjugated goat anti-human IgG $F(ab')_2$ and pNPP. The unrelated proteins, ovalbumin peptide (OVA) and human IgG Fc fragments, were used as control antigens to test non-specific binding (data not shown), and human recombinant Fab N28 anti-rotavirus was used as negative control (14).

To determine the ability of our Fab clones to competitively inhibit the binding of mouse mAb to EBV-VCA, we performed inhibition ELISA. After determining the dilution of mouse mAb (Argene, clone F3.23, France) that bound 90% of EBV-VCA protein in mouse mAb capture ELISA (1:100; data not shown), microtiter plates were coated with 5 μg per well of EBV-VCA, and 50 μl per well of serially diluted Fabs in PBS and 50 μl per well of diluted mouse mAb (1:50) were added. The plates were incubated for 1.5 h at room temperature (RT), washed, and incubated with HRP-conjugated goat anti-mouse IgG (ICN Pharmaceutical Inc., CA, USA) (1:2000) and 1-Step™ABTS [2-2′-azinobis(3-ethylbenzthiazoline-6-sulfonic acid) diammonium salt] (Pierce) substrates, then the absorbance at 405 nm was determined.

Western blotting analysis

One-half microgram aliquots of EBV-VCA protein loaded onto each lane were separated by 10% SDS–PAGE, followed by electrophoresis and transfer to a nitrocellulose membrane (Bio-Rad) by the semi-dry system (Bio-Rad). After blocking with 3% skimmed milk, the membrane was incubated overnight at 4°C with purified Fab fragment (1ug ml^{-1}). The membrane was subsequently incubated with HRP-labeled anti-human IgG $F(ab')_2$ (Pierce) for 1 h at RT and the reaction was developed and visualized with ECL-plus (Amersham Life Science, UK) (16).

Indirect immunofluorescence assay

Recombinant Fabs (10 μg ml^{-1}) were detected by indirect immunofluorescence assay (IFA) with FITC-conjugated goat anti-human IgG $F(ab')_2$ antibody (Jackson Immunoresearch, PA, USA). EBV-infected P3HR1 and Daudi cells [American Type Culture Collection (ATCC), VA, USA] were fixed with acetone after cytospin on glass slides, with EBV-negative Jurkat cells (ATCC) used as control. 4′-6-Diamidino-2-phenylindole (DAPI) (Wako) was used to counterstain the

nucleus. Mouse mAb was used as positive reference control and detected using PE-conjugated rabbit anti-mouse IgG antibody (Jackson Immunoresearch) (17).

Immunohistochemistry and in situ hybridization

Paraffin-embedded tumor tissue samples from five patients with EBV-positive lymphoid malignancies were used for immunohistochemical identification of EBV-VCA by our Fab clones and mouse mAb. They were one BL patient, two HL (mixed cellularity) patients and two diffuse large B cell lymphoma patients. As control, we used spleen samples from a patient with EBV-negative BL. Deparaffinized slides were treated for 10 min with 3% H_2O_2 to block endogenous peroxidase and 30 min with 3% skimmed milk. After antigen retrieval by autoclave heating, the slides were incubated for 1 h at RT with 10 μg ml^{-1} Fabs or 1:50 diluted mouse mAb. As control, slides were incubated with an anti-rotavirus Fab. After extensive washing with PBS, the slides were incubated for 1 h at RT with HRP anti-human IgG $F(ab)_2$ for Fabs and second antibody (Envision + Dual link system peroxidase, DAKO, Denmark) for mouse mAb. The slides were stained with DAB substrate (Envision DAB kit, DAKO) and counterstained with hematoxylin (DAKO). *In situ* hybridization (ISH) for EBV-encoded small RNA1 was performed simultaneously as described (18, 19).

Results

Selection of Fab fragments

After four rounds of panning, two Fab clones (Fab-aVCA1 and Fab-aVCA21) were considered positive for EBV-VCA. The reactivity of these Fab clones against the relevant antigen was higher than 1.0 optical density (OD), whereas their reactivity against human IgG Fc fragment and OVA were <0.3 OD by ELISA. Both purified Fab fragments appeared as clear bands of molecular weight 28 kDa on SDS–PAGE (Fig. 1).

Western blotting analysis of recombinant Fabs targeting EBV-VCA protein

Western blotting (WB) against EBV-VCA proteins was performed to define the targets of the recombinant monoclonal antibodies. Fab-aVCA1 recognized bands, of molecular weight 160, 85, 58 and 30 kDa (Fig. 2, lane 3), whereas Fab-aVCA21 detected bands of 85, 58 and 30 kDa (Fig. 2, lane 4). To determine why the Fab fragments recognized multiple bands, the EBV-VCA proteins were blotted with mouse mAb, which recognized EBV-VCA proteins of molecular weight 160, 85, 58, and 30 kDa (Fig. 2, lane 2), suggesting that the VCA protein may be proteolytically degraded (20).

Amino acid sequences of Fab H and L chains

The amino acid sequences of the V_H and V_L chains of both Fab clones were deduced from DNA sequencing and compared with the closest known germ line proteins (Fig. 3). The V_H chain sequence of Fab-aVCA1 was derived from the V_H4 family whereas the V_H chain sequence of Fab-aVCA21 was from the V_H3 family. The two Fab clones were found to share the same κ light chain. Homologies to the closest germ line gene were 94% for both V_L chains and 95 and 93% for the V_H chains of Fab-aVCA1 and Fab-aVCA21, respectively. The nucleotide sequence data of our Fabs reported in this paper have been submitted to the DDBJ database and were assigned the following accession number: AB266511 (Fab-aVCA1 light chain), AB266512 (Fab-aVCA1 heavy chain) and AB266513 (Fab-aVCA21 heavy chain).

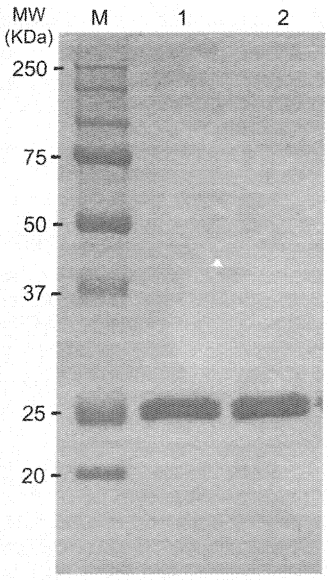

Fig. 1. SDS–PAGE analysis of purified Fab fragments. Fab fragments (2 μg) were subjected to 12% SDS–PAGE, and the gel was visualized with CBB staining. Both purified Fab fragments, Fab-aVCA1 and Fab-aVCA21, have molecular weights of ~28 kDa (M, molecular marker; lane 1, Fab-aVCA1; lane 2, Fab-aVCA21).

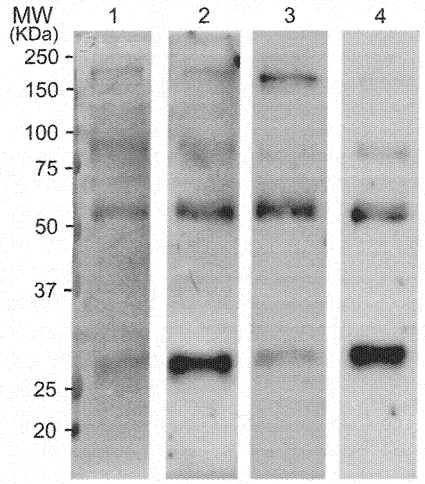

Fig. 2. Western blot analysis of EBV-VCA proteins with Fab-aVCA1 and Fab-aVCA21. EBV-VCA protein (0.5 μg) was separated by 10% SDS-PAGE, and transferred to a nitrocellulose membrane. After blocking, the membrane was incubated overnight at 4°C with purified Fab fragment (1 μg ml^{-1}), followed by incubation for 1 h at RT with HRP-labeled anti-human IgG $F(ab')_2$ and visualization with ECL system (lane 1, protein profiles of EBV-VCA; lane 2, mouse anti-VCA mAb; lane 3, Fab-aVCA1; lane 4, Fab-aVCA21).

A Variable heavy chain sequence

	FR1	CDR1	FR2	CDR2	FR3	CDR3	FR4
VH4-39	PGLVKPSETLSLTCTVSGGSIS	-SSSYYWG	WIRQPPGKGLEWIG	SIYYSGSTYYNPSLKS	RVTISVDTSKNQFSLKLSSVTAADTAVCAR		DYWGQGTPVT
Fab-aVCA1	.....D...	T.....A	.....	.F....G.F.....M.	.....A...L.....	EPTLGRGVWF	.S.....
VH3-30	GGVVQPGRSLRLSCAASGFTFS	SYGMH	WVRQAPGKGLEWVA	VISYDGSNKYYADSVKG	RFTISRDNSKNTLYLQMNSLRAEDTAVYYCAK		DVWGQGTTVT
Fab-aVCA21	.....KP.....	H.A..	.....	.....N.QH.....	.....K.....T..A.L.....	VDTPMAYGGI	.Y.....L..

B Variable light chain sequence

	FR1	CDR1	FR2	CDR2	FR3	CDR3	FR4
Vκ	GTLSLSPGERATLSC	RASQSVSSSYLA	WYQQKPGQAPRLLIY	GASSRAT	GIPDRFSGSGSGTDFTLTISRLEPEDFAVYYC	QQYGSSPRT	FGQTKVEIKRTVA
Fab-aVCA1	.....	.....	.....	...T...	.....I.....	.....	.....
Fab-aVCA21	.....	.....	.....	...T...	.....I.....	.....	.....

Fig. 3. Comparison of the deduced amino acid sequences of both V_H and V_L domains to the closest germ line sequence. (A) V_H sequences; (B) V_L sequences. Amino acid identity within a group is indicated by dots.

ELISA and inhibition ELISA

Binding of Fab-aVCA1 and Fab-aVCA21 to EBV-VCA was examined using ELISA. Both Fab fragments showed high affinity, concentration-dependent binding to EBV-VCA, whereas the negative control, Fab anti-rotavirus, did not bind to EBV-VCA (Fig. 4A). To further characterize the affinity of Fab-aVCA1 and Fab-aVCA21 to EBV-VCA, we compared their binding ability with that of mouse mAb (clone F3.23), which is specific for EBV-VCA, using inhibition ELISA. We found that Fab-aVCA21 significantly reduced the binding of mouse mAb to EBV-VCA, whereas Fab-aVCA1 showed a similar, but relatively weak effect, on binding (Fig. 4B).

Specificity of Fab fragments by IFA, immunohistochemistry and ISH

To further investigate the interaction of the purified Fab fragments and EBV-VCA, we assayed the binding of purified Fab fragments to the EBV-positive P3HR1 and Daudi cell lines and the EBV-negative Jurkat cell line by IFA. Confocal microscopy showed that both Fab-aVCA1 and Fab-aVCA21 stained P3HR1 and Daudi (Fig. 5), but not Jurkat cells (data not shown). In contrast, no staining was observed using Fab anti-rotavirus (Fig. 5). Immunohistochemically, we found that Fab-aVCA1 and Fab-aVCA21 specifically recognized EBV-VCA protein in EBV-infected lymphoma cells with good concordance with mouse mAb in five patients with EBV-positive lymphoid malignancies. Figure 6 showed staining of paraffin-embedded lymph node tissues from a patient with EBV-positive diffuse large B cell lymphoma by Fab-aVCA1 and Fab-aVCA21 (Fig. 6 B and C). Staining with Fab anti-rotavirus (Fig. 6 D) and staining of control tissues (spleen from a patient with EBV-negative BL) were negative (Fig. 6 G–I). These findings were confirmed by ISH (Fig. 6 E and J).

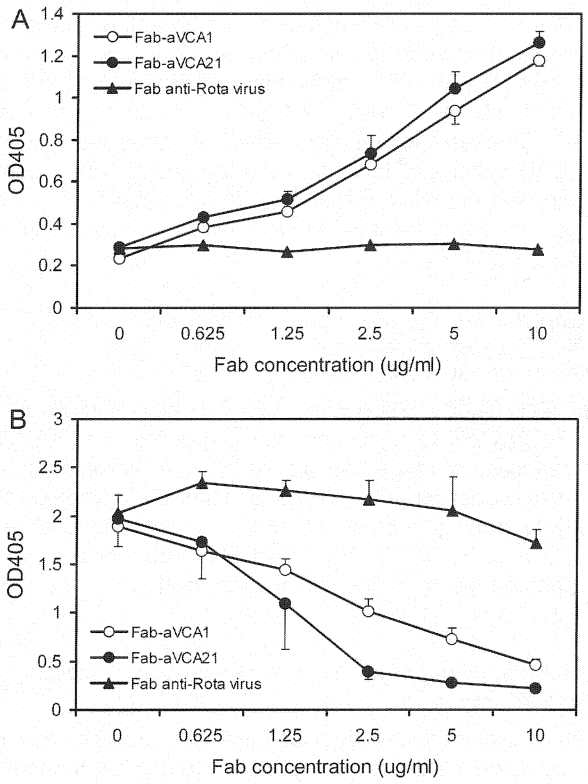

Fig. 4. Specificity of Fab fragments by ELISA. (A) Binding of Fab-aVCA1 and Fab-aVCA21 to EBV-VCA. Microtiter plates were coated with 5 μg μl^{-1} EBV-VCA protein, and two-fold serially diluted Fabs were added to the wells. Bound Fabs were detected by anti-human IgG $F(ab')_2$–HRP and measured by optical density at 405 nm. (B) Inhibition ELISA: Microtiter plates were coated with 5 μg per well EBV-VCA and blocked with 3% BSA/PBS, and to each well was added 50 μl serially diluted Fabs in PBS and 50 μ1 1:50 diluted mouse mAb. After incubation for 1.5 hour at RT, HRP-conjugated goat anti-mouse IgG was added and visualized by absorbance at 405 nm. Each experiment was done in triplicate. Error bars represent SEM.

Discussion

VCA is a complex of incompletely defined EBV late gene products associated with virion particles (21, 22) and expressed in the late period of EBV replication (17, 20). The presence of EBV-VCA in EB-related malignant cells may be associated with EBV reactivation, which usually entails virus replication and excretion. It is likely that the exposure of EBV-infected cancer cells to the immune system leads to an increase in titer of anti-VCA antibodies. In this regard, anti-VCA IgG titers have been reported to be associated with EB viral load in patients with HL, patients infected with HIV and children receiving solid-organ transplants (23–25). In addition, the presence of EBV-positive tumor cells has been associated with poorer survival in older patients with HL (26,

27) and advanced NPC (28). Therefore, new effective implications for diagnosis of EBV infection and potentially clinical marker to monitor the presence of EBV-related lymphoid malignancies are required.

Phage display is a rapid and convenient way to isolate recombinant mAbs specific for various antigens (8), including the isolation of a human monoclonal Fab fragment specific for EBV envelope glycoprotein, the gp350/220 antigen (29). We have successfully identified two EBV-specific Fab fragments by panning a Fab library against EBV-VCA, and subsequently characterized these fragments by DNA sequencing and serial approaches.

We have identified the genes encoding the Fab-aVCA1 and Fab-aVCA21 antibodies. Both Fab fragments share the same V_L chain, with homology to the closest germ line gene of 94%. The homologies of V_H chain of Fab-aVCA1 and Fab-aVCA21 were 95 and 93%, respectively. In addition, we found that both Fab-aVCA21 and Fab-aVCA1 specifically bind to EBV-VCA in a concentration-dependent manner, as well as significantly reducing the binding of mouse mAb to EBV-VCA, suggesting that Fab-aVCA1 and Fab-aVCA21 bind to VCA epitopes with high affinity, similar to that of mouse mAb. By WB, we detected minor differences in the proteins bound by both Fab fragments and mouse mAb, suggesting that reactive epitopes may differ in EBV-infected humans and EBV-immunized mice (11). Using IFA, we found that both Fab fragments could detect VCA protein in the EBV-positive P3HR1 cell line, which has been used for EBV serodiagnosis (30), as well as in Daudi cell line. These findings strongly suggest that our two human Fabs can recognize EBV-VCA with high affinity. Finally, we confirmed the specificity of these two Fab fragments in tissues from five patients with EBV-positive lymphoid malignancies by immunohistochemistry and ISH. These results indicate that these two Fab fragments are novel human EBV-VCA specific mAbs. Altogether, these results help us to further understand the molecular profiles of human anti-EBV-VCA antibody and may provide the insight for future study leading to intracellular expression of antibodies (31).

Hybridoma techniques to produce murine mAbs are quite expensive and require animal handling. In addition, the inherent immunogenicity of murine sequences in humans has presented obstacles to the clinical application of mouse mAbs. Human Fab should have reduced immunogenicity in humans, and may therefore have enhanced efficacy, safety and ease of use. In addition to phage display, transgenic mice can generate a full repertoire of human therapeutic mAbs and may facilitate the optimization of mAb production and open new therapeutic avenues (32, 33). Although further studies are necessary to determine whether our two Fab fragments specific to EBV-VCA have protective activity *in vitro and in vivo*, these results may provide building blocks for the development of novel diagnostic and therapeutic approaches.

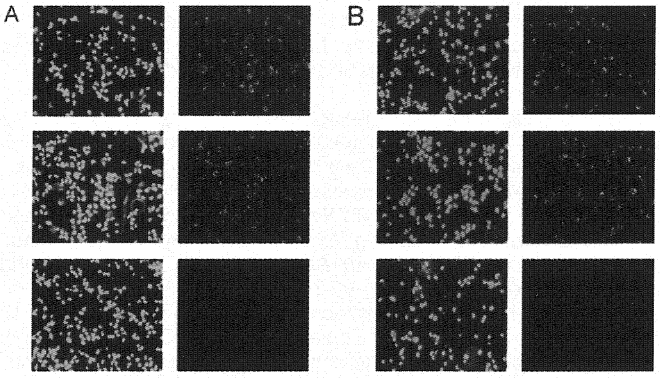

Fig. 5. Indirect immunofluorescence of EBV-infected P3HR1 (A) cells and Daudi cells (B) using recombinant Fab fragments. Recombinant Fabs (10 μg ml^{-1}) were detected by indirect immunofluorescence assay (IFA) with FITC-conjugated goat anti-human IgG $F(ab')_2$ antibody. EB virus-infected P3HR1 and Daudi cells were fixed with acetone after cytospin on glass slides. DAPI was used to counterstain the nucleus. (A) P3HR1 cells. (B) Daudi cells. Nuclei counterstained with DAPI (left panel), Fab-aVCA1, Fab-aVCA21 and Fab anti-rotavirus (right panel).

Acknowledgements

We gratefully thank Dennis R. Burton (The Scripps Research Institute, La Jolla, CA, USA) for the generous gift of the pCombs vector. This work was supported by grants from the Japanese Ministry of Education, Culture, Sports, Science and Technology (13557160,

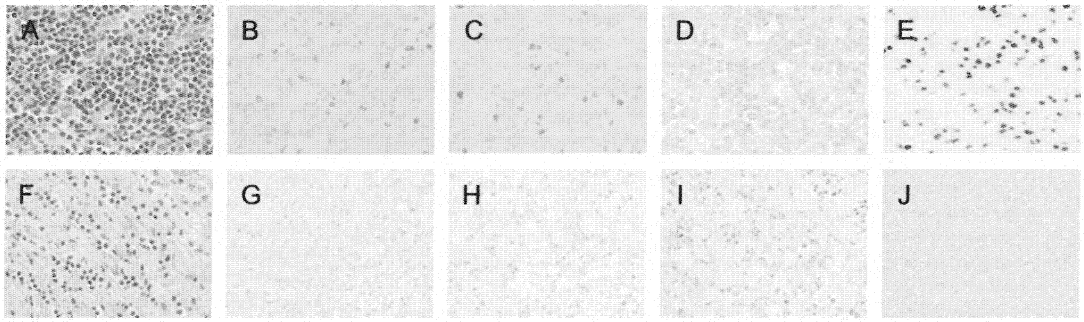

Fig. 6. EBV-VCA detection with Fab-aVCA1 and Fab-aVCA21 by IHC and EBAR detection by ISH study. Deparaffinized slides were treated for 10 min with 3% H_2O_2. After antigen retrieval, the slides were incubated with 10 μg ml^{-1} Fabs for 1 h at RT. After extensive washing with PBS, the slides were incubated for 60 min at RT with HRP anti-human IgG $F(ab')_2$ for Fabs. The slides were stained with DAB substrate and counterstained with hematoxylin. Immunohistochemistry of EBV-positive LN tissues (A–E) and EBV-negative spleen tissues (F–J) with Fab-aVCA1 (B and G), Fab-aVCA21 (C and H), Fab anti-rotavirus (D and I), as well as ISH studies of EBV-positive (E) and negative (J) lymphoma tissues. (A) and (F) are stained with H&E.

15024236, 15390313, 13877075, 15024236, 15390313 to H.U. and 17591060 to Y.M.), the Uehara Memorial Foundation (to H.U.), the Hokkoku Cancer Fund (to Y.M.) and Kanazawa Medical University Research Foundation (C2006-1 to H.U. and S2004-16 to Y.M.).

Abbreviations

AP	alkaline phosphatase
BL	Burkitt's lymphoma
DAPI	4′-6-Diamidino-2-phenylindole
EBV	Epstein–Barr virus
HL	Hodgkin's lymphoma
IFA	indirect immunofluorescence assay
ISH	*in situ* hybridization
NPC	nasopharyngeal carcinoma
OD	optical density
OVA	ovalbumin peptidep
pNPP	*p*-Nitrophenyl phosphate disodium salt
RT	room temperature
VCA	viral capsid antigen
WB	western blotting

References

1 Thompson, M. P. and Kurzrock, R. 2004. Epstein-Barr virus and cancer. *Clin. Cancer Res.* 10:803.
2 Williams, H. and Crawford, D. H. 2006. Epstein-Barr virus: the impact of scientific advances on clinical practice. *Blood* 107:862.
3 Sugimoto, M., Tahara, H., Ide, T. and Furuichi, Y. 2004. Steps involved in immortalization and tumorigenesis in human B-lymphoblastoid cell lines transformed by Epstein-Barr virus. *Cancer Res.* 64:3361.
4 Drouet, E., Brousset, P., Fares, F. *et al.* 1999. High Epstein-Barr virus serum load and elevated titers of anti-ZEBRA antibodies in patients with EBV-harboring tumor cells of Hodgkin's disease. *J. Med. Virol.* 57:383.
5 Hess, R. D. 2004. Routine Epstein-Barr virus diagnostics from the laboratory perspective: still challenging after 35 years. *J. Clin. Microbiol.* 42:3381.
6 Gross, A. J., Hochberg, D., Rand, W. M. and Thorley-Lawson, D. A. 2005. EBV and systemic lupus erythematosus: a new perspective. *J. Immunol.* 174:6599.
7 Chen, C. J., Lin, K. H., Lin, S. C. *et al.* 2005. High prevalence of immunoglobulin A antibody against Epstein-Barr virus capsid antigen in adult patients with lupus with disease flare: case control studies. *J. Rheumatol.* 32:44.
8 Paschke, M. 2006. Phage display systems and their applications. *Appl. Microbiol. Biotechnol.* 70:2.
9 Barbas, C. F. III 1993. Recent advances in phage display. *Curr. Opin. Biotechnol.* 4:526.
10 Zhang, M. Y., Xiao, X., Sidorov, I. A. *et al.* 2004. Identification and characterization of a new cross-reactive human immunodeficiency virus type 1-neutralizing human monoclonal antibody. *J. Virol.* 78:9233.
11 Higo-Moriguchi, K., Akahori, Y., Iba, Y., Kurosawa, Y. and Taniguchi, K. 2004. Isolation of human monoclonal antibodies that neutralize human rotavirus. *J. Virol.* 78:3325.
12 Flego, M., Di Bonito, P., Ascione, A. *et al.* 2005. Generation of human antibody fragments recognizing distinct epitopes of the nucleocapsid (N) SARS-CoV protein using a phage display approach. *BMC Infect. Dis.* 5:73.
13 Ditzel, H. J., Masaki, Y., Nielsen, H., Farnaes, L. and Burton, D. R. 2000. Cloning and expression of a novel human antibody-antigen pair associated with Felty's syndrome. *Proc. Natl Acad. Sci. USA* 97:9234.
14 Itoh, K., Nakagomi, O., Suzuki, K., Inoue, K., Tada, H. and Suzuki, T. 1999. Recombinant human monoclonal Fab fragments against rotavirus from phage display combinatorial libraries. *J. Biochem. (Tokyo)* 125:123.
15 Ditzel, H. J., Binley, J. M., Moore, J. P. *et al.* 1995. Neutralizing recombinant human antibodies to a conformational V2- and CD4-binding site-sensitive epitope of HIV-1 gp120 isolated by using an epitope-masking procedure. *J. Immunol.* 154:893.
16 Miyaji, M., Jin, Z. X., Yamaoka, S. *et al.* 2005. Role of membrane sphingomyelin and ceramide in platform formation for Fas-mediated apoptosis. *J. Exp. Med.* 202:249.
17 Liu, M. Y., Huang, Y. T., Sheen, T. S., Chen, J. Y. and Tsai, C. H. 2004. Immune responses to Epstein-Barr virus lytic proteins in patients with nasopharyngeal carcinoma. *J. Med. Virol.* 73:574.
18 Hirose, Y., Masaki, Y., Yoshioka, R. and Takiguchi, T. 1997. Aggressive natural killer cell lymphoproliferative disorder associated with Epstein-Barr viral RNA. *Am. J. Hematol.* 54:314.
19 Hirose, Y., Masaki, Y., Sawaki, T. *et al.* 2006. Association of Epstein-Barr virus with human immunodeficiency virus-negative peripheral T-cell lymphomas in Japan. *Eur. J. Haematol.* 76:109.
20 Johannsen, E., Luftig, M., Chase, M. R. *et al.* 2004. Proteins of purified Epstein-Barr virus. *Proc. Natl Acad. Sci. USA* 101:16286.
21 van Grunsven, W. M., van Heerde, E. C., de Haard, H. J., Spaan, W. J. and Middeldorp, J. M. 1993. Gene mapping and expression of two immunodominant Epstein-Barr virus capsid proteins. *J. Virol.* 67:3908.
22 Serio, T. R., Angeloni, A., Kolman, J. L. *et al.* 1996. Two 21-kilodalton components of the Epstein-Barr virus capsid antigen complex and their relationship to ZEBRA-associated protein p21 (ZAP21). *J. Virol.* 70:8047.
23 Besson, C., Amiel, C., Le-Pendeven, C. *et al.* 2006. Positive correlation between Epstein-Barr virus viral load and anti-viral capsid immunoglobulin G titers determined for Hodgkin's lymphoma patients and their relatives. *J. Clin. Microbiol.* 44:47.
24 Stevens, S. J., Blank, B. S., Smits, P. H., Meenhorst, P. L. and Middeldorp, J. M. 2002. High Epstein-Barr virus (EBV) DNA loads in HIV-infected patients: correlation with antiretroviral therapy and quantitative EBV serology. *AIDS* 16:993.
25 Rogers, B. B., Conlin, C., Timmons, C. F., Dawson, D. B., Krisher, K. and Andrews, W. S. 1997. Epstein-Barr virus PCR correlated with viral histology and serology in pediatric liver transplant patients. *Pediatr. Pathol. Lab. Med.* 17:391.
26 Jarrett, R. F., Stark, G. L., White, J. *et al.* 2005. Impact of tumor Epstein-Barr virus status on presenting features and outcome in age-defined subgroups of patients with classic Hodgkin lymphoma: a population-based study. *Blood* 106:2444.
27 Keegan, T. H., Glaser, S. L., Clarke, C. A. *et al.* 2005. Epstein-Barr virus as a marker of survival after Hodgkin's lymphoma: a population-based study. *J. Clin. Oncol.* 23:7604.
28 Yang, X., Goldstein, A. M., Chen, C. J. *et al.* 2006. Distribution of Epstein-Barr viral load in serum of individuals from nasopharyngeal carcinoma high-risk families in Taiwan. *Int. J. Cancer* 118:780.
29 Bugli, F., Bastidas, R., Burton, D. R., Williamson, R. A., Clementi, M. and Burioni, R. 2001. Molecular profile of a human monoclonal antibody Fab fragment specific for Epstein-Barr virus gp350/220 antigen. *Hum. Immunol.* 62:362.
30 Liao, G., Huang, J., Fixman, E. D. and Hayward, S. D. 2005. The Epstein-Barr virus replication protein BBLF2/3 provides an origin-tethering function through interaction with the zinc finger DNA binding protein ZBRK1 and the KAP-1 corepressor. *J. Virol.* 79:245.
31 Cattaneo, A. and Biocca, S. 1999. The selection of intracellular antibodies. *Trends Biotechnol.* 17:115.
32 Weiner, L. M. 2006. Fully human therapeutic monoclonal antibodies. *J. Immunother.* 29:1.
33 Sharon, J., Liebman, M. A. and Williams, B. R. 2005. Recombinant polyclonal antibodies for cancer therapy. *J. Cell. Biochem.* 96:305.

１．研究課題名：迷走神経によるグルカゴン様ペプチド１受容機構の分子生物学的検討
（研究番号 S2005-4）

２．キーワード：１）インクレチン（incretin）
２）グルカゴン様ペプチド１（glucagon-like peptide-1; GLP-1）
３）迷走神経（vagus）
４）節神経節（nodose ganglion）
５）神経化学受容（neural chemoreception）

３．研究代表者：中川　淳・医学部・助教授・内分泌代謝制御学（内分泌内科学）

４．研 究 目 的

我々は従来より、ある種の膵・消化管ホルモンは、門脈血中に放出→肝を通過→全身循環を経た後に標的器官に作用するのみならず、門脈領域に存在するホルモン感受性迷走神経求心路を介した神経性反射により作用発現し得る可能性を提唱してきた。取り分けグルコース濃度依存性インスリン分泌促進作用（インクレチン作用）や食欲抑制作用により糖尿病治療への応用が期待されているグルカゴン様ペプチド 1（GLP-1）に関しては早くから着目してきている。即ち、ラットを用いた電気生理学的実験より迷走神経肝臓枝による GLP-1 受容機構の存在を見出し、さらに迷走神経求心線維１次ニューロンの存在する節神経節（NG）において GLP-1 受容体遺伝子が発現していることを確認している。しかし、この NG での GLP-1 感受性ニューロンがどのような神経伝達物質により中枢（延髄孤束核）へ投射しているか等、不明な点は極めて多く、本機構の分子生物学的解明は現在端緒に付いたばかりである。本研究では主として、GLP-1 感受性 NG ニューロンでの中枢への神経伝達物質を同定することを目的とする。

５．研 究 計 画

迷走神経 GLP-1 受容機構に関与するニューロンがどのような神経伝達物質により延髄孤束核へ情報を伝達しているのかを同定するため、ラット NG で GLP-1 受容体遺伝子と神経伝達物質遺伝子の共発現の有無を２重染色 in situ hybridazation により検出する。GLP-1 は食欲抑制作用を示すことが知られているので、NG から孤束核への神経伝達物質も食欲抑制性である可能性が高い。従って，まず食欲抑制性神経伝達物質の NG での遺伝子発現を RT-PCR によりスクリーニングする。引き続き、これにより得られた知見に基づき、組織学的検索を行う。

・試料 cDNA…　自由摂食下の Wistar 系ラットより麻酔下に NG を摘出する。RT-PCR 用には、市販キットを用い総 RNA を抽出、cDNA を合成する。In situ hybridization 用には、OCT-compound に包埋，新鮮凍結切片を作製する。

・RT-PCR …　RT-PCR を用いて NG に発現する食欲抑制性神経伝達物質遺伝子の発現を検出する。目的とする神経伝達物質遺伝子として calcitonin gene-related peptide (CGRP)、cocaine- and amphetamine-regulated transcript (CART)、gastrin-releasing

peptide (GRP)、neurotensin/neuromedin N (NT/NMN), proopiomelanocortin (POMC) につき検索を行う。

・In situ hybridization … GLP-1 受容体 mRNA および神経伝達物質 mRNA に対する digoxigenin 標識および fluorescein 標識 cRNA プローブは、5'端に T7 または SP6 プロモーター配列を付加したプライマーによる RT-PCR 産物を鋳型として、T7- または SP6-RNA polymerase を用いて作製する。これら標識プローブを用い、ラット NG 新鮮凍結切片に対して２重染色 in situ hybridization を行う。

６．研究成果

RT-PCR 法により、ラット NG において、CGRP およびそのアイソフォームである calcitonin-related polypeptide-β (Calcb)、CART、NT/NMN 遺伝子の明瞭な発現が確認された。一方、GRP の発現はかなり弱く、POMC の発現は極めて僅かであった。

次いで、以上の RT-PCR の成績に基づき、ラット NG ニューロンにおけるこれら神経伝達物質遺伝子と GLP-1 受容体遺伝子の共発現の有無を、in situ hybridization を用いて検討した。標識 cRNA プローブは、T7 または SP6 プロモーター配列を付加したプライマーを用いた RT-PCR 産物を鋳型として作製した。In situ hybridization に関しては、TSA 法の採用により感度を上げることが可能となった。その結果、少なくとも CGRP と GLP-1 受容体とを同時に発現するニューロンが存在することが確認された。

なお、本研究の遂行に際し、副次的に、

１）ラット NG に発現するソマトスタチン受容体アイソフォームが主として SSTR2A であることを見出した。

２）グルカゴン様ペプチド２ (GLP-2) 受容体遺伝子は、NG には発現していないことを証明した。

また、本助成にて購入したサーマルサイクラーは、糖尿病細小血管症関連遺伝子に関する臨床研究にも利用された。

７．研究の考察・反省

本研究により、ラット NG において食欲抑制性神経伝達物質として CGRP、CART、NT/NMN 遺伝子が発現していることを RT-PCR にて確認した。そのうち少なくとも CGRP ニューロンの一部が GLP-1 受容体遺伝子を発現していることを、in situ hybridization にて明らかにした。

以上の知見に基づき引き続き解明されるべき課題は、門脈領域における GLP-1 情報が迷走神経を介して中枢 (延髄孤束核) に投射される際、はたして CGRP が神経伝達物質として働いているかどうか、という点になる。この点に関して、門脈内に GLP-1 を投与、延髄孤束核に出現する c-fos 陽性ニューロンと CGRP 陽性神経線維終末との関係を組織学的に検索することで証明できるのではないかと考えている。

迷走神経による GLP-1 受容機構の全容の理解には、迷走神経から延髄孤束核への連絡における神経伝達物質の同定を避けては通れないと考えている。この神経伝達物質を明らかにすることで、各種病態時における本機構の偏倚を検証することが可能となり、ひいては糖尿病や肥満症の病態解明や GLP-1 経路を介する新たな治療戦略の開発

に結びつくことを期待している。

８．研 究 発 表

な　　し

（延髄孤束核への連絡における CGRP の役割を明らかにした上での投稿を考えている）

・NG における SS 受容体アイソフォームに関しては投稿準備中

・NG で GLP-2 受容体遺伝子発現が認められないことは共同研究者により投稿準備中

・糖尿病細小血管症関連遺伝子に関する臨床研究については投稿済み、審査待ち

１．研究課題名：メタボリックシンドロームにおけるアディポネクチンの心筋修復再生機構の解明と臨床応用（研究番号　S2005-5）

２．キーワード：１）メタボリックシンドローム（metabolic syndrome）
２）アディポネクチン（adiponectin）
３）心筋修復再生（myocardial repair and regeneration）

３．研究代表者：高橋　孝・医学部・講師・総合内科学（総合診療科）

４．研 究 目 的

肥満(内臓脂肪蓄積)という危険因子は、糖尿病・高脂血症・高血圧症と重なり合って心血管系発作を招く可能性が大きく、メタボリックシンドローム(MS)という概念が提唱されている。

そこで、本研究は、MS において発生する障害心筋リモデリング、例えば、心肥大・心筋線維化・心拡大等に対する自己修復再生機構に脂肪由来の新規生理活性物質であるアディポネクチンが関与する機序を解明する。

次に、アディポネクチン転写活性薬物である Peroxisome proliferator-activated receptor-γ (PPAR-γ) アゴニストが臨床応用できるか否かを解明する。

５．研 究 計 画

(1) 肥満症を伴う心筋障害モデルマウスを用いた心筋修復再生機構におけるアディポネクチンの役割

(2) MS 剖検例における心筋修復機構へのアディポネクチンシグナルの関与

(1) 肥満/糖尿病モデルマウスを用いて心筋炎モデル・心筋梗塞モデルマウスを作成し、治療として PPAR-γアゴニスト(Pioglitazone, 20 mg/kg/day 経口) 連日投与あるいはアディポネクチン投与を実施する。アディポネクチン導入群やプラセボ群と比較して、PPAR-γアゴニスト投与群における心筋リモデリング(心筋肥大、間質線維化、アポトーシス)の程度・左室機能・アディポネクチン及び受容体(AdipoR1, AdipoR2)の組織局在・アディポネクチン及び mRNA の局所発現量・アディポネクチンの発現調節転写因子(PPAR-γ, LRH-1)の活性・血中アディポネクチン値の評価を行い、アディポネクチンによる心筋リモデリングの抑制効果を判定する。

幹細胞表面抗原である Sca-1 に対する免疫染色によって、Sca-1 陽性細胞の心臓内誘導局在を各群にて確認する。さらに、各群より心筋を単離培養し、Sca-1 を標的とする Flow cytometry によって全心筋由来細胞における Sca-1 陽性細胞の頻度を比較する。そして、心筋細胞に特異的な蛋白・遺伝子の発現に基づいて幹細胞の分化度を評価する。

(2) MS に合致する剖検例の心臓を用いて、心筋リモデリングの局所分布の相違と心外膜脂肪でのアディポネクチン発現性及び心筋でのアディポネクチン発現性・受容体:T-cadherin 発現性との関連性を解析することで、心筋修復機構へのアディポネクチンシグナルの関与を推定する。

６．研 究 成 果

(1) 肥満/糖尿病モデルマウスにおいて発症したウイルス性心筋炎は、重篤な心筋障害と低い生存率を示したが、組換えマウス全長アディポネクチン(30 μg/g/day 皮下投与)をウイルス接種と同時に連日補充することによって、心筋細胞におけるアディポネクチン受容体の発現増強と共に有意な障害心筋の修復が認められた。そして、アディポネクチン治療を受けた心筋炎では、プラセボ群と比較して、Sca-1 陽性細胞が有意に増加していた。以上より、アディポネクチン導入による障害心筋細胞に対する修復・再生の可能性が考慮された。

次に、PPAR-γアゴニスト(Pioglitazone, 20 mg/kg/day 経口)の 連日投与による心筋局所におけるアディポネクチン及び mRNA の局所発現を試みたが、障害心筋細胞を修復するに至るような同サイトカイン及び mRNA の心筋発現が得られなかった。

(2) 心筋梗塞や拡張型心筋症といった剖検例の心臓において、心外膜脂肪でのアディポネクチン発現を陽性シグナルとして、障害心筋自身におけるアディポネクチンとその受容体 T-cadherin の発現及び TNF-αの発現が免疫組織化学によって確認された(図を参照)。T-cadherin の発現は、正常心筋細胞においても認められたが、アディポネクチンや TNF-αといったアディポサイトカインのシグナル発現は、壊死に至っていない障害心筋において顕著であり、これらのシグナル発現の心筋修復機構への関与が示唆された。

＜心筋梗塞・拡張型心筋症の障害心筋細胞における
免疫組織化学を用いたアディポネクチン・アディポネクチン受容体・TNF-αの染色活性＞

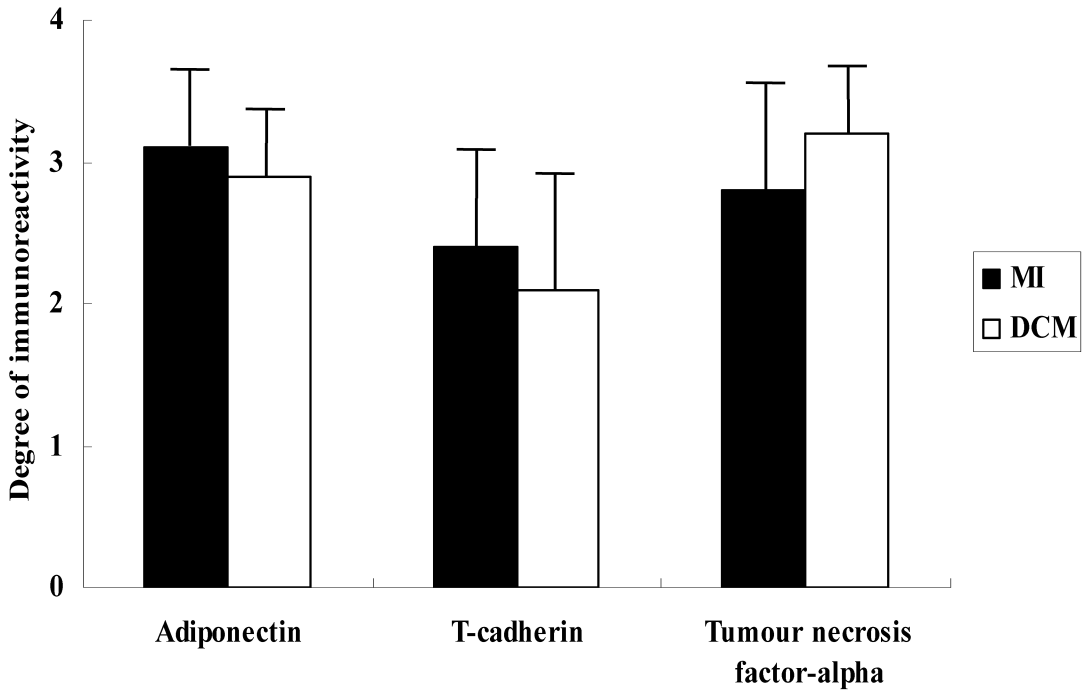

MI：心筋梗塞、DCM：拡張型心筋症

７．研究の考察・反省

(1) ウイルス性心筋炎による障害心筋におけるアディポネクチン及びmRNAの発現を誘導するようなPPAR-γアゴニスト(Pioglitazone)の至適投与量を今後決定する予定である。また、心筋梗塞モデルマウスにおいても局所におけるアディポネクチン発現誘導によって、障害心筋細胞に対する修復・再生作用が得られるかどうかを確認したい。

そして、単離培養した心筋細胞を用いて、心筋修復再生機構におけるアディポネクチンの役割を細胞分子レベルで検証する予定である。

(2) 今後は、MSに合致する剖検例の心臓を利用して、心筋修復機構へのアディポネクチンシグナルの関与を解析する必要がある。また、免疫組織化学のみならず in situ hybridization 法によってmRNA レベルでの心筋細胞内局在も検証したい。

８．研 究 発 表

Kanda T, Saegusa S, Takahashi T, Sumino H, Morimoto S, Nakahashi T, Iwai K, Matsumoto M. Reduced-energy diet improves survival of obese KKAy mice with viral myocarditis: induction of cardiac adiponectin expression. Int J Cardiol 2007; 119: 310-318. (MLDB)

Saegusa S, Yu F, Takahashi T, Sumino H, Moriya J, Kawaura K, Yamakawa J, Itoh T, Morimoto S, Nakahashi T, Iwai K, Matsumoto M, Kanda T. Oral administration of candesartan improve the survival of mice with viral myocarditis through modification of cardiac adiponectin expression. Cardiovasc Drugs Ther 2007; 21: 155-160. (MLDB)

Kanda T, Takahashi T, Sumino H, Nakahashi T, Iwai K, Morimoto S, Matsumoto M. Hepatocyte growth factor and visfatin in elderly bedridden patients. J Am Geriatr Soc 2007; 55: 963-965. (MLDB)

Morimoto S, Takahashi T, Okaishi K, Nakahashi T, Nomura K, Kanda T, Okuro M, Murai H, Nishino T, Matsumoto M. Tilting-induced decrease in systolic blood pressure in bedridden hypertensive elderly inpatients: effects of azelnidipine. Hypertens Res 2006; 29: 943-949. (MLDB)

Okuro M, Morimoto S, Takahashi T, Okaishi K, Nakahashi T, Murai H, Iwai K, Kanda T, Matsumoto M. Angiotensin I-converting enzyme inhibitor improves reactive hyperemia in elderly hypertensives with arteriosclerosis obliterans. Hypertens Res 2006; 29: 655-663. (MLDB)

Yu F, Takahashi T, Moriya J, Kawaura K, Yamakawa J, Kusaka K, Itoh T, Sumino H, Morimoto S, Kanda T. Angiotensin II receptor antagonist alleviates nonalcoholic

fatty liver in KKAy obese mice with type 2 diabetes. J Int Med Res 2006; 34: 297-302. (MLDB)

Yu F, Takahashi T, Moriya J, Kawaura K, Yamakawa J, Kusaka K, Itoh T, Morimoto S, Yamaguchi N, Kanda T. Traditional Chinese medicine and kampo: a review from the distant past for the future. J Int Med Res 2006; 34: 231-239. (MLDB)

Kusaka K, Itoh T, Kawaura K, Moriya J, Yamakawa J, Takahashi T, Oguchi M, Tonami H, Yamamoto I, Kanda T. Advanced esophageal carcinoma in 84 years old treated with chemoradiotherapy. J Int Med Res 2006; 34: 437-440. (MLDB)

Morimoto S, Takahashi T, Jackman HL, Erdös EG, Kanda T, Ohde H, Liu W-M, Okuro M, Nomura K, Matsumoto M. Extract from inflamed skin of rabbits increases enkephalin concentrations in cerebrospinal fluid in rats. J Kanazawa Med Univ 2005; 30: 141-146.

Takahashi T, Yu F, Saegusa S, Sumino H, Nakahashi T, Iwai K, Morimoto S, Kurabayashi M, Kanda T. Impaired expression of cardiac adiponectin in leptin-deficient mice with viral myocarditis. Int Heart J 2006; 47: 107-123. (MLDB)

Takahashi T, Yu F, Zhu S, Moriya J, Sumino H, Morimoto S, Yamaguchi N, Kanda T. Beneficial effect of brewers' yeast extract on daily activity in a murine model of chronic fatigue syndrome. Evid Based Complement Alternat Med 2006; 3: 109-115. (MLDB)

Honda H, Iwahashi J, Kashiwagi T, Imamura Y, Hamada N, Anraku T, Ueda S, Kanda T, Takahashi T, Morimoto S. Outbreak of human metapneumovirus infection in elderly inpatients in Japan. J Am Geriatr Soc 2006; 54: 177-180. (MLDB)

ELSEVIER

International Journal of Cardiology 119 (2007) 310–318

International Journal of Cardiology

www.elsevier.com/locate/ijcard

Reduced-energy diet improves survival of obese KKAy mice with viral myocarditis: Induction of cardiac adiponectin expression

Tsugiyasu Kanda [a,*], Seiichiro Saegusa [a], Takashi Takahashi [a], Hiroyuki Sumino [c], Shigeto Morimoto [b], Takeshi Nakahashi [b], Kunimitsu Iwai [b], Masayuki Matsumoto [b]

[a] *Department of General Medicine, Kanazawa Medical University, 1-1 Daigaku, Uchinada-machi, Kahoku-gun, Ishikawa 920-0293, Japan*
[b] *Department of Geriatric Medicine, Kanazawa Medical University, 1-1 Daigaku, Uchinada-machi, Kahoku-gun, Ishikawa 920-0293, Japan*
[c] *Department of Medicine and Biological Science, Gunma University Graduate School of Medicine, 3-39-22 Showa-machi, Maebashi, Gunma 371-8511, Japan*

Received 9 March 2006; received in revised form 24 July 2006; accepted 29 July 2006
Available online 31 January 2007

Abstract

Obesity is an important risk factor for heart disease. Whether weight loss affects the severity of heart failure induced by viral myocarditis is a matter of debate. We hypothesized that weight loss could improve cardiac dysfunction by inducing cardiac expression of a cardioprotective cytokine, adiponectin. We examined the relationship between weight loss by food restriction and heart failure due to viral myocarditis in obese KKAy mice. We intraperitoneally injected encephalomyocarditis virus (500 plaque-forming units/mouse) into KKAy mice fed ad libitum as a control (CF) or 60% restriction of that eaten by ad libitum (RF). The 14-day survival rate was 0% in FF, whereas it was 23% in RF ($P<0.01$). Heart weight/body weight ratio in RF was lower than that in FF on day 5 after viral inoculation ($P<0.05$). Histological scores for myocardial necrosis and inflammation on day 5 were significantly lower in RF than in FF ($P<0.05$). Circulating adiponectin level on day 0 was significantly elevated in RF compared with that in FF (32+9 vs. 22+2 μg/mL, $P<0.05$). Comparative expression of cardiac adiponectin mRNA in RF was significantly higher than that in FF (5.1+0.3 vs. 1+0.2, $P<0.05$). Cardiac tumor necrosis factor-alpha (TNF-alpha) mRNA in RF was significantly decreased compared with that in FF on day 5 ($P<0.05$). Cardiac expression of nuclear factor kappa B was reduced and that of peroxisome proliferator-activated receptor gamma mRNA was increased in RF in comparison with FF on day 0. Cardiac adiponectin mRNA was negatively correlated with cardiac TNF-alpha mRNA ($r=-0.555$; $P=0.0097$).

Weight loss improved the survival and myocardial damage in obese mice with viral myocarditis, with cardiac induction of adiponectin. The induction of adiponectin might provide benefit through a cardioprotective effect against acute heart failure due to viral myocarditis in obese subjects.

Keywords: Obesity; Food restriction; Myocarditis; Adiponectin

1. Introduction

Obesity is an important risk factor for heart disease including congestive heart failure. Weight loss in obese patients can improve or prevent many obesity-related risk factors for heart failure through an improvement of metabolic regulation and inflammation [1,2], and can improve cardiac function [3]. Nutritional homeostasis is linked to inflammatory and immune reaction. In a recent review, a weight-management strategy is the primary therapy in obese patients [4]. Inflammatory viral myocarditis is a frequent and the cause of dilated cardiomyopathy. However, little is known about the relation between obesity and acute heart failure due to viral myocarditis.

Adiponectin is an adipocyte-specific protein which was found to be inversely correlated with obesity and cardiovascular disease [5–7]. Adiponectin also possesses anti-inflammatory

* Corresponding author. Tel.: +81 76 286 2211x3841; fax: +81 76 286 2702.
E-mail address: kandat@kanazawa-med.ac.jp (T. Kanda).

0167-5273/$ - see front matter © 2006 Elsevier Ireland Ltd. All rights reserved.
doi:10.1016/j.ijcard.2006.07.181

and anti-atherogenic properties [7,8]. Thus, increasing evidence supports the notion that body-weight reduction increases circulating adiponectin, suggesting that its production is under feedback inhibition in obesity [9].

The purpose of this experiment was to show that determine whether weight loss improved survival and myocardial damage in an obese KKAy mouse model with viral myocarditis. We showed enhanced expression of peroxisome proliferator-activated receptor γ (PPARγ) and reduced expression of nuclear factor κB (NF-κB) in the myocardium of lean KKAy compared with obese KKAy mice, and that an0 adiponectin, was also upregulated in heart tissue, inversely correlated with cardiac tumor necrosis factor-α (TNF-α) mRNA level.

2. Methods

2.1. Animal model

Eight-week-old female KKAy mice were purchased from Clea (Tokyo, Japan). KKAy mice at 9 weeks of age, confirmed to exhibit hyperglycemia, were randomly divided into two groups ($n=16$ in each group): regular food ad libitum as a control (CF) and 60% restriction of that eaten by ad libitum (RF) for 2 weeks. The D variant of the encephalomyocarditis (EMC) virus (obtained from Y. Seto, Keio University, Tokyo, Japan) was stored at −70 °C in Eagle's MEM supplemented with 0.1% fetal bovine serum until use. The mice were inoculated intraperitoneally with 500 plaque-forming units of EMC virus in 0.1 ml saline. No virus was detected by assay of viral titer on day 14. The animals were placed in isolated cages and fed a diet and water. The University Committee on Animal Care of Kanazawa Medical University approved the entire experimental protocol.

2.2. Measurement of plasma adiponectin and glucose

Plasma adiponectin was measured by RIA (Linco, St. Charles, MO). Sensitivity was 1 ng/ml. Blood glucose concentration was determined by glucose oxidase method using a Fuji Dry Chem System (Medical System Co., Tokyo, Japan).

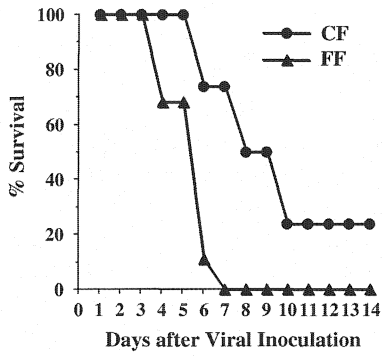

Fig. 1. Survival of KKAy mice after viral inoculation. Survival was significantly ($P<0.01$) improved in the group with 60% food restriction (RF) as compared with mice with food ad libitum as control (CF) after viral inoculation.

Table 1
Body weight and organ weight in KKAy mice after viral inoculation

	CF in KKAy mice		RF in KKAy mice	
Number	5	5	5	5
Days after inoculation	0	5	0	5
Body weight (g)	29.1+0.4	28.0+2.5	21.1+0.3*	22.8+0.2*
Thymus weight/Body weight ratio (mg/g)	2.83+0.22	1.99+0.27	2.29+0.15*	1.84+0.20
Spleen weight/body weight ratio (mg/g)	3.92+0.28	4.23+0.30	2.18+0.54*	4.25+0.46
Liver weight/body weight ratio (mg/g)	5.16+0.20	5.01+0.71	3.56+0.61*	4.66+0.93**
Blood glucose (mg/dl)	172+9	109+43	95+4*	103+22
Plasma adiponectin (μg/mL)	21.8+1.9	24.3+1.4	32.3+8.7*	27.4+0.4*

*$P<0.05$ vs. CF on the same day, CF; regular food ad libitum as a control, RF; 60% food intake.

2.3. Pathological examination

The heart and other organs were weighed. Body weight (BW) was also recorded. One half of each organ was fixed in 10% buffered formalin for tissue staining and for immunohistochemical studies; the other half was frozen for molecular study. Transverse sections of ventricular myocardium were graded for the severity of necrosis and mononuclear cell infiltration, with scoring from 1 to 4 as follows: grade 1, lesions involving <25% of the ventricular myocardium; grade 2, 25% to 50% of the myocardium; grade 3, 50% to 75% of the myocardium; and grade 4, 75% to 100% of the myocardium. The spleen, thymus, and liver were examined grossly and microscopically. Tissues were evaluated blindly by an experienced pathologist who was familiar with the grading of murine viral myocarditis and had no knowledge of the study design.

2.4. Measurement of myofiber diameter

In the lateral wall of the left ventricle, myocardial fiber diameter was determined by measuring the shortest diameter at the level of the nucleus of 50 myocardial fibers from each group with an ocular micrometer in stained cross-sections.

2.5. Immunohistochemical examination

To visualize the presence and anatomic localization of adiponectin within the myocardium, immunohistochemical studies were performed. Immunohistochemical staining was performed by the avidin biotin complex method (Vectastain ABC kit, Vector Laboratories, Burlingame, CA) previously described [10]. To minimize background staining, all sections were first blocked with normal goat serum for 20 min at room temperature. Next, the slides were incubated with an antibody directed against murine adiponectin (#ACRP303-A, Alpha-

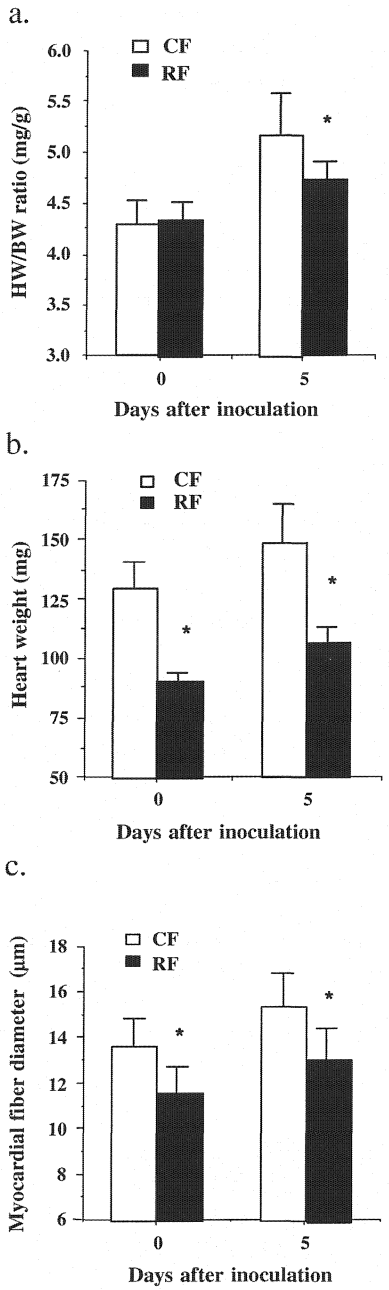

Fig. 2. Heart weight (HW), body weight (BW), and HW/BW ratio in KKAy mice after viral inoculation. HW/BW ratio and HW were significantly lower in RF than in CF ($P<0.01$). (Fig. 2-a, b). Myofiber diameter was significantly reduced in group RF than in group CF (Fig. 2-c, $P<0.01$).

Diagnostic International Inc., San Antonio, USA). Sections were counterstained with hematoxylin.

2.6. Viral titer in heart

The EMC viral titer in the heart was determined in terms of the viral cytopathic effect, and expressed as the tissue culture mean infectious dose (TCID50). On day 4 after inoculation ($n=3$ for each group), hearts were homogenized in 2 ml MEM. After centrifugation, the supernatants were added into 96-well microtiter plates containing human amnion cells in MEM supplemented with 10% fetal calf serum as described previously [10]. The microtiter plates were observed daily for 5 days for the appearance of any cytopathic effect.

2.7. Comparative expression levels of NF-κB, PPAR-γ, TNF-α, and adiponectin mRNA in heart

RNA extraction for each half of frozen cardiac tissue was performed as described by the manufacturer (RNeasy Mini Kit, QIAGEN Inc., Tokyo, Japan). Application of DNAase was performed during RNA extraction to avoid DNA contamination. The total RNA concentration was determined by measuring the optical density at 260 and 280 nm. Aliquots of 20 ml RNA from each tissue were used for production of cDNA. Comparative expression levels of PPAR-γ, NF-κB, TNF-α, and adiponectin mRNA in cardiac tissue from both groups were determined using quantitative real-time reverse transcriptase-polymerase chain reaction (RT-PCR) as described previously [10]. TaqMan MGB Probe (Applied Biosystems Inc., CA, USA) was applied for real-time PCR. We used a commercially available kit for NF-κB, PPAR-γ, TNF-α and adiponectin RT-PCR (Mm00440945 m1, Mm00456849 m1, Mm00443258 m1 and Mm00456425 m1, Applied Biosystems Inc.). Each threshold cycle number up to 50 cycles (Ct value) within the RT-PCR was examined for each mRNA level. The glyceraldehyde-3-phosphate dehydrogenase (GAPDH) gene was used as an endogenous internal standard, and was amplified with specific primers for the number of cycles. A negative control without template cDNA was always included. ΔCt values referred to differences between the Ct values for each target gene and the GAPDH gene. After confirming that the efficiency of amplification of each

Table 2
Histopathological and immunohistochemical findings in heart in KKAy mice

	CF in KKAy mice		RF in KKAy mice	
Number	5	5	5	5
Days after inoculation	0	5	0	5
Histopathological scores of heart				
Myocardial injury	0	2.1+0.6		1.1+0.4*
Inflammation	0	0.8+0.2		0.3+0.2*
Immunohistochemical staining of adiponectin				
Myocytes, myofibrils	+1	+2	+2	+3
Myocytes,	+1	+1	+1	+2
Epimysium	–	–	–	–
Interstitial cells	–	+1	–	+1
Inflammatory cells	+2	+2	+2	+2
Endothelial cells	–	–	–	–
Smooth muscle cells	–	–	–	–
Adventitia				

* $P<0.05$ vs. CF on same day.

molecule and GAPDH transcripts was approximately equal, the amount of NF-κB, PPAR-γ, TNF-α, or adiponectin transcript relative to the GAPDH transcript was determined using the comparative Ct method described in Perkin Elmer Applied Biosystems User Bulletin #2. Data are expressed as the fold-increase relative to the baseline value in the heart in mice with CF without viral inoculation.

2.8. Assay of natural killer (NK) cell activity

NK cell activity was assayed by a standard ^{51}Cr-release assay as described previously [10]. Briefly, YAC-1 tumor cells, which are NK-susceptible target cells, were labeled with ^{51}Cr and diluted to a concentration of 1×10^5 cells/ml in RPMI 1640 culture medium containing 10% fetal bovine serum. Spleen cells from mice (4 from each group) were suspended in the same medium and used as effector cells. Both the spleen cells and target YAC-1 cells were placed in round-bottomed 96-well microtiter plates at an effector cell/target cell ratio of 100:1, and incubated at 37 °C in a humidified chamber containing 5% CO_2 for 4 h. The cells were then harvested and counted in a gamma counter, and these procedures were repeated three times. The percentage of specific lysis was calculated as follows:

$$\% \text{ Lysis} = \text{Experimental release} - \text{Maximum spontaneous release} - \text{Spontaneous release} \times 100$$

2.9. Statistics

Data are presented as mean+S.D. Kaplan-Meier test was used to analyze differences in survival. The differences in scores of myocardial changes were examined by two-way analysis of variance. Scheffes' F test and Bonferroni/Dunn analysis were performed for confirmation. A value of $P<0.05$ was considered statistically significant.

3. Results

3.1. Survival

Survival was significantly improved in group RF as compared with group FF after viral inoculation ($P<0.01$, Fig. 1).

3.2. Organ weights

BW and HW in group RF on day 0, 3 and 5 after viral inoculation were significantly lower ($P<0.01$, Table 1, Fig. 2-b) than those in group CF. HW/BW ratio in group RF on day 0 was the same as that in group CF, but that in group RF on day 5 was significantly lower than that in group CF ($P<0.01$) (Fig. 2-a). Spleen weight/BW and thymus weight/BW ratios in group RF on day 0 were significantly lower ($P<0.01$) than those in group CF, but those on day 5 were not significantly different between the two groups. Liver weight/BW ratio on both days 0 and 5 was lower in group RF compared with group CF (Table 1).

3.3. Pathological findings

Myocardial necrosis with immune cell infiltration was observed in both groups on day 5. However, the score of myocardial necrosis on day 5 in group RF was significantly lower than that in group CF (Table 2, Fig. 3). Myofiber

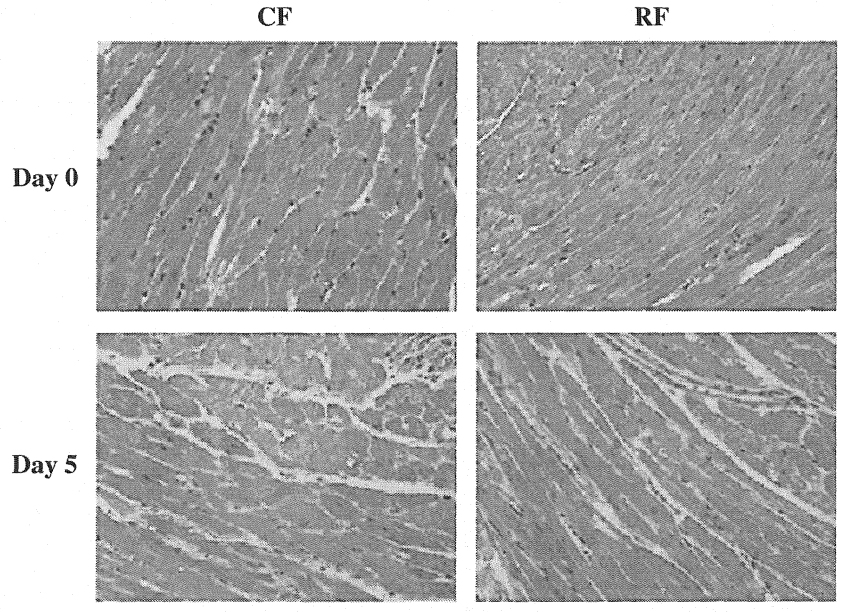

Fig. 3. Pathological findings in heart of KKAy mice after viral inoculation. Myocardial necrosis with immune cell infiltration was observed in both groups on day 5. However, myocardial necrosis on day 5 was reduced in group RF compared with group CF.

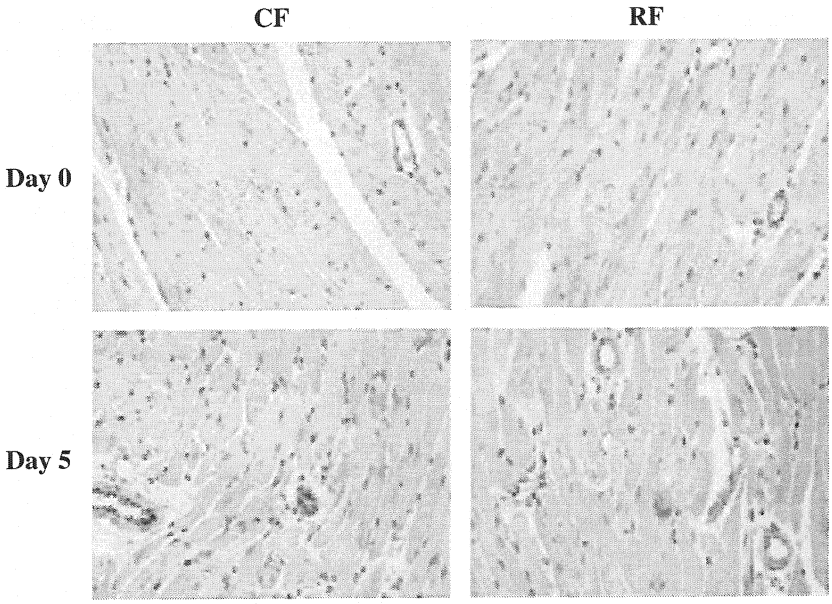

Fig. 4. Immunohistochemical findings. Localized expression of adiponectin in the heart was shown. Endothelial cells and myofibers showed positive expression in both groups on day 0.

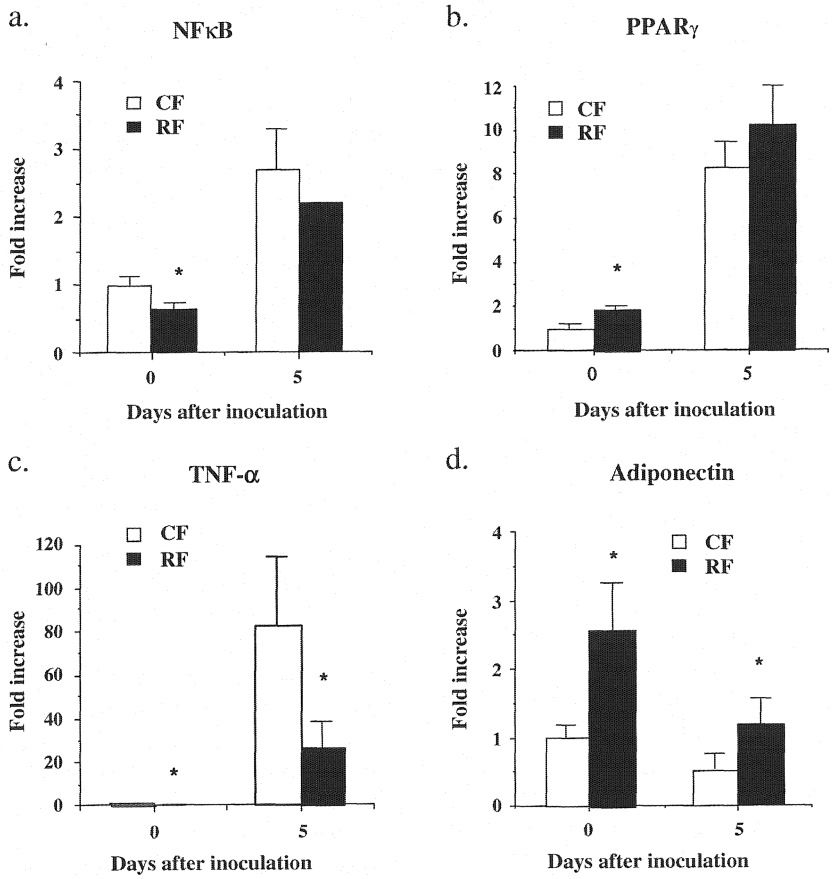

Fig. 5. Expression of cardiac NF-κB, PPAR-γ, TNF-α, and adiponectin mRNA by RT-PCR. The expression level of NF-κB mRNA in the heart in group RF was significantly lower than that in group CF on day 0 ($P<0.05$, $n=3$), those of PPAR-γ and adiponectin mRNA were significantly higher in group RF on day 0 ($P<0.05$, $n=3$), and that of adiponectin mRNA was significantly higher in group RF, but that of PPAR-γ mRNA was the same on day 5. TNF-α mRNA expression in the heart was significantly lower in RF than in CF on days 0 and 5 ($P<0.05$, $n=3$).

diameter was significantly smaller in group RF than in group FF ($P<0.05$, Fig. 2-c).

3.4. Immunohistochemical findings

Localized expression of adiponectin in the heart is shown in Table 2. Endothelial cells and myofibers showed positive adiponectin expression in both groups before viral infection (Fig. 4). Myofibers in group RF were slightly more positive than those in group CF. After infection, myofibers and the epimysium were highly positive and inflammatory cells were positive.

Immunohistochemical staining was scored by assessing the staining intensity. A staining intensity was rated as slight (+1), moderate (+2), and intense (+3) based on the intensity of staining uniformly visualized over the whole section. Back ground was considered as negative (0).

3.5. Expression of cardiac NF-κB, PPAR-γ, TNF-α, and adiponectin mRNA determined by RT-PCR

The expression level of NF-κB mRNA in the heart in group RF was significantly lower than that in group CF on day 0 ($P<0.05$, $n=3$), and those of PPAR-γ and adiponectin mRNA were significantly higher in group RF on day 0 ($P<0.05$, $n=3$). On day 5, the expression level of TNF-α

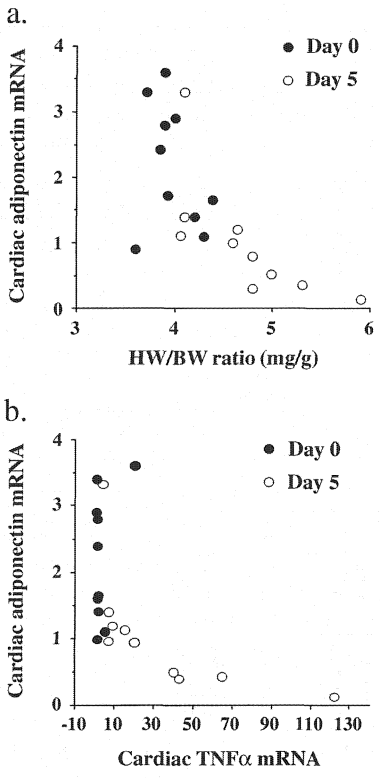

Fig. 6. Correlation of cardiac adiponectin and heart weight (HW)/body weight (BW) ratio, or TNF-α mRNA. There was a significant negative correlation between cardiac adiponectin mRNA and HW/BW ratio ($r=-0.493$; $P=0.0124$), and between cardiac adiponectin mRNA and TNF-α mRNA ($r=-0.555$; $P=0.0097$).

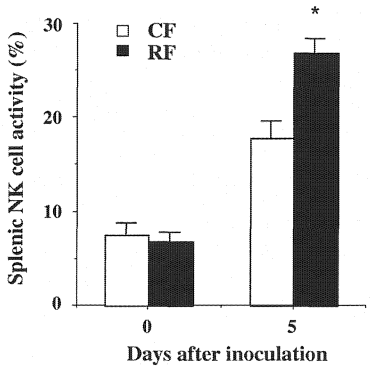

Fig. 7. Natural killer cell activity in spleen. NK cell activity in the spleen was significantly higher in group RF than in group FF on day 4 ($P<0.05$, $n=4$).

mRNA in the heart in group RF was still significantly lower than that in group CF ($P<0.05$, $n=3$, Fig. 5), and that of adiponectin mRNA was significantly higher in group RF, but PPAR-γ mRNA was the same in both groups (Fig. 5).

A significant negative correlation was found between cardiac adiponectin mRNA level and HW/BW ratio on day 0, 3 and day 5 after viral inoculation ($r=-0.701$; $P=0.0026$). There was also a significant negative correlation between cardiac adiponectin mRNA and TNF-α mRNA levels ($r=-0.555$; $P=0.0097$, Fig. 6).

3.6. Viral titer in heart

On day 4, the viral titer in the heart in group RF was significantly lower than that in group CF (3.2+0.2 vs. 3.6+0.2 TCID50/mg, $P<0.05$, $n=3$ for each).

3.7. NK cell activity in spleen

NK cell activity in the spleen in group RF was significantly higher than that in group CF on day 4 (27± 4% vs. 18±3%, $P<0.05$, $n=4$ for each, Fig. 7). There was no significant difference in NK cell activity on day 0.

4. Discussion

The present study showed that a restricted diet in obese KKAy mice improved the survival rate, decreased cardiac viral titer, increased splenic NK cell activity and reduced both myocardial necrosis and lymphocytic infiltration in mice with viral myocarditis. In addition, a reduced diet suppressed cardiac hypertrophy at the morphological and cellular levels. Therapeutic modulation of cardiac adiponectin might provide benefit through a cardioprotective effect against acute heart failure due to viral myocarditis in obese subjects. Cardiac adiponectin could be induced by activated PPARγ mRNA and reduced expression of NF-κB in the myocardium of mice with food restriction.

Obesity is increasingly viewed as an inflammatory state. General enhancement of adipose tissue-derived cytokine expression may be another plausible mechanism for the

inflammation/metabolic syndrome relationship. The role of adipose tissue as an endocrine organ capable of secreting a number of adipose tissue-specific or enriched hormones, known as adipokines, is gaining appreciation. An imbalance between increased inflammatory stimuli and decreased anti-inflammatory mechanisms is an intriguing working hypothesis. Adiponectin is negatively correlated with obesity, especially visceral fat masses and with lipid metabolism [11]. Adiponectin also suppresses activation of NF-κB [12]. Indeed, overweight rats showed higher PPARγ combined with inhibition of NF-κB [13].

Obesity frequently leads to left ventricular hypertrophy [14]. It associated with a chronically high cardiac workload due to the need to supply more blood to peripheral tissues. The high cardiac output is mainly a consequence of the greater requirements of increased lean body mass, and is maintained by an increased stroke volume and high normal heart rate, which is sustained by an increase in ventricular mass. The increase in left ventricular mass also implies an increase in non-muscular tissue, which plays a role in the development of electrical abnormalities, heart failure and sudden death. Obesity per se is a major risk factor for heart failure [14]. Our results showed that a reduced diet induced a reduction in cardiac hypertrophy in obese KKAy mice without infection. Therefore, weight reduction leads to decreased left ventricular mass and reduces the risk of cardiac death. A reduction of cardiac hypertrophy by adiponectin has been reported. Shibata et al. showed that adiponectin inhibits hypertrophic signaling in the myocardium through activation of AMP-activated protein kinase [15]. They also suggested that adiponectin could be used to treat cardiac hypertrophy such as hypertrophic cardiomyopathy associated with obesity-related diseases. Therefore, reduced diet in obese mice could inhibit cardiac hypertrophy through the induction of cardiac expression of adiponectin mRNA.

Food restriction and subsequent weight loss increased adiponectin expression of visceral fat in an obese rat model [16]. Previous observations showed that plasma adiponectin is decreased in obese rodents [17], and chronic caloric restriction is able to enhance the circulating level of this protein [18]. Also, in humans, weight loss increases plasma adiponectin level despite a reduction of adipose tissue [9]. All these observations taken together suggest that adiponectin expression is under feedback inhibition in obesity. The effect of weight loss on the metabolic syndrome attributes cardiovascular function [19]. In a cohort of outpatients, a higher body mass index was associated with higher mortality risk. Overweight and obese patients had a higher risk of death compared with those with a healthy weight [20]. Weight loss, particularly in persons who are severely obese, can improve cardiac structure and function [3]. In our results, adiponectin was expressed in the heart and was upregulated by food restriction in an obese mouse model.

Cardiac expression of adiponectin has been reported in autopsy cases [21,22]. Adiponectin was distributed in the interstitium of infarcted lesions at an early stage, and was present linearly both along the border of vital myocardium and at the periphery of surviving cardiomyocytes around the lesion in the granulation stage [21]. We have reported that adiponectin and its receptor were expressed in injured myocardium in autopsy cases of cardiomyopathy [22]. A recent report showed that adiponectin inhibited NF-κB activation and increased PPARγ expression in adipocytes [12]. Therefore, increased expression of cardiac adiponectin in food-restricted mice may suppress local inflammation via its regulation of the NF-κB and PPARγ transcription factors.

PPARγ is a transcription factor belonging to the nuclear receptor superfamily and is present in a variety of cells including myocardium [23,24]. Myocardium uses either fatty acid or glucose oxidation as the main energy source. Fatty acid oxidation is transcriptionally regulated by the fatty acid activated PPAR superfamily. We suggest that PPARγ may directly regulate cardiac inflammation, which plays a critical role in the progression of cardiac remodeling and dysfunction. A previous report showed that PPAR activators inhibit lipopolysaccharide-induced TNF-α expression in neonatal rat cardiac myocytes, and that this effect of PPARγ would be beneficial in preventing the development of congestive heart failure [23]. In the present study, we demonstrated that enhanced expression of PPARγ suppresses the development of heart failure due to viral myocarditis, associated with induced expression of cardiac adiponectin and suppressed cardiac TNF-α expression. Indeed, it has been reported that PPAR ligands could downregulate inflammatory responses, and stimulation of PPARγ blocked viral replication and TNF-α production in blood cells [25,26].

NF-κB is a central mediator of host immune responses, and activation of NF-κB enhances viral replication and evasion of immune responses [27]. Our data showed lower NF-κB mRNA in the heart of food-restricted mice than in obese mice. Decreased expression of cardiac NF-κB could reduce viral replication and inflammation in the heart through weight loss by food restriction. In a recent report, NF-κB was required for the hypertrophic response of cardiomyocytes in vitro [28]. Indeed, our data showed decreased heart weight and lower myofiber diameter by food-restriction in comparison with obese mice with downregulation of NF-κB expression.

Impaired immune function linked to obesity has been shown in both human and animal studies [29]. Diet control is also effective for impaired immune function including NK cell activity in obese animals [30]. A study of obese humans showed that removal of a significant amount of subcutaneous fat tissue had no effect on inflammatory markers [31]. Genesis of inflammatory reaction may be not due to adipose tissue but due to other organs, such as the heart, in obese subjects.

Cardiac expression of adiponectin mRNA was negatively correlated with cardiac TNF-α mRNA expression in this study. TNF-α is secreted primarily by myocytes and macrophages after injury [32]. Elevation of TNF-α has been shown to contribute to ventricular dysfunction, using TNF-α knockout mice [33]. A previous study has demonstrated that cardiac-specific expression of TNF-α results in

myocardial inflammation, cardiac hypertrophy, progressive dilatation, and increased apoptosis, leading to heart failure and death [34]. TNF-α play an important role in modulating left ventricular dysfunction [35]. A recent study showed a relation between adiponectin and TNF-α in adiponectin knockout mice [36], which demonstrated higher TNF-α expression in adipose tissue, and the administration of adiponectin resulted in a decrease in TNF-α expression. Thus, TNF-α and adiponectin are antagonists of each other, or one cytokine control the expression of the other [37]. Weight loss altered the cytokine expression in heart tissue, where adiponectin was inversely expressed with TNF-α.

The therapeutic implication of diet control in obese subjects is the prevention of acute heart failure with viral myocarditis with cardiac expression of adiponectin and TNF-α. Diet control is also beneficial in regulation of the immune reaction against cardiotropic viral infection.

Acknowledgements

This study was supported in part by a grant to promote research from Kanazawa Medical University (S2005-5), a grant for Project Research from the High-Technology Center of Kanazawa Medical University (H2004-7), and a Grant-in-Aid for Scientific Research (C) from the Ministry of Education, Science and Culture of Japan (T. Kanda, No. 17590767).

References

[1] Clinical guidelines on the identification, evaluation, and treatment of overweight and obesity in adults. The Evidence Report. National Institutes of Health. Obes Res 1998;6:51S–209S.
[2] Sjostrom CD, Lissner L, Wedel H, Sjostrom L. Reduction in incidence of diabetes, hypertension and lipid disturbances after intentional weight loss induced by bariatric surgery: the SOS Intervention Study. Obes Res 1999;7:477–84.
[3] Alpert MA, Terry BE, Kelly DL. Effect of weight loss on cardiac chamber size, wall thickness and left ventricular function in morbid obesity. Am J Cardiol 1985;55:783–6.
[4] Klein S, Burke LE, Bray GA, et al. Clinical implications of obesity with specific focus on cardiovascular disease: a statement for professionals from the American Heart Association Council on Nutrition, Physical Activity, and Metabolism: endorsed by the American College of Cardiology Foundation. Circulation 2004;110:2952–67.
[5] Arita Y, Kihara S, Ouchi N, et al. Paradoxical decrease of an adipose-specific protein, adiponectin, in obesity. Biochem Biophys Res Commun 1999;257:79–83.
[6] Lihn AS, Sterged T, Nyholm B, Pedersen SB, Richelsen B, Schmitz O. Adiponectin mRNA expression in subcutaneous adipose tissue is reduced in first-degree relatives of type 2 diabetic patients. Am J Physiol Endocrinol Metab 2003;284:E443–8.
[7] Ouchi N, Kihara S, Arita Y, et al. Novel modulator for endothelial adhesion molecules: adipocyte-derived plasma protein adiponectin. Circulation 1999;100:2473–6.
[8] Matsuzawa Y. Therapy insight: adipocytokines in metabolic syndrome and related cardiovascular disease. Nat Clin Pract 2006;3:35–42.
[9] Yang WS, Lee WS, Funahashi T, et al. Weight reduction increases plasma levels of an adipose-derived anti-inflammatory protein, adiponectin. J Clin Endocrinol Metab 2001;86:3815–9.
[10] Kanda T, McManus JE, Yang DC, et al. Modification of viral myocarditis in mice by interleukin-6. Circ Res 1996;78:848–58.
[11] Kwon K, Jung SH, Choi C, Park SH. Reciprocal association between visceral obesity and adiponectin: in healthy menopausal women. Int J Cardiol 2005;101:385–90.
[12] Ajuwon KM, Spurlock ME. Adiponectin inhibits LPS-induced NF-kappaB activation and IL-6 production and increases PPARgamma2 expression in adipocytes. Am J Physiol Regul Integr Comp Physiol 2005;288:R1220–5.
[13] Lamas O, Moreno-Aliaga MJ, Martinez JA, Marti A. NF-kappa B-binding activity in an animal diet-induced overweightness model and the impact of subsequent energy restriction. Biochem Biophys Res Commun 2003;311:533–9.
[14] Contaldo F, Pasanisi F, Finelli C, de Simone G. Obesity, heart failure and sudden death. Nutr Metab Cardiovasc Dis 2002;12:190–7.
[15] Shibata R, Ouchi N, Ito M, et al. Adiponectin-mediated modulation of hypertrophic signals in the heart. Nat Med 2004;10:1384–9.
[16] Milan G, Granzotto M, Scarda A, et al. Resistin and adiponectin expression in visceral fat of obese rats: effect of weight loss. Obes Res 2002;11:1095–103.
[17] Hu E, Liang P, Spiegelman BM. AdipoQ is a novel adipose-specific gene dysregulated in obesity. J Biol Chem 1996;271:10697–703.
[18] Berg AH, Combs TP, Du X, Brownlee M, Scherer PE. The adipocyte-secreted protein Acrp30 enhances hepatic insulin action. Nat Med 2001;7:947–53.
[19] Eyre Harmon, Kahn Richard, Robertson Rose Marie, et al. Preventing cancer, cardiovascular disease, and diabetes: a common agenda for the American Cancer Society, the American Diabetes Association, and the American Heart Association. Circulation 2004;109:3244–55.
[20] Curtis JP, Selter JG, Wang Y, et al. The obesity paradox: body mass index and outcomes in patients with heart failure. Arch Intern Med 2005;165:55–61.
[21] Ishikawa Y, Akasaka Y, Ishii T, et al. Changes in the distribution pattern of gelatin-binding protein of 28 kDa (adiponectin) in myocardial remodelling after ischaemic injury. Histopathology 2003;42:43–52.
[22] Takahashi T, Saegusa S, Sumino H, et al. Adiponectin, T-cadherin and tumor necrosis factor-alpha in damaged cardiomyocytes from autopsy specimens. J Int Med Res 2005;33:236–44.
[23] Takano H, Nagai T, Asakawa M, et al. Peroxisome proliferator-activated receptor activators inhibit lipopolysaccharide-induced tumor necrosis factor-alpha expression in neonatal rat cardiac myocytes. Circ Res 2000;87:596–602.
[24] Vidal-Puig AJ, Considine RV, Jimenez-Linan M, et al. Peroxisome proliferator-activated receptor gene expression in human tissues: effects of obesity, weight loss, and regulation by insulin and glucocorticoids. J Clin Invest 1997;99:2416–22.
[25] Ricote M, Li AC, Willson TM, Kelly CJ, Glass CK. The peroxisome proliferator-activated receptor is a negative regulator of macrophage activation. Nature 1998;391:79–82.
[26] Skolnik PR, Rabbi MF, Mathys JM, Greenberg AS. Stimulation of peroxisome proliferator-activated receptors alpha and gamma blocks HIV-1 replication and TNF alpha production in acutely infected primary blood cells, chronically infected U1 cells, and alveolar macrophages from HIV-infected subjects. J Acquir Immune Defic Syndr 2002;31:1–10.
[27] Hiscott J, Kwon H, Gein P. Hostile takeovers: viral appropriation of the NF-κB pathway. J Clin Invest 2001;107:143–51.
[28] Purcell NH, Tang G, Yu C, Mercurio F, diDonato JA, Lin A. Activation of NF-kB is required for hypertrophic growth of primary rat neonatal ventricular cardiomyocytes. Proc Natl Acad Sci U S A 2001;98:6668–73.
[29] Nieman DC, Henson DA, Nehlsen-Cannarella SL, et al. Influence of obesity on immune function. J Am Diet Assoc 1999;99:244–9.
[30] Lamas O, Martinez JA, Marti A. Energy restriction restores the impaired immune response in overweight (cafeteria) rats. J Nutr Biochem 2004;15:418–25.
[31] Klein S, Fontana L, Young VL, et al. Absence of an effect of liposuction on insulin action and risk factors for coronary heart disease. N Engl J Med 2004;350:2549–57.

[32] Kapadia SR, Oral H, Lee J, Nakano M, Taffet GE, Mann DL. Hemodynamic regulation of tumor necrosis factor-alpha gene and protein expression in adult feline myocardium. Circ Res 1997;81:187–95.
[33] Sun M, Dawood F, Wen WH, et al. Excessive tumor necrosis factor activation after infarction contributes to susceptibility of myocardial rupture and left ventricular dysfunction. Circulation 2004;110:3221–8.
[34] Yue P, Massie BM, Simpson PC, Long CS. Cytokine expression increases in nonmyocytes from rats with postinfarction heart failure. Am J Physiol 1998;275:H250–8.
[35] Yokoyama T, Vaca L, Rossen RD, Durante W, Hazarika P, Mann DL. Cellular basis for the negative inotropic effects of tumor necrosis factor-alpha in the adult mammalian heart. J Clin Invest 1993;92:2303–12.
[36] Maeda N, Shimomura I, Kishida K, et al. Diet-induced insulin resistance in mice lacking adiponectin/ACRP30. Nat Med 2002;8:731–7.
[37] Lihn AS, Richelsen B, Pedersen SB, et al. Increased expression of TNF-alpha, IL-6, and IL-8 in HALS: implications for reduced adiponectin expression and plasma levels. Am J Physiol Endocrinol Metab 2003;285:E1072–80.

Cardiovasc Drugs Ther (2007) 21:155–160
DOI 10.1007/s10557-007-6024-4

Oral Administration of Candesartan Improves the Survival of Mice with Viral Myocarditis through Modification of Cardiac Adiponectin Expression

Seiichiro Saegusa · Yu Fei · Takashi Takahashi · Hiroyuki Sumino · Junji Moriya · Ken Kawaura · Jun-ichi Yamakawa · Tohoru Itoh · Shigeto Morimoto · Takeshi Nakahashi · Kunimitsu Iwai · Masayuki Matsumoto · Tsugiyasu Kanda

Published online: 5 May 2007

Abstract
Purpose We examined the effects of the angiotensin II receptor type1 blocker candesartan on myocarditis injury in a murine model of acute myocarditis. We hypothesized that candesartan improves cardiac damage by inducing cardiac expression of adiponectin.
Methods and results We examined changes in heart failure caused by myocarditis in mice by candesartan based on induction of cardiac adiponectin expression. We intraperitoneally injected encephalomyocarditis virus in C3H mice, then orally administered candesartan (10 mg/kg/day) or vehicle (control). The 7 day survival rate was 18% in the control group, but 60% in the candesartan group. The heart weight/body weight ratio in the candesartan group was significantly lower than in the control group. Circulating adiponectin concentrations on day 7 were significantly higher in the candesartan group compared with the control group (7.91±0.61 vs. 6.04±2.26 μg/ml, $P<0.05$). Comparative expression of cardiac adiponectin mRNA in the candesartan group was significantly higher than in the control group on day 7 (55.4±41.3 vs. 5.3±7.7, $P<0.05$). Immunohistochemical staining and in situ hybridization showed that cardiac expression of adiponectin protein and mRNA was present in the candesartan group on day 7.
Conclusion Oral administration of candesartan improves survival and decreases myocardial damage in mice with viral myocarditits and induces expression of cardiac adiponectin. The induction of adiponectin might provide cardioprotective effects against acute heart failure due to viral myocarditis.

Key words candesartan · myocarditis · adiponectin · acute heart failure

S. Saegusa · Y. Fei · T. Takahashi · J. Moriya · K. Kawaura · J. Yamakawa · T. Itoh · T. Kanda (✉)
Departments of General Medicine, Kanazawa Medical University,
1-1, Daigaku, Uchinada-machi,
Kahoku-gun, Ishikawa 920-0293, Japan
e-mail: kandat@kanazawa-med.ac.jp

S. Morimoto · T. Nakahashi · K. Iwai · M. Matsumoto
Departments of Geriatric Medicine,
Kanazawa Medical University,
1-1, Daigaku, Uchinada-machi,
Kahoku-gun, Ishikawa 920-0293, Japan

H. Sumino
Department of Nursing,
Takasaki University of Health and Welfare,
501, Nakaorui-machi,
Takasaki-shi, Gunma 370-0033, Japan

Introduction

Acute myocarditis is a potentially lethal disease, and frequently precedes the development of dilated cardiomyopathy [1]. A murine model of vial myocarditis induced by the encephromyocardits (EMC) virus is associated with a high incidence of severe myocarditis, congestive heart failure, and dilated cardiomyopathy [2].

Recently, we and others have reported that treatment with angiotensin II type1 blockers (ARB) reduces viral-mediated myocardial injury [3, 4]. ARB has been shown to have anti-inflammatory properties in vitro and animal studies. In the setting of cardiovascular diseases, ARB reduce the expres-

sion of inflammatory cytokines including tumor necrosis factor-α (TNF-α) and its transcriptional factors [5–7].

Adiponectin is an anti-inflammatory and anti-atherogenic cytokine [8]. ARB treatment increases circulating adiponectin concentrations in human [9] and in mice [10, 11]. ARB treatment increases circulating adiponectin mRNA in fat tissue in hypertensive rats [12]. Our previous study showed that acute myocarditis is unknown. The purpose of this study was to examine the role of the ARB, candesartan, in mice with acute viral myocarditis, focusing on its effect on cardiac expression of adiponectin as well as cardiac TNF-α mRNA.

Materials and methods

Animal model

Eight-week-old C3H mice were purchased from Clea (Tokyo, Japan). At 9 weeks of age the mice were divided randomly into two groups (n=30 in each group) for either candesartan treatment at a daily dose of 10 mg/kg for 7 days starting from on the day of viral infection (candesartan group) or treatment with vehicle alone (control group). Uninfected mice (n=5) also were studied. The D variant of the encephalomycarditis (EMC) virus (obtained from Y. Seto, Keio University, Tokyo, Japan) was stored at −70°C in Eagle's MEM supplemented with 0.1% fetal bovine serum until use. The mice were injected intraperitoneally with 500 plaque-forming units of EMC virus in 0.1 ml of saline. No virus was detected by viral titer assay on day 14. The animals were placed in isolation cages and fed a standard diet and water. The University Committee on Animal Care of Kanazawa Medical University approved the entire experimental protocol.

Measurement of plasma adiponectin

Blood sample were obtained from all mice before killing by cervical distillation. All serum samples were stored at −80°C until analysis. The circulating concentrations of adiponectin were measured by enzyme linked immunosorbent assay (ELISA), according to the manufacturers' instructions (ELISA kit for mouse or rat adiponectin, Otsuka Pharmaceutical, Tokyo, Japan). This kit used for adiponectin demonstrated a sensitivity, intra-assay variation, and cross-reactivity of 0.25 ng/ml, <10%, and no responses for specimens from other animals including sheep, respectively.

Histologic examination

The body weight and heart weight were determined. One half of each organ was fixed in 10% buffered formalin for tissue staining and immunohistochemical studies; the other half was frozen for molecular analysis. Transverse sections of ventricular myocardium were graded for the severity of necrosis and mononuclear cell infiltration as follows: grade 1, lesions involving <25% of ventricular myocardium; grade 2, lesions involving 25–50% of the myocardium; grade 3, lesions involving 50–75% of the myocardium; and grade 4, lesions involving 75–100% of the myocardium.

Imunohistochemical examination

To visualize the present and anatomic localization of adiponectin within the myocardium, immunohistochemical studies were performed. Imunohistochemistry was performed by the avidin biotin complex method (Vectastain ABC kit, Vector laboratories, Burlingame, CA) as previously described [13]. To minimize background staining, all sections first were blocked with normal goat serum for 20 min at room temperature. Next, the slides were incubated with an antibody directed against murine adiponectin (#ACRP303-A, Alpha-Diagnostic International, San Antonio, Tx) or against murine TNF-α (#AF-410-NA, R&D systems, Minneapolis, MN). Sections were counterstained with hematoxylin.

In situ hybridization for adiponectin mRNA in the heart

To investigate the localization of adiponectin mRNA in the heart in heart, in situ hybridization was performed on myocardial sections using an adiponectin antisense RNA probe as reported previously [14].

Comparative expression levels of adiponectin and TNF-α mRNA in hearts

RNA extraction from half the frozen cardiac tissue was performed as described by the manufacturer (RNeasy Mini Kit, QIAGEN, Tokyo, Japan). DNAase treatment was

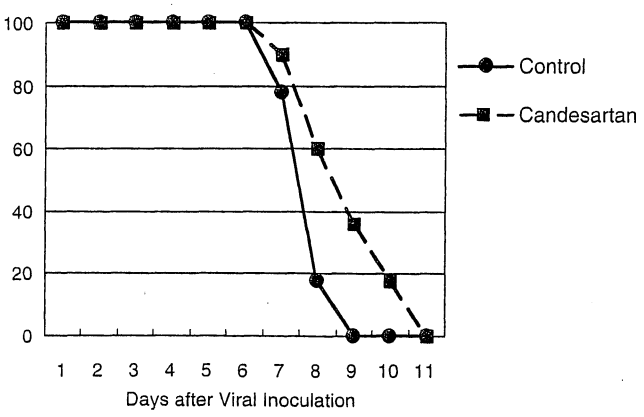

Fig. 1 Survival in mice after viral infection. Survival was significantly (P<0.05) improved in the Candesartan group

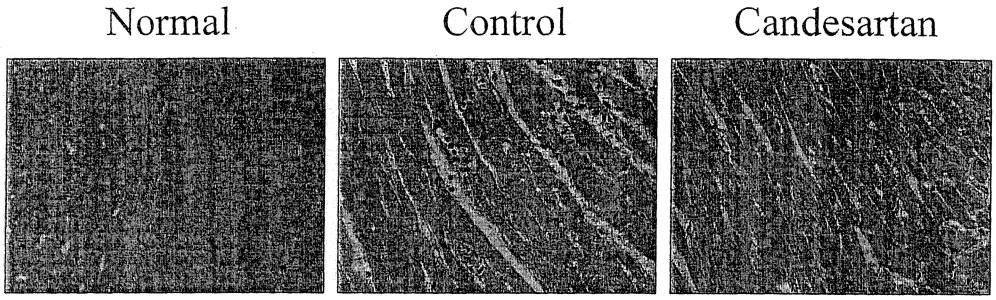

Fig. 2 Hematoxylin and eosin stains shows that myocardial injury with immune cell infiltration was observed in the Control group on day 7. However, the degree of myocardial injury was reduced on day 7 in the Candesartan group. Myofiber diameter was reduced in the Candesartan group compared with the Control group

performed during the RNA extraction to avoid DNA contamination. The total RNA concentration was determined by measuring the optical density of the sample at 260 and 280 nm. Aliquots of 20 μl RNA and TNF-α mRNA in cardiac tissue from both groups were determined using a quantitative real-time reverse transcriptase-polymerase chain reaction (RT-PCR) as described previously [13]. We used TaqMan MGB probe (Applied Biosystems, San Diego, CA) for the RT-PCR. We used a commercially available kit for adiponectin and TNF-α RT-PCR (Mm00443258 ml and Mn00456425 ml, Applied Biosystems, San Diego, CA). The glyceraldehydes-3-phosphate dehydrogenase (GAPDH) gene was used as an endogenous internal standard, and was amplified with specific primers. A negative control without templates cDNA was always included. The ΔCt values referred to differences between the Ct value for the target gene and the GAPDH transcripts were approximately equal, the amount of the adiponectin or TNF-α transcript relative to the GAPDH transcript was determined using the comparative Ct method as described in Perkin Elmer Applied Biosystem User Bulletin #2. Values are expressed as fold-increases relative to the baseline values for hearts frome uninfected normal mice.

Statistics

Data are reported as mean ± S.D. The Kaplan–Meier test was used to analyze differences in survival. The differences in the scores for myocardial changes were examined by two-way analysis of variance to reveal the combined effect of two different agents. Scheffes' F test and Bonferroni/Dunn analysis were used for confirmation. A value of $P<0.05$ was considered statistically significant.

Results

Survival

Survival was significantly improved in the candesartan group compared to the control group after viral infection ($P<0.05$, Fig. 1).

Organ weights

The body weight was significantly higher in the control group than in the uninfected normal mice and the heart weight was significantly greater in the control group than in

Table 1 Heart weight, histologic findings, and cytokine mRNA expression in mice 7 day after viral infection

	Normal	Control	Candesartan
Number	5	7	7
Body weight (g)	18.3±7.7	15.5±4.2[a]	17.5±3.3[a, b]
Heart weight (mg)	93.5±9.4	112.2±12.9[a]	97.4±10.6[a, b]
Heart weight/body weight ratio (mg/g)	5.1±0.7	7.2±1.1[a]	5.6±0.8[a, b]
Plasma adiponectin (μg/ml)	7.09±1.32	6.04±2.26[a]	7.91±0.61[a, b]
Histipathologic scores of the heart			
Myocardial injury	ND.	2.4±1.0[a]	1.5±0.7[a, b]
Inflammation	ND.	2.1±0.9[a]	1.1±0.4[a, b]
Myofiber diameter(μm)	12.6±1.2	15.4±1.9[a]	13.8±1.4[a, b]
Adiponectin mRNA	1±0.2	5.3±7.7[a]	55.4±41.3[a, b]
TNF-α mRNA	1±0.3	63.6±8.0	5.2±2.3[a, b]

Values are mean ± SD. [a] $P<0.05$ vs. normal group, [b] $P<0.05$ vs. Control
ND. non detectable

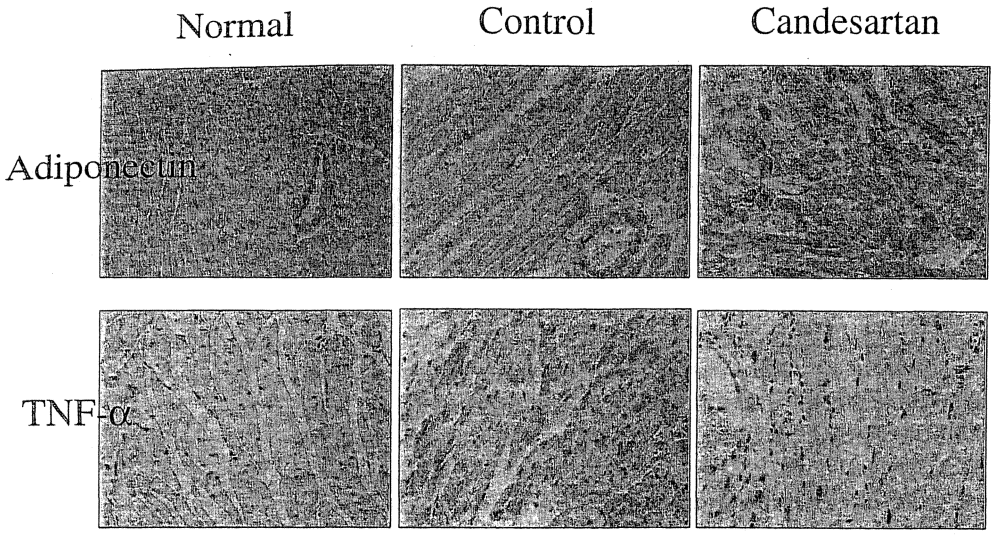

Fig. 3 Immunohistochemical staining in the heart of uninfected normal mice (Normal), untreated control mice on day 7 after viral infection (Control), and candesartan-treated mice (Candesartan). Immunohistochemical staining showed that cardiac expression of adiponectin and TNF-α was almost absent in normal mice, except in the vascular wall for adiponectin was strongly positive in the myocardium in the Candesartan group. Injured myocytes expressed TNF-α in the Control group on day 7, and endothelial cells and myofibers were weakly positive in the Candesartan group

normal mice (Fig. 2). The body weight and heart weight in the candesartan group on day 7 after viral infection was significantly lower than in the control group ($P<0.05$, Table 1).

Histological findings

Myocardial necrosis with immune cell infiltration was observed in both groups on day 7. However, the myocardial necrosis score on day 7 in the candesartan group was significantly lower than in the control group (Table 1). Myofiber diameter was significantly reduced in the candesartan group compared to the control group ($P<0.05$, Table 1).

Immunohistochemical findings

Cardiac expression of adiponectin protein was present in the candesartan group on day 7 but the finding was only slightly positive in the control group (Fig. 3). Staining in the normal heart was negative. Staining for cardiac TNF-α protein was strongly positive in the control group but was weakly positive in the candesartan group on day 7. In normal mice, staining for cardiac TNF-α protein was negative.

In situ hybridization for adiponectin mRNA in the heart

The genomic expression of adiponectin mRNA in transverse ventricular sections largely overlapped with that of adiponectin protein observed using the immunohistochemical and RT-PCR methods. Infected myocytes in the candesartan group were moderately to strongly positive on day 7. However, the absence of adiponectin mRNA was noted in myocytes from normal uninfected mice. There was hardly any adiponectin signal in the myocardium from control mice at the same time points (Fig. 4).

Expression of cardiac adiponectin and TNF-α mRNA by RT-PCR

Cardiac adiponectin mRNA expression was significantly higher in the candesartan group than in the control group. Cardiac TNF-α mRNA expression was significantly lower

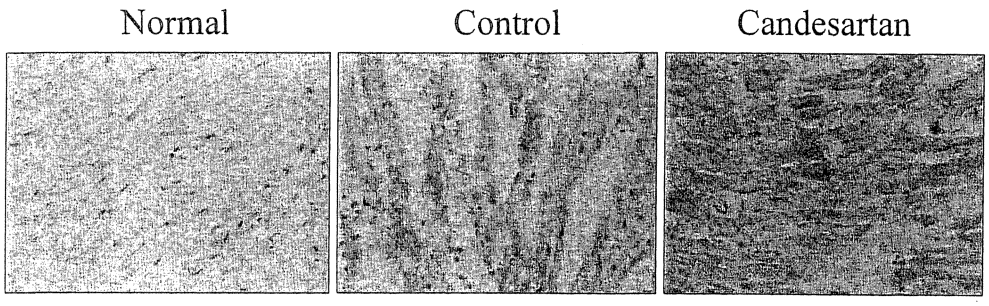

Fig. 4 Detection of adiponectin mRNA (normal) by in situ hybridization in myocardium from mice on day 7 after viral infection. Adiponectin mRNA was absent in myocytes from uninfected normal mouse. A moderate to strong signal for adiponectin mRNA was detected in myocytes from Candesartan treated mice 7 day after viral inoculation. There was a slightly positive adiponectin signal in the myocardium from infected control mice at the same time

in the candesartan group than in the control group (Table 1). Cardiac adiponectin and TNF-α mRNA expression were significantly increased in the control group compared to normal mice.

Discussion

We have shown that oral administration of candesartan improves survival rates, decreases myocardial necrosis, and decreases lymphocyte infiltration in mice with viral myocarditis. In addition, candesartan treatment increases the cardiac expression of adiponectin, which might provide cardioprotective effects against acute heart failure due to viral myocarditis by reducing the expression of cardiac TNF-α.

Adiponectin protein was distributed in the interstitium of infarcted lesions at an early stage. Adiponectin was found both along the border of viable myocardium and at the periphery of surviving cardiomyocytes around lesions at the granulative stage [15]. There was minimal expression of cardiac adiponectin by ISH after viral infection, the infected myocardium showed moderate to strong signal for adiponectin mRNA in myocytes from mice treated with candesartan on day7 in comparison with untreated myocardium. We also reported that adiponectin and its receptor are expressed in the injured myocardium in patients with cardiomyopathy [13]. Although the role of adiponectin in the myocardium is not clear, enhanced expression of cardiac adiponectin on the protein and mRNA level by candesartan treatment would be beneficial in the suppression in murine model of viral myocarditis.

Candesartan therapy has already been reported to reduce cardiac necrosis and inflammation in a murine model of viral myocarditis by Tanaka et al. [16]. However, they showed that the survival of mice receiving 10 mg/kg of candesartan did not improve significantly. Our data showed the improved survival by the same dose of candesartan. This difference may depend on haplotype of mice, which may affect the susceptibility of EMC virus infection.

Candesartan treatment reduces inflammation and lowers plasma CRP concentration in hypertensive patients [17]. Candesartan increases circulating adiponectin concentration in human [9, 18] and in diabetic mice [11]. Candesartan also increases adiponectin mRNA in fat tissue in hypertensive rat [12]. Our data showed that enhanced expression of myocardial adiponectin mRNA and protein was identified with the reduction of myocardial injury through candesartan treatment in a murine model of viral myocarditis. Candesartan could induced cardiac adiponectin expression in acute heart failure.

TNF-α is secreted primarily by myocytes and macrophages after injury [19]. Increased TNF-α expression contributes to extending ventricular dysfunction [20]. Previous studies have demonstrated that cardiac-specific expression TNF-α results in myocardial inflammation, cardiac hypertrophy, progressive dilation, and increased apoptosis, which leads to heart failure and death [21]. TNF-α may play an important role in modulating left ventricular dysfunction [22]. A recent study described the relationship between adiponectin and TNF-α in adiponectin knockout mice [23]. Adiponectin knockout mice demonstrated higher TNF-α expression and the administration of adiponectin resulted in decrease in TNF-α expression. Thus, TNF-α and adiponectin may be antagonist of each other or one cytokine may control the expression of the other [24].

We conclude that oral administration of candesartan is beneficial for the prevention of viral myocarditis through cardiac expression of the anti-inflammatory cytokine, adiponectin, which suppresses expression of the inflammatory cytokine, TNF-α. Further studies will be needed to clarify the cardiac adiponectin signaling by using agents to modify adiponectin regulation.

Acknowledgements This study was supported in part by a grant for promoted research from Kanazawa Medical University (S2005-5), a grant for Project Research from the High-technology Center of Kanazawa Medical University (H2004-7), and research grant from Grant-in-Aid for Scientific Research©, the Ministry of Education, Science and Culture of Japan (T. Kanda, No.17590767).

References

1. Nimata M, Kishimoto C, Yuan Z, Shioji K. Beneficial effects of olmesartan, a novel angiotensin II receptor type 1 antagonist, upon acute autoimmune myocarditis. Mol Cell Biochem 2004;259:217–22.
2. Kanda T, McManus JE, Yang DC, McManus BM, Imai S, Suzuki T, et al. Modification of viral myocarditis in mice by interleukin-6. Circ Res 1996;78:848–58.
3. Araki M, Kanda T, Imai S, Suzuki T, Murata K, Kobayashi I. Comparative effects of losartan, captopril, and enalapril on murine acute myocarditis due to encephalomyocarditis virus. J Cardiovasc Pharmacol 1995;26:61–5.
4. Shirai K, Watanabe K, Ma M, Wahed MI, Inoue M, Saito Y, et al. Effects of angiotensin-II receptor blocker candesartan cilexetil in rats with dilated cardiomyopathy. Mol Cell Biochem 2005;269:137–42.
5. Wu L, Iwai M, Nakagami H, Li Z, Chen R, et al. Roles of angiotensin II type 2 receptor stimulation associated with selective angiotensin II type 1 receptor blockade with valsartan in the improvement of inflammation-induced vascular injury. Circulation 2001;104:2716–21.
6. Lorenzo O, Ruiz-Ortega M, Suzuki Y, Ruperez M, Esteban V, Sugaya T, et al. Angiotensin III activates nuclear transcription factor-kappaB in cultured mesangial cells mainly via AT(2) receptors: studies with AT(1) receptor-knockout mice. J Am Soc Nephrol 2002;13:1162–71.
7. Berthonneche C, Sulpice T, Tanguy S, O'Connor S, Herbert JM, Janiak P, et al. AT1 receptor blockade prevents cardiac dysfunc-

tion after myocardial infarction in rats. Cardiovasc Drugs Ther 2005;19:251–9.
8. Ouchi N, Kihara S, Arita Y, Okamoto Y, Maeda K, Kuriyama H, et al. Adiponectin, an adipocyte-derived plasma protein, inhibits endothelial NF-kappaB signaling through a cAMP-dependent pathway. Circulation 2000;102:1296–301.
9. Cohn JN, Tognoni G. A randomized trial of the angiotensinreceptor blocker valsartan in chronic heart failure. N Engl J Med 2001;345:1667–75.
10. Yamamoto K, Shioi T, Uchiyama K, Miyamoto T, Sasayama S, Matsumori A. Attenuation of virus-induced myocardial injury by inhibition of the angiotensin II type 1 receptor signal and decreased nuclear factor-kappa B activation in knockout mice. J Am Coll Cardiol 2003;42:2000–6.
11. Yu F, Takahashi T, Moriya J, Kawaura K, Yamakawa J, Kusaka K, et al. Angiotensin-II receptor antagonist alleviates non-alcoholic fatty liver in KKAy obese mice with type 2 diabetes. J Int Med Res 2006;34:297–302.
12. Zorad S, Dou JT, Benicky J, Hutanu D, Tybitanclova K, Zhou J, et al. Long-term angiotensin II AT(1) receptor inhibition produces adipose tissue hypotrophy accompanied by increased expression of adiponectin and PPARgamma. Eur J Pharmacol 2006;552:112–22.
13. Takahashi T, Saegusa S, Sumino H, Nakahashi T, Iwai K, Morimoto S, et al. Adiponectin, T-cadherin and tumor necrosis factor-alpha in damaged cardiomyocytes from autopsy specimens. J Int Med Res 2005;33:236–44.
14. Takahashi T, Yu F, Saegusa S, Sumino H, Nakahashi T, Iwai K, et al. Impaired expression of cardiac adiponectin in leptin-deficient mice with viral myocarditis. Int Heart J 2006;47:107–23.
15. Ishikawa Y, Akasaka Y, Ishii T, Yoda-Murakami M, Choi-Miura NH, Tomita M, et al. Changes in the distribution pattern of gelatin-binding protein of 28 kDa (adiponectin) in myocardial remodelling after ischaemic injury. Histopathology 2003;42:43–52.
16. Tanaka A, Matsumori A, Wang W, Sasayama S. An angiotensin II receptor antagonist reduces myocardial damage in an animal model of myocarditis. Circulation 1994;90:2051–55.
17. Matsuzawa Y, Funahashi T, Kihara S, Shimomura I. Adiponectin and metabolic syndrome. Arterioscler Thromb Vasc Biol 2004;24:29–33.
18. Furuhashi M, Ura N, Higashiura K, Murakami H, Tanaka M, Moniwa N, et al. Blockade of the renin-angiotensin system increases adiponectin concentrations in patients with essential hypertension. Hypertension 2003;42:76–81.
19. Kapadia SR, Oral H, Lee J, Nakano M, Taffet GE, Mann DL. Hemodynamic regulation of tumor necrosis factor-alpha gene and protein expression in adult feline myocardium. Circ Res 1997;81:187–95.
20. Sun M, Dawood F, Wen WH, Chen M, Dixon I, Kirshenbaum LA, et al. Excessive tumor necrosis factor activation after infarction contributes to susceptibility of myocardial ruptureand left ventricular dysfunction. Circulation 2004;110:3221–8.
21. Yue P, Massie BM, Simpson PC, Long CS. Cytokine expression increases in nonmyocytes from rats with postinfarction heart failure. Am J Physiol 1998;275:H250–8
22. Yokoyama T, Vaca L, Rossen RD, Durante W, Hazarika P, Mann DL. Cellular basis for the negative inotropic effects of tumor necrosis factor-alpha in the adult mammalian heart. J Clin Invest 1993;92:2303–2312.
23. Maeda N, Shimomura I, Kishida K, Nishizawa H, Matsuda M, Nagaretani H, et al. Diet-induced insulin resistance in mice lacking adiponectin/ACRP30. Nat Med 2002;8:731–7.
24. Lihn AS, Richelsen B, Pedersen SB, Haugaard SB, Rathje GS, Madsbad S, et al. Increased expression of TNF-alpha, IL-6, and IL-8 in HALS: implications for reduced adiponectin expression and plasma levels. Am J Physiol Endocrinol Metab 2003;285: E1072–80.

on the facts and data mentioned above, we would suggest that ambulatory blood pressure monitoring be considered more often in the evaluation of patients with orthostatic hypotension.

Amir Kazory, MD
Marcelo E. Heinig, MD
A. Ahsan Ejaz, MD
Division of Nephrology, Hypertension and Transplantation
University of Florida
Gainesville, FL

REFERENCES

1. Ejaz AA, Haley WE, Wasiluk A et al. Characteristics of 100 consecutive patients presenting with orthostatic hypotension. Mayo Clin Proc 2004;79:890–894.
2. Jordan J, Shannon JR, Biaggioni I et al. Contrasting actions of pressor agents in severe autonomic failure. Am J Med 1998;105:116–124.
3. Rose KM, Eigenbrodt ML, Biga RL et al. Orthostatic hypotension predicts mortality in middle-aged adults. The Atherosclerosis Risk In Communities (ARIC) Study. Circulation 2006;114:630–636.
4. Suzuki Y, Kuwajima I, Aono T et al. Prognostic value of nighttime blood pressure in the elderly: A prospective study of 24-hour blood pressure. Hypertens Res 2000;23:323–330.
5. Aronow WS, Ahn C. Association of postprandial hypotension with incidence of falls, syncope, coronary events, stroke, and total mortality at 29-month follow-up in 499 older nursing home residents. J Am Geriatr Soc 1997;45: 1051–1053.

HEPATOCYTE GROWTH FACTOR AND VISFATIN IN ELDERLY BEDRIDDEN PATIENTS

To the Editor: Aged people have several hormonal alterations, although the endocrine function of adipose tissue in aged bedridden patients is not fully understood. Adipose tissue is now recognized as an endocrine organ that secretes multiple growth factors and cytokines, such as adiponectin, hepatocyte growth factor (HGF), and visfatin. Plasma adiponectin concentrations in women do not change significantly with age but were found to be positively related to the duration of time confined to bed in a previous report.[1] We investigated the clinical role of circulating HGF and visfatin in aged bedridden patients according to their clinical profiles and complications.

HGF is a well-known, potent, pleiotropic cytokine that exhibits mitogenic, motogenic, and morphogenic activities in a variety of cells.[2] There are several reports on the relationship between HGF and dementia[3] or cardiovascular diseases.[4] Recently, Jia and colleagues[5] reported that visfatin was significantly expressed in peripheral neutrophils of patients with sepsis. Visfatin was also expressed in lung tissues and associated with the susceptibility of acute lung injury.[6] Visfatin promoter polymorphism was reported to be associated with higher plasma levels of C-reactive protein in an analysis of patients with diabetes mellitus.[7]

We studied 154 bedridden patients who were admitted to geriatric wards and nursing homes in Osaka, Japan. Clinical diagnoses were defined using detailed physical examination and routine biochemical analyses of blood and urine, as well as clinical tools such as computed tomography. Blood pressure was examined at admission and at a subsequent examination. A diagnosis of Parkinson's disease was based on the assessment of experienced specialists for movement disorders. For the baseline magnetic resonance image, the number of lacunae was first counted and then graded as follows: absent = grade 0, 1 to 2 lacunae = grade 1, 3 to 5 lacunae = grade 2, and 6 or more lacunae = grade 3.[8] Mean time ± standard deviation confined to bed was 45.5 ± 40.3 months. Mean age of subjects was 80.3 ± 13.6, and 39 were male. All plasma analyses were performed in samples from fasting subjects. HGF and visfatin were measured using high-sensitive radioimmunoassay (Linco Research, St Louis, MO).[9] Plasma HGF levels were 0.40 ± 0.91 ng/mL, and visfatin levels were 50.3 ± 24.8 ng/mL.

Of 154 bedridden patients, the main cause of being confined to bed was cerebrovascular accident; others were respiratory disease, cardiovascular disease, Parkinson's disease, and dementia. In the entire group, no significant positive correlation was found between plasma HGF and visfatin concentration and age. Circulating levels of HGF were significantly related to the length of time confined to bed. Circulating visfatin was positively correlated with diastolic blood pressure in the examination, circulating adiponectin, and C-reactive protein using logarithmic transformation (Table 1).

Circulating levels of HGF were significantly related to Parkinson's disease, ischemic heart disease or dementia (Table 1). Moreover, logarithmic transformation of HGF levels was positively correlated with grade of lacunar infarction. Additionally, length of time confined to bed was positively associated with plasma HGF ($P = .03$) but was not associated with circulating visfatin ($P = .09$) in aged bedridden patients according to univariate analysis.

High levels of HGF have been associated with the genesis of Alzheimer's disease.[3] These reports may support the positive correlations between HGF and dementia in our results. For ischemic heart disease, HGF levels could predict long-term clinical outcome in patients with coronary revascularization.[4] Therefore, our findings of the correlation between HGF and cardiovascular disease, including lacunar infarcts, dementia, and ischemic heart disease, are incongruent with these studies. There are no reports on the relationship between HGF and Parkinson's disease. The variable symptoms and signs of Parkinson's disease suggest multiple causes or pathogenesis. Our findings, that circulating HGF was strongly correlated with Parkinson's disease, must be confirmed.

Treatment with mechanical force[6] or inflammatory cytokines up-regulated visfatin expression in a human cell line in vitro.[10] Visfatin-promoter polymorphism was reported to be associated with higher plasma levels of C-reactive protein in an analysis of diabetic patients.[7] These reports support our results—that visfatin level is associated with CRP levels. Furthermore, measurements of circulating visfatin after logarithmic transformation may be a marker of acute inflammation in aged bedridden patients. More investigations are necessary to access the mechanism of these findings and therapeutic implication for elderly bedridden patients.

Table 1. Univariate Analysis for Association Between Hepatocyte Growth Factor (HGF), Visfatin, and Clinical Characteristics in Bedridden Patients

Clinical Characteristics	HGF (ng/mL)	Log HGF (ng/mL)	Visfatin (ng/mL)	Log Visfatin (ng/mL)
	Proportional Value			
Age	0.975	0.115	0.302	0.291
Blood pressure, mmHg				
At admission				
Systolic	0.067	0.226	0.981	0.744
Diastolic	0.485	0.379	0.6330	0.900
Upon examination				
Systolic	0.555	0.972	0.554	0.292
Diastolic	0.518	0.887	0.619	0.039*
Serum albumin, g/dL	0.381	0.876	0.701	0.825
Total cholesterol, mg/dL	0.813	0.867	0.728	0.865
Blood urea nitrogen, mg/dL	0.977	0.620	0.344	0.117
Creatinine, mg/dL	0.237	0.179	0.694	0.179
Leukocyte counts, /m^3	0.208	0.192	0.355	0.314
Hemoglobin, g/dL	0.349	0.808	0.913	0.507
C-reactive protein, mg/dL	0.936	0.404	0.161	0.005*
Adiponectin, ng/mL	0.370	0.313	0.675	0.026*
HGF, ng/mL	NA	NA	0.320	0.733
Visfatin, ng/mL	0.320	0.401	NA	NA
Complications				
Pneumonia	0.762	0.055	0.829	0.064
Asthma	0.213	0.098	0.755	0.183
Parkinson's disease	<0.001*	<0.001*	0.459	0.842
Diabetes mellitus	0.965	0.574	0.468	0.729
Grade of lacunar infarction	0.402	0.004*	0.655	0.403
Renal failure	0.681	0.927	0.871	0.355
Atrial fibrillation	0.993	0.596	0.680	0.838
Ischemic heart disease	0.026	0.008*	0.297	0.792
Dementia	0.034*	0.019*	0.444	0.088
Arteriosclerosis obliterans	0.642	0.582	0.461	0.238

*$P<.05$.
NA = not assessed.

Tsugiyasu Kanda, MD
Takashi Takahashi, MD
Department of General Medicine
Kanazawa Medical University
Ishikawa, Japan

Hiroyuki Sumino, MD
Second Department of Internal Medicine
Gunma University School of Medicine
Gunma, Japan

Takeshi Nakahashi, MD
Kunimitsu Iwai, MD
Shigeto Morimoto, MD
Masayuki Matsumoto, MD
Department of Geriatric Medicine
Kanazawa Medical University
Ishikawa, Japan

ACKNOWLEDGMENTS

Financial Disclosure: Dr. Kanda was supported by a grant for Project Research from the High Technology Center of Kanazawa Medical University (H2004-7) and a research grant from Grant-in-Aid for Scientific Research, the Ministry of Education, Science and Culture of Japan (No. 17590767). Dr. Takahashi was supported by a grant for Promoted Research from Kanazawa Medical University (S2005-5). There is no conflict of interest regarding the present study.

Author Contributions: Study concept and design: Tsugiyasu Kanda and Takashi Takahashi. Acquisition of subjects and data: Shigeto Morimoto and Masayuki Matsumoto. Analysis and interpretation of data: Hiroyuki Sumino and Takeshi Nakahashi. Preparation of letter: Tsugiyasu Kanda and Kunimitsu Iwai.

Sponsor's Role: None.

REFERENCES

1. Kanda T, Takahashi T, Sumino H et al. Hypoadiponectinemia in bedridden female patients younger than 75. J Am Geriatr Soc 2005;53:2039–2041.
2. Zarnegar R, Michalopoulos GK. The many faces of hepatocyte growth factor: From hepatopoiesis to hematopoiesis. J Cell Biol 1995;129:1177–1180.
3. Tsuboi Y, Kakimoto K, Nakajima M et al. Increased hepatocyte growth factor level in cerebrospinal fluid in Alzheimer's disease. Acta Neurol Scand 2003;107:81–86.

4. Susen S, Sautiere K, Mouquet F et al. Serum hepatocyte growth factor levels predict long-term clinical outcome after percutaneous coronary revascularization. Eur Heart J 2005;26:2387–2395.
5. Jia SH, Li Y, Parodo J et al. Pre-B cell colony-enhancing factor inhibits neutrophil apoptosis in experimental inflammation and clinical sepsis. J Clin Invest 2004;113:1318–1327.
6. YeSQ, Simon BA, Maloney JP et al. Pre-B-cell colony-enhancing factor as a potential novel biomarker in acute lung injury. Am J Respir Crit Care Med 2005;171:361–370.
7. Zhang YY, Gottardo L, Thompson R et al. A visfatin promoter polymorphism is associated with low-grade inflammation and type 2 diabetes. Obesity (Silver Spring) 2006;14:2119–2126.
8. Takami S, Imai Y, Katsuya T et al. Gene polymorphism of the renin-angiotensin system associates with risk for lacunar infarction. The Ohasama Study. Am J Hypertens 2000;13:121–127.
9. Yamada A, Matsumoto K, Iwanari H et al. Rapid and sensitive enzyme-linked immunosorbent assay for measurement of HGF in rat and human tissues. Biomed Res 1995;16:105–114.
10. Ognjanovic S, Bao S, Yamamoto SY et al. Genomic organization of the gene coding for human pre-B-cell colony enhancing factor and expression in human fetal membranes. J Mol Endocrinol 2001;26:107–117.

LETHAL FECALOMA

To the Editor: Stercoral perforation of the colon is rarely reported in the surgical literature. Infrequently, a stercoral disease or ulceration with perforation may represent the underlying etiology. Age, comorbidity, systemic disorders, reduced "functional reserve," and poor tolerance to repeat surgical stresses are some of the medical factors that can lead to the high mortality rate (32–57%) related to this condition.[1] In the present study, we reported on the surgical management of eight stercoral perforations and indicate the importance of preventive treatment.

METHODS

We retrospectively reviewed the medical records of eight patients operated on for peritonitis due to perforation of a fecaloma in two hospitals between 2004 and 2006. The demographic, operative, pathological, and outcome details were recorded to assess the conditions of colonic perforation due to fecaloma.[2]

RESULTS

The mean age of the eight patients (5 women and 3 men) was 81 ± 5. Two patients came from a chronic nursing home or similar environment. All of the patients had a long history of chronic constipation preceding the stercoral perforation. Three patients were taking amitriptyline or others constipation sedatives, and two patients were in chronic renal failure. Three patients had neurological antecedents (1 psychotic, 1 depression, 1 dementia). Five patients had a lack of mobility. A diagnosis of acute abdomen was readily made with general peritonitis in five cases and local peritonitis in two. In four cases, a palpable impacted fecal mass was found on rectal examination. In one case, x-ray of the abdomen showed free air at; in another case, a pneumomediastinum was observed on the chest x-ray. In only five cases was observed pneumoperitoneum on a computed tomography scan.

Operative

In all cases, the perforation occurred in the sigmoid.

Treatment

All patients were operated on through a median incision. Hartman's procedure, which involves resection of the diseased rectosigmoid colon at the level of the peritoneal reflection, with creation of proximal end colostomy and suture of the distal rectal stump, was the standard technique used. This surgical approach was applied in the case of five patients. Exteriorization of perforation without resection was carried out in two cases; in the last case, a resection of the colon with double colostomy was achieved.

Mortality

Three patients died (33%) in the early postoperative course. All patients with exteriorization of perforation died. Five patients were alive, but four patients had a colostomy. The profiles of morbidity and mortality are shown in Table 1.

DISCUSSION

Observations reported in the present study underline the difficulty of determining precisely the true incidence of stercoral perforation. An explanation for the rarity of the disease is not apparent but almost certainly is underreported.[1,2] The first step of this pathology began by constipation that often pass unperceived, asymptomatic stercoral ulcer appeared in the second step (rarely they can lead to intestinal bleeding),[3] and in the final step, perforation of the colon occurred. The mean age of the patients in this study explains the greater rate of mortality than in Mauer's report.[2] Data reported in a French multicentric study showed that four independent preoperative risk factors of mortality exist: emergency surgery, loss of more than 10% of weight, neurological comorbidity, and age 70 and older.[4] Moreover, six independent risk factors for morbidity were found: age 70 and older, neurological comorbidity, hypoalbuminemia, cardiorespiratory comorbidity, long duration of surgery, and peritoneal contamination.[4] The study presented here is the anecdotal concept that stercoral ulceration and perforation are complications that develop in older individuals or in those with chronic pathologies (e.g., neurological and cardiorespiratory comorbidity). The perforation may have an atypical presentation (e.g., asthenic peritonitis) or result in few laboratory abnormalities (e.g., acute renal failure, hyperleukocytosis).[5] Moreover, an empty rectal fecaloma does not exclude perforation by fecaloma, although the most appropriate approach would be a preventive policy with active treatment of terminal constipation and fecaloma. Chronic constipation with fecal impaction is a mundane problem. Clinical symptoms such as anorexia, nausea, vomiting, abdominal pain, paradoxical diarrhea, and incontinence are among the most common symptoms in patients in institutions and should be carefully taken into account.[6] Although most impactions are in the rectal vault, the absence of palpable stool on rectal examination does not rule out a fecal impaction.[7] Although enemas and suppositories alone may eliminate the impaction, the manual fragmentation and extraction of the fecal mass is almost always indicated first.[6] Extraction of fecal mass may be made under local or general anesthesia.[6] The evolution of a bad extraction may continue to ischemic colitis and perforation.

Original Article

Tilting-Induced Decrease in Systolic Blood Pressure in Bedridden Hypertensive Elderly Inpatients: Effects of Azelnidipine

Shigeto MORIMOTO[1], Takashi TAKAHASHI[2], Kohya OKAISHI[3], Takeshi NAKAHASHI[1], Kohji NOMURA[1], Tsugiyasu KANDA[2], Masashi OKURO[1], Hiroshi MURAI[1], Tomoichi NISHINO[3], and Masayuki MATSUMOTO[1]

The object of this study was to examine blood pressure (BP) variability due to postural change in elderly hypertensive patients. The subjects studied were 154 elderly inpatients in a hospital for the elderly (48 male and 106 female; median age: 82 years), consisting of age- and sex-matched bedridden (n=39) and non-bedridden (n=39) normotensive controls and bedridden (n=38) and non-bedridden (n=38) hypertensive patients. BP and pulse rate (PR) were measured in the supine position, then again after a 2-min, 45 deg head-up tilt with the legs horizontal. The decrease in systolic BP (SBP) on tilting in the bedridden hypertensive group (median: −10 mmHg; range: −32 to 9 mmHg) was significantly (p<0.008) greater than those in the other three groups. Monotherapy with azelnidipine, a long-acting calcium channel blocker, for 3 months not only significantly reduced the basal BP and PR of hypertensive patients in the two groups, but also significantly (p<0.05) attenuated the tilt-induced decrease in the SBP to −3 mmHg (−19 to 25 mmHg) and enhanced the change in PR from −1 bpm (−10 to 7 bpm) to 1 bpm (−4 to 23 bpm) in the bedridden hypertensive group. Our findings indicate that tilt-induced decrease in SBP is a rather common phenomenon in bedridden elderly hypertensive patients, and that treatment with azelnidipine attenuates tilt-induced decrease in SBP, probably through an improvement of baroreceptor sensitivity. (*Hypertens Res* 2006; 29: 943–949)

***Key Words*: bedridden, head-up tilt, systolic blood pressure, hypertensive elderly, azelnidipine**

Introduction

Increased blood pressure (BP) variability on postural change is a recognized feature in the elderly, especially in those with hypertension (*1*). Moreover, many longitudinal epidemiological studies have shown that increased BP variability on postural change is associated with future cardiovascular events, including coronary heart disease (*2*), stroke (*3*), and even mortality (*4*), and is also recognized as a risk factor for cognitive impairment (*5*) and silent cerebrovascular disease (*6*). In addition, it has recently been reported that lying in a prone posture can lead to unregulated postural hypotension, which has the possibility of being a novel predictor of cardiovascular disease (*7*).

On the other hand, tilting-up of the upper body with the legs horizontal is a commonly performed maneuver in bedridden elderly subjects, and may prevent aspiration pneumonia (*8*).

From the [1]Departments of Geriatric Medicine and [2]General Medicine, Kanazawa Medical University, Ishikawa, Japan; and [3]Department of Medicine, Sengi-Hospital, Ishikawa, Japan.

This study was supported in part by a Grant-in-Aid for Scientific Research from the Ministry of Health, Labour and Welfare of Japan (to S.M.) and a grant for promoted research from Kanazawa Medical University (S2005-5 to T.T.).

Address for Reprints: Shigeto Morimoto, M.D. Ph.D., Department of Geriatric Medicine, Kanazawa Medical University, 1–1 Daigaku, Uchinada-cho, Kahoku-gun, Ishikawa 920–0293, Japan. E-mail: shigeto@kanazawa-med.ac.jp

Received May 2, 2006; Accepted in revised form August 9, 2006.

Table 1. Comparison of Clinical Factors among Normotensive and Hypertensive Inpatients with Non-Bedridden and Bedridden States in a Geriatric Hospital

	NB elderly (n=77)		B elderly (n=77)	
	N (n=39)	H (n=38)	N (n=39)	H (n=38)
Clinical background				
Age (years)	83 (72–93)	82 (70–93)	83 (71–91)	82 (70–92)
Male/female	12/27	12/26	12/27	12/26
Chronic conditions (n (%))				
Dementia	12 (30.8)	11 (28.9)	29 (74.4)$^{\dagger,\#}$	32 (84.2)$^{\dagger,\#}$
Stroke	7 (17.9)	9 (23.7)	29 (74.4)$^{\dagger,\#}$	22 (57.4)$^{\dagger,\#}$
Ischemic heart disease	4 (10.3)	11 (28.9)	8 (20.5)	9 (23.7)
Congestive heart failure	4 (10.3)	4 (10.5)	6 (15.4)	2 (5.3)
Hypoalbuminemia	5 (12.8)	0 (0.0)	11 (28.2)$^{\#}$	6 (15.8)
Diabetes mellitus	0 (0.0)	3 (7.9)	2 (5.1)	0 (0.0)

Values are expressed as median (range) in age. N, normotensives; H, hypertensives; NB, non-bedridden; B, bedridden. $^{\dagger}p<0.008$, *vs.* NB-N group. $^{\#}p<0.008$, *vs.* NB-H group.

However, little has been reported about the BP variability in completely bedridden elderly inpatients. In the present study, we compared variability of BP and pulse rate (PR) at the time of tilting-up of the upper body in non-bedridden and bedridden inpatients with and without hypertension in a hospital for the elderly. We also examined the effects of azelnidipine, a newly developed dihydropyridine-type calcium antagonist that acts without augmentation of the sympathetic nervous system (*9*, *10*), on variability of BP and PR in these hypertensive elderly inpatients.

Methods

Study Subjects

The study was conducted in Sengi-Hospital, a geriatric hospital serving as both a hospital and a long-term care facility for the elderly, which is a common combination of medical and care services in Japan (*11*). Katz's activities of daily living (ADL: bathing, dressing, going to the toilet, transfer, continence, feeding) (*12*) and the Braden scale (*13*) were assessed once a month in all inpatients in the hospital. The research protocol was approved by the Ethics Committee of the hospital. Patients aged 70 years and older, all of whom were Japanese with an admission period of 16 weeks or longer, were invited to participate in the study. All residents who gave informed consent (or whose family members gave consent) were enrolled. Both normotensive and hypertensive subjects were selected from bedridden residents. Control normotensive and hypertensive subjects were age- and sex-matched random samples of non-bedridden subjects admitted to the same hospital. The computerized admission lists served as the sampling frame, and we frequency matched the controls to the cases by sex and age (within ±2 years) at a ratio of 1:1. Hypertension was defined as systolic BP (SBP) ≥140 mmHg and/or diastolic BP (DBP) ≥90 mmHg measured in the supine position. Patients were defined as bedridden if they showed dependency in all sub-items in Katz's ADL (*12*), in addition to being permanently confined to bed (score: 1 or 2) according to the sub-item of "activity" score in the Braden scale (*13*). Patients were defined as non-bedridden if they showed independence in all of Katz's ADL items (*12*). None of the subjects had had any antihypertensive treatment for 2 months prior to enrollment. We excluded 1) subjects admitted to the hospital or at the start of the investigation with clinical diagnoses of Parkinsonism (*14*), Shy-Drager syndrome (*15*), amyloidotic polyneuropathy (*16*), or vitamin B_{12} deficiency (*17*); 2) subjects treated with any drug that may have contributed to or decreased the likelihood of orthostatic hypotension, such as diuretics, α-blockers or β-blockers; 3) subjects considered critically ill (*18*); 4) postoperative patients; and 5) patients admitted for less than 16 weeks.

Procedure for Modified Head-Up Tilt

Basal BP and PR of the elderly subjects were determined by averaging two determinations of supine BP measured with an automatic cuff-oscillometric BO recorder (HEM-705CP; OMRON Co., Ltd., Kyoto, Japan) after the subjects had rested for more than 30 min in the morning before breakfast. The responses of BP and PR were analyzed after a 2-min, 45 deg head-up tilt with the legs horizontal (0 deg) according to the procedure of Gotshall *et al.* (*19*). BP and PR were measured 2 min after the postural change (*20*). Tilt-induced hypotension was defined as a fall in SBP of 20 mmHg or greater and/or DBP of 10 mmHg or greater according to the consensus statement on the definition of orthostatic hypotension (*21*). The changes in BP and PR with the same head-up

Table 2. Comparison of Blood Pressure and Heart Rate at Time of Modified Head-Up Tilt among Normotensive and Hypertensive Inpatients with Non-Bedridden and Bedridden States in a Geriatric Hospital, and between before and after Azelnidipine Treatment

	NB elderly (n=77)		B elderly (n=77)	
	N (n=39)	H (n=38)	N (n=39)	H (n=38)
Before treatment				
Basal supine position				
Systolic BP (mmHg)	122 (106–136)	155 (139–199)†	119 (92–138)$^{\#}$	155 (146–203)$^{\dagger,\#}$
Diastolic BP (mmHg)	70 (54–89)	79 (64–97)†	72 (37–88)$^{\#}$	81 (58–100)$^{\dagger,\#}$
Heart rate (/min)	71 (53–86)	68 (58–86)	75 (58–106)	78 (56–114)
2 min after head-up tilt				
Systolic BP (mmHg)	124 (105–136)	165 (125–188)†	118 (94–162)$^{\#}$	151 (115–199)$^{\dagger,\#}$
Diastolic BP (mmHg)	72 (52–87)	82 (57–105)†	73 (51–93)$^{\#}$	81 (52–132)
Heart rate (/min)	67 (52–85)	66 (52–91)	74 (58–106)	76 (58–99)
Azelnidipine treatment				
Basal supine position				
Systolic BP (mmHg)	—	124 (108–168)$^{\$}$	—	133 (110–170)$^{\$}$
Diastolic BP (mmHg)	—	76 (63–99)$^{\$}$	—	81 (60–91)$^{\$}$
Heart rate (/min)	—	68 (49–86)	—	69 (45–89)$^{\$}$
2 min after head-up tilt				
Systolic BP (mmHg)	—	129 (114–174)$^{\$}$	—	130 (104–162)$^{\$}$
Diastolic BP (mmHg)	—	76 (57–98)$^{\$}$	—	79 (61–90)
Heart rate (/min)	—	69 (51–86)	—	72 (50–93)

Values are expressed as median (range). BP, blood pressure; N, normotensives; H, hypertensives; NB, non-bedridden; B, bedridden; —, no data. $^{\dagger}p<0.008$, *vs.* NB-N group. $^{\#}p<0.008$, *vs.* NB-H group. $^{\$}p<0.05$, *vs.* before treatment with azelnidipine in the same situation in NB-H or B-H groups.

tilt were also determined at 3 months after the start of administration of azelnidipine at a dose of 4 to 16 mg/day.

Data Collection

Operational definitions of each pre-existing potential risk factor for autonomic dysfunction, including stroke (motor deficit and evidence of cerebral hemispheric infarction on computed tomography and/or magnetic resonance imaging) (*22*, *23*), dementia (Mini-Mental State Examination score ≤23) (*17*), chronic ischemic heart disease (previous myocardial infarction or angina pectoris) (*24*), congestive heart failure (left ventricular ejection fraction <40% on echocardiography) (*25*), hypoalbuminemia (serum albumin level <30 g/l) (*26*), and diabetes mellitus (treated with insulin, oral hypoglycemic agent, or fasting blood glucose ≥7 mmol/l) (*26*, *27*), were established prior to data collection. Data were retrieved from medical records before the start of the examination. Personal physicians were involved in the diagnoses of these complications, which were further evaluated by a committee. Objective and routinely collected medical information was applied to augment the diagnostic accuracy. Only chronic conditions were recorded for the cases and respective controls.

Statistical Analyses

Data are expressed as the median and full range. The data were analyzed by Kruskal-Wallis χ^2 and Mann-Whitney U analysis as a multiple comparison using post hoc Bonferroni correction. p values were set at 0.008. Differences in changes of BP and PR by treatment with azelnidipine were assessed by nonparametric Wilcoxon test, and a value of $p<0.05$ was regarded as significant. Data were analyzed on a microcomputer running SPSS version 12 (SPSS, Chicago, USA).

Results

Clinical Characteristics of the Four Groups of Elderly Inpatients

Clinical characteristics of the subjects are shown in Table 1. Numbers of non-bedridden (NB) and bedridden (B) normotensive (N) elderly subjects were 39 (each 12 male and 27 female) and NB and B hypertensive (H) elderly subjects were 38 (each 12 male and 26 female). The median age was not significantly different among the four groups. The prevalence of dementia and chronic phase of stroke in the two bedridden groups (B-N and B-H) was significantly higher than that in

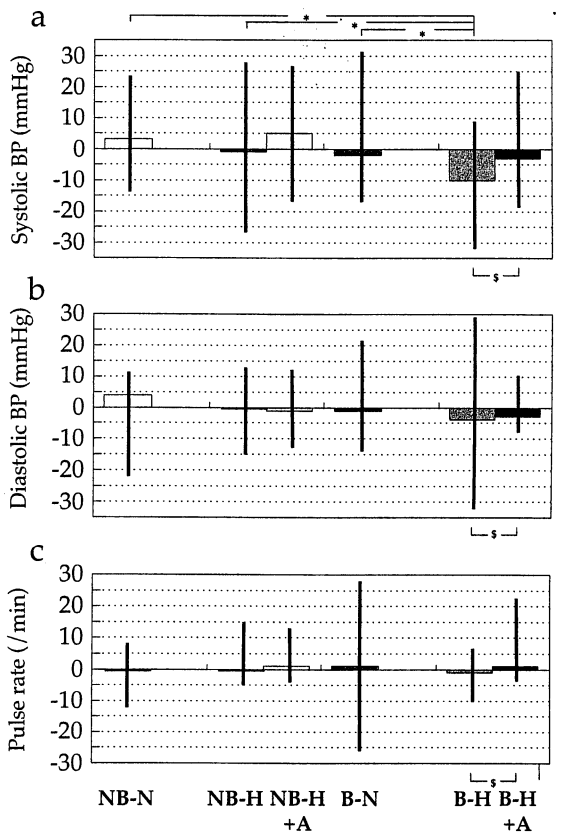

Fig. 1. *Changes in systolic blood pressure (SBP) (a) and diastolic blood pressure (DBP) (b) values and pulse rate (c) at 2 min after head-up tilt from the initial supine position in the four groups. Columns and bars represent the medians and full ranges in each group. NB-N, non-bedridden normotensive group; NB-H, non-bedridden hypertensive group; B-N, bedridden normotensive group; and B-H, bedridden hypertensive group. +A, after treatment with azelnidipine in groups NB-H and B-H.* *p < *0.008* vs. *the NB-H group.* $p < *0.05* vs. *before treatment with azelnidipine after the same maneuver in the NB-H or B-H groups.*

the non-bedridden groups (NB-N and NB-H), respectively, and the prevalence of hypoalbuminemia in the B-N group was significantly higher than that in the NB-H group (Table 1).

Changes in BP and PR by Modified Tilt in the Four Groups

Values in SBP, DBP, and PR at the basal supine position and at 2 min after the modified tilt are summarized in Table 2. Both the SBP and DBP values in the two hypertensive groups were significantly higher than those in the two normotensive groups, with the exception that the DBP in the B-H group at 2 min after the tilt was not significantly different from those of the other three groups.

Figure 1 summarizes the changes in SBP and DBP values and PR at 2 min after head-up tilt from the initial supine position in the four groups. Decreases in SBP in the B-H group (median: −10 mmHg; range: −32 to 9 mmHg) were significantly greater than those in either the NB-N group (4 mmHg, −14 to 24 mmHg, $p<0.001$), NB-H group (−1 mmHg, −26 to 28 mmHg, $p=0.001$) or B-N group (−2 mmHg, −17 to 31 mmHg, $p=0.001$), respectively.

On the other hand, the numbers of subjects with tilt-induced hypotension were not significantly different among the NB-N ($n=7$), NB-H ($n=6$), B-N ($n=5$), and B-H ($n=10$) groups by the Kruskal-Wallis test.

Effects of Azelnidipine on BP Change Induced by Head-Up Tilt

Treatment with azelnidipine, a new calcium channel blocker, not only significantly ($p<0.05$) decreased the SBP and DBP levels in the two groups, but also significantly attenuated the higher basal PR in the B-H group to a value comparable to that in the NB-N group (Table 2). Moreover, azelnidipine not only attenuated the tilt-induced prominent decrease in SBP observed before treatment of patients in the B-H group to a level comparable to that in the B-N group, but also significantly enhanced the tilt-induced change in PR to a value comparable to those in the other groups (Fig. 1).

All 10 patients with tilt-induced hypotension in the B-H group were assessed as not having hypotension after the treatment with azelnidipine ($p=0.003$), with significant increments in the tilt-induced changes in SBP (median, −20 mmHg, and range, [−32 to −7 mmHg], before the treatment; to −11 mmHg [−19 to 3 mmHg] after the treatment; $p=0.008$), in DBP (−10 mmHg [−32 to −7 mmHg] to −3 mmHg [−8 to 2 mmHg]; $p=0.005$), and in PR (−1 bpm [−10 to 7 bpm] to 0 bpm [−4 to 23 bpm]; $p=0.024$). Although administration of azelnidipine to the remainder of the 28 patients without tilt-induced hypotension in the B-H group also significantly enhanced the tilt-induced changes in SBP (−4 mmHg [−18 to 9 mmHg] to −2 mmHg [−16 to 25 mmHg]; $p=0.0014$) and in PR (0 bpm [−3 to 7 bpm] to 1 bpm [−1 to 6 bpm]; $p<0.001$), the increment in tilt-induced change in DBP (−1 mmHg [−9 to 5 mmHg] to 1 mmHg [−8 to 10 mmHg]) was not significant ($p=0.210$). Although 4 out of 6 patients with tilt-induced hypotension in the NB-H group were judged not to have hypotension after the treatment with azelnidipine, this difference was not statistically significant ($p=0.157$). Mann-Whitney U analysis and χ^2 analysis did not reveal any significant difference in the mean age or prevalence of the clinical factors, including male gender, dementia, stroke, ischemic heart disease, congestive heart failure, hypoalbuminemia, diabetes mellitus, or bedridden itself, between the 14 hypertensive elderly subjects (4 in the NB-H group and 10 in the B-H group) who showed improvement of the postural hypotension by azelnidipine and the 2 subjects in the NB-H group without the improvement.

Discussion

Our study demonstrated a greater decrease in SBP in the B-H group compared to the other three groups by a quite commonly used nursing maneuver of 45 deg head-up tilt with the legs horizontal. A greater decrease in BP by the head-up tilt is often seen in elderly hypertensive patients (*28*), and is caused by retarded sympathetic nerve activation mainly due to impaired baroreflex sensitivity (*28*), which cannot adjust decreases in cardiac output and arterial pressure due to redistribution of blood from the thoracic area to the deep intra- and inter-muscular vein of the legs by the tilt stress (*29*). The impaired baroreflex activation in these elderly hypertensive patients is represented at least in part by an inadequately lower increment in baroreflex-mediated PR despite a greater decrease in BP compared to that in normotensive elderly subjects (*30*). The elderly B-H patients in this study were characterized by a decrement of the median PR despite a significant decrement of SBP at the time of the tilt, which may be an ultimate feature of autonomic impairment (Fig. 1), suggesting that impaired baroreflex activation played a role in the prominent decrease in SBP in response to the head-up tilt in the B-H patients. On the other hand, increments in both SBP and DBP in response to head-up tilt were observed in NB-N subjects. This value was comparable to that in young normal subjects at the time of head-up tilt in a previous report (*28*). These findings suggest that normotensive healthy subjects, even at a very old age, show a normal autonomic response to the tilt stress, similar to that in young normal subjects.

In the present study, all the patients in the NB-H and B-H groups were treated with azelnidipine, a newly developed dihydropyridine-type calcium channel antagonist with a slowly developing and long-lasting hypotensive effect characterized by little reflex tachycardia (*9*, *10*, *31*). Treatment with azelnidipine not only significantly decreased basal SBP and DBP in patients in both hypertensive groups, but also significantly attenuated the higher basal PR of patients in the B-H group to a level comparable to that of subjects in the NB-N group (Table 2). This observation is partly compatible with a previous report that azelnidipine significantly decreased PR on 24-h ambulatory monitoring (*9*). Despite the significant decreases in BP and basal PR in the B-H patients, azelnidipine not only significantly attenuated the decrements of both SBP and DBP but also reversed the decrement of PR in response to the tilt (Fig. 1). Moreover, all the hypertensive patients with tilt-induced hypotension in the B-H group were judged as not having hypotension after the treatment with azelnidipine. In addition, these patients showed even greater attenuations of the tilt-induced decrements in SBP and DBP compared to those who were originally diagnosed as not having tilt-induced hypotension in the same group, although we used a rather strict criterion for the definition of tilt-induced hypotension—namely, a 20/10 mmHg or greater decline at the time of tilting compared to the spine BP, which is the criterion for orthostatic hypotension (*32*). These observations indicate that the augmenting effect of azelnidipine on the retarded sympathetic nerve activation was more effectively exerted on elderly B-H subjects who showed more severe decreases in BP by the postural change.

Although many antihypertensive agents are known to improve orthostatic hypotension in elderly hypertensive patients (*33*), the associations between dihydropyridine-type calcium blockers and postural hypotension are rather complicated: calcium blockers themselves sometimes induce postural hypotension (*34*), or have no effect on postural hypotension (*35*). Ferodipine (*36*, *37*) and nifedipine (*33*) even attenuate orthostatic hypotension. However, our study is the first to show a high prevalence of postural hypotension in long-term bedridden hypertensive elderly subjects, and the first to show an azelnidipine-induced improvement in postural hypotension among these subjects. The precise mechanism(s) by which azelnidipine improves the head-up-tilt–induced decreases in BP, especially in elderly B-H patients, is unknown. However, unlike in the case of most other long-acting dihydropyridine calcium channel antagonists, the antihypertensive efficacy of azelnidipine is characterized not only by an absence of reactive tachycardia, but also by suppressing effects on sympathetic nervous activity (*9*, *10*, *31*). The additive beneficial effects of the combination of azelnidipine and an angiotensin blocker have recently been described in a hypertensive rat-heart failure model (*38*). On the other hand, the sympathetic nervous activities in astronauts on the 12th and 13th spaceflights during the Neurolab space shuttle mission were actually enhanced compared to the pre-flight levels (*39*). According to these findings as well as the results on the recording of sympathetic nervous activity in subjects exposed to ground-based short- and long-term "stimulations" of microgravity induced by head-down tilt, Mano (*40*) reported that sympathetic neural control was lowered when subjects were exposed to short-term microgravity for several hours, but was enhanced after exposure to long-term microgravity for more than 3 days. In addition, he reported that the orthostatic intolerance based on impaired baroreflex functions in these subjects may have resulted from an exhaustion of the sympathetic nervous system by prolonged exaggerated sympathetic activity after exposure to long-term microgravity stress. He also indicated that the autonomic dysfunctions seen in bedridden subjects may be medicated by the same mechanism (*40*). Based on these observations, the beneficial effect of azelnidipine on the postural hypotension observed especially in elderly B-H patients may be the result of the augmenting effect of azelnidipine on baroreflex sensitivity through a suppression of the exaggerated sympathetic activity due to long-term microgravitational stress. It is also possible that the enhancing effect of azelnidipine on blood flow of the brain (*41*) may have contributed to the improvement of tilt-induced hypotension, since postural hypotension is associated with ischemic change in the brain on magnetic resonance imaging, such as periventricular white matter hyperintensity,

in older elderly subjects (*5*).

In the present study, we did not evaluate hemodynamic or humoral factors, such as echocardiographic measurements and circulating levels of catecholamines and factors associated with the renin-angiotensin-aldosterone system, at the time of tilting. We also did not estimate baroreflex function. These factors should be measured in the future to elucidate the beneficial effects of azelnidipine.

References

1. Masuo K, Mikami H, Habara N, Ogihara T: Orthostatic and postprandial blood pressure reduction in patients with essential hypertension. *Clin Exp Pharmacol Physiol* 1991; **18**: 155–161.
2. Rose KM, Tyroler HA, Nardo CJ, *et al*: Orthostatic hypotension and the incidence of coronary heart disease: the Atherosclerosis Risk in Communities study. *Am J Hypertens* 2000; **13**: 571–578.
3. Eguchi K, Kario K, Hoshide S, *et al*: Greater change of orthostatic blood pressure is related to silent cerebral infarct and cardiac overload in hypertensive subjects. *Hypertens Res* 2004; **27**: 235–241.
4. Masaki KH, Schatz IJ, Burchfiel CM, *et al*: Orthostatic hypotension predicts mortality in elderly men: the Honolulu Heart Program. *Circulation* 1998; **98**: 2290–2295.
5. Matsubayashi K, Okumiya K, Wada T, *et al*: Postural dysregulation in systolic blood pressure is associated with worsened scoring on neurobehavioral function tests and leukoaraiosis in the older elderly living in a community. *Stroke* 1997; **28**: 2169–2173.
6. Kario K, Eguchi K, Hoshide S, *et al*: U-curve relationship between orthostatic blood pressure change and silent cerebrovascular disease in elderly hypertensives: orthostatic hypertension as a new cardiovascular risk factor. *J Am Coll Cardiol* 2002; **40**: 133–141.
7. Tabara Y, Tachibana-Iimori R, Yamamoto M, *et al*: Hypotension associated with prone body position: a possible overlooked postural hypotension. *Hypertens Res* 2005; **28**: 741–746.
8. Grap MJ, Munro CL: Quality improvement in backrest elevation: improving outcomes in critical care. *AACN Clin Issues* 2005; **16**: 133–139.
9. Kuramoto K, Ichikawa S, Hirai A, Kanada S, Nakachi T, Ogihara T: Azelnidipine and amlodipine: a comparison of their pharmacokinetics and effects on ambulatory blood pressure. *Hypertens Res* 2003; **26**: 201–208.
10. Arita M, Hashizume T, Tanigawa K, Yamamoto H, Nishio I: A new Ca-antagonist, azelnidipine, reduced blood pressure during exercise without augmentation of sympathetic nervous system in essential hypertension: a randomized, double-blind, placebo-controlled trial. *J Cardiovasc Pharmacol* 1999; **33**: 186–192.
11. Kuroda K, Tatara K, Takatorige T, Zhao L, Shinsho F: Factors related to long-term stay in hospital by elderly people in a Japanese city. *Age Aging* 1992; **21**: 321–327.
12. Katz S, Downs TD, Cash HR, Grotz RC: Progress in development of the index of ADL. *Gerontologist* 1970; **10**: 20–30.
13. Bergstrom M, Braden BJ, Laguzza A, Holman B: The Braden scale for predicting pressure sore risk. *Nurs Res* 1987; **36**: 205–210.
14. Niimi Y, Ieda T, Hirayama M, *et al*: Clinical and physiological characteristics of autonomic failure with Parkinson's disease. *Clin Auton Res* 1999; **9**: 139–144.
15. Rosenthal MJ, Naliboff B: Postural hypotension: its meaning and management in the elderly. *Geriatrics* 1988; **43**: 31–42.
16. Carvalho MJ, van den Meiracker AH, Boomsma F, *et al*: Improved orthostatic tolerance in familial amyloidotic polyneuropathy with unnatural noradrenaline precursor L-threo-3,4-dihydroxyphenylserine. *J Auton Nerv Syst* 1997; **62**: 63–71.
17. Elmstahl S, Petersson M, Lilja B, Samuelsson SM, Rosen I, Bjuno L: Autonomic cardiovascular responses to tilting in patients with Alzheimer's disease and in healthy elderly women. *Age Ageing* 1992; **21**: 301–307.
18. Gilbert VE: Immediate orthostatic hypotension: diagnostic value in acutely ill patients. *South Med J* 1993; **86**: 1028–1032.
19. Gotshall RW, Wood VC, Miles DS: Modified head-up tilt test for orthostatic challenge of critically ill patients. *Crit Care Med* 1989; **17**: 1156–1158.
20. Gehrking JA, Hines SM, Benrud-Larson LM, Opher-Gehrking TL, Low PA: What is the minimum duration of headup tilt necessary to detect orthostatic hypotension? *Clin Auton Res* 2005; **15**: 71–75.
21. Tabara Y, Nakura J, Kondo I, Miki T, Kohara K: Orthostatic systolic hypotension and the reflection pressure wave. *Hypertens Res* 2005; **28**: 537–543.
22. Riedl B, Beckmann T, Neundorfer B, Handwerker HO, Birklein F: Autonomic failure after stroke—is it indicative for pathophysiology of complex regional pain syndrome? *Acta Neurol Scand* 2001; **103**: 27–34.
23. Hossain M, Ooi WL, Lipsitz LA: Intra-individual postural blood pressure variability and stroke in elderly nursing home residents. *J Clin Epidemiol* 2001; **54**: 488–494.
24. Rutan GH, Hermanson B, Bild DE, Kittner SJ, LaBaw F, Tell GS, CHS Collaborative Research Group: Orthostatic hypotension in older adults. The Cardiovascular Health Study. *Hypertension* 1992; **19**: 508–519.
25. Kassis E: Baroreflex control of the circulation in patients with congestive heart failure. *Dan Med Bull* 1989; **36**: 195–211.
26. Ogi M, Kojima S, Kuramochi M: Effect of postural change on urine volume and urinary sodium excretion in diabetic nephropathy. *Am J Kidney Dis* 1998; **31**: 41–48.
27. Morimoto S, Okaishi K, Onishi M, *et al*: Deletion allele of the angiotensin-converting enzyme gene as a risk factor for pneumonia in elderly patients. *Am J Med* 2002; **112**: 89–94.
28. Tonkin AL, Wing LM: Effects of age and isolated systolic hypertension on cardiovascular reflexes. *J Hypertens* 1994; **12**: 1083–1088.
29. Blomqvist CG, Stone HL: Cardiovascular adjustment to gravitation stress, in Shepherd JT, Abboud FM (eds): Handbook of Physiology, Section 2, Vol III. American Physiological Society, Bethesda, pp 1025–1063.
30. James MA, Potter JF: Orthostatic blood pressure changes and arterial baroreflex sensitivity in elderly subjects. *Age*

Ageing 1999; **28**: 522–530.
31. Oizumi K, Miyamoto M, Koike H: Antihypertensive effect of CS-905, a novel dihydropyridine calcium blocker, in conscious hypertensive dogs. *Jpn J Pharmacol* 1990; **53**: 264–266.
32. The Consensus Committee of the American Autonomic Society and the American Academy of Neurology: Consensus statement on thedefinition of orthostatic hypotension, pure autonomic failure, and multiple system atrophy. *Neurology* 1996; **46**: 1470.
33. Masuo K, Mikami H, Ogihara T, Tuck ML: Changes in frequency of orthostatic hypotension in elderly hypertensive patients under medications. *Am J Hypertens* 1996; **9**: 263–268.
34. Luukinen H, Koski K, Laippala P, Kivela SL: Prognosis of diastolic and systolic orthostatic hypotension in older persons. *Arch Intern Med* 1999; **159**: 273–280.
35. Cleophas TJ, van Marum R: Age-related decline in autonomic control of blood pressure: implications for the pharmacological management of hypertension in the elderly. *Drugs Aging* 2003; **20**: 313–319.
36. Koenig W, Binner L, Gabrielsen F, Sund M, Rosenthal J, Hombach V: Catecholamines and the renin-angiotensin-aldosterone system during treatment with felodipine ER or hydrochlorothiazide in essential hypertension. *J Cardiovasc Pharmacol* 1991; **18**: 349–353.
37. Kassis E, Amtorp O, Waldorff S, Fritz-Hansen P: Efficacy of felodipine in chronic congestive heart failure: a placebo controlled haemodynamic study at rest and during exercise and orthostatic stress. *Br Heart J* 1987; **58**: 505–511.
38. Kim-Mitsuyama S, Izumi Y, Izumiya Y, Yoshida K, Yoshiyama M, Iwao H: Additive beneficial effects of the combination of a calcium channel blocker and an angiotensin blocker on a hypertensive rat-heart failure model. *Hypertens Res* 2004; **27**: 771–779.
39. Ertl AC, Diedrich A, Biaggioni I, *et al*: Human muscle sympathetic nerve activity and plasma noradrenaline kinetics in space. *J Physiol* 2002; **538**: 321–329.
40. Mano T: Autonomic neural functions in space. *Curr Pharm Biotechnol* 2005; **6**: 319–324.
41. Oizumi K, Nishino H, Miyake S, *et al*: Hemodynamic changes following long-term administration of CS-905, a novel dihydropyridine calcium blocker, in conscious SHR. *Jpn J Pharmacol* 1990; **54**: 1–6.

Original Article

Angiotensin I–Converting Enzyme Inhibitor Improves Reactive Hyperemia in Elderly Hypertensives with Arteriosclerosis Obliterans

Masashi OKURO[1)], Shigeto MORIMOTO[1)], Takashi TAKAHASHI[2)], Kohya OKAISHI[1)], Takeshi NAKAHASHI[1)], Hiroshi MURAI[1)], Kunimitsu IWAI[1)], Tsugiyasu KANDA[2)], and Masayuki MATSUMOTO[1)]

Endothelial function in elderly hypertensive patients with arteriosclerosis obliterans has not been evaluated. We examined whether antihypertensive drugs improve vasodilatory response to reactive hyperemia of the limbs in elderly hypertensive patients (83±8 [SD] years) without (n=46, 0.9 ≤ ankle-brachial pressure index ≤1.4) and with (n=24) arteriosclerosis obliterans (ankle-brachial pressure index <0.2). Patients were randomized for treatment with monotherapy of either temocapril (14 with and 26 without arteriosclerosis obliterans) or amlodipine (10 with and 20 without arteriosclerosis obliterans) for 6 months. Blood flows of the forearms and legs were measured by strain-gauge plethysmography. The vasodilatory response to the release of compression of the forearms and thighs at 200 mmHg or 20 mmHg more than systolic blood pressure for 5 min and to sublingual administration of nitroglycerin (0.3 mg) was assessed. The maximum reactive hyperemic flow in 35 legs with arteriosclerosis obliterans was significantly (p<0.001) decreased compared to the value in legs in the control hypertensive subjects. Moreover, maximum reactive hyperemic flow in the forearms of patients with arteriosclerosis obliterans was significantly (p=0.002) decreased compared to that in the control subjects. Blood pressure was similarly decreased by treatment with temocapril or amlodipine. Response to nitroglycerin (0.3 mg) was not changed by either drug. Treatment with temocapril significantly improved maximum reactive hyperemic flow of not only the legs and forearms in control hypertensives but also the legs and forearms in patients with arteriosclerosis obliterans, and attenuated the worsening of activity of daily living in these patients, although treatment with amlodipine did not. These results suggest that the angiotensin-converting enzyme inhibitor temocapril has a beneficial effect on endothelial function in elderly patients with arteriosclerosis obliterans. (*Hypertens Res* 2006; 29: 655–663)

***Key Words*: antihypertensive drug, arteriosclerosis obliterans, elderly, hypertension, plethysmography**

Introduction

Arteriosclerosis obliterans has become one of the major health problems in the elderly, since the incidence of this disease increases with age (*1*), and since the disease not only causes decreased activity of daily living and quality of life, but is also a serious life-threatening condition due to its progressive nature and/or the high mortality of associated arterial lesions of cardiovascular organs (*2*). Arteriosclerosis obliterans frequently follows an inexorable downhill course (*3*, *4*), and, importantly, the Consensus Document of the European

From the Departments of [1)]Geriatric Medicine and [2)]General Medicine, Kanazawa Medical University, Ishikawa, Japan.

This study was supported in part by a Grant-in-Aid for Scientific Research from the Ministry of Health, Labour and Welfare of Japan (to S.M.) and a grant for promoted research from Kanazawa Medical University (S2005-5 to T.T.).

Address for Reprints: Shigeto Morimoto, M.D., Ph.D., Department of Geriatric Medicine, Kanazawa Medical University, 1–1 Daigaku, Uchinada-machi, Kahoku-gun, Ishikawa 920–0293, Japan. E-mail: shigeto@kanazawa-med.ac.jp

Received January 24, 2006; Accepted in revised form May 29, 2006.

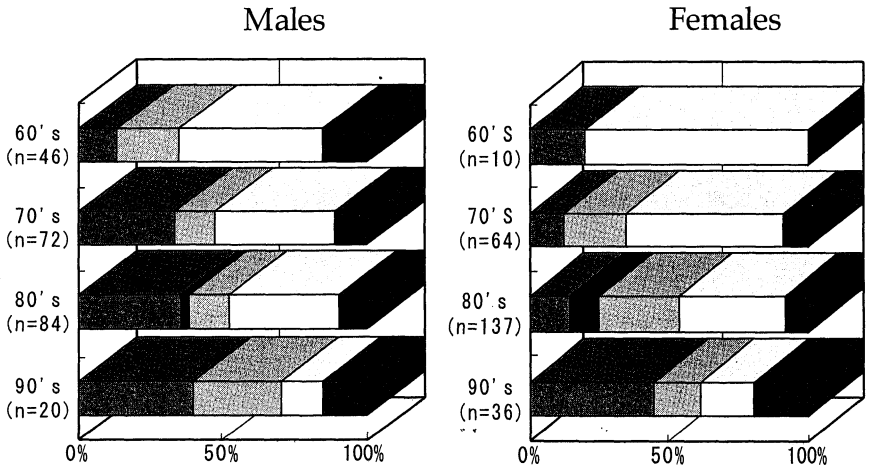

Fig. 1. *Prevalence of subjects with ABI>1.4 (■), 0.9≤ABI≤1.4 (□), 0.5≤ABI<0.9 (▒), 0.2≤ABI<0.5 (■), and ABI<0.2 (■) in males* (n=222) *and females* (n=247) *in their 60s, 70s, 80s and 90s respectively, in a hospital for the elderly.*

Working Group on Critical Limb Ischemia has concluded that there is no optimal medical therapy for this disease (*5*).

On the other hand, arteriosclerosis obliterans is highly associated with hypertension (*6*), and hypertension itself is a major risk for arteriosclerosis obliterans (*7–9*). It has been shown by microscopic examination that the endothelium of lesions of arteriosclerosis obliterans is impaired (*10*), and that endothelial function assessed by maximum reactive hyperemic flow is significantly decreased in patients with arteriosclerosis obliterans and/or hypertension (*11*). Among antihypertensive agents, angiotensin I–converting enzyme (ACE) inhibitors (*12*, *13*) and calcium antagonists (*13*, *14*) are known to maintain or even increase limb blood flow and to improve tolerability to exercise in patients with arteriosclerosis obliterans. Moreover, ACE inhibitors have been reported to have beneficial effects on endothelial function, as assessed by reactive hyperemia in middle-aged patients with essential hypertension (*15*) and in elderly patients with hypertension (*16*). However, there has been little study of the effects of these antihypertensive agents on endothelial function in this hypertension-associated disease.

In this study, we evaluated the effects of an ACE inhibitor, temocapril, and a calcium antagonist, amlodipine, on vasodilator responses in the limbs of elderly patients with hypertension with or without associated arteriosclerosis obliterans. These drugs were given as monotherapy for 6 months. We examined whether reactive hyperemia was impaired, and whether the antihypertensive agents affected the vasodilatory responses in these elderly subjects.

Methods

Study Population

The study was conducted in Sengi Hospital, which serves as both a hospital and a long-term care facility for the elderly; medical and care services are often combined in single facilities in Japan (*17*). Prior to the selection of subjects, we surveyed ankle-brachial pressure index (ABI) in 469 elderly inpatients aged 65 years or older (222 males and 247 females, including 46 males and 10 females in their 60s, 72 males and 64 females in their 70s, 84 males and 127 females in their 80s, and 20 males and 36 females in their 90s, with a mean [±SD] age of 82±9 years) in the hospital. ABI was measured as described below (*18*). Our classification of ABI was essentially based on the report of Resnick *et al.* (*18*), who used the three categories of ABI>1.4 (at least one leg), 0.9≤ABI≤1.4 (both legs), and ABI<0.9 (at least one leg). However, since about half (48%) of our subjects had an ABI<0.9, we further separated the category of ABI<0.9 into three classes, namely, 0.5≤ABI<0.9, 0.2≤ABI<0.5, and ABI<0.2 (at least one leg, respectively). The preliminary survey revealed that the numbers (%) of subjects with ABI>1.4, 0.9≤ABI≤1.4, 0.5≤ABI<0.9, 0.2≤ABI<0.5, and ABI<0.2 were 51 (12%), 191 (41%), 97 (21%), 16 (3%), and 114 (24%), respectively. Increases in age-related prevalence in those with ABI<0.2 were prominent both in males and females (Fig. 1). Moreover, the survey also disclosed that the percentage of subjects with 0.5≤ABI<0.9 was very small. Furthermore, none of the 113 subjects with 0.2≤ABI<0.9 showed any characteristic features of arteriosclerosis obliterans, such as intermittent claudication, pain at rest, or ulcer/gangrene of the lower extremities, although 12 (11%) of the 114 subjects with ABI<0.2 showed characteristic features of arteriosclerosis obliterans, *i.e.*, pain at rest (8 patients) and ulcer/gangrene (4 patients). Accordingly, we adopted rather strict criteria, using ABI<0.2 for selection of hypertensive patients with arteriosclerosis obliterans. The numbers (%) of subjects with hypertension, defined as a systolic blood pressure (SBP) of 140 mmHg or higher and/or diastolic blood pressure (DBP) of 90

mmHg or higher in the sitting position on at least three separate occasions and/or current use of antihypertensive drugs, were 19 (37%) out of 51 subjects with ABI>1.4, 67 (35%) out of the 191 with 0.9≤ABI≤1.4, 35 (36%) out of the 97 with 0.5≤ABI<0.9, 5 (31%) out of the 16 with 0.2≤ABI<0.5, and 57 (50%) out of the 114 with ABI<0.2. From among these hypertensive patients, we selected elderly patients with mild (140–159/90–99 mmHg) to moderate (160–179/100–109 mmHg) hypertension (mean±SD age: 83±8 years; age range: 68–94 years) without (n=46, 0.9≤ABI≤1.4) or with (n=24) arteriosclerosis obliterans (ABI <0.2, two legs in 11 subjects and one leg in 13 patients). Subjects showing pain at rest or ulcer/gangrene as features of arteriosclerosis obliterans, or those with diabetes mellitus (fasting blood glucose >7 mmol/l or treated with or current use of an antidiabetic drug) or hypercholesterolemia (total cholesterol >5.66 mmol/l) were excluded by clinical and laboratory examinations. None of the subjects had undergone amputation due to arteriosclerosis obliterans. Patients were randomized to treatment with initial doses of 2 mg temocapril (14 patients with and 26 patients without arteriosclerosis obliterans; Sankyo Co., Ltd., Tokyo, Japan) or 2.5 mg amlodipine (10 patients with and 20 patients without arteriosclerosis obliterans; Sumitomo Pharmaceutical Ltd., Osaka, Japan) once daily for 6 months. When the blood pressure was not decreased by 20/10 mmHg or to below 150/90 mmHg, the dose of drug was doubled. Blood pressure control was achieved in all hypertensive subjects with monotherapy of either drug. All patients had either never been treated (n=35) or had discontinued antihypertensive drugs—in this case, β-blockers (n=2), ACE inhibitors (n=17), or calcium antagonists (n=16)—for at least 4 weeks before the study. Biochemical factors were measured in blood collected in the morning after overnight fasting. The study protocol was approved by the ethical committee of the hospital. All subjects were Japanese, and only those who gave informed consent were enrolled in the study.

Measurement of Ankle and Arm Blood Pressures

At each ABI measurement, right arm blood pressures and bilateral ankle blood pressure (posterior tibial artery), measured by handheld Doppler ultrasonography (Imex Medical Systems, Golden, USA), were taken with the subject supine. If the absent pulse was verified, ankle blood pressure measures were taken on the dorsalis pedis. The means of the 2 measurements for each leg and for the arm were used to calculate ABI, and the lower of the 2 values was used to define ABI for each individual (*18*).

Blood Flow Measurements of the Forearm and Legs

The study was conducted in a dark, quiet, temperature-controlled (at 23°C) room. Subjects rested for 30 min in the supine position before the study. Blood flow of the right forearm and of both legs was measured by strain gauge plethysmography (model EC6; De Hokanson, Inc., Bellevue, USA) (*19*, *20*). Hand and foot circulations were excluded by wrist and ankle cuffs inflated to suprasystolic pressure. Mercury-in-silastic strain gauges that had been electrically calibrated were placed on the widest part of the right forearm and both lower legs at 5 cm and 8 cm below the antecubital and popliteal creases, respectively. Blood flows of forearm or legs were calculated from the rate of increase in forearm or leg volumes, while venous return was prevented by inflating the cuffs at upper arm or thigh to a venous-occlusion pressure of 50 mmHg. Flow measurements were recorded for 9 s every 15 s, and an average of 4 measurements was used for analysis. Endothelium-dependent vasodilatation was assessed by ischemia-induced reactive hyperemia. After a baseline recording of 4 min, ischemia was induced for 5 min by inflating the upper arm cuff to 200 mmHg or 20 mmHg more than SBP. Immediately after cuff deflation, maximal hyperemic blood flow was measured (peak flow), followed by continuous measurements for 3 min. At least 15 min after the last measurement, blood flow was measured to confirm that it had returned to the basal level. Then, endothelium-independent vasorelaxation was assessed after sublingual administration of nitroglycerin at 0.3 mg by one puff of a spray device (Miokol Spray; Toa Eiyo, Tokyo, Japan), and blood flows were measured for 5 min. The blood flow is expressed as ml of blood per min per 100 ml of limb volume (*15*, *20*, *21*).

Other Measurements

We evaluated activity of daily living according to the following four states of ambulation: walking, using a wheelchair, sitting on the bed, and bedridden. We also recorded known risk factors for arteriosclerosis obliterans, including dementia (Mini-Mental State Examination score≤23), chronic stage of stroke (motor deficit and evidence of cerebral hemispheric stroke on CT or MRI), and chronic ischemic heart disease (previous myocardial infarction or angina pectoris).

Statistical Analyses

Data are expressed as the mean±SD. Differences in changes of blood pressure and vasodilatory responses by treatment with antihypertensive drugs were assessed by analysis of variance with repeated measurements. Changes in ABI and activity of daily living were assessed by non-parametric Wilcoxon test. A value of $p<0.05$ was regarded as significant. Differences among the four groups were analyzed by Kruskal-Wallis χ^2 and Mann-Whitney U test for multiple comparisons with post-hoc Bonferroni correction. The statistical significance of p values was set at 0.008 for the analysis among four groups. Data were analyzed on a microcomputer running SPSS (SPSS Inc., Chicago, USA).

Table 1. Comparison of Clinical Factors between Hypertensive Patients with and without Arteriosclerosis Obliterans

	Control subjects		Arteriosclerotic patients	
	Amlodipine (n=20)	Temocapril (n=26)	Amlodipine (n=10)	Temocapril (n=14)
Clinical background				
Age (years)	82±7	83±8	83±7	83±8
Sex (male/female)	7/13	10/16	4/6	5/9
Total cholesterol (mmol/l)	4.89±0.32	4.86±0.30	4.85±0.29	4.87±0.28
Fasting blood glucose (mmol/l)	5.06±0.34	5.03±0.20	5.04±0.31	5.04±0.29
Dementia (n (%))	13 (65)	16 (62)	6 (60)	8 (57)
Chronic stage of stroke (n (%))	4 (20)	8 (31)	2 (20)	3 (21)
Ischemic heart disease (n (%))	7 (35)	8 (31)	3 (30)	3 (21)
Before				
SBP (mmHg)	161±12	162±13	162±14	162±12
DBP (mmHg)	82±7	84±8	83±7	82±6
Heart rate (bpm)	68±5	69±7	67±6	68±7
ABI	1.03±0.09	1.04±0.10	0.11±0.010#	0.10±0.01#
Activity of daily living (n (%))				
Walking	11 (55)	15 (57)	6 (60)	8 (57)
Using a wheelchair	5 (25)	6 (23)	2 (20)	4 (29)
Sitting on the bed	2 (10)	2 (8)	1 (10)	1 (7)
Bedridden	2 (15)	3 (12)	1 (10)	1 (7)
Six months				
SBP (mmHg)	138±10†	137±11†	138±10†	139±12†
DBP (mmHg)	72±7†	74±8†	72±9†	74±8†
Heart rate (bpm)	69±5	71±7	69±6	69±8
ABI	0.99±0.05	1.05±0.03	0.10±0.01#	0.13±0.01#,†
Activity of daily living (n (%))				
Walking	10 (50)	15 (57)	4 (40)	10 (72)
Using a wheelchair	3 (15)	5 (19)	1 (10)	2 (14)
Sitting on the bed	4 (20) *	3 (12)	2 (20) *	0 (0)
Bedridden	3 (15)	3 (12)	3 (30)	2 (14)

SBP, systolic blood pressure; DBP, diastolic blood pressure; bpm, beats per minute; ABI, ankle-brachial pressure index. Values are mean±SD. #$p<0.008$: significant difference *vs.* control groups by Kruskal-Wallis analysis. *$p<0.05$ and †$p<0.01$: significant difference *vs.* before.

Results

Table 1 shows the backgrounds of the groups of hypertensive elderly patients with and without arteriosclerosis obliterans treated with amlodipine or temocapril. There was no statistically significant difference among the four groups in age, male/female ratio, circulating concentration of total cholesterol or glucose, activity of daily living, or prevalence of dementia, chronic phase of stroke, or chronic ischemic heart disease. Of course, the ABI values in the two groups with arteriosclerosis obliterans were significantly ($p<0.008$) reduced compared to those in the two control groups (Table 1).

The values of basal blood flow (Fig. 2a), nitroglycerin-induced increase in blood flow (Fig. 2b), and maximum reactive hyperemic flow (Fig. 2c) in the 35 affected legs of the 24 hypertensive patients with arteriosclerosis obliterans were significantly ($p<0.001$ in each) decreased compared to the respective values in the 92 legs of 46 age- and sex-matched elderly hypertensive control subjects. Although the basal and nitroglycerin-induced increases in blood flow in the right forearm were similar in the two hypertensive groups, maximum reactive hyperemic flow in the right forearm in the 24 patients with arteriosclerosis obliterans was significantly ($p<0.01$) decreased compared to that in the 46 control subjects.

Baseline values (ml/min/100 ml) of blood flow in the legs and forearms before treatment in patients with arteriosclerosis obliterans (1.8±0.4 and 3.9±0.5 in the amlodipine-treated group and 1.9±0.5 and 4.0±0.4 in the temocapril-treated group) and patients without arteriosclerosis obliterans (3.2±0.4 and 4.1±0.4 in the amlodipine-treated group and 3.3±0.4 and 4.2±0.5 in the temocapril-treated group) were

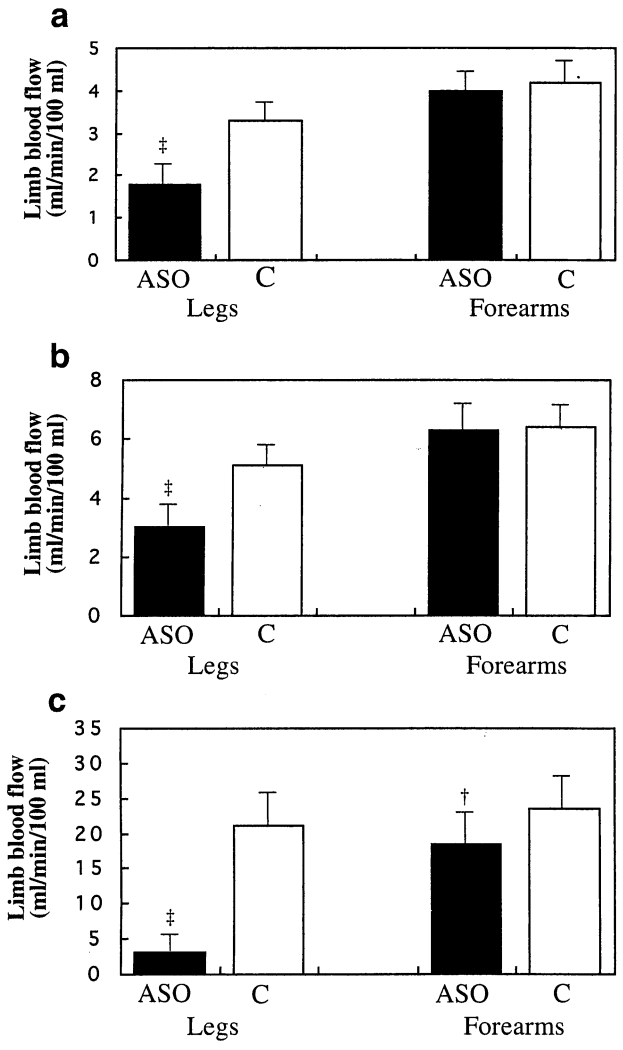

Fig. 2. *Comparison of basal blood flow (a), nitroglycerin-induced increase in blood flow (b), and maximum reactive hyperemic flow (c) between legs with arteriosclerosis obliterans (ASO,* n=*35, solid bars) and legs in control hypertensive patients (C,* n=*92, open bars) (left), and between the right forearms in ASO patients* (n=*24) and control patients* (n=*46) (right).* †p<*0.01,* ‡p<*0.001: significant differences between hypertensive elderly patients with and without ASO.*

similar in the two drug groups. Basal blood flow in the affected legs of patients with arteriosclerosis obliterans (n=14 in the amlodipine-treated group and n=21 in the temocapril group) was again significantly lower compared to that in the legs of patients without arteriosclerosis obliterans in the respective drug groups.

Blood pressure was well controlled by 2.5 mg (n=6 in the group with arteriosclerosis obliterans and n=12 in the control group) or 5 mg (n=4 in the group with arteriosclerosis obliterans and n=8 in the control group) amlodipine, or 2 mg (n=11 in the group with arteriosclerosis obliterans and n=22 in the control group) or 4 mg (n=3 in the group with arteriosclerosis obliterans and n=5 in the control group) temocapril. Monotherapy of either amlodipine or temocapril for 6 months produced a similar reduction of blood pressure (Table 1).

Treatment with temocapril slightly but significantly increased the ABI value in patients with arteriosclerosis obliterans, although amlodipine did not significantly change the ABI value in patients with arteriosclerosis obliterans (Table 1). On the other hand, basal blood flow and nitroglycerin-induced increase in blood flow (Fig. 3a) in the legs and forearm were not significantly changed by either drug. Treatment with temocapril significantly improved maximum reactive hyperemic flow (ml/min/100 ml) of not only the legs (21.8±3.8 *vs.* 24.9±3.7, p<0.001) and forearm (24.2±3.6 *vs.* 27.3±3.6, p<0.01) in control hypertensive subjects, but also in the affected legs (2.8±2.2 *vs.* 5.8±2.5, p<0.001) and forearms (18.2±3.8 *vs.* 22.3±2.9, p<0.01) of patients with arteriosclerosis obliterans, although treatment with amlodipine did not affect maximum reactive hyperemic flow (Fig. 3b). Moreover, the activities of daily living were slightly but significantly decreased in control subjects and patients with arteriosclerosis obliterans treated with amlodipine for 6 months, but not in the other two groups treated with temocapril (Table 1).

Discussion

As a diagnostic criterion for arteriosclerosis obliterans, ABI<0.9 is often used (*18*, *22*). According to one report, the prevalence of asymptomatic arteriosclerosis obliterans defined by an ABI value <0.9 was only 3.4% in subjects aged 65 years or more who were inhabitants of rural communities in Japan (*22*). However, our preliminary survey in 469 inpatients of an elderly hospital aged 65 years or older revealed that about half of the elderly subjects would have been diagnosed with arteriosclerosis obliterans if this criterion had been adopted. Moreover, subjects with 0.2≤ABI<0.9 did not show any characteristic features of arteriosclerosis obliterans. Furthermore, only 3% of the total subject group had 0.2≤ABI<0.5. According to these findings, we selected subjects with ABI<0.2 as subjects with arteriosclerosis obliterans in this study. Furthermore, subjects with apparent rest pain or ulcer/gangrene were excluded from the present study, and thus most of the remaining subjects would be classified as stage I or II in Fontaine classification. However, we did not adopt the Fontaine classification for staging of the severity of arteriosclerosis obliterans, since many of the inpatients of the elderly hospital were not capable of complaining about intermittent claudication or rest pain of the lower extremities, and in some cases not capable of walking, due to rather high prevalence of dementia and chronic phase of stroke (Table 1). Instead, we analyzed the activity of daily living in the four groups, and found no statistically significant difference in this parameter among the four groups. This observation suggests that decreased activity of daily living due to arteriosclerosis

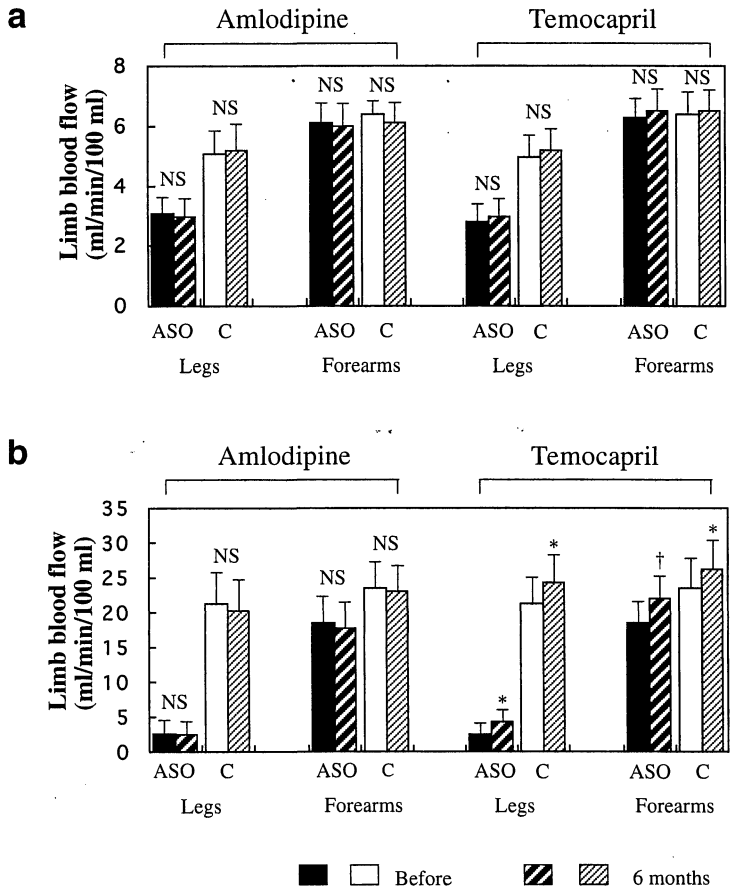

Fig. 3. *Changes of blood flow in legs and forearms in response to sublingual administration of nitroglycerin (a), and of reactive hyperemic response (b), before and after 6 months of treatment with amlodipine or temocapril. ASO, patients with arteriosclerosis obliterans; C, control patients.* *$p<0.05$, †$p<0.01$: *significant differences between before and after 6 months of treatment; NS: not significant.*

obliterans itself was not a direct cause of the differences seen in the basal and reactive hyperemic blood flow in this study.

There may be two possible mechanisms which could explain the decreased reactive hyperemia in the diseased legs. Since we measured ankle blood pressure at the lower part of the main coarctation sites of arteriosclerosis obliterans (*23*), the first possibility is that the endothelial function had already reached an almost maximal level because of the decreased blood stream due to coactation of the upper part of the legs which would have resulted in a decrease in reactive hyperemia after complete occlusion by the cuff. The second possibility is that the decreased reactive hyperemia in the diseased legs was one of the general findings of the reduced vasodilatory endothelial function represented by those in upper extremities, since vasodilatory responses to reactive hyperemia were significantly decreased not only in the diseased legs but also in the forearms of patients with arteriosclerosis obliterans. The results of several reports may lend support to this latter mechanism. Postischemic hyperemia in human limbs is thought to be partly mediated by nitric oxide (NO), since inhibition of NO synthesis by N^G-monomethyl-L-arginine has been shown to decrease reactive hyperemic flow (*24*), although the participation of other mechanisms, including endothelium-dependent vasodilating substances such as prostaglandins (*25*) and endothelium-stimulating substances such as adenosine (*26*), has also been reported. Impaired endothelial function in hypertensive patients has been demonstrated by several investigators (*15*, *27–29*). Moreover, aging itself is also a causal factor for decreased endothelial function (*30*). Furthermore, a generalized decrease of endothelial function was also reported in patients with thromboangiitis obliterans (Buerger's disease), another occlusive arterial disease (*31*). In the present study, on the other hand, treatment with temocapril slightly but significantly increased the ABI value, and improved the reactive hyperthermia even in the legs with arteriosclerosis obliterans without any significant change in basal blood flow, suggesting that this ACE inhibitor improves not only the generalized decrease in endothelial function in patients with arteriosclerosis obliterans, but also might improve the decreased reactivity of the endothelial function

due to defatigation by continuous stimulation of the decreased blood stream.

Our results also showed that the reactive hyperemia in the legs and forearms in control hypertensive subjects as well as in the affected legs and forearms of patients with arteriosclerosis obliterans was improved by 6 months of treatment with an ACE inhibitor, temocapril, but not by a calcium antagonist, amlodipine. Moreover, significant decreases in the activity of daily living observed both in control subjects and patients with arteriosclerosis obliterans treated with amlodipine for 6 months were apparently attenuated by treatment with the ACE inhibitor. Treatment with amlodipine and temocapril produced a similar blood pressure reduction after 6 months of treatment. Both drugs are long-acting antihypertensive agents that are usually given once a day. Therefore, it is unlikely that the difference in duration of normotension can explain the results obtained in this study. ACE inhibitors reduce circulating and tissue levels of angiotensin II (*32*), the most potent vasoconstrictor, which causes sequential production of other vasoconstricting factors such as endothelin (*33*) and prostaglandin H_2 (*34*) from endothelial cells, and production of superoxide, an inactivator of NO, *via* the stimulation of reduced nicotine amide adenine dinucleotide oxidase (*35*). Moreover, ACE inhibitors induce accumulation of bradykinin (*36*), which causes the release of endothelium-derived relaxing factor from the endothelium (*37*) and the ACE inhibitor–induced increase in reactive hyperemia (*38*). These mechanisms may participate in the improvement of vasodilatory responses to reactive hyperemia in temocapril-treated elderly patients with hypertension. Interestingly, it has also recently been reported that brachial flow-mediated vasodilation is significantly correlated with coronary endothelial function and fibrinolytic activity in response to bradykinin in 14 diabetic and 63 non-diabetic subjects (*39*). The results of our study are partly compatible with previous reports demonstrating the beneficial effects of ACE inhibitors on endothelial function as assessed by reactive hyperemia in middle-aged patients with essential hypertension (*15*) and in elderly patients with hypertension (*16*). Moreover, treatment with temocapril might improve the decreased reactivity of endothelial function due to defatigation by continuous stimulation of the decreased blood stream.

In the present study, on the other hand, treatment with amlodipine had no effects on reactive hyperemia in the legs and forearms of elderly hypertensive patients with and without arteriosclerosis obliterans. Since amlodipine (*40*) and other calcium antagonists (*41*) are reported to enhance *in vitro* endothelial synthesis of NO, the reason for the difference in the vasodilatory response between the two antihypertensives is uncertain. However, our results are partly compatible with the clinical observations that treatment with amlodipine failed to improve forearm reactive hyperemia (*15*) and L-arginine–induced increase in renal plasma flow (*42*) in patients with essential hypertension.

In the present study, however, we did not measure factors related to the renin-angiotensin system or bradykinin. Further studies including evaluations of local or systemic levels of these factors are required to elucidate the precise mechanism of the efficacy of ACE inhibitors for improvement of vasodilatory responses to reactive hyperemia, especially in elderly hypertensive patients with arteriosclerosis obliterans, since ACE inhibitors suppress local and systemic formation of angiotensin II (*32*) and degradation of bradykinin (*36*) and since local bradykinin has been reported to play a role in the ACE inhibitor–induced improvement of endothelial function in humans (*38*). Moreover, because they were asymptomatic, despite their rather low ABI values, the majority of elderly inpatients with arteriosclerosis obliterans in this study were not treated with anti-platelet drugs, anticoagulants, or prostaglandins, which are standard prescriptions for younger patients with this disease. The efficacies of these drugs for prevention of progression and treatment of arteriosclerosis obliterans in oldest–old patients like our subjects have not been examined.

Reactive hyperemia-induced increase in forearm blood flow is a frequently used marker of endothelium-dependent vasorelaxation, especially because its measurement is noninvasive (*43*, *44*). However, it has certain limitations compared with the reference method of forearm blood flow measurement during intra-arterial infusion of acetylcholine. Hyperemic blood flow is not exclusively dependent on the endothelium, because in addition to endothelium-derived vasoactive agents, other local metabolic factors may contribute to vasodilatation after ischemia. Furthermore, the placement of the arm occlusion (upper *vs.* lower arm) and the age of the investigated subjects may influence the correlation of hyperemic forearm blood flow with endothelium-mediated vasorelaxation.

References

1. Makino H, Aoki M, Hashiya N, *et al*: Increase in peripheral blood flow by intravenous administration of prostaglandin E1 in patients with peripheral arterial disease, accompanied by up-regulation of hepatocyte growth factor. *Hypertens Res* 2004; **27**: 85–91.
2. Lambert GE: Management alternatives of infrainguinal arteriosclerosis obliterans in the elderly. *Surg Clin North Am* 1986; **66**: 293–303.
3. Dormandy J, Mahir M, Ascady G, *et al*: Fate of the patient with chronic leg ischaemia: a review article. *J Cardiovasc Surg (Torino)* 1989; **30**: 50–57.
4. Rutherford RB, Flanigan DP, Gupta SK, *et al*, Ad Hoc Committee on Reporting Standards, Society for Vascular Surgery/North American Chapter, International Society for Cardiovascular Surgery: Suggested standards for reports dealing with lower extremity ischemia. *J Vasc Surg* 1986; **4**: 80–94.
5. No Authors Listed: Second European Consensus Document on Chronic Critical Leg Ischemia. *Circulation* 1991; **84** (4 Suppl): IV1–IV26.

6. Hozawa A, Ohmori K, Kuriyama S, *et al*: C-reactive protein and peripheral artery disease among Japanese elderly: the Tsurugaya Project. *Hypertens Res* 2004; **27**: 955–961.
7. Olin JW: Antihypertensive treatment in patients with peripheral vascular disease. *Cleve Clin J Med* 1994; **61**: 337–344.
8. Qian SX, Iwai T, Endo M, Sato S, Muraoka Y, Inoue Y: Comparison of arteriosclerosis obliterans of lower limbs between China and Japan. *Bull Tokyo Med Dent Univ* 1990; **37**: 19–26.
9. National High Blood Pressure Education Program Working Group: National High Blood Pressure Education Program Working Group report on hypertension in the elderly. *Hypertension* 1994; **23**: 275–285.
10. Uchida Y, Nakamura F, Morita T: Observation of atherosclerotic lesions by an intravascular microscope in patients with arteriosclerosis obliterans. *Am Heart J* 1995; **130**: 1114–1119.
11. Milio G, Cospite V, Cospite M: Hypertension and peripheral arterial disease: a plethysmographic study. *Angiology* 1997; **48**: 241–245.
12. Roberts DH, Tsao Y, McLoughlin GA, Breckenridge A: Placebo-controlled comparison of captopril, atenolol, labetalol, and pindolol in hypertension complicated by intermittent claudication. *Lancet* 1987; **2**: 650–653.
13. Bernardi D, Bartoli P, Ferreri A, Geri AB, Ieri A: Assessment of captopril and nicardipine effects on chronic occlusive arterial disease of the lower extremity using Doppler ultrasound. *Angiology* 1988; **39**: 942–952.
14. Lewis P, Psaila JV, Davies WT, Morgan RH, Woodcock JP: Nifedipine in patients with peripheral vascular disease. *Eur J Vasc Surg* 1989; **3**: 159–164.
15. Iwatsubo H, Nagano M, Sakai T, *et al*: Converting enzyme inhibitor improves forearm reactive hyperemia in essential hypertension. *Hypertension* 1997; **29**: 286–290.
16. Deng YB, Wang XF, Le GR, Zhang QP, Li CL, Zhang YG: Evaluation of endothelial function in hypertensive elderly patients by high-resolution ultrasonography. *Clin Cardiol* 1999; **22**: 705–710.
17. Kuroda K, Tatara K, Takatorige T, *et al*: Factors related to long-term stay in hospital by elderly people in a Japanese city. *Age Aging* 1992; **21**: 321–327.
18. Resnick HE, Lindsay RS, McDermott MM, *et al*: Relationship of high and low ankle brachial index to all-cause and cardiovascular disease mortality: the Strong Heart Study. *Circulation* 2004; **109**: 733–739.
19. Hokanson DE, Summer DS, Strandness DEJ: An electrically calibrated plethysmograph for direct measurement of limb blood flow. *IEEE Trans Biomed Eng* 1975; **22**: 25–29.
20. Wassmann S, Hilgers S, Laufs U, Bohm M, Nickenig G: Angiotensin II type 1 receptor antagonism improves hypercholesterolemia-associated endothelial dysfunction. *Arterioscler Thromb Vasc Biol* 2002; **22**: 1208–1212.
21. Komai N, Ohishi M, Moriguchi A, *et al*: Low-dose doxazosin improved aortic stiffness and endothelial dysfunction as measured by noninvasive evaluation. *Hypertens Res* 2002; **25**: 5–10.
22. Fujiwara T, Saitoh S, Takagi S, *et al*: Prevalence of asymptomatic arteriosclerosis obliterans and its relationship with risk factors in inhabitants of rural communities in Japan: Tanno-Sobetsu study. *Atherosclerosis* 2004; **177**: 83–88.
23. Elsman BH, Legemate DA, van der Heyden FW, de Vos H, Mali WP, Eikelboom BC: The use of color-coded duplex scanning in the selection of patients with lower extremity arterial disease for percutaneous transluminal angioplasty: a prospective study. *Cardiovasc Intervent Radiol* 1996; **19**: 313–316.
24. Tagawa T, Imaizumi T, Endo T, Shiramoto M, Harasawa Y, Takeshita A: Role of nitric oxide in reactive hyperemia in human forearm vessels. *Circulation* 1994; **90**: 2285–2290.
25. Kilbom A, Wennmalem A: Endogenous prostaglandins as local regulators of blood flow in man; effect of indomethacin on reactive and functional hyperemia. *J Physiol* 1976; **257**: 109–121.
26. Carlsson I, Sollevi A, Wennmalm A: The role of myogenic relaxation, adenosine and prostaglandins in human forearm reactive hyperemia. *J Physiol* 1987; **389**: 147–161.
27. Panza JA, Quyyumi AA, Brush JE Jr, Epstein SE: Abnormal endothelium-dependent vascular relaxation in patients with essential hypertension. *N Engl J Med* 1990; **323**: 22–27.
28. Linder L, Kiowski W, Buhler FR, Luscher TF: Indirect evidence for the release of endothelium-derived relaxing factor in human forearm circulation *in vivo*: blunted response in essential hypertension. *Circulation* 1990; **81**: 1762–1767.
29. Iiyama K, Nagano M, Yo Y, *et al*: Impaired endothelial function with essential hypertension assessed by ultrasonography. *Am Heart J* 1996; **132**: 779–782.
30. Celermajer DS, Sorensen KE, Spiegelhalter DJ, Georgakopoulos D, Robinson J, Deanfield JE: Aging is associated with endothelial dysfunction in healthy men years before the age-related decline in women. *J Am Coll Cardiol* 1994; **24**: 471–476.
31. Makita S, Nakamura M, Murakami H, Komoda K, Kawazoe K, Hiramori K: Impaired endothelium-dependent vasorelaxation in peripheral vasculature of patients with thromboangiitis obliterans (Buerger's disease). *Circulation* 1996; **94**: 11211–11215.
32. Zhou JL, Froomes P, Casley D, *et al*: Perindopril chronically inhibits angiotensin-converting enzyme in both the endothelium and adventitia of the internal mammary artery in patients with ischemic heart disease. *Circulation* 1997; **96**: 174–182.
33. Hahn AW, Resink TJ, Scott-Burden T, Powell J, Dohi Y, Buhler FR: Stimulation of endothelin mRNA and secretion in the rat vascular smooth muscle cells: a novel autocrine function. *Cell Regul* 1990; **1**: 649–659.
34. Lin L, Mistry M, Stier CT Jr, Nasjletti A: Role of prostanoids in renin-dependent and renin-independent hypertension. *Hypertension* 1991; **17**: 517–525.
35. Griendling K, Ollerenshaw JD, Minieri CA, Alexander RW: Angiotensin II stimulates NADH and NADPH activity in cultured vascular smooth muscle cells. *Circ Res* 1994; **74**: 1141–1148.
36. Kitakaze M, Node K, Takashima S, Minamino T, Kuzuya T, Hori M: Cellular mechanisms of cardioprotection afforded by inhibitors of angiotensin converting enzyme in ischemic hearts: role of bradykinin and nitric oxide. *Hypertens Res* 2000; **23**: 253–259.
37. Mombouli JV, Illiano S, Nagao T, Scott-Burden T, Van-

houtte PM: Potentiation of endothelium-dependent relaxations to bradykinin by angiotensin I converting enzyme inhibitors in canine coronary artery involves both endothelium-derived relaxing and hyperpolarizing factors. *Circ Res* 1992; **71**: 137–144.
38. Hornig B, Kohler C, Drexler H: Role of bradykinin in mediating vascular effects of angiotensin-converting enzyme inhibitors in humans. *Circulation* 1997; **95**: 1115–1118.
39. Tarutani Y, Matsumoto T, Takashima H, Yamane T, Horie M: Brachial artery flow-mediated vasodilation is correlated with coronary vasomotor and fibrinolytic responses induced by bradykinin. *Hypertens Res* 2005; **28**: 59–66.
40. Zhang X, Hintze TH: Amlodipine releases nitric oxide from canine coronary microvessels: an unexpected mechanism of action of a calcium channel–blocking agent. *Circulation* 1998; **97**: 576–580.
41. Yang J, Fukuo K, Morimoto S, Niinobu T, Suhara T, Ogihara T: Pranidipine enhances the action of nitric oxide released from endothelial cells. *Hypertension* 2000; **35**: 82–85.
42. Higashi Y, Oshima T, Sasaki S, *et al*: Angiotensin-converting enzyme inhibition, but not calcium antagonism, improves a response of the renal vasculature to L-arginine in patients with essential hypertension. *Hypertension* 1998; **32**: 16–24.
43. Higashi Y, Sanada M, Sasaki S, *et al*: Effect of estrogen replacement therapy on endothelial function in peripheral resistance arteries in normotensive and hypertensive postmenopausal women. *Hypertension* 2001; **37**: 651–657.
44. Cortella A, Zambon S, Sartore G, *et al*: Calf and forearm blood flow in hypercholesterolemic patients. *Angiology* 2000; **51**: 309–318.

The Journal of International Medical Research
2006; 34: 297 – 302

Angiotensin-II Receptor Antagonist Alleviates Non-alcoholic Fatty Liver in KKAy Obese Mice with Type 2 Diabetes

F YU[1,4], T TAKAHASHI[1], J MORIYA[1], K KAWAURA[1], J YAMAKAWA[1], K KUSAKA[1], T ITOH[1], H SUMINO[3], S MORIMOTO[2] AND T KANDA[1]

[1]Department of General Medicine and [2]Department of Geriatric Medicine, Kanazawa Medical University, Ishikawa, Japan; [3]Department of Medicine and Biological Science, Gunma University Graduate School of Medicine, Gunma, Japan; [4]Department of Traditional Chinese Medicine, Second Affiliated Hospital of China Medical University, Liaoning, China

We examined the effects of the angiotensin-II receptor antagonist candesartan on non-alcoholic fatty liver (NAFL) and circulating adiponectin concentrations in KKAy obese mice with type 2 diabetes mellitus. The KKAy mice were randomly assigned to receive either candesartan at a once-daily dose of 10 mg/kg (n = 5) or placebo (n = 5). The differences in liver weight, histological evaluation of hepatic lipid infiltration, serum adiponectin concentration and hepatic adiponectin mRNA levels between the two groups were determined on day 7 after treatment was initiated. Candesartan-treated mice demonstrated significantly lower liver weights and reduced lipid droplets in hepatic cells compared with control mice. The circulating adiponectin levels and hepatic expression of adiponectin mRNA were significantly higher in candesartan-treated mice than control mice. These results suggest that candesartan might alleviate NAFL through elevation of circulating adiponectin levels in KKAy obese mice with type 2 diabetes mellitus.

KEY WORDS: CANDESARTAN; ANGIOTENSIN-II RECEPTOR ANTAGONIST; NON-ALCOHOLIC FATTY LIVER; OBESITY; DIABETES; ADIPONECTIN

Introduction

Non-alcoholic fatty liver (NAFL) is emerging as one of the most common liver diseases in industrialized countries,[1] and it is recognized as one of the leading causes of chronic liver disease.[2] Although NAFL may occur in non-obese patients,[3] most cases of NAFL are associated with obesity, type 2 diabetes mellitus,[4] hyperlipidaemia[5] and insulin resistance.

Adiponectin is an approximately 30-kDa protein that circulates in plasma as multimeric complexes at relatively high concentration (2 – 10 μg/ml), and it plays a crucial role in the association between obesity, type 2 diabetes mellitus and insulin resistance.[6] Recent intensive research on obesity has shown that hypoadiponectinaemia is associated with many cardiovascular and metabolic complications,

including NAFL,[7,8] although the pathogenic relationship between obesity, metabolic syndrome and cardiovascular diseases remains poorly understood.

Angiotensin-II, the main peptide of the renin–angiotensin system, is a true cytokine that regulates cell growth, inflammation and fibrosis,[9] and it plays an important role in the pathophysiology of various cardiovascular disorders, such as hypertension and atherosclerosis. It has been reported that blockade of the renin–angiotensin system increases adiponectin concentrations in patients with essential hypertension.[10] However, the role of an angiotensin-II receptor antagonist on NAFL and circulating adiponectin levels in obese patients with type 2 diabetes remains unknown. The purpose of this study was to examine the effects of an angiotensin-II receptor antagonist, candesartan, on NAFL in KKAy obese mice with type 2 diabetes, focusing on its effect on adiponectin levels.

Materials and methods

ANIMALS AND TREATMENTS

Nine-week-old female KKAy mice weighing 40 – 42 g were purchased from Clea Japan Inc. (Tokyo, Japan), and maintained at the animal centre at Kanazawa Medical University (Ishikawa, Japan). Food and water were freely available. Ethical approval for this study was obtained from the animal experimental committee at Kanazawa Medical University. All mice were randomly assigned to receive either candesartan 10 mg/kg once daily (n = 5) or placebo (n = 5). Candesartan, which was provided by Takeda Chemical Industries Ltd (TCV-116, Lot No. HB982; Osaka, Japan), was dissolved with gum arabic in distilled water and diluted with water to the appropriate concentration. Candesartan was administrated orally with an oesophageal tube. Arabic gum dissolved in water was used as the placebo treatment.

LIVER WEIGHTS AND HISTOLOGICAL EXAMINATION OF THE LIVER

The mice were weighed on day 7 after treatment and then killed by cervical dislocation. Livers were removed immediately and weighed, and the ratio of liver weight (LW) to body weight (BW) was calculated for each animal.

Liver specimens were fixed for 24 h in 10% buffered formalin and embedded in paraffin. The remaining liver tissue was frozen in liquid nitrogen and stored at –80 °C until molecular analysis. Haematoxylin and eosin-stained liver sections were graded blindly under the light microscope for the degree of fatty change, inflammation and necrosis as described previously.[8] Ten low-power fields (magnification × 100) per liver were examined by an experienced pathologist who had no knowledge of our study design. The degree of lipid infiltration was graded from 0 to 4 as follows: grade 0, no fat present; grade 1, lipid infiltration involving < 25%; grade 2, lesions involving 25 – 50%; grade 3, lesions involving 50 – 75%; and grade 4, lesions involving 75 – 100%. Oil Red O staining was performed on frozen sections in order to confirm the distribution of lipid droplets.

BLOOD SAMPLE ASSAY

On day 7 after treatment, blood samples were obtained from all mice before they were killed. All serum samples were stored at –80 °C until analysis. Blood glucose concentrations were determined by a glucose oxidation method using a Fuji Dry Chem System (Medical System Co., Tokyo, Japan). Circulating adiponectin levels were measured by enzyme-linked immunosorbent assay (ELISA) according to the manufacturer's instructions (ELISA kit for mouse or rat adiponectin; Otsuka Pharmaceutical Co., Ltd, Tokyo, Japan).

The ELISA adiponectin kit had a limit of sensitivity of 0.25 ng/ml and an intra-assay variation of < 10%, and there was no cross-reactivity with specimens from other animals, including sheep.

ADIPONECTIN MRNA EXPRESSION ANALYSIS

RNA extraction from frozen hepatic tissues was performed as described by the manufacturer (RNeasy Mini Kit, Qiagen Inc., Tokyo, Japan). DNase was used during the RNA extraction to avoid DNA contamination. Total RNA concentration was determined by measuring the optical density at 260 and 280 nm. Aliquots of RNA (20 µl) from the liver tissue were used to produce cDNA. Comparative expression levels of adiponectin mRNA in liver from both groups of animals were determined using a quantitative real-time reverse transcriptase polymerase chain reaction (RT-PCR) as described previously.[11] TaqMan MGB Probe (Applied Biosystems Inc., Foster City, CA, USA) was used for real-time PCR. We used a commercially available kit for adiponectin RT-PCR (Mm00456425_m1, Applied Biosystems Inc.). The threshold cycle number up to 50 cycles (C_t value) within the RT-PCR was examined for the adiponectin mRNA levels. The glyceraldehyde-3-phosphate dehydrogenase (GAPDH) gene was used as an endogenous internal standard, which was amplified with specific primers for the number of cycles. A negative control that did not contain template cDNA was always included. ΔC_t values referred to the differences between the C_t values for the target gene and the GAPDH gene. After confirming that the amplification efficiencies of the target molecule and GAPDH transcripts were approximately equal, the amount of the adiponectin transcript relative to the GAPDH transcript was determined using the comparative C_t method described in Perkin Elmer Applied Biosystems User Bulletin #2 (1997). Data are expressed as fold increases relative to a baseline value in liver from a normal C57BL/6J mouse without fatty liver (assigned the value of 1).

STATISTICAL ANALYSIS

All data are expressed as the mean ± SD. Statistical analyses were performed by using an unpaired Student's *t*-test for differences in liver weight, serum adiponectin level and hepatic expression of adiponectin mRNA, and by the Kruskal–Wallis test for the difference in histological score of hepatic lipid infiltration. A value of $P < 0.05$ was considered to be statistically significant.

Results

LIVER WEIGHT

Administration of candesartan had no obvious effect on the mean body weight, measured on day 7, between the treatment and control groups (Table 1). On day 7, the mean liver weight and the LW/BW ratios of the candesartan-treated mice were significantly lower compared with those of the control mice ($P < 0.05$ and $P < 0.01$, respectively; Table 1).

HISTOLOGICAL EXAMINATION OF THE LIVER

Histological evaluation of the livers showed obvious microvesicular and macrovesicular steatosis and occasional foci of inflammation and necrosis in the control mice (Fig. 1A). On day 7 after administration of candesartan, there was markedly reduced lipid accumulation in hepatic cells associated with an improvement in necro-inflammation ($P < 0.05$; Table 1) (Fig. 1B).

BLOOD GLUCOSE AND SERUM ADIPONECTIN LEVELS

Blood glucose levels in the candesartan-treated mice were non-significantly lower

TABLE 1:
Effects of candesartan (10 mg/kg once daily) on body weight, liver weight, liver weight to body weight ratio and histological scores of hepatic lipid infiltration on day 7 in KKAy obese mice with type 2 diabetes mellitus

Group	*n*	BW (g)	LW (g)	LW/BW (%)	Histological scores
Candesartan	5	38.88 ± 0.93	1.72 ± 0.13[a]	4.42 ± 0.24[b]	2.4 ± 0.8[a]
Control	5	41.18 ± 2.78	2.29 ± 0.31	5.56 ± 0.45	3.5 ± 0.6

Values are mean ± SD.
BW, body weight; LW, liver weight; LW/BW, liver weight to body weight ratio.
[a]$P < 0.05$, [b]$P < 0.01$ compared with control mice.

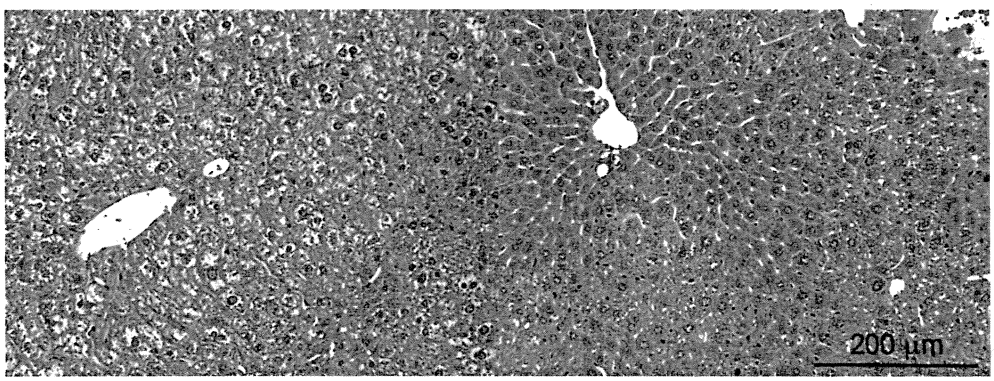

FIGURE 1: Photomicrograph showing microvesicular and macrovesicular steatosis and occasional foci of inflammation and necrosis in control KKAy obese mice with type 2 diabetes mellitus (A) and reduced lipid accumulation in hepatic cells associated with improvement in necro-inflammation in candesartan-treated KKAy obese mice with type 2 diabetes mellitus (B). (Original magnification, × 200; scale bar indicates 200 µm)

than in the control mice (236 ± 52 mg/dl versus 268 ± 52 mg/dl, respectively). On day 7, serum adiponectin levels were significantly increased in the candesartan-treated mice compared with the control mice ($P < 0.05$; Fig. 2A).

HEPATIC ADIPONECTIN MRNA LEVELS

As shown in Fig. 2B, liver adiponectin mRNA levels were significantly elevated in the candesartan-treated mice on day 7 compared with control mice ($P < 0.05$).

Discussion

'Non-alcoholic fatty liver' is the preferred term to describe the spectrum of liver damage, ranging from hepatic steatosis to steatohepatitis, liver fibrosis, and cirrhosis, which is associated with obesity, insulin resistance, type 2 diabetes and metabolic syndrome.[12] In this study, we observed that treatment with candesartan, an angiotensin-II receptor antagonist, was associated with a significantly decreased liver weight and ratio of liver weight to body weight, in addition to reduced lipid infiltration in the liver,

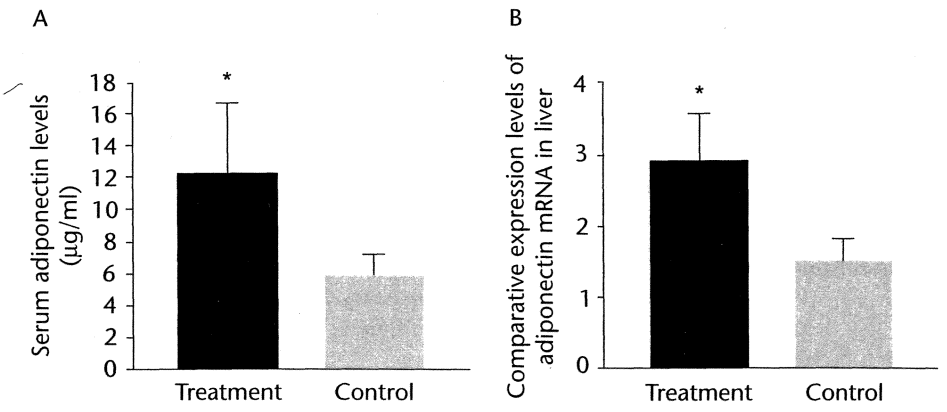

FIGURE 2: The effects of candesartan on circulating serum adiponectin concentrations (A) and hepatic expression levels of adiponectin mRNA (B) in KKAy obese mice with type 2 diabetes mellitus. The treatment group was administered candesartan orally at a daily dose of 10 mg/kg, while the control group was given placebo. Data are the mean ± SD. *$P < 0.05$ compared with control mice

compared with control treatment. Consistent with our data, Yokohama *et al.*[13] have reported the beneficial effect of the angiotensin receptor blocker in seven subjects with non-alcoholic steatohepatitis and hypertension. Histological assessment showed improvement of hepatic necro-inflammation in five patients, reduction of hepatic fibrosis in four individuals, and disappearance of iron deposition in two subjects. Another study also showed that the angiotensin receptor blocker could improve overproduction and accumulation of triglyceride in the liver with insulin resistance in Zucker fatty rats.[14]

In the present investigation, we found that serum adiponectin concentrations and hepatic expression levels of adiponectin mRNA were significantly higher in candesartan-treated mice than in control mice, suggesting that the angiotensin receptor blocker might alleviate NAFL through the increase of circulating adiponectin levels. Serum adiponectin levels are reduced under conditions of insulin resistance such as NAFL,[12] despite an elevated mass of fat cells. Delivery of recombinant adiponectin into mice with NAFL or alcoholic fatty liver has been shown dramatically to alleviate hepatomegaly and steatosis and to significantly attenuate inflammation and the increased levels of serum alanine aminotransferase.[8] Although the mechanisms are unclear, our study shows that blockade of the renin–angiotensin system could elevate circulating adiponectin levels under conditions of insulin resistance, including obesity, diabetes and NAFL. Our results are compatible with those previously described.[10]

To the best of our knowledge, the present study is the first to demonstrate the effects of an angiotensin-II receptor antagonist on NAFL and circulating adiponectin levels under conditions of obesity and diabetes. Further investigation in a large number of subjects with NAFL is required in order to elucidate the potential therapeutic effects of the renin–angiotensin system inhibition.

Acknowledgements

This study was supported in part by a grant for Promoted Research from Kanazawa Medical University (S2005-5); a grant for Project Research from the High-Technology Center of Kanazawa Medical University (H2004-7); and a Grant-in-Aid for Scientific Research (C) from the Ministry of Education, Science, Sports, and Culture of Japan (No. 17590767).

Conflicts of interest

No conflicts of interest were declared in relation to this article.

• Received for publication 14 November 2005 • Accepted subject to revision 2 December 2005
• Revised accepted 4 January 2006

References

1 Fong DG, Nehra V, Lindor KD, Buchman AL: Metabolic and nutritional considerations in non-alcoholic fatty liver. *Hepatology* 2000; **32:** 3 – 10.
2 Powell EE, Cooksley WG, Hanson R, Searle J, Halliday JW, Powell LW: The natural history of nonalcoholic steatohepatitis: a follow-up study of forty-two patients for up to 21 years. *Hepatology* 1990; **11:** 74 – 80.
3 Sheth SG, Gordon FD, Chopra S: Nonalcoholic steatohepatitis. *Ann Intern Med* 1997; **126:** 137 – 145.
4 Marceau P, Biron S, Hould FS, Marceau S, Simard S, Thung SN, *et al*: Liver pathology and the metabolic syndrome X in severe obesity. *J Clin Endocrinol Metab* 1999; **84:** 1513 – 1517.
5 Kelley DE, McKolanis TM, Hegazi RA, Kuller LH, Kalhan SC: Fatty liver in type 2 diabetes mellitus: relation to regional adiposity, fatty acids, and insulin resistance. *Am J Physiol Endocrinol Metab* 2003; **285:** E906 – E916.
6 Matsuzawa Y, Funahashi T, Kihara S, Shimomura I: Adiponectin and metabolic syndrome. *Arterioscler Thromb Vasc Biol* 2004; **24:** 29 – 33.
7 Pineiro R, Iglesias MJ, Gallego R, Raghay K, Eiras S, Rubio J, *et al*: Adiponectin is synthesized and secreted by human and murine cardiomyocytes. *FEBS Lett* 2005; **579:** 5163 – 5169.
8 Xu A, Wang Y, Keshaw H, Xu LY, Lam K, Cooper GJ: The fat-derived hormone adiponectin alleviates alcoholic and nonalcoholic fatty liver diseases in mice. *J Clin Invest* 2003; **112:** 91 – 100.
9 Ruiz-Ortega M, Lorenzo O, Suzuki Y, Ruperez M, Egido J: Proinflammatory actions of angiotensins. *Curr Opin Nephrol Hypertens* 2001; **10:** 321 – 329.
10 Furuhashi M, Ura N, Higashiura K, Murakami H, Tanaka M, Moniwa N, *et al*: Blockade of the renin-angiotensin system increases adiponectin concentrations in patients with essential hypertension. *Hypertension* 2003; **42:** 76 – 81.
11 Takahashi T, Zhu SJ, Sumino H, Saegusa S, Nakahashi T, Iwai K, *et al*: Inhibition of cyclooxygenase-2 enhances myocardial damage in a mouse model of viral myocarditis. *Life Sci* 2005; **78:** 195 – 204.
12 Yoon D, Lee SH, Park HS, Lee JH, Park JS, Cho KH, *et al*: Hypoadiponectinemia and insulin resistance are associated with nonalcoholic fatty liver disease. *J Korean Med Sci* 2005; **20:** 421 – 426.
13 Yokohama S, Yoneda M, Haneda M, Okamoto S, Okada M, Aso K, *et al*: Therapeutic efficacy of an angiotensin II receptor antagonist in patients with nonalcoholic steatohepatitis. *Hepatology* 2004; **40:** 1222 – 1225.
14 Ran J, Hirano T, Adachi M: Angiotensin II type 1 receptor blocker ameliorates overproduction and accumulation of triglyceride in the liver of Zucker fatty rats. *Am J Physiol Endocrinol Metab* 2004; **287:** E227 – E232.

Address for correspondence
Dr T Kanda
Department of General Medicine, Kanazawa Medical University, 1-1 Daigaku, Uchinada-machi, Kahoku-gun, Ishikawa 920-0293, Japan.
E-mail: kandat@kanazawa-med.ac.jp

The Journal of International Medical Research
2006; 34: 231 – 239

Traditional Chinese Medicine and Kampo: A Review from the Distant Past for the Future

F YU[1,4], T TAKAHASHI[1], J MORIYA[1], K KAWAURA[1], J YAMAKAWA[1], K KUSAKA[1], T ITOH[1], S MORIMOTO[2], N YAMAGUCHI[3] AND T KANDA[1]

[1]Department of General Medicine, [2]Department of Geriatric Medicine, and [3]Department of Serology, Kanazawa Medical University, Ishikawa, Japan; [4]Department of Traditional Chinese Medicine, Second Affiliated Hospital of China Medical University, Liaoning, China

Traditional Chinese medicine (TCM) is a complete system of healing that developed in China about 3000 years ago, and includes herbal medicine, acupuncture, moxibustion and massage, etc. In recent decades the use of TCM has become more popular in China and throughout the world. Traditional Japanese medicine has been used for 1500 years and includes Kampo-yaku (herbal medicine), acupuncture and acupressure. Kampo is now widely practised in Japan and is fully integrated into the modern health-care system. Kampo is based on TCM but has been adapted to Japanese culture. In this paper we review the history and characteristics of TCM and traditional Japanese medicine, i.e. the selection of traditional Chinese herbal medicine treatments based on differential diagnosis, and treatment formulations specific for the 'Sho' (the patient's symptoms at a given moment) of Japanese Kampo – and look at the prospects for these forms of medicine.

KEY WORDS: TRADITIONAL CHINESE MEDICINE; KAMPO; SELECTION OF TREATMENT BASED ON THE DIFFERENTIAL DIAGNOSIS; FORMULATION CORRESPONDING TO SHO

Introduction

According to the definition given by the World Health Organization, traditional medicine includes a diversity of health practices, approaches, knowledge and beliefs and incorporates plant, animal and/or mineral-based medicines, spiritual therapies, manual techniques and exercises, which are applied singly or in combination to maintain well-being and to treat or prevent illness.[1] The National Center for Complementary and Alternative Medicine, established at the National Institutes of Health in the USA in October 1998, re-categorized traditional medicine as complementary and alternative medicine.

Traditional Chinese medicine (TCM), one of the oldest continuously surviving traditions, originated as a means of maintaining good health and treating diseases in Chinese communities and has been adopted recently by other ethnic groups worldwide.[2] TCM is a complete system of healing that developed in China about 3000 years ago and reached a coherent, codified form about 2000 years ago. It includes

herbal medicine, acupuncture, moxibustion and massage, etc. In recent decades, the use of TCM has become more popular in its own right and also as a complement to Western medicine throughout the world.[3] TCM has been adopted in modified form in Far Eastern countries, such as Korea and Japan.[4]

Traditional Japanese medicine has been used for 1500 years and includes Kampo, acupuncture and acupressure (Shiatsu). The word 'Kampo' (also written 'Kanpo') refers to the herbal system used in China that developed during the Han dynasty (between 206 BC and AD 220); today the word is also used to describe a unique system of Japanese herbal medicine. Kampo is widely practised in Japan, where it is fully integrated into the modern health-care system.

Throughout the history of TCM and Kampo, the basic theories and the methods of diagnosis and treatment have differed considerably from those of Western medicine. Western medicine uses disease-based diagnosis, while TCM and Kampo emphasize patient-based diagnosis.

Kampo is based on TCM but is adapted to Japanese culture. It can be characterized as a simplified, positivistic and pragmatic version of Chinese herbal medicine.[5] The process of diagnosis and treatment differs between TCM and Kampo. In TCM the treatment is according to the differential diagnosis, whereas Kampo uses a treatment 'formulation corresponding to Sho'; Sho is the patient's symptoms at a given moment. In this paper we review these two forms of traditional medicine.

Zheng and Sho

'Sho' and 'Zheng' in Japanese and Chinese are derived from the same word, but over time they have come to acquire different meanings.

The disease, the symptom and the syndrome are the basic ideas of TCM. The meanings of 'disease' and 'symptom' are similar to those in Western medicine. Zheng, which can generally be translated as 'syndrome', is the basic unit and the key term in TCM theory, with a unique meaning. Zheng is the clinical outcome of the disease at any moment, and it generally encompasses the aetiology, pathology and disease location. After analysing the patient's history and all the symptoms and signs, doctors using TCM recognize not only the disease, but also the more important Zheng. The same disease may have many different Zheng because of differences in symptoms and signs at different stages of the disease. On the other hand, different diseases may have the same Zheng, so that in TCM different diseases can sometimes be treated with the same formulation. The analysis of the patient's history and all the symptoms and signs is referred to as the 'differentiation of Zheng'. All treatments in TCM are based on the differentiation of Zheng and all formulae used for treatment are based upon this 'treatment principle' (for an example, see Fig. 1).

The concept of 'Sho' comes from the Zheng of TCM, but is simpler because of the simplified Kampo theory. Sho is the patient's symptoms at any moment, recognized in terms of Qi (well-being, energy, illness, vigour), Blood and Water; the eight categories (Yin–Yang, hypofunction and hyperfunction, heat and cold, superficies and interior); the five parenchymatous viscera; and the six stages of the disease (Taiyang, Shaoyang, Yangming, Taiyin, Shaoyin, Jueyin).[6,7] Sho is broadly defined as Kampo diagnosis in the epistemic framework of the Kampo view of illness, and provides information on which to base the treatment.[6,7] Recently there has been a trend to name the Sho in terms of a formula, such as 'Kakkonto Sho', which denotes treatment of the patient's symptoms with Kakkonto.

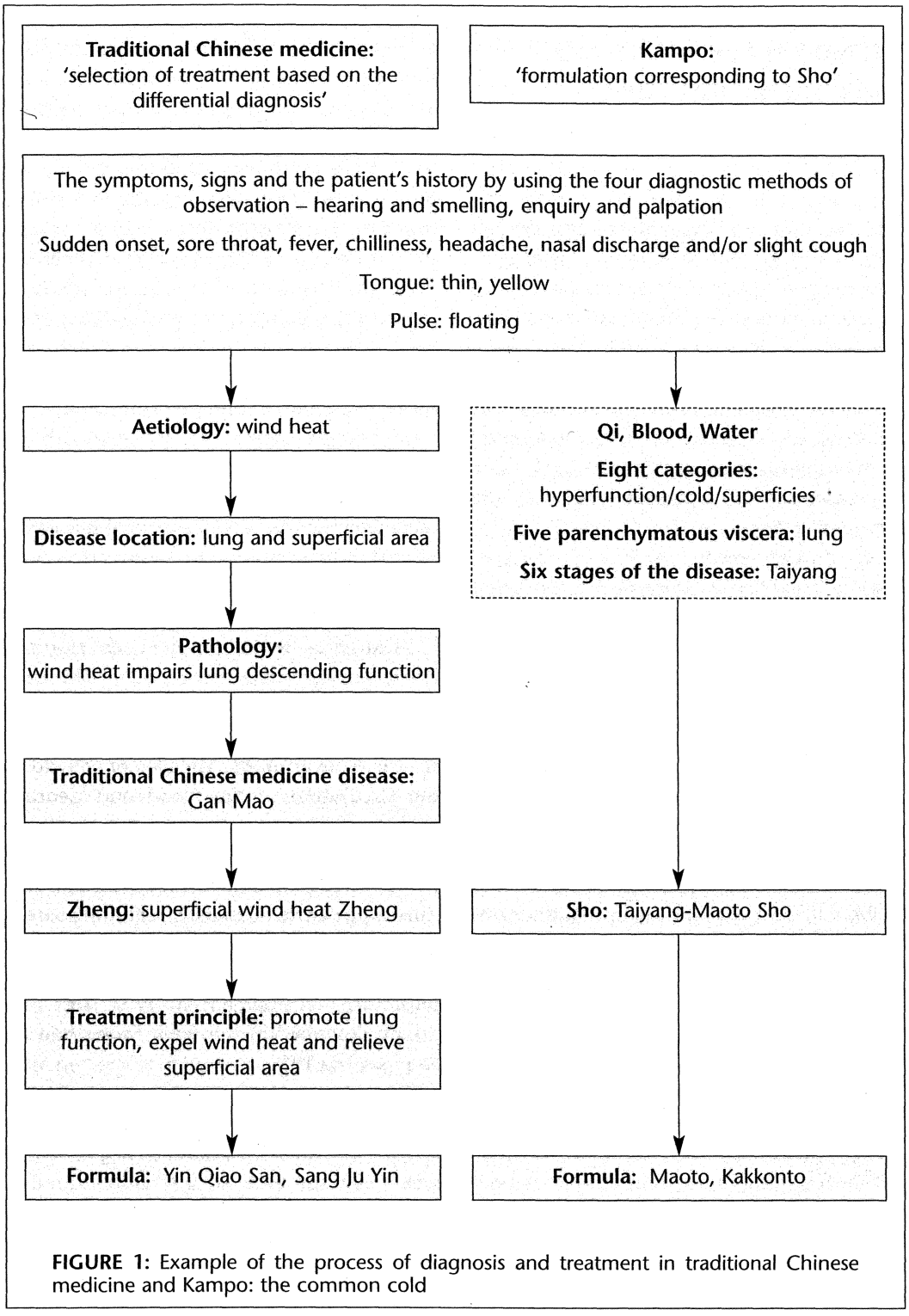

FIGURE 1: Example of the process of diagnosis and treatment in traditional Chinese medicine and Kampo: the common cold

'Selection of treatment based on the differential diagnosis' and the 'formulation corresponding to Sho'

In TCM, after having recognized the particular Zheng, the Chinese practitioner then confirms the 'treatment principle'. According to this principle, it is possible to choose formulae for treatment and adjust the herbs used in the formula, or make a new formulation adapted to the patient's particular condition. This step is called the 'selection of treatment' in TCM. The process from diagnosis to treatment in TCM is called the 'selection of treatment based on the differential diagnosis' (Fig. 1).

In Kampo medicine, the process of diagnosis and treatment is called 'formulation corresponding to Sho'. When treating a patient, Japanese practitioners recognize the Kampo diagnosis (Sho) and choose the most suitable formula. The relationship between these steps is regarded as similar to that of lock and key. Each pathological condition is thus related to its prescription.[6,7] Japanese practitioners generally tend to check the symptoms and name of the disease, and choose Kampo drugs (Fig. 1).[8]

We will now explain the development of the different methods of diagnosis and treatment in TCM and Kampo.

Origin and development of traditional Chinese medicine and Kampo

During the development of TCM, ancient authorities, well-known doctors, researchers and philosophers inherited their predecessor's writings, tested their techniques, and in turn added their own experience and knowledge, which they handed on to posterity.[8] By about 2000 years ago TCM had been codified into a system; the major classic medical manuscripts and drug books were completed at this time, and these are still used today.

In the sixth century AD Japan imported the culture of Chinese medicine, mainly via the Korean Peninsula. During the period between the seventh century and the Edo Period (1603 – 1867), the latest medicine from China was always taken up eagerly in Japan; it was accepted immediately and used virtually without modification.[8] This imported Chinese medicine was modified to meet local needs and became known as Kampo. In the Meiji period (1868 – 1912) the government adopted Western medicine, and during this period of repression Kampo medicine became divided into three parts: herbal medicine; acupuncture and acupressure. Today 'Kampo' refers only to herbal medicine.[8]

TCM has never stopped developing. However, the new theory of TCM that developed after the Meiji period was not accepted in Japan because of the policies of the Meiji government. The idea of activating the circulation of the blood and clearing away static blood was promoted by Wang Qing-ren (1768 – 1831) in the Qing dynasty (1644 – 1911). The theory of *Wen Bing Xue* (meaning 'Warm Disease' [febrile disease]), the most modern of the four areas of classical study, is regarded as the most important development in TCM since the theory described in the book *Shang Han Za Bing Lun* (AD 190).

After World War II, Kampo medicine ushered in a new age in Japan. In 1967, the health insurance authorities began reimbursement for four Kampo drug formulae prescribed by doctors. Reimbursement was available for 147 formulae in 1987[8] and about 200 formulae in 2000. Thereafter, Kampo spread steadily and rapidly.

Basic theory

TCM has developed over 3000 years. The tradition has been well conserved and the system of recognition/healing has become comprehensive. TCM can be characterized as holistic, with emphasis on the integrity of the human body and the close relationship between the human body and its social and natural environment. It focuses on health maintenance, and in the treatment of disease it emphasizes the enhancement of the body's resistance to disease.[9] The theoretical basis of TCM originates from the ancient Chinese philosophy of Yin–Yang and the five elements. The major TCM theories are covered systematically, including Qi, Blood, Body Fluids, Essence, Shen, the Zang Fu internal organ theory (Zangxiang), aetiology and pathogenesis, as well as the principles of the prevention and treatment of diseases.

As mentioned above, the theory of TCM was unified in China. However, a unified theory of Japanese traditional medicine has not been established in Japan.[8] Kampo medicine is simpler and more informal than TCM and emphasizes practice rather than theory.[10] The main theories of Kampo are the three substances (Qi, Blood, Water), the eight categories, the five parenchymatous viscera and the six stages of disease. Among the reasons for the simplification of Kampo may be the policies of the Meiji government. Theories such as the *Wen Bing Xue* theory and the idea of activating the blood circulation and clearing away static blood were not accepted after this period in Japan. Another reason is that a theory based on the treatment theory of *Shang Han Lun* (included in the book *Shang Han Za Bing Lun*, called *Sho Kan Ron* in Japanese) was followed by the classical school that gained power in the Edo era, a school that still constitutes the mainstream in Japanese Kampo medicine.[8]

Formulae

Most of the formulae used in Japan come from *Shang Han Za Bing Lun*. In China there is a broader range of sources, including medical manuscripts and well-known formulae.

In TCM there is a large number of excellent classic formulae. Herb formulae (typically 10 – 15 herbs) are prescribed in such a way that each herb is used to its greatest advantage, which improves the results of the treatment and reduces any adverse effects of the other herbs. Doctors usually change the formulae according to changes in the patient's condition and the treatment principle. This makes it possible to treat complicated diseases and to carry out patient-based treatment, in which the doctor thinks about the patient's particular characteristics, such as their age, general health and constitution, and the social and natural setting. It also contributes to the making of entirely new formulations.

The herb formulae prescribed by the doctor may take different forms in China. Many of them are decoctions, while others are powdered herbs, pills and tablets, and so on. There is also the ready-to-use form, which is different from that used in Japan. It is based on a single herb rather than a fixed formula, and the doctor can adjust the formula easily.

The *Shang Han Lun* and *Jin Gui Yao Lue* (both are part of *Shang Han Za Bing Lun*) formulae are among the principal focal points of Kampo medicine. Today, many Kampo practitioners use these books and prescribe their formulae. The herbs in these formulae (typically five to nine herbs) are categorized mainly in modern texts as surface-relieving herbs, heat-clearing herbs, moisture-draining herbs and tonics.

Formal recognition by the Japanese Ministry of Health has strongly influenced the practice of Kampo during the past 30 years. As a result, Japanese practitioners

focus their attention on about 200 formulae. Most of the modern formulae are of the ready-to-use type produced in factories.

Education

According to the Chinese State Administration of TCM, there were 34 universities or colleges for TCM and pharmacology in 2003. These universities or colleges provide 14 professional programmes for undergraduates. Twenty-three of the schools provide programmes for master's degrees and 13 provide doctorate programmes. In China, every Western medical school contains a department of TCM.

On the other hand, in Japan there is no systematic programme exclusively teaching Kampo medicine and no special license course for Kampo physicians. Under the laws governing medical practitioners, only allopathic (conventional) physicians may practise medicine, including Kampo medicine.[1] However, there are no restrictions on the types of medical procedure allopathic physicians may use in their practice.[1] A national survey in 1998 reported that 18 medical schools had either an elective or a required class on complementary and alternative medicine – mainly Kampo medicine and/or acupuncture.[11] Recently, more medical universities have begun to provide education in Kampo medicine along with Western medicine.

Evidence-based medicine

The clinical efficacies of Western medicine and TCM have been assessed in widely different ways in the past.[3] Evidence-based medicine is the integration of the best research evidence with clinical expertise and patient values. Large randomized, controlled trials (RCTs) are generally accepted as the gold standard. Although it is difficult to carry out RCTs because of the changeability of Zheng, scientific studies on the efficacy and safety of TCM using the RCT method are increasing in number in China.

In the 1970s, departments of oriental medicine were established in teaching hospitals for the training of physicians. In these institutions, clinical research was undertaken on how to use traditional Kampo formulae for the treatment of various health problems.[10] The research models used in Japan for studying Kampo are all Western, and the approach is based on conventional Western disease nosology and on conventional immunology.[10] The results of various clinical and laboratory studies have led to expansion of the use of traditional formulae in doctors' offices and hospitals in the mainstream of Japanese medicine.[10]

Discussion

Some ideas have penetrated deeply during the formation and development of TCM. The first is the idea of the 'whole', which focuses on the integrity of the human body and the close relationship between the human body and its social and natural environment. The second is the idea of 'dynamic balance', which emphasizes movement in the integrity and changeability of the Zheng.[9] The third, and most important, idea is the 'selection of treatment based on the differential diagnosis'.

Kampo medicine accepts the 'whole' idea taken from TCM, and emphasizes the relationship between the human body and its social and natural environment. It regards the disease state as an imbalanced state, and the process of Kampo treatment is intended to correct this imbalance or to help the individual patient return to the equilibrium state. The Zheng is changeable during the disease process.[6,7] These ideas are similar to those of TCM. The symptom–formula correspondence is regarded as another characteristic in which Kampo medicine[12] differs from TCM (Table 1).

TABLE 1:
Characteristics of traditional Chinese medicine and Kampo

	Traditional Chinese medicine	Kampo
Characteristics	System codified and complete	Simplified and pragmatic
Characteristics of ideas	Ideas of the 'whole' and the 'dynamic balance'	
	'Selection of treatment based on the differential diagnosis'	'Formulation corresponding to Sho'
Focal point	Syndrome (Zheng)	Disease and symptom
Basic theory	Yin–Yang and the five elements Qi, Blood, Body fluids, Essence, Shen The Zang Fu internal organ theory Aetiology and pathogenesis Prevention and treatment principles for diseases	Three substances (Qi, Blood, Water) Eight categories Five parenchymatous viscera Six stages of disease
Formulae	Many classic formulae Typically 10 – 15 herbs Decoctions and ready-to-use herbs (easy to adjust)	Limited formulae Typically 5 – 9 herbs Ready-to-use formulae (relative fixation, i.e. relative adjustment to the Sho)
Education	Systematic traditional Chinese medicine programme	Western medicine programme
Evidence-based medicine	Emphasizes experience in combination with evidence	Emphasizes evidence from clinical and laboratory studies

As drugs covered by the National Health Insurance System (NHIS) in Japan can only be prescribed by medical doctors trained in Western medicine, there is a tendency for them to use Kampo formulae without paying much attention to the TCM interpretations of the symptoms of the patient.[12] Therefore, the mainstream of Kampo relies not so much on the rigorous interpretation of the disease state in terms of the basic TCM concepts as on the direct practical effects of the formula itself.[12] Terasawa pointed out that 'In Japan, it is not possible for a physician to use TCM's system of three elements/eight categories in order for his or her Kampo formulae to be covered by NHIS'.[12] Kampo medicine places more emphasis on the results of clinical and laboratory studies. However, all the clinical and laboratory studies are carried out on the basis of the disease alone. Whereas the Zheng is changeable and the same disease may have different Zheng, it is impossible to reveal the entire Zheng from the results of the clinical and laboratory studies. Sometimes the doctor cannot find a suitable key to the particular lock because of the limited number of formulae covered by the NHIS.

In the West, the practice of Chinese herbal medicine has been strongly influenced by Kampo. One reason is that Kampo was introduced before the licensing of acupuncture was established, and a second reason is the convenience of the ready-to-use formulae. A third reason may

be that the idea of the symptom–formula correspondence in Kampo is easier to master than TCM's idea of the 'selection of treatment based on the differential diagnosis'. Another reason, in our opinion, is that Kampo used with evidence-based medicine is easily accepted in the West because the research models and methods used in Japan for studying Kampo are thoroughly Western[10]. The practice of TCM with evidence-based medicine in China is more difficult than in Japan because of the large number of formulae used and the individualization of treatment.

Traditional medicine has faced the crisis and challenge of historical continuity and modernization. Its practitioners in China and Japan have worked hard to find the best approach. One approach is to combine the Zheng with the disease. In some diseases, such as fatty liver, the patient has no special symptoms and signs. In other conditions, such as early cancer, there are also no special symptoms and signs – or there may be only general discomfort – and the therapeutic result will differ according to whether the Zheng or the disease is considered. On the other hand, if the emphasis is placed heavily upon the disease, it will be difficult to tailor the treatment to the particular patient. This makes a TCM or Kampo medicine merely a kind of combined herb drug, like any Western drug, and TCM will have no appeal. Combining the differentiation of Zheng with the diagnosis of the disease would achieve the best therapeutic effect.[9]

A second approach is to combine traditional experience with modern evidence. In TCM, there is a history of more than 3000 years of unique experience and there are hundreds of excellent classic formulae. Because of its unique system and the methods it uses for diagnosis and treatment, TCM does not find ready acceptance in the West. The demonstration of statistically significant effects seems necessary for the improvement and acceptance of TCM.[13] Modern drugs are good for curing diseases with a clear cause and pathology but not for curing diseases due to multiple factors, and these have become more common.[9] TCM is not a perfect way of identifying specific pathogens and pathological changes. It seeks disturbances in the human body by analysing all symptoms and signs,[9] and this make it possible to treat diseases due to multiple pathogenic factors and some diseases that are not very well understood. This is the advantage and unique appeal of TCM and Kampo.

The third approach is the establishment of an animal model that has the Zheng of the human condition in addition to showing a model form of the disease. In TCM and Kampo practice, it sometimes happens that a formula that has been shown to be effective in animal experiments or RCTs does not achieve the desired effect in humans, and sometimes even produces the converse effect. One important reason for this is the existence of Zheng. Therefore, the establishment of a model with the Zheng seems to be necessary and important in TCM and Kampo studies.

We need to keep alive the history of TCM and Kampo and at the same time make advances in the practice of these forms of medicine. Although the practice of Kampo in Japan is different from that of TCM in China, all efforts that we can make will aid the development of TCM and Kampo.

Acknowledgements

The authors were supported in part by a grant for Promoted Research from Kanazawa Medical University (S2005-5), a grant for Project Research from the High-Technology Center of Kanazawa Medical University (H2004-7), and a research grant from

Grant-in-Aid for Scientific Research (C) from the Ministry of Education, Science, Sports, and Culture of Japan (No. 17590767).

Conflicts of interest

No conflicts of interest were declared in relation to this article.

• Received for publication 13 December 2005 • Accepted subject to revision 6 January 2006
• Revised accepted 24 January 2006

References

1 World Health Organization: Legal status of traditional medicine and complementary/alternative medicine: a worldwide review. WHO Document WHO/EDM/TRM/2001.2; 2001; pp1 – 159.
2 Chan K: Chinese medicinal materials and their interface with Western medical concepts. *J Ethnopharmacol* 2005; **96:** 1 – 18.
3 Leung KF, Liu FB, Zhao L, Fang JQ, Chan K, Lin LZ: Development and validation of the Chinese Quality of Life Instrument. *Health Qual Life Outcomes* 2005; **3:** 26.
4 Park J, Park HJ, Lee HJ, Emst E: What's in a name? A systematic review of the nomenclature of Chinese medical formulae. *Am J Chin Med* 2002; **30:** 419 – 427.
5 Terasawa K: Evidence-based reconstruction of Kampo medicine: Part I – Is Kampo CAM? *Evid Based Complement Alternat Med* 2004; **1:** 11 – 16.
6 Ishibashi A, Kosato H, Ohno S, Sakaguchi H, Yamada T, Matsuda K: General introduction to Kampo. In: *Introduction to Kampo*, 1st edn. (Sato Y, Hanawa T, Aria M, Cyong JC, Fukuzawa M, Mitani K, *et al*, eds). Tokyo: Elsevier Japan, 2005; pp2 – 15.
7 Terasawa K, Itoh T, Nagasaka K, Kita T, Tosa H, Imadaya A, *et al*: Diagnosis and treatment. In: *Introduction to Kampo*, 1st edn. (Sato Y, Hanawa T, Aria M, Cyong JC, Fukuzawa M, Mitani K, *et al*, eds). Tokyo: Elsevier Japan, 2005; pp17 – 52.
8 Horiguchi K, Tsutani K: A cultural perspective: conceptual similarities and differences between traditional Chinese medicine and traditional Japanese medicine. In: *What will Influence the Future of Alternative Medicine? A World Perspective* (Eskinazi D, ed). Singapore: World Scientific, 2001; pp41 – 55.
9 Lu AP, Jia HW, Xiao C, Lu QP: Theory of traditional Chinese medicine and therapeutic method of diseases. *World J Gastroenterol* 2004; **10:** 1854 – 1856.
10 Kenner D: The role of traditional herbal medicine in modern Japan. *Acupunct Today* 2001; **2:** 1 – 5.
11 Tsuruoka K, Tsuruoka Y, Kajii E: Complementary medicine education in Japanese medical schools: a survey. *Complement Ther Med* 2001; **9:** 28 – 33.
12 Terasawa K: Evidence-based reconstruction of Kampo medicine: Part II – The concept of Sho. *Evid Based Complement Alternat Med* 2004; **1:** 119 – 123.
13 Cheng JT: Review: drug therapy in Chinese traditional medicine. *J Clin Pharmacol* 2000; **40:** 445 – 450.

Address for correspondence
Dr T Kanda
Department of General Medicine, Kanazawa Medical University, 1-1 Daigaku, Uchinada-machi, Kahoku-gun, Ishikawa 920-0293, Japan.
E-mail: kandat@kanazawa-med.ac.jp

The Journal of International Medical Research
2006; 34: 437 – 440

Advanced Oesophageal Carcinoma in an 84-year-old Treated with Chemoradiotherapy

K KUSAKA[1], T ITOH[1], K KAWAURA[1], J MORIYA[1], J YAMAKAWA[1], T TAKAHASHI[1], M OGUCHI[2], H TONAMI[2], I YAMAMOTO[2] AND T KANDA[1]

[1]Department of General Medicine, and [2]Department of Radiology, Kanazawa Medical University, Ishikawa, Japan

We present a case of advanced oesophageal cancer with cardiac invasion in an 84-year-old male presenting with dysphagia and general malaise. Histological analysis of an endoscopic biopsy specimen revealed a poorly differentiated squamous cell carcinoma. Computed tomography indicated a thickened oesophageal wall that was compressing the left atrium, suggesting invasion of the heart, and oesophagography revealed a polypoid lesion 9 cm in length. No distant metastases were seen on computed tomography. The patient was given chemotherapy with 10 mg/m^2 cisplatin on days 1 and 4 every week for 5 weeks and concurrent radiotherapy at a dose of 2 Gy five times per week (total dose 52 Gy). After 4 weeks, the mass was no longer visible on oesophagography or endoscopic examination. The patient was free of recurrence and metastases for 4.5 years. In conclusion, chemoradiotherapy may be curative in elderly patients with unresectable oesophageal carcinoma.

KEY WORDS: CHEMORADIOTHERAPY; OESOPHAGEAL CARCINOMA; ELDERLY

Introduction

Surgical resection is the standard treatment for oesophageal cancer, but is associated with complete remission in < 20% of patients with advanced disease.[1] In recent years, a combination of chemotherapy and concurrent radiotherapy has been reported to be potentially curative for unresectable oesophageal cancer.[1,2] We report a case of advanced oesophageal cancer with cardiac involvement in an elderly patient treated with chemoradiotherapy without resection. The patient survived for 4.5 years without any recurrences or metastases.

Case report

An 84-year-old male with dysphagia and general malaise was referred to our hospital in June 2001. Endoscopic examination revealed an advanced oesophageal cancer located in the lower thoracic oesophagus. Histological analysis of an endoscopic biopsy specimen revealed a poorly differentiated squamous cell carcinoma.

A computed tomography (CT) scan indicated a thickened oesophageal wall that was compressing the left atrium, suggesting invasion of the heart. Oesophagography revealed a polypoid lesion 9 cm in length (Fig. 1A). On endoscopy, the lesion was seen at a distance of 32 cm from the canine teeth (Fig. 2A). No distant metastases were seen on CT, and the cancer was classified as stage 4 using the Tumour, Node and Metastasis (TMN) staging system.

The patient was given chemotherapy with 10 mg/m^2 cisplatin on days 1 and 4 every week for 5 weeks and concurrent radiotherapy at a dose of 2 Gy five times per week (total dose 52 Gy). After 4 weeks, no stenotic mass lesion was seen in the oesophagus on oesophagography and endoscopic examination showed no malignant mass. An endoscopic biopsy examination confirmed that there were no remnant cancer cells in the mucosa.

No additional treatment was given. No local progression or lymph node or distant metastases were detected on follow-up oesophagographies (Fig. 1B), endoscopic examinations (Fig. 2B) and CT scans over a 4.5-year period.

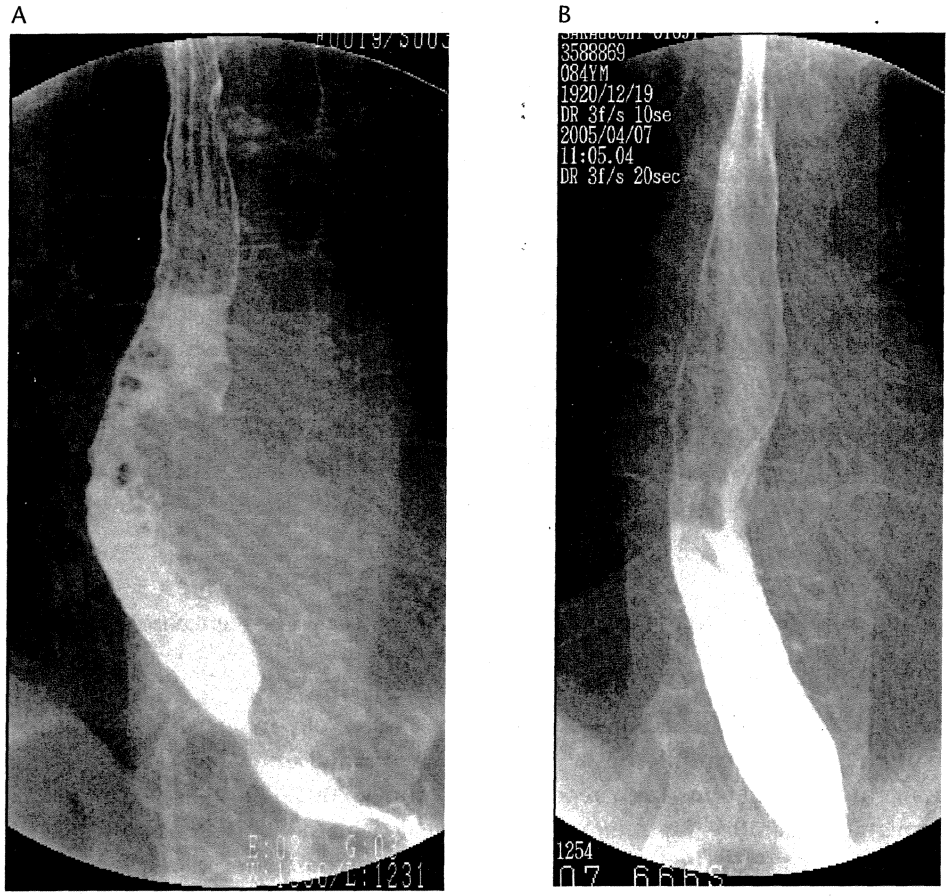

FIGURE 1: Oesophagography showing a polypoid lesion (A); oesophagography 3 years and 10 months after chemoradiotherapy, the stenotic lesion is no longer present (B)

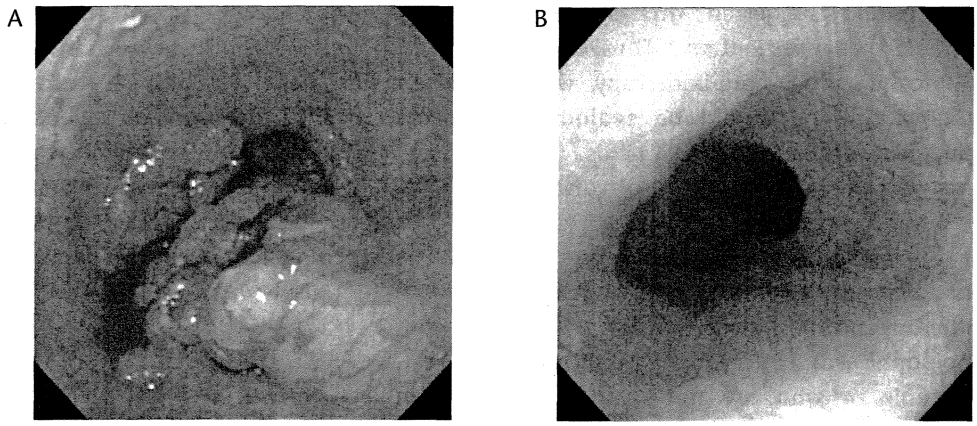

FIGURE 2: Oesophageal endoscopy showing a polypoid lesion at a distance of 32 cm from the canine teeth (A); oesophageal endoscopic examination 3 years and 10 months after chemoradiotherapy confirms the absence of the malignant mass (B)

Discussion

Treatment for patients with oesophageal cancer remains unsatisfactory.[3] Although surgery with or without chemoradiotherapy is generally accepted as a reasonable option for patients with locoregional oesophageal cancer, the 5-year survival rate is only around 20%.[1] Patients with oesophageal cancer are usually managed with palliative intent. Particular attention should be given to alleviating the common problem of dysphagia, which causes significant morbidity.[4] The case presented here demonstrates that chemoradiotherapy alone may be appropriate for elderly patients with unresectable oesophageal cancer.

A comparative prospective randomized trial of chemoradiotherapy versus radiotherapy alone in oesophageal cancer was performed by the Radiation Therapy Oncology Group (RTOG);[2,5] it compared radiation at a dose of 50 Gy plus concurrent 5-fluorouracil and cisplatin with radiation alone at a dose of 64 Gy for 5 weeks. Patients receiving chemoradiation had a greater median survival than those receiving radiation alone. A subsequent follow-up study[6] confirmed an improved 5-year survival rate in those receiving chemoradiation (26% versus 0%). More recently, the RTOG published the results of a randomized prospective trial[7] in which patients receiving 5-fluorouracil and cisplatin were randomized to receive concurrent radiotherapy at a dose of either 64.8 Gy or 50.4 Gy; the higher radiation dose was not associated with an increase in survival and the standard dose was considered to be preferable in terms of the patients' quality of life.[6]

The use of chemoradiotherapy given as a definitive treatment or in combination with surgery may improve locoregional control and survival compared with radiotherapy.[2,8] A prospective phase II study of pre-operative chemoradiotherapy consisting of 5-fluorouracil and cisplatin and 46.5 – 48 Gy of radiotherapy followed by surgery for patients

with resectable oesophageal squamous cell carcinoma suggested this strategy warrants further investigation.[9] Thus, long-term outcome of chemoradiotherapy, with or without surgery, should be evaluated in prospective randomized trials for subjects with operable oesophageal cancers in the future.

In conclusion, non-operative managements such as cisplatin-based chemoradiotherapy may be appropriate in patients with oesophageal cancer that is clearly unresectable or who are not candidates for surgery.

Acknowledgements

This study was supported in part by a grant for Promoted Research from Kanazawa Medical University (S2005-5), a grant for Project Research from the High-Technology Center of Kanazawa Medical University (H2004-7), and a research grant from Grant-in-Aid for Scientific Research (C) from the Ministry of Education, Science, Sports, and Culture of Japan (No. 17590767).

Conflicts of interest

No conflicts of interest were declared in relation to this article.

• Received for publication 25 January 2006 • Accepted subject to revision 6 February 2006
• Revised accepted 16 March 2006

References

1 Poplin EA, Khanuja PS, Kraut MJ, Herskovic AM, Lattin PB, Cummings G, *et al*: Chemoradiotherapy of esophageal carcinoma. *Cancer* 1994; **74**: 1217 – 1224.
2 Cooper JS, Guo MD, Herskovic A, Macdonald JS, Martenson JA Jr, Al-Sarraf M, *et al*: Chemoradiotherapy of locally advanced esophageal cancer: long-term follow-up of a prospective randomized trial (RTOG 85-01). Radiation Therapy Oncology Group. *JAMA* 1999; **281**: 1623 – 1627.
3 Wobst A, Audisio RA, Colleoni M, Geraghty JG: Oesophageal cancer treatment: studies, strategies and facts. *Ann Oncol* 1998; **9**: 951 – 962.
4 Sherman CA, Turrisi AT, Wallace MB, Reed CE: Locally advanced esophageal cancer. *Curr Treat Options Oncol* 2002; **3**: 475 – 485.
5 Herskovic A, Martz K, al-Sarraf M, Leichman L, Brindle J, Vaitkevicius V, *et al*: Combined chemotherapy and radiotherapy compared with radiotherapy alone in patients with cancer of the esophagus. *N Engl J Med* 1992; **326**: 1593 – 1598.
6 Fournel P, Robinet G, Thomas P, Souquet PJ, Lena H, Vergnenegre A, *et al*: Randomized phase III trial of sequential chemoradiotherapy compared with concurrent chemoradiotherapy in locally advanced non-small-cell lung cancer: Groupe Lyon-Saint-Etienne d'Oncologie Thoracique-Groupe Francais de Pneumo-Cancerologie NPC 95-01 Study. *J Clin Oncol* 2005; **23**: 5910 – 5917.
7 Minsky BD, Pajak TF, Ginsberg RJ, Pisansky TM, Martenson J, Komaki R, *et al*: INT 0123 (Radiation Therapy Oncology Group 94-05) phase III trial of combined-modality therapy for esophageal cancer: high-dose versus standard-dose radiation therapy. *J Clin Oncol* 2002; **20**: 1167 – 1174.
8 Geh JI: The use of chemoradiotherapy in oesophageal cancer. *Eur J Cancer* 2002; **38**: 300 – 313.
9 Swisher SG, Ajani JA, Komaki R, Nesbitt JC, Correa AM, Cox JD, *et al*: Long-term outcome of phase II trial evaluating chemotherapy, chemoradiotherapy, and surgery for locoregionally advanced esophageal cancer. *Int J Radiat Oncol Biol Phys* 2003; **57**: 120 – 127.

Address for correspondence
Dr T Kanda
Department of General Medicine, Kanazawa Medical University, 1-1 Daigaku, Uchinada-machi, Kahoku-gun, Ishikawa 920-0293, Japan.
E-mail: kandat@kanazawa-med.ac.jp

J Kanazawa Med Univ 30 : 141−146, 2005

Extract from Inflamed Skin of Rabbits Increases Enkephalin Concentrations in Cerebrospinal Fluid in Rats

Shigeto Morimoto[1], Takashi Takahashi[2], Herbert L. Jackman[3], Ervin G. Erdös[3], Tsugiyasu Kanda[2], Hironori Ohde[4], Wei-Min Liu[1], Masashi Okuro[1], Kohji Nomura[1] and Masayuki Matsumoto[1]

Abstract: A non-protein extract from inflamed skin of rabbits inoculated with vaccinia virus (EISRV) is widely employed to combat pain and allergic conditions. To investigate whether enkephalin could be involved in the analgesic activity of EISRV, we examined concentrations of Met^5-enkephalin and Leu^5-enkephalin in cerebrospinal fluid in male Wistar rats after intraperitoneal EISRV injection. EISRV increased both Met^5-enkephalin and Leu^5-enkephalin concentrations in a dose- and time-dependent manner. Although not statistically significant, there appeared to be a trend towards lowered activity of neutral endopeptidase (E.C.3.4.24.11), the major inactivator of enkephalins in the brain, in cerebrospinal fluid of rats treated with EISRV. There were no significant changes in thalamic mRNA levels of proenkephalin and prodynorphin after EISRV treatment. Thus, the antinociceptive effect of EISRV is possibly in part due to the accumulation of Met^5-enkephalin and Leu^5-enkephalin in cerebrospinal fluid, mediated through inhibition of neutral endopeptidase activity.

Key Words: non-protein extract, enkephalin, neutral endopeptidase, cerebrospinal fluid, rats

Introduction

A protein-free extract from inflamed skin of rabbits inoculated with vaccinia virus (EISRV, Rosemorgen) is widely employed to combat pain and allergic conditions in human subjects in Japan. Antinociceptive effects of EISRV have been observed in mice assessed by the tail pressure method(1). EISRV normalizes the decreased nociceptive threshold in temperature stressed mice(2), and increases the pain threshold and tolerance to cold-induced pain in normal volunteers(3). Complex regional pain syndrome type I induced by pacemaker implantation, with a good response to EISRV and methylprednisolone, is described as a case presentation(4). Because bradykinin is an important mediator of allergic reactions and pain induction, possibly the mechanism of EISRV action is linked to inhibition of kinin release(5). The analgesic action of EISRV is recently reported to be at least in part due to the enhancement of noradrenergic and serotonergic descending pain inhibitory pathways in adjuvant-induced arthritic rat, a chronic pain model with inflammation(6). In addition, pre-administration of EISRV reduced the hyperalgesic effect of antiserum to β-endorphin on both nociceptive thermal stimulus and nociceptive electro-skin stimulus(7), suggesting that EISRV may affect endogenous opioid peptide release or metabolism.

Endogenous opioid peptides such as β-endorphin, Met^5-enkephalin, and Leu^5-enkephalin are well known to play important roles in the modification of pain perception and analgesia threshold. To investigate whether Met^5-enkephalin and Leu^5-enkephalin could be involved in the analgesic activity of EISRV, we examined the levels of Met^5-enkephalin and Leu^5-enkephalin in cerebrospinal fluid (CSF) in rats after EISRV injection.

[1] *Departments of Geriatric Medicine, Kanazawa Medical University*
[2] *General Medicine, Kanazawa Medical University*
[3] *Departments of Pharmacology and Anesthesiology, University of Illinois College of Medicine*
[4] *Research Institute, Fujimoto Pharmaceutical Corp*
Correspondent to: Shigeto Morimoto, Department of Geriatric Medicine, Kanazawa Medical University 1-1 Daigaku, Uchinada-machi, Kahoku-gun, Ishikawa 920-0293, Japan
Accepted: January 17, 2006

Materials and Methods

1 Materials

EISRV (Rosemorgen) was a product (12 U/ml) from raw material solution provided by Fujimoto Diagnostics, Inc., Osaka, Japan. Before use, the agent was diluted in saline to different concentrations as follows.

2 Animals and treatment

Male Wistar rats aged 11 weeks were purchased from Charles River Japan, Inc. (Tokyo, Japan). All experiments involving animals were conducted in accordance with NIH guidelines for the care and use of experimental animals, and all animal experiments were approved by Osaka University Animal Care and Use Committee. To examine the dose-dependent effect of EISRV on concentrations of opioid peptides in CSF, rats were randomly divided into four groups (n=6 in each group), receiving intraperitoneal injection of 1.5 ml EISRV at doses of 0, 10, 20, and 50 U/kg body weight, respectively. At 30 or 120 min after EISRV administration (n=3 for each subdivision at each time point), the rats were anesthetized by intraperitoneal injection of sodium pentobarbital (100 mg/kg), and CSF was withdrawn from the cisternal space using a 26-gauge needle inserted through the atlanto-occipital membrane. Using this technique, 150-250 μl CSF was routinely withdrawn per rat. To examine the time-dependent effect of EISRV, rats were injected intraperitoneally with 1.5 ml EISRV at a dose of 50 U/kg. The CSF samples were collected as above at 0, 30, 60, 90, and 120 min after EISRV administration (n=5 for each time point). And to examine assay for activity of neutral endopeptidase 24.11 (NEP) in CSF of rats, the CSF samples were collected 0, 90 and 120 min after EISRV (50 U/kg) administration (n=14 or 15 for each point). The CSF samples were stored at -80℃ until determination.

3 Radioimmunoassay

CSF concentrations of Met^5-enkephalin and Leu^5-enkephalin were determined by radioimmunoassay using RIA kits from Phoenix Pharmaceuticals, Inc. (Mountain View, CA). For Met^5-enkephalin assay, 50 μl CSF was diluted with 50 μl RIA buffer, and for Leu5-enkephalin assay, 20 μl CSF was diluted with 80 μl RIA buffer. The concentrations of Met^5-enkephalin and Leu^5-enkephalin were expressed as pg/ml.

4 Determination of neural endopeptidase activity

To examine whether EISRV may affect opioid peptide concentration via alteration of their catabolism, activity of neutral endopeptidase (NEP) (E.C. 3.4.24.11) in CSF samples was determined by a reported method(8,9). On the day of NEP assay, CSF samples were thawed and used immediately. Each sample was assayed in duplicate using 10 μlCSF, 50 μl of 100 mmol/L 2-[N-morpholino]-ethansulfonic acid buffer with 0.1% Triton X-100 at pH 6.5, 100 μl of 100 mmol/L substrate Glutaryl-Ala-Ala-Phe-(methoxy-naphthylamine) and water to a final volume of 250 μl. Reaction mixtures were incubated at 37℃ for 6 h and the reaction was stopped by the addition of 25 μl of 2.5 x 10^{-5} mol/L phosphoramidon. Phe-(methoxy-naphthylamine) was developed by adding leucine aminopeptidase and the resultant fluorescence was read in a spectrophotofluorometer at wavelengths of 340 nm for excitation and 425 nm for emission. A third 10 μl aliquot of each CSF sample was assayed as above but with the addition of 25 μl of phosphoramidon before the substrate was added; this was done to enhance the specificity of the NEP assay. Standard preparations of NEP were run as part of the assay for quality control. The activity of the enzyme was expressed as pmol/h/10 μl CSF.

5 Analysis of mRNA levels of proenkephalin and prodynorphin

Total RNA was extracted from rat thalamus by standard procedures using ISOGEN (Nippon Gene, Tokyo, Japan)(10). The concentration of RNA was estimated from the absorbance at 260 nm. The first strand of DNA was reverse transcribed (RT) from 1 μl total RNA using random 9-mer primers and avian myeloblastosis virus reverse transcriptase (Takara Shuzo Co., Shiga, Japan), followed by polymerase chain reaction (PCR) amplification using synthetic gene specific primers for rat proenkephalin (forward 18-mer, 5'-CTT GGG TCC TGC CTC CTG-3'; reverse 20-mer, 5'-GCT CCT TTG CTT CGT CTT CC-3') and prodynorphin (forward 19-mer, 5'-CGG GGC TTT TGG TCT TTT C-3'; reverse 19-mer, 5'-CCT GTG CGG CTT CAT CAT T-3') with the following schedule: denaturation, annealing and extension at 94℃, 63℃ and 72℃ for 40 s, 1 min and 1 min 30 s, respectively, for 30 cycles. The RT-PCR products were electrophoresed on 2% agarose gel containing ethidium bromide and visualized by UV-induced fluorescence. The relative intensity was analyzed by NIH Image 1.55 software.

6 Statistical analyses

Results are expressed as mean ±S.D. One-way ANOVA with Fisher's PLSD post hoc test was used to determine the statistical significance of differences. Student's t-test was also used for comparison between two groups. A value of $P < 0.05$ was considered to be significant.

Results

EISRV increases met⁵-enkephalin and leu⁵-enkephalin levels in CSF in a time- and dose-dependent manner

As shown in Fig. 1, EISRV increased concentrations of Met⁵-enkephalin and Leu⁵-enkephalin in CSF in a dose-dependent and time-dependent manner. An increasing trend towards Met⁵-enkephalin level was observed at 30 min, which became significant at over 60 min after EISRV administration. Leu⁵-enkephalin level did not change at 30 min but tended to somewhat increase after 60 min, and the increase became significant at 120 min after the injection. The non-significant trend of Leu⁵-enkephalin at the time points of 60 and 90 min, however, may have resulted

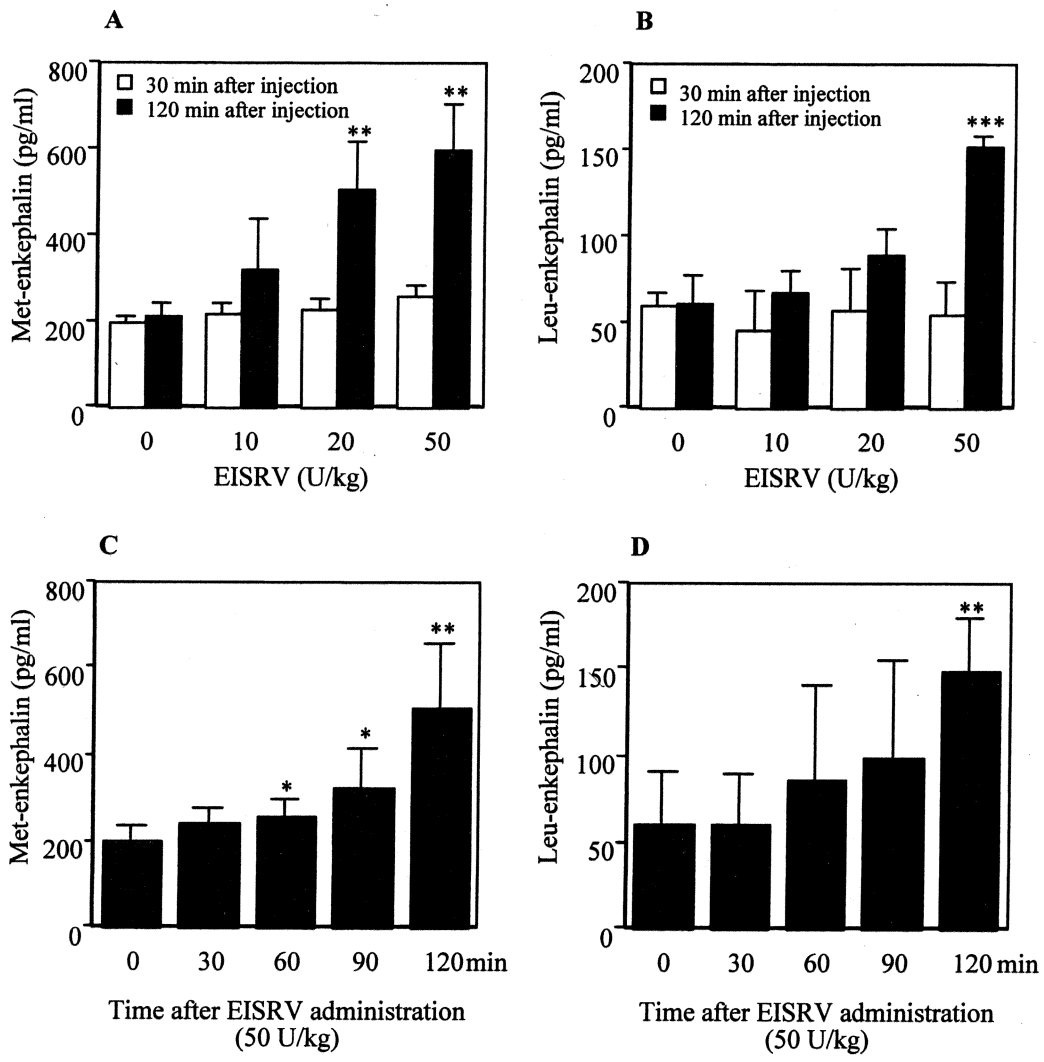

Fig. 1. Dose- and time-dependent effect of EISRV on concentrations of Met⁵-enkephalin and Leu⁵-enkephalin in CSF in rats.
Rats were injected intraperitoneally with EISRV, and CSF was withdrawn under sodium pentobarbital anesthesia from the cisternal space through the atlanto-occipital membrane. A and B: Dose-dependent changes of Met⁵-enkephalin and Leu⁵-enkephalin concentrations, n = 3 for each treatment, C and D: Time-dependent changes of Met⁵-enkephalin and Leu⁵-enkephalin concentrations, n = 5 for each treatment. Results are expressed as mean ±S.D. $^{*}P < 0.05$, $^{**}P < 0.01$ and $^{***}P \leq 0.001$ vs. control levels (0 U/kg or 0 min) by ANOVA.

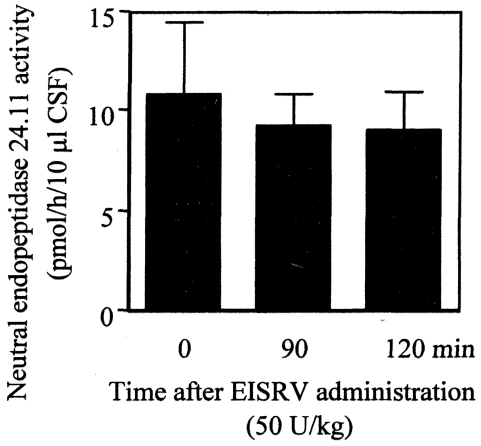

Fig. 2. Effect of EISRV on neutral endopeptidase activity in CSF in rats.
Rats were injected intraperitoneally with EISRV (50 U/kg) and CSF was withdrawn under sodium pentobarbital anesthesia from the cisternal space through the atlanto-occipital membrane. Neutral endopeptidase activity was determined using Glutaryl-Ala-Ala-Phe-methoxy-naphthylamine as the substrate. Results are expressed as mean ±S.D., n = 14 or 15.

from the large variation in its concentration in CSF. At the dose of 50 U/kg and 120 min after injection of EISRV, Met^5-enkephalin was 2.86-fold and Leu^5-enkephalin was 2.48-fold higher than the basal concentrations.

Experiments in NEP

Although not significant by one way ANOVA (P = 0.1092), NEP had a trend towards lower activity in CSF of rats treated with EISRV (50 U/kg) at 90 or 120 min compared to controls (0 min and without EISRV treatment), with P values of 0.087 at 90 min and 0.056 at 120 min. The reduction of mean NEP activity showed a time-dependent trend with activities of 85% of the control level at 90 min and 83% at 120 min (Fig. 2).

Thalamic mRNA concentrations of proenkephalin and prodynorphin

The RT-PCR produced a 583 base-pair product from proenkephalin mRNA and a 256 base-pair product from prodynorphin mRNA. The mRNA levels of proenkephalin and prodynorphin in rat thalamus showed no significant alteration after EISRV treatment (Fig. 3).

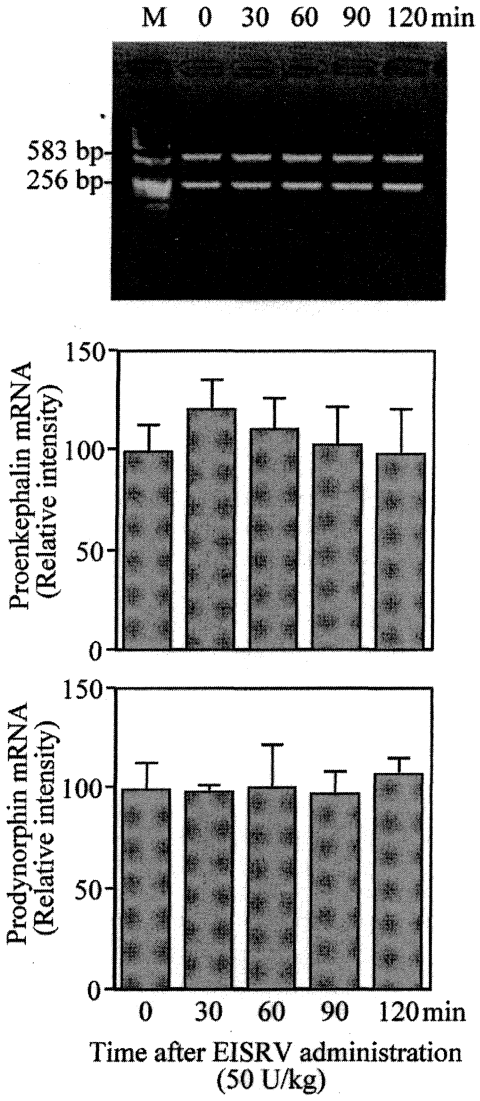

Fig. 3. Effect of EISRV on thalamic mRNA levels of proenkephalin and prodynorphin.
Rats were injected intraperitoneally with EISRV (50 U/kg) and killed at the indicated times. Total RNA was extracted from thalamic tissues and the mRNA levels of proenkephalin and prodynorphin were analyzed by reverse transcription polymerase chain reaction (RT-PCR). Top: RT-PCR products electrophoresed on 2% agarose gels containing ethidium bromide. A 583 base-pair single band for proenkephalin and a 256 base-pair band for prodynorphin in each lane were visualized by UV fluorescence. M: size marker. Bottom: relative intensities of RT-PCR products analyzed by NIH Image 1.55 software. Values are mean ±S.D., n = 3. There is no significant difference between the time points (by ANOVA).

Discussion

EISRV (Rosemorgen) is a non-protein extract from the inflamed skin of rabbits inoculated with vaccinia virus, and contains components of amino acids, peptides, and nucleic acid bases. Although the component that account for its antinociceptive effect remains unclear, EISRV has been widely used as a sedative analgesic because of its lack of marked side effects. EISRV is an inhibitor of the kallikrein-kinin system, because it inhibits the release of bradykinin(5). EISRV improves methacholine-induced hypersecretion and histamine-evoked sneeze response, and may be effective for treatment of nasal allergy(11). Evidence suggests that EISRV may act at the supraspinal level rather than on the spinal cord(1,12). Previous *in vitro* studies have indicated that EISRV inhibits two major naturally occurring enkephalin inactivators: neutral endopeptidase 24.11 and angiotensin I converting enzyme(13), indicating that the antinociceptive effect of EISRV may involve the metabolism of enkephalins, which are well known to be important moderators of pain perception and analgesia threshold.

The present study provides the first evidence that EISRV enhanced levels of Met^5-enkephalin and Leu^5-enkephalin in CSF in a dose-dependent and time-dependent manner when given by intraperitoneal injection. The duration of the increase of enkephalin concentration is consistent with that reported by others(14), who observed that when EISRV was injected into mice intraperitoneally 30 min prior to inducing pain responses, hyperalgesia was suppressed to the control level. The delay may be due to the time required for EISRV to permeate the blood-brain barrier and to reach an effective level in the CSF.

NEP is a metallopeptidase that cleaves peptides at the amino side of hydrophobic amino acids(8,9). It inactivates enkephalin by hydrolyzing it to Tyr^1-Gly^2-Gly^3 and Phe^4-Leu^5/Met^5. It is probably the major inactivator of enkephalins in the brain. In the present study, there appeared to be a trend towards lowering of NEP activity in CSF by EISRV administration, suggesting a possible inhibitory effect of EISRV on enkephalin catabolism *in vivo*. We consider that the non-significant change in the mean NEP activity was due to the requirement of a long incubation time for the diluted CSF samples that could lead to the dissociation of a reversible inhibitor from the enzyme. Further investigation regarding the inhibition of NEP activity in other tissue (i.e. brain) by EISRV administration needs to be performed in future. In addition, NEP is a membrane-bound enzyme; the inhibitor could be effective on cell membranes and obviously, just a small portion of the enzyme would be released into the CSF. It is possible that in other types of assays approaching physiological conditions more, the inhibition would have been more apparent. The *in vivo* effect of EISRV should be explored further.

No obvious change was observed in the thalamic mRNA levels of proenkephalin and prodynorphin during the experiment. The results of mRNA levels of proenkephalin and prodynorphin need to be reconfirmed using the real-time quantitative RT-PCR in future. Although the effect of EISRV on enkephalin expression in other parts of the brain can not be excluded, combined with the previous report(13), the inhibition of NEP activity may, at least partly, explain the accumulation of Met^5-enkephalin and Leu^5-enkephalin in CSF after EISRV administration.

In conclusion, the above findings suggest that EISRV enhances enkephalins (analgesic peptides) by probably inhibiting NEP in brain to eventually elicit analgesic effects.

We thank Ms. Taeko Kaimoto for her technical assistance and Ms. Tomoko Adachi for her secretarial assistance. This study was supported in part by a grant-in-aid for scientific research from the Ministry of Health, Labour and Welfare of Japan (to Dr. Shigeto Morimoto) and a grant for promoted research from Kanazawa Medical University (S2005-5 to Dr. Takashi Takahashi).

References

1. Shimazu S, Watanabe H, Kinoshita C et al: Antinociceptive effects of Rosemorgen. Jpn Pharmacol Ther 1997; **25**: 819-26.
2. Ohara H, Kawamura M, Namimatsu A et al: Mechanism of hyperalgesia in SART stressed (repeated cold stress) mice: antinociceptive effect of neurotropin. Jpn J Pharmacol 1991; **57**: 243-50.
3. Thiebauld C, Vandeput J, Lintermans J et al: Action of neurotropin on cold-induced pain in normal volunteers: a double-blind placebo study. Fundam Clin Pharmacol 1990; **4**: 141-6.
4. Okada M, Suzuki K, Hidaka T et al: Complex regional pain syndrome type I induced by pacemaker implantation, with a good response to steroids and neurotropin. Intern Med 2002; **41**: 498-501.
5. Nishikawa K, Reddigari SR, Silverberg M et al: Effect of neurotropin on the activation of the plasma kallikrein-kinin system. Biochem Pharmacol 1992; **43**: 1361-9.
6. Miura T, Okazaki R, Yoshida H et al: Mechanisms of analgesic action of neurotropin on chronic pain in adjuvant-induced arthritic rat: roles of descending noradrenergic and serotonergic systems. J Pharmacol Sci 2005; **97**: 429-36.
7. Litvinova SV, Aristova VV, Kaliuzhnyi AL et al: The antihyperalgesic and selective analgesic effects of neurotropin. Farmakol Toksikol 1991; **54**: 13-5.
8. Erdös EG, Skidgel RA: Neutral endopeptidase 24.11 (enkephalinase) and related regulators of peptide hormones. FASEB J 1989; **3**: 145- 51.
9. Dragovic T, Deddish PA, Tan F et al: Increased expression of neprilysin (neutral endopeptidase 24.11) in rat and human hepatocellular carcinomas. Lab Invest 1994; **70**: 107-13.
10. Jiang B, Morimoto S, Yang J et al: Parathyroid hormone-related protein upregulates interleukin-1β-induced nitric oxide synthesis. Hypertension 1997; **30**: 922-7.

11. Namimatsu A, Go K, Hata T: Regulatory effect of neurotropin on nasal mucosal hypersensitivity in guinea pigs caused by SART (intermittent exposure to cold) stress. Jpn J Pharmacol 1992; **59**: 371-7.
12. Hata T, Kita T, Itoh E et al: Mechanism of the analgesic effect of neurotropin, Jpn J Pharmacol 1988; **48**: 165-73.
13. Jackman HL, Jiang B, Morimoto S et al: Novel pharmacological effects of Rosemorgen. Jpn Pharmacol Ther 1996; **24**: 2581-90.
14. Takahashi H, Shibata M, Ohkubo T et al: Effect of neurotropin on hyperalgesia induced by prostaglandin E2, naloxone, melatonin and dark condition in mice. Jpn J Pharmacol 1987; **43**: 441-4.

１．研究課題名：遺伝疾患原因遺伝子の探索（研究番号　S2005-6）

２．キーワード：１）ナンセンス変異（nonsense mutation）
２）NMD（nonsense mediated mRNA decay）
３）RNAi（RNAi）
４）DNA マイクロアレイ（DNA microarray）
５）DNA チップ（DNA chip）

３．研究代表者：石垣　靖人・総合医学研究所・講師・共同利用部門

４．研 究 目 的

本研究の目的は網羅的遺伝子発現解析法と RNAi による遺伝子発現ノックダウンを組み合わせることによって、劣性遺伝疾患を引きこしているナンセンス変異遺伝子を迅速に同定するための方法論を確立することにある。ナンセンス変異を持つ遺伝子から転写された mRNA は、Upf1,2,3 あるいは SMG1 等と呼ばれるタンパク質群との相互作用により分解に導かれる。この現象は NMD と呼ばれており、ナンセンス変異をもつ遺伝子の発現はほぼ消失している。NMD の活性を阻害剤や RNAi によって抑制してやると、処理前に消失していた変異をもつ遺伝子の発現が回復することを見いだして来た。このことを利用し、DNA マイクロアレイシステムによる網羅的な遺伝子発現解析を行うことによって、未知のナンセンス変異遺伝子を検出する方法の確立を目指した。

５．研 究 計 画

培養細胞における遺伝子発現を網羅的に解析することによって、変異遺伝子の探索が可能な系を立ち上げる。必要な系として、発現解析系と効率の良い mRNA 代謝系のノックダウンが必要であるため、RNAi の適用方法を工夫した。最終的には変異既知の細胞を利用して、実際に既知ナンセンス変異遺伝子が検出可能かどうかを検討する。

６．研 究 成 果

網羅的遺伝子発現解析系を立ち上げ、総合医学研究所の先生方のご尽力により、検索等に必要なソフトウエア(GeneSpring GX)とデータベース(Ingenuity Pathways Analysis)を整備することができた。RNAi によるノックダウン系の効率が低かったので、複数回誘導する系に切り替えて高い効率をもつノックダウン系を確立できた。

これらを活用して DNA マイクロアレイ解析を行うことによって、既知のナンセンス遺伝子を絞り込めることを明らかにした。ノックダウン系および阻害剤を利用した DNA マイクロアレイ解析は既知のナンセンス変異遺伝子をゲノム全体から発現する２万個以上の転写産物から 100 個未満まで絞り込むことが可能であることが明らかとな

った。以上の結果は、国際学会１（20th IUBMB)、国際会議１（First meeting of the Anglo-Japanese Werner syndrome consortium)、国内学会２カ所（日本薬学会、北陸先天異常研究会学術集会）等に報告し、特に希少な劣性遺伝疾患でナンセンス変異の存在が疑われる疾患の原因遺伝子解析に関して、この技術を活用した共同研究を推進中である。

７．研究の考察・反省

研究過程でがん細胞における同様の解析が他の研究者によって論文発表されてしまい、オリジナリティが低くなってしまった。今後さらに迅速に実験が進められるように努力することと、追加の実験を行うことによって、これまでの報告よりも洗練された実験系として、論文として報告して行きたい。さらに、DNA マイクロアレイが有効なツールであることは明らかとなり、その解析方法にも習熟したが、他の網羅的な解析手法（パスウエイ解析やプロテオミクスなど）と連結することによって、データに大量に付随するノイズを解消して行く手法を開発して行きたい。

８．研 究 発 表

石垣靖人．ナンセンス変異依存 mRNA 分解機構(NMD)の機構と役割について．金医大誌 2005；30：320-325.

金医大誌（J Kanazawa Med Univ）30：320－325, 2005

ナンセンス変異依存mRNA分解機構 (NMD) の機構と役割について

石　垣　靖　人

要　約：例えば色素性乾皮症，Werner症候群，血管拡張性失調症などの劣性遺伝疾患ではmRNAの読み枠の途中で終止コドンを生むナンセンス変異が原因遺伝子に見いだされ，その発現は，mRNAレベルでほぼ消失していることが知られている。これはナンセンス変異をもつ遺伝子のmRNAが細胞内で選択的に分解されていることが原因であるが，この分解経路のことをRNAサーベイランス，またはナンセンス変異依存mRNA分解機構 (Nonsense-mediated mRNA decay)，略してNMDと呼ぶ。現在考えられているNMDのモデルでは，はじめにスプライシングに伴ってエキソンとエキソンのつなぎ目にタンパク質の複合体 (Exon junction complex) が結合する。この複合体を介してNMD関連因子がmRNA上へ集結する。このあとの翻訳で，リボソームがナンセンス変異で停止すると，変異の3'側に結合するNMD関連因子と相互作用して変異mRNAだけを選択的に分解に導く。この時，リン酸化および脱リン酸化反応が分解へのスイッチとして機能すると考えられている。ナンセンス変異は遺伝疾患で見いだされるだけでなく，スプライシングの失敗やRNA編集の結果として，常に生体内のmRNA上に生まれているらしい。NMDはこのような遺伝情報のノイズを排除しており，遺伝情報の品質管理に必須な機構であると考えられている。

キーワード：　mRNA分解，ナンセンス変異，NMD，RNAサーベイランス

はじめに

遺伝情報の設計図ともいえるDNAの配列はRNAに写し取られ，RNAの配列をもとにアミノ酸がつなげられていってタンパク質が合成される。細胞は，この遺伝情報の流れを常に監視しており，異常を修復し不良品を排除することにより遺伝情報の「品質管理」を行っている。

mRNAはDNA配列をもとに合成されるが，5'末端にキャップ構造と呼ばれる修飾をうけ，スプライシングによってイントロン配列が除かれてエキソン配列のみがつなげられていき，3'末端に長いアデニン鎖 (ポリA) が付けられる。タンパク質はアミノ酸がmRNAの3塩基の組み合わせ (コドン) に基づいてつなげられていくことにより完成される。コドンの中にはアミノ酸をコードしない組み合せが3種あり，ここでリボソームが行うアミノ酸の連結が終了することから，特に「終止コドン」と呼ばれる。タンパク質合成 (翻訳) は初めの「開始コドン」からはじまって「終止コドン」で終了するが，何らかの理由で開始コドンと本来の終止コドンの間に新たに終止コドンができることがある。このようなタイプの変異は特に「ナンセンス変異」と呼ばれる (図1)。

ナンセンス変異は，多くのヒト劣性遺伝疾患でゲノムDNAの原因遺伝子配列中に見いだされ，遺伝疾患で同定される変異のおよそ3割がナンセンス変異であると言われている。また，RNA合成時の読み間違い，スプライシングの失敗，RNA編集などによっても細胞内に頻繁に生成していると推測されている。さらに，B細胞の免疫グロブリン遺伝子やT細胞のレセプター遺伝子で起こる遺伝子再構成においても，組換えを終えた遺伝子に高い頻度でナンセンス変異が生成することが知られている (1)。なお，ナンセンス変異は狭義には新たに終止コドンを生むようなDNA配列上の変異と定義されているが，転写後にmRNA配列の読み枠内に生成してしまった新たな終止コドンは，特にPremature terminationコドン (PTC) と呼ばれることもある。本総説では混乱を避けるためにPTCを用いずにナンセンス変異で統一して記述した。

金沢医科大学総合医学研究所共同利用部門RIセンター
石川県河北郡内灘町大学1-1
平成18年2月28日受理

1．ナンセンス変異依存mRNA分解とは

ナンセンス変異をもつmRNAがタンパク質に翻訳されていくと，本来のタンパク質よりも短いポリペプチド鎖が合成される

表1．ナンセンス変異依存mRNA分解 (NMD) の特徴

変異を持つ mRNA の選択的分解機構である。
酵母からヒトにまで保存された機構である。
変異が存在しても転写活性は低下しない。pre-mRNA 量も減少しない。
分解にはスプライシング（イントロンの存在）が必要である。
変異の位置によっては分解されない場合がある（図2 参照）。
翻訳反応が必要である。
タンパク質合成および PI-3 型キナーゼ阻害剤で阻害できる。

が，部分的には正常な配列を持っているために正常な全長をもつタンパク質の働きを競合阻害する可能性がある。このように生体にとって有害な変異型のタンパク質の生成を防ぐために，細胞は変異のあるmRNAを選びだして分解してしまう特別なRNA分解経路を持っている。これがナンセンス変異依存mRNA分解機構 (Nonsense-mediated mRNA decay; 以下NMDと省略) あるいはRNAサーベイランスと呼ばれるシステムである(2)。実際には，変異をもつmRNAの分解速度が速くなっているため，ナンセンス変異をもつ遺伝子のmRNA量は正常に比べて極端に減少しており，タンパク質はほぼ完全に消失していわゆるnull”の状態となっている。実際NMDの標的となるようなナンセンス変異をもつ遺伝疾患原因遺伝子の発現を調べてみると，患者由来細胞において消失している一方，両親の細胞においては半

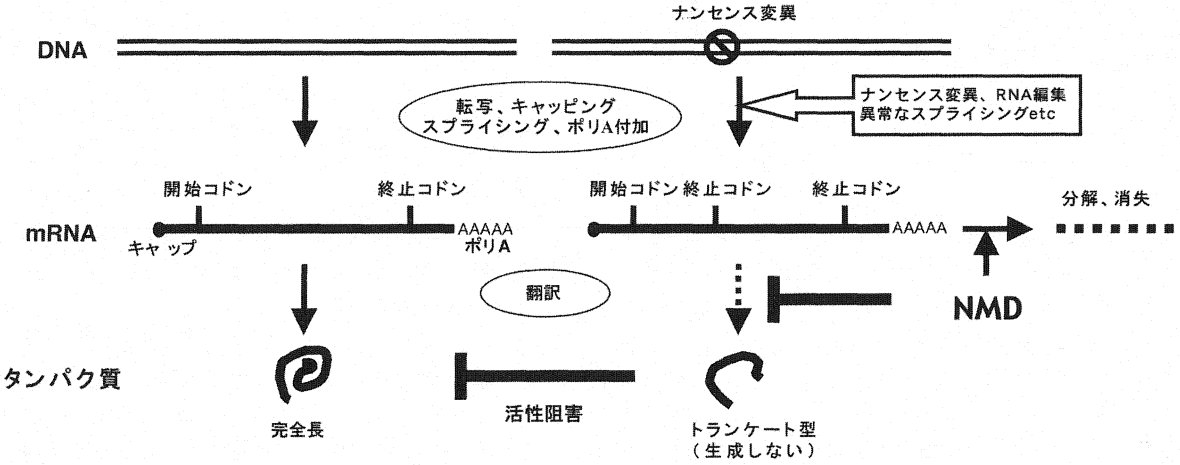

図1．ナンセンス変異の生成とNMDの役割
ナンセンス変異はDNA上の変異，RNA編集，スプライシング異常などの結果により生成する。読み枠の途中で終止コドンが生成すると，トランケート型のタンパク質が生成して完全長の働きを阻害してしまう。このためNMDが進化の過程で獲得され，mRNAをいちいちチェックして変異型を選択的に分解するようになったと考えられる。

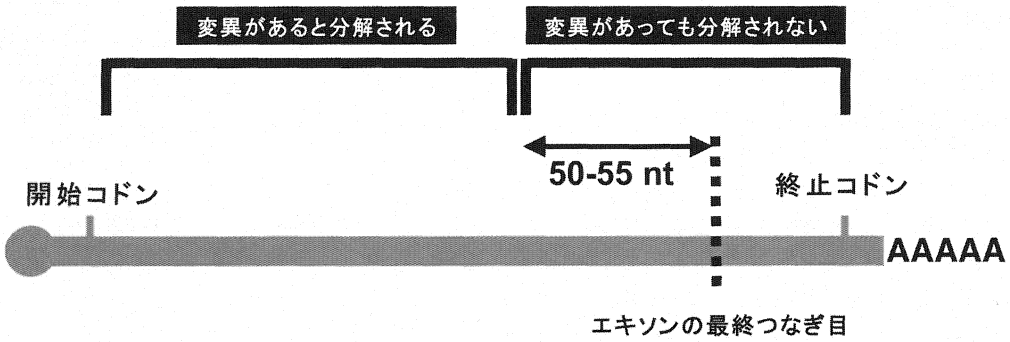

図2．NMDが変異を認識できるmRNA上の領域
NMDは全てのナンセンス変異を認識できるわけではない。最終エキソン内の変異と，エキソンのつなぎ目から50から55塩基上流までに存在する変異は認識できず，mRNAの分解も起きない。

減が観察される。原因遺伝子のmRNAが選択的に分解されているので，通常は開始コドンからナンセンス変異による終止コドンまでの配列に基づいた短い翻訳産物は検出できない (図1)。

ヒト細胞におけるNMDの機構は変異遺伝子を培養細胞へ導入した実験系で様々な角度から検討され，幾つかの特徴が明らかにされてきた (表1)。まず，NMDはmRNAの積極的な分解によってmRNAが消失する現象であり，ナンセンス変異が存在しても転写活性は影響を受けていない。従って転写されてスプライシングを受ける前のpre-mRNAの量も減少していない。また，cDNAにナンセンス変異を導入して細胞内で発現させても分解を受けないが，イントロンを含む配列を発現させると分解を受けるので，スプライシングを受けたmRNAのみで起きる現象である。また，NMDが起こるためにはmRNA配列上でのナンセンス変異の位置が重要である。興味深いことに，ナンセンス変異が最終エキソンに位置するmRNAの場合，たとえ変異が本来の終止コドンの上流にあっても分解は受けない。さらに図2に示したように一番下流のエキソンとエキソンのつなぎ目からおおよそ50～55塩基上流までにあるナンセンス変異も認識されないことが明らかになった(3)。

一方，NMDによる変異mRNAの分解はタンパク質合成阻害剤やPI(Phosphatidylinositol)-3型キナーゼ阻害剤によって特異的に抑制されるので，翻訳とリン酸化を伴う反応である(4,5)。例えば色素性乾皮症A群患者のうちナンセンス変異をもつ患者から採取した細胞に，タンパク質の合成阻害剤であるシクロヘキシミドやエメチン，あるいはPI-3キナーゼ特異的な阻害剤であるワルトマニンを処理すると消失していた原因遺伝子*XPA*のmRNA量が速やかに回復してくる (未発表データ)。タンパク質合成以外のステップでコドンが読みとられる機構はまず存在しないと考えられるので，翻訳の阻害剤がNMDを抑制することは，ナンセンス変異の認識はリボソームがひとつひとつのコドンを読み取るタンパク質合成過程で起きることを強く示唆する。以上のような特徴が明らかにされると共に，酵母や線虫の変異体の解析からNMD関連因子が次々に同定されるようになり，次項で述べるようにヒトにおけるオルソログがつぎつぎと同定されてきた。

2．NMD関連因子

ヒト，酵母，線虫におけるNMD関連因子について表2にまとめた。酵母において初めて見いだされたUpf1，2，3は複合体を形成してmRNAに結合し，変異を持つmRNAの識別に中心的な役割を果たすと考えられている。酵母での配列情報をもとにクローニングされたヒトUpf1は，リボソームが終止コドンまで翻訳を終えたときに働く翻訳終結因子eRF1，eRF3と結合し，またATPase活性，5'→3'ヘリケース活性を持ちRNAに結合できることが報告されている(6,7)。ヘリケースドメインに変異を持つUpf1のcDNAを細胞へ導入して強発現させるとNMDの活性に対してドミナント・ネガティブな効果を持つことから，このヘリケース活性はNMDの誘導に重要である(8)。またヒトUpf1は細胞内でリン酸化制御を受けることも報告されている(4)。

タンパク質間の相互作用の解析から，ヒトでもUpf1，Upf2，Upf3またはUpf3Xは細胞内で強固に結合するので，スプライシングを受けたmRNAに複合体を形成して結合し，NMDを引き起こすと考えられる。ただし，免疫染色の結果によると，それぞれの細胞内での局在場所は異なっており，Upf1は細胞質に，Upf2は核周辺に，Upf3は核内に局在が認められることから，核から細胞質へmRNAが輸送されていく過程で段階的に複合体が形成されると考えられている(9)が，確実な証明があるわけではない。Upf1，2，3のmRNA上への結合はスプライシングによってエキソンとエキソンのつなぎ目付近に形成されるExon junction complex (EJC) を介して行われる。実際，スプライシング後のmRNA上に形成されるEJC内にUpf3が検出される(10)ので，以降のUpf2，Upf1あるいはは SMG1の結合はUpf3を介してmRNA上で起こると考えられている。一方，β-グロビン遺伝子の終止コドン下流にMS2コートタンパク質の結合配列を挿入し，MS2コートタンパク質と融合させたUpf1，Upf2，Upf3，Upf3Xのいずれかと共に細胞内に導入すると，挿入されたMS2コートタンパク質結合配列の上流に終止コドンがあるmRNAに対してのみ分解が誘導される。したがって，Upf複合体がmRNA上に局在し，ナンセンス変異であるかないかにかかわらず上流に存在する終止コドンを認識した時に変異と判断されてmRNAを分解に導くと考えられている(11)。

一方SMG1はPI-3型キナーゼファミリーのひとつであり，ヒトSMG1のキナーゼドメインに突然変異を入れて発現させるとNMDが抑制されること，SMG1がUpf1，Upf2，Upf3と結合することから，直接Upf1に結合してリン酸化を行っており，この制御はNMDに必要であるとされている。ワルトマニンなどのPI-3キナーゼ阻害剤は，SMG1に作用してUpf1のリン酸化を阻害しNMDを抑制すると考えられている。この系を用いてNMD

表2． ヒトおよびモデル生物における主要なNMD関連因子とその機能

ヒト	線虫	酵母	機能など
SMG1/ATX	SMG-1		PI-3型キナーゼ、Upf1をリン酸化 DNA傷害センサー
Upf1	SMG-2	Upf1	ATPase、ヘリケース活性 Upf2、eRF1、eRF3、SMG-1と結合
Upf2	SMG-3	Upf2	Upf1、Upf3と結合
Upf3 Upf3X	SMG-4	Upf3	核-細胞質間シャトリング Upf2、EJCと結合
SMG5	SMG-5		Upf1脱リン酸化に関与
SMG6	SMG-6		Upf1脱リン酸化に関与
SMG7	SMG-7		Upf1脱リン酸化に関与
EJC (Exon junction complex)			スプライシングに伴ってmRNA上にUpf複合体が結合する足場を提供する
Staufen1			RNA結合タンパク質 Upf1に結合
		Hrp1/Nab4	DSE配列に結合してUpf複合体と相互作用しNMDを誘導
		Pub-1	STE配列に結合してNMDを阻害

の阻害がトランケート型蛋白質の蓄積を導くことが初めて示されている(5)。ヒトにおける他のSMGオルソログについては，脱リン酸化に働くことが最近報告されているが，リン酸化と脱リン酸化が具体的に分子レベルでどのようにしてNMDに働くのかは未だに明らかではない(12)。この他にRNA結合タンパク質Staufen1や酵母特異的なHrp1，Pub1などが関与することが知られている(13,14)。

3．NMDの機構モデル

2．および3．での知見を基にして現時点で考えられている哺乳類動物細胞でのNMDのモデルを図3に示した。転写されたpre-mRNAがスプライシングを受けることによって，それぞれのエキソンのつなぎ目にEJCが形成され，そこを足場としてUpf3，Upf3Xが結合し，核膜付近でUpf2が会合し，続いてUpf1がリクルートされてUpf複合体が形成される。mRNAにUpf複合体が結合している段階では，キャップ構造にCap binding complex (CBC) が結合しており，ポリA配列にはPABP2 (Poly A binding protein-2) が結合している。やがてCBCが結合したmRNAにおいて初めての翻訳反応 (Pioneer round translation) がはじまると，リボソームの進行に伴って各EJCは次々とはずされていくが，リボソームが終止コドンに到達して停止すると，下流のEJCを足場として形成されたUpf複合体と翻訳装置の間に相互作用が起きて変異が認識されると考えられている(15,16,17)。ナンセンス変異を持つことが確認されたmRNAは，キャップ構造をはずされ，ポリA配列の分解を経ずに5'→3'方向への分解が起こる。SMG1はこれらのステップのいずれかでUpf複合体中のUpf1をリン酸化すると予想される。ナンセンス変異をもたないmRNAでは，リボソームが正常な終止コドンに達することで翻訳の終結が起こり，下流にEJCを介したUpf複合体が結合していないために分解には導かれない。やがて，細胞質でCBCは翻訳開始因子であるeIF4Eへと置換される。この品質保証されたmRNAには，eIF4Gをはじめとする他の翻訳開始因子が集結し，ポリA配列にはPABP1 (Poly A binding protein-1) が結合して細胞質における活発な翻訳が始まると考えられる。おそらくはNMDを回避するため大部分の正常な終止コドンが最終エキソンに存在する事実と，実験的に最終エキソン中のナンセンス変異がNMDに認識されないことはこのモデルを支持している(18)。

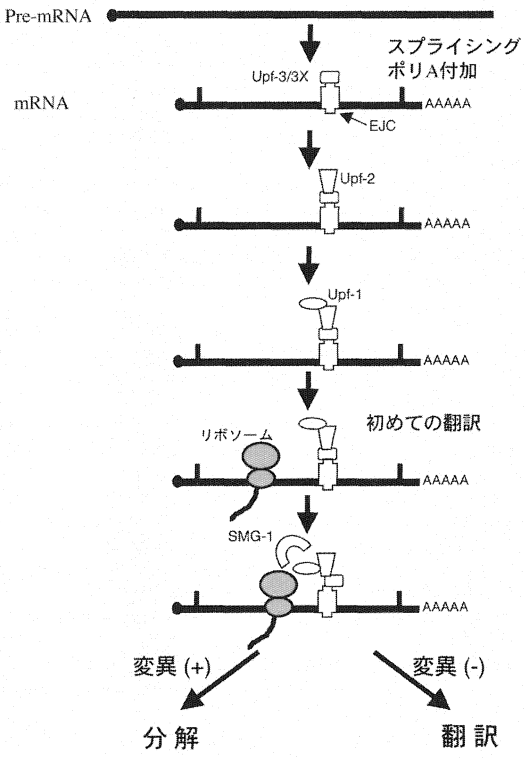

図3．NMDのモデル
EJCを利用してUpf3→Upf2→Upf1の順番でmRNA上に複合体が形成される。ナンセンス変異による終止コドンで停止したリボソームとUpf複合体は相互作用し，そこにSMG1がリクルートされてUpf1をリン酸化する。これが引き金となってmRNAの分解が起こると考えられている。EJCは最後のエキソンのつなぎ目以降の配列には形成されないために，図2で示したようにつなぎ目付近と最終エキソンの終止コドンはNMDに認識されないと考えられている。

4．変異mRNA分解以外のNMDまたはNMD関連因子の役割

上に述べたように，NMDはスプライシング，mRNA輸送，翻訳，タンパク質のリン酸化制御などを巻き込んだ複雑なシステムであることが次第に明らかになってきている。現時点では，ナンセンス変異を持つmRNAの排除がNMDの役割であることに疑いはないとしても，一方でNMD関連因子はNMD以外の生命現象にも寄与していることが報告されている。線虫では一部の*smg*突然変異体がRNA interference (RNAi) による遺伝子発現のノックダウンを保てないこと(19)が報告されており，NMD関連因子がNMD以外のRNA分解経路に寄与する可能性がある。また，酵母のUpf変異体では，染色体末端に位置して細胞分裂寿命を決定するテロメア配列の短縮が報告されている(20)。さらに，Upf1によってキネトコア構成タンパク質の発現量が制御されていること(21)やSMG1が細胞周期チェックポイントを制御するPI-3キナーゼであるATMやATRと類似の配列を持ちDNA傷害センサーとして機能すること(22)，またUpf1がDNAポリメラーゼδと結合する(23)等の報告から，NMDとは一見無関係に見える老化や細胞周期チェックポイントなどの生命現象にもNMD，またはNMD関連因子が寄与する可能性が考えられている。

おわりに

NMDにおける今後の課題としては，NMDにかかわる一連の反応が細胞内のどこで起きているか，という「場」の問題がある。教科書的には翻訳が細胞質で起きる以上，翻訳を必要とす

るNMDは細胞質で起きると考えるのがひとまず自然である。しかし，一部の研究者は細胞の核内で翻訳が起きうると主張していること(24,25)とあわせて，核分画から精製したRNAを解析するとNMDが観察されることから，核あるいは核膜上でNMD，すなわち初めての翻訳反応が起きている可能性は否定できない。ただし，従来の生化学的な解析では不純物の混入を否定しきれないので，この問題を解決するためには別の方法論によるアプローチが必要である。

また，NMDの標的となるナンセンス変異がゲノムあるいはトランスクリプトーム全体でどれくらい存在しているのかも未だに定量的な解析結果は報告されていない。DNAマイクロアレイを利用した遺伝子発現量の解析では個体差の大きい遺伝子は千個以上存在するが，これらすべてがナンセンス変異を持つとは考えにくく，おそらくは一塩基多型 (SNPs) などによる発現量の変動も反映していると考えている。NMD関連因子をRNAiを利用してノックダウンすると多数の遺伝子発現変動がおきることが報告されている(26)が，この結果はNMDの標的となるナンセンス変異がゲノム配列中にかなりの頻度で存在している可能性と同時に，NMDが変異に関係なく遺伝子の発現量を調節している可能性を示唆する。今後は，NMDの分子レベルでの機構解明が進むと共に，遺伝情報の発現や品質管理における役割がさらに明らかにされていくことが期待される(27,28)。

本総説中の未発表データの研究については金沢医科大学奨励研究S2005-6，武田科学振興財団，科学研究費補助金16590045, 17019022, 14035221からのご支援をいただきました。深く感謝致します。また，様々な面で助けていただきました金沢医科大学総合医学研究所所長の松井忍先生，同研究所共同利用部門長中川秀昭先生をはじめとする研究所の皆様にもこの場をお借りして感謝致します。ありがとうございました。

文　　献

1. Li S, Wilkinson MF: Nonsense surveillance in lymphocytes? Immunity 1998; **8**: 135-41.
2. Maquat LE: Nonsense-mediated mRNA decay. Curr Biol 2002; **12:** 196-7.
3. Maquat LE: Nonsense-mediated mRNA decay in mammals. J Cell Sci 2005; **118**: 1773-6.
4. Pal M, Ishigaki Y, Nagy E et al: Evidence that phosphorylation of human Upfl protein varies with intracellular location and is mediated by a wortmannin-sensitive and rapamycin-sensitive PI 3-kinase-related kinase signaling pathway. RNA 2001; **7**: 5-15.
5. Yamashita A, Ohnishi T, Kashima I et al: Human SMG-1, a novel phosphatidylinositol 3-kinase-related protein kinase, associates with components of the mRNA surveillance complex and is involved in the regulation of nonsense-mediated mRNA decay. Genes Dev 2001; **15**: 2215-28.
6. Czaplinski K, Ruiz-Echevarria MJ, Paushkin SV et al: The surveillance complex interacts with the translation release factors to enhance termination and degrade aberrant mRNAs. Genes Dev 1998; **12**: 1665-77.
7. Bhattacharya A, Czaplinski K, Trifillis P et al: Characterization of the biochemical properties of the human Upf1 gene product that is involved in nonsense-mediated mRNA decay. RNA 2000; **6**: 1226-35.
8. Sun X, Perlick HA, Dietz HC et al: A mutated human homologue to yeast Upf1 protein has a dominant-negative effect on the decay of nonsense-containing mRNAs in mammalian cells. Proc Natl Acad Sci U S A 1998; **95**: 10009-14.
9. Serin G, Gersappe A, Black JD et al: Identification and characterization of human orthologues to Saccharomyces cerevisiae Upf2 protein and Upf3 protein (Caenorhabditis elegans SMG-4). Mol Cell Biol 2001; **21**: 209-23.
10. Gehring NH, Neu-Yilik G, Schell T et al: Y14 and hUpf3b form an NMD-activating complex. Mol Cell 2003; **11**: 939-49.
11. Lykke-Andersen J, Shu MD, Steitz JA: Human Upf proteins target an mRNA for nonsense-mediated decay when bound downstream of a termination codon. Cell 2000; **103**: 1121-31.
12. Ohnishi T, Yamashita A, Kashima I et al: Phosphorylation of hUPF1 induces formation of mRNA surveillance complexes containing hSMG-5 and hSMG-7. Mol Cell 2003; **12**: 1187-200.
13. Kim YK, Furic L, Desgroseillers L et al: Mammalian Staufen1 recruits Upf1 to specific mRNA 3'UTRs so as to elicit mRNA decay. Cell 2005; **120**: 195-208.
14. Ruiz-Echevarria MJ, Peltz SW: The RNA binding protein Pub1 modulates the stability of transcripts containing upstream open reading frames. Cell 2000; **101**: 741-51.
15. Ishigaki Y, Li X, Serin G et al: Evidence for a pioneer round of mRNA translation: mRNAs subject to nonsense-mediated decay in mammalian cells are bound by CBP80 and CBP20. Cell 2001; **106**: 607-17.
16. Lejeune F, Ishigaki Y, Li X et al: The exon junction complex is detected on CBP80-bound but not eIF4E-bound mRNA in mammalian cells: dynamics of mRNP remodeling. EMBO J 2002; **21**: 3536-45.
17. Buhler M, Wilkinson MF, Muhlemann O: Intranuclear degradation of nonsense codon-containing mRNA. EMBO Rep 2002; **3**: 646-51.
18. Nagy E, Maquat LE: A rule for termination-codon position within intron-containing genes: when nonsense affects RNA abundance. Trends Biochem Sci 1998; **23**: 198-9.
19. Domeier ME, Morse DP, Knight SW et al: A link between RNA interference and nonsense-mediated decay in Caenorhabditis elegans. Science 2000; **289**: 1928-31.
20. Lew JE, Enomoto S, Berman J: Telomere length regulation and telomeric chromatin require the nonsense-mediated mRNA decay pathway. Mol Cell Biol 1998; **18**: 6121-30.
21. Dahlseid JN, Puziss J, Shirley RL et al: Accumulation of mRNA coding for the ctf13p kinetochore subunit of Saccharomyces cerevisiae depends on the same factors that promote rapid decay of nonsense mRNAs. Genetics 1998; **150**: 1019-35.
22. Brumbaugh KM, Otterness DM, Geisen C et al: The mRNA surveillance protein hSMG-1 functions in genotoxic stress response pathways in mammalian cells. Mol Cell 2004; **14**: 585-98.
23. Carastro LM, Tan CK, Selg M et al: Identification of delta helicase as the bovine homolog of HUPF1: demonstration of an interaction with the third subunit of DNA polymerase delta. Nucleic Acids Res 2002; **30**: 2232-43.
24. Ibbora FJ, Jackson DA, Cook PR: Coupled transcription and translation within nuclei of mammalian cells. Science 2001; **293**: 1139-42
25. Iborra FJ, Jackson DA, Cook PR: The case for nuclear translation. J Cell Sci 2004; **117**: 5713-20.
26. Mendell JT, Sharifi NA, Meyers JL et al: Nonsense surveillance regulates expression of diverse classes of mammalian transcripts and mutes genomic noise. Nat Genet 2004; **36**: 1073-8.
27. Wilkinson MF: A new function for nonsense-mediated mRNA-decay factors. Trends Genet 2005; **21**: 143-8.
28. Lejeune F, Maquat LE: Mechanistic links between nonsense-mediated mRNA decay and pre-mRNA splicing in mammalian cells. Curr Opin Cell Biol 2005; **17**: 309-15.

Mechanism and Role of Nonsense-mediated mRNA Decay (NMD)

Yasuhito Ishigaki

Medical Research Institute, Kanazawa Medical University, Uchinada, Ishikawa 920-0293, Japan

Some cases of recessive genetic disease are caused by nonsense-mutation (premature stop codon) and mRNA that contains this type of mutation is rapidly degraded by a mRNA decay pathway termed nonsense-mediated mRNA decay (NMD, or RNA surveillance). The biological role of NMD is thought to be the knocking down of abnormal mRNA that encodes potentially deleterious truncated protein. In addition to naturally occurring nonsense-containing mRNAs originating from genetic mutations, abnormally spliced mRNAs and some edited mRNAs are also degraded by NMD. NMD pathway is dependent on pre-mRNA splicing, PI-3 kinase dependent phosphorylation and translation. Splicing deposits a complex at 50-55nt upstream of exon-exon junction, and this exon junction complex (EJC) recruits NMD factors (Upf1, Upf2 and Upf3s) onto mRNA molecule. NMD seems to occur when translation terminates at stop codon derived from nonsense mutation. The terminated ribosome is thought to interact with junction-bound NMD factors via translation termination factors (eRF1 and eRF3). For eliciting abnormal mRNA degradation, the phosphorylation of NMD factors by PI-3 type kinase, SMG-1/ATX is also required. Although previously thought of as a pathway that rids the cell of deleterious mRNAs arising from mutations and processing errors, recent research suggests a more general and evolutionarily important role for NMD in the control of overall gene expression.

Key Words: mRNA decay, NMD, nonsense mutation, premature termination codon, RNA surveillance

１．研究課題：G１期の癌細胞に対する放射線効果増強法の開発---53BP1 を標的として
（研究番号　S2005-7）

２．キーワード：１）細胞周期（cell cycle）
２）放射線照射（X-irradiation）
３）DNA 二重鎖切断（DNA double strand break ）
４）非相同末端結合修復（non-homologous end joining）
５）53BP1

３．研究代表者：岩淵　邦芳・医学部・助教授・ゲノム医科学（生化学）

４．研究目的

X 線照射などにより発生する DNA 二重鎖切断に対して、細胞は、相同組み換え、非相同末端結合の 2 つの修復経路を備えている。相同組み換え修復経路は、DNA 複製時の姉妹染色分体を鋳型として損傷部位を修復するため、その修復は正確であるが、姉妹染色分体が存在する細胞周期 S、G2 期にしか機能しない。一方、非相同末端結合修復経路は､修復の正確性には欠けるものの G1 期を含めたすべての細胞周期に機能している。これを細胞周期側からみてみると、G1 期には 2 つの修復経路のうちの一方しか機能していないことがわかる。したがって、G1 期の細胞は S、G2 期に比べて DNA 二重鎖切断に対して感受性が強いと考えられる。実際、非相同末端結合修復経路に関与する蛋白質を欠損した細胞は､G1 期に極めて強い X 線感受性を示すことが知られている。以上より、もし非相同末端結合修復経路を癌細胞特異的に抑制することができれば、G1 期で停止しているため抗癌剤が効かない休眠中（dormant）の癌細胞に対する、有効な放射線効果増強療法の開発につながることが期待される。一方私は、私の発見した 53BP1 の機能解析の過程で、53BP1 欠損細胞が G1 期に極めて強い X 線感受性を示すことを見出した。このことは、53BP1 が非相同末端結合修復に関与していることを示唆しており、さらに、53BP1 の機能抑制法の開発が、G1 期癌細胞に対する放射線効果増強療法の開発につながることを意味している。本研究は、非相同末端結合修復における 53BP1 の機能を明らかにするとともに、将来的には、53BP1 を標的とした新しい放射線効果増強療法を開発することを目的とする。

５．研究計画

ニワトリ DT40 細胞株は、標的の遺伝子を容易に欠損させることができる。DT40 細胞株を用いて、非相同末端結合修復経路に関与する蛋白質の遺伝子、Ku70、Artemis、DNA ligase IV、および、53BP1 それぞれを欠損させた細胞株を樹立する。2 つの蛋白質が同じ経路で機能しているか否かを知るために、Ku70/53BP1、Artemis/53BP1、DNA ligase IV/53BP1 などの二重遺伝子欠損細胞株も樹立し､エピスターシス解析を行う。エピスターシス解析では、たとえば、Ku70/53BP1 二重遺伝子欠損細胞株の G1 期 X 線感受性が、53BP1 遺伝子欠損株、Ku70 遺伝子欠損株ぞれぞれの G1 期 X 線感受性を足し合わせた程度の場合、53BP1 と Ku70 は non-epistatic であり異なった経路で機能して

いると判断する。逆に、Ku70/53BP1 二重遺伝子欠損細胞株の G1 期 X 線感受性が、53BP1 遺伝子欠損株、Ku70 遺伝子欠損株いずれかのそれと一致すれば、53BP1 と Ku70 は epistatic であり同一経路で機能している（言い換えれば共同で機能している）と判断する。X 線に対する感受性は、コロニー形成法で判定する。細胞周期の G1 期への同調は、ノコダゾール 8 時間処理後、ノコダゾールを除いた後、ミモシン 8 時間処理することにより行う。細胞への X 線照射には、本学血液センターの X 線照射装置を使用する。

６．研究成果

53BP1 欠損細胞は、G1 期に極めて強い X 線感受性を示したが、DNA 二重鎖切断に対するチェックポイント異常は認めず、相同組換え修復も障害されていなかった。一方、DNA 二重鎖切断のマーカーとして知られているリン酸化 H2AX foci の消失が遅れることから、53BP1 欠損細胞では、非相同末端結合修復が障害されていると考えられた。エピスターシス解析の結果、G1 期細胞に生じた DNA 二重鎖切断に対しては、すでに知られている①Ku70/Ku80 を介した core 非相同末端結合修復経路　②Artemis を介した Artemis 依存性非相同末端結合修復経路以外に、新たに③53BP1 依存性非相同末端結合修復経路が存在することが明らかになった。①②③の 3 経路はいずれも非相同末端結合修復経路に特異的な DNA ligase IV につながることから、非相同末端結合修復経路の sub-pathway を構成していると考えられた。Ku70/Ku80 と結合し①の経路に関与することが知られている DNA-PK は、②の経路にも関与し、Artemis を活性化していることが示唆された。したがって、遺伝子欠損のない DT40 細胞を G1 期に同調させ DNA-PK 阻害剤である Wortmannin 存在下で 1 Gy の X 線照射を行うと、①②の経路が働かなくなり、コロニー形成が極端に減少した。しかし③の 53BP1 依存性修復経路が残っているため、コロニー形成は 0 にはならなかった。ところが 53BP1 欠損細胞で同様の実験を行うと①②③すべての修復経路が機能しないため、1 Gy という低線量にも関わらずコロニー形成が全く認められなくなった。以上より 53BP1 依存性非相同末端結合修復経路は、確かに G1 期に発生した DNA 二重鎖切断の修復に関与していること、①②の経路と異なり Wortmannin 抵抗性であること、更には、G1 期細胞は①②③の非相同末端結合修復経路以外の修復経路を持たないことが明らかになった。

７．研究の考察・反省

53BP1 が関与する新たな非相同末端結合修復経路を発見した。G1 期細胞は 3 つの非相同末端結合修復経路をどのように使い分けているのであろうか。ひとつには、DNA 二重鎖切断端の形態の違いによる使い分けが考えられる。これまでのところ、Ku 依存性修復経路は断端処理の必要がない断端の結合に、Artemis 依存性修復経路は断端処理の必要な断端の修復に関与しているのではないかと考えられている。しかし、私の実験では、53BP1 依存性経路は、明らかにそれ以外の 2 経路とは異なっている。したがって、Artemis が認識できず、53BP1 だけが認識できるような断端形態があるのではないかと考える。3 経路の機能分担の問題は、53BP1 の機能を明らかにするうえでの今後の大きな課題である。

本研究は、DNA-PK 阻害剤存在下で 53BP1 の機能を抑えると、G1 期細胞は X 線照射に対して無防備な状態になることを示している。同様の現象がヒト癌細胞でもみられるかどうかを明らかにする必要があるが、今後、siRNA を用いた治療法や、ヒトに投与可能な DNA-PK 阻害剤の開発が進めば、本研究の成果は以下のような方法で癌治療に利用できよう。たとえば、DNA-PK に異常がある癌細胞に対しては、53BP1 阻害剤を投与した上で、１Gy 以下の低線量の全身 X 線照射を行う。すると正常細胞は Ku 依存性修復経路、Artemis 依存性修復経路が機能しているため DNA 二重鎖切断を修復できるが、全身に転移した癌細胞で G1 期にいるものは DNA 二重鎖切断修復能を全く持たないため、完全に死滅してしまう。逆に 53BP1 に異常のある癌細胞では、DNA-PK 阻害剤を X 線照射前に投与する。このような放射線増感療法と、S、M 期の癌細胞を標的としている従来の抗癌剤療法とを併用すれば、癌の治療成績をさらに向上させることができるのではないかと考える。

８．研究発表

Iwabuchi K, Hashimoto M, Matsui T, Kurihara T, Shimizu H, Adachi N, Ishiai M, Yamamoto K, Tauchi H, Takata M, Koyama H, Date T. 53BP1 contributes to survival of cells irradiated with X-ray during G1 without Ku70 or Artemis.Genes Cells. 2006; 11: 935-948. (MLDB)

53BP1 contributes to survival of cells irradiated with X-ray during G1 without Ku70 or Artemis

Kuniyoshi Iwabuchi[1,*], Mitsumasa Hashimoto[1], Tadashi Matsui[1], Takayuki Kurihara[2], Hiroko Shimizu[3], Noritaka Adachi[5], Masamichi Ishiai[6], Ken-ichi Yamamoto[3], Hiroshi Tauchi[4], Minoru Takata[6], Hideki Koyama[5] and Takayasu Date[1]

[1]*Department of Biochemistry, and* [2]*Medical Research Institute, Kanazawa Medical University, Daigaku 1-1, Uchinada, Kahoku-gun, Ishikawa 920-0293, Japan*

[3]*Department of Molecular Pathology, Cancer Research Institute, Faculty of Medicine, Kanazawa University, Kanazawa, Ishikawa, 920-0934, Japan*

[4]*Department of Environmental Sciences, Faculty of Science, Ibaraki University, Bunkyo 2-1-1, Mito, Ibaraki 310-8512, Japan*

[5]*Kihara Institute for Biological Research, Graduate School of Integrated Science, Yokohama City University, Totsuka-ku, Yokohama 244-0813, Japan*

[6]*Department of Immunology and Molecular Genetics, Kawasaki Medical School, Kurashiki, Okayama 701-0192, Japan*

Ionizing radiation (IR) induces a variety of DNA lesions. The most significant lesion is a DNA double-strand break (DSB), which is repaired by homologous recombination or nonhomologous end joining (NHEJ) pathway. Since we previously demonstrated that IR-responsive protein 53BP1 specifically enhances activity of DNA ligase IV, a DNA ligase required for NHEJ, we investigated responses of 53BP1-deficient chicken DT40 cells to IR. 53BP1-deficient cells showed increased sensitivity to X-rays during G1 phase. Although intra-S and G2/M checkpoints were intact, the frequency of isochromatid-type chromosomal aberrations was elevated after irradiation in 53BP1-deficient cells. Furthermore, the disappearance of X-ray-induced γ-H2AX foci, a marker of DNA DSBs, was prolonged in 53BP1-deficient cells. Thus, the elevated X-ray sensitivity in G1 phase cells was attributable to repair defect for IR-induced DNA-damage. Epistasis analysis revealed that 53BP1 plays a role in a pathway distinct from the Ku-dependent and Artemis-dependent NHEJ pathways, but requires DNA ligase IV. Strikingly, disruption of the *53BP1* gene together with inhibition of phosphatidylinositol 3-kinase family by wortmannin completely abolished colony formation by cells irradiated during G1 phase. These results demonstrate that the 53BP1-dependent repair pathway is important for survival of cells irradiated with IR during the G1 phase of the cell cycle.

Introduction

Ionizing radiation (IR) induces a variety of DNA lesions, including single- and double-strand breaks, DNA-protein cross-links and various base damage (Friedberg *et al.* 1995). A DNA double-strand break (DSB) is one of the most serious threats to cells because it can result in loss or rearrangement of genetic information, leading to cell death or carcinogenesis. DSBs can arise during normal cellular processes, such as DNA replication and meiosis. In addition, DSBs occur during V(D)J and class switch recombination, processes required for normal development of the immune repertoire (Lieber *et al.* 2003). DSBs also activate signaling responses, termed cell-cycle checkpoints, which monitor DNA damage and transduce signals to coordinate repair and cell cycle progression (Shiloh 2003).

Upon exposure to IR, p53-binding protein 1 (53BP1) (Iwabuchi *et al.* 1994, 1998) is rapidly redistributed to sites of DSBs and is hyperphosphorylated in an ataxia telangiectasia mutated protein (ATM)-dependent manner (Schultz *et al.* 2000; Xia *et al.* 2000; Anderson *et al.* 2001; Rappold *et al.* 2001). ATM, a protein defective in the heritable disorder ataxia telangiectasia, is a central signaling kinase in the response to DSBs (Shiloh 2003). Studies using *53BP1*−/− mouse embryonic fibroblasts or small interfering RNA to inhibit 53BP1 expression have revealed that 53BP1 is required for the accumulation of p53 protein, G2/M checkpoint arrest, the intra-S-phase checkpoint in response to IR damage (DiTullio *et al.* 2002; Fernandez-Capetillo *et al.* 2002; Wang *et al.* 2002), and IR-stimulated phosphorylation of at least a subset of ATM substrates, including Chk2, BRCA1 and

Communicated by: Fumio Hanaoka

**Correspondence*: E-mail: kuni-kmu@kanazawa-med.ac.jp

DOI: 10.1111/j.1365-2443.2006.00989.x

SMC1 (DiTullio *et al.* 2002; Wang *et al.* 2002). The checkpoint defects observed in 53BP1-deficient cells are modest and restricted to responses to low doses of IR, suggesting that 53BP1 has other functions in the response to IR-induced DNA damage.

DSBs are repaired by two major pathways: homologous recombination (HR) and non-homologous end joining (NHEJ) (Jeggo 1998; Jackson 2002). HR primarily uses the undamaged sister chromatid as a DNA template allowing for accurate repair of the lesions (Johnson & Jasin 2000), and functions in late S-G2 phase (Rothkamm *et al.* 2003). NHEJ is an error-prone joining of DNA ends with the use of little or no sequence homology. NHEJ requires the DNA ligase IV (Lig IV)/Xrcc4 complex and DNA-dependent protein kinase (DNA-PK), which consists of the DNA end-binding subunits of Ku (Ku70 and Ku80) and the catalytic subunit (DNA-PKcs). In addition to participating in the rejoining of DSBs during V(D)J recombination, NHEJ plays a major role in the repair of IR-induced DSBs, especially during the G1 phase of the cell cycle when sister chromatids are not available (Rothkamm *et al.* 2003). It is thought that broken DNA termini are recognized by the Ku heterodimer, which then recruits DNA-PKcs, activating its kinase activity. This large complex protects the DNA ends from nuclease attack while facilitating the recruitment of the Lig IV/Xrcc4 heterodimer (Lieber *et al.* 2003; Downs & Jackson 2004). Cells lacking any of these factors show pronounced IR sensitivity and have an impaired ability to rejoin IR-induced DNA DSBs (Lobrich & Jeggo 2005).

Artemis (Moshous *et al.* 2001), a protein with nuclease activity, forms a physical complex with DNA-PKcs. The endonuclease activity of Artemis is required for processing the hairpin intermediate generated during V(D)J recombination (Ma *et al.* 2002), and it also appears to function similarly in end-processing during IR-induced DNA DSB repair (Riballo *et al.* 2004). Riballo *et al.* (2004) identified Artemis as a downstream component of ATM-dependent signaling in DSB repair. They also proposed a model for the repair of IR-induced DSBs during the G1 phase in mammalian cells, in which the majority of DSBs are rejoined by NHEJ. This process requires what they refer to as the "core NHEJ," which is composed of Lig IV/Xrcc4, Ku70/Ku80, and DNA-PKcs, wherein DNA-PKcs plays a nonessential but facilitating role. In addition, a subfraction of DSBs that require end-processing by Artemis is repaired by ATM/Artemis-dependent NHEJ. This ATM/Artemis-dependent repair pathway also requires proteins locating to sites of DSBs, including 53BP1.

We showed in a previous study that the ligation reaction catalyzed by recombinant Lig IV/Xrcc4 is enhanced by a purified polypeptide corresponding to the domain of 53BP1 responsible for focus formation (Iwabuchi *et al.* 2003). This suggests that 53BP1 participates in a DNA damage repair pathway. To investigate the role of 53BP1 in repair of IR-induced DNA damage in vertebrate cells, we analyzed the X-ray sensitivity of 53BP1- and various NHEJ-deficient cells. We show that there is a 53BP1-dependent repair pathway that is distinct from the Ku-dependent, and Artemis-dependent pathways. This 53BP1-dependent repair pathway substantially contributes to survival of cells irradiated with IR during G1 phase.

Results

Generation of 53BP1-deficient DT40 clones

Exon 9 of the two 53BP1 alleles in DT40 cells was targeted for disruption (Fig. 1A). Southern blot analysis using a probe for introns 5 or 10 confirmed the disruption of the 53BP1 alleles (Fig. 1B). Reverse transcriptase-polymerase chain reaction (RT-PCR) analysis revealed the presence of exons 6 to 9 but not exons 9 to 14 or 9 to 28 in 53BP1 transcripts (Fig. 1C). Because this transcript carried an in-frame stop codon in exon 9, the predicted translation product lacks the C-terminal region, which includes the kinetochore binding (Jullien *et al.* 2002), DNA-binding, nuclear localization (Iwabuchi *et al.* 2003) and two BRCT domains (Koonin *et al.* 1996). Mice expressing the truncated 53BP1, which lacks these C-terminal functional domains, have been reported to show a 53BP1 knockout phenotype (Morales *et al.* 2003). These data suggest that the *53BP1–/–* cells are 53BP1-null DT40 mutants. These *53BP1–/–* cells grew with similar kinetics as the wild-type DT40 cells (Fig. 1D).

Cell cycle stage-specific X-ray sensitivity in 53BP1-deficient cells

To determine whether *53BP1–/–* cells have defects in their responses to IR-induced DNA damage, we examined their X-ray sensitivity using a colony formation assay. Unsynchronous *53BP1–/–* and wild-type cells showed similar sensitivity to X-ray (Fig. 2A, left panel). In contrast, as reported previously (Adachi *et al.* 2001; Tauchi *et al.* 2002), *Lig IV–/–* and HR-deficient *Nbs1–/–/–* cell lines were hypersensitive to X-rays (Fig. 2A, right panel). Also, as previously described (Takata *et al.* 1998), *Ku70–/–* cells showed a characteristic biphasic pattern

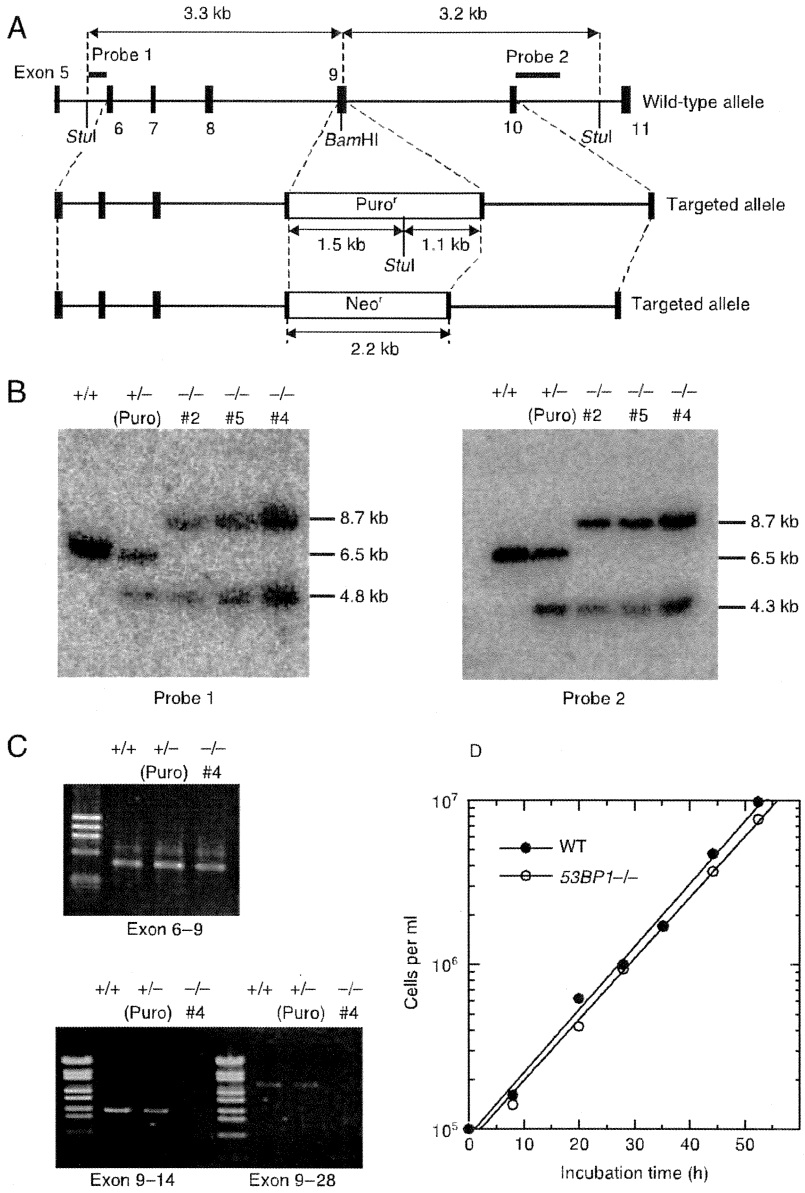

Figure 1 Generation of *53BP1−/−* clones. (A) Schematic representation of a partial restriction map of the chicken *53BP1* locus and configuration of the targeted loci. (B) Southern blot analysis of wild-type (+/+), heterozygous mutant (+/−), and homozygous mutant (−/−) clones. *Stu*I-digested genomic DNA was hybridized with probe 1 or 2 shown in panel A. (C) RT-PCR analysis of the indicated genotype with primer sets that amplify exons 6–9, 9–14, and 9–28. (D) Growth rates of wild-type DT40 (WT) and *53BP1−/−* cells.

of X-ray sensitivity (Fig. 2A, left panel), reflecting the presence of a resistant subpopulation. Also, as previously described (Takao *et al.* 1999; Ishiai *et al.* 2004), *ATM−/−* and *Artemis−/−* cells showed modest increases in sensitivity to X-irradiation (Fig. 2A, right panel).

We next examined X-ray sensitivity at various stages of the cell cycle (Fig. 2B). Cell lines deficient in the NHEJ pathway are reported to have increased sensitivity to IR in the G1-early S phase, a period when HR plays only a modest role in DSB repair and cell survival (Takata *et al.* 1998; Rothkamm *et al.* 2003). Cells were synchronized in the G1 phase with mimosine after release from nocodazole treatment. After release from mimosine treatment, synchronously progressing cells were X-irradiated at various time points and then seeded on plates. Wild-type cells showed a relatively constant sensitivity throughout the cell cycle. In contrast, like *Ku70−/−* (Takata *et al.* 1998), *Lig IV−/−* (Adachi *et al.* 2001) and *Artemis−/−* cells, *53BP1−/−* cells exhibited elevated sensitivity to X-rays in the G1 phase.

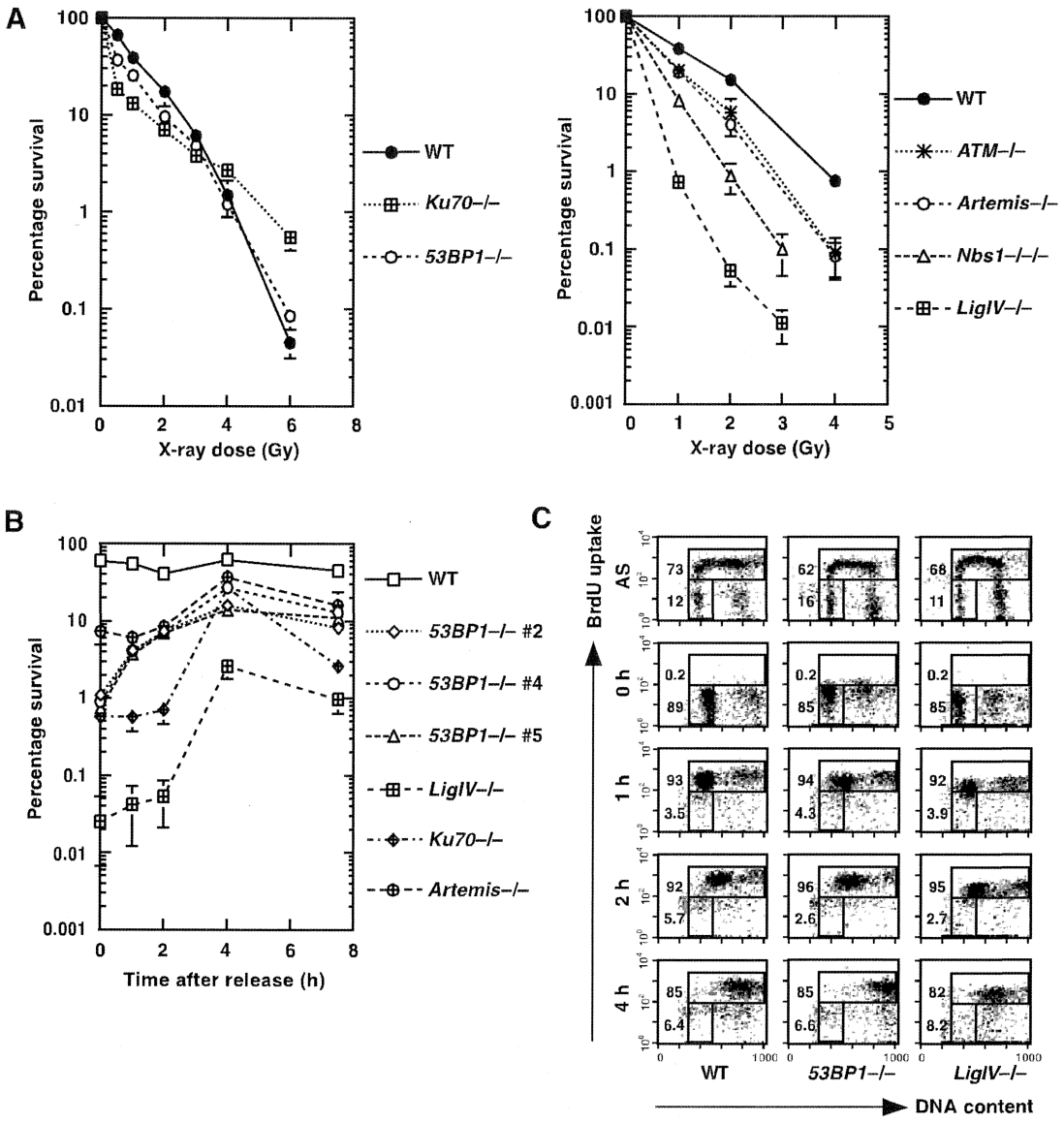

Figure 2 Cell cycle stage-specific X-ray sensitivity in *53BP1−/−* cells. (A) X-ray sensitivity in asynchronous cells. Asynchronous cells were treated with the indicated doses of X-radiation and subjected to a colony formation assay. Results represent the mean ± standard deviation (SD) from three independent experiments. (B) X-ray sensitivity in different stages of the cell cycle. Cells synchronized in G1 phase were released into the cell cycle at time 0. The cells were then treated with 1 Gy of X-radiation at various time points and were subjected to a colony formation assay. Results represent the means ± SD from three independent experiments. (C) Kinetics of the increase in DNA content and BrdU uptake from G1 to late S phase. Asynchronous (AS) and synchronous cells were pulse-labeled with BrdU for 15 min before cell harvest. Harvested cells were fixed and stained with fluorescein isothiocyanate-conjugated anti-BrdU antibody and propidium iodide. Cells synchronized in G1 phase were released into the cell cycle at time 0, and pulse-labeled with BrdU at the indicated time points after the cell-cycle release. The upper and lower gates in each panel identify cells in S and G1 phases, respectively. Numbers show the percentages of the cells falling in each gate.

Flow cytometric analysis of the DNA content and bromodeoxyuridine (BrdU) uptake following release from mimosine revealed that wild-type, *53BP1–/–*, and *Lig IV–/–* cells progress similarly in the S phase (Fig. 2C). In spite of this, in contrast to *Artemis–/–*, *Ku70–/–*, and *Lig IV–/–* cells, the *53BP1–/–* cells showed better resistance to X-rays in early and middle S phases than in the G1 phase. Specifically, as shown in Fig. 2B, the X-ray resistance of *53BP1–/–* cells 1 h after release from mimosine treatment (early S phase) recovered to 26% to 30% of the most resistant level (observed 4 h after release, which is during late S phase), and there was a 50% to 65% recovery 2 h after release from mimosine treatment (middle S phase). In contrast, the X-ray resistance of *Artemis–/–*, *Ku70–/–*, and *Lig IV–/–* cells remained at a low level in early and middle S phases and recovered in the late S phase (Fig. 2B). A similar difference in the recovery of X-ray resistance in the early S phase was observed between *53BP1–/–* and *Lig IV–/–* cells synchronized with nocodazole alone (data not shown). These data suggest that 53BP1-deficient cells lack a DNA-damage response that substantially contributes to survival of cells irradiated with IR during the G1 phase.

Intact intra-S and G2/M checkpoints in 53BP1-deficient cells

We next asked whether checkpoint defects contribute to this relatively G1-phase-specific hypersensitivity in *53BP1–/–* cells. The intra-S phase checkpoint was examined by measuring radiation-induced inhibition of DNA synthesis 1 h after X-irradiation (Fig. 3A). *53BP1–/–* cells were indistinguishable from wild-type cells in the suppression of DNA synthesis by X-irradiation, indicating that the intra-S phase checkpoint is intact in *53BP1–/–* cells, whereas intra-S phase checkpoint-deficient *Nbs1–/–/–* cells showed reduced inhibition of radiation-induced DNA synthesis. With respect to the G2/M checkpoint, we examined the mitotic index at various times after X-irradiation of the cells (Fig. 3B). The fractions of mitotic cells in non-irradiated wild-type and *53BP1–/–* cells increased constantly with time after the addition of colcemid. After X-irradiation, most of the wild-type and *53BP1–/–* cells did not enter mitosis for several hours, indicating that the G2/M checkpoint is not impaired in 53BP1-deficient cells. The presence of intact intra-S- and G2/M-phase checkpoints in 53BP1-deficient cells is consistent with the idea that the elevated radiosensitivity in the G1 phase is due to a defect in repair rather than the cell cycle checkpoints.

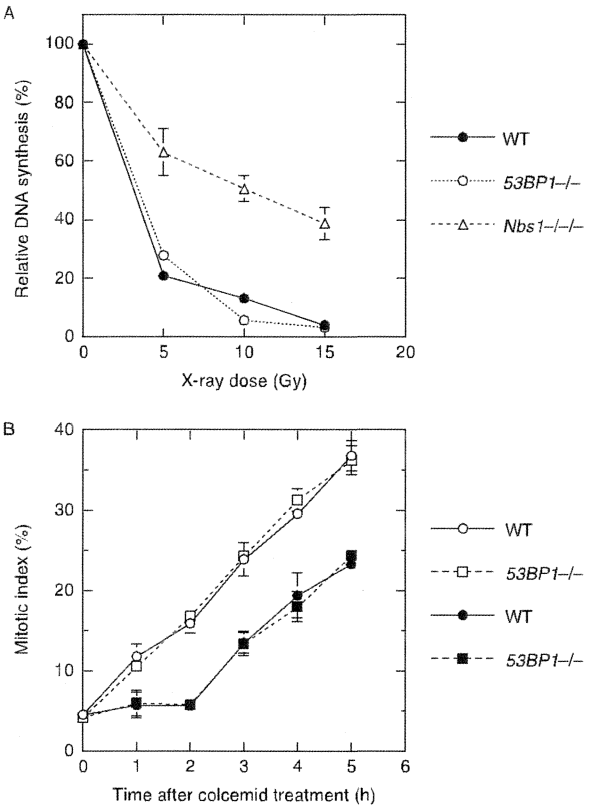

Figure 3 Intact intra-S and G2/M checkpoints in *53BP1–/–* cells. (A) Arrest of DNA synthesis in *53BP1–/–* cells after irradiation. Cells were X-irradiated as indicated and labeled with [^{3}H]thymidine 1 h after the irradiation. Results represent the mean ± SD from three independent experiments. Standard deviations are too small to plot for results of WT and *53BP1–/–* cells. (B) G2/M arrest in *53BP1–/–* cells. Asynchronous cells were unexposed (open symbols) or exposed to 0.5 Gy of X-irradiation (closed symbols). Colcemid was added at the time of irradiation, and mitotic indices were counted at the times indicated. Results represent the mean ± SD from three independent experiments.

HR is not impaired in 53BP1-deficient cells

It is now widely accepted that most of the lethal effects of IR can be attributed to strand breaks, in particular to DSBs (Friedberg *et al.* 1995). To investigate the involvement of 53BP1 in HR, one of the major pathways in DSB repair, we examined targeted integration efficiency using the chicken *Nbs1* and *Rad18* loci (Table 1). A targeting construct was transfected into wild-type and *53BP1–/–* cells, and genomic DNA was analyzed by PCR with a set of primers for the antibiotic-resistant

Table 1 Targeted integration frequencies

Locus	Selection marker	Targeted integration/ transformants analyzed	
		Wild-type	*53BP1–/–*
Nbs1	Bsr	27/34 (79.4%)	46/61 (75.4%)
Rad18	Ecogpt	14/27 (51.9%)	12/22 (54.5%)

Targeting constructs for indicated loci were transfected into cells of the indicated genotype. Drug resistant transformants were randomly picked up and targeted integration events were determined by PCR. Selection markers are Bsr for blasticidin and Ecogpt (*E. coli* gpt) for mycophenolic acid resistance.

Table 2 Spontaneous and X-ray-induced chromosomal aberrations

Genotype	Time (h)†	Isochromatid		Chromatid		
		Breaks	Gaps	Breaks	Gaps	Exchange
Spontaneous*						
Wild-type		0	0	0	0	0
53BP1–/–		0	0	0	0	0
X-ray-induced (1 Gy)						
Wild-type	0–3	2	5	12	2	0
	3–6	1	4	3	0	0
	6–9	4	4	1	0	1
53BP1 –/–	0–3	3	6	15	6	0
	3–6	3	6	3	1	0
	6–9	14	8	2	1	1

The number of aberrations per 100 mitotic cells is presented.
*Cells were treated with colcemid for 3 h to enrich mitotic cells.
†Cells were treated with colcemid during the indicated periods after X-irradiation. Each time duration corresponds the cell population irradiated at the cell cycle stages: 0–3, G2/M-late S: 3–6, S: 6–9, early S-G1 (Takata *et al.* 1998).

marker gene and a site upstream of the 5′-end of the targeting gene in the targeting construct. The targeting frequencies of *53BP1–/–* cells were comparable to those of wild-type cells in these two loci, indicating that gene targeting by HR is not impaired in *53BP1–/–* cells. Intact HR as a result of gene conversion has been reported in 53BP1-deficient mouse embryonic fibroblasts (Ward *et al.* 2004).

Increased levels of X-ray-induced chromosomal aberrations in 53BP1-deficient cells

To obtain evidence for a defect in the repair activity in *53BP1–/–* cells, we examined chromosomal aberrations (Table 2). Spontaneous chromosomal aberrations, which are frequently observed in DT40 cells deficient in the HR pathway (Sonoda *et al.* 2001), were not observed in either wild-type or *53BP1–/–* cells, providing further support for the idea that 53BP1 is not involved in HR; however, there were more radiation-induced chromosomal aberrations in *53BP1–/–* cells than in wild-type DT40 cells. The most significant difference was an elevated frequency of isochromatid-type breaks and gaps in *53BP1–/–* cells irradiated during G1-early S phase (6–9 h) (Table 2). The increase in isochromatid-type aberrations suggest that 53BP1 is involved in a repair pathway that plays a major role during G1-early S phase (Takata *et al.* 1998).

Impaired disappearance of X-ray-induced γ-H2AX foci in 53BP1-deficient cells

Phosphorylation of H2AX, a variant form of the histone H2A, is an early response to DSBs (Rogakou *et al.* 1998).

Phosphorylated H2AX (γ-H2AX) can be observed by immunofluorescence microscopy as discrete nuclear foci. Recent studies indicate that there is a correlation between the number of foci and the number of DSBs induced by IR and that the rate of disappearance of foci reflects the cellular activity of DSB repair, especially in non-replicating, G1-arrested cells (Rothkamm & Lobrich 2003). Although foci are also formed at single strand DNA sites in an ATR (ataxia-telangiectasia-Rad3-related)-dependent manner (Ward & Chen 2001; Limoli *et al.* 2002), measurement of the rate at which foci disappear is also useful in replicating cells for monitoring their ability to repair DSBs induced by IR (Rothkamm *et al.* 2003). To obtain further evidence for a defect in the repair activity in *53BP1–/–* cells, we performed immunofluorescence analysis of the γ-H2AX focus induced by X-ray in *53BP1–/–* cells (Fig. 4). G1-synchronized cells were released into the cell cycle and subsequently irradiated with 1 Gy of X-rays. We then counted the number of γ-H2AX foci at various time points. Without irradiation, G1-synchronized wild-type, *53BP1–/–*, *Ku70–/–*, and *Artemis–/–* cells showed 7.6, 6.8, 8.5, and 8.1 γ-H2AX foci per cell, respectively. In all cell-lines, the number of γ-H2AX foci 30 min after 1 Gy of X-irradiation increased to as many as 20 per cell (Fig. 4). Because flow cytometry showed that DT40 cells contain approximately half the amount of DNA as human fibroblasts (data not shown), 15 X-ray-induced γ-H2AX foci in DT40 cells is comparable to the 35 initial DSBs per Gy reported in human fibroblasts (Lobrich *et al.* 1993). *Ku70–/–* cells were markedly delayed in disappearance of γ-H2AX foci, confirming that the core NHEJ repairs the majority of IR-induced DSBs. There were fewer foci persisting 8 h after irradiation in *53BP1–/–* and *Artemis–/–* cells than in *Ku70–/–* cells but substantially more than in wild-type cells. These findings suggest that *53BP1–/–* cells have defects in the repair of IR-induced DSBs. The number of foci persisting 8 h after irradiation roughly correlated with the radiosensitivities of cells irradiated in the G1 phase (Figs 4 and 5A,B).

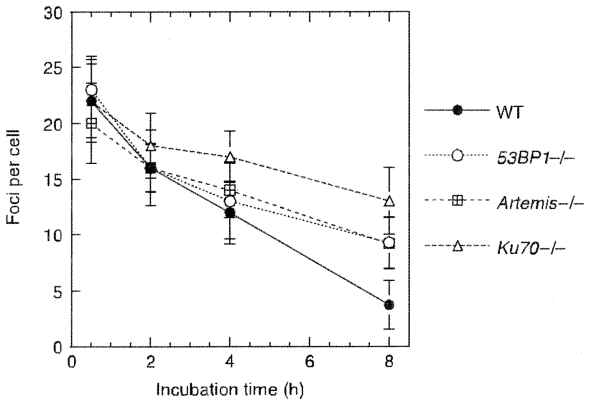

Figure 4 Impaired disappearance of X-ray-induced γ-H2AX foci in 53BP1-deficient cells. G1-phase cells were treated with 1 Gy of X-irradiation, and the number of γ-H2AX foci was counted at the indicated times. The mean number of foci per cell ± standard error is shown from the analysis of more than 40 nuclei.

53BP1 plays a role in a pathway distinct from the Ku-dependent and Artemis-dependent pathways but functions with DNA ligase IV in a common pathway

To determine whether 53BP1 functions in the core NHEJ pathway, we carried out epistasis-type analysis using *53BP1–/–* and *Ku70–/–* cells as well as cells deficient in both *53BP1* and *Ku70* (*53BP1–/– Ku70–/–* cells) (Fig. 5A). When cells were irradiated in G1 phase, *53BP1–/–* and *Ku70–/–* cells were more sensitive to irradiation than wild-type cells, and *Ku70–/–* cells were more sensitive than *53BP1–/–* cells. In addition, *53BP1–/– Ku70–/–* cells were more sensitive than either of the single mutants. Thus, 53BP1 and Ku70 are nonepistatic in cell survival, suggesting the existence of a 53BP1-dependent pathway that is independent of the core NHEJ pathway.

To determine the relationship between ATM and Artemis in cell survival, we performed epistasis-type analysis using cells irradiated in the G1 phase (Fig. 5B). Both *ATM–/–* and *Artemis–/–* cells were more sensitive to X-rays than wild-type cells, and *Artemis–/–* cells were more sensitive than *ATM–/–* cells. *ATM–/– Artemis–/–* cells had a similar sensitivity to X-rays as *Artemis–/–* cells. Thus, ATM and Artemis are epistatic for cell survival, supporting the previous findings that they function in a common DSB repair pathway (Riballo *et al.* 2004). We next examined whether 53BP1 functions in the ATM/Artemis-pathway (Fig. 5C). *53BP1–/–* cells were more sensitive than *ATM–/–* cells and were slightly more sensitive to a low dose (1 Gy) and slightly less sensitive to a high dose (3 Gy) of X-irradiation than *Artemis–/–* cells. In addition, *53BP1–/– Artemis–/–* cells were more sensitive than either of the single mutants, indicating that 53BP1 and Artemis are nonepistatic in cell survival. *53BP1–/– ATM–/–* cells had a similar sensitivity to low doses (less than 1 Gy) of X-rays as *53BP1–/–* cells. However, *53BP1–/– ATM–/–* cells were more sensitive to high doses (more than 2 Gy) of X-irradiation than either of the single mutants. These data suggest that 53BP1

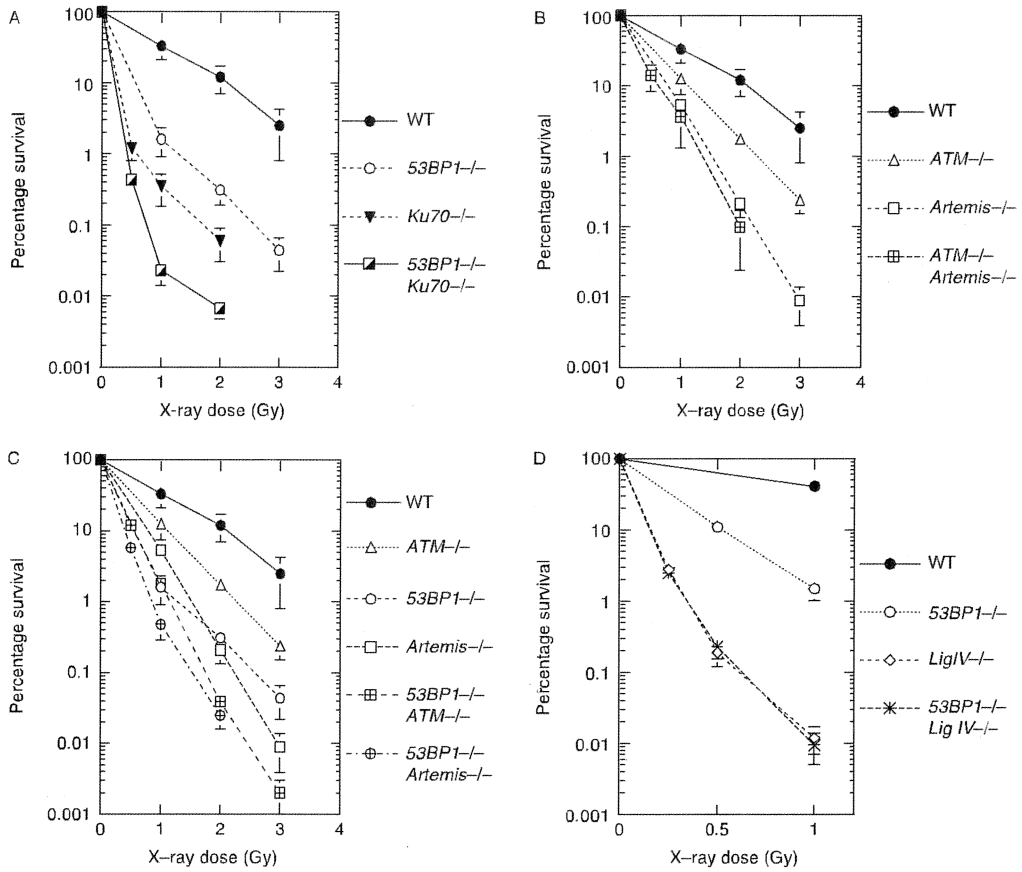

Figure 5 The 53BP1-dependent pathway is different from the Ku-dependent and Artemis-dependent pathways, but requires Lig IV. G1-phase cells were irradiated and subjected to a colony formation assay. Epistasis analysis between 53BP1 and Ku70 (A), ATM and Artemis (B), 53BP1 and either ATM or Artemis (C), and 53BP1 and Lig IV (D). Results represent the means ± SD from three independent experiments. Results shown in (A–C) were from the experiments performed at the same time.

functions in a pathway different than the ATM/Artemis-pathway at least in high doses of X-irradiation.

We next asked whether the 53BP1-dependent pathway requires Lig IV (Fig. 5D). We found that *53BP1–/– Lig IV–/–* cells had the same degree of X-ray sensitivity as *Lig IV–/–* cells. The epistasis-type analysis therefore strongly suggests that Lig IV is required for the 53BP1 dependent-repair pathway.

53BP1-dependent repair pathway is resistant to wortmannin

Wortmannin is an inhibitor of the phosphatidylinositol 3-kinase family, which includes DNA-PK (Sarkaria *et al.* 1998). It is thought that DSB ends are recognized by the Ku70/Ku80 heterodimer, which then recruits DNA-PKcs to sites of DNA DSBs, after which the kinase activity of DNA-PK is stimulated by association with DNA ends (Lieber *et al.* 2003; Downs & Jackson 2004). To confirm importance of the 53BP1-dependent repair pathway in cell survival, we next examined the effect of wortmannin on the X-ray sensitivity of cells receiving 1 Gy of X-rays at the G1 phase (Fig. 6A, left panel).

Wortmannin reduced the fraction of surviving wild-type cells from 57% to 5% due to the inhibition of DNA repair by wortmannin-sensitive end-joining pathways. No effect of wortmannin was observed on the survival of *Ku70–/–* cells after X-irradiation. However, wortmannin significantly reduced colony formation by *ATM–/–* cells after irradiation. These results suggest that, under these experimental conditions, the possible inhibition of ATM by wortmannin (Sarkaria *et al.* 1998) does not significantly affect colony formation and that, as shown previously (Hashimoto *et al.* 2003), DNA-PK is a major target of wortmannin. *53BP1–/–* cells without wortmannin treatment were slightly more sensitive to

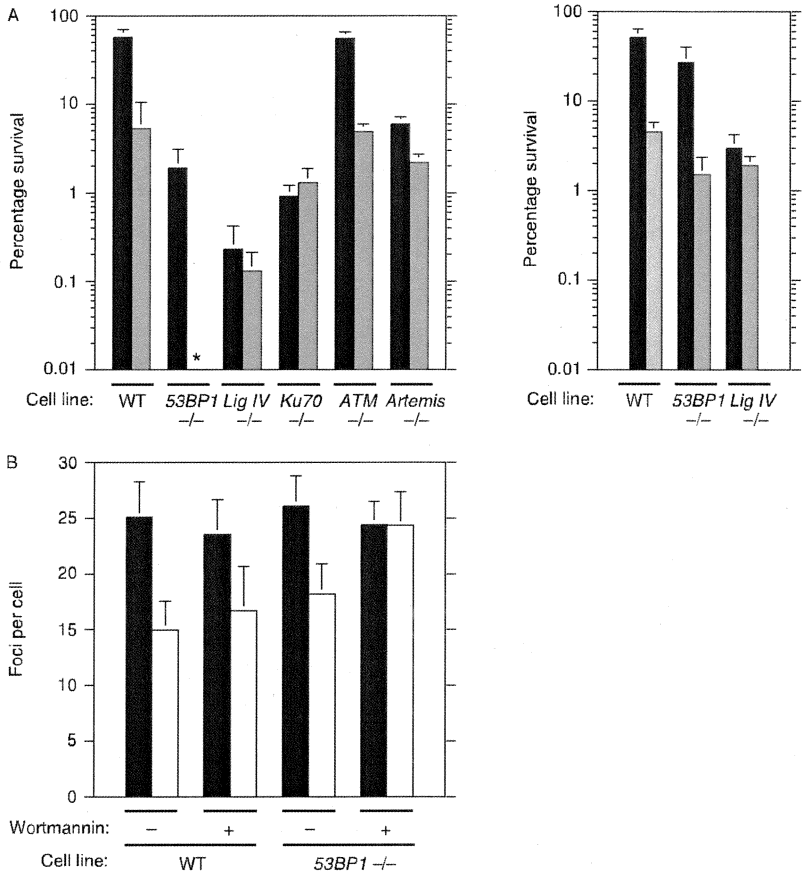

Figure 6 The 53BP1-dependent repair pathway is resistant to wortmannin. (A) Effect of wortmannin on X-ray sensitivity. Cells were synchronized in G1 phase and released into the cell cycle. G1 (left panel)- and late S (right panel)- phase cells were treated with 1 Gy of X-radiation, cultured for 1 h in the presence (□)or absence (■) of wortmannin, and subsequently subjected to a colony formation assay. Colony formation was not observed in wortmannin-treated *53BP1−/−* cell culture (*), indicating that the surviving cell fraction was less than 0.01%. Results represent the means ± SD of three independent experiments. (B) Effect of wortmannin on disappearance of γ-H2AX foci. G1-phase cells were treated with 1 Gy of X-radiation in the presence (+) or absence (−) of wortmannin. After fixing part of cells 30 min postirradiation, the remaining cells were washed, subsequently cultured at 39.5 °C, and fixed 4 h after irradiation. The number of γ-H2AX foci was counted at 30 min (■) and 4 h (□) after irradiation. The mean number of foci per cell ± standard error is shown from the analysis of more than 40 nuclei.

X-rays than wortmannin-treated wild-type cells. Strikingly, wortmannin-treated *53BP1−/−* cells were extremely sensitive to 1-Gy irradiation; no colony formation was observed, indicating that less than 0.01% of the cells survived. Colony formation was not observed even when ten-fold more cells were seeded on larger plates (data not shown). Thus, the cells were more than 100-fold more sensitive to X-rays than wortmannin-treated or untreated *Lig IV−/−* cells. Wortmannin treatment of *Artemis−/−* cells increased the X-ray sensitivity, suggesting that there is an Artemis-independent, wortmannin-sensitive repair pathway, probably the core NHEJ. Collectively, these data suggest that, in contrast to the Artemis-dependent and the core NHEJ pathways, the 53BP1-dependent pathway is resistant to wortmannin. Colony formation was observed in wortmannin-treated, 53BP1-deficient cells receiving 1 Gy of X-rays at the late S phase (Fig. 6A, right panel).

Finally, to determine whether damaged DNA remained unrepaired in wortmannin-treated *53BP1−/−* cells, we examined the effect of wortmannin on disappearance of γ-H2AX foci after X-irradiation (Fig. 6B). G1-synchronized cells were released into the cell cycle and subsequently irradiated with 1 Gy of X-rays in the presence or absence of wortmannin. More than 20 γ-H2AX foci per cell were observed 30 min after irradiation in both wild-type and *53BP1−/−* cells. At 4 h after irradiation, the number of foci per cell decreased to 15.0, 16.7 and 18.2 in wortmannin-untreated, wortmannin-treated wild-type and wortmannin-untreated *53BP1−/−* cells, respectively. However, wortmannin-treated *53BP1−/−* cells showed 24.4 foci per cell at 4 h after irradiation. These data are consistent with the hypersensitivity to X-ray of wortmannin-treated *53BP1−/−* cells, and suggest that damaged DNA remains unrepaired in wortmannin-treated *53BP1−/−* cells.

Discussion

53BP1 was originally identified in a yeast-two hybrid screen as a protein that interacts with p53, through the 53BP1's BRCT repeats (Iwabuchi *et al.* 1994, 1998). 53BP1 is thought to be a human counterpart of *Saccharomyces cerevisiae* checkpoint protein Rad9 because of the similarity

in their BRCT repeats (Koonin *et al.* 1996). This possibility is supported by accumulating evidence that 53BP1 plays an important role in checkpoint signaling (Mochan *et al.* 2004). In a previous study, we observed that the 53BP1 domain responsible for focus formation enhances the ligation reaction catalyzed by recombinant Lig IV/Xrcc4 (Iwabuchi *et al.* 2003). In this study, we show that 53BP1 plays a role in repair of IR-induced DNA damage in a pathway distinct from the core NHEJ and the ATM/Artemis-dependent pathways, and that the 53BP1-dependent repair pathway contributes to survival of cells irradiated with IR during the G1 phase of the cell cycle.

53BP1 may be involved in repair of DNA damage induced by IR

53BP1–/– cells exhibited increased radiosensitivity in the G1 phase. This may be due to defective repair for X-ray-induced DNA damage, because the *53BP1–/–* cells have apparently normal intra-S and G2/M checkpoints. Because HR plays an essential role in repair of DSBs induced by replication processes, DT40 cells deficient in the HR pathway frequently show an increase in spontaneous chromosomal breaks (Sonoda *et al.* 2001). Such spontaneous chromosomal aberrations, however, were not observed in 53BP1-deficient cells. Furthermore, gene targeting by HR is not impaired in 53BP1-deficient cells. These results suggest that 53BP1 is not required for HR. Rather, several of our findings suggest the involvement of 53BP1 in NHEJ:

1 *53BP1–/–* cells exhibit elevated radiosensitivity in the G1 phase when HR plays only a modest role in DSB repair and cell survival.

2 *53BP1–/–* cells exhibit an elevated frequency of isochromatid-type breaks and gaps in cells irradiated during the G1-early S phase.

3 epistasis analysis shows that Lig IV is required for the 53BP1-dependent pathway.

4 *53BP1–/–* cells have a reduced ability to rejoin X-ray-induced DNA DSBs.

However, the possibility is not excluded that 53BP1 is involved in the suppression of IR-induced apoptosis or repair of other IR-induced DNA damage than DSBs, for example single-strand breaks, DNA-protein cross-links and various base damages.

53BP1 plays a role in a pathway that is distinct from both the core NHEJ and ATM/Artemis-dependent pathways

We propose that 53BP1 functions in repair of IR-induced DNA damage in a pathway distinct from both

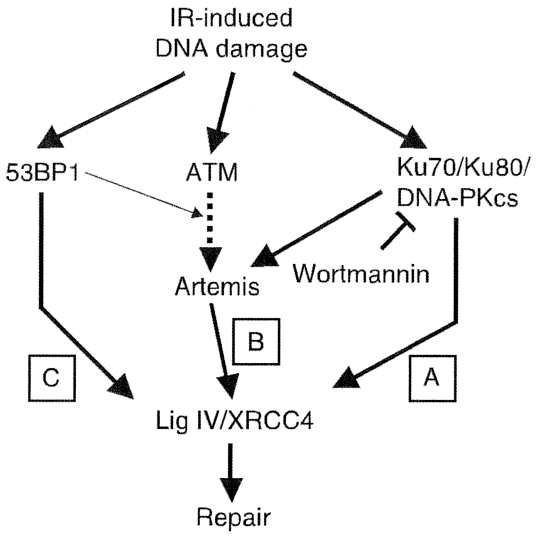

Figure 7 Model of the repair pathways for IR-induced DNA damage in G1 phase cells. A, B and C represent the core NHEJ, ATM/Artemis-dependent and 53BP1-dependent pathways, respectively. The dotted arrow represents the minor pathway in DT40 cells. The thin arrow represents a possible interaction resulting from the scaffold function of 53BP1. The two perpendicular lines represent an inhibition.

the core NHEJ and ATM/Artemis-dependent pathways in the G1 phase cells (Fig. 7). The core NHEJ (Riballo *et al.* 2004) (pathway A in Fig. 7) is well-known and involves the Ku70/Ku80 heterodimer, DNA-PKcs, and the Lig IV/Xrcc4 complex. In mammalian cells, the majority of DSBs induced by IR in G1-phase cells are rejoined rapidly by the core NHEJ, whereas approximately 10% of the DSBs are repaired over a prolonged time. Recently, it was reported that this slower end-joining process requires ATM and Artemis (Riballo *et al.* 2004). *Artemis–/–* DT40 cells show increased radiosensitivity in the G1 and early S phase, supporting the involvement of Artemis in NHEJ. Furthermore, our epistasis-type analysis supports the idea that Artemis plays a role in a common pathway with ATM.

These findings are consistent with studies in mammalian cells showing that there is a second pathway dependent on ATM and Artemis (Riballo *et al.* 2004) (pathway B in Fig. 7). However, in DT40 cells, *Artemis–/–* cells are more sensitive than *ATM–/–* cells, and wortmannin treatment provides more impact on the colony formation by *ATM–/–* cells than by *Artemis–/–* cells, when cells are irradiated in the G1 phase. Therefore, it appears that there are, in addition to ATM, other upstream regulators of Artemis in DT40 cells. Artemis nuclease activity has been shown to be modified upon phosphorylation by DNA-PK *in vitro* (Ma *et al.* 2002), and DNA-PK is

likely to be the major target of wortmannin in our colony formation assay. Thus, Artemis may be regulated by DNA-PK in DT40 cells. Indeed, DNA-PK is known to be involved in the Artemis-dependent pathway in mammalian cells (Riballo *et al.* 2004). DNA-PK and ATM may play redundant roles in modulating Artemis function.

The increase in the radiosensitivity of wild-type, *ATM−/−*, and *53BP1−/−* cells by wortmannin could be due to inhibition of both the core NHEJ and Artemis-dependent pathways. However, the ability of wortmannin-treated wild-type and *ATM−/−* cells but not *53BP1−/−* cells to form colonies indicates that there is a pathway that is dependent on 53BP1 and resistant to wortmannin (pathway C in Fig. 7). In *53BP1−/−* mammalian cells, addition of inhibitors of ATM or DNA-PK does not affect DSB repair activity (Riballo *et al.* 2004). This contradicts our results in DT40 cells. The discrepancy may be due to redundancy between DNA-PK and ATM in the modulation of Artemis, as discussed above. Importantly, since colonies are formed by wortmannin-treated wild-type cells, the 53BP1-dependent pathway may be the third pathway in NHEJ. Alternatively, 53BP1 may play dual roles in repair of IR-induced DNA damage: roles in repair of DSBs, and in repair of other DNA damages than DSBs. In this model, 53BP1 may function in the Artemis-dependent NHEJ pathway, as suggested by Riballo *et al.* in mammalian cells (Riballo *et al.* 2004).

In *Artemis−/−* cells, the core NHEJ and 53BP1-dependent pathways are functional, and wortmannin inhibits the core NHEJ pathway, resulting in a reduction in the number of colonies. However, in the presence of wortmannin, *Artemis−/−* cells are more sensitive than wild-type cells to X-rays, suggesting that Artemis has a DNA-PK-independent function. Wortmannin-treated *Ku70−/−* cells are more sensitive to X-rays than wortmannin-treated wild-type cells. This suggests that the Ku70/Ku80 complex also has a DNA-PK-independent function.

53BP1 may function as a backup pathway towards the Lig IV/Xrcc4 complex

Colony formation in *Lig IV−/−* cells suggests the presence of a Lig IV-independent end-joining pathway. The severe radiosensitivity of wortmannin-treated *53BP1−/−* cells suggests that Lig IV-independent repair does not function in these cells. In *Lig IV−/−* cells, the absence of Lig IV may allow access of other DNA ligase(s) to sites of ligation reaction. The DNA-PKcs protein but not the kinase activity of DNA-PK is required for recruitment of the Lig IV/Xrcc4 complex to chromatin (Drouet *et al.* 2005). In contrast, the DNA-PK kinase activity is required for functional end-joining in DSB repair (Chan *et al.* 2002). In wortmannin-treated cells, even though the Lig IV/Xrcc4 complex is present at ligation sites, the ligation reaction might be inhibited due to the lack of upstream signals produced by DNA-PK kinase activity. Thus, the severe radiosensitivity of wortmannin-treated *53BP1−/−* cells might be due to the defect in the 53BP1-dependent pathway as well as the inability of other DNA ligases to access sites of the ligation reaction due to the binding of non-functional Lig IV/Xrcc4 complexes. 53BP1 may function as a backup pathway towards the Lig IV/Xrcc4 complex, when upstream phosphorylation signals for this complex are weak or absent.

Finally, the 53BP1-dependent pathway made a larger contribution to cell survival in G1 than in early S phase, suggesting that the 53BP1-dependent pathway is regulated at the G1 to S phase transition by mechanisms distinct from the other two pathways. Recently, it has been shown that 53BP1-deficient mice have intact V(D)J recombination but impaired class switch recombination (Manis *et al.* 2004; Ward *et al.* 2004). It is unclear whether the 53BP1-dependent repair pathway identified in this study is involved in class switch recombination. If, as proposed, class switch recombination occurs in the G1 phase of the cell cycle (Petersen *et al.* 2001), it is possible that, in vertebrates, class switch recombination is the main stage at which 53BP1 participates in DNA damage repair.

Experimental procedures

Targeting constructs

Sequence information for chicken *53BP1* genomic DNA and cDNA was obtained from GenBank (accession no. AADN-01085436) and the Biotechnology and Biological Sciences Research Council (BBSRC) ChickEST Database (sequence ID 055102.1 for exons 6 to 10, 350592.1 for exons 12 to 14, and 356837.3 for exons 21 to 28), respectively. Sequence information for chicken *Ku70* genomic DNA was obtained from GenBank (accession no. NW-060209). The genomic DNA fragment for exons 6–10 of the chicken *53BP1* was generated by PCR using genomic DNA extracted from wild-type DT40 cells. Targeting constructs for *53BP1* were generated by inserting a drug selection marker gene at the *Bam*HI site in exon 9 of the *53BP1* genomic DNA fragment. Targeting constructs for *Ku70* were designed as previously described (Takata *et al.* 1998).

Cell culture and colony formation assay

Cells were cultured in RPMI1640 medium (Nissui) supplemented with 10% fetal calf serum (Valley Biomedical Inc.), 1%

chicken serum (Medical and Biological Laboratories), and 10 μM β-mercaptoethanol at 39.5 °C. DNA transfection and selection were performed as previously described (Buerstedde & Takeda 1991). X-irradiation at 150 kV and 20 mA was performed at a dose rate of 1.9 Gy/min with an X-ray irradiator (Hitachi Medico). The colony formation assay was performed as previously described (Hashimoto *et al.* 2003). Briefly, an appropriate number of cells were plated in 1.5% methylcellulose (Sigma)-containing medium immediately after irradiation. After incubation at 39.5 °C for 7 days, the surviving cell fractions were calculated by comparing the numbers of colonies formed in the irradiated cultures with those in a non-irradiated control. For wortmannin treatment, cultures were adjusted to 10 μM wortmannin (Sigma) just before receiving 1 Gy of irradiation. After irradiation, cells were cultured for 1 h at 39.5 °C, washed three times with phosphate-buffered saline (PBS) containing 5% calf serum (GibcoBRL), and subsequently seeded on the methylcellulose plates. For a non-irradiated control, cells treated with wortmannin were cultured for 1 h at 39.5 °C without irradiation, washed three times as described above and subsequently seeded on the methylcellulose plates. After incubation at 39.5 °C for 7 days, the surviving cell fractions were calculated as described above.

Chromosomal aberration assay

The chromosomal aberration assay was performed as previously described (Takata *et al.* 1998). Briefly, 1.0 μg/mL of colcemid (Sigma) was added in cultures 3 h before cell harvest. Harvested cells were incubated in 1 mL of 0.9% sodium citrate for 15 min at room temperature and fixed in 5 mL of freshly prepared 3 : 1 mixture of methanol and acetic acid. The cell suspension was dropped on to an ice-cold wet glass slide and immediately flame dried. Slides were stained with 3% Giemsa solution at pH 6.4 for 10 min.

Cell cycle synchronization

To enrich cells in prometaphase, cells were cultured in medium containing 1.0 μg/mL nocodazole (Sigma) for 8 h. For G1 phase synchronization, cells treated with nocodazole were washed three times with PBS containing 5% calf serum and then cultured in medium containing 0.8 mM mimosine (Sigma) for 8 h. Synchronized cells were washed three times as described above and cultured in medium to release them into the cell cycle.

Flow cytometric analysis and DNA synthesis assay

Cells were labeled for 15 min with 10 μM BrdU (Sigma). Cells were then harvested and fixed with 70% ethanol at 4 °C. Fixed cells were incubated as follows: (i) 4 N HCl containing 0.5% Triton X-100 for 30 min at room temperature (ii) fluorescein isothiocyanate-conjugated anti-BrdU antibody (Becton Dickinson) for 1 h at room temperature, and (iii) 5 μg/mL propidium iodide in PBS for 10 min at room temperature. After each incubation, cells were washed with PBS containing 1% bovine serum albumin. Flow cytometric analysis was performed using a FACScan (Becton Dickinson), and data were displayed using Cell Quest software (Becton Dickinson). DNA synthesis assays were performed as previously described (Tauchi *et al.* 2002) with the following minor modifications: cells were irradiated with X-rays, incubated for 1 h, and labeled with [^{3}H]thymidine for 30 min.

G2/M checkpoint assay and γ-H2AX staining

In the G2/M checkpoint assay, non-irradiated or irradiated cells were cultured in medium containing 0.1 μg/mL colcemid and collected at 1-h intervals. Cells were attached to the surface of a slide glass by centrifugation, fixed in 4% paraformaldehyde for 10 min, permeabilized in PBS containing 1% Nonidet P-40, and stained with 4′,6′-diamino-2-phenylindole. To determine the percentage of mitotic cells (mitotic index), more than 200 nuclei were counted using a fluorescence microscope (Olympus). For γ-H2AX staining, cells were fixed as described above and then treated with 70% ethanol for 10 min. After a brief rinse with PBS, cells were permeabilized as described above, blocked in 3% bovine serum albumin at room temperature for 20 min, and then incubated with anti-γ-H2AX antibody (2 μg/mL, Upstate, clone JBW301) at room temperature for 1 h. After extensive washing, cells were incubated with tetramethylrhodamine isothiocyanate-conjugated secondary antibody (Dako) at room temperature for 1 h. Cells were counterstained with 4′,6′-diamino-2-phenylindole, and foci of nonapoptotic nuclei were counted by eye using a fluorescence microscope with an oil-immersion objective lens (PlanApo 100X).

Acknowledgements

We thank Dr H. Kitao (Kawasaki Medical School) for technical assistance. This work was supported in part by grants-in-aid from the Ministry of Education, Culture, Sports, Science and Technology of Japan, the Hokkoku Foundation for Cancer Research, and the Grant for Promoted Research from Kanazawa Medical University (S2005-7).

References

Adachi, N., Ishino, T., Ishii, Y., Takeda, S. & Koyama, H. (2001) DNA ligase IV-deficient cells are more resistant to ionizing radiation in the absence of Ku70: Implication for DNA double-strand break repair. *Proc. Natl. Acad. Sci. USA* **91**, 6098–6102.

Anderson, L., Henderson, C. & Adachi, Y. (2001) Phosphorylation and rapid relocalization of 53BP1 to nuclear foci upon DNA damage. *Mol. Cell. Biol.* **21**, 1719–1729.

Buerstedde, J.M. & Takeda, S. (1991) Increased ratio of targeted to random integration after transfection of chicken B cell lines. *Cell* **67**, 179–188.

Chan, D.W., Chen, B.P., Prithivirajsingh, S., *et al.* (2002) Autophosphorylation of the DNA-dependent protein kinase catalytic subunit is required for rejoining of DNA double-strand breaks. *Genes Dev.* **16**, 2333–2338.

DiTullio, R.A., Mochan, T.A., Venere, M., *et al.* (2002) 53BP1 functions in an ATM-dependent checkpoint pathway that is

constitutively activated in human cancer. *Nat. Cell Biol.* **12**, 998–1002.

Downs, J.A. & Jackson, S.P. (2004) A means to a DNA end: the many roles of Ku. *Nat. Rev. Mol. Cell Biol.* **5**, 367–378.

Drouet, J., Delteil, C., Lefrancois, J., Concannon, P., Salles, B. & Calsou, P. (2005) DNA-dependent protein kinase and XRCC4-DNA ligase IV mobilization in the cell in response to DNA double strand breaks. *J. Biol. Chem.* **280**, 7060–7069.

Fernandez-Capetillo, O., Chen, H.T., Celeste, A., *et al.* (2002) DNA damage-induced G2/M checkpoint activation by histone H2AX and 53BP1. *Nat. Cell Biol.* **12**, 993–997.

Friedberg, E.C., Walker, G.C. & Siede, W. (1995) DNA damage. In: *DNA Repair and Mutagenesis* (eds E.C. Friedberg, G.C. Walker & W. Siede), pp. 1–58. Washington, D.C.: American Society for Microbiology.

Hashimoto, M., Rao, S., Tokuno, O., *et al.* (2003) DNA-PK: the major target for wortmannin-mediated radiosensitization by the inhibition of DSB repair via NHEJ pathway. *J. Radiat. Res.* **44**, 151–159.

Ishiai, M., Kimura, M., Namikoshi, K., *et al.* (2004) DNA cross-link repair protein SNM1A interacts with PIAS1 in nuclear focus formation. *Mol. Cell. Biol.* **24**, 10733–10741.

Iwabuchi, K., Bartel, P.L., Li, B., Marraccino, R. & Fields, S. (1994) Two cellular proteins that bind to wild-type but not mutant p53. *Proc. Natl. Acad. Sci. USA* **91**, 6098–6102.

Iwabuchi, K., Basu, B.P., Kysela, B., *et al.* (2003) Potential role for 53BP1 in DNA end-joining repair through direct interaction with DNA. *J. Biol. Chem.* **278**, 36487–36495.

Iwabuchi, K., Li, B., Massa, H.F., Trask, B.J., Date, T. & Fields, S. (1998) Stimulation of p53-mediated transcriptional activation by the p53-binding proteins, 53BP1 and 53BP2. *J. Biol. Chem.* **273**, 26061–26068.

Jackson, S.P. (2002) Sensing and repairing DNA double-strand breaks. *Carcinogenesis* **23**, 687–696.

Jeggo, P.A. (1998) DNA breakage and repair. *Adv. Genet.* **38**, 185–211.

Johnson, R.D. & Jasin, M. (2000) Sister chromatid gene conversion is a prominent double-strand break repair pathway in mammalian cells. *EMBO J.* **19**, 3398–3407.

Jullien, D., Vagnarelli, P., Earnshaw, W.C. & Adachi, Y. (2002) Kinetochore localisation of the DNA damage response component 53BP1 during mitosis. *J. Cell Sci.* **115**, 71–79.

Koonin, E.V., Altschul, S.F. & Bork, P. (1996) BRCA1 protein products ... Functional motifs.... *Nat. Genet.* **13**, 266–268.

Lieber, M.R., Ma, Y., Pannicke, U. & Schwarz, K. (2003) Mechanism and regulation of human non-homologous DNA end-joining. *Nat. Rev. Mol. Cell Biol.* **4**, 712–720.

Limoli, C.L., Giedzinski, E., Bonner, W.M. & Cleaver, J.E. (2002) UV-induced replication arrest in the xeroderma pigmentosum variant leads to DNA double-strand breaks, γ-H2AX formation, and Mre11 relocalization. *Proc. Natl. Acad. Sci. USA* **99**, 233–238.

Lobrich, M., Ikpeme, S., Haub, P., Weber, K.J. & Kiefer, J. (1993) DNA double-strand break induction in yeast by X-rays and alpha-particles measured by pulsed-field gel electrophoresis. *Int. J. Radiat. Biol.* **64**, 539–546.

Lobrich, M. & Jeggo, P.A. (2005) Harmonising the response to DSBs: a new string in the ATM bow. *DNA Repair (Amst.)* **4**, 749–759.

Ma, Y., Pannicke, U., Schwarz, K. & Lieber, M.R. (2002) Hairpin opening and overhang processing by an Artemis/DNA-dependent protein kinase complex in nonhomologous end joining and V(D)J recombination. *Cell* **108**, 781–794.

Manis, J.P., Morales, J.C., Xia, Z., Kutok, J.L., Alt, F.W. & Carpenter, P.B. (2004) 53BP1 links DNA damage-response pathway to immunoglobulin heavy chain class-switch recombination. *Nat. Immunol.* **5**, 481–487.

Mochan, T.A., Venere, M., DiTullio, R.A. & Halazonetis, T.D. (2004) 53BP1, an activator of ATM in response to DNA damage. *DNA Repair (Amst.)* **3**, 945–952.

Morales, J.C., Xia, Z., Lu, T., *et al.* (2003) Role for BRCA1 C-terminal repeats (BRCT) protein 53BP1 in maintaining genomic stability. *J. Biol. Chem.* **278**, 14971–14977.

Moshous, D., Callebaut, I., de Chasseval, R., *et al.* (2001) Artemis, a novel DNA double-strand break repair/V(D)J recombination protein, is mutated in human severe combined immune deficiency. *Cell* **105**, 177–186.

Petersen, S., Casellas, R., Reina-San-Martin, B., *et al.* (2001) AID is required to initiate Nbs1/γ-H2AX focus formation and mutations at sites of class switching. *Nature* **414**, 660–665.

Rappold, I., Iwabuchi, K., Date, T. & Chen, J. (2001) Tumor suppressor p53 binding protein 1 (53BP1) is involved in DNA damage-signaling pathways. *J. Cell Biol.* **153**, 613–620.

Riballo, E., Kuhne, M., Rief, N., *et al.* (2004) A pathway of double-strand break rejoining dependent upon ATM, Artemis, and proteins locating to γ-H2AX foci. *Mol. Cell* **16**, 715–724.

Rogakou, E.P., Pilch, D.R., Orr, A.H., Ivanova, V.S. & Bonner, W.M. (1998) DNA double-stranded breaks induce histone H2AX phosphorylation on serine 139. *J. Biol. Chem.* **273**, 5858–5868.

Rothkamm, K., Kruger, I., Thompson, L.H. & Lobrich, M. (2003) Pathways of DNA double-strand break repair during the mammalian cell cycle. *Mol. Cell. Biol.* **23**, 5706–5715.

Rothkamm, K. & Lobrich, M. (2003) Evidence for a lack of DNA double-strand break repair in human cells exposed to very low x-ray doses. *Proc. Natl. Acad. Sci. USA* **100**, 5057–5062.

Sarkaria, J.N., Tibbetts, R.S., Busby, E.C., Kennedy, A.P., Hill, D.E. & Abraham, R.T. (1998) Inhibition of phosphoinositide 3-kinase related kinases by the radiosensitizing agent wortmannin. *Cancer Res.* **58**, 4375–4382.

Schultz, L.B., Chehab, N.H., Malikzay, A. & Halazonetis, T.D. (2000) p53-binding protein 1 (53BP1) is an early participant in the cellular response to DNA double-strand breaks. *J. Cell Biol.* **151**, 1381–1390.

Shiloh, Y. (2003) ATM and related protein kinases: safeguarding genome integrity. *Nat. Rev. Cancer* **3**, 155–168.

Sonoda, E., Takata, M., Yamashita, Y.M., Morrison, C. & Takeda, S. (2001) Homologous DNA recombination in vertebrate cells. *Proc. Natl. Acad. Sci. USA* **98**, 8388–8394.

Takao, N., Kato, H., Mori, R., *et al.* (1999) Disruption of ATM in p53-null cells causes multiple functional abnormalities in cellular response to ionizing radiation. *Oncogene* **18**, 7002–7009.

Takata, M., Sasaki, S., Sonoda, E., *et al.* (1998) Homologous recombination and non-homologous end-joining pathways of DNA double-strand break repair have overlapping roles in the maintenance of chromosomal integrity in vertebrate cells. *EMBO J.* **17**, 5497–5508.

Tauchi, H., Kobayashi, J., Morishima, K., *et al.* (2002) Nbs1 is essential for DNA repair by homologous recombination in higher vertebrate cells. *Nature* **420**, 93–98.

Wang, B., Matsuoka, S., Carpenter, P.B. & Elledge, S.J. (2002) 53BP1, a mediator of the DNA damage checkpoint. *Science* **298**, 1435–1438.

Ward, I.M. & Chen, J. (2001) Histone H2AX is phosphorylated in an ATR-dependent manner in response to replicational stress. *J. Biol. Chem.* **276**, 47759–47762.

Ward, I.M., Reina-San-Martin, B., Olaru, A., *et al.* (2004) 53BP1 is required for class switch recombination. *J. Cell Biol.* **165**, 459–464.

Xia, Z., Morales, J.C., Dunphy, W.G. & Carpenter, P.B. (2000) Negative cell cycle regulation and DNA-damage inducible phosphorylation of the BRCT protein 53BP1. *J. Biol. Chem.* **276**, 2708–2718.

Received: 28 February 2006
Accepted: 11 May 2006

１．研究課題名：副嗅球における感覚情報処理様式の内因性光計測法による解明
（研究番号 S2005-8）

２．キーワード：１）副嗅球（accessory olfactory bulb）
２）内因性光応答（intrinsic optical response）
３）２分化（dichotomy）
４）フェロモン（pheromone）
５）尿刺激（urinary stimulation）

３．研究代表者：須貝外喜夫・医学部・助教授・生理機能制御学 （生理学Ⅰ）

４．研 究 目 的

脊椎動物には主嗅覚系と鋤鼻系の２つの独立した嗅覚系がある。主嗅覚系の一次中枢である主嗅球において、内因性光信号計測法により、“ニオイ地図”が形成されていることが最近確実となってきた。一方、“フェロモン”を受容する鋤鼻系の一次中枢である副嗅球(AOB)では、どのような情報処理機構がされているのだろうか？申請者はこれまでスライス標本を用い、AOB における興奮の信号伝播、区分化およびオシレーション電位等の成果を報告した。これらはすべて *in vitro* 系における研究であった。今回の研究目的は、*in vivo* 系の標本を用い、フェロモン等の自然刺激による感覚情報が AOB で実際にどのように処理されるかを調べることである。予備的実験の結果は、内因性光信号計測法が、AOB においても適用可能なことを示した。

５．研 究 計 画

麻酔下でラット AOB 表面の骨を薄く削り、頭部を傾け AOB を外側面から観測した。したがって硬膜は無傷である。内因性光信号の計測には、646 nm の光を脳表面に照射し、その反射光をビデオカメラで計測した。刺激には 2-heptanone、メス混合尿およびオス混合尿を用いた。刺激物質のラット外鼻腔への提示には以下の 2 種類の方法でおこなった。1：刺激物質をシリンジに入れ、シリンジ駆動装置により鼻先 1～2cm の位置で 5 秒間、その揮発性成分を与えた。刺激終了後や無刺激時には脱臭したクリーンエアーを常時与えた。2：尿で湿らせたろ紙を鼻先へ接触させて刺激を行った。計測の際には、無刺激と刺激からなる試行を交互に繰り返し、6～8 試行行った。なお、刺激間隔は 3～6 分とした。1 の方法は揮発性成分による刺激、2 の方法は主に不揮発性成分による刺激となる。また、光学計測終了後、活性部位のマーキングを行った。還流固定後、AOB 切片を作成し組織学的検索から AOB 内での位置を確認した。

６．研 究 成 果

20 匹のラット（オス 15 匹、メス 5 匹、体重 200-300g）を用いた。

１）シリンジを用いた揮発性成分に対する内因性光応答

0.3% 2-heptanone および 5%オス尿刺激に対し応答は再現性を有して AOB 領域に観察され、組織学的検索から活性化部位は、ラットの性差に関わらず AOB 前半部

(aAOB)であった。一方、2%メス尿刺激は、オスラットではaAOBとAOB尾側部付近の2箇所で応答を引き起こしたが、メスラットではaAOBでだけ応答を引き起こした。3種の物質の応答強度や範囲は濃度依存性に増大する傾向がみられた。

２）不揮発性成分による尿刺激に対する内因性光応答

ろ紙によるオスおよびメス尿刺激に対する活性化部位は、尿中の揮発性成分とは異なり、主にaAOBより後半部に再現性を有して見られた。マーキング部位のレクチン(RCA_{120})による組織化学的検索からAOB後半部(pAOB)の吻側(pAOBr)であることがわかった。

７．研究の考察・反省

揮発性物質や尿中の揮発性成分の刺激に対し、内因性光応答は主にaAOBで観察された。また、オスラットではオス尿に対しては主にaAOBに応答が見られたが、メス尿に対する応答はaAOBとpAOBの尾側部付近に見られた。この活性化部位は、以前に発表したラットAOBの3つの区分化の内、pAOBの尾側部(pAOBc)であると考えられ、pAOBcの機能の一つを示していると推測されるが、さらなる実験が必要である。一方、ろ紙を用いた不揮発性成分による尿刺激はpAOBrに応答を引き起こした。以上の結果は、揮発性成分はaAOB、不揮発性成分はpAOBrでそれぞれ情報処理されている可能性を示す。鋤鼻器感覚上皮の表層に発現しているV1R受容体は揮発性低分子物質（フェロモン）を感知し、aAOBにその情報は伝えられ、またV2R受容体は不揮発性蛋白様物質を感知し、pAOBに伝えられると考えられているが、これを裏付ける。今後、今回の結果をさらに確証づけるためニューロン応答の記録をおこなう計画である。

８．研究発表

Sugai T, Yoshimura H, Kato N, Onoda N. Component-dependent urine response in the rat accessory olfactory bulb. NeuroReport 2006; 17: 1663-1667. (MDLB)

須貝外喜夫, 小野田法彦. 内因性光計測法によるラット副嗅球の尿刺激に対する応答. 日本味と匂学会誌 2005; 12: 459-460.

須貝外喜夫, 吉村　弘, 加藤伸郎. ラット副嗅球の尿刺激に対する応答と機能的区分化. 日本味と匂学会誌 2006; 13: 569-570.

Component-dependent urine responses in the rat accessory olfactory bulb

Tokio Sugai[a], Hiroshi Yoshimura[b], Nobuo Kato[a] and Norihiko Onoda[a]

Departments of [a]Physiology and [b]Oral and Maxillofacial Surgery, Kanazawa Medical University, Uchinada, Ishikawa, Japan

Correspondence and requests for reprints to Dr Tokio Sugai, PhD, Department of Physiology, Kanazawa Medical University, Uchinada, Ishikawa 920-0293, Japan
Tel: +81 76 286 2211; fax: +81 76 286 3523; e-mail: tokio@kanazawa-med.ac.jp

Sponsorship: This work was supported by a Grant for Promoted Research from Kanazawa Medical University (S2005-8).

Received 27 June 2006; revised 25 July 2006; accepted 26 July 2006

To investigate how pheromonal information is processed in the rat accessory olfactory bulb, we optically imaged intrinsic signals to obtain high-resolution maps of activation induced by urinary stimulation. Application of volatile components in male urine mainly induced activation in the anterior accessory olfactory bulb, irrespective of the sex, whereas volatile female urine elicited activation not only in the anterior but also to some extent in the caudal part of the posterior accessory olfactory bulb of male, but not female, rats. Nonvolatile components of both male and female urine induced activation mainly in the rostral part of the posterior and to a lesser extent in the anterior accessory olfactory bulb, irrespective of the sex. These results indicate that volatile and nonvolatile urinary components activate the anterior and posterior subdivisions of the accessory olfactory bulb, respectively. *NeuroReport* 17:1663–1667 © 2006 Lippincott Williams & Wilkins.

Keywords: dichotomy, intrinsic optical imaging, pheromone, vomeronasal system

Introduction

The vomeronasal system is thought to be involved mainly but not exclusively in the detection of pheromones [1] and it plays an important role in instinctive behaviors related to reproduction and social dominance [2]. The peripheral structure of the vomeronasal system is the vomeronasal organ, located in the rostral portion of the nasal septum. Vomeronasal receptor cells reside within the epithelium of the vomeronasal organ, and project axons to the accessory olfactory bulb, which is a specialized region of the dorsocaudal main olfactory bulb.

The vomeronasal system exhibits a distinct anatomical and molecular dichotomy that is distinguished by the location of the cell body within the vomeronasal epithelium. Apical vomeronasal receptor neurons coexpress the V1R class of vomeronasal receptors [3,4] with the G-protein subunit $G\alpha_{i2}$ and project axons to the anterior subdivision of the accessory olfactory bulb, whereas basal vomeronasal receptor neurons coexpress the V2R class of receptors [5–7] with $Go\alpha$ and project axons to the posterior subdivision of the accessory olfactory bulb.

We previously demonstrated heterogeneity in the anterior and posterior subdivisions of the accessory olfactory bulb in the guinea pig [8] and rat [9], using electrophysiological and optical recordings with voltage-sensitive dye. The innervation of a single mitral cell is restricted to either the anterior or the posterior accessory olfactory bulb [10]. Although these two segregated subdivisions are thought to respond to different stimuli and mediate differential behaviors, the biological significance of the dichotomy of the accessory olfactory bulb remains unknown.

One of the major sources of pheromones seems to be urine, and volatile and nonvolatile urinary substances that produce definite endocrine or behavioral responses in rodents have been identified [11,12]. To examine responses to urine in the accessory olfactory bulb might provide a cue to the anatomical and molecular dichotomy of this region. We attempted to detect urine-induced responses using optical imaging of intrinsic signals, which has been an established method for signal detection in the main olfactory bulb [13] and the sensory cortices [14–18].

Methods

Experimental procedures

The animal protocols used in this study complied with all pertinent institutional and Japanese governmental regulations, and the number of animals used was minimized. Male and female Wistar rats (n=23, 250–310 g) were anesthetized with Na-barbiturate (35 mg/kg, intraperitoneally). The skull overlying the accessory olfactory bulb was thinned with a dental drill. The surgical procedure and experimental details have been described previously [18]. Briefly, a specially designed head attachment was fixed to the skull with stainless-steel screws and dental cement, and then the head was fixed on the stereotaxic frame using an overhead device [19] and tilted until the camera field was as horizontal as possible.

Intrinsic signals (absorption changes at 646 nm of light) in the accessory olfactory bulb were recorded through silicone oil. Images were obtained using a video camera (CS8310, Tokyo Electronic Industry, Tokyo, Japan) and digitized with an IBM/PC-compatible computer equipped with a video frame grabber board (Pulsar, Matrox, Quebec, Canada). The imaged area was $4.26 \times 3.2\,mm^2$ and contained 320×240 pixels. An image (at 567 nm) of surface blood vessels in the region of interest was generated before intrinsic signal imaging. The intrinsic signal images were obtained at 500 μm below the cortical surface where the accessory olfactory bulb is located.

Stimulation

Compressed air was dehydrated through silica gel, deodorized through activated charcoal, then humidified, and finally blown into the animal's nose. Different odors were applied using two procedures. 2-Heptanone and male or female urine were used as odor stimuli. First, all stimuli were diluted 0.1–10% (volume %) with an odorless mineral oil or distilled water, and 1 ml of each was stored in 30-ml syringes. As a control, mineral oil and distilled water, 1 ml of each, was stored in separate syringes. Vapor was delivered from the syringe that was placed 1–2 cm in front of the nostrils, and motor-driven under the control of a pulse generator. During stimulus application, clean air was discontinued to ensure the inhalation of volatile compounds. Second, the nostrils were placed in direct contact with filter paper that had been moistened with urine (3–5%) to ensure the application of nonvolatile components in the urine. Before any stimulation, we confirmed that the distilled water and mineral oil did not elicit a response.

Each trial consisted of obtaining a pair of records with and without stimulation at a 3-min interval. This trial was repeated 6 to 8 times. For each record, 18 frames (500 ms each) were collected for 9 s. The stimulation was applied at frames 3 to 14 from the start (6 s in duration).

Data analysis of intrinsic signals

Details of data processing have been described elsewhere [18]. Briefly, individual images from frames 4–18 within a pair of records were divided by individual mean images obtained from frames one and two to improve the signal–noise ratio (relative image). Individual relative images with and without stimulation were separately averaged. The average relative image without stimulation was subtracted from that with stimulation and averaged across six to eight trials (differential image). The averaged reflectance intensities of individual pixels (320×240) with and without stimulation were also compared using a *t*-test. A Gaussian spatial filter was used to eliminate nonspecific darkening (increased light absorption) and high-frequency noise [16–18]. Regions containing pixels that appeared to be significant ($P < 0.05$) were defined as active.

We applied a spatial correlation analysis [20] to calculate the spatial correlation coefficient (SCC) to test reproducibility. The SCC values indicate correlations between active regions. Here, we considered that a value of $0.2 < SCC < 1.0$ indicated a significant degree of domain overlap ($P < 0.01$), that of $-0.2 > SCC > -1.0$, a significant degree of domain segregation or avoidance ($P < 0.01$) and that of $0.2 > SCC > -0.2$, no significant correlation (a near-random relationship).

Histological reconstruction

After optical recording, a glass pipette was inserted about 500 μm below the surface into the center of each active region and brilliant blue dye was deposited. The animal was then perfused with 4% paraformaldehyde under deep anesthesia. Serial frontal sections at 50 μm thickness were photographed and histologically analyzed. Sections were also histologically examined using *Ricinus communis* agglutinin (RCA_{120}; 0.5–1 μg/ml) lectin [9]. The posterior accessory olfactory bulb of the rat can be subdivided into the rostral two-thirds and caudal one-third on the basis of RCA_{120} histochemistry [9].

Results

Activation in response to 2-heptanone (0.3%) was evident in the accessory olfactory bulb beneath the cortex (red arrow in Fig. 1a). The differential images demonstrated an optical response to 2-heptanone but not to mineral oil (Fig. 1c). Active regions calculated as being significant ($P < 0.05$) were superimposed onto the image of the surface and blood vessels (red spots in Fig. 1b). The same stimulus was applied three times to demonstrate the reproducibility of the optical responses (Fig. 1d). Significant spatial correlations indicated domain overlap among the three patterns (SCC=0.320, 0.317 and 0.214 between those colored red and green, red and blue, and green and blue). To precisely locate optical responses, a blue spot was deposited through the glass pipette inserted about 500 μm below the surface into the center of the active region (yellow triangle in Fig. 1d). A histological sagittal section (Fig. 1e) confirmed that the spot was in the anterior accessory olfactory bulb. The results were similar in all preparations (n=6). The active region (Fig. 1f–h) and intensity of the optical responses to 2-heptanone increased with concentrations tested in the range of 0.1–1% (n=2).

Male urine delivered from the syringe elicited optical responses in the anterior accessory olfactory bulb of the male rat. Figure 2Aa shows that the active regions obtained from three trials superimposed with different colors are significantly reproducible. Male urine also elicited optical responses in the anterior accessory olfactory bulb of another male rat (n=5; Fig. 2Ab), whereas female urine induced responses not only in the anterior region but also in the caudal part of the posterior region of the accessory olfactory bulb in the same animal (Fig. 2Ac). A histological section of the male rat accessory olfactory bulb confirmed that optical responses to urine were generated from the anterior region and the caudal part of the posterior region of the accessory olfactory bulb (Fig. 2Cc). The extent of active regions increased with increasing concentrations of male urine in the range of 1–5% (n=2; Fig. 2Ba–c). In the female rat (n=4), urine from either male or female rats elicited optical responses in the anterior accessory olfactory bulb alone (Fig. 2Ca and b). These results indicated that the application of 2-heptanone and urine delivered from the syringe elicited optical responses mainly in the anterior accessory olfactory bulb.

Next, placing the nostrils of a male rat in contact with filter papers moistened with 5% male or female urine elicited optical responses in the accessory olfactory bulb (Fig. 3a and b, respectively). The optical responses of the same rat to 2-heptanone delivered from the syringe are also obtained (Fig. 3c), and the active region contours are

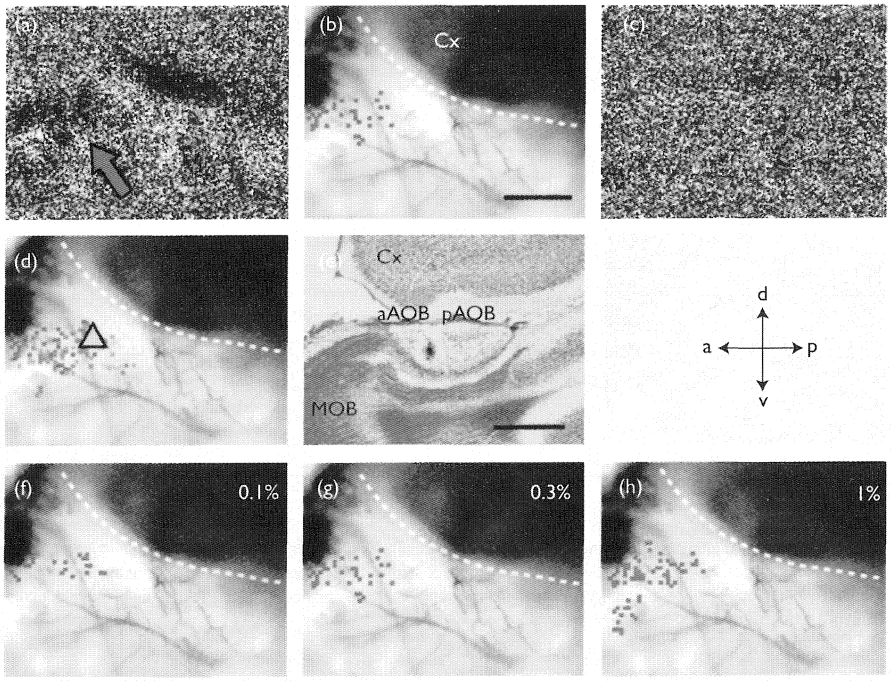

Fig. 1 Optical images of intrinsic signals in response to 2-heptanone in rat accessory olfactory bulb. (a) Differential image in response to 0.3% 2-heptanone. (b) Image of active spots (active region) superimposed on cortical surface. (c) Differential image after mineral oil application. (d) To determine reproducibility, 2-heptanone was applied in three trials. Each response was indicated with a different color. Center of active region was marked (yellow triangle). (e) Photograph of sagittal section indicates that marked spot is located in the anterior accessory olfactory bulb. Yellow dashed line is the boundary between anterior and posterior accessory olfactory bulb. (f–h) Regions activated by various concentrations of 2-heptanone. Concentrations (%) are indicated in upper right corners. a, anterior; aAOB, anterior accessory olfactory bulb; Cx, cortex; d, dorsal; p, posterior; pAOB, posterior accessory olfactory bulb; v, ventral; MOB, main olfactory bulb. Scale bar: 1 mm.

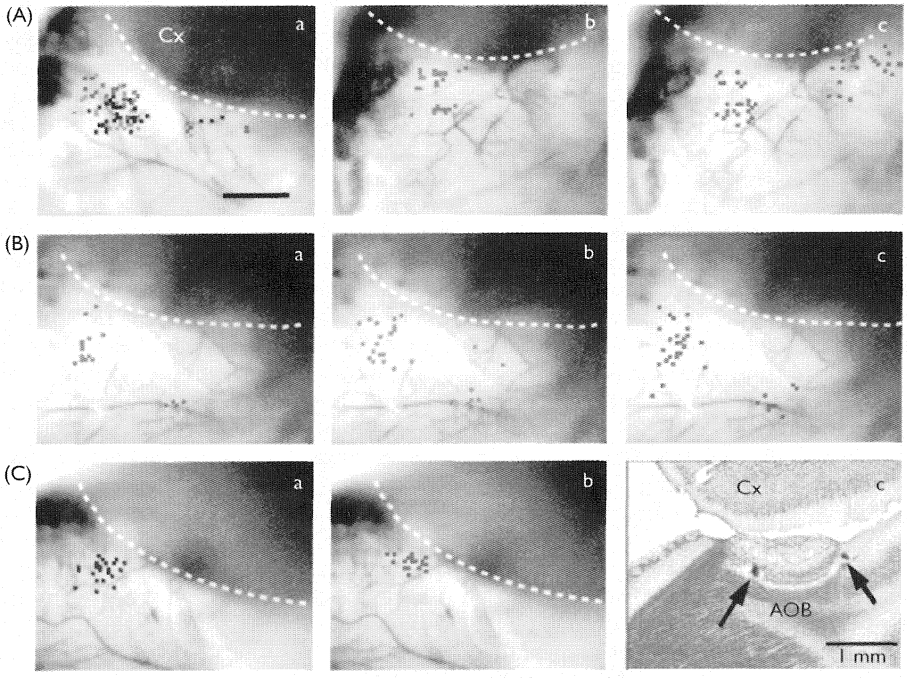

Fig. 2 Optical images of intrinsic signals in response to urine. (A) Active regions obtained from male rat accessory olfactory bulb. (a) Male urine (5%) was applied three times to determine reproducibility. Spatial correlation coefficient values were 0.211, 0.203 and 0.230 between patterns represented by red and green, red and blue, and green and blue, respectively. Optically active regions obtained from another animal in response to male (b) and female (c) urine (5%). (B) Active maps obtained from male urine at different concentrations. (a) 1%; (b) 5%; (c) 10%. Active pixels in lower portion are outside of accessory olfactory bulb. (C) Active maps obtained from female rat in response to male (a) and female (b) urine. (c) Photograph of sagittal section indicates that two marked spots were in anterior subdivision and the caudal part of the posterior subdivision of the accessory olfactory bulb. Direction and scale bar are same as shown in Fig. 1. Cx, cortex; AOB, accessory olfactory bulb.

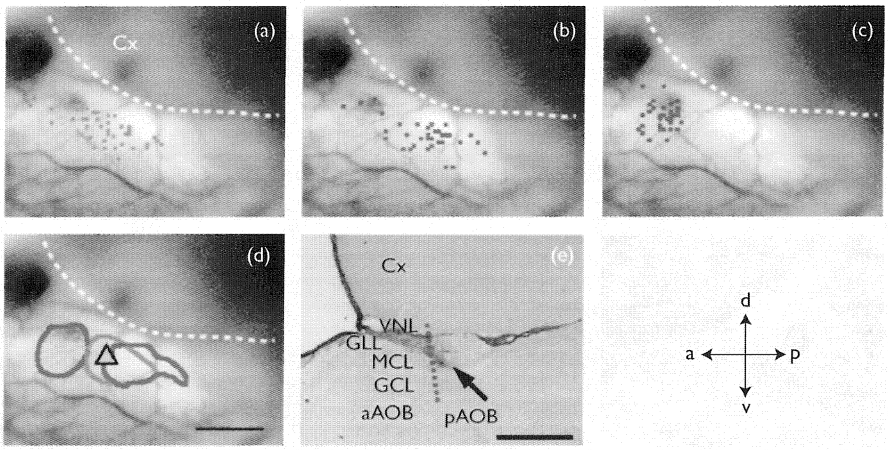

Fig. 3 Optical responses to filter paper moistened with male (a) and female (b) urine (5%). (c) Optical response for 2-heptanone (0.1%) with syringe in the same preparation. (d) Superimposed contours of active regions in (a), (b) and (c). Colors correspond to those in (a), (b) and (c). Center of active region for urine stimulation with moistened filter paper was marked (yellow triangle) to locate optical response. (e) Photograph of sagittal section indicates that marked spot (arrow) is in the rostral part of the posterior accessory olfactory bulb. Section was stained with RCA_{I20} lectin. Dotted line shows boundary between two subdivisions. GCL, granule cell layer; GLL, glomerular layer; MCL, mitral cell layer; VNL, vomeronasal nerve layer; RCA_{I20}, *Ricinus communis* agglutinin; Cx, cortex; aAOB, anterior accessory olfactory bulb; pAOB, posterior accessory olfactory bulb; a, anterior; d, dorsal; p, posterior; v, ventral. Direction and scale bar are same as shown in Fig. 1.

superimposed (Fig. 3d), implying that the region activated by urine on filter paper was located more posteriorly than that induced by 2-heptanone. Furthermore, the SCC value between the two patterns shown in (a) and (c) was −1.00, indicating that two distributions were significantly segregated. These results indicated strongly that the active region induced with nonvolatile components in urine differs from that induced with volatile stimulation. A histological examination using RCA_{I20} revealed that the active region was the rostral part of the posterior accessory olfactory bulb [20]. Similar results were obtained from four additional preparations.

Discussion

Here, we mapped optical images of intrinsic signals from the accessory olfactory bulb in response to urinary stimulation. Volatile and nonvolatile components of urine preferentially activated the anterior and the posterior accessory olfactory bulbs, respectively, irrespective of whether mapping was performed in male or female rats. These results indicate that the dichotomy in the vomeronasal system is involved in recognition of distinct categories of pheromone, such as volatile versus nonvolatile. Our results are consistent with the notion that lipophilic volatile ligands activate vomeronasal receptor neurons coexpressing $G\alpha i2$ and V1R whereas nonvolatile major urinary proteins, such as α_{2u}-globulin, activate vomeronasal receptor neurons coexpressing $Go\alpha$ and V2Rs [21].

The activity-dependent signals obtained in our optical recordings are likely to arise from effects of the blood oxygenation level, such as the metabolic rate of oxygenation in the brain. Histological examinations indicated that the optical responses originated primarily from neural activities in deep layers of the accessory olfactory bulb, such as the external plexiform/mitral and granule cell layers. Intrinsic optical responses have been observed from the glomeruli in the glomerular layer of the main olfactory bulb [13]. Circular activities reflecting glomerular activity were not, however, observed in the accessory olfactory bulb. This difference in optical responses between the accessory and main olfactory bulbs might be explained by the previously published findings from slice preparations of the main and accessory olfactory bulbs stained with voltage-sensitive dye. Electrical stimulation of the olfactory nerve layer elicited large responses in amplitude and duration in the glomerular layer of the rat main olfactory bulb [22], whereas electrical stimulation of vomeronasal nerve layer produced large responses in the external/mitral cell layers in the accessory olfactory bulb, and the glomerular responses were relatively small [8,9].

A recent study of mice using functional magnetic resonance imaging (fMRI) revealed that a mixture of urinary pheromones and odorants in urine elicited significant signals in limited regions of the main olfactory bulb and in large regions of the accessory olfactory bulb [20]. Our findings of optical responses to volatile urine components in the anterior accessory olfactory bulb closely correlate with those of the fMRI study. The fMRI results also implied that both the main olfactory and the vomeronasal systems respond to volatile compounds but with different selectivity, suggesting a greater integration of the two olfactory pathways than has traditionally been believed. Furthermore, c-fos immunoreactivity is preferentially located in the anterior accessory olfactory bulb of mice exposed to mouse urine [23]. As the anterior accessory olfactory bulb receives inputs from the receptor neurons in the apical part of the vomeronasal epithelium, it follows that volatile compounds mainly activate the vomeronasal receptor neurons expressing V1R receptor proteins [4,24]. The activated locations in the accessory olfactory bulb shown by fMRI in these and the present studies are also consistent with the finding [25] that the vomeronasal receptor neurons activated by mouse urinary pheromones are located in the apical zone.

2-Heptanone, which has a fruity odor quality, is known as one of the prospective mouse urinary pheromones. The present experiments showed that this compound elicited optical responses in the anterior accessory olfactory bulb of

rats. Although vomeronasal receptor cells can be activated by a subset of common odors [1], our studies have raised the possibility that 2-heptanone may be a rat urinary pheromone.

We previously reported that the rat posterior accessory olfactory bulb can be separated into the rostral and caudal parts [9]. We showed here that volatile female urine elicits optical responses not only in the anterior subdivision but also in the caudal part of the posterior subdivision. Furthermore, these responses were observed in the male, but not female, rat. Although this finding might reflect the biological significance of the caudal part of the posterior accessory olfactory bulb, further detailed examinations are required to establish this notion as a fact.

Conclusions

We attempted to detect urine-induced responses in the rat accessory olfactory bulb using optical imaging of intrinsic signals. We found that volatile and nonvolatile components of urine preferentially activated the anterior and posterior accessory olfactory bulbs, respectively, irrespective of whether mapping was made in male or female rats, indicating that the dichotomy in the vomeronasal system is involved in recognition of distinct categories of pheromone, such as volatile versus nonvolatile.

Acknowledgements

The authors thank Mr H. Adachi and Mr S. Muramoto for excellent technical assistance.

References

1. Sam M, Vora S, Malnic B, Ma W, Novotny MV, Buck LB. Odorants may arouse instinctive behaviors. *Nature* 2001; **412**:142.
2. Halpern M, Martinez-Marcos A. Structure and function of the vomeronasal system: an update. *Prog Neurobiol* 2003; **70**:245–318.
3. Dulac C, Axel R. A novel family of genes encoding putative pheromone receptors in mammals. *Cell* 1995; **83**:195–206.
4. Rodriguez I, Del Punta K, Rothman A, Ishii T, Mombaerts P. Multiple new and isolated families within the mouse superfamily of V1R vomeronasal receptors. *Nat Neurosci* 2002; **5**:134–140.
5. Herrada G, Dulac C. A novel family of putative pheromone receptors in mammals with a topographically organized and sexually dimorphic distribution. *Cell* 1997; **90**:763–773.
6. Matsunami H, Buck LB. A multigene family encoding a diverse array of putative pheromone receptors in mammals. *Cell* 1997; **90**:775–784.
7. Ryba NJP, Trindelli R. A new multigene family of putative pheromone receptors. *Neuron* 1997; **19**:371–379.
8. Sugai T, Sugitani M, Onoda N. Subdivisions of the guinea-pig accessory olfactory bulb revealed by the combined method with immunohistochemistry, electrophysiological, and optical recordings. *Neuroscience* 1997; **79**:871–885.
9. Sugai T, Sugitani M, Onoda N. Novel subdivisions of the rat accessory olfactory bulb revealed by the combined method with lectin histochemistry, electrophysiological and optical recordings. *Neuroscience* 2000; **95**:23–32.
10. Jia C, Halpern M. Segregated populations of mitral/tufted cells in the accessory olfactory bulb. *Neuroreport* 1997; **8**:1887–1890.
11. Novotny M, Harvey S, Jemiolo B, Alberts J. Synthetic pheromones that promote inter-male aggression in mice. *Proc Natl Acad Sci USA* 1985; **82**: 2059–2061.
12. Vandenbergh JG, Whitsett JM, Lombardi JR. Partial isolation of a pheromone accelerating puberty in female mice. *J Reprod Fertil* 1975; **43**:515–523.
13. Rubin BD, Katz LC. Optical imaging of odorant representations in the mammalian olfactory bulb. *Neuron* 1999; **23**:499–511.
14. Bonhoeffer T, Grinvald A. The layout of iso-orientation domains in Area 18 of cat visual cortex: optical imaging reveals a pinwheel-like organization. *J Neurosci* 1993; **13**:4157–4180.
15. Maloneck D, Grinvald A. Interactions between electrical activity and cortical microcirculation revealed by imaging spectroscopy: implications for functional brain mapping. *Science* 1996; **272**:551–554.
16. Tsunoda K, Yamane Y, Nishizaki M, Tanifuji M. Complex objects are represented in macaque inferotemporal cortex by the combination of feature columns. *Nat Neurosci* 2001; **4**:832–838.
17. Yoshimura H, Sugai T, Fukuda M, Segami N, Onoda N. Cortical spatial aspects of optical intrinsic signals in response to sucrose and NaCl stimuli. *Neuroreport* 2004; **15**:17–20.
18. Sugai T, Miyazawa T, Fukuda M, Yoshimura H, Onoda N. Odor-concentration coding in the guinea-pig piriform cortex. *Neuroscience* 2005; **130**:769–781.
19. Onoda N, Imamura K, Obata E, Iino M. Response selectivity of neocortical neurons to specific odors in the rabbit. *J Neurophysiol* 1984; **52**: 638–652.
20. Xu F, Schaefer M, Kida I, Schaefer J, Liu N, Rothman DL, *et al.* Simultaneous activation of mouse main and accessory olfactory bulbs by odors or pheromones. *J Comp Neurol* 2005; **489**:491–500.
21. Krieger J, Schmitt A, Lobel D, Gudermann T, Schultz G, Breer H, *et al.* Selective activation of G-protein subtypes in the vomeronasal organ upon stimulation with urine-derived compounds. *J Biol Chem* 1999; **274**: 4655–4662.
22. Senseman DM. High-speed optical imaging of afferent flow through rat olfactory bulb slice: voltage-sensitive dye signals reveal periglomerular cell activity. *J Neurosci* 1996; **16**:313–324.
23. Dudley CA, Moss RL. Activation of an anatomically distinct subpopulation of accessory olfactory bulb neurons by chemosensory stimulation. *Neuroscience* 1999; **91**:1549–1556.
24. Peele P, Salazar I, Mimmack M, Keverne EB, Brennan PA. Low molecular weight constituents of male mouse urine mediate the pregnancy block effect and convey information about the identity of the mating male. *Eur J Neurosci* 2003; **18**:622–628.
25. Leinders-Zufall T, Lane AP, Puche A, Ma W, Novotny MV, Shipley MT, *et al.* Ultrasensitive pheromone detection by mammalian vomeronasal neurons. *Nature* 2000; **405**:792–796.

１．研究課題名：Rab38 遺伝子異常によって起きる肺病変の検討（研究番号　S2005-9）

２．キーワード：１）Rab38 低分子量 G タンパク質（Rab38　Small G protein）
２）肺サーファクタント（lung surfactant）
３）チョコレート・マウス（*chocolate* mouse）
４）ルビー・ラット（*Ruby* rat）
５）ヘルマンスキー・パドラック症候群（Hermansky-Pudlak syndrome）

３．研究代表者：長内　和弘・医学部・助教授・呼吸機能治療学（呼吸器内科学）

４．研 究 目 的

低分子量 G タンパク質ファミリーは細胞の重要な生命活動である増殖・分化、収縮・形態変化、小胞輸送・分泌などの諸機能を制御している。我々は *rab* ファミリーに属する新低分子量 G タンパク質(Rab38, Genbank Accession No. M94043)が肺組織の中でも肺胞 II 型上皮細胞とクララ細胞に特異的に発現していることを報告した(Osanai K, et al. Am J of Pathol 2001, 158:1665.)。最近、Loftus らはこの Rab38 核酸配列の点突然変異によりマウスに眼皮膚型白皮症が発生することを報告した(Loftus SK, et al. Proc Natl Acad Sci U S A. 99:4471, 2002)。Rab38 が発現していることが知られている肺胞 II 型上皮細胞と皮膚メラノサイトは、それぞれ secretory lysosome に属する層状封入体とメラノゾームという細胞内小器官を持つ。Secretory lysosome の形成異常によって引き起こされる疾患はいくつか知られており、いずれも多臓器にわたる病変を形成し、常染色体劣性遺伝形式を示す。白皮症をともなう呼吸器疾患としては常染色体劣性遺伝疾患である Hermansky-Pudlak 症候群が知られているが、その責任遺伝子は単一ではない。白皮症マウスの成績より、この Rab38 が同疾患の責任遺伝子の１つである可能性もある。本研究の目的は、我々の発見した Rab38 が肺の中でも肺胞 II 型上皮細胞とクララ細胞という分化した上皮細胞（末梢気道上皮）に発現されていることに注目し、Rab38 遺伝子変異動物を用いてその肺病変を検討することである。

５．研 究 計 画

１）Rab38 遺伝子点突然変異マウスおよびラットでの肺病変の観察

アメリカ、チャールズリバー研究所より Rab38 遺伝子点突然変異マウス(C57BL/6J$^{cht/cht}$)を購入し、繁殖させる。またチャールズ・リバー・ジャパン社より Rab38 遺伝子変異(ルビー)ラットである Long Evans Cinammon/Crj を購入する。それぞれの動物の肺病変の有無、肺サーファクタント合成能、輸送・分泌を観察するほか、LPS、ブレオマイシン、シリカ投与による実験間質性肺炎・肺肺線維症に変化がおきるかどうか検討する。

２）単離培養肺胞 II 型上皮細胞での肺サーファクタント分泌能の検討

ラット肺から肺胞 II 型上皮細胞を単離・培養し、マトリゲル膜上に培養し、途中から上皮側を気相にして、II 型肺胞上皮細胞を培養すると細胞は長期間 II 型細

胞の分化機能を維持すると報告されている。分化機能は SP-A, SP-B, SP-C の発現を RealTime-PCR 法で確認する。[^{3}H]コリンを培地に加えると細胞は肺サーファクタント主成分である[^{3}H]フォスファチジル･コリンを合成し層状封入体に蓄える。この分泌活性を検討する。

３）外来性 Rab38 遺伝子の強制発現細胞における II 型細胞機能変化の解析

アデノベクター(カナダ、Microbix 社)に Rab38-cDNA を 293 細胞への co-transfection にて組み込み、増殖・単離したベクターを培養 II 型細胞にトランスフェクションし、細胞形態の観測、サーファクタント・プロテインやフォスファチジルコリンの産生能、層状封入体への輸送、分泌能などを解析する。また Rab38-cDNA の GTP 結合部位のドメインに点突然変異を与えるようなプライマーを設定し、PCR を行い、上記アデノベクターに組み込み、培養肺胞 II 型上皮細胞にトランスフェクションする。これにより II 型細胞は点突然変異を有する Rab38 を高発現するようになると期待され、内因性の正常 Rab38 の機能を拮抗的に阻害すると考えられる。この後、細胞形態の観測、サーファクタント・プロテインやフォスファチジルコリンの産生能、層状封入体への輸送、分泌能などを解析する。

６．研 究 成 果

ルビーラットの形質を有する Fawn-Hooded(FH)ラットおよび Long Evans Cinnamon/Crj(LEC/Crj)ラット尻尾よりゲノム DNA を抽出し PCR 法で DNA 解析したところ、Rab38 遺伝子エキソン 1 のアミノ酸翻訳開始コドン ATG が ATA に変異しており核酸の点突然変異が起きていた。同ラット肺組織タンパク質のウエスターン・ブロットを施行したところ Rab38 タンパク質の欠損が確かめられた。FH ラットおよび LEC/Crj ラットの眼は野生型に比し深赤色でルビー色をしており、体毛はシナモン色をしており眼皮膚型白皮症の特徴を備えていた。出血時間はすべて 15 分以上に延長していた。すなわち Hermansky-Pudlak 症候群のモデル動物の形質を備えていた。LEC/Crj ラット肺には気腫性肺病変が起きており、肺胞 II 型上皮細胞は腫大し、胞体内には大型の層状封入体が充満していた。また気管支肺胞洗浄液、層状封入体分画、全肺ホモジネート中の肺サーファクタントのウエスターン・ブロットを施行したところ、SP-B タンパク質が細胞内に貯留し、気腔への分泌が障害されていた。単離培養 II 型上皮細胞からの肺サーファクタントの分泌活性を検討したところ、LEC/Crj 由来細胞では無刺激では分泌が優意に低下していたが、アゴニスト刺激では逆に著明に亢進していた。これらのことからラットにおいて Rab38 タンパク質が欠損すると眼皮膚型白皮症、出血異常、気腫性肺病変が起きることが知られた。したがって、もしヒトにおいて Rab38 の高度の機能不全を起こすような遺伝子異常が起こると眼皮膚型白皮症、易出血性、間質性肺炎・肺線維症を呈する Hermansky-Pudlak 症候群が発症すると推測された。

７．研究の考察・反省

本研究によって Rab38 遺伝子遺伝子突然変異動物が Hermansky-Pudlak 症候群のモデル動物であることが確立された。今後は Rab38 が小胞輸送にはたす役割の分子機序の解明が必要である。またヒトでの Hermansky-Pudlak 症候群患者の中に Rab38 遺伝子異

常を有する症例がないかどうか検討しなければならない。Hermansky-Pudlak 症候群はまれな疾患であるため症例を経験することが困難である。国内外の病院、研究機関などとの提携・協力が必要と思われる。

８．研 究 発 表

Osanai K, Voelker D. Analysis and expression of Rab38 in oculocutaneous lung disease. Small GTPases in Disease. Methods in Enzymology 2007. (in press) (MLDB)

長内和弘、八田理恵子、樋口純子、土原一真、及川　卓、井口晶晴、関　利満、高橋昌克、黄　正寿、栂　博久、高橋敬治. 肺サーファクタントの細胞内処理過程における障害によって引き起こされる肺疾患. 日本界面医学会雑誌　2006；37：4-6.

長内和弘、八田理恵子、三輪知子、戸部勇保、関　利満、高橋昌克、黄　正寿、栂　博久、樋口純子.Rab38 欠損ラットにおける肺病変の検討.分子呼吸器病 2007;11:61-63.

長内和弘、八田理恵子、井口晶晴、関　利満、高橋昌克、黄　正寿、栂　博久、樋口純子. Rab38 低分子量 G タンパク質の遺伝子突然変異マウスにおける肺サーファクタント輸送異常と気腫性肺病変. 分子呼吸器病 2006；10：47-50.

長内和弘. II 型肺胞上皮細胞における細胞内蛋白移送と関連疾患の検討. 分子呼吸器病 2006；10：11-15.

１．研究課題名：ニトロソチオールの作用と体内動態（研究番号　S2005-10）

２．キーワード：１）一酸化窒素（nitric oxide）
２）ニトロソチオール（nitrosothiols）
３）アセチルコリン（acetylcholine）
４）NOC7（NOC7）
５）ウサギ（rabbit）

３．研究代表者：石橋　隆治・医学部・助教授・生体情報薬理学（薬理学）

４．研 究 目 的

血管張力の調節因子として重要な役割を演じている一酸化窒素(NO)は血管内皮で産生される。様々な病態、例えば動脈硬化や糖尿病などで内皮機能が低下するとNO産生も低下し、さらにそれぞれの病態の悪化を招くことは良く知られている。この時の補充療法として、外部からNO供与体を投与しようと云う考えがあるものの、古典的な亜硝酸剤などは作用時間や耐性等の問題もある。そこで近年脚光を浴びているのが、もともと生体内にもNOキャリアーとして存在するニトロソチオール(R-SNO)類である。生体内ではNOは局所で作用する以外に、チオールと結合してR-SNOとなって安定化し、遠方にもその生物活性が運ばれると考えられている。実際、持続的なNO放出体として様々なR-SNOの合成が試みられ、血行動態に対する基本的な作用は検討されているものの、生体内のNO動態の詳細は明らかになっていない。そこで、内因性のR-SNOを含め、様々なR-SNOの作用と、その生体内動態を解明し、外因性R-SNOを応用した治療の新たな可能性を明らかにすることが目的である。

５．研 究 計 画

先ず、生体試料からのR-SNOの定量技術を確立する。

次に、様々なR-SNOを投与し、これに対する生体内の生体内NOキャリアーである低分子R-SNO（ニトロソシステイン；Cys-SNO、ニトロソグルタチオン;G-SNO）や高分子R-SNO(ニトロソアルブミン; Alb-SNO)の変化を明らかにする。

実験にはウサギを用い、心血行動態パラメータの他に、上記物質を定量する。投与薬物は生体内R-SNO（高分子および低分子)、および合成されたR-SNOとする。また、R-SNOによる作用を観察する際の対照として、内皮細胞のNO放出を促すアセチルコリン、さらにはNO放出剤やNO溶液の注入も行う。

６．研 究 成 果

R-SNOの定量にはHPLCとSavilleの方法を組み合わせた測定装置を用いた。低分子

R-SNO は ODS カラムで分離した後に水銀を加えて-SNO を切り離して NO_2^- とし、これを Griess 試薬で発色させて定量した。高分子 R-SNO はゲル濾過カラムで分離し、水銀で-SNO を切り離して NO_2^- にするが、その後に ODS カラムで除タンパクしてから Griess 試薬で発色させて定量した。Cys-SNO と G-SNO それぞれの検出限界は 1nM、Alb-SNO の検出限界は 5nM であった。

R-SNO の分解を抑制するために EDTA やチオール保護剤の NEM を使用して麻酔下のウサギから動静脈血を採血したが、血中に R-SNO の存在は確認できなかった。これは採血後に急速な分解が起こるためではないかと考え、今度は NEM をウサギに直接注入してみた。すると、血圧は低下し、心拍数も低下の傾向を示した。この状態で採血しても、R-SNO は全く検出できなかった。これらの結果から、血液中には 1nM 以上の低分子の R-SNO と 5nM 以上の高分子 R-SNO は存在しないということことがわかった。

次に、比較的安定な R-SNO である Alb-SNO を投与したらどうなるかを調べてみた。

ウサギに Alb-SNO を累積的に投与すると、30nmoles/kg から用量依存性に血圧が低下したが、心拍数には変化は認めらなかった。この結果から、血圧に全く変化の見られない 10nmoles/kg と、明らかに変化が見られる 300nmoles/kg の Alb-SNO を投与したときの血中 R-SNO の変化を調べてみた。10nmoles/kg の投与では血圧に何の変化も認められないが、3 分後に採血した血液の中には 100nM 以上の Alb-SNO が検出された。300nmoles/kg の投与では血圧は持続的に低下した。このとき、血中には 5000nM 程度の Alb-SNO が検出され、さらに、G-SNO も低濃度であるが、検出された。

次に、アセチルコリンで内皮からの NO 産生を刺激したらどうなるかを調べてみた。アセチルコリンを持続注入すると、用量依存性に血圧は低下した。しかし、R-SNO はアセチルコリンの最大量（30μg/kg/min）を注入した際にも全く検出できなかった。

さらに、NO ガスで飽和した溶液をウサギに直接投与してみた。すると、血圧が全く低下しない量(3ml/kg)でも血中に Alb-SNO が出現した。血圧の低下は最大でも 10%に足らないものの、このときには血中の Alb-SNO は 200nM 以上というレベルで検出された。しかし、低分子の R-SNO は全く検出できなかった。

最後に、生体内で NO を放出する NOC7 を投与した。NOC7 は用量依存性に血圧を低下させたが、その作用がほぼ最大になる 1μg/kg の投与量で初めて Alb-SNO が血中に出現した。その後はさらに Alb-SNO の血中濃度が増加していくものの、血圧の低下は既に頭打ちとなっていた。

７．研究の考察・反省

外因性に R-SNO を投与した結果から、血中に R-SNO が存在さえすれば、我々の測定系は確かにこれらを検出できるということが確認できた。しかし、同時に、定常状態のウサギの血液中には 1nM 以上の低分子 R-SNO と 5nM 以上の高分子 R-SNO は存在しないということも明らかになった。また、アセチルコリンで内皮からの NO 産生を刺激し

て血圧を低下させても R-SNO は全く検出されないこと、NOC7 による NO 放出では血圧がかなり低下してからようやく R-SNO が検出されること、また、100nM 以上の Alb-SNO が存在しても、血行動態には変化がないということや、NO 溶液を投与すると 200nM 以上の R-SNO が出現するにも拘わらず血圧の低下は非常に少ないことなどが分かった。

以上の結果をまとめると、生理学的状態ではごく少量の NO が平滑筋とその近傍だけに到達し、R-SNO は検出できる量存在しないと考えられる。しかし、何らかの方法で余剰な NO が存在すると、初めて R-SNO が検出できるようになることが明らかとなった。ところが、R-SNO の potency は決して高いものではなく、かなりの濃度になって初めて作用をあわすようになる。これらの事実より、R-SNO は、生体において循環動態の調節に重要な役割を担っているとは考えがたいと思われる。従って、今回検討した R-SNO を循環器疾患の治療に応用することは難しいのではないかと考えられる。今後は R-SNO 以外の新たな生体内 NO キャリアーを模索し、その生体内に於ける意義を検討したい。

８．研 究 発 表

Shibamoto T. Ishibashi T. Shimo T. Cui S. Takano H. Tsuchida H. Nishio M and Kurata Y. N^{G}-Nitro-L-arginie methyl ester potentiates anaphylactic venoconstriction in rat perfused livers. Clin Exp Pharmacol Physiol 2006; 33: 1073-1077. (MLDB)

１．研究課題名：ヒトモノクローナル抗体によるアルツハイマー病治療法の開発
（研究番号　S2005-11）

２．キーワード：１）アルツハイマー病（Alzheimer’s disease）
２）モノクローナル抗体（monoclonal antibody）
３）アミロイドβ蛋白（amyloid β protein）
４）受動免疫療法（passive immunization）

３．研究代表者：朝倉　邦彦・医学部・助教授・生体感染防御学（微生物学）
（現：藤田保健衛生大学）

４．研 究 目 的

1999 年に Schenk らは、アルツハイマー病モデルマウスをアミロイドβ(Aβ)蛋白で免疫すると、脳内のAβ沈着量が減少することを報告した。さらには抗Aβ抗体を投与しても同様の有効性が認められた。2001 年よりAβワクチンによる臨床治験が行われたが、ワクチン療法開始後髄膜脳炎をきたす症例が多数報告されるに至り、この副作用克服のためにその発症メカニズムの解明が急がれている状態である。

一方、我々はアルツハイマー病患者においてAβ蛋白に対するＢ細胞応答が健常対照や認知症をきたさない他の神経疾患群に比べて有意に低下していることを示し、抗Aβ抗体投与によるアルツハイマー病の受動免疫療法の可能性を示す結果を得ている。本研究では、これまでの多発性硬化症研究における抗体作製技術を活かしてヒト抗 Aβモノクローナル抗体をヒト抗体遺伝子改変マウス（マウス由来の抗体をまったく産生しないマウス）を用いて直接作製し、アルツハイマー病治療への応用（受動免疫療法確立）を目標とする。このマウスを用いることにより、キメラ抗体やヒト化(humanized)抗体作製の必要がなく、またAβワクチン療法にみられた髄膜脳炎発症の可能性もないため、早い段階で臨床応用の可能性があると考えられる。

５．研 究 計 画

ヒトAβN末端合成ペプチド（Aβ3-9 あるいはAβ5-11）にウシサイログロブリンを conjugate したものを抗原としてヒト抗体遺伝子トランスジェニックマウス（KM マウス）を免疫し、抗体価の上昇したマウスの脾細胞を X63 Ag8.653 ミエローマ細胞と細胞融合を行い、多数のハイブリドーマを作製する。得られたハイブリドーマ上清を用いて、免疫抗原との反応性を ELISA によりスクリーニングを行い、陽性細胞は１次および２次クローニング・スクリーニングを行う。陽性クローンは、Aβ1–40あるいはAβ1-42 の合成ペプチドとの反応性を調べ、さらにアルツハイマー病患者の脳切片を用いて組織染色を行い最終的に陽性のクローンを得る。得られた陽性クローンは、その抗体の H 鎖、L 鎖の可変領域の塩基配列を RACE 法により決定する。また、治療に用いるため大量培養して、上清より抗体を精製し、アルツハイマー病モデルマウスに投与し老人斑の減少効果を検討する。

６．研 究 成 果

ヒトAβN末端合成ペプチド（Aβ3-9あるいはAβ5-11）で免疫したヒト抗体遺伝子トランスジェニックマウスを免疫し、抗体価の上昇したマウスの脾細胞を X63 Ag8.653 ミエローマ細胞と細胞融合を行い、数個のハイブリドーマを作製した。２次、３次クローニングを行い、免疫抗原 Aβ3-9 あるいは Aβ5-11 と強く反応する 1 クローンを得た。このクローンが産生する抗体は、Aβ1-40 と Aβ1-42 とも非常に強く反応した。アルツハイマー病患者の大脳切片を用いた免疫染色では、薄い染色性が認められた。RACE 法による免疫グロブリン可変領域の解析から、この抗体はヒト IgG1 抗体で、H 鎖は VH6 によりコードされていることが明らかとなった。

７．研究の考察・反省

ヒト抗体遺伝子トランスジェニックマウス（KM マウス）を免疫することにより、抗体遺伝子を組み換える必要なく、直接マウスから完全なヒト抗 Aβモノクローナル抗体を得ることができた。同様の手法を用いて、今後複数のヒト抗 Aβモノクローナル抗体を得られることができれば、これらの抗体の複合体を用いて治療を行うことが可能と考えられ、抗体治療の場合常に問題となる、抗イディオタイプ抗体の産生を抑制できる可能性があると考えられた。

今後は、アルツハイマー病モデルマウスなどを用いて、これらの抗体の ex vivo および in vivo での作用を検討する必要がある。

８．研 究 発 表

Asakura K, Murayama H, Himeda T, Ohara Y. Expression of L* protein of Theiler's murine encephalomyelitis virus in the chronic phase of infection. J Gen Virol 2007; 88: 2268-2274. (MLDB)

Takano-Murayama M, Ohara Y, Asakura K, Okuwa T. Theiler's murine encephalomyelitis virus (TMEV) leader (L) protein amino acid residue 57regulates subgroup-specific virus growth on BHK-21 cells. J Virol 2006; 80: 12025-12031. (MLDB)

Takano-Maruyama M, Ohara Y, Asakura K, Okuwa T. Leader (L) and L* proteins of Theiler's murine encephalomyelitis virus (TMEV) and their regulation of the virus' biological activities. J Neuroinflammation 2006; 3: 19-26. (MLDB)

Journal of General Virology (2007), **88**, 2268–2274 DOI 10.1099/vir.0.82381-0

Expression of L* protein of Theiler's murine encephalomyelitis virus in the chronic phase of infection

Kunihiko Asakura,[1] Harunobu Murayama,[2] Toshiki Himeda[1]† and Yoshiro Ohara[1]

Correspondence
Yoshiro Ohara
ohara@kanazawa-med.ac.jp

[1]Department of Microbiology, Kanazawa Medical University, Ishikawa 920-0293, Japan
[2]Division of Pathology, Sendai City Hospital, Miyagi 984-0075, Japan

The DA strain and other members of the TO subgroup of Theiler's murine encephalomyelitis virus synthesize the L* protein from an alternative initiation codon. L* is considered to play a key role in viral persistence and demyelination in susceptible strains of mice, although this hypothesis is still controversial. By using a mutant virus that expresses FLAG epitope-tagged L*, it was demonstrated previously that L* is expressed exclusively in neurons *in vivo* in the acute phase of infection in the central nervous system (CNS). However, in the mutant virus, the C-H-C-C zinc-binding motif in the leader protein (L) was disrupted by the insertion of the FLAG epitope, resulting in clearance of the virus from the CNS. Therefore, a further two mutant viruses were newly generated, expressing FLAG epitope-tagged L* in which the C-H-C-C zinc-binding motif within L is spared. Both mutant viruses caused persistence and demyelination successfully in spinal cords and enabled us to identify L* immunohistochemically in the demyelinating lesions.

Received 13 July 2006
Accepted 2 April 2007

INTRODUCTION

Theiler's murine encephalomyelitis virus (TMEV) belongs to the genus *Cardiovirus* of the family *Picornaviridae* (Ohara *et al.*, 1988). TMEV is classified into two subgroups, TO and GDVII, based on different biological activities. The DA strain and other members of the TO subgroup cause a biphasic disease with an acute, subclinical encephalomyelitis, followed by a chronic demyelination in the spinal cords of mice (Obuchi & Ohara, 1998; Roos, 2002; Oleszak *et al.*, 2004). TMEV contains a large open reading frame (ORF), translated as a long precursor polyprotein that undergoes autoproteolytic processing to yield all of the viral proteins required to fulfil the viral life cycle. In the TO subgroup, an additional protein, designated L*, was found to be translated from an alternative ORF starting 13 nt downstream of the initiation codon AUG of the virus polyprotein ORF and ending in the VP2-encoding region (Kong & Roos, 1991). The L* ORF is conserved in all TO subgroup strains analysed (Michiels *et al.*, 1995). In GDVII subgroup strains, the AUG initiation codon for the translation of the alternative ORF is substituted for ACG, therefore no L* synthesis occurs. The role of L* is still poorly understood and controversial. DA (DAFL3 clone; Roos *et al.*, 1989) with a mutation at the L* initiation codon, designated DAL*-1, fails to synthesize L* and has attenuated demyelinating activity in the central nervous system (CNS), suggesting that L* plays a key role for viral persistence and demyelination (Chen *et al.*, 1995b; Ghadge *et al.*, 1998). A mutant virus from a different DA clone, DA1, which also fails to synthesize L*, has a weak influence on virus persistence (van Eyll & Michiels, 2000).

We have shown previously that L* is required for virus growth in cells of the macrophage lineage (Takata *et al.*, 1998; Obuchi *et al.*, 2000; Himeda *et al.*, 2005), the target cell of DA persistence. We also generated polyclonal rabbit anti-L* antibody (α-L*) and demonstrated that L* is not incorporated into virions and is associated with microtubules *in vitro* (Obuchi *et al.*, 2001). *In vivo* expression of L* in the CNS was confirmed by immunoprecipitation with α-L* in the acute phase of infection. Additionally, expression of L* in the acute phase of infection was analysed immunohistochemically by using a mutant virus (DA/3 × FLAGL*) expressing FLAG epitope-tagged L*. A double-immunolabelling study demonstrated that L* colocalizes with the viral antigen and is expressed exclusively in neurons (Asakura *et al.*, 2002).

We extended our previous observation and found that the mutant virus DA/3 × FLAGL* does not persist or cause demyelination in the CNS. Therefore, in this study, we generated a further two mutant viruses expressing FLAG epitope-tagged L* to analyse the expression of L* *in vivo* in the chronic phase of infection.

†Present address: Department of NeuroBiology and Therapeutics, Institute of Health Biosciences, The University of Tokushima Graduate School, Tokushima 770-8505, Japan.

METHODS

Construction of plasmid DNA clones and viruses. All constructs were generated on the basis of a parental infectious cDNA clone, pDAFL3 (Roos *et al.*, 1989). As shown in Fig. 1, in a construct designated DA/3 × FLAGL*, which was generated previously (Asakura *et al.*, 2002), a 3 × FLAG epitope sequence was tagged directly to the N terminus of L*, resulting in the disruption of the zinc-binding motif in L. A further two constructs, DA/3 × FLAGL*4 and DA/3 × FLAGL*5, were designed to express FLAG epitope-tagged L* and L with an intact zinc-binding motif. Namely, the spacer sequence, consisting of 9 nt (CTTGCAAAC), was inserted between the 3 × FLAG epitope and L* sequences, in order not to disrupt the zinc-binding motif in L. The ORF coding for L* starts with two AUG codons in the same frame separated by 9 nt (van Eyll & Michiels, 2002). In DA/3 × FLAGL*4, only the first AUG was changed to ACG, as shown in Fig. 1. Therefore, a truncated 15 kDa protein could be synthesized in addition to a full-length, 18 kDa L*. In DA/3 × FLAGL*5, the second AUG codon was changed to ACG in order not to synthesize the truncated 15 kDa L*. Comparison of the two mutant viruses makes clear the influence of the truncated 15 kDa L*. For the above modification, an overlap-extension PCR was applied as described previously (Asakura *et al.*, 2002). The clones with correctly sized insert were sequenced completely on both strands. Plasmid DNAs were linearized with *Xba*I (TOYOBO) and viral RNA was synthesized by using T7 RNA polymerase (Promega). BHK-21 cells were then transfected with the synthesized RNA by using Lipofectin (Gibco) according to the manufacturer's instructions. Virus was purified by a standard plaque technique, propagated on BHK-21 cells and used in the following experiments.

Kinetics of virus growth. BHK-21 cells in a six-well culture plate were infected with viruses at an m.o.i. of 10 p.f.u. per cell. The cells were scraped at various times (0, 3, 6, 12, 24 and 48 h) post-infection (p.i.) and the mixtures of culture supernatants and cell lysates were harvested by freezing and thawing. The lysates were then assayed for infectivity on BHK-21 cells by a standard plaque assay.

Immunoblotting. Extracted proteins from BHK-21 cells infected with mutant viruses were separated by SDS-PAGE under reducing conditions on 15 % acrylamide gels and transferred to nitrocellulose membranes by electroblotting. The membranes were incubated with a mouse anti-FLAG M2 mAb (Sigma) and the mouse anti-VP1 capsid protein mAb DAmAb2 (kindly provided by Dr Raymond Roos, University of Chicago, IL, USA) overnight at 4 °C after blocking with Tris-buffered saline containing 5 % non-fat dry milk and 0.05 % Tween 20 for 1 h at room temperature. Bound antibody was then detected with biotinylated anti-mouse IgG and horseradish peroxidase-conjugated streptavidin (both from Jackson ImmunoResearch) using the Enhanced Chemiluminescence (ECL) system (Amersham Biosciences).

The expression of L* in each mutant virus was compared with an image analyser. L* expression was adjusted to the expression of capsid protein VP1. The relative ratios were compared with that of DA/3 × FLAGL*.

Animal experiments. SJL/J mice were purchased from Jackson Laboratories. The experiments were approved by the Kanazawa Medical University Institutional Animal Care and Use Committee. Four-week-old mice were injected intracerebrally with 2×10^5 p.f.u. virus in a 10 µl volume. At 21, 45, 90 and 180 days p.i., mice were sacrificed and perfused with physiological saline followed by 10 % formalin. Formalin-fixed brain tissues were dehydrated and embedded in paraffin. The entire spinal cord was also removed from the spinal canal, sectioned into lengths of a few millimetres and embedded in paraffin.

Histological study. To detect inflammatory-cell infiltration and demyelination, haematoxylin–eosin (H–E) and Klüver–Barrera (K–B) stains were performed on 4 µm paraffin-embedded tissue sections. In addition, autoclave-pretreated tissue sections were subjected to the following immunohistochemical analysis. Briefly, the sections were incubated with DAmAb2 or anti-FLAG M2 mAb overnight at 4 °C, followed by incubation with peroxidase-conjugated secondary antibody (EnVision+; DAKO) for 30 min at room temperature and the bound antibodies were detected by 3,3′-diaminobenzidine tetrahydrochloride (DAB). To exclude non-specific bindings of secondary antibody with endogenous mouse antibodies, the serial sections were also stained without primary antibodies as a control. To identify L*-expressing cells, double labelling was also performed. The sections were subsequently incubated with biotinylated BS-1 lectin for macrophage/microglia (Vector Laboratories) or rabbit polyclonal anti-glial fibrillary acidic protein (GFAP) antibody for astrocytes (DAKO) overnight at 4 °C, followed by incubation with alkaline phosphatase-conjugated streptavidin (Jackson ImmunoResearch) or secondary antibody (Histofine; Nichirei). The bound lectin or antibody was detected by using a New Fuchsin substrate kit (Nichirei). All sections were counterstained with haematoxylin.

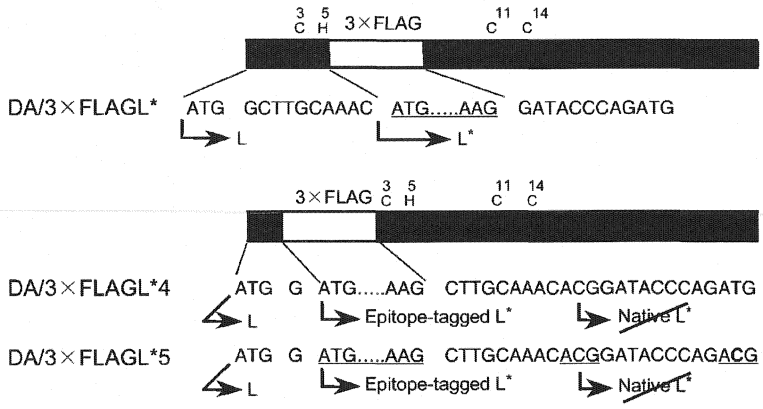

Fig. 1. Schematic diagram of mutant constructs. In pDA/3×FLAGL*, the 3×FLAG epitope sequence (ATG.....AAG) was tagged directly to the N terminus of the L* protein, resulting in disruption of the zinc-binding motif in the L protein. In the two other constructs (DA/3×FLAGL*4 and DA/3×FLAGL*5), the spacer sequence (CTTGCAAAC) was inserted between the 3×FLAG epitope and the L* sequences in order not to disrupt the zinc-binding motif in L. In these two constructs, the initiation codon ATG of L* was changed to ACG in order not to synthesize the native L*. Another ATG is located 9 nt downstream of the first ATG, which could synthesize a truncated 15 kDa L*. In DA/3×FLAGL*5, the second ATG codon was also changed to ACG in order not to translate the truncated 15 kDa L*.

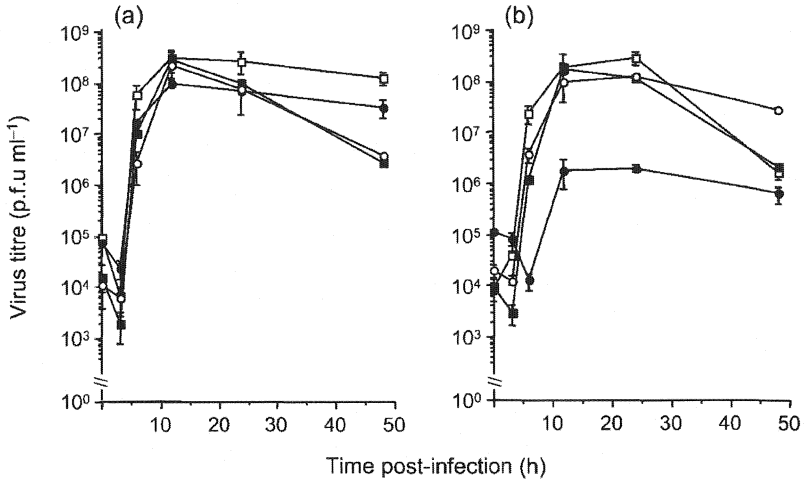

Fig. 2. Growth kinetics of wild-type DA (□) and mutant (●, DA/3×FLAGL*; ■, DA/3× FLAGL*4; ○, DA/3×FLAGL*5) viruses on BHK-21 (a) and L929 (b) cells. Cells were infected with each virus (10 p.f.u. per cell). A mixture of culture supernatants and cell lysates of infected cells at various time points (0, 3, 6, 12, 24 and 48 h p.i.) was subjected to titre determination by plaque assay. Values represent the mean ± SD of triplicate samples.

Quantitative analysis of demyelinated lesions in spinal cords. On each section with K–B staining, the areas of white matter or demyelinated lesion were quantified by using a digital image-analysis system (Mitani Corp.) attached to a Nikon photomicroscope. The ratio of the area of demyelinated lesion to the area of white matter was calculated.

RT-PCR. One microgram of total RNA isolated from virus-infected SJL/J mouse spinal cords was denatured at 94 °C for 5 min, chilled on ice and reverse-transcribed into cDNA in a reaction mixture containing 50 U Moloney murine leukemia virus reverse transcriptase (Invitrogen), 10 μM dithiothreitol, 0.7 μM dNTPs and DA virus-specific primers (5′ primer, DA940–960 nt; 3′ primer, DA1311–1331 nt) at 42 °C for 60 min. The reaction was terminated by heating at 72 °C for 5 min. Two microlitres of the reaction mixture was subjected to the following PCR: 30 cycles of denaturation at 94 °C for 1 min, annealing at 55 °C for 1 min and extension at 72 °C for 2 min.

RESULTS

In vitro growth kinetics of mutant viruses in BHK-21 and L929 cells

We compared the growth kinetics of mutant viruses (DA/3 × FLAGL*, DA/3 × FLAGL*4 and DA/3 × FLAGL*5) in BHK-21 and L929 cells. Plaque sizes of all mutant viruses were slightly reduced in comparison with that of wild-type DA in BHK-21 cells. In L929 cells, the plaque size of DA/3 × FLAGL* was extremely small, although plaques of DA/3 × FLAGL*4 and DA/3 × FLAGL*5 were almost the same size as those in BHK-21 cells (data not shown). All of the mutant viruses showed growth kinetics similar to those of wild-type DA in BHK-21 cells; the same growth pattern of DA/3 × FLAGL* as that of DA was reported previously (Asakura *et al.*, 2002). The titres reached their peak at 12 h p.i. and decreased gradually thereafter. The peak titres of mutant viruses were similar to that of DA (Fig. 2a). In contrast, in L929 cells, DA/3 × FLAGL* showed an approximately 2-log reduction of peak titre, as shown in Fig. 2(b). DA/3 × FLAGL*4 and DA/3 × FLAGL*5, carrying intact zinc-binding motifs, showed peak titres and growth patterns similar to those of DA.

In vitro detection of L* by immunoblotting with anti-FLAG mAb

Proteins extracted from BHK-21 cells infected with each virus were loaded on an SDS/polyacrylamide gel. Immunoblotting with DAmAb2 showed similar levels of VP1 capsid protein production in BHK-21 cells infected with DA/3 × FLAGL*, DA/3 × FLAGL*4 or DA/3 × FLAGL*5, according to the intensity of bands detected by an image analyser (Fig. 3a, lower panel). L* was detectable by immunoblotting with anti-FLAG mAb in BHK-21 cells infected with each virus (Fig. 3a, upper panel). The expression of L* in DA/3 × FLAGL*4- or DA/3 × FLAGL*5-infected cells, adjusted to the expression of VP1 capsid protein, increased by approximately 30 % in comparison with that in DA/3 × FLAGL*-infected cells (Fig. 3b).

Clinical observation and histological study in the chronic phase of infection

SJL/J mice were inoculated intracerebrally with 2×10^5 p.f.u. of each virus; wild-type DA and all types of mutant virus, including DA/3 × FLAGL*, pathologically caused acute encephalitis within 7 days (data not shown). During the chronic stage of disease, mice were observed clinically every week. At 21 and 45 days p.i., mice infected with wild-type DA, DA/3 × FLAGL*4 or DA/3 × FLAGL*5 showed no visible appearance changes or clinical signs. At 90 days p.i., some of the mice showed minimal change in fur and mild ataxia, but not paralysis. However, after several months of infection, mice started showing scruffy appearance, incontinence and extremity paralysis with stiff movement. There were no clinical differences observed among mice infected with wild-type DA, DA/3 × FLAGL*4 or DA/3 × FLAGL*5.

Transverse or longitudinal spinal-cord sections from infected mice were prepared and studied histologically.

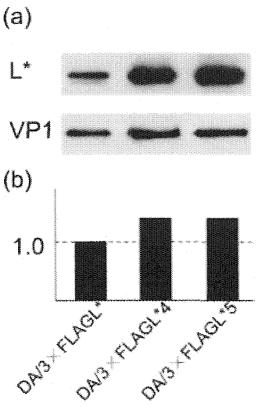

Fig. 3. (a) Immunoblotting with anti-FLAG M2 mAb and anti-TMEV VP1 mAb DAmAb2. Proteins extracted from BHK-21 cells infected with DA or mutant viruses were separated by SDS-PAGE (15% gel). Bound antibodies were detected with biotinylated secondary antibodies and horseradish peroxidase-conjugated streptavidin by using enhanced chemiluminescence. Expression of L* was adjusted to expression of the VP1 capsid protein. (b) Expression of L* in each mutant virus was compared by using an image analyser. The relative ratio of the expression of L* in DA/3×FLAGL*-infected cells to that in DA/3×FLAGL*4- or DA/3×FLAGL*5-infected cells was evaluated.

At 21 and 45 days p.i., less severe inflammatory-cell infiltration was observed in the spinal cords of mice infected with DA/3 × FLAGL*4 or DA/3 × FLAGL*5 than in those infected with wild-type DA by H–E staining. At 90 days p.i., however, similar inflammatory-cell infiltration was observed in all virus-infected groups (data not shown). At 21 and 45 days p.i., demyelinated lesions were not identified by K–B staining in the mice infected with mutant viruses. However, minor demyelinated lesions were occasionally observed at 90 days p.i. Extensive demyelinated lesions were identified in the entire spinal cords of mice infected with both DA/3 × FLAGL*4 and DA/3 × FLAGL*5 at 180 days p.i. As shown in Fig. 4, the lateral and anterior columns at thoracic-cord level were demyelinated in mice infected with both DA/3 × FLAGL*4 (Fig. 4a) and DA/3 × FLAGL*5 (Fig. 4b). These demyelinated areas were similar to those observed in mice infected with wild-type DA (data not shown). Serial-section staining with viral antigen revealed viral persistence in the spinal-cord white matter (Fig. 4a and b, insets). Double staining with anti-FLAG mAb and BS-1 lectin demonstrated that L* and lectin are colocalized, suggesting that L* is expressed in lectin-positive cells (macrophage/microglia) (Fig. 4c). Subsequent double staining demonstrated that L*-positive cells are GFAP-negative (Fig. 4d).

At 180 days p.i., demyelinated lesions in each virus-infected mouse were quantified. As shown in Table 1, approximately 17–20% of white matter was demyelinated in the spinal cords of mice infected with DA/3 × FLAGL*4 or DA/3 × FLAGL*5. Among these experimental groups, including the wild-type DA-infected group, there was no statistical significance in the percentage area of demyelinated lesion/area of white matter.

Identification of mutant virus genomes in chronically infected CNS tissues

To further confirm the presence of virus genomes in the chronic phase of infection, we isolated total RNA from the spinal cords of mice infected chronically with DA/3 × FLAGL*4, DA/3 × FLAGL*5 or wild-type DA at 180 days p.i., and performed RT-PCR with virus-specific primers. The predicted PCR products (461 bp for DA/3 FLAGL*4 or DA/3 × FLAGL*5, which contain 69 bp extra inserted sequence) were detected as clear, single bands (Fig. 5, lanes 1 and 2). For wild-type DA, a band of the predicted size (392 bp) was detected (Fig. 5, lane 3). Further sequencing analysis of PCR products confirmed that these PCR products of 461 bp are derived from DA/3 × FLAGL*4 and DA/3 × FLAGL*5 (data not shown). These results indicated that there was no wild-type DA virus contamination in mice infected with DA/3 × FLAGL*4 or DA/3 × FLAGL*5.

DISCUSSION

L* is considered to play a key role in viral persistence and demyelination in susceptible strains of mice (Chen *et al.*, 1995b; Ghadge *et al.*, 1998; van Eyll & Michiels, 2002), although this hypothesis is controversial (van Eyll & Michiels, 2000). Our previous study (Asakura *et al.*, 2002) demonstrated, by using a mutant virus, DA/3 × FLAGL*, which expresses FLAG epitope-tagged L*, that L* is expressed *in vivo* in the acute phase of infection in the CNS. We extended our observation to detect the expression of L* in the chronic phase of infection. However, we did not find any inflammation or demyelination in the CNS of DA/3 × FLAGL*-inoculated mice at 45 and 90 days p.i. In addition, RT-PCR detected no TMEV genome (data not shown).

L is synthesized by members of the genera *Cardiovirus* and *Aphthovirus*, but not by members of other genera of the family *Picornaviridae*. TMEV strains have an L protein composed of 76 aa located in the N terminus of the polyprotein. It is a highly acidic protein (Ohara *et al.*, 1988). Kong *et al.* (1994) have observed that L of TMEV is required for viral spread in L929 cells, but not in non-interferon (IFN)-responsive BHK-21 cells. Based on the fact that DA (TMEV) L has a putative C-H-C-C zinc-binding motif, they demonstrated that DA virus with a mutation in the motif displayed a restricted viral infection in L929 cells. Chen *et al.* (1995a) extended this observation and demonstrated that L of TMEV is a metalloprotein and that zinc binds a C-H-C-C motif that is conserved among cardioviruses. In the DA subgroup, van Pesch *et al.* (2001) introduced point mutations in the zinc-binding motif without affecting the L* alternative ORF. They reported

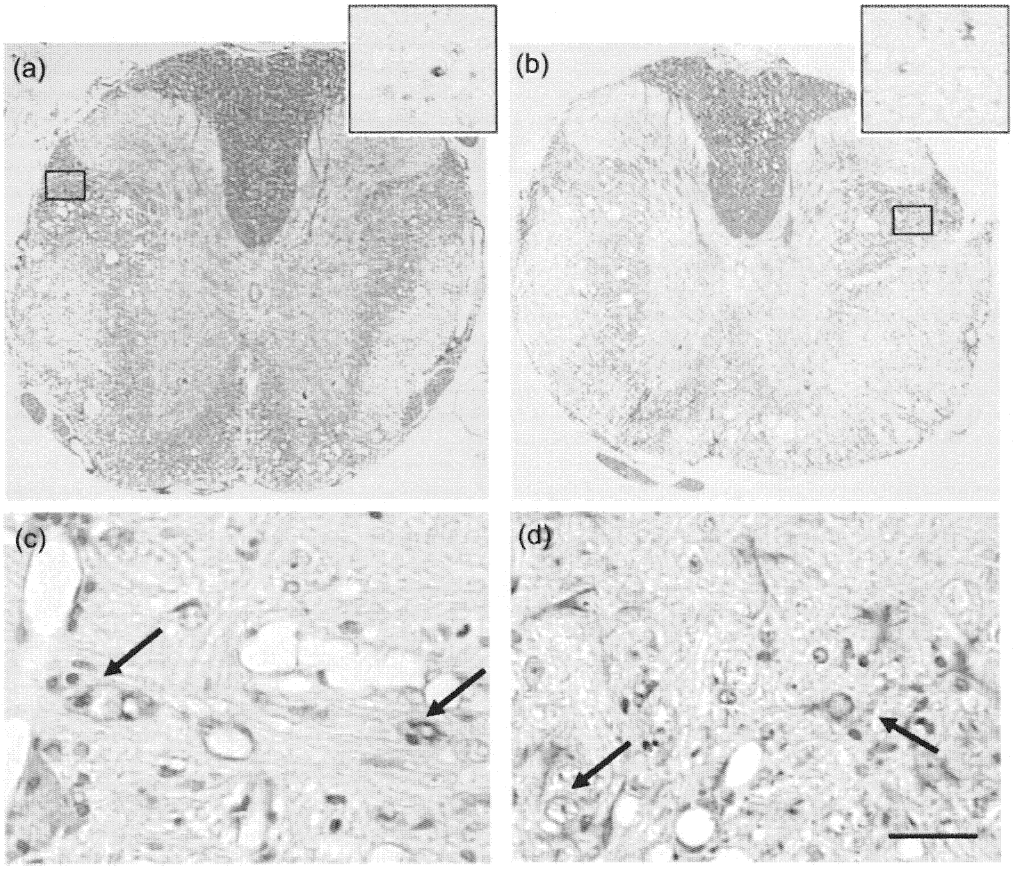

Fig. 4. Histological and immunohistochemical study of SJL/J mice infected with DA/3×FLAGL*4 and DA/3×FLAGL*5 at 180 days p.i. (a, b) Light micrographs showing representative K–B staining of transverse spinal-cord sections in mice infected with DA/3×FLAGL*4 (a) or DA/3×FLAGL*5 (b). Extensive demyelinated lesions were observed in the lateral and anterior columns at thoracic-cord level in mice infected with DA/3×FLAGL*4 and DA/3×FLAGL*5. Serial-section immunohistochemical staining using a mAb against the VP1 capsid protein demonstrated viral persistence in the spinal-cord white matter (a and b, insets). (c) Double staining with anti-FLAG mAb (L*, brown) and BS-1 lectin (macrophage/microglia, red). Arrows indicate an L* and BS-1 lectin double-positive cell. (d) Double staining with anti-FLAG mAb (L*, brown) and anti-GFAP antibody (astrocytes, red). Arrows indicate L*-positive and GFAP-negative cells (d). Bar, 50 μm.

that L inhibits the production of IFN-α/β by infected L929 cells and specifically inhibits transcription of the IFN-α4 and IFN-β genes, which are known be activated early in response to viral infection. They additionally demonstrated that mutation of the zinc finger was sufficient to block anti-IFN activity (van Pesch *et al.*, 2001). A more recent

Table 1. Quantitative analysis of demyelinated lesions in mice infected with wild-type or mutant viruses at 6 months p.i.

Values represent the mean ± SEM. Among these experimental groups, there was no statistical significance in the percentage area of demyelinated lesion/area of white matter by Student's *t*-test.

Virus	No. mice	Area of white matter (mm^2)	Area of demyelinated lesion (mm^2)	Area of demyelinated lesion/ area of white matter (%)
Wild-type DA	9	9.27 ± 0.33	1.61 ± 0.42	16.2 ± 3.0
DA/3 × FLAGL*4	7	11.10 ± 0.43	2.09 ± 1.03	17.6 ± 3.1
DA/3 × FLAGL*5	9	10.03 ± 0.56	2.13 ± 0.37	20.2 ± 4.7

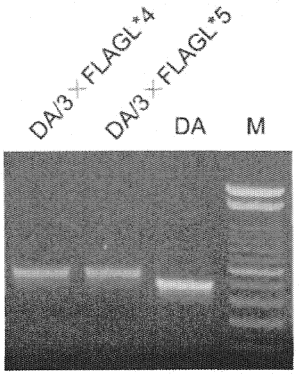

Fig. 5. Persistent infection of mutant viruses in the spinal cords of mice. Total RNA was isolated from the spinal cords of SJL/J mice infected with DA/3×FLAGL*4 or DA/3×FLAGL*5. Total RNA isolated from the spinal cord of an SJL/J mouse infected with wild-type DA was used as a positive control to exclude the possibility of wild-type DA contamination in the mice tested. A PCR product of the predicted size [461 bp length for DA/3×FLAGL*4 (lane 1) or DA/3×FLAGL*5 (lane 2)] was detected. In the wild-type DA, a band of the predicted size (392 bp) was detected (lane 3). M, 100 bp ladder marker (TOYOBO).

study showed that L interferes with trafficking of the cytoplasmic IFN-regulatory factor 3, a factor critical for transcriptional activation of IFN-α/β genes (Delhaye *et al.*, 2004).

In this study, as shown in Fig. 2, only the growth of DA/3 × FLAGL* was restricted in L929 cells. In DA/3 × FLAGL* virus, the epitope tag was inserted immediately after the initiation codon of L*, which is located 13 nt downstream of the initiation codon of L, i.e. in the middle of the zinc-binding motif, leading to complete disruption of zinc binding (Fig. 1). Although the data are not shown, RT-PCR demonstrated that transcription of the immediate-early IFN genes IFN-α4 and INF-β is preserved in DA/3 × FLAGL*-infected L929 cells, suggesting strongly that disruption of the zinc-binding motif by insertion of the FLAG epitope induced no virus persistence or demyelination. The present data are supporting evidence that the zinc-binding motif within L plays an important role for TMEV persistence (van Pesch *et al.*, 2001).

In order to analyse L* expression *in vivo* in the chronic phase of infection, we generated a further two mutant viruses expressing epitope-tagged L*. In these mutants, the zinc-binding motif within L is conserved, as shown in Fig. 1. As expected, these mutants persisted in the spinal cords of SJL/J mice and caused inflammation and demyelination.

As shown in Table 1, the mutant viruses caused demyelination at 180 days p.i., similar to that caused by wild-type DA. In addition, demyelination caused by the two mutant viruses was not significantly different. The data suggest that tagging of the FLAG epitope does not alter the biological activities of wild-type DA (virus persistence and demyelination), leading to the physiological expression of L*. The expression and localization of L* can be studied in mice inoculated with these mutant viruses.

When injected intracerebrally into SJL/J mice, mutant virus-specific RNA containing the epitope tag was identified in the spinal cords by RT-PCR (without wild-type DA virus contamination). Although the mice infected with DA/3 × FLAGL*4 or -5 showed less severe clinical signs and pathological findings at 21, 45 and 90 days p.i. in comparison with wild-type DA-infected mice, after several months of infection, mice showed severe clinical signs, including spastic paraparesis and severe inflammatory demyelination in the spinal cords by histological study. This observation was further confirmed by quantitative analysis of demyelinated lesions at 180 days p.i. (Table 1).

The present study demonstrated that L* is expressed in lectin-positive and GFAP-negative cells (macrophage/microglia). Although the cell types where TMEV antigen resides in the chronic phase of infection are still to be confirmed, several reports suggest strongly that these are macrophages: the recovery of infectious virus from infiltrating mononuclear cells (Clatch *et al.*, 1990), the predominant viral load in macrophages (Lipton *et al.*, 1995) and clearance of virus by the depletion of infiltrating macrophages (Rossi *et al.*, 1997). Therefore, it is suggested that, in the chronic phase of infection, L* is colocalized with TMEV capsid antigen in macrophage/microglia cells. As L* is reported to remain without being incorporated into virions (Obuchi *et al.*, 2001), L* in the cytoplasm of macrophage/microglia cells may have some effect(s) on the biological activities of DA (persistence and demyelination) through interaction with some host factor(s) of macrophages.

The precise mechanisms of TMEV-induced persistent infection and demyelination are yet to be elucidated. The functions of L and L* are also not yet fully understood. The mutant viruses generated in the present study showed similar behaviour to that of wild-type DA both *in vitro* and *in vivo*, and L* was visualized in the chronic phase of infection. These viruses may be useful to pursue further elucidation of the role(s) of L and L*.

ACKNOWLEDGEMENTS

This work was supported by a grant from the Neuroimmunological Research Committee of the Ministry of Health, Labor and Welfare, a Grant for Promoted Research from Kanazawa Medical University (S2005-11) and a Grant for Hightechnology Research Center from Kanazawa Medical University (H2006-7). We thank Ms S. Saito for technical assistance.

REFERENCES

Asakura, K., Murayama, H., Himeda, T. & Ohara, Y. (2002). Epitope-tagged L* protein of Theiler's murine encephalomyelitis virus is

expressed in the central nervous system in the acute phase of infection. *J Virol* **76**, 13049–13054.

Chen, H.-H., Kong, W.-P. & Roos, R. P. (1995a). The leader peptide of Theiler's murine encephalomyelitis virus is a zinc-binding protein. *J Virol* **69**, 8076–8078.

Chen, H.-H., Kong, W.-P., Zhang, L., Ward, P. L. & Roos, R. P. (1995b). A picornaviral protein synthesized out of frame with the polyprotein plays a key role in a virus-induced immune-mediated demyelinating disease. *Nat Med* **1**, 927–931.

Clatch, R. J., Miller, S. D., Metzner, R., Dal Canto, M. C. & Lipton, H. L. (1990). Monocytes/macrophages isolated from the mouse central nervous system contain infectious Theiler's murine encephalomyelitis virus (TMEV). *Virology* **176**, 244–254.

Delhaye, S., van Pesch, V. & Michiels, T. (2004). The leader protein of Theiler's virus interferes with nucleocytoplasmic trafficking of cellular proteins. *J Virol* **78**, 4357–4362.

Ghadge, G. D., Ma, L., Sato, S., Kim, J. & Roos, R. P. (1998). A protein critical for a Theiler's virus-induced immune system-mediated demyelinating disease has a cell type-specific anti-apoptotic effect and a key role in virus persistence. *J Virol* **72**, 8605–8612.

Himeda, T., Ohara, Y., Asakura, K., Kontani, Y., Murakami, M., Suzuki, H. & Sawada, M. (2005). A lentiviral expression system demonstrates that L* protein of Theiler's murine encephalomyelitis virus (TMEV) is essential for virus growth in a murine macrophage-like cell line. *Virus Res* **108**, 23–28.

Kong, W.-P. & Roos, R. P. (1991). Alternative translation initiation site in the DA strain of Theiler's murine encephalomyelitis virus. *J Virol* **65**, 3395–3399.

Kong, W. P., Ghadge, G. D. & Roos, R. P. (1994). Involvement of cardiovirus leader in host cell-restricted virus expression. *Proc Natl Acad Sci U S A* **91**, 1796–1800.

Lipton, H. L., Twaddle, G. & Jelachich, M. L. (1995). The predominant virus antigen burden is present in macrophages in Theiler's murine encephalomyelitis virus-induced demyelinating disease. *J Virol* **69**, 2525–2533.

Michiels, T., Jarousse, N. & Brachic, M. (1995). Analysis of the leader and capsid coding regions of persistent and neurovirulent strains of Theiler's virus. *Virology* **214**, 550–558.

Obuchi, M. & Ohara, Y. (1998). Theiler's murine encephalomyelitis virus and mechanisms of its persistence. *Neuropathology* **18**, 13–18.

Obuchi, M., Yamamoto, J., Odagiri, T., Uddin, M. N., Iizuka, H. & Ohara, Y. (2000). L* protein of Theiler's murine encephalomyelitis virus is required for virus growth in a murine macrophage-like cell line. *J Virol* **74**, 4898–4901.

Obuchi, M., Odagiri, T., Asakura, K. & Ohara, Y. (2001). Association of L* protein of Theiler's murine encephalomyelitis virus with microtubules in infected cells. *Virology* **289**, 95–102.

Ohara, Y., Stein, S., Fu, J., Stillman, L., Klaman, L. & Roos, R. P. (1988). Molecular cloning and sequence determination of DA strain of Theiler's murine encephalomyelitis viruses. *Virology* **164**, 245–255.

Oleszak, E. L., Chang, J. R., Friedman, H., Katsetos, C. D. & Platsoucas, C. D. (2004). Theiler's virus infection: a model for multiple sclerosis. *Clin Microbiol Rev* **17**, 174–207.

Roos, R. P. (2002). Pathogenesis of Theiler's murine encephalomyelitis virus-induced disease. In *Molecular Biology of Picornaviruses*, pp. 427–435. Edited by B. L. Semler & E. Wimmer. Washington, DC: American Society for Microbiology.

Roos, R. P., Stein, S., Ohara, Y., Fu, J. & Semler, B. L. (1989). Infectious cDNA clones of the DA strain of Theiler's murine encephalomyelitis virus. *J Virol* **63**, 5492–5496.

Rossi, C. P., Delcroix, M., Huitinga, I., McAllister, A., van Rooijen, N., Claassen, E. & Brahic, M. (1997). Role of macrophages during Theiler's virus infection. *J Virol* **71**, 3336–3340.

Takata, H., Obuchi, M., Yamamoto, J., Odagiri, T., Roos, R. P., Iizuka, H. & Ohara, Y. (1998). L* protein of the DA strain of Theiler's murine encephalomyelitis virus is important for virus growth in a murine macrophage-like cell line. *J Virol* **72**, 4950–4955.

van Eyll, O. & Michiels, T. (2000). Influence of the Theiler's virus L* protein on macrophage infection, viral persistence, and neurovirulence. *J Virol* **74**, 9071–9077.

van Eyll, O. & Michiels, T. (2002). Non-AUG-initiated internal translation of the L* protein of Theiler's virus and importance of this protein for viral persistence. *J Virol* **76**, 10665–10673.

van Pesch, V., van Eyll, O. & Michiels, T. (2001). The leader protein of Theiler's virus inhibits immediate-early alpha/beta interferon production. *J Virol* **75**, 7811–7817.

１．研究課題名：タイラーウイルス受容体の同定　（研究番号　S2005-12）

２．キーワード：１）　タイラーウイルス（Theiler's virus, TV）
２）　L 蛋白（L protein）
３）　ウイルス増殖（kinetics of virus growth）
４）　ウイルス RNA のカプシドへの取込み（RNA encapsidation）

３．研究代表者：高野　真澄・医学部・助手・生体感染防御学（微生物学）

４．研 究 目 的

タイラーウイルス（TV）は、マウスに急性致死性灰白脳脊髄炎を引き起こす GDVII 亜群と、脊髄に持続感染・脱髄を引き起こす DA 亜群に分類される。

我々は、ウイルス非構成蛋白による DA 株固有の持続感染・脱髄発症機構について解析、研究を進めてきた。一方、組換えウイルスを用いた研究により、ウイルスの受容体結合想定領域が各亜群固有の生物学的性状の決定に重要であることが示されている。従って、TV 受容体を同定することは各亜群固有の生物学的性状の決定機構の解明に必須であるとして、本計画を立案した。しかし、計画遂行の過程で、TV の非構成蛋白で両亜群間で最もアミノ酸配列が異なる L がウイルス増殖に関わっていることが分かってきた。

そこで、本研究は、L 蛋白の性状を明らかにすることにより、最終的には各亜群固有の生物学的性状の決定機構の解明を目的とする。

５．研 究 計 画

組換えウイルスを用いた L 蛋白の性状の解明

1) Site-directed mutagenesis によって DA 株 L 蛋白の 57 番目のセリンをプロリンに置換した組換えウイルス（DAL_{pro}）と GDVII 株 L 蛋白の 57 番目のプロリンをセリンに置換した組換えウイルス（GDVIIser）を作製する。
2) TV を BHK-21 細胞に感染させ、経時的に感染細胞と培養上清を回収し、プラークアッセイによってウイルス増殖を検討する。
3) TV 特異的プライマーを用いた半定量的 RT-PCR によってウイルスの複製を解析する。
4) L-[^{35}S]メチオニンと L-[^{35}S]システインで感染細胞をパルスラベルし、ウイルスと細胞の蛋白合成を解析する。
5) L-[^{35}S]メチオニンと L-[^{35}S]システイン標識した感染細胞の溶解液をショ糖密度勾配遠心法により分画し、カプシドの合成とウイルス粒子の成熟について解析する。

６．研 究 成 果

DAL_{pro} ウイルスと GDVIIser ウイルスの BHK-21 細胞における増殖を調べたところ、DAL_{pro} ウイルスは GDVII 株と同等の増殖を示し、最終的にタイターが親株 DA 株の約 10 倍に達した。一方、GDVIIser ウイルスは DA 株と同等の増殖を示した。つまり、L 蛋白の 57 番目のアミノ酸は両亜群間の増殖の違いに関与している。さらにウイルス

増殖に関して詳細に調べた結果、L 蛋白の変異は、ウイルスゲノム RNA の複製、ウイルス蛋白の合成、カプシド合成には影響を与えず、ウイルスゲノムがカプシドに取り込まれ成熟したウイルス粒子となる過程に影響を及ぼしていた。つまり、DAL_{pro}、GDVII 株では GDVIIser、DA 株と比較して、成熟したウイルス粒子が効率良く産生されていた。これらの結果から、L 蛋白の 57 番目のアミノ酸残基がウイルス RNA のカプシドへの取込みの制御に重要であることが明らかとなった。

７．研究の考察・反省

組換えウイルスはマウス脳内接種した時、急性期には GDVIIser ウイルスは致死性の急性灰白脳脊髄炎を引き起こし、DAL_{pro} ウイルスは症状がなかった。このことは、L の 57 番目のアミノ酸残基は TV の in vivo における急性期の性状を規定していないことを示す。DAL_{pro} ウイルスの慢性期症状についてさらに検討をしていきたいと考えている。

８．研 究 発 表

Takano-Maruyama M, Ohara Y, Asakura K, Okuwa T.
Theiler's murine encephalomyelitis virus leader protein amino acid residue 57 regulates subgroup-specific virus growth on BHK-21 cells. J Virol 2006; 80: 12025-12031. (MLDB)

Takano-Maruyama M, Ohara Y, Asakura K, Okuwa T.
Leader (L) and L* proteins of Theiler's murine encephalomyelitis virus (TMEV) and their regulation of the virus' biological activities. J Neuroinflammation 2006; 3: 19-26. (MLDB)

JOURNAL OF VIROLOGY, Dec. 2006, p. 12025–12031 Vol. 80, No. 24
0022-538X/06/$08.00+0 doi:10.1128/JVI.00693-06

Theiler's Murine Encephalomyelitis Virus Leader Protein Amino Acid Residue 57 Regulates Subgroup-Specific Virus Growth on BHK-21 Cells[▽]

Masumi Takano-Maruyama, Yoshiro Ohara,* Kunihiko Asakura, and Takako Okuwa

Department of Microbiology, Kanazawa Medical University, Ishikawa 920-0293, Japan

Received 5 April 2006/Accepted 15 September 2006

Strains of Theiler's murine encephalomyelitis virus (TMEV) are divided into two subgroups, TO and GDVII. TMEV strains show subgroup-specific virus growth and cell tropism and induce subgroup-specific diseases. Using site-directed mutagenesis, we demonstrated that the amino acid at position 57 of the leader protein (L^{57}), which is located at the most N-terminal part of the polyprotein, regulates subgroup-specific virus growth on BHK-21 cells. Further study suggested that L^{57} may regulate viral RNA encapsidation, although it does not affect the synthesis of viral proteins or the assembly of viral intermediates.

Theiler's murine encephalomyelitis virus (TMEV) belongs to the genus *Cardiovirus* of the family *Picornaviridae* and is divided into two subgroups on the basis of their different biological activities (23, 26, 30). GDVII subgroup strains cause acute and fatal polioencephalomyelitis in mice following intracerebral inoculation. In the few surviving mice, no virus persistence or demyelination is observed. In contrast, TO or DA subgroup strains induce a biphasic central nervous system disease. In the acute phase, the virus infects mainly neurons and causes mild polioencephalomyelitis. During the chronic phase, the virus persists in the spinal cord of susceptible strains of mice and causes demyelination. In addition, virus growth differs in vitro between strains of the two subgroups. On baby hamster kidney (BHK-21) cells, GDVII subgroup strains grow well at a titer that is 10-fold higher than that of DA subgroup strains. Furthermore, GDVII subgroup strains produce larger plaques (2.5 mm in diameter), whereas DA subgroup strains produce smaller plaques (less than 0.5 mm) (18).

Leader protein (L) is located at the most N-terminal portion of the polyprotein in members of the *Aphthovirus* and *Cardiovirus* genera of the picornaviruses (17). L is known to enable virus growth on specific cell lines because it inhibits alpha/beta interferon (IFN-α/β) transcription (35). Although the capsid proteins have over 94% homology at the amino acid level, the homology of L between TO and GDVII subgroup strains is only 85% (20). The sequence difference between leader proteins of the two subgroups may account for TMEV subgroup-specific biological activities.

There are 11 amino acid (aa) residue differences distributed over the total 76 aa of L between the two subgroup strains (20). One of the amino acid residues is proline, which is known to have an important influence on protein structure; *cis-trans* isomerization at a proline residue alters the protein structure. In addition, proline has the highest reverse turn probability (9). GDVII L contains eight proline residues, whereas DA L contains seven, since aa position 57 (L^{57}) is a proline in the case of the GDVII strain but is a serine in the case of the DA strain.

We questioned whether the difference in L^{57} regulates the structure of L and thereby affects TMEV subgroup-specific biological activities. Therefore, by generating a series of mutant viruses, we studied the possibility that L^{57} is a determinant of subgroup-specific virus growth.

MATERIALS AND METHODS

Cells and virus assay. BHK-21 cells, a baby hamster kidney-derived fibroblast cell line permissive for TMEV infection, were maintained in Eagle's minimum essential medium (Nissui, Tokyo, Japan) supplemented with 5% calf serum (Invitrogen, Carlsbad, CA). A standard plaque assay was performed at 37°C for 3 days.

Mutant viruses. A series of mutant cDNAs are shown in Fig. 1. $pDAL_{Pro}$ and $pDAL_{Pro}/L^*$-1 were generated by site-directed mutagenesis using a full-length DA infectious cDNA (pDAFL3) (29) and pDAL*-1 (8), respectively, as a template. pDAL*-1 is a mutant construct in which the only difference from pDAFL3 is a change of the AUG at nucleotide (nt) 1079, the initiation codon of the L* protein, to ACG.

In the case of $pDAL_{Pro}$, the segment spanning from XhoI to MscI sites was amplified by PCR using the following primers, containing a single nucleotide substitution changing serine to proline: primers A (5′-CTC GAG CAA TCA ACC TGA AAC-3′) and B (5′-AGA CAC CTC CGT CCT CGC CAG-3′) and primers C (5′-GTT TCA GGT TGA TTG CTC GAG-3′) and D (5′-AAC ATG CAG AGT AAC GCG AAG-3′) (the nucleotide inducing a single amino acid substitution of serine to proline is underlined). The PCR products were hybridized after purification using a QIAquick gel extraction kit (QIAGEN, United Kingdom). The hybridized DNA was then amplified by PCR with primers A and D. The PCR product and pDAFL3 were digested with XhoI and MscI (TOYOBO, Osaka, Japan), and the digested PCR fragment was replaced with the corresponding fragment in pDAFL3. In the case of $pDAL^*\text{-}1/L_{Pro}$, the XhoI- and MscI-digested fragment amplified by PCR as described above was replaced with the corresponding fragment in pDAL*-1. This point mutation of L did not change the amino acid sequence of L*, which is synthesized out of frame with the polyprotein only in TO subgroup strains (23, 25, 30).

$pGDVIIL_{Ser}$ was constructed by using a full-length GDVII infectious cDNA, pGDVIIFL2 (11), as a template. The segment spanning from KpnI to MscI sites was also amplified by PCR using the following primers: primers E (5′-TGA ACC CCT GAA TGG CGA TC-3′) and F (5′-CGG ACA CTA GTA CTC AAT CTC-3′) and primers G (5′-GAG ATT GAG TAC TAG TGT CCG-3′) and H (5′-GAT TGT CAG CAT TGA TCT TGG TG-3′) (the nucleotide inducing a single amino acid substitution of proline to serine is underlined). The PCR product and pGDVIIFL2 were digested with KpnI and MscI (TOYOBO), and the digested PCR fragment was replaced with the corresponding fragment in pGDVIIFL2.

In $pDAL_{Pro}$, $pDAL^*\text{-}1/L_{Pro}$, and $pGDVIIL_{Ser}$, PCR-amplified segments and the regions adjacent to the sites of ligation were sequenced completely on both

* Corresponding author. Mailing address: Department of Microbiology, Kanazawa Medical University, 1-1 Uchinada, Ishikawa 920-0293, Japan. Phone: 81-76-286-2211. Fax: 81-76-286-3961. E-mail: ohara@kanazawa-med.ac.jp.

[▽] Published ahead of print on 27 September 2006.

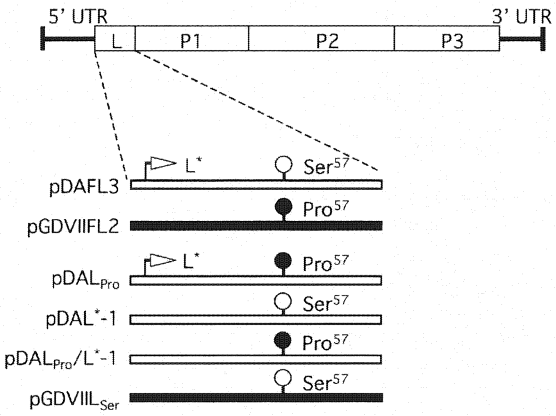

FIG. 1. Series of parental and mutant cDNAs. The position of the TMEV coding area is shown at the top. pDAFL3 and pGDVIIFL2 are parental cDNAs derived from DA and GDVII, respectively. DA and GDVII genomes are shown as open and solid bars, respectively. pDAL*-1 has a mutation changing the initiation codon AUG of L* to ACG; therefore, it fails to synthesize L*. Mutant constructs DAL_{Pro} and DAL_{Pro}/L*-1 were generated by introducing a mutation at nt 1234, leading to a predicted change in the amino acid residue at position 57 (L^{57}) from the serine of DA to proline. Another mutant construct, $GDVIIIL_{Ser}$, was generated by introducing a mutation into nt 1236, leading to a predicted change in L^{57} from the proline of GDVII to serine. UTR, untranslated region.

strands. No unexpected mutations were observed. The plasmids were linearized with XbaI (TOYOBO), and viral RNA was synthesized by T7 RNA polymerase (Promega, Madison, WI). BHK-21 cells were then transfected with the synthesized RNA using Lipofectin (Invitrogen) according to the manufacturer's instructions. Virus was purified by a standard plaque purification technique described previously (2). The sizes of plaques before and after the purification were identical. Purified virus was propagated on BHK-21 cells and used in the following experiments.

Kinetics of virus growth. The kinetics of growth of parental and mutant viruses on BHK-21 cells were examined as previously described (22). A 35-mm-diameter plastic culture dish containing 1×10^6 cells was infected at a multiplicity of infection (MOI) of 10 PFU per cell. At the indicated times, the infected cells with supernatants were harvested, and plaque formation on BHK-21 cells was assayed after freezing and thawing three times.

RT-PCR. BHK cells were infected with parental and mutant viruses at an MOI of 10 PFU per cell. Total RNA was isolated from the infected cells at the indicated times (0, 3, 6, 9, and 12 h) after infection using TRIzol reagent (Invitrogen) according to the manufacturer's instruction. Viral RNA synthesis and mRNA expression of mouse β-actin were analyzed by semiquantitative reverse transcription (RT)-PCR. cDNA was synthesized using M-MLV reverse transcriptase (Invitrogen). The 1/20 volume of each RT mixture was subjected to the PCR (94°C for 10 s, 60°C for 20 s, and 72°C for 60 s) using the following primers: 5′-TCAACTCTGACATCCTCACTCTCG-3′ and 5′-GACGTCCGTG AACCTTGTAGTCAA-3′ for TMEV RNA and 5′-ATGGATGACGATATCG CT-3′ and 5′-ATGAGGTAGTCTGTCAGGT-3′ for mouse β-actin as a control. The number of cycles was determined to be 32, since the preliminary data showed that the cycle number was sufficient before the plateau of amplification.

Pulse-labeling experiment for viral and cellular proteins. BHK-21 cells were infected with virus at an MOI of 10 PFU/cell. The infected cells were incubated in methionine- and cysteine-free medium (Sigma-Aldrich, St. Louis, MO) for 30 min prior to the indicated times, followed by incubation for 1 h in medium containing 75 μCi of L-[^{35}S]methionine and L-[^{35}S]cysteine (GE Healthcare Bio-Science, Piscataway, NJ). The radiolabeled cells were scraped, washed twice with ice-cold phosphate-buffered saline (PBS), and lysed in lysis buffer (5 mM Tris-HCl [pH 7.4], 150 mM NaCl, 1% sodium deoxycholate, 1 mM EDTA, 1% NP-40,) for 30 min on ice. After centrifugation at 15,000 rpm for 10 min at 4°C, the radiolabeled proteins in the supernatant were separated by sodium dodecyl sulfate (SDS)–12% polyacrylamide gel electrophoresis (PAGE) and analyzed by autoradiography. The analysis was performed in triplicate.

Determination of viral assembly intermediates by sucrose gradient. Subconfluent BHK-21 cells (3×10^6 cells in a 25-cm^2 flask) were infected with viruses at an MOI of 10 PFU per cell and incubated for 3 h. The infected cells were incubated in methionine- and cysteine-free medium for 30 min prior to the addition of 100 μCi of L-[^{35}S]methionine and L-[^{35}S]cysteine. Following radiolabeling for 4 h, the cells were lysed in 400 μl of lysis buffer as described above. The supernatants were layered onto 5 to 20% or 15 to 30% linear sucrose gradients in lysis buffer (11 ml). Gradients were centrifuged in an SW41 rotor (Beckman, Fullerton, CA) at 35,000 rpm for 16 h or 18,000 rpm for 10 h. Fractions (0.3 ml each) were collected by pumping from the bottom of the sucrose gradient. An aliquot (0.1 ml) of each fraction was counted using a scintillation counter.

Western blotting. The proteins extracted from 5×10^4 infected cells were separated on a Tris-Tricine gel and transferred onto a polyvinylidene difluoride membrane (Millipore, Billerica, MA). The membrane was blocked with 5% skim milk in Tris-buffered saline–Tween (50 mM Tris-HCl [pH 7.4], 0.45% sodium chloride, and 0.05% Tween 20) for 1 h and incubated at room temperature for 2 h with polyclonal rabbit anti-L antibody (see below), followed by incubation with horseradish peroxidase-conjugated donkey anti-rabbit immunoglobulin G antibody (Jackson Immunoresearch Laboratory, West Grove, PA) for 1 h. Signals were detected using ECL Western blotting detection reagents (GE Healthcare Bio-Science) according to the manufacturer's instructions. In order to generate anti-L antibody, L of the DA strain was expressed as a fusion protein with maltose-binding protein in a bacterial expression plasmid, pMALc2X (New England Bio Labs, Beverly, MA). The L fusion protein was used to immunize a rabbit. The anti-L antibody detected the L of both GDVII and DA strains.

Immunoprecipitation. Lysis buffer (0.2 ml) was added to a part of each fraction (0.2 ml) of the sucrose gradients. The fractions were then incubated for 1 h at 4°C with protein G (GE Healthcare Bio-Science), which was incubated with the rabbit preimmune sera. The supernatants were separated by centrifugation and then incubated for 3 h at 4°C with protein G, which was incubated with polyclonal rabbit anti-GDVII antibody. The anti-GDVII antibody was raised against GDVII particles purified on a cesium chloride gradient and then dialyzed in PBS. This antibody detected DA as well as GDVII viral capsid proteins. The immunoprecipitates were washed twice with ice-cold PBS, and the proteins were then separated by SDS–15% PAGE. The gels were fixed and subjected to autoradiography.

RESULTS

Growth kinetics and plaque formation of parental and mutant viruses. To examine the effect(s) of L^{57} (proline or serine) on virus growth on BHK-21 cells, growth kinetics were first evaluated (Fig. 2A). DAL_{Pro}, DAL_{Pro}/L*-1, and GDVII viruses, which contain proline at L^{57}, showed very similar patterns of growth. The titers of these viruses ranged from 2.5 to 9.3×10^6 PFU/ml at 6 h postinfection (p.i.) and gradually increased thereafter, reaching a peak of 7.0 to 8.8×10^8 PFU/ml at 24 h p.i. On the other hand, the yield of viruses containing serine at L^{57} was lower; the titer of these viruses ranged from 2.8 to 4.9×10^5 PFU/ml at 6 h p.i. and reached a peak of only 6.0 to 8.4×10^7 PFU/ml at 24 h p.i. Despite a varying genome background, the overall yield of the viruses containing proline at L^{57} was approximately 10-fold higher than that of the viruses containing serine at the corresponding position. In addition, the size of the plaques correlated with virus growth (Fig. 2B). The plaque size of GDVII, DAL_{Pro}, and DAL_{Pro}/L*-1 viruses, in which L^{57} is proline, was 2 to 4 mm in diameter. In contrast, the size of plaques of DA, DAL*-1, and $GDVIIIL_{Ser}$ viruses, in which L^{57} is serine, was 0.5 to 1 mm in diameter.

In summary, the growth of the DA strain is enhanced by the replacement of serine with proline at L^{57}, and the growth of the GDVII strain is suppressed by the replacement of proline with serine. Therefore, the overall data suggest that L^{57} regulates virus growth on BHK-21 cells.

Viral RNA replication and viral protein synthesis. To address which step of virus multiplication is influenced by L^{57}, we

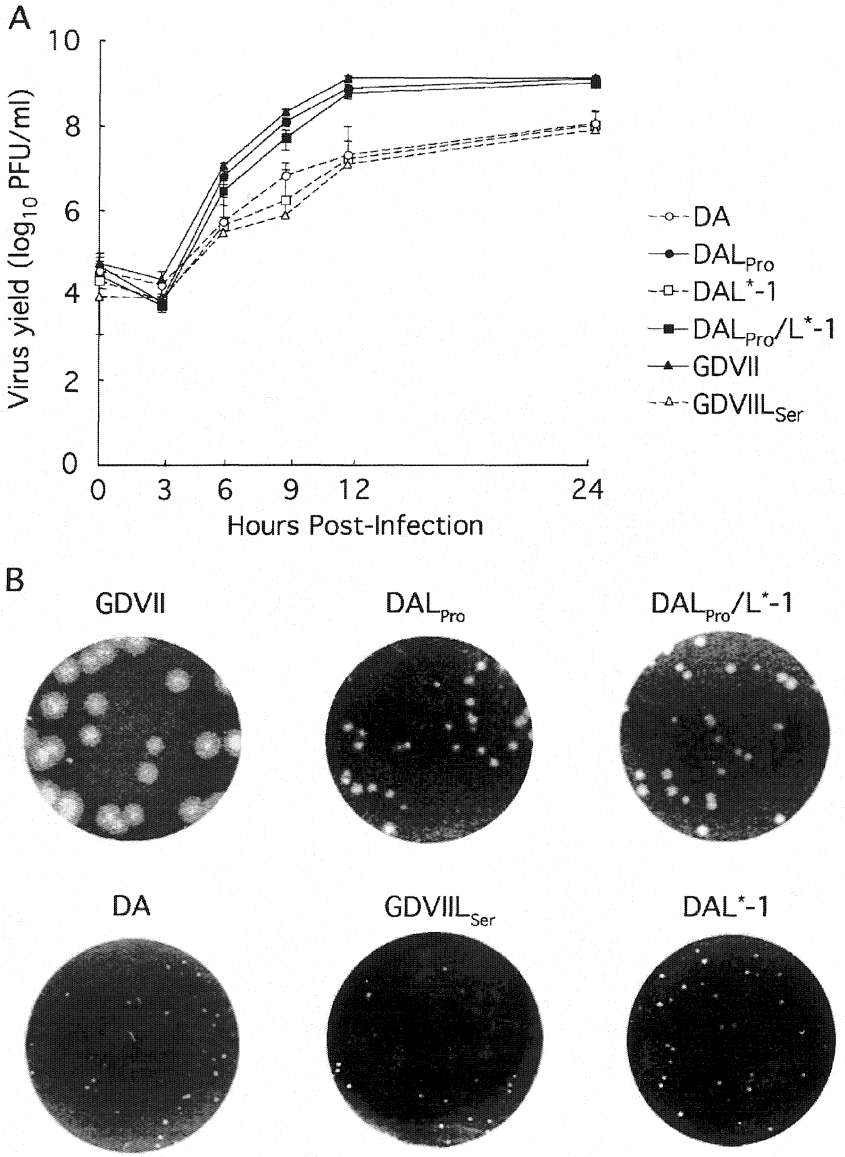

FIG. 2. (A) Kinetics of parental and mutant virus growth on BHK-21. Cells were infected with each virus at an MOI of 10 PFU per cell. At the indicated times, the infected cells with the supernatants were harvested, and plaque formation on BHK-21 cells was assayed after freezing and thawing three times. The growth curves of DAL_{Pro} (●), DAL_{Pro}/L*-1 (■), and GDVII (▲) viruses, in which L^{57} is proline, were drawn with solid lines and closed symbols. Those of DA (○), DAL*-1 (□), and $GDVIIL_{Ser}$ (△) viruses, in which L^{57} is serine, were drawn with dotted liens and open symbols. (B) Plaque sizes of parental and mutant viruses on BHK-21. Results were obtained with a 10^{-6} or 10^{-7} dilution of parental and mutant viruses.

examined viral RNA replication and protein synthesis of parental and mutant viruses on BHK-21 cells. We first evaluated viral RNA replication at 0, 3, 6, 9, and 12 h p.i. by semiquantitative PCR. No significant differences in the amplified bands were observed among all six viruses throughout the time course. The representative data at 6 h p.i. are shown in Fig. 3A.

We next evaluated virus protein synthesis at 0. 3, 6, 9, and 12 h p.i. in a pulse-labeling experiment (Fig. 3B). At 3 h p.i., viral proteins started to be prominent, although cellular proteins were still synthesized. At 6 h p.i., host protein shutoff appeared, and in parallel, viral proteins became prominent. This tendency was observed up to 12 h p.i. There were no significant differences in the amounts of viral proteins synthesized by all six viruses that had either proline or serine at L^{57}. The similarity in kinetics suggested that there were no significant differences in viral protein processing among the samples. To further confirm the processing of L, the amounts of L were examined by Western blotting using rabbit anti-L antibody at 7.5 h p.i. L was detected in equal amounts among all the viruses (Fig. 3C). In summary, the data demonstrate that L^{57} does not affect viral RNA replication and the synthesis and processing of viral proteins.

Virion assembly. The efficiency of virion assembly may account for the regulation of virus growth by L^{57}. Therefore, we examined the mature virion and assembly intermediates by sedimentation of infected BHK-21 cell lysates on sucrose den-

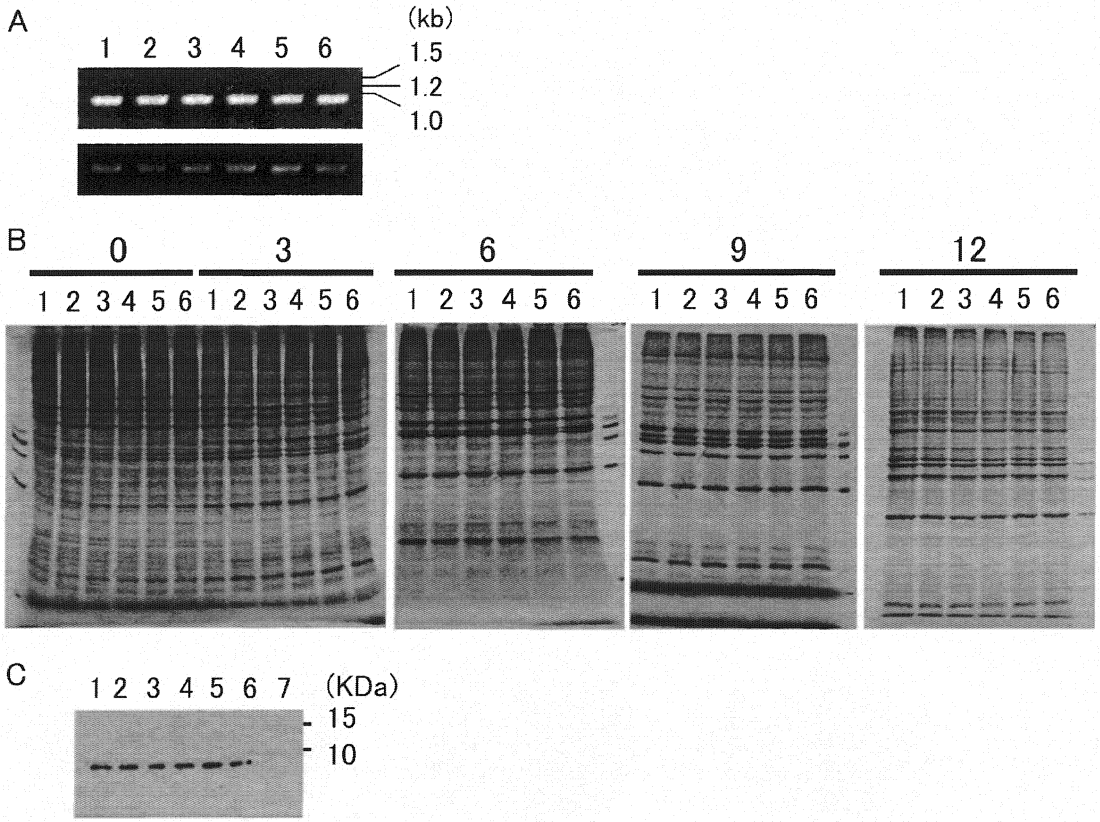

FIG. 3. Viral replication and protein synthesis in infected BHK-21 cells. (A) TMEV genomic RNA (upper panel) and β-actin mRNA (lower panel). BHK-21 cells were infected with DA, DAL_{Pro}, DAL*-1, DAL_{Pro}/L*-1, GDVII, or $GDVIII_{Ser}$ virus at an MOI of 10 PFU per cell. At 6 h p.i., the infected cells were harvested, and total RNA was extracted from cells infected with parental and mutant viruses. Reverse-transcribed cDNA was subjected to RT-PCR as described in the text. (B) TMEV protein synthesis. BHK-21 cells were also infected with those viruses at an MOI of 10 PFU per cell. The number at the top indicates hours p.i. The cells were labeled with [^{35}S]methionine for 1 h from the indicated time as described in the text. (C) L synthesis. Lysates from BHK-21 cells 7.5 h p.i. were subjected to Western blotting using anti-L antibody as described in the text. In A, B, and C, lane 1 shows DA-infected BHK-21 cells, lane 2 shows DAL*-1-infected cells, lane 3 shows DAL_{Pro}-infected cells, lane 4 shows DAL_{Pro}/L*-1-infected cells, lane 5 shows GDVII-infected cells, and lane 6 shows $GDVIII_{Ser}$-infected cells. Lane 7 in C shows noninfected BHK-21 cells as a negative control.

sity gradients. The fractionation from 5 to 20% sucrose gradients identified two peaks: one peak corresponded to the 5S protomer (fraction 16), and the other peak corresponded to the 14S pentamer (fractions 3 to 9). The patterns of the sedimentation profiles of the protomers and pentamers of six viruses were very similar (Fig. 4A).

To confirm whether these fractions contain assembly intermediates, immunoprecipitation using anti-GDVII antibody followed by SDS-PAGE was performed. VP0, VP1, and VP3 were clearly detected in the corresponding fractions (Fig. 4B).

Since no significant differences were observed in the assembly of the protomer and pentamer among all the viruses, virions and empty capsids in the lysates of infected cells were examined (Fig. 5). The fractions from 15 to 30% sucrose gradients showed two peaks corresponding to empty capsids (fractions 17 to 19) and mature virions (fraction 3) (Fig. 5A). No significant differences were detected in the 75S empty capsid peaks among all the viruses. However, the counts of the mature virion peaks of DAL_{Pro}, DAL_{Pro}/L*-1, and GDVII viruses were approximately threefold higher than those of $GDVIII_{Ser}$, DAL*-1, and DA viruses. Fraction 3 was shown to contain mature virions, since VP2 and VP4 were detected by immunoprecipitation (Fig. 5B). Immunoprecipitation of fractions 17 and 19 also detected VP0, the precursor protein of VP2 and VP4, suggesting that fractions 17 to 19 contain empty capsids (Fig. 5B).

In summary, the amount of mature virions of DA was enhanced by the replacement of serine with proline at L^{57}, and the amount of mature virions of GDVII was suppressed by the replacement of proline with serine at L^{57}. These data suggest that L^{57} may regulate the efficiency of viral RNA encapsidation.

DISCUSSION

Using a series of mutant viruses, we demonstrated a correlation between virus growth on BHK-21 cells and L^{57} (proline or serine). $GDVIII_{Ser}$, in which proline is replaced with serine at L^{57}, showed the same pattern of virus growth as DA. On the other hand, DAL_{Pro} and DAL_{Pro}/L*-1, in which proline is replaced with serine, showed the same pattern of enhanced virus growth as GDVII. However, the plaque sizes of DAL_{Pro} and DAL_{Pro}/L*-1 were not as large as that of GDVII (Fig. 2B). The size of the plaque reflects not only the growth of virus but

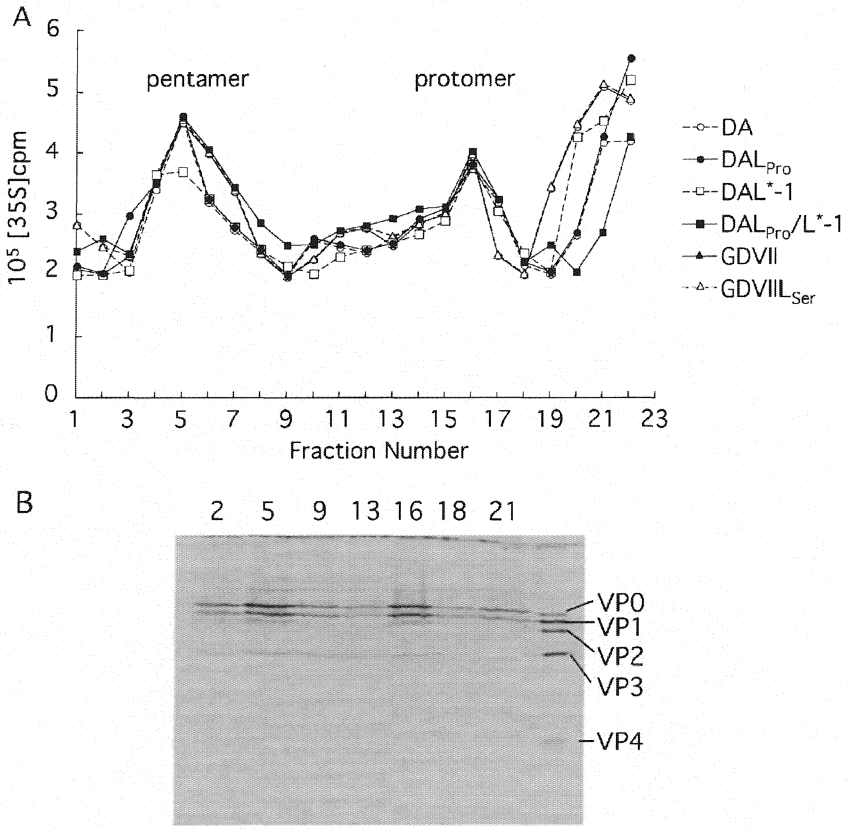

FIG. 4. Sucrose gradient sedimentation of capsid precursors synthesized during infection. (A) Virus assembly intermediates, the 5S protomer, and the 14S pentamer were detected in lysates of BHK-21 cells (3×10^6 cells) infected with DA, DAL_{Pro}, DAL*-1, DAL_{Pro}/L*-1, $GDVIIL_{Ser}$, or GDVII virus at an MOI of 10 PFU per cell. The infected cells were radiolabeled as described in the text. Lysates were fractionated on 5 to 20% gradients. (B) Confirmation of viral assembly intermediates by immunoprecipitation. Representative data for DAL_{Pro}-infected cells are shown. The numbers at the top indicate the fraction numbers. The fractions were immunoprecipitated and then analyzed by SDS-PAGE.

also the cell-to-cell extension of virus. A sequence(s) other than that of L^{57} may affect the extension of virus. In addition, we examined the in vivo phenotypes of those mutants. DAL_{Pro} and DAL_{Pro}/L*-1 caused acute encephalomyelitis and mainly infected neurons. However, mice showed no apparent clinical signs in the acute stage and survived. On the other hand, $GDVII_{Ser}$ caused acute fatal encephalomyelitis with severe neuronal damage, like the parental GDVII strain (data not shown). This indicates that L^{57} does not regulate in vivo phenotypes of TMEV. Further studies on in vivo phenotypes of those mutant viruses will be important and are now in progress.

TMEV L plays a role in host cell-restricted infection. L-deleted DA mutant virus cannot grow efficiently in L929 cells (16), which can produce IFN. L-deleted DA mutant virus growth is relatively unaffected in BHK-21 cells (6), which have a defect in IFN synthesis. The L of the DA strain inhibits the transcription of IFN-α/β by interfering in the nuclear localization of the transcription factor IFN regulatory factor 3 (10). The zinc-binding motif of L, Cys^3-His^5-Cys^{11}-Cys^{14}, which is located 44 aa upstream of L^{57}, has the function of inhibiting IFN-α/β transcription (35). In this study, it was demonstrated that L regulates subgroup-specific virus growth on BHK-21 cells. Thus, the L of TMEV works as a multifunctional regulator.

In the present study, the growth pattern on BHK-21 cells was not changed in viruses that expressed or failed to express L*, suggesting that L* does not influence the virus growth on BHK-21 cells. These results show that L* is not important for TMEV subgroup-specific virus growth on BHK-21 cells, although L* is an essential protein for virus growth on macrophages (13, 24, 32) and plays a role in virus persistence and demyelination (8, 23, 30).

L^{57}, whether it is proline or serine, did not affect viral RNA replication, the synthesis of viral proteins, or the assembly of viral intermediates; however, the peak of 150S mature virions was regulated with L^{57}. The pulse-labeling experiment showed that the amounts of VP0, VP2, and VP4 were the same among all the viruses (Fig. 3B), suggesting that the cleavage of VP0 into VP2 and VP4, which is required for virus assembly, was normally processed. It was, however, previously reported that neither virions nor empty capsids were detected in L929 cells infected with L-deleted GDVII mutant virus (3). Those investigators speculated that L may be responsible for the assembly. Since L is present in our mutant viruses, amino acid residue(s) other than L^{57} may be involved in the formation of empty capsids.

In picornaviruses, it is thought that RNA encapsidation and the replication process of positive-strand RNA are linked to each other (21, 33). The newly synthesized progeny RNA is encapsidated into the capsid proteins as soon as RNA is syn-

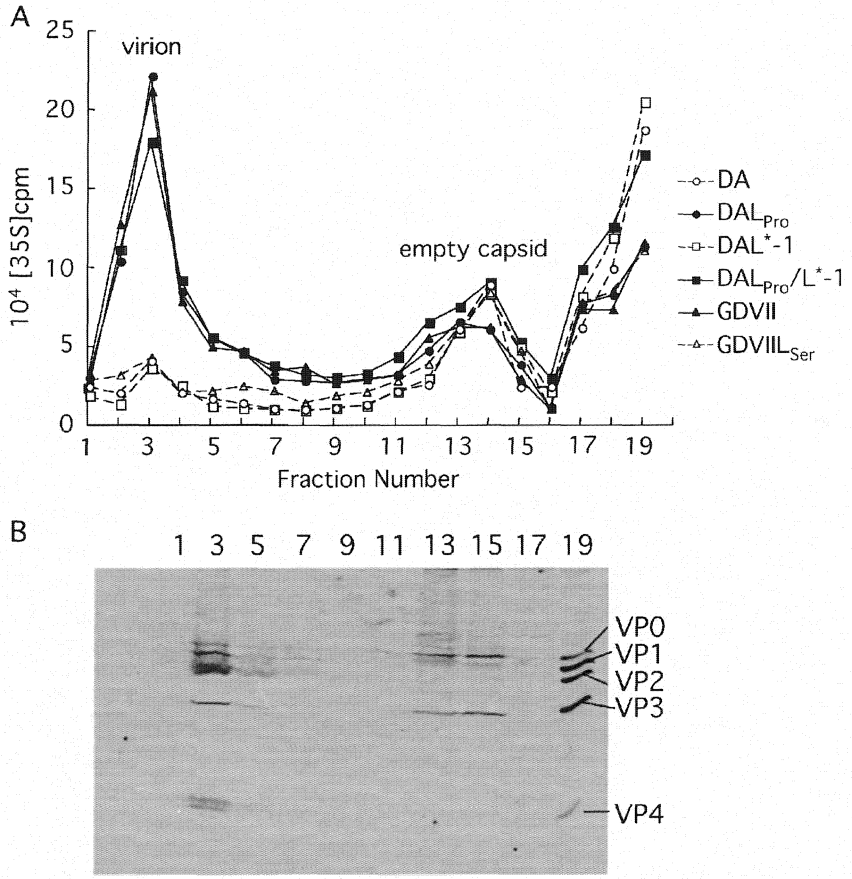

FIG. 5. Analysis of virion assembly by sucrose gradient sedimentation. (A) The 75S empty capsid and 150S virion were detected in lysates of BHK-21 cells (3×10^6 cells) infected with parental and mutant viruses at an MOI of 10 PFU per cell. The infected cells were radiolabeled as described in the text. Lysates were fractionated on 15 to 30% gradients. (B) Confirmation of empty capsids and virions by immunoprecipitation. Representative data for DAL_{Pro}-infected cells are shown. The numbers at the top indicate the fraction numbers. The fractions were immunoprecipitated and then analyzed by SDS-PAGE.

thesized. In the case of Aichi virus, which belongs to the genus *Kobuvirus* of the family *Picornaviridae*, L is involved in viral RNA replication and encapsidation, since the accumulation of empty capsids was observed in the case of an L-deleted mutant virus (31). In this study, the peaks of empty capsids are almost similar among all the viruses. In addition, no accumulation of empty capsids was observed in the viruses containing serine at L^{57}. Therefore, TMEV L plays a role in viral RNA encapsidation distinct from that of Aichi virus L.

The action of L on viral RNA encapsidation also differs from that of poliovirus 2C protein (PV2C), which is responsible for the binding of newly synthesized viral RNA to the vesicular membranes and for the organization of the replication complex, thereby affecting the efficiency of viral RNA encapsidation (4, 5, 34). The membrane- and RNA-binding domains present within PV2C (28) were not found in TMEV L. Therefore, L of TMEV differs from PV2C in its role in viral RNA encapsidation. Further studies are required in order to clarify the mechanism(s) of L-regulated TMEV RNA encapsidation.

Proline has unique conformational and structural properties. Since L^{57} of GDVII is a proline residue that has the highest reverse turn probability, GDVII L may be structurally distinct from DA L (9). In addition, *cis-trans* isomerization at a proline residue alters the protein structure. This structural change plays an important role in protein-protein interactions, ligand-receptor binding, and interconversion of the open and closed states of the ion channel (7, 15, 19). A structural difference in L may alter the utilization and/or interference of cellular and viral proteins, resulting in the change of viral RNA encapsidation efficiency.

Another potentially important reason for the influence of L^{57} might relate to the phosphorylation of the serine. Phosphorylation of serine can regulate protein-protein interactions as well as kinase, phosphatase, and protease activities (1, 12, 14). Therefore, the phosphorylation of serine at position 57 may foster the binding of L to some host protein(s), resulting in a decrease in TMEV RNA encapsidation.

Finally, previous works (16, 27) reported that the entire substitution of DAL for GDVIIL does not give any differences in in vitro and in vivo phenotypes. As described above, a single amino acid change of L (either proline or serine) may change the structure and property of L or may be compensated for by another divergent amino acid residue of L. This could lead to the alteration of phenotypes of mutants in the present study.

The identification of binding partners of L may provide new insights into RNA encapsidation and may also lead to an

increase in our understanding of the pathogenesis of TMEV-induced diseases.

ACKNOWLEDGMENTS

We thank M. Higashino, K. Asakura, and S. Saito for technical assistance.

This study was supported by a grant-in-aid for scientific research from the Ministry of Education, Science, Sports, and Culture; a grant from the Neuroimmunological Research Committee of the Ministry of Health, Labor, and Welfare; a grant for promoted research from Kanazawa Medical University (S2005-12), and a grant for project research from the High-Technology Center of Kanazawa Medical University (2004-7).

REFERENCES

1. **Amaravadi, R., and C. B. Thompson.** 2005. The survival kinases Akt and Pim as potential pharmacological targets. J. Clin. Investig. **115:**2618–2624.
2. **Asakura, K., H. Murayama, T. Himeda, and Y. Ohara.** 2002. Epitope-tagged L* protein of Theiler's murine encephalomyelitis virus is expressed in the central nervous system in the acute phase of infection. J. Virol. **76:**13049–13054.
3. **Badshah, C., M. A. Calenoff, and K. Rundell.** 2000. The leader polypeptide of Theiler's murine encephalomyelitis virus is required for the assembly of virions in mouse L cells. J. Virol. **74:**875–882.
4. **Banerjee, R., A. Echeverri, and A. Dasgupta.** 1997. Poliovirus-encoded 2C polypeptide specifically binds to the 3′-terminal sequences of viral negative-strand RNA. J. Virol. **71:**9570–9578.
5. **Bienz, K., D. Egger, M. Troxler, and L. Pasamontes.** 1990. Structural organization of poliovirus RNA replication is mediated by viral proteins of the P2 genomic region. J. Virol. **64:**1156–1163.
6. **Calenoff, M. A., C. S. Badshah, M. C. Dal Canto, H. L. Lipton, and M. K. Rundell.** 1995. The leader polypeptide of Theiler's virus is essential for neurovirulence but not for virus growth in BHK cells. J. Virol. **69:**5544–5549.
7. **Cameron, A. M., F. C. Nucifora, Jr., E. T. Fung, D. J. Livingston, R. A. Aldape, C. A. Ross, and S. H. Snyder.** 1997. FKBP12 binds the inositol 1,4,5-trisphosphate receptor at leucine-proline (1400–1401) and anchors calcineurin to this FK506-like domain. J. Biol. Chem. **272:**27582–27588.
8. **Chen, H.-H., W.-P. Kong, L. Zhang, P. L. Ward, and R. P. Roos.** 1995. A picornaviral protein synthesized out of frame with the polyprotein plays a key role in a virus-induced immune-mediated demyelinating disease. Nat. Med. **1:**927–931.
9. **Creighton, T. E.** 1984. Proteins: structural and molecular principles. W. H. Freeman and Co., New York, N.Y.
10. **Delhaye, S., V. van Pesch, and T. Michiels.** 2004. The leader protein of Theiler's virus interferes with nucleocytoplasmic trafficking of cellular proteins. J. Virol. **78:**4357–4362.
11. **Fu, J. L., S. Stein, L. Rosenstein, T. Bodwell, M. Routbort, B. L. Semler, and R. P. Roos.** 1990. Neurovirulence determinants of genetically engineered Theiler viruses. Proc. Natl. Acad. Sci. USA **87:**4125–4129.
12. **Gazina, E. V., J. E. Fielding, B. Lin, and D. A. Anderson.** 2000. Core protein phosphorylation modulates pregenomic RNA encapsidation to different extents in human and duck hepatitis B viruses. J. Virol. **74:**4721–4728.
13. **Himeda, T., Y. Ohara, K. Asakura, Y. Kontani, M. Murakami, H. Suzuki, and M. Sawada.** 2005. A lentiviral expression system demonstrates that L* protein of Theiler's murine encephalomyelitis virus (TMEV) is essential for virus growth in a murine macrophage-like cell line. Virus Res. **108:**23–28.
14. **Hiscott, J., H. Kwon, and P. Genin.** 2001. Hostile takeovers: viral appropriation of the NF-κB pathway. J. Clin. Investig. **107:**143–151.
15. **Howard, B. R., F. F. Vajdos, S. Li, I. Sundquist, and C. P. Hill.** 2003. Structural insights into the catalytic mechanism of cyclophilin A. Nat. Struct. Biol. **10:**475–481.
16. **Kong, W. P., G. D. Ghadge, and R. P. Roos.** 1994. Involvement of cardiovirus leader in host cell-restricted virus expression. Proc. Natl. Acad. Sci. USA **91:**1796–1800.
17. **Leong, L. E. C., C. T. Cornell, and B. L. Semler.** 2002. Processing determinants and functions of cleavage products of picornavirus polyproteins, p. 187–197. *In* B. L. Semler and E. Wimmer (ed.), Molecular biology of picornaviruses. ASM Press, Washington, D.C.
18. **Lipton, H. L.** 1980. Persistent Theiler's murine encephalomyelitis virus infection in mice depends on plaque size. J. Gen. Virol. **46:**169–177.
19. **Lummis, S. C. R., D. L. Beene, L. W. Lee, H. A. Lester, R. W. Broadhurst, and D. A. Dougherty.** 2005. *Cis-trans* isomerization at a proline opens the pore of a neurotransmitter-gated ion channel. Nature **438:**248–252.
20. **Michiels, T., N. Jarousse, and M. Brahic.** 1995. Analysis of the leader and capsid coding regions of persistent and neurovirulent strains of Theiler's virus. Virology **214:**550–558.
21. **Nugent, C. I., K. L. Johnson, P. Sarnow, and K. Kirkegaard.** 1999. Functional coupling between replication and packaging of poliovirus replicon RNA. J. Virol. **73:**427–435.
22. **Obuchi, M., Y. Ohara, T. Takegami, T. Murayama, H. Takada, and H. Iizuka.** 1997. Theiler's murine encephalomyelitis virus subgroup strain-specific infection in a murine macrophage-like cell line. J. Virol. **71:**729–733.
23. **Obuchi, M., and Y. Ohara.** 1998. Theiler's murine encephalomyelitis virus and mechanisms of its persistence. Neuropathology **18:**13–18.
24. **Obuchi, M., J. Yamamoto, T. Odagiri, M. N. Uddin, H. Iizuka, and Y. Ohara.** 2000. L* protein of Theiler's murine encephalomyelitis virus is required for virus growth in a murine macrophage-like cell line. J. Virol. **74:**4898–4901.
25. **Obuchi, M., T. Odagiri, K. Asakura, and Y. Ohara.** 2001. Association of L* protein of Theiler's murine encephalomyelitis virus with microtubules in infected cells. Virology **289:**95–102.
26. **Oleszak, E. L., J. R. Chang, H. Friedman, C. D. Katsetos, and C. D. Platsoucas.** 2004. Theiler's virus infection: a model for multiple sclerosis. Clin. Microbiol. Rev. **17:**174–207.
27. **Paul, S., and T. Michiel.** 2006. Cardiovirus leader proteins are functionally interchangeable and have evolved to adapt to virus replication fitness. J. Gen. Virol. **87:**1237–1246.
28. **Rodríguez, P. L., and L. Carrasco.** 1995. Poliovirus protein 2C contains two regions involved in RNA binding activity. J. Biol. Chem. **270:**10105–10112.
29. **Roos, R. P., S. Stein, Y. Ohara, J. Fu, and B. L. Semler.** 1989. Infectious cDNA clones of the DA strain of Theiler's murine encephalomyelitis virus. J. Virol. **63:**5492–5496.
30. **Roos, R. P.** 2002. Pathogenesis of Theiler's murine encephalomyelitis virus-induced disease, p. 427–435. *In* B. L. Semler and E. Wimmer (ed.), Molecular biology of picornaviruses. ASM Press, Washington, D.C.
31. **Sasaki, J., S. Nagashima, and K. Taniguchi.** 2003. Aichi virus leader protein is involved in viral RNA replication and encapsidation. J. Virol. **77:**10799–10807.
32. **Takata, H., M. Obuchi, J. Yamamoto, T. Odagiri, R. P. Roos, H. Iizuka, and Y. Ohara.** 1998. L* protein of the DA strain of Theiler's murine encephalomyelitis virus is important for virus growth in a murine macrophage-like cell line. J. Virol. **72:**4950–4955.
33. **Troxler, M., D. Egger, T. Pfister, and K. Bienz.** 1992. Intracellular localization of poliovirus RNA by in situ hybridization at the ultrastructural level using single-stranded riboprobes. Virology **191:**687–697.
34. **Vance, L. M., N. Moscufo, M. Chow, and B. A. Heinz.** 1997. Poliovirus 2C region functions during encapsidation of viral RNA. J. Virol. **71:**8759–8765.
35. **van Pesch, V., O. van Eyll, and T. Michiels.** 2001. The leader protein of Theiler's virus inhibits immediate-early alpha/beta interferon protection. J. Virol. **75:**7811–7817.

Journal of Neuroinflammation

BioMed Central

Review

Open Access

Leader (L) and L* proteins of Theiler's murine encephalomyelitis virus (TMEV) and their regulation of the virus' biological activities

Masumi Takano-Maruyama, Yoshiro Ohara*, Kunihiko Asakura and Takako Okuwa

Address: Department of Microbiology, Kanazawa Medical University, Uchinada, Ishikawa 920-0293, Japan

Email: Masumi Takano-Maruyama - maru0812@kanazawa-med.ac.jp; Yoshiro Ohara* - ohara@kanazawa-med.ac.jp; Kunihiko Asakura - kasakura@kanazawa-med.ac.jp; Takako Okuwa - tokuwa@kanazawa-med.ac.jp

* Corresponding author

Published: 16 August 2006

Journal of Neuroinflammation 2006, **3**:19 doi:10.1186/1742-2094-3-19

Received: 05 January 2006
Accepted: 16 August 2006

This article is available from: http://www.jneuroinflammation.com/content/3/1/19

Abstract

Theiler's murine encephalomyelitis virus (TMEV) is divided into two subgroups on the basis of their different biological activities. GDVII subgroup strains produce fatal poliomyelitis in mice without virus persistence or demyelination. In contrast, TO subgroup strains induce demyelinating disease with virus persistence in the spinal cords of weanling mice. Two proteins, whose open reading frames are located in the N-terminus of the polyprotein, recently have been reported to be important for TMEV biological activities. One is leader (L) protein and is processed from the most N-terminus of the polyprotein; its function is still unknown. Although the homology of capsid proteins between DA (a representative strain of TO subgroup) and GDVII strains is over 94% at the amino acid level, that of L shows only 85%. Therefore, L is thought to be a key protein for the subgroup-specific biological activities of TMEV. Various studies have demonstrated that L plays important roles in the escape of virus from host immune defenses in the early stage of infection. The second protein is a 17–18 kDa protein, L*, which is synthesized out-of-frame with the polyprotein. Only TO subgroup strains produce L* since GDVII subgroup strains have an ACG rather than AUG at the initiation site and therefore do not synthesize L*. 'Loss and gain of function' experiments demonstrate that L* is essential for virus growth in macrophages, a target cell for TMEV persistence. L* also has been demonstrated to be necessary for TMEV persistence and demyelination. Further analysis of L and L* will help elucidate the pathomechanism(s) of TMEV-induced demyelinating disease.

Introduction

Theiler's murine encephalomyelitis virus (TMEV) belongs to the genus *Cardiovirus* of the family *Picornaviridae* and is classified into two subgroups of strains [1-4]. Although the sequence identity between strains from these two subgroups is 90.4% at the nucleotide (nt) level and 95.7% at the amino acid (AA) level [5,6], these subgroup strains induce widely different biological activities. GDVII subgroup strains produce acute fatal polioencephalomyelitis in mice without virus persistence or demyelination. On the other hand, TO subgroup strains cause a milder polioencephalomyelitis followed by virus persistence and demyelination. The pathological features of this demyelination are reminiscent of the human demyelinating disease, multiple sclerosis (MS) (Fig. 1) [1-4]. Although several other viruses are known to induce demyelination

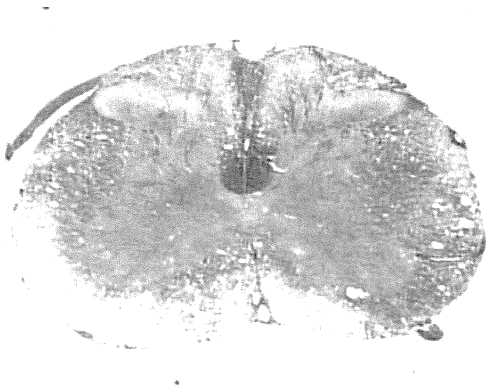

Figure 1
Theiler's murine encephalomyelitis virus (TMEV)-induced demyelination. Spinal cord from a female SJL/J mouse 6 months postinoculation (p.i.) with DA strain of TMEV. Severe demyelination and scattered inflammatory cell infiltration are observed in the white matter (Klüver-Barrera stain, x40).

[7], TMEV-induced demyelinating disease serves as an excellent animal model for MS [1-4]. However, the precise mechanisms of virus persistence and demyelination still remain unknown.

Since infectious cDNAs were constructed from the late 1980s to the early 1990s [8-11], various studies using recombinant viruses between GDVII and DA (or BeAn) strains have been carried out to clarify the region responsible for those biological activities. The studies have demonstrated that capsid proteins, especially VP1 and VP2, are important for virus persistence and demyelination [1,3]. In addition to these structural proteins, two proteins designated leader (L) and L* that are located in the N end of the polyprotein (Fig. 2) also play a role in TMEV biological activities [2,3,12].

The present review focuses on the roles of L and L* in regulating the biological activities of TMEV.

TMEV: properties and biological activities

The TMEV virion is an icosahedron approximately 28 nm in diameter with no lipid-bilayer envelope. A single-stranded RNA is packaged in the shell that consists of four capsid proteins, VP1, VP2, VP3 and VP4 [13]. Neutralizing epitopes have been identified [14-16], the nt and predicted AA sequence determined [5,9,17,18], and full-length infectious cDNAs have been constructed [8-11]. In addition, the three-dimensional structure was resolved by means of X-ray crystallography in the early 1990s [19,20]. The RNA genome is positive sense and approximately 8,100 nt long. An open reading frame (ORF) between the 5' and 3' non-coding regions is translated into a long polyprotein, which is then cleaved into L, P1, P2 and P3. The 5' terminus is covalently linked to VPg, which plays a role in RNA replication. The 3' non-coding region has a poly (A) tract. The coding regions for L and L* are located at the most 5' terminus of the polyprotein coding region (Fig. 2). Details of this will be described later.

GDVII subgroup strains, typified by the GDVII strain, are highly virulent and cause an acute fatal polioencephalomyelitis in mice after intracerebral and peripheral routes of inoculation. After an incubation period of usually less than 2 weeks, infected mice show circling, cachexia, and ruffled hair with a progressive flaccid paralysis. Neither virus persistence nor demyelination is observed in the few surviving mice. Histopathological examination reveals severe necrosis of neurons of the hippocampus, cortex, and spinal cord anterior horn, with microgliosis, neuronophagia, and inflammatory cell infiltration [1-4].

On the other hand, TO subgroup strains cause a biphasic disease after intracerebral inoculation. The early disease, which appears 1–2 weeks postinoculation (p.i.), has clinical and pathological features that are similar to those seen with the GDVII subgroup strains, but milder. Mice recover from the early disease and then develop a chronic, progressive white matter demyelinating disease 1–2 months p.i. Clinical signs include spastic paralysis, inactivity and urinary incontinence. The demyelination mainly affects the spinal cord, with an unexplained sparing of the cerebellar hemispheric white matter. These pathological findings are reminiscent of MS, that is, inflammatory cell infiltration and loss of myelin in the face of relative preservation of axons [1-4]. Therefore, this demyelinating disease is considered to be an excellent animal model for MS, as noted above.

The target cell for DA persistence

Both subgroup strains of TMEV infect mainly neurons during the acute stage of infection [1-4]. It is of interest that DA viral antigen and RNA that are present in neurons during the acute stage of infection disappear from neurons in the chronic demyelinating stage, presumably because these cells are cleared, perhaps by apoptosis. The cellular localization of DA viral antigen and RNA in the chronic demyelinating stage is somewhat controversial. There are two proposals: viral persistence in oligodendrocytes and/or viral persistence in macrophages. Immunoelectron microscopic study have shown viral antigen in oligodendrocytes at 45 days p.i. or later. Based on this, Rodriguez and coworkers proposed that a "gdying-back" process might occur in virus-infected oligodendrocytes [21,22], resulting in demyelination. In nude mice, demyelination occurs without evidence of myelin stripping by macrophages, suggesting that the demyelination occurs secondary to a lytic infection of oligodendrocytes [23].

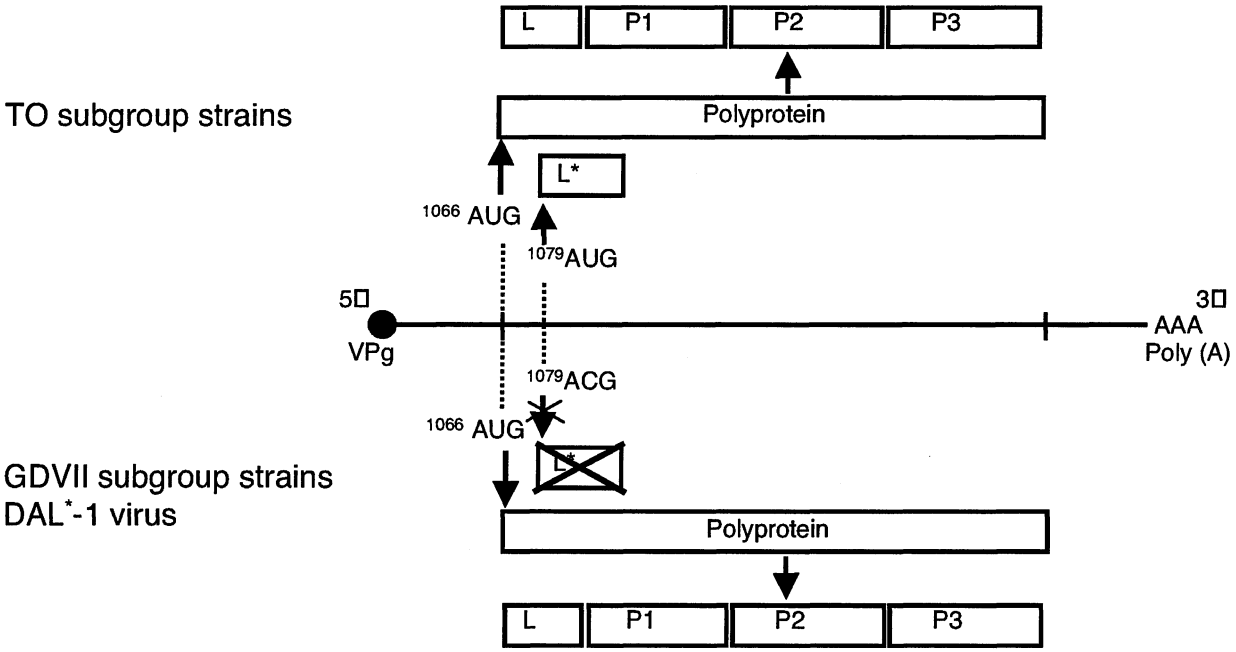

Figure 2
TMEV genome and two different initiation sites. All the TMEVs have an authentic initiation site at nucleotide (nt) 1066, from which the polyprotein is translated followed by cleavage into L, P1, P2 and P3. DA subgroup strains synthesize a small 17–18 kDa protein, L*, from an alternative, out-of-frame, initiation site, which is located at nt 1079. In contrast, GDVII subgroup strains or DAL*-1 virus do not synthesize L* since the L* initiating AUG is replaced with ACG.

Also, in nude mice, electron microscopic studies have demonstrated paracrystalline arrays of picornavirus in degenerating glial cells, many of which were identified as oligodendrocytes. A lytic infection of oligodendrocytes has been proposed as a cause of the demyelination [24]. On the other hand, a number of studies have found that the virus persists in macrophages. Using ultrastructural immnohistochemical techniques, researchers have observed viral inclusions in macrophages in and around demyelinating lesions [25]. Two-color immunofluorescent staining has shown that viral antigen is predominantly within macrophages infiltrating demyelinating lesions [26]. Infectious virus can be recovered from infiltrating mononuclear cells isolated directly from the central nervous system (CNS) [27]. Cultured primary brain macrophages can be efficiently infected with the DA strain without the induction of a significant cytopathic effect [28]. The importance of macrophages in late demyelinating disease is further emphasized by the observation that depletion of blood-borne macrophages by dichloromethylene diphosphonate prevents virus persistence in mice infected with the DA strain [29]. From these data, it appears likely that macrophages are the major cells containing persistent viral genome. Therefore, the mechanism by which DA survives in macrophages may clarify DA persistence.

L and picornaviruses

The aphthoviruses and caridioviruses are the only members of the *Picornaviridae* family that contains an L coding region at the most 5' terminus of the ORF [13]. In the case of foot-and-mouth disease virus (FMDV), an aphthovirus, L has two proteolytic functions. One is autocatalytic cleavage from the viral polyprotein [30,31], and the second is cleavage of the p220 component of the cap-binding protein complex [32], resulting in the shut off of host protein synthesis. On the other hand, the function of L of the cardioviruses is not well defined.

L has been implicated in other functions of picornaviruses. FMDV L is involved in inhibiting phosphorylation of eukaryotic initiation factor 2 by double-strand RNA-dependent protein kinase [33]. L of cardioviruses inhibits the expression of alpha/beta interferon (IFN α/β) (see later discussion), which is a critical tool to inhibit viral spread. L of mengovirus, which also belongs to the genus *Cardiovirus*, has been reported to inhibit the iron/ferritin-mediated activation of NFκB [34]. The functions of L of

TMEV and the other cardioviruses remain incompletely clarified.

The properties of TMEV L

TMEV L, which is processed from the most N-terminus of the polyprotein, consists of 76 amino acids [17,18] (Fig. 2). The release of L occurs rapidly. However, it lacks autocatalytic activity [35].

Although the identity of capsid proteins between DA and GDVII strains is over 94% at the AA level, that of L shows only 85% identity [5,6]; the low identity of the AA sequence of L between both TMEV subgroups suggests that L may contribute to the determination of the DA subgroup-specific biological activities, such as attenuated neurovirulence, viral persistence and demyelination. In addition, the identity of TMEV L with L of EMCV, which belongs to the same cardiovirus genus, is ~35 % although that of the entire coding region is about 60%. TMEV L contains a zinc-binding motif Cys-His-Cys-Cys that, interestingly, is present in L from all the cardioviruses [6,36].

Our unpublished data demonstrate that L is synthesized with the same kinetics as capsid proteins and is not incorporated into the virion. L is synthesized in the cytoplasm of host cells and, in part, transferred into the nucleus [37]. The data suggest that L may function through its interactions with cellular protein(s).

The biological activities of TMEV L

A mutant DA or GDVII virus with a deletion of L causes poor growth in the L929 mouse fibroblast cell line that produces IFN α/β, but not in BHK-21 cells producing no IFN α/β [38,39]. Since L of DA strain has been reported to inhibit the transcription of IFN α/β [36,40], the replication of virus is suppressed under pressure of IFN α/β. L prevents transcription of IFN α/β because of its interference with the nuclear localization of IFN regulatory factor 3 (IRF-3), a transcription factor required for the expression of IFN α/β [37]. The zinc-binding motif within L directly binds zinc ions and is a key factor in the inhibition of IFN α/β expression [36,37,40,41].

The importance of IFN α/β in the animal's host cell defense from TMEV infection has been demonstrated in TMEV infections of IFN α/β receptor-deficient mice [42]. These mice die of overwhelming encephalomyelitis following intracerebral inoculation with DA strain because of enhanced virus replication. Similarly, DA virus with a mutation in the zinc-binding motif of L is cleared from the CNS since the mutation induces the transcription of IFN α/β, resulting in production of IFN α/β [36].

The inhibition of IFN α/β by L, however, is not enough to allow TMEV to escape all host defense mechanisms. Indeed, DA strain is cleared after the first phase of disease in genetically resistant C57BL/6 mice in which L is expressed. Disruption of β_2-microglobulin gene in resistant mice, which fail to express class I MHC molecules and therefore lack $CD8^+$ T lymphocytes, abrogates resistance to the DA strain, allowing the virus to persist [43]. This report suggests that class I-restricted $CD8^+$ T lymphocytes are important for persistent infection, in addition to inhibition of IFN α/β by L.

*The properties of L**

During an investigation of polyprotein processing, Roos et al identified a small 17–18 kDa protein that is synthesized *in vitro* in rabbit reticulocyte lysates programmed from *in vitro*-derived transcripts of full-length clones of DA strain cDNA [35]. DA subgroup strains have an alternative translation initiation site at nt 1079, in addition to the authentic initiation site for the polyprotein at nt 1066 [44] (Fig. 2). This alternative initiation site is out-of-frame with the polyprotein and is used to translate the 17–18 kDa protein, designated L*. The synthesis of L* is TO subgroup-specific because this alternative initiation site is not present in GDVII subgroup strains (where the L* AUG is substituted by an ACG) (Fig. 2) [6,44]. Therefore, this DA subgroup-specific out-of-frame protein is thought to play an important role in characterizing the different biological activities of TMEV subgroups, especially viral persistence and demyelination.

There were initial difficulties in generating an anti-L* antibody, perhaps related to a relative lack of antigenicity or to extreme hydrophobicity resulting in solubility problems. These difficulties were overcome with the production of a rabbit polyclonal antibody against synthetic peptides corresponding to amino acid residues 70–88 (the computer-predicted antigenic site) [45,46]. Studies employing this antibody have demonstrated that L* is synthesized with kinetics similar to that of other viral proteins, although in a lesser amount. After synthesis, L* remains stable in the cytoplasm and is not incorporated into virions. Immunofluorescent staining and immunoblotting of microtubule preparations have demonstrated that L* is associated with microtubules. Experiments employing transient expression of L* have suggested that the 5' one third of the L* coding region is responsible for this association [46].

The role of L in virus growth in macrophages*

We examined the growth patterns of DA (which persists in the CNS) and GDVII (which does not persist) strains in J774-1 cells, a representative mouse macrophage cell line, since macrophages are the target cells for virus persistence, as described above [25-29]. The growth curves clearly demonstrated that DA strain grows well in J774-1 cells, while GDVII strain does not. On the other hand, both

strains grew well equally in BHK-21 cells [47]. These results are of interest since virus growth is necessary for the maintenance of the viral genome, which is essential for virus persistence [48]. TMEV subgroup-specific virus growth was studied in various other cell lines including neural cells. The results demonstrated that enhanced DA growth compared to GDVII is only observed in macrophage cell lines. Therefore, the TMEV subgroup-specific virus growth is also host cell-dependent [49].

The role of L* in TMEV subgroup-specific virus growth was further studied in a 'loss of function' experiment using a mutant virus, DAL*-1, which has an ACG rather than AUG at the initiation site of L* coding region, and therefore does not synthesize L*. Takata et al found that the DAL*-1 virus failed to grow in J774-1 cells, whereas the virus grew well in BHK-21 cells [50]. In addition, DAL*-1 virus failed to grow in other macrophage cell lines, suggesting that L* plays an important role in host cell-dependent subgroup-specific infection [49].

In order to carry out a 'gain of function' experiment to further confirm the role of L* in host cell-dependent subgroup-specific virus growth, Obuchi et al constructed a recombinant virus, DANCL*/GD, which has DA 5' noncoding and L* coding regions in the background of GDVII (with synthesis of L*). DANCL*/GD virus had enhanced growth activity in J774-1 cells compared to GDVII, suggesting that L* is important for the subgroup-specific virus growth in macrophages [45]. However, a pitfall of L* in studies such as these involving L* is that the sequence of L* overlaps with that of polyprotein (L and a part of P1). Therefore, it is impossible to evaluate the role of L* without affecting the nt sequence of the corresponding coding region of the polyprotein. In order to overcome this situation, we recently established an L*-expressing J774-1 cell line. GDVII and DAL*-1 viruses do not grow in control cells, which do not express L*, whereas virus growth is enhanced in L*-expressing cells [51]. van Eyll et al also have shown that L* ORF is required for virus growth in macrophage cell lines [52]. Therefore, L* is essential for host cell-dependent subgroup-specific virus growth, which is likely to play an important role in TMEV pathogenesis.

L and apoptosis of macrophages*

TMEV is reported to induce apoptosis *in vitro* and *in vivo*. Tsunoda et al detected the apoptosis *in vivo* and suggested that the apoptosis of neurons may be responsible for the fatal outcome of GDVII infection [53]. Apoptosis has also been found during the chronic stage of DA infection [54]. Of interest, the majority of apoptotic cells ($CD3^+$T cells) were uninfected, suggesting an activation-induced cell death.

The role of L* in apoptosis is studied in both 'loss of function' and 'gain of function' experiments. In a 'loss of function' experiment, a macrophage cell line, P388D1, was infected by wild type DA (which synthesizes L*) as well as DAL*-1 and GDVII viruses (neither of which synthesizes L*). DAL*-1 and GDVII viruses induced DNA laddering 12 hrs p.i., however, wild type DA did not. TUNEL-staining demonstrated that DAL*-1 and GDVII viruses caused apoptosis in 38% and 43% of P388D1 cells, respectively, while only 6% of DA-infected cells were apoptotic. These studies suggest that L* has an anti-apoptotic activity in macrophage cells [55]. In contrast to these findings, TMEV infection of microglia does not induce apoptosis [56]. The differing results may relate to special properties of microglia that are distinct from those of circulating macrophages.

Himeda et al established L*-expressing P388D1 cells to confirm the anti-apoptotic activity of L* in a 'gain of function' experiment [57]. DAL*-1 virus induced prominent DNA laddering in control cells that do not express L*, but failed to do so in L*-expressing P388D1 cells. The activity of caspase-3 was raised in the control cells and was inhibited by a caspase family inhibitor, Z-VAD-FMK, whereas caspase activity was significantly decreased in L*-expressing cells. The authors speculate that the major apoptotic pathway following TMEV infection may be a death receptor-mediated pathway since no cytochrome c release was detected.

The role of L in virus persistence and demyelination*

A challenging issue that remains is whether L* plays a role in virus persistence and demyelination. An initial question that required answering is whether L* is expressed *in vivo*. Asakura et al first demonstrated the expression of L* *in vivo* by means of immunoprecipitation and immunoblotting studies using anti-L* antibody [58]. These studies also localized L* in the mouse CNS during the acute stage of infection. L* was identified in neurons and colocalized with capsid protein, VP1.

L* was found to play an important role in virus persistence and demyelination by employing a 'loss of function' experiment. DAL*-1 virus produces an early acute polioencephalomyelitis similar to the parental DA, however, the viral RNA genome is no longer detected in the spinal cord of mice 6 weeks p.i. [55]. In addition, there is minimal if any evidence of demyelination or inflammation in the spinal cord [59]. L* appears to inhibit the generation of H-2K-restricted TMEV-specific cytotoxic T cells, therefore permitting a persistent infection to occur in susceptible mouse strains [60]. However, it is also reported that wild type-DA (which expresses L*) induces H-2K-restricted TMEV-specific cytotoxic T cells [61], In addition, the above findings regarding L* were also called into

question by Michiels and colleagues because the absence of the L* AUG initiation codon in a mutant DAL*-1 virus generated from a different DA infectious clone had only a weak influence on virus persistence [62]. The discrepancy is due to one nt sequence of the two viruses (Roos, R., personal communication). Further studies by van Eyll et al [52] using DA virus mutants with a stop codon in the L* reading frame (leading to a truncated L*) confirmed the key role of L* in virus persistence and demyelination.

Yamasaki et al. reported a utilization of the L* translation initiation vs. the polyprotein's AUG [63]. These investigators proposed that L* (rather than the polyprotein) is preferentially synthesized in certain CNS cells (e.g. microglial cells) following infection with DA subgroup strains. The production of only small amounts of capsid protein in certain cells would foster virus persistence and lead to restricted expression of the virus in the chronic stage.

The above data indicate that L* is a key determinant of TMEV persistence, subsequently leading to an inflammatory demyelination in the CNS, similar to that in MS. However, all the *in vivo* data that have been obtained to date are from 'loss of function' experiments. Additional data through by 'gain of function' experiments, such as those involving L*-expressing transgenic mice, would be valuable in order to confirm the role of L* protein *in vivo*.

From the above data regarding L and L*, it is speculated that DA strain could escape from host immune defense(s) through the inhibition of IFN α/β by L in the early stage of infection. DA that had escaped from early immune attack could then maintain its genome in macrophages with the aid of L* in the chronic stage of infection. The presence of TMEV genome in macrophages could trigger a cascade of immune system, leading to immune-mediated demyelination.

Conclusion

Both DA and GDVII subgroup strains of TMEV synthesize L, which consists of 76 AA and is processed from the most N-terminus of the polyprotein. L contains a zinc-binding motif, Cys-His-Cys-Cys, which is conserved among all cardioviruses and directly binds to zinc ions. L prevents transcription of IFN α/β through interference of the nuclear localization of IRF-3, a transcription factor important for the expression of IFN α/β.

DA subgroup strains synthesize L*, which is out of frame with the polyprotein. GDVII subgroup strains have an ACG rather than AUG corresponding to the initiation codon of L*, resulting in no synthesis of L*. A 'loss of function' experiment using mutant DA virus that fails to synthesize L*, as well as a 'gain of function' experiment using an L*-expressing macrophage cell line, demonstrated that L* has anti-apoptotic activity and is required for virus growth in macrophages. *In vivo* experiments using mutant DA virus, in which L or L* is not synthesized, also demonstrated that these are key proteins regulating the DA subgroup-specific biological activities, i.e., virus persistence and demyelination. Further studies clarifying the roles of L and L* will elucidate the pathomechanism(s) of TMEV-induced demyelinating disease, and may also provide insights into our understanding for MS.

Abbreviations

L: leader protein

L*: L* protein

TMEV: Theiler's murine encephalomyelitis virus

CNS: central nervous system

Competing interests

The author(s) declare that they have no competing interests.

Authors' contributions

MT conceived this review and wrote the initial draft with KA under the direction of YO. YO and TO modified, wrote and submitted the final draft. All authors read and approved the final version.

Acknowledgements

Supported by a Grant from the Neuroimmunological Research Committee of the Ministry of Health, Labor and Welfare, a Grant for Project Research from High-Technology Center of Kanazawa Medical University (H2005-7), and a Grant for Promoted Research from Kanazawa Medical University (S2005-12).

References

1. Lipton HL, Jelachich ML: **Molecular pathogenesis of Theiler's murine encephalomyelitis virus-induced demyelinating disease in mice.** *Intervirol* 1997, **40**:143-152.
2. Obuchi M, Ohara Y: **Theiler's murine encephalomyelitis virus and mechanisms of its persistence.** *Neuropathology* 1998, **18**:13-18.
3. Roos RP: **Pathogenesis of Theiler's murine encephalomyelitis virus-induced disease.** In *Molecular Biology of Picornaviruses* Edited by: Semler BL, Wimmer E. Washington DC: ASM Press; 2002:p427-435.
4. Oleszak EL, Chang JR, Friedman H, Katsetos CD, Platsoucas CD: **Theiler's virus infection: a model for multiple sclerosis.** *Clin Microbiol Rev* 2004, **17**:174-207.
5. Pevear DC, Borkowski J, Calenoff M, Oh CK, Ostrowski B, Lipton HL: **Insights into Theiler's virus neurovirulence based on a genomic comparison of the neurovirulent GDVII and less virulent BeAn strains.** *Virology* 1988, **165**:1-12.
6. Michiels T, Jarousse N, Brahic M: **Analysis of the leader and capsid coding regions of persistent and neurovirulent strains of Theiler's virus.** *Virology* 1995, **214**:550-558.
7. Johnson RT: **Postinfectious Demyelinating Disease.** In *Viral Infections of the Nervous System* 2nd edition. Edited by: Johnson RT. Philadelphia: Lippincott-Raven; 1998:p181-210.
8. Roos RP, Stein S, Ohara Y, Fu J, Semler BL: **Infectious cDNA clones of the DA Strain of Theiler's murine encephalomyelitis virus.** *J Virol* 1989, **63**:5492-5496.

9. Fu J, Stein S, Rosenstein L, Bodwell T, Routbort M: **Neurovirulence determinants of genetically engineered Theiler viruses.** *Proc Natl Acad Sci USA* 1990, **87**:4125-4129.
10. Calenoff MA, Faaberg KS, Lipton HL: **Genomic regions of neurovirulence and attenuation in Theiler murine encephalomyelitis virus.** *Proc Natl Acad Sci USA* 1990, **87**:978-982.
11. McAllister A, Tangy F, Aubert C, Brahic M: **Genetic Mapping of the ability of Theiler's virus to persist and demyelinate.** *J Virol* 1990, **64**:4252-4257.
12. Ohara Y, Himeda T, Asakura K: **A small out-of-frame protein regulating the biological activities in a mouse model for human demyelination disease.** *Curr Top Virol* 2004, **4**:123-132.
13. Leong LEC, Cornell CT, Semler BL: **Processing determinants and functions of cleavage products of picornavirus polyproteins.** In *Molecular Biology of Picornaviruses* Edited by: Semler BL, Wimmer E. Washington DC: ASM Press; 2002:p187-197.
14. Nitayaphan S, Toth MM, Roos RP: **Neutralizing monoclonal antibodies to Theiler's murine encephalomyelitis viruses.** *J Virol* 1985, **53**:651-657.
15. Nitayaphan S, Toth MM, Roos RP: **Localization of a neutralization site of Theiler's murine encephalomyelitis viruses.** *J Virol* 1985, **56**:887-895.
16. Ohara Y, Senkowski A, Fu J, Klaman L, Goodall J, Toth M, Roos RP: **Trypsin-sensitive neutralization site on VP1 of Theiler's murine encephalomyelitis viruses.** *J Virol* 1988, **62**:3527-3529.
17. Pevear DC, Calenoff M, Rozhon E, Lipton HL: **Analysis of the complete nucleotide sequence of the picornavirus Theiler's murine encephalomyelitis virus indicates that it is closely related to cardioviruses.** *J Virol* 1987, **61**:1507-1516.
18. Ohara Y, Stein S, Fu J, Stillman L, Klaman L, Roos RP: **Molecular cloning and sequence determination of DA strain of the Theiler's murine encephalomyelitis viruses.** *Virology* 1988, **164**:245-255.
19. Grant RA, Filman DJ, Fujinami RS, Icenogle JP: **Three-dimensional structure of Theiler virus.** *Proc Natl Acad Sci USA* 1992, **89**:2061-2065.
20. Luo M, He C, Toth KS, Zhang CX, Lipton HL: **Three-dimensional structure of Theiler murine encephalomyelitis virus (BeAn strain).** *Proc Natl Acad Sci USA* 1992, **89**:2409-2413.
21. Rodriguez M, Leibowitz JL, Lampert PW: **Persistent infection of oligodendrocytes in Theiler's virus-induced encephalitis.** *Ann Neurol* 1983, **13**:426-433.
22. Rodriguez M: **Virus-induced demyelination in mice: "gDying back"h of oligodendrocytes.** *Mayo Clin Proc* 1985, **60**:433-438.
23. Roos RP, Wollmann R: **DA strain of Theiler's murine encephalomyelitis virus induces demyelination in nude mice.** *ANN Neurol* 1984, **15**:494-499.
24. Rosenthal A, Fujinami RS, Lampert PW: **Mechanism of Theiler's virus-induced demyelination in nude mice.** *Lab Invest* 1986, **54**:515-522.
25. Dal Canto MC, Lipton HL: **Ultrastructural immunohistochemical localization of virus in acute and chronic demyelinating Theiler's virus infection.** *Am J Pathol* 1982, **106**:20-29.
26. Lipton HL, Twaddle G, Jelachich ML: **The predominant virus antigen burden is present in macrophages in Theiler's murine encephalomyelitis virus-induced demyelinating disease.** *J Virol* 1995, **69**:2525-2533.
27. Clatch RJ, Miller SD, Metzner R, Dal Canto MC, Lipton HL: **Monocytes/macrophages isolated from the mouse central nervous system contain infectious Theiler's murine encephalomyelitis virus (TMEV).** *Virology* 1990, **176**:244-254.
28. Levy M, Aubert C, Brahic M: **Theiler's virus replication in brain macrophages cultured in vitro.** *J Viro* 1992, **66**:3188-3193.
29. Rossi CP, Delcroix M, Huitinga I, McAllister A, van Rooijen N, Claassen E, Brahic M: **Role of macrophages during Theiler's virus infection.** *J Virol* 1997, **71**:3336-3340.
30. Strebel K, Beck E: **A second protease of foot-and-mouth disease virus.** *J Virol* 1986, **58**:893-899.
31. Piccone ME, Zellner M, Kumosinski TF, Mason PW, Grubman MJ: **Identification of the active-site residues of the L proteinase of foot-and-mouth disease virus.** *J Virol* 1995, **69**:4950-4956.
32. Devaney MA, Vakharia VN, Lloyd RE, Ehrenfeld E, Grubman MJ: **Leader protein of foot-and- mouth disease virus is required for cleavage of the p220 component of the cap-binding protein complex.** *J Virol* 1988, **62**:4407-4409.
33. Chinsangaram J, Koster M, Grubman MJ: **Inhibition of L-deleted foot-and-mouth disease virus replication by alpha/beta interferon involves double-stranded RNA-dependent protein kinase.** *J Virol* 2001, **75**:5498-5503.
34. Zoll J, Melchers WJG, Galama JMD, van Kuppeveld FJM: **The mengovirus leader protein suppresses Alpha/Beta interferon production by inhibition of the iron/ferritin-mediated activation of NF-kB.** *J Virol* 2002, **76**:9664-9672.
35. Roos RP, Kong W-P, Semler BL: **Polyprotein processing of Theiler's murine encephalomyelitis virus.** *J Virol* 1989, **63**:5344-5353.
36. van Pesch V, van Eyll O, Michiels T: **The leader protein of Theiler's virus inhibits immediate-early alpha/beta interferon production.** *J Virol* 2001, **75**:7811-7817.
37. Delhaye S, van Pesch V, Michiels T: **The Leader protein of Theiler's virus interferes with nucleocytoplasmic trafficking of celler proteins.** *J Virol* 2004, **78**:4357-4362.
38. Kong W-P, Ghadge GD, Roos RP: **Involvement of cardiovirus leader in host cell-restricted virus expression.** *Proc Natl Acad Sci USA* 1994, **91**:1796-1800.
39. Calenoff MA, Badshah CS, Dal Canto MC, Lipton HL, Rundell MK: **The Leader polypeptide of Theiler's virus is essential for neurovirulence but not for virus growth in BHK cells.** *J Virol* 1995, **69**:5544-5549.
40. van Pesch V, Michiels T: **Characterization of interferon-α 13, a novel constitutive murine interferon-α subtype.** *J Biol Chemistry* 2003, **278**:46321-46328.
41. Chen H-H, Kong W-P, Roos RP: **The leader peptide of Theiler's murine encephalomyelitis virus is a zing-binding ptotein.** *J Virol* 1995, **69**:8076-8078.
42. Fiette L, Aubert C, Müller U, Huang S, Aguet M, Brahic M, Bureau J-F: **Theiler's virus infection of 129Sv mice that lack the interferon α/β or interferon γ receptors.** *J Exp Med* 1995, **181**:2069-2076.
43. Fiette L, Aubert C, Brahic M, Rossi CP: **Theiler's virus infection of β_2-microglobulin-deficient mice.** *J Virol* 1993, **67**:589-592.
44. Kong W-P, Roos RP: **Alternative translation initiation site in the DA strain of Theiler's murine encephalomyelitis virus.** *J Virol* 1991, **65**:3395-3399.
45. Obuchi M, Yamamoto J, Odagiri T, Uddin MN, Iizuka H, Ohara Y: **L* protein of Theiler's murine encephalomyelitis virus is required for virus growth in a murine macrophage-like cell line.** *J Virol* 2000, **74**:4898-4901.
46. Obuchi M, Odagiri T, Asakura K, Ohara Y: **Association of L* protein of Theiler's murine encephalomyelitis virus with microtubules in infected cells.** *Virology* 2001, **289**:95-102.
47. Obuchi M, Ohara Y, Takegami T, Murayama T, Takada H, Iizuka H: **Theiler's murine encephalomyelitis virus subgroup strain-specific infection in a murine macrophage-like cell line.** *J Virol* 1997, **71**:729-733.
48. Ahmed R, Morrison LA, Knipe DM: **Virus persistence.** In *Viral Pathogenesis* Edited by: Natanson N, Ahmed R, Holmes KV, Gonzalez-Scrano F, Murphy FA, Griffin DE, Robinson HL. Philadelphia: Lippincot-Raven; 1997:P181-205.
49. Obuchi M, Yamamoto J, Uddin MN, Odagiri T, Iizika H, Ohara Y: **Theiler's murine encephalomyelitis virus (TMEV) subgroup strain-specific infection in neural and non-neural cell lines.** *Microbiol Immunol* 1999, **43**:885-892.
50. Takata H, Obuchi M, Yamamoto J, Odagiri T, Roos RP, Iizuka H, Ohara Y: **L* protein of the DA strain of Theiler's murine encephalomyelitis virus is important for virus growth in a murine macrophage-like cell line.** *J Virol* 1998, **72**:4950-4955.
51. Himeda T, Ohara Y, Asakura K, Kontani Y, Murakami M, Suzuki H, Sawada M: **A lentiviral expression system demonstrates that L* protein of Theiler's murine encephalomyelitis virus (TMEV) is essential for virus growth in a murine macrophage-like cell line.** *Virus Res* 2005, **108**:23-28.
52. van Eyll O, Michiels T: **Influence of the Theiler's virus L* protein on macrophage infection, viral persistence, and neurovirulence.** *J Virol* 2000, **74**:9071-9077.
53. Tsunoda I, Kurtz CIB, Fujinami RS: **Apoptosis in acute and chronic central nervous system disease induced by Theiler's murine encephalomyelitis virus.** *Virology* 1997, **228**:388-393.
54. Schlitt BP, Felrice M, Jelachich ML, Lipton HL: **Apoptotic cells, including macrophages, are prominent in Theiler's virus-**

induced inflammatory, demyelinating lesions. *J Virol* 2003, **77**:4383-4388.
55. Ghadge GD, Ma L, Sato S, Kim J, Roos RP: **A protein critical for a Theiler's virus-induced immune system-mediated demyelinating disease has a cell type-specific antiapoptotic effect and a key role in virus persistence.** *J Virol* 1998, **72**:8605-8612.
56. Ohara Y, Himeda T, Asakura K, Sawada M: **Distinct cell death mechanisms by Theiler's murine encephalomyelitis virus (TMEV) infection in microglia and macrophage.** *Neurosci Lett* 2002, **327**:41-44.
57. Himeda T, Ohara Y, Asakura K, Kontani Y, Sawada M: **A lentiviral expression system demonstrates that L* protein of Theiler's murine encephalomyelitis virus (TMEV) has an anti-apoptotic effect in a macrophage cell line.** *Microb Pathog* 2005, **38**:201-207.
58. Asakura K, Murayama H, Himeda T, Ohara Y: **Epitope-tagged L* protein of Theiler's murine encephalomyelitis virus is expressed in the central nervous system in the acute phase of infection.** *J Virol* 2002, **76**:13049-13054.
59. Chen H-H, Kong W-P, Zhang L, Ward PL, Roos RP: **A picornaviral protein synthesized out of frame with the polyprotein plays a key role in a virus-induced immune-mediated demyelinating disease.** *Nat Med* 1995, **1**:927-931.
60. Lin X, Roos RP, Pease LR, Wettstein P, Rodriguez M: **A Theiler's virus alternatively initiated protein inhibits the generation of H-2K-restricted virus-specific cytotoxicity.** *J Immunol* 1999, **162**:17-24.
61. Kang B-S, Lyman MA, Kim BS: **Differences in avidity and epitope recognition of CD8+ T cells infiltrating the central nervous systems of SJL/J mice infected with BeAn and DA strains of Theiler's murine encephalomyelitis virus.** *J Virol* 2002, **76**:11780-11784.
62. van Eyll O, Michiels T: **Non-AUG-Initiated internal translation of the L* protein of Theiler's virus and importance of this protein for viral persistence.** *J Virol* 2002, **76**:10665-10673.
63. Yamasaki K, Weihl CC, Roos RP: **Alternative translation initiation of Theiler's murine encephalomyelitis virus.** *J Virol* 1999, **73**:8519-8526.

１．研究課題名：発達期歯牙喪失の大脳新皮質－辺縁系機能連関への影響に関する研究
(S2005-13)

２．キーワード：１）脳梁膨大後野（retrospleial cortex）
２）大脳皮質視覚野（visual cortex）
３）膜電位振動（voltage oscillation）
４）カフェイン（caffeine）
５）ラット（rat）

３．研究代表者：吉村　弘・医学部・助教授・顎口腔機能病態学（口腔科学）

４．研 究 目 的

あらゆる動物は、生命維持のための成分を口腔から摂取するように進化してきた。歯牙が萌出するまさにその時期は、親から独立して一個の個体として生きていくための重要な準備期間である。この時期になんらかの形で咀嚼機能が障害されるか、または低下すると、やがて健全な情動発育に対して影響をおよぼす可能性が考えられる。

ヒトを含めて、動物が事象を認知して、そして行動に移していく一連の過程に、大脳新皮質と大脳辺縁系の機能連関は最も重要であると考えられる。情動をつかさどる中心は大脳辺縁系であり、外部環境の脳内描出は大脳新皮質が中心となる。本研究において、発達期の咀嚼機能の低下が、大脳新皮質と大脳辺縁系の機能連関におよぼす影響を調べた。

５．研 究 計 画

Wister 系ラットを用いて実験をおこなった。(1) 抜歯を施行せず､固形飼料で飼育した正常飼育群と、(2) 生後 2～3 週に上顎歯牙を抜歯して､流動食で飼育した抜歯群、の 2 種類の群を準備した。

脳梁膨大後野は、大脳新皮質と海馬の中間に位置しており、これらの領域のインターフェースとして機能していると考えられている。上記 2 群より､大脳皮質視覚野と脳梁膨大後野を含むスライスを作製し、フィールド電位計測法および膜電位変化を検知することのできる光学的計測法を用いて、発達期歯牙喪失の大脳新皮質と脳梁膨大後野間の発達形成への影響を調べた。

６．研 究 成 果

【結果 1】

正常に歯牙が萌出し、固形飼料を与えて飼育した正常ラットから、大脳皮質視覚野および脳梁膨大後野を含む脳スライスを作製し､カフェイン存在下で 1 次視覚野の白質を低頻度で刺激すると、図 1 に示すような膜電位振動が誘発される。正常に発育した場合、１次視覚野を出発した信号は、2 次視覚野を経て、脳梁膨大後野 RSG まで到達する。このとき､Oc2M､RSA､RSG それぞれの領域においても振動現象が観察される (図 2)。

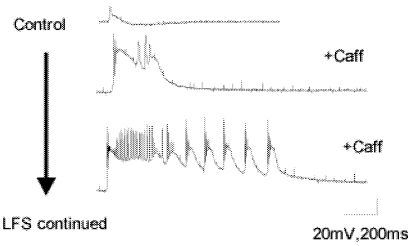

図 1:正常ラットの脳スライスからの細胞内電位計測
1次視覚野単一ニューロンからの細胞内電位記録。カフェイン存在下、1次視覚野への入力線維を反復刺激すると、8～10Hzの膜電位振動が誘発される。

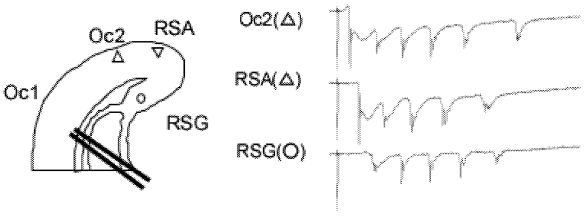

図 2:正常ラットの脳スライスからのフィールド電位計測
左:カフェイン存在下で1次視覚野の白質を低頻度で反復刺激し、2次視覚野(Oc2)、脳梁膨大後野(RSA、RSG)からフィールド電位計測をおこなった。
右上段:1次視覚野への入力線維刺激により、Oc2においても8～10Hzの膜電位振動が誘発される。
右中段、下段:視覚野から脳梁膨大後野への興奮伝播。視覚野の興奮が脳梁膨大後野に伝播し、そこにおいても振動性興奮が引き起こされている。

【結果 2】

生後 2～3 週に上顎歯牙を抜歯して、流動食で飼育した抜歯群から脳スライスを作製し、上記とまったく同様の方法で信号応答を観察した。1 次視覚野の白質刺激により 1 次視覚野と外側の 2 次視覚野（Oc2L）に振動性応答が出現したが、脳梁膨大後野 RSA と RSG においては、正常コントロールにみられたような振動性応答は出現しなかった（図 3A)。

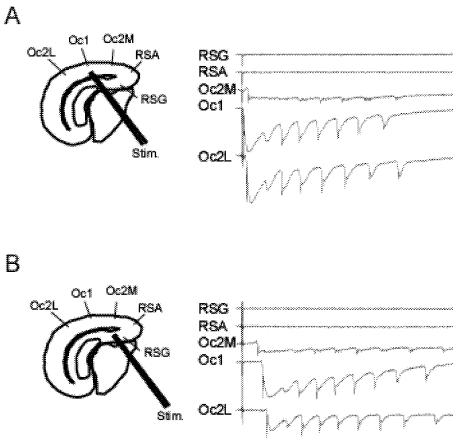

図 3:抜歯ラットを用いた実験
A:1次視覚野への入力線維刺激による振動性興奮伝播。視覚野Oc1-Oc2Lにおける
振動性興奮は誘発されているが、Oc2Mおよび脳梁膨大後野における振動発現が著しく抑制されている。
B:脳梁膨大後野への刺激による振動性興奮伝播。脳梁膨大後野における応答は小さいが、視覚野Oc1-Oc2Lにおいては十分振動性興奮は誘発されている。
視覚野-脳梁膨大後野間の相互線維連絡は存在するが、Oc2Mおよび脳梁膨大後野での振動発現能力が著しく阻害されていることがわかる。
Oc1、Oc2:視覚野　RSA、RSG:脳梁膨大後野

RSG を刺激した場合、Oc1 と Oc2L においては十分な振動性応答を認めたが、RSA と RSG においては著明な応答を認めなかった。1 次視覚野と脳梁膨大後野の間で、線維連絡は存在しているが、脳梁膨大後野における振動性活動発現能力が著しく低下していた（図 3B)。

【結果 3】

正常ラットの場合について、1 次視覚野の白質刺激を継続したときの、脳梁膨大後野におけるニューロン活動の変化を調べたところ、1 次視覚野との間で Shortcut（近道）が形成され、視覚野から RSG への到達時間が約 30 msec 短縮された（図 4）[2]。さらに、振動性活動は NMDA 受容体の活動に依存しており、皮質間の連絡の強化に関わっていることがわかった[1]。

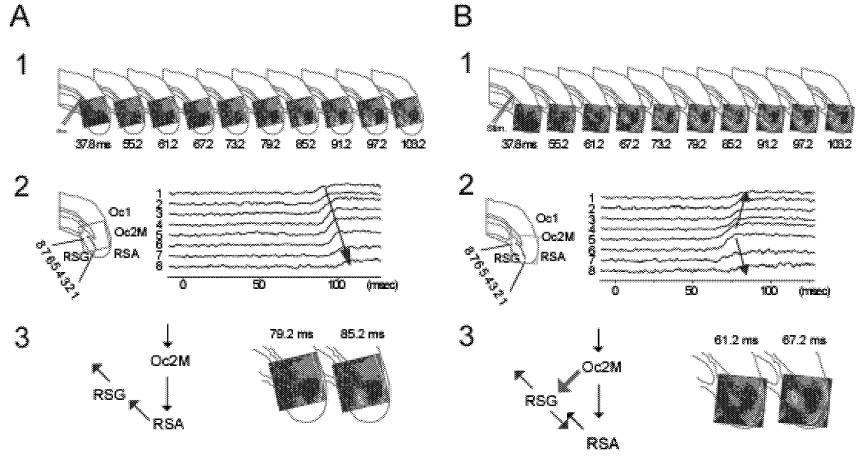

図 4：Shortcut（近道）の発現（正常ラット脳梁膨大後野における振動性活動の働き）
1次視覚野刺激による脳梁膨大後野への信号伝播と振動性活動が繰り返されると、Oc2MからRSAを経由してRSAに入力する経路（A）にOc2Mから直接RSGに入力する経路（B）があらたに生じる。このことにより、視覚野で引き起こされた興奮のRSGへの到達時間が約30msec短縮された。

7．研究の考察・反省

脳梁膨大後野は大脳新皮質と海馬の中間に位置し、傍辺縁系に属している。脳梁膨大後野は、記憶や情動発現に重要な働きを担っていると考えられているが、本研究結果から、発達期にう蝕等により多数歯牙を喪失すると、脳梁膨大後野の機能が低下する可能性が示された。結果 3 より、脳梁膨大後野は外部環境情報と記憶や情動情報の処理効率を上昇させる働きを持つということが示唆されるので、発達期の口腔機能低下は、脳梁膨大後野の機能低下を介して情動発達を遅らせる可能性が考えられる。今後、実際に行動を評価して、局所神経回路の変化と行動パターンの関連性を調べる必要がある。

8．研 究 発 表

Yoshimura H, Honjo M, Segami N, Kaneyama K, Sugai T, Mashiyama Y and Onoda N. Cyclic AMP-dependent attenuation of oscillatory-activity-induced intercortical strengthening of horizontal pathways between insular and parietal cortices. Brain Res 2006; 1069: 86-95. (MLDB)

Yoshimura H, Mashiyama Y, Kaneyama K, Nagao T, Segami N. Opening of shortcut circuits between visual and retrosplenial granular cortices of rats. NeuroReport 2007; 18: 1315-1318. (MLDB)

BRAIN RESEARCH 1069 (2006) 86–95

available at www.sciencedirect.com

SCIENCE DIRECT®

www.elsevier.com/locate/brainres

BRAIN RESEARCH

Research Report

Cyclic AMP-dependent attenuation of oscillatory-activity-induced intercortical strengthening of horizontal pathways between insular and parietal cortices

Hiroshi Yoshimura[a,b,*], Makoto Honjo[a], Natsuki Segami[a], Keiseki Kaneyama[a], Tokio Sugai[b], Yuichi Mashiyama[a], Norihiko Onoda[b]

[a]Department of Oral and Maxillofacial Surgery, Kanazawa Medical University, Uchinada-cho, Ishikawa 920-0293, Japan
[b]Department of Physiology, Kanazawa Medical University, Uchinada-cho, Ishikawa 920-0293, Japan

ARTICLE INFO

Article history:
Accepted 2 November 2005
Available online 4 January 2006

Keywords:
Insular cortex
Parietal cortex
Caffeine
cAMP
Oscillation
Optical recording

ABSTRACT

Cyclic AMP (cAMP) is a key intracellular second messenger, and the intracellular cAMP signaling pathway acts to modulate various brain functions. We have previously reported that low-frequency insular cortex stimulation in rat brain slices switches on a voltage oscillator in the parietal cortex that delivers signals horizontally back and forth under caffeine application. The oscillatory activities are N-methyl-D-aspartate (NMDA) receptor-dependent, and the role of oscillation is to strengthen functional intercortical connections. The present study investigated actions of the cAMP signaling pathway on caffeine-induced strengthening of intercortical connections and tried to confirm the role of oscillation on intercortical strengthening by focusing on the cAMP pathway. After induction of parietal oscillation by insular cortex stimulation in caffeine-containing medium, application of membrane-permeable cAMP analog, bromo-cAMP, diminished oscillatory signal delivery from the parietal cortex, but initial insulo-parietal signal propagation remained strong. When oscillatory activities were reduced with co-application of caffeine and bromo-cAMP from the beginning, initial insulo-parietal propagation was established, but amplitudes of propagating wavelets and propagating velocity were reduced. Thus, cAMP-dependent diminution of caffeine-induced NMDA-receptor-dependent oscillatory signal delivery causes attenuation of intercortical strengthening of horizontal pathways between insular and parietal cortices. This finding suggests that the intracellular cAMP signaling pathway has the ability to regulate extracellular communications at the network level, and also that full expression of strengthened intercortical signal communication requires sufficient NMDA-receptor-dependent oscillatory neural activities.

1. Introduction

In general, one of the roles of intracellular signaling pathways is to regulate extracellular signal communication (Bhella and Iyengar, 1999; Butcher and Sutherland, 1962). Such signal regulation enables cells to make feedback or feedforward loops for cellular interaction and communication. Cyclic AMP (cAMP) is a critical intracellular second messenger, and the

* Corresponding author. Department of Oral and Maxillofacial Surgery, Kanazawa Medical University, Uchinada-cho, Ishikawa 920-0293, Japan. Fax: +81 76 286 2010.
E-mail address: hyoshimu@kanazawa-med.ac.jp (H. Yoshimura).

0006-8993/$ – see front matter © 2005 Elsevier B.V. All rights reserved.
doi:10.1016/j.brainres.2005.11.048

cAMP signaling pathway modulates various biological functions (Butcher and Sutherland, 1962; Cho et al., 2002; Crump et al., 2001; Frey et al., 1993; Mao and Wang, 2002; Renden and Broadie, 2003; Wang et al., 1999). In the brain, neurotransmitters and receptors dominantly intermediate extracellular signal communication at the synapses, and the cAMP signaling pathway largely operates at the synapses. The cAMP signaling pathway may thus have the ability to regulate extracellular signal communication in the brain via modulation of synaptic activities (Evans and Morgan, 2003; Ma et al., 1999; Thakur et al., 2004; Yoshimura and Kato, 2000).

Caffeine displays several pharmacological actions and can invade the synapses in the brain (Fredholm et al., 1999; Nehlig and Boyet, 2000). We recently demonstrated that caffeine enhances intercortical neural activities between primary and secondary visual cortices (Yoshimura et al., 2003a, 2005b). In those studies, we reported that intercortical horizontal connections are functionally opened and strengthened by caffeine-induced α-range voltage oscillations. The oscillatory signal deliveries that activate N-methyl-D-aspartate (NMDA) receptor components to surrounding areas cause strengthening of functional neural connections (Yoshimura et al., 2003a, 2005a,b). One important action of caffeine is thus the opening and strengthening of intercortical signal communications by way of driving NMDA-receptor-dependent neural oscillators.

Since synapses are major sites where both the cAMP signaling pathway and caffeine operate and since caffeine has the ability to affect the cAMP signaling pathway (Beavo and Reifsnyder, 1990; Butcher and Sutherland, 1962; Fredholm et al., 1999), increased intracellular cAMP level by pharmacological manipulation in addition to application of caffeine might induce up- or down-regulation of synaptic activities. We have focused attention on areas between the gustatory insular cortex where chemosensory information is processed and the parietal oral somatosensory cortex where somatosensory information is processed (Hanamori et al., 1999; Katz et al., 2001; Kosar et al., 1986; Ogawa and Wang, 2002; Paxinos

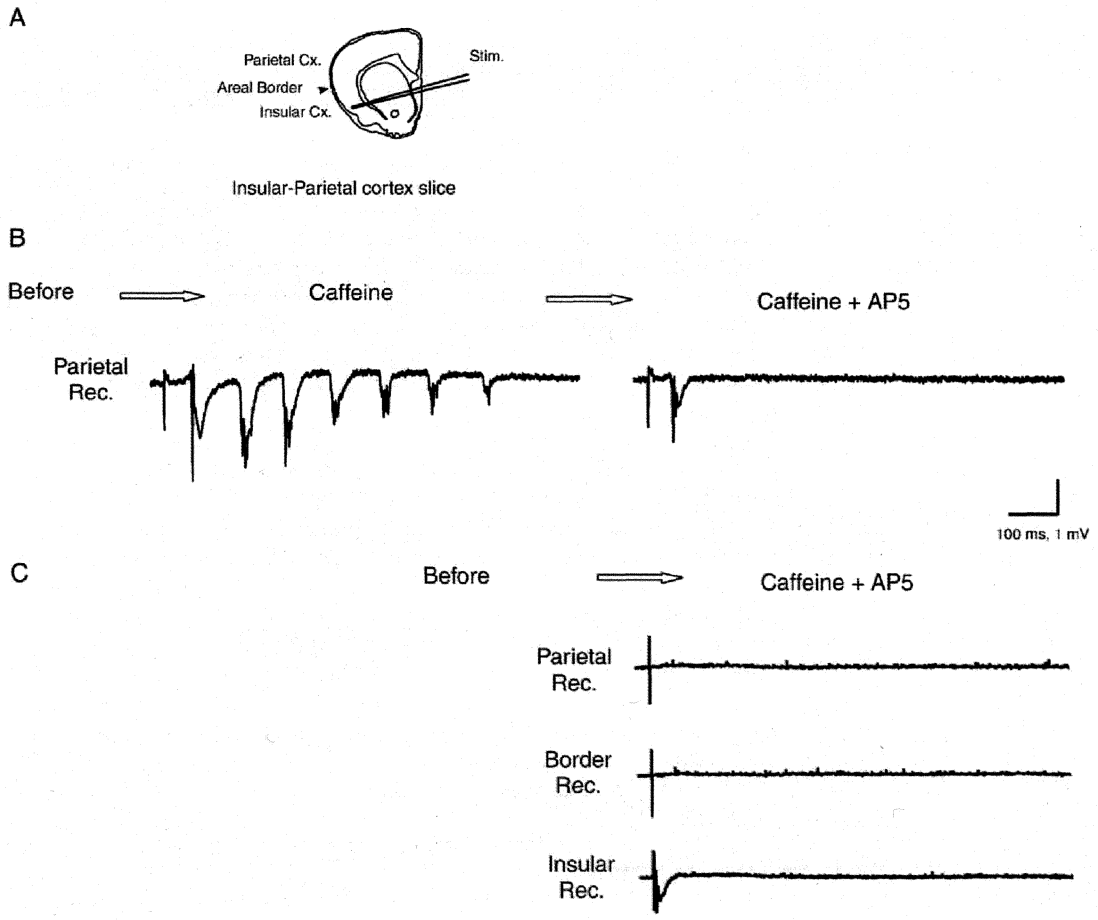

Fig. 1 – Comparing insulo-parietal signal propagation under caffeine application and NMDA receptor blockade after establishing voltage oscillation in the parietal cortex with propagation under application of caffeine and NMDA receptor blockade from the beginning. (A) Brain slices including insular and parietal cortices and electrical stimulation site. Low-frequency stimulation was delivered to the insular cortex, and field potentials were recorded from layer II/III in the insular cortex, parietal cortex and areal border. (B) After induction of parietal oscillation in caffeine-containing medium, D-AP5, an NMDA receptor blocker, was added. Note that initial insulo-parietal component remained. (C) Caffeine and D-AP5 co-applied to medium from the beginning. Note that initial component did not penetrate the parietal cortex.

et al., 1997; Remple et al., 2003; Shi and Cassell, 1998; Swanson et al., 1992; Yamamoto et al., 1981; Yoshimura et al., 2004b; Zilles and Wree, 1995) We recently reported that insulo-parietal neural connections are functionally strengthened after oscillatory activities in the parietal cortex (Yoshimura et al., 2003b, 2004a). The present study investigated how intracellular cAMP elevation affects opening and strengthening of insulo-parietal connections to examine whether cAMP pathways have the ability to regulate extracellular signal communications at the intercortical network level. In addition, we tried to verify that NMDA-receptor-dependent oscillatory activities cause strengthening of intercortical signal communications by focusing on the intracellular cAMP signaling pathway.

2. Results

Low-frequency intracortical electrical stimulation was delivered to layer IV in the gustatory insular cortex, and field potentials were recorded from layer II/III in the parietal cortex (Fig. 1A). In normal medium, a small solitary potential was observed only in the gustatory insular cortex and did not propagate horizontally toward the parietal cortex (24/24 slices, not shown). After application of caffeine into the medium, the evoked potential was enlarged, and the potential propagated from the insular cortex to the parietal cortex. However, marked oscillation was only generated in the parietal cortex (22/24 slices). These propagation and oscillation have been precisely described in our previous report, and histological identification of the stimulation and recording sites has also been demonstrated (Yoshimura et al., 2003b, 2004a). The same kinds of propagation and oscillation are induced in both the insulo-parietal cortex and primary–secondary visual cortex (Yoshimura et al., 2003a, 2005b). We have repetitively reported that later oscillatory components are entirely NMDA-receptor-dependent in both the parietal and visual cortices (Yoshimura et al., 2003a,b, 2004a, 2005b). The present findings again confirmed this. Oscillation in the parietal cortex was induced in caffeine-containing medium after low-frequency stimulation to the insular cortex. After oscillation in the parietal cortex stabilized, D-2-amino-5-phosphonovaleric acid (D-AP5), a blocker of NMDA receptor, was applied to the medium. Approximately 30 min later, the insulo-parietal signal propagation remained, but oscillatory activities in the parietal cortex were depressed (Fig. 1B; "Caffeine + AP5"; 12/12 slices). The remaining initial response was non-NMDA-receptor-dependent since additional application of 6-cyano-7-nitroquinoxaline-2,3-dione (CNQX), a blocker of non-NMDA receptor, completely depressed the initial response (15/15 slices, not shown).

In the visual cortex, co-application of caffeine and D-AP5 from the beginning abolishes not only induction of oscillatory signal deliveries from the secondary visual cortex, but also

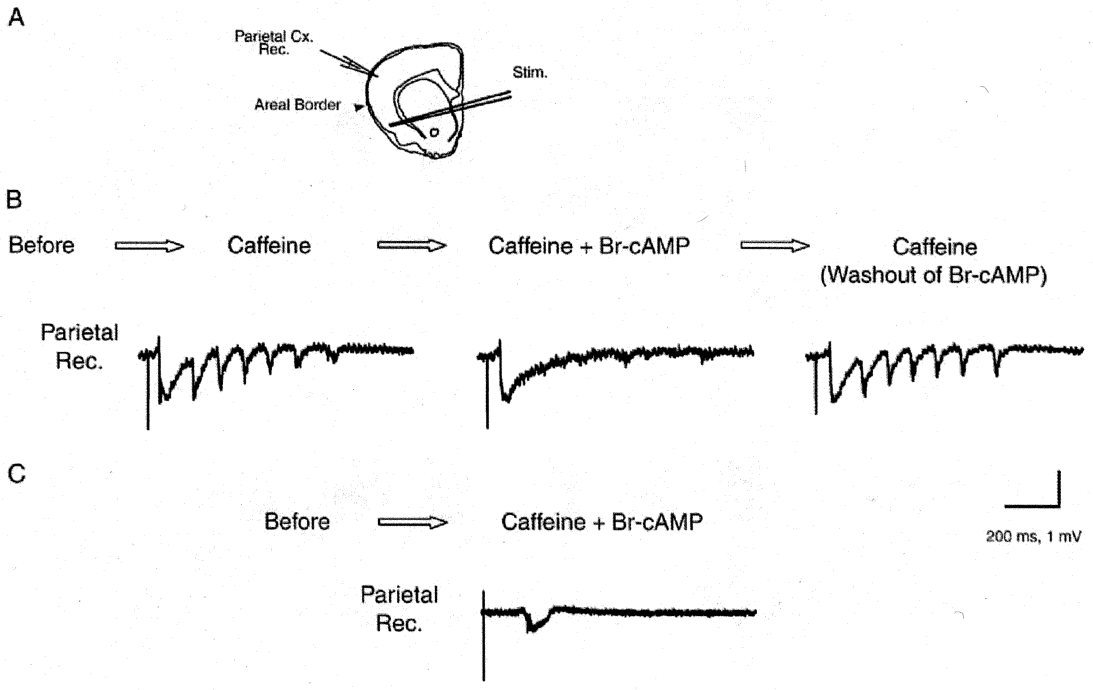

Fig. 2 – Comparing effects of bath application of bromo-cAMP on responses in parietal cortex evoked by insular cortex stimulation under co-application of caffeine and bromo-cAMP after caffeine conditioning with effects under co-application of caffeine and bromo-cAMP from the beginning. (A) Location of stimulation and recording electrodes. (B) After inducing marked parietal oscillations in caffeine-containing medium, bromo-cAMP was added to the medium. When oscillatory phases were depressed, bromo-cAMP was washed out from medium. (C) Bromo-cAMP co-applied with caffeine from the beginning. Note that induction of oscillatory activities was depressed, but depression of oscillatory activities was incomplete, and initial response with smaller amplitude and longer latency was observed.

opening horizontal signal pathways from the primary visual cortex to the secondary visual cortex (Yoshimura et al., 2005b). In the same way, co-application of caffeine and D-AP5 from the beginning in the present study abolished not only induction of parietal oscillation, but also opening horizontal signal pathways from the insular cortex to the parietal cortex (Fig. 1C). The present study offered new confirmation that NMDA-receptor-dependent oscillatory activities cause opening and strengthening of intercortical horizontal signal pathways between the insular and parietal cortices.

The intracellular cAMP pathway is a key second messenger pathway that modulates neuron functions. We have previously reported that synaptic efficiency in the visual cortex is modulated by increases in intracellular cAMP (Yoshimura and Kato, 2000). In the next experiment, effects of intercellular cAMP elevation on propagation and oscillation between insular and parietal cortices were investigated. Oscillation in the parietal cortex was induced in the same way as described above, and, after oscillation in the parietal cortex stabilized, bromo-cAMP, a membrane permeable cAMP analog, was applied to the medium. Approximately 30 min later, insulo-parietal signal propagation remained, but oscillatory activities in the parietal cortex were depressed. Depressed oscillatory activities recovered with washout of bromo-cAMP from the medium (Fig. 2B; 7/7 slices). Application of bromo-cAMP thus reversibly diminished oscillatory activities in the parietal cortex.

NMDA-receptor-dependent oscillatory signal deliveries contribute to strengthening of corticocortical signal pathways between the primary and secondary visual cortices (Yoshimura

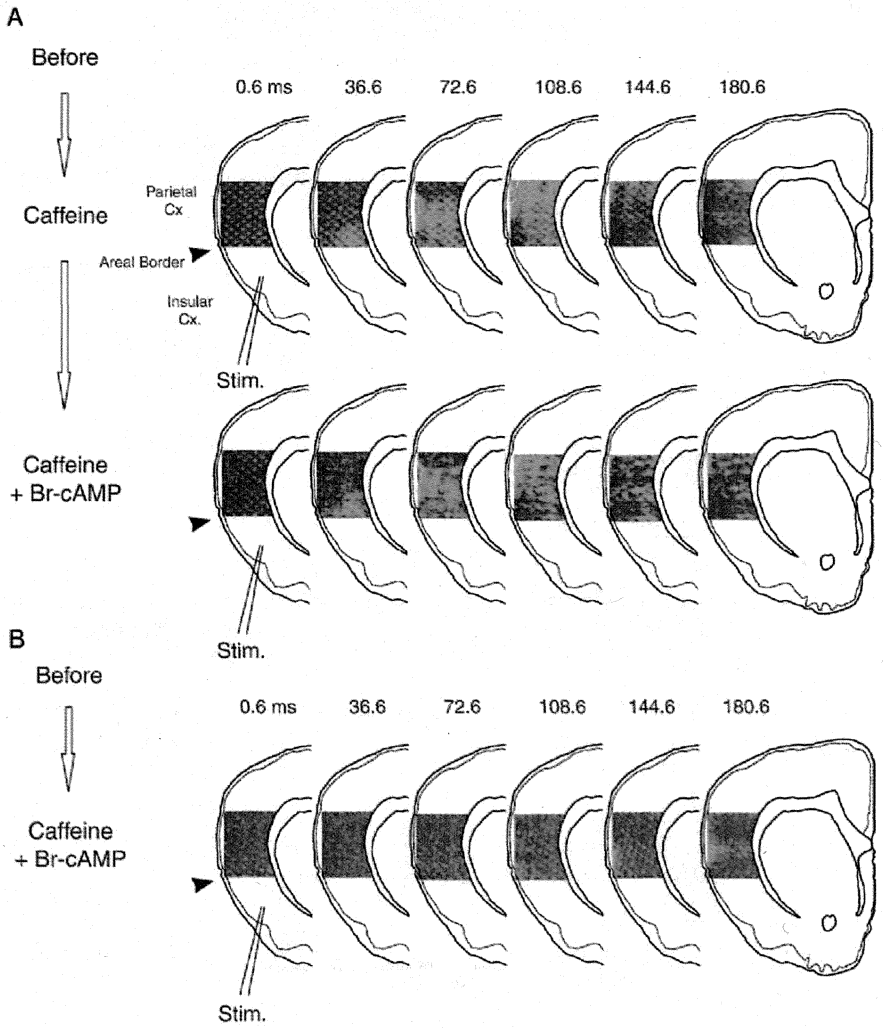

Fig. 3 – Comparing spatiotemporal dynamics of initial voltage signal propagation in parietal cortex under co-application of caffeine and bromo-cAMP after caffeine conditioning with dynamics under co-application of caffeine and bromo-cAMP from the beginning. (A) After caffeine conditioning, initial signal evoked by insular cortex stimulation propagated into parietal cortex along layer II/III (upper). After additional application of bromo-cAMP, initial evoked signal propagated into parietal cortex in the same way (lower). (B) When caffeine and bromo-cAMP were co-applied from the beginning, initial evoked signal managed to propagate into parietal cortex, but intensity of optical response and propagating velocity was reduced, compared with the case for caffeine application preceded by bromo-cAMP.

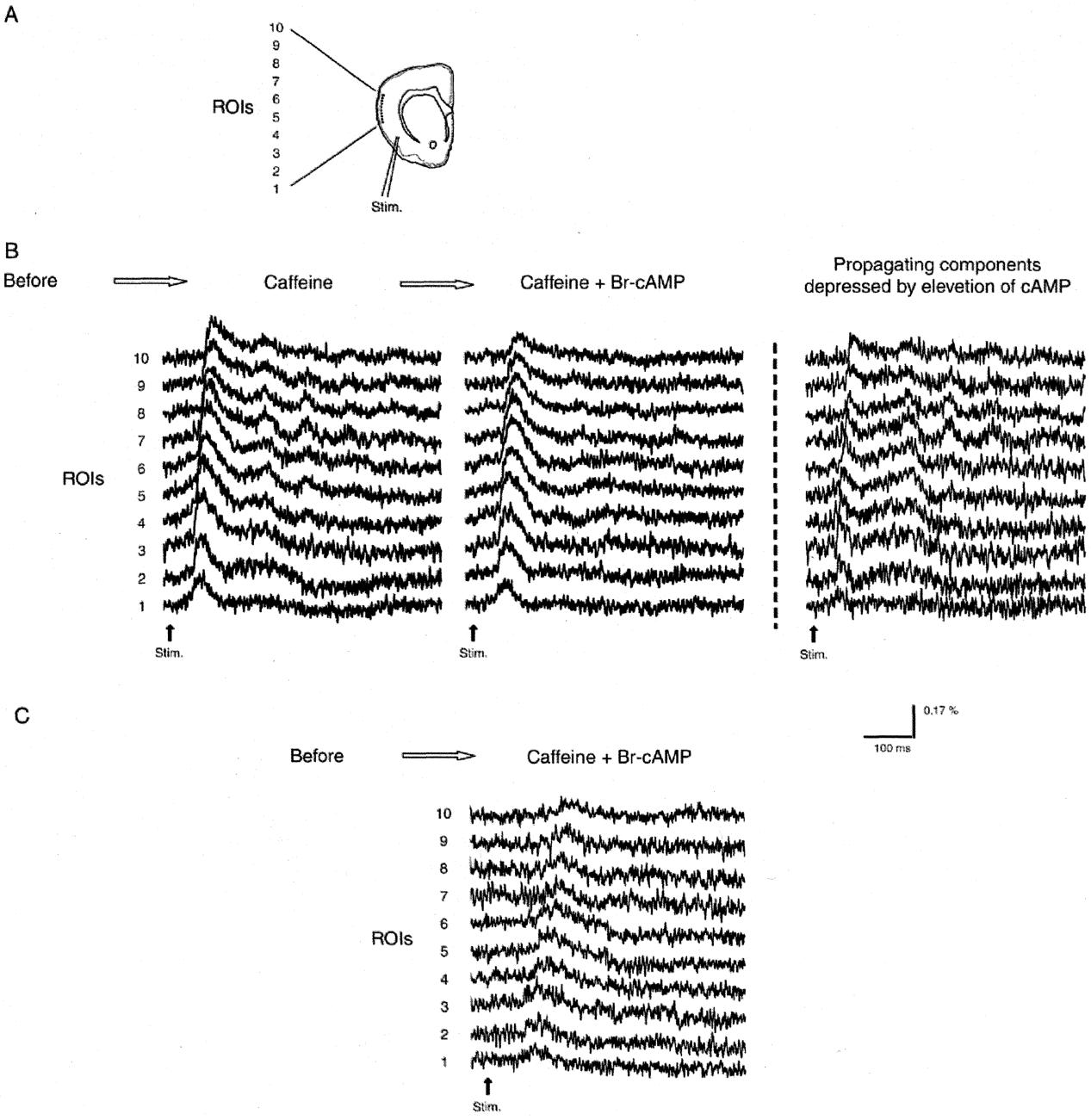

Fig. 4 – Comparing time courses of optical responses in parietal cortex obtained from optical recordings as shown in Fig. 3 under co-application of caffeine and bromo-cAMP after caffeine conditioning with time courses under co-application of caffeine and bromo-cAMP from the beginning. (A) Regions of interest (ROIs) 1–10 are shown in an illustration of insulo-parietal cortex slice. (B) Time courses of optical responses obtained from ROIs were arranged vertically. Left: after caffeine conditioning, initial signal evoked by insular cortex stimulation propagated into parietal cortex, and later oscillatory components were generated in parietal cortex and propagated toward insular cortex. Precise analysis of propagation is described in Thakur et al. (2004). Center: after additional application of bromo-cAMP, initial evoked signal propagated into parietal cortex in the same way, but later oscillatory components were largely depressed. Right: propagating components depressed by elevation of cAMP were obtained by subtracting "Caffeine" recordings from "Caffeine + bromo-cAMP" recordings. (C) When caffeine and bromo-cAMP were co-applied from the beginning, initial evoked signal managed to propagate into parietal cortex, but amplitudes of optical response and propagating velocity were reduced compared with the case of caffeine application preceded by bromo-cAMP.

et al., 2004a) and between the insular and parietal cortices (Fig. 1). Since elevation of intracellular cAMP depressed oscillatory components (Fig. 2B), we presumed that depression of oscillation induction by cAMP elevation might depress intercortical strengthening between the insular and parietal cortices. When bromo-cAMP was co-applied with caffeine from the beginning, induction of oscillatory activities was depressed, but depression of oscillatory activities was incomplete. With co-application of caffeine and D-AP5 from the beginning, no oscillatory activity occurred (Fig. 1C), whereas co-application of caffeine and bromo-cAMP from the beginning yielded oscillatory activities with two or three wavelets occurring every several episodes (not shown, Fig. 2C). In addition, amplitude of the initial wavelet arriving in the parietal cortex was significantly smaller with co-application of caffeine and bromo-cAMP from the beginning (0.3 ± 0.1 mV, mean ± standard error of the mean; $n = 7$) than with addition of bromo-cAMP after oscillation generation in caffeine-containing medium (1.1 ± 0.1 mV; $n = 7$). Incomplete induction of oscillation thus generates incomplete intercortical strengthening between the insular and parietal cortices.

The next experiments investigated how application of bromo-cAMP affects establishment of insulo-parietal signal pathways by observing spatiotemporal patterns of voltage signals, using optical recording methods with voltage-sensitive dye. Electrical stimulation was delivered to the insular cortex, and optical responses were observed from the area including parietal cortex. In caffeine-containing medium, evoked signals penetrated the parietal cortex and predominantly traveled along layer II/III (Fig. 3A; upper panel). After additional application of bromo-cAMP, evoked signals predominantly traveled along layer II/III in the same way as in medium containing caffeine only (Fig. 3A; lower panel). Conversely, in medium with co-application of caffeine and bromo-cAMP from the beginning, evoked signals traveled slowly, and intensity of optical responses was weak, compared with additional application of bromo-cAMP after caffeine conditioning (Fig. 3B).

To investigate the precise spatiotemporal properties of optical signals, time courses of signal intensity recorded from region of interests (ROIs; Fig. 4A) were aligned tangentially (Figs. 4B, C). Time courses of signal intensity in the case of

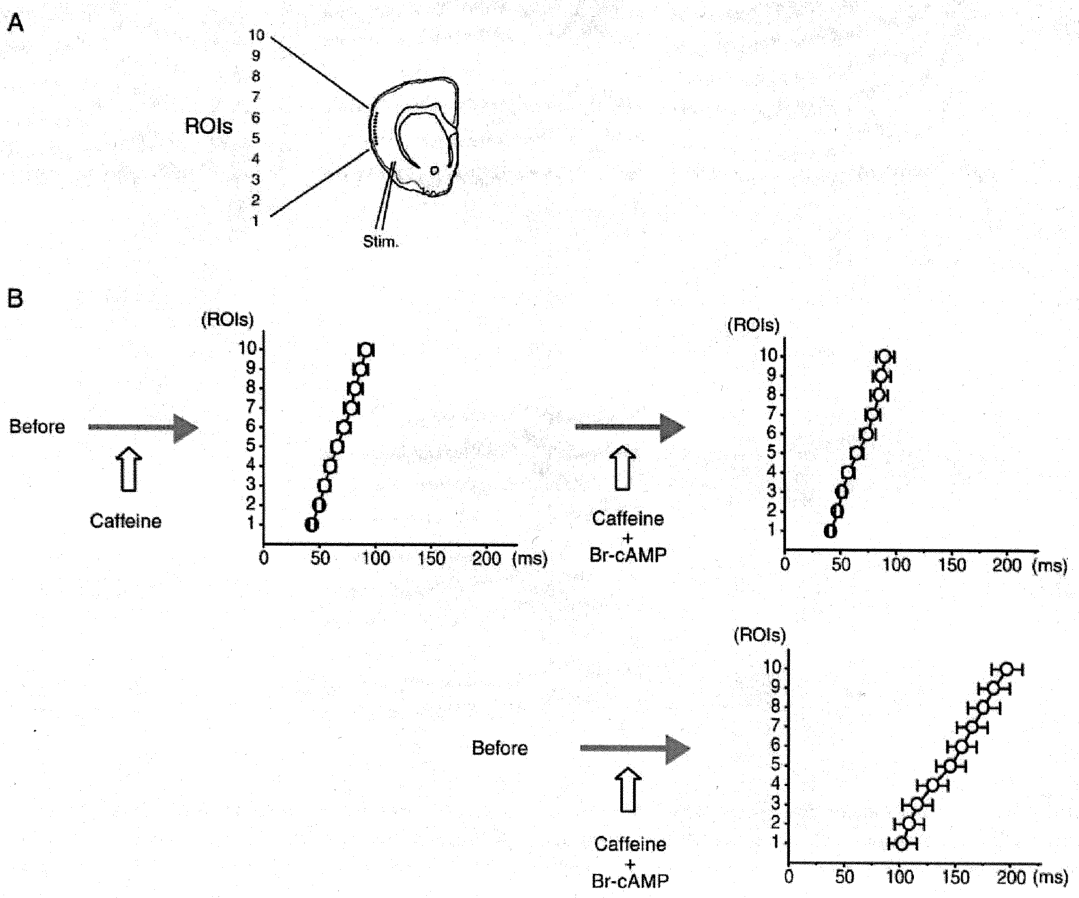

Fig. 5 – Comparing averaged time-to-peak of initial voltage signal propagation in parietal cortex under co-application of caffeine and bromo-cAMP after caffeine conditioning with time-to-peak under co-application of caffeine and bromo-cAMP from the beginning. (A) Regions of interests (ROI 1–10) are shown in an illustration of insulo-parietal cortex slice. (B) Mean time (open circle) and standard deviation (cap) were plotted. When caffeine and bromo-cAMP were co-applied from the beginning, mean time at each ROI was delayed, and mean propagating velocity was reduced (lower), compared with the case of caffeine application preceded by bromo-cAMP (upper).

caffeine application preceded by bromo-cAMP were collected from the same data displayed in Fig. 3A (upper panel). The results show that oscillation elicited by insular cortex stimulation comprises 2 components: an initial signal propagation from the insular cortex to the parietal cortex and later oscillatory signals generated in the parietal cortex that propagate bi-directionally in horizontal directions (Fig. 4B; left). This observation is consistent with the findings of our recent report (Yoshimura et al., 2004a). After addition of bromo-cAMP into the medium, initial signal propagation from the insular cortex to the parietal cortex persisted, but later waves diminished (Fig. 4B; center panel). Time courses of propagating components depressed by cAMP elevation were obtained by subtracting time courses in medium with additional bromo-cAMP from time courses in medium with caffeine alone (Fig. 4B; right panel). This clearly shows that part of the initial propagating components from the insular cortex to the parietal cortex and the greater part of oscillatory propagating components were depressed by elevations of intracellular cAMP. These results show that the dominant targets of increases in intracellular cAMP are local areas generating NMDA-receptor-dependent signal flows from the parietal cortex.

Time courses of signal intensity with co-application of caffeine and bromo-cAMP from the beginning were aligned tangentially (Fig. 4C). Time courses were collected from the same data displayed in Fig. 3B. The results show that delivery of oscillatory signals from the parietal cortex was diminished, and both amplitudes of propagating signal and propagating velocity decreased compared with caffeine application preceded by bromo-cAMP.

Time-to-peaks of the first waves recorded at ROIs over different slices were averaged. After induction of parietal oscillation in caffeine-containing medium, first waves propagated from ROI 1 to ROI 10 (Fig. 5B; upper left; $n = 7$). Mean propagating velocity of the first wave from ROI 1 to ROI 10 was 63.4 ± 8.2 mm/s. After additional application of bromo-cAMP, first waves propagated in the same way (Fig. 5B; upper right; $n = 7$), and propagating velocity was 62.7 ± 11.9 mm/s. This shows that additional application of bromo-cAMP did not

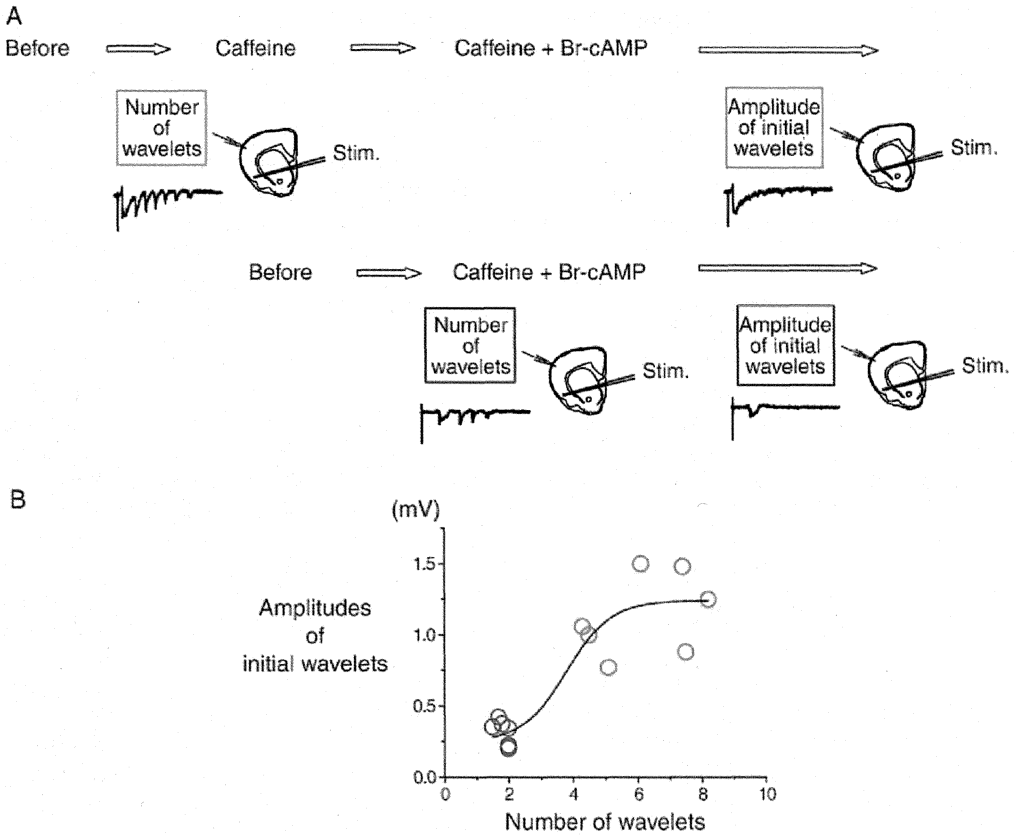

Fig. 6 – Relationship between number of wavelets of oscillatory activities after caffeine application and amplitudes of initial wavelets arriving in the parietal cortex from the insular cortex under co-application of caffeine and bromo-cAMP. (A) Schematic of timings and sites of data acquisition for preparation of part (B). Data were collected from field potential recordings, e.g., time course responses in Fig. 2. (B) Blue circle: amplitude of initial wavelets under additional application of bromo-cAMP to caffeine-containing medium was plotted against mean number of wavelets of oscillatory activities for several episodes before application of bromo-cAMP. Red circle: bromo-cAMP was bath-applied to caffeine-containing medium from the beginning. Amplitudes of initial wavelets were plotted against mean number of wavelets of oscillatory activities for several episodes. Blue squares in panel A correspond to blue circles in panel B, and red squares in panel A correspond to red circles in panel B. Note that signal propagation with sufficient amplitude requires sufficient oscillatory activities.

affect the propagating velocity of first waves. Conversely, in the case of co-application of caffeine and bromo-cAMP from the beginning, first waves managed to propagate from ROI 1 to ROI 10 (Fig. 5B; lower; $n = 7$), but propagating velocity (30.2 ± 2.7 mm/s) was significantly reduced compared with caffeine application preceded by bromo-cAMP ($P < 0.05$).

To clarify the dependence of oscillatory activities on intercortical strengthening of signal communication, relationships between number of wavelets of oscillatory activities under caffeine application and amplitudes of initial wavelets arriving in the parietal cortex from the insular cortex under co-application of caffeine and bromo-cAMP were investigated (Fig. 6). Once stable signal propagation and oscillation were established in medium with caffeine alone, initial propagation with sufficient amplitude was observed (1.1 ± 0.1 mV; $n = 7$) even after addition of bromo-cAMP. However, when caffeine and bromo-cAMP were co-applied from the beginning, induction of oscillatory activities was not stable. Oscillatory activities with 2–3 wavelets occurred every several episodes rather than every episode, and, consequently, although initial signal propagation to the parietal cortex was observed, amplitudes of initial wavelets were small (0.3 ± 0.01 mV; $n = 7$) (Fig. 2). Mean amplitude and wavelet numbers were calculated from data acquired from respective slices ($n = 7$) and plotted (Fig. 6). Incomplete induction of oscillation was seen to produce incomplete amplitude of propagating signals, suggesting a dependence of oscillatory activity on intercortical strengthening of signal communication.

3. Discussion

In the intercortical areas between primary and secondary visual cortices, the components of the horizontal pathway that is strengthened after NMDA-receptor-dependent oscillatory signal delivery using our experimental protocol are non-NMDA-receptor-dependent (Yoshimura et al., 2005b). In the same way in the present study, components of the horizontal pathway between the insular and parietal cortices that is strengthened after NMDA-receptor-dependent parietal oscillation are non-NMDA-receptor-dependent. Interestingly, increases in intracellular cAMP barely affected non-NMDA-receptor-dependent pathways that had been already strengthened but markedly diminished NMDA-receptor-dependent oscillatory activities (Figs. 2–6).

Functional glutamate receptors are expressed in both neurons and glial cells (Noda et al., 2000; Steinhäuser and Gallo, 1996). In addition, astrocytes can modulate neural synaptic activities by releasing glutamate in a Ca^{2+}-dependent manner (Parpura and Haydon, 2000). GABA receptors in inhibitory networks are modulated by activation of cAMP pathways (Cuove et al., 2002). These findings indicate that application of caffeine and bromo-cAMP might modulate synaptic activities by way of various intra- and extracellular pathways. We thus cannot even conclude that targets of cAMP under caffeine application are restricted to excitable neurons, let alone conclude that cAMP, caffeine and NMDA receptors are operating in the same neurons. However, since NMDA receptor activity-dependent neural oscillations induced by caffeine and the depression of NMDA-receptor-dependent neural activities with cAMP increases are effects produced by assemblies of various causes present in intra- and extracellular pathways, we can safely say that the dominant target of cAMP increases is NMDA-receptor-related neural activities.

The cAMP signaling pathway modulates neural functions at both channel and receptor levels, such as single channel activities (Greengard et al., 1991; Kavalali et al., 1997), probability of synaptic transmission (Abrams et al., 1991; Frey et al., 1993; Renden and Broadie, 2003; Yoshimura and Kato, 2000) and synaptic targeting of NMDA receptors (Crump et al., 2001). However, evidence that the cAMP signaling pathway regulates neural activities at the long-range intercortical network level has been lacking. In the process of establishing intercortical strengthening in our experimental model, we have described causality as follows: NMDA-receptor-dependent oscillatory signal deliveries cause strengthening of non-NMDA-receptor-dependent intercortical pathways (Yoshimura et al., 2005a,b). Thus, considering the relationship between cause and effect, increased cAMP levels directly affect the cause itself and as a result affect the effect. Since the dominant target of cAMP is considered to be NMDA receptor activities under the present experimental conditions, activation of intracellular cAMP signaling pathways can be interpreted as resulting in the induction of down-regulation in NMDA-receptor-activity-dependent strengthening of extracellular intercortical signal communications by way of diminishing NMDA-receptor-dependent oscillatory signal deliveries. This is important evidence that shows intracellular signaling pathways regulate extracellular signaling pathways between intercortical regions in the brain. NMDA receptors may act as an intermediary between actions of intracellular cAMP signaling pathways and extracellular signaling pathways at the cortical network level.

Induction of functional synapses mediated by non-NMDA receptors requires NMDA receptor activation in the hippocampus (Liao et al., 2001; Lu et al., 2001; Nicoll and Malenka, 1999). In the same way, strengthening of non-NMDA-receptor-dependent intercortical pathways in the present study required NMDA-receptor-dependent oscillatory signal deliveries from the parietal cortex. Plastic changes might thus underlie intercortical strengthening, as we previously reported (Yoshimura et al., 2005a,b). Blockade of NMDA receptor activities from the beginning completely abolished oscillatory activities and disturbed opening of signal pathways between insular and parietal cortices (Fig. 1). Compared with NMDA receptor blockade, manipulation of cAMP increases in the present experimental condition could not completely abolish oscillatory activities (Figs. 2, 6). Due to incomplete blockade of oscillation induction by cAMP increases, evoked signals from the insular cortex might manage to penetrate the parietal cortex after caffeine conditioning with increased cAMP. However, due to the attenuation of NMDA-receptor-dependent oscillatory activities by cAMP increases during caffeine conditioning, signal propagating velocity from the insular cortex to the parietal cortex in addition to amplitude of the propagating signals was reduced, compared with the case in which sufficient NMDA-receptor-dependent oscillatory signals were delivered during caffeine conditioning before manipulation of cAMP increases (Figs. 5, 6). Increases in intracellular cAMP levels could not completely abolish

opening of insulo-parietal signal communication but attenuated strengthening of insulo-parietal signal communication under caffeine application. These findings suggest that full expression of opening and strengthening of intercortical signal pathways requires sufficient NMDA-receptor-dependent oscillatory neural activities.

Caffeine displays several neuropharmacological actions (Fredholm et al., 1999; Nehlig and Boyet, 2000; Yoshimura, 2005). Among these actions, either blockade of adenosine A1 receptors or blockade of phosphodiesterases (PDEs) by caffeine induces increased intracellular cAMP levels. In general, one result of the increase in intracellular cAMP by caffeine is facilitation of synaptic activities (Fredholm et al., 1999; Moraidis and Bingmann, 1994). In the present results, however, additional increase in cAMP by bromo-cAMP application to the medium with caffeine resulted in depression of synaptic activities. A discrepancy therefore seems to exist between the actions of these manipulations, application of caffeine alone and co-application of caffeine and bromo-cAMP. However, the two manipulations produce different spatiotemporal conditions of increased cAMP and may drive a different stream of signaling pathways. As we have discussed previously (Yoshimura and Kato, 2000), determination of the direction of neuron excitability by cAMP may be dependent on the manner in which cAMP is increased.

4. Experimental procedures

All experiments were performed in accordance with the guidelines for the ethical use of animals approved by the Japanese Physiological Society. Details of the experimental procedures have been described previously by us (Yoshimura et al., 2001, 2002, 2003b, 2004a). Brains were quickly removed from Wistar rats and soaked into cold medium (2–4 °C) containing: NaCl, 124 mM; KCl, 3.3 mM; KH_2PO_4, 1.25 mM; $MgSO_4$, 1.3 mM; $CaCl_2$, 2 mM; $NaHCO_3$, 26 mM; and D-glucose, 10 mM; saturated with 95% O_2 and 5% CO_2. Coronal slices (350 μm thick) that included the insular and parietal cortices anterior to the middle cerebral artery were produced from rat brains isolated on postnatal day 27–35. Micropipettes for field potential recordings were filled with 3 M NaCl and inserted into the upper layer of the insular or parietal cortex (6–10 MΩ). Synaptic responses were evoked by single pulse stimulation at 0.03–0.3 Hz, recorded with a bridge-equipped Axoclamp-2B amplifier (Axon Instruments, Foster City, USA), digitized by an AD Digidata 1200 converter (Axon Instruments) at a rate of 2.5–5 kHz and stored in a personal computer for off-line analysis. For experimental purposes, the following drugs (purchased from Wako, Osaka, Japan) were added to medium: caffeine, 3.0 mM; D-2-amino-5-phosphonovaleric acid (D-AP5), 15 μM; 6-cyano-7-nitroquinoxaline-2,3-dione (CNQX), 20 μM; and bromo-cAMP, 40 μM.

High-speed optical recording methods with voltage-sensitive dyes were used to observe the spatiotemporal dynamics of neural activities. Details of the optical recording system used in this study have been described elsewhere (Thakur et al., 2004; Wang et al., 1999; Yoshimura et al., 2004a). Before optical recording began, slices were incubated with 0.125 mg/ml of NK2761 voltage-sensitive dye (Nihon Kanko, Okayama, Japan) for 20 min then transferred to the recording chamber. The camera unit of the optical imaging system (Fujix HR Deltaron 1700; Fuji Photo Film, Tokyo, Japan) contained a photodiode array of 128 × 128 elements. With a ×10 objective lens, the whole array corresponded to a 2.24 × 2.24 mm^2 area of tissue. Light for absorption measurements, generated by a tungsten–halogen lamp (150 W), passed through a heat absorption filter and a narrow band interference filter before being focused on the preparation. Illumination was controlled by an electromagnetic shutter to avoid dye bleaching or photodynamic damage. A run constituted the average of 16 responses elicited by cortical stimulation. Neural activity was recorded as the change in intensity of transmitted light hitting each photodiode. Images were captured every 0.6 ms. Recordings are shown as averages over 16 traces. Relative increases in optical signal were expressed as a time-sequence for the whole image or were plotted against time for each region of interest (ROI).

Acknowledgments

This work was supported by a Health Science Research Grant from the Ministry of Health, Labour and Welfare of Japan (Comprehensive Research on Aging and Health, H-17-Chouju-018) and Grants from Kanazawa Medical University (Grant for Promoted Research No. S2005-13).

REFERENCES

Abrams, T.W., Karl, K.A., Kandel, E.R., 1991. Biochemical studies of stimulus convergence during classical conditioning in *Aplysia*: dual regulation of adenylate cyclase by Ca^{2+}/calmodulin and transmitter. J. Neurosci. 11, 2655–2665.

Beavo, J.A., Reifsnyder, D.H., 1990. Primary sequence of cyclic nucleotide phosphodiesterase isozymes and the design of selective inhibitors. Trends. Pharmacol. Sci. 11, 150–155.

Bhella, U.S., Iyengar, R., 1999. Emergent properties of networks of biological signaling pathways. Science 283, 381–387.

Butcher, R.W., Sutherland, E.W., 1962. Adenosine-3′,5′-phosphate in biological materials. J. Biol. Chem. 273, 1244–1250.

Cho, K., Brown, M.W., Bashir, Z.I., 2002. Mechanisms and physiological roles of enhancement of mGlu5 receptor function by group II mGlu receptor activation in rat perirhinal cortex. J. Physiol. 540, 895–906.

Cuove, A., Thomas, P., Calver, A.R., Hirst, W.D., Pangalos, M.N., Walsh, F.S., Smart, T.G., Moss, S.J., 2002. Cyclic AMP-dependent protein kinase phosphorylation facilitates GABA(B) receptor–effector coupling. Nat. Neurosci. 5, 415–424.

Crump, F.T., Dillman, K.S., Craig, A.M., 2001. cAMP-dependent protein kinase mediates activity-regulated synaptic targeting of NMDA receptors. J. Neurosci. 21, 5079–5088.

Evans, G.L., Morgan, A., 2003. Regulation of the exocytotic machinery by cAMP-dependent protein kinase: implication for presynaptic plasticity. Biochem. Soc. Trans. 31, 824–827.

Fredholm, B.B., Bättig, K., Holmén, J., Nehlig, A., Zvartau, E.E., 1999. Action of caffeine in the brain with spatial reference to factors that contribute to its widespread use. Pharmacol. Rev. 51, 83–133.

Frey, U., Huang, Y.Y., Kandel, E.R., 1993. Effects of cAMP stimulate a late stage of LTP in hippocampal CA1 neurons. Science 260, 1661–1664.

Greengard, P., Jen, J., Nairn, A.C., Stevens, C.F., 1991. Enhancement of the glutamate response by cAMP-dependent protein kinase in hippocampal neurons. Science 253, 1135–1138.

Hanamori, T., Kunitake, T., Kato, K., Kannan, H., 1999. Responses of neurons in the insular cortex to gustatory, visceral, and nociceptive stimuli in rats. J. Neurophysiol. 79, 2535–2545.

Katz, D.B., Simon, S.A., Nicolelis, M.A.L., 2001. Dynamic and multimodal responses of gustatory cortical neurons in awake rats. J. Neurosci. 21, 4478–4489.

Kavalali, E.T., Hwang, K.S., Plummer, M.B., 1997. cAMP-dependent enhancement of dihydropyridine-sensitive calcium channel availability in hippocampal neurons. J. Neurosci. 17, 5334–5348.

Kosar, E., Grill, H.J., Norgren, R., 1986. Gustatory cortex in the rat: I. Physiological properties and cytoarchitecture. Brain Res. 379, 329–341.

Liao, D., Scannevin, R.H., Huganir, R., 2001. Activation of silent synapses by rapid activity-dependent synaptic recruitment of AMPA receptors. J. Neurosci. 21, 6008–6017.

Lu, W., Man, H., Ju, W., Trimble, W.S., MacDonald, J.F., Wang, Y.T., 2001. Activation of synaptic NMDA receptors induces membrane insertion of new AMPA receptors and LTP in cultured hippocampal neurons. Neuron 29, 243–254.

Ma, L., Zablow, L., Kandel, E.R., Siegelbaum, S.A., 1999. Cyclic AMP induces functional presynaptic boutons in hippocampal CA3–CA1 neuronal cultures. Nat. Neurosci. 2, 24–30.

Mao, L., Wang, J.Q., 2002. Glutamate cascade to cAMP response element-binding protein phosphorylation in cultured striatal neurons through calcium-coupled group I metabotropic glutamate receptors. Mol. Pharmacol. 62, 473–484.

Moraidis, I., Bingmann, D., 1994. Epileptogenic actions of xanthines in relation to their affinities for adenosine A1 receptors in CA3 neurons of hippocampal slices (guinea pig). Brain Res. 640, 140–145.

Nehlig, A., Boyet, S., 2000. Dose–response study of caffeine effects on cerebral functional activity with a specific focus on dependence. Brain Res. 858, 71–77.

Nicoll, R.A., Malenka, R.C., 1999. Expression mechanisms underlying NMDA receptor-dependent long-term potentiation. Ann. N. Y. Acad. Sci. 868, 515–525.

Noda, M., Nakanishi, H., Nabekura, J., Akaike, N., 2000. AMPA–kainate subtypes of glutamate receptor in rat cerebral microglia. L. Neurosci. 20, 251–258.

Ogawa, H., Wang, X.D., 2002. Neurons in the cortical taste area receive nociceptive inputs from the whole body as well as the oral cavity in the rat. Neurosci. Lett. 322, 87–90.

Parpura, V., Haydon, P.G., 2000. Physiological astrocytic calcium levels stimulate glutamate release to modulate adjacent neurons. Proc. Natl. Acad. Sci. U. S. A. 97, 8629–8634.

Paxinos, G., Watson, C., 1997. The Rat Brain in Stereotaxic Coordinates, 4th ed. Academic Press, San Diego.

Remple, M.S., Henry, E.C., Catania, K.C., 2003. Organization of somatosensory cortex in the laboratory rat (*Rattus norvegicus*): evidence for two lateral areas joined at the representation of the teeth. J. Comp. Neurol. 467, 105–118.

Renden, R.B., Broadie, K., 2003. Mutation and activation of Gαs similarly alters pre- and postsynaptic mechanisms modulating neurotransmission. J. Neurophysiol. 89, 2620–2638.

Shi, C.J., Cassell, M.D., 1998. Cortical, thalamic, and amygdaloid connections of the anterior and posterior insular cortex. J. Comp. Neurol. 399, 440–468.

Steinhäuser, C., Gallo, V., 1996. News on glutamate receptors in glial cells. Trends Neurosci. 19, 339–345.

Swanson, L.W., 1992. Brain Maps: Structure of the Rat Brain, 2nd ed. Elsevier, Amsterdam.

Thakur, P., Stevens, D.R., Sheng, Z.H., Rettig, J., 2004. Effects of PKA-mediated phosphorylation of Snapsin on synaptic transmission in cultured hippocampal neurons. J. Neurosci. 24, 6476–6481.

Wang, S.J., Cheng, L.L., Gean, P.W., 1999. Cross-modulation of synaptic plasticity by beta-adrenergic and 5-HT1A receptors in the rat basolateral amygdala. J. Neurosci. 19, 570–577.

Yamamoto, T., Yuyama, N., Kawamura, Y., 1981. Cortical neurons responding to tactile, thermal and taste stimulation of the rat's tongue. Brain Res. 221, 202–206.

Yoshimura, H., 2005. The potential of caffeine for functional modification from cortical synapses to neuron networks in the brain. Curr. Neuropharmacol. 3, 309–316.

Yoshimura, H., Kato, N., 2000. Diverse roles of intracellular cAMP in early synaptic modulations in the rat visual cortex. J. Physiol. (London) 522, 417–426.

Yoshimura, H., Sugai, T., Onoda, N., Segami, N., Kato, N., 2001. Synchronized population oscillation of excitatory synaptic potentials dependent on calcium-induced calcium release in rat neocortex layer II/III neurons. Brain Res. 915, 94–100.

Yoshimura, H., Sugai, T., Onoda, N., Segami, N., Kato, N., 2002. Age-dependent occurrence of synchronized population oscillation of synaptic potentials in the rat visual cortex. Dev. Brain Res. 136, 63–68.

Yoshimura, H., Kato, N., Sugai, T., Segami, N., Onoda, N., 2003a. Age-dependent emergence of oscillatory signal flow between the primary and secondary visual cortices in rat brain slices. Brain Res. 990, 172–181.

Yoshimura, H., Kato, N., Sugai, T., Segami, N., Onoda, N., 2003b. Age-dependent appearance an insulo-parietal cortical signal propagation that elicits a synchronized population oscillation in the parietal cortex of rats. Dev. Brain Res. 143, 241–245.

Yoshimura, H., Kato, N., Sugai, T., Honjo, M., Sato, J., Segami, N., Onoda, N., 2004a. To-and-fro optical voltage signal propagation between the insular gustatory and parietal oral somatosensory areas in rat cortex slices. Brain Res. 1015, 114–121.

Yoshimura, H., Sugai, T., Fukuda, M., Segami, N., Onoda, N., 2004b. Cortical spatial aspects of optical intrinsic signals in response to sucrose and NaCl stimuli. NeuroReport 15, 17–20.

Yoshimura, H., Sugai, T., Honjo, M., Segami, N., Onoda, N., 2005a. NMDA receptor-dependent oscillatory signal outputs from the retrosplenial cortex triggered by a non-NMDA receptor-dependent signal input from the visual cortex. Brain Res. 1045, 12–21.

Yoshimura, H., Sugai, T., Segami, N., Onoda, N., 2005b. Strengthening of non-NMDA receptor-dependent horizontal pathways between primary and lateral secondary visual cortices after NMDA receptor-dependent oscillatory neural activities. Brain Res. 1036, 60–69.

Zilles, K., Wree, A., 1995. Cortex, In: Paxinos, G. (Ed.), The Rat Nervous System, 2nd ed. Academic Press, Inc. San Diego, pp. 649–685.

Opening of shortcut circuits between visual and retrosplenial granular cortices of rats

Hiroshi Yoshimura, Yuichi Mashiyama, Keiseki Kaneyama, Toshikazu Nagao and Natsuki Segami

Departments of Oral and Maxillofacial Surgery, Kanazawa Medical University, Uchinada-cho, Kanazawa, Ishikawa 920-0293, Japan

Correspondence to Hiroshi Yoshimura, PhD, Department of Oral and Maxillofacial Surgery, Kanazawa Medical University, Uchinada-cho, Kanazawa, Ishikawa 920-0293, Japan
Tel: +81 76 286 2211; fax: +81 76 286 2010; e-mail: hyoshimu@kanazawa-med.ac.jp

Received 21 April 2007; accepted 2 May 2007

Traveling neural signals may try to find suitable paths of propagation in cortical circuits. We examined the behavior of electrically evoked signals from primary visual cortex (Ocl) to granular retrosplenial cortex (RSG) in rat brain slices under caffeine application. With continued electrical stimulation, evoked signals propagated from Ocl to RSG along the upper layer of the secondary visual cortex (Oc2) and agranular retrosplenial cortex (RSA), but on further continuation of stimulation, a new shortcut pathway along the deep layer between Oc2 and RSG was opened. Circuitry changes reduced the signal traveling time by about 40 ms. Cortical neural circuits between Ocl and RSG may thus have the ability to open a shortcut circuit in a use-dependent manner. *NeuroReport* 18:1315–1318 © 2007 Lippincott Williams & Wilkins.

Keywords: caffeine, cortical circuit, rat, retrosplenial cortex, shortcut, visual cortex

Introduction

In general, neural signals in the brain propagate along neural circuits via synaptic transmissions. Selection of traveling routes may depend on the spatial conformation of neural connections and efficiency of synaptic transmission. The most prominent property of the brain may be that structure and function are variable according to synaptic activities [1–5]. Traveling neural signals may thus try to find suitable paths of propagation during repetitive synaptic activities.

The visual and retrosplenial cortices are thought to be concerned with processing spatial information and episodic memory [6]. Properties of use-dependent change are required of neural circuits between these cortices. We recently used rat brain slices to reveal that the granular retrosplenial cortex (RSG) has the ability to deliver *N*-methyl-D-aspartate (NMDA) receptor-dependent oscillatory signals, and oscillatory activities are important for opening and strengthening neural pathways between Ocl and RSG [7]. This suggests that plastic changes at the network level occur in these areas. However, precise spatiotemporal signal traveling routes and modes of change were unclear. This study investigated how traveling neural signals find suitable paths of propagation during the process of opening and strengthening neural pathways from Ocl to RSG.

Materials and methods

All experiments were performed in accordance with the guidelines for the ethical use of animals approved by the Japanese Physiological Society. Wistar rats (27 to 32 days old) were decapitated under ether anesthesia, and the brains were quickly removed and soaked in a cold medium (2–4°C) comprising (in mM): NaCl 124, KCl 3.3, NaH_2PO_4 1.25, $MgSO_4$ 1.3, $CaCl_2$ 2, $NaHCO_3$ 26, and D-glucose 10, saturated with 95% O_2–5% CO_2. Brain slices (thickness, 300 μm) including visual cortex, retrosplenial cortex, postsubiculum, and subiculum were prepared. The slices were placed in a submerged-type chamber set on the stage of an IMT-2 upright microscope (Olympus, Tokyo, Japan) and perfused with the medium (30°C; 5 ml/min). Caffeine (Wako, Osaka, Japan) at a concentration of 3.5 mM was added to the perfusion medium. For simulation, a bipolar tungsten electrode was inserted into the border region between the grey and white matter in Ocl. Electrical stimulation was delivered at a frequency of 0.2–0.02 Hz. The duration and intensity of stimuli were 80 μs and 250–350 μA, respectively.

High-speed optical recording methods were used with voltage-sensitive dyes to observe the spatiotemporal dynamics of spreading neural activities. Details of the optical recording system used in this study have been described elsewhere [7–9]. The optical imaging system (Fujix HR Deltaron 1700; Fuji Photo Film, Tokyo, Japan) contains a photodiode array of 128 × 128 elements, corresponding to a 2.26 × 2.26 mm^2 area of tissue. Images are captured every 0.6 ms. The recordings shown represent averages over 16 traces. Relative increases in optical signal were expressed as a time sequence of the whole image, or were plotted against time for each pixel of interest.

Results

As reported previously, oscillatory activities and strengthening of horizontal pathways were induced in a caffeine-containing medium [7–9]. In this study, the recording

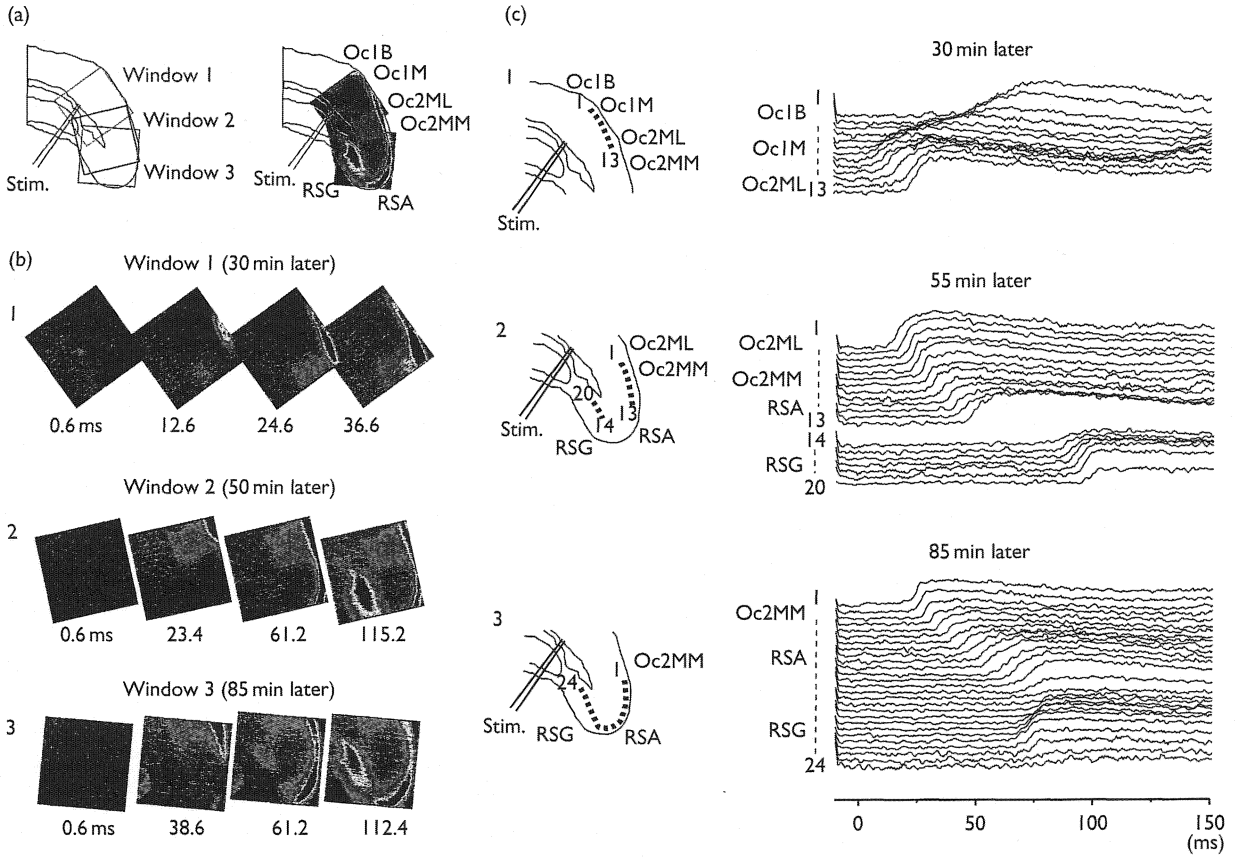

Fig. 1 Spatiotemporal dynamics of signal propagation from Oc1 to RSG. (a) Recording areas 'Window 1', 'Window 2', and 'Window 3' and stimulation site are indicated in a line drawing of the slice (left). Representative pseudocolor images of optical signals recorded from the three windows were superimposed on a line drawing of the slice (right). (b) Selected optical images were arranged. Optical images of 'Window 1' were recorded 30 min after LFS start (upper), whereas images of 'Window 2' were recorded 50 min after LFS start (middle) and those of 'Window 3' were recorded 85 min after LFS start (lower). (c) Signal flows from visual cortex to RSG along high intensity are demonstrated in pseudocolor images of Windows 1–3. Time courses of optical responses obtained from ROIs in Windows 1–3 are arranged horizontally in the upper layers of Oc2M and RSA and the deep layer of RSG, as indicated in the line drawing on the left. LFS, low frequency stimulation; ROI, region of interest; RSA, agranular retrosplenial cortex; RSG, granular retrosplenial cortex.

windows were moved for every recording session to observe dynamic neural activities in Oc1, medial secondary visual cortex (Oc2M), agranular retrosplenial cortex (RSA), and RSG. After induction of stable oscillation, horizontal signal propagation was strengthened, and spatiotemporal activities were observed through 'Window 1' 30 min after start of caffeine application and repetitive stimulation (0.2–0.02 Hz) to white matter in Oc1 (Fig. 1b-1). About 50 min later, spatiotemporal activities were observed through 'Window 2'. The initial signal propagated to the RSG via Oc2M and RSA along layers II/III (Fig. 1b-2). About 85 min later, spatiotemporal activities were observed through 'Window 3' (Fig. 1b-3). The initial signal propagated to the RSG similar to that observed in 'Window 2'. The representative optical images of Windows 1–3 were superimposed (Fig. 1a right). This showed that intense signal travel in the upper layers of Oc2M and RSA, and the deep layer of RSG. Time courses of optical responses for intense signal traveling paths were selected as regions of interests (ROIs) and arranged (Fig. 1c). Transitions of peak time for waves indicate the direction of wave propagation. A strange result was that the onset time of RSG activities in Window 2 (ROI 18) differed from that in Window 3 (ROI 20), despite identical stimulation sites.

To investigate precisely the properties of propagation, optical images from 'Window 2' and 'Window 3' were selected and arranged in detail every 6 ms (Fig. 2a-1 and b-1). The dynamics of RSG activation were clearly different between 'Window 2' and 'Window 3'. In 'Window 2', RSG began to activate from a signal from RSA, whereas in 'Window 3' RSG began to activate from a signal from Oc2M. Time courses of optical responses on intense signal traveling routes along the horizontal direction in RSG were selected as ROIs 1–8 (Fig. 2a-2 left, b-2 left). The transition of peak time in 'Window 2' showed that the initial signal propagated from RSA to RSG, whereas in 'Window 3' the signal propagated bidirectionally from ROI 6. Focusing on ROI 6, the arrival time was 98 ms in 'Window 2' (Fig. 2a-2), compared with 63 ms in 'Window 3' (Fig. 2b-2). This clearly showed that a shortcut from Oc2 to RSG had been opened (Fig. 2b-3; red arrow). Anatomically, Oc1 and RSG have been confirmed as connected [10]. This study successfully visualized two signal-traveling routes from Oc1 to RSG.

In the present experiments, the phenomena described above were observed in eight slices from six animals. In many slices, using the same protocol as in the present experiment, signals propagated from Oc1 to RSG. In those cases, we adopted data in which the areas of both surface

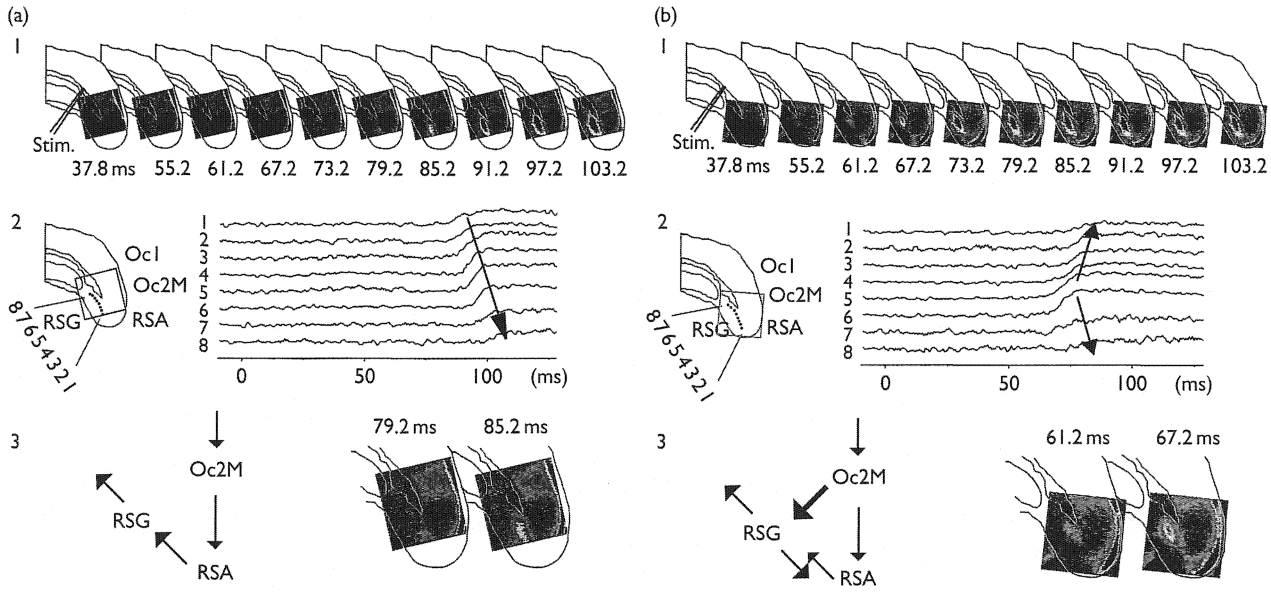

Fig. 2 Emergence of shortcut from visual cortex to RSG on continuation of LFS to Ocl. (a-1) Optical images from 'Window 2' recorded 50 min after LFS start were arranged to show precisely signal propagation from Oc2 to RSG. (a-2) Time courses of optical responses obtained from ROIs arranged horizontally in the deep layer of RSG, as indicated in the line drawing on the left. (a-3) Illustration of signal flow from Ocl to RSG (left). Representative optical images at 79.2 and 85.2 ms after stimulation were superimposed on line drawings (right). (b-1) Optical images from 'Window 3' recorded 85 min after LFS start were arranged to show precisely signal propagation from Oc2M to RSG. (b-2) Time courses of optical responses obtained from ROIs arranged horizontally in the deep layer of RSG, as indicated in the line drawing on the left. (b-3) Illustration of signal flow from Ocl to RSG (left). Representative optical images at 61.2 and 67.2 ms after stimulation were superimposed on line drawings (right). Note that the shortcut from Oc2M to RSG is newly induced (red arrow). LFS, low frequency stimulation; ROI, region of interest; RSG, granular retrosplenial cortex.

and shortcut traveling routes were included in the recording windows of the same slice. Figure 3 shows the arrival time of signals to RSG from Ocl via surface and shortcut routes obtained from eight slices. This indicates that, when a shortcut is opened, the arrival time from Ocl to RSG is significantly reduced (t-test, $P<0.01$, $n=8$) by a mean ($\pm$SD) of 40.7 ± 9.6 ms.

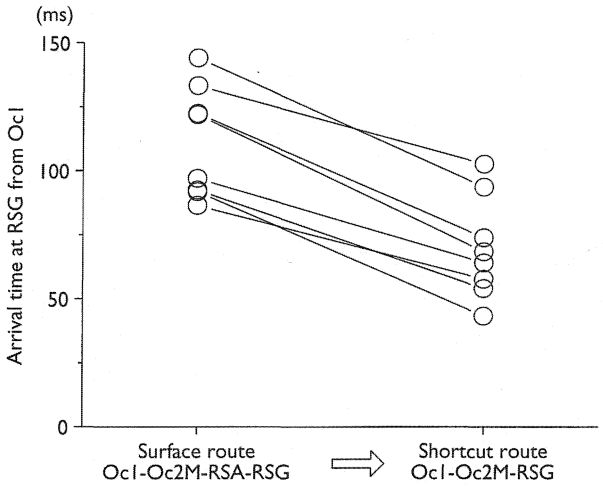

Fig. 3 Reduction of arrival time at RSG from Ocl by opening the shortcut. Arrival times recorded from the same slice before and after opening the shortcut were plotted with open circles, and the pair of circles was connected with a solid line. Data obtained from eight slices were superimposed. Time reduction was obtained by subtracting arrival time via the shortcut from arrival time via the surface route. Mean ($\pm$SD) reduction in arrival time was 40.7 ± 9.6 ms, and arrival time at RSG was significantly reduced ($P<0.01$; $n=8$, t-test) by the opening of shortcut circuits. RSG, granular retrosplenial cortex.

Discussion

We have developed an experimental protocol in which the synesthetical application of caffeine and repetitive electrical stimulation finely elicit long-range signal flows in cortical circuits of brain slices, as described previously [7–10]. Indeed, this is a rather drastic method, but has revealed the dynamic ability of cortical neural networks that is masked during normal experimental conditions. In addition, optical recording methods finely visualize the spatio-temporal network activities of neurons. Under our experimental conditions, we have found and reported that NMDA receptor-dependent oscillatory activities originating from the medial and lateral Oc2 cause opening and strengthening of intercortical signal communications [8,9]. The opening and strengthening are thought to be use-dependent changes, as they require repetitive oscillatory activities [7,9], and as the induction of the oscillatory activities requires both the repetitive NMDA receptor activation and calcium-induced calcium release [11]. The oscillatory origins located near the brain surface, lateral secondary visual cortex (Oc2L) and Oc2M, act as booster and relay stations for neural signals [8,9]. We thus call the origins the intermediaries.

Another intermediary is also located in the deep layer of the RSG. This deep intermediary also delivers NMDA receptor-dependent oscillatory signals (not shown, see Ref. [7]). At first, the surface route, in which signals propagate from the surface intermediary (Oc2M) to the

deep intermediary (RSG) via RSA, was opened in a use-dependent manner. Although this is a roundabout path, the fact that the signal traveling route was use-dependent opened from Oc1 to RSG is important. Neuroanatomically, it was demonstrated that RSG receives innervations from Oc1 [10]. This study proposes a new concept of use-dependent cortical changes, in which traveling neural signals may try to find suitable paths of propagation during repetitive signal traveling. In other words, cortical shortcuts are opened in a use-dependent manner. RSG is in contact with OC2M at the deep layer. As these two areas are able to deliver NMDA receptor-dependent oscillatory signals, both may be prepared for making shortcuts between the visual and retrosplenial cortices [7,8]. The most functional merit of a shortcut is the accomplishment of rapid arrival at the hippocampal formation from the visual cortex. Increases in synaptic efficiency alone cannot achieve such reductions in the arrival time.

Spatial refinement with the opening of a shortcut and subsequent reductions in signal traveling time may be an important strategy. The roles of network oscillation in the brain for synapse plasticity have recently started to be elicited [12]. We have recently proposed the 'Neural oscillator-dependent plasticity hypothesis' [9,13]. This hypothesis might be relevant for the currently proposed brain strategy, as neural oscillation that is convenient to produce temporal and spatial coding might underlie spatial circuitry changes. The spatial changes are based on synaptic selection for choosing appropriate connections between neurons, and the synaptic selection is based on intracellular trafficking [14]. The delivery of NMDA receptor-dependent oscillatory signals from oscillators [7–9] might represent a convenient method for driving the appropriate intracellular traffic.

Conclusion

By applying caffeine and electrical stimulation to rat brain slices and using an optical recording system, we have demonstrated the two signal-traveling pathways from Oc1 to RSG. One is a roundabout pathway along which signals propagate from the upper layer of Oc2M and RSA to the deep layer of the RSG, whereas the other is a shortcut pathway along which signals directly propagate from the deep layer of Oc2M to the deep layer of RSG. The shortcut pathway was opened after repetitive signal propagation. The cortical area between the visual cortex and hippocampal formation may have the ability to change the properties of neural circuits for the reduction of signal traveling time according to synaptic activities.

Acknowledgements

This work was supported by a Health Science Research Grant from the Ministry of Health, Labour and Welfare of Japan (Comprehensive Research on Aging and Health, H-17-Chouju-018), and grants from Kanazawa Medical University (Grant for Promoted Research No. S2005-13).

References

1. Bliss TPV, Collingridge GL. A synaptic model of memory: long term potentiation in the hippocampus. *Nature* 1993; **361**:31–39.
2. Singer W. Development and plasticity of cortical processing architectures. *Science* 1995; **270**:758–764.
3. Buonomano DV, Merzenich MM. Cortical plasticity: from synapses to maps. *Annu Rev Neurosci* 1998; **21**:149–186.
4. Malenka RC, Nicoll RA. Long-term potentiation: a decade of progress? *Science* 1999; **285**:1870–1874.
5. Martin SJ, Grimwood PD, Morris GM. Synaptic plasticity and memory: an evaluation of the hypothesis. *Annu Rev Neurosci* 2000; **23**:649–711.
6. Chen LL, Lin LH, Green EJ, Barnes CA, McNaughton BL. Head-direction cells in the rat posterior cortex. I. Anatomical distribution and behavioral modulation. *Exp Brain Res* 1994; **101**:8–23.
7. Yoshimura H, Sugai T, Honjo M, Segami N, Onoda N. NMDA receptor-dependent oscillatory signal outputs from the retrosplenial cortex triggered by a non-NMDA receptor-dependent signal input from the visual cortex. *Brain Res* 2005; **1045**:12–21.
8. Yoshimura H, Kato N, Sugai T, Segami N, Onoda N. Age-dependent emergence of oscillatory signal flow between the primary and secondary visual cortices in rat brain slices. *Brain Res* 2003; **990**:172–181.
9. Yoshimura H, Sugai T, Segami N, Onoda N. Strengthening of non-NMDA receptor-dependent horizontal pathways between primary and lateral secondary visual cortices after NMDA receptor-dependent oscillatory neural activities. *Brain Res* 2005; **1036**:60–69.
10. Van Groen T, Wyss JM. Connections of the retrosplenial granular A cortex in the rat. *J Comp Nurol* 1990; **300**:593–606.
11. Yoshimura H, Sugai T, Onoda N, Segami N, Kato N. Synchronized population oscillation of excitatory synaptic potentials dependent on calcium-induced calcium release in rat neocortex layer II/III neurons. *Brain Res* 2001; **915**:94–100.
12. Buzsaki G, Draguhn A. Neuronal oscillations in cortical networks. *Science* 2004; **304**:1926–1929.
13. Yoshimura H. The potential of caffeine for functional modification from cortical synapses to neuron networks in the brain. *Curr Neuropharmacol* 2005; **3**:309–316.
14. Jontes JD, Phillips GR. Selective stabilization and synaptic specificity: a new cell-biological model. *Trends in Neurosci* 2006; **29**:186–191.

１．研究課題名：筋細胞再生におけるCa依存性プロテアーゼの動態の解析（研究番号　S2005-14）

２．キーワード：１）α-Fodrin（alpha fodrin）
２）プロテアーゼ（protease）
３）炎症性筋疾患（Inflammatory myopathy）
４）免疫染色（immunohistological study）

３．研究代表者：村田　顕也・医学部・講師・脳脊髄神経治療学　（神経内科学）

４．研究目的

筋ジストロフィーや炎症性ミオパチーをはじめとする筋疾患の機能予後は、筋線維壊死と再生が如何に効率よいバランスで推移するかに起因する。再生が不十分であれば筋線維萎縮に陥り最終的に筋力低下を引き起こす。これまで、各種筋疾患における筋崩壊の機序の検討は多数あるが、筋再生の観点からの検討は非常に少ない。

カルパインは、カルシウム依存性プロテアーゼの一種で、活性化に必要なカルシウム濃度の差異によりカルパイン I、IIに分類される。これまで、カルパインに代表されるカルシウム依存性プロテアーゼは、筋線維崩壊に一義的に作用するものと考えられてきた。筋ジストロフィー患者にカルパイン阻害剤を実際投与する治験も施行されたが、進行予防にはいたらなかった。しかし、近年、カルパインは筋崩壊作用に加え筋再生作用を有していることが示唆された。カルパインの濃度により、本来筋崩壊に関与するカルパインを、筋再生に利用でき、今までとは全く別の観点から筋疾患治療を行う可能性が想定される。

以上のことより、カルパインは筋再生にも関与し、しかも、アイソザイムによりその作用機序が異なることが推測される。

５．研究計画

１．カルシウム依存性プロテアーゼの骨格筋への関与の検討
１）カルパイン活性の測定　２）カルパイン基質の検討　３）ブビカイン投与後の実験的筋壊死モデルでの検討

２．カルパイン活性阻害薬の作用の検討
１）　培養筋を用いての検討
生検筋培養後、筋芽細胞を精製する。筋管細胞への分化の課程でカルパイン活性阻害薬であるカルパスタチンを投与し作用を検討する。
２）　実験的筋壊死モデルでの検討
前述の実験的筋壊死モデルにカルパイン活性阻害薬であるカルパスタチンを投与し壊死再生課程の変化を検討する。

６．研究成果

多発筋炎/皮膚筋炎（PM/ DM）、横紋筋融解症（Rhab）、Duchenne型筋ジストロフィー（DMD）の生検筋を用い、1）m-calpainおよび・μ-calpain、2）α-fodrin、3）myosin heavy chain developmental（MHC-d）の発現を免疫組織学的に検討した。特にα-fodrinは、intact α

-fodrin (280 kDa)に加え、calpain、caspase 3 により切断された 150 kDa α-fodrin 分解産物 (SBDP150s) をそれぞれ選択的に認識する抗体を使用した。さらに各疾患の生検筋の膜分画を抽出し各種・α-fodrin 抗体を使用しウエスタンブロットを行った。

m-μcalpain やα-fodrin は正常対照の筋細胞膜にも発現していたがその程度は軽度であった。一方、疾患群ではα-fodrin は小径化した筋線維の筋細胞膜に、calpain は筋細胞質にそれぞれ発現していた。PM/DM,Rhab では calpain, α-fodrin 共に陽性である筋線維は同時に再生のマーカーである MHC-d も陽性を示したが、DMD では、必ずしも MHC-d が陽性とは限らなかった。筋細胞膜のα-fodrin は calpain により分解された SBDP150 のみを認識する抗体とも反応した。ウエスタンブロットでは、各疾患群にて 150kDa のα-fodrin 断片化産物が認められたが、このバンドも calpain 由来の SBDP150 を認識する抗体とのみ反応した。

以上のことから、筋細胞膜の安定性を維持するために、α-fodrin は絶えず形成され続けるが、calpain により、筋細胞膜はそれぞれ最も適した状態に再構成される。先天的筋疾患である DMD と異なり、PM/DM, Rhab といった後天性筋疾患では同時に筋細胞質の再生を伴うなどその発現パターンは疾患により異なっていた。calpain による・α-fodrin の分断化は筋線維再生と関係なく進行し、各疾患での筋細胞膜の特性を構成するのに重要であることが判明した。

７．研究の考察・反省

今回での検討では、生検筋での検討が主で、α-fodrin の発現動態や、発現機序を検討するのみになってしまい、培養細胞での検討が行えなかった。現在培養筋での検討を施行中である。

８．研 究 発 表

まだ、当研究結果による論文はアクセプトされていません。

現在論文はほぼ完成し、Neurology に投稿準備中です。

１．研究課題名：Anthracycline 系抗腫瘍剤に対する耐性獲得機序およびその克服に関する研究　（研究番号：S2005-15）

２．キーワード：１）アポトーシス（apoptosis）
２）アンソラサイクリン（anthracycline）
３）シスプラチン（cisplatinum）
４）リピッドラフト（lipid raft）
５）スフィンゴミエリン（sphingomyelin）

３．研究代表者：福島　俊洋・医学部・講師・血液免疫制御学（血液免疫内科学）

４．研 究 目 的

成人急性白血病は化学療法により 70-80%に完全寛解が得られるようになったものの、多くが再発するため完治に至る症例は 20-30%に過ぎない。その主たる原因は白血病細胞が抗腫瘍剤に対し耐性を獲得することである。成人急性白血病に対する key drug である daunorubicin など、anthracycline 系抗腫瘍剤に対する耐性獲得機序のひとつに、P-glycoprotein(PGP)の過剰発現による抗腫瘍剤の細胞外へのくみ出し亢進が知られている。申請者らはこれまでに anthracycline 系の新規抗腫瘍剤 idarubicin が PGP の過剰発現した細胞においても良好に細胞内にとどまること、cyclosporin A やその誘導体 PSC-833 により idarubicin の細胞内の貯留はさらに高まり耐性克服に有用であることなどを明らかにしてきた。このような薬理学的特性が評価され、世界的にみても idarubicin は成人急性骨髄性白血病に対する第一選択薬となったが、idarubicin の使用をもってしても治療成績は十分とは言えない。抗がん剤耐性機序の解明と新たな腫瘍殺傷法の開発が血液系悪性腫瘍治療に必須である。我々の研究室では、細胞膜マイクロドメイン（リピッドラフト）の解析を通じて細胞アポトーシスのシグナル経路の検討を行っている。その結果、Fas 依存性アポトーシスにおけるリピッドラフトの関与を証明した。ある種の抗癌剤は Fas 依存性アポトーシスを誘導するが、薬剤耐性を獲得した場合この過程に障害が生じると推察される。我々は、下記に示す如く、リピッドラフトの主要構成脂質であるスフィンゴミエリンの欠失細胞(WR-MOCK)とスフィンゴミエリン合成酵素遺伝子を導入した合成回復株(WR22)を樹立しえた。両細胞を用いて、アポトーシスにおける Fas およびラフトの凝集過程、DISC 形成過程を明らかにし、抗癌剤シスプラチンに対する感受性をその耐性機序を解析する。細胞膜リピッドラフトを制御することにより、抗がん剤耐性を克服しうる治療法の確立を目指す。

５．研 究 計 画

A）スフィンゴミエリン欠失細胞株における Fas 誘導 apoptosis の解析

１） スフィンゴミエリン欠質細胞株（WR-MOCK）細胞にスフィンゴミエリン合成酵素遺伝子を導入し、スフィンゴミエリン合成回復株(WR22)を樹立した。

２） WR22 および WR-MOCK 細胞における細胞膜リピッドラフトを confocal

microscopy による解析を行う。

3） 両細胞における Fas 誘導シグナルの差異を検討する。

4） 細胞膜リピッドラフトを sucrose gradient により分離し、ラフト内移行 Fas の相違を解析する。

B）スフィンゴミエリン欠失細胞株のシスプラチン感受性の検討とそのメカニズムの解析

1） WR22 および WR-MOCK 細胞のシスプラチン感受性を検討する。

2） WR22 および WR-MOCK 細胞のアポトーシスにおけるシスプラチンと Fas 架橋刺激の相加作用を検討する。

3） シスプラチン誘導細胞死における DISC 形成能およびカスパーゼ活性の相違を検討する。

4） シスプラチン誘導細胞死におけるカスパーゼ活性を測定する。

5） 抗アポトーシス作用を有する FLIP, Bcl2 量を WR22 および WR-MOCK 細胞において検討する。

6．研 究 成 果

A）スフィンゴミエリン欠失細胞株細胞株における Fas 誘導 apoptosis の解析

1） スフィンゴミエリン欠質細胞およびコントロール細胞を抗 Fas 抗体（CH11）で刺激し、apoptosis を sub G1 法で FACS で解析し、両細胞における apoptosis の差異を明らかにした。Fas 架橋刺激による DISC 形成、Caspase 活性、ミトコンドリア膜電位の低下は、WR-MOCK 細胞で有意に低下していた。

2）細胞膜リピッドラフトおよび Fas 凝集の confocal microscopy による解析

スフィンゴミエリン欠失細胞株におけるリピッドラフトの形態および機能を明らかにした。細胞膜でのスフィンゴミエリンの局在を明らかにするために、スフィンゴミエリンに特異的に結合する MBP 結合 lysenin と PE 標識抗 MBP 抗体を用いて染色した。Fas 架橋刺激による Cluster 形成を FITC-, PE-標識 Fas 抗体で検出し、ラフト構成における ganglioside GM1 とスフィンゴミエリンおよび Fas の動態を明らかにした。その結果、WR-MOCK 細胞では有意に Fas 凝集が低下していた。

3） Fas 誘導シグナルの差異の検討:Fas 架橋刺激に伴う、FADD、 Caspase-8 と Fas との結合を Western blotting および免疫沈降法を用いて検討した。リピッドラフトを sucrose gradient 法により分画し、ganglioside GM1 量とスフィンゴミエリン量を比較検討した。Fas 刺激に伴う FADD や Caspase などのシグナル伝達物質のリピッドラフトへの移行を検討した。WR-MOCK 細胞では有意に Fas 刺激による caspase-8, caspase-3 活性が抑制されていた。また、Fas に会合する FADD、Caspase-8 量も低下していた。これらの結果は、Fas によるアポトーシスがスフィンゴミエリン欠失細胞では障害されていること示している。

B）スフィンゴミエリン欠失細胞株のシスプラチン感受性の検討とそのメカニズムの解析

1） 2.5 μg/ml、 5μg/ml 濃度のシスプラチン存在下に WR22 および WR-MOCK 細胞の感受性を検討したところ、両細胞とも用量依存性のアポトーシスが誘導された。

2） 25 μg/ml、 50μg/ml 濃度の Fas 抗体存在下で WR22 および WR-MOCK 細胞のアポ

トーシスを検討したところ、WR22 細胞では用量依存性のアポトーシスが認められたが、WR-MOCK 細胞のアポトーシスは著明に低下していた。

3） WR22 および WR-MOCK 細胞を低濃度の Fas 抗体と 2.5 μg/ml、 5μg/ml 濃度のシスプラチン存在下で刺激を加えたところ、WR22 細胞では相乗的なアポトーシスが誘導された。

4） Fas 誘導アポトーシスにおける DISC 形成能に及ぼすシスプラチンの影響を検討したところ、シスプラチンはむしろ DISC 形成を抑制する傾向が認められた。

5） 同様に，Fas 誘導アポトーシスにおけるカスパーゼ活性を検討したところ，シスプラチンはむしろカスパーゼ活性を抑制する傾向が認められた。

以上の結果より、Fas 誘導アポトーシスとシスプラチンによる細胞死との間に異なるメカニズムが存在する可能性が伺われた。

7．研究の考察・反省

上記の結果より、細胞膜スフィンゴミエリンは Fas 誘導アポトーシスに深く関与していることが明らかとなった。その欠質は，Fas を介した細胞のアポトーシスの障害に直結するという結果を得た。シスプラチンは単独でも細胞死を誘導しうるが、Fas との共刺激により相乗的に細胞死を誘導出来る事が明らかになった。しかし、この相乗効果は単に Fas 誘導アポトーシスの増強によるものではない事も判明した. 今後は，シスプラチン誘導細胞死の経路を明らかにしたい. ある種の抗癌剤は細胞膜表面への Fas の発現増加および凝集増強を介して腫瘍細胞のアポトーシスを誘導している。抗癌剤耐性機序に、この Fas 誘導アポトーシスの障害が関わっている可能性が強く示唆され。細胞膜リピッドラフトを制御しうる薬物は、抗がん剤抵抗性を獲得した腫瘍細胞をアポトーシスに引き込む可能性がある。今後、リピッドラフト制御に関わる薬剤の検討を行い、抗がん剤耐性機序の克服を目指す。手法を開発する。これらの研究成果を白血病細胞のみならず悪性リンパ腫や固形腫瘍の細胞に広げていくことで癌化学療法全体の成績向上が期待される。

１．研究課題名：電位非依存性陽イオンチャネル蛋白質 TRP の細胞増殖における機能解析
（研究番号　S2005-16）

２．キーワード：１）容量性 Ca^{2+}流入（capacitative Ca^{2+} entry）
２）細胞増殖（cell proliferation）
３）Ca^{2+}拮抗薬（Ca^{2+} channel blocker）
４）TRP 蛋白質（transient receptor potential（TRP）protein）

３．研究代表者：吉田　純子・医学部・講師・生体情報薬理学（薬理学）

４．研 究 目 的

Ca^{2+}は筋収縮や分泌ばかりでなく、細胞の増殖においても重要な二次メッセンジャーとして働いている。細胞外から細胞内へのCa^{2+}流入を担うCa^{2+}透過性チャネルには、電位依存性 Ca^{2+}チャネルと電位非依存性陽イオンチャネルの二種類があるが、近年、後者を介しておこるCa^{2+}流入が、細胞の増殖に深く関わっていることが明らかになってきた。

我々は、電位依存性 Ca^{2+}チャネルを欠くヒト扁平上皮がん細胞 A431 を標的細胞として用いた研究から、ある種のCa^{2+}拮抗薬が、当該細胞の増殖と核酸合成を抑制することを見いだした。また、その作用に電位非依存性陽イオンチャネルを介する容量性Ca^{2+}流入抑制の機構が関与していることを明らかにしてきた。

本研究では、Ca^{2+}拮抗薬の示すがん細胞増殖抑制作用の機序を詳細に解析することにより、電位非依存性陽イオンチャネルの細胞増殖に果たす役割を明らかにすることを目的とした。

５．研 究 計 画

１）ヒト扁平上皮がん A431 細胞に発現する電位非依存性陽イオンチャネルの解析

これまでの電気生理学的解析により、A431 細胞には電位依存性 L 型 Ca^{2+}チャネルが無く、細胞内 Ca^{2+}貯蔵部位（ストア）の枯渇刺激や G 蛋白質共役受容体刺激で活性化される電位非依存性陽イオンチャネルがあることが示唆されている。近年、電位非依存性陽イオンチャネルの分子実体として transient receptor potential（TRP）蛋白質ファミリーがクローニングされ、そのサブファミリーメンバーの細胞増殖における役割が明らかにされてきた。そこで、RT-PCR 法や Western blot 法にて、A431 細胞に TRP 蛋白質の発現が認められるか否かを調べる。また、small interfering RNA（siRNA）を用いた RNA 干渉法によって TRP 蛋白質と A431 細胞の Ca^{2+}動態や細胞増殖との関連を調べる。

２）Ca^{2+}拮抗薬のヒト扁平上皮がん A431 細胞周期進行に対する影響

我々はこれまでに、ジヒドロピリジン系 Ca^{2+}拮抗薬であるアムロジピンが A431 細胞の増殖と核酸合成を抑制し、当該細胞を皮下移植したヌードマウスの生存日数を延長させることを報告した（Yoshida et al., Eur. J. Pharmacol., 472: 23-31, 2003）。またこの作用に、Ca^{2+}拮抗薬による容量性 Ca^{2+}流入抑制機構が関与していることを示

唆した（Yoshida et al., Eur. J. Pharmacol., 492: 103-112, 2004)。細胞内 Ca^{2+} 濃度の上昇は細胞周期進行においても必要であるため、本研究では Ca^{2+} 拮抗薬の細胞増殖抑制作用機序を解析するための一端として、アムロジピンの A431 細胞の細胞周期進行に及ぼす影響を調べる。細胞周期はフローサイトメトリー法により、細胞周期関連因子の発現と活性の解析はそれぞれ Western blot 法と in vitro kinase assay 法にて行う。

６．研 究 成 果

１）ヒト扁平上皮がん A431 細胞に発現する電位非依存性陽イオンチャネルの解析

7 つのサブファミリーからなる TRP スーパーファミリー蛋白質のうち、細胞内 Ca^{2+} 貯蔵部位（ストア）の枯渇刺激や G 蛋白質共役受容体刺激で活性化される Ca^{2+} 透過性イオンチャネルの分子実体として TRPC サブファミリーが示されている。

そこで、RT-PCR 法にて A431 細胞の TRPC(1-7)サブファミリーメンバーの発現を調べた。その結果、陽性コントロールとしてのヒト脳には TRPC2 を除くすべての TRPC サブファミリーメンバーの発現が認められたのに対し、A431 細胞では、TRPC1 と TRPC5 の発現が認められた。また、TRPC1 と TRPC5 蛋白質の発現は両抗体を用いた Western blot 法により確認された。更に、L 型 Ca^{2+} チャネルのαサブユニットに対するプライマーを用いた PCR では増幅産物は認められず、A431 細胞は L 型 Ca^{2+} チャネルを発現していないことが確認された（Yoshida et al., Eur. J. Pharmacol., 510: 217-222, 2005)。

TRPC サブファミリーメンバーは、ホモまたはヘテロ四量体の形で Ca^{2+} 透過性イオンチャネルを形成していることが報告されている。A431 細胞で発現が確認された TRPC1 と TRPC5 の遺伝子産物が実際に Ca^{2+} 透過性イオンチャネルを形成し、容量性 Ca^{2+} 流入を担っているか否かを確認するため、両遺伝子に対する siRNA を用いて RNA 干渉法による解析を行った。TRPC1 については、加えた siRNA の濃度に依存して遺伝子の発現抑制が認められたが、TRPC5 でははっきりと siRNA の効果が認められなかった。今後、siRNA による発現抑制条件を確立した上で、両遺伝子の細胞内 Ca^{2+} 動態や細胞増殖における役割を引き続き解析していく予定である。

２）Ca^{2+} 拮抗薬のヒト扁平上皮がん A431 細胞周期進行に対する影響

Ca^{2+} 拮抗薬アムロジピンは A431 細胞の核酸合成と増殖を抑制し、その作用に L 型 Ca^{2+} チャネル遮断作用以外の機序、すなわち容量性 Ca^{2+} 流入の抑制が関係していることが解っている（Yoshida et al., Eur. J. Pharmacol., 492: 103-112, 2004)。細胞内 Ca^{2+} 濃度の上昇は、細胞周期進行においても必要であるため、アムロジピンの A431 細胞周期に対する影響をフローサイトメトリー法にて調べた。

その結果、アムロジピンは A431 細胞の細胞周期を G1 期で停止させることが解った。次に、G1 期から S 期進行に必須である pRB（retinoblastoma protein）のリン酸化レベルを Western blot 法で調べたところ、pRB のリン酸化レベルがアムロジピン処置によって有意に低下することが解った。この時、cyclin D1、cyclin dependent kinase 4 (CDK4) および 転写因子 E2F1 のタンパク質発現レベルも低下した。一方、CDK inhibitors の１つである p21 タンパク質の発現は亢進した。更に、in vitro kinase assay 法にて cyclin/CDK 複合体の活性を調べた。その結果、cyclin D1/CDK4 および

cyclin E/CDK2 複合体のキナーゼ活性は共に低下した。以上の結果から、アムロジピンの G1 期停止作用が、CDK inhibitor p21 の発現亢進、cyclin/CDK 複合体のキナーゼ活性の低下とそれに引き続く pRB のリン酸化抑制によってもたらされることが明らかになった（Yoshida et al., Biochem. Pharmacol., 73: 943-953, 2007)。

７．研究の考察・反省

イオンチャネルと細胞増殖の関連を明らかにするため、Ca^{2+}拮抗薬の示す細胞増殖抑制作用に着目して研究を進めた。上記のようにこれまでに、① Ca^{2+}拮抗薬アムロジピンが、本来の標的である電位依存性 L 型 Ca^{2+}チャネルをもたないヒト扁平上皮がん A431 細胞の増殖を in vitro および in vivo で抑制すること、② その作用機序に容量性 Ca^{2+}流入機構の抑制が関与していること、③ A431 細胞には容量性 Ca^{2+}流入チャネルの分子実体と考えられる TRPC1 と TRPC5 が発現していること、④ アムロジピンが A431 細胞の細胞周期を G1 期で停止させること、等が明らかになった。アムロジピンは、降圧薬として臨床使用される際に抗動脈硬化作用を示すが、その機序の１つとして血管平滑筋細胞の増殖抑制の関与が示唆されている点で非常に興味深い。今後、Ca^{2+}拮抗薬による細胞増殖抑制の機序を更に解明することによって、Ca^{2+}透過性イオンチャネルや細胞内 Ca^{2+}シグナリング関連因子を分子標的とする新規抗動脈硬化薬や抗がん薬の創薬に新たな情報を提供できるものと期待される。

８．研 究 発 表

吉田純子、石橋隆治、西尾眞友. カルシウム拮抗薬の多様な作用 -その細胞増殖抑制作用を中心に- 金沢医大誌 2005; 30: 420-426.

Yoshida J, Ishibashi T, Nishio M. G1 cell cycle arrest by amlodipine, a dihydropyridine Ca^{2+} channel blocker, in human epidermoid carcinoma A431 cells. Biochem Pharmacol 2007; 73: 943-953. (MLDB)

金医大誌（J Kanazawa Med Univ）30：420－426, 2005

カルシウム拮抗薬の多様な作用
－その細胞増殖抑制作用を中心に－

吉田純子，石橋隆治，西尾眞友

要　約：細胞内Ca^{2+}イオンは筋収縮，分泌，および細胞の増殖・分化などの情報伝達において重要な二次メッセンジャーとして働いている。その細胞内濃度の恒常性は，細胞膜に存在するCa^{2+}透過性イオンチャネルやイオントランスポーターおよび細胞内Ca^{2+}貯蔵部位からの遊離や取り込み機構によって保たれる。高血圧，狭心症，不整脈の治療薬の一つであるCa^{2+}拮抗薬は電位依存性L型 Ca^{2+}チャネルに結合し，細胞内へのCa^{2+}流入を抑えて血管平滑筋や心筋細胞の興奮性を低下させる。しかし，近年，ある種のCa^{2+}拮抗薬がL型 Ca^{2+} チャネル遮断ではなく，抗酸化作用や血管平滑筋の増殖抑制作用を介して動脈硬化や血管再狭窄に対する予防効果を示すことが明らかにされてきた。また，がん細胞に対する増殖抑制作用も報告され，ヒトがん細胞を用いた我々の基礎的研究結果からもCa^{2+}拮抗薬のがん細胞増殖抑制作用が示唆されている。本総説では，Ca^{2+}拮抗薬の多様な薬理作用，特に細胞増殖抑制作用について概説し，細胞内Ca^{2+}濃度を調節する分子群が，抗動脈硬化薬や抗腫瘍薬の新しい分子標的となる可能性を展望した。

キーワード：　カルシウム拮抗薬，細胞増殖，容量性カルシウム流入，TRP蛋白質，細胞内カルシウム貯蔵部位

1．はじめに

細胞内Ca^{2+}イオンは筋収縮，分泌，細胞の増殖・分化およびアポトーシスなどの情報伝達において重要な二次メッセンジャーとして働いている。細胞内Ca^{2+}濃度の恒常性は，細胞膜に存在するCa^{2+}透過性チャネル，Ca^{2+}-ATPaseおよびイオン交換体と，細胞内Ca^{2+}貯蔵部位（ストア）である小胞体（endoplasmic reticulum；ER）に存在するCa^{2+}-ATPase (sarcoendoplasmic Ca^{2+}-ATPase; SERCA)，イノシトール(1,4,5)三リン酸(IP_3)受容体，およびリアノジン受容体を介する取り込みや遊離機構によって制御されている(1-4)。通常，細胞質内Ca^{2+}濃度は低く維持されている（<100 nM）が，いったん刺激が加わると細胞膜Ca^{2+}チャネルを介して細胞外から細胞内にCa^{2+}が流入し，上昇した細胞質内の遊離Ca^{2+}は直接，あるいはCa^{2+}-calmodulin複合体を形成して，種々のシグナル伝達系の酵素活性や転写活性を制御する(4-6)。この細胞外からのCa^{2+}の流入経路を形成する細胞膜Ca^{2+}チャネルには，電位依存性Ca^{2+}チャネルの他に，非選択的陽イオンチャネルに分類されるリガンド作動性チャネル，受容体作動性チャネル (receptor-operated channels; ROCs) およびストア枯渇性チャネル (store operated channels; SOCs) がある。

現在，狭心症や高血圧の重要な治療薬の一つとして臨床使用されているCa^{2+}拮抗薬は，細胞膜の電位依存性L型Ca^{2+}チャネルのα1サブユニットに特異的結合部位を持ち，細胞内へのCa^{2+}流入を抑えることによって冠状動脈はじめすべての血管平滑筋の弛緩を引き起こす。しかし，放射標識Ca^{2+}拮抗薬を用いた結合実験やCa^{2+}拮抗薬による機能修飾解析の結果から，Ca^{2+}拮抗薬がL型Ca^{2+}チャネルだけでなく種々の細胞内器官と相互作用する可能性が，すでに1980年代に指摘されていた(7)。近年，ある種のCa^{2+}拮抗薬が動脈硬化の進展や血管形成術後の再狭窄を予防すること(8,9)，また，in vitroおよびin vivoの実験においてCa^{2+}拮抗薬が抗腫瘍作用を示すこと(10-15)などが報告されるようになってきた。本総説では，これらの作用の一つであるCa^{2+}拮抗薬の細胞増殖抑制作用の機序について，著者らが得た知見(16-18)とあわせて概観するとともに，細胞内Ca^{2+}濃度の調節に関わる分子群が抗動脈硬化薬や抗腫瘍薬の新しい分子標的となる可能性について考察を試みた。

2．Ca^{2+}拮抗薬の抗動脈硬化作用

多くの動物実験によって，動脈硬化に対してCa^{2+}拮抗薬が予防的な作用を示すことが明らかになっている(8,19)。また臨床研究においても，ニフェジピン，ニカルジピンなどのCa^{2+}拮抗薬が冠動脈造影法により評価した冠動脈病変の発生や軽度病

金沢医科大学生体情報薬理学（薬理学）
石川県河北郡内灘町大学1-1
平成18年3月6日受理

変の進行を予防することが示唆された(19-21)。また近年，冠動脈疾患患者を対象に行った臨床研究成績から，長時間作用型Ca^{2+}拮抗薬アムロジピンが動脈肥厚の進展を有意に抑制することが報告され(9)，アムロジピンの動脈硬化抑制作用を初めて臨床的に証明したものとして注目された。第三世代Ca^{2+}拮抗薬に分類されるアムロジピンは，化学構造上，ユニークな特徴を有し，血管拡張作用以外に多くの作用を示す。集積しつつある基礎的研究のデータによると，アムロジピンの抗動脈硬化作用の機序については，① 抗酸化作用，② 内皮細胞の一酸化窒素 (NO) 産生刺激作用，③ 内皮細胞由来の細胞外マトリックス分解酵素であるマトリックスメタロプロテアーゼ-1 (MMP-1) 産生を抑制する作用，④ 平滑筋細胞の増殖を抑制する作用など複数の可能性が示唆されている(8)。① の抗酸化作用を示す理由として，アムロジピンの化学構造上の特徴が挙げられている。アムロジピンは正に荷電したアミノ基を持つため，負の電荷を持つ細胞膜リン脂質に高い親和性をもち，過酸化の標的となる膜の高度不飽和脂肪酸の近傍に位置することが可能で，その酸化を効率的に抑制しうるという(8,22)。また，② のアムロジピンのNO産生刺激作用には，一酸化窒素合成酵素 (eNOS) の発現亢進と，抗酸化作用を介するNOの半減期延長という両方の作用(23)が関与する。更に，アンギオテンシン変換酵素 (ACE=キニナーゼII) 阻害薬と類似の作用を持つことが示唆された。すなわちアムロジピンのNO産生刺激効果が，NOS阻害薬やブラジキニン受容体阻害薬によって有意に抑制されることから，アムロジピンはブラジキニン活性の上昇を介してNO合成系を刺激し，内皮細胞のNO産生を促進することが示唆された(24,25)。動脈硬化の発生・進展に血管内皮機能の低下が深く関わっており，血管保護作用をもつ生理活性物質NOの放出も内皮機能の低下に伴って低下する。アムロジピンによって産生を促進されるNOが，血管拡張作用，血小板凝集抑制作用，細胞増殖抑制作用や細胞接着阻止作用を介して，動脈硬化抑制効果に寄与していると考えられる(26,27)。また，③ アムロジピンが，MMP-1産生を抑制することが明らかにされている。MMP-1は動脈硬化プラークの線維成分であるコラーゲンを分解するため，MMP-1活性の上昇によって動脈硬化巣の線維成分が減少し，プラークの安定性が低下する。不安定化した動脈硬化プラークの破裂とそれに続く血栓性閉塞が，心筋梗塞や不安定狭心症といった急性冠症候群の主要な成因となることから，プラークを安定化させるような治療が急性冠症候群の予防に必要となる。アムロジピンは，インターロイキン-1β (IL-1β) で刺激した際にみられるMMP-1の発現とコラーゲンの分解活性を共に有意に抑制することが，ヒト培養血管内皮細胞を用いた実験で確認されている(28)。

3．Ca^{2+}拮抗薬の血管平滑筋細胞増殖抑制作用

動脈硬化の進展において，血管平滑筋の遊走・増殖が重要な要因と考えられている。動脈の中膜を構成している血管平滑筋は，酸化等による変性をうけた低比重リポ蛋白 (low density lipoprotein; LDL) の刺激により中膜から内膜に遊走し，表現形を本来の収縮型から合成型に変えてここで盛んに分裂し，動脈硬化プラークのサイズを増大させて病変部の肥厚を進展させる。動物モデルを用いた研究や臨床研究により，Ca^{2+}拮抗薬の作用の一部として，④ 血管平滑筋の遊走・増殖を抑えることによって動脈硬化の進展を抑制することが示された(19,29-31)(前項2．Ca^{2+}拮抗薬の抗動脈硬化作用)。ラット大動脈平滑筋細胞では，血清，トロンビン，線維芽細胞増殖因子 (FGF) 刺激で誘導される増殖がアムロジピン処理によって有意に抑制される(32)。Stepien らは，ラット胸部大動脈平滑筋細胞を用いて細胞内Ca^{2+}動態を観察し，トロンビンで誘発されるthapsigargin (小胞体のCa^{2+}-ATPase (SERCA) 阻害薬) 感受性細胞内Ca^{2+}貯蔵部位 (ストア) からのCa^{2+}遊離やthapsigarginによるストア枯渇性Ca^{2+}流入が共にアムロジピンで抑制されることを示した。そして，アムロジピンがSERCAに直接作用してその酵素活性を抑制している可能性を示唆した(33)。彼らはまた，ヒト血管平滑筋細胞において，アムロジピンがSERCAやL型Ca^{2+}チャネルなど複数の分裂シグナル関連蛋白に作用して細胞増殖抑制効果を示すことを示唆した(34)。また，アムロジピン，ジルチアゼム，ベラパミルは初代ヒト血管平滑筋細胞の転写因子であるNF-IL6やNF-κBの活性化を介して抗炎症サイトカインとしてのインターロイキン-6 (IL-6) 遺伝子発現を亢進させる(35)。細胞周期回転の抑制因子であるp21 (Waf1/Cip1) は，動脈硬化においても重要な役割をしていることが示されているが(36,37)，最近，アムロジピンがヒト肺血管平滑筋細胞のグルココルチコイドレセプターを介してp21 (Waf1/Cip1) の遺伝子発現を亢進することが報告され(38)，抗動脈硬化作用の新しいメカニズムの可能性として注目されている。

4．Ca^{2+}拮抗薬の抗腫瘍作用

TaylorとSimpsonは，アムロジピン，ジルチアゼム，ベラパミルがヒト乳癌細胞HT-39の試験管内増殖を抑制するとともに，ヌードマウスに移植した同腫瘍の増殖を有意に抑制することを報告した(15)。ベラパミル，ニフェジピン，ジルチアゼムは，ヒト脳腫瘍細胞の試験管内増殖を抑制し(13)，ヒト脳腫瘍患者由来初代脳腫瘍細胞の血清，上皮増殖因子 (EGF) および血小板由来増殖因子 (PDGF) 刺激による増殖を抑制する(10,12)。更に，ジルチアゼムとベラパミルでは，ヌードマウスに移植された初代脳腫瘍細胞の増殖に対して抑制作用を示す(11)ことが報告された。また，ベラパミルはヒト前立腺癌細胞LNCaP(14)や，ヒト直腸ガン (HCT) 細胞の増殖を抑制した(39)。Ca^{2+}拮抗薬の腫瘍細胞増殖抑制作用の機序として，これらの報告の中では細胞内Ca^{2+}シグナリングの修飾が示唆されているものの，詳細な作用機序は明らかにされていない。

5．Ca^{2+}拮抗薬のヒト扁平上皮ガン細胞 (A431) に対する細胞増殖抑制作用

5－1．ジヒドロピリジン系Ca^{2+}拮抗薬のA431細胞増殖抑制作用

著者らは，いくつかのCa^{2+}拮抗薬がヒト扁平上皮がん細胞A431細胞の増殖と核酸合成を抑制することを見いだした(17)。各種Ca^{2+}拮抗薬のA431細胞増殖と核酸合成に対する影響をそれぞれ，MTT (3-(4,5-dimethylthiazol-2-yl)-2,5-diphenyl tetrasodium) による比色法と核酸前駆体5-bromo-2'-deoxyuridine (BrdU) の細胞内への取り込み活性を指標として調べたところ，ジヒドロピリジン系のアムロジピン，ニカルジピンおよびニモジピンが濃度依存性に同細胞の増殖と核酸合成を抑制したが (50%増殖抑制濃度；20-30 μM)，同濃度のフェニルアルキルアミン系のベラパミル，ベンゾジアゼピン系のジルチアゼムでは増殖抑制作用はみられなかった。興味あることに，同じジヒドロピリジン系でもニフェジピンは，同細胞の増殖になんの影響ももたらさなかった。この結果が，ジヒドロピリジン系Ca^{2+}拮抗薬の化学構造上の相違によるものか，あるいはA431細胞の標的分子の特性に起因するものなのかは現在のところ明らかではないが，ジヒドロピリジン系Ca^{2+}拮抗薬のA431細胞増殖抑制作用機序を解析する上で，ニフェジピンは有用なnegative controlになると思われる。

5－2．ジヒドロピリジン系Ca^{2+}拮抗薬の細胞内Ca^{2+}動態に及ぼす影響

Ca^{2+}拮抗薬は本来，電位依存性L型Ca^{2+}チャネルの α1サブユニットに結合し，興奮性細胞内へのCa^{2+}流入を抑制して細胞膜の興奮性を低下させる。しかし，電気生理学的解析よりA431細胞にはCa^{2+}拮抗薬が結合するべきL型Ca^{2+}チャネルがないとされている(40)。一方，この細胞には電気的性質の異なる2種のCa^{2+}透過性チャネル，すなわちストア枯渇性Ca^{2+}チャネル (store-operated Ca^{2+} channels; SOCs) とCRAC (calcium release-activated Ca^{2+}) チャネルが存在することがMozhayevaら(41-43)のパッチクランプ法による一連の電気生理学的解析によって示されている。2つのチャネルは，細胞内Ca^{2+}貯蔵部位 (ストア) の枯渇刺激または，ホスホリパーゼC (PLC) 共役アゴニストであるuridine 5'- triphosphate (UTP) によるG蛋白質共役型受容体刺激によって共に活性化される。ちなみに，SOCsを介するCa^{2+}流入は，電気回路におけるcapacitator (コンデンサー) に例えて容量性Ca^{2+}流入 (capacitative Ca^{2+} entry:CCE) と呼ばれる(1)。CRACチャネルはCa^{2+}高選択性の容量性Ca^{2+}流入チャネルの1つである。そこで，容量性Ca^{2+}流入がCa^{2+}拮抗薬によって影響されるか否かを調べるために，まず，ストア枯渇薬であるcyclopiazonic acidやthapsigarginを用いて実験を行った。両試薬は，小胞体にCa^{2+}を汲みいれるポンプCa^{2+}-ATPase (SERCA) を阻害することによって細胞内Ca^{2+}貯蔵部位 (ストア) のCa^{2+}を枯渇させ，ストア枯渇性Ca^{2+}流入を惹起させる。Ca^{2+}蛍光指示薬fura-2またはfluo-3を負荷したA431細胞に両試薬を適用して細胞内Ca^{2+}動態を解析すると，増殖抑制活性を示したアムロジピン，ニカルジピンおよびニモジピンは，cyclopiazonic acidまたはthapsigargin によって惹起されるストア枯渇性Ca^{2+}流入を有意に減弱させることがわかった。一方，増殖抑制活性を示さなかったニフェジピン，ベラパミル，ジルチアゼムにこのような作用は認められなかった。この結果から，Ca^{2+}拮抗薬による細胞増殖抑制に，ストア枯渇刺激で惹起されるCa^{2+}流入の抑制作用が関連していることが示唆された。

次に，PLC共役アゴニストUTP を用いて，G蛋白質共役型受容体刺激によって起こるCa^{2+}反応へのCa^{2+}拮抗薬の影響を検討した。UTPはGq蛋白質共役受容体に結合し，PLCβの活性化を介してIP_3を産生する。産生したIP_3は小胞体のIP_3受容体を刺激，細胞内Ca^{2+}貯蔵部位 (ストア) である小胞体からCa^{2+}を遊離させることによって容量性Ca^{2+}流入を引き起こす。増殖抑制作用をもつCa^{2+}拮抗薬アムロジピンを培養液に加えて1時間前培養した細胞では，UTPによる容量性Ca^{2+}流入が減弱した。このようにストア枯渇刺激とPLC共役アゴニスト刺激によっておこる容量性Ca^{2+}流入がいずれもアムロジピン処理によって抑制されたことから，アムロジピンなどのCa^{2+}拮抗薬がSOC，CRACのいずれかあるいは両方を介するCa^{2+}流入を抑えることによって増殖抑制作用を示している可能性が示された(16)。

5－3．ジヒドロピリジン系Ca^{2+}拮抗薬アムロジピンのA431細胞移植ヌードマウスに対する抗腫瘍作用

A431細胞を皮下移植したヌードマウスに，腫瘍移植3日後よりジヒドロピリジン系Ca^{2+}拮抗薬アムロジピン (10 mg/kg) を20日間にわたって腹腔内投与したところ，腫瘍の増殖は対照群に比べて有意に抑制され，マウスの生存日数は有意に延長した(16)。実験中，対照群とアムロジピン投与群のマウスの体重には有意の差は見られなかったものの，アムロジピン投与開始後14日目から，注射後に痛み反応としてのストレッチング反応を示すマウスが現れた。この機序については明らかではないが，アムロジピンの慢性投与によってACE (＝キニナーゼII) が阻害され，キニン産生が高まった結果とも考えられる。アムロジピンにはACE (＝キニナーゼII) 阻害作用があり，その結果産生するブラジキニンが，ブラジキニンB_2受容体刺激を介してNO産生を高めることが示唆されている(25)。したがって，A431移植ヌードマウスにおけるアムロジピンの抗腫瘍作用にNOが関与している可能性も否定できない。NOの腫瘍に対する効果については，促進と抑制作用の両論がある(44)が，最近，NO合成酵素 (NOS2 (=iNOS)) とその制御因子p53をノックアウトしたマウスにおいて，癌の自然発生が高まることが示されており(45)，NOの癌新生抑制効果を示唆した報告として興味深い。

6．容量性カルシウム流入を担うTRP蛋白質

容量性Ca^{2+}流入の抑制が，ジヒドロピリジン系Ca^{2+}拮抗薬の

細胞増殖抑制作用と関連しているとした著者らの実験結果は，一方で，A431細胞の容量性Ca^{2+}流入を担うCa^{2+}透過性チャネルの分子実体とその細胞増殖との関連に関心を抱かせた。

容量性Ca^{2+}流入を担うストア枯渇性チャネル (store operated channels; SOCs) や受容体作動性チャネル (receptor-operated channels; ROCs) の分子実体として近年明らかになったのがtransient receptor potential (TRP) 蛋白質である。*trp*遺伝子は，1989年，ショウジョウバエの光受容器異常変異株の原因遺伝子として同定された(46)。ショウジョウバエ*trp*変異株では光応答電位が，持続的 (sustained) ではなく一過性 (transient) の変化しか示さず，細胞外からのCa^{2+}流入が減弱するが，この遺伝子産物TRP蛋白質はショウジョウバエの光受容反応カスケードの最終段階で機能するCa^{2+}流入チャネルであることが明らかになった(47)。その後，脊椎動物でも多くのTRPホモログがクローニングされてイオンチャネルTRPスーパーファミリーを形成するに至っている。TRPスーパーファミリーはTRPC (canonical), TRPM (melastatin), TRPV (vanilloid), TRPML (mucolipin), TRPP (polycystin), TRPA (ankyrin) とTRPN (no mechanoreceptor potential C, or NOMPC) イオンチャネルと呼ばれる7つのサブファミリーからなる(48)。すべてのTRPsはC末端に共通のTRPドメイン (25個のアミノ酸からなる) と中央に6回膜貫通領域 (5-6番目の間にポアドメイン) を持ち，ヘテロ四量体としてCa^{2+}およびMg^{2+}透過性のイオンチャネルを形成する。TRPチャネルは，酵母からヒトに至るあらゆる生物の興奮性細胞，非興奮性細胞に存在し，痛覚，浸透圧，温度，pH，酸化還元状態の変化，さらに増殖・分化刺激のtransducerとして機能していると考えられている(48,49)。

そこで，細胞増殖との関連が示唆されているTRPCサブファミリー (TRPC1－7)(49)について，著者らは，RT-PCRとウエスタンブロットによる発現解析を行った。その結果，A431細胞にTRPC1，TRPC5遺伝子と蛋白質が発現していることが明らかになった(18)。一方，TRPVサブファミリーの1つであるTRPV6がCRACの分子的実体を担っている可能性が提唱されている(50)が，RT-PCRによる発現解析ではA431細胞に増幅産物は検出されなかった。従って，TRPC1とTRPC5がおそらくヘテロ四量体を形成してA431細胞の容量性Ca^{2+}流入を担っているのではないかと推測される。しかし，直接的な証明には両遺伝子に対するアンチセンスオリゴヌクレオチドやsiRNAを用いたRNA干渉法による解析が必要であろう。

7．TRP蛋白質の細胞増殖における機能

肺動脈血管平滑筋の増殖による肺血管中膜肥厚は，肺高血圧患者における肺血管抵抗の増強に深く関与している。そのメカニズムの一つとして，肺動脈血管平滑筋細胞の増殖におけるTRPチャネル蛋白質の機能解析が進んでいる(51)。ヒト肺動脈血管の平滑筋細胞を血清と増殖因子を含む培地で培養すると，無血清培地で培養した場合に比べ細胞増殖が促進される。この時，cyclopiazonic acidによって惹起される細胞内Ca^{2+}貯蔵部位(ストア) からのCa^{2+}遊離とストア枯渇性のCa^{2+}流入が共に高まって，cyclopiazonic acidによる単一チャネル電流が増大するとともに，TRPC1のmRNA発現が亢進した(52)。また，TRPC1に対するアンチセンスオリゴヌクレオチドでTRPC1発現を抑制すると，同細胞のcyclopiazonic acid誘発容量性Ca^{2+}流入や増殖が低下する(53)。ラット肺動脈平滑筋細胞をPDGFで刺激して増殖させると，c-Jun/STAT3の活性化を介してTRPC6の発現が亢進し，それに伴って容量性Ca^{2+}流入も増大した(54)。また，ヒト肺動脈内皮細胞では，酸化ストレスが容量性Ca^{2+}流入とストア枯渇性Ca^{2+}電流の増加を引き起こし，同時にTRPC4遺伝子および蛋白質の発現を亢進させることから，酸化ストレスによる肺高血圧の肺血管リモデリングに内皮細胞TRPが関与することが示唆された(55)。

肺動脈平滑筋ばかりでなく，気管支平滑筋細胞 (ラット) を用いた実験でも，その収縮や増殖にTRPC1が関与していることが示されて(56)おり，気管支喘息とTRPチャネル蛋白質の関連が注目される。また，胎児神経幹細胞 (ラット) では，basic fibroblast growth factor (bFGF)/bFGF受容体刺激を介して細胞内へのCa^{2+}流入と細胞増殖が促進されること，このCa^{2+}流入にTRPC1が寄与していることが報告された(57)。このように，平滑筋細胞や神経細胞の分裂刺激にTRP蛋白質が深く関わっていることを示すデータが増えている。

8．細胞内Ca^{2+}ストアの細胞増殖における機能

細胞が増殖するためには，細胞質から小胞体にCa^{2+}を移動させるポンプであるCa^{2+}- ATPase (SERCA) が働いて細胞内Ca^{2+}貯蔵部位 (ストア) にCa^{2+}が充分に満たされていることが必要である(4)。Legrand らは，ヒト前立腺癌細胞LNCaPにおいて，SERCAの機能が細胞の増殖に密接に関係することを初めて示した。つまり，EGFは濃度依存性にLNCaPの増殖を促進するが，EGFを含まない培地中で培養した細胞では，小胞体のCa^{2+}含量が低下するばかりでなく，SERCAのアイソフォームSERCA1, 2a, 2b, 3のうちSERCA2b発現も低下する(58)。この結果から，SERCAが前立腺癌治療の新しい分子標的となる可能性が示唆された。実際，SERCA機能を直接抑制してCa^{2+}貯蔵部位 (ストア) を枯渇させるthapsigarginは，確かに細胞増殖を抑制するが，正常細胞にも毒性を示す。そこで，thapsigarginにペプチドを結合させて無毒性のプロドラッグを設計する試みがある。すなわち，前立腺癌に高発現するserine protease prostate-specific antigen (PSA) のような癌特異的プロテアーゼによって分解されて，その場ではじめて活性化されるようなプロドラッグ (PSA-activated thapsigargin prodrugs) を作成して，癌治療に用いようとするものである(59)。また，thapsigarginの誘導体をlead compoundsとして，SERCAの膜貫通疎水性部位に結合し，Ca^{2+}輸送を阻止するような強力かつ特異的SERCA阻害薬の開発も進められている(60)。

9．細胞増殖抑制のための戦略

SERCAを阻害する（上記8.）以外に，容量性Ca^{2+}流入を抑制することも，細胞増殖制御の戦略の一つとなりうる。Carboxyamidotriazole (CAI) は，容量性Ca^{2+}流入抑制作用を持つ新しい抗腫瘍物質として開発された(61)。CAIは，血管内皮細胞の増殖を抑制して血管新生を抑制(62-64)したり，小細胞肺がん細胞(65)やヒト肝がん細胞(66)の増殖を抑制する。また，進行がんに対する第Ⅰ相試験(67)や再発卵巣癌に対する第Ⅱ相試験(68)も行われている。

その他に，ジヒドロピリジン系Ca^{2+}拮抗薬ニトレンジピンやニフェジピンの種々誘導体を合成し，ヒト前骨髄性白血病細胞(HL60) のadenosine triphosphate (ATP) で惹起される容量性Ca^{2+}流入とイノシトールリン酸代謝を指標にして，より強力で選択的な容量性Ca^{2+}流入抑制物質の探索を試みた研究もある(69)。

現在のところ，CAIやCa^{2+}拮抗薬がTRP蛋白質の機能を修飾するという報告は見あたらない。しかし，両物質が容量性Ca^{2+}流入を抑制すること，TRP蛋白質が容量性Ca^{2+}流入を担っていること，細胞増殖においてTRP蛋白質が機能していること，増殖因子受容体刺激とTRP蛋白質が連関していること，また最近の，Ca^{2+}拮抗薬アムロジピンがEGF受容体リン酸化を抑制することによって心筋肥大を改善するという報告(70)等を勘案すると，TRP蛋白質を介する増殖シグナリングにCa^{2+}拮抗薬が関わる可能性は充分想定されよう。

10．おわりに

細胞の増殖には細胞質内Ca^{2+}イオン濃度の上昇は必須であるが，Ca^{2+}イオンがあまりにも普遍的な二次メッセンジャーであるために，細胞増殖抑制を目的とするCa^{2+}シグナル調節薬は未だ無い。しかし，本総説で紹介した多くの知見は，細胞内Ca^{2+}貯蔵部位である小胞体のCa^{2+}取り込み機構に関わる分子群や，細胞内への容量性Ca^{2+}流入を担うチャネルの分子実体であるTRP蛋白質が，細胞増殖を抑制するための分子標的になる可能性を強く示唆している。我々は，Ca^{2+}拮抗薬アムロジピンが，本来の標的である電位依存性Ca^{2+}チャネルを持たないヒトがん細胞の増殖をin vitroおよびin vivoで抑制することを見いだし，その作用機序に容量性Ca^{2+}流入機構の抑制が関与することを示唆した。本薬物が，電位依存性Ca^{2+}チャネル遮断以外の機序を介して血管平滑筋細胞の異常増殖を抑制し，抗動脈硬化作用を示すことが示唆されている点で非常に興味深い。今後，Ca^{2+}拮抗薬による細胞増殖抑制の機序が更に解明されれば，抗動脈硬化薬や抗腫瘍薬の開発に有用な情報を提示できるものと期待される。

本稿に引用した我々の研究は，平成13年金沢医科大学奨励研究費 (S2001-13)，平成14-15年度日本学術振興会基盤研究C (14570091) および平成17年度金沢医科大学奨励研究 (萌芽) 費 (S2005-16) の助成によりなされた。

文　献

1. Putney JW Jr, Broad LM, Braun FJ et al: Mechanisms of capacitative calcium entry. J Cell Sci 2001; **114**: 2223-9.
2. Putney JW Jr, Bird GS: The inositol phosphate-calcium signaling system in nonexcitable cells. Endocr Rev 1993; **14**: 610-31.
3. Clapham DE: Calcium signaling. Cell 1995; **80**: 259-68.
4. Lipskaia L, Lompre AM: Alteration in temporal kinetics of Ca^{2+} signaling and control of growth and proliferation. Biol Cell 2004; **96**: 55-68.
5. Agell N, Bachs O, Rocamora N et al: Modulation of the Ras/Raf/MEK/ERK pathway by Ca^{2+}, and calmodulin. Cell Signal 2002; **14**: 649-54.
6. Munaron L, Antoniotti S, Lovisolo D: Intracellular calcium signals and control of cell proliferation: how many mechanisms? J Cell Mol Med 2004; **8**: 161-8.
7. Zernig G: Widening potential for Ca^{2+} antagonists: non-L-type Ca^{2+} channel interaction. Trends Pharmacol Sci 1990; **11**: 38-44.
8. Mason RP, Marche P, Hintze TH: Novel vascular biology of third-generation L-type calcium channel antagonists: ancillary actions of amlodipine. Arterioscler Thromb Vasc Biol 2003; **23**: 2155-63.
9. Pitt B, Byington RP, Furberg CD et al: Effect of amlodipine on the progression of atherosclerosis and the occurrence of clinical events. PREVENT Investigators. Circulation 2000; **102**: 1503-10.
10. Jensen RL, Petr M, Wurster RD: Calcium channel antagonist effect on in vitro meningioma signal transduction pathways after growth factor stimulation. Neurosurgery 2000; **46**: 692-702.
11. Jensen RL, Wurster RD: Calcium channel antagonists inhibit growth of subcutaneous xenograft meningiomas in nude mice. Surg Neurol 2001; **55**: 275-83.
12. Jensen RL, Origitano TC, Lee YS et al: In vitro growth inhibition of growth factor-stimulated meningioma cells by calcium channel antagonists. Neurosurgery 1995; **36**: 365-73.
13. Lee YS, Sayeed MM, Wurster RD: Inhibition of cell growth and intracellular Ca^{2+} mobilization in human brain tumor cells by Ca^{2+} channel antagonists. Mol Chem Neuropathol 1994; **22**: 81-95.
14. Rybalchenko V, Prevarskaya N, Van Coppenolle F et al: Verapamil inhibits proliferation of LNCaP human prostate cancer cells influencing K^+ channel gating. Mol Pharmacol 2001; **59**: 1376-87.
15. Taylor JM, Simpson RU: Inhibition of cancer cell growth by calcium channel antagonists in the athymic mouse. Cancer Res 1992; **52**: 2413-8.
16. Yoshida J, Ishibashi T, Nishio M: Antitumor effects of amlodipine, a Ca^{2+} channel blocker, on human epidermoid carcinoma A431 cells in vitro and in vivo. Eur J Pharmacol 2004; **492**: 103-12.
17. Yoshida J, Ishibashi T, Nishio M: Antiproliferative effect of Ca^{2+} channel blockers on human epidermoid carcinoma A431 cells. Eur J Pharmacol 2003; **472**: 23-31.
18. Yoshida J, Ishibashi T, Imaizumi N et al: Capacitative Ca^{2+} entries and mRNA expression for TRPC1 and TRPC5 channels in human epidermoid carcinoma A431 cells. Eur J Pharmacol 2005; **510**: 217-22.
19. Waters D, Lesperance J: Calcium channel blockers and coronary atherosclerosis: from the rabbit to the real world. Am Heart J 1994; **128**: 1309-16.
20. Waters D, Lesperance J, Francetich M et al: A controlled clinical trial to assess the effect of a calcium channel blocker on the progression of coronary atherosclerosis. Circulation 1990; **82**: 1940-53.
21. Lichtlen PR, Hugenholtz PG, Rafflenbeul W et al: Retardation of angiographic progression of coronary artery disease by nifedipine. Results of the International Nifedipine Trial on Antiatherosclerotic Therapy (INTACT). INTACT Group Investigators. Lancet 1990; **335**: 1109-13.
22. Mason RP: Atheroprotective effects of long-acting dihydropyridine-type calcium channel blockers: evidence from clinical trials and basic scientific research. Cerebrovasc Dis 2003; **16** Suppl 3: 11-7.
23. Berkels R, Taubert D, Bartels H et al: Amlodipine increases endothelial nitric oxide by dual mechanisms. Pharmacology 2004; **70**: 39-45.
24. Zhang X, Hintze TH: Amlodipine releases nitric oxide from canine coronary microvessels: an unexpected mechanism of action of a calcium channel-blocking agent. Circulation 1998; **97**: 576-80.
25. Xu B, Xiao-hong L, Lin G et al: Amlodipine, but not verapamil or nifedipine,

dilates rabbit femoral artery largely through a nitric oxide- and kinin-dependent mechanism. Br J Pharmacol 2002; **136**: 375-82.
26. Zhang XP, Loke KE, Mital S et al: Paradoxical release of nitric oxide by an L-type calcium channel antagonist, the R+ enantiomer of amlodipine. J Cardiovasc Pharmacol 2002; **39**: 208-14.
27. Kato M, Matsumoto A, Nakajima T et al: Amlodipine increases nitric oxide production in exhaled air during exercise in patients with essential hypertension. Am J Hypertens 2004; **17**: 729-33.
28. Ikeda U, Hojo Y, Ueno S et al: Amlodipine inhibits expression of matrix metalloproteinase-1 and its inhibitor in human vascular endothelial cells. J Cardiovasc Pharmacol 2000; **35**: 887-90.
29. Schachter M: Calcium antagonists and atherosclerosis. Int J Cardiol 1997; **62** Suppl 2: S9-15.
30. Schachter M: Vascular smooth muscle cell migration, atherosclerosis, and calcium channel blockers. Int J Cardiol 1997; **62** Suppl 2: S85-90.
31. Kahn MB, Boesze-Battaglia K, Stepp DW et al: Influence of serum cholesterol on atherogenesis and intimal hyperplasia after angioplasty: inhibition by amlodipine. Am J Physiol Heart Circ Physiol 2005; **288**: H591-600.
32. Stepien O, Gogusev J, Zhu DL et al: Amlodipine inhibition of serum-, thrombin-, or fibroblast growth factor-induced vascular smooth-muscle cell proliferation. J Cardiovasc Pharmacol 1998; **31**: 786-93.
33. Stepien O, Marche P: Amlodipine inhibits thapsigargin-sensitive Ca^{2+} stores in thrombin-stimulated vascular smooth muscle cells. Am J Physiol Heart Circ Physiol 2000; **279**: H1220-7.
34. Stepien O, Zhang Y, Zhu D et al: Dual mechanism of action of amlodipine in human vascular smooth muscle cells. J Hypertens 2002; **20**: 95-102.
35. Eickelberg O, Roth M, Mussmann R et al: Calcium channel blockers activate the interleukin-6 gene via the transcription factors NF-IL6 and NF-kappaB in primary human vascular smooth muscle cells. Circulation 1999; **99**: 2276-82.
36. Condorelli G, Aycock JK, Frati G et al: Mutated p21/WAF/CIP transgene overexpression reduces smooth muscle cell proliferation, macrophage deposition, oxidation-sensitive mechanisms, and restenosis in hypercholesterolemic apolipoprotein E knockout mice. FASEB J 2001; **15**: 2162-70.
37. Nathe TJ, Deou J, Walsh B et al: Interleukin-1beta inhibits expression of p21 (WAF1/CIP1) and p27 (KIP1) and enhances proliferation in response to platelet-derived growth factor-BB in smooth muscle cells. Arterioscler Thromb Vasc Biol 2002; **22**: 1293-8.
38. Ziesche R, Petkov V, Lambers C et al: The calcium channel blocker amlodipine exerts its anti-proliferative action via p21 (Waf1/Cip1) gene activation. FASEB J 2004; **18**: 1516-23.
39. Cao QZ, Niu G, Tan HR: In vitro growth inhibition of human colonic tumor cells by verapamil. World J Gastroenterol 2005; **11**: 2255-9.
40. Lückhoff A, Clapham DE: Calcium channels activated by depletion of internal calcium stores in A431 cells. Biophys J 1994; **67**: 177-82.
41. Kaznacheyeva E, Zubov A, Nikolaev A et al: Plasma membrane calcium channels in human carcinoma A431 cells are functionally coupled to inositol 1,4,5-trisphosphate receptor-phosphatidylinositol 4,5-bisphosphate complexes. J Biol Chem 2000; **275**: 4561-4.
42. Kaznacheyeva E, Zubov A, Gusev K et al: Activation of calcium entry in human carcinoma A431 cells by store depletion and phospholipase C-dependent mechanisms converge on ICRAC-like calcium channels. Proc Natl Acad Sci U S A 2001; **98**: 148-53.
43. Mozhayeva MG, Kiselyov KI: Involvement of Ca^{2+}-induced Ca^{2+} release in the biphasic Ca^{2+} response evoked by readdition of Ca^{2+} to the medium after UTP-induced store depletion in A431 cells. Pflügers Arch 1998; **435**: 859-64.
44. Hussain SP, Hofseth LJ, Harris CC: Radical causes of cancer. Nat Rev Cancer 2003; **3**: 276-85.
45. Hussain SP, Trivers GE, Hofseth LJ et al: Nitric oxide, a mediator of inflammation, suppresses tumorigenesis. Cancer Res 2004; **64**: 6849-53.
46. Montell C, Rubin GM: Molecular characterization of the Drosophila trp locus: a putative integral membrane protein required for phototransduction. Neuron 1989; **2**: 1313-23.
47. Hardie RC, Minke B: Novel Ca^{2+} channels underlying transduction in Drosophila photoreceptors: implications for phosphoinositide-mediated Ca^{2+} mobilization. Trends Neurosci 1993; **16**: 371-6.
48. Pedersen SF, Owsianik G, Nilius B: TRP channels: An overview. Cell Calcium 2005; **38**: 233-52.
49. Clapham DE: TRP channels as cellular sensors. Nature 2003; **426**: 517-24.
50. Yue L, Peng JB, Hediger MA et al: CaT1 manifests the pore properties of the calcium-release-activated calcium channel. Nature 2001; **410**: 705-9.
51. Landsberg JW, Yuan JX: Calcium and TRP channels in pulmonary vascular smooth muscle cell proliferation. News Physiol Sci 2004; **19**: 44-50.
52. Golovina VA, Platoshyn O, Bailey CL et al: Upregulated TRP and enhanced capacitative Ca^{2+} entry in human pulmonary artery myocytes during proliferation. Am J Physiol Heart Circ Physiol 2001; **280**: H746-55.
53. Sweeney M, Yu Y, Platoshyn O et al: Inhibition of endogenous TRP1 decreases capacitative Ca^{2+} entry and attenuates pulmonary artery smooth muscle cell proliferation. Am J Physiol Lung Cell Mol Physiol 2002; **283**: L144-55.
54. Yu Y, Sweeney M, Zhang S et al: PDGF stimulates pulmonary vascular smooth muscle cell proliferation by upregulating TRPC6 expression. Am J Physiol Cell Physiol 2003; **284**: C316-30.
55. Fantozzi I, Zhang S, Platoshyn O et al: Hypoxia increases AP-1 binding activity by enhancing capacitative Ca^{2+} entry in human pulmonary artery endothelial cells. Am J Physiol Lung Cell Mol Physiol 2003; **285**: L1233-45.
56. Sweeney M, McDaniel SS, Platoshyn O et al: Role of capacitative Ca^{2+} entry in bronchial contraction and remodeling. J Appl Physiol 2002; **92**: 1594-602.
57. Pla AF, Maric D, Brazer SC et al: Canonical transient receptor potential 1 plays a role in basic fibroblast growth factor (bFGF)/FGF receptor-1-induced Ca^{2+} entry and embryonic rat neural stem cell proliferation. J Neurosci 2005; **25**: 2687-701.
58. Legrand G, Humez S, Slomianny C et al: Ca^{2+} pools and cell growth. Evidence for sarcoendoplasmic Ca^{2+}-ATPases 2B involvement in human prostate cancer cell growth control. J Biol Chem 2001; **276**: 47608-14.
59. Denmeade SR, Isaacs JT: The SERCA pump as a therapeutic target: making a "smart bomb" for prostate cancer. Cancer Biol Ther 2005; **4**: 14-22.
60. Singh P, Mhaka AM, Christensen SB et al: Applying linear interaction energy method for rational design of noncompetitive allosteric inhibitors of the sarco- and endoplasmic reticulum calcium-ATPase. J Med Chem 2005; **48**: 3005-14.
61. Kohn EC, Liotta LA: L651582: a novel antiproliferative and antimetastasis agent. J Natl Cancer Inst 1990; **82**: 54-60.
62. Faehling M, Kroll J, Fohr KJ et al: Essential role of calcium in vascular endothelial growth factor A-induced signaling: mechanism of the antiangiogenic effect of carboxyamidotriazole. FASEB J 2002; **16**: 1805-7.
63. Oliver VK, Patton AM, Desai S et al: Regulation of the pro-angiogenic microenvironment by carboxyamido-triazole. J Cell Physiol 2003; **197**: 139-48.
64. Antoniotti S, Fiorio PA, Pregnolato S et al: Control of endothelial cell proliferation by calcium influx and arachidonic acid metabolism: a pharmacological approach. J Cell Physiol 2003; **197**: 370-8.
65. Moody TW, Chiles J, Moody E et al: CAI inhibits the growth of small cell lung cancer cells. Lung Cancer 2003; **39**: 279-88.
66. Enfissi A, Prigent S, Colosetti P et al: The blocking of capacitative calcium entry by 2-aminoethyl diphenylborate (2-APB) and carboxyamidotriazole (CAI) inhibits proliferation in Hep G2 and Huh-7 human hepatoma cells. Cell Calcium 2004; **36**: 459-67.
67. Desai AA, Innocenti F, Janisch L et al: A phase I trial of pharmacokinetic modulation of carboxyamidotriazole (CAI) with ketoconazole in patients with advanced cancer. Cancer Chemother Pharmacol 2004; **54**: 377-84.
68. Hussain MM, Kotz H, Minasian L et al: Phase II trial of carboxyamidotriazole in patients with relapsed epithelial ovarian cancer. J Clin Oncol 2003; **21**: 4356-63.
69. Harper JL, Camerini-Otero CS, Li A-H et al: Dihydropyridines as inhibitors of capacitative calcium entry in leukemic HL-60 cells. Biochem Pharmacol 2003; **65**: 329-38.
70. Liao Y, Asakura M, Takashima S et al: Amlodipine ameliorates myocardial hypertrophy by inhibiting EGFR phosphorylation. Biochem Biophys Res Commun 2005; **327**: 1083-7.

Antiproliferative Action of Ca^{2+} Channel Blockers

Junko Yoshida, Takaharu Ishibashi and Matomo Nishio

Department of Pharmacology, Kanazawa Medical University, Uchinada, Ishikawa 920-0293, Japan

Ca^{2+} plays a central role in many fundamental cellular processes including muscle contraction, secretion, and cellular differentiation and proliferation. The intracellular Ca^{2+} homeostasis is controlled by Ca^{2+} permeable ionic channels and transporters in the plasma membrane and by Ca^{2+} release and uptake of internal Ca^{2+} stores. Ca^{2+} channel blockers, due to their inhibitory effects on the voltage-dependent L-type Ca^{2+} channels, have been used therapeutically to control hypertension, angina, and tachyarrhythmia. Recent data, however, have demonstrated that Ca^{2+} channel blockers have antiatherosclerotic and antiproliferative action, beyond their blood pressure-lowering effect. We demonstrated that some dihydropyridine Ca^{2+} channel blockers inhibit the growth and DNA synthesis of human epidermoid carcinoma A431 cells in part by inhibiting capacitative Ca^{2+} entry.The possible strategies based on lowering the intracellular Ca^{2+} concentration would be considered to arrest cell growth and proliferation, which potentially lead to prevent atherosclerotic vasculardisease or tumor growth.

Key Words: Ca^{2+} channel blockers, proliferation, capacitative Ca^{2+} entry, TRP protein, intracellular Ca^{2+} store

BIOCHEMICAL PHARMACOLOGY 73 (2007) 943–953

available at www.sciencedirect.com

ScienceDirect

journal homepage: www.elsevier.com/locate/biochempharm

G1 cell cycle arrest by amlodipine, a dihydropyridine Ca^{2+} channel blocker, in human epidermoid carcinoma A431 cells

Junko Yoshida *, *Takaharu Ishibashi*, *Matomo Nishio*

Department of Pharmacology, Kanazawa Medical University, Daigaku 1-1, Uchinada, Ishikawa 920-0293, Japan

ARTICLE INFO

Article history:
Received 30 August 2006
Accepted 11 December 2006

Keywords:
Calcium channel blocker
G1 cell cycle arrest
pRB
$p21^{Waf1/Cip1}$
Cyclin dependent kinase
Human epidermoid carcinoma A431 cells

ABSTRACT

We demonstrated previously that amlodipine, a dihydropyridine Ca^{2+} channel blocker, exhibits antitumor effects on human epidermoid carcinoma A431 cells both *in vitro* and *in vivo*, in part through inhibition of capacitative Ca^{2+} entry. In this study, we examined the effects of amlodipine on cell cycle distribution and cell cycle regulatory molecules in A431 cells, since a rise in intracellular Ca^{2+} is required at several points during cell cycle progression. Flow cytometric analysis revealed that treatment with amlodipine (20–30 μM, for 24 h) induced G1 phase cell accumulation. The amlodipine-induced G1 arrest was associated with a decrease in phosphorylation of retinoblastoma protein (pRB), a regulator of G1 to S phase transition, reduction of protein levels of cyclin D1 and cyclin dependent kinase 4 (CDK4), G1 specific cell cycle proteins, and increased expression of $p21^{Waf1/Cip1}$, an inhibitory protein of CDK/cyclin complexes. *In vitro* kinase assay revealed that amlodipine significantly decreased CDK2-, CDK4-, and their partners cyclin E- and cyclin D1-associated kinase activities. The amlodipine-induced reductions in cyclin D1 protein expression and in CDK2 kinase activity were reproduced by a dihydropyridine derivative, nicardipine, having an inhibitory effect on A431 cell growth, but not by nifedipine, lacking the antiproliferative activity. Our results demonstrate that amlodipine caused G1 cell cycle arrest and growth inhibition in A431 cells through induction of $p21^{Waf1/Cip1}$ expression, inhibition of CDK/cyclin-associated kinase activities, and reduced phosphorylation of pRB.

1. Introduction

Ca^{2+} channel blockers have been used for the treatment of hypertension, angina pectoris and ventricular tachyarrhythmias based on their inhibitory effect on Ca^{2+} entry by interacting with plasma membrane voltage-dependent L-type Ca^{2+} channels (L-type VDCCs). In animal models and clinical trials, some Ca^{2+} channel blockers also retard the development of atherosclerosis in part due to their inhibition of smooth muscle cell proliferation [1–4]. The antiproliferative effect of Ca^{2+} channel blockers has been shown also in tumor cell lines, such as HT-39 human breast cancer cells [5], human brain tumor cells [6–9], and LNCaP human prostate cancer cells [10]. We have demonstrated recently that dihydropyridine derivatives, such as amlodipine, nicardipine and nimodipine, inhibited the growth and DNA synthesis of human epidermoid carcinoma A431 cells, whereas verapamil (phenylalkylamine), diltiazem (benzodiazepine), and interestingly, nifedipine (dihydropyridine) did not show such effects [11]. Since intracellular Ca^{2+} is indispensable for the proliferation of various cell types, we examined in our previous study the effect of Ca^{2+} channel blockers on intracellular free Ca^{2+} concentration ($[Ca^{2+}]_i$) by single-cell Ca^{2+}-imaging. Fluorometric measurement of $[Ca^{2+}]_i$ revealed that Ca^{2+} channel

* *Corresponding author*. Tel.: +81 76 218 8107; fax: +81 76 286 8191.
E-mail address: yayuyo@kanazawa-med.ac.jp (J. Yoshida).
0006-2952/$ – see front matter
doi:10.1016/j.bcp.2006.12.011

blockers with antiproliferative activity specifically blunted Ca^{2+} influx through the store-operated Ca^{2+} channels (SOCs) evoked by thapsigargin, an endoplasmic reticulum (ER) Ca^{2+}-ATPase inhibitor [11]. In addition, amlodipine, but not nifedipine, attenuated Ca^{2+} responses elicited by stimulation of Gq protein coupled receptors with uridine 5′-triphosphate (UTP) in A431 cells, suggesting that amlodipine also attenuated Ca^{2+} entry through receptor-activated cation channels [12].

In electrophysiological studies, some investigators demonstrated that A431 cell line lacks dihydropyridine-sensitive VDCCs [13], but has plasma membrane Ca^{2+} permeable channels, named I_{SOC} and I_{CRAC} channels instead, both of which are activated by store depletion and stimulation of phospholipase C-coupled receptors [14,15]. The mammalian homologs of the *Drosophila* canonical transient receptor potential (TRPC) channel family have been implicated as molecular candidates for SOCs and receptor-activated cation channels in excitable and non-excitable cells [16–22]. Our reverse transcription-polymerase chain reaction (RT-PCR) analysis revealed that A431 cells express mRNAs of TRPC1 and TRPC5 out of seven members of TRPC subfamily, but the cells actually do not express mRNAs for the α and β subunits of L-type VDCC. TRPC1 and TRPC5 are expressed probably in heteromultimers in A431 cells and may function as SOCs and/or receptor-activated cation channels. Thus, we suggested that inhibition of capacitative Ca^{2+} entry through SOCs like TRPCs could be partly involved in the antiproliferative effect of Ca^{2+} channel blockers in A431 cells [23].

To explore the mechanisms underlying the antiproliferative effect of amlodipine further, we investigated here the effect of amlodipine on the cell cycle progression in A431 cells, because a rise in intracellular Ca^{2+} is required at several points during cell cycle progression [20,24]. The results showed that amlodipine induced G1 cell cycle arrest and decreased the phosphorylation level of retinoblastoma protein, essential for the G1 to S phase transition. Then, we examined the effects of amlodipine on the cell cycle regulatory molecules: cyclin D1, cyclin dependent kinase 4 (CDK4), cyclin E, CDK2, $p21^{Waf1/Cip1}$, and their-associated kinase activities. We also examined the effects of intracellular Ca^{2+} modulators, such as thapsigargin [25], an ER Ca^{2+}-ATPase inhibitor, and 2-aminoethoxydiphenyl borate, a SOC inhibitor, to elucidate whether or not these substances emulate the action of amlodipine on the cell cycle regulatory machinery.

2. Materials and methods

2.1. Reagents

Amlodipine vesilate, donated by Sumitomo Pharmaceutical (Ibaraki, Japan), and nifedipine were dissolved in dimethyl sulfoxide (DMSO) each at concentration of 100 mM. Nicardipine was dissolved in distilled water at 10 mM. Thapsigargin and 2-aminoethoxydiphenyl borate (2-APB; Tocris Cookson Inc., Ellisville, MO) were dissolved in DMSO at a concentration of 10 mM and 100 mM, respectively.

The antibodies used for Western blot were mouse monoclonal anti-pRB, rabbit polyclonal anti-phospho pRB, mouse monoclonal anti-cyclin D1, mouse monoclonal anti-CDK4, rabbit polyclonal anti-E2F1 (Cell Signaling Technology, Beverly, MA) and rabbit polyclonal anti-$p21^{Waf1/Cip1}$ (Santa Cruz Biotechnology, Santa Cruz, CA). To confirm equal loading of protein for every immunoblot, mouse monoclonal anti-β-actin antibody (Sigma–Aldrich Inc., St. Louis, MO) was used. Horseradish peroxidase-conjugated goat anti-mouse IgG or horseradish peroxidase-conjugated goat anti-rabbit IgG (Santa Cruz Biotechnology) was used as the secondary antibody for Western blot. For immunoprecipitation and *in vitro* kinase assays, we used mouse monoclonal anti-cyclin D1 (Cell Signaling Technology), mouse monoclonal anti-CDK4, mouse monoclonal anti-CDK2, and rabbit polyclonal anti-cyclin E antibodies (Santa Cruz Biotechnology).

2.2. Tumor cell lines

Human epidermoid carcinoma A431 cells were cultured as described previously [11,12,26]. Briefly, the cells were cultured in Dulbecco's modified Eagle medium (DMEM), containing 10% heat-inactivated fetal bovine serum (FBS), 2 mM L-glutamine, 12.7 mM *N*-2-hydroxyethylpiperazine-*N*′-2-ethanesulfonic acid (HEPES), 0.12% sodium bicarbonate, 100 U/ml penicillin G and 100 μg/ml streptomycin, at 37 °C in humidified air containing 5% CO_2. Cells were seeded at a density of 3×10^5/plate in 10 cm diameter plastic culture dishes and passaged every 3–4 days.

2.3. Flow cytometric analysis of DNA content

The cells (2.5×10^5 cells) were grown in 5 ml of DMEM containing 10% FBS for 24 h and treated either with vehicle or agents for the indicated time. For flow cytometry, cells were trypsinized, pelleted by centrifugation, and resuspended in 0.5 ml of PBS. The same volume of 70% ethanol in PBS was added to the cell suspension and fixed for 30 min at 4 °C. After washing the cells with PBS, cells were resuspended in 1 ml of 2.5 mg/ml RNAse for 1–2 h at room temperature. The pelleted cells were suspended in 0.5–1.0 ml of 50 μg/ml propidium iodide and analyzed using a FACSCalibur Flow Cytometer (Becton Dickinson Immunocytometry Systems, Mountain View, CA). The cell cycle distribution was determined by Modifit cell cycle analysis software (Becton Dickinson Immunocytometry Systems).

2.4. Preparation of total cell lysate and Western blot analysis

The cells (5×10^5 cells) were grown in 10 ml of DMEM containing 10% FBS for 24 h and treated either with vehicle or agents for the indicated time. The cells were lysed in 0.1–0.5 ml of mammalian cell lysis/extraction reagent (CelLytic™-M; Sigma–Aldrich Inc.) containing protease inhibitors (Protease inhibitor cocktail; Sigma–Aldrich Inc.), 1 mM phenylmethylsulfonyl fluoride (PMSF) and 1 mM Na_3VO_4. The extract was centrifuged at $12{,}500 \times g$ for 15 min at 4 °C to remove insoluble material. The protein concentration of the supernatant was determined with the Bio-Rad protein assay reagent (Bio-Rad Laboratories, Hercules, CA). For Western blot analysis, the cell lysate (10–25 μg protein) was denatured in 5× sample buffer (625 mM Tris–HCl, 10% SDS, 25% glycerol,

0.015% bromophenol blue, and 5% 2-mercaptoethanol, pH 6.8) at 95 °C for 5 min, then electrophoretically separated on a polyacrylamide gel (PAG Mini "DAIICH" 4/20 or 15/25: Daiichi Pure Chemical Co., Tokyo, Japan). The protein was transferred to a nitrocellulose membrane, probed with primary antibodies followed by incubation with secondary antibodies conjugated with horseradish peroxidase. Immunoreactive bands were visualized through enhanced chemiluminescence system (Amersham Biosciences Corp., Piscataway, NJ) and laser densitometry (Molecular Dynamics, Sunnyvale, CA). The intensities of bands were analyzed utilizing Molecular Dynamic's ImageQuant Software.

2.5. *Immunoprecipitation and in vitro kinase assays*

Cell lysates containing equal amounts of protein (200–300 μg in each case) were immunoprecipitated with specific anti-CDK2, anti-cyclin E, anti-CDK4 or anti-cyclin D1 antibody at 4 °C for 1 h. Twenty microliter of Protein G PLUS-agarose (Santa Cruz Biotechnology) were added to the immunoprecipitate and rocked on a platform at 4 °C for 1 h or overnight. The immunoprecipitates were washed thrice with radioimmunoprecipitation assay buffer (150 mM NaCl, 10 mM Tris, 1 mM ethylenediaminetetraacetic acid [EDTA], 1 mM ethylene glycol bis (beta-aminoethyl ether)-N,N,N′,N′-tetraacetic acid [EGTA], 0.2 mM sodium vanadate, 0.2 mM PMSF, 0.5% NP40, and 1% Triton X-100, pH 7.4), and twice with kinase buffer (in mM: 50 HEPES, pH 7.4, 10 $MgCl_2$, 2.5 EDTA, and 1 dithiothreitol [DTT] for CDK2- and cyclin E-associated kinase assays, 50 HEPES, pH 7.4, 10 $MgCl_2$, 2.5 EDTA, 1 DTT, 10 β-glycerophosphate, and 1 NaF for CDK4- and cyclin D1-associated kinase assays). The immunoprecipitate was added with 20 μl kinase reaction buffer (kinase buffer containing 20 μM ATP, 5 μCi of [γ^{32}P]-ATP (Amersham Biosciences Corp.), and 1 μg glutathione S-transferase tagged RB protein (GST-RB: Santa Cruz Biotechnology) or 2 μg histone H1 (Calbiochem, La Jolla, CA), and incubated at 37 °C for 30 min. The reaction was stopped by the addition of 5× sample buffer and heated at 95 °C for 5 min. The samples were separated on a 4–20% polyacrylamide gel (PAG Mini "DAIICH" 4/20: Daiichi Pure Chemical Co.). Gels were dried, exposed to a PhosphorImager screen overnight. Radiolabeled GST-RB and histone H1 bands were analyzed with ImageQuant Software (Molecular Dynamics).

3. Results

3.1. *Amlodipine induces a G1 arrest in cell cycle progression of human epidermoid carcinoma A431 cells*

We showed previously that treatment of A431 cells with amlodipine for 48 h inhibited cell growth in a concentration-dependent manner with an IC_{50} value of 25 μM [11]. Since the mean percentages of growth rates at 20 and 30 μM of amlodipine in A431 cells were 70.6 ± 6.4 and 34.8 ± 5.7 (±S.E.M.), respectively, we used in this study mainly 20 and 30 μM of amlodipine concentrations. First, to determine whether the growth inhibitory effect of amlodipine would be cell cycle phase-specific or not, exponentially growing A431 cells were treated with either vehicle or 30 μM of amlodipine for 7 h, 24 h and 48 h and analyzed by flow cytometry. As shown in Fig. 1A, treatment of A431 cells with amlodipine increased G1 phase cell population at 24 h and 48 h, but not at 7 h. The cell numbers at 24 h and 48 h treatment with 30 μM amlodipine were decreased by 89.3% and 38.8% of control, respectively. However, the amlodipine-induced G1 cell cycle arrest at 48 h was relatively similar to that at 24 h. At the 24 h of optimum treatment time, G1 cell cycle arrest by amlodipine was concentration-dependent (Fig. 1B). To assess the effect of amlodipine on the synchronized cells, A431 cells were incubated in FBS-free DMEM for 24 h and then stimulated with 10% FBS in the absence or presence of amlodipine. As shown in Fig. 2A, the A431 cells synchronized at G0 phase progressed into the S phase after 24 h of serum addition. On the other hand, in A431 cells incubated with serum plus 20 μM or 30 μM amlodipine for 24 h, an increase in G1 phase cell population was observed with a slight decrease in the S phase cells. The decrease in cell number by amlodipine treatment (20 μM and 30 μM) was nearly equal (Fig. 2A and B). Thus, the amlodipine-induced G1 cell cycle arrest was confirmed in synchronized A431 cells.

3.2. *Effects of amlodipine on phosphorylation of retinoblastoma protein (pRB), a regulator of G1 to S transition, and other cell cycle regulatory molecules*

Since phosphorylation of retinoblastoma protein (pRB) by G1 specific cyclin dependent kinases (CDKs) is important for the G1 to S phase transition, we examined the effect of amlodipine on the phosphorylation of pRB by Western blot analysis using an antibody that recognizes the pRB phosphorylated at serine 780 residue. The phosphorylated state of pRB was evaluated as the ratio of phosphorylated pRB to unphosphorylated one. Treatment of A431 cells with amlodipine for 22–24 h decreased the phosphorylation of pRB (Fig. 3A), decreased the protein expression of cyclin D1, and increased the expression of $p21^{Waf1/Cip1}$, an inhibitory protein of CDK-cyclin complexes, while the protein level of internal control β-actin remained relatively unchanged (Fig. 3A). $p27^{Kip1}$, a member of CDK-cyclin complex inhibitors, was consistently undetectable in A431 cells (data not shown). Time-course experiments showed that the effects of amlodipine on these molecules were time-dependent (Fig. 3B). Since the reduction in cyclin D1 protein expression by amlodipine was apparent as early as 4 h treatment, we examined the effect of other dihydropyridine Ca^{2+} channel blockers on cyclin D1 protein expression. A similar effect was observed at 4 h treatment of nicardipine, which has an antiproliferative effect on A431 cells; however, such effect could not be observed with nifedipine, a dihydropyridine derivative lacking antiproliferative potency (Fig. 3C). Furthermore, Western blot analysis revealed that amlodipine treatment reduced the protein levels of CDK4 and E2F1, a transcription factor essential for progression through G1 and into the S phase of the cell cycle (Fig. 3D).

3.3. *Effects of amlodipine on cyclin-dependent kinase activities in A431 cells*

Phosphorylation of pRB is regulated by activation of CDKs and their heterodimeric cyclin partners. To elucidate whether the

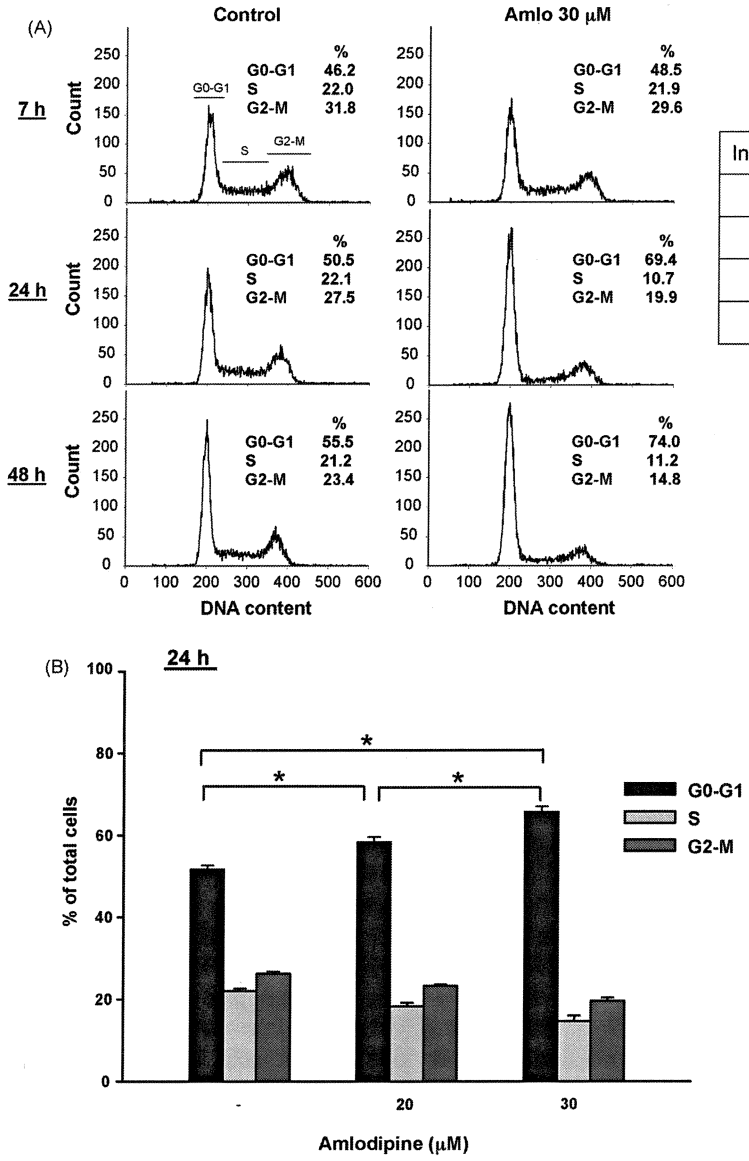

Cell number (x10^5 cells)

Incubation time (h)	Control	Amlo 30 μM
0	2.5	2.5
7	2.5	2.5
24	2.8	2.5
48	9.8	3.8

Fig. 1 – Effects of amlodipine on cell cycle in A431 cells. Cells were cultured in complete medium and treated with either vehicle (0.03% DMSO) or amlodipine. After the indicated time of incubation, cells were collected, and cellular DNA was stained with propidium iodide and analyzed for cell cycle distribution. 1 × 10^4 cells were analyzed for each condition. (A) Representative histogram plotting cell count *vs.* DNA content after 7 h, 24 h, and 48 h of incubation of A431 cells with 30 μM of amlodipine (Amlo 30 μM). The percentage of cells present in G0-G1, S, and G2-M phases are shown. The table shows the cell number determined by trypan blue exclusion in the same dishes. (B) Summary of data for amlodipine-induced G1 cell cycle arrest in A431 cells at 24 h treatment. Values are mean ± S.E.M. of four independent experiments. *P < 0.05 by one-way analysis of variance followed by Fisher's PLSD.

amlodipine-induced reduction in the pRB phosphorylation is due to inhibition of CDK-cyclin activities, we examined the effects of amlodipine on CDKs- and their partner cyclin-associated kinase activities. An *in vitro* kinase assay using CDK4 and cyclin D1-immunoprecipitates and GST-RB as a substrate showed that treatment of A431 cells with amlodipine significantly decreased the CDK4- and its partner cyclin D1-associated kinase activities (Fig. 4A). In addition, *in vitro* kinase assay using CDK2 and cyclin E-immunoprecipitates and histone H1 as a substrate revealed that amlodipine treatment resulted in a decrease in CDK2- and its partner cyclin E-associated kinase activities (Fig. 4A). The possibility that the decrease in kinase activity was due to reduced protein expression was ruled out by Western blotting on CDK4-, cyclin D1-, CDK2- and cyclin E-immunoprecipitates; the levels of immunoprecipitated proteins were not difference among vehicle (Control)-, 20 μM amlodipine-, and 30 μM amlodipine-treated cells (data not shown). Similar results to amlodipine (reductions of both cyclin D1- and CDK2-associated kinase activities) were observed for nicardipine (30 μM),

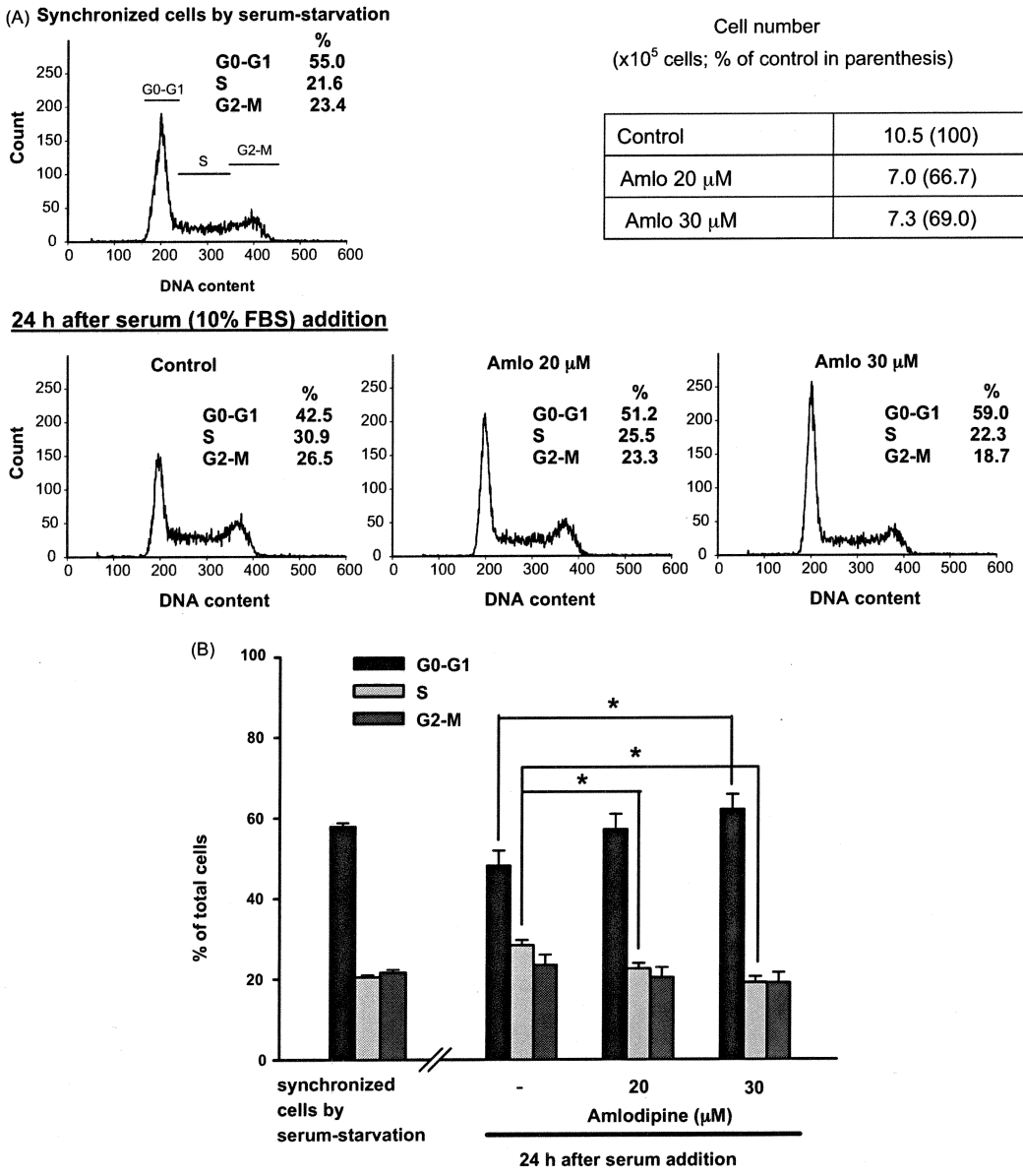

Cell number
(x10^5 cells; % of control in parenthesis)

Control	10.5 (100)
Amlo 20 μM	7.0 (66.7)
Amlo 30 μM	7.3 (69.0)

Fig. 2 – Effects of amlodipine on cell cycle in synchronized A431 cells by serum-starvation. Cells were incubated in fetal bovine serum (FBS)-free DMEM for 24 h and stimulated with 10% FBS for 24 h in the absence or presence of amlodipine. (A) Representative histogram plots of cell count vs. DNA content after serum-starvation and 24 h incubation with 10% FBS in the absence or presence of amlodipine (Amlo 20 and 30 μM). Numbers represent percentages of cells in G0-G1, S, and G2-M phases. The table shows the cell number at 24 h after serum addition determined by trypan blue exclusion in the same dishes. (B) Quantitative analysis of amlodipine-induced G1 cell cycle arrest in synchronized A431 cells. Values are mean ± S.E.M. of four independent experiments. *P < 0.05 by one-way analysis of variance followed by Fisher's PLSD.

an antiproliferative dihydropyridine derivative, but not for nifedipine, a derivative of the same class lacking antiproliferative activity (Fig. 4B). These results were consistent with those by Western blot analysis showing that their effects on the cyclin D1 protein expression correlated with their inhibitory effects on cell growth (Fig. 3C). Taken together, these data suggest that a reduction in cyclin D1 protein expression, as well as inhibition of cyclin D1- and CDK2-associated kinase activities, may be involved in the antiproliferative effect of amlodipine in A431 cells.

3.4. *Effects of thapsigargin, an inhibitor of endoplasmic reticulum (ER) Ca^{2+}-ATPase, and 2-aminoethoxydiphenyl borate (2-APB), an inhibitor of store-operated Ca^{2+} channels, on cell cycle regulatory molecules*

In our reported Ca^{2+} imaging assay in A431 cells, we observed that amlodipine did not only attenuate the capacitative Ca^{2+} entry elicited by thapsigargin, an ER Ca^{2+}-ATPase inhibitor, but also induced Ca^{2+} release from thapsigargin-sensitive Ca^{2+} stores [12], i.e., in fluo-3-loaded A431 cells, application of

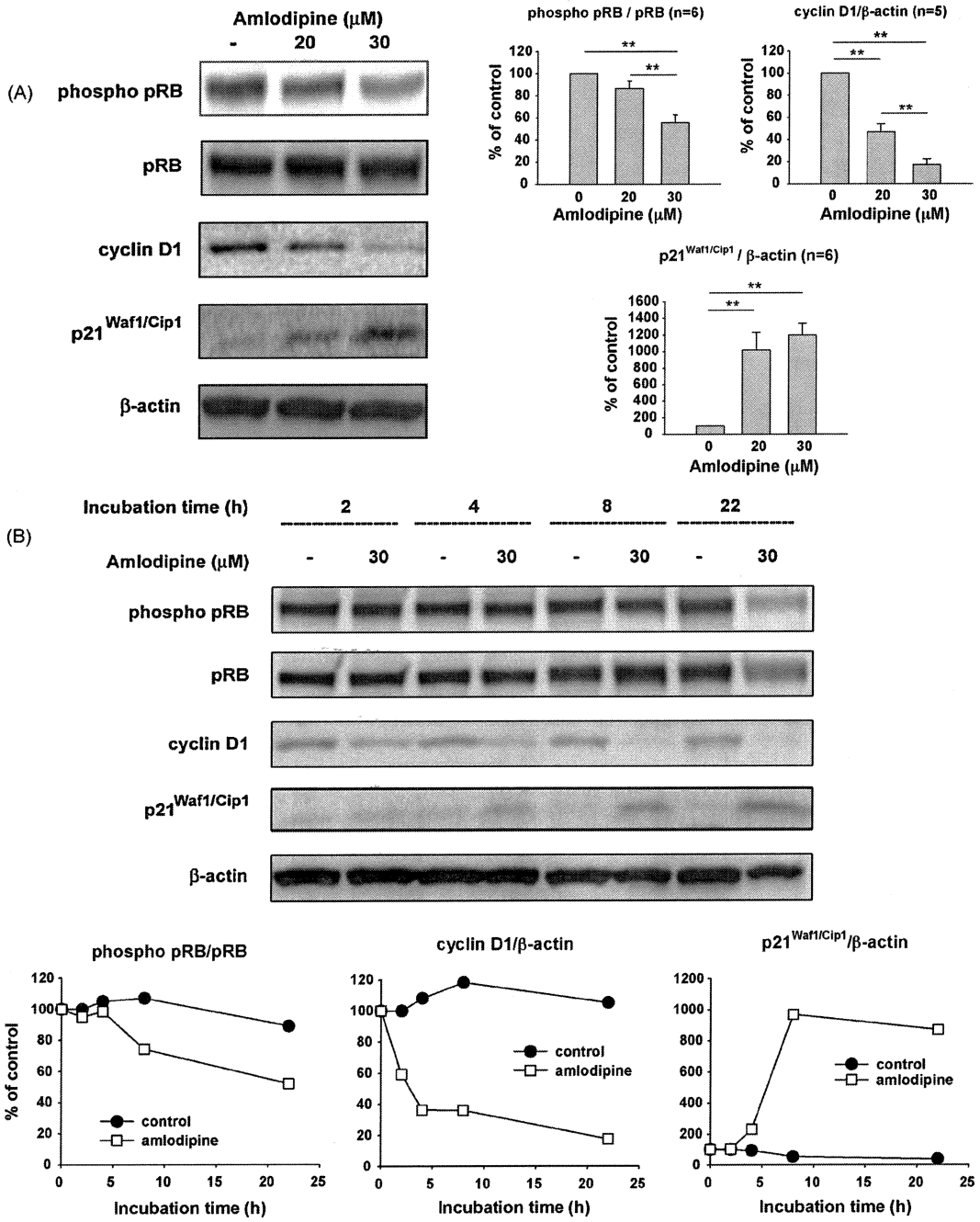

Fig. 3 – Effects of amlodipine on G1 cell cycle regulatory proteins in A431 cells. (A) Left: A431 cells were cultured in complete medium and treated with either vehicle or amlodipine (20 and 30 μM) for 22–24 h. The cell lysates were subjected to SDS-PAGE followed by Western blot analysis with antibodies for phosphorylated and non-phosphorylated form of retinoblastoma protein (phospho pRB and pRB, respectively), cyclin D1 and $p21^{Waf1/Cip1}$. β-actin was used to verify equal gel loading. Right: bars represent the ratio of phosphorylated pRB to pRB, and protein levels of cyclin D1 and $p21^{Waf1/Cip1}$ normalized to β-actin. Values are mean ± S.E.M. of five to six independent experiments. $^{**}P < 0.01$ by one-way analysis of variance followed by Fisher's PLSD. (B) Results of time-course studies of amlodipine-induced inhibition of pRB phosphorylation, reduction in cyclin D1 protein expression, and upregulation of $p21^{Waf1/Cip1}$ in A431 cells. Data are representative results of two independent experiments. (C) Effects of other dihydropyridine Ca^{2+} channel blockers (CCBs) on cyclin D1 protein expression in A431 cells. A431 cells were incubated in complete medium and treated with either 0.03% DMSO (–) or 30 μM amlodipine (Amlo), 30 μM nifedipine (Nife), 0.3% of methanol (MeOH, solvent for the dilution of nifedipine) and 30 μM nicardipine (Nicar) for 4 h, to examine their effects on cyclin D1 protein level. Data are representative results of three to four independent experiments. The graph on the right shows cyclin D1 protein levels normalized to β-actin. (D) Effects of amlodipine treatment (22–24 h) on the protein expression of cyclin dependent kinase 4 (CDK4) and transcription factor E2F1 in A431 cells. Data are representative results of three independent experiments. The graphs on the right show protein levels for CDK4 and E2F1 normalized to β-actin.

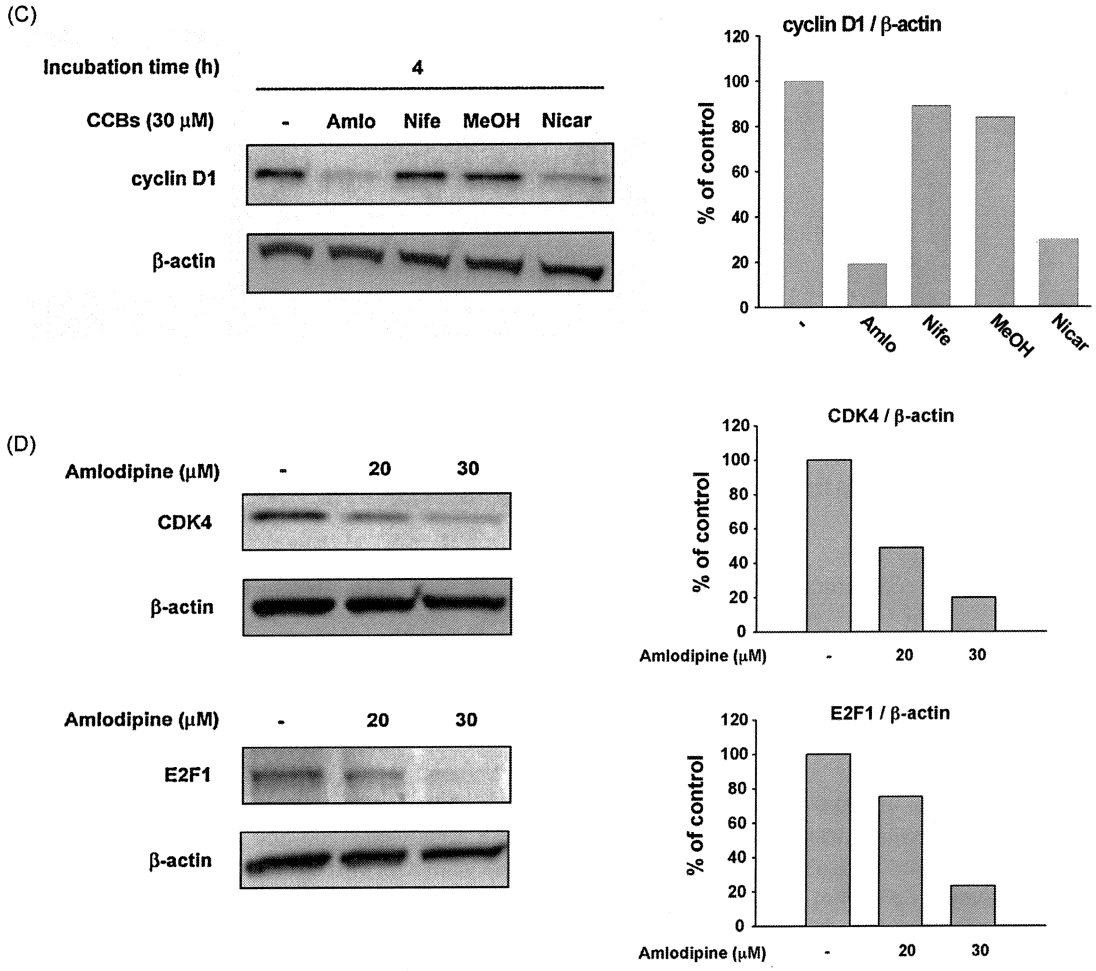

Fig. 3. (Continued).

amlodipine in Ca^{2+}-free medium elicited a transient rise in $[Ca^{2+}]_i$. Thapsigargin applied thereafter caused no rise in $[Ca^{2+}]_i$, and vice versa [12]. Therefore, to assess whether the effects of amlodipine on cell cycle regulatory molecules were due to the Ca^{2+}-releasing effect from thapsigargin-sensitive Ca^{2+} stores or the inhibitory effect on SOCs, we examined the effects of thapsigargin and 2-aminoethoxydiphenyl borate (2-APB), a SOC inhibitor, on the cell cycle machinery. 2-APB at 50 μM has been shown to inhibit effectively the thapsigargin-induced capacitative Ca^{2+} entry in A431 cells [23]. To this end, A431 cells were preincubated with 1 μM thapsigargin or 50 μM 2-APB for 15 min, then incubated for another 24 h with vehicle or amlodipine, and these cells were used in Western blot analysis and *in vitro* kinase assay. Western blot analysis showed that thapsigargin reduced the phosphorylation level of pRB and protein level of cyclin D1, and predominantly upregulated the $p21^{Waf1/Cip1}$ protein expression, while 2-APB showed a modest effect (Fig. 5A). In *in vitro* CDK2 kinase assay using histone H1 as a substrate, thapsigargin showed a considerable reduction in histone H1 phosphorylation, whereas 2-APB decreased the phosphorylation slightly (Fig. 5B). These results imply that the effects of amlodipine on cell cycle regulatory molecules were similar to those of thapsigargin, an ER Ca^{2+}-ATPase inhibitor, rather than those of 2-APB, a SOC inhibitor. That is, the amlodipine-induced effects on cell cycle machinery could not be fully reproduced by inhibiting Ca^{2+} entry with SOC inhibitors, such as 2-APB.

4. Discussion

We have demonstrated that some dihydropyridine Ca^{2+} channel blockers, such as amlodipine, nicardipine and nimodipine, inhibited human epidermoid carcinoma A431 cell growth and DNA synthesis *in vitro* [11], and intraperitoneal injection of amlodipine into nude mice bearing A431 xenografts retarded tumor growth and prolonged the survival of these mice [12]. Several electrophysiological studies [13,14] and our RT-PCR assay [23] indicated that A431 cells do not express L-type VDCCs, which are sensitive to Ca^{2+} channel blockers. Our single cell Ca^{2+} imaging analysis demonstrated that antiproliferative Ca^{2+} channel blockers specifically attenuated Ca^{2+} responses to thapsigargin, an ER Ca^{2+}-ATPase inhibitor, and UTP, a Gq-protein-coupled receptor agonist. It is thus suggested that inhibition of capacitative Ca^{2+} entry through SOCs in A431 cells could be involved in part in the antiproliferative effect of Ca^{2+} channel blockers, such as amlodipine [11,12].

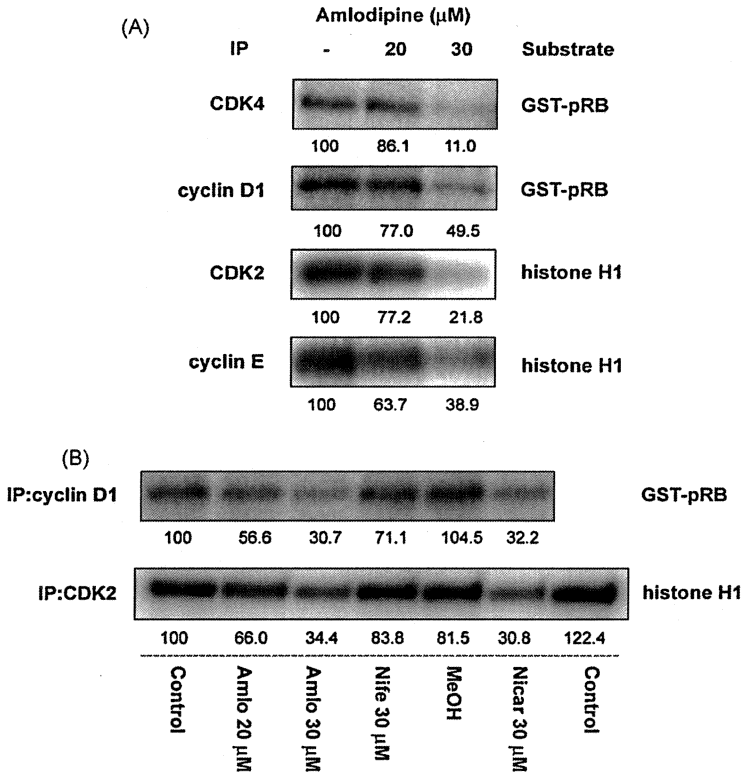

Fig. 4 – Effects of amlodipine on CDK- and cyclin-associated kinase activities. A431 cells were cultured in complete medium and treated with either vehicle (0.03% DMSO) or amlodipine for 24 h. Cell lysate (200–300 μg protein) were immunoprecipitated with antibodies for CDK4, cyclin D1, CDK2 and cyclin E. *In vitro* kinase assays were performed on their immunoprecipitates using GST-RB or histone H1 as a substrate as described in Section 2. (A) Representative scanning data of a PhosphorImager screen (three independent experiments). Kinase activities are expressed as % of the control (vehicle) and the values are shown below each scan. (B) Effects of other dihydropyridine Ca^{2+} channel blockers on cyclin D1-, and CDK2-associated kinase activities. A431 cells were cultured in complete medium and treated with either 0.03% DMSO (Control) or amlodipine (Amlo 20 and 30 μM), nifedipine (Nife 30 μM), 0.3% methanol (MeOH, solvent for the dilution of nifedipine) and nicardipine (Nicar 30 μM) for 24 h. Cyclin D1- and CDK2-associated kinase assays were performed as described in A. Data are representative results of each of two independent experiments. Kinase activities in each treatment (% of the control (vehicle)) are shown below each scan. IP, immunoprecipitation.

Since a rise in intracellular Ca^{2+} is required at several points during cell cycle progression [24], flow cytometric analysis was performed to determine whether amlodipine affects the cell cycle progression or not. Cell cycle analysis revealed that treatment of A431 cells with amlodipine retarded the cell cycle progression at G1 phase in concentration- and time-dependent manners (Figs. 1 and 2). As cells progress through G1 to S phase, cyclin-CDK complexes, such as cyclin D1-CDK4/6 and cyclin E-CDK2 complexes, are sequentially activated and phosphorylate retinoblastoma protein (pRB) on serine and threonine residues [27]. The hyperphosphorylated pRB releases active E2F transcription factors, which, in turn stimulate the transcription of numerous genes whose products are required for the G1 to S transition and S phase progression [28]. There are two families of cyclin-CDK inhibitors, the Cip/Kip and INK4 families, both of which regulate cell cycle progression [29]. Members of the Cip/Kip family, such as $p21^{Waf1/Cip1}$, $p27^{Kip1}$ and $p57^{Kip2}$, bind to cyclin-CDK complexes and inhibit their activities. Then, we examined the effects of amlodipine on some of these cell cycle regulatory molecules by Western blot analysis and *in vitro* kinase assay.

Treatment of A431 cells with amlodipine resulted in reduction of the phosphorylated level of pRB and protein expression of cyclin D1, CDK4 and E2F1 transcription factor. Concomitantly, the protein expression of $p21^{Waf1/Cip1}$, a member of the Cip/Kip family of cyclin-CDK inhibitors, was significantly upregulated (Fig. 3A, B and D). Although $p27^{Kip1}$ is reported to be upregulated in response to antiproliferative signals [30], it was consistently undetectable in A431 cells (data not shown). A reduction in cyclin D1 protein level as early as 4 h incubation was observed by nicardipine, another dihydropyridine derivative, but not by nifedipine, another dihydropyridine lacking antiproliferative activity (Fig. 3C). These results suggest that the reduction in cyclin D1 protein expression correlates with the growth inhibitory effect of Ca^{2+} channel blockers.

In *in vitro* kinase assay using CDK4- and cyclin D1-immunoprecipitates and GST-RB as a substrate, treatment of A431 cells with amlodipine (20 and 30 μM, for 22–24 h) resulted in decreases in the CDK4-, and its partner cyclin D1-associated kinase activities (Fig. 4A). We also determined CDK2- and its partner cyclin E-associated kinase activities

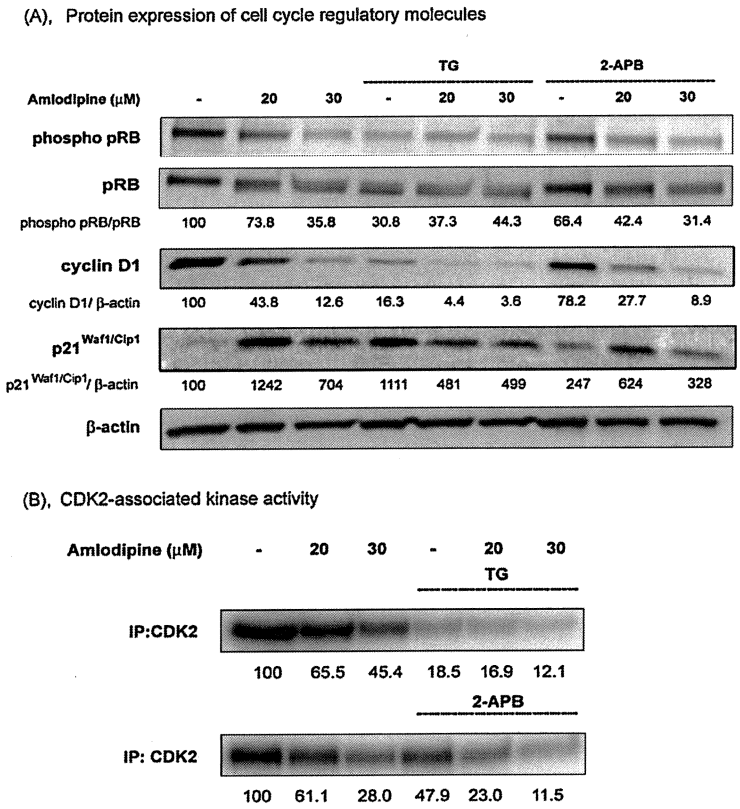

Fig. 5 – Effects of thapsigargin and 2-APB on the G1 cell cycle regulatory molecules in A431 cells. The cells were preincubated with 1 μM thapsigargin (TG) or 50 μM 2-APB for 15 min, then 0.03% DMSO (–) or amlodipine (20 and 30 μM) was added, and the cells were incubated for another 24 h. Cell lysates were used for Western blot analysis (A) and *in vitro* CDK2-associated kinase assay with histone H1 as a substrate (B). Data in A and B are representative results of each of two independent experiments. The ratio of phosphorylated pRB to pRB, and protein levels for cyclin D1 and $p21^{Waf1/Cip1}$ normalized to β-actin band are shown as % of control (vehicle) below each scan in A. CDK2-associated kinase activities (% of the control [vehicle]) are shown below each scan in B. IP, immunoprecipitation.

using their immunoprecipitates and other substrate histone H1. CDK2, but not CDK4, specifically phosphorylates histone H1 as well as pRB [31]. Amlodipine treatment effectively decreased the CDK2- and cyclin E-associated kinase activities in A431 cells (Fig. 4A). Taken together, these results indicate that amlodipine treatment inhibited both cyclinD1-CDK4 and cyclin E-CDK2 kinase activities, which led to a reduction in the level of pRB phosphorylation, thereby G1 cell cycle arrest in A431 cells. In addition, this amlodipine-induced reduction in the cyclin-CDK kinase activities might be due to upregulation of $p21^{Waf1/Cip1}$, a cyclin-CDK inhibitor. Although the ability of $p21^{Waf1/Cip1}$ is known to be induced through tumor suppressor gene p53-dependent and -independent pathways, the amlodipine-induced upregulation of $p21^{Waf1/Cip1}$ in A431 cells appear to be independent of p53, because p53 in A431 cells was shown to be mutant at codon 273 [32]. As far as we know, this is the first study reporting the involvement of $p21^{Waf1/Cip1}$ upregulation in tumor cell growth inhibition by amlodipine, a Ca^{2+} channel blocker.

Recently, amlodipine was reported to exert an antiproliferative effect on human lung vascular smooth muscle cells via $p21^{Waf1/Cip1}$ gene activation [33]. The study demonstrated that amlodipine induced $p21^{Waf1/Cip1}$ promoter activity through the activation of the glucocorticoid receptor and a transcription factor, CCAAT/enhancer binding protein alpha (C/EBPα). Since the role of the negative cell cycle regulator $p21^{Waf1/Cip1}$ has been also demonstrated in atherosclerosis [34,35], it is possible that $p21^{Waf1/Cip1}$ is the key molecule that mediates the anti-atherosclerotic and antitumor actions of Ca^{2+} channel blockers, such as amlodipine.

To explore possible targets for amlodipine, we also examined the effects of thapsigargin and 2-APB, a SOC inhibitor, on the cell cycle regulatory molecules. Based on the protein expression of cell cycle regulatory molecules and CDK2-associated kinase activity, the effects of amlodipine were rather similar to those of thapsigargin than those of 2-APB (Fig. 5A and B). We showed previously that amlodipine resulted in Ca^{2+} release from thapsigargin-sensitive Ca^{2+} stores [12]. Is the Ca^{2+}-releasing effect involved in amlodipine-induced effects on cell cycle regulatory molecules? Indeed, Ca^{2+} pool content in ER, as well as cytosolic Ca^{2+}, is a critical factor for cell growth and progression through the cell cycle [36,37]. Legrand et al. [38] were the first group to demonstrate that intracellular Ca^{2+}-ATPases (SERCAs) and Ca^{2+} pool content are closely associated with prostate cancer LNCaP cell growth. When LNCaP cell growth was inhibited by serum deprivation, the Ca^{2+} pool content was reduced and expression of SERCA2b, an isoform of SERCAs, was decreased

[38]. We reported previously that treatment of A431 cells with thapsigargin (1 μM, 48 h) resulted in inhibition of cell growth by up to 50% of the control, due to the depletion of Ca^{2+} stores, and at this dose, thapsigargin tended to augment the antiproliferative effect of amlodipine [11]. However, RT-PCR analysis, performed as described previously [23], using a set of primers for SERCA2b (GenBank accession no. **NM_001681**) showed no detectable changes in mRNA expression of SERCA2b in A431 cells incubated with amlodipine (data not shown). The result indicates at least that the Ca^{2+} releasing effect of amlodipine did not cause a decrease in SERCA2b gene expression, leading to Ca^{2+} store depletion.

Although the exact target(s) of amlodipine is not clear at present, amlodipine may interact with unknown molecules in the thapsigargin-sensitive ER and/or plasma membrane SOCs. It is possible that amlodipine interacts with a molecule involved in Ca^{2+} signaling between Ca^{2+} store depletion and activation of plasma membrane SOCs. Consequently, amlodipine may inhibit capacitative Ca^{2+} entry, resulting in growth inhibition of A431 cells.

In conclusion, our study demonstrated that amlodipine induced $p21^{Waf1/Cip1}$ expression and thereby inhibited CDK/cyclin-associated kinase activities, which led to a reduction in pRB phosphorylation resulting in G1 cell cycle arrest and growth inhibition in A431 cells. Although the direct target of amlodipine is not known at present, amlodipine would be a lead compound for the development of selective inhibitors of store-operated Ca^{2+} influx. Further studies are needed to explore the mechanisms underlying the antiproliferative property of amlodipine. Such studies should provide more definitive data for the development of new antiatherogenic and antitumor drugs acting through inhibition of Ca^{2+} signaling.

Acknowledgments

We thank Ms. Yasuko Shinzawa for secretarial assistance. This work was supported in part by a Grant-in-Aid for Scientific Research from the Ministry of Education, Culture, Sports, Science and Technology of Japan (18590247) and by a Grant for Specially Promoted Research from Kanazawa Medical University (S2005-16).

REFERENCES

[1] Marche P, Stepien O. Calcium antagonists and vascular smooth muscle cell reactivity. Z Kardiol 2000;89:140–4.
[2] Stepien O, Marche P. Amlodipine inhibits thapsigargin-sensitive CA^{2+} stores in thrombin-stimulated vascular smooth muscle cells. Am J Physiol Heart Circ Physiol 2000;279:H1220–7.
[3] Stepien O, Zhang Y, Zhu D, Marche P. Dual mechanism of action of amlodipine in human vascular smooth muscle cells. J Hypertens 2002;20:95–102.
[4] Zhang YZ, Gao PJ, Wang XY, Stepien O, Marche P, Zhang ZL, et al. The inhibitory mechanisms of amlodipine in human vascular smooth muscle cell proliferation. Hypertens Res 2000;23:403–6.
[5] Taylor JM, Simpson RU. Inhibition of cancer cell growth by calcium channel antagonists in the athymic mouse. Cancer Res 1992;52:2413–8.
[6] Jensen RL, Petr M, Wurster RD. Calcium channel antagonist effect on in vitro meningioma signal transduction pathways after growth factor stimulation. Neurosurgery 2000;46:692–702.
[7] Jensen RL, Wurster RD. Calcium channel antagonists inhibit growth of subcutaneous xenograft meningiomas in nude mice. Surg Neurol 2001;55:275–83.
[8] Jensen RL, Origitano TC, Lee YS, Weber M, Wurster RD. In vitro growth inhibition of growth factor-stimulated meningioma cells by calcium channel antagonists. Neurosurgery 1995;36:365–73.
[9] Lee YS, Sayeed MM, Wurster RD. Inhibition of cell growth and intracellular Ca^{2+} mobilization in human brain tumor cells by Ca^{2+} channel antagonists. Mol Chem Neuropathol 1994;22:81–95.
[10] Rybalchenko V, Prevarskaya N, Van Coppenolle F, Legrand G, Lemonnier L, Le Bourhis X, et al. Verapamil inhibits proliferation of LNCaP human prostate cancer cells influencing K^+ channel gating. Mol Pharmacol 2001;59:1376–87.
[11] Yoshida J, Ishibashi T, Nishio M. Antiproliferative effect of Ca^{2+} channel blockers on human epidermoid carcinoma A431 cells. Eur J Pharmacol 2003;472:23–31.
[12] Yoshida J, Ishibashi T, Nishio M. Antitumor effects of amlodipine, a Ca^{2+} channel blocker, on human epidermoid carcinoma A431 cells in vitro and in vivo. Eur J Pharmacol 2004;492:103–12.
[13] Moolenaar WH, Aerts RJ, Tertoolen LG, de Laat SW. The epidermal growth factor-induced calcium signal in A431 cells. J Biol Chem 1986;261:279–84.
[14] Gusev K, Glouchankova L, Zubov A, Kaznacheyeva E, Wang Z, Bezprozvanny I, et al. The store-operated calcium entry pathways in human carcinoma A431 cells: functional properties and activation mechanisms. J Gen Physiol 2003;122:81–94.
[15] Kaznacheyeva E, Zubov A, Gusev K, Bezprozvanny I, Mozhayeva GN. Activation of calcium entry in human carcinoma A431 cells by store depletion and phospholipase C-dependent mechanisms converge on I_{CRAC}-like calcium channels. Proc Natl Acad Sci USA 2001;98:148–53.
[16] Ma HT, Patterson RL, van Rossum DB, Birnbaumer L, Mikoshiba K, Gill DL. Requirement of the inositol trisphosphate receptor for activation of store-operated Ca^{2+} channels. Science 2000;287:1647–51.
[17] Parekh AB, Putney Jr JW. Store-operated calcium channels. Physiol Rev 2005;85:757–810.
[18] Pedersen SF, Owsianik G, Nilius B. TRP channels: an overview. Cell Calcium 2005;38:233–52.
[19] Vennekens R, Voets T, Bindels RJ, Droogmans G, Nilius B. Current understanding of mammalian TRP homologues. Cell Calcium 2002;31:253–64.
[20] Clapham DE. TRP channels as cellular sensors. Nature 2003;426:517–24.
[21] Montell C. The venerable inveterate invertebrate TRP channels. Cell Calcium 2003;33:409–17.
[22] Ambudkar IS. Ca^{2+} signaling microdomains: platforms for the assembly and regulation of TRPC channels. Trends Pharmacol Sci 2006;27:25–32.
[23] Yoshida J, Ishibashi T, Imaizumi N, Takegami T, Nishio M. Capacitative Ca^{2+} entries and mRNA expression for TRPC1 and TRPC5 channels in human epidermoid carcinoma A431 cells. Eur J Pharmacol 2005;510:217–22.
[24] Kahl CR, Means AR. Regulation of cell cycle progression by calcium/calmodulin-dependent pathways. Endocr Rev 2003;24:719–36.

[25] Thastrup O, Cullen PJ, Drøbak BK, Hanley MR, Dawson AP. Thapsigargin, a tumor promoter, discharges intracellular Ca^{2+} stores by specific inhibition of the endoplasmic reticulum Ca^{2+}-ATPase. Proc Natl Acad Sci USA 1990;87:2466–70.
[26] Yoshida J, Ishibashi T, Nishio M. Growth-inhibitory effect of a streptococcal antitumor glycoprotein on human epidermoid carcinoma A431 cells: involvement of dephosphorylation of epidermal growth factor receptor. Cancer Res 2001;61:6151–7.
[27] Ekholm SV, Reed SI. Regulation of G1 cyclin-dependent kinases in the mammalian cell cycle. Curr Opin Cell Biol 2000;12:676–84.
[28] Nevins JR, Leone G, DeGregori J, Jakoi L. Role of the Rb/E2F pathway in cell growth control. J Cell Physiol 1997;173: 233–6.
[29] Sherr CJ, Roberts JM. CDK inhibitors: positive and negative regulators of G1-phase progression. Genes Dev 1999;13:1501–12.
[30] Polyak K, Lee MH, Erdjument-Bromage H, Koff A, Roberts JM, Tempst P, et al. Cloning of p27Kip1, a cyclin-dependent kinase inhibitor and a potential mediator of extracellular antimitogenic signals. Cell 1994;78: 59–66.
[31] Ewen ME. Where the cell cycle and histones meet. Genes Dev 2000;14:2265–70.
[32] Park DJ, Nakamura H, Chumakov AM, Said JW, Miller CW, Chen DL, et al. Transactivational and DNA binding abilities of endogenous p53 in p53 mutant cell lines. Oncogene 1994;9:1899–906.
[33] Ziesche R, Petkov V, Lambers C, Erne P, Block LH. The calcium channel blocker amlodipine exerts its anti-proliferative action via $p21^{(Waf1/Cip1)}$ gene activation. FASEB J 2004;18:1516–23.
[34] Condorelli G, Aycock JK, Frati G, Napoli C. Mutated p21/WAF/CIP transgene overexpression reduces smooth muscle cell proliferation, macrophage deposition, oxidation-sensitive mechanisms, and restenosis in hypercholesterolemic apolipoprotein E knockout mice. FASEB J 2001;15:2162–70.
[35] Nathe TJ, Deou J, Walsh B, Bourns B, Clowes AW, Daum G. Interleukin-1 beta inhibits expression of $p21^{WAF1/CIP1}$ and $p27^{KIP1}$ and enhances proliferation in response to platelet-derived growth factor-BB in smooth muscle cells. Arterioscler Thromb Vasc Biol 2002;22:1293–8.
[36] Lipskaia L, Lompré AM. Alteration in temporal kinetics of Ca^{2+} signaling and control of growth and proliferation. Biol Cell 2004;96:55–68.
[37] Short AD, Bian J, Ghosh TK, Waldron RT, Rybak SL, Gill DL. Intracellular Ca^{2+} pool content is linked to control of cell growth. Proc Natl Acad Sci USA 1993;90:4986–90.
[38] Legrand G, Humez S, Slomianny C, Dewailly E, Vanden Abeele F, Mariot P, et al. Ca^{2+} pools and cell growth. Evidence for sarcoendoplasmic Ca^{2+}-ATPases 2B involvement in human prostate cancer cell growth control. J Biol Chem 2001;276:47608–14.

２００５　平成１７年度金沢医科大学共同研究成果報告書
奨励研究成果報告書

平成 19 年 12 月発行
編　集　　研究推進評価委員会
発行所　　金沢医科大学出版局
石川県河北郡内灘町大学１丁目１番地